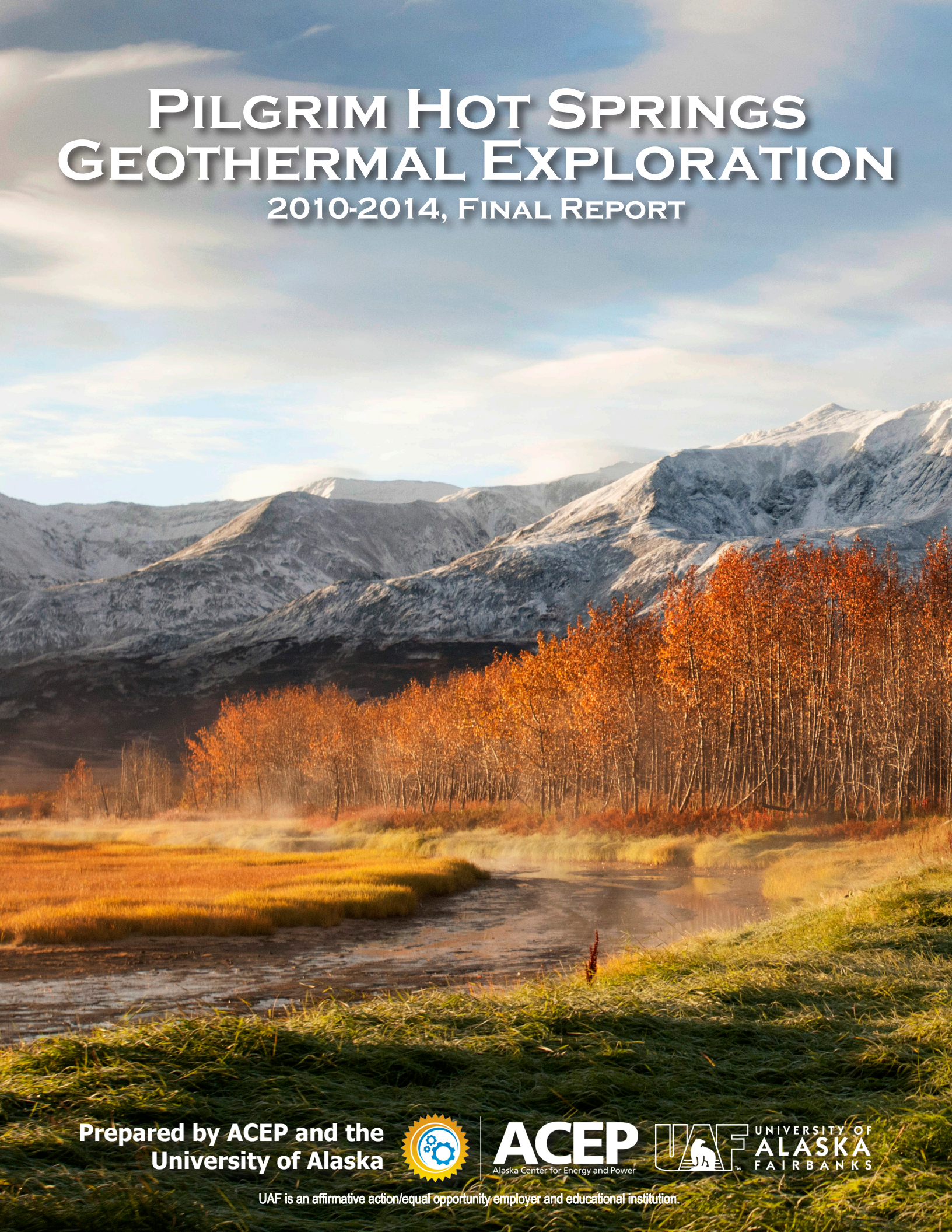
Pilgrim Hot Springs Geothermal Exploration

2010-2014, Final Report



Prepared by ACEP and the University of Alaska

ACEP
Alaska Center for Energy and Power

UAF University of Alaska Fairbanks

UAF is an affirmative action/equal opportunity employer and educational institution.

Geothermal Exploration at Pilgrim Hot Springs 2010 to 2014: Final Report

Prepared by the Alaska Center for Energy and Power at the University of Alaska Fairbanks

Acknowledgments

Activities described in this report were made possible with funding from a variety of federal, state, local, private and tribal sources including the U.S. Department of Energy under DE-EE0002846, "Validation of Innovative Exploration Techniques, Pilgrim Hot Springs, Alaska" and DE-EE0000263, "Southwest Alaska Regional Geothermal Energy Project, Pilgrim Hot Springs, Alaska," The Alaska Energy Authority through RSA R1108 and R1215, the City of Nome, Bering Straits Native Corporation, White Mountain Native Corporation, Sitnasuak Native Corporation, Potelco, Inc., and the Norton Sound Economic Development Corporation.

The geothermal exploration described in this report required a significant amount of planning and organization, and would not have been possible without the generous support from numerous individuals and organizations. The importance of local people and groups on the Seward Peninsula to this project's success cannot be overstated. The employees of Bering Straits Native Corporation were generous with never-ending useful snippets of local knowledge as well as logistical support, in addition to the monetary support already described. Assistance from Robert Bensin, Kevin Bahnke, Larry Pederson, Matt Ganley, and Jerald Brown was indispensable and deserves special mention. The support of staff from the Norton Sound Economic Development Corporation and the City of Nome, especially John Handeland of the Nome Joint Utility Service and Mayor Denise Michels, were instrumental in overcoming logistical and funding challenges. Unaatuq, LLC and its board of directors have continued to have the vision required to keep the project moving forward. Unaatuq board member Roy Ashenfelter provided logistical support and boat transport up and down the Pilgrim River.

Mary's Igloo Native Corporation, whose land abuts the hot spring property was an important project partner and allowed land access for project activities. Mary's Igloo Native Corporation tribal member Dora Mae Hughes and her family members provided important cultural background and shared stories about the regional history. Louis Green Sr. willingly shared his knowledge of the Pilgrim Hot Springs site and its history and provided logistical support. Chuck Fagerstrom freely shared his knowledge and was always willing to share site history and stories. Bryant Hammond and Amy Russell from Kawerak provided additional local support. University of Alaska faculty member Dr. Catherine Hanks assisted with technical editing and offered her expertise on the geology of the Seward Peninsula. Joe Batir and others from Southern Methodist University assisted with well logging and allowed ACEP to use high quality geothermal logging equipment. Jo Price and Graphite One Resources willingly shared data that they acquired to assist with the development of a regional geothermal understanding. In addition, former University of Alaska faculty members Dr. Ronald Daanen and Jo Mongraine were heavily involved and instrumental in project planning and data collection.

The staff of the U.S. Geologic Survey (USGS) assisted in a variety of ways. Art Clark and the USGS drilling team made the initial stages of the project possible. John Glen and his crew accomplished an extensive set of geophysical surveys and interpretations and provided technical assistance at various stages of the project.

The University of Alaska Fairbanks Geophysical Institute including Anupma Prakash, Christian Haselwimmer and Jeff Benowitz and graduate students Josh Miller and Arvind Chittambakkam

worked tirelessly to complete the remote sensing and conceptual modeling, adding an important piece to the body of knowledge about Pilgrim Hot Springs.

Ryan Purcella of Baker Hughes and Mark Kumataka provided valuable engineering guidance related to well pumping and flow testing. Additional technical assistance was provided by Bill Cummings, and Dr. Dave Blackwell. Cheryl Thompson, collections assistant at the Carrie M. McLain Memorial Museum in Nome, was extremely helpful, providing assistance with historical research and obtaining historic photos. Ethan Berkowitz assisted with organizing and maintaining positive momentum during the final round of drilling and Howard Trott contributed his time and supplied equipment used in the flow testing.

Joel Renner and Fran Pedersen spent long hours on a technical review of this report for which we are very grateful. A special thank you goes out to Dick Benoit who provided endless advice and technical assistance and who was always willing to answer his phone when we called.

Table of Contents

Acknowledgments i
List of Figures v
List of Tables vi
Terms and Acronyms vii
1. EXECUTIVE SUMMARY 1
2. BACKGROUND – KRUZGAMEPA HOT SPRINGS 2
2.1 Geothermal Exploration History 4
3. GEOLOGIC SETTING 6
3.1 Regional Geologic Setting 6
3.2 Local Geology 8
4. SUBSURFACE TEMPERATURES 8
4.1 Updated Temperature Logging 11
5. REMOTE SENSING 14
5.1 Satellite-based Geothermal Anomaly Mapping 15
5.2 Airborne Forward Looking Infrared Surveys 17
6. GEOPHYSICAL SURVEYS 27
6.1 Gravity Surveys 28
6.2 Airborne Magnetic and Electromagnetic Surveys 29
6.3 Magnetotellurics Survey 31
7. DRILLING ACTIVITIES 35
7.1 Permitting 36
7.2 Legacy Wellhead Repairs 36
7.3 Shallow Temperature Survey 37
7.4 Deep Drilling 40
8. WATER CHEMISTRY 42
9. FLOW AND INTERFERENCE TESTING 44
9.1 Interference Testing of Wells PS-3, PS-4, and MI-1 45
9.2 Interference Testing of PS-3, PS-13-1, and PS-13-3 46
9.3 Flow Testing of PS-13-1 46
9.4 Temperature and Pressure Monitoring in PS-13-2 52
9.5 Temperature and Pressure Monitoring in PS-13-3 52
9.6 Historic Hot Springs Temperature Monitoring 54
9.7 Flow Testing Conclusions 55

10. PILGRIM GEOTHERMAL SYSTEM CONCEPTUAL MODEL 56
10.1 Conceptual Model History 56
10.2 Current Pilgrim Geothermal System Understanding 61
11. EXPORTING GEOTHERMAL ENERGY TO NOME 64
11.1 Geothermal Power Economics 64
11.2 Wind-Diesel-Geothermal Microgrid Modeling 64
11.3 Transmission from Pilgrim Hot Springs to Nome 65
12. LESSONS LEARNED 65
13. CONCLUSIONS 66
14. REFERENCES 68

APPENDICES

APPENDIX A Well Schematics
APPENDIX B Well Temperature Profiles
APPENDIX C Well Locations and Descriptions
APPENDIX D Wellhead Repair Description
APPENDIX E Geophysical Survey Report
APPENDIX F 2012 Mud Logging Records
APPENDIX G Geophysical Well Logs for 2011 and 2012 Drilling
APPENDIX H September 2013 Interference Testing
APPENDIX I February 2014 Interference Testing
APPENDIX J 2012 Drilling Logs
APPENDIX K 2013 Geophysical Logs
APPENDIX L Fugro MT Report
APPENDIX M A Conceptual Model of Pilgrim Hot Springs: Joshua Miller Master Thesis
APPENDIX N Reservoir Simulation Modeling: Arvind Chittambakkam Thesis
APPENDIX O Tectono-thermal History of Pilgrim Hot Springs, Alaska
APPENDIX P Wind-Geothermal-Diesel Microgrid Development: Jeremy VanderMeer Thesis
APPENDIX Q Fuel Oil Volatility – Complications for Evaluating a Proposed Power Purchase Agreement for Renewable Energy in Nome, Alaska
APPENDIX R High Voltage Direct Current Transmission Assessment at Pilgrim Hot Springs
APPENDIX S Wind-Geothermal-Diesel Microgrid Development

List of Figures

Figure 1. The location of Pilgrim Hot Springs on the Seward Peninsula. 2
Figure 2. Index maps showing the topography and regional geology. 6
Figure 3. Topographic map of the area surrounding Pilgrim Hot Springs, ... 7
Figure 4. Map of all drill holes and well locations 10
Figure 5. The1982 temperature logs from the original wells..... 11
Figure 6. Temperature profiles of all holes and wells 12
Figure 7. Map showing the approximate margin of the very shallow thermal aquifer..... 13
Figure 8. Plan view temperature maps of Pilgrim Hot Springs 14
Figure 9. A time series of ASTER visible to near-infrared imagery 16
Figure 10. A subset of an ASTER wintertime false color composite image 16
Figure 11. Landsat 7 satellite images of the Pilgrim Hot Springs 17
Figure 12. Low-emissivity thermal blankets 18
Figure 13. Field calibration and validation data sites for the primary target area 19
Figure 14. Comparison of a FLIR-derived temperatures profile 19
Figure 15. Mosaicked FLIR surface temperature data..... 20
Figure 16. FLIR (left) and optical data (right) from the fall 2010 survey 21
Figure 17. Processed airborne images for parts of the study area 22
Figure 18. A simplified conceptual model of the Pilgrim geothermal system 23
Figure 19. A total surface energy budget model for the Pilgrim geothermal system 24
Figure 20. The effect of wind speed on heat flux 27
Figure 21. Gravity stations are labeled on a topographic map 28
Figure 22. Isostatic residual gravity map..... 29
Figure 23. Magnetic field maps from Glen et al. (2014) 30
Figure 24. Magnetic lineations interpreted from maximum horizontal gradients 30
Figure 25. Airborne EM resistivity slices..... 31
Figure 26. Magnetotellurics site locations. 32
Figure 27. Resistivity at Profile D from a 1D MT inversion. 32
Figure 28. Resistivity maps at 25 m and 50 m from the blind 3D MT inversion. 33
Figure 29. Resistivity maps at 100 m, 150 m, 200 m, and 300 m 34
Figure 30. Resistivity maps at 400 m, 500 m, 750 m, and 1000 m 35
Figure 31. Areas of leaking, scale, and corrosion are shown on PS-4..... 37
Figure 32. The PS-4 completed replacement valve installation. 37
Figure 33. Installing Geoprobe holes at Pilgrim Hot Springs..... 38
Figure 34. Location of Geoprobe holes and their temperatures in Fahrenheit at 60 feet. 39
Figure 35. The temperature logs from all Geoprobe holes 40
Figure 36. The mixing trend between sodium and chloride is shown for all samples..... 43
Figure 37. Chloride content is shown along with well temperature 44
Figure 38. PS-3 downhole pressure during interference testing. 45
Figure 39. PS-3 temperature response during 2013 interference testing. 46
Figure 40. Surface equipment used for the airlift of PS-13-1..... 47
Figure 41. Downhole pressure and temperature record of PS-13-1..... 49
Figure 42. PS-13-1 downhole pressure and temperature 49
Figure 43. Downhole pressure and temperature at the end of the second airlift 50
Figure 44. Detailed flowing and static logs from PS-13-1 51
Figure 45. PS-13-2 pressure and temperature response during PS-13-1 flow testing. 53

Figure 46. PS-13-3 pressure and temperature response during PS-13-1 flow testing. 53
Figure 47. The historic hot spring pool..... 54
Figure 48. Hot spring pool temperatures during the September 2014 flow testing..... 55
Figure 49. Conceptual model from Miller et al. (2013a). 58
Figure 50. Regional conceptual model cartoon from Glen et al. (2014). 59
Figure 51. The current conceptual model of Pilgrim Hot Springs..... 63

List of Tables

Table 1. FLIR heat flux estimates. 26
Table 2. Permits and approvals..... 36
Table 3. Pilgrim Hot Springs well chemistry in PPM 42
Table 4. Well productivity data 52

Terms and Acronyms

ACEP	Alaska Center for Energy and Power
ASTER	Advanced Spaceborne Thermal Emission and Reflection Radiometer
DOE	U.S. Department of Energy
NETL	National Energy Technology Lab
EM	Electromagnetic
ETM+	Enhanced Thematic Mapper
FLIR	Forward looking infrared radiometry
gpm	Gallons per minute
IGRF	International Geomagnetic Reference Field
Kauweraq	The region of the central Seward Peninsula (also spelled Kawerak)
MHG	Maximum horizontal gradient
MT	Magnetotellurics
MW_e	Megawatt electric
MW_{th}	Megawatt thermal
PGS	Pilgrim Geothermal System
PHS	Pilgrim Hot Springs
SMU	Southern Methodist University
TG	Temperature gradient
UAF	University of Alaska Fairbanks
Unaatuq	Inupiaq word (also spelled Oonuktuak) meaning hot water/ hot spring. Also refers to the group of Native Alaskan and non-profit organizations that own Pilgrim Hot Springs.
USGS	United States Geological Survey
VNIR	Visible and near-infrared

1. EXECUTIVE SUMMARY

This document is the final report for the Pilgrim Hot Springs (PHS) geothermal exploration project, funded by the U.S. Department of Energy (DOE), The Alaska Energy Authority, the City of Nome, Bering Straits Native Corporation, White Mountain Native Corporation, Sitnasuak Native Corporation, Potelco, Inc., and the Norton Sound Economic Development Corparation. The first round of funding in 2009 was awarded under Alaska Energy Authority RSA R1108 and R1215 and DOE award DE-EE0002846. In 2013, DOE award DE-EE0000263 along with match money from the six other organizations listed above was awarded. This report details the activities that occurred as part of the first and second rounds of funding for geothermal exploration at PHS in 2010 and 2013. The project objectives were to test innovative geothermal exploration techniques for low-to-moderate-temperature geothermal resources and conduct resource evaluations of PHS.

A variety of methods including geophysical surveys, remote sensing techniques, and heat budget modeling estimated that the geothermal resource might support electrical power generation of approximately 2 MWe using a binary power plant. Further flow testing of the deep geothermal aquifer is needed to verify this estimate.

Eight new wells were drilled around the PHS site to a maximum depth of 1294 feet. Five of these wells use sealed casing and can be used only to collect temperature logs. The other three wells have perforated casing and are capable of measuring temperature as well as artesian flow. A maximum temperature of 91°C (196°F) was measured in two different wells: in the shallow thermal aquifer at approximately 120 feet in depth and in the deep aquifer at approximately 1100 feet in depth. These wells were drilled in what is believed to be the vicinity of the upwelling zone, but both wells show a temperature reversal between the shallow and deep thermal aquifers, suggesting they are not directly over the main area of upwelling. Based on data collected to date, the main upwelling zone is likely northwest of well PS-13-1 in a swampy area that has been inaccessible for drilling.

As in past surveys, geothermometry from water samples collected suggests maximum system temperatures could be as high as 145°C (293°F), based on Na-K-Ca geothermometry. The most concentrated geothermal fluid with 3500 ppm (parts per million) chloride continues to be collected from the traditional thermal hot spring located directly south of the church. Thermochronology data analyzed by University of Alaska Fairbanks (UAF) researchers suggest that the Pilgrim geothermal system (PGS) is relatively young, and core samples collected from the drilling indicate that temperatures have likely reached approximately 150°C (302°F) in the past 1000 years.

In 2014, a power purchase agreement was signed between the City of Nome and Pilgrim Geothermal LLC, who has sent a letter of intent to the landowners to develop the resource. Modeling by the UAF power integration program, examined the effect of adding a geothermal generation source to the existing wind-diesel islanded grid in Nome. Adding 2 MW of geothermal power to the Nome grid displaces approximately 1 million gallons of diesel fuel per year (VanderMeer and Mueller-Stoffels, 2014).

Flow testing of the shallow thermal aquifer reached maximum flow rates of 350 gpm (gallons per minute), and sustained flow rates of 300 gpm for 7.5 hours. Based on the observed flow rates and minimum pressure decline, it appears likely that the shallow thermal aquifer could sustain this flow long term, opening up the potential for on-site direct geothermal heating or electrical power generation.

2. BACKGROUND – KRUZGAMEPA HOT SPRINGS

Pilgrim Hot Springs, formerly known as Kruzgamepa Hot Springs, is located on Alaska's Seward Peninsula about 60 miles north of Nome and 75 miles south of the Arctic Circle (Figure 1). The site has a long, colorful human history, which has included use as a traditional Native Alaskan gathering place, a farm, a dancehall and roadhouse, a Catholic orphanage and mission, and most recently as a recreational bathing and hunting site. The lush and tall local vegetation, dominated by cottonwood trees, contrasts with the otherwise treeless tundra of the western Seward Peninsula and is visible from miles away. Since the late 1970s, the area has seen two extensive geothermal exploration efforts that have extended road access to the site from the Nome-Taylor Highway.

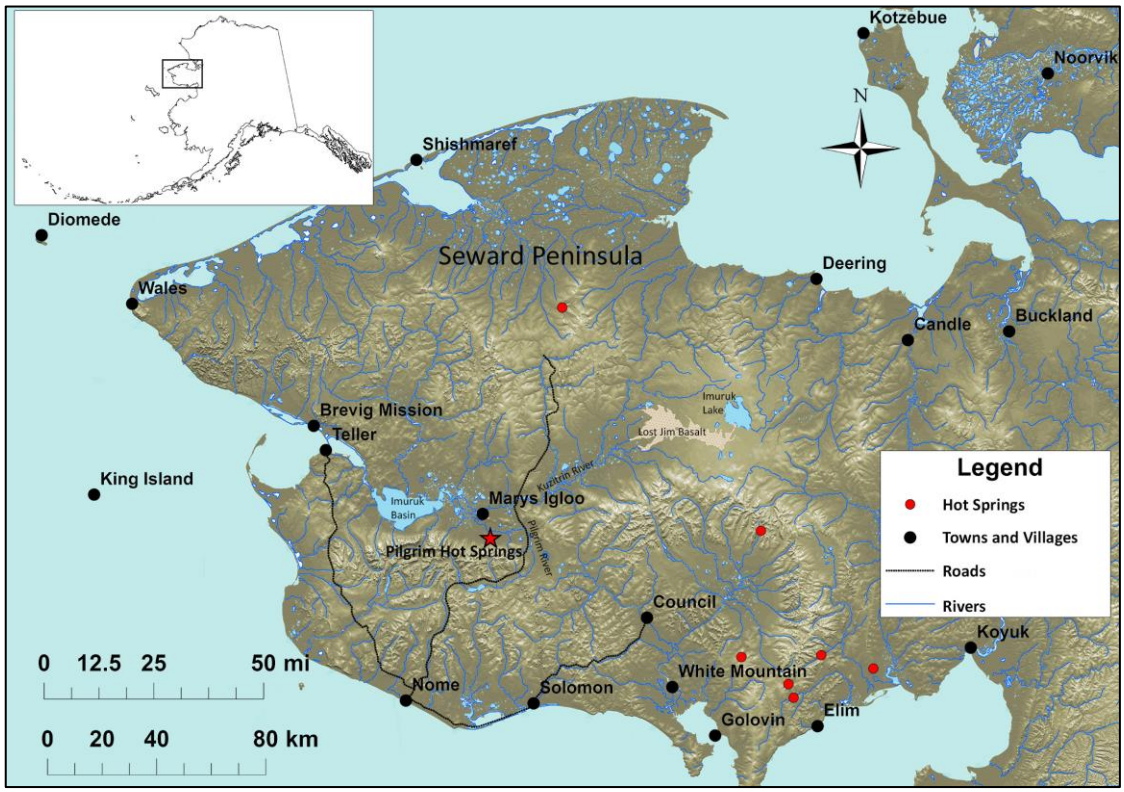


Figure 1. The location of Pilgrim Hot Springs on the Seward Peninsula.

Before outsiders came to the region, the people of Kauweraq (the region of the central Seward Peninsula) used the area known as Oonuktuak (also spelled Unaatuq), also known as Kruzgamepa and later as Pilgrim Hot Springs. Traditionally, the hunting camp served as a

tropical oasis for the Kauweramuit (the people of Kauweraq) (D. Hughes, personal communication, February 17, 2015). During the winter months, Oonuktuak was an ideal living area with fresh water, plenty of wood for heat, and bountiful hunting and fishing. After successful ceremonial caribou hunts, other native groups such as the King Islanders would visit the area (Ray, 1992).

Pressure from commercial whaling and hunting significantly reduced the marine mammal population in the region, and local government officials became concerned about the well-being of the region's native inhabitants. In 1892, reindeer from northeastern Siberia were first introduced, after Dr. Sheldon Jackson, the Commissioner of Education in Alaska, received congressional approval. A reindeer station was established at Teller, about 40 miles west of the hot springs (Bucki, 2004). Later reindeer fairs were held, the first of which took place in 1915 at Pilgrim Hot Springs (Van Stone et al., 2000).

Modern development at the hot springs began around the year 1900, during the Nome Gold Rush, when a family homesteaded 160 acres and worked the land, raising cows, chickens, pigs, and horses (Bland, 1972). After several years, the land was leased or sold to a series of people who developed a roadhouse. During the gold rush period, a bathhouse, greenhouse, roadhouse (hotel), and stables were built on the site. The facilities were frequented by the miners, their "fancy ladies," and gamblers who reached the area by dog team. A railroad once passed within 8 miles of the site. In 1908, the roadhouse and saloon-dancehall burned to the ground. By this time, the gold rush was ebbing and a second roadhouse was constructed to serve travelers (National Register of Historic Places, 1977). By the late 1910s, mining on the Seward Peninsula had greatly diminished, and eventually, after another series of transactions, the land was deeded to the Catholic Church by two brothers with no heirs.

In 1917 and 1918, an influenza epidemic decimated the area's Native Alaskan adult population. On April 22, 1918, a Canadian priest and pastor of a Nome church, Father Bellarmine Lafortune, S.J, moved out to the hot springs to build an orphanage (*The Alaskan Shepherd*, 2009). Many buildings were moved from a mission that existed in the village of Mary's Igloo, several miles north of the hot springs, to the present-day site. Additional buildings were constructed using lumber from a nearby mining site as well as the on-site timber (National Register of Historic Places, 1977). During this time, the site became known as Pilgrim Hot Springs (PHS). Eventually the orphanage included a machine shop, student dormitories, nun and priest quarters, a sizable church that now dominates the site, a variety of lesser buildings, a cemetery, and reportedly an unmarked or lost burial ground where victims of the Spanish influenza outbreak were interred. Some of the buildings were reportedly heated with the natural springs; others were heated using wood stoves. Historic photos show huge piles of firewood stacked near the church and a substantial treeless area around the springs, now heavily wooded. Toward the latter stages of the orphanage, firewood became scarce in the region (*The Alaskan Shepherd*, 2009). The orphanage was largely self-sustaining thanks to the gardens that flourished on the permafrost-free soil, producing legendary crops of potatoes, cabbages, turnips, and other vegetables. The population averaged about 100 youth and 20 adults then (National Register of Historic Places, 1977). A field of shoulder-high oats was growing in the thawed area in September 1915 (Waring, 1917). The orphanage closed in 1941; however, caretakers continued to grow produce, and up to

7 airplane flights a day ferried this produce to Nome (Bland, 1972), as there was no road access at the time.

During World War II, military forces used the site for rest and recreational purposes. In 1969, Pilgrim Springs Ltd. signed a 99-year lease on the property with the Catholic Church to develop the site as a historical resort (Bland, 1972). This plan never materialized, but the land continued to be farmed by a number of caretakers. In 2010, Unaatuq LLC, a consortium of Alaska Native and nonprofit entities from the Seward Peninsula, purchased the property and decaying buildings for $1.9 million from the Fairbanks Catholic Diocese after the Diocese filed for Chapter 11 bankruptcy (Smetzer, 2010). Since acquiring the property, Unaatuq has been investigating various options for the development and preservation of the site. Throughout the site's history, it has continuously been used for bathing and recreational purposes.

2.1 Geothermal Exploration History

The first recorded description and map of the hot springs dates from 1915, after the local area had already seen significant development (Waring, 1917). Waring apparently reached the site via light carts pulled by dog teams on the old railroad grade that passed 8 miles east of the hot springs. Waring described a permafrost-free area 100 yards wide and a half-mile long, and measured a maximum spring temperature of 156°F. The visible single-point discharge in 1915 was only about 8 gpm, but additional diffuse discharge increased this amount to an estimated 60 gpm. The water was reported clear with a slight hydrogen sulfide odor. Waring collected a thermal water sample for chemical analysis. This analysis, now a century old, is remarkably similar to modern analyses of the thermal water (Table 3).

In 1968, the Catholic Church leased the geothermal rights to C. J. Phillips of Nome (Kirkwood, 1979). However, no significant exploratory work occurred under this lease, which ultimately was revoked. The U.S. Geological Survey (USGS) designated the hot springs as a Known Geothermal Resource Area in the 1970s.

In the early 1970s, initial evaluation of the geothermal resource commenced. The USGS revisited some of the thermal springs in central and western Alaska and published a new chemical analysis of the PHS thermal water (Miller et al., 1975). The quartz and Na-K-4/3Ca geothermometers from this analysis predicted subsurface hot springs temperatures of 137°C and 120°C. In October 1973, Harding-Lawson Associates ran two resistivity lines and concluded that a fault crossed the area and down-dropped bedrock from a depth of 100 feet to 600 feet (Kirkwood, 1979). In 1974, a 2250-foot-long north–south seismic refraction line and surface magnetic profile were run (Forbes et al., 1975). Forbes et al. measured a maximum temperature of 80°C in the thermal pool and deployed a portable seismograph for two nights to try to detect any tremors. They found the area quiet.

The first major geothermal studies at PHS were led by the Geophysical Institute at the University of Alaska, the Alaska Division of Geological and Geophysical Survey, and the State Division of Energy and Power Development in 1979, using funding from the Alaska Division of Energy and Power and the U.S. Department of Energy. During the 45-day field season, a variety of geological, geochemical, geophysical, hydrological, and shallow drilling studies were performed at the site (Turner and Forbes, 1980). In the fall of 1979, the first two wells at PHS were drilled

to a maximum depth of 160 feet and initially flowed, allowing the first analysis of subsurface thermal water (Kline et al., 1980).

During a 30-day field season in 1980, the central Seward Peninsula was evaluated on a more regional scale for its geothermal potential (Wescott and Turner, 1981). This helicopter-supported work included geologic, geophysical, and geochemical studies near PHS. It also incorporated a remote sensing component (Dean et al., 1982).

In 1982, a 7-mile-long road was at last constructed from the Nome-Taylor Highway to Pilgrim Hot Springs, allowing reasonable access for a drilling rig and associated equipment capable of drilling larger-diameter and deeper wells (P. Eagan, personal communication, April 29, 2015). During summer 1982, four wells were drilled to a maximum depth of 1001 feet (Kunze and Lofgren, 1983; Lofgren, 1983). These wells were flowed, brief interference tests were conducted, and chemical analyses were obtained (Economides, 1982; Economides et al., 1982). This work represented the end of the first major exploration effort at PHS, as the maximum measured well temperature of 91°C was far too low for electrical power generation with the technology that existed at the time.

Pilgrim Hot Springs attracted very little geothermal interest between 1983 and the early 2000s, with the exception of a comprehensive water and gas sampling program conducted in 1993 (Liss and Motyka, 1994). In the early 2000s, interest in the PGS gradually revived with the National Renewable Energy Laboratory sponsoring a site visit (Huttrer, 2002) and the Alaska Energy Authority funding a preliminary development feasibility study (Dilley, 2007). In 2008, the Nome Region Energy Assessment concluded that geothermal energy was a potentially economic option for the region (Sheets et al., 2008).

In 2006, the first geothermal power plant in Alaska was installed at Chena Hot Springs, near Fairbanks. The project was able to generate electricity using 165°F (73°C) fluid, effectively making it the lowest temperature geothermal power plant in the world and demonstrating that generating electricity from low temperature geothermal resources was technically and economically feasible (Holdmann, 2007). Following this success, overall interest in developing Alaska's low-to-moderate temperature resources increased, and the Alaska Center for Energy and Power (ACEP) secured grant funding from the U.S. Department of Energy and the Alaska Energy Authority to resume exploration of the PGS. This work began in 2010, with repairs to the existing wellheads so that those wells could be relogged and flow tested. Remote sensing studies also began at this time (Haselwimmer et al., 2011), followed by numerical modeling of existing data (Daanen et al., 2012). The USGS also collected additional geophysical data around the hot springs (Glen et al., 2012). In 2011, two 500-foot temperature gradient holes were drilled to evaluate the northern part of the thermal anomaly where the thermal upwelling was then expected to be located.

In 2012, three deep holes were drilled in an attempt to precisely define the location of the thermal upwelling beneath the shallow thermal anomaly (Miller et al., 2013a; Miller et al., 2013b; Benoit et al., 2014a). Recent modeling efforts used data from the deep holes drilled in 2012 (Chittambakkam et al., 2013). In 2013, additional funding became available through the U.S. Department of Energy. ACEP drilled a deep, large-diameter well and two shallower wells

to locate and produce fluid directly from the deep thermal upwelling (Benoit et al., 2014b). These holes failed to penetrate or precisely locate the thermal upwelling, but were completed as possible future production wells for direct-use projects. In September 2014, these three wells were flow tested and monitored for interference.

3. GEOLOGIC SETTING

3.1 Regional Geologic Setting

The central Seward Peninsula is underlain by a Precambrian metamorphic complex, intruded by Cretaceous granitic rocks (Amato and Miller, 2004; Till et al., 2011). In the vicinity of Pilgrim Hot Springs (PHS), Quaternary alluvial fill overlies this basement complex. The metamorphic and intrusive rocks are well exposed in the Kigluaik Mountains 2.5 miles south of the PGS and on Mary's Mountain and Hen and Chickens Mountain 2.5 miles north of the hot springs (Figure **2**). Nowhere is the alluvial fill dissected to the point that any meaningful thickness can be viewed in any detail at the surface.

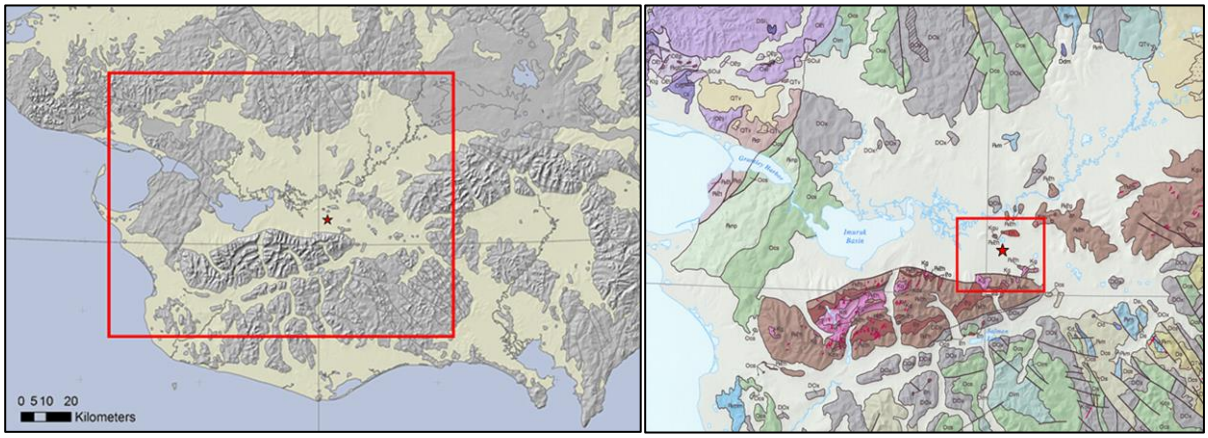


Figure 2**.** Index maps showing the topography and regional geology.The red box in the left panel shows the area in the geologic map on right. The location of Pilgrim Hot Springs is shown by the red star. Map after Till et al. (2011). The red box in the right panel outlines the area of Figure 3.

The dominant regional structural feature near PHS is the east–west trending Kigluaik-Bendeleben system of normal faults. These normal faults are interpreted as due to regional north-south extension (Ruppert, 2008), which led Wescott and Turner (1981) to propose that the central part of the Seward Peninsula is a 250 km long east-west striking rift system. The Kigluaik section of the fault system uplifts the Kigluaik Mountains in the south relative to the Imuruk Basin in the north, where the hot springs are located.

Hudson and Plafker (1978) divided the Kigluaik section of the fault system into three segments. The western and central section's show clear surface traces and post Wisconsin or Holocene vertical displacements up to 10 m. The eastern section, which passes about 2.5 miles south of PHS, has less definable surface traces, being more obscured by glacial deposits (Hudson and Plafker, 1978). The eastern section is more complex, with two distinct northward steps, giving

the range front an en echelon system of at least three mappable faults. Geomorphic features suggest that displacement of the western en echelon section is younger than displacement of the eastern section. The vertical displacement on the Kigluaik fault zone is at least several hundred meters and probably exceeds 1200 m. While it is tempting to hypothesize that this major extensional structure somehow plays a role in the geothermal system, no serious arguments for this have yet been made.

Up to 320 m of Quaternary alluvium ranging from clay to gravel in size and consisting of alluvial, fluvial, glaciolacustrine, and brackish lagoon sediments has been drilled in the immediate vicinity of PHS (Miller et al., 2013a, 2013b).

The volcanic rocks closest to the PGS are the Holocene Lost Jim basaltic lava flows (Till et al., 2011). These flows cover 88 square miles and lie about 30 miles northeast of the PGS. They are outside of the boundary of Figure **2**. This distance from the PGS makes it unlikely that the Lost Jim lava flows represent a possible direct magmatic heat source for the PGS. The northern horn of the Seward Peninsula also hosts the world's largest maar craters, dated at 21,000 years (Rozell, 2006), but these craters are much farther away. If there is a magmatic heat source for the PGS, no author has yet tried to make a convincing case for its existence

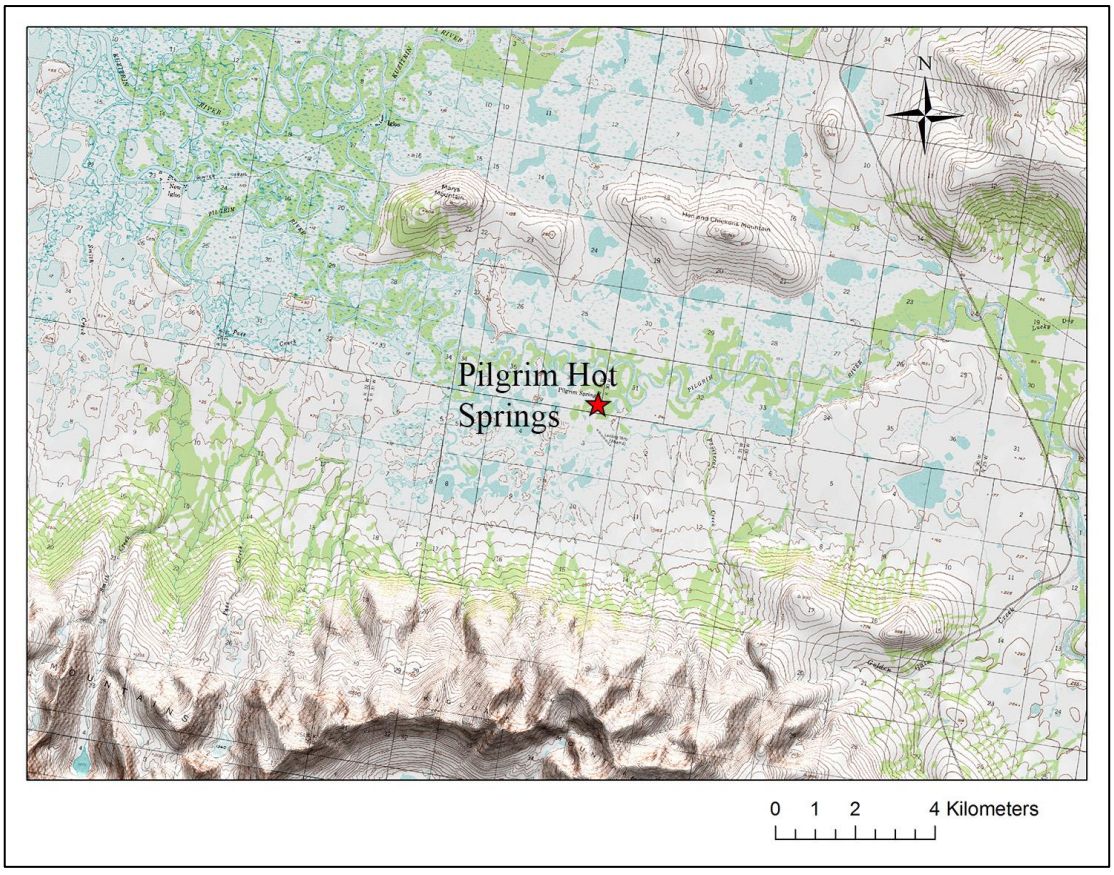


Figure 3**.** Topographic map of the area surrounding Pilgrim Hot Springs, indicated by the red star.

3.2 Local Geology

The localized surficial geology surrounding the PGS consists of a flat, wide valley covered mostly by thermokarst lakes, permafrost tundra, and muskeg swamps (Miller et al., 2013b). The most striking local surface feature is a thaw in the permafrost, covering an area of about one-half square mile (~0.58 mi^2 or 1.5 km^2) that allows anomalous vegetation such as cottonwood trees, alders, grass, and various wildflowers to thrive.

The most extensive published surficial geology description of the PGS suggests that the hot springs might be located near the western edge of an actively subsiding north-south striking graben, apparently resulting from north–south-trending faults (Kline et al., 1980). The publication offers eight brief lines of evidence as support, but unfortunately, contains no maps, photos, and/or diagrams to back the evidence, nor has any been reported in more recent publications. Swanson et al. (1980, p.11) suggest that "many of the canyons found on the north flank of the Kigluaik Mountains are apparently controlled by north–south-trending faults." However, the 2011 geologic map of the Seward Peninsula (Till et al., 2011) shows no north–south-trending faults in the Kigluaik Mountains, casting serious doubt on the earlier suggestion. In spite of the 2011 map, inferred or buried north–south-trending faults are shown by Miller et al. (2013a) and are included in discussion by Glen et al. (2014). Thus, at this time, north–south-trending structures have been proposed by several researchers, but no recent geological work has focused on the Pilgrim Valley to confirm the existence of these structures, and a more recent geologic map did not give them any credence.

On a smaller scale, the local geology has been evaluated with several recent drill holes to a maximum depth of 350 m (Miller et al., 2013a, 2013b). This evaluation primarily focused on the stratigraphy of the Quaternary alluvium and showed that metamorphic bedrock is present at a depth of about 320 m. Particle sizes in the alluvium range from clay to gravel, with sand, silt, and clay predominating. The sand is locally indurated with silica cement near most of the deeper wells that have been drilled. The most laterally extensive silt and clay unit is located about 164 feet (50 m) above the top of the metamorphic basement.

4. SUBSURFACE TEMPERATURES

Above the top of the metamorphic bedrock at depths of about 1050 feet (320 m) the thermal fluid flow pattern has become much better defined by the activities described in this report. Some type of vertical or near-vertical permeable channel allows the thermal fluid to rise to the surface through a sequence of unconsolidated Quaternary fluvial material. If any elongation or dip accompanies this channel, it has not yet been recognized. It is possible that the access limitations for drill-hole locations allow some northwest–southeast elongation, which could be hypothesized as evidence for a fault. Drilling and temperature logging completed between 1979 and 2014 have delineated a 2 square mile permafrost-free area and a series of thermal aquifers overlying each other within this location. All holes and wells that were drilled between 1979 and 2013 are shown in Figure 4.

The oldest well logs are from September 1982, when flowing and static temperature logs were obtained from the first six wells using a FENWAL model UUT-51J1 thermistor instrument, with

an estimated absolute accuracy of about 1°C (Lofgren, 1983) (Figure 5).A few logs from this era are questionable, especially below a depth of 200 feet in the PS-5 well log, but overall these well logs give a valuable baseline dataset with which to measure long-term aquifer temperatures.

All existing and new holes and wells, except for PS-2, were repeatedly logged between 2011 and 2014. In general, temperature profiles matched the profiles reported in Woodward-Clyde (1983). Recent well logs were obtained using two different instruments. Many logs were obtained using one of three Kuster K-10 memory tools owned by the Alaska Center for Energy and Power. The Kuster tools are extremely robust, can be used up to 150°C (302°F) and 5000 psi, and can remain downhole for long periods. This tool measures temperature and pressure with an accuracy of 0.2°C. The Kuster tools were used with a strong reel of aircraft cable that could be operated by hand by one person. Once retrieved from the hole, the Kuster tool is disassembled and the data are downloaded onto a computer.

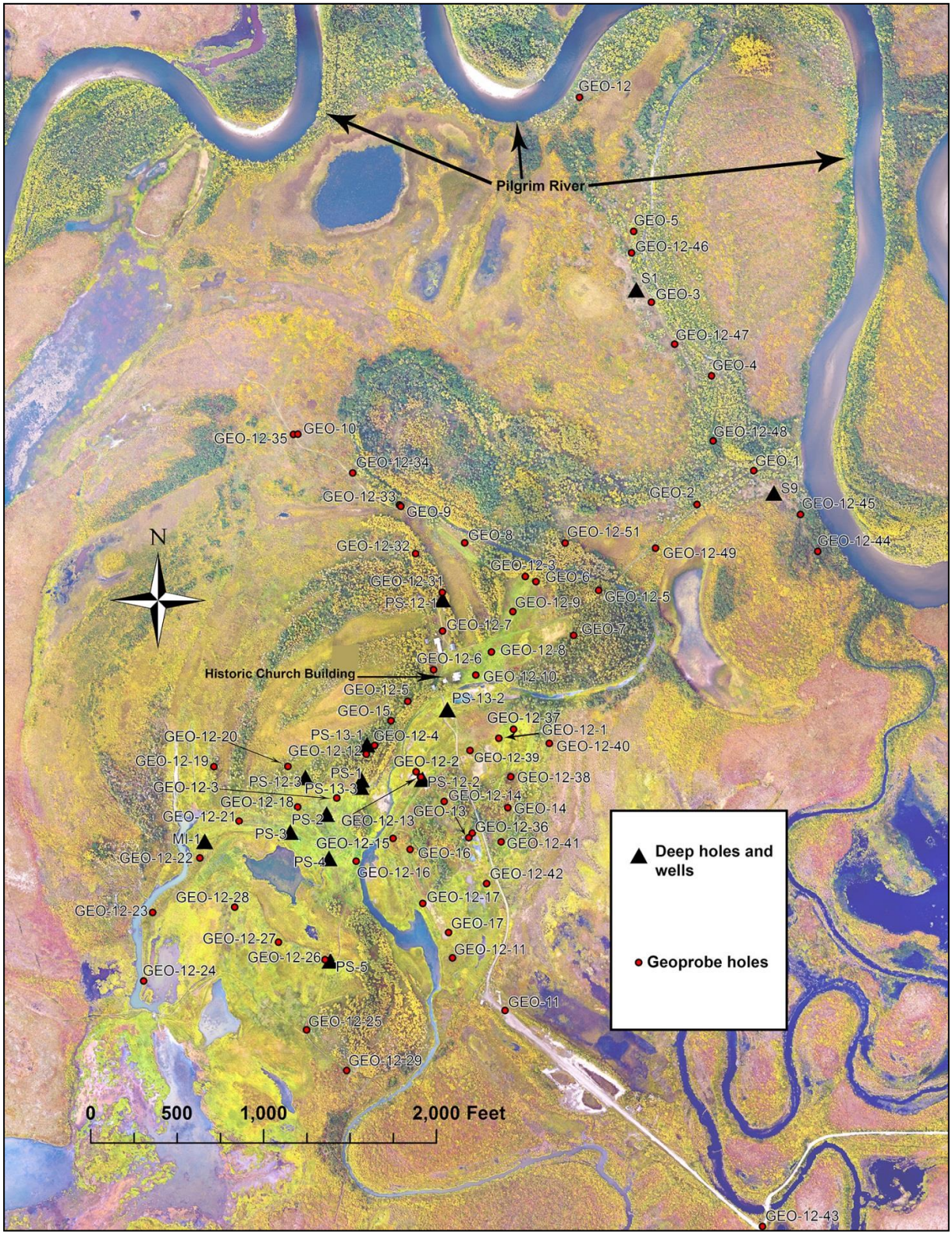


Figure 4. Map of all drill holes and well locations at Pilgrim Hot Springs.

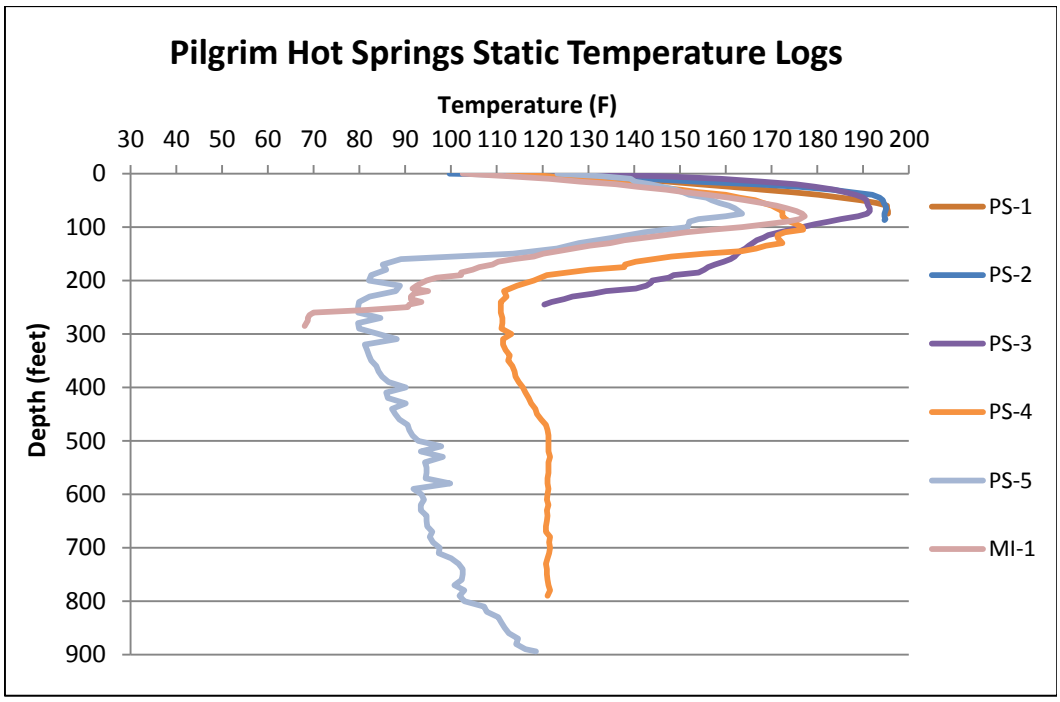


Figure 5. The1982 temperature logs from the original wells drilled at Pilgrim Hot Springs from 1979–81.

The second tool was a light and simple portable wireline temperature measurement tool with surface readout, custom built for Southern Methodist University (SMU). The tool employs a platinum thermistor with a reported accuracy of ±.01°C depending on the depth. It is simply referred to here as the SMU tool. Both types of equipment were compared with one another, and the readings were virtually identical.

4.1 Updated Temperature Logging

A presentation of all available PHS temperature profiles to a depth of 160 feet (Figure 6) reveals a confusing picture, but highlights a hot shallow aquifer of varying depths. The thermal anomaly consists of a shallow aquifer 10 to 20 feet deep (Figure 7) above an aquifer 55 to 90 feet deep, which is referred to here as the shallow thermal aquifer (Benoit et al., 2014a). The shallow thermal aquifer is the primary geothermal discharge zone of the geothermal fluid within the PGS.

The shallow thermal aquifer can be subdivided into northern and southern portions based on the shape of the static temperature profiles measured in the associated holes and wells. While these northern and southern shallow thermal aquifers have different characteristics, they are likely not independent aquifers and are certainly hydraulically connected. Where the holes and wells penetrate the shallow thermal anomaly and show a temperature reversal, the temperature profiles define the aquifer temperature, depth, and thickness. These data were used to create an aquifer temperature map showing the flow direction and the division of the northern and southern shallow aquifers (Figure 8).

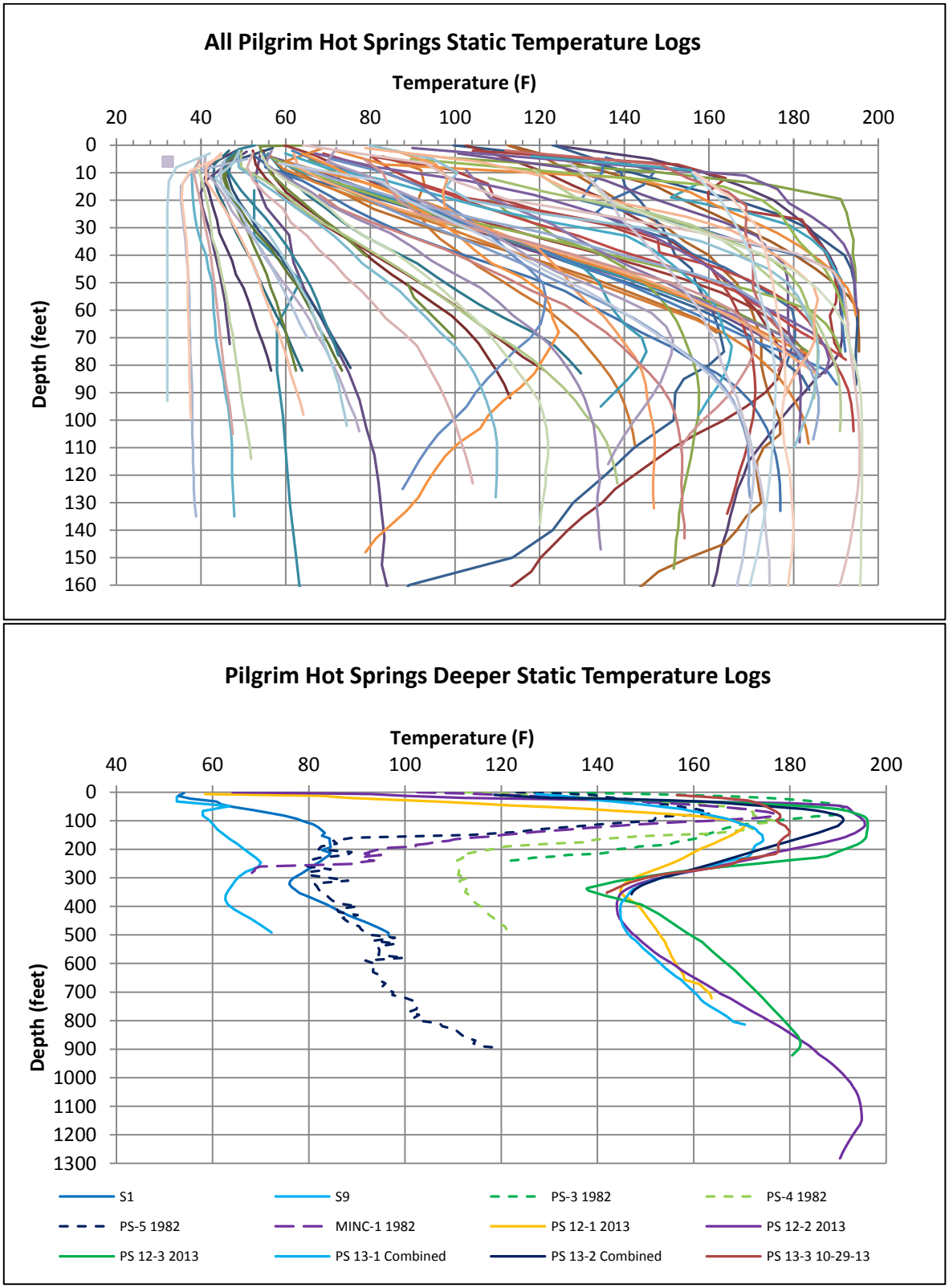


Figure 6. Temperature profiles of all holes and wells drilled to date at Pilgrim Hot Springs are shown. The temperature profiles in the top graph define the shallow and very shallow thermal aquifers shown in Figure 8 and Figure 7. The bottom graph shows all the deep holes and wells drilled to date. These profiles show the temperature minimum data that were used to create Figure 8.

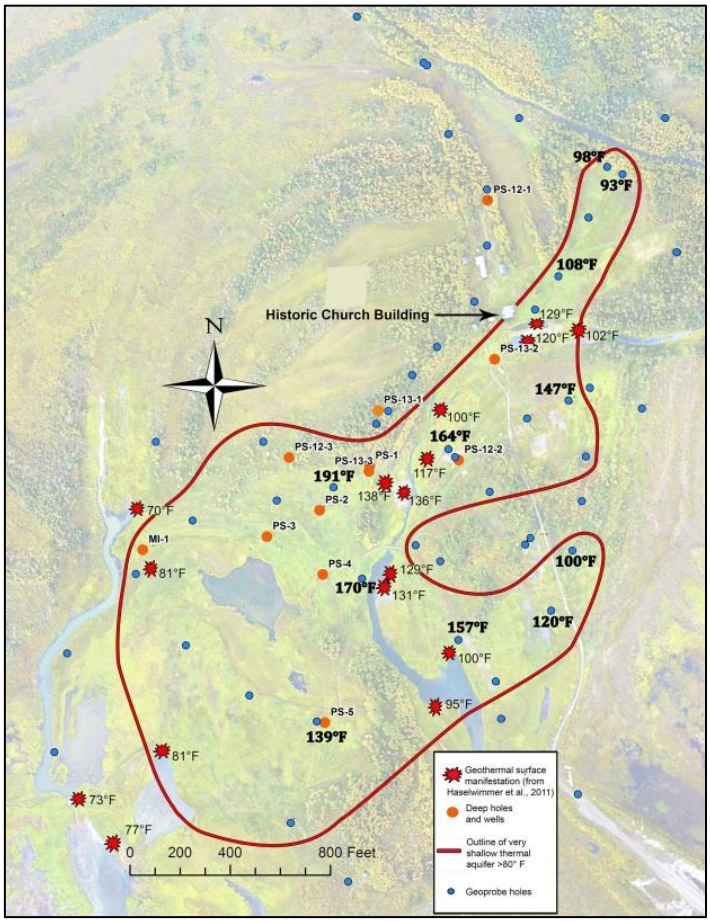


Figure 7**.** Map showing the approximate margin of the very shallow thermal aquifer, the temperatures within this aquifer, and the temperatures of thermal water measured at the surface. The red boundary closely approximates a temperature of 80°F (27°C).

The hottest measured temperatures in the shallow aquifer occur near the boundary of the northern and southern thermal aquifers, indicating that both are supplied from the same upwelling source and represent thermal fluid moving through permeable intervals of varying thicknesses and depths. Overall, temperature distribution of the shallow thermal aquifer appears to show primitive waters rising in its center and flowing out laterally (Figure 8). The weaker thermal aquifers penetrated by the remote northeasterly S1 and S9 holes are most likely a continuation of the northern aquifer

The deep holes that have been drilled at PHS show temperature minimums in between depths of 220 and 400 feet (Figure 6). While only the 12 deepest holes penetrate the temperature minimum to a depth where positive gradients occur, they allow the creation of plan view map showing temperature minimum contours (Figure 8).

The temperature minimums measured between the shallow and deep thermal aquifers, and shown in Figure 6, provide the best dataset to define the location of the upwelling zone in Figure 8. Since 91°C (196°F) fluid has been measured in the deep thermal aquifer at the top of bedrock, and 91°C fluid has been measured in the shallow thermal aquifer, there must be a zone where the 91°C fluid emerges from a fracture of some type in the metamorphic bedrock and travels between those two aquifers. The two maps in Figure 8 suggest that the thermal fluid is rising through bedrock in the northwest swampy area and flowing northeast and south through the shallow thermal aquifer.

The temperature profile from well PS-12-2 shows identical temperatures of 90°C (194°F) at depths of 126 feet and 1148 feet, indicating that the geothermal fluid loses no heat as it rises from the top of bedrock to the shallow thermal aquifer. Therefore, we speculate that the hottest and most saline fluid samples collected from the thermal springs and the shallow thermal aquifer have probably not been diluted by any shallow groundwater within the unconsolidated

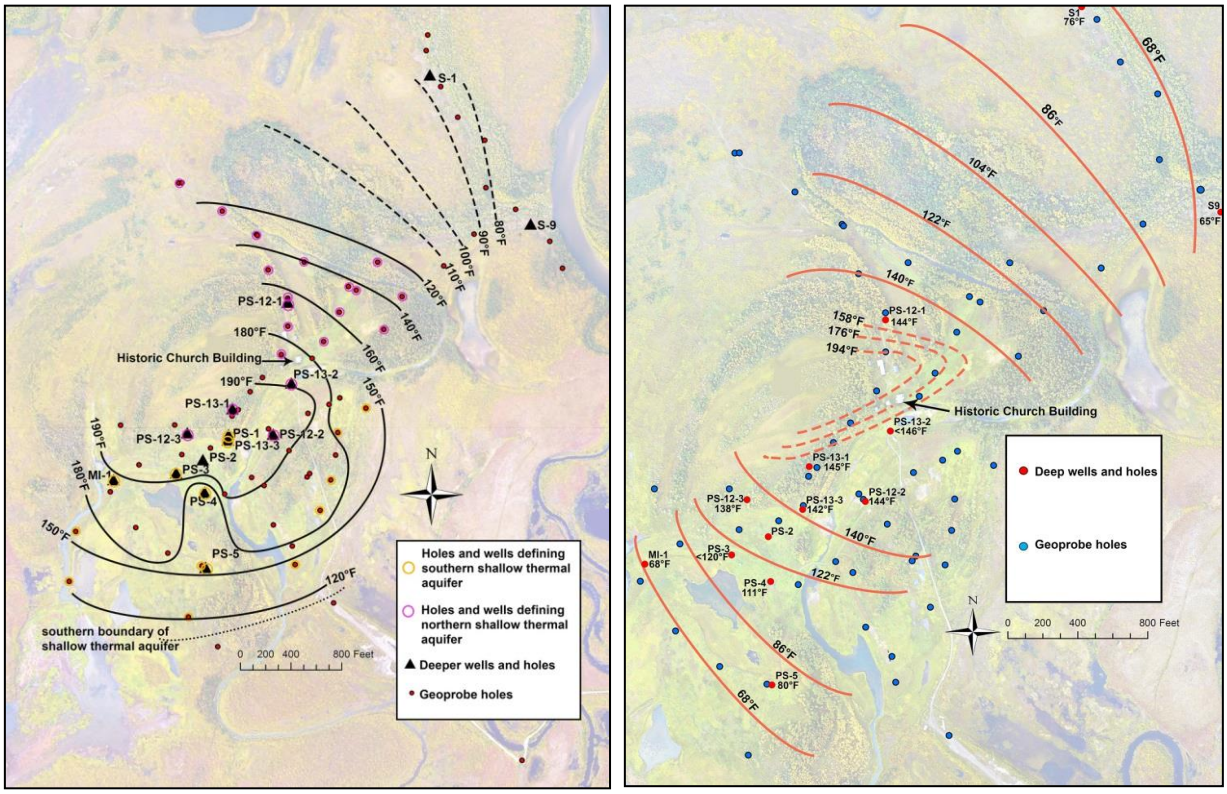


Figure 8. Plan view temperature maps of Pilgrim Hot Springs. The temperature contour map on the left shows the shallow thermal aquifer at the hot springs, and is based on the shallow temperature maximum. On the right, temperature minimum contours are shown at the hot springs. Known temperature contours are shown as solid lines. Hypothetical higher temperature contours are shown as the closely spaced dashed lines These minimum temperature contours, based on deep holes and wells, in conjunction with the shallow aquifer temperature profiles, indicate the direction of thermal water flow and help pinpoint the likely upwelling zone northwest of the area where past drilling occurred.

Quaternary fluvial material. This indicates that pressures are higher within the plumbing hosting the thermal flow than in the surrounding Quaternary material.

5. REMOTE SENSING

The first calculations of heat loss and potential power output of the Pilgrim geothermal system (PGS) were developed from 1979 data (Harrison and Hawkins, 1980; Osterkamp et al., 1980). Harrison and Hawkins (1980) indirectly measured the surface discharge downstream from the main area of PHS at 67 gpm and used a hot water temperature of 81°C to calculate admittedly crude numbers of 1.5 and 2.2 MW due to thermal water surface discharge. A 10 MW total vertical heat flow from the thawed area around the springs was also determined. Harrison and Hawkins (1980) indicate that this total vertical heat flow is probably a serious underestimate, as it did not include the power removed by groundwater movement. It is now known that 91°C would be a more accurate original thermal water temperature. Osterkamp et al. (1980), using a

more systemwide approach to estimate the heat loss, analyzed the temperature and salinity increases in the Pilgrim River after it had passed through the geothermal area. This approach resulted in minimum total accessible power values of 350 to perhaps 500 MW. However, Osterkamp et al. admit that these numbers are highly uncertain, and caution that the values "should not result in unbridled optimism."

The first remote sensing efforts at PHS occurred in 1980 with radar and infrared surveys (Dean et al., 1982). The radar study identified numerous lineaments near the PGS that have received little or no recent attention. The high altitude (60,000 ft) infrared work indicated the presence of two large and unusually warm areas along the Pilgrim River north of the hot springs, but provided no quantitative thermal data.

Remote sensing work since 2010 has extended the traditional use of remote sensing for geothermal exploration by developing methods for acquiring and processing remote sensing images (Haselwimmer et al., 2011). These methods identified various surface signatures associated with the geothermal systems and derived first-order quantitative estimates of thermal fluxes. Permafrost-free areas, snowmelt areas in early spring, anomalous vegetation patterns, and heated ground and water bodies were identified as areas that warrant further study. The temperature images derived from remote sensing provided the basis for heat budget modeling. This helped to focus the field efforts for further investigation and helped to target drilling activities and develop a conceptual heat flow model.

5.1 Satellite-based Geothermal Anomaly Mapping

Satellite images from Landsat, Advanced Spaceborne Thermal Emission and Reflection Radiometer (ASTER), and WorldView-2 (WV-2) were processed and used to identify areas of persistent high temperature, areas of snowmelt in winter images, and areas of greener vegetation in springtime images. An iterative approach to the use of satellite data followed by airborne surveys and traditional ground-based exploration was recommended as a routine part of a systematic geothermal exploration program.

5.1.1 Analysis of Landsat 7 Data

A search of the Landsat 7 archive for ETM+ images from the PGS region yielded 18 scenes, which had been acquired between August 1999 and July 2010. Eleven datasets were selected for further analysis of cloud and snow-free images.

The discrimination of thermal anomalies was undertaken using the image "stacking" approach (Prakash et al., 2011). This included pre-processing the band 6L thermal data for each dataset using the three-step procedure described by Chander et al. (2009). Thermal hot spot images for each year were integrated to identify temporally persistent thermal anomalies most likely to represent geothermal sources. A thermally anomalous pixel identified in data from three different years was labeled persistent. The ETM+ data highlight five persistent thermal anomalies located within the broad region of the PGS. These anomalies were later investigated in detail during the aerial FLIR survey.

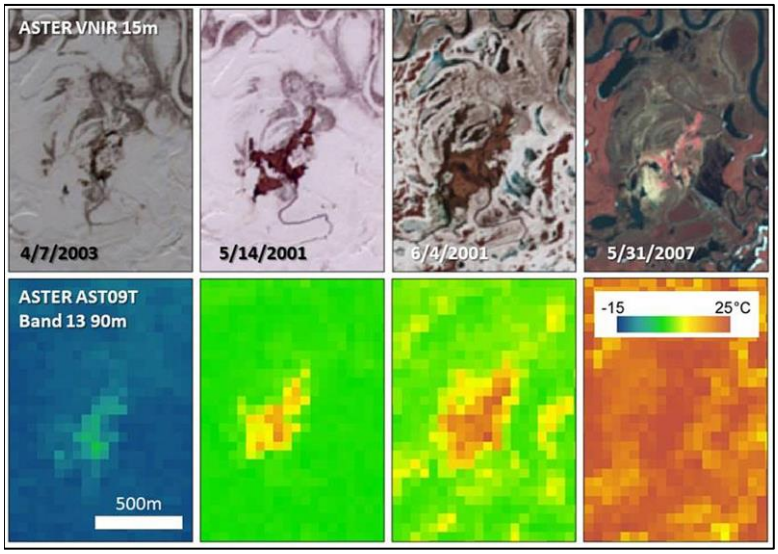


Figure 9. A time series of ASTER visible to near-infrared imagery (top) and thermal (bottom) data from Pilgrim Hot Springs, showing snow-free areas and vegetation growth anomalies associated with geothermally heated ground.

5.1.2 Analysis of ASTER Data

The ASTER multispectral thermal infrared data were acquired over the PHS site to identify geothermal anomalies (Figure 9). The 90 m spatial resolution of the ASTER thermal bands is lower than that of Landsat 7; however, as a multispectral instrument, ASTER is routinely used to acquire data during its nighttime ascending orbit, minimizing the effects of solar heating. The five ASTER thermal bands also enable the effects of emissivity to be accounted for within geothermal anomaly detection. The ASTER data delineated potential surface indicators of geothermal activity such as snowmelt anomalies, anomalous river ice melt, and areas of vegetation growth in the PGS region.

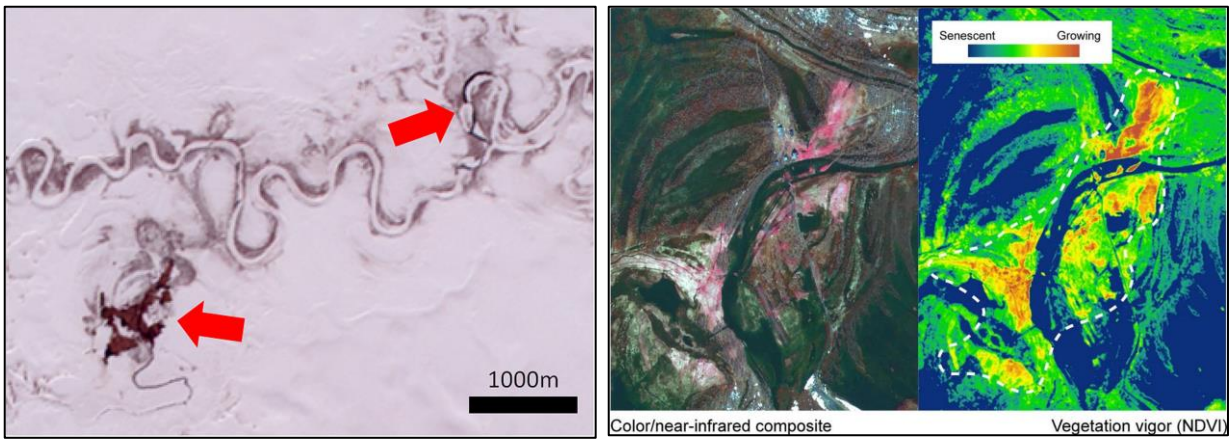


Figure 10. A subset of an ASTER wintertime false color composite image with 15 m spatial resolution is shown on the left. Prominent snow-free areas are indicated with red arrows. The left arrow points to the area near the hot springs. The right arrow points to a persistent snow-free region. A WV-2 color infrared image acquired in May 2010 is shown on the right. Healthy green vegetation (bright pink/reddish tones) and senescent vegetation (dark brownish red tones) are clearly visible (left). The processed WV-2 image (right) shows vegetation vigor, the dashed white line marking the approximate limit of vigorous nontundra vegetation. This map (right) is a color-coded Normalized Difference Vegetation Index (NDVI) image, where NDVI = (Near-infrared – Red) / (Near-infrared + Red).

5.1.3 Analysis of WorldView-2 Data

Analysis of high-resolution VNIR (visible and near-infrared) data was completed using the commercial WV-2 satellite data. Images from WV-2 are acquired in the visible and near-infrared region of the electromagnetic spectrum at a spatial resolution of 1.2 m. The presence of the near-infrared band and high spatial resolution makes the dataset suitable for detailed vegetation mapping. Data were acquired during May 2010 and defined vegetation growth anomalies associated with geothermally heated ground (Figure 10). This work was validated with shallow-temperature survey measurements during the 2011 and 2012 field seasons that outlined the extent of the shallow and very shallow thermal aquifers (Benoit et al., 2014a).

5.2 Airborne Forward Looking Infrared Surveys

Forward Looking Infrared Radiometer (FLIR) data collected from airborne surveys were used to calculate the geothermal potential of the PGS using a thermal budget model. Airborne surveys were conducted in fall 2010 and spring 2011, and data were mosaicked and processed to create high-resolution optical and thermal images. Thermal data-processing algorithms used by the volcanology community were adapted to compute heat flux.

Airborne surveys were planned around high- and low-priority survey areas (Figure 11) to provide flexibility in case of poor weather conditions. The primary survey area covered a region approximately 27 km^2, centered on the main PGS site encompassing the most likely geothermal anomalies detected from the Landsat 7 ETM+ data (red polygons in Figure 11). The secondary survey area covered a region approximately 175 km^2, including the sites of the other thermal anomalies detected from Landsat.

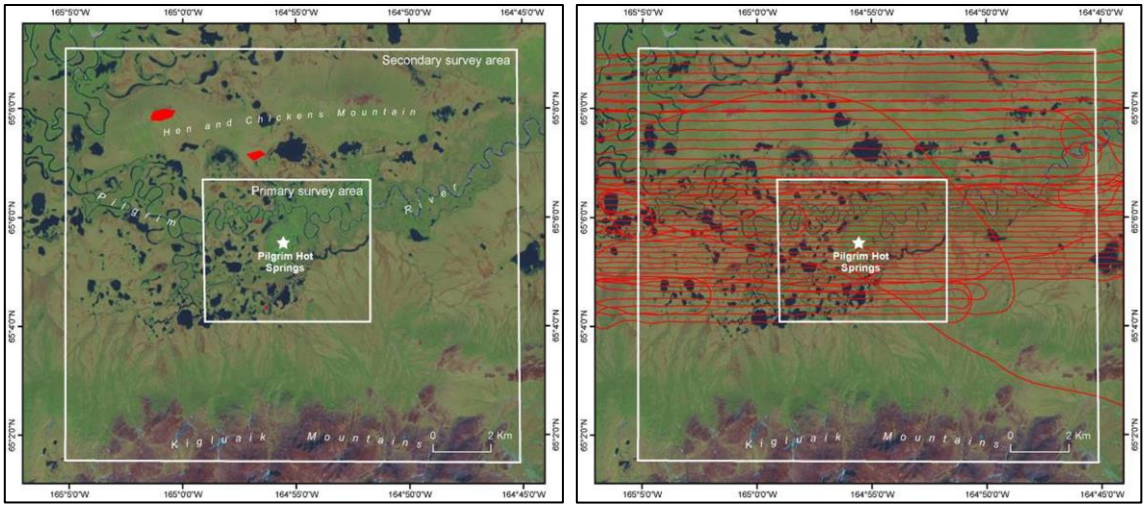


Figure 11. Landsat 7 satellite images of the Pilgrim Hot Springs region. The left image shows the extent of the primary and secondary survey areas; thermal anomalies detected from Landsat 7 satellite data are indicated by red filled polygons. On the right are the flight line locations for the aerial survey over the hot springs; cloud and turbulence restricted data acquisition over the southern half of the secondary survey area.

The first airborne survey was undertaken from September 9–15, 2010, using the Nome Airport as the base for flight operations. Favorable weather conditions enabled acquisition of data over the entire primary survey area and the northern portion of the secondary survey area. Flights over the southern portion of the secondary area were not possible due to persistent cloud cover and turbulence around the northern flanks of the Kigluaik Mountains. The FLIR images were successfully acquired along all the flight lines shown in Figure 11. Optical imagery was acquired for most of the flight lines; however, technical issues led to some gaps in the imagery in the northern part of the secondary survey area.

Thermal images were acquired using a FLIR Systems A320 camera that records emitted thermal infrared radiation in the 7.5 to 13 µm wavelength region. The FLIR has a 320 × 240 pixel sensor with a 25 µm sensor pitch and 18 mm lens. Visible images were acquired using a Nikon D700 digital camera with an 85 mm f/1.8 lens fixed at infinity. The FLIR and D700 cameras were positioned side-by-side in a fixed nadir-looking mount within the aircraft. The FLIR camera was set to continuously record thermal images at a frame rate of 5 Hz, and Topoflight Navigator software triggered the shutter of the D700 camera at pre-programmed intervals along the flight lines. A Crossbow NAV440 GPS/IMU unit recorded the position, roll, pitch, and yaw of the plane during the survey. A flying height of about 1000 m yielded an approximate spatial resolution of 1.4 m for the thermal imagery and 20 cm for the optical imagery.

The second airborne survey was flown in April 2011 and was restricted to a small area centered on the PGS property. During this survey, optical images were acquired at 20 cm resolution and FLIR data were acquired at 1.2 m spatial resolution. In-flight GPS data were recorded and time synced with the optical and FLIR image frames.

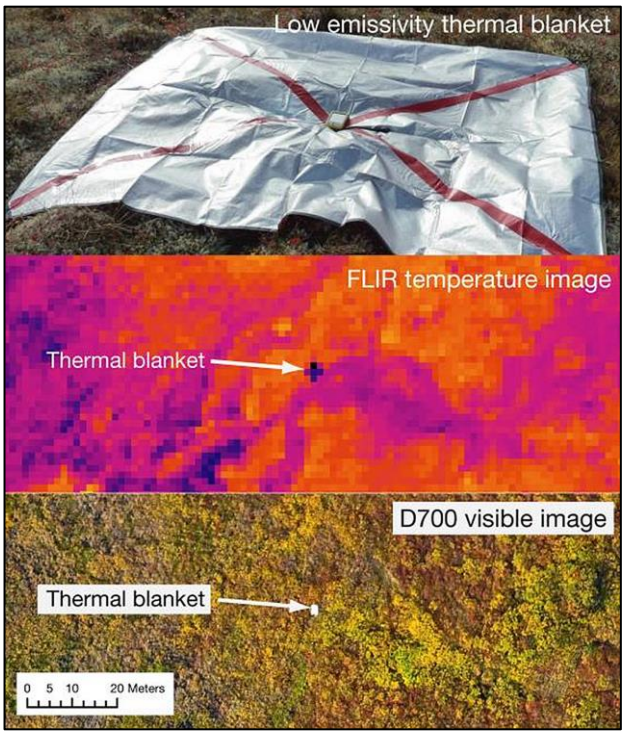


Figure 12. Low-emissivity thermal blankets (cold targets) were used as ground control points for registration of airborne FLIR and optical image data.

5.2.1 Field Calibration and Validation

Concurrent with the fall 2010 airborne survey, a field party of three undertook ground calibration and validation work in support of the airborne FLIR and optical data collection. Accurate geographic positions of well-spaced and notable ground features and thermal blankets (Figure 13) were recorded using portable Garmin and Trimble GPS receivers. These ground control points enabled georegistration of the FLIR and optical data. Thermal blankets provided geo-located "cool" targets readily delineated from the FLIR data (Figure 12).

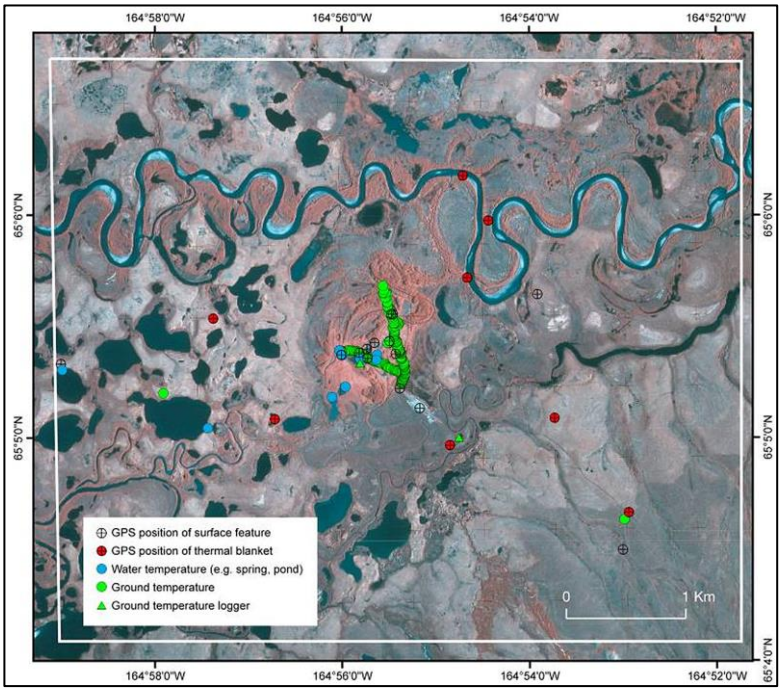


Figure 13. Field calibration and validation data sites for the primary target area of the Pilgrim Hot Springs survey; the data are overlain on a high resolution color near-infrared aerial photograph (AHAP) of the study area.

Wind speed, temperature, and humidity measurements were recorded throughout the collection period to calibrate the thermal data. Ground and water temperatures were recorded using TEGAM thermocouple sensors. Several ground temperature profiles were also recorded near the main hot spring site to compare against the retrieved FLIR surface temperature data, enabling further calibration as needed (Figure 13). Two HOBO temperature-logging systems provided continuous measurements of ground temperatures after the survey had been completed.

The region around the main hot springs site and an area about 3.5 km northeast along the Pilgrim River, where field observations provided some evidence for a geothermal anomaly, were the priority regions (Figure 15). Initial processing of the FLIR data required knowledge of the surface temperatures and humidity values as inputs to the ThermaCam research software. The average flying height was also integrated to correct for atmospheric absorption and emission.

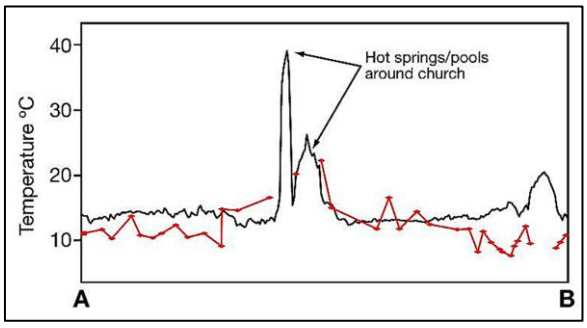


Figure 14. Comparison of a FLIR-derived temperatures profile (black line) with a field temperature profile (red line) for a selected profile line.

A comparison of collected FLIR surface temperature values with ground-based temperature profiles shows agreement to within about 5°C (Figure 14).

For the first airborne survey, the surface temperature images were manually georegistered to a high-resolution aerial photograph of the region from the Alaska High-Altitude Aerial Photography (AHAP) program and then mosaicked using ArcGIS software. There was significant overlap of the individual FLIR frames, associated with the 5 Hz acquisition rate. A high-quality mosaic

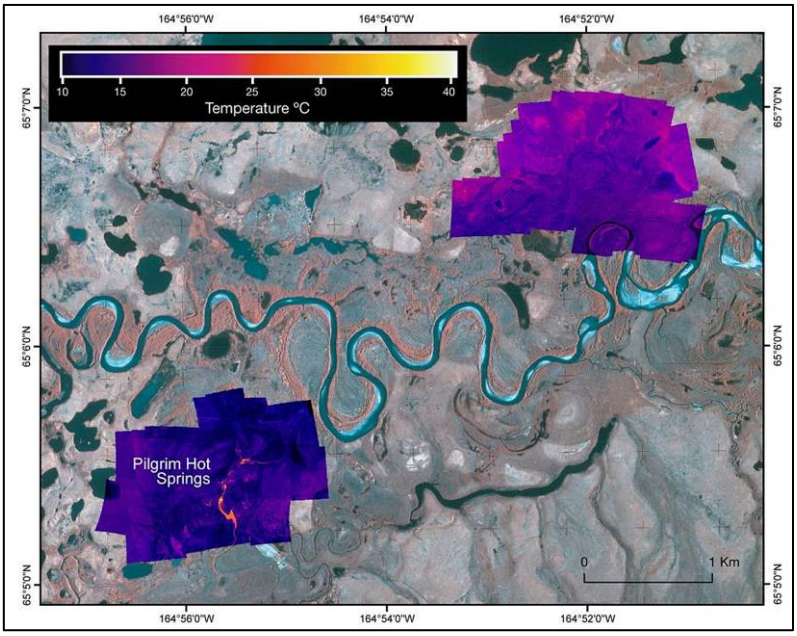


Figure 15. Mosaicked FLIR surface temperature data for the main Pilgrim Hot Springs site (bottom left) and possible geothermal area to the northeast (top right).

image was obtained using every fifth image. Color in the visible images was adjusted to improve the contrast, then georeferenced against the AHAP aerial photograph and mosaicked together with a minimum of overlap.

A semi-automated methodology was used to mosaic the spring 2011 images. The in-flight time synced GPS information was synchronized with the optical and FLIR sensor systems to georeference each image. To mosaic the images together, 2d3 software was used. Due to logistical challenges, the second round of field validation work was delayed until August 2011.

This fieldwork included:

- Gathering in situ measurements of hot spring temperatures.
- Validating the locations of springs mapped from FLIR data, and acquiring in situ thermal images of hot springs and pools.
- Measuring the outflow rate of hot springs.
- Validating the extent of snowmelt anomalies and inferred geothermally heated ground using 1.20 cm shallow temperature probes.
- Recording the temperature and conductivity of the Pilgrim River as well as local streams and locating outflow of saline geothermal waters.

5.2.2 Mapping Using Airborne Images

The main surface geothermal features such as hot springs, wells, pools, and areas of hot ground can be clearly delineated using the fall 2010 FLIR imagery with its 1.3 m resolution. The surface water temperatures in the images are as high as 40.5°C (105°F). The FLIR imagery helped

researchers to delineate geothermal features that would be difficult to map using visual imagery alone. Examples of such features include:

- Upwelling thermal plumes within pools of water
- Temperature gradients within pools and streams indicating the flow paths and mixing of hot and cool waters
- Subtle thermal features that may represent previously unmapped small springs
- Areas of hot ground away from the main spring complex.

The optical images acquired during the same period provide useful complementary information, especially about land cover in the area (Figure 16).

The analysis of the FLIR data from the area northeast of the main PHS site (Figure 15) provided little evidence for current geothermal activity. The range of surface temperatures is consistent with the different surface types (vegetation, soil, water ponds), and there are no obvious thermal anomalies. Nevertheless, the ground cover present in this region is similar to the ground cover near the hot springs, and it is not found elsewhere in the region.

The April 2011 survey was completed in early spring when the region usually is still covered by a thick blanket of snow. The survey timing proved useful for mapping areas of snowmelt (Figure 17), a direct indicator of surface heating from the very shallow geothermal aquifer. Snowmelt areas also correspond to permafrost-free areas and anomalous vegetation growth not regularly found on the Seward Peninsula. The spring FLIR data were more useful than the fall FLIR data in identifying the limits of the very shallow thermal aquifer (Figure 17).

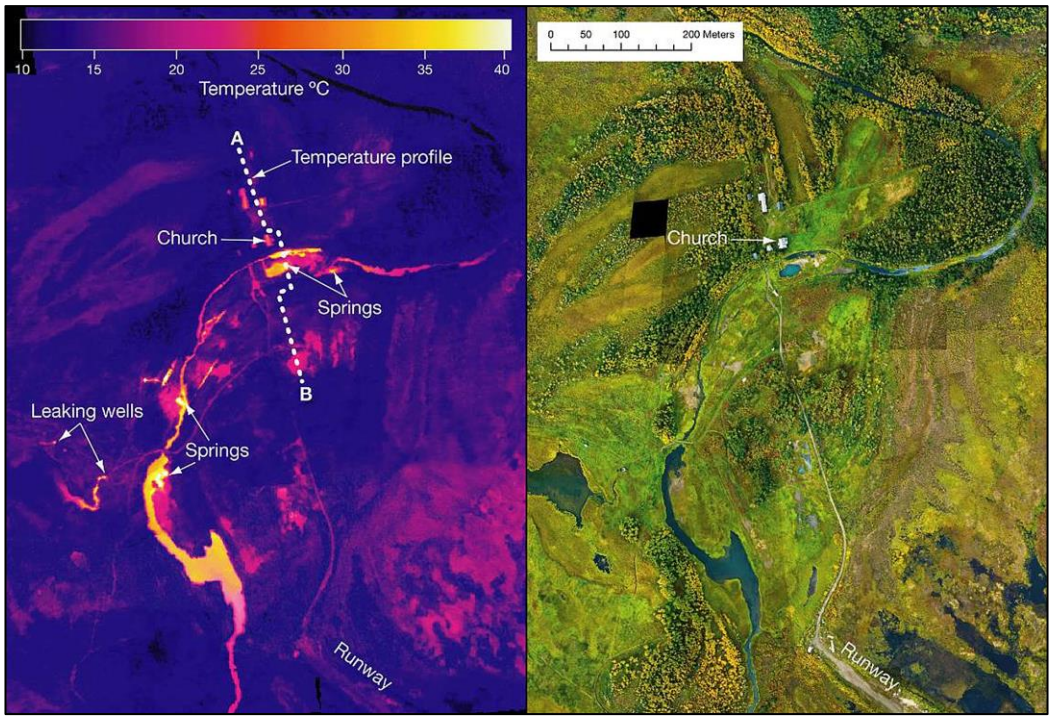


Figure 16. FLIR (left) and optical data (right) from the fall 2010 survey over the main Pilgrim Hot Springs site. The FLIR data effectively delineate surface features associated with the geothermal system, such as hot springs, pools, and warm ground.

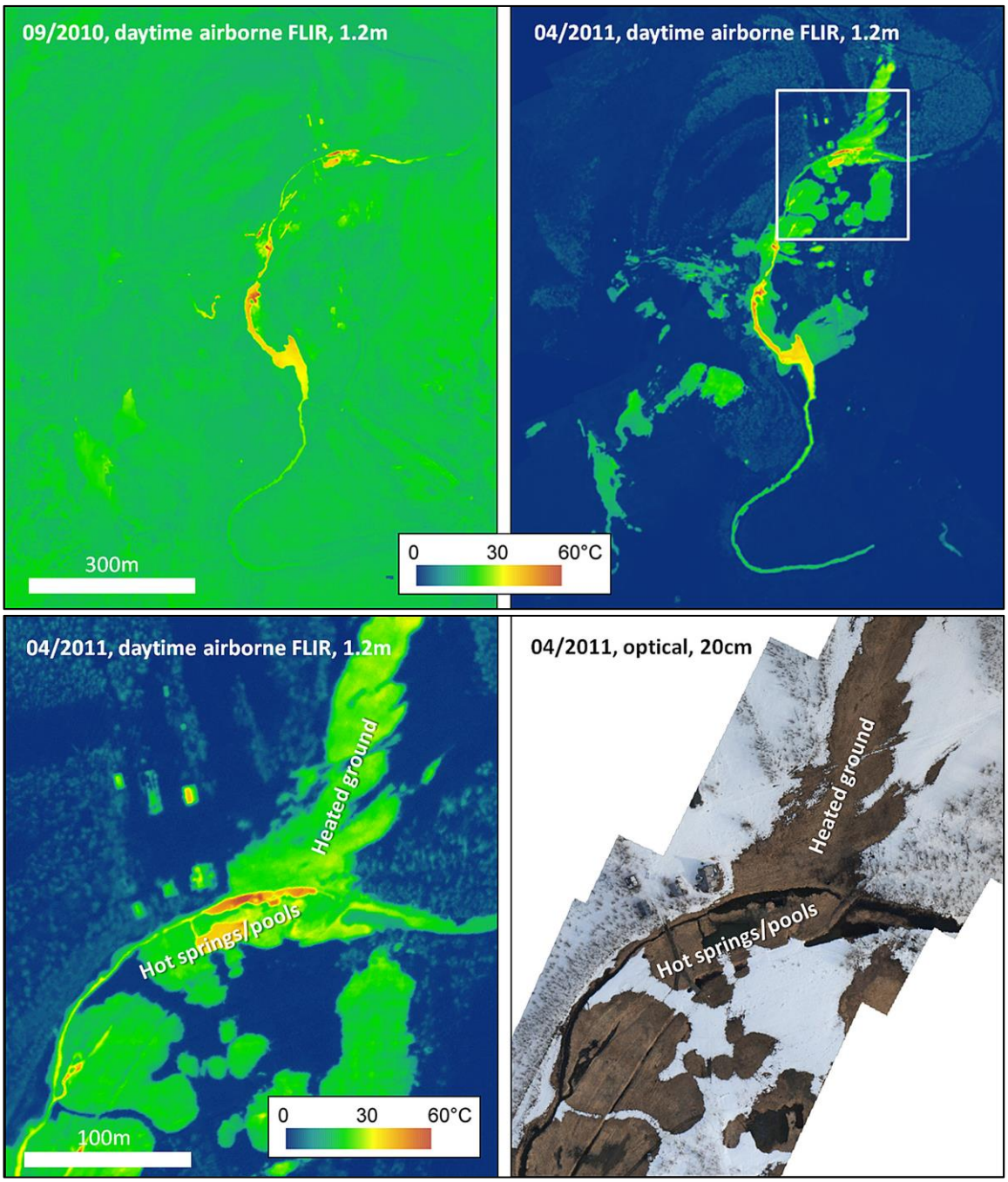


Figure 17. Processed airborne images for parts of the study area. Top left: Temperature map from September 2010 FLIR survey. Top right: Temperature map from April 2011 FLIR survey. The April 2011 image more clearly reveals the limits of the shallow hot aquifer. Bottom left: Subset of the April 2011 image, indicated with a white box in top right panel. Bottom right: Optical image of the area corresponding to the image in the bottom left panel. The optical image reveals underlying soils (brown), as the snow has melted over these areas due to geothermal heating.

5.2.3 Heat Budget Modeling

A heat budget model was developed to quantify the radiant and convective heat flux and the flow rate of surface geothermal waters (Figure 18).

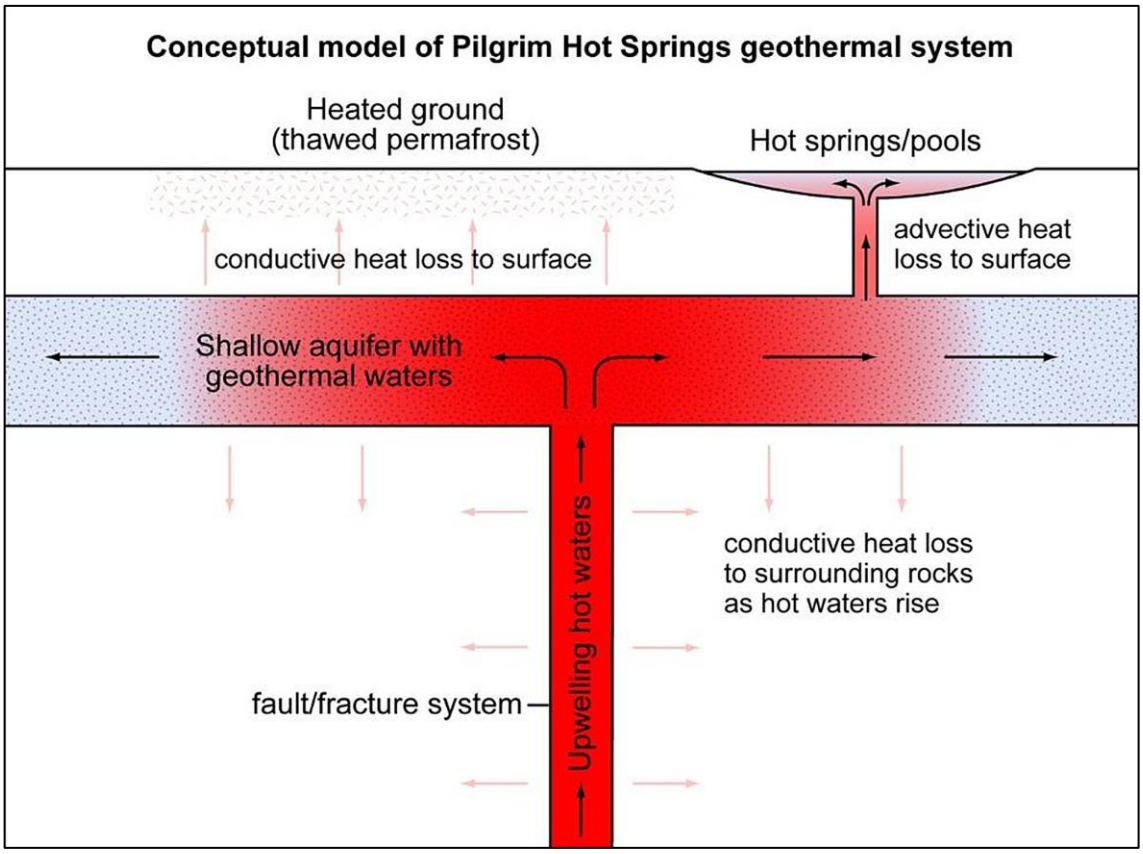


Figure 18. A simplified conceptual model of the Pilgrim geothermal system used for numerical calculations of thermal flux from the processed FLIR data.

An initial model treated all hot pixels in the same way, regardless of whether they were associated with heated ground or hot water. Upon further examination, it became clear that hot ground and hot water gain and lose heat differently, and the thermal flux estimations for these features need different approaches. An improved heat flux modeling process was developed (Haselwimmer et al., 2011; Haselwimmer and Prakash, 2011). Both approaches are discussed in this section.

Initially, heat loss was estimated from the geothermal system by correcting for background temperature and the natural radiative heat loss of the earth and sun. Using a modified Stefan-Boltzmann equation (see below) with fixed values for surface emissivity and background temperature, the radiant flux was calculated for each pixel representing a geothermal feature:

$$M = \varepsilon\sigma(Th^4 - Tb^4)$$

where

M = radiant flux density (W/m^2)
ε = emissivity
σ = Stefan-Boltzmann constant
Th^4 = temperature of pixel in Kelvin
Tb^4 =temperature of background in Kelvin

To delineate the pixels associated with geothermal areas, a mask was created using a temperature threshold applied to the FLIR image. The background temperature value used in the thermal flux calculation was the average temperature value from the non-geothermal areas (not including anthropogenic and other non-geothermal temperature anomalies). The radiant flux value for each geothermal pixel was summed to calculate the total radiant flux, which amounted to 6.2×10^5 Watts. This method underestimated the thermal flux associated with the hot waters, so a sensitivity analysis was not performed (Haselwimmer et al., 2011).

Upon further consideration, we concluded that the convective component was likely the dominant heat transfer component. Later model development attempted to establish methods for estimating the convective heat flux from geothermal hot springs and pools. Pixels associated with hot waters and hot ground are easily separated on the FLIR image mosaics. These water pixels were isolated for further analysis.

Adapting an approach applied to volcanic crater lakes (e.g., Patrick et al., 2004), an energy budget model was developed to quantify the convective heat flux along with the flow rate of the surface geothermal waters at PHS (Figure 19). Complete details about the thermal model used for the quantitative analysis are presented in Haselwimmer and Prakash (2011) and are briefly

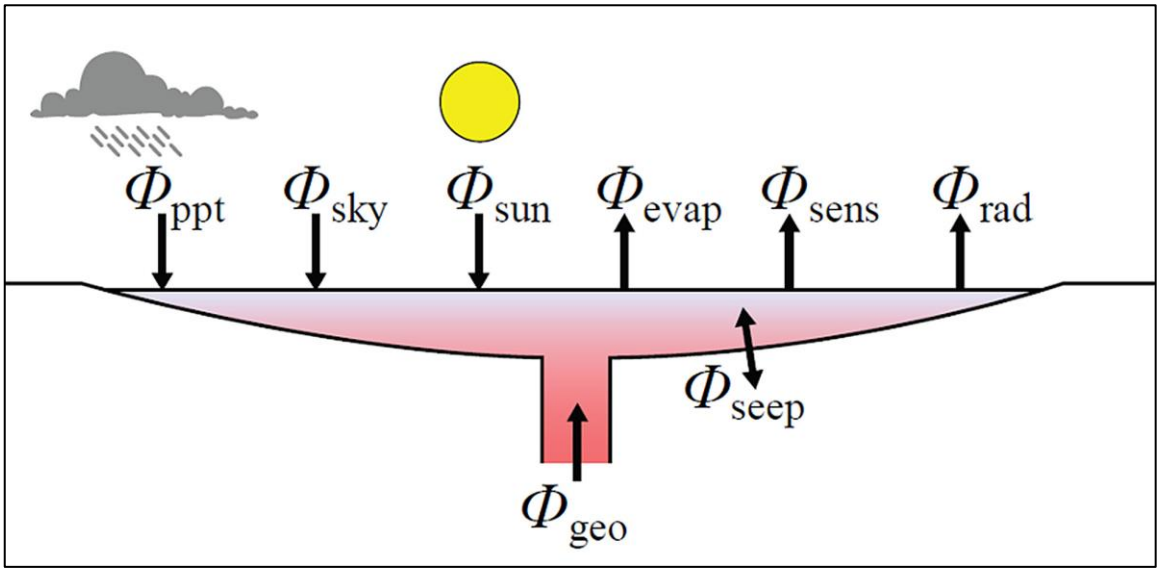


Figure 19. A total surface energy budget model for the Pilgrim geothermal system. Refer to the main text for an explanation of each term.

described below.
The total heat budget for a water body (in Watts) expressed as

$$\Phi_{total} = \Phi_{geo} + \Phi_{ppt} + \Phi_{seep} + \Phi_{evap} + \Phi_{sens} + \Phi_{rad} + \Phi_{sun} + \Phi_{sky}$$

where

Φ_{geo} = heat input from geothermal fluids
Φ_{ppt} = heat input from precipitation
Φ_{seep}= heat flux from seepage
Φ_{evap}= heat loss from evaporation
Φ_{sens}= heat loss via sensible heat transfer
Φ_{rad} = heat loss by radiation
Φ_{sun} = heat input from solar radiation
Φ_{sky} = heat input from atmospheric radiation

Simplifying this model further, Φ_{ppt} and Φ_{seep} were removed, as these heat fluxes are small.

The temperature of surface non-geothermal waters was used to account for Φ_{sun} and Φ_{sky} terms. Pixels associated with geothermal surface waters were isolated, and the geothermal heat flux density was calculated in W/m^2on a pixel-by-pixel basis using the following equation:

$$q_{geo} = (q_{rad} + q_{evap} + q_{sens}) - (q_{radAmb} + q_{evapAmb} + q_{sensAmb})$$

where
q_{rad}, q_{evap}, q_{sens} and q_{radAmb}, $q_{evapAmb}$, $q_{sensAmb}$ are radiative, evaporative, and sensible heat fluxes for each pixel at the ambient temperature of non-geothermal waters.

Further, q_{rad}, the radiative heat flux, was calculated using the Stefan-Boltzmann equation:

$$q_{rad} = \varepsilon\sigma T^4$$

where

$\sigma = 5.67 \times 10^{-8}$ (Stefan-Boltzmann constant in $W/m^2 K^{-4}$)
ε = water emissivity(0.98)
T = water temperature (°C).

Also, $q_{evap+sens}$, the evaporative and sensible heat fluxes, were calculated using the formula presented by Ryan et al. (1974):

$$q_{evap+sens} = [\lambda(T_{sv}-T_{av})^{1/3} + b_o W_2][e_s - e_2 + C(T_s - T_a)]$$

where

$\lambda = 2.7$ (constant)
$b_o = 3.2$ (constant)
W_2 = wind speed at 2 m height (m/s)
e_s = vapor pressure of water at T_s (mbar)
e_2 = vapor pressure of water at 2 m height (mbar)
$C = 0.61$ (constant)
T_s = water surface temperature (°C)
T_a = air temperature (°C)
T_{sv} = virtual water surface temperature (°C)
T_{av} = virtual air temperature (°C)

This model was applied to both FLIR datasets. The total heat flux is the sum of heat fluxes for each pixel, representing the hot water at the surface.

Flow Rates

Assuming a fixed hot springs temperature of 81°C and water at the ambient air temperature, the flow rate (*V*) in m^3/s was calculated from the total geothermal heat flux (Φ_{geo}) using the following equation:

$$V = [\Phi_{geo} / (h_s - h_{amb})] / \rho_w$$

where

h_s = enthalpy of hot spring water
h_{amb} = enthalpy of water at ambient temperature
ρ_w = density of water (kg/m^3)

Heat Budget Modeling Results

The computed heat flux/flow rate estimates are generally higher than the in situ observations. This difference is likely caused by underestimating in situ measurements of the total outflow rate of the hot springs. These calculated results are quite conservative as they assume a wind speed of 0 m/s, which is unrealistic for the PHS area. The nearest meteorological station about 50 km northeast of PHS reports an average annual wind speed of 3.18 m/s. Therefore, the true heat flux is likely to be higher than estimated in the following table:

Table 1. FLIR heat flux estimates.

Source of estimate	Total heat flux	Flow rate	Notes
Airborne FLIR - Fall 2010	**3.62 MW**	**0.43 feet^3/s**	Conservative estimate assuming wind = 0
Airborne FLIR - Spring 2011	**3.67 MW**	**0.44 feet^3/s**	Conservative estimate assuming wind = 0
1979 flow rate measurement [9]	2.00 MW	0.15 feet^3/s	Hot stream gauged at Site 1 (See panel 3)
1983 flow rate measurement [10]	-	0.20 - 0.50 feet^3/s	Hot stream gauged at Site 1
08/2011 flow rate measurement	-	0.39 feet^3/s	Hot stream gauged at Site 2

Heat flux estimates are sensitive to wind speeds, as shown in Figure 20. Using a wind speed of 1.5 m/s, the heat flux estimated using FLIR data is 6.96 MW, which corresponds to a flow rate of 0.90 ft^3/s, equivalent to 404 gpm.

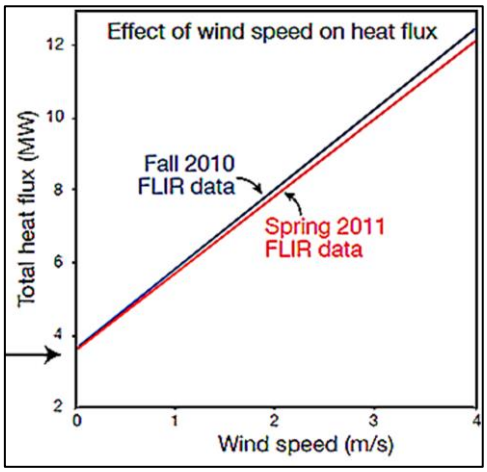


Figure 20. The effect of wind speed on heat flux is estimated from fall 2010 and spring 2011 FLIR data for the Pilgrim geothermal system area.

5.2.4 Discussion

Aerial FLIR surveys have been a useful tool in the initial stages of geothermal exploration at PHS. For geothermal exploration using aerial FLIR surveys at systems similar to PHS, 1 to 2 m spatial resolution appears to be sufficient to estimate heat flux using the steps outlined above.

A springtime FLIR survey is likely more useful than a fall FLIR survey for identifying blind geothermal resources in high-latitude snow-covered regions where the hot ground contrasts well with cooler snow-covered areas.

Combined optical and FLIR airborne surveys offer a relatively inexpensive addition to geothermal resource exploration for targeting further field-based data collection strategies. In logistically challenging areas, such as many areas of Alaska, these surveys may be the most cost-effective method for the first phase of geothermal exploration.

While airborne surveys were limited to the use of optical and FLIR cameras, the future use of multispectral or hyperspectral imaging sensors, consisting of several spectral bands in the near- and shortwave-infrared regions, may better characterize the vegetation signatures and alteration minerals associated with the geothermal activity.

Heat budget modeling performed in this study estimated that heat flux and flow rates of geothermal waters can be transferred to the characterization of both low-temperature and high-temperature geothermal resources.

6. GEOPHYSICAL SURVEYS

In collaboration with the USGS, ACEP conducted geophysical surveys between 2010 and 2013, including a gravity survey in 2010, a high-resolution airborne magnetic and electromagnetic (EM) survey in 2011, and a magnetotellurics (MT) survey in 2012. The goal of these surveys was to provide the regional geophysical framework of the area and help delineate key local and regional structures controlling hydrothermal fluid flow, and characterize the basin geometry and depth to bedrock.

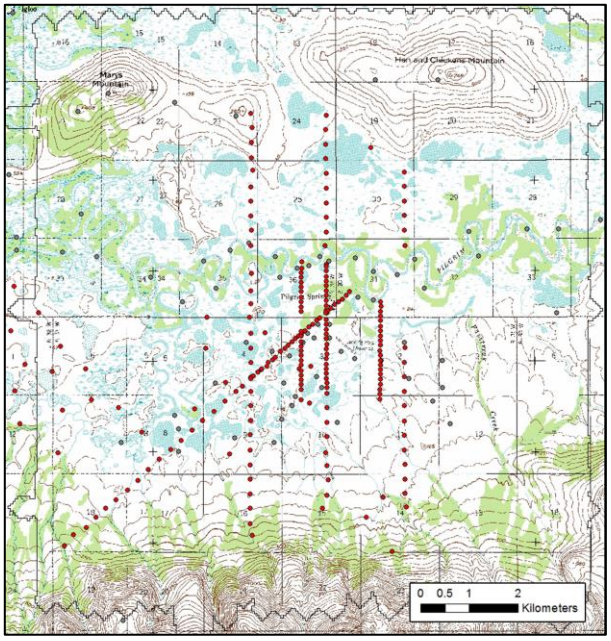


Figure 21. Gravity stations are labeled on a topographic map of the Pilgrim Hot Springs region. Stations shown by red dots are from the 2010 survey. The earlier stations are shown by gray dots.

6.1 Gravity Surveys

The PGS gravity data were obtained in 1979 and 1980 (Kienle and Lockhart, 1980; Lockhart, 1981) and in 2010 by the USGS. In 1979, 122 stations were occupied along several traverses made on foot and by helicopter, boat, and car. In 1980, one 43 km long north–south regional line was run through PHS (Figure 21). Stations in 1979 were generally along lines, and most stations were 1 to 3 km apart. In the immediate vicinity of the thermal springs, stations were more closely spaced. Station spacing along the 1980 line was anywhere from 1 to 5 km apart. These surveys lacked precise elevation control. Two sets of closely spaced gravity contours trending east–northeast and north–northeast and intersecting a short distance southwest of the thermal area were hypothesized to result from a down dropped basement fault block (Kienle and Lockhart, 1980).

The 295 USGS gravity stations in 2010 were located along five north–south lines and one northeast–southeast line, with an additional scattering of more regional points. These data have been merged with the 1979 and 1980 data (Glen et al., 2014). The additional data generally confirmed the earlier contour pattern, with a pronounced gravity low centered about 4 km southwest of the thermal springs being the dominant feature in the valley (Figure 22).The second and more dominant regional gravity feature is along the Kigluaik Mountains range front 2½ miles south of the thermal springs.

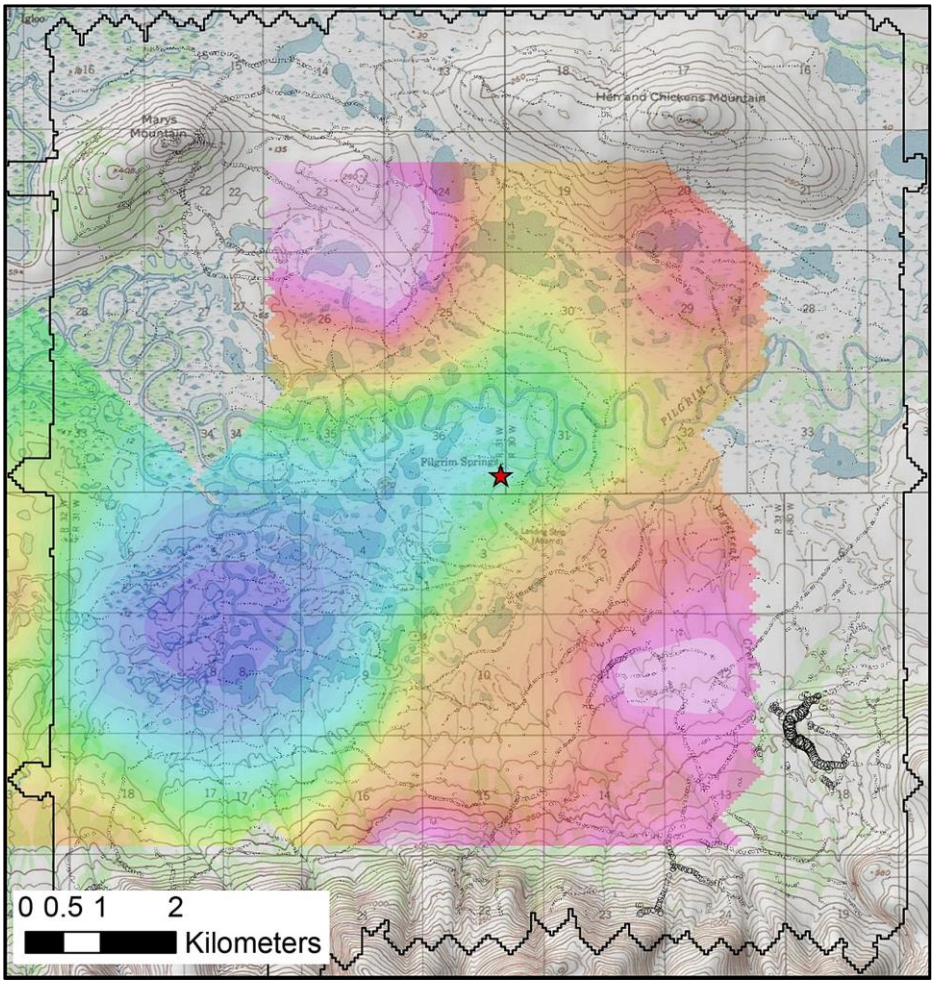


Figure 22. Isostatic residual gravity map from Glen et al. (2014) used to map the structural basin. Light blue (immediately below Pilgrim Hot Springs) correlates to a basin depth to basement at 320 m (corroborated with drilling contact). Southwest of the hot springs, the deeper basin, indicated by dark blue, is estimated at about 800 m depth. Shallow areas are represented by red.

6.2 Airborne Magnetic and Electromagnetic Surveys

In October 2011, airborne and electromagnetic surveys were flown over the hot springs area. The USGS was primarily responsible for managing this program and interpreting the data. Survey details can be found in Appendix E. About 556 km were flown along north–south lines with east–west tie lines. The mean survey drape of the instrument was 38.2 m. The contractor, Fugro, performed the basic data processing, and the USGS applied additional processing with derivative and filtering methods (Glen et al., 2014).

Aeromagnetic data usually provide the most complex and ambiguous geophysical data normally used in geothermal exploration, and the PHS aeromagnetic results live up to this reputation. Glen et al. (2014) note magnetic highs in the vicinity of the PGS and further northwest, and a pronounced magnetic low along the Kigluaik Mountains range front on a reduced-to-pole

magnetic field map (Figure 23). A residual reduced-to-pole magnetic map shows a more complicated pattern of shallow-sourced anomalies, with a small magnetic low in the immediate vicinity of the thermal springs (Figure 23). Two narrow northeast–southwest-trending anomalies northwest and north–northeast of the hot springs have magnetic signatures in good alignment with mapped mafic dikes in the Kigluaik Mountains (Glen et al., 2014) and may represent possible dikes that either have not yet been found on the surface or do not quite reach the surface.

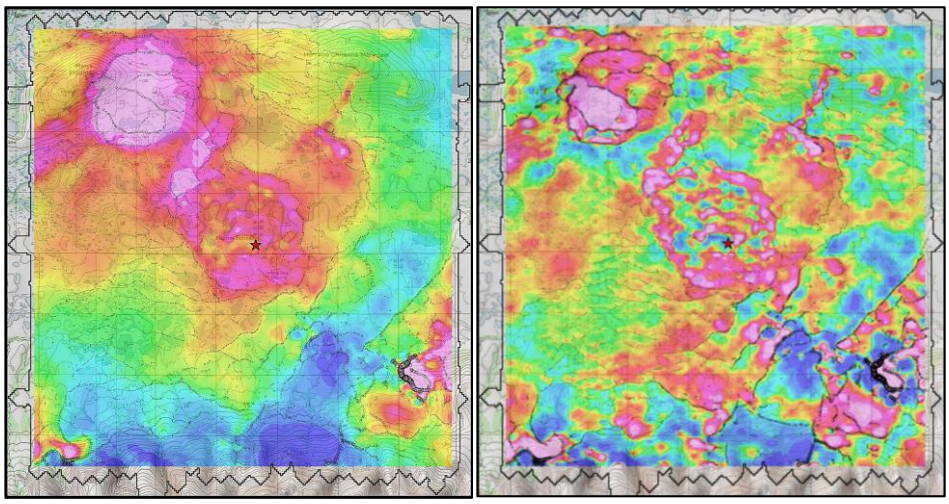


Figure 23. Magnetic field maps from Glen et al. (2014). Magnetic highs appear as reds and pinks, gravity lows as blues and purples, in the reduced-to-pole magnetic anomaly map (left). Magnetic highs appear as reds and pinks, gravity lows as blues and purples, in the differential reduced-to-pole map (right).

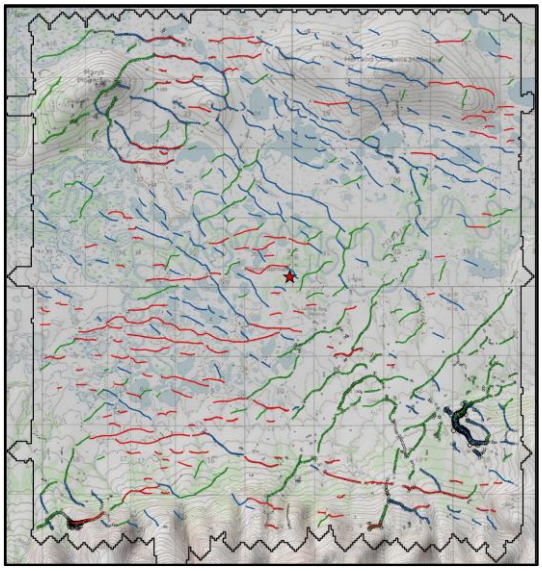


Figure 24. Magnetic lineations interpreted from maximum horizontal gradients of pseudogravity. Colored by trend (EW, red; NW, blue; NE, green). From Glen et al. (2014).

A magnetic lineation map based on maximum horizontal gradients shows that the PGS is in a somewhat unique position, where two trends terminate as they intersect a third trend. A broad east–west trend is largely terminated by a northeast–southwest trend, and a northwest–southeast trend is terminated by a northeasterly trend (Figure 24). The same generalized trends are present on the isostatic gravity map (Figure 22), giving additional credence to these regional magnetic trends.

The depth extent of the electromagnetic survey is in the range of 20 to 125 m (Figure 3 in Glen et al., 2014). The most striking low resistivity in the survey area is centered on the PGS and is approximately co-located with the thawed area at shallow depths near 15 m (Figure 25). A much larger but less intense shallow resistivity anomaly is located north and northeast of the center of the PGS, and overlies the known, but

largely unexplored, northeastern thermal anomaly. At a slightly greater depth of 35 m, the northeastern thermal anomaly area is the dominant low-resistivity area, and the core of the known PGS is no longer particularly low in resistivity (Figure 25). The presumed upflow area is in this region and will be discussed later in this report.

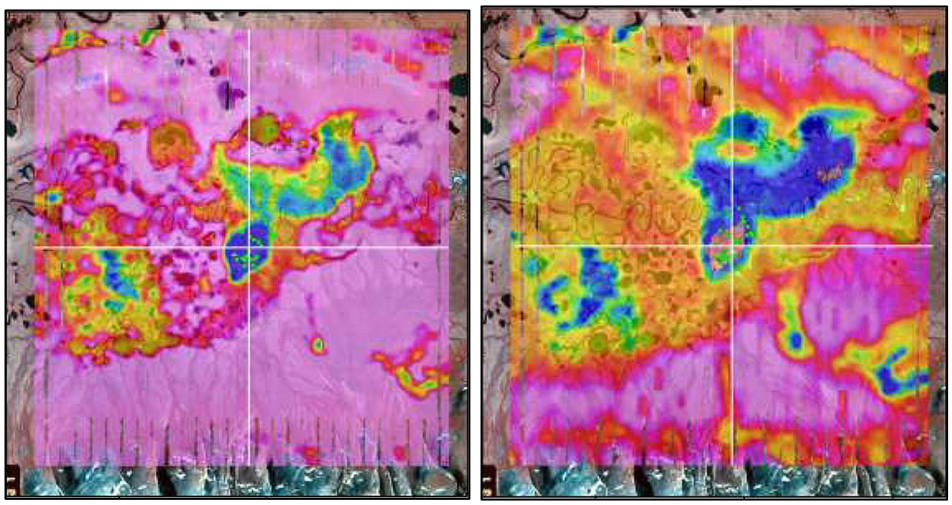


Figure 25. Airborne EM resistivity slices shown at 15 m (left) and at 35 m (right). From Glen et al. (2014).

Two areas west–southwest and southwest of the PGS have interesting low-resistivity values at a depth of 15 m, and it is speculated that they result from graphitic metamorphic rocks (Glen et al., 2014). The higher-resistivity rocks reflect metamorphic bedrock and coarser-grained glacial outwash sediments. Unfortunately, the electromagnetic survey was not capable of penetrating to depths near the PGS, which would have helped locate the upwelling zone, but the survey does offer the possibility that other and possibly even larger thermal areas are in the Pilgrim Valley.

6.3 Magnetotellurics Survey

In August 2012, Fugro obtained 59 magnetotellurics (MT) soundings at the PGS. Spacing between sites varied from about 300 feet to about 1800 feet, with less-dense coverage away from the center of the known thermal anomaly (Figure 26). The outer ring of MT sites was specifically chosen to extend beyond the known limits of the shallow thermal anomaly in all directions except toward the northeast. No sites were occupied north of the Pilgrim River, as the intent was to locate the upwelling of the PGS, not to study the more inaccessible northeastern thermal anomaly.

At a depth of 25 m, approximately the known depth of the shallow thermal aquifer, the MT data show a nearly circular low-resistivity area about 900 m in diameter, with resistivities as low as 2 Ohm-m. The MT is probably responding to the high salinity of the PHS thermal fluid. The area with resistivity less than about 5 Ohm-m is a good approximation of the 49°C (120°F) temperature contour defining the shallow thermal aquifer. Above about 5 Ohm-m, the resistivity contours are tight, rapidly climbing to values above 100 Ohm-m. The high resistivity values probably reflect the low-salinity permafrost surrounding the thermal anomaly.

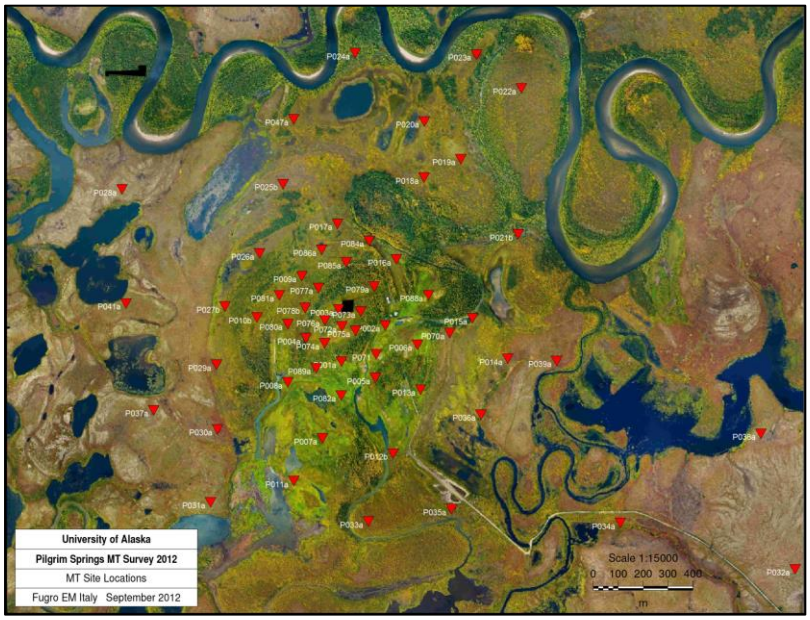


Figure 26. Magnetotellurics site locations.

The sharp margins of the MT anomaly are also clearly defined in cross-sectional view (Figure 27). The temperature contours at shallow depths generally behave in a sharply bounded fashion, near the edge of the shallow thermal aquifer (Figure 28). The obvious exception to the sharp boundaries for both datasets is toward the northeast, where the shallow thermal aquifer has its greatest known length. The MT anomaly also extends that direction. The MT data show a short "nose" extending southwest of the PS-5 hole that was not picked up by the temperature data. At a depth of 50 m, a short distance below the shallow thermal aquifer the resistivity increased slightly, but the circular anomaly core is still present (Figure 28).

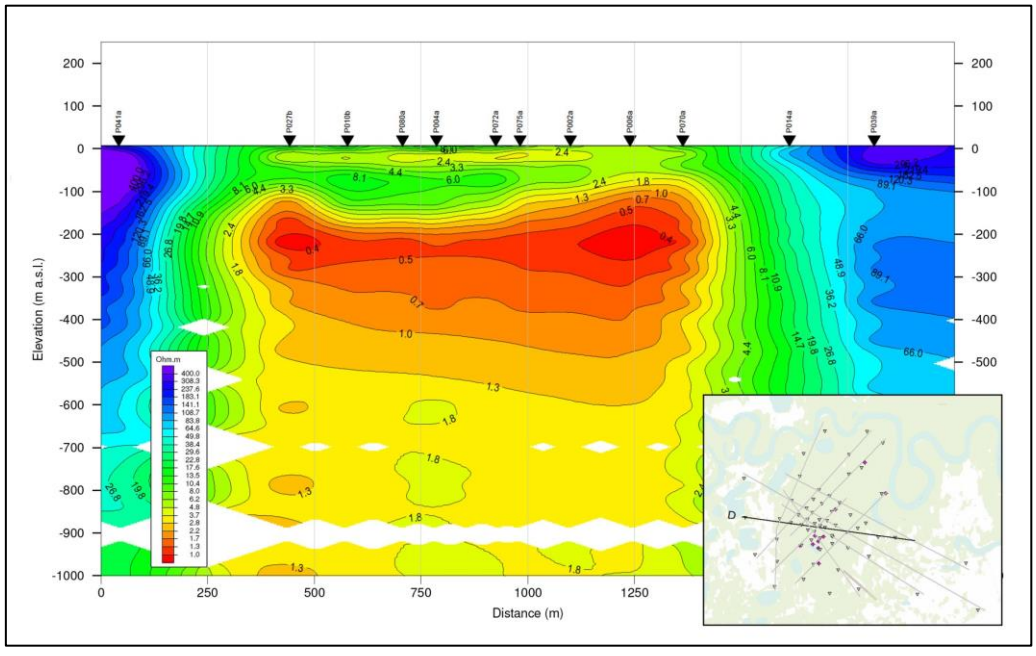


Figure 27. Resistivity at Profile D from a 1D MT inversion.

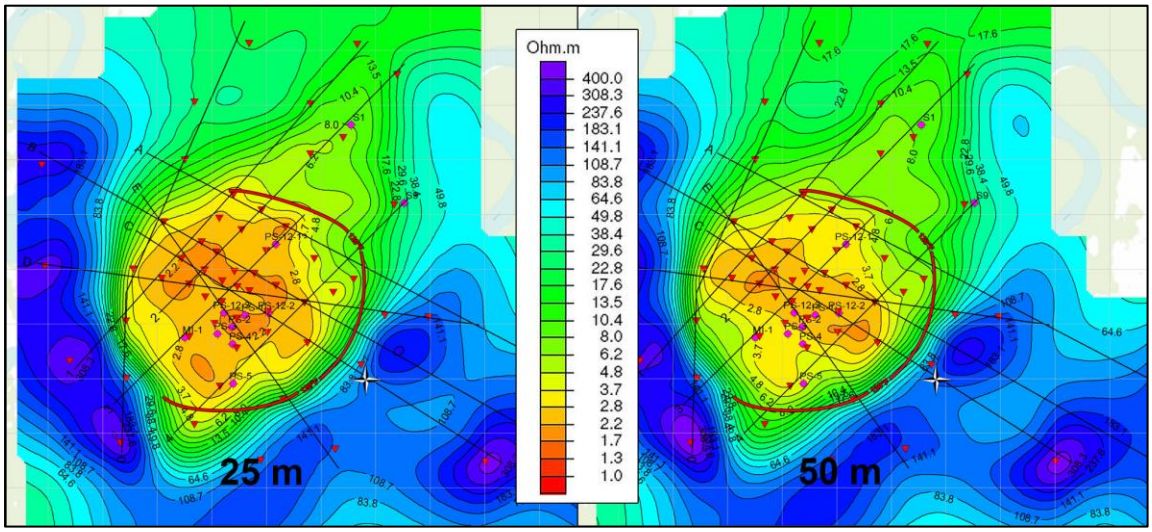


Figure 28. Resistivity maps at 25 m and 50 m from the blind 3D MT inversion. The red line represents the 49°C (120°F) temperature contour in the shallow thermal aquifer. The straight black lines are the MT transects.

The thermal minimum in the deeper PGS wells occurs near a depth of 100 m. At this depth, the MT shows the smallest areal extent of less than 3 Ohm-m resistivity of any of the depths (Figure 29). The lowest resistivity values are now centered about 85 m southeast of well PS-12-2. At depths between 100 and 300 m, which are within the Quaternary alluvium, the area of less than 5 Ohm-m gradually expands and moves toward the northwest (Figure 29). Between depths of 300 and 500 m, in the metamorphic bedrock, the lowest resistivity values shift noticeably about 0.5 km to the southwest; by 500 m, they are centered beneath well PS-5 (Figure 29 and Figure 30). By a depth of 1000 m, the lowest resistivity values have radically shifted east and northwest of the shallow thermal anomaly (Figure 30).

Since the MT survey was run to help locate the upwelling zone, the question of whether this survey was successful must be addressed. While MT clearly succeeded in locating and outlining the shallow thermal anomaly, there is no clear evidence that MT located the thermal upwelling. The small volume of low-resistivity values near PS-12-2 at depths of 100 to 200 m within the alluvium cannot directly represent thermal upwelling, given the temperature profile of PS-12-2. The large horizontal shifts of low-resistivity areas below 300 m in metamorphic basement rocks may represent some larger-volume conductor(s) other than hot water. The full Fugro (2012) report, which discusses this topic in detail, is included as Appendix L.

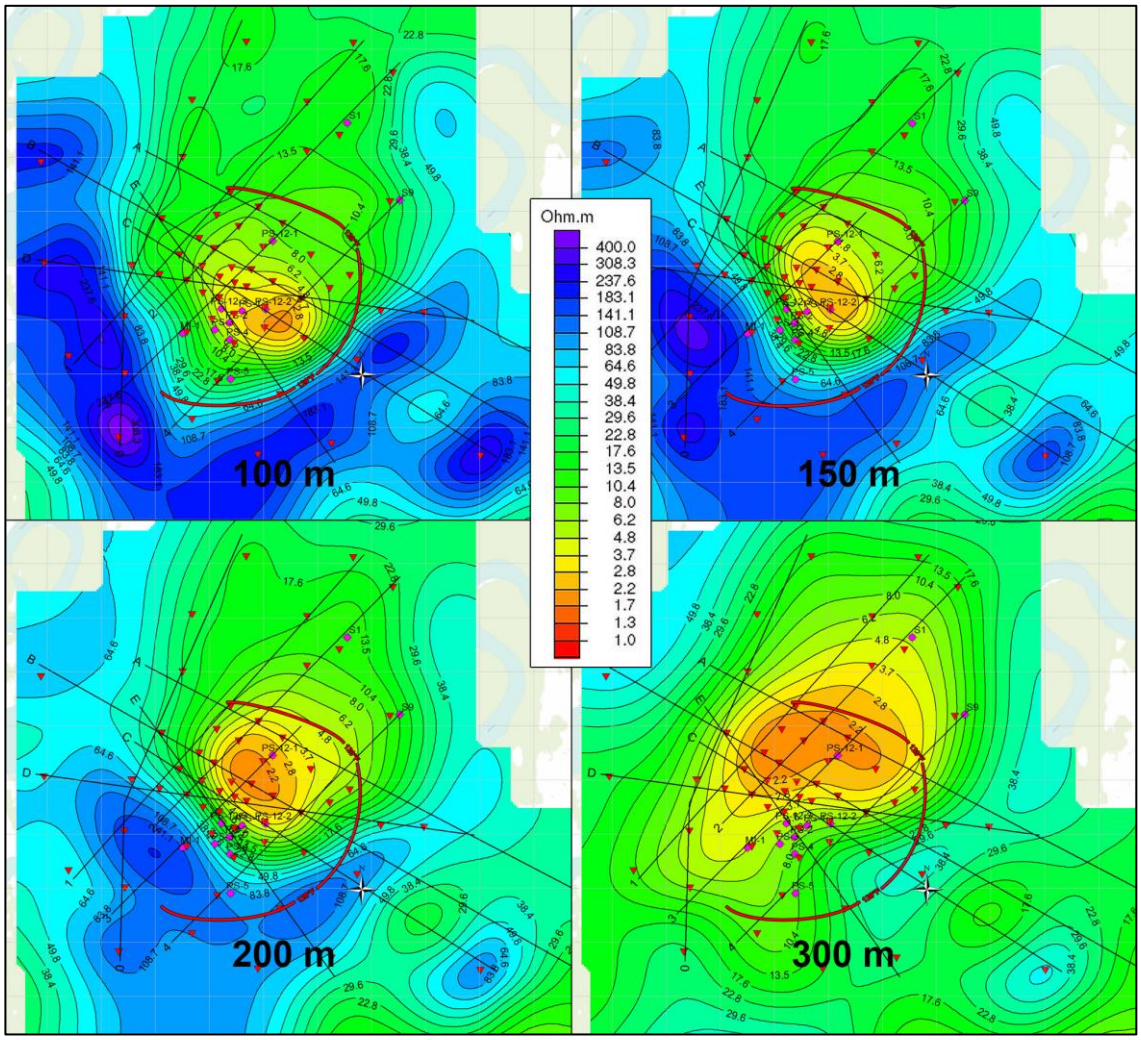


Figure 29. Resistivity maps at 100 m, 150 m, 200 m, and 300 m depths from the blind 3D MT inversion. The red line represents the 49°C (120°F) temperature contour in the shallow thermal aquifer.

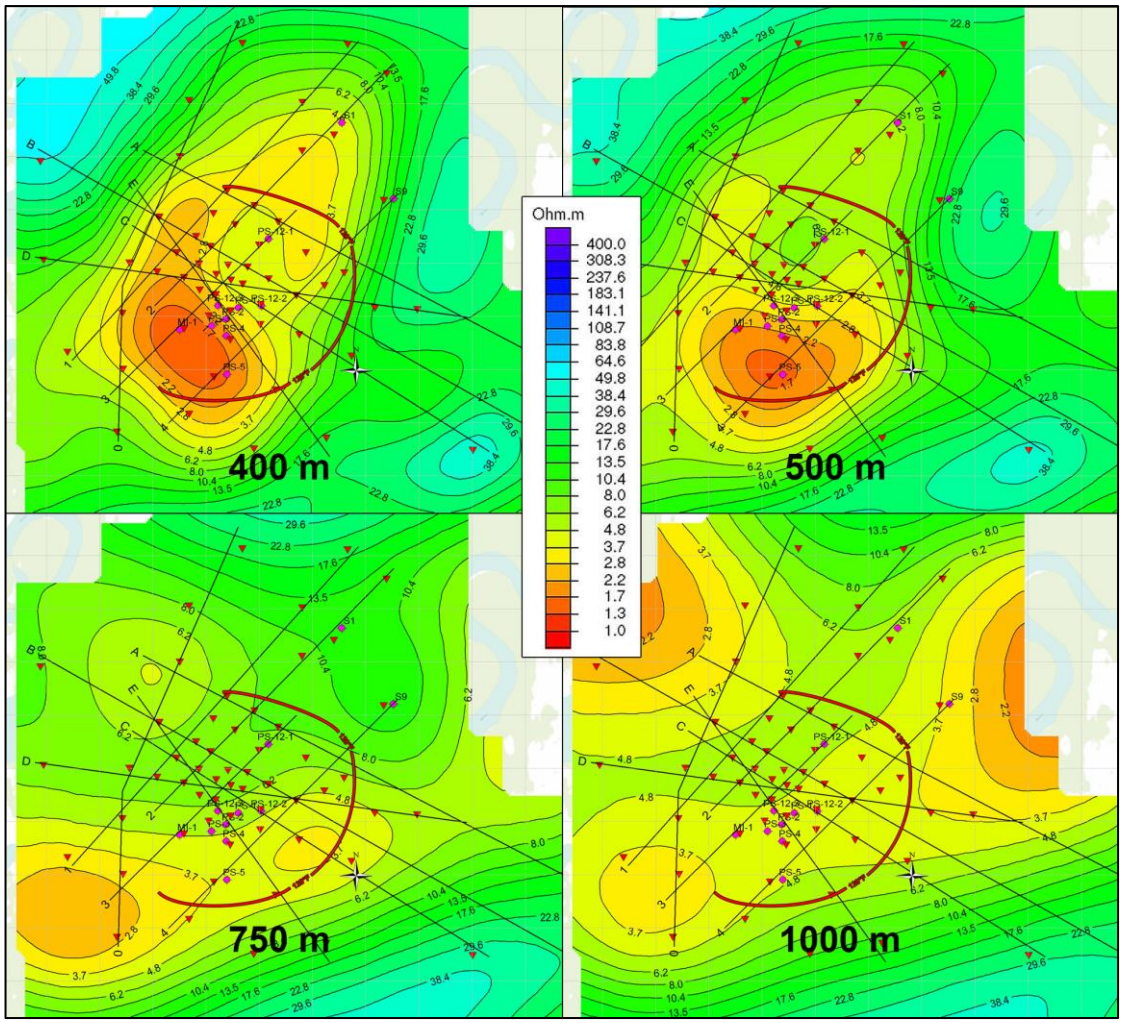


Figure 30. Resistivity maps at 400 m, 500 m, 750 m, and 1000 m depths from the blind 3D MT inversion. The red line represents the 49°C (120°F) temperature contour in the shallow thermal aquifer.

7. DRILLING ACTIVITIES

The bulk of the money and effort invested in the geothermal exploration project at PHS was used for drilling activities, with the aim of obtaining accurate subsurface temperature data and identifying the main upwelling zone. Drilling ranged from very shallow activities carried out with a simple gasoline-powered backpack drill, to large-diameter drilling that required a large rotary drill rig and mud circulation systems capable of drilling a 14-inch-diameter well to bedrock. Additionally, the valves on the wellheads of the wells drilled in 1979 and 1982 were replaced to cease uncontrolled artesian flows and allow the wells to be logged in a static state. The deep holes and wells that have been drilled at the site since 1979 are shown on Figure 4.

7.1 Permitting

Before any of the drilling activities described in this report could occur, a variety of permits and land usage agreements had to be secured. Permits were obtained in several phases as drilling plans were refined and new data were input into geothermal models of the area. Land use permits were also obtained so that UAF and its contractors could legally perform activities associated with geothermal exploration on the landholdings of various entities. The land use agreements, permits, and waivers that were obtained for this project are summarized in Table 2.

Table 2. Permits and approvals

Entity	Permit or Approval
Alaska Oil and Gas Conservation Commission	Permits to drill
Alaska Department of Environmental Conservation	Storage/discharge of drilling waste solids, Waste water discharge approval/ waiver
National Environmental Policy Act	Project review
Department of Natural Resources	Temporary water use permit for drilling makeup water and flow testing
Alaska Department of Fish and Game	Project approval, Waiver of fish habitat permit for flow test
U.S. Bureau of Land Management	Permit for road or trail improvements, Gravel pit use
U.S .Army Corp of Engineers	Verification that project is in Nationwide Permit 6 accordance
Mary's Igloo Native Corporation	Land use permit
Unaatuq, LLC	Exploration license
Bering Straits Native Corporation	Exploration license
State Historic Preservation Office	Finding of no historic properties effected

7.2 Legacy Wellhead Repairs

During 1979 and 1982, six wells penetrating the shallow thermal aquifer were drilled to depths of 1000 feet. These wells were never plugged and were abandoned. Due to a lack of maintenance, the wellheads were in extremely poor condition when examined by ACEP in 2009. The wellheads had to be repaired to control artesian flows and permit new static temperature logs and water samples.

During an initial site visit in July of 2010, an assessment of each well was made and work plans were developed. Wellhead repairs occurred September 13–18, 2010. The team completing the repairs was able to replace the master gate valves on wells PS-1, PS-3, PS-4, and MI-1. Wells PS-2 and PS-5 were not found to be leaking, and the team was not able to replace the gate valves because of swampy conditions around the wells, which restricted heavy equipment access. At each of the four repaired wellheads, the team removed the existing gate valves while pumping down the water and installed new stainless steel valves. Detailed repair descriptions for each well are given in Appendix D. Images from the repair of well PS-4 are shown in Figure 31 and Figure 32.



Figure 31. Areas of leaking, scale, and corrosion are shown on PS-4.



Figure 32. The PS-4 completed replacement valve installation.

Multiple static and flowing temperature and pressure logs were obtained for all wells except for PS-2, where the wellhead has sunk into the soft ground and the master valve is inoperable. Water samples were collected from these wells and from the natural hot springs for chemical analysis.

7.3 Shallow Temperature Survey

At shallow depths, the PGS is dominated by a strong lateral flow of geothermal water, identified three decades ago when the first six wells were drilled into the system. The maximum temperature of this shallow aquifer is slightly below boiling, and the depth to the most hydraulically conductive part of the aquifer is less than 100 feet. This combination of factors produces very high shallow-temperature gradients above the thermal aquifer and sharp temperature declines below the aquifer.

The smooth nature of the six early shallow temperature profiles strongly suggests that the aquifer began transmitting hot water in the relatively recent past and that the lower temperatures beneath the aquifer are a result of downward conduction of heat from the aquifer—not a flow of cold water beneath the thermal aquifer. If there were a counterflow of cold water, complexity such as isothermal segments in the temperature profile separated by short intervals of extremely high temperature gradients would be expected. This combination of characteristics at PHS allows the possibility of defining the shallow thermal aquifer with abnormally shallow holes compared with most other geothermal systems. Characterizing the shallow thermal aquifer allows definition of the directions of thermal fluid flow within the aquifer and recognition of the hottest part, which most likely would overlie thermal upwelling beneath the aquifer.

The absence of bedrock and coarse conglomerate in the vicinity of PHS is also an important factor that allowed consideration of low-cost and unconventional drilling techniques. The flat,

swampy topography at PHS is an advantage to the extent that it minimizes topographic effects at shallow depths; however, it also inhibits access to much of the area with machinery.

The first shallow temperature holes at PHS were installed in 1979, when about 70 “pipes” were hand driven to a maximum depth of 5 to 9.5 m (Harrison and Hawkins, 1979; Osterkamp et al., 1980). An isothermal map at a depth of 4.5 m was prepared, outlining the central part of the shallow thermal anomaly with temperatures between 30°C and 80°C (86°F–176°F). Effort was focused on the heart of the shallow thermal anomaly, and none of the holes was deep enough to penetrate into or beneath the shallow thermal aquifer.

7.3.1 Backpack Drilling Program

Two additional shallow temperature surveys were attempted in April 2011 using a small backpack-mounted drill. Thirty-one holes were drilled to depths of 3 m while the area was still snow-covered and could be accessed by snowmobile. However, a number of challenges arose including holes collapsing before tubing could be installed and snow depths of 2 m. These challenges limited the ability to install as many holes as desired to a uniform depth, which presents difficulty with interpretation. The backpack-drilling effort did not produce results much better than the effort made in the 1970s.

7.3.2 Geoprobe Drilling Program

Discussion with USGS project partners revealed that they had a self-contained track-mounted direct-drive Geoprobe unit, touted as capable of driving pipes to depths of less than 30 m. The unit is highly mobile, and at a weight of 5000 pounds, was light enough to travel on trails in the PHS area with minimal impact. The Geoprobe unit drives small-diameter sealed pipes into the ground without the need for circulatory fluids (Figure 33), eliminating the mud system that traditional drill rigs require.



Figure 33. Installing Geoprobe holes at Pilgrim Hot Springs.

During the summer of 2011, sixteen Geoprobe holes with an outer pipe diameter of 2.25 inches (5.7 cm) and a hole diameter of 1.5 inches (3.81 cm) were installed to a maximum depth of 109

feet. Locations and temperatures are shown in Figure 34. Prior to the end of the 2011 season, all holes were decommissioned by pulling the pipes and sealing the holes with grout as the pipes were removed.

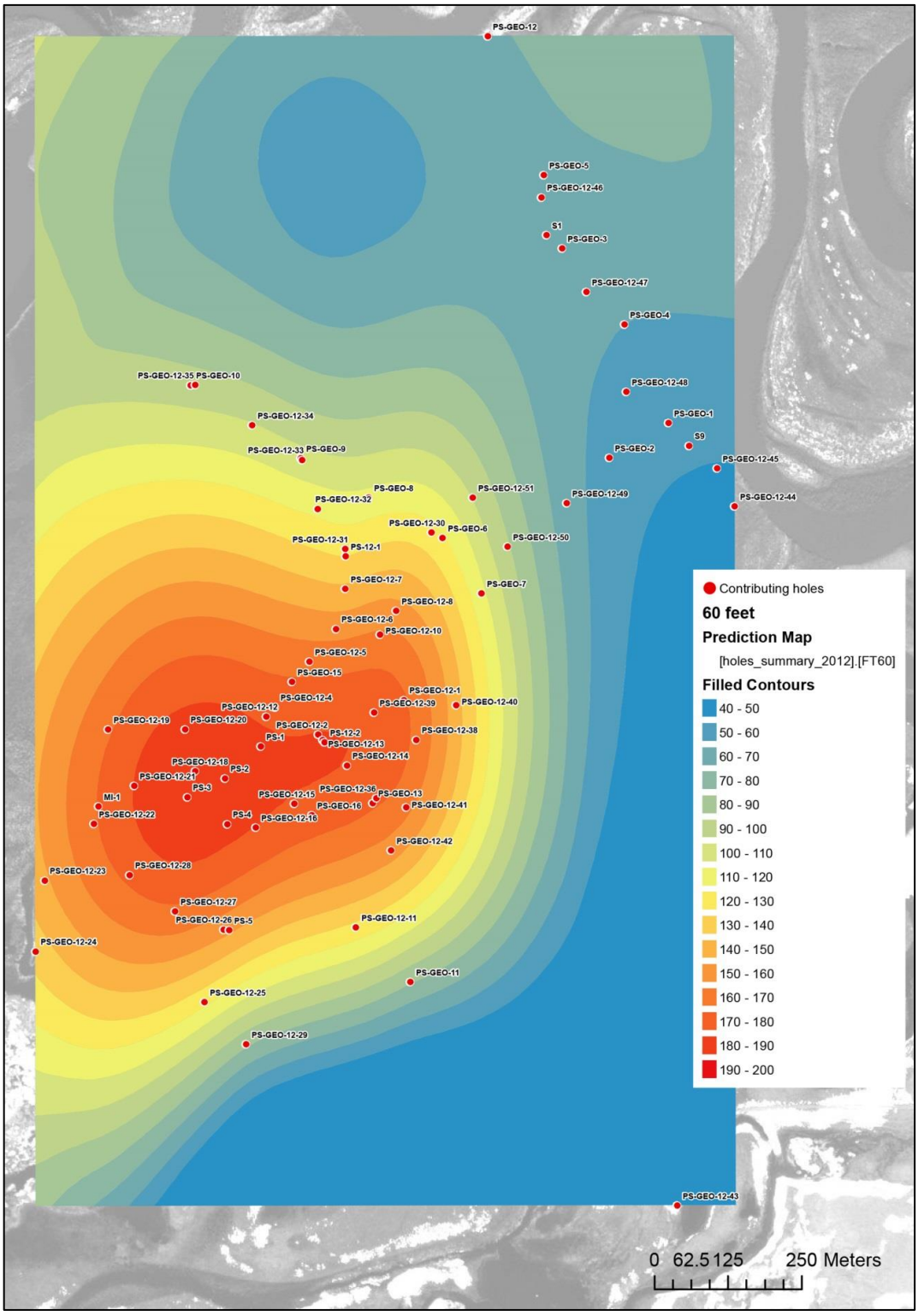


Figure 34. Location of Geoprobe holes and their temperatures in Fahrenheit at 60 feet.

Nearly all of the Geoprobe holes from 2011 failed to reach beyond 80 feet deep; none penetrated into or beneath the shallow thermal aquifer. In 2012, smaller pipe (1.25 in. outer diameter; 0.5 in. inner diameter) was used in 54 holes, enabling deeper penetration (Figure 34). The deepest hole reached 154 feet. The majority of these holes still have positive temperature gradients, but some have encountered isothermal conditions indicative of having penetrated the shallow thermal aquifer, documenting its maximum temperature (Figure 35). Phase 2 drilling produced known depths of the aquifer, so it was possible to extrapolate some of the Geoprobe hole temperature profiles and better define the flow pattern within the shallow thermal aquifer. All Geoprobe locations and depths are shown in Appendix C.

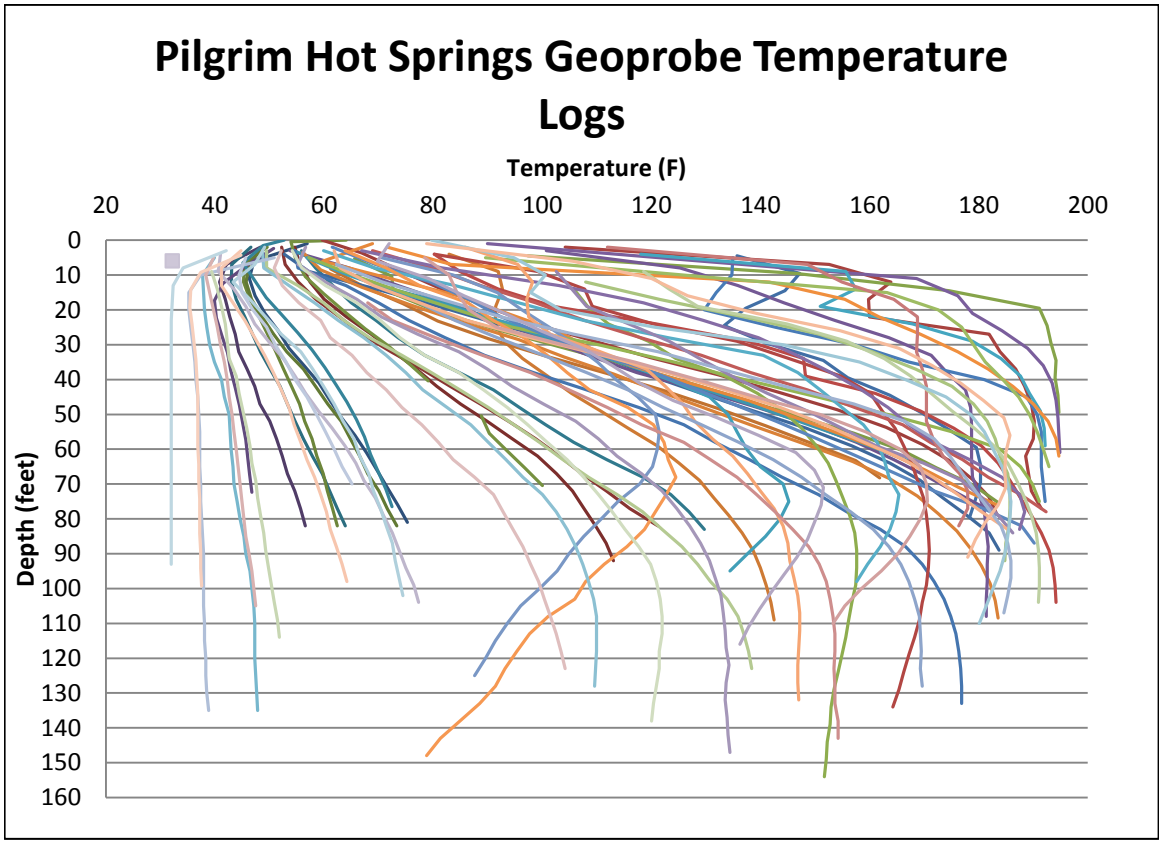


Figure 35. The temperature logs from all Geoprobe holes show a wide variety of temperatures and profile shapes. A shallow thermal aquifer of varying depths and characteristics is clearly visible.

7.4 Deep Drilling

Deep drilling at PHS occurred over three different field seasons: 2011, 2012, and 2013. Holes and wells drilled more than 500 feet in total depth required permits from the Alaska Oil and Gas Conservation Commission, while those shallower than 500 feet did not. During 2012, a blowout preventer (BOP) was required when drilling below 1000 feet. In 2013, a waiver was obtained, and a BOP was not required. Drilling in 2011 and 2012 was accomplished with USGS Alaska Rural Energy Project equipment and personnel. This drilling was done with an Atlas Copco CS-

1000-P6L drill rig, while in 2013, drilling was done by MW Drilling using their Schramm Model T555 Rotadrill rig based out of Anchorage, Alaska. Well schematics and detailed descriptions for each well are found in Appendix A.

In June 2011, prior to drilling activities, researchers from ACEP and the USGS conducted an aerial inspection of PHS via helicopter to locate suitable temperature gradient (TG) hole drilling locations. Nine possible drill sites were identified. The initial drilling targets were northeast of the historic hot springs, located on land owned by the Mary's Igloo Native Corporation. This decision was based on data from the 1982 drilling effort, especially the cool temperatures and low bottom-hole gradient measured in well PS-5 (Figure **5**). Drilled in 1982, PS-5 was the deepest well that had been drilled during that effort; it also recorded the coolest temperatures. This information clearly showed that the upwelling zone could not be located south of the existing well field. The upwelling zone appeared to be located northeast of the existing wells, with evidence for this supported by the appearance of a thawed zone in the northeast area.

In 2011, drilling was sited as far north as logistically possible, where the USGS drill rig could access the area using existing primitive roads and trails. Drilling took place just southwest of the Pilgrim River and resulted in TG holes S-1 and S-9 (Figure 4). The temperatures measured in these holes were significantly cooler than the temperatures measured in the existing wells, suggesting that these two holes were too far to the northeast and that the upwelling zone must be closer to the historic hot springs.

In 2012, three TG slim holes were drilled on the PHS property owned by Unaatuq, LLC. Drilling logs for these wells are shown in Appendix J. The 2012 drilling activities moved farther to the south, with the first hole (PS-12-1) located slightly north of the historic orphanage buildings and the second and third holes (PS-12-2 and PS-12-3) drilled near the existing well field. The equilibrated temperature profiles (shown in Appendix B) collected from these three wells show temperature reversals beneath the shallow thermal aquifer, indicating that they are not directly over the upwelling zone.

The holes drilled in 2011 and 2012 used sealed casing cemented in place. The holes were only permitted as TG holes and were not intended to have the ability to access fluids in the geothermal aquifer. Once drilling was completed, the casing was filled with water so that a temperature probe could be lowered into the hole to record accurate static aquifer temperature profiles. Wells drilled in 2012 were at first assigned names by the Alaska Oil and Gas Conservation Commission: TG-1, PS-12-3, and PS-12-9. In order to be consistent with the existing nomenclature, the names of these wells were changed so that TG-1 became PS-12-1, PS-12-3 became PS-12-2, and PS-12-9 became PS-12-3.

In 2013, an attempt was made to drill a large-diameter well into the predicted upwelling zone and test fluid production from the aquifer above the bedrock. The drilling methods used were similar to those used in 2011 and 2012, but makeup water was pumped from the slough on the property in accordance with state and federal regulations. The first drill site was chosen based on data from the wells drilled in 2012, which suggested that those wells surrounded the upwelling. When the first well drilled in 2013—PS-13-1—encountered the usual large temperature reversal and showed lower temperatures than hoped, it was completed in the shallow aquifer. Two more

small-diameter wells were drilled in 2013 to 400 feet. All wells drilled in 2013 showed temperature reversals, indicating that they were not directly over the upwelling. All three holes drilled in 2013 used perforated casing or well screen and have artesian flows. Details about each deep TG hole and well are described in Appendix A.

8. WATER CHEMISTRY

The geochemistry of the thermal fluid at PHS is one of the primary reasons why so much effort over so many years has been put into exploring this geothermal system. In addition to its relatively hot surface temperature, thermal fluid at PHS has the highest predicted quartz geothermometer temperature (137°C) and one of the highest Na-K-Ca geothermometer temperatures (146°C) of the thermal springs on the mainland of Alaska (Miller et al., 1975). Chemical analyses of PHS thermal waters now cover a century (Waring, 1917; Miller et al., 1975; Liss and Motyka, 1994; Benoit et al., 2014b), and an extensive water chemistry database has been assembled (Table 3). The thermal water at PHS is relatively high in sodium and chloride, but stable isotope analyses of thermal and cold waters at this location show that the thermal water is derived from local meteoric runoff and not from seawater (Miller et al., 1975; Liss and Motyka, 1994). Only three noncondensible gas samples from PHS thermal waters have been analyzed, and these contain mostly methane and nitrogen and are relatively high in hydrogen (Liss and Motyka, 1994). Gas geothermometry results indicate subsurface temperatures from 113°C to 230°C (235°F–446°F). The surface flowing temperatures and brine chemistry of some of the PHS wells have changed with time (Liss and Motyka, 1994), but these changes have since been shown to result from changes in fluid entry points in those wells (Benoit et al., 2014b).

Table 3. Pilgrim Hot Springs well chemistry in PPM

Sample	Date	T°C	pH	Na	K	Ca	Mg	Li	B	SiO_2	HCO_3	CO_3	SO_4	CL	F
Spring	1915	70		1590	61	545	7.4			87	21		25	3450	
Spring	1972	82	6.75	1450	61	530	1.4	4.0	2.4	100	30.1		24	3346	4.7
Spring	1982	55	6.8	1660	59	542	1.0	4.5	2.2	91	36		15	3360	4.3
Spring	1993	42	6.5	1580	65	569	1.5	4.0	2.7	86	19		18	3530	4.7
Spring	1993	55	6.8	1660	59	542	1.0	4.5	2.2	91	36		15	3360	4.3
Spring	2012		6.65	1480	62.8	508	0.38	3.6	2.0	86	14		22	3350	4.6
Spring	2014	73	6.63	1400	58	460	1.00	3.4	2.1	80	15			3500	
PS-1	1979	90.5	6.4	1828	75	518	0.9	3.9	2.5	95	16		16	3590	4.8
PS-1	1982	92	7.5	1720	60	511	0.9	4.7	2.3	94	30		19	3420	4.4
PS-1	1993	82	7.1	1560	65	545	0.6	4.2	2.4	90	20		7	3460	5.3
PS-1	2010	79	7.1	1530	61.6	519	1.21	3.5	2.2	83	27.8		14.3	3460	4.5
PS-2	1979	90	6.4	1820	75	516	0.9	3.9	2.3	101	19		15	3540	4.8
PS-2	1982	96	7.3	1510	57	516	0.9	4.7	2.3	92	26		19	3420	4.5
PS-3	1982	75	8.0	592	25	260	0.4	2.0	1.0	60	36		15	1430	1.3
PS-3	1993	65	6.8	1100	43	441	0.6	3.2	1.5	67	27		6	2450	2.9
PS-3	2010	67	7.0	1140	40.9	412	0.85	2.8	1.7	71	23.7		10.8	2650	3.0
PS-4	1982	48	8.6	115	4.8	23	0	0.3	0.5	35	80		11	284	0.5
PS-4	1993	45	8.6	146	7.8	98	0.2	0.2	0.2	27	48		1	386	0.3
PS-4	2010	44	8.52	152	5.9	73	0.14	0.5		28	34		9.4	353	0.4
PS-4	2013	44.6	8.47	128	5.5	45	0	0.4	0.2	29	39.9	1.5	9.3	260	0.6
PS-5	1993	32	9.6	36	1.1	2	0.2	0.1	0.6	21	81		5	6	0.5
PS-5	2010	30	9.6	36	1.09	1	0	0.1		20	49.6		5.4	2	0.5
MI-1	1982	22	9.7	16	0.5	5	0	0.1		21	37		9	5	0.2
MI-1	1993	31	8.3	29	1.5	23	0.6	0.2	0.1	20	32		10	66	0.2
MI-1	2010	29	7.8	130	4.4	93	0	0.5		21	25.8		9.5	337	0.2
PS 12-3	2012	65.5	7.52	731	29.9	281	0.78	1.8	1.0	51	30.6		8.2	1640	1.9
PS 13-1 (open to 1036 ft)	2013	70.5	7.51	537	26.1	236	0.4	1.4	0.8	54	25.1		9.3	1300	1.4
PS13-1	2013	77	7.27	1090	50.9	370	0.7	2.6	1.5	79	22.8		12.4	2500	3.3

Sample	Date	T°C	pH	Na	K	Ca	Mg	Li	B	SiO_2	HCO_3	CO_3	SO_4	CL	F
(shallow Completion)															
PS 13-1 300 gpm	2014	79	7.26	1000	35.0	250		2.0	1.5	59	18			2500	
PS 13-1 60 gpm	2014	77	7.05	950	37.0	250		2.1	1.4	67	15			2300	
PS 13-2	2013	71	8.95	124	25	49	0	0.3	0.2	62	39.4	11.1	5.8	265	0.5
PS 13-2 55 gpm	2014	69	7.52	53	3.1	9		0.2	0.1	54	62		5.5	*65*	
PS 13-3	2013	79	7.27	1070	46.3	373	0.7	2.5	1.4	74	22.1		12.3	2424	3.0
PS 13-3 60 gpm	2014	78	6.97	920	37.0	280		2.2	1.3	66	16			2200	

There is an obvious mixing trend between dilute cold groundwater, and primitive geothermal fluid, exemplified by sodium and chloride contents (Figure 36) and temperature (Figure 37) (Liss and Motyka, 1994). The same relationship is shown in cross plots involving all other chemical species except sulfate, which has more scatter. Flowing temperature profiles show little or no mixing of different fluids within the wellbores (Benoit et al., 2014b) and thin discrete aquifers with discrete chemistries that are supplying the PHS wells.

The mixing trend shown in Figure 36 does not fall along the line of charge balance where sodium ions equal the chloride ions. The thermal fluid at PHS is deficient in sodium, and this deficiency is balanced by an abundance of calcium, causing the apparent mixing to diverge from the Na-Cl line. The calcium content of the primitive geothermal fluid is greater than 525 ppm, and exceptionally high when compared with most other low-salinity geothermal waters throughout the world.

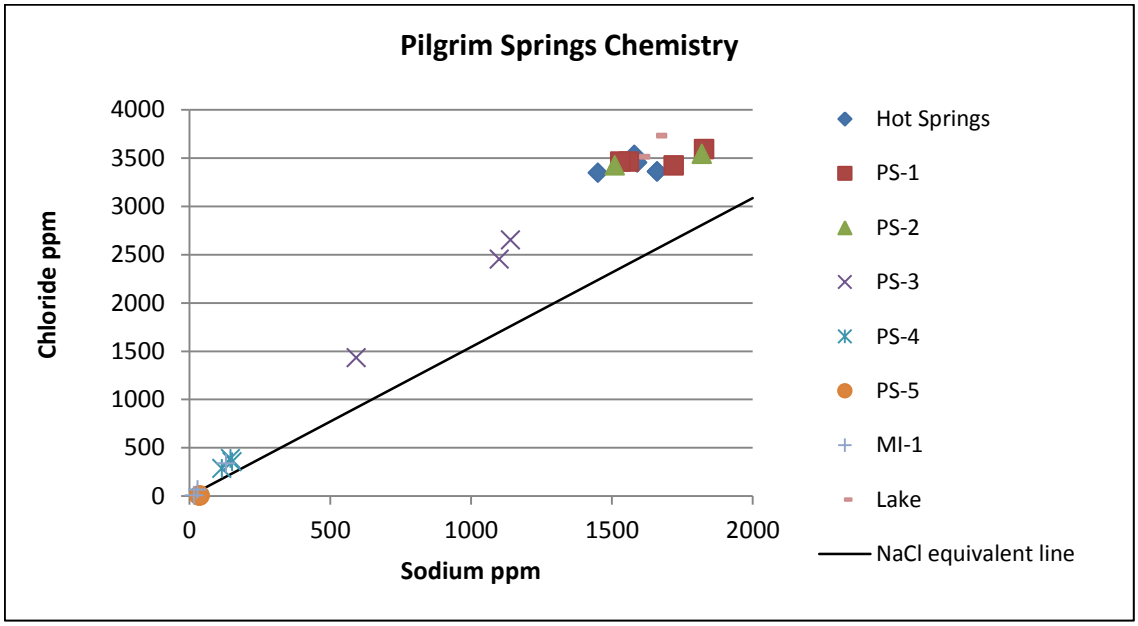


Figure 36. The mixing trend between sodium and chloride is shown for all samples collected from the Pilgrim Hot Springs site.

A major disappointment of recent exploration at PHS has been the inability to find the more optimistic temperatures predicted by geothermometry. The exceptionally high gas geothermometry values have always been viewed as questionable (Liss and Motyka, 1994), but the low magnesium content and the neutral chloride nature of the thermal fluid along with the

quartz and the Na-K-1/3Ca geothermometry appeared to credibly predict temperatures of 130 to 145°C (266°F–293°F). To date, all drilling to depths as great as 1294 feet has resulted in a measured maximum temperature of only 91°C (196°F). To compound the frustration of this finding, temperature profiles in the deeper wells cannot be extrapolated to significantly greater depths to predict reliably where these higher temperatures may be present. Of course, it is always possible that higher temperatures are located at a much greater depth or lateral separation.

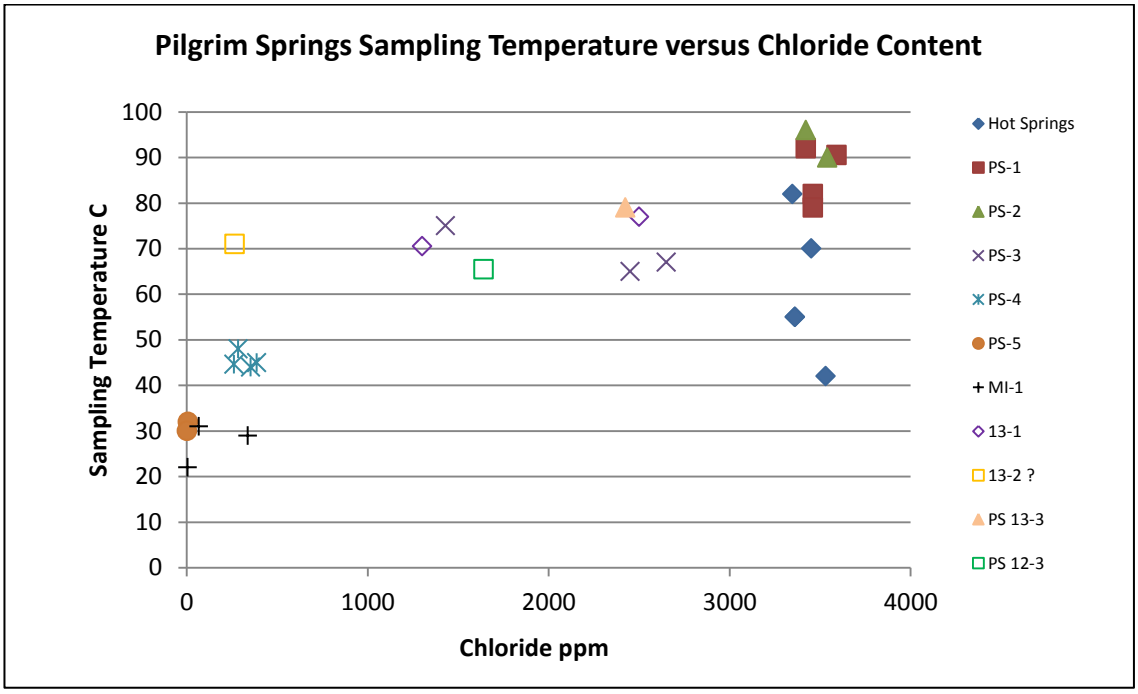


Figure 37. Chloride content is shown along with well temperature. The PS-13-2 chloride content appears to be low, given its temperature.

However, other geothermometers might be more appropriate for PHS. The chalcedony geothermometer predicts subsurface temperatures of 99°C to 111°C (210°F–232°F), and the Na-K-4/3Ca geothermometer gives values near 120°C (248°F). The 120°C value is still 29°C above the maximum measured temperature and begs the question of whether the geothermometer is valid for the PGS brine chemistry. The 525 ppm of calcium in the PGS water is an obvious suspect in raising the question of whether thermal waters with exceptionally high calcium content provide accurate geothermometry calculations.

9. FLOW AND INTERFERENCE TESTING

The first flow testing and interference testing of the PGS were performed in 1982, when well PS-1 was flowed at 30 to 35 gpm and pressures were recorded in well PS-2. Type-curve matching of the drawdown gave an estimated permeability of 4.5 darcys (Economides et al., 1982). In 1982, the productivity of the wells ranged from 2.5 to 19 gpm/ft, and the transmissivity of the wells ranged from 300 to 40,000 gpd/ft (Kunze and Lofgren, 1982).

9.1 Interference Testing of Wells PS-3, PS-4, and MI-1

Three interference tests using downhole temperature and pressure monitoring were performed in September 2013 (Benoit, 2013). The first test involved "static" pressure and temperature monitoring of well PS-3, with wells MI-1 and PS-4 being flowed with different start and stop times over a period of two and a quarter days. The second test involved flowing well PS-4 for 3 hours and monitoring wells PS-1 and PS-5. The third test was a mirror image of the first test, with well PS-3 being flowed for 3.5 hours and downhole pressure and temperature monitoring in wells PS-4 and MI-1.

The interference tests conducted on September 7, 8, 9, 11, and 22 generally confirmed the observations made by Woodward-Clyde during their flow tests in 1982. Examples of the temperature and pressure responses during these tests are shown as Figure 38 and Figure 39. Wells PS-1 and PS-2, completed in the shallow thermal aquifer, do not quickly or obviously communicate with the deeper and cooler aquifers exposed in wells PS-3, 4, 5 and MI-1. More precise tools available in 2013 have shown that wells MI-1, PS-3, and PS-4 have a rapid but barely detectable pressure communication of 0.1 to 0.25 psi. This communication occurs at flow rates of 50 to 100 gpm from individual wells.

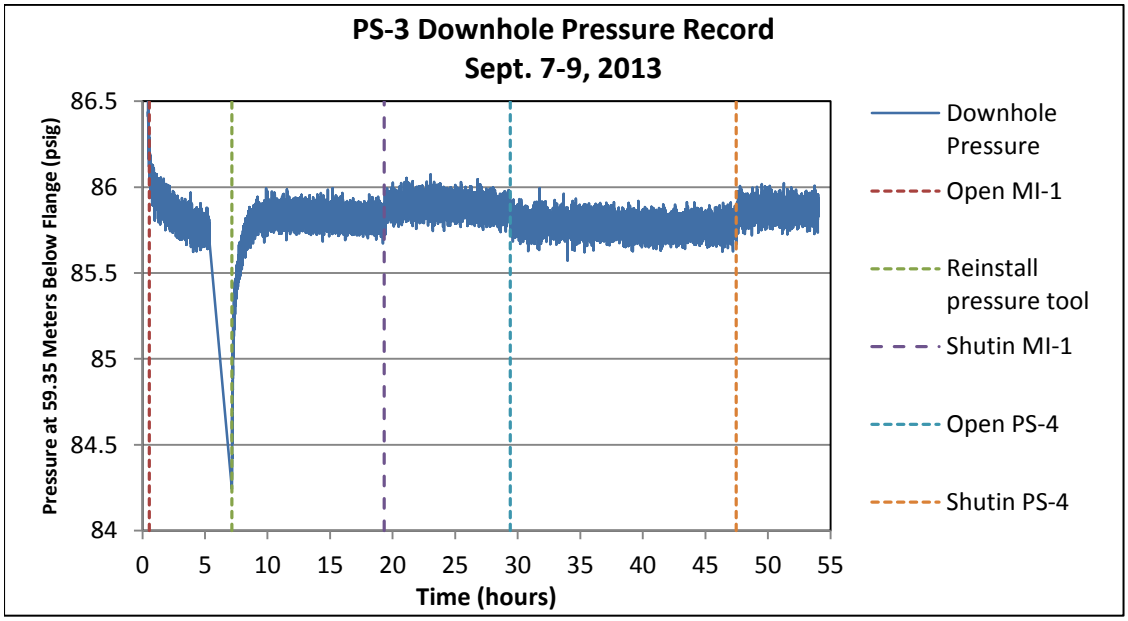


Figure 38. PS-3 downhole pressure during interference testing.

This small pressure communication creates a much stronger and surprising temperature change in the static well PS-3 when wells MI-1 and PS-4 are flowed. The speed with which this temperature communication occurs indicates that the small changes in pressure create flow rate changes that quickly change the water flow past the tool in the "static" PS-3 well. More likely, the temperature changes are related to flow rates and mixing than to a single fluid entry changing its temperature. No obvious temperature changes appear in well PS-4 when PS-3 is flowed. Well MI-1 showed some small temperature changes when PS-3 was flowed, but these changes are not

as clearly related to starting and stopping PS-3 flow. Wells PS-3, PS-4, and MI-1 have relatively similar depth permeable intervals, which is a first-cut explanation for their measurable short-term communication. Some background temperature and pressure trends in the PHS wells are not understood and will require additional and/or longer-term monitoring to understand. The full flow-testing report for September 2013 is shown in Appendix H.

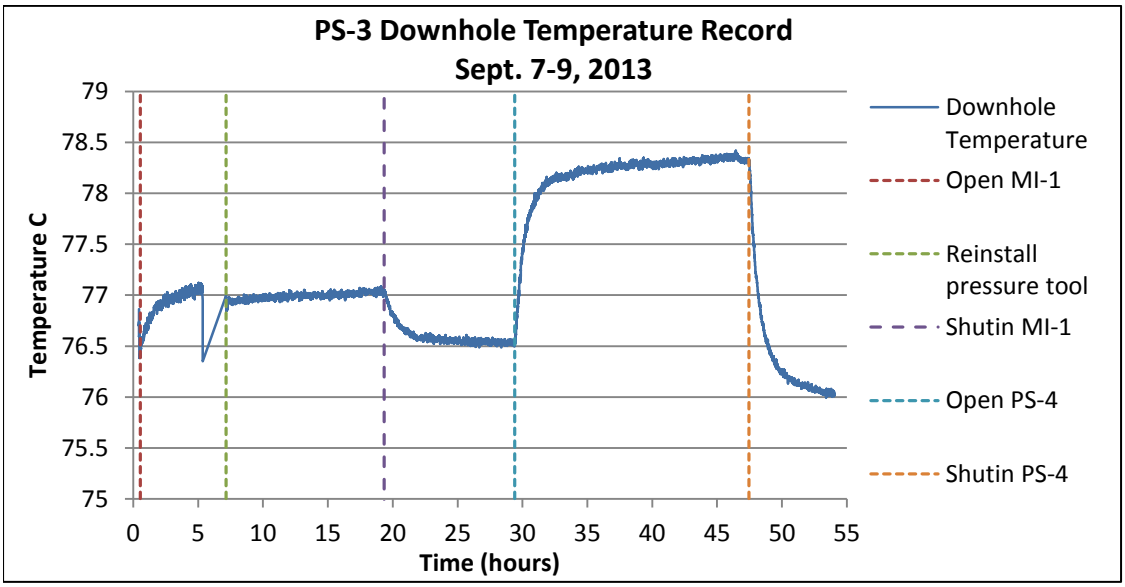


Figure 39. PS-3 temperature response during 2013 interference testing.

9.2 Interference Testing of PS-3, PS-13-1, and PS-13-3

Interference testing and flow testing of the 2013 wells were conducted twice about 6 months apart. The first testing occurred in February 2014 during a winter trip to the hot springs. The purpose of this trip was primarily for collecting equilibrated temperature logs of the 2013 wells, and time available for flow testing was limited. The temperature and pressure were monitored in wells PS-3, PS-13-1, and PS-13-3, while well PS-13-1 and later well PS-13-3 were allowed to flow at natural artesian rates of 50 to 70 gpm (Appendix I). Flows were visually estimated, as no flow metering was available. Well PS-13-3 was allowed to flow for just under 5 hours, and immediately after the flow was cut off, well PS-13-1 was opened and allowed to flow overnight for 12 hours. At artesian flow rates, the recorded pressure and temperature effects between the wells were extremely minimal, on the order of 0.2 psi and 0.02°C. In each well, productivity was approximately 20 gal/psi. Productivity will be discussed in further detail in the next section.

9.3 Flow Testing of PS-13-1

To date, the most significant flow test at the PGS was conducted between September 15 and 17, 2014, by airlifting well PS-13-1. The airlift was accomplished using thin-wall 1-inch-diameter aluminum tubing with a dispersion head on the bottom and an Atlas Copco trailer-mounted air compressor rated at 100 psi and 185 cfm. This hardware was supplied by Howard Trott of Potelco and rented locally in Nome. A 6-inch Krohne magnetic flow meter (magmeter), supplied by ACEP, was used to measure the flow rates. The surface equipment is shown in Figure 40. The

5-inch-diameter dispersion head was backed up with 1/8 inch aircraft cable to prevent accidental loss of the downhole equipment in the well.

The air-water mixture flowed with considerable turbulence into the first tank shown in Figure 40. As the water flowed into the second tank, no turbulence occurred, and the tank provided adequate head to push the water through the magmeter and out a 240-foot-long 6-inch PVC pipeline to flow through a hot springs pond, where the water cooled.

The first airlift only lasted about an hour, as the flow was limited by a constriction in the flow line downstream of the second tank. Expansion of the flow line caused a short flexible hose to partially collapse, reducing the flow rate out of the second tank. This first test was more a test of the equipment than a test of the resource. The aluminum tubing was run to a depth of 12.2 m below the top of the standpipe (8.8 m below ground level). The average airlift flow rate during the first test was 172 gpm, and the magmeter readings were confirmed by measuring that it took 18 seconds to fill a 55-gallon drum from the discharge of the pipeline into the flow through a hot springs pond. Pumping at a higher air rate increased the flow rate to 177 gpm, but resulted in the water overflowing the top of the wellhead standpipe.



Figure 40. Surface equipment used for the airlift of PS-13-1. The magmeter is in the silver spool between the black and white parts of the flow line. The black large-diameter hose serving as a standpipe on top of the wellhead was needed to prevent water from overflowing the top of the wellhead, which could not be sealed. The clamp holding the aluminum tubing is visible on top of the standpipe. The blue hoses are the air lines coming from the air compressor.

While the well was being airlifted and the wellhead appeared to be stable, a Kuster tool was run to a depth of 30 m below the top of the master gate, with the heavier aircraft cable used as a backup in case the small 1/16-inch-diameter cable normally used on the reel was cut. The Kuster tool hung in the well just over a half hour before the air was cut off. Once the air was cut off, the well resumed its natural artesian flow of 55 gpm, and the Kuster tool remained hanging in the well overnight to record pressure buildup. There was no wing valve on the flow line to allow the well to be shut in

with the aluminum tubing and Kuster tool hanging inside it.

On the morning of September 16, additional flow line parts were obtained in Nome, and the line was modified to remove the constriction. The aluminum tubing in the well was deepened from 12.2 m to 21.9 m below the top of the standpipe on the wellhead (18.6 m below ground level). This depth was about the maximum practical for one person on a large A-frame ladder to raise and lower the downhole equipment; it was also the maximum depth at which the on-hand larger-diameter aircraft cable could be used to hold and protect the Kuster tool.

In the second test, there was adequate confidence to run the Kuster tool into the well under artesian flow conditions before starting the airlift. The air volume was quickly increased in three steps to find the maximum airlift rate that would not flow water out the top of the wellhead. This flow rate was about 300 gpm. The highest flow rate reported briefly by the magmeter was about 350 gpm. The 300 gpm airlifted flow rate was held for about 7.5 hours, until the air compressor was almost out of diesel fuel at 01:00 hours on September 17. After the compressor was shut off, the well continued artesian flow until after the Kuster tool was retrieved late in the morning on September 17. Also on that morning, the downhole hardware was pulled out of the well.

Airlifting increased the scatter in the pressure and temperature data as compared with the unassisted artesian flow (Figure 41 and Figure 42). During the first airlift, it is unclear if there was any decline trend in the downhole pressure. The first 15 minutes of downhole data indicate a decline, but perhaps this was simply the tool equilibrating to the downhole conditions (Figure 42). During the second 15 minutes, no decline is evident. At 19:00, the amount of air being pumped was increased for 2 minutes to assess the plumbing system at higher flow rates and was then shut off (Figure 42). The amount flowing through the meter increased by only about 5 gpm to 177 gpm, but water occasionally geysered at the top of the wellhead. A constriction in the soft 6-inch hose between the two tanks limited the flow through the meter. The downhole flowing temperatures were measured below the air injection depth and, therefore, were not cooled by the air injection, as the surface-measured temperatures were. The maximum downhole temperature measured during the first airlift was 78.28°C (Figure 42).

Immediately upon shutting off the air, the temperature took a 0.2°C decline and then quickly climbed for the next 13 minutes to its maximum value of 78.8°C, then quickly cooled. The temperature was down to 77°C when the tool was removed the following morning and showed a range of 1.7°C during this logging. During the airlift, the temperature increased slightly. After airlifting ceased, the bulk of the temperature change occurred, first with a short 0.2°C decrease, probably related to the short increased volume airlift, and then with a 0.8°C increase followed by a long decline until the temperature was about 1°C lower than during the airlifting. During this decline, the well was flowing under natural artesian conditions. This variation of temperatures with flow rates demonstrates that there is more than one feed zone for this well, with differing temperatures. Higher temperatures coincide with higher flow rates. A similar response was seen upon stopping the second airlift (Figure 43); however, this response lacked the sharp initial drop in temperature as seen at the end of the first airlift (Figure 42).

The maximum temperature recorded after stopping the second airlift was 79.8°C, or 1.0°C hotter than seen after the first airlift stopped (Figure 41). After the second airlift was finished, the

artesian flow temperature declined to 76.9°C, about 0.25°C cooler than that seen after the end of the first airlift.

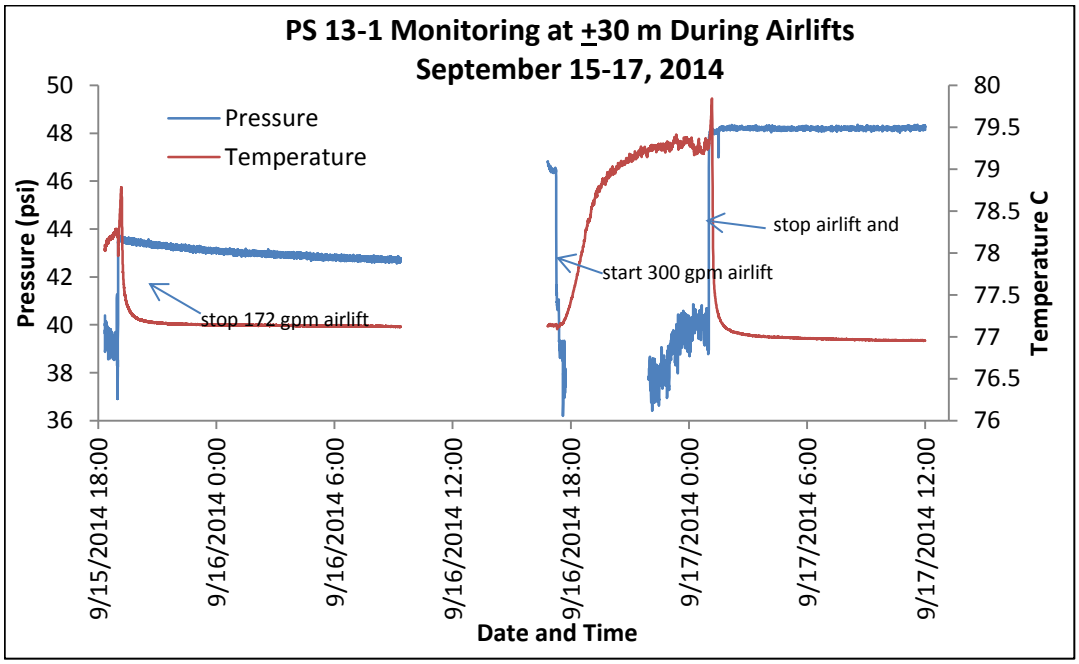


Figure 41. Downhole pressure and temperature record of PS-13-1 during the two airlifts.

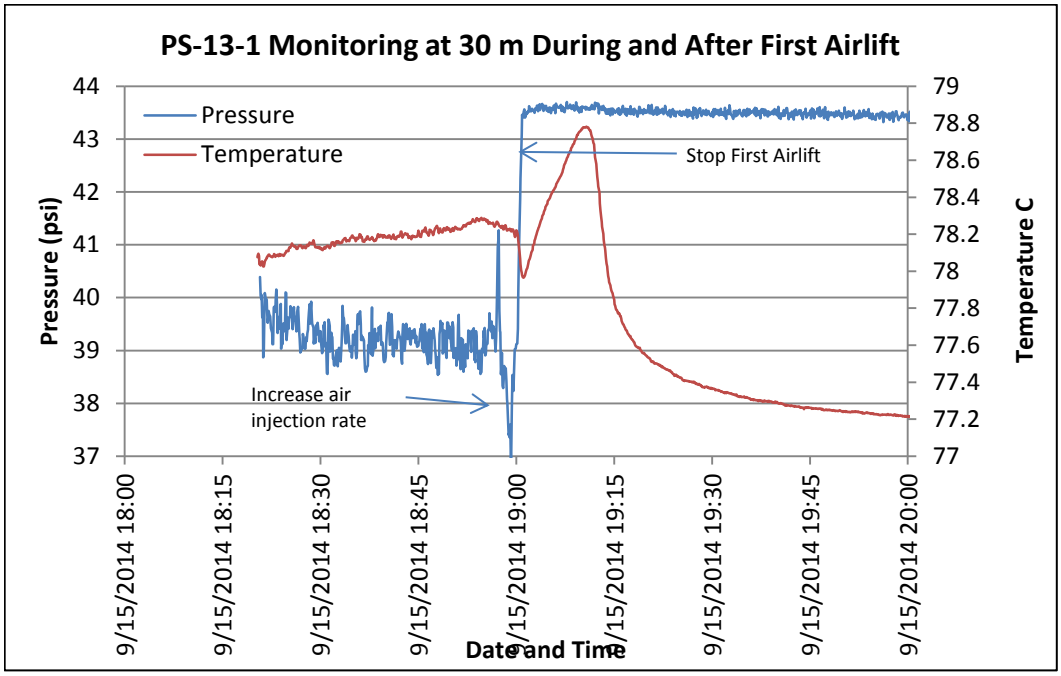


Figure 42. PS-13-1 downhole pressure and temperature record just before and after stopping the first airlift at 19:02 hours on September 15, 2014.

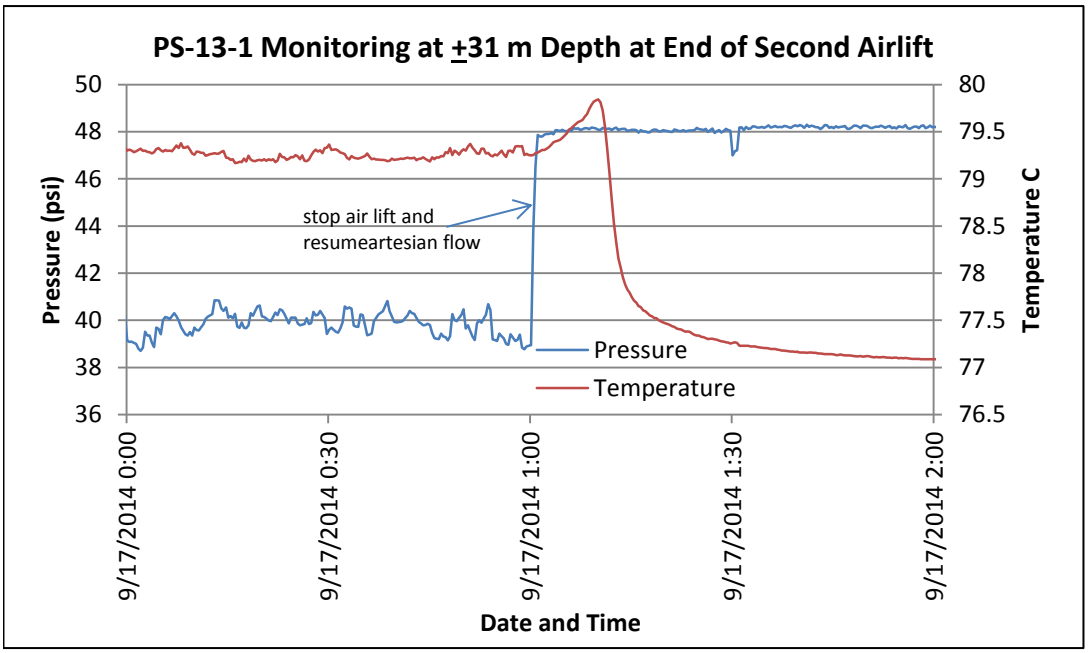


Figure 43. Downhole pressure and temperature at the end of the second airlift at 01:00 hours on September 17, 2014.

This temperature variability points to a fairly complex interplay between two or more feed zones with differing temperatures. This idea led to a detailed flowing log run on the morning of September 18, before the well was shut in and the artesian flow was stopped. This artesian flowing log and a static log run on September 7, 2014, show some of the details of the fluid entry points (Figure 44).

The flowing SMU log shows multiple sharp reversals in temperature gradient between depths of 56 and 67 m, which define all the possible fluid entry points. The top of the screen in the wells is at 57.3 m, which is in good agreement with the flowing temperature log. Due to minimal divergence between the flowing and static logs between depths of 65 and 67 m, any fluid entry point in that interval is suspect, as the temperature readings were not stable in that and shallower intervals. The deepest significant fluid entry is at a depth near 65 m, and the shallowest major entry as defined by temperature is near 60 m. All of the defined fluid-entry temperatures are between 77.02°C and 77.18°C on the flowing log. However, the static temperatures in this interval range from 77.4°C to 77.7°C. During airlifting, temperatures as high as 78.25°C to 79.3°C were measured, which had to have come from shallower depths in the well, perhaps as shallow as 35 or 40 m. This fluid would then have had to flow down the outside of the uncemented 14-inch casing and enter the screened interval between 57.3 and 72.5 m (see Appendix A for well schematic). The maximum temperature measured during the airlifting operations was the 79.8°C spike shortly after ceasing the airlift. This temperature is only 0.18°C hotter than the maximum measured tempeature of 79.62°C during the static log prior to flowing the well. Thus, we now have a good idea as to the origin of the fluid producing the temperature spike.

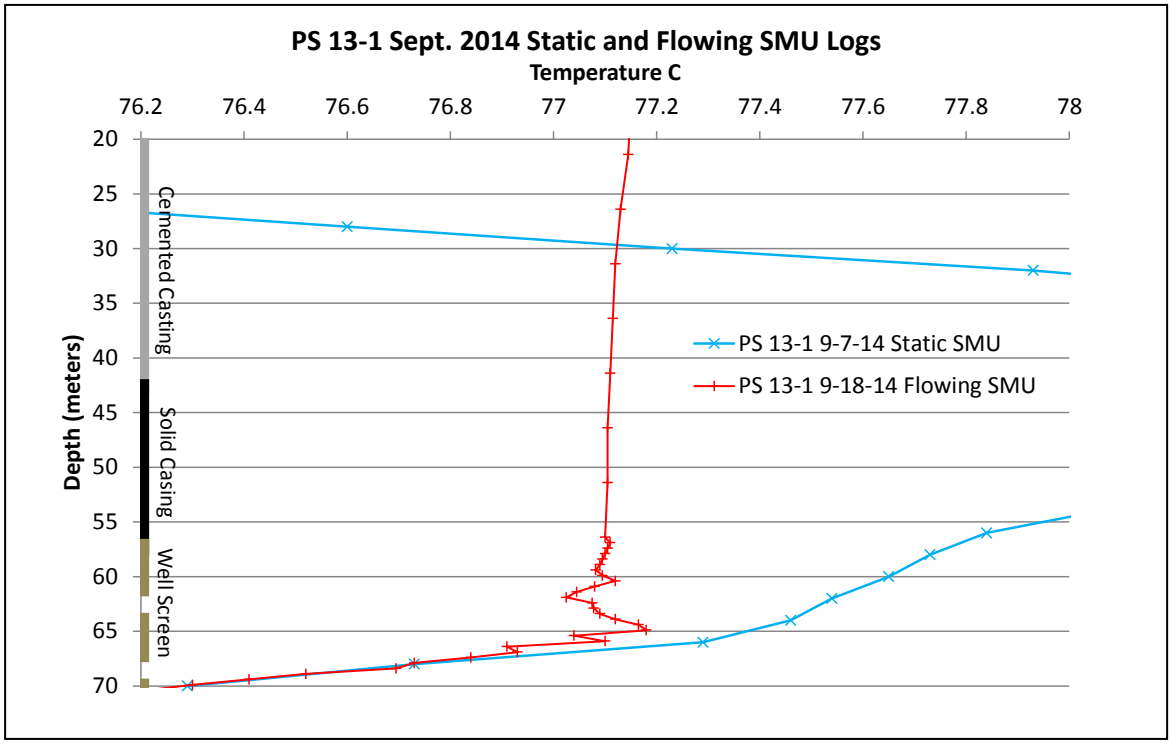


Figure 44. Detailed flowing and static logs from PS-13-1 run in September 2014 with precision SMU logging equipment. The flowing log was run during artesian flows, and the depths were increased by 1.4 m to have exactly the same bottomhole depth as the static log, as this is the most important part of the hole for this discussion.

It was decided that during the airlift the internal wellbore conditions would probably be too severe for the small SMU tool and its delicate electrical cable. The primary use of the Kuster tool was for pressure monitoring, so it was not moved during the airlifting. However, during any future airlift, a traversing Kuster survey should be run.

Four major flow rate changes were monitored with downhole pressure changes in PS-13-1 during September 2014. The first was done on September 15, prior to the airlifting, and involved opening up the well so that it could artesian flow. During this flow, the rate was somewhere between 60 and 75 gpm, as measured with a 5-gallon bucket. Three major flow rate changes were then monitored during airlifting while the Kuster tool was downhole (Figure 41, Table 4) and the magmeter was providing the flow rate data. The first flow rate change was the cessation of the first airlift, the second was the start of the second airlift, and the third was the end of the second airlift. All of these changes had natural artesian flow either before or after. None of the changes involved the larger change of going from a static condition to the airlift.

The productivity measurement involving the lowest flow rate and the smallest downhole pressure change was between 20.4 and 25.5 gpm/psi. The next largest flow rate change was at the end of the first airlift, and it produced a productivity value of 22.2 gpm/psi, the same as the average value of the cessation of artesian flow. The two largest flow rate changes at the start and stop of the second airlift give virtually identical and higher productivity values of 27.5 and 27.2 gpm/psi.

These values are quite encouraging, as the well did not give lower productivity values as higher flow rate changes occurred, indicating that the well is capable of flowing at significantly higher rates. However, the values do not indicate that the temperatures seen during testing are sustainable over the long term.

Table 4. Well productivity data

	Start Artesian Flow	**Stop First Airlift**	**Start Second Airlift**	**Stop Second Airlift**
Starting Flow Rate	0	172	65	300
Ending Flow Rate	60 – 75?	55	300	60?
Change in Flow Rate	60 – 75?	117	235	240
Pressure Before Change	103.40	38.27	46.45	39.4
Pressure After Change	100.46	43.54	37.91	48.23
Change in Pressure	2.94	5.27	8.54	8.83
Productivity (gpm/psi)	20.4 – 25.5	22.2	27.5	27.2

The pressure record in PS-13-1 shows a 2 psi increase after 22:30 hours on September 16 (Figure 41). This increase reflects the thin cable holding the tool breaking, and the tool moving part of a meter downhole until it was held by the thicker aircraft cable, which turned out to be useful backup for the Kuster tool.

9.4 Temperature and Pressure Monitoring in PS-13-2

Two hours after the first airlift of well PS-13-1, a Kuster tool was hung in well PS-13-2 near a depth of 30 m to monitor its downhole temperature and pressure for a few days during the expected longer and more voluminous second airlift. This PS-13-2 record is exceptionally complex for a well that was not flowing (Figure 45). The start and stop of the second airlift is marked by sharp pressure changes of about 0.2 psi. No net longer-term pressure change occurred between the pressure prior to the airlift and pressures near the end of the monitoring period.

During the airlift, a curious temperature increase and decline was recorded that requires a much deeper understanding of the hydrology to explain (Figure 45). Equally large or larger temperature changes occurred when the airlift was not in progress.

9.5 Temperature and Pressure Monitoring in PS-13-3

A Kuster tool was also hung in PS-13-3 after the first airlift of PS-13-1 to document the downhole pressure and temperature changes (Figure 46). This record shows a sharp 0.2 psi reaction to both the start and stop of the airlift. There is no longer-term net pressure change from the start of monitoring to the end. A tiny 0.05°C temperature rise was associated with the higher

flow that did not reverse after the airlift. Also, three tiny temperature spikes occurred after 20:00, close to one day apart, that are not understood.

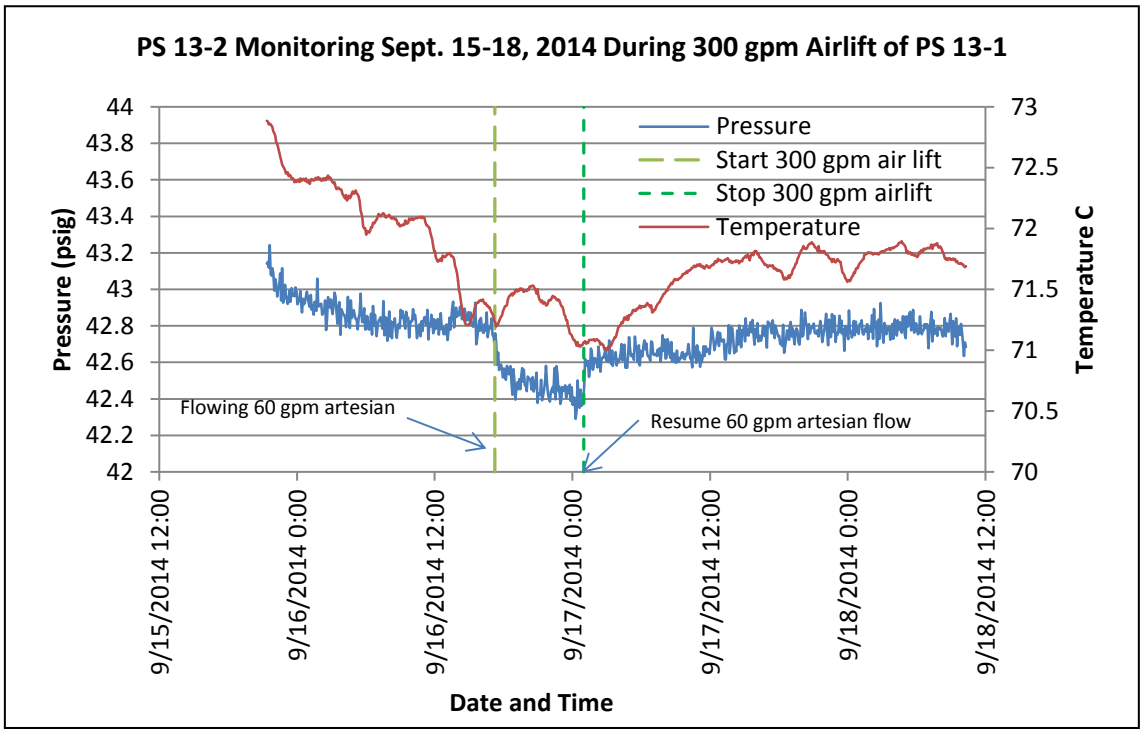


Figure 45. PS-13-2 pressure and temperature response during PS-13-1 flow testing.

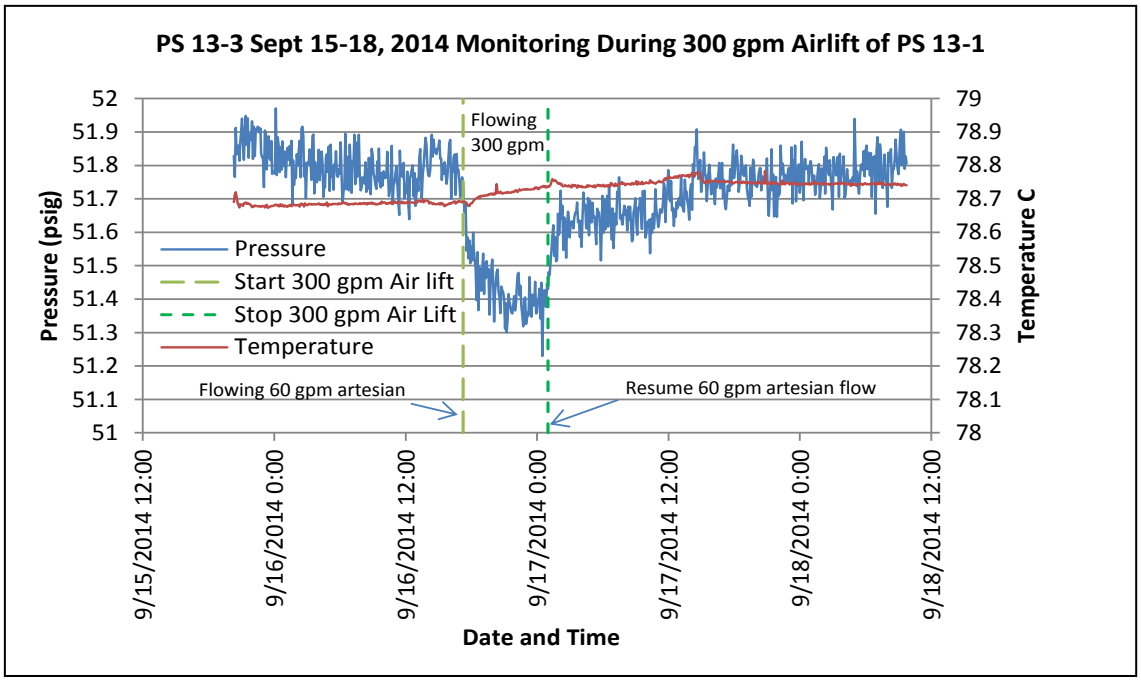


Figure 46. PS-13-3 pressure and temperature response during PS-13-1 flow testing.

9.6 Historic Hot Springs Temperature Monitoring

A small Hobo brand temperature monitoring probe was placed in the discharge area in the historic hot spring pool at PHS during testing of the wells. The pool is located 750 feet northeast of well PS-13-1. During the testing period, the sensor was placed in the northwest corner of the pool, about 2 feet below the water surface (Figure 47).



Figure 47. The historic hot spring pool temperature was monitored during flow testing of PS-13-1.

Researchers Chris Pike and Dick Benoit also used a presision temperature measuring probe owned by Southern Methodist University to measure temperatures in the bottom of the pool, inserting the probe several inches into the sandy bottom of the pool and recording the temperatures. A maximum temperature of 73°C (163°F) was encountered in the extreme eastern edge of the pool.

The water temperature of the pool was monitored between September 9 and 18, 2014, with a brief interuption during the early morning hours of September 16 to download data. During the time that the temperature was being recorded, the hot spring pool was being used by the public for soaking and relaxation activities. Chris Pike, an ACEP staff member, monitored the temperature probe on a nightly basis to ensure that it was still in position. During a brief period

on September 12, the probe was removed from the spring. The data collected show that the pool temperature varied for unknown reasons, but mostly stayed between 38°C and 43°C (100°F–110°F) (Figure 48).

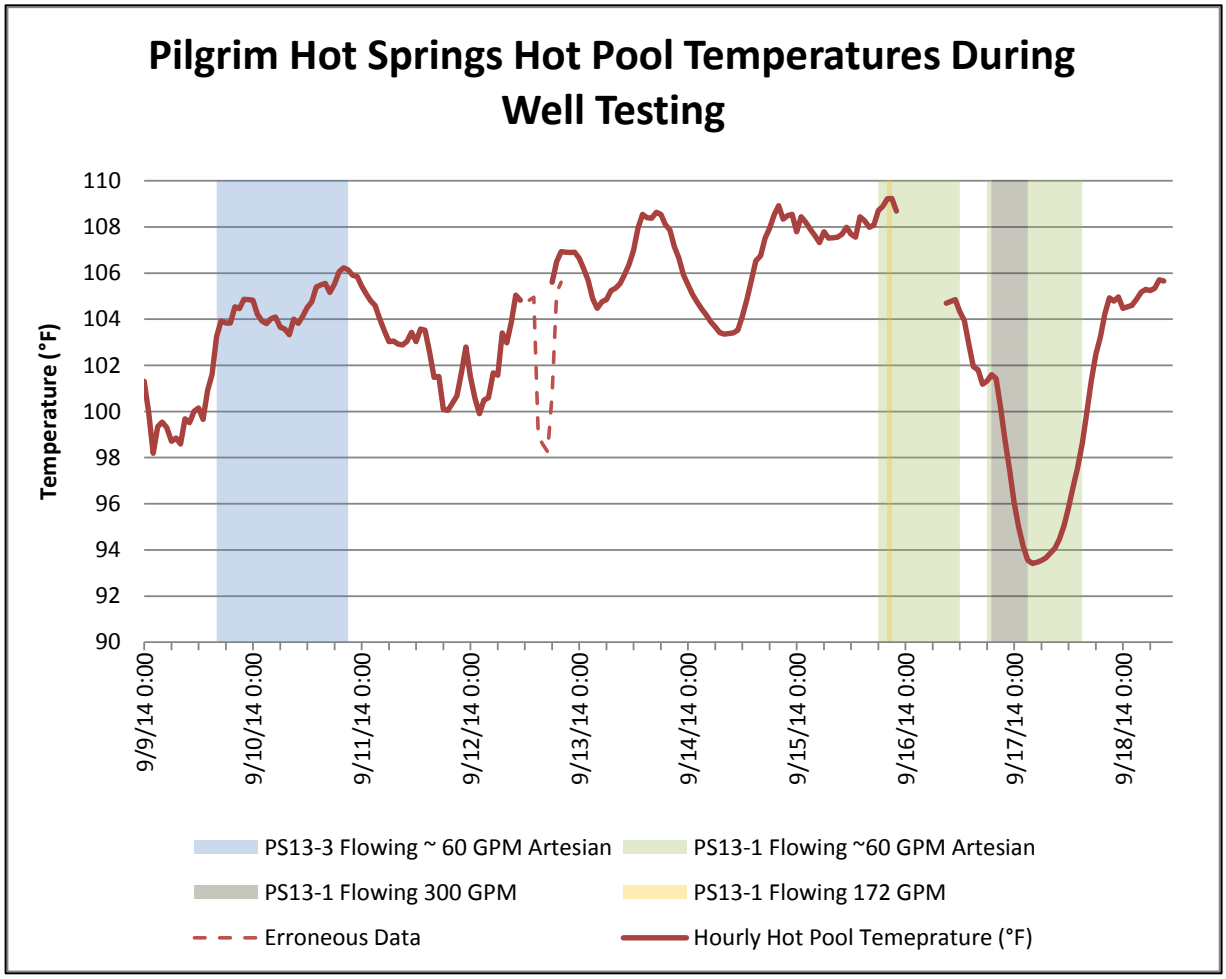


Figure 48. Hot spring pool temperatures during the September 2014 flow testing. The lowest temperature recorded occurred when the greatest flow rates were being pumped from PS-13-1.

During the 300 gpm flow testing, the pool temperature dropped and did not stabilize and begin to rise again until after airlift pumping was stopped. During this time, the pool dropped to its coolest recorded temperature, below 34°C (94°F) (Figure 48). Further testing is needed to draw a difinitive correlation between the temperature of the hot spring pool and the flow of the wells. However, pumping of water from the shallow thermal aquifer likely impacts the flow of hot water into the pool.

9.7 Flow Testing Conclusions

Well PS-13-1 was airlifted for over 7 hours at an average flow rate of 300 gpm, which represented about the largest flow that could have been achieved with available equipment. A

longer flow test would have been more desireable, and help to better define the resource however, due to time and funding constraints it was not possible. We acknowledge this weakness and recommend future flow testing prior to substantial investment in anything other than small scale power generation.
Repeated productivity measurements with flow rate changes of 60 to 240 gpm gave values of 20.4 to 27.5 gpm/psi which indicate a productive well. It is encouraging that the productivity values associated with the higher flow rates had the highest values. During the airlift, most of the fluid must have entered the wellbore in the main shallow thermal aquifer and flowed down through the sediments along the blank casing to enter the screened part of the well below 57.3 m.

The airlift test impacted wells PS-13-2 and PS-13-3 nearby with a 0.2 psi pressure decline. Apparently, temperature impacts also occurred, but the indicators are not convincingly explicable with the available data.

10. PILGRIM GEOTHERMAL SYSTEM CONCEPTUAL MODEL

10.1 Conceptual Model History

Conceptual speculation about the PGS dates to its first recorded visit by geologist G. A. Waring, who was interested in the geothermal system (Waring, 1917). Waring noted that the sulfate-to-chloride and the calcium-to-sodium ratios in the thermal water were much different from seawater and that the relatively high salinity was not due to "an admixture with sea water" (p.74). Also, Waring speculated that "beneath the river alluvium the bedrock may be gneiss, intruded by a granitic mass … the heated water rises along the fractured contact zone between the two kinds of rock"(p.75). Waring drew no schematic diagrams of the PGS.

In the early 1970s, the USGS embarked on a program to improve the understanding of geothermal systems in the United States; it developed long-lasting conceptual understandings of the PGS even if it did not draw a specific conceptual model. In Alaska, Miller et al. (1975) assessed the geochemistry of many of the known springs and their regional geologic setting. In terms of regional setting, the proximal relationship between thermal springs and granitic plutons was recognized. Miller et al. (1975) presented the first stable isotope analysis of the Pilgrim thermal water, which showed the water to be derived from local rain and snowmelt. The thermal fluid is not a mixture of meteoric water and seawater. Miller et al. (1975) presented the first predicted PGS subsurface temperatures—137°C (279°F) based on the quartz geothermometer and 146°C (295°F) based on the Na-K-Ca geothermometer—and concluded that the thermal water must be at depths of 9000 to 15,000 feet (3.3 to 5.3 km) to reach these temperatures, based on a gradient of 30°C–50°C/km. Finally, Miller et al. (1975) observed that "most, if not all, of the hot springs are characterized by reservoirs of limited extent and relatively low temperatures in comparison with temperatures of geothermal systems presently being exploited for power generation"(p.12).

The first conceptual model of the PGS was bravely put forth following the 1979 field season, with the focus on small-scale and very shallow convection cells and a water balance model (Osterkamp et al., 1980). The water balance model (Figure 14 from Osterkamp et al., 1980) allows for the possibility of rising hot water being impacted by subpermafrost cold recharge and

recirculation of thermal water. Various power estimates were made. The geothermometry from PHS and the first two wells drilled in late 1979 indicated the presence of a deeper and hotter 145°C–150°C (293°F–302°F) reservoir (Motyka et al., 1980).

The second conceptual understanding of the PGS was developed in 1982 after the first six wells had been drilled and flow tested (Figure 3 from Economides, 1982). The primary result was the recognition of the shallow reservoir of laterally flowing thermal aquifer and the exceptionally bold conclusion was that "the existence of a hot water zone of about 150°C (302°F) and at a depth of around 5000 feet is now virtually certain" (Economides, 1982; Economides et al., 1982, p.30). In fact, a more specific depth of 4875 feet was stated, based on extrapolating the positive temperature gradients beneath the shallow thermal aquifer. The researchers also stated that "locating the hot water source for the shallow zone is relatively unimportant, since the fluid at depth provides a high temperature source formation extending aerially at least as far as the total area drilled" (p.28). Regrettably, the total area drilled by 1982 amounted to only a few square acres.

Liss and Motyka (1994) relied upon geochemical data to suggest that Tertiary–Quaternary marine sediments might underlie PHS and that the PGS might have subsurface temperatures as hot as 190°C–230°C (374°F–446°F) based on a Mg-Li geothermometer and admittedly suspect noncondensible gas geothermometry. More recent drilling at PHS did not encounter Tertiary–Quaternary marine sediments. Liss and Motyka (1994) also noted a $^{3}He/^{4}He$ value of 0.9, which suggested a mantle component of helium. No work was performed on the PGS from 1993 until 2010.

Following this nearly two-decade hiatus, Daanen et al. (2012) utilized the COMSOL Multiphysics finite element package to develop the first numerical model of the PGS. This modeling assumed steady-state conditions with an ongoing flow of cold water toward the geothermal system being required to maintain the high negative-temperature gradients beneath the shallow thermal aquifer. The model indicated that potentially 38 MW of thermal energy moves through the shallow groundwater system near PHS. Concurrently, Chittambakkam et al. (2013) utilized the TOUGH2 simulator and assumed similar steady-state conditions to estimate a total heat loss of 26 MW (Appendix N).

Unfortunately, more recent geologic studies have brought new information to light which does not coincide with the results of these modeling efforts. In the case of Daanen et al. (2012), the observed vertical temperature distribution given in their Figure 3 shows no shallow lateral flow and implies that it should be possible to drill a well below PS-1 with near isothermal temperatures of 90°C (194°F), which was disproven by the drilling of well PS-13-3. In the case of Chittambakkam et al. (2013), their simulated temperatures in Figures 12 and 13 do not show 90°C water flowing from depth to the surface. Instead, there is an unexplained cooling and then reheating of the thermal upwelling.

Benowitz et al. (2013) used thermochronology modeling to constrain the tectonic regime responsible for the PGS. They conclude that the thermal anomaly is related to the youthful extensional setting of the Kigluaik range front fault and is not thermally equilibrating, suggesting that the hottest temperatures have not been accessed (Appendix O).

Miller et al. (2013a) present the most complete and detailed conceptual picture of the upper 700 feet of the PGS (Figure 49). In their model, an areally restricted near-vertical thermal upwelling transmits 90°C water almost to the surface. There is a near-cylindrical thermal anomaly with a radius of 500 to 800 m extending outward from this upwelling that, by the distance of the temperature decline to 20°C (68°F), is basically vertical. Also shown in the Miller et al. (2013a) model (Figure 49) is a strong flow of cold groundwater beneath the shallow aquifer flowing toward the thermal upwelling from both east and west and then flowing north toward the Pilgrim River. This is the steady-state model wherein the thermal anomaly and static temperature profiles of the various wells could remain in the described condition for an indefinite period provided the relative flow rates of hot and cold water remain more or less constant. One other challenge for the model developed by Miller et al. (2013a) is that three recent wells drilled to locate thermal upwelling do not show it located where it is shown in the model (Benoit et al., 2014a).

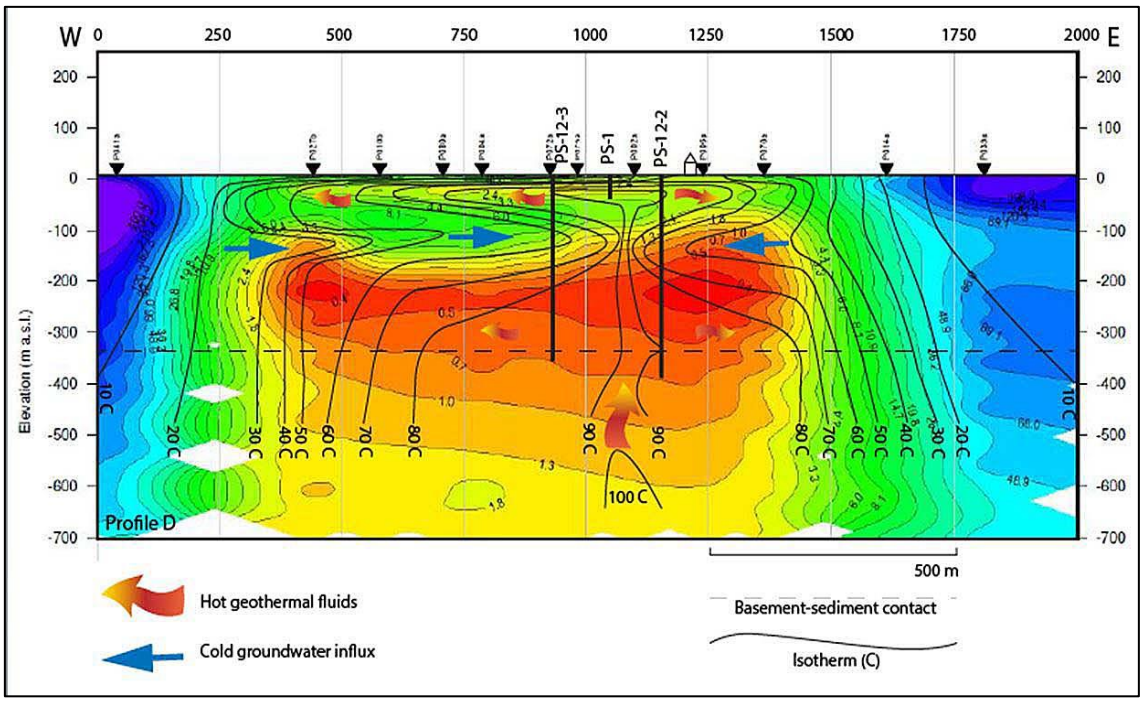


Figure 49. Conceptual model from Miller et al. (2013a).

All subsurface temperature data acquired to date were used to create the plan view maps shown in Figure 8. These maps show temperature contours of the shallow thermal aquifer and the temperature minimum, measured from the deep wells. These data along with modifications to the Miller et al. (2013a) model were used to create Figure 51, which shows the current understanding of the PHS upwelling.

The model in Figure 51 shows temperature contours across the thermal anomaly, using a northwest to southeast cross section. The upwelling is shown in the area northwest of PS-13-1, where no subsurface exploration has been attempted due to swampy conditions and challenging access. Numerous Geoprobe and temperature gradient holes south and east of PS-13-1 allow a

high degree of confidence in the subsurface temperatures. North and west of PS-13-1, no drilling activities have taken place, and the temperatures shown are estimates that could occur, based on the conditions given in the model.

Glen et al. (2014) developed a more regional conceptual model of the overall geothermal system (Figure 50). This model consists of a diffuse downward flow of meteoric water through basement rocks, along range-bounding faults that separate the Kigluaik Mountains and Hen and Chickens Mountain from the Imuruk Basin. Hot fluid is shown diffusely rising through bedrock beneath the valley; it becomes focused in a narrow inferred northeast-trending structure that is diagonal across the basin, and then rises obliquely in a northeasterly direction. The proposed northeastward hot flow direction is largely based on a prominent gravity low southwest of PHS, which suggests 800 m depth to bedrock (Figure 22). Fluid then flows along the shallowing and narrowing bedrock contact toward the northeast, where close to the surface location of the hot springs it is further concentrated into north- and northeast-trending structures that allow it to rise steeply through approximately 300 m of clay-rich alluvium to the surface. This model is constrained by drill-hole data only in a small area near the hot springs. No temperature or quantitative depth distribution of the thermal fluid is shown in the Glen et al. conceptual model.

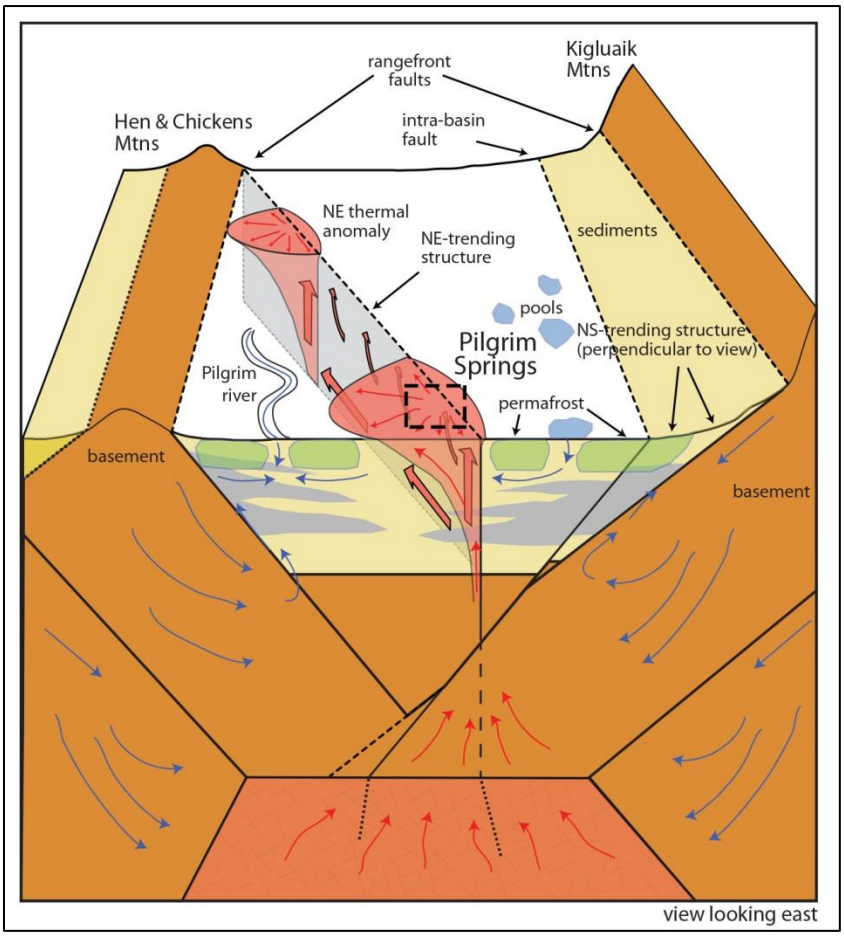


Figure 50. Regional conceptual model cartoon from Glen et al. (2014).

The culmination of this report is to present as complete a conceptual model as possible of the PGS. This model uses to the maximum extent the previous efforts and covers the range from regional aspects to quite detailed local features within the thermal area.

There is no doubt that the thermal fluid at PHS comes from a local meteoric source. Whether this fluid is recharged from the Kigluaik Mountains to the south or from the Pilgrim River Valley is unknown, as not enough local meteoric isotopic samples have been collected from these areas. Discriminating between these two possibilities will first require determining if there are measurable isotopic differences between precipitation falling on the south and north sides of the Kigluaik Mountains. Obviously, this information is of more academic than practical interest in trying to develop the PGS, which is why it was not pursued as an integral part of the recent exploration effort.

To date, drilling efforts at PHS have been unsuccessful in finding the estimated subsurface temperatures of 140°C to 150°C (284°F–302°F) that have provided much of the impetus for extensive exploration of this location over the past 40 years. Perhaps the higher temperatures are a relatively large lateral distance away from the thermal springs or at much greater depths. If so, the direction to go is uncertain. Even if a location lateral to the thermal springs were known, the costs to access it by road would likely be high. Alternatively, perhaps the quartz and NA-K-1/3Ca geothermometers may not have been appropriate for the PGS, and more conservative predictions, such as the chalcedony and Na-K-4/3Ca geothermometer, should have been used. In this case, the predicted subsurface temperatures would be near boiling at depth. Another possibility is that somehow the exceptionally high calcium content in the PHS water is impacting the accuracy of the cation geothermometers. A lower base temperature of perhaps 100°C (212°F) for the geothermal system does not require the meteoric water to descend to depths of 9000 to 15,000 feet, as calculated by Miller et al. (1975); it still would have to go as deep as 10,000 feet. Unfortunately, no background heat flow holes are anywhere near PHS to constrain the regional background temperature gradient.

In west-central Alaska, Miller et al. (1975) observed that "apparently fracture systems were not developed or are not sufficiently open in well-foliated regionally metamorphosed rocks to allow deeply circulating hot water to gain access to the surface" (p.6). In the 40 years since this observation was first printed, very few producing geothermal fields have been hosted by foliated metamorphic rocks. The few examples of wells producing from foliated rocks are not highly productive. This makes it more challenging and risky to drill into the metamorphic bedrock beneath PHS to produce from fractured bedrock. To date, the bedrock samples recovered from PHS drilling have been metamorphic, not granitic. Granitic rocks and other volcanic and sedimentary rocks in west-central Alaska regularly host geothermal systems. However, no geophysical interpretation or discussion has yet argued granitic rocks are present beneath PHS.

The structure(s) controlling the thermal fluid flow remain poorly understood, though there is agreement that the east–west-trending Kigluaik range-front fault is the dominant structure in the vicinity of the PGS, and is probably close to optimal orientation for the critical failure needed to create open space for thermal fluid flow. Structures trending north–south or northeast–southwest would be much less likely to pull apart to create the needed open space for fluid flow. Structures oriented in these less optimal directions would need to be in more complex local settings for

permeability. Intersections of single narrow faults present small targets and are unlikely to have enough areal extent for development as geothermal fields. This kind of geometry would require some second permeability, such as a connection to nearby permeable formations, to store enough fluid to develop a viable production/injection strategy. The dip of the Kigluaik range-front fault at depth is unknown, so it is highly speculative to draw it at a low enough angle for realistic penetration by a well near the thermal springs. If other east–west-trending faults are present beneath the Pilgrim Valley, they have not created a density contrast large enough to be recognized on the gravity map.

It is interesting to speculate on the nature of the local structure or feature at PHS that is transmitting the thermal water from the top of the metamorphic rocks at 320 m to the surface. Nobody has yet described any surficial indication of such a structure, which must be either very young or somehow continuously active to maintain its permeability. Miller et al. (2013a) recognize a 1 m high north–south terrace that is near the west edge of the thermal anomaly near the postulated north–south-trending fault, but also note that the terrace could be the result of frost heaving. This feature must penetrate and keep open multiple layers of soft clay above the bedrock. It is difficult to describe a feature that has proven so elusive. The drilling and temperature results to date indicate this feature is most likely northwest of where drilling has occurred. If the zone of upwelling is located between the already drilled wells, then it is likely so small that whether it represents a viable target becomes a question.

10.2 Current Pilgrim Geothermal System Understanding

With the background presented thus far, the conceptual model based on our current understanding of the PGS contains the following components:

1. Local meteoric water must travel to depths of 15,000 feet to provide a resource temperature of 150°C (302°F) if the regional temperature gradient is 30°C–50°C/km (Miller et al., 1975). If a lower resource temperature near 100°C (212°F) is present then the water may only need to travel as deep as 10,000 feet. Whether the cold water flows down a single fault in a concentrated manner or through myriad small fractures in bedrock is only of academic interest, as no developer's activities are likely to impact this flow.

2. The area of the top hundred or so feet near the discharge point of the PGS has been quite well characterized. Some thermal water is actually able to reach the surface and discharge through the thermal springs. This water reaches the near surface with a temperature of 91°C (196°F). Some thermal water is discharged into a very shallow aquifer several feet or meters below the surface and spreads laterally over a fairly large area. Most of the thermal water is discharged through the shallow thermal aquifer near a depth of 100 feet. Most likely, this shallow aquifer is charged not too far to the northwest of well PS-13-1. Where the water that percolates through the shallow aquifer eventually travels is unknown, as this has not been the primary purpose of recent exploration. It is suspected, however that this water travels to local sloughs, natural hot springs, and the Pilgrim River. The amount of water discharged onto the surface and into the shallow subsurface amounts to about 20 to 40 MW thermal.

3. The nature of the feature or features allowing the thermal water to rise through the Quaternary alluvium is unknown. Individual faults or intersecting structures have been previously proposed, but as noted, the proposed ideas are somewhat questionable and nobody has yet strongly argued the case for these features.

4. The northeast thermal anomaly is real, but so little is known about it at this time that it is unclear if it is part of the same geothermal system as the PGS. If it is part of the same system, then the argument for a northeast-trending structure becomes stronger. If the northeast thermal anomaly is not actually part of the PGS, then the possible northeast trend might actually be misleading.

5. The sharply declining temperatures beneath the shallow thermal aquifer can be interpreted in two ways. A steady-state model requires that cold water be flowing beneath the shallow thermal aquifer to remove the heat. A transient model does not require such cold groundwater flow. Arguments against the steady-state model are based on two facts. First, the original static temperature profiles in the deeper wells were all very smooth and showed none of the complexity that moving water imparts to them. Once the wellbores connected various zones of permeability, then water movement in the static temperature profiles became obvious (Benoit et al., 2014b). Second, the hot and cold flowing water would be competing for the same permeability channels near the thermal upwelling, presumably in gravel and sandy layers. The thermal water clearly has enough pressure to flow up to the surface but there are no recognized cold springs near the thermal springs. If there were abundant cold water with artesian pressure coming from the Kigluaik Mountains, only a perfect seal or a near-perfect pressure balance could separate the two hydrologies. With the amount of gravel described by Miller et al. (2014a), this seems quite unlikely. An argument might be proposed that having 100 m of permafrost surrounding the thaw bulb offers the best available protection from invading cold water at shallow depths.

To place the proceeding arguments into a picture, we know there must be a thermal upwelling, and by default, the most likely place for its location is a modest distance to the northwest of well PS-13-1 (Figure 51). The nature of the permeability in this channel is uncertain. Faults or fault intersections have been hypothesized, but no convincing evidence has been presented for verification. The thermal water must have circulated deeply within the metamorphic or metamorphic/granitic bedrock. It is not known at what depth the thermal water became concentrated into the focused flow we see near the surface. Whether it has diffusely flowed along the top of the bedrock or has risen as concentrated flow through the upper part of the bedrock is speculative.

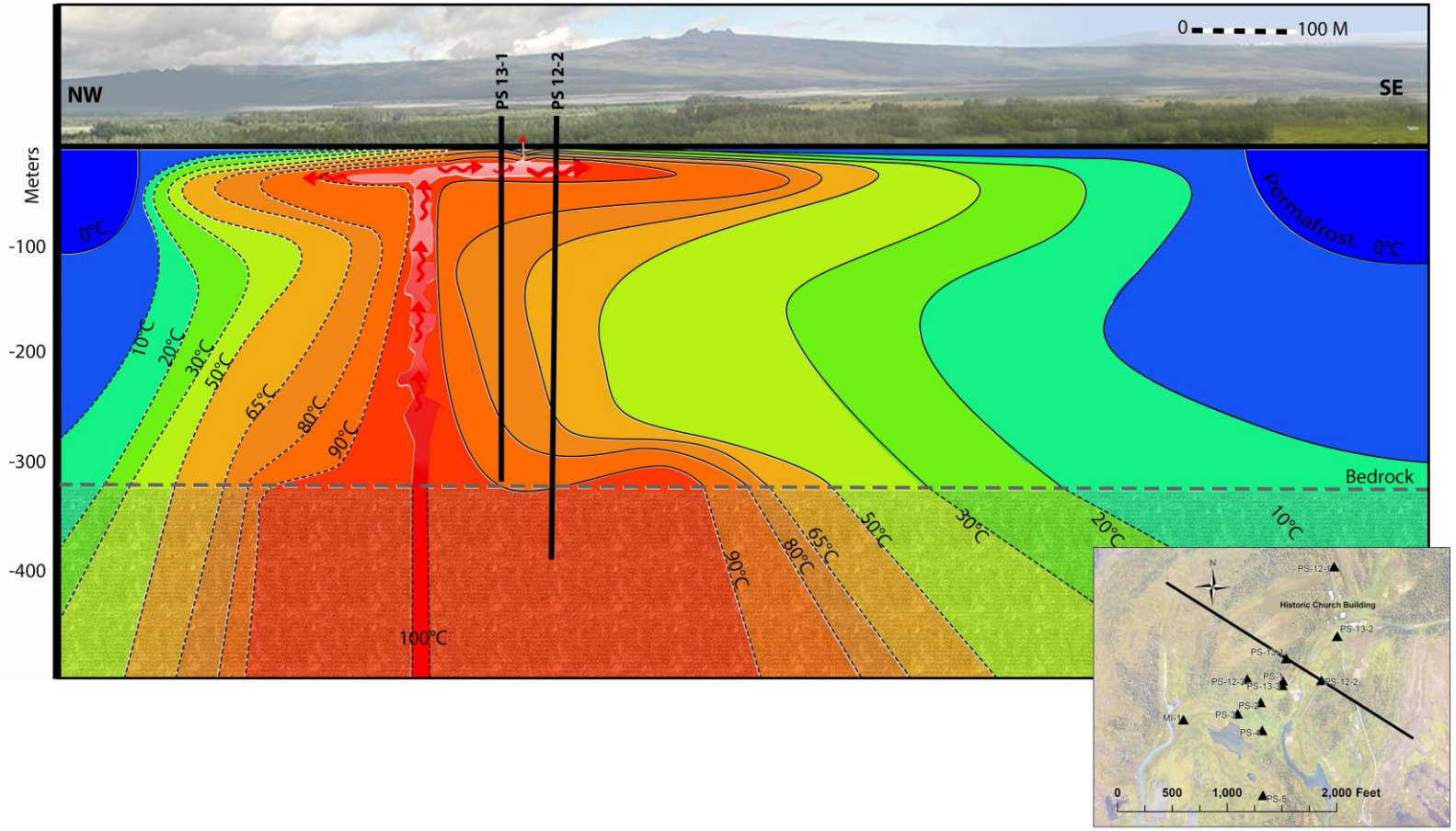


Figure 51. The current conceptual model of Pilgrim Hot Springs as shown in a cross-sectional view looking from southwest to northeast. This model, which is based on all data acquired through September 2014, indicates that the main upwelling zone is in the swampy area northwest of PS-13-1. Bedrock is represented by the dashed horizontal line at approximately 320 m in depth. The dashed temperature contours represent areas where the temperatures have not been well measured.

11. EXPORTING GEOTHERMAL ENERGY TO NOME

Like most rural areas of Alaska, Nome relies on a diesel microgrid for its electrical power. The diesel fuel that powers this grid is shipped long distances during a short period when the sea is ice free and is stored in bulk fuel storage tanks until it is used for home heating or electricity generation. Rural communities in Alaska face challenging logistics, limited infrastructure, and poor economies of scale. These factors coupled with high oil prices equate to expensive energy prices that make economic development challenging in many of Alaska's rural communities.

In 2008, the Nome Region Energy Assessment, funded by the U.S. Department of Energy and the National Energy Technology Laboratory, concluded that geothermal energy was a potentially economic option for the region, depending on the size of the power plant that the geothermal resource could support (Sheets et al., 2008). Following the success of the Chena Hot Springs project, a preliminary feasibility study was performed in conjunction with the Nome Regional Energy Assessment report (Dilley, 2007).

To support landowners and the City of Nome in their decision-making process regarding possible development options, several studies related to the integration of 2 MW of geothermally generated electricity into the existing Nome grid and the economics of the project have been conducted in conjunction with the geothermal exploration described in this report.

11.1 Geothermal Power Economics

In 2012, a private developer representing Potelco Power and Telecommunications expressed interest in developing a geothermal project at PHS. Potelco believed the project could be economically viable, and transmission infrastructure could be constructed between PHS and Nome if the resource could provide at least 2 MWe. Potelco created Pilgrim Geothermal LLC, under which development activities would take place. The City of Nome negotiated a power purchase agreement with Pilgrim Geothermal LLC to purchase 2 MW of geothermally generated electricity. To determine if this energy would be cheaper for their ratepayers than traditional electrical power generated with diesel generators, UAF economist Antony Scott modeled the price of Nome diesel versus the price of Arctic North Slope crude and then used this information to project possible future Nome diesel prices based on U.S. Department of Energy crude oil price predictions. The work provided a framework for decision makers as they weighed the pros and cons of integrating a geothermal generation source into the Nome grid. Indeed, from a utility point of view, the most compelling aspect of adding geothermal is the opportunity to reduce the price volatility that results from the fluctuating price of diesel (Scott, 2015). This was the first attempt to quantify diesel price risk in remote locations that receive only a few fuel deliveries per year. The full report is shown in Appendix Q.

11.2 Wind-Diesel-Geothermal Microgrid Modeling

In 2013, Nome increased its nameplate wind power capacity to 2.7 MW to provide a portion of the annual average load of 4 MW. To model the effect of 2 MW of geothermal power, which had been negotiated as a take or pay power purchase agreement, UAF researchers created a time step simulation model using two years of Nome grid data. As with the economic analysis explained in

the previous section, the grid modeling was intended to serve as a guide to Nome decision makers as they decided if the integration of geothermally generated electricity was beneficial to the utility's ratepayers. A non-load following 2 MWe geothermal generation scheme was modeled in conjunction with the installed wind and diesel capacity. The Nome utility wished to observe the effect of possible geothermal power on its ability to fully utilize the wind resource, which would soon be owned, maintained, and controlled by them, and minimize the wind that would need to be "dumped." Researchers also modeled the utility's ability to fully use the wind if it added smaller generators to the diesel powerhouse. According to VanderMeer and Mueller-Stoffels (2014), "adding to the diesel generator fleet to create smaller, more consistent differences between the combined capacities of diesel generator combinations resulted in less diverted wind energy, more displaced diesel generated energy, a higher diesel generator load factor, and more diesel generator switching" (p.4). This modeling allowed the utility to determine the value of adding geothermal generation, while still considering the decrease in performance due to increased switching and decreased load factor.

11.3 Transmission from Pilgrim Hot Springs to Nome

The remote location of PHS, 60 miles north of Nome, complicates any future development of a power generation facility. While the site is accessible via road, the transmission infrastructure must be constructed from PHS to Nome if any power generated on-site is to be purchased and consumed in Nome. A transmission option that has been investigated in hopes of lowering the infrastructure cost of transmission in rural Alaska is a high-voltage direct current (HVDC) transmission line. Conventional alternating current (AC) transmission requires three- or four-wire transmission infrastructure, while HVDC transmission requires one or two wires. This could reduce cost through wire savings and reduced structural loads, requiring fewer poles and saving money in materials and construction time (Polar Consult Alaska, 2012). This research is discussed in detail in Appendix R.

12. LESSONS LEARNED

The remote location of Pilgrim Hot Springs, short snow-free construction season, thick layer of Quaternary alluvial fill above the bedrock which included multiple permeable layers, and limited accessibility, necessitated careful operational planning. During the course of the research at Pilgrim Hot Springs it has become clear that some parts of the project were highly successful, and other elements of the project could have been done differently and more efficiently. Many of the lessons learned are detailed below in the hopes that future geothermal exploration in the area can benefit from this experience. These lessons learned include:

- The combination of the aerial FLIR and optical remote sensing data used in conjunction with the geoprobe exploration was an efficient and relatively cost-effective way to define the extent and temperatures of the shallow thermal aquifer. A slightly larger geoprobe unit might have been able to consistently penetrate through the temperature maximum of the shallow thermal aquifer and enable data collection as deep as 200 feet without the need for a full drill rig. If this unit had been used in the springtime when temperatures were cool and the ground was still firm, exploration northwest of PS13-1 might have been possible.

- FLIR surveys served the dual purpose of finding hot seeps and allowing the heat flux associated with the PGS to be modeled. Two surveys were performed, one in the spring and one in the fall time. The spring survey was the most useful for mapping areas of snowmelt that correspond to permafrost-free areas and anomalous vegetation growth not regularly found on the Seward Peninsula.
- Flow testing wells at flow rates exceeding the natural artesian flows proved to be challenging at PHS given the remoteness of the location, cost limitations, and temperatures. Basic water well pumps were not rated for the temperatures encountered at Pilgrim and required a rig on site to install. The lightweight air lifting apparatus that was utilized worked very well, however it did require close monitoring and regular refueling every couple hours. Flowing the well at rates greater than 300 gpm would have required additional manpower and equipment. The 6-inch Krohne magnetic flow meter that was used during this flow test was extremely reliable, effective, and accurate as well as user friendly.
- The 525 ppm of calcium in the Pilgrim water is an obvious suspect in raising the question of whether thermal waters with exceptionally high calcium contents provide accurate geothermometry calculations. Given the inability to encounter the temperatures predicted by established geothermometry techniques, additional research is warranted to see if there are other geothermal systems where high levels of calcium caused overly optimistic geothermometry estimates.
- The drilling associated costs consumed the most time and financial resources. The legacy wellhead repairs allowed researchers to utilize the wells that were drilled in the 1970's and 1980's for temperature and flow testing, and improved our understanding of the field. In addition, we were able to characterize subtle long term changes that have occurred over time. The temperature gradient slim holes were an economic way to measure temperatures at the top of bedrock. Ideally one or two more additional slim holes would have been drilled near where PS13-1 was eventually drilled and northwest of this area to help guide the later drilling of the large diameter well capable of flowing large quantities of geothermal fluid.
- The Alaska Oil and Gas Conservation Commission regulates geothermal exploration and drilling in the same way as oil and gas associated activities are regulated, regardless of depth, or the temperatures and pressures that one is likely to encounter. Applying the same standards that the oil and gas industry is bound to for low temperature geothermal exploration creates a situation where this type of exploration becomes cost prohibitive and disincentivizes the development of small geothermal resources. Revisiting the regulations associated with geothermal exploration in Alaska is warranted.

13. CONCLUSIONS

Geothermal exploration at Pilgrim Hot Springs (PHS) has significantly increased the understanding of this resource and enabled the planning of possible next steps, which are being carried out at the time this report is being written.

- Initial project planning included the consideration of helicopter supported drilling based on the belief that the area of upwelling could be north of the Pilgrim River. Slim hole drilling was able to define the edges of the shallow thermal aquifer and the depth of the

deep aquifer at PHS. Bedrock was encountered on several occasions which had not occurred during previous drilling at the site.

- The possible upwelling area was constrained by drilling and the most likely upwelling zone feeding PHS is located slightly northwest of well PS13-1 (Figure 51). This idea is supported by the plan view temperature maps in Figure 8, which describe the flow direction of the thermal fluids.
- We continue to believe the site is capable of supporting two megawatts of electrical power generation. The economic viability of exporting this power to Nome remains a question that private industry is best suited to answer. Repeated productivity measurements of well PS13-1with flow rate changes of 60 to 240 gpm gave values of 20.4 to 27.5 gpm/psi which indicate good productivity. A longer flow test would have been more desireable, and helped to better define the resource, however, due to time and funding constraints it was not possible. We acknowledge this weakness and recommend future flow testing prior to substantial investment in anything other than small scale power generation.
- The landowners at PHS are investigating different on-site development options and are currently moving forward with plans to begin producing agricultural products on the site. This could include the construction of greenhouses to produce food for export to local communities, tourism infrastructure, and community facilities. Traditionally, the export of geothermal power has occurred in the form of electricity; however, using the heat energy at PHS to grow food for the region could be a creative way to export the "energy" and supply a much-needed commodity that otherwise is shipped into the region. The high cost of food transported to the area is heavily impacted by the price of petroleum.
- Pilgrim Geothermal, LLC has indicated that it is planning additional drilling activities to identify the future production-well location for a large-scale geothermal electric power plant. Future exploration could rely on angle drilling from the existing drill to access the northwest target area.

14. REFERENCES

Amato, J.M., and Miller, E.L., 2004, Geologic map and summary of the evolution of the Kigluaik Mountains gneiss dome, Seward Peninsula, Alaska, Geological Society of America Special Papers, Vol. 380, pp. 295–306.

Benoit, D., 2013, Sept. 2013 interference testing of the 1982 Pilgrim wells, Unpublished report to ACEP, 16 pp.

Benoit, D., Pike, C., and Holdmann, G., 2014a, The Pilgrim thermal anomaly, Geothermal Resources Council Transactions, Vol. 38, pp. 470–486.

Benoit, D., Pike, C., and Holdmann, G., 2014b, Fluid-entry temperatures, depths, and water chemistry at Pilgrim Hot Springs, Alaska, Geothermal Resources Council Transactions, Vol. 38, pp. 487–495.

Benowitz, J., Haselwimmer, C., Metcalf, J., O'Sullivan, P.B., Flowers, R., Holdmann, G., Miller, J., 2014, Tectono-thermal history of Pilgrim Hot Springs, Alaska, Alaska Space Grant Conference, Juneau Alaska.

Bland, L.L., 1972, Special historical and cultural inventory of Imuruk Basin, Final Report, Phase II, Anchorage, Alaska, Human Environmental Resource Services, Inc.

Bucki, C., Finstad, G., and Smith, T.A., 2004, Reindeer roundup! A K–12 educator's guide to reindeer in Alaska. Reindeer Research Program, Alaska Agricultural and Forestry Experiment Station, School of Natural Resources and Agricultural Sciences, University of Alaska Fairbanks.

Chander, G., Markham, B.L., and Helder, D.L., 2009, Summary of current radiometric calibration coefficients for Landsat MSS, TM, ETM+, and EO-1 ALI sensors. Remote Sensing of Environment, Vol. 113, No. 5, pp. 893–903

Chittambakkam, A., Daanan, R.P., Haselwimmer, C., Prakash, A., and Holdmann, G., 2013, Development of a reservoir simulation model at Pilgrim Hot Springs, Alaska, using TOUGH 2, Proceedings of 38th Workshop on Geothermal Reservoir Engineering Stanford University, Stanford, California, February 11–13, 2013, 13 pp.

Daanen, R.P., Chittambakkan, A., Haselwimmer, C., Prakash, A., Mager, M., and Holdmann, G., 2012, Use of COMSOL multiphysics to develop a shallow preliminary conceptual model for exploration at Pilgrim Hot Springs, Alaska, Geothermal Resources Council Transactions, Vol. 36, pp. 631–635.

Dean, K.G., Forbes, R.B., Turner, D.L., Eaton, F.D., and Sullivan, K.D., 1982, Radar and infrared remote sensing of geothermal features at Pilgrim Springs, Alaska, Remote Sens. Environ., Vol. 12, No. 5, pp. 391–405.

Dilley, L.M., 2007, Preliminary feasibility report Pilgrim Hot Springs Nome, Alaska, Report for Alaska Energy Authority, 16 pp.
Economides, M.J., 1982, Drilling and reservoir engineering analysis of Pilgrim Hot Springs, Alaska, Report Submitted to the Division of Energy and Power Development, Donald Markle, Project Manager, 28 pp.

Economides, M.J., Economides, C.A.E., Kunze, J.F., and Lofgren, B., 1982, A fieldwide reservoir engineering analysis of the Pilgrim Hot Springs, AK, Proceedings of the 8th Geothermal Reservoir Engineering Workshop, Stanford University, Stanford, CA, pp. 25–30.

Forbes, R.B., Gedney, L., Van Wormer, D., and Hook, J., 1975, A geophysical reconnaissance of Pilgrim Springs, Alaska, University of Alaska, Geophysical Institute, February, Geophysical Institute Report UAG-R231.

Fugro Electro Magnetics Sri, 2012, Pilgrim Hot Springs, Alaska, Magnetotelluric (MT) Survey, Unpublished final report for the University of Alaska.

Glen, J., McPhee, D., and Athens, N., 2012, Airborne geophysical studies of the Pilgrim geothermal area, unpublished draft report for the University of Alaska Fairbanks, 38 pp.

Glen, J.M.G., McPhee, D.K., and Bedrosian, P.A., 2014, Geophysical investigations of the geologic and hydrothermal framework of the Pilgrim Springs geothermal area, Alaska, Proceedings 39th Workshop on Geothermal Reservoir Engineering Stanford University, Stanford, California, February 24–26, 2014, 9 pp.

Harrison, W., and Hawkins, D., 1980, Water and heat flow measurements and their relationship to power estimates at Pilgrim Springs, Alaska. Technical Report, University of Alaska, Geophysical Institute.

Haselwimmer, C.E., and Prakash, A., 2011, Use of airborne thermal imaging to quantify heat flux and flow rate of surface geothermal fluids at Pilgrim Hot Springs, Alaska, *in* AGU Fall Meeting.

Haselwimmer, C., Prakash, A., and Holdmann, G., 2011, Geothermal exploration at Pilgrim Hot Springs, Alaska, using airborne thermal infrared remote sensing, Geothermal Resources Council Transactions, Vol. 35, pp. 805–810.

Holdmann, G., 2007, The Chena Hot Springs 400kW geothermal power plant: experience gained during the first year of operation, Geothermal Resources Council Transactions, Vol. 31, pp. 515–519.

Hudson, T., and Plafker, G., 1978, Kigluaik and Bendeleben Faults, Seward Peninsula, *in* Johnson, K.M., ed., The United States Geological Survey in Alaska – Accomplishments during 1977, U.S. Geol. Survey Circular 722B, pp. B47–B50.

Huttrer, G.W., 2002, Summary descriptions of geothermal conditions at Kwiniuk and Pilgrim Hot Springs and beneath Kotzebue, Alaska, Unpublished report to the National Renewable Energy Laboratory; Contract ECE-2-32078-01, 5 pp.

Kienle, J., and Lockhart, A., 1980, Gravity survey of the Pilgrim Springs geothermal area, Alaska, *in* Turner, D.L., and Forbes, R.B., 1980, A geological and geophysical study of the geothermal energy potential of Pilgrim Springs, Alaska, University of Alaska Fairbanks, Geophysical Institute Report UAG R-271, pp. 73–79.

Kirkwood, P., 1979, The status of Pilgrim Springs, U.S. Department of Energy Topical Report DOE/DP/01540-3, Work performed under Contract No. EY-77-C-08-1540, 29 pp.

Kline, J.T., 1981, Surficial geology of the lower Pilgrim valley and vicinity, western Seward Peninsula, Alaska, Alaska Division of Geological and Geophysical Survey Open File Map AOF-140, 2 sheets.

Kline, J., Reger, R., McFarlane, R., and Williams, T., 1980, Surficial geology and test drilling at Pilgrim Springs, Alaska, in a geological and geophysical study of the geothermal energy potential of Pilgrim Springs, Alaska, Report to U.S. Department of Energy and Alaska Division of Energy and Power Development January 1980, pp. 21–28.

Kunze, J.F., and Lofgren, B.E., 1983, Pilgrim Springs, Alaska, geothermal; resource exploration, drilling, and testing, Geothermal Resources Council S Transactions, Vol. 7, pp. 301–304.

Liss, S.A., and Motyka, R.J., 1994, Pilgrim Springs KGRA, Seward Peninsula, Alaska: Assessment of fluid geochemistry, Geothermal Resources Council Transactions, Vol. 18, pp. 213–219.

Lockhart, A., 1981, Gravity survey of the central Seward Peninsula, *in* Wescott, E., and Turner D.L., Geothermal reconnaissance survey of the central Seward Peninsula, Alaska, Geophysical Institute Report UAG-R284, pp. 61–72.

Lofgren, B., (Woodward-Clyde), 1983, Geothermal energy development at Pilgrim Springs, Alaska, PHASE II: results of drilling testing and resource confirmation, Report submitted to State of Alaska Division of Energy and Power Development April 15, 1983.

Miller, J.K., Prakash, A., Daanen, R., Haselwimmer, C., Whalen, M., Benoit, C., Cumming, W., Clark, A.C., Mager, M., and Holdmann, G., 2013a, Geologic model of the geothermal anomaly at Pilgrim Hot Springs, Seward Peninsula, Alaska, Proceedings, 38th Workshop on Geothermal Reservoir Engineering Stanford University, Stanford, California, February 11–13, 2013, 9 pp.

Miller, J.K., Prakash, A., and Haselwimmer, C., 2013b, Investigating low-temperature hydrothermal alteration in drill cuttings from Pilgrim Hot Springs, Alaska, using a suite of low cost analytical techniques, Geothermal Resources Council Transactions, Vol. 37, pp. 989–995.

Miller, T.P., Barnes, I., and Patton, W.W., 1975, Geologic setting and chemical characteristics of hot springs in west-central Alaska, Jour. Research U.S. Geol. Survey Vol. 3, No. 2, Mar–Apr 1975, pp. 149–162.

Motyka, R.J., Forbes, R.B., and Moorman, M., 1980, Geochemistry of Pilgrim Springs thermal waters, *in* Turner, D.L., and Forbes, R.B., eds., A geological and geophysical study of the geothermal energy potential of Pilgrim Springs, Alaska, University of Alaska, Geophysical Institute Report UAG R–271, pp. 43–52.

National Register of Historic Places, 1977, Pilgrim Hot Springs Kruzgamepa, Teller, Seward Peninsula, Alaska, National Register #BEN-014.

Osterkamp, T.E., Gosink, J.P., Forbes, R., Gaffi, R., Hanscom, J., Kane, M., and Kline, J.T., 1980, A reconnaissance study of the hydrothermal characteristics and accessible power of Pilgrim Springs, Alaska, *in* A Geological and Geophysical Study of the Geothermal Energy Potential of Pilgrim Springs, Alaska, University of Alaska, pp. 113–156.

Patrick, M., Dean, K., and Dehn, J., 2004, Active mud volcanism observed with Landsat 7 ETM+, Journal of Volcanology and Geothermal Research, Vol. 131, No. 3–4, pp. 307–320.

Polar Consult Alaska Inc., 2012, HVDC Transmission Systems for Rural Alaska Applications. Version1.1, Anchorage, Alaska.

Prakash, A., Schaefer, K., Witte, W.K., Collins, K., Gens, R., and Goyette, M.P., 2011, A remote sensing and GIS based investigation of a boreal forest coal fire. International Journal of Coal Geology, Vol. 86, No. 1, pp. 79–86.

Ray, D.J., 1992, The Eskimos of Bering Strait, 1650–1898. University of Washington Press.

Rozell, N., 2006, Volcanoes, permafrost, earthquakes shape Alaska, Alaska Science Forum Article No. 1785, January 12, 2006, 2 pp.

Ruppert, N.A., 2008, Stress map for Alaska from earthquake focal mechanisms, *in* Active Tectonics and Seismic Potential of Alaska, Geophys. Monogr. Ser., Vol. 179, edited by Freymueller, J.T., pp. 351–367.

Ryan, P.J., Harleman, D.R.F., and Stolzenbach, K.D., 1974, Surface heat loss from cooling ponds, Water Resources Research, Vol. 10, No. 5, pp. 930–938.

Scott, A.G., 2015, Fuel oil volatility – Complications for evaluating a proposed power purchase agreement for renewable energy in Nome, AK, Innovating Energy Access for Remote Areas: Discovering Untapped Resources, 89.

Sheets, B. et al., 2008, Nome Regional Energy Assessment. DOE/NETL-2007/1284, p. 153.

Smetzer, M.B., 2010, Fairbanks Catholic diocese sells Pilgrim Hot Springs as part of bankruptcy plan, Fairbanks Daily News-Miner, March 10.

Stefano, R.R., 1974, Low temperature utilization of geothermal water in Alaska at Pilgrim Hot Springs, Presented at General Short Course on Geothermal Resources, Boise, Idaho, available from Idaho Dept. of Water Resources, Boise, Idaho, and Ralph R. Stefano, Stefano and Associates, Inc., Anchorage, Alaska, 14 pp.

Swanson, S.E., Turner, D.L., Forbes, R.B., Maynard, D., 1980, Bedrock geology of the Pilgrim Springs geothermal area, Alaska, Geophysical Institute, University of Alaska Fairbanks, UAG R-271, Fairbanks, Alaska.

The Alaskan Shepherd, 2009, Pilgrim Hot Springs: Building a future on the past, Vol. 47, pp.1–8,

Till, A.B., Dumoulin, J.A., Werdon, M.B., and Bleick, H.A., 2011, Bedrock geologic map of the Seward Peninsula, Alaska, and accompanying conodont data, U.S. Geological Survey Scientific Investigations Map 3131, 2 sheets, scale 1:500,000, 1 pamphlet, 75 pp., and database, available at http://pubs.usgs.gov/sim/3131/.

Turner, D.L., and Forbes, R.B., 1980, A geological and geophysical study of the geothermal energy potential of Pilgrim Springs, Alaska, University of Alaska Fairbanks, Geophysical Institute Report UAG R-271, 165 pp.

VanderMeer, J.B., and Mueller-Stoffels, M., 2014, Wind-geothermal-diesel hybrid microgrid development: A technical assessment for Nome, AK. In review

Van Stone, J.W., Kakaruk, J.A., and Lucier, C.V., 2000, Reindeer fairs on Seward Peninsula, Alaska, 1915–1918, Arctic Anthropology, pp. 60–77.

Waring, G.A., 1917, Mineral springs of Alaska, U.S. Geological Survey Water Supply Paper.

Wescott, E., and Turner, D., 1981, Geothermal reconnaissance survey of the Central Seward Peninsula, Alaska, Report UAG R-284 to Division of Geothermal Energy, U.S. Department of Energy Under Cooperative Agreement DE-FC07-79-ET27034.

Woodward-Clyde, 1983, Results of drilling, testing, and resource confirmation: Geothermal energy development at Pilgrim Springs, Alaska, Woodward-Clyde Report, 102 pp.

Appendix A
Pilgrim Hot Springs Well Diagrams and Information

Note:
It was standard practice for the drill crews to use English units in all driller logs and diagrams throughout the project. The schematics below have converted depths to metric units, however casing sizes and hole diameters has been left in English units.

Temperature Gradient Hole S-9

Temperature gradient hole S-9 was cased with 6-in diameter steel conductor casing to a depth of approximately 10 meters. An attempt was made to retrieve core samples however drillers were unable to continuously core in S9 due to the encountered soil conditions (disaggregated gravel, silt and sand), which was not unexpected. Drillers switched to rotary drilling and finished S9. Non-screened 2 inch casing was set from total depth to land surface and grouted into place. The casing was filled with water and used to measure subsurface temperatures with a thermal gauge.

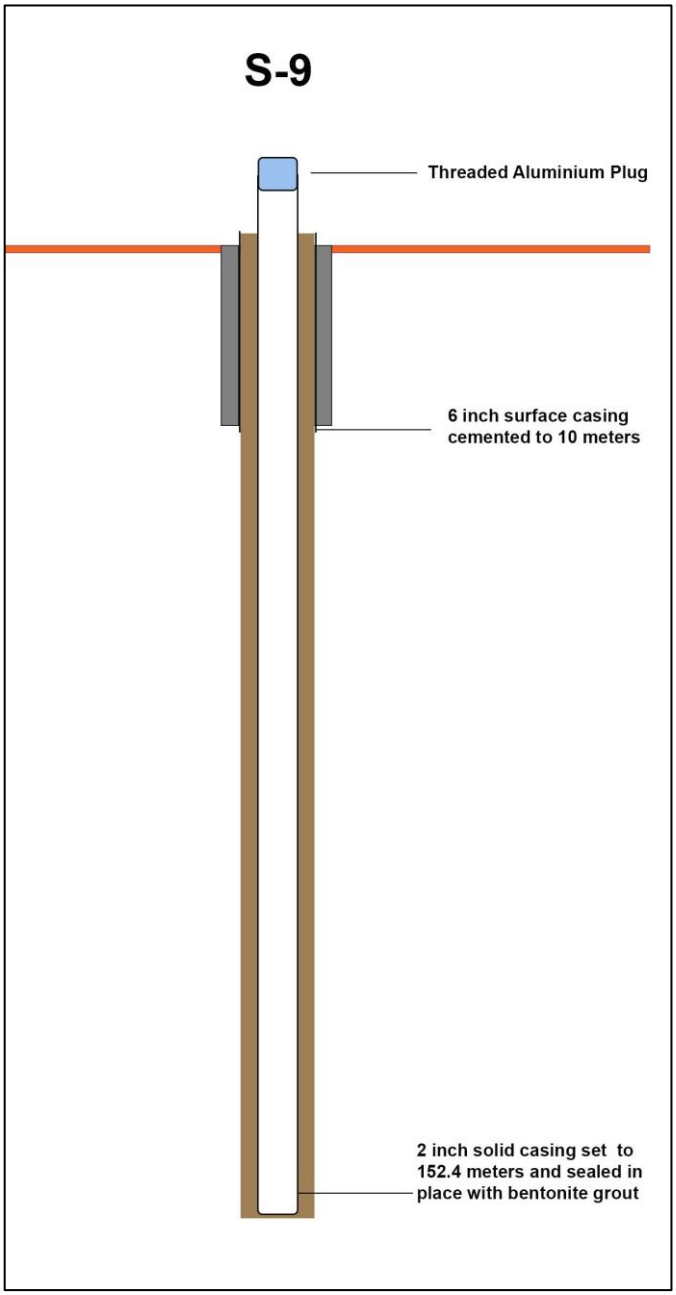


Figure 1. Temperature gradient hole S-9.

Temperature Gradient Hole S-1

Temperature gradient hole S-1 was cased with 6-in diameter steel conductor casing to a depth of 10 meters. S-1 was drilled entirely using rotary drilling due to the expectation that drillers would encounter the same unconsolidated soil conditions that were found in S-9. A non-screened 2 inch casing was set from total depth to land surface and grouted into place. The casing was filled with water and used to measure subsurface temperatures with a thermal gauge.

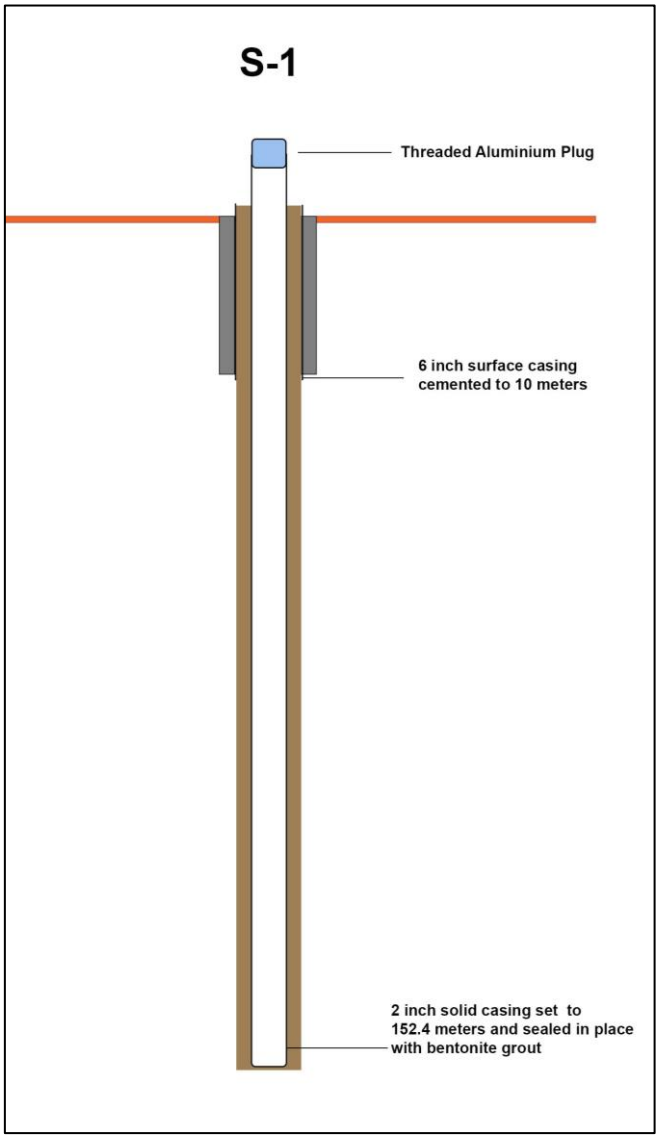


Figure 2. Temperature gradient hole S-1.

Deep Hole PS 12-1

PS12-1 was originally permitted to go as deep as 762 meters. The decision to drill to a shallower depth was made during the drilling process based on the measured down-hole temperatures and blow out preventer (BOP) damage that necessitated repairs. Drilling below 304.8 meters (1000 feet) was only permitted with the use of an annular blow out preventer. The hole was drilled on the Pilgrim Hot Springs property in the extreme end of the church campus, as far from the historic buildings as logistically possible. The hole was permitted as TG-1however the name was later officially changed to PS12-1 to be consistent with the other wells that were drilled. The well was spudded on July 3, 2012. Ten inch surface casing was driven to a depth of 3 meters. A 9 7/8 inch hole was drilled to 30.5 meters and the 6 5/8" conductor casing was cemented in place. After the cement set, a 6 inch hole was drilled to 304.8 meters, reaching total depth on July 11. 304.8 meters of HW casing was run into the hole and geolite cement was pumped through the casing to the surface. After the cement was set, the top was tagged at 182.9 meters with a 3 7/8" bit. The cement was drilled out to 301.7 meters. The well was completed by flushing the hole and filling the casing with water to enable future logging activities.

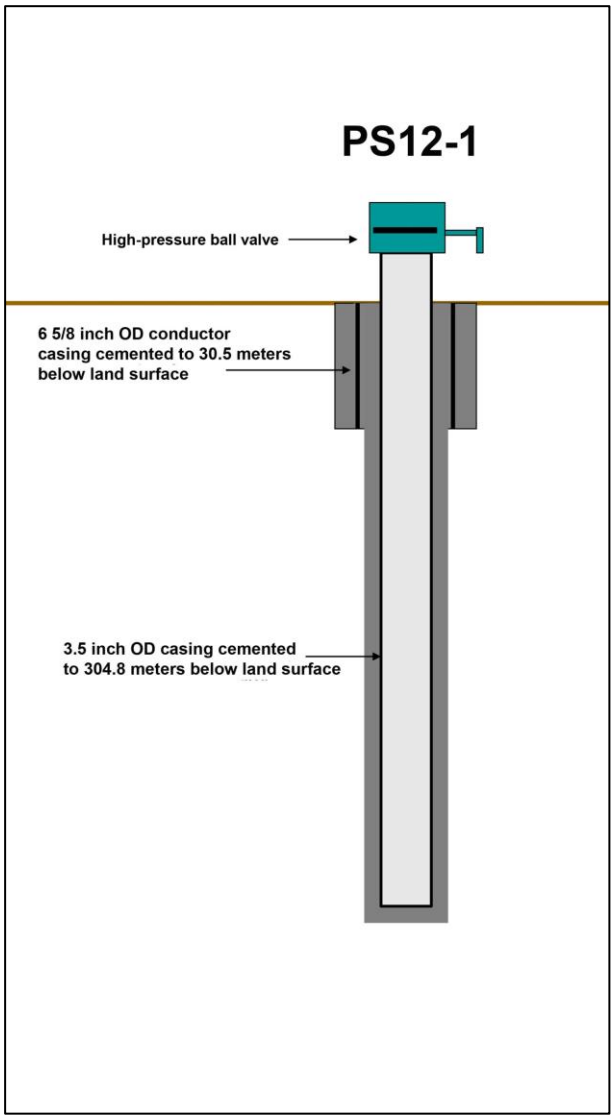


Figure 3. A schematic of hole PS 12-1.

On 27 July the drillers installed the BOP to the HQ casing on the well, as was required for drilling below 304.8 meters. A failed blow out preventer test required the BOP to be repaired. As a result, the drill rig was moved to begin drilling hole PS12-2.

Deep Hole PS 12-2

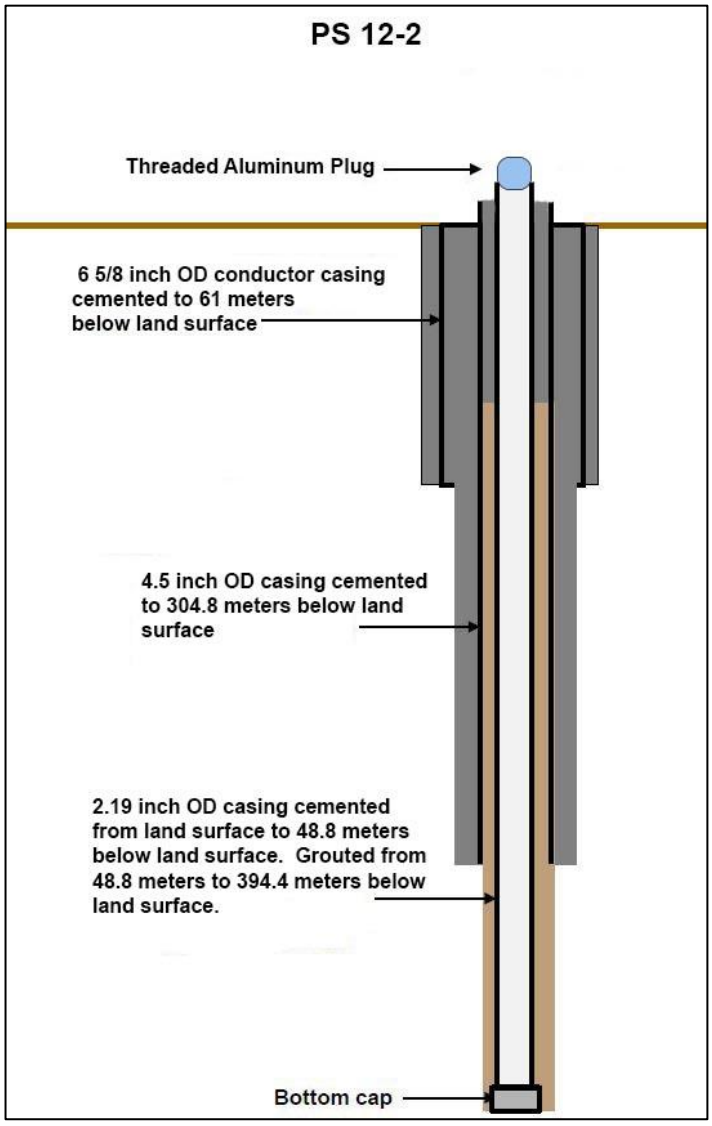


Figure 4. A schematic of hole PS 12-2.

Well PS12-2 was located south of the historic structures at Pilgrim Hot Springs, approximately 317 meters (1040 feet) south of PS12-1. PS12-2 was originally referred to as PS12-3 in permitting paperwork. The name was later changed to correspond with the order that the wells were drilled. The hole was spudded on August 1, 2012 and 10 inch surface casing was cemented in place. The hole was drilled with a 9 7/8" bit to 62 meters and 6 inch casing was cemented to this depth. Below this, the hole was drilled with a 5 7/8" bit to 308 meters. HW casing with a drillable aluminum shoe was cemented to the bottom of the hole and the BOP was installed to the top of this casing and tested in accordance with regulations. Basement was reached at about 317 meters. The hole was drilled to 380.7 meters with a 3 7/8" bit before the rig was changed to a coring set up. The hole was cored from 380.8 meters to 394.4 meters thru biotite schist and other metasedimentary basement rock. The hole was completed with sealed BQ casing to 394.7 meters and filled with water.

Deep Hole PS 12-3

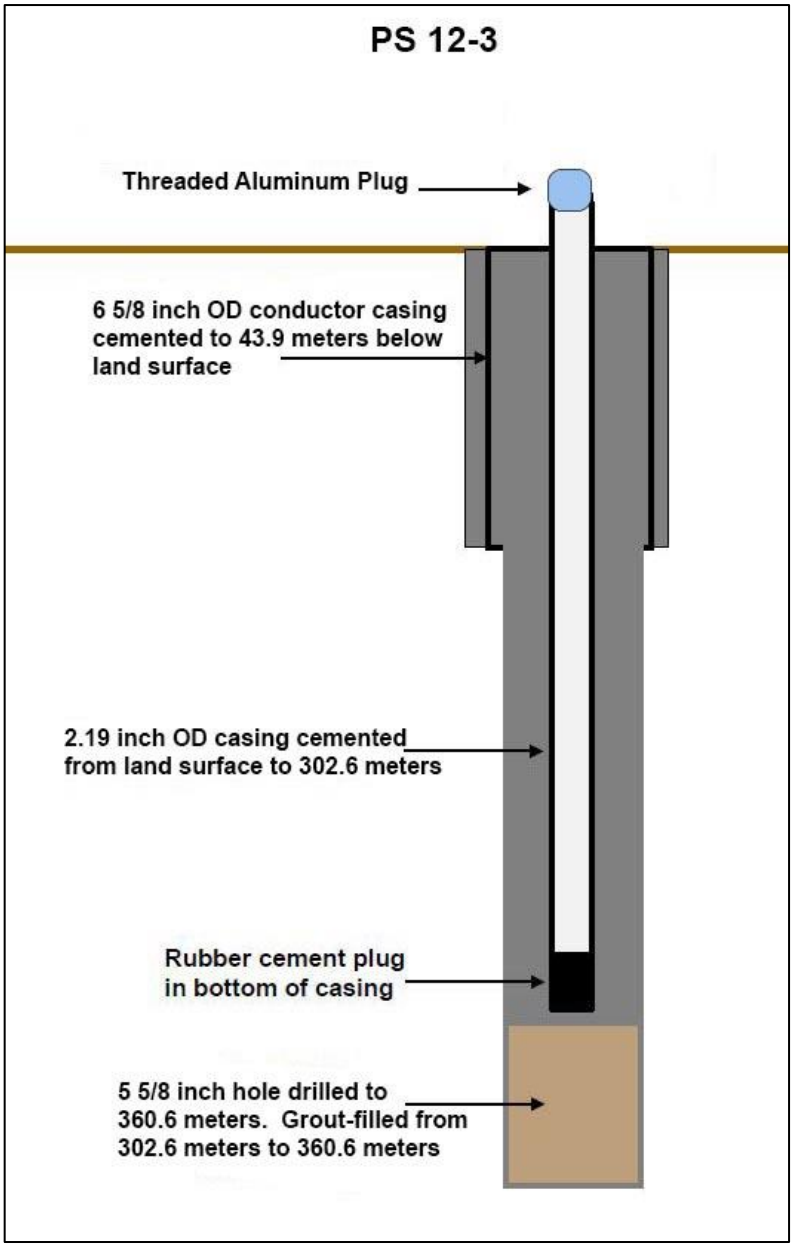


Figure 5. A schematic of Hole PS12-3

Well PS12-3 was spudded on August 17, 2012. Five feet of 10 inch surface casing was set in place. Using a 9 7/8" bit, the hole was drilled to 43.9 meters and six inch casing was cemented in place. When cement was set, the hole was drilled with a 5 5/8 inch tricone bit to basement rock that was encountered at 330.1 meters. Drilling logs report that numerous sections of hard indurated sandstone were encountered between 80.2 meters and the top of the basement rock. The well was drilled to a total depth of 360 .6 meters. During geophysical logging the caliper probe became stuck in the hole at 324.6 meters. In an attempt to free the probe the BQ rods with a reaming shoe attached was run 302.6 meters into the hole. Mud was circulated through the rods to try and wash out the logging probe. When circulation was completed, drillers discovered that the rods were stuck. Rather than risk fracturing the rods and totally losing the hole, rods were left at this depth to enable temperature logging. To complete the hole, cement was pumped through the rods followed by a cement plug and water on August 28th. The following day, water began flowing at an estimated 150 gpm from the annular area. Drillers killed the flow with mud, then sealed the area with cement.

Well PS 13-1

Well PS 13-1 was drilled to 315.8 meters with the intent of being a deep, large-diameter well capable of producing 2000 gpm of 90°C fluid from unconsolidated Quaternary sediments near a depth of 300 m in the immediate vicinity of the upwelling area of the geothermal system. Unfortunately, the well was not located directly above the upwelling area and after running several temperature logs, the well was recompleted at a depth of 74 m to produce from the vicinity of the shallow thermal aquifer.

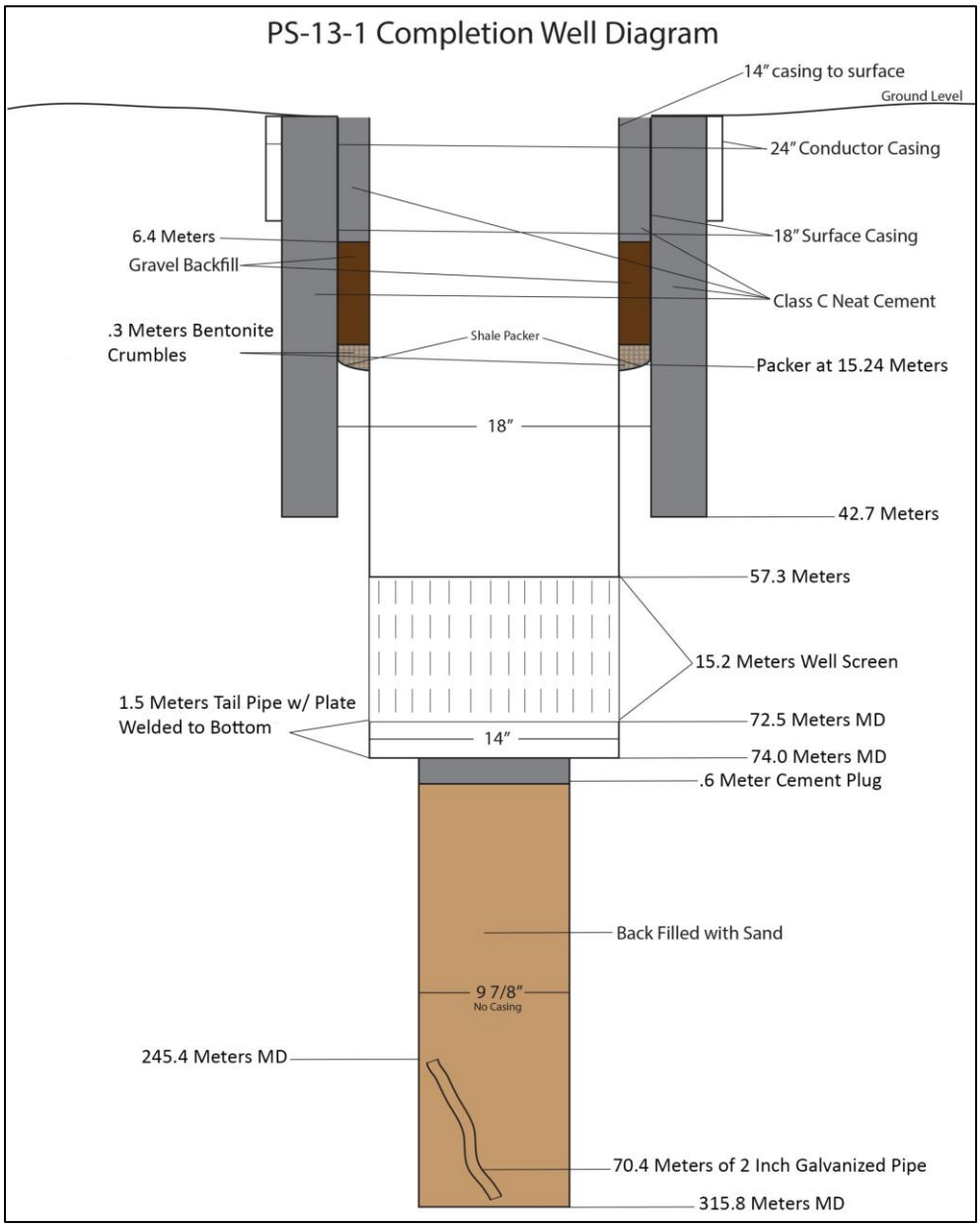


Figure 6. Well PS 13-1

The well was spudded on September 7, 2013 when 6.1 meters of 24 inch conductor casing was set. The Alaska Oil and Gas Conservation Commission, the state agency which permits geothermal exploratory drilling, required completing a 22" hole to 42.7 meters and cementing in 18 inch casing before drilling a slim hole to bedrock. This 22 inch hole section was completed by expanding a pilot hole from 9 7/8 inch to 22 inches in several drilling passes. Surface casing installation was completed when 42.7 meters of 18" casing was cemented in place on September 18th.

The next stage of the hole was drilled with a 9 7/8" bit from the bottom of the surface casing to the top of bedrock, which was encountered at 315.8 meters. Researchers completed a series of geophysical and temperature logs in order to gather down hole temperature data and make decisions about the final completion of the hole.

Due to lower than desired temperatures at the bottom of the hole and complications caused by a section of 2 inch pipe which fell into the hole when a coupling failed during testing, the decision was made to develop the hole in the shallow thermal aquifer. The bottom of the hole was backfilled and a cement plug was set at 77.4 meters.

The hole was completed by installing 14" blank production casing to a depth of 57.3 meters below the surface. There is 15.2 meters of 14" well screen between 57.3 meters and 72.5 meters which allows the well to access the shallow thermal aquifer. A blank 1.5 meter long 14" tailpipe is installed to the top of a cement plug at the bottom of the current completion. The 14" casing was sealed from the surface to 15.2 meters with bentonite, gravel backfill, and cement as shown in Figure 6. PS13-1 was completed on October 24, 2013. Initially the well flowed 40-50 gpm at 75°C. Over time, the artesian flow and the temperature have increased. Artesian flows at the completion of the September 2014 flow testing were between 60-70 gpm and temperatures at these flow rates were 77°C. A detailed flow test description is included later in this report.

The hole has the potential to be used by the land owners as a shallow production hole for future onsite power production or for onsite direct use applications. The completed hole could also have the potential to be used as a future injection hole for larger scale geothermal electrical generation.

Temperature Gradient Well PS 13-2

When it became obvious that downhole temperatures at the top of bedrock in PS 13-1 were less than 90 °C, indicating that the well was not over the upwelling, the decision to drill an additional temperature gradient well east of PS13-1 was made in order to obtain temperature data in an area where the shallow thermal aquifer had not been penetrated. PS 13-2 was spudded on October 14, 2013 and completed on October 17, 2013. It was drilled to a total depth of 122.8 m. Blank 6" casing was driven into the ground while simultaneously drilling with mud. The 6 inch casing had steel tabs welded on the outside of the casing which were intended to draw bentonite crumbles into the ground on the outside of the casing. The six inch casing was driven 69.18 meters before it hit what was believed to be a layer of indurated sandstone and could not drive any more. The hole was drilled open hole below this to TD at 122.8 meters. A string of 4" casing is installed from the wellhead to the total depth and is perforated in alternate 3 meter (10 foot) sections below 69.18 m. A six inch gate valve is installed on the wellhead. Upon completion, the well was allowed to flow under artesian conditions. It had a wellhead pressure of approximately 4 psi and flowed at approximately 70 gpm at 68.9°C. As of September 2014, this temperature and flow rate had remained consistent.

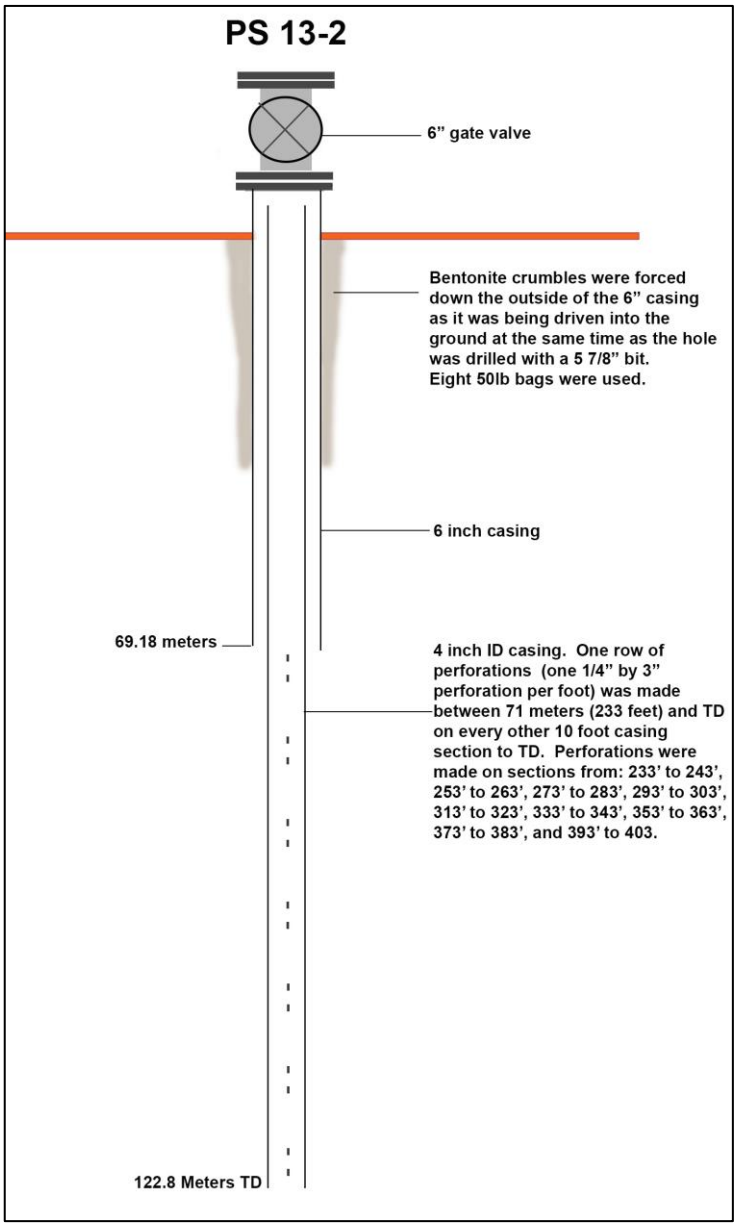


Figure 7. Temperature gradient well PS 13-2.

Temperature Gradient Well PS13-3

PS13-3 was spudded on October 25, 2013 and completed on October 27, 2013. This was the final well that was drilled during the 2013 season. It was located directly beside PS-1 which was drilled to 48.8 meters. PS-1 flows artesian at about 90°C and had no temperature turnover (see Appendix B). PS 13-3 was drilled as a temperature gradient hole to collect deeper temperature data from this area and help isolate the area of upflow. The well was drilled to a depth of 121.9 m. It was drilled using the same process as PS 13-2. Six inch blank casing was driven to 18.3 meters while bentonite crumbles were forced down the outside of the casing with steel tabs welded on the outside of the casing. Four inch casing with slots cut in every other 3 meter (10 foot) joint below 18.3 meters was installed from the surface to total depth. A six inch gate valve on the wellhead prevented the well from flowing after it had been completes. The well was allowed to flow artesian to develop. It flowed 79°C at 60gpm. The temperature and flow rate has remained unchanged over time.

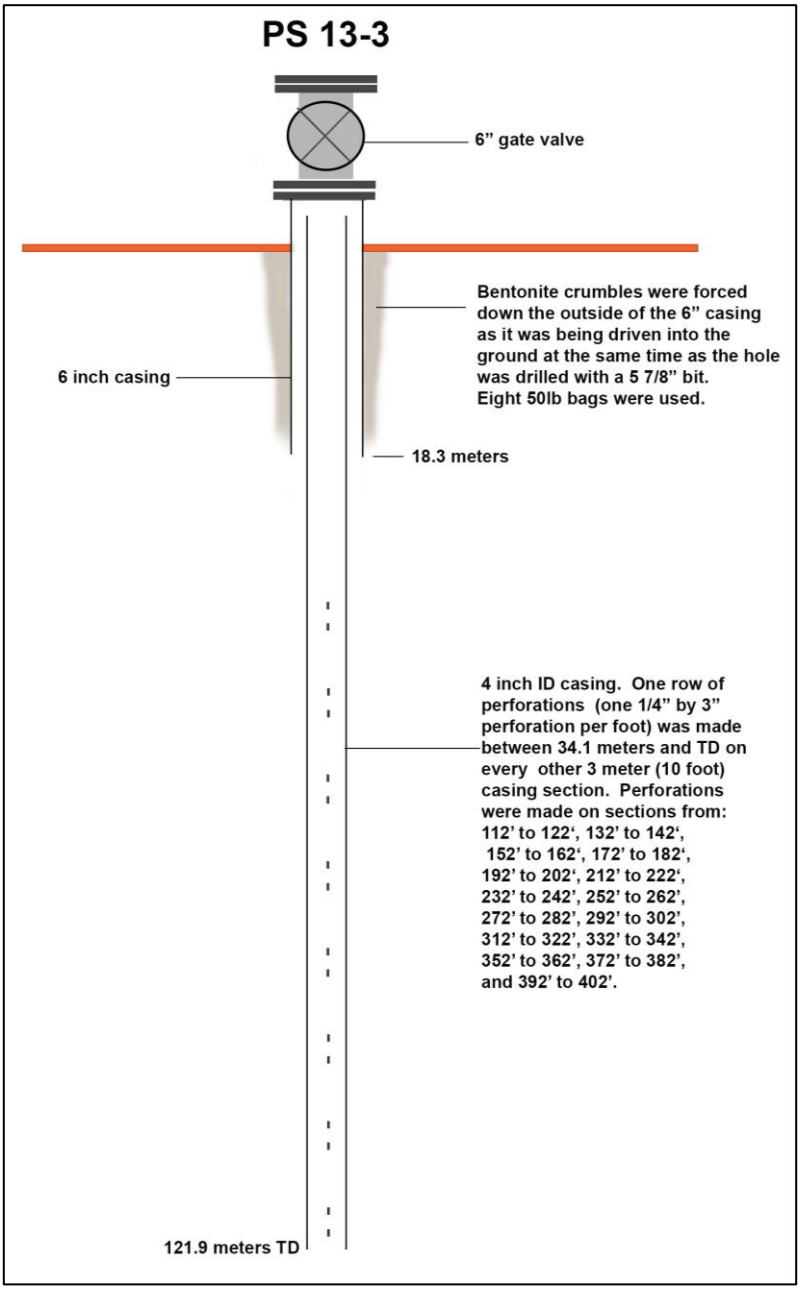


Figure 8. Temperature gradient well PS 13-3.

Appendix B
Pilgrim Hot Springs Well Temperature Profiles and Fluid Entry Points

PS-1

PS-1 was drilled to 48.8 meters in 1979 and its casing was perforated between depths of 18.3 and 30.5 meters in 1982. The well has been blocked below a depth of 23 meters since prior to the 1982 logging. It is not known if this obstruction blocks all flow from greater depths or not.

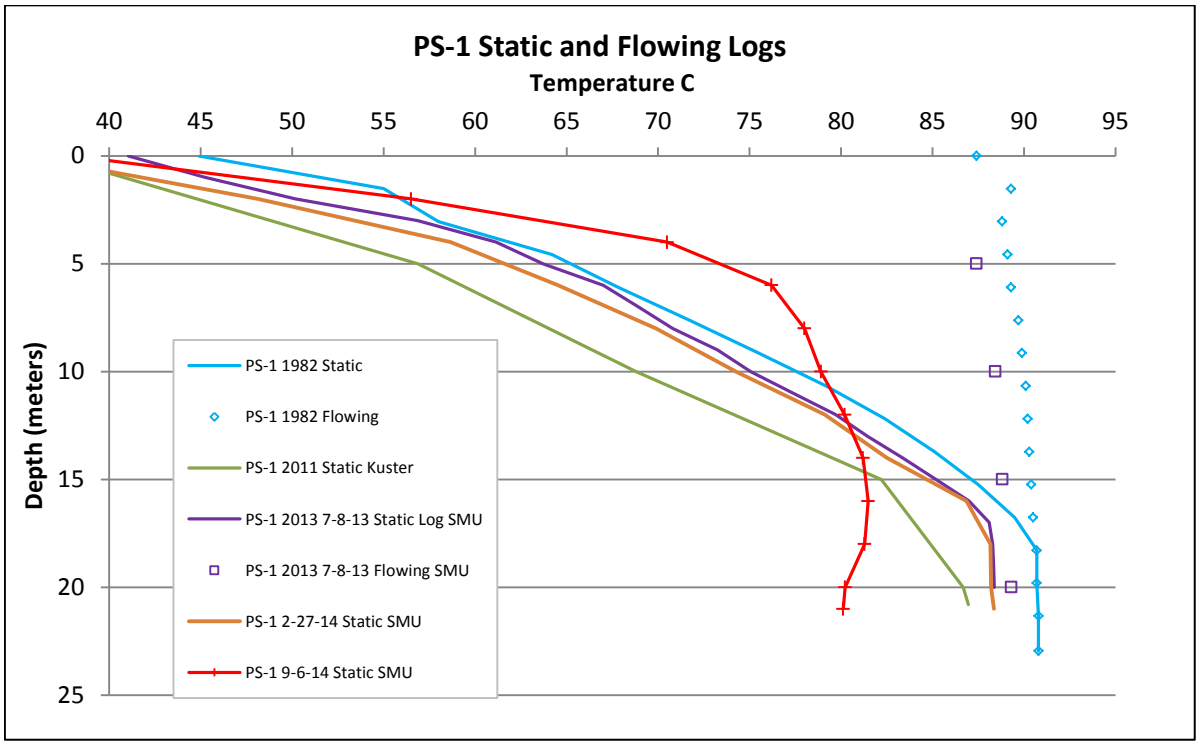


Figure 1. PS-1 temperature logs between 1982 and 2014.

Fluid enters the PS-1 well below a depth of 18 meters during flowing conditions.
Static temperature logs in Figure 1 show that the highest recorded temperatures were measured in 1982, when the well was first logged. Until 2014, the well temperatures appeared to have decreased by several degrees Celsius however the overall temperature profile in the well had the same shape that was recorded in 1982. Logging during September 2014 recorded a drastically different temperature profile with bottom hole temperatures almost 11°C cooler than measured in 1982. Most of this cooling had occurred since the previous logs were measured in February 2014. PS-1 is located approximately 4.6 meters northwest of the PS 13-3 well, and it is believed that the cooling is due to a cooler upflow in the PS 13-3 well which is flowing out into the shallow thermal aquifer and cooling the nearby area.

PS-2

Well PS-2 has not been logged since 1982. The wellhead, which is not leaking, sunk into the ground prior to 1993 (Liss and Moytka, 1994) and the master valve was not able to be replaced . The temperature log that was collected in 1982 is shown in Figure 2. It is very similar to the temperature log from PS-1 measured in 1982.

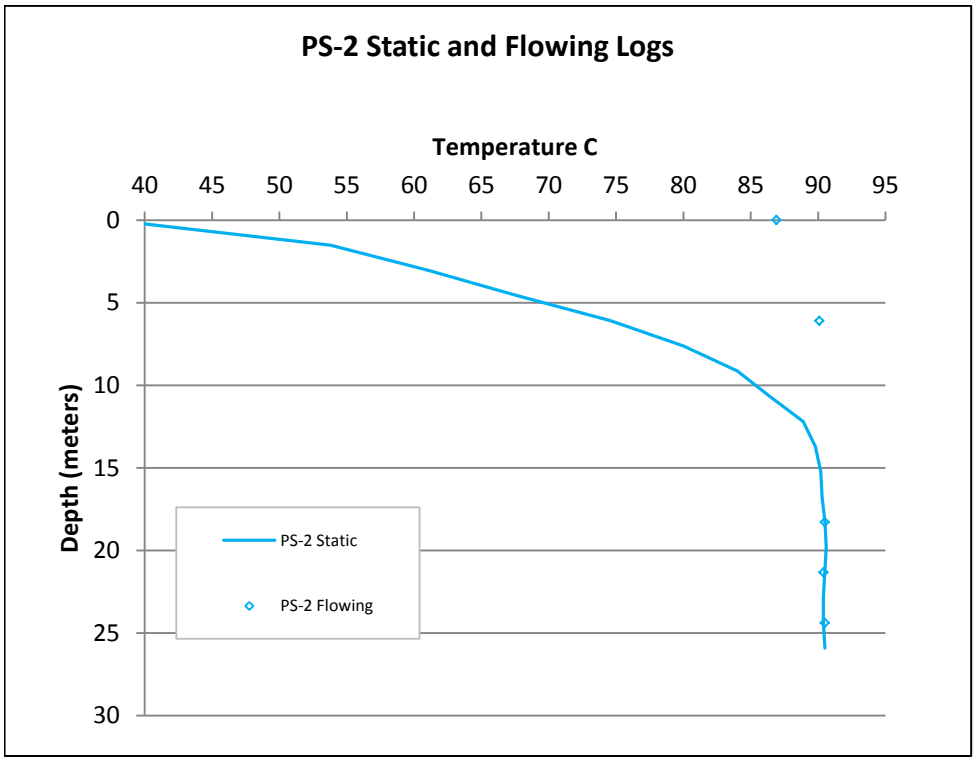


Figure 2. The 1982 PS-2 temperature log.

PS-3

PS-3 was drilled in 1982 to a depth of 79.2 meters and has cemented casing to a depth of 51 meters. A 3 inch slotted liner is present from 51 to 79.2 meters. The casing in PS-3 was intentionally cemented through the shallow thermal aquifer. The 1982 flowing log, with relatively few data points, showed ± 60 °C fluid entering the wellbore near 60 meters. The high positive and negative temperature gradients beneath the shallow thermal aquifer define obvious fluid entry points. The decline of 4 °C above a depth of 8 meters is questionable in the 1982 flowing log. Between 1982 and 2011, the shape of the PS-3 static temperature profile changed. However, the logging of PS-3 after 2011 has produced a series of temperature logs that are all relatively similar to each other. The most obvious feature is the development of a down flow in the wellbore between 40 meters and 56 meters while static. Three fluid entries are shown in the 2013 flowing log at 62 meters, 56 meters, and 45 meters.

PS-3 was extensively logged during interference flow testing in the fall of 2013. This logging discovered that the static temperatures below the cemented casing in PS-3 change when the PS-4 well is flowed or shut in. Temperatures immediately increase in PS-3 when PS-4 starts to flow and decrease when PS-4 is shut in. The total measured temperature change is 3.5 °C. This is additional proof of the dynamic condition of the lower part of the PS-3 hole when it is static at the surface (Benoit et al., 2014).

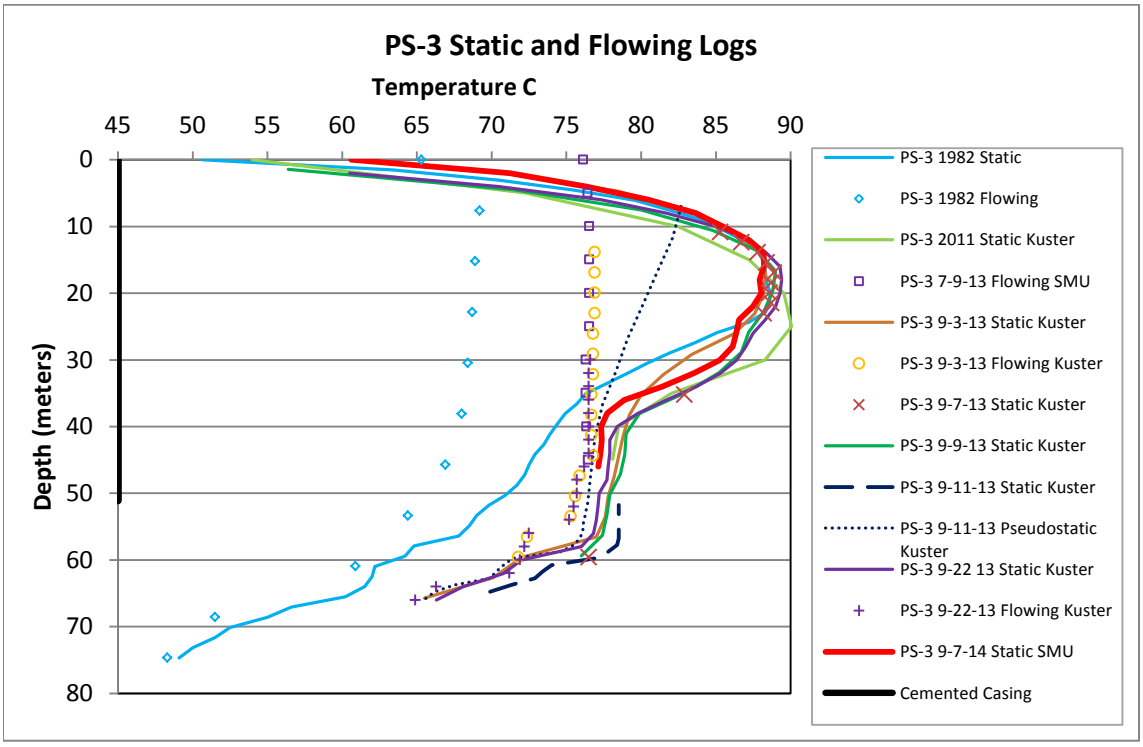


Figure 3. The PS-3 temperature logs collected between 1982 and 2014.

PS-4

PS-4 was originally drilled to 258.5 meters however it has never been logged below 145 meters due to an obstruction in the wellbore. It is interesting to note that this blockage occurs at the same point where the original log shows the beginning of an isothermal trend which extends to the bottom of the hole, presumably due to circulation within the wellbore. The well has solid casing from the surface to 57.1 meters and is uncased below this depth. An old soaking tub was fed by this well for decades and the well flowed approximately 50 gpm into this tub year-around.

Below 112 meters all the flowing and static logs closely overlap indicating no significant fluid movement (Figure 4). In 1982 there appears to have been one 44°C fluid-entry near 65 meters where the 1982 static and flowing logs diverge. The Sept. 9, 2013 flowing logs also show a 44°C fluid entry near 60 meters but below this fluid entry cooler temperatures are now present as opposed to warmer temperatures in 1982. The high positive and negative temperature gradients below 60 meters in 2013 do not allow for any significant vertical fluid movement in that part of the wellbore and therefore suggest that only a single temperature fluid is entering the PS-4 wellbore. The differences between the 1982 static profile and the Sept. 9, 2013 flowing logs below 60 meters beg the question of whether there may have been some fluid movement between 65 and 95 meters (where the temperatures are nearly isothermal) during the 1982 static logging that masked cooler true formation temperatures. The 2013 SMU flowing log was run shortly after flow commenced. This may explain modestly higher flowing temperatures than measured in 1982 and on Sept. 9, 2013.
The notable negative temperature gradient in the bottom of the 2014 log was confirmed with follow up measurements.

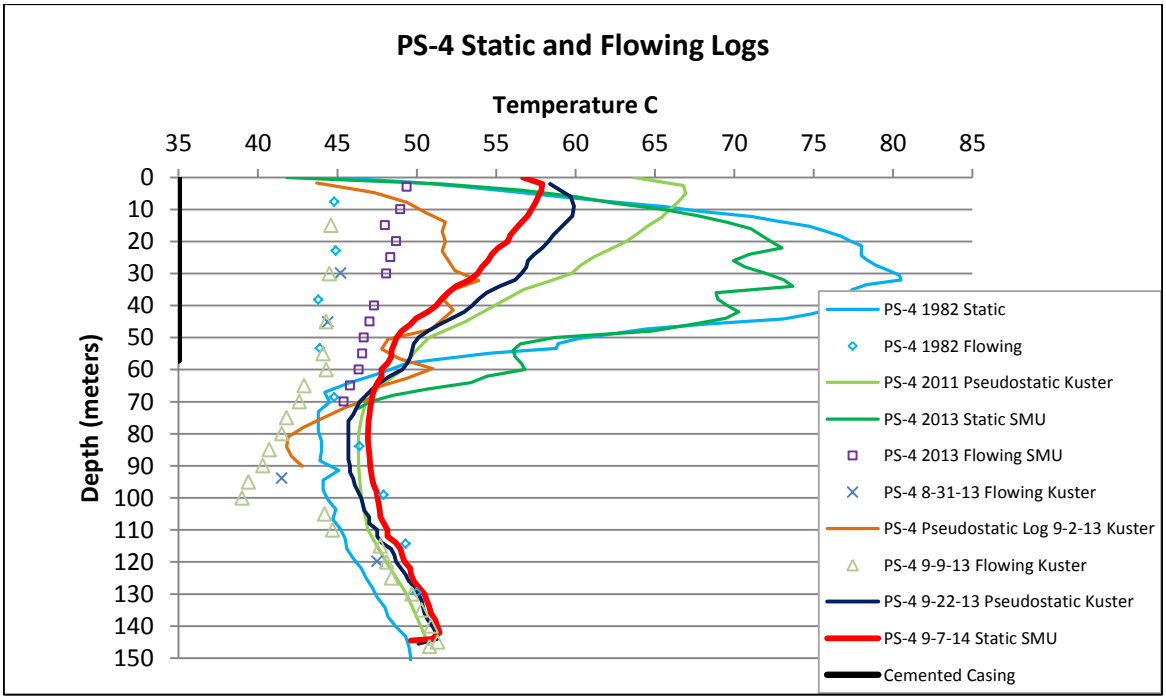


Figure 4. PS-4 temperature logs.

PS-5

Well PS-5 was the deepest well drilled during the exploration in the 1970's and 1980's, reaching a total depth of 305 meters. A solid uncemented liner is present from 54.25 to 179.2 meters and 3 inch slotted liner is present from 179.2 to 299 meters. The well has not been logged as often as the other wells at Pilgrim Hot Springs due a wellhead that was inaccessible to logging tools at the beginning of the study period. The temperature profile from 1982 shows a series of spikes which have never been repeated and could be anomalous. Until September of 2014, it appeared that the fringes of the shallow aquifer were cooling based on the 2013 cooling trends observed in wells PS-5 and MI-1, however the September 2014 temperature log showed the highest temperatures ever measured in well PS-5. The shallowest fluid-entry point, and the one that controls the combined fluid-entry temperature, is near the thin cement plug at a depth of 173 meters and has a temperature of 34°C. Two deeper and slightly warmer fluid-entry points are present at 214 and 234 meters and potentially allow the mixing of fluids from different depths relatively deep within the wellbore.

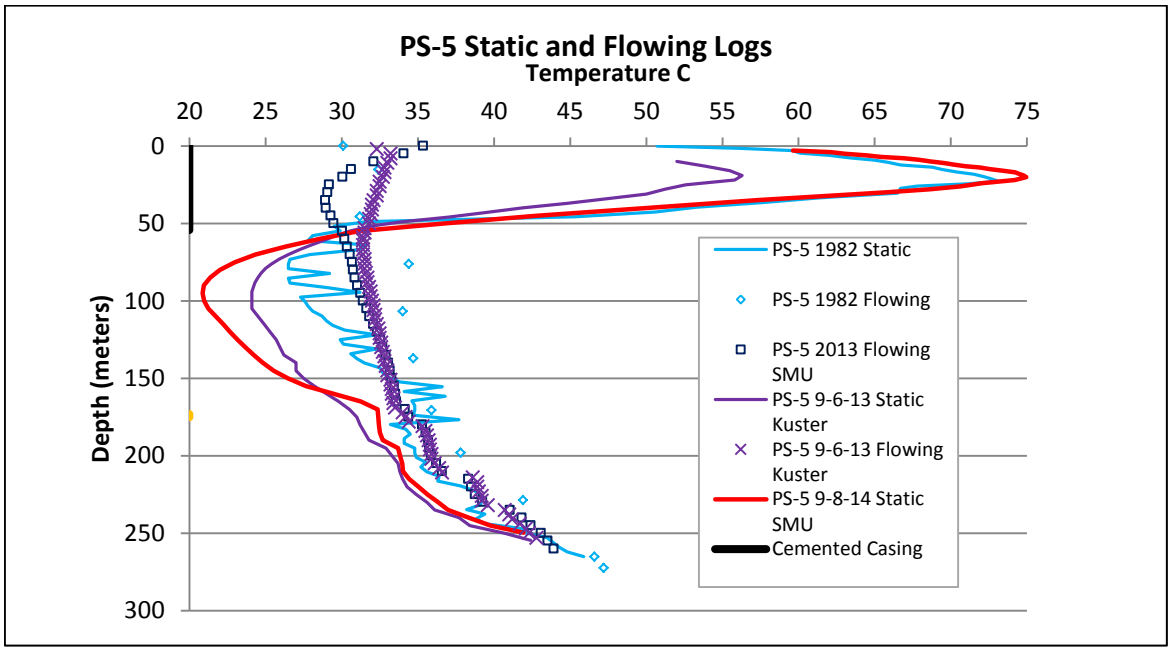


Figure 5. PS-5 temperature logs collected between 1982 and 2014.

MI-1

The MI-1 well was drilled to 93.6 meters with cemented casing to 24.4 meters and a slotted liner below this. Like the PS-5 well, MI-1 is at the periphery of the shallow thermal aquifer. Until, 2014, it appeared that this aquifer was cooling. In September of 2014 however, the second highest temperature ever recorded in MI-1 was measured. One possible reason for the sudden increase in the well temperature was the removal of the hot tub near well PS-4. Water from PS-4 had been flowing into the tub at a constant rate of between 50 and 100 gpm for decades which appears to have cooled the margins of the shallow thermal aquifer. The hot tub was removed in October 2013 and the flow from PS-4 was stopped.

Flowing temperature profiles show the most obvious fluid-entry points near depths of 61 and 76 m with a combined fluid-entry temperature of 28°C that has not changed since 1982. Fluids currently enter at depths of 76 and 61 meters and exit at about 70 and 42 meters when the well is not flowing at the surface. This fluid must be rising in the wellbore as the amount of cooling increases upward in the two intervals.

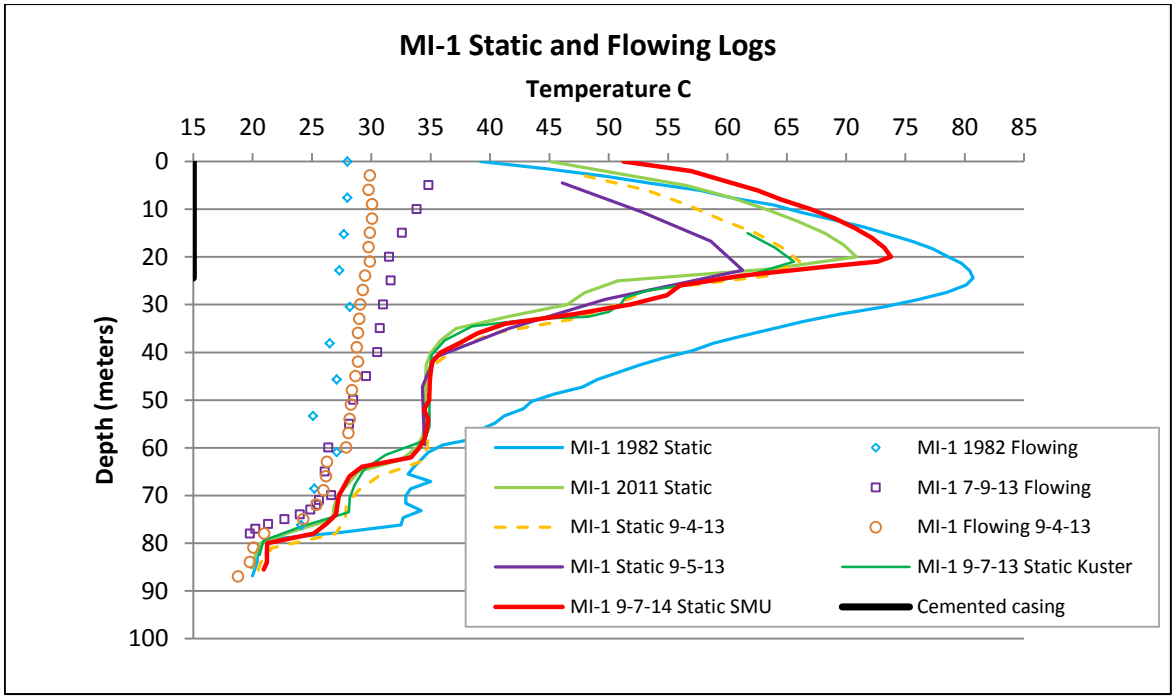


Figure 6. MI-1 temperature logs collected between 1982 and 2014.

S-1

S-1 was logged in 2011 and 2014. The two logs are very similar and show a shallow thermal aquifer 50 meters deep, however it is significantly cooler and slightly deeper than the shallow

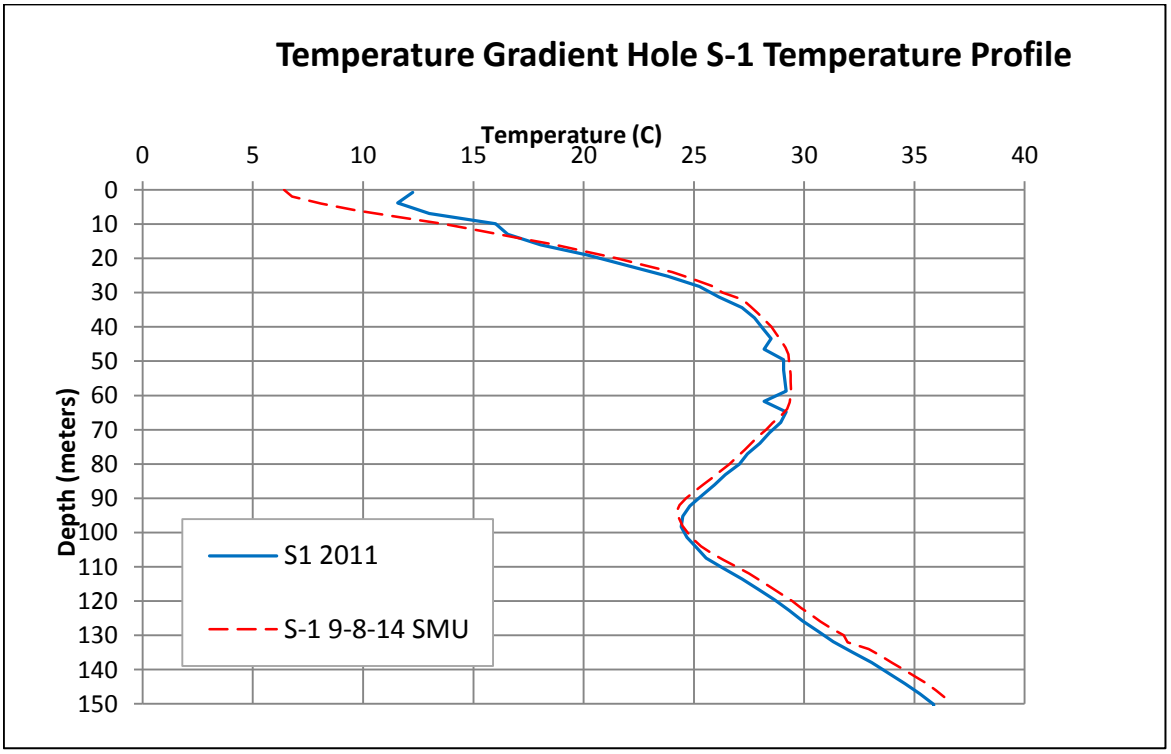


Figure 7. The S-1 temperature logs.

thermal aquifer measured in the wells further south. The low temperatures that were measured indicate the hole is located far from any upwelling zone.

S-9

Temperature gradient hole S-9 was logging in 2011 and 2014. While the lower part of the S-9 profiles are very similar, the upper part of the 2014 S-9 profile is much different and cooler from

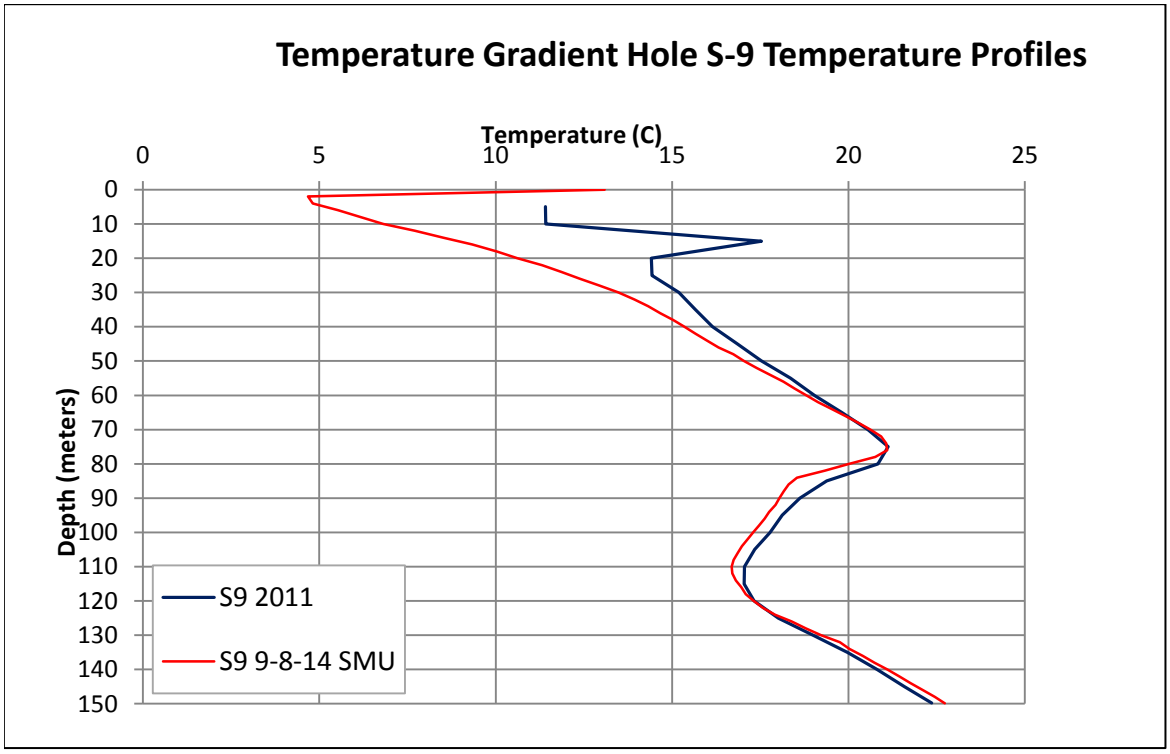


Figure 8. Temperature log of the S-9 hole.

the 2011 S-9 log. The new profile does not show the very shallow aquifer seen at 15 meters in the 2011 log. The sealed casing in this well prevented data from being gathered about fluid entry points. The 2014 log is now believed to most accurately represent the equilibrated tempertures in the local S-9 area.

PS 12-1

The temperature gradient holes drilled in 2012, PS12-1, PS12-2, and PS12-3 all have similar shaped temperature profiles. PS 12-1 was the first hole drilled during the summer of 2012, however it failed to encounter the 90°C + temperatures that had already been measured in the wells drilled 25 years earlier. The familiar shallow thermal aquifer is easily identified however the temperatures measured in this hole are below 80°C. The sealed casing does not allow for the discrimination of fluid entry points.

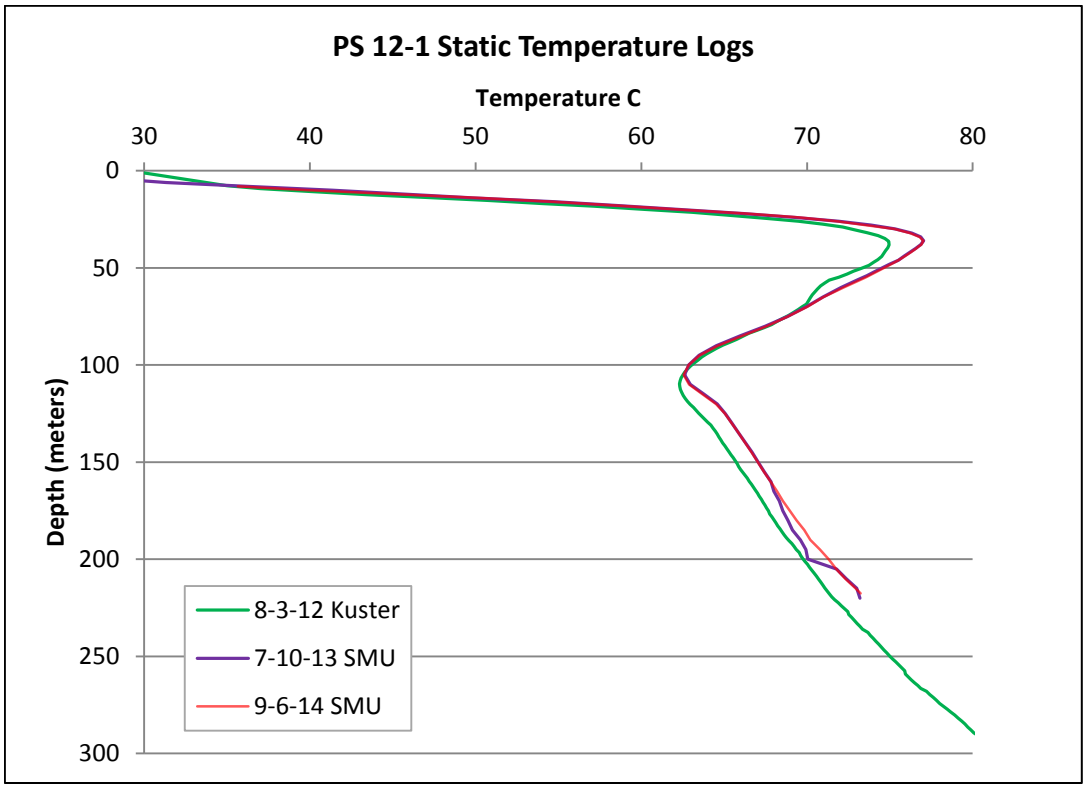


Figure 9. Temperature logs of the PS12-1 temperature gradient hole.

PS 12-2

Temperature gradient hole PS12-2 is the deepest well that has been drilled to date at Pilgrim Hot Springs and enabled the collection of core from the basement metasedimentary rock. The temperature profile clearly defines a shallow thermal aquifer with temperatures exceeding 90°C as well as a deeper thermal aquifer where temperatures are the same as the shallow thermal aquifer. The temperature measured in the deeper aquifer in this well is the hottest deep temperature encountered to date, exceeding 90°C, and provides one of the few data points for temperatures in this deep aquifer.

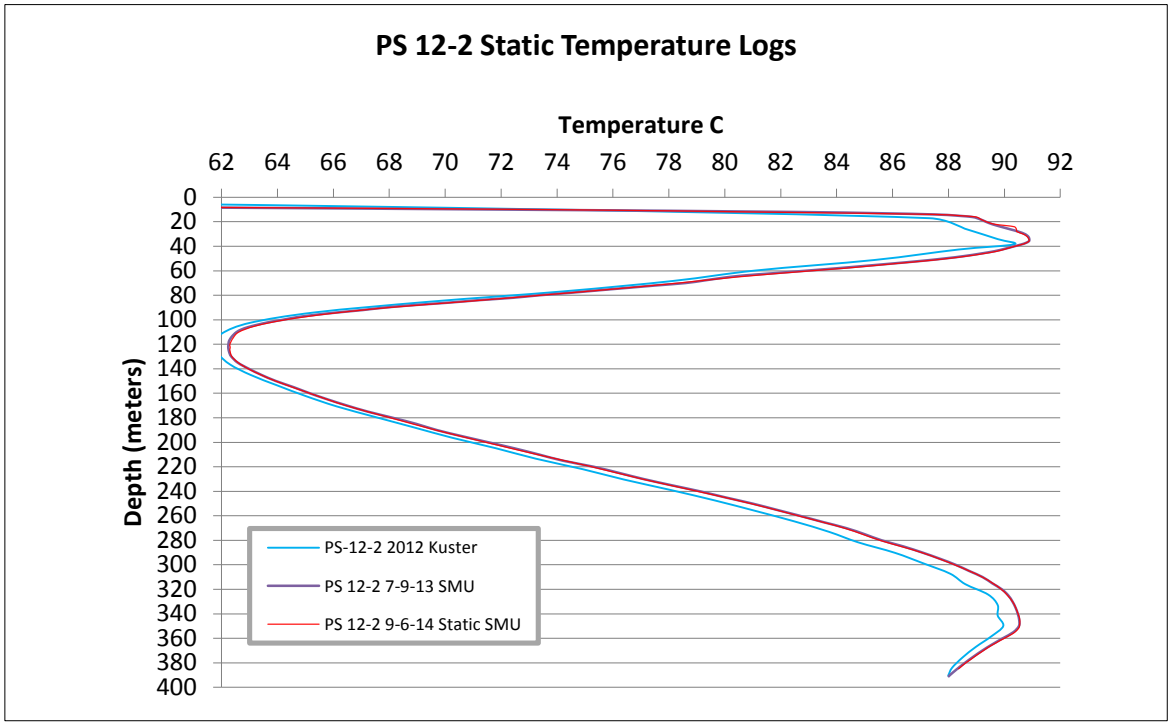


Figure 10. Temperature logs of the PS12-2 temperature gradient hole**.**

PS 12-3

The temperature gradient hole PS12-3 showed high temperatures in the shallow thermal aquifer. The 2013 and 2014 temperature logs were identical and show much better detail in the shallow thermal aquifer than the equilibrated initial 2012 temperature log. The temperatures measured in the shallow thermal aquifers are very similar in wells PS12-2 and PS 12-3.

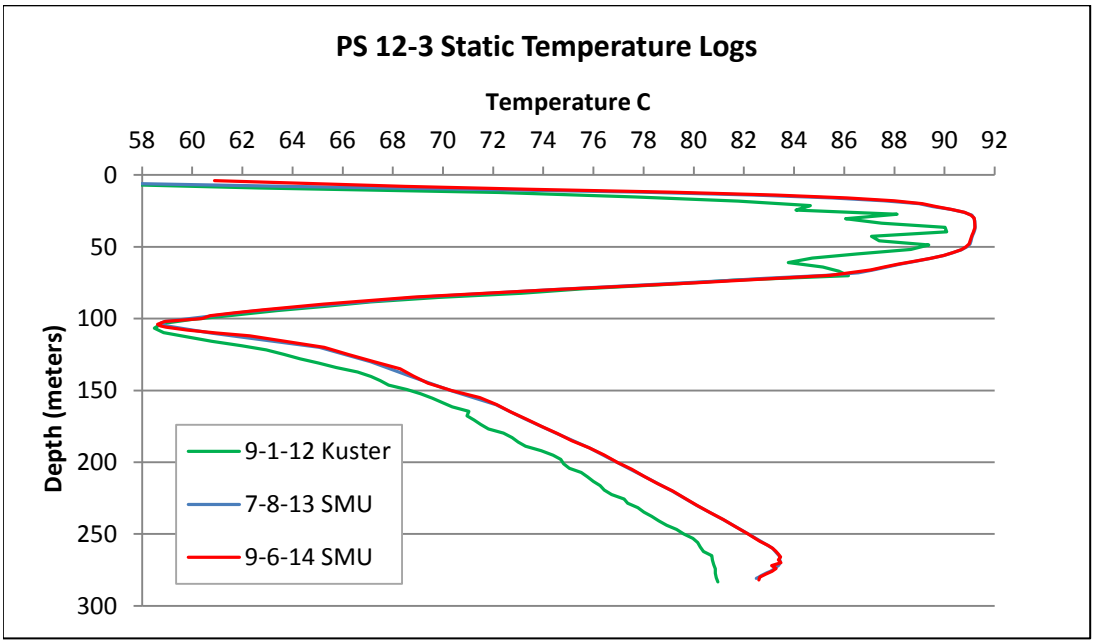


Figure 11. Temperature logs of the PS12-3 temperature gradient hole.

PS 13-1

The PS13-1 well was initially completed at a depth of 317 meters and then recompleted at a much shallower depth. There appears to be a shallow upflow in parts of the wellbore that is masking the true static formation temperatures in the area. This upflow appears to have cooled during 2014 as there was about half a degree of cooling between the February and September 2014 flowing logs (Figure 13). This upflow theory is further supported by the nearby GeoProbe hole PS-GEO-12-13 being 5-7 degrees hotter than any of the PS13-1 static logs (Figure 12). The flowing logs were run with the well flowing about 60 gpm.

The most important logs from this hole that help researchers make decisions regarding future uses of this well are the logs run after the hole was completed with well screen between 57.3 and 72.5 meters. A second graph showing these logs in more detail is presented as Figure 13. The fuid inflow point is between 60 and 65 meters.

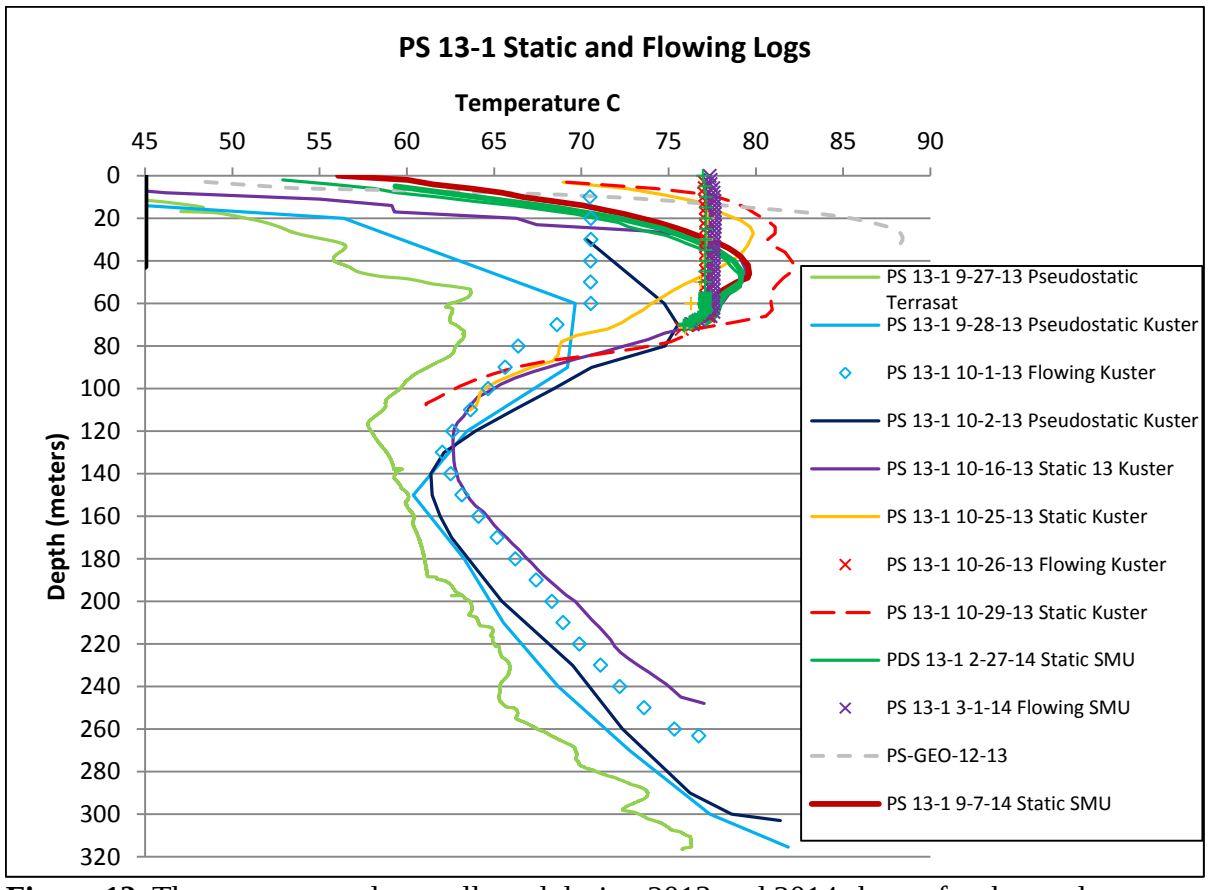


Figure 12. The temperature logs collected during 2013 and 2014 shown for the total depth which the well was originally drilled to.

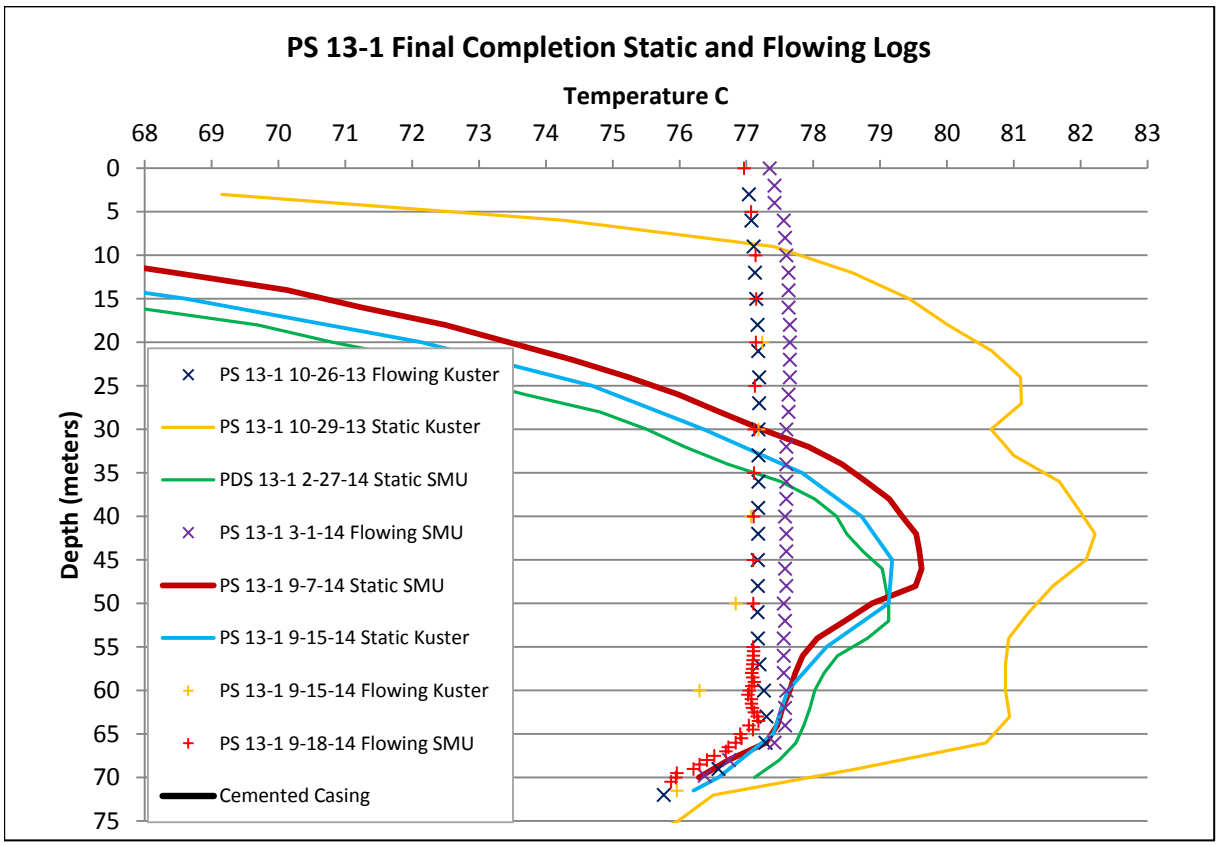


Figure 13. The PS13-1 temperature logs zoomed to the completed depth to show fluid entry depth details.

PS 13-2

A number of temperature logs were collected from PS 13-2 in the year after it was drilled. Temperatures in the well were unstable and readings indicate moving fluid within the well bore. All the static logs are cooler than the nearby GeoProbe hole that was logged in 2011. The artesian flow rate in this well is 60 -100 gpm, and fluid entry points appear to be at 85 meters, 80 meters, and 70 meters in depth.

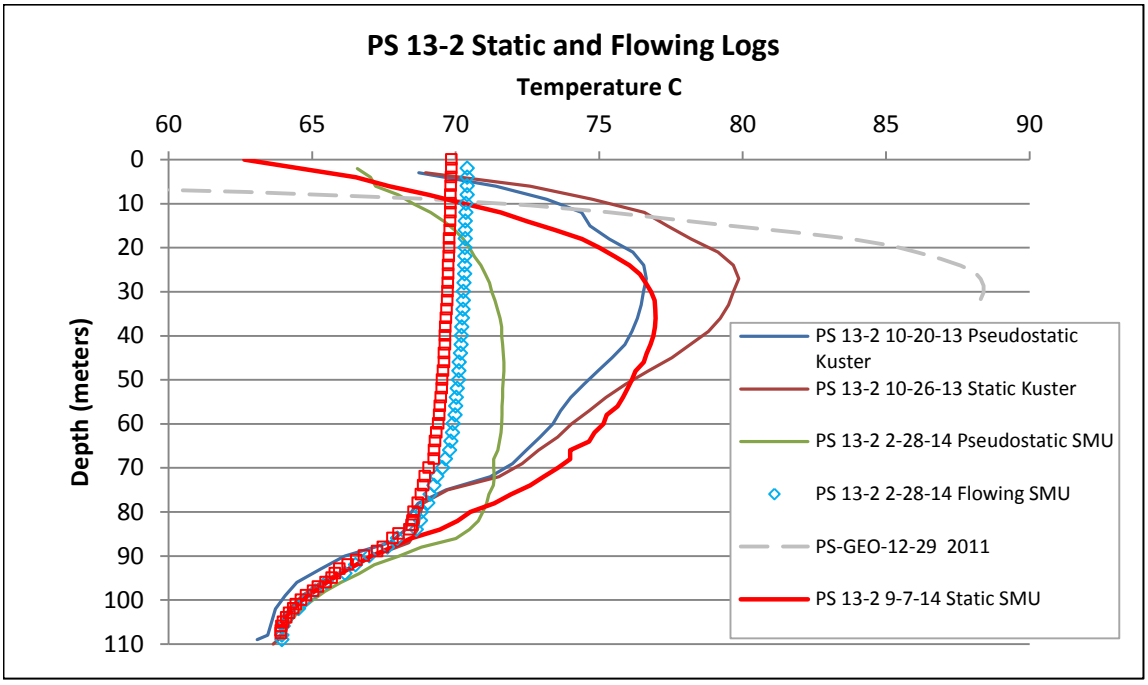


Figure 14. PS13-2 temperature logs.

PS 13-3

Logging in PS 13-3 shows that an up-flow has developed in the well. This is shown in the temperature logs by the declining maximum temperature and the development of isothermal sections. This upflow is reducing the shallow aquifer temperature in the immediate vicinity of the well, as shown by the temperature log of PS-1 (Figure 1). The well flows artesian at about 60 gpm, but the fluid entry points are difficult to observe. The most obvious point is near 60 meters.

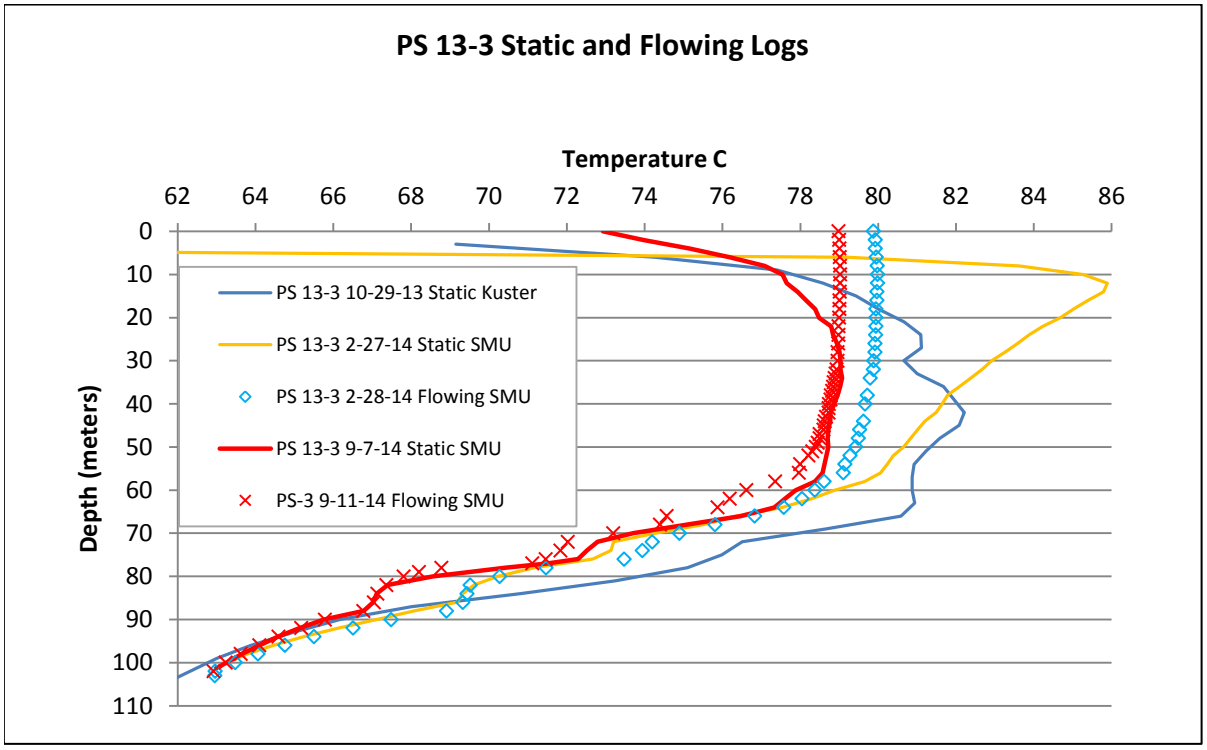


Figure 15. PS13-3 temperature logs.

Appendix C
Pilgrim Hot Springs Well Details and Locations

Holes and Wells Drilled to Date at Pilgrim Hot Springs

1979					
Hole Name	Date Drilled	Latitude	Longitude	Depth (ft)	Notes
PS-1	November 1979	65°5'25.747"	164°55'39.407"	150	Cased to TD, perforated in 1982 between 60 and 100 feet. Accessible in July 2013 to 69 feet.
PS-2	November 1979	65°5'24.004"	164°55'44.083"	150	Cased to TD, perforated in 1982 between 60 and 105 feet. Wellhead valve inoperable. Last logged in 1982.
1982					
PS-3	25 June-4 July 1982	65°5'22.973"	164°55'48.986"	260	Accessible in July 2013 to 147 feet.
PS-4	7 July-23 July 1982	65°5'21.484"	164°55'43.784"	881	Accessible in September 2013 to 480 feet.
PS-5	23 July-28 July 1982	65°5'15.656"	164°55'43.613"	1001	Accessible in July 2013 to 853 feet.
MI-1	15 July-18 July 1982	65°5'22.462"	164°56'0.557"	307	Accessible in September 2013 to 280 feet.
2011 Deep Holes					
S1	Aug 2011	65° 5' 53.8146"	164° 55' 2.1354"	502	See figure??
S9	Aug 2011	65° 5' 42.2442"	164° 54' 43.6032"	491	See figure??
2012 Deep Holes					
PS12-1	July 3, 2012-July 14, 2012	65°5'36.203"	164°55'28.379"	1000	In July 2013, accessible to 721 ft. See figure??
PS12-2	Aug 1, 2012-Aug 15, 2012	65°5'25.98"	164°55'31.116"	1295	In July 2013 accessible to 1282 ft. See figure??
PS12-3	Aug 17, 2012-Aug 29, 2012	65°5'26.088"	164°55'46.921"	1183	In July 2013 accessible to 921 ft. See figure??
2013 Holes					
PS 13-1	7 September-24 October 2013	65°05’28.3”	164°55’38.3”	1036	In February 2012 accessible to 231 ft. See figure??
PS 13-2	14-17 October 2013	65°05’29.9”	164°55’27.6”	400	In February 2012 accessible to 357 ft. See figure??
PS 13-3	25-27 October 2013	65°05’25.8”	164°55’38.9”	400	In February 2012 accessible to 338 ft. See figure??

Geoprobe holes were named in a similar fashion to deeper temperature gradient holes. The geoprobe holes drilled in 2011 use the prefix 'PS-GEO.' Geoprobe holes from 2012 confusingly use the prefix 'PS-GEO-12' followed by the geoprobe hole number. The hole names along with the dates drilled and location are shown in **Table 1** and **Table 2**

Table 1

2011 Geoprobe Holes					
Geoprobe Hole Name	Date Drilled	Latitude	Longitude	Depth (ft)	Notes
PS-GEO-1	10 August 2011	65° 5' 43.5006"	164° 54' 46.3212"	82	
PS-GEO-2	14 August 2011	65° 5' 41.5782"	164° 54' 53.9994"	82	
PS-GEO-3	15 August 2011	65° 5' 53.0988"	164° 55' 0.1194"	81	
PS-GEO-4	17 August 2011	65° 5' 48.9012"	164° 54' 52.0194"	82	
PS-GEO-5	18 August 2011	65° 5' 57.1194"	164° 55' 2.5212"	82	
PS-GEO-6	20 August 2011	65° 5' 37.2006"	164° 55' 15.78"	109	
PS-GEO-7	21 August 2011	65° 5' 34.1406"	164° 55' 10.6788"	92	
PS-GEO-8	23 August 2011	65° 5' 39.4188"	164° 55' 25.3812"	83	
PS-GEO-9	24 August 2011	65° 5' 41.5782"	164° 55' 34.2006"	82	
PS-GEO-10	26 August 2011	65° 5' 45.6"	164° 55' 48.4998"	75	
PS-GEO-11	26 August 2011	65° 5' 12.7998"	164° 55' 19.9992"	75	
PS-GEO-12	30 August 2011	65° 6' 4.7586"	164° 55' 9.7962"	76.5	
PS-GEO-13	31 August 2011	65° 5' 22.6314"	164° 55' 24.8802"	68.3	
PS-GEO-14	31 August 2011	65° 5' 24.3492"	164° 55' 19.6062"	90	
PS-GEO-15	1 September 2011	65° 5' 29.2986"	164° 55' 35.3706"	78.7	
PS-GEO-16	1 September 2011	65° 5' 21.9768"	164° 55' 32.808"	75.3	
PS-GEO-17		65° 5' 17.25"	164° 55' 27.6132"		Broken hole, No tip

Table 2

2012 Geoprobe Holes					
Geoprobe Hole Name	Date Drilled	Latitude	Longitude	Depth (ft)	Notes
PS-GEO-12-1	12 June 2012	65° 5' 28.2984"	164° 55' 20.7984"	79.5	
PS-GEO-12-2	14 June 2012	65° 5' 26.4006"	164° 55' 32.0016"	77	
PS-GEO-12-3	14 June 2012	65° 5' 24.8994"	164° 55' 42.7008"	49.5	
PS-GEO-12-4	15 June 2012	65° 5' 27.8982"	164° 55' 37.599"	78	
PS-GEO-12-5	15 June 2012	65° 5' 30.4008"	164° 55' 33.099"	68	
PS-GEO-12-6	15-16 June 2012	65° 5' 32.2002"	164° 55' 29.6004"	108.5	
PS-GEO-12-7	19 June 2012	65° 5' 34.3998"	164° 55' 28.401"	133	
PS-GEO-12-8	19 June 2012	65° 5' 33.2016"	164° 55' 21.7986"	134	
PS-GEO-12-9	29 June 2012	65° 5' 35.4978"	164° 55' 18.9012"	154	
PS-GEO-12-10	19 June 2012	65° 5' 31.8984"	164° 55' 23.901"	108	
PS-GEO-12-11	21 June 2012	65° 5' 15.7986"	164° 55' 27.0978"	95	
PS-GEO-12-12	20 June 2012	65° 5' 27.3978"	164° 55' 38.7006"	76	

PS-GEO-12-13	20 June 2012	65° 5' 26.0982"	164° 55' 31.3998"	76	
PS-GEO-12-14	20 June 2012	65° 5' 24.6978"	164° 55' 28.1994"	104	
PS-GEO-12-15	20 June 2012	65° 5' 22.5996"	164° 55' 35.1006"	75	
PS-GEO-12-16	21 June 2012	65° 5' 21.3"	164° 55' 40.1016"	61	
PS-GEO-12-17	21 June 2012	65° 5' 18.8982"	164° 55' 31.1016"	59	
PS-GEO-12-18	23 June 2012	65°5'24.426"N	164°55'47.992"	62	
PS-GEO-12-19	24 June 2012	65°5'26.717"	164°55'59.35"	87	
PS-GEO-12-20	25 June 2012	65°5'26.73"	164°55'49.19"	78	
PS-GEO-12-21	23 June 2012	65°5'23.6"	164°55'55.945"	65	
PS-GEO-12-22	26 June 2012	65°5'21.486"	164°56'1.291"	83	
PS-GEO-12-23	26 June 2012	65°5'18.421"	164°56'7.599"	98	
PS-GEO-12-24	26 June 2012	65°5'14.511"	164°56'8.825"	148	
PS-GEO-12-25	27 June 2012	65°5'11.724"	164°55'46.848"	125	
PS-GEO-12-26	28 June 2012	65°5'15.71"	164°55'44.284"	82	
PS-GEO-12-27	28 June 2012	65°5'16.725"	164°55'50.635"	92	
PS-GEO-12-28	28 June 2012	65°5'18.702"	164°55'56.496"	84	
PS-GEO-12-29	27 June 2012	65°5'9.384"	164°55'41.363"	135	
PS-GEO-12-30	29 June 2012	65°5'37.489"	164°55'17.238"	132	
PS-GEO-12-31	30 June 2012	65°5'36.598"	164°55'28.429"	128	
PS-GEO-12-32	30 June 2012	65°5'38.83"	164°55'32.041"	143	
PS-GEO-12-33	1 July 2012	65°5'41.497"	164°55'34.01"	123	
PS-GEO-12-34	1 July 2012	65°5'43.404"	164°55'40.502"	147	
PS-GEO-12-35	2 July 2012	65°5'45.609"	164°55'47.899"	128	
PS-GEO-12-36	2 July 2012	65°5'22.902"	164°55'24.395"	82	
PS-GEO-12-37	3 July 2012	65°5'28.803"	164°55'18.822"	107	
PS-GEO-12-38	3 July 2012	65°5'26.107"	164°55'19.195"	110	
PS-GEO-12-39	3 July 2012	65°5'27.6"	164°55'24.701"	104	
PS-GEO-12-40	10 July 2012	65°5'28.001"	164°55'14.002"	116	
PS-GEO-12-41	13 July 2012	65°5'22.403"	164°55'20.501"	110	
PS-GEO-12-42	13 July 2012	65°5'20.026"	164°55'22.472"	91	
PS-GEO-12-43	13 July 2012	65°5'0.5"	164°54'45.297"	135	Hit permafrost
PS-GEO-12-44		65°5'38.902"	164°54'37.702"	105	
PS-GEO-12-45		65°5'40.999"	164°54'40"	114	
PS-GEO-12-46	3 August 2012	164°55'2.801"	65°5'55.9"	104	
PS-GEO-12-47	3 August 2012	65°5'50.701"	164°54'56.999"	102	
PS-GEO-12-48	5 August 2012	65°5'45.2	164°54'51.802	98	
PS-GEO-12-49	5 August 2012	65°5'39.098"	164°54'59.601"	70	
PS-GEO-12-50	5 August 2012	65°5'36.701"	164°55'7.298"	123	
PS-GEO-12-51	5 August 2012	65°5'39.401"	164°55'11.799"	138	
PS-GEO-12-52	8 August 2012	N 65 05' 04.3"	W 164 54' 03.6"	6	Permafrost
PS-GEO-12-53	8 August 2012	N 65 05' 06.0"	W 164 54'19.1"	93	Cold Temps, Permafrost
PS-GEO-12-54	8 August 2012	N 65 05' 05.1"	W 164 54' 38.8"	99	Nearly Isothermal @ about 36° F

Appendix D
Pilgrim Hot Springs Well Head Repairs

Pilgrim Hot Springs Geothermal Exploration Project

Pilgrim Hot Springs Wellhead Repair

Prepared by: Dan Brotherton, Arctic Drilling, Inc. & Markus Mager, ACEP

Fairbanks Alaska, September 2010



Alaska Center for Energy and Power
University of Alaska
PO Box 755910
Fairbanks, AK 99775-5910

Pilgrim Hot Springs Wellhead Repair

Prepared by: Dan Brotherton, Arctic Drilling, Inc. & Markus Mager, ACEP

Overview

This task was completed in two phases, including:

1) an initial site visit in July 2010 to assess the condition of the six existing wells and develop a work plan for replacing the wellhead assemblies as needed, and

2) a second trip to the site to complete the work outlined in the work plan. This trip took place September 13th-18th. The goal was to stop the wells from leaking, and make them accessible for instrumentation as part of the DOE funded project 'Innovative Geothermal Exploration of Pilgrim Hot Springs, Alaska'. This report details the work performed on the individual wellheads during the September trip, which included replacing the gate valves on 4 of the 6 wells, including PS-1, PS-3, PS-4 and MI-1. At this time, none of the wells are leaking to the surface although there are still weak points which need to be addressed in the future. Recommendations for future work are outlined in this report.
The team performing the work included Dan Brotherton from Arctic Drilling, Richard Eggert, and Max Iyapana from Bering Straits Development Company (BSDC), and Markus Mager from ACEP.

For each of the four wellheads that were repaired, the team removed the existing gate valves by pumping down the water level in order to access the well and installing new, stainless steel valves. A detailed work description for each well can be found on the following pages. The team did not alter the configuration of the wellheads except for installing an additional fitting on top of the blind flanges capping the gate valves that can accept a 3" stainless standpipe with a tee and a valve to allow future installation of monitoring and logging equipment. A 1" access port with a plug was also built into the top of the blind flange.

We recommend installing chains and locks on all the new valves and that all valves should be tested for functionality (opened/closed) at least once a year. Winterization of all the wells is necessary in order to prevent freezing and cracking of the gate valves. A plan for winterization has been forwarded in a separate communication that is attached to this report.

Mobilization

All new valves (6), parts, tools and supplies, totaling 3,842lbs, were purchased or rented by ACEP and shipped to Nome via Northern Air Cargo (NAC). Additional heavy equipment such as 4 wheelers, trailers, a bobcat and an air compressor were rented in Nome from BSDC. All parts, tools and equipment were transported to the side on September 13th and 14th and staged at the central staging area (Figure 1). Repair work began on the 15th, and was completed on the 18th.



Figure 1. Central staging area for repairs.

PS-4 (Completed September 14-15th)

PS-4 supplies the water for the hot tub from a 2in lower valve. The well was leaking from a ½ inch hole in the blind flange on top of the 10in well gate valve and from the corroded 2in valves on each side of the 10in casing underneath the 10in valve (Figure 2).

The lower bolt flange of the 10in valve was covered with mineral buildup and corrosion scale. There was a small pond around the well at the level of the 2in side valves from the constant leaking and overflow from the tub. The team laid down timbers and planks to create a stable work platform and removed mineral build up and rust scale from the lower bolt flange (Figure 3). After various failed attempts to release the old 10in valve from the well flange, the bolts had to be cut off with a torch (Figure 4 & 5).

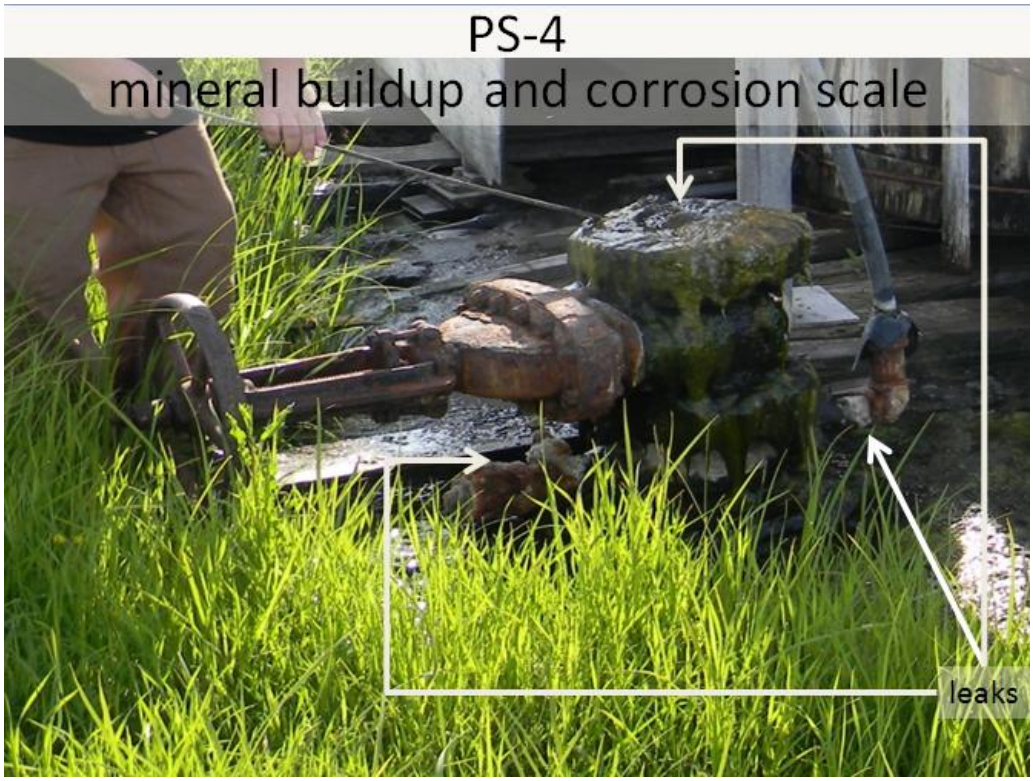


Figure 2. Arrows show areas of leaking on PS-4.



Figure 3. Removing buildup and scale and attempting unsuccessfully to cut the flange bolts with a Sawzall.



Figure 4. Cutting bolts to remove old gate valve.



Figure 5. Removing gate valve with Bobcat – note artesian flow from well.

PS-4 has an inner 8in and an outer 10in casing. The outer casing is corroded and thin. The 8in/10in annulus (space between the two casings) continued to produce water after the water level inside the 8in casing was drawn down. This indicates a likelihood that they are set to different depths and water is produced from a different production zone in the annular space than through the main hole. In order to weld on new 2in nipples, this water would need to be drawn down. We were able to partly draw this water down with a 1in suction tube, but it was ultimately decided to not risk changing the 2in nipples after it was determined they are corroded but still sound (probably just as sound as the casing). Dan was not confident that the casing could be welded given its state of deterioration, so rather than risk creating a difficult to stop leak, the original nipples were left in place and only the 2in valves were replaced with new stainless 2" valves (Figure 6).

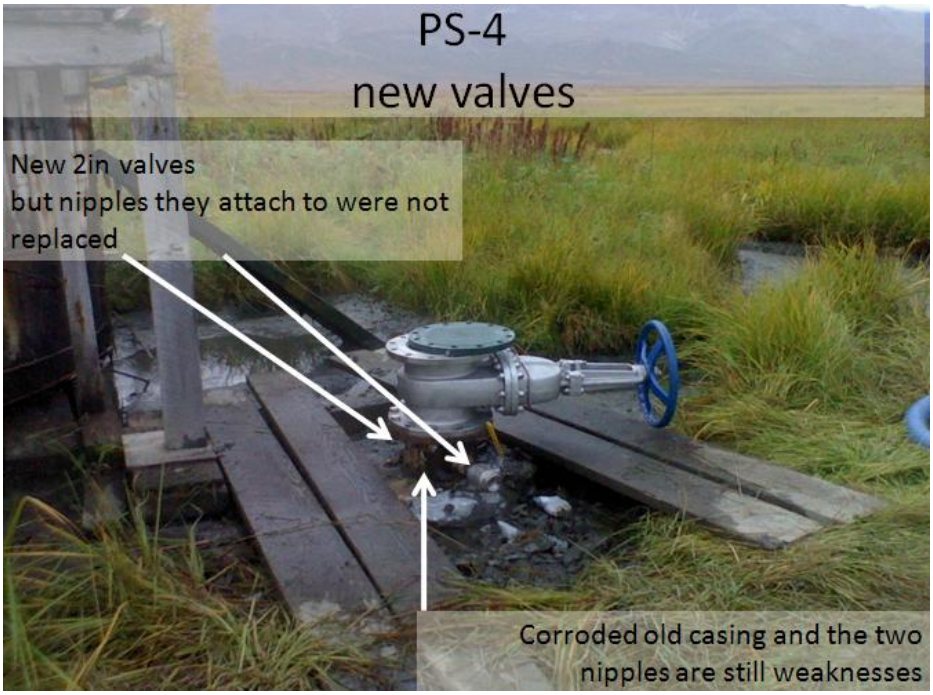


Figure 6. New valves.

The flange on this well is partly eaten away but still appears to be sound. The well is artesian and produces clear water. We installed a new 10in stainless steel valve with reducer flange on top connected to a 3in threaded nipple with a stainless cap. The well has no visible leaks and has been re-connected to the hot tub via one of the new 2in valves.

Further repairs on this wellhead will be needed in the near future. The 10in casing and the 2in nipples are thin and will eventually start leaking with no way to control or stop the flow. Dan recommends that the 8-10in annulus be cemented from the bottom up to the top via tremie pipe which would seal off the corroded outer casing from the well water and would extend the life of the well.

We are also recommending locks on the 2in valves to guarantee flow to the hot tub, prevent accidently closure (or opening) and to prevent well freeze up since this well will presumably not be shut in through the winter. If this is the case, it is imperative that the 2in valve remains open to prevent the new gate valve from freezing.

PS-3 (Completed September 15-16th)

Prior to repairs, this well was leaking through the standpipe at the top of the well and later, after we started to remove buildup and scale (Figure 8), from a hole in the side of the 10in valve (Figure 7). We were unable to plug this leak so we dug a sump hole to drain the fluid and temporarily pump it away from the well and surrounding work space.



Figure 7. Image showing leaks and corroded standpipe.



Figure 8. Removing scale and buildup.

There was significant corrosion to several of the bolts connecting the existing gate valve to the wellhead flange, which necessitated cutting them off with a torch. We were able to drive out some of the bolts once they were cut, but several posed additional challenges and had to be removed in chunks. The torch was damaged during this process.

Eventually we were able to remove the old 10in valve and replace it with the new stainless valve and bolts. The lower flange of the wellhead is severely corroded and the new flange bolts are exposed. The flange thickness is about half of original thickness and there is barely enough material left to secure new flange bolts (Figure 9). The well was completed with a new capped gate valve and blind flange, with a 3in nipple and cap. There is a 2in valve below the flange which was left in place as it is not currently leaking. Dan was not confident the well casing is sound enough to permit replacement of this valve.

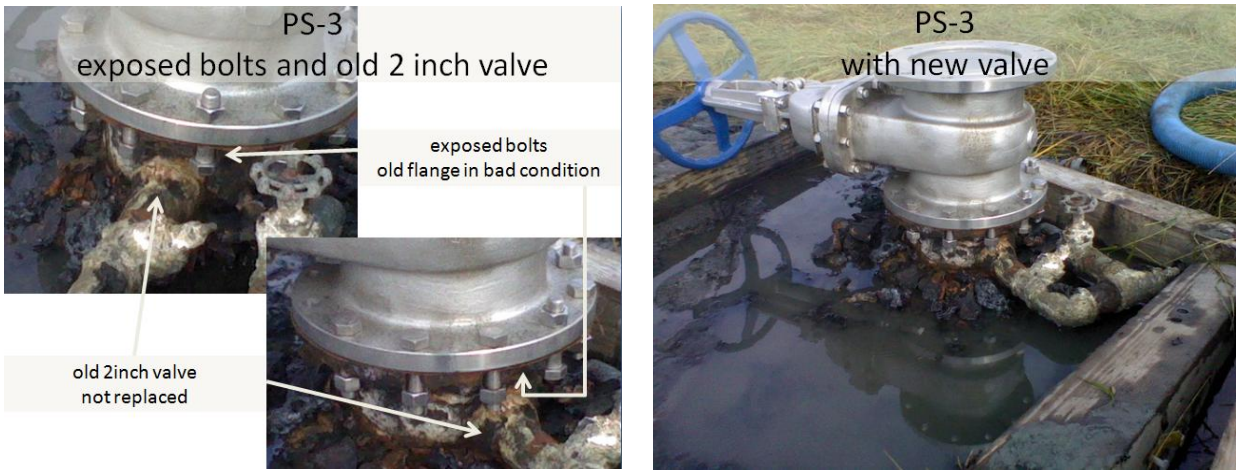


Figure 9. Exposed bolts, new valves.

PS-3 is hotter than PS-4 and produces clear water. There is also a 6in inner casing in this well that comes to the top of the 10in casing. Once the old valve was replaced, there were no visible leaks. Figure 10 shows a comparison of the old PS-4 valve flange and the old PS-3 valve flange.



Figure 10. Old 10in valves from PS-3 and PS-4. Note severe corrosion on lower PS-3 flange.

Further repairs will be needed to this wellhead soon. Dan recommends cementing the 6-10" annulus from the bottom up with tremie pipe so that the side valve can be removed and the main well flange can be replaced. This will protect the well from a permanent leak if one develops from the corroded casing.

MI-1 (Completed September 16-18th)

This well is located on adjacent Mary's Igloo Native Corporation land. The top of the 10in gate valve was split in half, probably due to a freeze break. We were able to open and close the old gate valve but could not completely stop the flow of the well. MI-1 is colder than PS-4, and the water temperature of this artesian well appears to fluctuate. When flowed for a short period of time it produced gray, silty fluids. The well has no visible inner well casing.

Due to leaks in the wellhead, a small pond had formed around the well several inches deep. We cleaned out an existing trench leading away from the well and the pond drained away to ground level. We built a work platform around the well and removed mineral build up, rust and scale from the bolts. Dan cut the bolts and drove them out with the torch. We removed and replaced the 10in valve with new stainless steel valve and bolts (Figure 11). The new gate valve is capped with a blind flange with 3in welded nipple and cap.





Figure 11. Work commences on MI-1. Note artesian flow prior to pumping.

Prior to repairs, the well was also leaking from several holes corroded through the casing below the gate valve flange. These leaks continued after installing, capping and shutting the new gate valve. The casing is paper thin midway between the flange and the cement. Dan welded a sleeve around the casing from about 2in above the cement level up to the flange, totaling about 14in. In order to weld on the sleeve, he completely removed the side valve, nipple and weldolet from the 10in casing. The sleeve stopped the leaks temporarily but the casing below the sleeve is thin and remains a significant weakness (Figure 12).

Dan recommends installing a 6in inner casing and cementing the annulus from the bottom to the top via tremie in order to prevent further leaking once the casing corrodes further.





Figure 12. Casing conditions of MI-1.

PS-1 (Completed September 18th)

PS-1 is the hottest of the repaired wells. This well was buried past the valve handle and covered with several inches of mineral buildup. Before repairs, it leaked out of a corroded two inch elbow from the top of the wellhead, as well as the remains of a 2in valve and a 1in hole in the top of the well cap (Figure 13). These holes were plugged with sticks driven into the openings after some of the mineral build up was removed. We then excavated around the well to just below the lower valve flange covering an 8ft by 10ft area, dug a sump hole for the water pump and laid down blocking and timbers for a work platform. We removed the mineral build up and de-scaled what remained of the bolts (Figure 14).



Figure 13. PS-1 after excavation but before repair work.



Figure 14. Removing scale and buildup prior to replacing gate valve.

When the gate valve was removed, it was evident that the lower flange was almost completed corroded away with no bolt heads remaining and the bolt threads visible from the side of the flange. We used the torch to remove the bolts, removed the old gate valve, cleaned up the flange as much as possible, and installed the new 6in stainless valve topped with a stainless blind flange, 3in nipple and cap (Figure 15).



Figure 15. New valve installed on PS-1. Note collapsed suction hose due to high temperatures.

This well has a 4in inner casing inside the 6in outer casing, and does not have any lower casing 2in valves. There is not much left of the well flange, just barely enough to bolt on the new valve. The well is sealed and does not

leak at this time. We backfilled around the well but not to the previous level so it is possible to access valve handle. We left the remaining dirt piled to the side of the excavated area.

Dan recommends installing a short (18in) spool section underneath the new gate valve to raise the valve above ground level and permit the well to be backfilled to ground level. This would also eliminate the standing water around the well, which is now below grade. He also recommends cementing the 4in-6in annulus and welding on a new casing flange in order to prevent future leaks.

PS-2

This well is buried but inaccessible with rubber tired backhoe. We did not attempt to dig up this well. The wellhead valve is not corroded or leaking. We will attempt to make it accessible for instrumentation in 2011.



Figure 16. PS-2 buried but not leaking. We will need to excavate and replace valve before this well can be accessed with instruments.

PS-5

This well is also not corroded or leaking so we did not replace the valve at this time. We will attempt to make it accessible for instrumentation in 2011.



Figure 17. PS-5 still appears to be in good shape, but not accessible by instrumentation.

Winterization Plan for Wellheads (Dick Benoit and Gwen Holdmann)

The trick to keeping a wellhead from freezing and then breaking during sub freezing weather is to inject a liquid that is both less dense than water and has a very low freezing point into the wellhead. This fluid needs to be environmentally benign so that when (not if) it is spilled or leaks out of the wellhead it does no environmental damage. Typically a food grade vegetable oil has been used in the lower 48. A small pump is used to pump the oil into the highest opening in the wellhead but if the pressures are very low even a hand operated pump may be enough to do the job. We expect this to be the case for the Pilgrim wells. This pump obviously needs to be able to overcome the internal wellhead pressure and can pump at low rates. You will need to know how much oil has been pumped into the wellhead. Enough oil needs to be pumped into the wellhead to push or displace the water down the well to a point below the freezing level, which is probably not more than a few feet. Therefore, it is necessary to calculate the volume of the wellhead above ground and a few feet of wellbore below ground. We expect this might amount of a few tens of gallons per well. It is important to check the wellhead for leaks, no matter how slow, before injecting the vegetable oil. If the oil leaks out of the wellhead then the water will flow back up in the wellhead and freeze. We recommend doing this on the 4 wells with new gate valves prior to hard freeze-up.

Appendix E
USGS Geophysical Survey Report

Airborne Geophysical Studies of the Pilgrim Springs Geothermal Area

Jonathan Glen, Darcy K. McPhee, and Noah D. Athens
U.S. Geological Survey

DOE Phase 1 report on Task 2.3

SUMMARY

We report on preliminary results from an airborne magnetic and EM survey of the Pilgrim Springs geothermal area (figs. 1-4) that provide the regional geophysical framework of the area and help delineate key structures controlling hydrothermal fluid flow and to characterize the basin geometry and depth to bedrock. Data analysis and modeling, that will comprise future activities as part of this research, will include 2D potential field studies (joint gravity and magnetic modeling) along selected transects, regional geophysical mapping of structures, and 3D potential field and EM modeling.

INTRODUCTION

Geology

Most of the Seward Peninsula is composed of Precambrian metamorphic basement and overlying Paleozoic carbonates (fig. 3). Cretaceous alkalic intrusive rocks occur along the eastern part of the peninsula. The Pilgrim River Valley is covered by alluvial fill. The nearest outcrops to Pilgrim Springs consist of plutonic and high-grade metamorphic rocks that occur 2.5 mi to the south in the Kigluaik Mountains, and low-grade metamorphic rocks that outcrop 2.5 mi to the north at Hen-and-Chicken Mountain.

The Imurk Basin and Pilgrim River Valley are interpreted (Turner and Forbes, 1980) as a graben or half-graben structure that is bound on the south by the Kigluaik Fault – a major rangefront normal fault (~65km long) that separates the basin from the Kigluaik Mountains to the south. Other local-scale features, inferred from the geophysics (see discussion below), lie adjacent to Pilgrim Springs and may represent important structures controlling local hydrothermal fluid flow.

Although there is no direct evidence of volcanic activity in the Imuruk Basin-Pilgrim River Valley region, the geothermal anomaly at Pilgrim Springs and nearby thawed regions, and high lake temperatures to the north and northeast are indicative of high heat flow in the region that is thought to be, in a general sense, related to recent volcanism in surrounding areas. Alternatively, the source of heat may be radiogenic, derived from the Precambrian basement and Cretaceous intrusive rocks that outcrop in the surrounding uplands and are inferred to floor the Pilgrim Valley.

PREVIOUS STUDIES

A number of geologic and geophysical reconnaissance studies were performed in the mid-70's through early 80's to assess the origin, character and potential of geothermal resources of the Seward Peninsula and the Pilgrim Springs area, in particular. Geophysical investigations included gravity, magnetic, seismic and resistivity studies.

Gravity data

Gravity studies were performed in 1979 and 1980 to assess the depth to bedrock in the Pilgrim River Valley in the vicinity of Pilgrim Springs (Lockhart, 1981; Kienle and Lockhart, 1980). Data were collected (122 stations in 1979, and 184 stations in 1980) regionally and along several traverses by helicopter, boat, car, and on foot. Station spacing along traverses acquired during the 1980 survey was 1-5km, though much more closely spaced stations were taken in the vicinity of Pilgrim Springs during the 1979 campaign (<1km in places). The gravity data from the 1979 campaign reveal a ~10 mgal triangular-shaped gravity low located immediately southwest of Pilgrim Springs that is characterized by ENE-trending and NE-trending gradients along its northern and southern margins, respectively. Kienle and Lockhart (1980) suggest that these gradients reflect basement normal faults, bounding the low, that have accommodated several hundred meters of vertical offset resulting in downdropping of the basin. It is implied that the location of the springs is controlled by the intersection of these two basement structures.
A gravity profile along a 45 km traverse across Pilgrim Valley (from the 1980 study) reveals a gravity high near the center of the valley suggesting a horst in the middle of the graben. Regional gravity traverses at Imurk, Noxapaga and Pilgrim areas, which all cross the proposed rifts of Turner and Swanson (1981), reveal significant gravity lows. Lockhart (1981) suggests these lows are due to low density fill in structurally-controlled basins, consistent with geologic and seismic evidence for such in the Kuzitrin flats and Pilgrim River Valley, and consistent with the regional rift-graben model of Turner and Swanson (1981).

Magnetic data

An aeromagnetic grid compilation was made in 1995 (grid spacing of 250m) and provided by John Cady under contract to the State of Alaska, Division of Geological and Geophysical Surveys. The original data are not available (the compilation consists of surveys flown in the late 1960s and early 1970s). The survey that was likely used in this compilation (covering the Pilgrim Springs area) is that described by Cady and Hummel (1976) which was flow at 300m above ground with a flightline spacing of 1.2km along E-W trending flightlines. A base station was not available for this survey. While useful for interpreting regional structures, this grid is of insufficient resolution to resolve features like those at Pilgrim Springs inferred from the gravity. Ground magnetic measurements (<30 discrete measurements taken at 100ft intervals) were collected along a single N-S profile extending across and south of Pilgrim Springs (Kirkwood, 1979) that indicates a ~50 gamma magnetic low near the hot springs interpreted to be due to leaching of magnetic minerals in the sands and silts by hydrothermal fluids.

NEW STUDIES

More recently, the USGS has been engaged in geophysical studies of the Pilgrim Springs geothermal area to delineate structures that may provide pathways or barriers to fluid flow and control the location of the springs. This effort entailed the compilation, re-reduction, and editing of existing gravity data, in addition to the collection, in 2010, of new potential field data (including several hundred new gravity data and over 150 km of ground magnetic data), regionally and along several detailed profiles around Pilgrim Springs. In 2011-2012 the USGS, in collaboration with ASCEP, was responsible designing, supervising, and analyzing a high-resolution airborne magnetic and EM survey.

Ground studies

Gravity data

The USGS collected 295 gravity stations in the early spring of 2010 using two Scintrex CG-5 gravimeters. Data were collected at 100 to 300m spacing along several profiles in the vicinity of the springs, in addition to regionally throughout the entire project area. Profiles are oriented north south with the exception of one northeast trending profile that extends north east trending profile NEB (Fig. 5). Gravity highs occur over the crystalline rock of the Kigluiaks Mts., Mary's Mountain and the Hens and Chickens Mountain. A local elongate gravity low extends from Pilgrim Springs, where it is ~4.5 mGal southwestward where the lowest values (~10 mGal) occur ~4km southwest of the springs. These values would suggest basin thicknesses of ~ 350 m to ~800m beneath the springs and deepest parts of the gravity low, respectively (assuming a density contrasot of 0.4 g/cc between basement and fill). The margins of the low are characterized by northeast-trending gradients that probably reflect the edges of fault –bounded structural blocks. The southeastern edge of the low near the springs, in particular, lies very close to the springs and may provide an important pathway conveying deep fluids to the surface.

Magnetic data

Ground magnetic data were collected using a Geometrics® G858 cesium vapor magnetometer sampling at 0.1 second intervals. In wooded or otherwise difficult-to-traverse areas data were collected on foot. The majority of the data, however, were obtained using a custom-designed snowmachine-towed magnetometer system developed specifically for this purpose.
The height of the magnetometer above the ground surface was about 2 m. A portable Geometrics® G856 proton-precession base-station magnetometer was used to record diurnal variations of the Earth's magnetic field during the ground-magnetic surveys. Diurnal variations recorded by the base-station magnetometer were removed and the data were filtered to remove cultural "noise", such as culverts and fences. Ground magnetic data were collected along several traverses s in the vicinity of the springs. Ground magnetic traverses are shown in figure 6.

Airborne magnetic survey

Data acquisition

An airborne geophysical survey, was flown by FugroArborne Surveys from October 16th to November 1st, 2011 over the Pilgrim Springs area. Data were acquired using Fugro's RESOLVE system (fig. 7) that is equipped with a multi-coil, multi-frequency electromagnetic system, and high sensitivity cesium magnetometer.

The onboard Cesium vapor magnetometer sampled at a rate of 10 Hz, with a sensitivity of 0.01 nT, while a base Cesium magnetometer recorded the earth's magnetic field at 1 Hz for diurnal corrections. A GPS electronic navigation system recorded GPS time and satellite data for differential correction of survey positions, yielding a post-survey flight path determined to within ±2 m.

Flightlines were oriented North-South with East-West tielines. The mean survey drape was 38.2 m (Range: 0.4 – 123 m, stdev 8.5 m), though there was an increase in drape at south due to steep terrain. The total coverage of these areas amounted to approximately 556 km.

This new magnetic survey provides significant improvement over existing surveys (fig. 9) in this area by including diurnal corrections, differential GPS positions, tighter flight line spacing (1/4 & 1/8 mile flightline spacing; 2.5 mi tieline spacing), and lower flight elevations (60 meters - helicopter; 40 meters above ground - bird).

Processing

Fugro performed basic processing of the magnetic data that included removal of an IGRF field and light-line leveling. The USGS performed additional processing applying a variety of derivative and filtering methods, described below, that aid in interpretation by helping to delineate structures and to constrain their geometry. These various transformations were applied to the total magnetic field anomaly grid (fig. 8) that was derived from the leveled, and IGRF- and diurnally-corrected data.

Pseudogravity - PSG

The Pseudogravity (PSG) or magnetic potential transformation (fig. 10) is applied to magnetic data in order to isolate broad magnetic features that are often masked by high-amplitude shallow magnetic sources. The PSG transform converts a magnetic anomaly into one that would be observed if the magnetic distribution of the body were replaced by an identical density distribution. This significantly simplifies the interpretation of magnetic sources, however, there are significant assumptions that can limit the use of this method.

Difference maps

Difference or residual maps (fig. 11) are useful for emphasizing surface and near-surface sources. They are produced by upward-continuing the observed anomalies and subtracting the result from the original grid. This effectively removes the contribution of deeper sources.

Maximum Horizontal Gradients-maxspots

Maximum horizontal gradients (MHG) are used to map the edges of sources (fig. 12). MHG reflect abrupt lateral changes in the density or magnetization of the underlying rocks, and tend to lie over the edges of bodies with near vertical boundaries (Blakely and Simpson, 1986). They are calculated for both gravity and magnetic data to estimate the extent of buried sources, and to define the boundaries of geophysical domains, and internal domain structures.

Reduced to Pole - R2P

The Reduced to Pole transformation (figs. 13-14) centers magnetic anomalies over their sources.

Domains

We have characterized geophysical domains throughout the study area (fig. 15), in part with the MHG method, but also with other filtering and derivative methods that aid in highlighting the regional structural grain. Regions with a consistent anomaly trend, amplitude, or frequency content are defined as distinct geophysical terranes, and assumed to represent discrete crustal blocks with similar physical properties or sources.
Geophysically-defined boundaries may take several forms, such as:
1) A stepped anomaly that forms along an edge of a large crustal block with relatively uniform density or magnetic properties (e.g., dip-slip fault, or edge of a batholith or caldera).
2) A long, narrow, linear anomaly generated over a source whose vertical extent is much greater that its width (e.g., a dike or alteration zone along a fault).
3) A linear feature observed as the abrupt termination, and/or alignment of numerous high and low anomalies of different sizes and intensity (e.g., lateral fault).

Match filter

Match filtering (fig. 16) us used to separate potential field anomalies by depth to their sources, isolating anomalies arising from different crustal levels. A matched-filtering technique (Syberg, 1972; Phillips, 2001) applied to the frequency spectrum of potential field data can be used to isolate anomalies arising from different crustal levels, provided that the depths of anomaly sources are sufficiently distinct.

Depth to source estimations

As part of our ongoing work we are applying a number of different methods for estimating the depth to magnetic sources (including Euler deconvolution, and tilt derivative methods).

Preliminary Results

The various filtering methods applied reveal a number of interesting features spanning the shallow to mid-crustal levels. The longest wavelength features are revealed by the pseudogravity (PSG) transformation (fig. 10), that shows a broad high extending southeastwards from Mary's Mountain to Pilgrim Springs. Similar highs within the survey area are seen further to the southeast over the flanks of parts of the Kigluaik Mountains. A prominent low is observed over

the Kigluaik Mountains due south of the springs and northeast-trending elongate low bounds the springs to the southeast. This low is flanked by sharp gradients at its margins and is sub-parallel to the trend of gravity low described above. Maximum horizontal gradients (MHG) of the PSG reveal much more detail (figs. 10-12) and can be used to locate sharp contrasts in magnetic properties that occur, for example, at faults or contacts. Regionally, the MHG can be used to define structural domains (fig. 15). A series of northest-trending structures is clearly observed in this region southeast of the springs. In contrast, a dominant northwest tending fabric characterizes the northeastern portion of the survey area between the springs and Hen and Chickens Mountain. This trend is similar to that seen far north and south of the study area and may reflect deep basement structures (fig. 17). The area south of the springs, however, is dominantly characterized by east-west-trending range-front-parallel structures (fig. 15) that are likely late Cenozoic features associated with north-south extension that formed the basin. A similar E-W trend extends into the area immediately over the springs. Regionally, the springs are characterized by a magnetic high (fig. 13), but this is punctuated by several EW trending magnetic lows, the most prominent occurring directly over the springs (fig. 14). The lows may result from the demagnetization of magnetic material along range-front parallel faults that dissect the basin.

A set of northeast narrow magnetic highs (fig. 18), located between the springs and Marys Mountain, have a signature consistent with mafic dikes. Furthermore, their trends are similar to the trends of Tertiary dikes that outcrop in the Kigluaik Mountains (fig. 18). Indeed, based on the trend of the Precambrian metamorphic belt that forms the Kigluaik and Bendeleben Mountains (including the Hen and Chickens and Mary Mountains, fig. 3) it is expected that the Pilgrim Valley is floored by these same rocks.

Conceptual models

Its not clear what is the origin of the heat responsible for Pilgrim Springs. Despite the lack of direct evidence of volcanic activity in the Imuruk Basin-Pilgrim River Valley region, it has been suggested that the springs are related to recent volcanism in surrounding areas. The regional magnetic map provides some support that volcanic activity may have occurred more local to the springs than is suggested by surface geologic mapping (Fig. 19). 10-15 km north of Pilgrim Springs is an area, concealed by Quaternary sediments that has a very similar magnetic character to other areas of Tertiary volcanic outcrop. Nonetheless, Precambrian basement and Cretaceous intrusive rocks that outcrop in the surrounding uplands and are inferred to floor the Pilgrim Valley form a likely source of radogenic heat that could feed the springs locally. A promising source may lie beneath the deepest parts of the basin inferred from the gravity data (fig. 20), located just a few kilometers sowthwest of the springs. Joint potential field mapping (fig. 21) and future modeling should help delineate subsurface structures and basin geometry that can be used to test fluid flow models and constrain possible sources and pathways of geothermal fluids.

Airborne electromagnetic (EM) data

Airborne electromagnetic (AEM) systems transmit a magnetic field into the earth. This primary magnetic field induces currents in the ground that produce secondary magnetic fields measured by receiver coils on the airborne system. The receivers record both the in-phase and quadrature (out-of-phase) response as referenced to the transmitted signal. The result of an AEM survey is

an electrical resistivity image of the subsurface. Electrical resistivity is not only sensitive to conductive mineral content, but also to ice, clay content, porosity, permeability, saline fluids, and temperature.

We collected frequency-domain airborne electromagnetic (EM) data using Fugro's Resolve system. This system is sensitive to the frequency range of 400 Hz to 140 kHz. Data were collected using six coil pairs that measure signals at a sample rate of 10 seconds at six frequencies (400 Hz, 1800 Hz, 3300 Hz, 8200 Hz, 40,000 Hz, and 140,000 Hz) and at a nominal altitude of 37 meters. All frequencies were recorded in a coplanar configuration except 3300 Hz, which was recorded in a coaxial configuration. The coplanar configuration utilizes the vertical magnetic dipole field and is sensitive to massive conductive bodies and horizontal layering whereas the coaxial configuration utilizes a horizontal magnetic dipole field which is sensitive to vertical conductive objects in the ground such as thin, steeply dipping conductors perpendicular to the flight direction. The in-phase and quadrature response for each transmitter-receiver coil-pair at each frequency was recorded. The data were processed by Fugro to account for system drift and calibrations.

Processing

The following products were received from Fugro: Quadrature and in-phase raw data, noise information, apparent resistivity, apparent depth, differential resistivity, and preliminary depth sections. We have begun to analyze and interpret the above products and have performed preliminary inversion on several profiles across the survey region.

Apparent resistivity maps (Figure 22) were calculated using a pseudo-layer, half-space model defined by Fraser (1978). This model consists of a highly resistive layer (air) overlying a conductive half-space (Earth). Inputs are in-phase and quadrature components of the coplanar coil-pair at a given frequency. The air layer is fixed at a very high resistivity and data are inverted for two parameters: depth to the surface and half-space (apparent) resistivity. Higher frequencies are sensitive to shallow depths whereas lower frequencies are sensitive to greater depths of investigation.

Preliminary results

Preliminary interpretation of apparent resistivity and differential resistivity maps shows low resistivities around Pilgrim Springs. This conductive region extends to tens of meters below the surface and the most conductive regions extend to the north and northeast. Higher temperatures in this region likely give rise to more conductive sediments and the EM data are sensitive to saline geothermal fluids as well. More moderate resistivities characterize the regions surrounding rivers and streams. These moderate to low resistive areas are likely due to variations in clay content of the sediments.

The high resistivities (> 1000 ohm-m) associated with the mountain ranges (Figure 22,23) reflect the bedrock that comprises these ranges. An equally resistive region exists between the range front of the Kigluaik Mountains and the dense stream channels surrounding Pilgrim Springs. Although subtle topography exists in this region, it is north of the Kigluaik range front. This region of high resistivity is likely indicative of regions of resistive permafrost at depth. This interpretation agrees with permafrost mapping in the area and further work will be done regarding using the airborne EM data to map permafrost regions at depth.

An east-west trending, low resistivity (100-200 ohm-m) trend exists on both the apparent resistivity and the differential resistivity maps at all frequencies and depths, respectively. This linear trend follows the base of the Kigluaik Mountains and is preliminarily interpreted to indicate a range-front fault. Fault zones can be conductive when they are comprised of rocks that are fractured and may have hosted fluid flow and subsequent mineralization.
Several conductive anomalies appear in the data at greater depths that are more subdued or missing at shallow depths. These include the conductive regions to the southeast of Pilgrim Springs, the area east of Pilgrim Springs at the eastern edge of the map, the region immediately north of Mary's Mountain, and a narrow conductive conduit that appears at depth between Pilgrim Springs and the conductive region north of Mary's Mountain. Although these anomalies require further investigation and modeling before interpretations can be made, they may indicate regions of higher permeability or alteration at depth.
Full inversion of the airborne EM data will yield densely sampled models of electrical resistivity along the survey flight lines. We performed one-dimensional (1D) inversions along ten profile lines for all of the frequencies at given locations (Figure 24). In-phase and quadrature data along each profile were inverted using the laterally-constrained inversion of Auken et al. (2005). Data were inverted for 20-layer models starting from a 50 ohm.m halfspace and with no prior model. In-phase and quadrature data errors were defined as the maximum of a percent error and an absolute error floor. The resulting 1D models were stitched together to form a quasi two-dimensional (2D) resistivity depth section (Figure 25).

FUTURE WORK

Mapping and Modeling

We are in the process of developing two-dimensional geophysical models of the subsurface to define the shape and structure of buried units, to locate faults, and to delineate changes in the basement geology. Planned 2D and 3D modeling (using forward and inverse methods) of the data derived from the airbone survey, combined with high-resolution ground magnetic and gravity data will yield a structural model of the subsurface that can be used for testing fluid flow scenarios. In addition, the combined potential field and EM interpretations will help to identify deeper crustal structures most likely responsible for transporting hydrothermal fluids from their source to the springs, and will enable us to constrain viable heat source and transport models.

By providing a region-wide geologic and geophysical framework, this work will allow for more informed decisions regarding drill-site planning. By identifying structures that may be important targets for drilling, this work may significantly influence drilling strategies and priorities. In addition to directly aiding geothermal studies, this work will be useful to a wide range of ongoing and future regional geologic investigations related to geothermal systems in active extensional basins.

CONCLUSIONS

The aim of this study is to provide 1) a regional geophysical characterization of the area around Pilgrim Springs, and 2) a detailed assessment of the crustal cross-section along selected profiles,

with the goal of characterizing the geometry of the basin, and identifying intra-basin and basin-bounding structures that may provide pathways for hydrothermal fluid flow associated with the hot springs.

In 2011-2012 the USGS, in collaboration with ASCEP, was responsible designing, supervising, and analyzing a high-resolution airborne magnetic and EM survey. The airborne survey provides high resolution data related to the magnetic and resistivity structures spanning the shallow (upper 100m) to mid-crustal levels.

Data analysis and modeling will comprise future activities of this research that will include 2D potential field modeling along selected transects, regional geophysical mapping of structures, and 3D potential field and EM modeling.

Figure 1: Topographic index map showing the location of Pilgrim Springs (red star) on the Seward Peninsula.

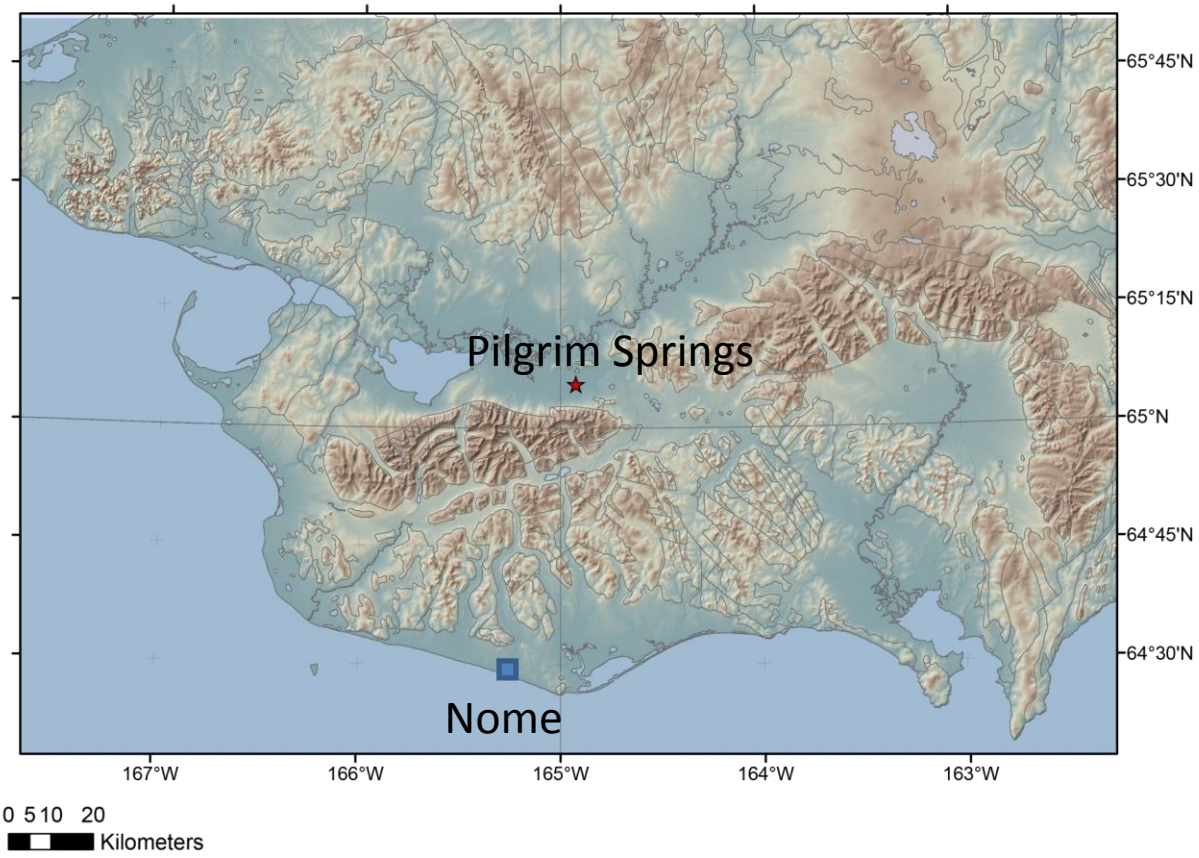


Figure 2: Index map index map showing the distribution of sediments (tan colored areas) on shaded topographic relief. Red box shows the area outlined in figure 4.

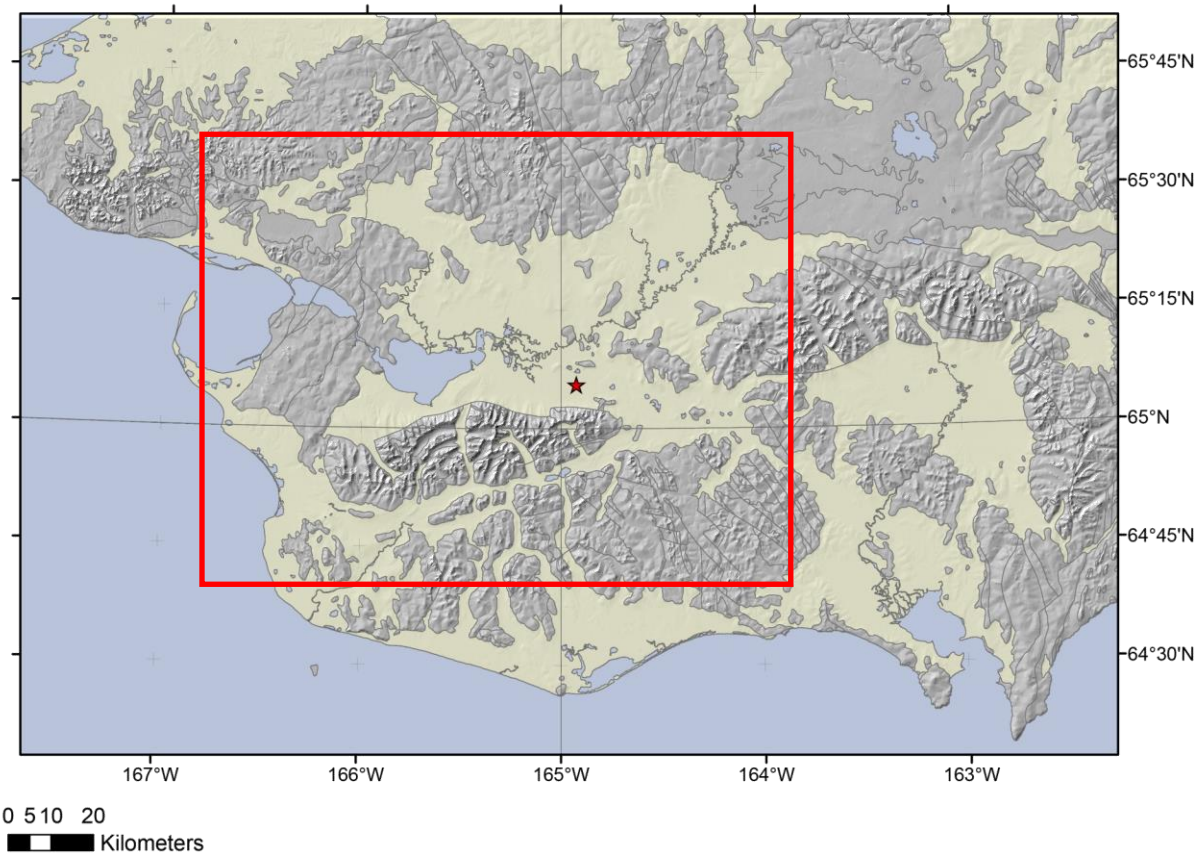


Figure 3: Geologic map of the area surrounding Pilgrim Springs (red star). Map after Till et al. (2010). Red box shows the area outlined in figure 5.

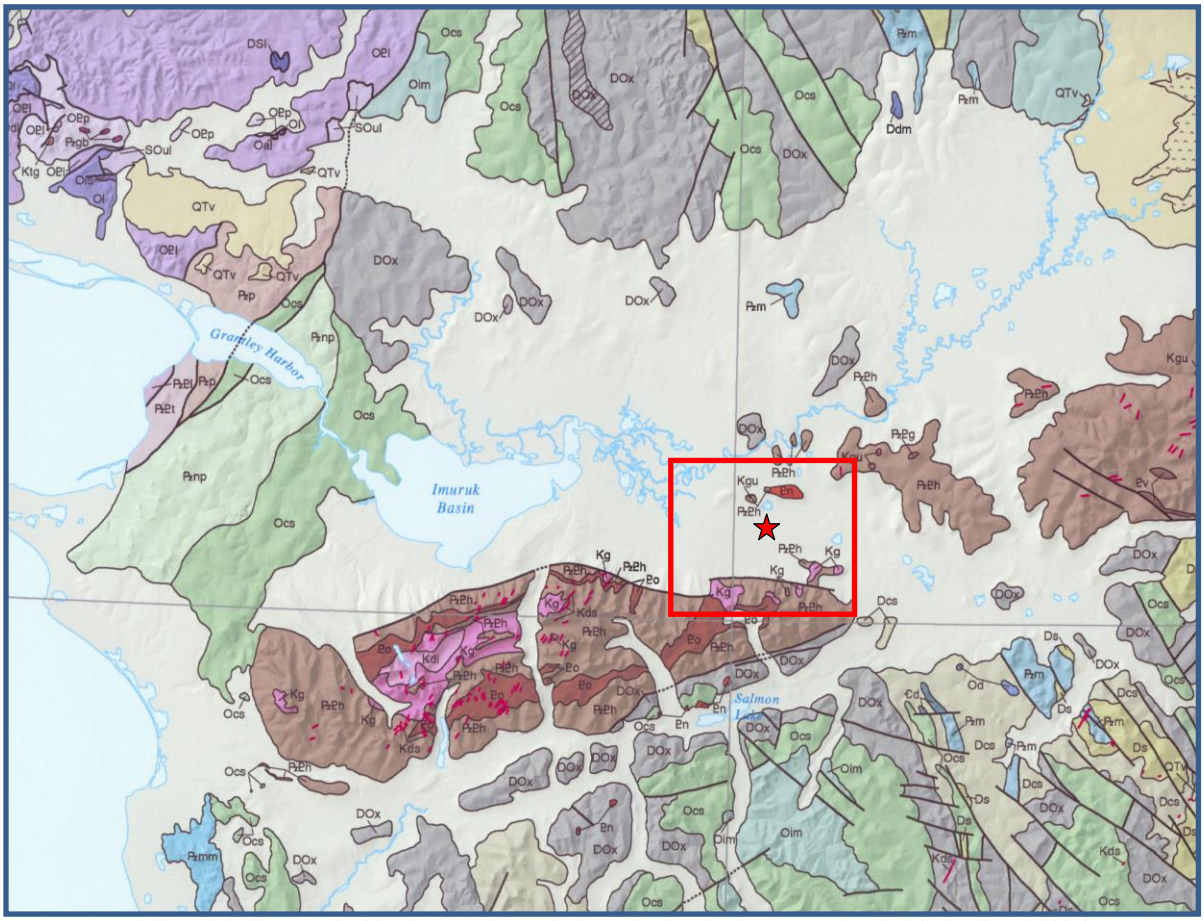


Figure 4: Topographic map of the area surrounding Pilgrim Valley. Pilgrim Springs is indicated by a red star.

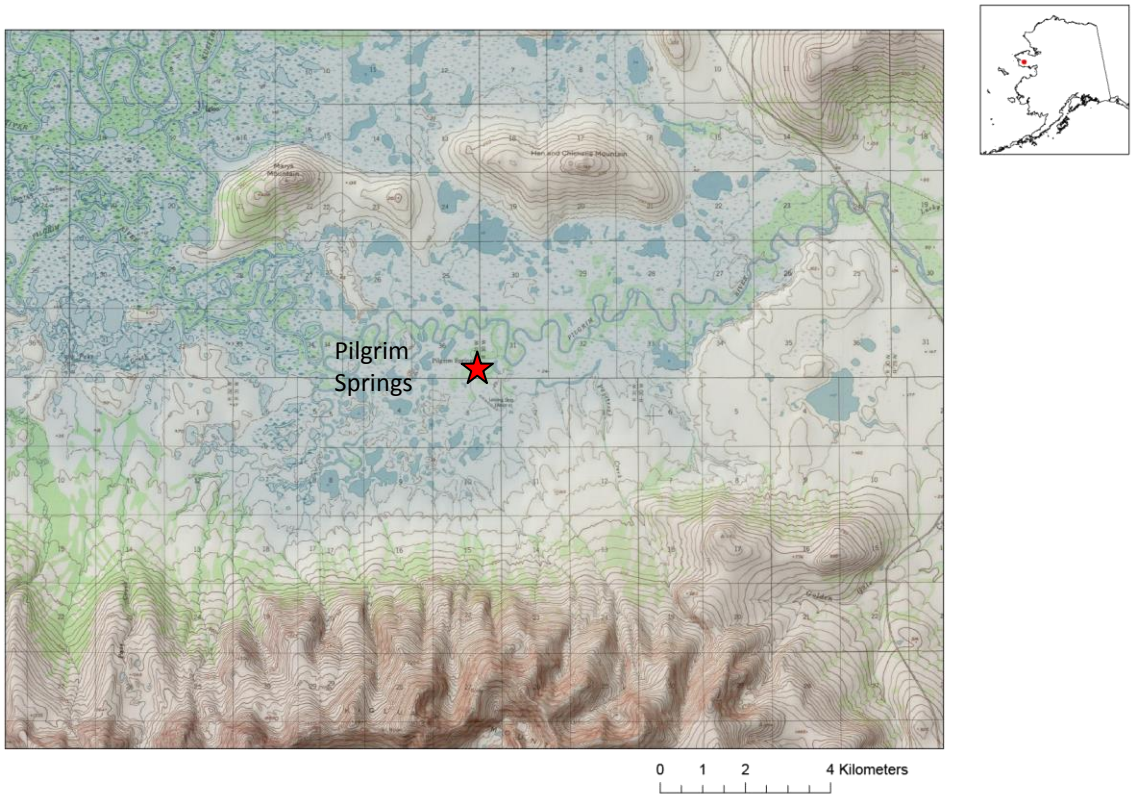


Figure 5: Isostatic gravity map of the pilgrim Springs area (upper panel). New gravity stations collected in the spring of 2010 are show in red. Grey symbols indicate existing gravity data. gravity profiles are labeled in the lower panel. Gravity highs appear as reds and pinks, gravity lows as blues and purples.

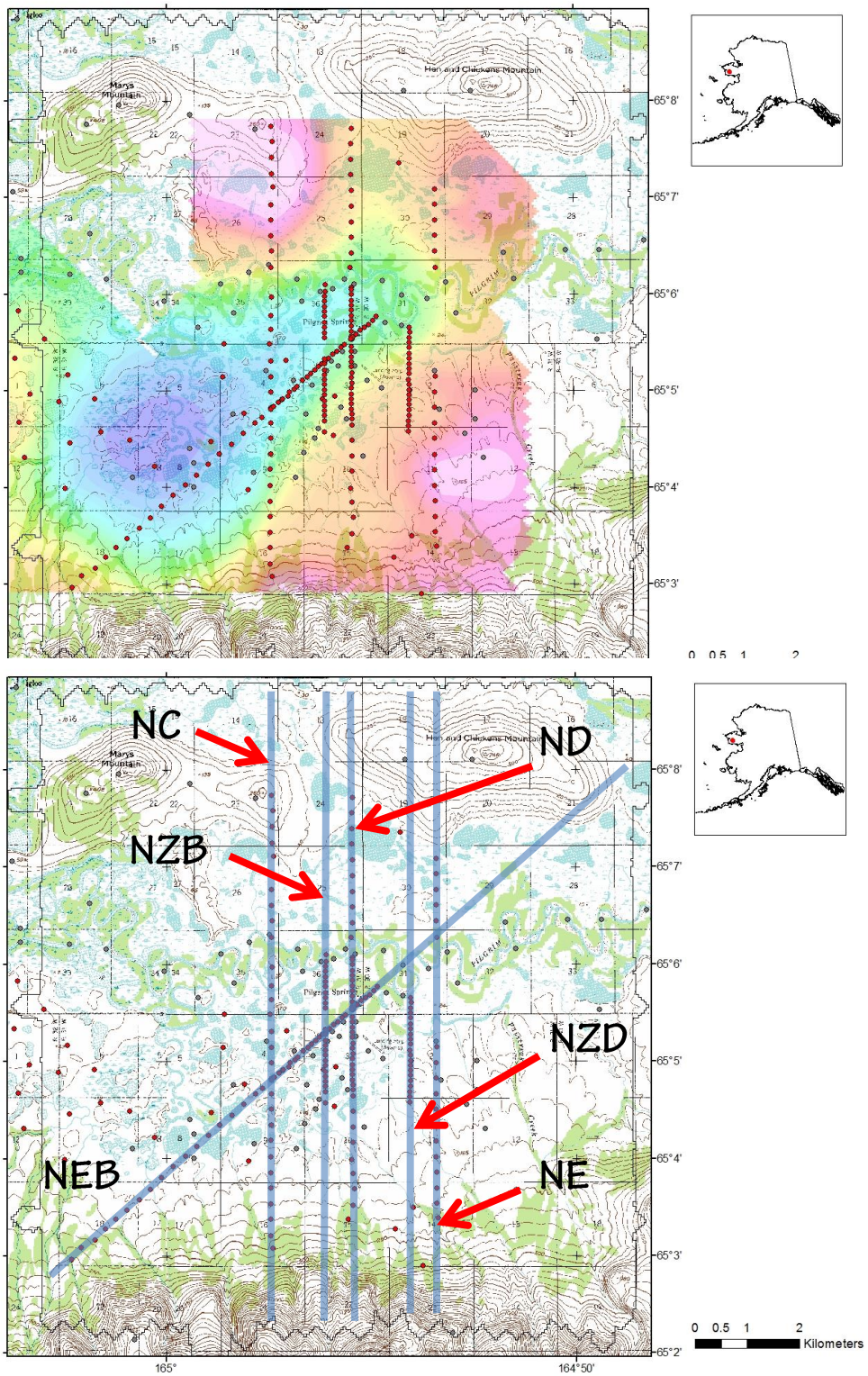
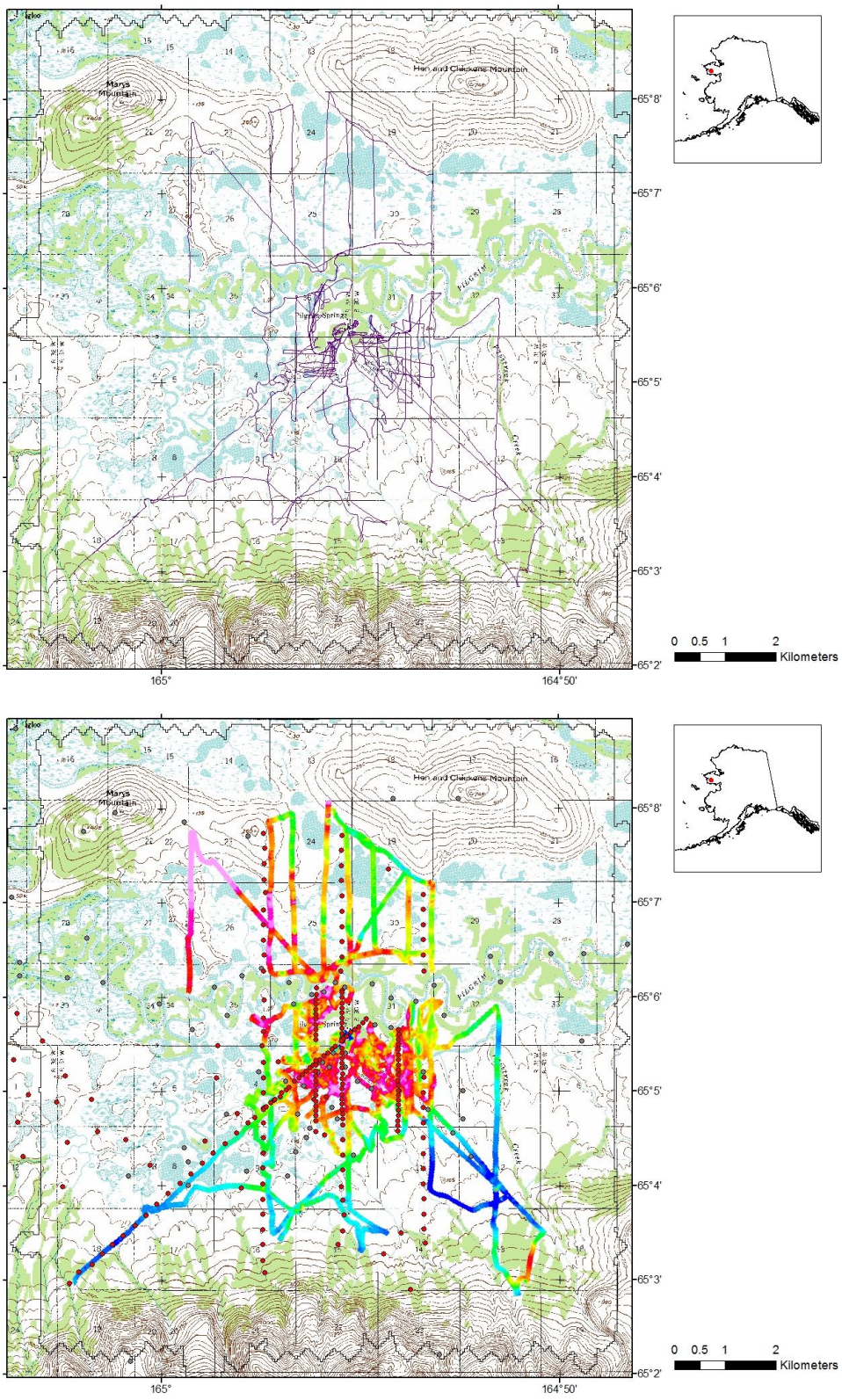


Figure 6: Map showing ground magnetic traverses in the pilgrim Springs area (upper panel). Magnetic field anomalies plotted along magnetic traverses (lower panel). Magnetic highs appear as reds and pinks, gravity lows as blues and purples.



FIGURES

Figure 7a: Fugro Airborne Surveys RESOLVE system on the ground in the Pilgrim Valley



Figure 7b: Fugro Airborne Surveys RESOLVE system just after takeoff



Figure 8: Magnetic field anomaly map derived from data obtained during the airborne survey flown for this study. Magnetic highs appear as reds and pinks, gravity lows as blues and purples.

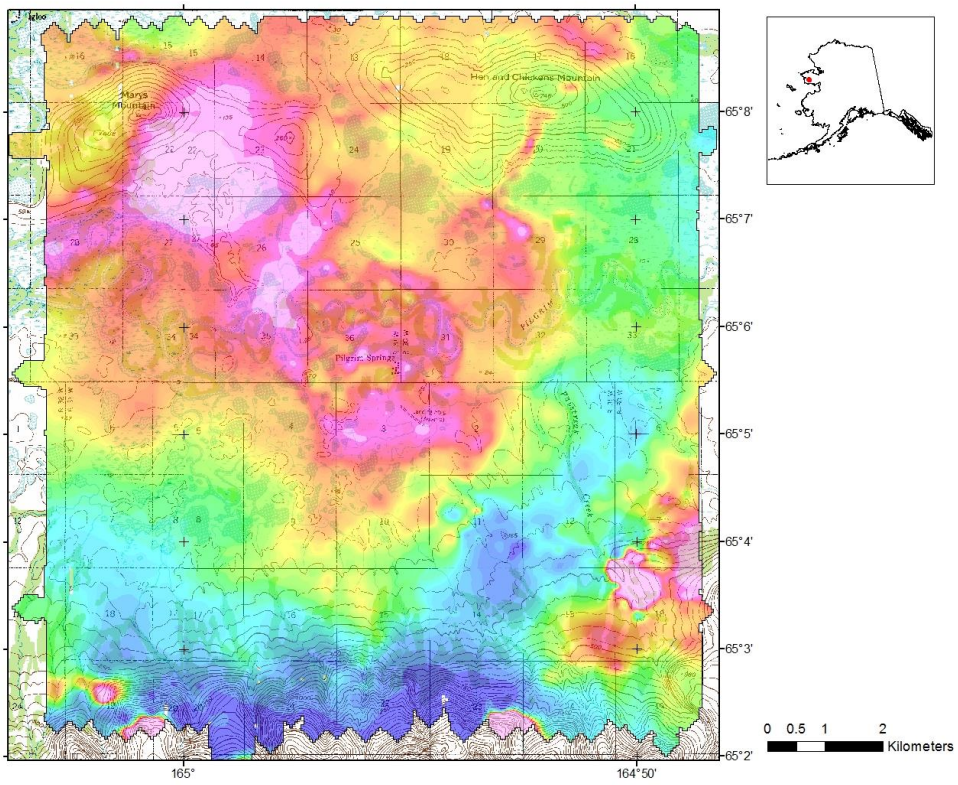


Figure 9: Regional magnetic anomaly map derived from surveys flown in the late 1960's and early 1970's (Cady, 1977). Magnetic highs appear as reds and pinks, gravity lows as blues and purples.

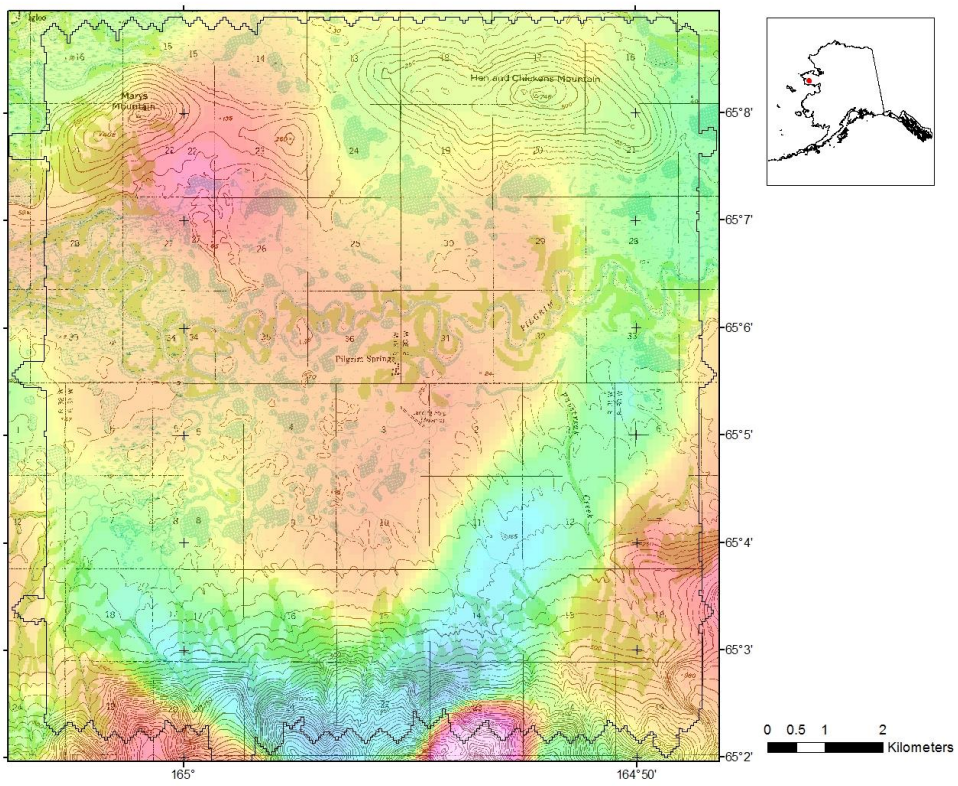


Figure 10: Pseudogravity map. Pseudogravity highs appear as reds and pinks, gravity lows as blues and purples.

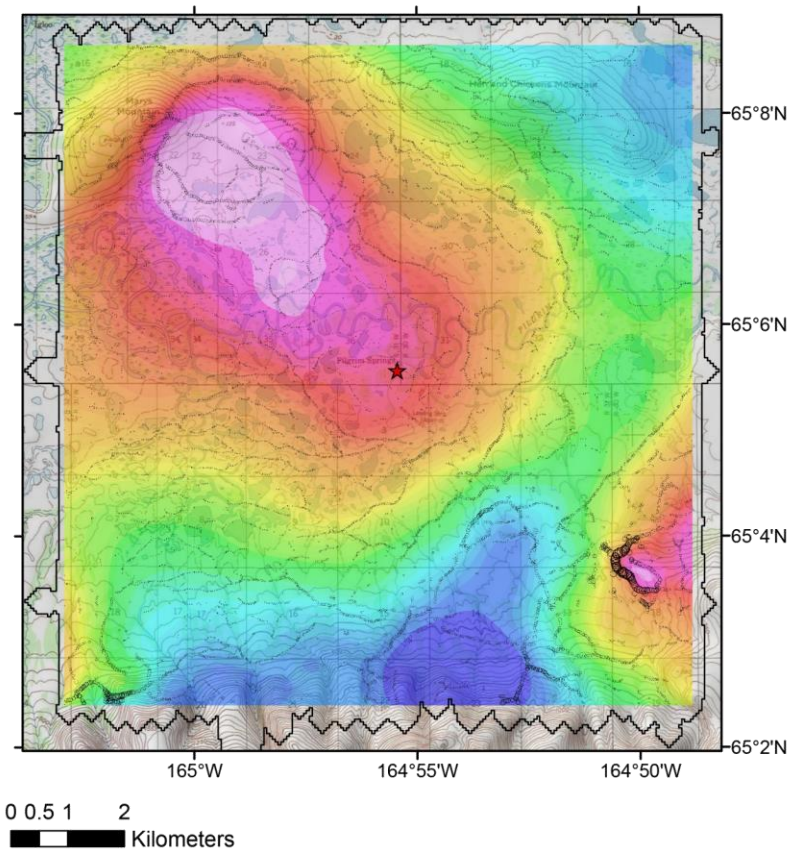


Figure 11: Differential Pseudogravity with spots of maximum horizontal gradient. Pseudogravity highs appear as reds and pinks, gravity lows as blues and purples.

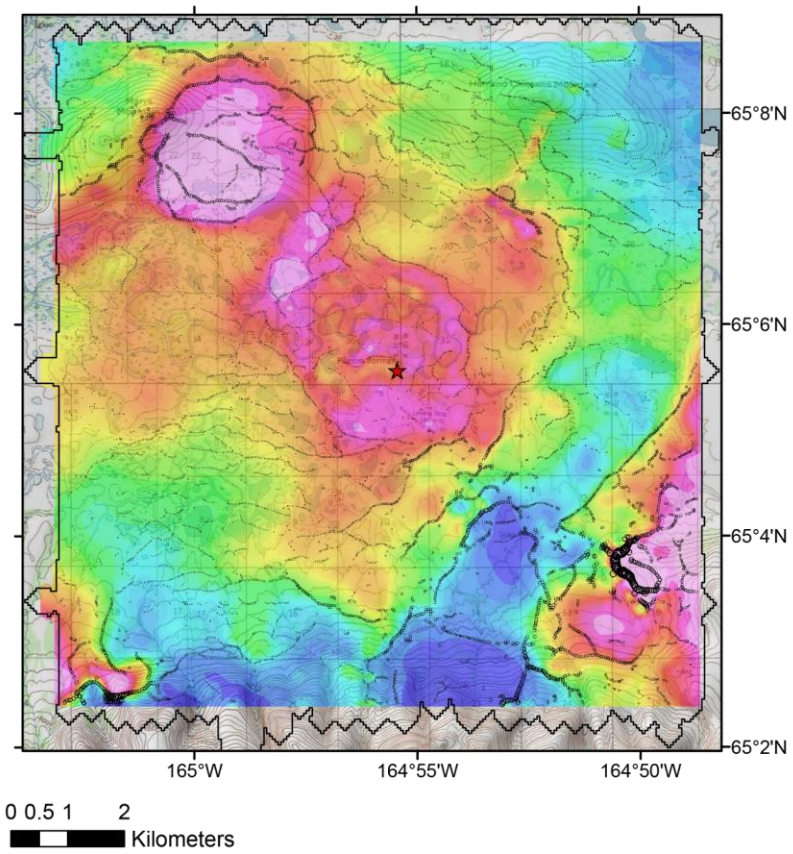


Figure 12: Differential Pseudogravity maps with magnetic lineations interpreted from maximum horizontal gradients. Pseudogravity highs appear as reds and pinks, gravity lows as blues and purples.

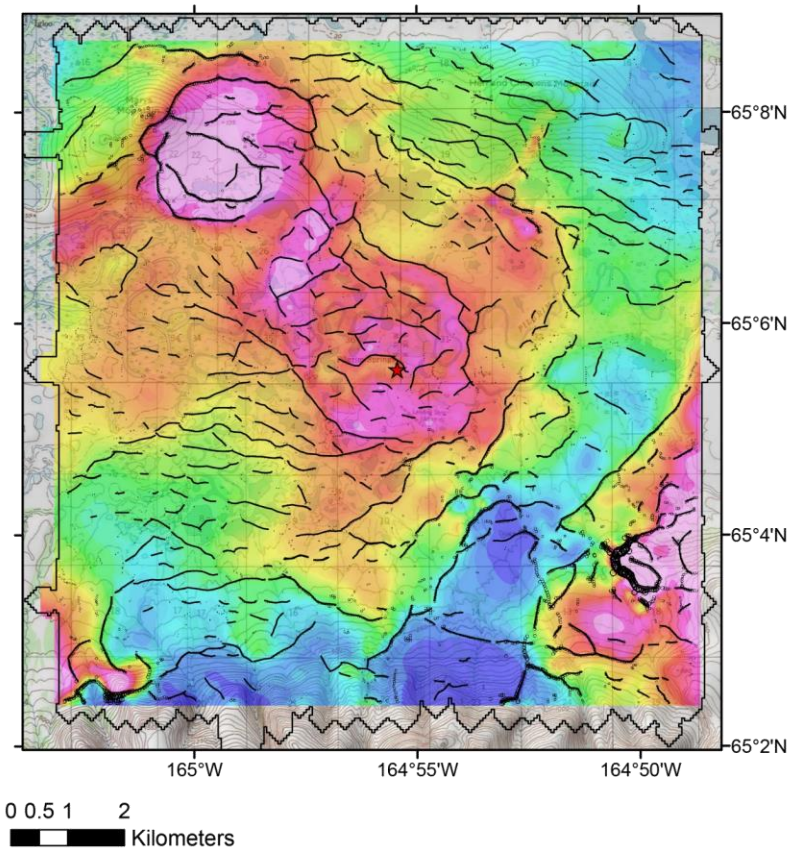


Figure 13: Reduced to pole magnetic anomaly map. Magnetic highs appear as reds and pinks, gravity lows as blues and purples.

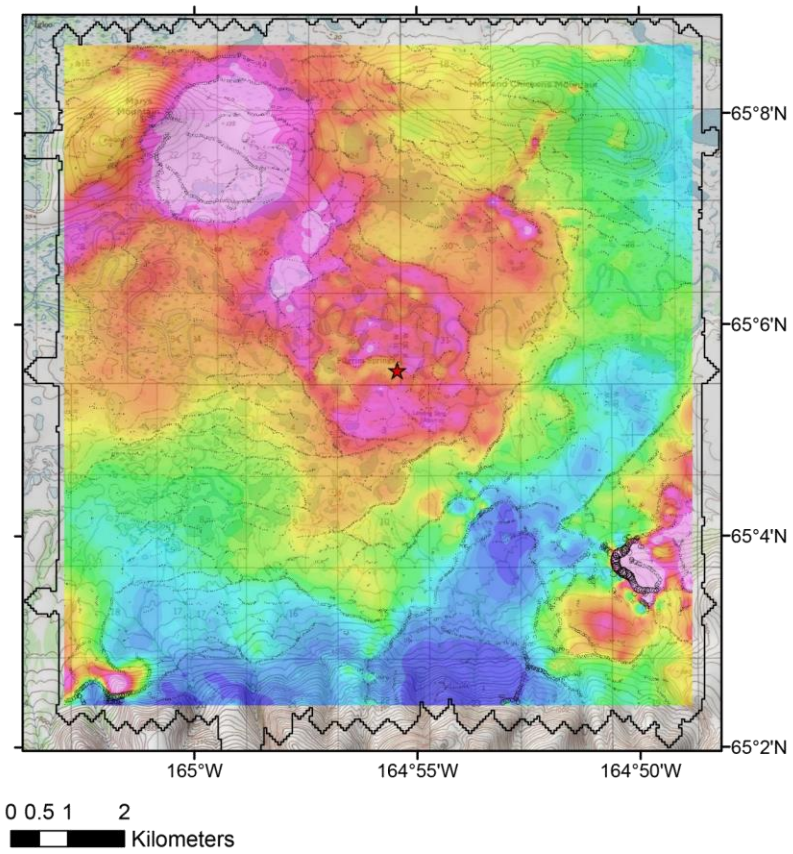


Figure 14: Differential Reduced to Pole. Magnetic highs appear as reds and pinks, gravity lows as blues and purples.

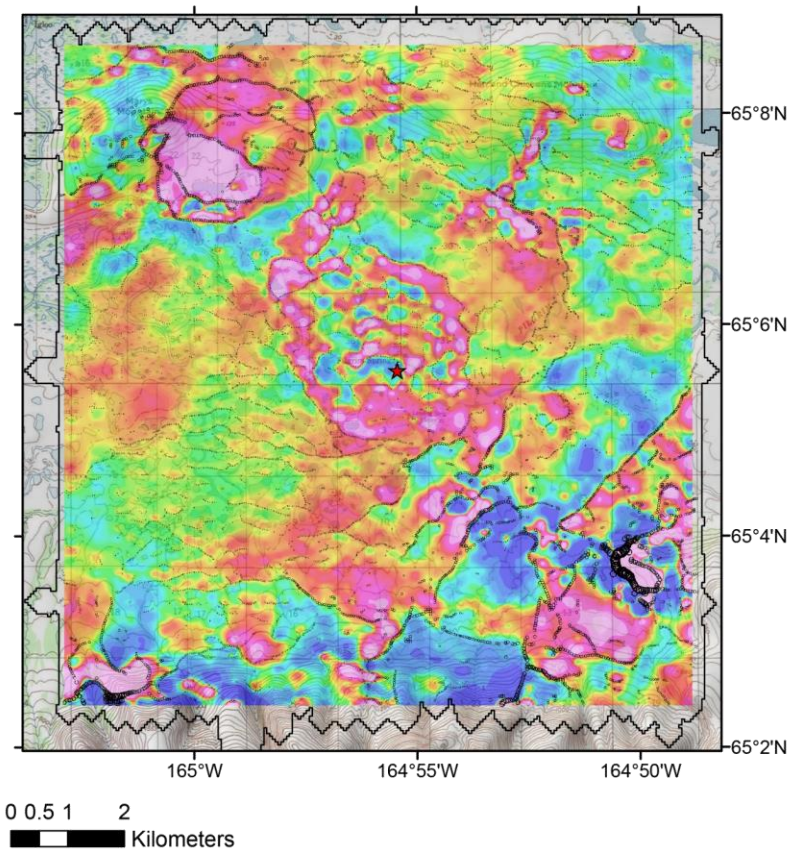


Figure 15: Magnetic lineations interpreted from maximum horizontal gradients, colored by trend (EW – red; NW – blue; NE – green).

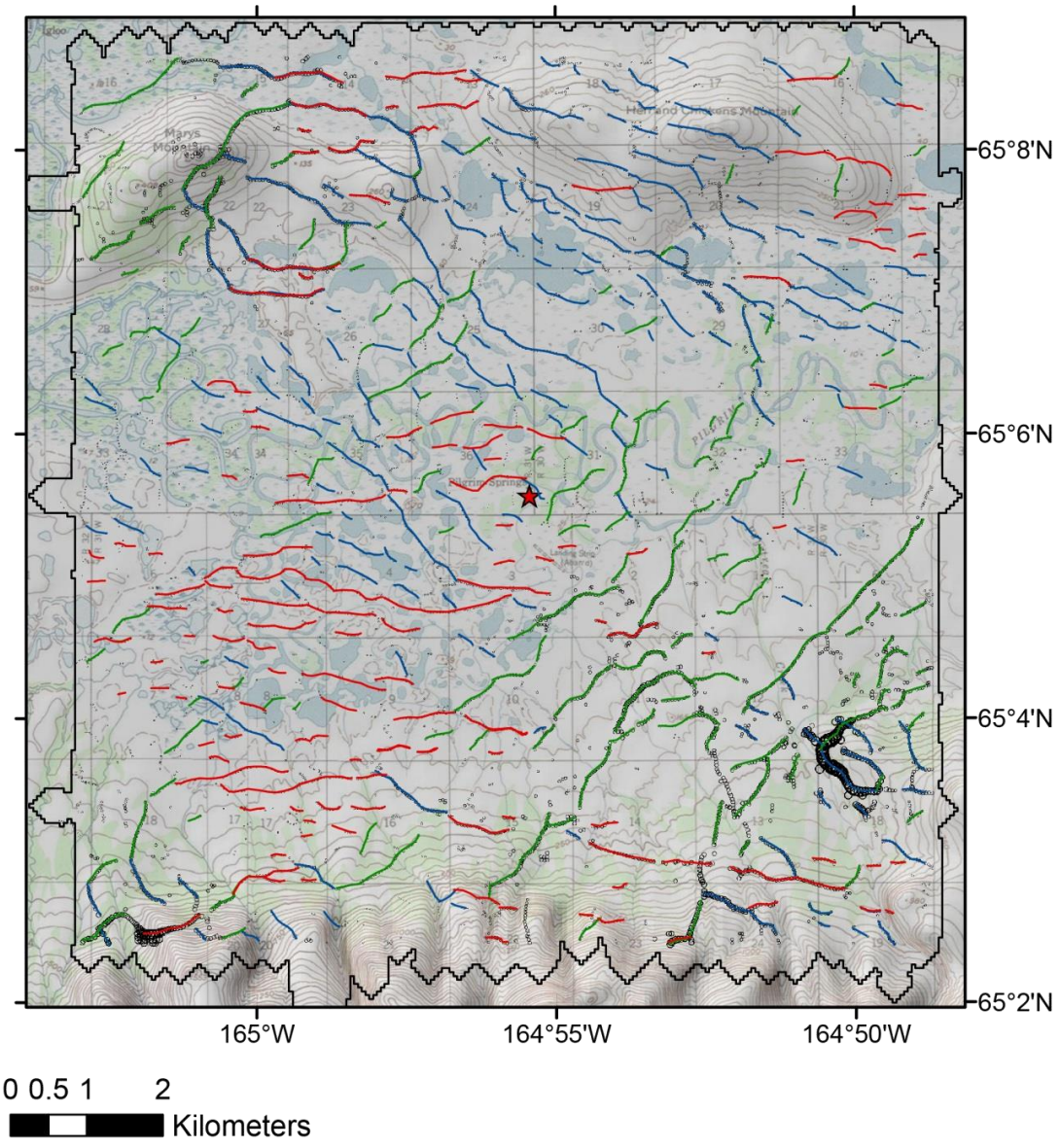


Figure 16: Match filtered band pass of magnetic reduced to pole grid, yielding deep (upper panel), intermediate (middle panel), and shallow (lower panel) sourced anomalies. Magnetic highs appear as reds and pinks, gravity lows as blues and purples.

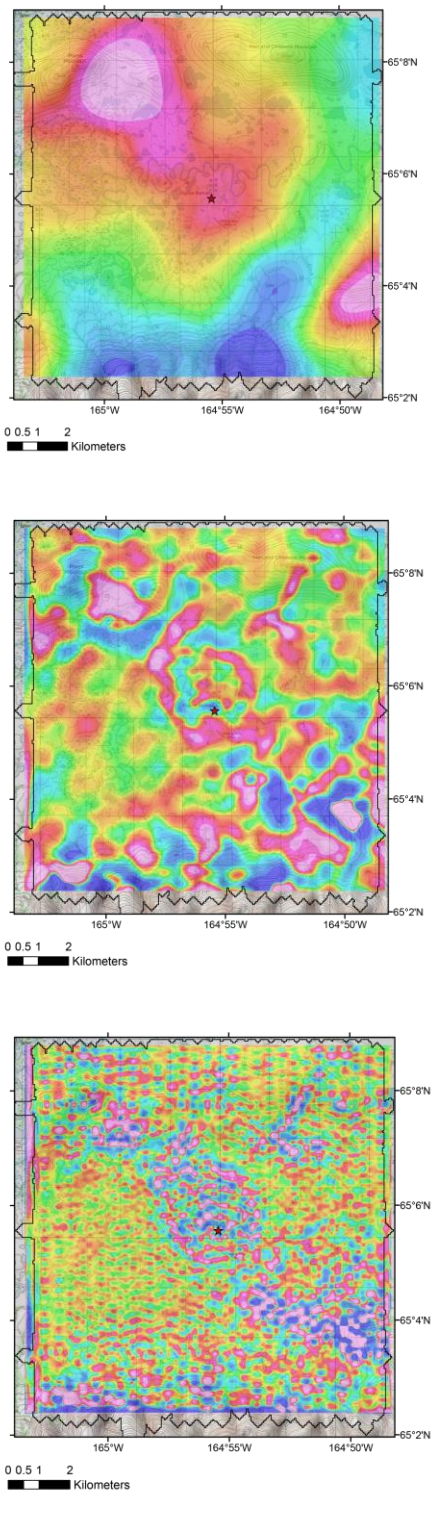
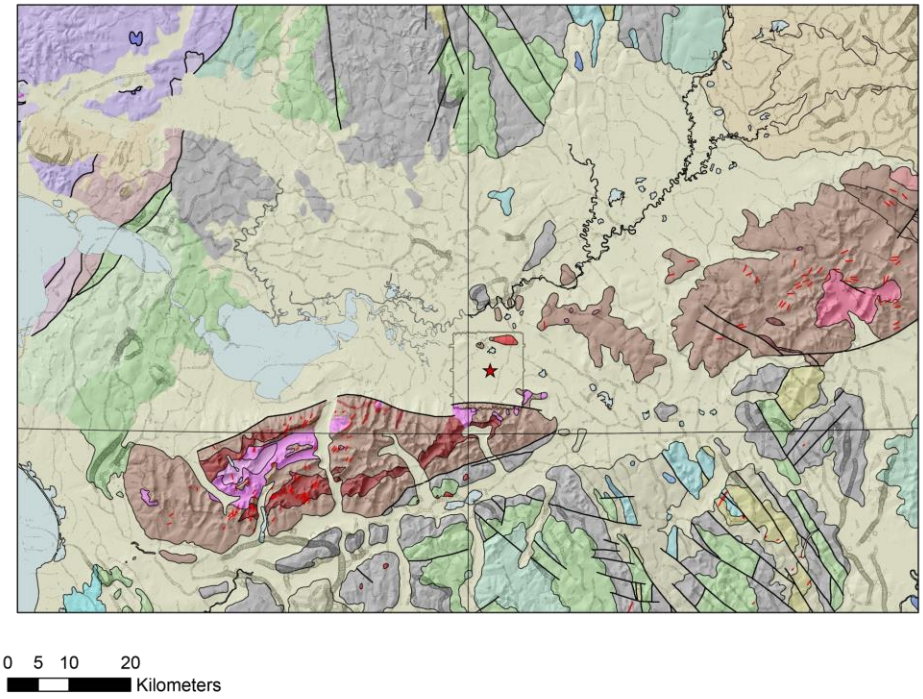


Figure 17: Geologic map (upper panel) and shaded reliev (lower panel) of the Pilgrim Springs area superimposed with spots of maximum horizontal gradients of the magnetic field. A prominent regional northwest trending fabric can be seen extending across Pilgrim Springs.



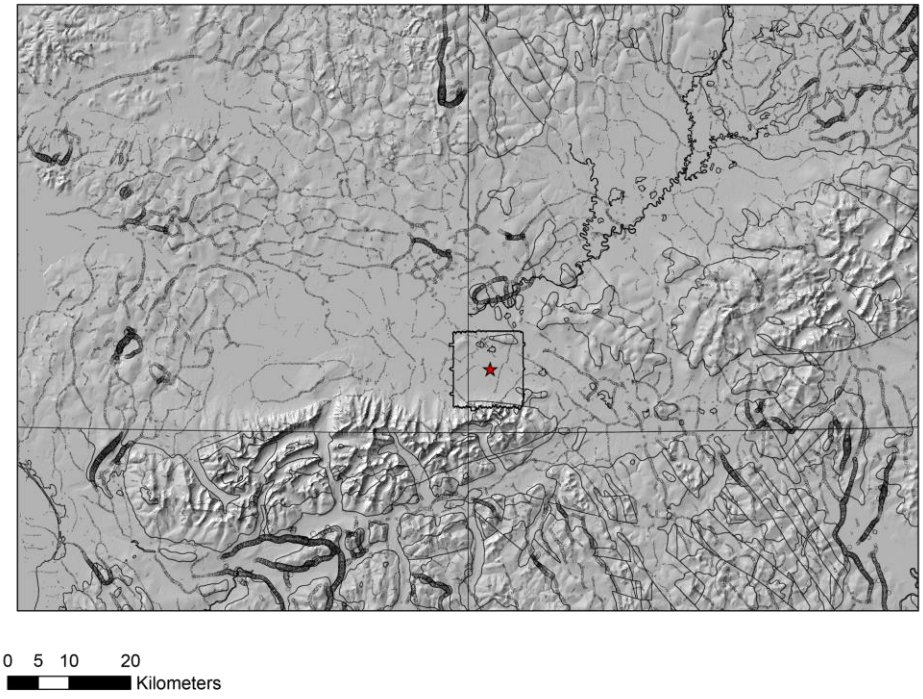


Figure 18: Map showing mafic dikes in the Kigluaik Mountains (red lines). Inset in the upper left shows a rose diagram of dike trends. Inset in the lower right shows the differential magnetic anomaly map with arrows highlighting possible dikes.

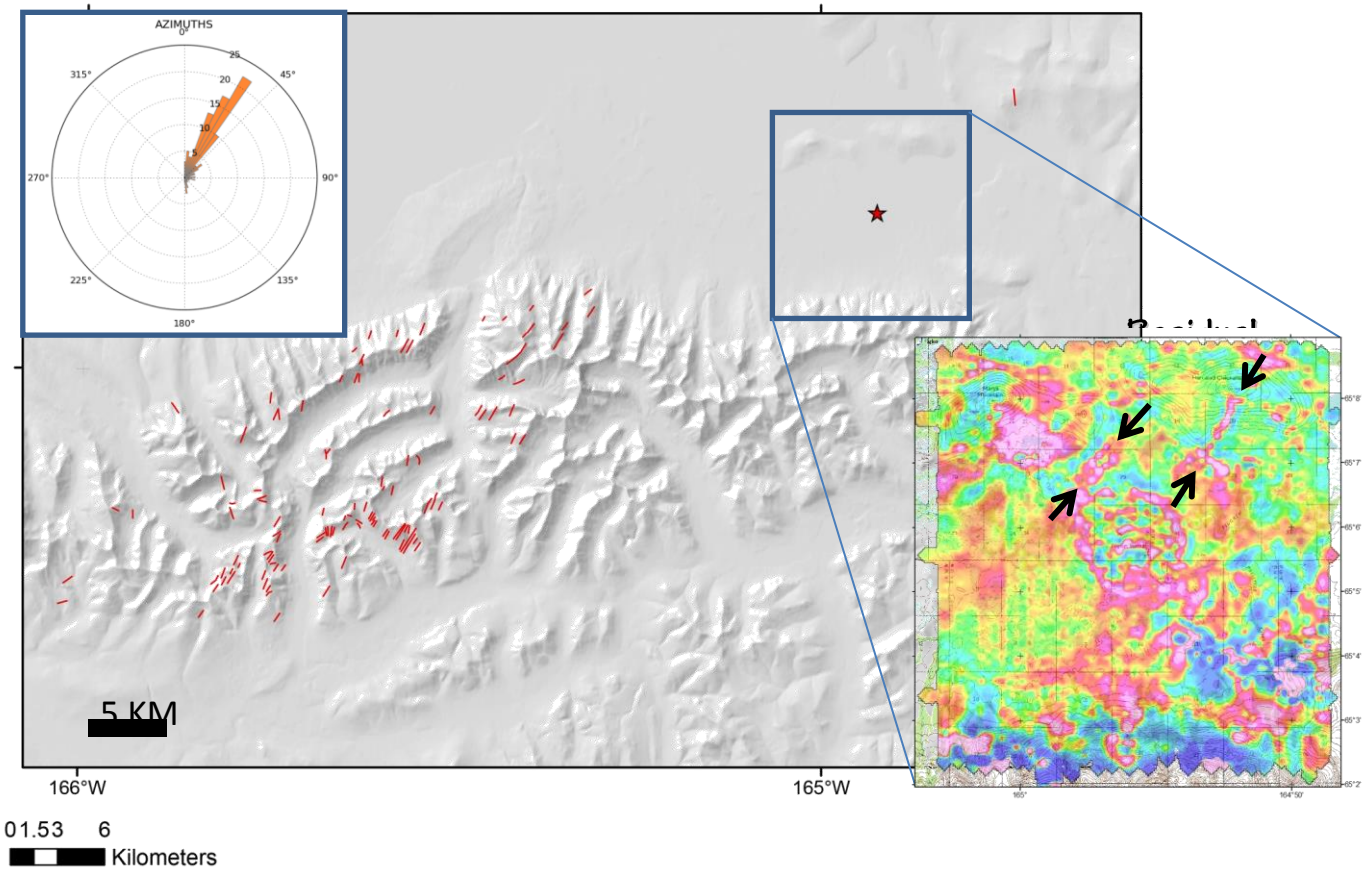
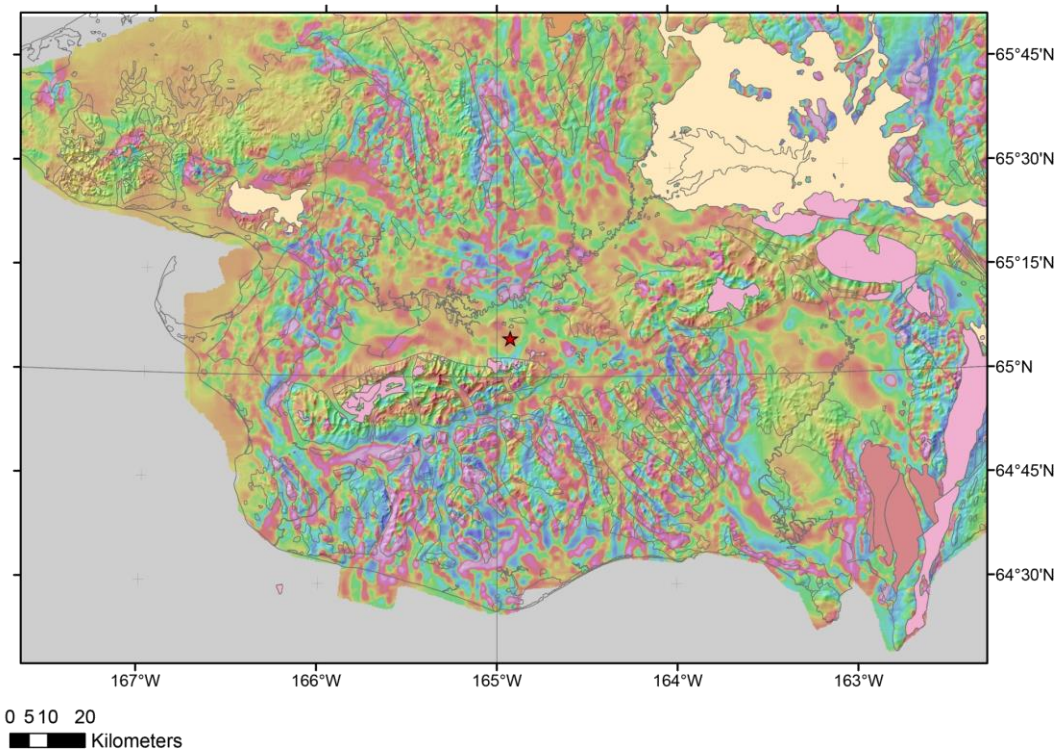


Figure 19: Upper panel: Regional magnetic map of the southern Seward Peninsula (After Cady, 1977). Magnetic highs appear as reds and pinks, gravity lows as blues and purples. Also shown areQuaternary and Tertiary volcanics (tan plygons) and Mesozoic intrusive rocks (pink and red polygons); Lower panel: area north of Pilgrim Springs that has a similar magnetic character as other areas covered by Tertiary volcanics.



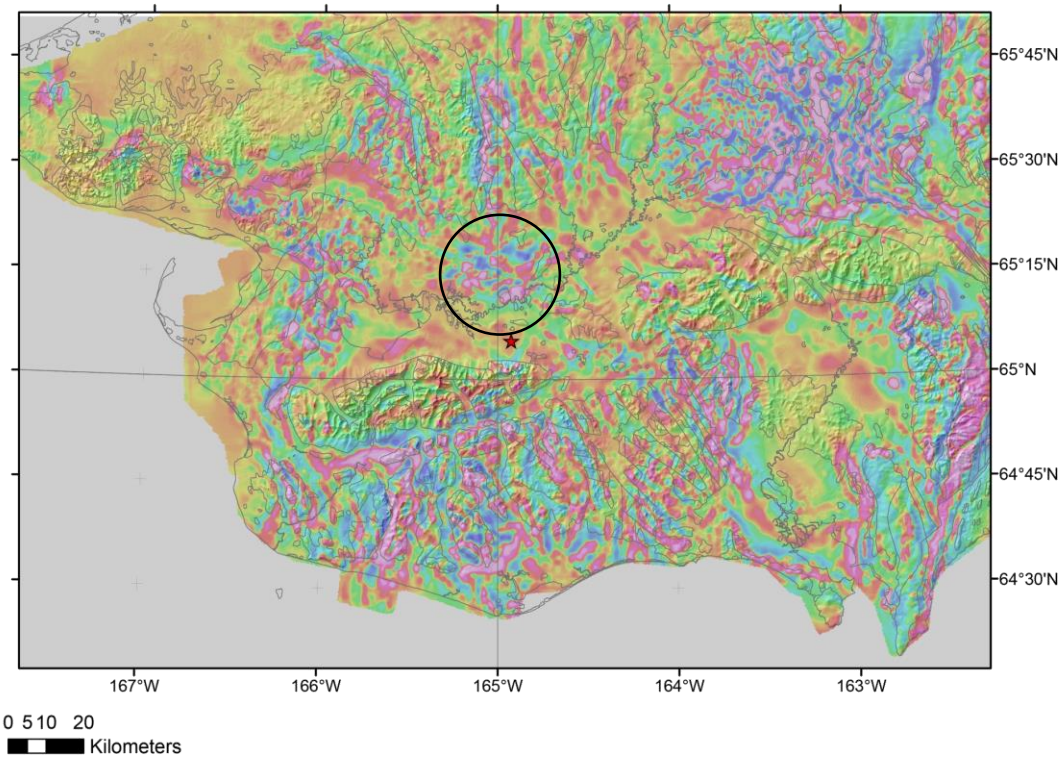


Figure 20: Isostatic residual gravity map used to map the structural basin.

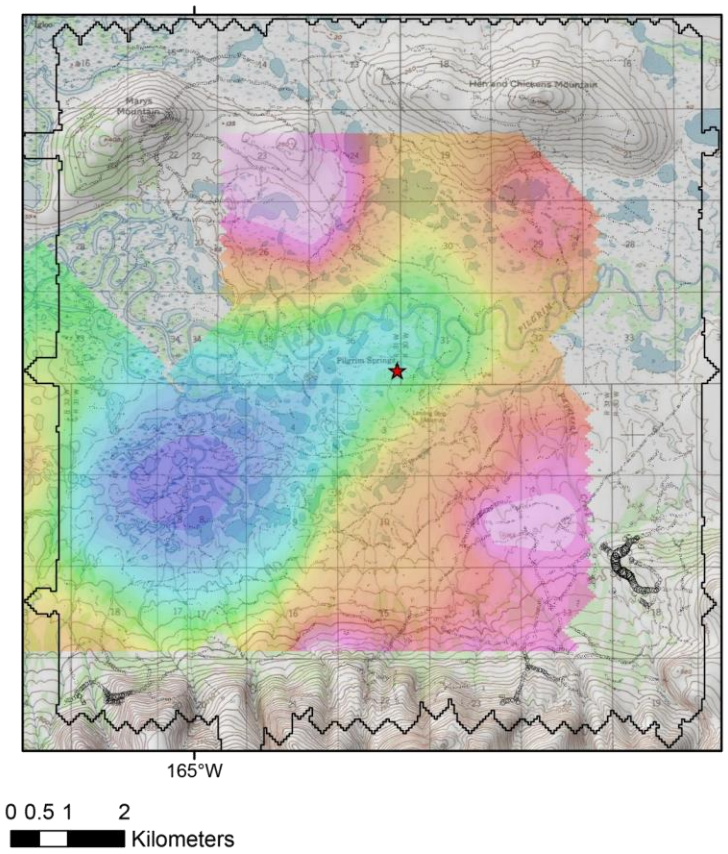
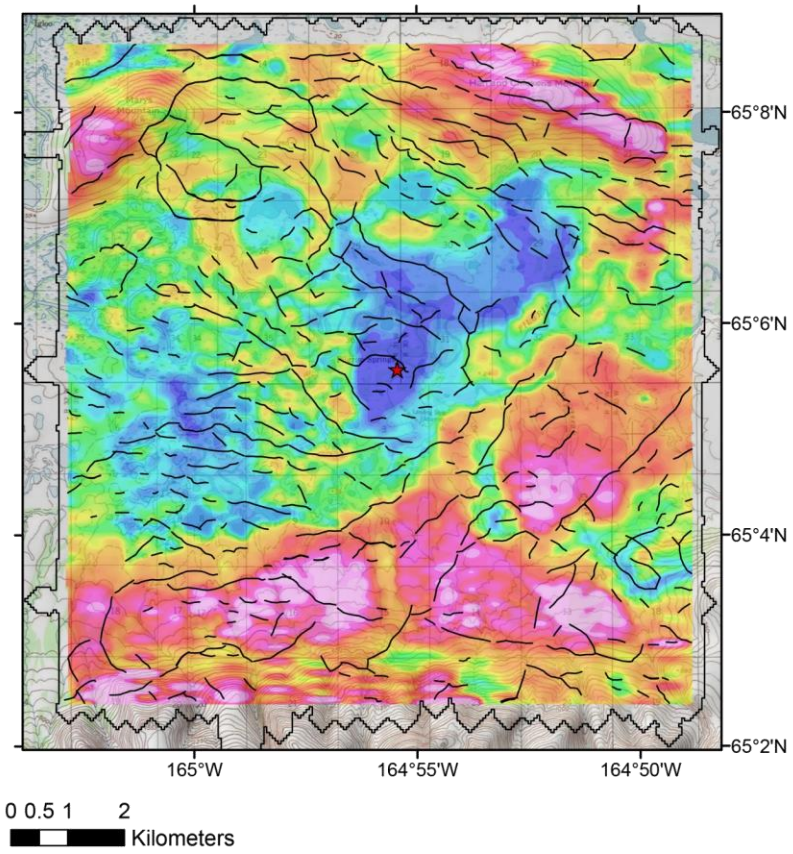
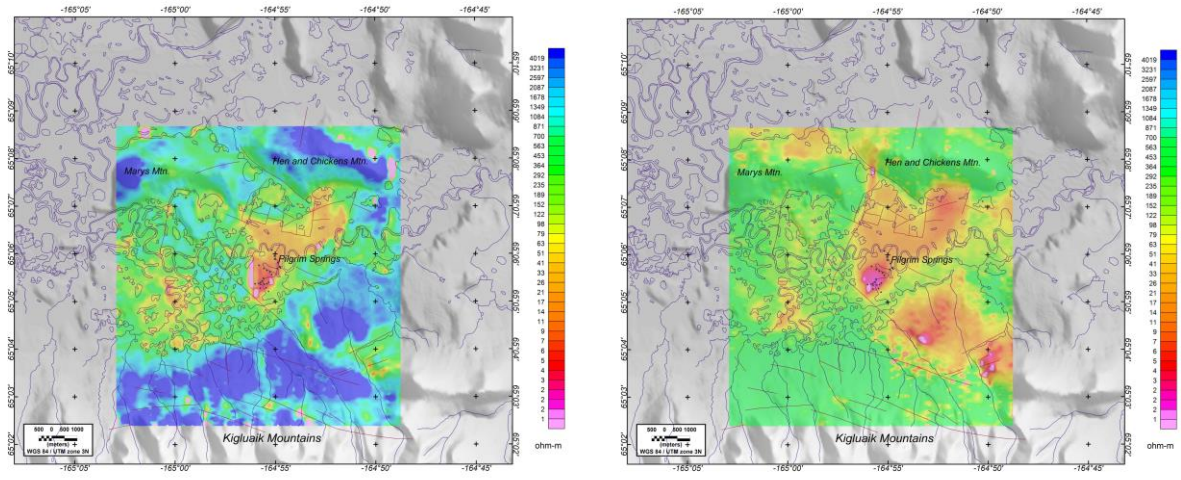


Figure 21: Map showing Differential resistivity depth slice at 5m superimposed with magnetic lineations to aid the correlation of potential-field & EM features.



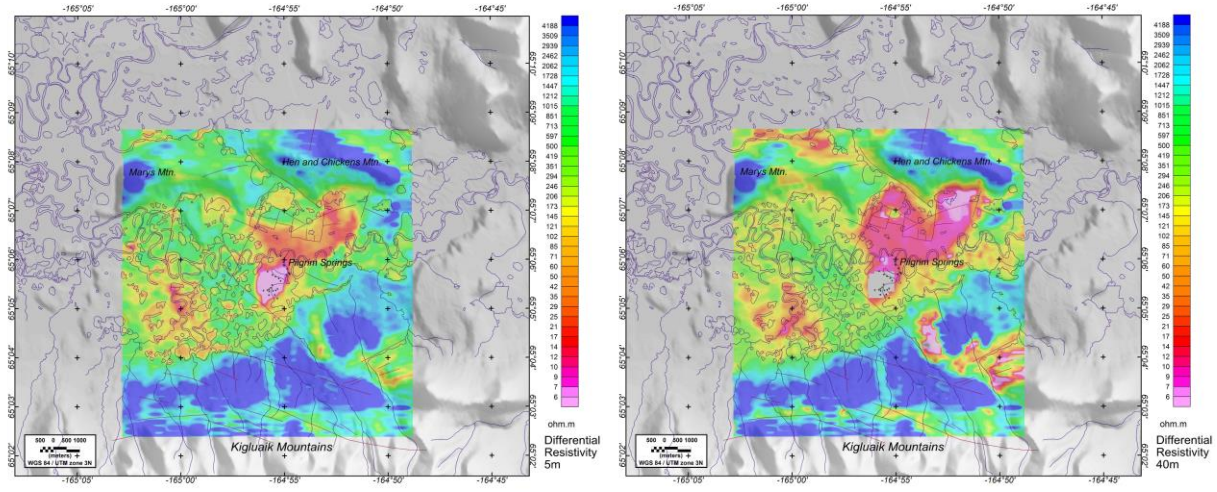


(a) (b)

Figure 22: Apparent resistivity at 140 KHz (a) and 400 Hz (b) overlayed on topography. Waterways and stream channels are shown in blue and faults are shown in red. Wells are shown with black dots. (need more info about faults and wells)

Apparent resistivity maps show regions of low resistivity (high conductivity) around Pilgrim Springs. At 140 KHz, the areas near rivers and streams are characterized by moderate resistivities (50-300 ohm-m) whereas the Hen and Chickens Mountain, Marys Mountain, and the Kigluaik Mountains are characterized by high resistivities (> 1000 ohm-m). At 400 Hz, the mountainous areas are less resistive. This is likely due to the lack of sensitivity of the data at low frequency as opposed to the mountains getting more conductive at depth. However, more conductive regions southeast of Pilgrim Springs appear in the map that are not seen at higher frequencies.

In addition to apparent resistivity, differential resistivity maps (Figure B) were made from the data delivered from Fugro. Differential resistivity (Huang and Fraser, 1996) is a transformation of apparent resistivity to an approximation of layer resistivity at an apparent depth. The method approximates the effect of shallow layer conductance determined from higher frequencies to estimate the deeper resistivity (Huang and Fraser, 1996).



(a) (b)

Figure 23: Differential resistivity maps at 5 m (a) and 40 m (b) overlayed on topography.

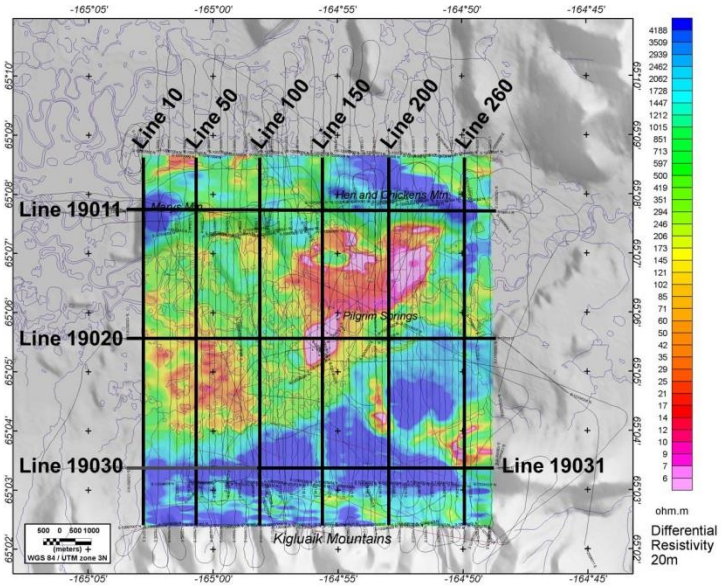


Figure 24: Map showing location of preliminary 1D models (black lines) overlayed on the 20 m differential resistivity depth section.

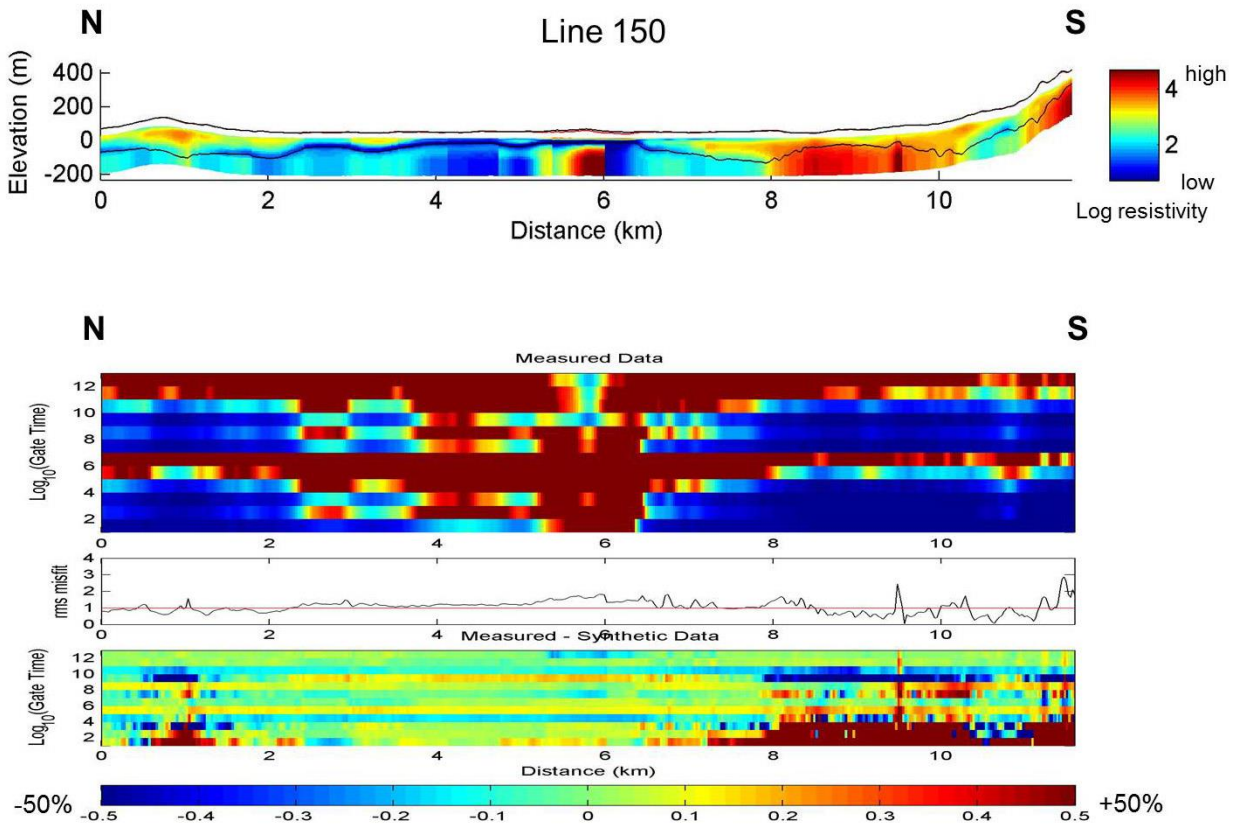


Figure 25: 1D inversion along line 150. The top panel shows the model with a 2:1 vertical exaggeration with a log color scale from 5-50,000 ohm-m. The black line shows a relative measure of depth of investigation. Any model structure below this line is considered unreliable. The black and red lines above the model section are the measured and inverted bird altitude. Note that the resistivity color scale is reversed from that in Figures A-C. The second panel shows the measured data (in-phase and quadrature) from high to low frequency on the y-axis. The third panel shows the data misfit (black) relative to the target misfit (red). The lower panel shows the data misfit by frequency along the line. The color scale at the bottom goes from -50% to +50%. Preliminary interpretation of the 1D models along line 150 shows various features in the data (Figure E). The XX bedrock of Hen and Chickens and the Kigluaik Mountains are highly resistivity (>1000 ohm-m; note, the resistivity color scale is reversed from that on Figures A-C). Pilgrim Springs is highly conductive, so much so that data are not resolved beneath a few meters. The highly resistive region south of Pilgrim Springs is interpreted to be permafrost and a less resistive feature shows up between this region of permafrost and the Kigluaik Mountains, likely an indication of a range-front fault. The low resistivity (high conductivity) zone north of Pilgrim Springs may be a region of high clay content and alteration.
1D inversion of the entire dataset (work in progress) will allow for a more thorough interpretation of the region as well as joint interpretation with the aeromagnetic data.

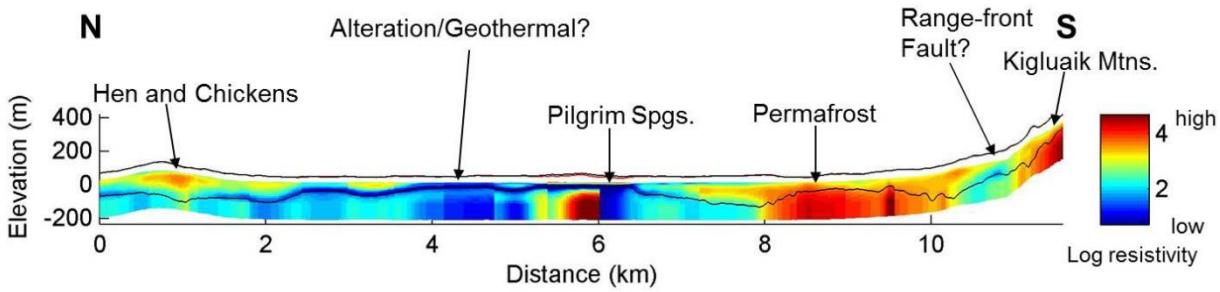


Figure 26: Interpretation of 1D model along line 150. Vertical exaggeration = 2.

REFERENCES

Auken, E., Christiansen, A.V., Jacobsen, B.H., Foged, N., and Sorensen, K.I., 2005, Piecewise 1D laterally constrained inversion of resistivity data, Geophysical Prospecting, v. 53, no. 4, p. 497-506.

Cady, J. W., and Hummel, C.L., 1976, Magnetic studies of selected geologic and aeromagnetic features in southwest Seward Peninsula, west-central Alaska: U.S. Geological Survey Open-File Report 76-425, scale 1:125,000.

Dean, K.G., R.B. Forbes, and D.L. Turner, 1981, Application of Radar and Infrared Airborne Remote Sensing to Geothermal Research on Pilgrim Springs, Alaska, Geophysical Institute, University of Alaska Fairbanks, AK, 1981.

Dean, K.G., R.B. Forbes, D.L. Turner, F.D. Eaton, and K.D. Sullivan, 1982, Radar and Infrared Remote Sensing of Geothermal Features at Pilgrim Springs, Alaska, Remote Sens. Environ., 12(5), 391-405.

Dilley, 2007, Preliminary Feasibility Report: Pilgrim Hot Springs – Nome, Alaska. Report to Alaska Energy Authority, 33p.

Economides, M., 1982, Drilling and Reservoir Engineering Analysis of Pilgrim Hot Springs, Alaska, University of Alaska Fairbanks, Fairbanks, Alaska.

Economides, M.J., Economides, C.A.E., Kunze, J.F. and Lofgren, B., 1982, A Fieldwide Reservoir Engineering Analysis of the Pilgrim Hot Springs, AK, Proceedings of the 8th Geothermal Reservoir Engineerring Workshop, Stanford University, Stanford, CA, pp. 25-30.

Forbes , R.B. , L. Gedney, D. Van Wormer, J. Hook, 1975, A Geophysical Reconnaissance o f Pilgrim Springs, Alaska, University o f Alaska, Geophysical Institute, February, 1975. Alaska Geophysical Institute Report UAG-R231.

Forbes, Wescott, Turner & Kienle, 1979, Geological & Geophysical Assessment of the Geothermal Potential of Pilgrim Springs, Alaska: Unpublished preliminary report to Alaska Division of Energy and Power Development and U.S. Department of Energy. No number.

Fraser, D.C., 1978, Resistivity mapping with an airborne multicoil electromagnetic system, Geophysics: v.43, no.1, p. 144-172.
Huang, H. and Fraser, D.C., 1996, The differential parameter method for multifrequency airborne resistivity mapping, Geophysics: vol. 61, no.1, p. 100-109.

Hudson, T. L., 1977, Geologic map of Seward Peninsula, Alaska,: U.S. Geological Survey Open-File Report OF 77-0796-A, unpaged, 1 sheet, scale 1:1,000,000.

Kienle, J., and Lockhart, A., 1980, Gravity survey of the Pilgrim Springs Geothermal area, Alaska, *in* Turner, D.L., and Forbes, R.B., 1980, A geological and geophysical study of the

geothermal energy potential of Pilgrim Springs, Alaska: Fairbanks, University of Alaska Geophysical Institute Report UAG R-271, p. 73-79.

Kirkwood, P., The Status of Pilgrim Hot Springs, 1979. http://www.osti.gov/bridge/servlets/purl/5528250-hFGhNB/5528250.pdf

Kline, J.T., 1981, Surficial geology of the lower Pilgrim valley and vicinity, western Seward Peninsula, Alaska, Alaska Division of Geological and Geophysical Survey Open File Map AOF-140, 2 sheets. .

Kline, J.T., Reger, R.D., McFarlane, R.M. and Williams, T., 1980, Surficial Geology and Test Drilling at Pilgrim Springs, Alaska, Geophysical Institute, University of Alaska Fairbanks, UAG R-271, Fairbanks, Alaska.

Kunze, J.F., and Lofgren, B.E., 1983, Pilgrim Springs, Alaska, geothermal; resource exploration, drilling, and testing: Geothermal Resources Council S Transactions, v. 7, p. 301–304.

Lockhart, A., 1981, Gravity Survey of the central Seward Peninsula, *in* Wescott, E., and Turner D.L., Geothermal reconnaissance survey of the central Seward Peninsula, Alaska: 'Alaska Geophysical Institute Report UAG-R284.', p61-72.

Lockhart, A., & Kienle, J., 1981, Deep Seismic Refraction Profile in the Pilgrim River, Geophysical Institute, University of Alaska Fairbanks, UAG R-284, Fairbanks, AK.

Motyka, R.J., Forbes, R.B., and Moorman, M., 1980, Geochemistry of Pilgrim Springs thermal waters, in Turner, D.L., and Forbes, R.B. eds., A geological and geophysical study of the geothermal energy potential of Pilgrim Springs,Alaska: Fairbanks, University of Alaska Geophysical Institute Report UAG R–271, p. 43–52.

Stefano, R.R. 1974, Low Temperature Utilization of Geothermal Water in Alaska at Pilgrim Hot Springs. Presented at General Short Course on Geothermal Resources, Boise, Idaho. Available from Idaho Dept. of Water Resources, Boise, Idaho and Ralph R. Stefano, Stefano and Associates, Inc., Anchorage, Alaska. 14 p.

Swanson, S.E., Turner, D. L., Forbes, R. B., Maynard, D., 1980, Bedrock Geology of the Pilgrim Springs Geothermal Area, Alaska, Geophysical Institute, University of Alaska Fairbanks, UAG R-271, Fairbanks, Alaska.

Turner, D.L., and Forbes, R.B., 1980, A geological and geophysical study of the geothermal energy potential of Pilgrim Springs, Alaska: Fairbanks, University of Alaska Geophysical Institute Report UAG R-271, 165 p.

Turner and Swanson, S.E., 1981, Continental Rifting, *in* Wescott, E., and Turner D.L., Geothermal reconnaissance survey of the central Seward Peninsula, Alaska: 'Alaska Geophysical Institute Report UAG-R284.', p7-36.

Wescott, E., and Turner D.L., 1981, Geothermal reconnaissance survey of the central Seward Peninsula, Alaska: Alaska Geophysical Institute Report UAG-R284.

Appendix F
2012 Mud Logging

Well Nam	TG-1
Logger:	Joshua Miller

Project Name:

Pilgrim Hot Springs Geothermal Anomaly Assessment



Depth From (ft)	To (ft)	Sizes of grain diameters (mm) clay 0.002	silt (vfL-fL 0.031	fU 0.063	0.125	mL 0.25	mU 0.35	cL 0.5	cU 0.71	vcL 1	vcU 1.41	Clasts 2	Clast Size	Lithology	Color	Shape	Sorting	Por.	Por. (%	d^2	mm^2	m^2	Darcy	Comment
0	5	50%						2%	2%	2%	4%	30%	10%	2-5mm	qtz, schist	brown	angular	moderate	34	0.34	0.4833	0.164	1.643E-07	1.9E-07	organics
5	15	30%	30%					2%	2%	2%	4%	20%	10%	2-8mm	qtz, mica, schist	brown	angular	moderate	34	0.34	0.3171	0.108	1.078E-07	1.3E-07	
15	25	5%	5%							60%	10%	10%	10%	2-10mm	schist, qtz, mica	gray	angular	poor	30.7	0.307	0.7546	0.232	2.316E-07	2.7E-07	15-23 ft gravel, 23-25ft silty clay
25	35	40%	45%		5%	5%						5%	0%	10-15mm	qtz, schist	gray	angular	poor	30.7	0.307	0.0108	0.003	3.321E-09	3.9E-09	gray silty clay all 10ft very sticky clay matrix
35	45	25%	25%			2%	2%	2%	2%	1%	1%	40%	2-12mm	qtz, schist	gray	subangular	v. poor	27.9	0.279	0.7544	0.210	2.105E-07	2.5E-07	gray silty clay to 39 ft interbedded with small gravel to 45 ft
45	55	40%		2%	2%	2%	2%	1%	1%	15%	15%	20%	2-18mm	mica, schist, qtz	brown	subangular	poor	30.7	0.307	0.6244	0.192	1.917E-07	2.2E-07	interbedded SAA to 50 ft, brown smooth clay to 55 ft
55	65	65%					10%	10%	15%	2-10mm	qtz, schist, granite	brown-grey	subangular	v. poor	27.9	0.279	0.2941	0.082	8.205E-08	9.6E-08	clay with woody debris, silt has qtz, muscovite, amphiboles, altered copper-colored mica. Brown clay to 60ft, interbedded gravel and silt+fine sand to 65ft. Fining sequences?
65	75	60%		2%	2%	2%	1%	1%	1%	1%	10%	20%	20-18mm	schist, qtz	light brown	subangular	poor	30.7	0.307	0.3324	0.102	1.021E-07	1.2E-07	clay with organics, clay is balled up, silt s SAA but more muscovite. Brown clay +sand to 72ft, gravel 72-75ft
75	85	40%	40%						1%	1%	3%	15%	2-12mm	schist, granite, qtz	dark gray	subangular	moderate	34	0.34	0.1388	0.047	4.720E-08	5.5E-08	clay with organics that include wood and seeds. Gray clay with some fine sand interbedded at small intervals of gravel through section
85	95	30%	35%						5%	5%	5%	20%	2-15mm	schist, qtz	light gray	subangular	moderate	34	0.34	0.322	0.109	1.095E-07	1.3E-07	organics (balled up). Silt has more amphiboles than above. Smooth gray clay to 90ft with some small gravels interbedded to 95ft-clay was tight and hot
95	100	15%	15%						5%	15%	30%	20%	2-20mm	schist, qtz	dark gray	subround	poor	30.7	0.307	1.0271	0.315	3.153E-07	3.7E-07	gravel is mostly schist. Matrix has more fine sand than silt. Clayey sand to 100ft with gravel
100	110	5%	5%							20%	20%	50%	2-19mm	qtz, schist, granite, mica, amphibolite		subround	v. well	40.8	0.408	2.2012	0.898	8.981E-07	1.1E-06	gravel 100-110ft
110	120	5%	5%						10%	30%	30%	20%	2-17mm	qtz, schist, granite, green stained schist, mica, amphibole		angular	moderate	34	0.34	1.4296	0.486	4.861E-07	5.7E-07	gravel 110-120ft. Good vertical fining up sequence
120	130	30%	20%						10%	20%	15%	5%	2-5mm	qtz, schist, granite		angular	moderate	34	0.34	0.3473	0.118	1.181E-07	1.4E-07	organics present (~5cm root ball), few large clasts. First 4ft-gravel, last 6ft- gray clay
130	140								10%	40%	40%	10%	2-8mm	qtz, schist, granite		subangular	moderate	34	0.34	1.5252	0.519	5.186E-07	6.1E-07	130-135ft silty clay, 135-140ft coarse gravel. Some organics in clay
140	150						10%	10%	20%	20%	20%	20%	2-14mm	qtz, schist, granite		angular	poor	30.7	0.307	1.2299	0.378	3.776E-07	4.4E-07	140-147ft gravel, 147-150ft fine sandy clay to gravel at bottom. Trace silt
150	160	10%	25%	25%						15%	15%	10%	2-9mm	qtz, schist, granite	dark gray	subangular	poor	30.7	0.307	0.3425	0.105	1.051E-07	1.2E-07	silty brown clay at top to 152ft. 152-158ft silty coarse sand and gravel
160	170	7%	8%						15%	15%	15%	40%	2-17mm	granite, schist, qtz	gray	angular	poor	30.7	0.307	1.6145	0.496	4.956E-07	5.8E-07	all gravel with finer sandy matrix in middle 8 ft. Pyrite abundant
170	180	60%							10%	10%	20%	20%	2-16mm	schist, granite, sandstone	dark gray	angular	poor	0.01	0.0001	0.4124	0.000	4.124E-11	4.8E-11	Smooth dark gray mud, all clay. sandstone-indurated sand. 170-174ft gravel, 174-180 ft smooth gray clay
180	190	70%							10%	10%	10%	10%	2-8mm	schist, granite, pyrite	gray	subangular	poor	30.7	0.307	0.1957	0.060	6.009E-08	7.0E-08	Smooth dark gray mud, clay. interbedded smooth clay and gravels
190	200	80%									10%	10%	2-22mm	qtz, schist, granite, pyrite	gray	subangular	poor	30.7	0.307	0.1174	0.036	3.603E-08	4.2E-08	gray smooth mud. Sticky clay. pyrite very abundant
200	210	80%								10%	5%	5%	2-10mm	schist, pyrite, qtz	dark gray	subangular	poor	30.7	0.307	0.074	0.023	2.273E-08	2.7E-08	little to no silt. Grains are ~50% pyrite. Clay saturated. 200-206ft dark gray smooth clay. 206-210ft interbedded with coarse sand
210	220	10%			5%	5%	5%	5%	20%	20%	20%	10%	2-15mm	qtz, mica, schist, granite	dark gray	angular	moderate	34	0.34	0.784	0.267	2.666E-07	3.1E-07	210-220 coarse sand with lenses of 6 inches of clayey sand or gravel
220	230	5%							15%	30%	30%	20%	2-10mm	qtz, mica, schist, granite	dark gray	angular	poor	30.7	0.307	1.5119	0.464	4.642E-07	5.4E-07	no pyrite. Gravel 110-226ft, finer sand+smaller gravel intervals to 230ft
230	240	5%							15%	30%	30%	20%	2-10mm	qtz, mica, schist, granite	dark gray	angular	poor	30.7	0.307	1.5119	0.464	4.642E-07	5.4E-07	all gravels with some clayey sand intervals
240	250	5%							15%	30%	30%	20%	2-10mm	qtz, mica, schist, granite	dark gray	angular	poor	30.7	0.307	1.5119	0.464	4.642E-07	5.4E-07	all gravels with some clayey sand intervals
250	260	30%			2%	2%	2%	2%	1%	1%	10%	50%	2-20mm	qtz, schist, angular, poorly sorted	dark gray	angular	poor	30.7	0.307	1.4	0.430	4.298E-07	5.0E-07	finer gravel 250-260ft
260	270	40%		2%	2%	2%	4%			10%	10%	30%	2-10mm	qtz, schist,	light gray	angular	v. poor	27.9	0.279	0.7475	0.209	2.085E-07	2.4E-07	. Clay has organics (roots) smoother clay + finer sediment to 267ft, 267-270ft gravel
270	280	30%							10%	30%	20%	10%	2-5mm	qtz, schist	light gray	angular	moderate	34	0.34	0.7286	0.248	2.477E-07	2.9E-07	clay has some organics (roots). Some pyrite. Clayey sand and some gravel layers
280	290	25%								10%	60%	5%	2-10mm	qtz, schist	gray-brown	subangular	moderate	34	0.34	1.0952	0.372	3.724E-07	4.4E-07	clay has some organics (roots). Some pyrite. Clayey sand and some gravel layers
290	300							5%	5%	20%	40%	30%	2-9mm	qtz, schist, granite, pyrite		subangular	moderate	34	0.34	2.0292	0.690	6.899E-07	8.1E-07	no clay collected from wellhead-saturated and washed out? 290-296ft clay or fine sand, 296-300ft coarse sand and gravel, iron stained qtz grains common
300	310	15%	15%					7%	7%	6%	40%	10%	2-17mm	qtz, schist, granite, pyrite	light brown	subangular	v. poor	27.9	0.279	0.8348	0.233	2.329E-07	2.7E-07	300-308 ft gravel, 305-310ft silty clay. Mud contains hairlike roots
310	320	5%	5%			2%	2%	2%	4%	50%	20%	10%	2-6mm	qtz, schist		subangular	poor	30.7	0.307	1.0693	0.328	3.283E-07	3.8E-07	320-330 all gravel/coarse sand
320	330			5%					5%	30%	10%	50%		qtz, schist, granite		subangular	well	39	0.39	2.1894	0.854	8.539E-07	1.0E-06	320-330ft gravel with a saturated clay matrix
330	340	2%	3%						10%	40%	20%	25%	2-10mm	qtz, schist, granite		subangular	well	39	0.39	1.5724	0.613	6.133E-07	7.2E-07	interbedded intervals of gravel and sand
340	350	2%	3%						10%	40%	20%	25%	2-12mm	qtz, schist, granite		subangular	poor	30.7	0.307	1.5724	0.483	4.827E-07	5.7E-07	interbedded intervals of gravel and sand
350	360	10%	10%						5%	20%	30%	25%	2-10mm	qtz, schist, granite	brown-dark gray	subangular	poor	30.7	0.307	1.3498	0.414	4.144E-07	4.9E-07	interbedded intervals of gravel and sand
360	370	12%	13%						5%	10%	10%	50%	2-12mm	granite, qtz	dark gray	subangular	poor	30.7	0.307	1.6404	0.504	5.036E-07	5.9E-07	SAA except more silty clay matrix
370	380	50%							5%	5%	20%	20%	2-10mm	schist, granite	dark gray	subangular	poor	30.7	0.307	0.5906	0.181	1.813E-07	2.1E-07	interbedded clay and coarse sand layers
380	390	50%						10%		10%	20%	10%	2-10mm	schist, granite, qtz	dark gray	subangular	poor	30.7	0.307	0.4007	0.123	1.230E-07	1.4E-07	clay dominant, gravel interbeds
390	400	25%	25%					5%	20%	20%	5%	2-4mm		qtz, schist, gneiss?	dark gray	angular	moderate	34	0.34	0.3916	0.133	1.331E-07	1.6E-07	390-406 silty clay with a ~ inch lens of gravel
400	410	50%		5%	5%					10%	20%	10%		schist, granite, qtz	brown	angular	poor	30.7	0.307	0.3509	0.108	1.077E-07	1.3E-07	saturated brown mud, not sticky. Gray-brown
410	420	50%		5%	5%			10%	10%	10%	10%			schist, qtz, granite	brown	subangular	poor	30.7	0.307	0.1387	0.043	4.258E-08	5.0E-08	brown mud with organics, hair roots. Sticky ,denser than above. Silty clay with coarser sand intervals
420	430	25%	25%		10%					10%	20%	10%	2-12mm	schist, qtz, granite	gray	subangular	moderate	34	0.34	0.3633	0.124	1.235E-07	1.4E-07	brown to gray transition, better sorting
430	440	15%	5%					10%	20%	20%	10%	2-14mm		schist, qtz, qtz, granite, mica flakes	gray	subangular	moderate	34	0.34	0.7671	0.261	2.608E-07	3.1E-07	mixed, last 3 ft-more gravel
440	450	20%	10%	2%	2%	2%	2%	2%	10%	10%	20%	20%	2-14mm	schist, qtz, granite, mica, pyrite	gray	subangular	poor	30.7	0.307	0.7784	0.239	2.390E-07	2.8E-07	organics. SAA
450	460	75%								5%	10%	10%	2-14mm	schist, mica, pyrite, abundant qtz,	dark gray	angular	poor	30.7	0.307	0.1541	0.047	4.730E-08	5.5E-08	much more clay
460	470	45%	5%						10%	10%	20%	10%	2mm	schist, granite, qtz, pyrite	dark gray	subangular	poor	30.7	0.307	0.4296	0.132	1.319E-07	1.5E-07	layer of cobble. Organics
470	480	40%			5%	5%			20%	20%	10%			qtz, schist, pyrite, organic hair roots	dark gray	subangular	moderate	34	0.34	0.2526	0.086	8.587E-08	1.0E-07	pyrite abundant
480	490	40%		5%						25%	25%	5%	2-5mm	qtz, schist	dark gray	subangular	moderate	34	0.34	0.4991	0.170	1.697E-07	2.0E-07	some fine hair roots (hair like). Mostly clay with coarse sand through section
490	500	30%		5%						50%	10%	5%	2-5mm	qtz, schist, pyrite	dark gray	subangular	well	39	0.39	0.5547	0.216	2.163E-07	2.5E-07	SAA with finer sand
500	510	15%	20%							30%	30%	5%	2-5mm	qtz, granite, schist, pyrite	dark gray	subround	moderate	34	0.34	0.6881	0.234	2.339E-07	2.7E-07	qtz is half iron-stained. smooth 500-510ft- coarse sand with high clay matrix
510	520	15%	20%							30%	30%	5%	2-5mm	qtz, granite, schist, pyrite	dark gray	subround	moderate	34	0.34	0.6881	0.234	2.339E-07	2.7E-07	smooth 500-510ft- coarse sand with high clay matrix
520	530	10%	10%						10%	25%	40%	5%	2-5mm	qtz, schist	brown-dark gray	subround	poor	30.7	0.307	0.9767	0.300	2.999E-07	3.5E-07	coarse grained gravel until the bottom where silty brown-dark gray clay dominates
530	540	15%	20%						5%	10%	40%	10%	2-10mm	qtz, schist,	dark gray	subround	poor	30.7	0.307	0.8208	0.252	2.520E-07	3.0E-07	mud is saturated. SAA until 538ft where large gravels were felt interbedded with clay to 540 ft
540	550	15%	20%						5%	10%	40%	10%	2-10mm	qtz, schist,	dark gray	subround	poor	30.7	0.307	0.8208	0.252	2.520E-07	3.0E-07	coarse sand/small gravel with some silty clay intervals
550	560	20%	20%							10%	20%	30%	2-5mm	qtz, schist, greenschist	brown	subangular	poor	30.7	0.307	0.9773	0.300	3.000E-07	3.5E-07	coarser grained gravel and silty clay intervals
560	570	60%	15%			2%	2%	2%	4%	5%	10%			qtz, schist	dark gray	subround	poor	30.7	0.307	0.0611	0.019	1.877E-08	2.2E-08	schist and qtz are green and oxidized
570	580	30%	30%							10%	10%	20%	2-10mm	schist, qtz, pyrite	dark gray	subround	moderate	34	0.34	0.4237	0.144	1.440E-07	1.7E-07	570-580ft dominantly smooth clay with some coarse sand
580	590	50%				2%	2%	2%	4%	10%	20%	10%	2-12mm	qtz, schist, pyrite	gray-brown				0	0.4012	0.000	0.000E+00	0.0E+00	abundant pyrite (occurs at VcL-VcU size). More organic clay appears more brown at base of section. Gravel at top but interbedded with clay through hole. Brown clay at bottom
590	600	25%	25%			1%	1%	1%	2%	10%	20%	15%	2-5mm	qtz, schist, pyrite	dark gray	subround	poor	30.7	0.307	0.5119	0.157	1.571E-07	1.8E-07	very smotth clay through the interval
600	610	30%	20%							25%	15%	10%	2-5mm	qtz, schist, pyrite	dark gray	subround	moderate	34	0.34	0.4466	0.152	1.519E-07	1.8E-07	brown organic clay horizons interbedded. 600-608ft Smooth clay, 608-610ft interbedded with gravel
610	620	25%		25%		4%	4%	4%	3%	25%	5%	5%	2-5mm	qtz, schist, pyrite	brown-dark gray	subangular	v. poor	27.9	0.279	0.2521	0.070	7.032E-08	8.2E-08	sandy clay 610-618ft, 615-620ft small gravel
620	630	10%		15%		6%	6%	6%	7%	10%	20%	20%	2-5mm	qtz, schist	brown-dark gray				0	0.8233	0.000	0.000E+00	0.0E+00	no pyrite, clay saturated. Sandy clay throughout hole with minor gravel
630	640	80%	10%							2%	3%	5%	2-4mm	qtz, schist	dark gray	subangular	moderate	34	0.34	0.0279	0.009	9.482E-09	1.1E-08	smooth, thick steel gray clay. Smooth clay throughout
640	650	30%	50%			10%				2%	3%	5%	2-5mm	schist, qtz, pyrite	dark gray	subangular	poor	30.7	0.307	0.0414	0.013	1.270E-08	1.5E-08	pyrite abundant + vcU/vcL. Smooth clay with intervals of coarser grains
650	660	25%		25%		2%	2%	2%	4%		20%	20%	2-7mm	qts, pyrite, schist	dark gray				0	0.5605	0.000	0.000E+00	0.0E+00	sandy clay throughout
660	670	15%		20%		1%	1%	1%	2%	30%	30%			qtz, pyrite, sandstone	light brown	angular	well	0.01	0.0001	0.5793	0.000	5.793E-11	6.8E-11	sandy clay throughout.
670	680	20%		20%						10%	20%	30%		qtz, pyrite, sandstone	light brown	angular	moderate	0.01	0.0001	0.99	0.000	9.900E-11	1.2E-10	sandy clay throughout. Sandstone is dark brown.
680	690	70%								20%	5%	5%	2-4mm	qtz, pyrite, sandstone	light brown	angular	well	0.01	0.0001	0.1383	0.000	1.383E-11	1.6E-11	one pyrite is 5mm in size. Interbedded smooth light brown clay + sandy clay with coarse grains
690	700	40%								30%	25%	5%	2-7mm	qtz pyrite, schist, sandstone	light brown	angular	well	0.01	0.0001	0.5675	0.000	5.675E-11	6.6E-11	one pyrite is 5mm in size. Interbedded smooth light brown clay + sandy clay with coarse grains. Clay is saturated
700	710	80%								10%	5%	5%	2-5mm	qtz, pyrite, sandstone	dark brown	angular	poor	0.01	0.0001	0.074	0.000	7.404E-12	8.7E-12	smooth clay.
710	720	80%								10%	5%	5%	2-5mm	qtz, pyrite, sandstone	dark brown	angular	poor	0.01	0.0001	0.074	0.000	7.404E-12	8.7E-12	smooth clay. More pyrite than above (vcL)
720	730	35%				2%	2%	2%	4%	50%	5%			qtz, pyrite, schist	dark brown	angular	well	39	0.39	0.3864	0.151	1.507E-07	1.8E-07	smooth clay. Same amount of pyrite as above (vcL)
733	753	20%	25%	30%				5%	5%	5%	5%	5%	2-5mm	qtz, schist, pyrite	dark gray	subangular	poor	30.7	0.307	0.0949	0.029	2.913E-08	3.4E-08	abundant pyrite and organics (sticks, grass, bark). Saturated
753	763	25%		25%	5%				10%	15%	15%	5%	2-10mm	schist, qtz, pyrite, granite	dark gray	subangular	poor	30.7	0.307	0.308	0.095	9.456E-08	1.1E-07	saturated.
763	773	30%							25%	30%	10%	5%	2-5mm	qtz, pyrite, schist	dark gray	subangular	moderate	34	0.34	0.5171	0.176	1.758E-07	2.1E-07	Organics (grass, bark). Clay is smooth
773	783	60%				2%	2%	2%	4%	20%	10%			qtz, pyrite, schist	dark gray	subangular	moderate	34	0.34	0.1541	0.052	5.241E-08	6.1E-08	very little recovery, sampled trench
783	793	60%				2%	2%	2%	4%	20%	10%			qtz, pyrite, schist	dark gray	subangular	moderate	34	0.34	0.1541	0.052	5.241E-08	6.1E-08	had to sample from diverter
800	810	80%			5%				3%	3%	4%	5%		schist, granite, qtz, pyrite	dark gray	subangular	poor	30.7	0.307	0.0465	0.014	1.426E-08	1.7E-08	dark gray, smooth, soft, saturated clay
810	820	80%							3%	3%	4%	10%	2-9mm	qtz, schist, pyrite	dark gray	subangular	poor	30.7	0.307	0.0957	0.029	2.937E-08	3.4E-08	dark gray, smooth, soft, saturated clay
820	830	50%			10%				10%	10%	10%	10%	2-15mm	qtz, schist, pyrite	dark gray	subangular	poor	30.7	0.307	0.2762	0.085	8.478E-08	9.9E-08	smooth mud with orgranics (root fibers). Cobbles at 823ft
830	840	60%			2%	2%	2%	4%		10%	10%	10%	2-10mm	qtz, schist, pyrite, granite	dark gray	subangular	poor	30.7	0.307	0.2272	0.070	6.976E-08	8.2E-08	some dense lumps of clay
840	850	55%				1%	1%	1%	2%	10%	10%	20%	2-14mm	schist, pyrite, qtz	dark gray	subangular	poor	30.7	0.307	0.4453	0.137	1.367E-07	1.6E-07	cobbles half way through
850	860	80%							5%	5%	5%	5%	2-11mm	qtz, pyrite, schist	gray-brown	subangular	moderate	34	0.34	0.0664	0.023	2.256E-08	2.6E-08	smooth. Organics (root fibers0
860	870	80%							5%	5%	5%	5%	2-11mm	qtz, pyrite, schist	gray-brown	subangular	moderate	34	0.34	0.0664	0.023	2.256E-08	2.6E-08	denser and thicker than above. Cobbles at 862ft.
870	880	80%							5%	5%	5%	5%	2-5mm	qtz, pyrite, schist, granite	dark gray	subangular	moderate	34	0.34	0.0664	0.023	2.256E-08	2.6E-08	qtz is half stained. A lot of roots. Dark brown clay cloggining diverter until this point. Likely present in other intervals but too sticky to wash up.
880	890	75%	5%						5%	5%	5%	5%	2-16mm	qtz, schist, pyrite	brown	subangular	moderate	34	0.34	0.0671	0.023	2.282E-08	2.7E-08	qtz is half iron stained. Pyrite is abundant. Clay is dense, sticky, and organic rich. Coarse grains at base.
890	900	65%	5%							10%	15%	5%	2-12mm	qtz, schist, pyrite	brown	angular	well	39	0.39	0.1717	0.067	6.696E-08	7.8E-08	thick organic-rich clay, roots. Very clay rich with some fine grains, strands of gray clay and coarse grains.
900	910	55%	5%			1%	1%	3%		5%	25%	5%	2-5mm	qtz, schist, pyrite	brown	angular	moderate	34	0.34	0.2768	0.094	9.412E-08	1.1E-07	sticky clay with roots. Smooth until 903ft where coarser sandy intervals began to interbed in 2 inch layers
910	920	50%				1%	1%	1%	2%	20%	20%	5%	2-6mm	qtz, schist, pyrite	brown	subangular	well	39	0.39	0.3699	0.144	1.443E-07	1.7E-07	Roots. More sandy clay and intervals of coarse grains.
920	930	40%				2%	2%	1%		40%	10%	5%	2-4mm	qtz, pyrite, schist	brown	angular	well	39	0.39	0.434	0.169	1.693E-07	2.0E-07	Roots. More sandy clay and intervals of coarse grains. More gravel at bottom of hole although not reflected in cuttings.
930	940	40%				2%	2%	1%		40%	10%	5%	2-4mm	qtz, pyrite, schist	brown	angular	well	39	0.39	0.434	0.169	1.693E-07	2.0E-07	intervals of gravel but not on shaker table: may be at bottom of slough
940	950	40%				2%	2%	1%		40%	10%	5%	2-4mm	qtz, pyrite, schist	brown	angular	well	39	0.39	0.434	0.169	1.693E-07	2.0E-07	sandy clay through the hole.
950	960	75%							5%	15%	3%	2%	2-4mm	qtz, green epidote or chlorite, pyrite, schist, granite	brown				0	0.0725	0.000	0.000E+00	0.0E+00	roots. stems. Intervals of smooth clay and coarser sandy clay
960	970	20%		20%			1%	1%	3%	40%	10%	5%	2-4mm	qtz, green grains, pyrite, schist, granite	brown	angular	well	39	0.39	0.4676	0.182	1.824E-07	2.1E-07	organic rich with roots and stems. Intervals of smooth clay and coarser sandy clay
970	980	25%	25%			1%	1%	1%	2%	15%	20%	10%	2-5mm	qtz, pyrite, schist	brown	angular	moderate	34	0.34	0.4428	0.151	1.506E-07	1.8E-07	sandy clay with gravel intervals
980	990	25%	25%			1%	1%	1%	2%	15%	20%	10%	2-5mm	qtz, pyrite, schist	brown	angular	moderate	34	0.34	0.4428	0.151	1.506E-07	1.8E-07	sandy clay with gravel intervals
990	1000	30%	30%						5%	20%	15%			qtz, pyrite, schist	brown	angular	well	39	0.39	0.2088	0.081	8.142E-08	9.5E-08	some roots. Sandy clay through hole
1005	TD																							

Well Name:	PS-12-3
Logger:	Joshua Miller

Project Name:

Pilgrim Hot Springs Geothermal Anomaly Assessment

6.441

Depth From (ft)	Depth To (ft)	Sizes of grain diameters (mm) clay 0.002	silt (vfL-fL) 0.031	0.063	fU 0.125	mL 0.25	mU 0.35	cL 0.5	cU 0.71	vcL 1	vcU 1.41	Clasts 2	Clast Size	Lithology	Color	Grain Shape	Sorting	Por. (%	Por.	d^2	mm^2	m^2	Comment
0	5								10%	20%	65%	5%	2 mm	qtz, schist		subangular	well	30.7	0.307	1.6576563	0.5089	5E-07	mica flakes common
5	15	5%							5%	20%	20%	50%	2-25 mm	qtz, schist	grey-brown	subround	poor	30.7	0.307	2.3031098	0.70705	7E-07	some schist flakes are green
15	25							10%	10%	15%	15%	50%	2-10 mm	schist, qtz, phyllite		subround	moderate	34	0.34	2.1978063	0.74725	7E-07	
25	35	10%	10%	5%	5%				10%	10%	10%	40%	2-15 mm	qtz, schist, phyllite, pyrite		subround	v. poor	30.7	0.307	1.2649501	0.38834	4E-07	25'-27' clays with abundant pyrite; 27'-35' coarse grains
35	45	60%							5%	5%	10%	20%	2-15 mm	schist, qtz, pyrite	dark grey	round	poor	30.7	0.307	0.3940073	0.12096	1E-07	35'-40' SAA; 40'-45' dark grey clay
45	55	30%		5%	5%	5%	5%	5%	5%	5%	5%	30%	2-20 mm	schist. Qtz, pyrite, phyllite	dark grey	subround	v. poor	30.7	0.307	0.674041	0.20693	2E-07	grey to brown clay transitions; pyrite vcU size
55	65	10%		5%	5%	5%	5%	5%	5%	20%	20%	20%	2-21 mm	schist, qtz, pyrite	dark grey	subround	v. poor	30.7	0.307	0.9645204	0.29611	3E-07	interbedded clays and gravels; wood present; schist appears green
65	75	5%	5%	5%	5%	5%	5%	5%	5%	20%	20%	20%	2-16 mm	schist, qtz, phyllite, pyrite	light grey	subround	poor	30.7	0.307	0.9673706	0.29698	3E-07	indurated sands; green schists; abundant pyrite
75	85	15%	10%	10%	10%				10%	10%	15%	20%	2-15 mm	qtz, schist, phyllite, pyrite	dark grey	subangular	moderate	34	0.34	0.6475421	0.22016	2E-07	indurated sands; grey-brown clay present; pyrite less abundant
85	95	15%	10%	10%	10%				10%	10%	15%	20%	2-15 mm	qtz, schist, phyllite, pyrite	dark grey	subangular	moderate	34	0.34	0.6475421	0.22016	2E-07	indurated sands; grey-brown clay present; pyrite less abundant
95	105	15%	10%	10%	10%				10%	10%	15%	20%	2-15 mm	qtz, schist, phyllite, pyrite	dark grey	subangular	moderate	34	0.34	0.6475421	0.22016	2E-07	indurated sands; grey-brown clay present; pyrite less abundant
105	115	10%	10%	10%	10%	5%	5%			15%	15%	20%	2-15 mm	schist, qtz, granite, pyrite	brown	subround	poor	30.7	0.307	0.661945	0.20322	2E-07	105'-109' indurated sand; 109'-115' less indurated, easier drilling
115	125					10%	10%	10%	10%	20%	20%	20%	2-19 mm	qtz, schist, granite		subangular	moderate	34	0.34	1.129969	0.38419	4E-07	schist appears green; no clay present
125	135	20%				10%	10%		10%	10%	10%	30%	2-12 mm	qtz, schist, phyllite, pyrite	brown	subangular	v. poor	30.7	0.307	0.9455618	0.29029	3E-07	125'-130' gravel; 130'-135' brown clay
135	145	20%	10%	10%	10%					10%	10%	30%	2-12 mm	schist, qtz, phyllite, pyrite, ss	grey-brown	subround	poor	0.01	0.0001	0.7452869	7.5E-05	7E-11	135'-145' interbedded clays and gravel with gravels dominant at base of section
145	155	40%	10%	5%	5%					10%	15%	15%	2-14 mm	schist, qtz, phyllite, pyrite, ss	grey	subangular	moderate	0.01	0.0001	0.390375	3.9E-05	4E-11	145'-151' gravel; 151'-155' grey silty sandy clay
155	165	20%	10%	5%	5%				10%	15%	15%	20%	2-10 mm	qtz, schist, granite, pyrite	dark grey	subround	poor	30.7	0.307	0.7147012	0.21941	2E-07	interbedded clays and small gravels
165	175	10%	5%						5%	15%	15%	50%	2-20 mm	qtz, schist, granite, pyrite	light brown	subround	poor	30.7	0.307	1.9565016	0.60065	6E-07	165'-170' small gravels; 170'-175' large gravels
175	185	10%	5%	5%					10%	10%	10%	50%	2-10 mm	ss, qtz, schist, pyrite	brown-grey	subround	poor	0.01	0.0001	1.7342256	0.00017	2E-10	indurated sands; lithic arenite composition
185	195	70%				5%	5%	5%	5%			10%	2-15 mm	schist, qtz, pyrite	grey-brown	subangular	v. poor	30.7	0.307	0.0852056	0.02616	3E-08	185'-189' grey clay; 189'-195' interbedded clay and gravel
195	205	70%				5%	5%	5%	5%			10%	2-15 mm	schist, qtz, pyrite	grey-brown	subangular	v. poor	30.7	0.307	0.0852056	0.02616	3E-08	interbedded clay and gravels
205	215	90%								5%	5%			pyrite, schist, organics	dark grey	angular	moderate	34	0.34	0.0149573	0.00509	5E-09	Driller start depth 204'; clay with minor sand; some roots
215	225	10%	10%	5%	5%	5%	5%	5%	5%	15%	15%	20%	2-12 mm	ss, granite, schist, pyrite	dark grey	angular	poor	0.01	0.0001	0.7477061	7.5E-05	7E-11	215'-216' clay; 216'-221' indurated sand; 221'-225' clay
225	235	10%							10%	15%	15%	50%	2-15 mm	schist, qtz, granite	dark grey	angular	moderate	0.01	0.0001	2.0526293	0.00021	2E-10	225'-230' "hardest drilling at PHS" indurated sand; 230'-235' easier drilling
235	245	10%							10%	15%	15%	50%	2-15 mm	schist, qtz, granite	dark grey	angular	moderate	0.01	0.0001	2.0526293	0.00021	2E-10	indurated sand, consistent; 43 minutes to Kelly Bush
245	255	10%							10%	15%	15%	50%	2-15 mm	schist, qtz, granite	dark grey	angular	moderate	34	0.34	2.0526293	0.69789	7E-07	mud thinning quickly, high flow from aquifer?
255	265						5%	5%	10%	20%	20%	40%	2-15 mm	qtz, schist, ss		angular	poor	0.01	0.0001	1.9474203	0.00019	2E-10	down to 15 minutes to Kelly Bush
265	275	20%	5%			5%	5%	10%	10%	10%	10%	25%	2-8 mm	schist, qtz, ss, granite, pyrite	grey	angular	moderate	0.01	0.0001	0.7991466	8E-05	8E-11	265'-273' gravels (induration?); 273'-275' grey clay
275	285	30%	20%			5%	5%	5%	5%	10%	10%	10%	2-10 mm	qtz, schist, ss, pyrite	grey	subangular	poor	30.7	0.307	0.2897669	0.08896	9E-08	interbedded grey silty clay and gravels
285	295	50%	25%	5%	5%					5%	5%	5%	2-10 mm	schist, qtz, granite, phyllite	light grey	subangular	moderate	34	0.34	0.0569538	0.01936	2E-08	mostly clay in bottom 2/3
295	305	20%	10%	5%	5%	5%	5%		10%	20%	10%	10%	2-5 mm	qtz, schist, granite, pyrite	grey	subangular	poor	30.7	0.307	0.428894	0.13167	1E-07	schist appears green
305	315						5%	5%	5%	30%	30%	25%	2-10 mm	granite, qtz, schist		subangular	moderate	34	0.34	1.692601	0.57548	6E-07	small gravels throughout section; no pyrite; little silt
315	325								5%	5%	80%	10%	2-5 mm	qtz, schist, ss		subangular	well	0.01	0.0001	1.9979823	0.0002	2E-10	SAA with epidote (?) in granite clasts
325	335	5%					5%	5%	5%	20%	20%	40%	2-10 mm	granite, schist, qtz, minor pyrite	brown	angular	moderate	34	0.34	1.849872	0.62896	6E-07	SAA with gravel dominantly granite clasts and slight silty brown clay matrix
335	345	45%	5%	5%	5%	5%				15%	15%	5%	2-4 mm	granite, schist, qtz, muscovite	brown	angular	poor	30.7	0.307	0.2360502	0.07247	7E-08	335'-345' brown slightly silty clay interbedded with sand; contains altered and unaltered muscovite grains with a copper color and metallic luster
345	355	25%	10%	5%		5%	5%	5%		15%	15%	15%	2-8 mm	qtz, granite, schist	brown	subangular	poor	30.7	0.307	0.5230906	0.16059	2E-07	345'-350' brown silty, slightly sandy clay; 350'-355' gravels dominate
355	365		5%	5%	5%		5%	5%	5%	10%	10%	50%	2-10 mm	ss, qtz, schist		subround	poor	0.01	0.0001	1.768767	0.00018	2E-10	gravels that coarsen upwards; ss is sublitharenite with weak induration and mica-rich with brown silty, clayey matrix
365	375		5%	5%	5%	5%	5%	5%	5%	15%	15%	35%	2-5 mm	ss, granite, minor qtz		subangular	poor	0.01	0.0001	1.3524527	0.00014	1E-10	gravels dominantly ss
375	385	35%				5%	5%			10%	10%	35%	2-5 mm	ss, granite	grey	angular	poor	0.01	0.0001	0.9442009	9.4E-05	9E-11	375'-382' gravels of mostly ss; 382'-385' brown saturated smooth clay
385	395	30%	20%						5%	30%	10%	5%	2-3 mm	qtz, granite, ss	grey	subangular	moderate	0.01	0.0001	0.3402389	3.4E-05	3E-11	dominantly coarse sand with increasing clay content to bottom
395	405	30%	10%	10%					5%	5%	5%	35%	2-5 mm	schist, qtz, pyrite	grey	subangular	moderate	34	0.34	0.749956	0.25499	3E-07	395'-400' grey, sandy clay; 400'-405' small gravels
405	415	15%	10%						5%	10%	10%	50%	2-13 mm	qtz, ss, schist, pyrite	brown	subround	moderate	34	0.34	1.638144	0.55697	6E-07	mostly gravel with brown silty clay present; organics (grass)
415	425	15%	10%	5%	5%				5%	25%	25%	10%	2-8 mm	qtz, schist, ss, pyrite	brown	subround	well	39	0.39	0.7238606	0.28231	3E-07	dominantly coarse sand with increasing clay content to bottom
425	435	10%	5%	5%	5%	5%	5%	5%	5%	15%	20%	20%	2-5 mm	qtz, schist, minor pyrite	brown	subangular	well	39	0.39	0.8717023	0.33996	3E-07	interbedded coarse sand to gravels with brown sandy clay intervals
435	445	20%	5%	5%				5%	5%	20%	20%	20%	2-10 mm	qtz, schist, minor pyrite	brown	subangular	poor	30.7	0.307	0.8979458	0.27567	3E-07	interbedded coarse sand to gravels with brown sandy clay intervals
445	455	20%	5%	5%				5%	5%	20%	20%	20%	2-10 mm	qtz, schist, minor pyrite	brown	subangular	poor	30.7	0.307	0.8979458	0.27567	3E-07	interbedded coarse sand to gravels with brown sandy clay intervals
455	465				5%	5%	5%			30%	35%	20%	2-10 mm	qtz, granite, pyrite	brown	subround	well	39	0.39	1.5122851	0.58979	6E-07	little to no clay; dominantly coarse sand
465	475	60%	10%							10%	10%	10%	2-14 mm	qtz, granite, pyrite, schist, ss	grey	subangular	moderate	0.01	0.0001	0.1982921	2E-05	2E-11	94 F overnight temperature
475	485	60%	25%							5%	5%	5%	2-5 mm	qtz, pyrite, schist, ss	light grey	subangular	moderate	0.01	0.0001	0.0526473	5.3E-06	5E-12	Very silty grey clay; low recovery from well head
485	495	70%			5%	5%			5%	5%	10%			qtz, ss, pyrite, schist	dark grey	subangular	moderate	0.01	0.0001	0.0608362	6.1E-06	6E-12	Dark grey clay with little to no silt and brown streaks
495	505	65%	5%		5%	5%			5%	5%	10%			qtz, pyrite, granite, schist	light grey	subangular	moderate	34	0.34	0.0615536	0.02093	2E-08	altered mica flakes with copper, metallic luster
505	515	90%							5%	5%				qtz, pyrite, schist	dark grey	subangular	well	39	0.39	0.0076213	0.00297	3E-09	dominantly dark grey clay
515	525	80%			5%					5%	5%	5%	2-9 mm	qtz, schist, pyrite	dark grey	subangular	moderate	34	0.34	0.0521437	0.01773	2E-08	515'-524' dark grey clay; 524' gravels
525	535	50%		5%	5%				10%	10%	10%	10%	2-7 mm	qtz, schist, pyrite, granite	dark grey	subangular	poor	30.7	0.307	0.2729018	0.08378	8E-08	interbedded with increasing coarse sand and gravels to bottom
535	545	40%							10%	20%	20%	10%	2-5 mm	qtz, schist, pyrite, granite	brown	subangular	poor	30.7	0.307	0.5682144	0.17444	2E-07	Altered mica flakes with copper, metallic luster abundant; brown organic clay with hair-like roots present; beginning of 20 ft joints to Kelly Bush in pipe sections
545	555	80%							5%	5%	10%			qtz, pyrite, schist	light brown	subangular	moderate	34	0.34	0.0520296	0.01769	2E-08	dominantly brown smooth clay
555	565	20%				10%	10%	5%	5%	10%	20%	20%	2-14 mm	qtz, schist, pyrite	dark grey	subangular	poor	30.7	0.307	0.8152284	0.25028	3E-07	mostly coarse sand and gravels; altered micas
565	575	60%			5%	5%			5%	5%	10%	10%	2-5 mm	qtz, schist, pyrite	dark grey	subangular	poor	30.7	0.307	0.1993176	0.06119	6E-08	more dark grey clay than above
575	585	65%	10%							5%	5%	15%	2-4 mm	qtz, pyrite, ss	grey	subangular	moderate	34	0.34	0.18054	0.06138	6E-08	grey silty clay dominant
585	595	65%	10%							5%	5%	15%	2-4 mm	qtz, pyrite, ss	grey	subangular	moderate	34	0.34	0.18054	0.06138	6E-08	grey silty clay dominant
595	605	65%	10%						5%	10%	10%			qtz, pyrite, ss	grey	subangular	moderate	34	0.34	0.0789048	0.02683	3E-08	grey silty clay dominant
605	615	65%	10%						5%	10%	10%			qtz, pyrite, ss	grey	subangular	moderate	34	0.34	0.0789048	0.02683	3E-08	grey silty clay dominant
615	625	30%	10%							25%	25%	10%	2-3 mm	qtz, schist, pyrite	brown	subangular	well	39	0.39	0.6499584	0.25348	3E-07	615'-620' brown silty clay; 620'-625' coarse sand
625	635	5%	5%						5%	10%	35%	35%	10%	2-6 mm	qtz, schist		angular	well	39	0.39	1.3019951	0.50778	5E-07	coarse sand
635	645	5%	5%						5%	5%	30%	30%	20%	2-5 mm	qtz, schist, pyrite	brown	angular	moderate	34	0.34	1.4045805	0.47756	5E-07	dominantly coarse sand with some brown silty clay matrix
645	655	25%	5%						5%	5%	25%	25%	10%	2-7 mm	qtz, schist, pyrite	brown	subangular	moderate	34	0.34	0.7483115	0.25443	3E-07	dominantly coarse sand with increasing clay content to bottom
655	665	55%	10%						5%	5%	5%	15%	2-8 mm	qtz, schist, pyrite	brown	subangular	poor	30.7	0.307	0.235419	0.07227	7E-08	brown silty clay interbedded with coarse sand and gravel
665	675	40%	10%						10%	10%	10%	20%	2-10 mm	qtz, chloritic schist, pyrite	brown	subangular	poor	30.7	0.307	0.5125128	0.15734	2E-07	brown silty clay interbedded with coarse sand and gravel
675	685	40%	10%						10%	10%	10%	20%	2-10 mm	qtz, chloritic schist, pyrite	brown	subangular	poor	30.7	0.307	0.5125128	0.15734	2E-07	brown silty clay interbedded with coarse sand and gravel
685	695	25%	5%					5%	10%	15%	15%	25%	2-10 mm	qtz, schist, pyrite	brown	subangular	moderate	34	0.34	0.9207362	0.31305	3E-07	less brown, slightly silty clay and more coarse sand
695	705	25%	5%					5%	10%	15%	15%	25%	2-10 mm	qtz, schist, pyrite	brown	subangular	moderate	34	0.34	0.9207362	0.31305	3E-07	less brown, slightly silty clay and more coarse sand
705	715	30%	10%	5%	5%			5%	5%	15%	20%	10%	2-8 mm	qtz, schist, granite, pyrite	brown	subround	poor	30.7	0.307	0.4632164	0.14221	1E-07	705'-710' brown, silty, sandy clay; 710'-715' more coarse sand
715	725	40%	10%	5%	5%					20%	20%			qtz, pyrite, schist	brown	round	well	39	0.39	0.2453221	0.09568	1E-07	brown silty, sandy clay interbedded with coarse sand
725	735	40%	10%	5%	5%					20%	20%			qtz, pyrite, schist	brown	round	well	39	0.39	0.2453221	0.09568	1E-07	brown silty, sandy clay interbedded with coarse sand
735	745	20%	10%	5%	5%					30%	30%			qtz, pyrite, schist	brown	round	well	39	0.39	0.5415488	0.2112	2E-07	brown silty, sandy clay interbedded with coarse sand
745	755	20%	10%	5%	5%					30%	30%			qtz, pyrite, schist	brown	round	well	39	0.39	0.5415488	0.2112	2E-07	brown silty, sandy clay interbedded with coarse sand
755	765	80%								5%	5%	10%	2-11 mm	qtz, schist, pyrite, granite	dark grey	subangular	moderate	34	0.34	0.1037484	0.03527	4E-08	65 C overnight temperature in well; dominantly dark grey/brown smooth clay with minor coarse sand and gravel
765	775	80%								5%	5%	10%	2-11 mm	qtz, schist, pyrite, granite	dark grey	subangular	moderate	34	0.34	0.1037484	0.03527	4E-08	dominantly dark grey/brown smooth clay with minor coarse sand and gravel
775	785	80%								5%	5%	10%	2-11 mm	qtz, schist, pyrite, granite	dark grey	subangular	moderate	34	0.34	0.1037484	0.03527	4E-08	dominantly dark grey/brown smooth clay with minor coarse sand and gravel
785	795	80%								5%	5%	10%	2-11 mm	qtz, schist, pyrite, granite	dark grey	subangular	moderate	34	0.34	0.1037484	0.03527	4E-08	dominantly dark grey/brown smooth clay with minor coarse sand and gravel
795	805	80%			5%	5%			5%	5%				qtz, schist, pyrite	brown	subangular	moderate	34	0.34	0.0112042	0.00381	4E-09	brown, smooth clay with fine root organics and minor interbedding of coarser grains; some schist appears green again
805	815	80%			5%	5%			5%	5%				qtz. Schist, pyrite	brown	subangular	moderate	34	0.34	0.0112042	0.00381	4E-09	brown, smooth clay with fine root organics and minor interbedding of coarser grains; some schist appears green again
815	825	90%										10%	2 mm	qtz, granite, pyrite, schist	dark grey	subangular	well	39	0.39	0.0407232	0.01588	2E-08	some oxidation in streaks in clay
825	835	90%										10%	3 mm	qtz, granite, pyrite, schist	dark grey	subangular	well	39	0.39	0.0407232	0.01588	2E-08	some oxidation in streaks in clay
835	845	50%	10%	5%	5%					15%	20%	5%	2-5 mm	qtz, schist, pyrite	brown	angular	poor	30.7	0.307	0.2975703	0.09135	9E-08	brown, silty, sandy clay with coarse sand intervals
845	855	50%	10%	5%	5%					15%	20%	5%	2-5 mm	qtz, schist, pyrite	brown	angular	poor	30.7	0.307	0.2975703	0.09135	9E-08	brown, silty, sandy clay with coarse sand intervals
855	865	50%	10%	5%	5%					15%	20%	5%	2-5 mm	qtz, schist, pyrite	brown	angular	poor	30.7	0.307	0.2975703	0.09135	9E-08	brown, silty, sandy clay with coarse sand intervals
865	875	15%	10%	5%						30%	30%	10%	2-10 mm	qtz, pyrite, schist	brown	subangular	moderate	34	0.34	0.8640632	0.29378	3E-07	mostly coarse sand, brown silty, sandy clay and minor gravels
875	885	15%	10%	5%						30%	30%	10%	2-10 mm	qtz, pyrite, schist	brown	subangular	moderate	34	0.34	0.8640632	0.29378	3E-07	mostly coarse sand, thick brown silty, sandy clay and minor gravels
885	895	15%	10%	5%						30%	30%	10%	2-10 mm	qtz, pyrite, schist	brown	subangular	moderate	34	0.34	0.8640632	0.29378	3E-07	mostly coarse sand, thick brown silty, sandy clay and minor gravels
895	905	10%	5%	5%				10%	10%	10%	10%	30%	2-20 mm	qtz, schist, granite, pyrite	brown-grey	subround	moderate	34	0.34	0.9348956	0.31786	3E-07	lots of organics; transition from brown clay to grey clay on bottom
905	915	10%	5%	5%				10%	10%	10%	10%	30%	2-8 mm	qtz, schist, granite, pyrite	brown-grey	subangular	moderate	34	0.34	0.9348956	0.31786	3E-07	mostly coarse sand
915	925	10%	5%	5%				10%	10%	10%	10%	30%	2-8 mm	qtz, schist, granite, pyrite	grey	subangular	moderate	34	0.34	0.9348956	0.31786	3E-07	mostly coarse sand
925	935	15%	10%	5%						25%	25%	25%	2-8 mm	qtz, pyrite, granite	light grey	round	moderate	34	0.34	1.2299919	0.4182	4E-07	mostly coarse sand
935	945	20%	10%	5%	5%				10%	10%	10%	10%	2-4 mm	qtz, schist, pyrite	dark grey	subround	moderate	34	0.34	0.27552	0.09368	9E-08	very clean, vitreous qtz fragments (vcU-vcL); epidote, hornblende grains?
945	955	50%	10%						10%	10%	10%	10%	2-10 mm	qtz, schist, pyrite	dark grey	round	moderate	34	0.34	0.2663592	0.09056	9E-08	blue-green color to sample (epidote, hornblende?)
955	965	50%	10%						10%	10%	10%	10%	2-10 mm	qtz, schist, pyrite	dark grey	round	moderate	34	0.34	0.2663592	0.09056	9E-08	blue-green color to sample (epidote, hornblende?)
965	975	50%	10%						10%	10%	10%	10%	2-10 mm	qtz, schist, pyrite	dark grey	round	moderate	34	0.34	0.2663592	0.09056	9E-08	blue-green color to sample (epidote, hornblende?)
975	985	50%	10%						10%	10%	10%	10%	2-10 mm	qtz, pyrite	dark grey	round	moderate	34	0.34	0.2663592	0.09056	9E-08	almost entirely qtz fragments of clean, vitreous quality
985	995	50%	10%						10%	10%	10%	10%	2-10 mm	qtz, pyrite	dark grey	round	moderate	34	0.34	0.2663592	0.09056	9E-08	almost entirely qtz fragments of clean, vitreous quality; increasing pyrite content
995	1005	50%	10%						10%	10%	10%	10%	2-10 mm	qtz, pyrite	dark grey	round	moderate	34	0.34	0.2663592	0.09056	9E-08	almost entirely qtz fragments of clean, vitreous quality; increasing pyrite content
1005	1015		10%	5%	5%	5%	5%	10%	20%	20%	20%			qtz, schist, phyllite, pyrite		subangular	poor	30.7	0.307	0.5133723	0.15761	2E-07	drill mud very hot at 68 C
1015	1025	15%	15%	5%	5%				5%	5%	20%	30%		schist, granite, qtz		subangular	moderate	34	0.34	0.4869946	0.16558	2E-07	
1025	1035									10%	20%	70%		biotite, qtz, mafics, muscovite		angular	moderate	34	0.34	1.582564	0.53807	5E-07	BEDROCK contact at 1030'?; biotite has copper metallic luster alteration; no clay
1035	1045		5%	5%							30%	60%		biotite, qtz, mafics, muscovite		angular	well	39	0.39	1.3241105	0.5164	5E-07	flakes of soft, white, thin mineral; calcite(?)
1045	1055							10%	10%	40%	40%			biotite, qtz, mafics, muscovite		angular	well	39	0.39	1.177225	0.45912	5E-07	flakes of soft, white, thin mineral; calcite(?)
1055	1065							10%	10%	40%	40%			biotite, qtz, mafics, muscovite		angular	well	39	0.39	1.177225	0.45912	5E-07	flakes of soft, white, thin mineral; calcite(?)
1065	1075							10%	10%	40%	40%			biotite, qtz, mafics, muscovite		angular	well	39	0.39	1.177225	0.45912	5E-07	flakes of soft, white, thin mineral; calcite(?); drill bit pulled at end of shift revealed all teeth broken off, worn smooth, and reason for long drilling times for every section
1073	1083							10%	10%	40%	40%			qtz, schist, biotite, pyrite		angular	moderate	34	0.34	1.177225	0.40026	4E-07	switch to diamond bit
1083	1093							10%	10%	40%	40%			qtz, schist, biotite, pyrite		angular	moderate	34	0.34	1.177225	0.40026	4E-07	slow drilling
1093	1103							10%	10%	40%	40%			qtz, schist, biotite, pyrite		angular	moderate	34	0.34	1.177225	0.40026	4E-07	slow drilling
1103	1113							10%	10%	40%	40%			qtz, schist, biotite, pyrite		angular	moderate	34	0.34	1.177225	0.40026	4E-07	slow drilling
1113	1123							10%	10%	40%	40%			qtz, schist, biotite, pyrite		angular	moderate	34	0.34	1.177225	0.40026	4E-07	slow drilling
1123	1133							10%	10%	40%	40%			qtz, schist, biotite, pyrite		angular	moderate	34	0.34	1.177225	0.40026	4E-07	slow drilling
1133	1143							10%	10%	40%	40%			qtz, schist, biotite, pyrite		angular	moderate	34	0.34	1.177225	0.40026	4E-07	slow drilling
1143	1153							10%	10%	40%	40%			qtz, schist, biotite, pyrite		angular	moderate	34	0.34	1.177225	0.40026	4E-07	slow drilling
1153	1163							10%	10%	40%	40%			qtz, schist, biotite, pyrite		angular	moderate	34	0.34	1.177225	0.40026	4E-07	muscovite more common
1163	1173							10%	10%	40%	40%			qtz, schist, biotite, pyrite, muscovite		angular	moderate	34	0.34	1.177225	0.40026	4E-07	increasing muscovite
1173	1183							10%	10%	40%	40%			qtz, schist, biotite, pyrite, muscovite		angular	moderate	34	0.34	1.177225	0.40026	4E-07	abundant muscovite
1183	1193							10%	10%	40%	40%			qtz, schist, biotite, pyrite		angular	moderate	34	0.34	1.177225	0.40026	4E-07	slow drilling
1193	1203							10%	10%	40%	40%			qtz, schist, biotite, pyrite		angular	moderate	34	0.34	1.177225	0.40026	4E-07	slow drilling
1203	1213							10%	10%	40%	40%			qtz, schist, biotite, pyrite		angular	moderate	34	0.34	1.177225	0.40026	4E-07	slow drilling
1213	1223							10%	10%	40%	40%			qtz, schist, biotite, pyrite		angular	moderate	34	0.34	1.177225	0.40026	4E-07	slow drilling
1223	1233							10%	10%	40%	40%			muscovite, biotite, qtz		angular	moderate	34	0.34	1.177225	0.40026	4E-07	slow drilling
1233	1243							10%	10%	40%	40%			muscovite, biotite, qtz		angular	moderate	34	0.34	1.177225	0.40026	4E-07	30 minutes faster on drilling this section; fracture in bedrock?
1243	1253																						Cored basement
1253	1263																						Cored basement
1263	1273																						Cored basement
1273	1283																						Cored basement
1283	1293																						Cored basement
1296 TD																							Cored basement; TD 1296'

Well Name:	PS-12-9
Logger:	Joshua Miller

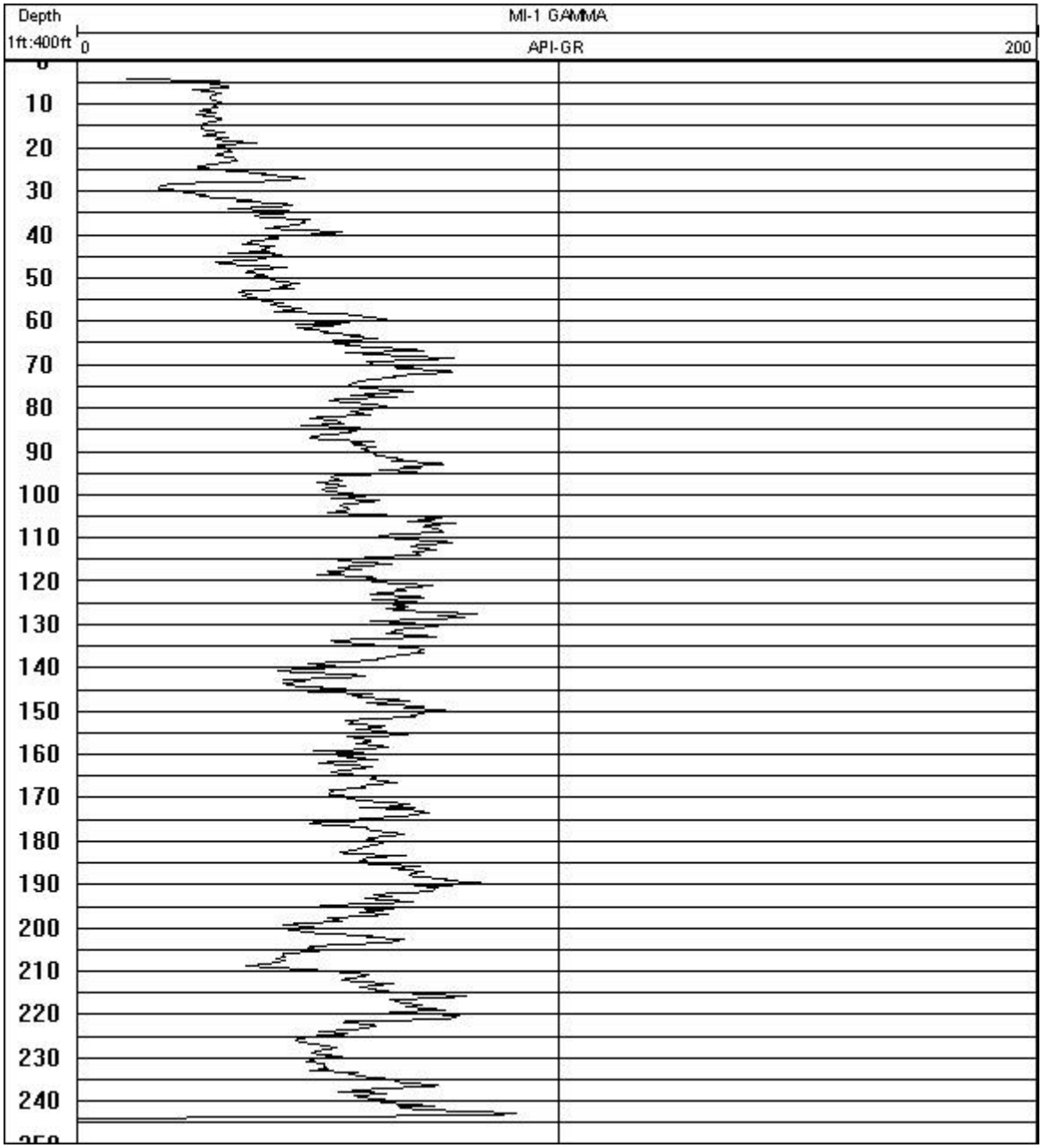
Project Name:

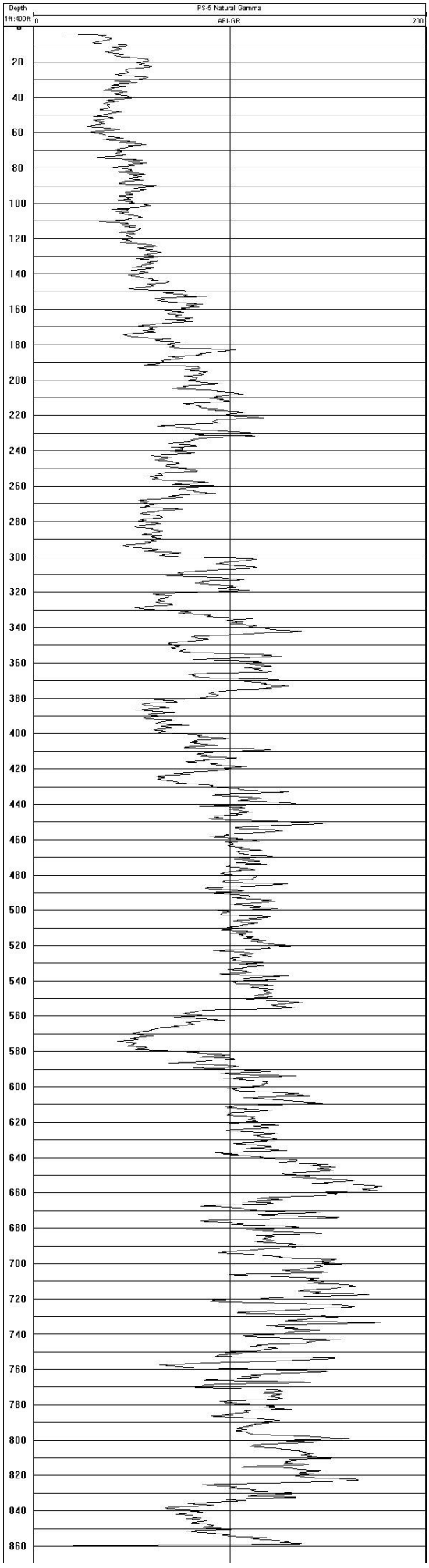
Pilgrim Hot Springs Geothermal Anomaly Assessment

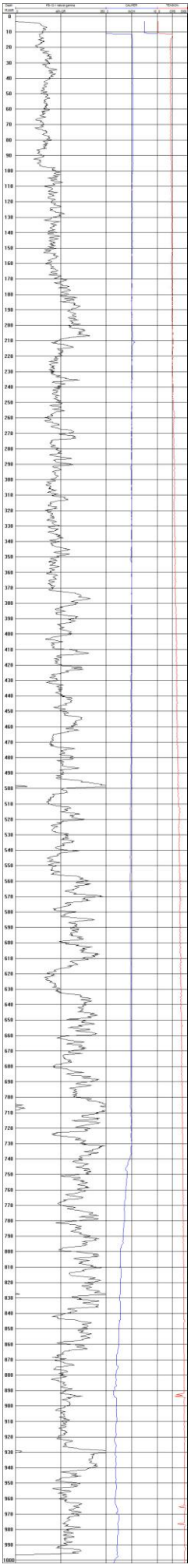


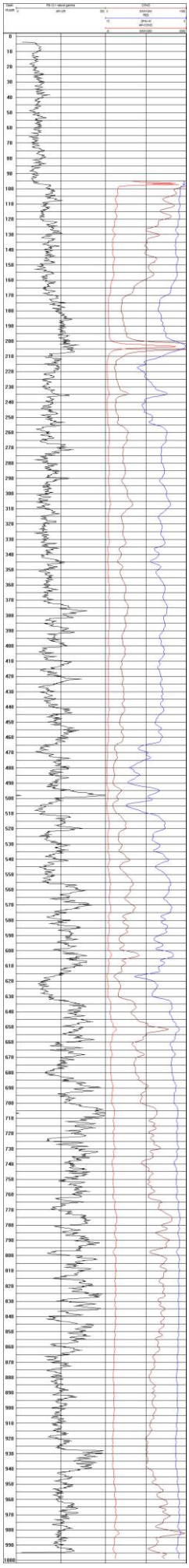
Depth		Sizes of grain diameters (mm)																					
		clay	silt (vfL-	fL	fU	mL	mU	cL	cU	vcL	vcU	Clasts											
From (ft)	To (ft)	0.002	0.031	0.063	0.125	0.25	0.35	0.5	0.71	1	1.41	2	Clast Size	Lithology	Color	Shape	Sorting	Por.	Por. (%)	d^2	mm^2	m^2	Comment
4	14		5%	10%	5%	10%	10%	10%	10%	15%	15%	10%	2-4 mm	qtz, schist, organics	N/A	subround	poor	30.7	0.307	0.57244356	0.175740173	2E-07	tree bark
14	24	20%				5%	5%	5%	5%	10%	10%	40%	2-5mm	qtz, phyllite, schist	brown	round	v. poor	27.9	0.279	1.28119761	0.357454133	4E-07	14'-22' gravels, 22'-24' thick brown clay
24	34	30%	15%	20%					5%	10%	10%	10%	2-7 mm	qtz, schist, pyrite	brown-grey	subround	v. poor	27.9	0.279	0.244381923	0.068182556	7E-08	thick clay (brown) top 2', last 8' thick grey clay
34	44	30%	10%	10%				5%	5%	5%	5%	30%	2-10 mm	ss, qtz, pyrite	grey-brown	subround	v. poor	0.01	0.0001	0.625681	6.25681E-05	6E-11	grey-brown clay 34'-44' intebedded ss clasts
44	54							5%	5%	10%	10%	70%	2-10 mm	ss, qtz	grey-brown	round	poor	0.01	0.0001	2.89510225	0.00028951	3E-10	almost entirely ss clasts
54	64	25%	25%					5%	5%	5%	5%	30%	2-15 mm	ss, qtz, schist, pyrite	grey-brown	round	poor	0.01	0.0001	0.622915563	6.22916E-05	6E-11	silty grey-brown with ss clasts
64	74	25%	25%					5%	5%	5%	5%	30%	2-15 mm	qtz, ss, schist, pyrite	grey-brown	round	poor	0.01	0.0001	0.622915563	6.22916E-05	6E-11	silty grey-brown with ss clasts
74	84	35%	30%				5%	5%	5%	5%	5%	10%	2-10 mm	ss, schist, qtz, pyrite	grey-brown	subangular	poor	0.01	0.0001	0.16687225	1.66872E-05	2E-11	74'-79' v .indurated sands, 79'-84' grey-brown clay
84	94	50%					5%	5%	5%	5%	5%	25%	2-12 mm	ss, qtz, pyrite	grey	subangular	v. poor	0.01	0.0001	0.48930025	4.893E-05	5E-11	84'-89' grey clay, 89'-94' indurated gravels
94	104					100%								ss, pyrite, schist	brown	round	v. well	0.01	0.0001	0.0625	0.00000625	6E-12	94'-104' well indurated ss
104	114						5%	5%	5%	5%	5%	75%	2-15 mm	qtz, phyllite, pyrite, ss	brown	subangular	moderate	0.01	0.0001	2.88490225	0.00028849	3E-10	104'-109' indurated, 109'-114' gravels
114	124							5%	5%	30%	35%	25%	2-5 mm	qtz, schist, pyrite	brown	subangular	moderate	34	0.34	1.833316	0.62332744	6E-07	114'-124' gravels
124	134						5%	5%	5%	25%	25%	35%	2-10 mm	qtz, schist, ss, granite	brown	subround	moderate	0.01	0.0001	1.90578025	0.000190578	2E-10	124'-134' fines bottom up
134	144						5%	5%	5%	25%	25%	35%	2-10 mm	qtz, schist, ss, granite	brown	subround	moderate	0.01	0.0001	1.90578025	0.000190578	2E-10	SAA
144	153		70%		5%	5%					10%	10%	2-15 mm	ss, mafics, qtz	grey	subround	moderate	0.01	0.0001	0.145504103	1.45504E-05	1E-11	Weak induration; 151'-153' gravels
153	163		20%		5%	5%	5%				10%	50%	2-5 mm	ss, qtz, schist		subround	poor	0.01	0.0001	1.40801956	0.000140802	1E-10	153'-159' gravels; 159'-163' silty indurated ss
163	173			25%	25%	25%	25%							ss, qtz, mafics, mica	grey	subangular	moderate	0.01	0.0001	0.038809	3.8809E-06	4E-12	Increasingly indurated from 171'-173'
173	183			25%	25%	25%	25%							ss, qtz, mafics, mica	grey	subangular	moderate	0.01	0.0001	0.038809	3.8809E-06	4E-12	Weakly indurated
183	193	10%		15%	25%	25%	25%							ss, qtz, mafics, mica	grey	subangular	poor	0.01	0.0001	0.03644281	3.64428E-06	4E-12	Increasingly indurated to bottom of section; clay layer @ 189' <1 ft thick
193	203	20%		15%	15%	25%	25%							ss, qtz, mafics, mica	grey	subangular	poor	0.01	0.0001	0.03189796	3.1898E-06	3E-12	Increasingly indurated to bottom of section; clay layer @ 197' <1 ft thick with more interbedded clay at 199'-203'
203	213	20%	20%	15%	15%	15%	15%							ss, qtz, mafics, mica	grey	subangular	poor	0.01	0.0001	0.01557504	1.5575E-06	2E-12	Weakly indurated; Dominantly ss 209'-213'
213	223		10%	15%	15%	15%	15%				10%	20%	2-15 mm	ss, mafics, qtz	grey	round	poor	0.01	0.0001	0.43864129	4.38641E-05	4E-11	213'-215' ss; 215'-221' sand, coarse sand, gravels; 221'-223' gravel
223	233									30%	30%	40%	2-15 mm	schist, qtz	grey	subround	moderate	0.01	0.0001	2.319529	0.000231953	2E-10	Strongly indurated gravels
233	243									30%	30%	40%	2-15 mm	schist, qtz	grey	angular	moderate	0.01	0.0001	2.319529	0.000231953	2E-10	Strongly indurated gravels
243	253									30%	30%	40%	2-15 mm	schist, qtz	grey	angular	moderate	0.01	0.0001	2.319529	0.000231953	2E-10	Strongly indurated gravels "like bedrock"
253	263									30%	30%	40%	2-15 mm	schist, qtz	grey	angular	moderate	0.01	0.0001	2.319529	0.000231953	2E-10	Strongly indurated gravels "like bedrock"
263	273			25%	25%	25%	25%							ss,qtz, mafics, pyrite	light grey	angular	moderate	0.01	0.0001	0.038809	3.8809E-06	4E-12	Strongly indurated
273	283		50%	25%	25%									ss, phyllite, pyrite	black	angular	well	0.01	0.0001	0.00390625	3.90625E-07	4E-13	Very indurated, like siltstone
283	293		50%	25%	25%									ss, phyllite, pyrite	black	angular	well	0.01	0.0001	0.00390625	3.90625E-07	4E-13	Very indurated, like siltstone; broke through at 287'-289.5' and lost most of drilling mud
293	303		50%	25%	25%									ss, phyllite, pyrite	black	angular	well	0.01	0.0001	0.00390625	3.90625E-07	4E-13	Very indurated, like siltstone
303	313		50%	25%	25%									ss, phyllite, pyrite	black	angular	well	0.01	0.0001	0.00390625	3.90625E-07	4E-13	Very indurated, like siltstone
313	323		20%	10%	10%	10%	10%	10%	10%	10%	10%			qtz, ss	grey	angular	v. poor	0.01	0.0001	0.199809	1.99809E-05	2E-11	313'-315' ss; 315'-323' coarse sand
323	333		50%	25%	25%									ss, qtz	grey	angular	well	0.01	0.0001	0.00390625	3.90625E-07	4E-13	Silty ss
333	343		50%	25%	25%									ss, qtz	grey	angular	well	0.01	0.0001	0.00390625	3.90625E-07	4E-13	Silty ss
343	353		10%	10%	5%					25%	25%	25%	2-5 mm	qtz, mafics, ss	grey	angular	poor	0.01	0.0001	1.25025923	0.000125026	1E-10	343'-350' gravels; 350'-353' siltstone
353	363		50%	25%	25%									qtz, mafics, ss	grey	angular	well	0.01	0.0001	0.00390625	3.90625E-07	4E-13	Silty ss
363	373		50%	25%	25%									qtz, mafics, ss	grey	angular	well	0.01	0.0001	0.00390625	3.90625E-07	4E-13	363'-368' silty ss; 368'-373' silty sand
373	383		15%	10%	10%	10%	20%							qtz, mafics, ss	grey	angular	poor	0.01	0.0001	0.014030403	1.40304E-06	1E-12	Samlpe return not good, washed out by high flow from aquifer?
383	393		15%	10%	10%	10%	20%							qtz, mafics, ss	grey	angular	poor	0.01	0.0001	0.014030403	1.40304E-06	1E-12	Samlpe return not good, washed out by high flow from aquifer?
393	403		30%	10%	20%	20%	20%							qtz, mafics, ss	grey	subangular	poor	0.01	0.0001	0.02579236	2.57924E-06	3E-12	Silty sand
403	413							25%	25%	25%	25%			qtz, mafics, pyrite	grey	round	moderate	34	0.34	0.819025	0.2784685	3E-07	Coarse sand
413	423							10%	25%	25%	25%	15%	2-4 mm	qtz, mafics, pyrite	grey	round	moderate	34	0.34	1.2769	0.434146	4E-07	Coarse sand and gravels
423	433							10%	25%	25%	25%	15%	2-4 mm	qtz, mafics, pyrite	grey	round	moderate	34	0.34	1.2769	0.434146	4E-07	Coarse sand and gravels
433	443							10%	25%	25%	25%	15%	2-4 mm	qtz, mafics, pyrite, ss	grey	round	moderate	0.01	0.0001	1.2769	0.00012769	1E-10	Coarse sand and gravels; some slighthly indurated lenses, v. thin
443	453		30%	10%	20%	20%	20%							qtz, mafics, pyrite	grey	round	poor	30.7	0.307	0.02579236	0.007918255	8E-09	Silty sand
453	463	20%							25%	25%	30%			qtz, mafics, pyrite	grey	subround	v. poor	27.9	0.279	0.72403081	0.202004596	2E-07	Coarse sand until 260'-263' grey clay lenses
463	473		10%	10%	20%	30%	30%							qtz, mafics, pyrite, ss	grey	subround	poor	0.01	0.0001	0.04596736	4.59674E-06	5E-12	Sandy silt with indurated lenses below 465'
473	483		10%	10%	20%	30%	30%							qtz, mafics, pyrite, ss	grey	subround	poor	0.01	0.0001	0.04596736	4.59674E-06	5E-12	Sandy silt with indurated lenses below 475'
483	493							25%	25%	25%	25%			ss, qtz, mafics, pyrite	grey	subround	moderate	0.01	0.0001	0.819025	8.19025E-05	8E-11	Indurated coarse sand
493	503		20%	20%	20%	20%	10%	10%						qtz, mafics, pyrite	grey	subangular	poor	30.7	0.307	0.03196944	0.009814618	1E-08	Mostly silty sand, some coarse
503	513		20%	20%	20%	20%	10%	10%						qtz, mafics	grey	subangular	poor	30.7	0.307	0.03196944	0.009814618	1E-08	Mostly silty sand, some coarse
513	523		20%	10%	10%	10%	10%	10%	10%	10%	10%			qtz, mafics	grey	subangular	poor	30.7	0.307	0.199809	0.061341363	6E-08	Mostly silty sand, some coarse
523	533		10%	10%	10%	10%	10%	10%	10%	10%	10%	10%	2-5 mm	qtz, mafics	grey	subangular	poor	30.7	0.307	0.41460721	0.127284413	1E-07	Mostly silty sand; gravels at 531'-533'
533	543		10%	10%	10%							70%	2-5 mm	qtz, mafics	grey	subangular	poor	30.7	0.307	2.02179961	0.62069248	6E-07	533'-541' gravels; 541'-543' silty sand
543	553							5%	5%	10%	10%	70%	2-5 mm	qtz, mafics	grey	subangular	poor	30.7	0.307	2.89510225	0.888796391	9E-07	Coarse sand and gravels
553	563		20%	10%	10%	10%	10%	10%	10%	10%	10%			qtz, mafics	grey	subangular	v. poor	27.9	0.279	0.199809	0.055746711	6E-08	Silty sand increasing in coarse sand to bottom
563	573		20%	10%	10%	10%	10%	10%	10%	10%	10%			qtz, mafics	grey	subangular	v. poor	27.9	0.279	0.199809	0.055746711	6E-08	Silty sand increasing in coarse sand to bottom
573	583		20%	10%	10%	10%	10%	10%	10%	10%	10%			qtz, mafics	grey	subangular	v. poor	27.9	0.279	0.199809	0.055746711	6E-08	Silty sand
583	593		20%	10%	10%	10%	10%	10%	10%	10%	10%			qtz, mafics	grey	subangular	v. poor	27.9	0.279	0.199809	0.055746711	6E-08	Silty sand
593	603		20%	10%	10%	10%	10%	10%	10%	10%	10%			qtz, mafics	grey	subangular	v. poor	27.9	0.279	0.199809	0.055746711	6E-08	Silty sand
603	613		20%	10%	10%	10%	10%	10%	10%	10%	10%			qtz, mafics	grey	subangular	v. poor	27.9	0.279	0.199809	0.055746711	6E-08	Silty sand
613	623		20%	10%	10%	10%	10%	10%	10%	10%	10%			qtz, mafics	brown	subangular	v. poor	27.9	0.279	0.199809	0.055746711	6E-08	Silty sand
623	633		20%	10%	10%	10%	10%	10%	10%	10%	10%			qtz, mafics	grey	subangular	v. poor	27.9	0.279	0.199809	0.055746711	6E-08	Silty sand
633	643		10%	10%	10%	10%	10%	10%	10%	10%	10%	10%	2-4 mm	qtz, mafics	grey	subangular	v. poor	27.9	0.279	0.41460721	0.115675412	1E-07	Silty sand top half; vcL-gravels bottom half
643	653		10%	5%	5%	5%	5%	5%	5%	20%	20%	20%	2-4 mm	qtz, mafics	grey	subangular	v. poor	27.9	0.279	0.970225	0.270692775	3E-07	Dominantly gravels with some silt and sand
653	663		20%	10%	10%	10%	10%	10%	10%	10%	10%			qtz, mafics	brown	subangular	v. poor	27.9	0.279	0.199809	0.055746711	6E-08	Silty sand to coarse sand
663	673		20%	10%	10%	10%	10%	10%	10%	10%	10%			qtz, mafics	brown	subangular	v. poor	27.9	0.279	0.199809	0.055746711	6E-08	Silty sand to coarse sand
673	683		5%	5%	5%	5%	5%	20%	20%	20%	15%			qtz, mafics	brown	subangular	v. poor	27.9	0.279	0.482260803	0.134550764	1E-07	Coarse sand with some silt; coarse grains increase to bottom
683	693		20%	20%	20%	20%	10%	5%	5%					qtz, mafics	brown	subangular	poor	30.7	0.307	0.03583449	0.011001188	1E-08	Silty sand with some mL-cU
693	703		20%	20%	20%	20%	10%	5%	5%					qtz, mafics	brown	subangular	poor	30.7	0.307	0.03583449	0.011001188	1E-08	Silty sand with some mL-cU
703	713		30%	30%	20%	10%	10%							qtz, mafics	brown	subangular	moderate	34	0.34	0.01281424	0.004356842	4E-09	Silty sand with less mL-cU
713	723		20%	10%	10%	10%	10%	10%	10%	10%	10%			qtz, mafics	brown	subangular	v. poor	27.9	0.279	0.199809	0.055746711	6E-08	Silty sand with more coarse sand
723	733		20%	10%	10%	10%	10%	10%	10%	10%	10%			qtz, mafics	brown	subangular	v. poor	27.9	0.279	0.199809	0.055746711	6E-08	Silty sand with more coarse sand
733	743		25%	25%	20%	20%	5%	5%						qtz, mafics	grey	subangular	poor	30.7	0.307	0.019881	0.006103467	6E-09	Silty sand with very small % mL-cL
743	753		25%	25%	20%	20%	5%	5%						qtz, mafics	grey	subangular	poor	30.7	0.307	0.019881	0.006103467	6E-09	Silty sand with very small % mL-cL
753	763		20%	10%	10%	10%	10%	10%	10%	10%	10%			qtz, mafics	grey	subangular	v. poor	27.9	0.279	0.199809	0.055746711	6E-08	Silty sand with higher % of coarse sand
763	773		30%	10%	10%	10%	10%	10%	10%					qtz, mafics	grey	subangular	v. poor	27.9	0.279	0.09554281	0.026656444	3E-08	SAA with less coarse sand
773	783		30%	20%	20%	10%								qtz, mafics	grey	subangular	poor	30.7	0.307	0.01739761	0.005341066	5E-09	SAA with no coarse sand
783	793		10%	10%	10%	5%	5%	15%	15%	15%	15%			qtz, mafics	grey	subangular	v. poor	27.9	0.279	0.35390601	0.098739777	1E-07	Over 50% cL-vcU with silt and fine sand
793	803		20%	20%	20%	20%	10%	5%	5%					qtz, mafics	grey	subangular	v. poor	27.9	0.279	0.03583449	0.009997823	1E-08	Silty sand with less mL-cU
803	813		20%	20%	20%	20%	20%							qtz, mafics	grey	subangular	poor	30.7	0.307	0.02683044	0.008236945	8E-09	Silty with no coarse sand
813	823			5%	5%	5%	5%	20%	20%	20%	20%			qtz, mafics	grey	subangular	v. poor	27.9	0.279	0.58277956	0.162595497	2E-07	Coarse sand with some fines
823	833	10%	10%	10%	10%	10%	15%	15%	10%	10%				qtz, mafics	grey	subangular	v. poor	27.9	0.279	0.25441936	0.070983001	7E-08	fL-vcU sand
833	843		5%	5%	5%	5%	5%	15%	15%	15%	15%	15%	2-5 mm	qtz, mafics	grey	subangular	v. poor	27.9	0.279	0.781367603	0.218001561	2E-07	Coarse sand, gravels, less fines than above
843	853	15%	15%	15%	15%	15%	10%	10%	10%	5%	5%			qtz, mafics	grey	subangular	v. poor	27.9	0.279	0.120304923	0.033565073	3E-08	Finer sand with little coarse sand
853	863	15%	15%	15%	15%	15%	10%	10%	10%	5%	5%			qtz, mafics	grey	subangular	v. poor	27.9	0.279	0.120304923	0.033565073	3E-08	Finer sand with little coarse sand
863	873	15%	15%	15%	15%	15%	10%	10%	10%	5%	5%			qtz, mafics	grey	subangular	v. poor	27.9	0.279	0.120304923	0.033565073	3E-08	Finer sand with little coarse sand
873	883	15%	15%	15%	15%	15%	10%	10%	10%	5%	5%			qtz, mafics	grey	subangular	v. poor	27.9	0.279	0.120304923	0.033565073	3E-08	Finer sand with little coarse sand
883	893	15%	15%	15%	15%	15%	10%	10%	10%	5%	5%			qtz, mafics	brown	subangular	v. poor	27.9	0.279	0.120304923	0.033565073	3E-08	Finer sand with little coarse sand
893	903	10%	10%	10%	10%	10%	10%	10%	10%	15%	15%			qtz, mafics	brown	subangular	v. poor	27.9	0.279	0.31854736	0.088874713	9E-08	Coarse sand with finer silt
903	913	5%	5%	5%	5%	5%	15%	15%	20%	25%				qtz, mafics	brown	subangular	v. poor	27.9	0.279	0.600547503	0.167552753	2E-07	Less silt
913	923								25%	25%	50%	2-10 mm		qtz, mafics, ss	brown	subangular	moderate	0.01	0.0001	2.56800625	0.000256801	3E-10	coarse sand and gravels dominate; Inudrated at 917' to bottom
923	933					10%	10%	10%	10%	20%	20%	20%	2-10 mm	qtz, mafics, ss	brown	subangular	poor	0.01	0.0001	1.129969	0.000112997	1E-10	Very strongly indurated coarse sand
933	943					10%	10%	10%	10%	20%	20%	20%	2-10 mm	qtz, mafics, ss	brown	subangular	poor	0.01	0.0001	1.129969	0.000112997	1E-10	Very strongly indurated coarse sand
943	953					10%	10%	10%	10%	20%	20%	20%	2-10 mm	qtz, mafics, ss	brown	subangular	poor	0.01	0.0001	1.129969	0.000112997	1E-10	Very strongly indurated coarse sand
953	963					10%	10%	10%	10%	20%	20%	20%	2-10 mm	qtz, mafics, ss	brown	subangular	poor	0.01	0.0001	1.129969	0.000112997	1E-10	Indurated to 960'
963	973					10%	10%	10%	10%	20%	20%	20%	2-10 mm	qtz, mafics, ss	brown	subangular	poor	0.01	0.0001	1.129969	0.000112997	1E-10	Weakly indurated
973	983					10%	10%	10%	10%	20%	20%	20%	2-10 mm	qtz, mafics, ss	brown	subangular	poor	0.01	0.0001	1.129969	0.000112997	1E-10	Weakly indurated
983	993		15%	15%	15%	15%	10%	10%	10%	5%	5%			qtz, mafics	brown	subangular	v. poor	27.9	0.279	0.120304923	0.033565073	3E-08	Silty sand; some coarse sand
993	1003		15%	15%	15%	15%	10%	10%	10%	5%	5%			qtz, mafics	brown	subangular	v. poor	27.9	0.279	0.120304923	0.033565073	3E-08	Silty sand; some coarse sand
1003	1013		15%	15%	15%	15%	10%	10%	10%	5%	5%			qtz, mafics	brown	subangular	v. poor	27.9	0.279	0.120304923	0.033565073	3E-08	Silty sand; some coarse sand
1013	1023		15%	15%	15%	15%	10%	10%	10%	5%	5%			qtz, mafics	brown	subangular	v. poor	27.9	0.279	0.120304923	0.033565073	3E-08	Silty sand; some coarse sand
1023	1033		10%	10%	10%	10%	10%	10%	10%	15%	15%			Almost entirely qtz, mafics	brown	subangular	v. poor	27.9	0.279	0.31854736	0.088874713	9E-08	90% quartz, angular grains; bedrock or close to it?
1033	1043		10%	10%	10%	10%	10%	10%	10%	15%	15%			Almost entirely qtz, mafics	brown	subangular	v. poor	27.9	0.279	0.31854736	0.088874713	9E-08	Mostly quartz sand
1043	1053		10%	10%	10%	10%	10%	10%	10%	15%	15%			Almost entirely qtz, mafics	brown	subangular	v. poor	27.9	0.279	0.31854736	0.088874713	9E-08	Mostly quartz sand
1053	1063		10%	10%	10%	10%	10%	10%	10%	15%	15%			Almost entirely qtz, mafics	brown	subangular	v. poor	27.9	0.279	0.31854736	0.088874713	9E-08	Mostly quartz sand
1063	1073			5%	5%	5%	5%	5%	25%	25%	25%			Almost entirely qtz, mafics, ss, pyrite	light grey	subangular	v. poor	0.01	0.0001	7.13011136	7.13011E-05	7E-11	fine weakly indurated ss (10%); 90% quartz and pyrite
1073	1083			5%	5%	5%	5%	5%	25%	25%	25%			Almost entirely qtz, mafics, pyrite	light grey	subangular	v. poor	27.9	0.279	0.71301136	0.198930169	2E-07	Bedrock; no ss; dominantly qtz, pyrite, micas
1083	1093			5%	5%	5%	5%	5%	25%	25%	25%			Almost entirely qtz, mafics, pyrite	light grey	subangular	v. poor	27.9	0.279	0.71301136	0.198930169	2E-07	Bedrock; no ss; dominantly qtz, pyrite, micas
1093	1103			5%	5%	5%	5%	5%	25%	25%	25%			Almost entirely qtz, mafics, pyrite	light grey	subangular	v. poor	27.9	0.279	0.71301136	0.198930169	2E-07	Bedrock; no ss; dominantly qtz, pyrite, micas
1103	1113			5%	5%	5%	5%	5%	25%	25%	25%			Almost entirely qtz, mafics, pyrite	light grey	subangular	v. poor	27.9	0.279	0.71301136	0.198930169	2E-07	Bedrock; no ss; dominantly qtz, pyrite, micas
1113	1123			5%	5%	5%	5%	5%	25%	25%	25%			Almost entirely qtz, mafics, pyrite	light grey	subangular	v. poor	27.9	0.279	0.71301136	0.198930169	2E-07	Bedrock; no ss; dominantly qtz, pyrite, micas
1123	1133			5%	5%	5%	5%	5%	25%	25%	25%			Almost entirely qtz, mafics, pyrite	light grey	subangular	v. poor	27.9	0.279	0.71301136	0.198930169	2E-07	Bedrock; no ss; dominantly qtz, pyrite, micas
1133	1143			5%	5%	5%	5%	5%	25%	25%	25%			Almost entirely qtz, mafics, pyrite	light grey	subangular	v. poor	27.9	0.279	0.71301136	0.198930169	2E-07	Bedrock; no ss; dominantly qtz, pyrite, micas
1143	1153			5%	5%	5%	5%	5%	25%	25%	25%			Almost entirely qtz, mafics, pyrite	light grey	subangular	v. poor	27.9	0.279	0.71301136	0.198930169	2E-07	Bedrock; no ss; dominantly qtz, pyrite, micas
1153	1163			5%	5%	5%	5%	5%	25%	25%	25%			Almost entirely qtz, mafics, pyrite	light grey	subangular	v. poor	27.9	0.279	0.71301136	0.198930169	2E-07	Bedrock; no ss; dominantly qtz, pyrite, micas
1163	1173			5%	5%	5%	5%	5%	25%	25%	25%			Almost entirely qtz, mafics, pyrite	light grey	subangular	v. poor	27.9	0.279	0.71301136	0.198930169	2E-07	Bedrock; no ss; dominantly qtz, pyrite, micas
1173	1183			5%	5%	5%	5%	5%	25%	25%	25%			Almost entirely qtz, mafics, pyrite	light grey	subangular	v. poor	27.9	0.279	0.71301136	0.198930169	2E-07	Bedrock; no ss; dominantly qtz, pyrite, micas
1183	1193			5%	5%	5%	5%	5%	25%	25%	25%			Almost entirely qtz, mafics, pyrite	light grey	subangular	v. poor	27.9	0.279	0.71301136	0.198930169	2E-07	Bedrock; no ss; dominantly qtz, pyrite, micas
1196 TD		(although cased and cemented at 996' due to hole collapse while drilling)																					

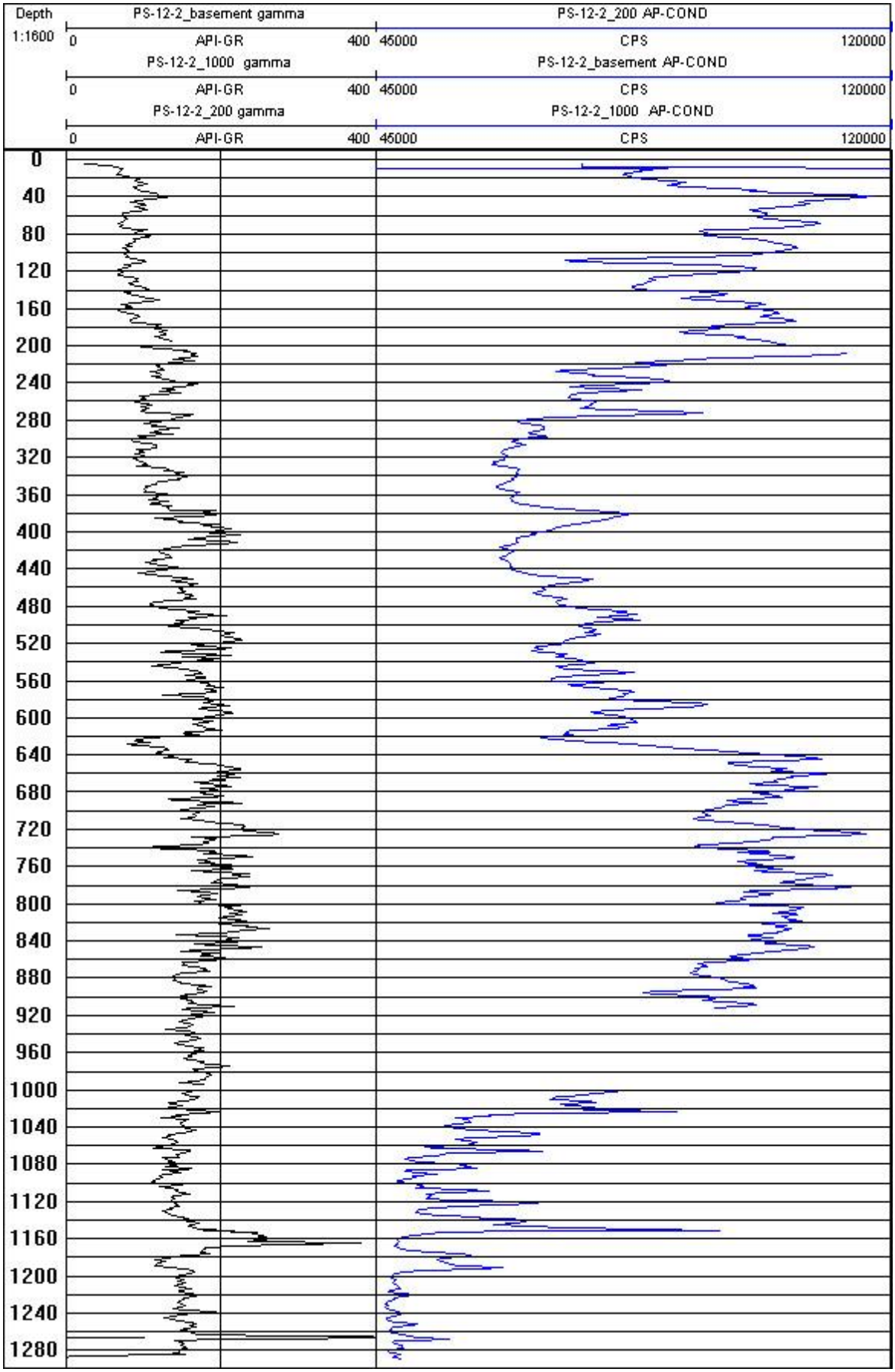
Appendix G
2011 and 2012 Electronic Well Logs

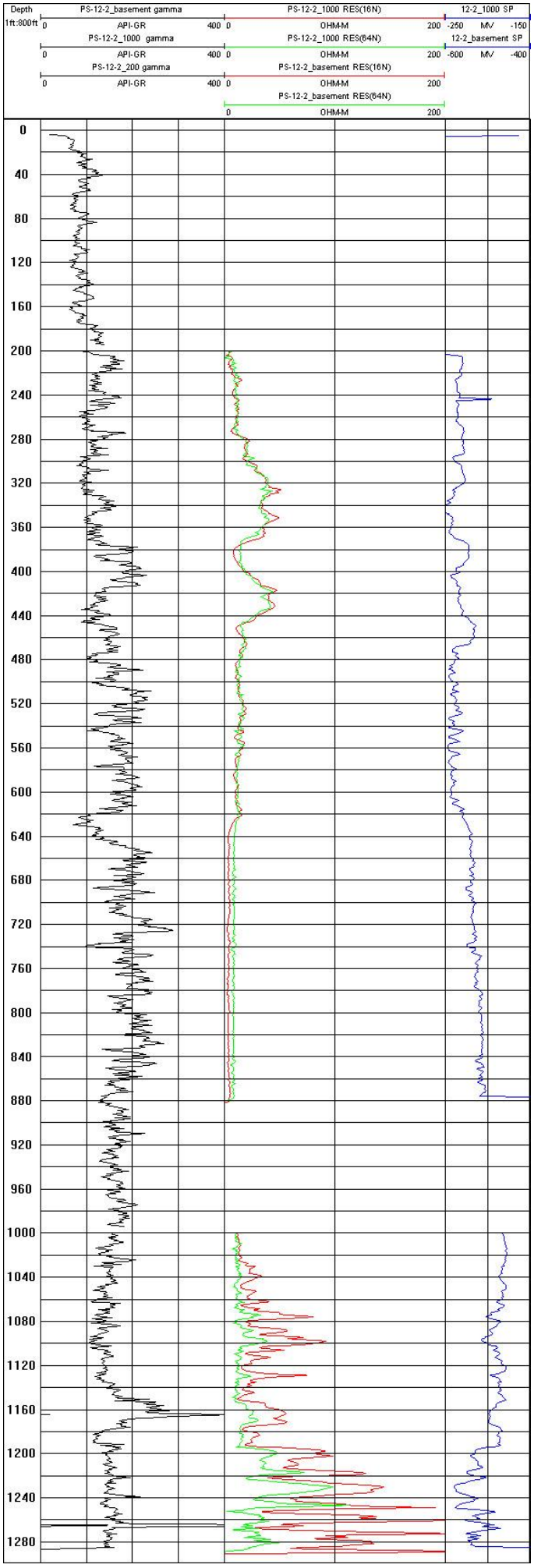

Depth
1ft:400ft
MI-1 GAMMA
0
API-GR
200
10
20
30
40
50
60
70
80
90
100
110
120
130
140
150
160
170
180
190
200
210
220
230
240

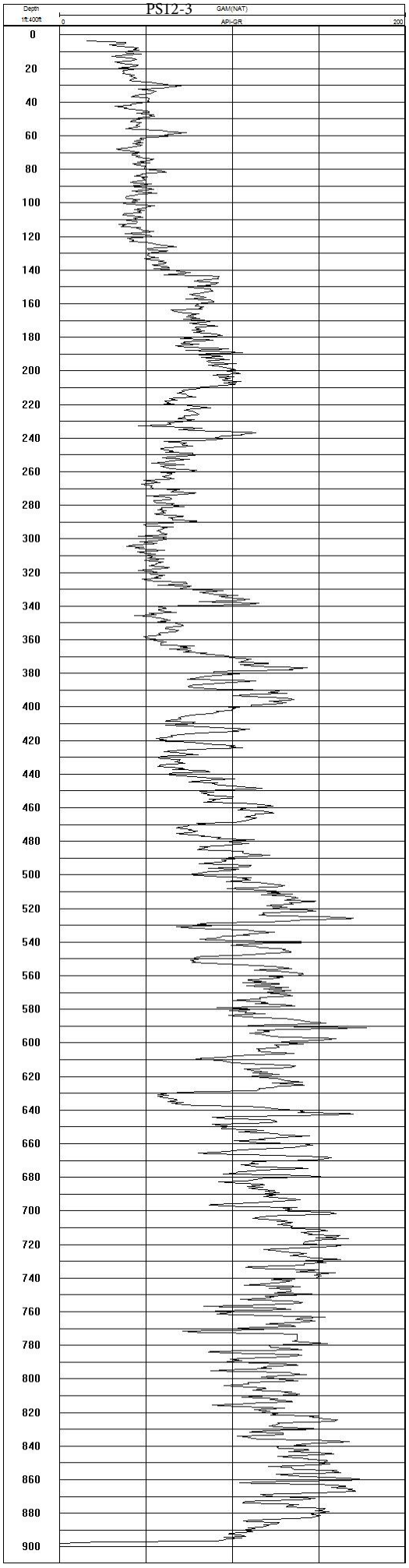

Depth
1ft:400ft
PS-5 Natural Gamma
0
API-GR
200
0
20
40
60
80
100
120
140
160
180
200
220
240
260
280
300
320
340
360
380
400
420
440
460
480
500
520
540
560
580
600
620
640
660
680
700
720
740
760
780
800
820
840
860

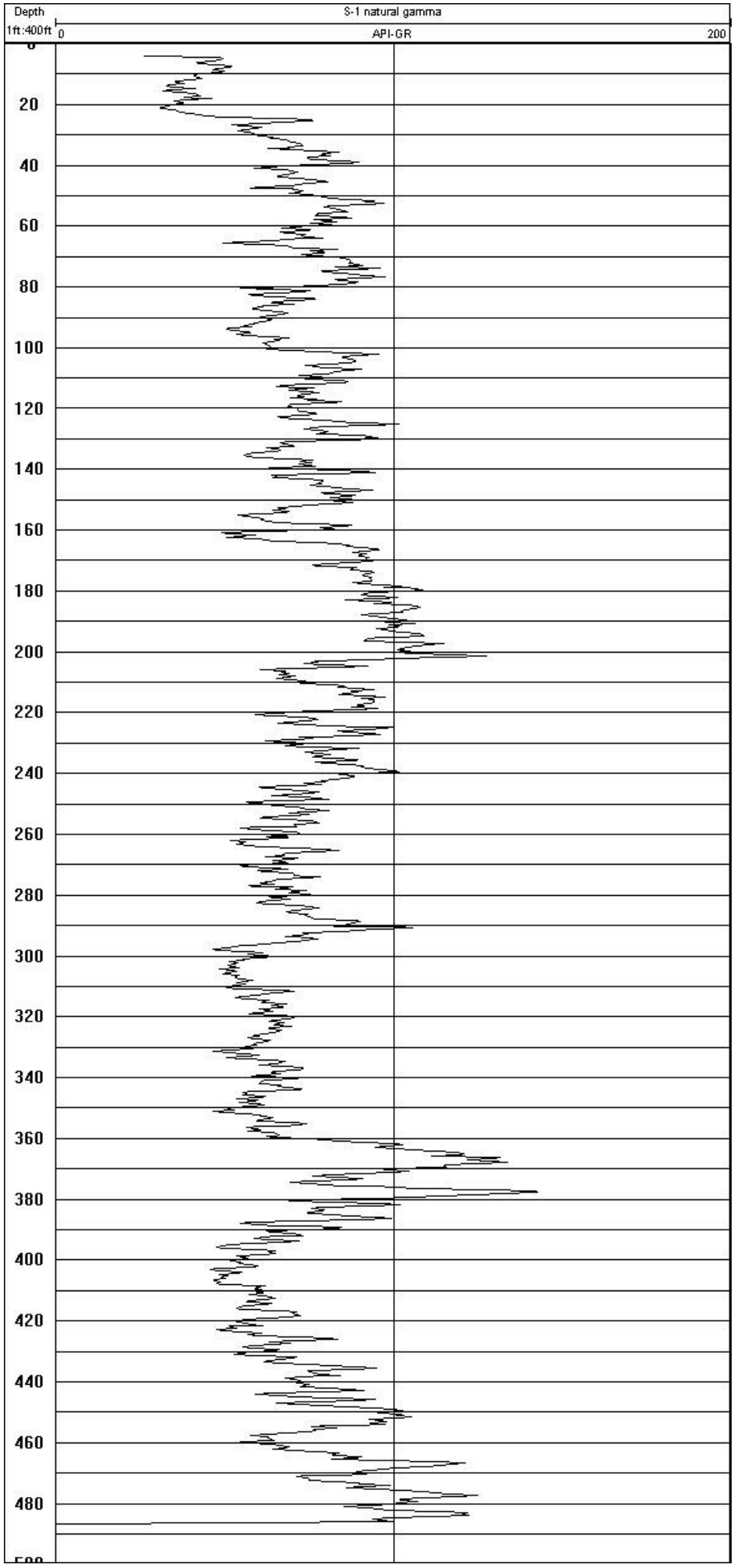


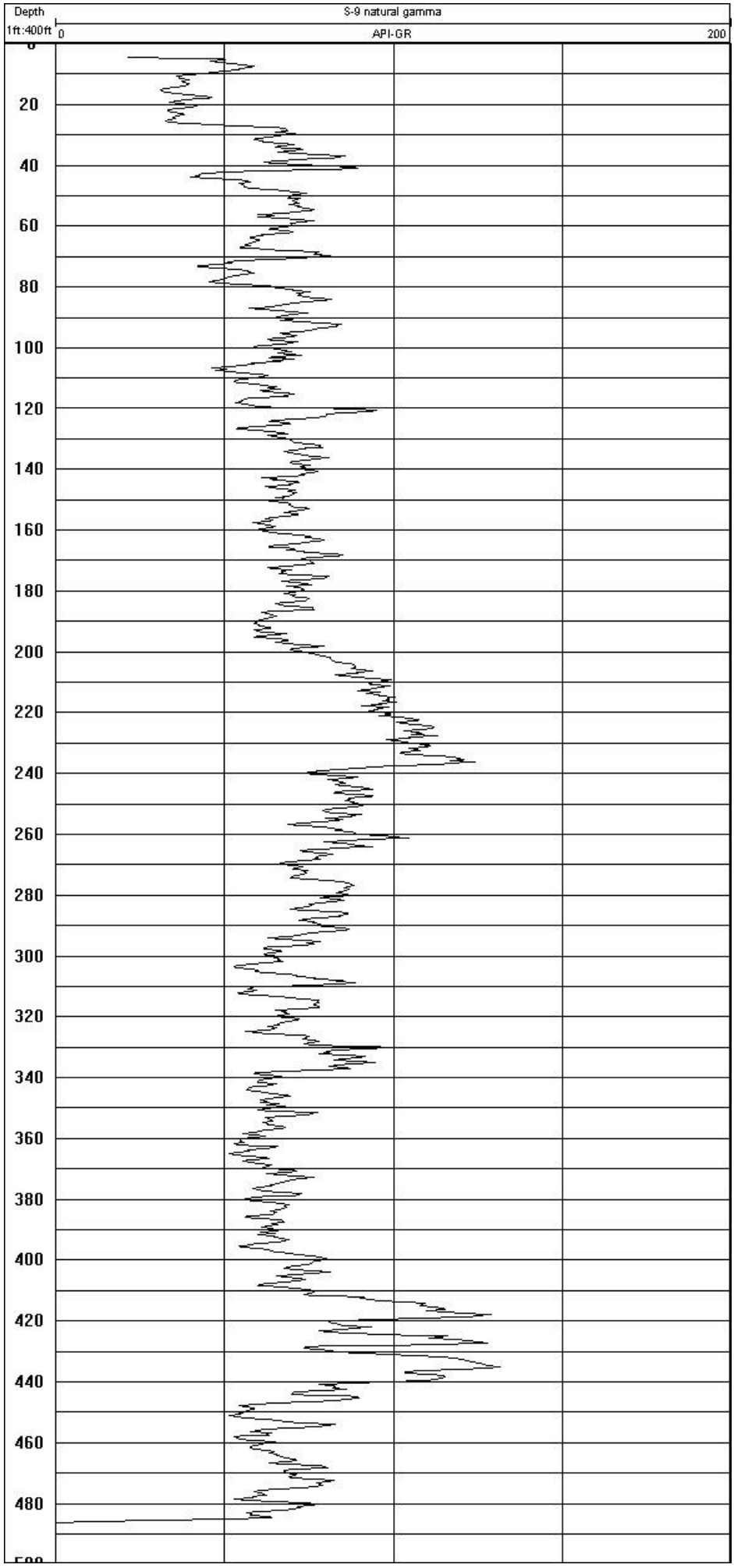



Depth
1:1600
PS-12-2_basement gamma
0
API-GR
400
PS-12-2_1000 gamma
0
API-GR
400
PS-12-2_200 gamma
0
API-GR
400
PS-12-2_200 AP-COND
45000
CPS
120000
PS-12-2_basement AP-COND
45000
CPS
120000
PS-12-2_1000 AP-COND
45000
CPS
120000
0
40
80
120
160
200
240
280
320
360
400
440
480
520
560
600
640
680
720
760
800
840
880
920
960
1000
1040
1080
1120
1160
1200
1240
1280


Depth
1ft:800ft
PS-12-2_basement gamma
0
API-GR
400
PS-12-2_1000 gamma
0
API-GR
400
PS-12-2_200 gamma
0
API-GR
400
PS-12-2_1000 RES(16N)
0
OHM-M
200
PS-12-2_1000 RES(64N)
0
OHM-M
200
PS-12-2_basement RES(16N)
0
OHM-M
200
PS-12-2_basement RES(64N)
0
OHM-M
200
12-2_1000 SP
-250
MV
-150
12-2_basement SP
-600
MV
-400
0
40
80
120
160
200
240
280
320
360
400
440
480
520
560
600
640
680
720
760
800
840
880
920
960
1000
1040
1080
1120
1160
1200
1240
1280


PS12-3
Depth
1ft:400ft
GAM(NAT)
0
API-GR
200
0
20
40
60
80
100
120
140
160
180
200
220
240
260
280
300
320
340
360
380
400
420
440
460
480
500
520
540
560
580
600
620
640
660
680
700
720
740
760
780
800
820
840
860
880
900


Depth
1ft:400ft
S-1 natural gamma
0
API-GR
200
20
40
60
80
100
120
140
160
180
200
220
240
260
280
300
320
340
360
380
400
420
440
460
480


Depth
1ft:400ft
S-9 natural gamma
0
API-GR
200
20
40
60
80
100
120
140
160
180
200
220
240
260
280
300
320
340
360
380
400
420
440
460
480

Appendix H
2013 Interference Testing and Interpretation

Sept. 2013 Interference Testing of the 1982 Pilgrim Wells

By

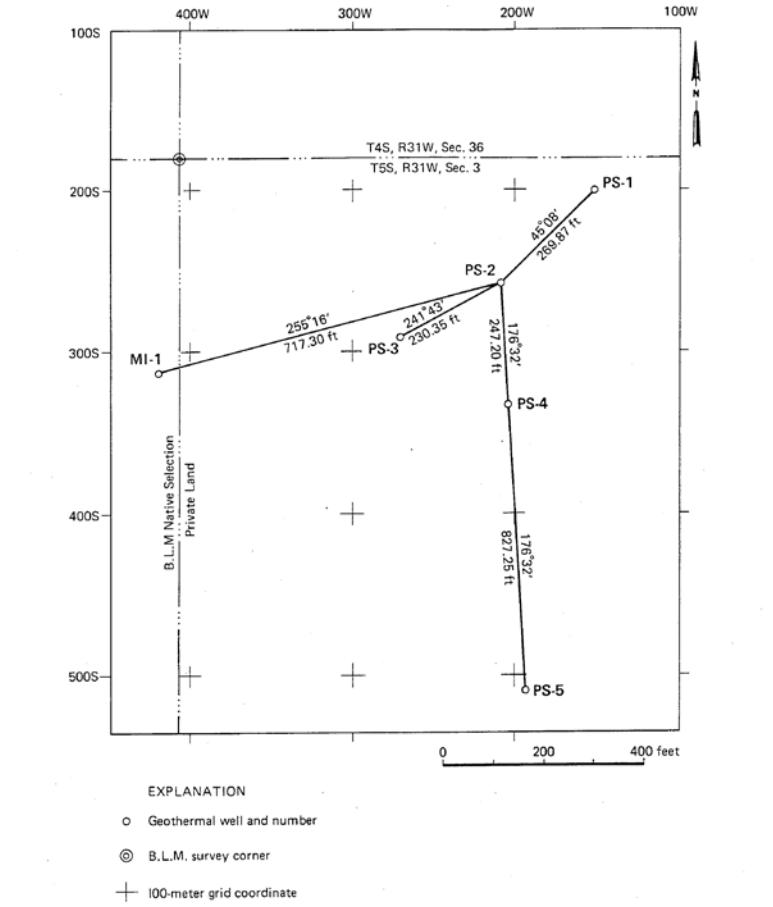
Dick Benoit

Sept. 23, 2013

INTRODUCTION

Between Sept. 7 and 22, 2013 three interference tests with downhole temperature and pressure monitoring were performed primarily utilizing the wells drilled by Woodward Clyde in 1982. These are the first true interference tests performed at Pilgrim, other than a half hour test monitoring a 2.7 psi pressure decline in well PS-2 when PS-1 was flowed for 31 minutes at 30-35 gpm in 1982. Additional interference tests were performed in 1982 between other wells but the results were "more subtle". The three wells drilled by ACEP in 2012 were not utilized in these new interference tests as they are lined with steel pipe that is capped on the bottom. There presently is no opportunity for these three wells to communicate with the hydrologic system. These tests were run partly as preliminary tests of the available equipment for a more extensive test later in 2013 of the PS 13-1 well and to develop a greater familiarity of the hydrological relationships between the existing wells. The spatial relationships between these wells are shown on Figure 1.

Figure 1 (from Woodward and Clyde, 1983)



Project No. 15267A	Pilgrim Springs	SURVEYED LOCATION OF SIX GEOTHERMAL WELLS WITH RESPECT TO WELL PS-2	Figure 4
Woodward-Clyde Consultants			

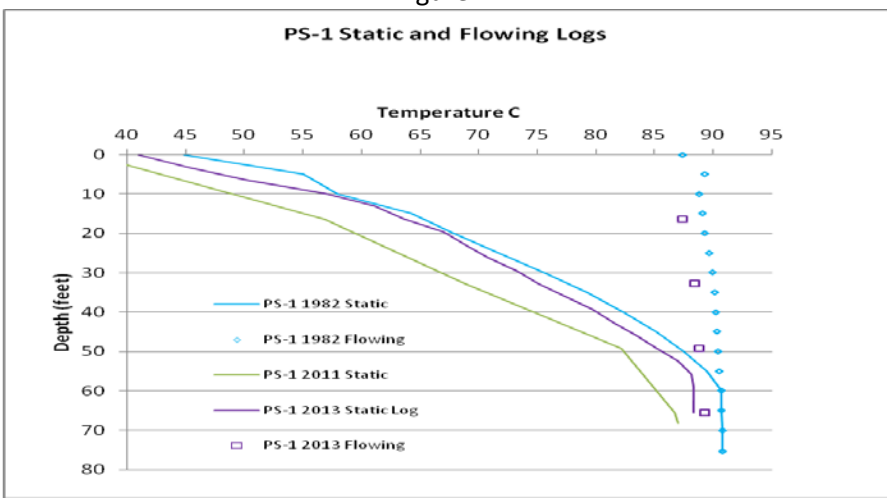
The first 2013 interference test was performed between Sept. 7 and 9 and consisted of artesian flow from the MI-1 and PS-4 wells at different times and monitoring of the PS-3 well located between them. The second test was performed on Sept. 11 and was planned with knowledge from the first test. The second test consisted of artesian flow from the PS-4 well and monitoring the PS-1, PS-3, and PS-5 wells. The third test was performed on Sept. 22 and consisted of flowing the PS-3 well and monitoring the PS-4 and MI-1 wells. The third interference test was a mirror image or inverse of the first test. The number of monitoring wells was limited by the availability of three Kuster gauges. Prior to discussing the interference tests in detail the background knowledge of the wells involved needs to be presented.

WELL BACKGROUND

PS-1

PS-1 was the first well drilled at Pilgrim in 1979. It was drilled to 160' but is currently only open to a depth of 75.3'. PS-1 has perforated casing between depths of 60 and 100'. Temperature profiles from PS-1 are simple, showing only a rapid temperature rise to the top of the shallow thermal aquifer at a depth of 60' and an isothermal temperature of 90.8 C in 1982 within the aquifer (Figure 2). In 2013 the hottest temperature measured in PS-1 was 88.3 C, allowing a possible 2.5 C of cooling, assuming the 1982 and 2013 instruments were both properly calibrated. PS-1 has the highest flowing surface temperatures of the wells discussed in this report. In 1982 it flowed at a rate of 30-35 gpm.

Figure 2



PS-3

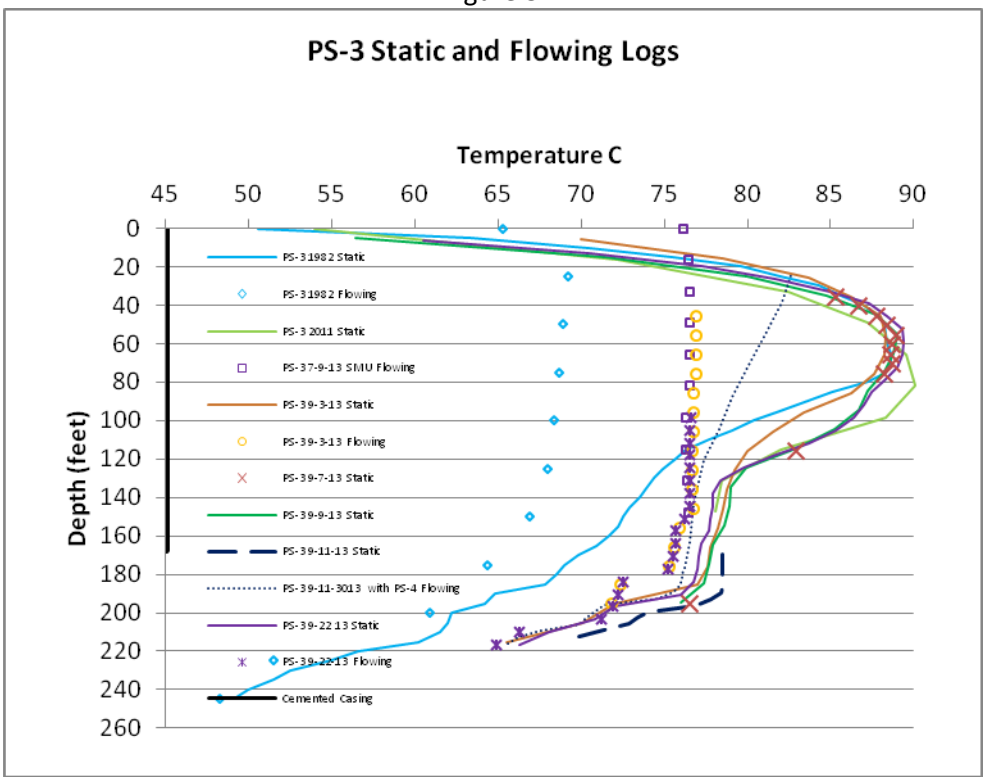
PS-3 was drilled in 1982 to a depth of 260' and has casing cemented to a depth of 167.5'. A 3" slotted liner is present beneath the casing. The static temperature profiles show a marked difference between 1982 and 2013 (Figure 3). In 1982 there was no obvious vertical fluid flow beneath the shallow thermal aquifer. Vertical fluid movement between 130 and 185' is one of the most dominant aspects of all of the 2011 and 2013 static temperature profiles. The shallow aquifer in PS-3 has shown little or no change in temperature since 1982. In 2013 PS-3 has, by a small margin, the highest shallow aquifer temperature of the wells drilled in 1979 and 1982. The separation between the 1982 and 2013 static

logs below a depth of 180' indicates that there have been hydrologic changes in PS-3 that may extend below the currently accessible depth of 222'.

The 2013 flowing PS-3 logs indicate 2 or 3 fluid entries ranging from 72 to 77 C and show the second highest surface flowing temperature (76 C) of the wells described in this report. The most striking fluid entry on the flowing temperature profile is a short distance beneath the casing, near a depth of 180' and there is also a deeper fluid entry near 190' as shown by the divergence between the flowing and static logs at that depth. The flowing temperatures are all lower than the static temperatures above a depth of 190'. A small but consistent offset in the 2013 flowing log suggests a minor fluid entry may also be present near a depth of 155' but this is within the cased and cemented interval. PS-3 has a relatively high flow rate which minimizes the temperature changes as the fluid rises through the hotter formation hosting the shallow thermal aquifer. It is uncertain as to why the 2013 flowing temperatures are several degrees hotter than the 1982 flowing temperatures. Perhaps with the well open to a greater depth in 1982 cooler flow could enter the well below the current open depth.

One particularly interesting feature of PS-3 is that the static temperatures below the casing increase by 2-3 C when PS-4 was flowing at a high rate on Sept. 11, 2013. This is discussed in more detail later.

Figure 3



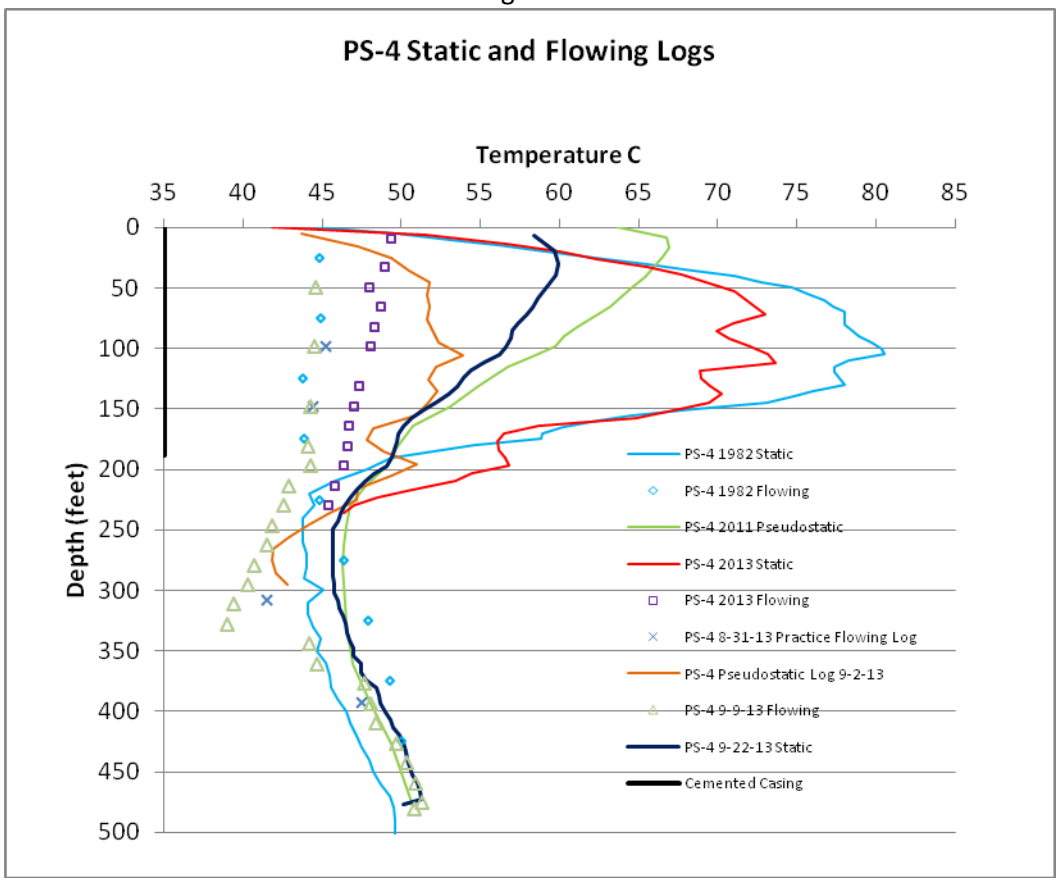
PS-4

PS-4 was drilled in 1982 to a depth of 881' and has cemented casing to a depth of 187.4'. Openhole is present beneath the cemented casing and 70.2' of steel were left in the bottom of the hole. The deepest this hole has apparently been logged is 480' where it was found to be blocked in 1982 and in 2013. Static temperature logs (Figure 4) show this well has a fairly thick and complex shallow thermal

aquifer with 3 zones of concentrated flow between depths of 60 and 140'. Some of the static logs are clearly influenced by recent flow or ongoing leakage from the wellhead during the "static" logging. In 1982 the maximum shallow aquifer temperature was 80.5 C. In 2013 the maximum temperature measured in this aquifer was 73.7 C, indicating a high possibility of some cooling. A thin and cooler zone of lateral flow is present near a depth of 200'.

The 1982 flowing log with widely spaced data points does not show any clearly defined fluid-entry depths and is quite different from the 2013 flowing logs. The divergence between the 1982 flowing and 1982 static logs suggests the most likely fluid entry was present near a depth of 220'. The 9-9-13 flowing log indicates two fluid entries near depths of 330 and 375'. A change in slope in the 9-9-13 flowing log near the bottom of the cemented casing also hints at a lesser entry. The main fluid-entry shown on the 9-9-13 log has a temperature of 39 C near a depth of 330'.

Figure 4



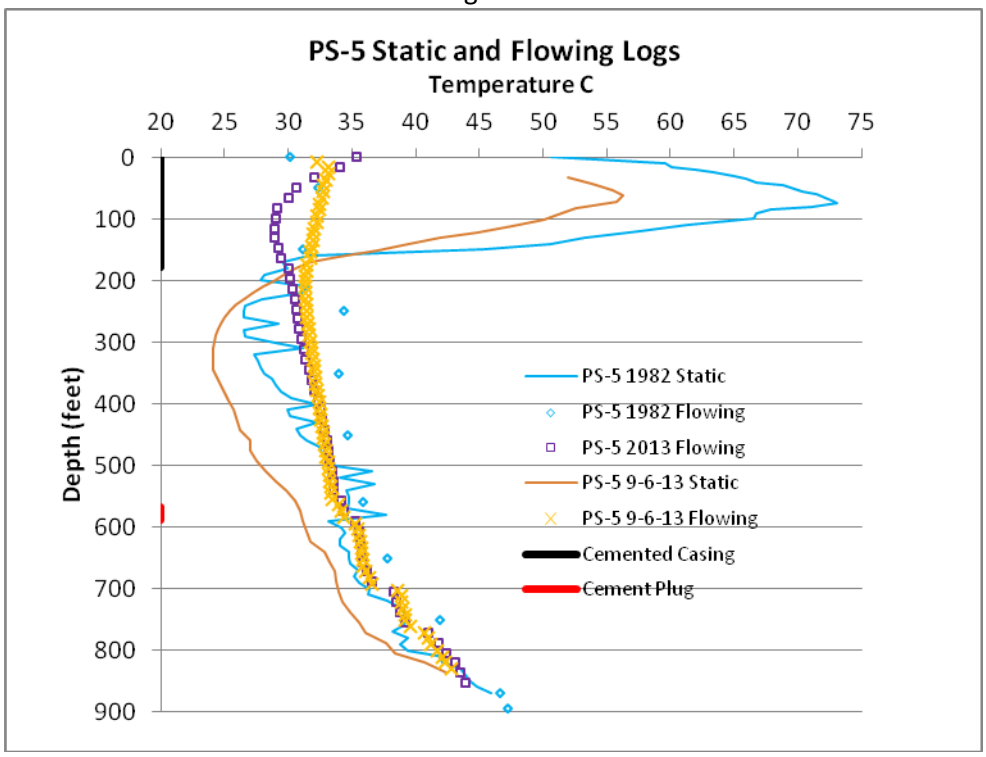
PS-5

PS-5 was drilled in 1982 to a depth of 1001' and casing was cemented to a depth of 178'. Six inch blank casing extends down to a depth of 588' and there is a 20' thick cement plug just above 6' casing shoe. Below the 6" casing there is 441' of slotted liner. This was the deepest of the 1982 wells. In 1982 it had the coolest shallow thermal aquifer temperature (73.1 C) indicating it was drilled furthest from the thermal upwelling (Figure 5). Unfortunately, the 1982 static log clearly had some problems as evidenced by the spiky character below 180' which is completely lacking in the 2013 logs. Whether these problems

also impacted the log above a depth of 180' is impossible to know. Logs obtained in 2013 appear to suggest that the shallow thermal aquifer has cooled by perhaps 15 C since 1982. Below about 800' the 1982 and 2013 temperatures are similar.

Two 2013 flowing logs indicate up to five discrete fluid inflows near depths of 560, 600, 700, 780, and perhaps 830' with temperatures between 34 and 44 C. As these combined fluid entries rise above 560' the fluid first loses temperature to the surrounding cooler formation and then gains temperature from the hotter formations above a depth of 200'. These are by far the deepest fluid entries in the group of wells discussed in this report.

Figure 5



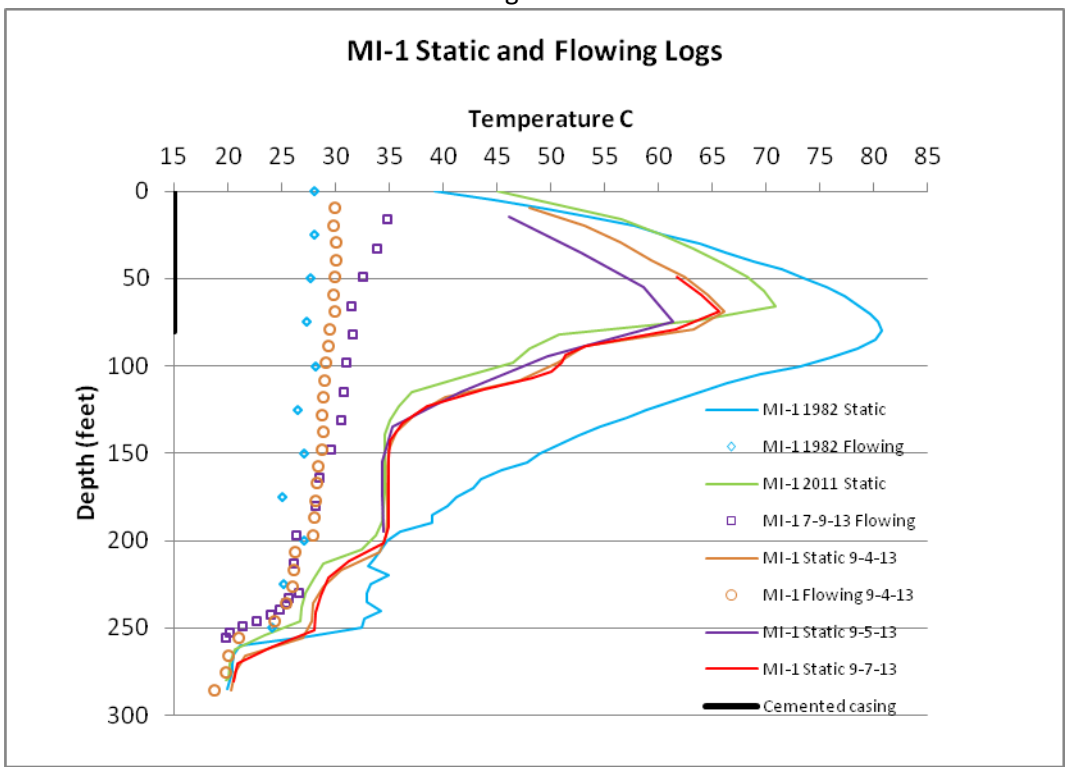
MI-1

The MI-1 well was drilled in 1982 to a depth of 307' and has cemented casing to a depth of 80 feet. There is a thin cement plug just above a depth of 232' but there are also slots in the liner above this plug which could allow fluid to enter the wellbore between the cement plug and the bottom of the cemented casing. A series of 5 static logs and 3 flowing logs run between 1982 and 2013 show a strong and simple lateral flow of thermal water at depths of 65 to 80 feet. In 1982 this aquifer had a temperature of 80.7 C. The aquifer temperature in 2011 was 70.9 C and the highest aquifer temperature measured in the 2013 logging program was 66.1 C. This suggests that the aquifer at this location has cooled significantly since 1982. Below a depth of 140' the static MI-1 temperature profiles are now characterized by 3 intervals of vertical flow with temperatures below 35 C. The deepest flow may continue below the maximum logged depth of 280'. These flows are most likely within the wellbore and become progressive cooler with increasing depth. The 1982 static temperature profile showed two zones of

vertical flow. There apparently has been a change in the hydrology of the well between 1982 and 2011. The MI-1 flowing and static temperatures are all very similar below a depth of about 260'.

The 2013 flowing logs show the shallowest fluid entry to be near a depth of 200' and a deeper entry near 250'. The flowing logs show a small increase in temperature as the water moves up through hotter near surface formation.

Figure 6



A summary table of wellbore characteristics (Table 1) shows the wells have a large range of completion and flowing characteristics. Well PS-1 is shallowest and has the highest fluid-entry and surface flowing temperature. PS-3 has the second highest temperatures. Well PS-5 has the deepest and second coolest fluid entries. The three wells with the most similar fluid-entry depths are PS-3, PS-4, and MI-1.

Table 1

Well	Well TD feet	Cemented Casing Depth feet	Fluid Entry Intervals feet	Surface Flowing Temperature C	Fluid Entry Tempeatures C
PS-1	150	?	>55	87	91
PS-3	260	167.5	150? 180 200?	76	75.3
PS-4	881	187.4	187? 330 375	45	39
PS-5	1001	178	560 600	33	35.4-44

			700 780 830		
MI-1	307	80	200 250?	30	28

September 7 – 9, 2013 Interference Test

Between Sept. 7 and 9, 2013 an interference test was run at Pilgrim Hot Spring with the PS-3 well being monitored downhole for 2 ¼ days while the MI-1 and PS-4 wells were individually flowed at separate times.

The test began on the morning of Sept. 7 with a static downlog in the MI-1 well after it had been shut in for two days. This static log was run to both check how fast the well returned to a static temperature profile and to also obtain another downhole pressure falloff curve when the well commenced flowing. After a static downlog to 85.5m the Kuster tool (E1477) was hung at 241' below the master gate of MI-1. This depth is between the MI-1 fluid-entry zones. At 14:54:23 hours the top of the MI-1 well lubricator was opened for flow out the top of the lubricator. The flow was visually estimated to be about 50 gpm but appeared to decline to about 30 gpm at 1908 hours on Sept. 7 when the Kuster tool was pulled out of MI-1. While pulling the tool up no stops were made but the temperatures recorded every 5 seconds progressively increased from 25.36 C to 29.34 C at the surface. These temperatures are in close agreement with the other flowing temperatures logs in MI-1.

Kuster tool (E1476) was installed in PS-3 194.75' below the flange at 1448 hours on Sept. 7, about 6 minutes before the MI-1 flow started. This tool was temporarily pulled from the hole at 1943 hours on Sept. 7 to download data. There appeared to be a small pressure decline in PS-3 due to MI-1 flowing and the decision was made to reinstall Kuster tool E1476 at 194.75' and continue flowing the MI-1 well overnight and then shutin the MI-1 well to see if a pressure buildup could also be detected in PS-3.

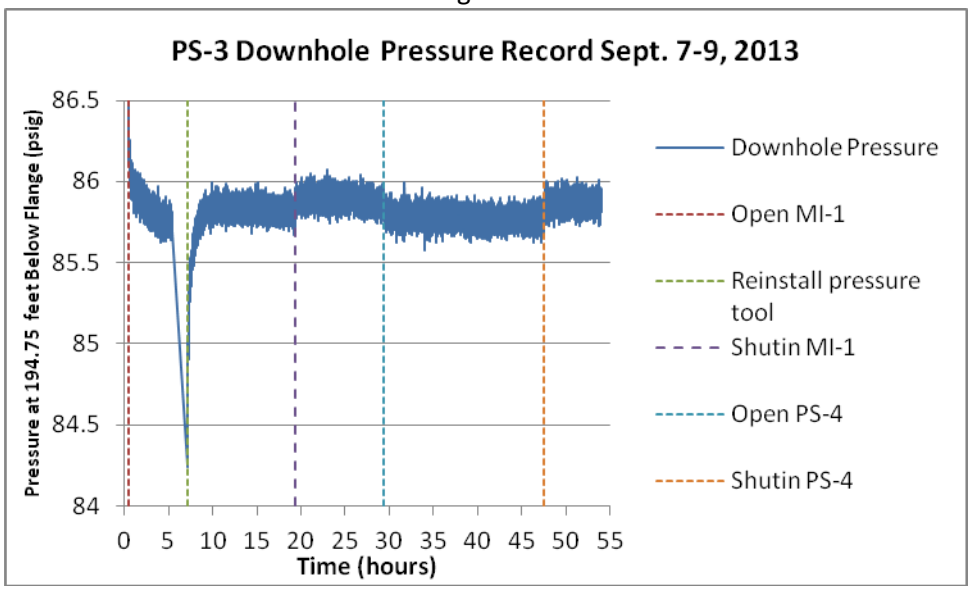
On the evening of Sept. 7 Jeremy Stariwat arrived in camp to run electrical logs but the electrical line logging tools did not get to Nome. About mid day on Sept. 8 the Mt. Sopris logging tools arrived in camp. At 1848 hours on Sept. 8 the PS-4 well was opened to full flow of perhaps 100 gpm and a temperature/conductivity log was run in PS-4 to 463' with some difficulty as the down logging rate was only 8 ft/min and the tool kept hanging up. The tool only briefly worked during the uplog which was finished shortly before sunset. The flow rate from PS-4 noticably declined during the hour and a half we were logging on site. During this decline the fluid produced by PS-4 was silty.

On the morning of Sept. 9 PS-4 was logged with the gamma and resistivity tool while the well continued to flow but the flow rate had decreased noticeably to about 50 gpm from the previous evening and the fluid was now clear. At 1252 hours on Sept. 4 PS-4 was shutin. As soon as the 2" side outlet valve was closed the water was able to reach the top of the PS-4 lubricator and start leaking there. After PS-4 was shut in the flow rate from a couple of wellhead leaks was about 3 gpm.

The Kuster tool was pulled from PS-3 at 1926 hours on Sept. 9 effectively completing the interference test.

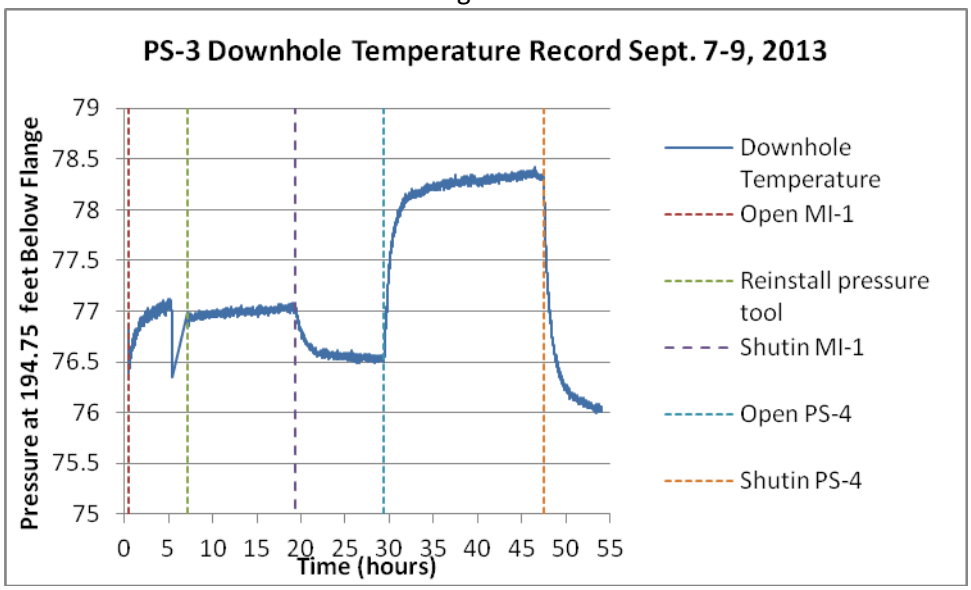
The pressure record from PS-3 shows that sharp and clear but small pressure changes on the order of a tenth of two of a psi occurred in PS-3 as both the MI-1 and PS-4 wells were opened to flow and shutin (Figure 7).

Figure 7



The temperature record shows surprising and more substantial changes (Figure 8). An almost instantaneous increase of about 0.5 C was associated with flowing and shutting in MI-1 and a larger nearly instantaneous increase of 1.9 C occurred when PS-4 was flowed. The temperature nearly instantaneously started to decline in PS-3 at a depth of 194.75' when PS-4 was shutin. This temperature change was over 2.4 C.

Figure 8

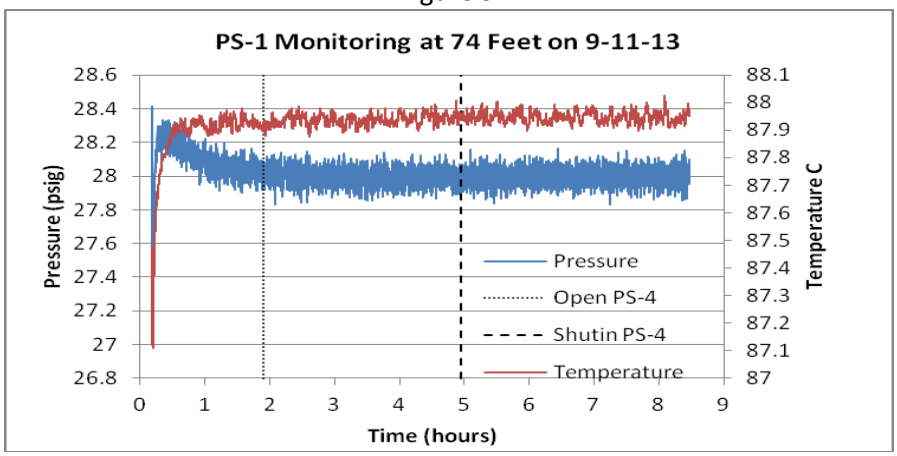


Sept. 11, 2013 Interference Test

A second and shorter interference test was run on Sept. 11 to look for responses in the PS-1 and PS-5 wells and to better document the temperature changes in the PS-3 well. The PS-4 well was flowed for 3 hours and monitoring continued for another three hours.

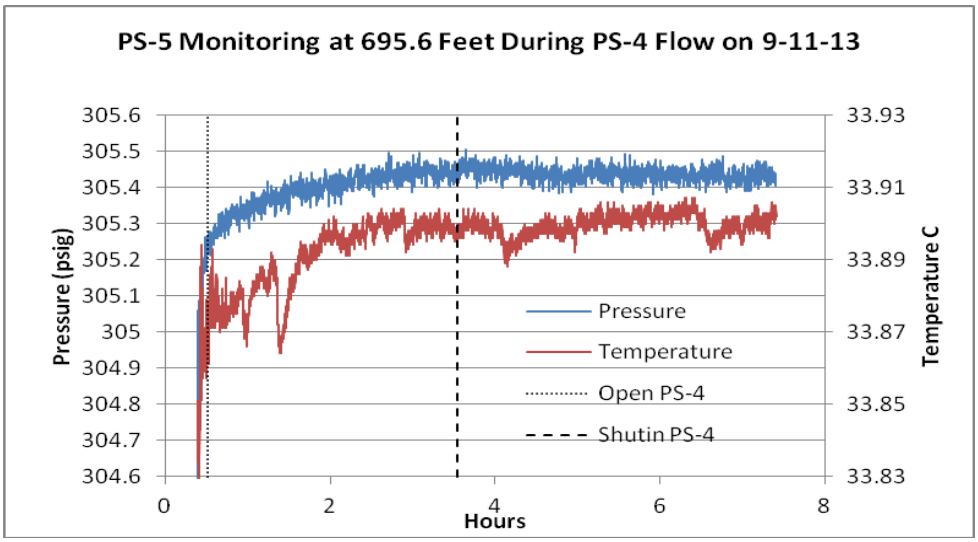
No traversing temperature logs were made in PS-1 while tool E 1476 was being installed or retrieved but the highest temperature noted during this time was 88.0 C. This was only 0.38 C less than the maximum static temperature measured in July with the SMU equipment.
The tool was hung at a depth of 74', about 1.3' above the open TD of the hole. This depth is not known or proven as a permeable interval. During the monitoring the pressures showed an initial decline of about 0.2 psi prior to flowing PS-4 (Figure 9). Once PS-4 was flowing the pressure remained constant, with no hint of a pressure change when PS-4 was shutin. The origin of the pressure decline prior to starting to flow PS-4 is uncertain. Temperatures in PS-1 showed no response to PS-4 flowing.

Figure 9



Kuster tool E1474 was hung in well PS-5 at a depth of 695.6' for monitoring. This depth was selected as being close to the most obvious inflow in the well and therefore most likely to detect any possible temperature change. There is a 0.2 psi pressure increase that may be temporally associated with opening up PS-4 to flow (Figure 10). There is also a tiny temperature change. However, there is no hint pressure or temperature response within 3 hours of shutting PS-4. Temperatures varied sharply and irregularly during the monitoring, if only by a couple hundredths of a degree. This may be interpreted as evidence of some background fluid flow at 695.6'. The pressure response near the start of monitoring is the inverse of that seen in PS-1 (Figure 9). What this may or may not imply is uncertain.

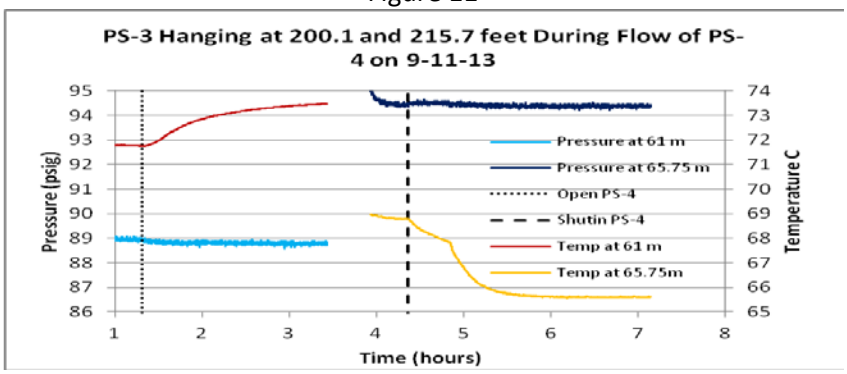
Figure 10



Kuster tool E1477 was installed in PS-3 and due to time constraints no traversing downlog was run. The tool in PS-3 was hung at a depth of 200.1', 5.35' deeper than during the Sept. 7-9 interference test. While PS-4 was flowing the tool in PS-3 was used to make a traversing down and up log to document over what depth interval the temperature changes occur. This explains the apparent data gap in Figure 11. During this traverse the cable slipped through the depth counter and the tool was hung at a greater depth for the second half of the monitoring. This explains the offset of lower temperture and higher pressure after the data gap. It was necessary to make a correction to the depths once the tool was pulled back up to the surface. While the Kuster tool was in PS-3 there was a 2-3 gpm leak through the lubricator.

The pressure and temperature monitoring in PS-3 on Sept. 11 confirmed the Sept. 7 small pressure changes and large temperature changes (Figures 7 and 8). There is a second sharp inflection on the

Figure 11

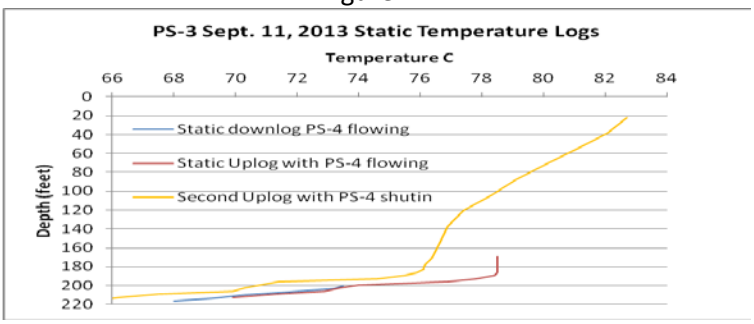


temperature curve near 5 hours (Figure 11) after PS-4 was shut in on Sept. 11 that is of unknown origin.

A comparison of the PS-3 traversing logs while PS-4 is flowing and after the flow from PS-4 was shutin shows that the temperature differences extend over at least the depth from the current bottom of the well up to 170' (Figure 12). This demonstrates that there is vertical flow within the PS-3 wellbore during this logging and it is known that the lubricator was leaking 2 – 3 gpm of hot water during the static logs. These two Sept. 11 temperature logs suggest that some fluid is either entering the well below its currently accessible bottom of 222' and its drilled total depth of 307' or is entering the wellbore near a

depth of 190’ and then flowing both up and down the well from 190’. This fluid either increases its temperature or perhaps its flow rate when PS-4 is flowing. It is highly unlikely that there is a downflow of water inside the cased and cemented part (above 167.5’) of PS-3.

Figure 12



September 22, 2013 Interference Test

On September 22 the third interference test was performed by flowing well PS-3 for 3.5 hours and monitoring the downhole pressures in PS-4 and MI-1.

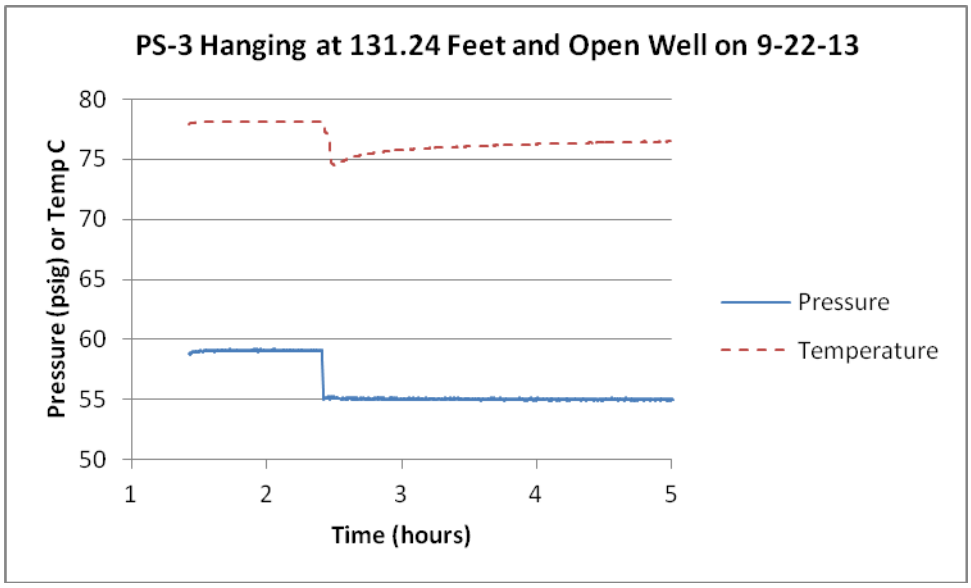
A detailed “static” downlog was run in the PS-4 well with Kuster tool E1474prior to the flowing of PS-3. PS-4 had been static with a 1-2 gpm wellhead leak for about 16 hours (since the flow to the hot tub was cut off). The tool was hanging at a depth of 406.8’ when PS-3 was opened for flow and while PS-3 was flowing a traversing up log between depths of 477 and 226’ was run to determine if there was any change in temperature in the well below the cased interval. The Kuster tool was hanging at 226’ when PS-3 was shutin and stops were made coming out of the hole to finish an uplog to the surface.

There were no traversing logs made in MI-1. Kuster tool E1477 was quickly lowered to a depth of about 200’ in MI-1 and hung there until it was quickly pulled back up to the surface after PS-3 was shutin.

Kuster Tool E1476 was used to make a detailed static downlog of PS-3 to its total open depth and was hung at a depth of 131’ prior to opening the 2” side valve on PS-3 so it could flow. During flow the tool was pulled up to 98’ and a detailed flowing downlog was made to the bottom of the hole at 217’. Then the tool was pulled up to 197’ and hung there while PS-3 was shutin. Following shutin, the tool was simply pulled up to the surface with no stops.

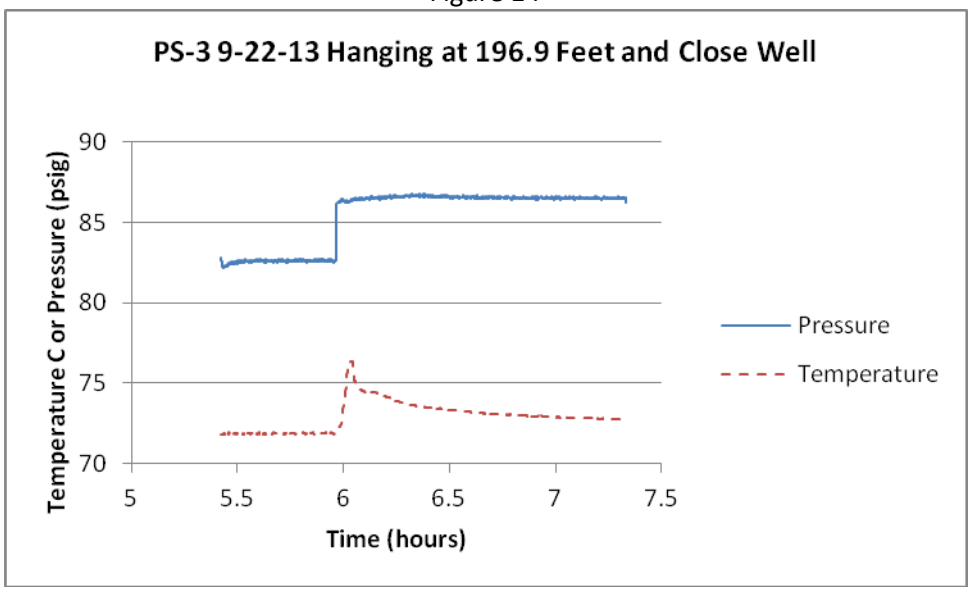
The PS-3 pressure record is complicated by the responses being measured at differeing depths when the flow began and was terminated. When the well was opened there was an immediate 4 psi pressure decline and a temperature decline up to 3.6 C due to cooler water from greater depths flowing up past the tool (Figure 13). The flowing temperture at 131.24’ did not stablize but over the longer term appears to be about 1.5 C. The measuring depth of 131.24’ is inside the casing and above the highest inflow point so it represents the total combined flow of the well.

Figure 13



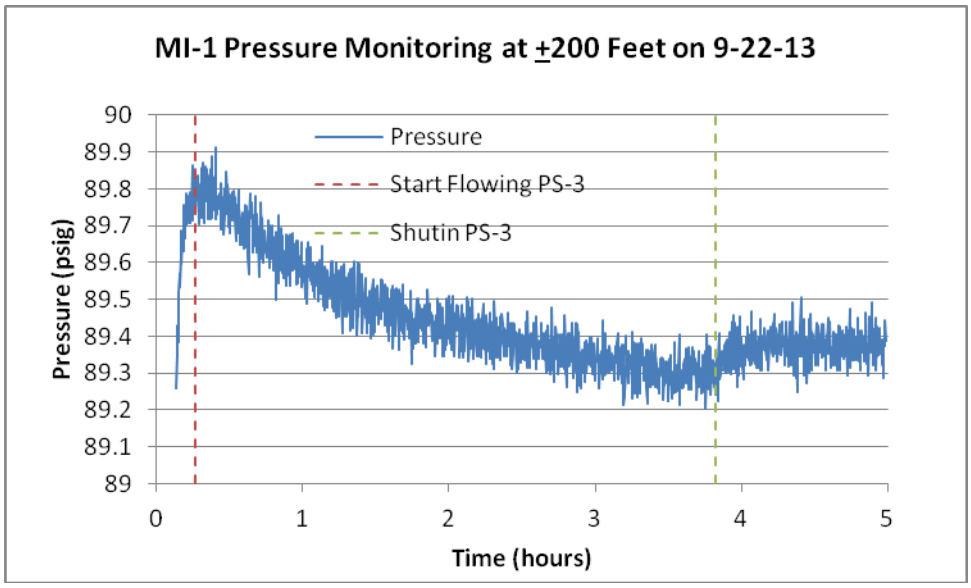
Upon shut in of PS-3 the temperature and pressure changes were reversed with an immediate 4 psi increase and a more gradual and smaller temperature increase (Figure 14). The smaller temperature increase may simply be a function of the measurement being beneath the most obvious inflow point in the well.

Figure 14



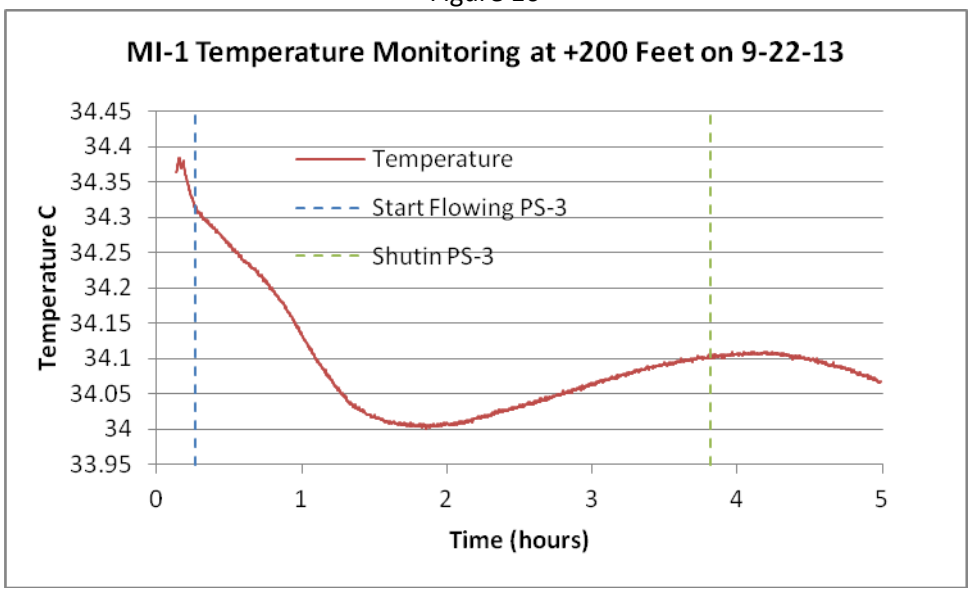
The MI-1 pressure record shows a small and sharp pressure increase of 0.1 psi when PS-3 was shutin (Figure 15). This 0.1 psi is comparable to the change seen when MI-1 was flowed on Sept. 7 and PS-3 was monitored (Figure 7). A possible much large pressure change might be associated with the start of flow from PS-3 but it appears to be superimposed on another longer term decline of uncertain origin.

Figure 15



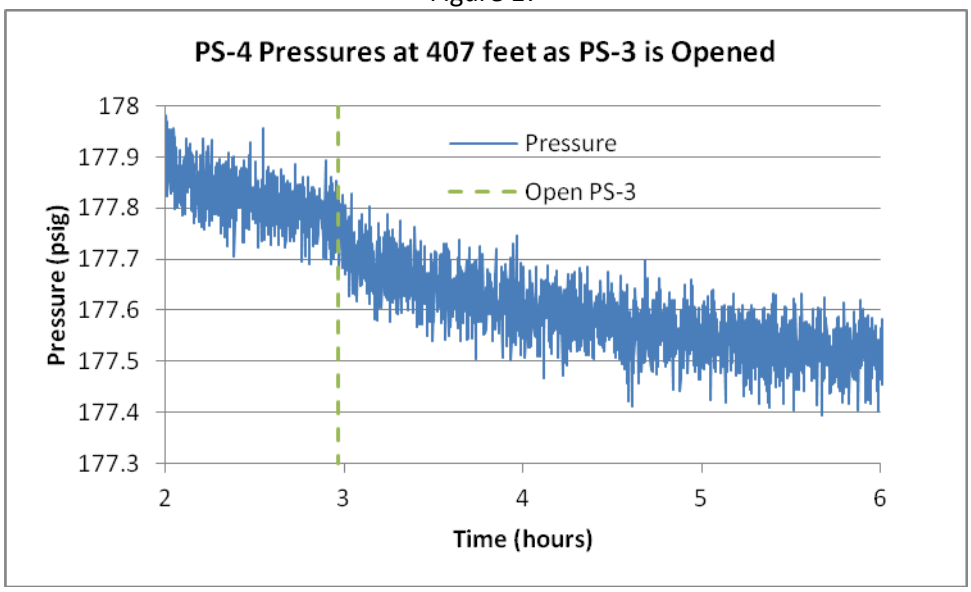
There might also be a small temperature change in MI-1 associated with flow from PS-3 (Figure 16)but if there is the change is superimposed on background trend that is difficult to interpretate given the short length of the monitoring period.

Figure 16



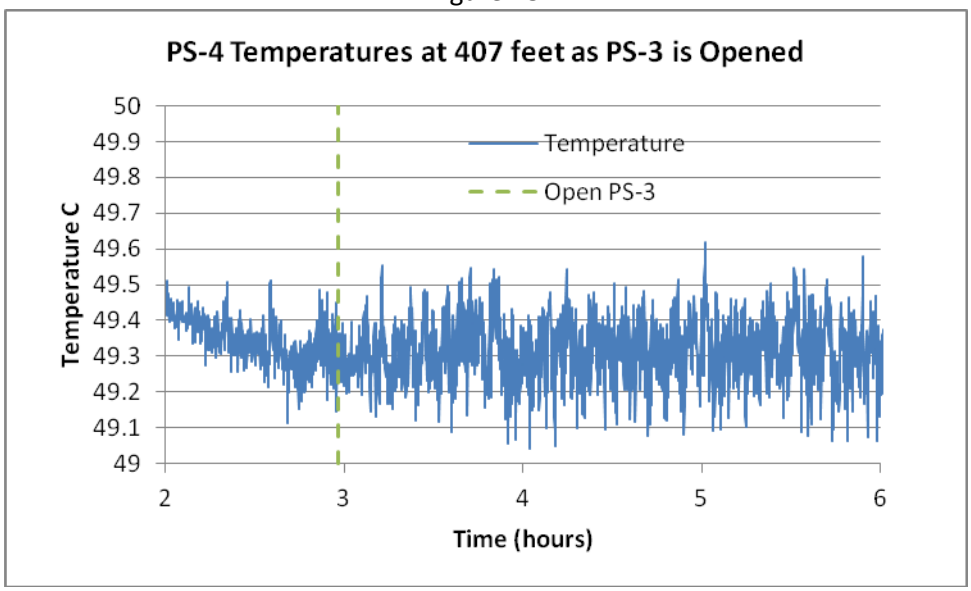
The PS-4 pressure record shows a pressure decline of 0.26 psi following the opening of PS-3 over a few hours (Figure 17). This appears to be a larger and slower change than was seen when the wells were reversed on Sept. 9 (Figure 7).

Figure 17



There was no obvious temperature change in PS-4 at 407' when PS-3 was opened (Figure 18).

Figure 18



When PS-3 was shutin there was a rapid pressure increase of about 0.8 psi (Figure 19) and a possible very small temperature increase at a depth of 223' (Figure 20). This temperature change is far smaller than was seen in PS-3 when PS-4 was opened and shutin (Figure 8).

Figure 19

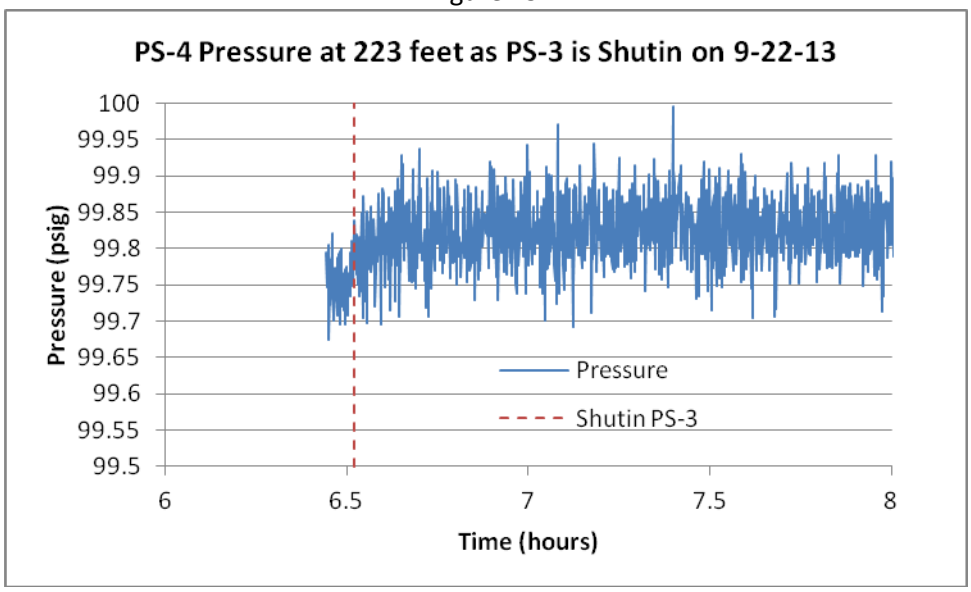
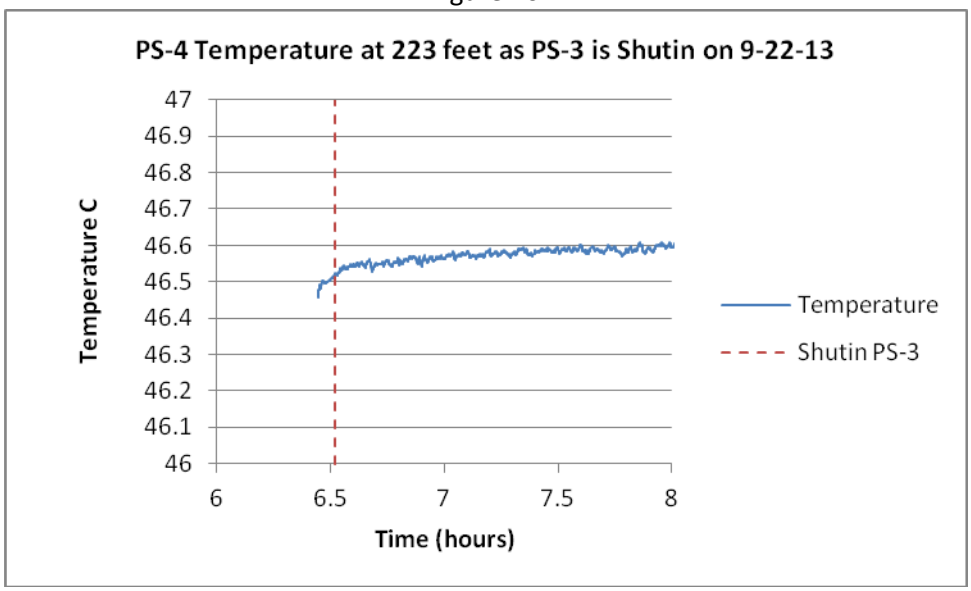


Figure 20



CONCLUSIONS

The Sept. 7-9, 11, and 22 interference tests have generally confirmed observations made by Woodward-Clyde during 1982 flow testing. The shallow PS-1 and PS-2 wells, completed in the shallow thermal aquifer, do not quickly or obviously communicate with the deeper and cooler aquifers exposed in the PS-3, 4, 5 and MI-1 wells. More precise tools available in 2013 have shown that the MI-1, PS-3, and PS-4 wells have a rapid but barely detectable pressure communication of 0.1 to 0.25 psi. This communication occurs at flow rates of 50 – 100 gpm from individual wells.

This small pressure communication creates a much stronger and surprising temperature change in the static PS-3 well when the MI-1 and PS-4 wells are flowed. The speed with which this temperature

communication occurs indicates that the small changes in pressure create flow rate changes which quickly change the water flow past the tool in the “static” PS-3 well. It is more likely that the temperature changes are related to flow rates and mixing than to a single fluid-entry changing its temperature. There are no obvious temperature changes in the PS-4 well when PS-3 is flowed. Well MI-1 showed some small temperture changes when PS-3 was flowed but these changes are not as clearly related to starting and stopping PS-3 flow. The PS-3, PS-4, and MI-1 wells have relatively similar depth permeable intervals which is a first cut explanation for their measurable short term communication. There are some background temperature and pressure trends in the Pilgrim wells that are not understood and will require additional and/or longer term monitoring to understand.

During the upcoming possible flow test of PS 13-1 it will be interesting to see if there are temperature or pressure changes in the wells monitored during this test. It is intuitively more likely that the PS-1 well will respond to PS 13-1 flowing than the other wells simply because the PS-1 chemistry indicates it is most closely connected to the deeper geothermal system.

Appendix I

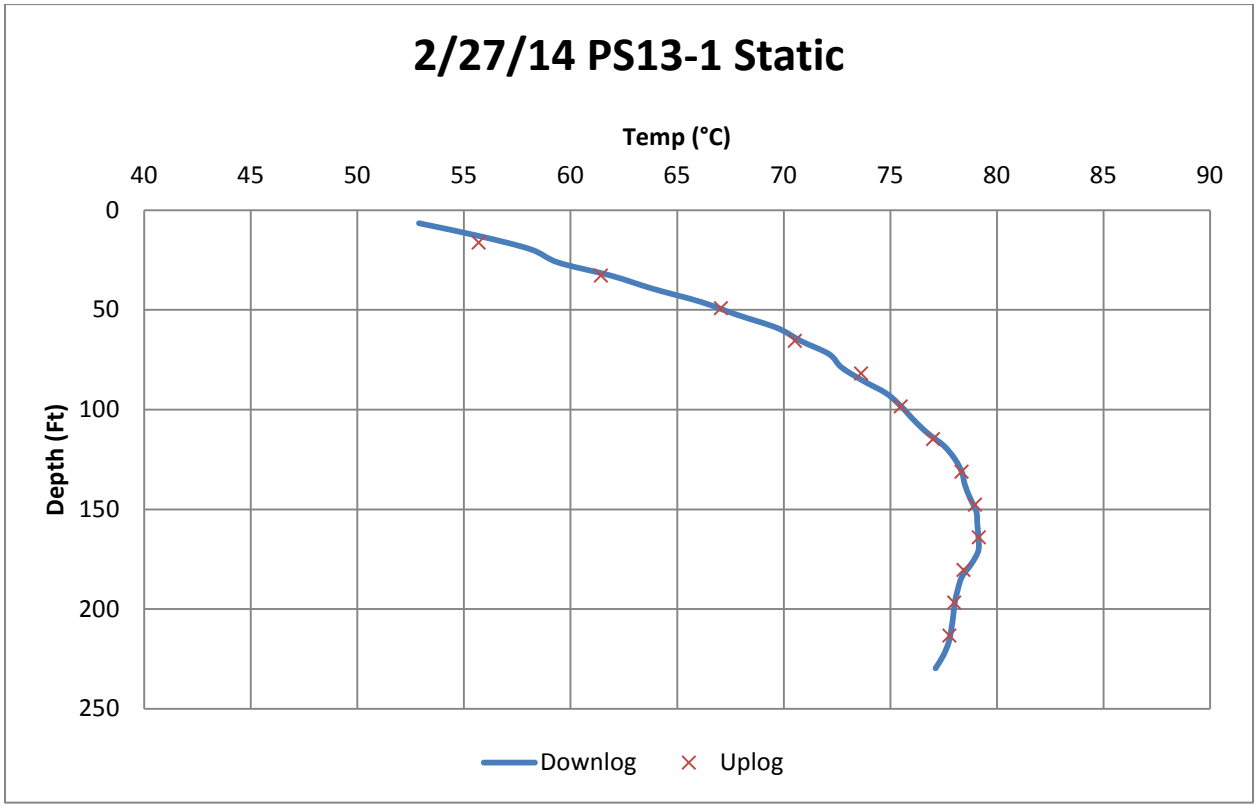
February 2014 Interference Testing

Pilgrim Hot Springs February 2014 Trip Report and Temperature Interpretations
By Chris Pike
March 11, 2014

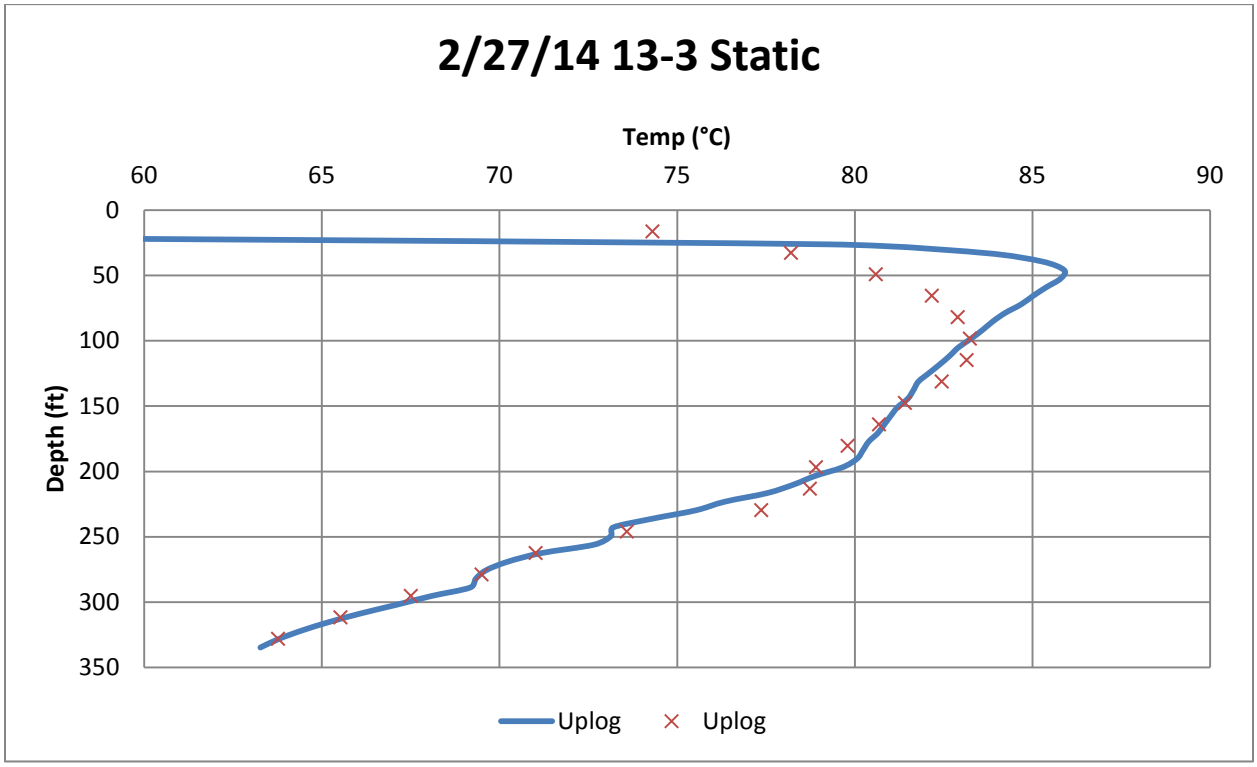
On Thursday February 27th Chris Pike, assisted by John Wallukk, made a trip to Pilgrim Hot Springs via snow machine for the purpose of logging the geothermal wells. Temperatures were pleasant and warm, above freezing for most of the trip. The snow machines were trailered up the Kugarak Road to mile 28 because of minimal snow cover close to Nome. From mile 28 to the turn off for the Pilgrim Hot Springs spur road the snow cover was excellent. On the Pilgrim road, snow drifts were 6-8 ft deep in many places until the road dropped into the Pilgrim Valley where snow cover was minimal and gravel was showing in many places. The first task was to obtain static well logs of PS 13-1, PS 13-2, PS 13-3 and PS-1 using the surface read wire logging equipment supplied by Southern Methodist University.

Static Well Logging

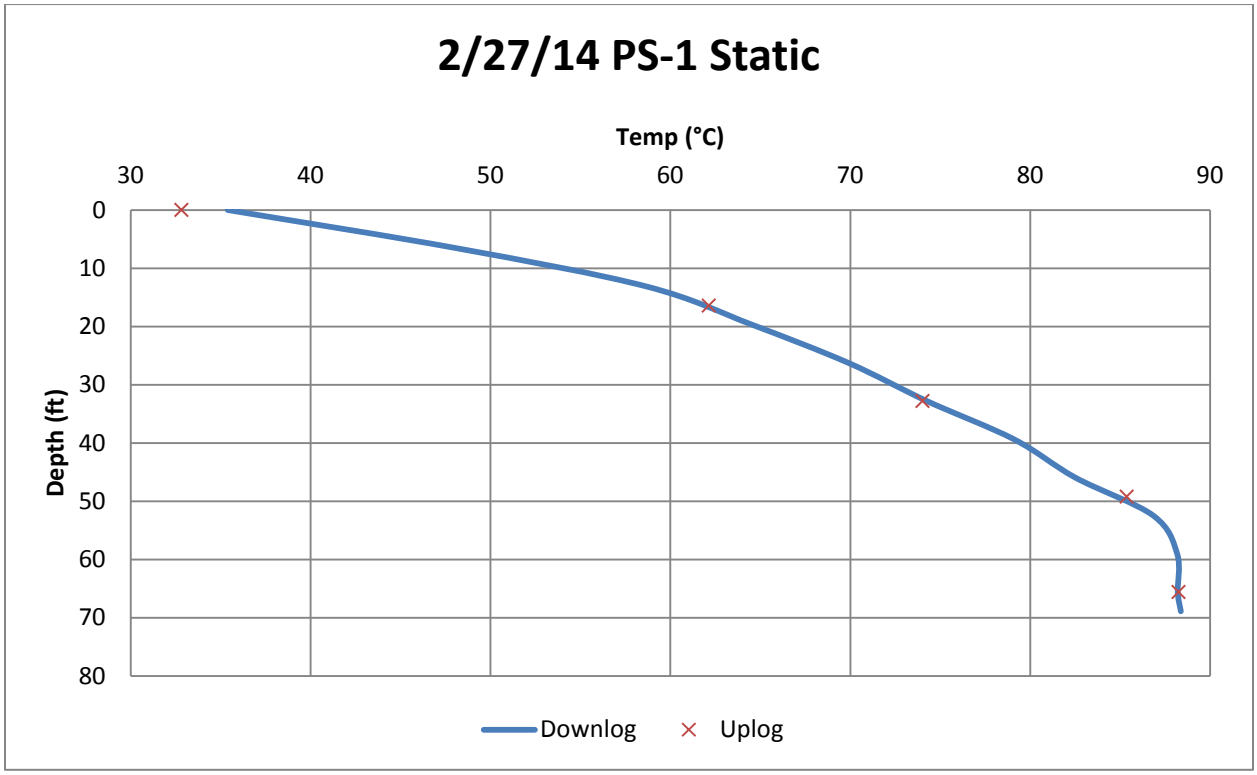
Well PS 13-1 was logged at 16:00 on 2/27/14. The ambient temperature at the time of logging was 38 degrees Fahrenheit with light gusty winds and sunshine. The well is located at coordinates:
N 65° 05' 28.3" W164° 55' 38.3" . PS 13-1 was completed to a depth of 243', with 14" stainless steel well screen installed between depths of 188' to 238' and solid 14" casing from the top of the screen to the surface. The temperature profile measured during this logging exercise is shown below:



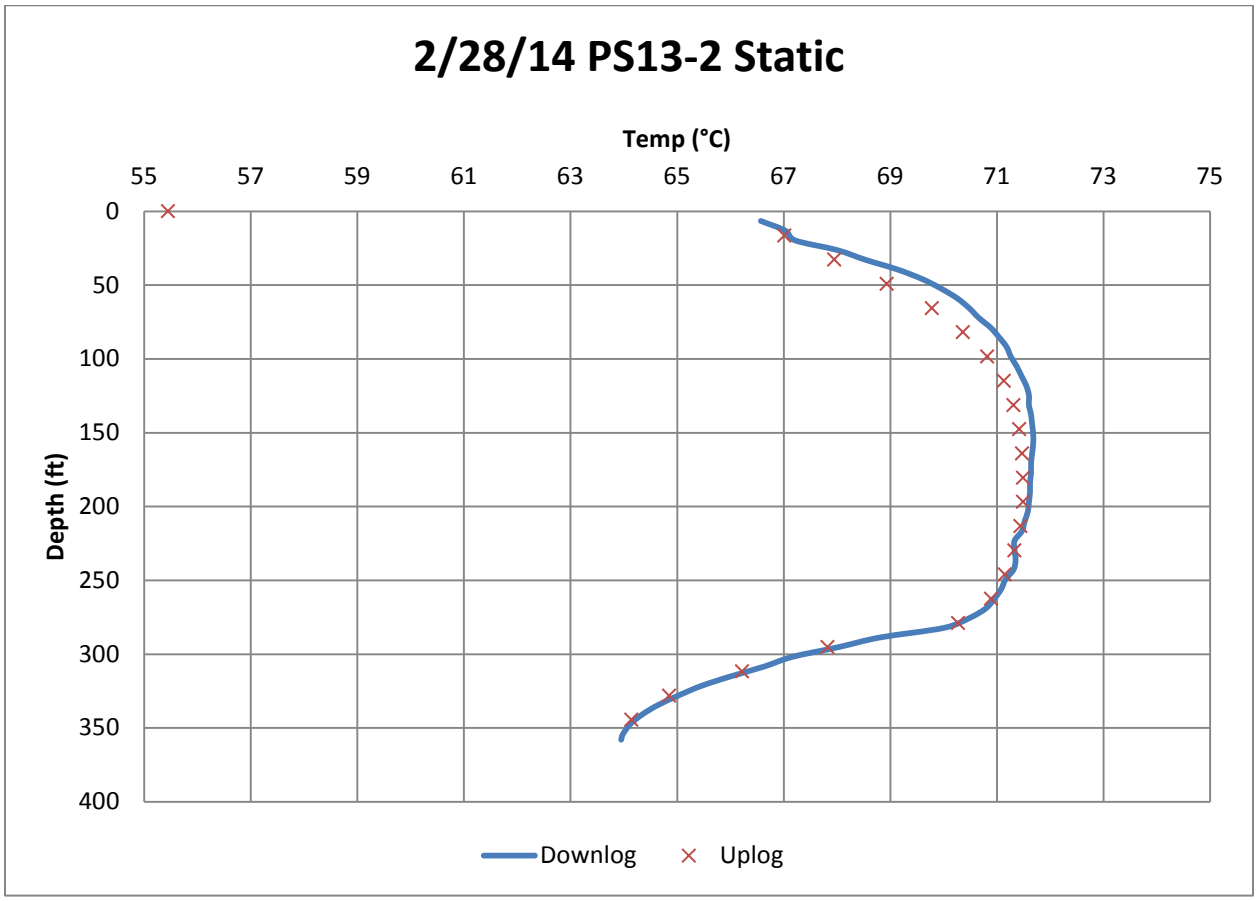
Well PS 13-3 was logged next beginning at 17:40 on 2/27/14. The well is located at coordinates: N 65° 05’ 25.8” W 164° 55’ 38.9”. The well was initially drilled to a depth of 400’. Solid 6” casing was installed from the surface to a depth of 60 feet. Inside the 6” casing 4” casing was installed from the surface to the bottom of the hole at 402.5 feet. The 4” casing was perforated from the bottom of the 6” casing to the bottom of the hole. Perforations were made ¼” wide by 3” long, once per foot on every other 10 foot section of casing. Of note is that when the static logging equipment was installed on the well and the gate valve was opened, gas of unknown type was forced out of the top of the pipe for about 20-30 min until water came out through a small leak in the stand pipe that had been installed to facilitate static logging. This may account for the different temperature profiles observed during the down log and up log. (During the static log, <1/2 quart/ min leaked from this pipe) The temperature profile measured during this logging exercise is shown below:



Well PS-1, which was drilled in 1979 was logged beginning at 19:24 on 2/27/14. This well has been logged numerous times in the past however a slight maximum temperature drop has been suspected so it was decided to take the time to perform an initial static log of the well. A 5' section of 2" pipe was attached to the top of the well head as this well does not have sufficient artesian head to flow out of a pipe of this height. The temperature profile measured during this logging exercise is shown below:



Upon arrival at Pilgrim Hot Springs, Well PS 13-2 was leaking about 1-2 gallons per minute due to a leaky valve and a failed gasket on the flange above the gate valve. A simple replacement gasket was made from scrap rubber material available on site and the well had been in a static state since 20:00 hours on the evening of 2/27/14. The well was logged beginning at 10:00 on 2/28/14. During the static log, the well was leaking about 1 quart/min. Ambient temperature was 33 degrees Fahrenheit with light snow and rain and winds at 10 mph out of the east. PS 13-2 is located at N 65° 05' 29.9" W 164° 55'27.6". The well was drilled to a total depth of 403 ft. Solid 6" casing was installed from ground level to a depth of 227'. Inside the 6" casing, 4" casing was installed from the wellhead to total depth. The 4" casing was perforated from the bottom of the 6" casing to the total depth. Perforations were made in a single row, ¼" wide by 3"long, one perforation per foot on every other 10 foot section of casing. (During the static log, 1 quart/ min leaked from this pipe) The temperature profile measured during this logging exercise is shown below:



Interference Testing

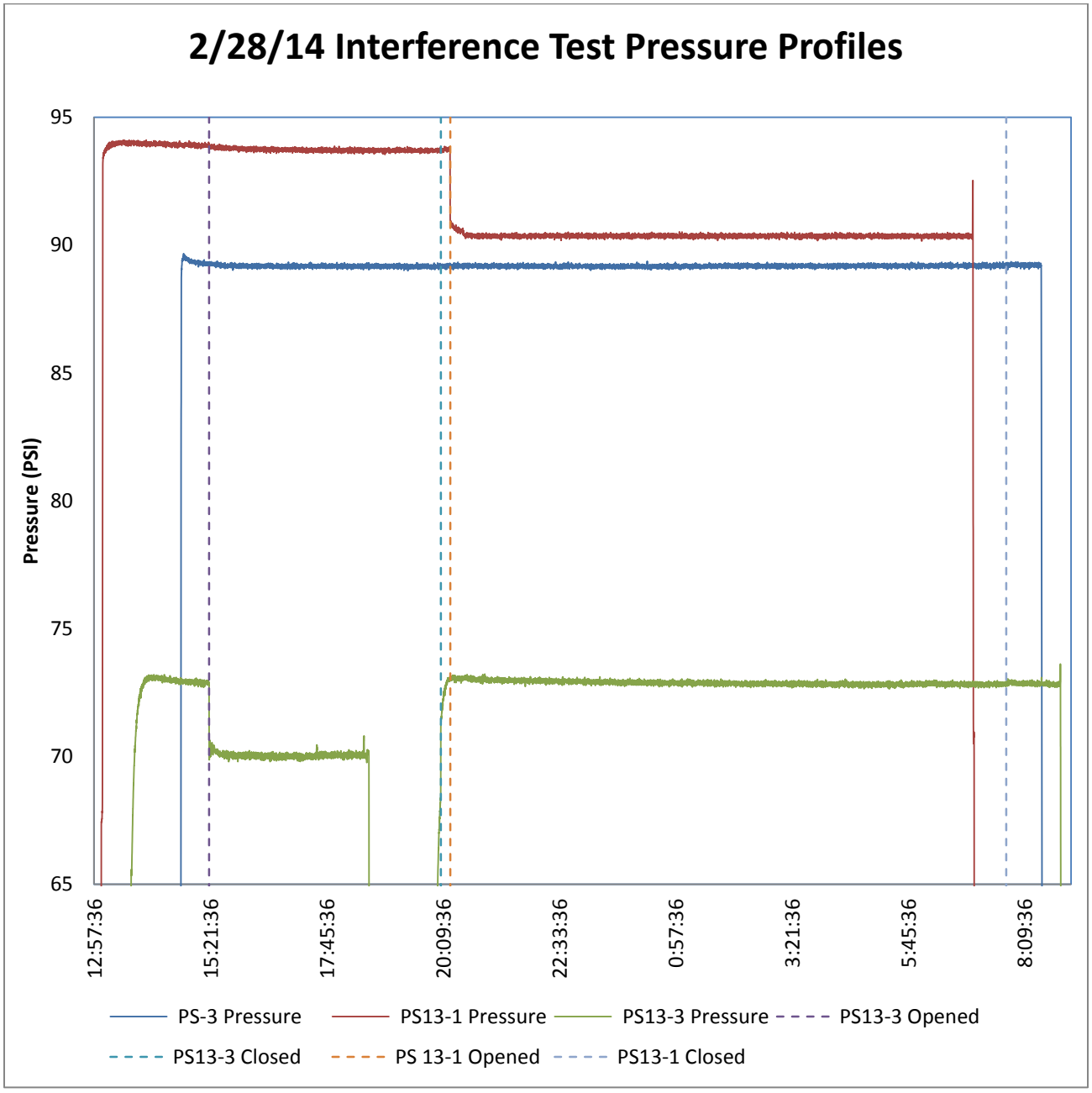
Following the static well logging exercise, interference testing was performed by flowing wells PS13-3 and PS13-1 while Kuster temperature and pressure gauges were placed in wells PS-3, PS 13-3 and PS13-1. Kuster #1476 was placed at a depth of 210 feet below ground level in well PS13-1. Kuster #1477 was placed 161 feet below ground level in well PS13-3. Kuster #1474 was placed 200 feet below ground level in well PS-3.

At 15:20 on 2/28/14 well PS13-3 was opened and water flowed from a 2" hose connected to a diverter valve 44" above ground level in the well head. After 10 minutes, the water flowed consistently at an estimated 50 gpm. The measured temperature was 173.5°F (78.6°C). At 17:30 on the same day the flow from well PS 13-3 appeared unchanged and the temperature of the water was measured at 174.2°F (79°C). At 18:30, the flow appeared unchanged and the temperature was measured at 175°F (79.4°C). At 18:38, the Kuster probe was removed from the hole so that a flowing log of PS 13-3 could be collected using the logging equipment from Southern Methodist University. The flowing log procedures are described in greater detail below. The Kuster probe was reinserted into well PS 13-3 to the previous depth of 161 feet below ground level at approximately 20:03. The flow was cut off from the well at 20:07 on 2/28/14.

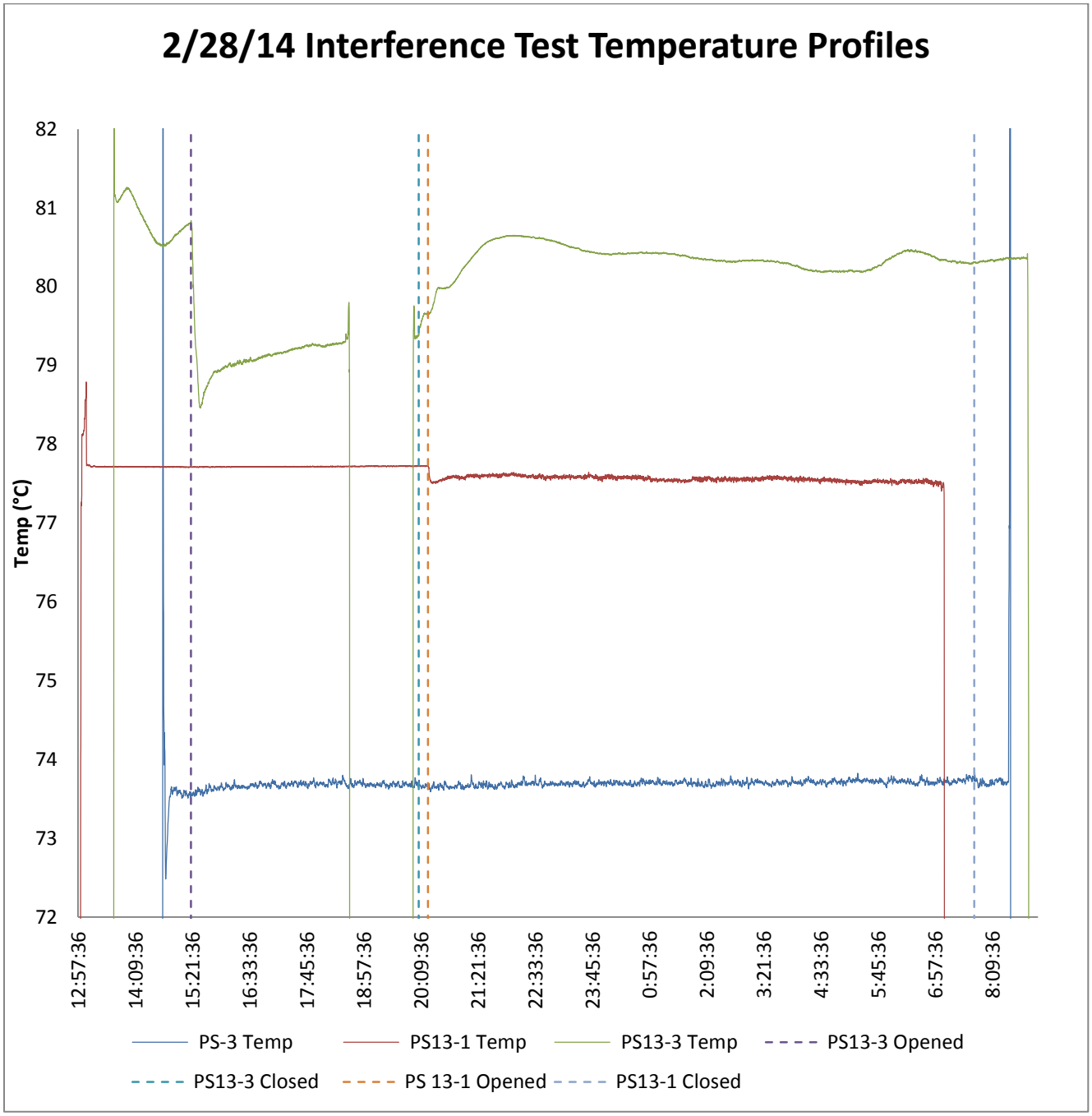
The 4" diverter valve on the PS 13-1 wellhead was opened at 20:18:40 on 2/28/14. It was estimated that water was flowing at a rate of 30-50 gpm. At 20:26 the water temperature was measured at 149°F (65°C). The well was allowed to flow overnight. At 06:58 on 3/1/14 the flow appeared unchanged and the temperature was measured at 170.8°F (77.1°C). Immediately after the temperature was measured, the Kuster logger was removed from well PS 13-1 at approximately 07:15AM and a flowing well log was collected.

Well PS 13-2 was opened at 07:54 on 3/1/14 and it flowed at an estimated 100gpm from a 2" diverter valve above the wellhead as well as from an open standpipe that was attached to the wellhead. At 08:17, the temperature was measured at 157°F (69.4 °C) and the flow appeared to have increased very slightly. The Kuster probes were removed from well PS-3 at 08:35 on 3/1/14 and from well PS 13-3 at 09:00 on 3/1/14.

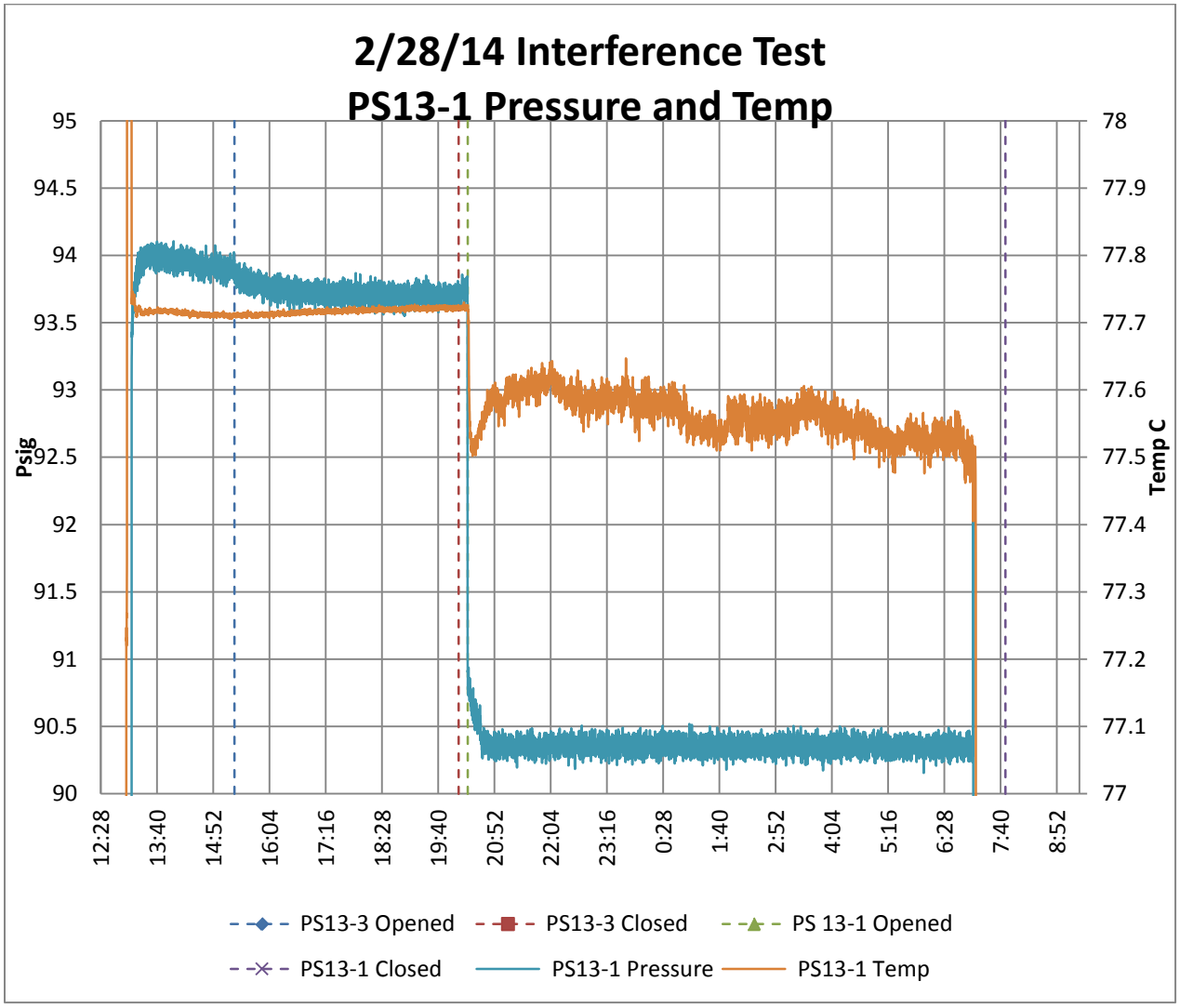
Well Interference Test Pressure Profiles



Well Interference Test Temperature Profiles



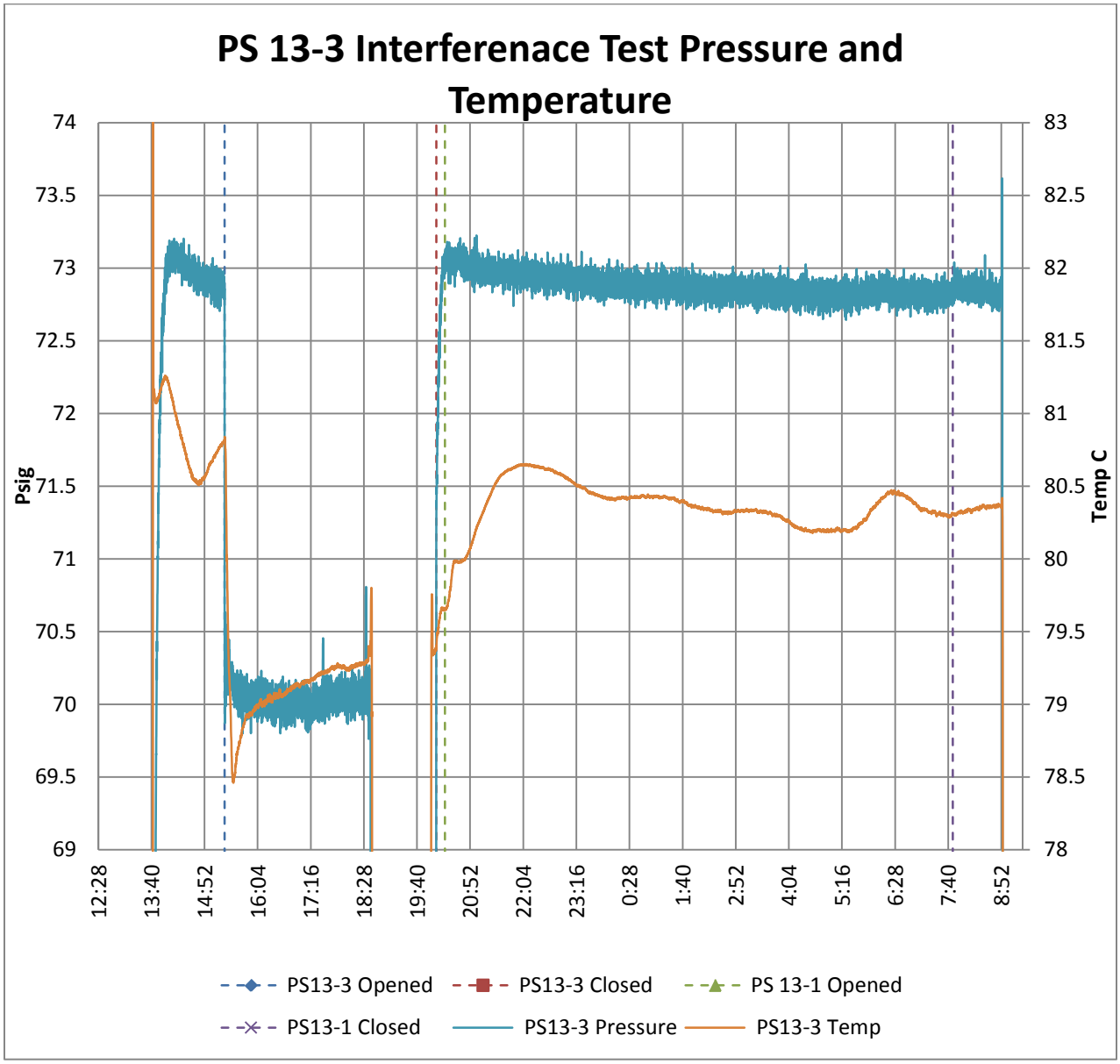
PS13-1



Based on this graph, when well PS13-3 was allowed to flow, the pressure in PS13-1 decreased by approximatly .2 PSI and the temperature in PS 13-1 increased very slighty; on the order of 2 hundreths of a degree .

When well PS13-1 was flowed, the pressure in PS13-1 immediately dropped from 93.55psi to 90.55 psi then continued to drop and stabalized at 90.4 psi as the well continued to flow. The temperature in the well immediately dropped from 77.72 degrees to 75.52 degrees. As the well continued to flow the temperature in PS 13-1 fluxuated by about .15 degrees C.

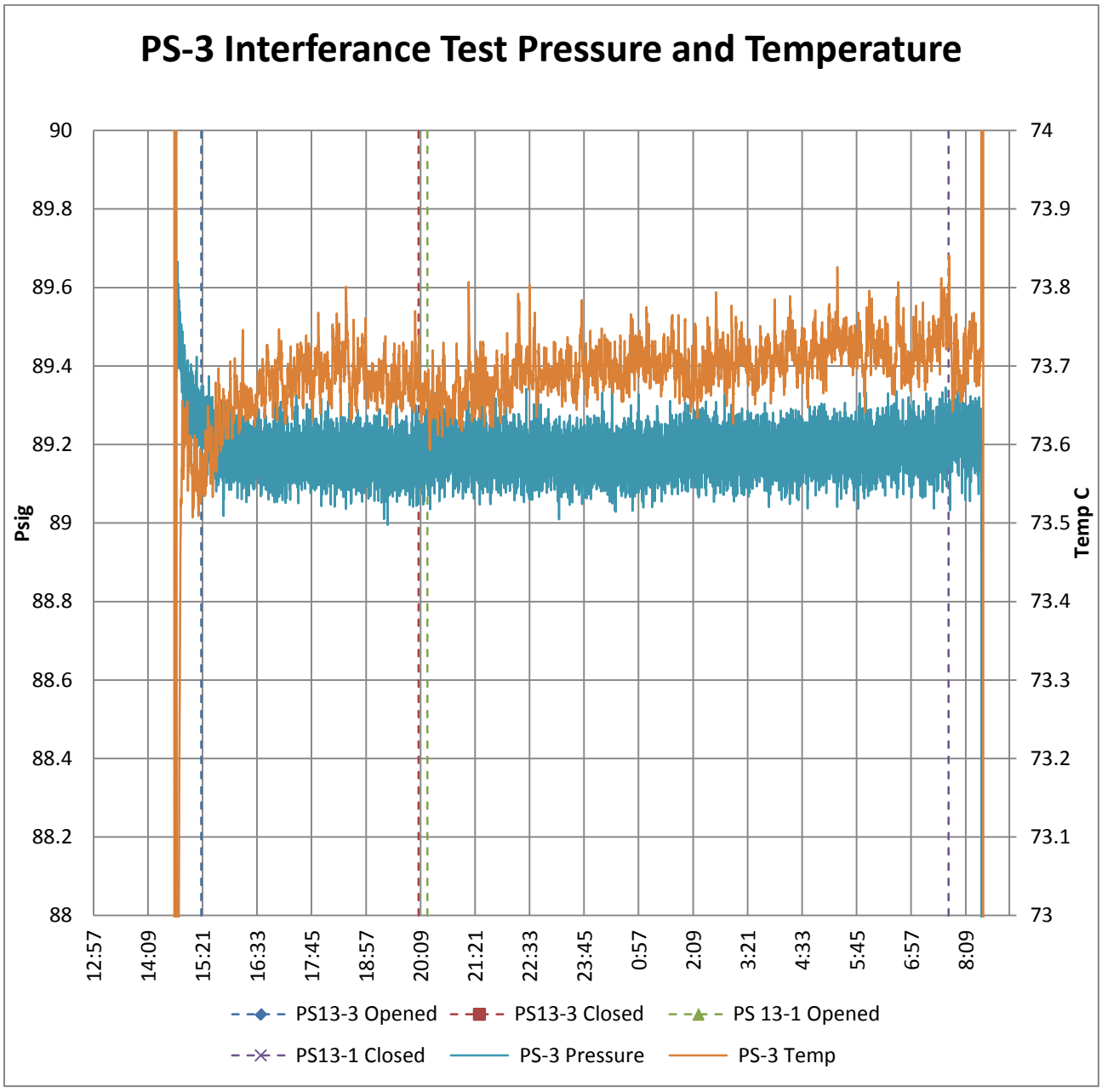
PS 13-3



The pressure and temperature profiles of well PS13-3 are shown above. When well PS 13-3 was allowed to flow, the pressure and temperatures in the well also dropped. When the well was opened, the pressure immediately dropped from 72.9 psi to approximatly 70 psi. The temperature, which appears to fluxuate slightly at the depth where the probe was placed dropped quickly (althought not instantaniously) from 80.8 degrees to 78.5 degrees. During the following three hours when the well continued to flow, the water temperature at the probe depth slowly climbed to approximatly 79.4 degrees at which point the probe was removed from the well.

When well PS13-1 was opened the pressure inside PS 13-3 appears to slowly drop by approximatly .25 psi. While it appears the temperature in PS13-3 rises when PS13-1 was opened, the temperature ossilates and it is impossible to make any conclusions given the short time scale of the test.

PS-3



The graph above shows the temperature and Pressure in PS-3 during the interferance test when PS13-1 and PS13-3 were allowed to flow. Based upon the data aquired and the length of time which it was

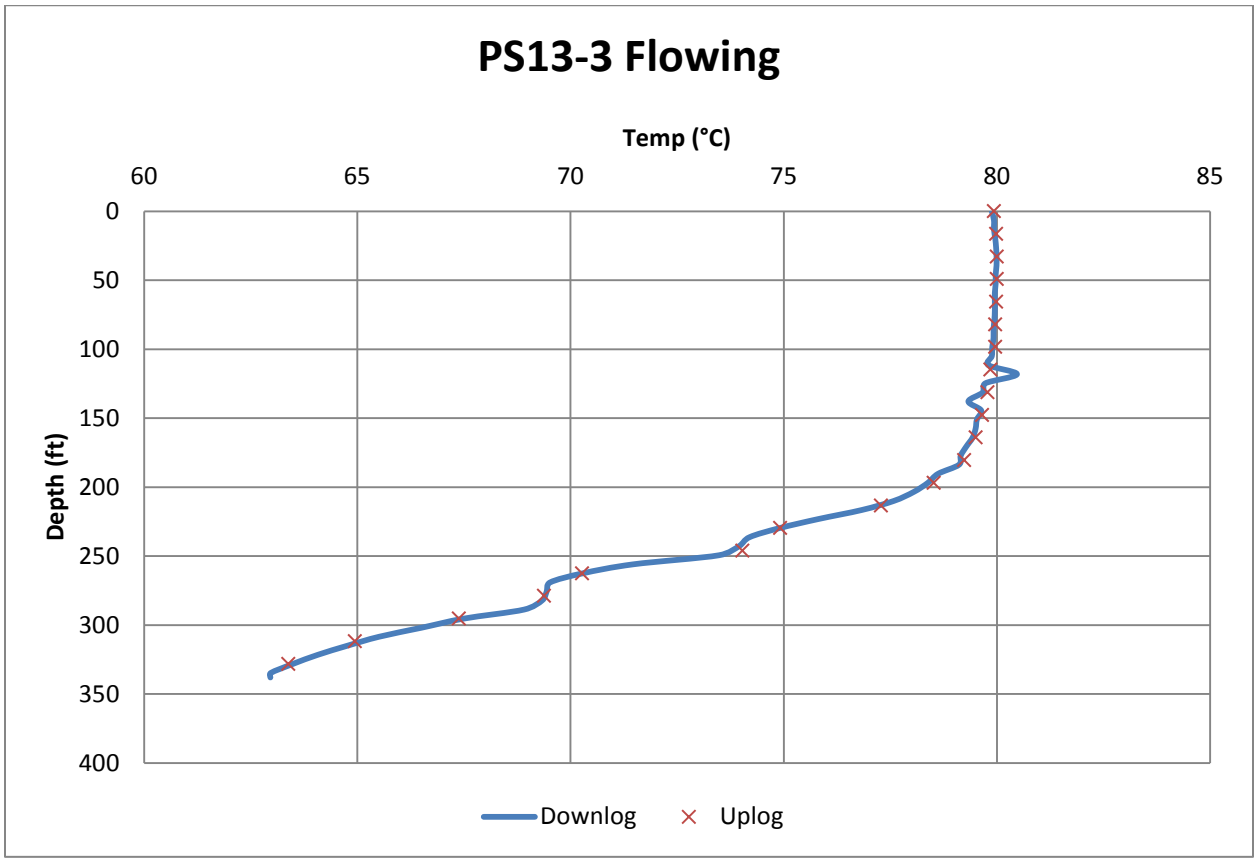
aquired for, nothing conclusive can be said about the response of PS-3 when the other wells were flowing.

Interference Testing Conclusions

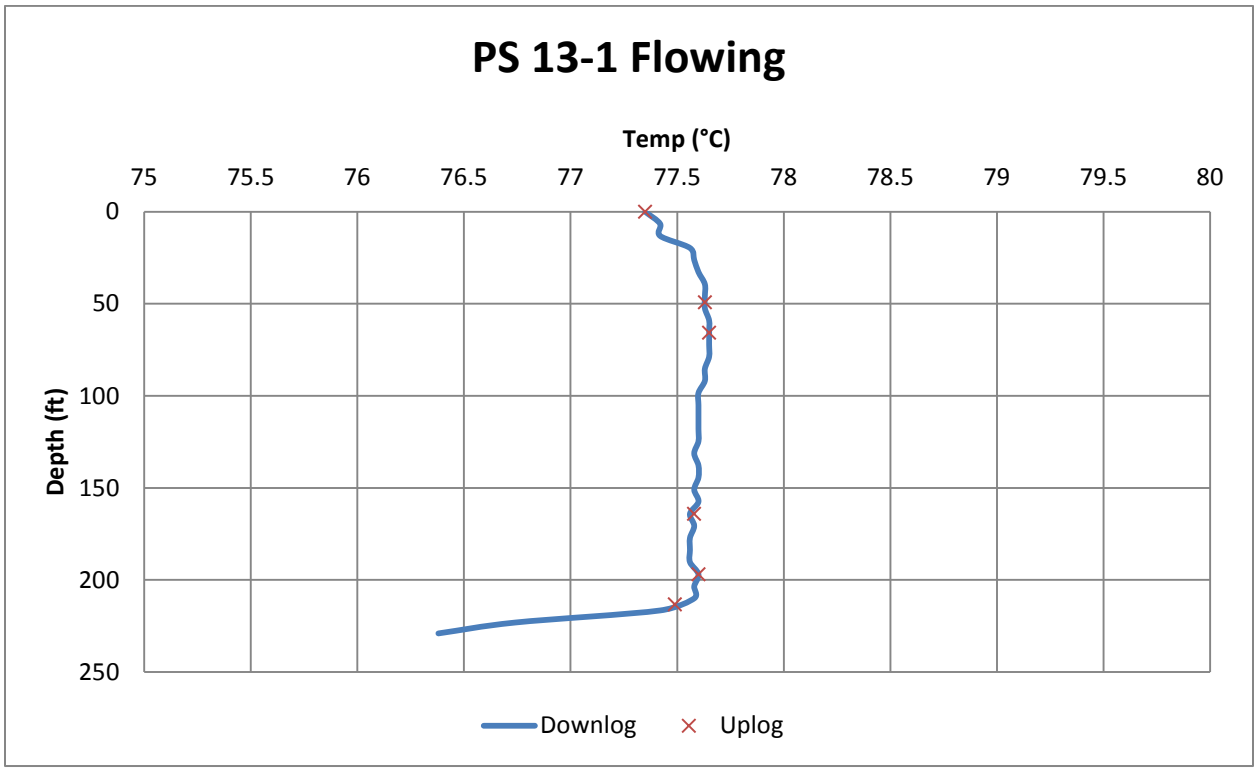
The most notable event that occurred durign the interference testing was the rise in temperatures (although small) in wells PS13-1 and PS 13-3 when well PS13-3 was flowed. It should be noted however that well PS 13-3 only flowed four hours at a flow of approximatly 50 gpm. A longer test with greater flows, perhaps increased by pumping the wells would increase the certainty of the results and the changes in temperatures and pressures overtime would likely be amplified as various wells are pumped. This type of testing would also allow the monitoring of drawdown.

Flowing Well Logs

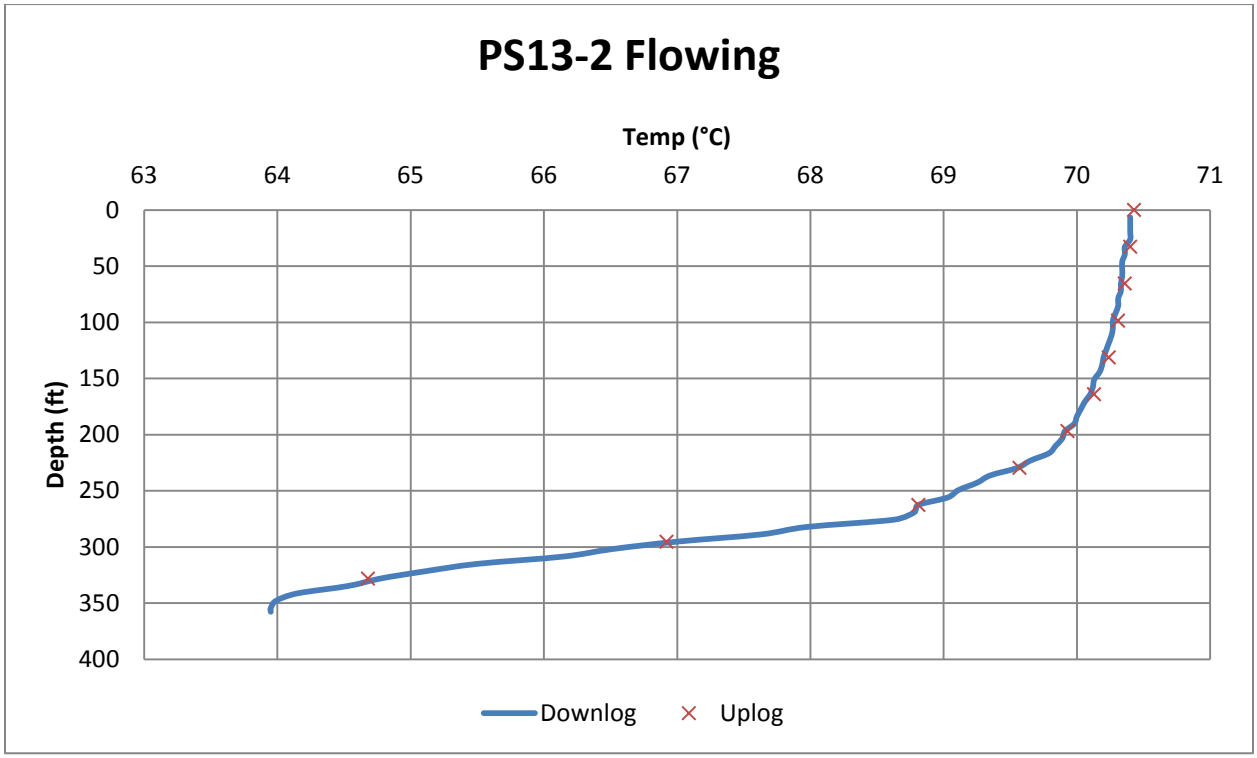
A flowing log of Well PS 13-3 was collected at 18:57 on 2/28/14 using precision well logging equipment provided by southern Methodist University. The well construction has been described above. The well was allowed to begin flowing at 15:20 on 2/28/14 and was flowing at an estimated 50 gpm from a 2" diverter valve located about 5 Ft above the ground at the time the well log was taken. The temperature profile measured during this logging exercise is shown below:



A flowing well log of well PS 13-1 was recorded at 07:18 on 3/1/14. The ambient air temperature at the time of the log was 29°F with light winds. The well had been allowed to flow beginning at 20:18 on 2/18/14 and was flowing at an estimated 30-50 gpm from a 4" diverter valve located on the wellhead. The temperature profile measured during this logging exercise is shown below:



A flowing log was recorded for well PS 13-2 at 11:43 on 3/1/14. The well was initially opened at 07:54 on the same morning. The well was estimated to be flowing at about 100gpm. Field notes indicate that 20 minutes after flow began, the flow appeared to increase slightly, but by the time the log was run, the flow had slightly decreased from its initial rate. The temperature profile measured during this logging exercise is shown below:



Appendix H
2012 and 2013
Drilling Logs

Drilling Logs for Pilgrim Hot Springs Wells TG-1, PS-12-3, and PS-12-9		
Date	**Activity description**	**Hours worked**
5-Jun	Art and Jeff arrive in Nome. Pick up two rental vehicles. Inspect snow conditions on Pilgrim access road (still considerable).	12
6-Jun	Working in town on equipment preparation. Load Louie Green's backhoe onto our trailer for transport to PHS to dig snow from access road. Northland barge arrives in Nome.	12
7-Jun	Equipment preparation continues. Haul Louie's backhoe and unload at PHS access road intersection.	12
8-Jun	Pick up dump truck at Northland. Start equipment engines in town. Drive to site to check on Louie's progress. Drill crew flies from Denver to Anchorage.	12
9-Jun	Pick up remaining three rental vehicles. Crew arrives in Nome on morning flight. Still working on equipment preparation in Nome. Louie has access road dug to the BLM gravel pit. Begin moving equipment to the pit as it's ready. Get backhoe from Northland.	12
10-Jun	Continue equipment prep in Nome (Geoprobe hydraulics etc). Move backhoe to access road and begin working with Louie to clear snow. Move more equipment to BLM gravel pit.	12
11-Jun	Continue equipment prep in Nome. Begin hauling gravel for access road repair. Locate and mark first ten geoprobe sites.	12
12-Jun	Using rented loader, begin mining rock from MINC site at top of Golden Gate and hauling it for access road improvement. Continue work in Nome and moving equipment to BLM gravel pit. Move supplies from Northland to Icy View.	12
13-Jun	Move geoprobe to PHS and drive first well to 80 ft. Continue access road repair work, moving equipment to BLM pit, and painting rig in Nome.	12
14-Jun	Geoprobe 3 sites. Continue access road repair work. Move more supplies from Northland to Icy View.	12
15-Jun	Pick up pipe at Northland and move it, and additonal equipment, to BLM pit. Continue access road work. Geoprobe 2 sites.	13
16-Jun	Finish getting supplies from Northland. Continue access road work and geoprobing. Install new culvert at churchyard springs crossing.	12
17-Jun	Continue road work. Begin moving equipment from BLM pit to PHS runway parking area. Continue geoprobing using 2-pipe method.	12
18-Jun	Continue geoprobe work (plugging and driving with larger points). Move trailers to chuchyard area and begin moving into Nun's Quarters. Continue access road work.	13
19-Jun	More geoprobe work and access road work. Move two loads of pipe from Nome to runway staging area.	12
20-Jun	Continued geoprobe and access road work. Move two more loads of pipe from Nome to runway staging area.	12
21-Jun	Continued geoprobe and access road work. Move loader to BSNC gravel pit on main road to get smaller material. Move pallets of cement and drill mud from Nome to runway staging area.	12
22-Jun	Continue geoprobe and access road work using smaller BSNC material. Move drill rig from Nome to runway staging area. Install mast extension and large-diameter tires for improved site access. Waiting on AOGCC permit-	12
23-Jun	Continue geoprobe work. Move loader to BLM pit in anticipation of gaining access to this material on 6/25. Begin rig and pipe pallet construction.	12
BEGIN WORK ON TG-1, PERMIT NO.: 212-077		
24-Jun	Continue geoprobe work. Begin moving equipment into churchyard area in preparation to move to well TG-1. Continue pallet construction etc.	12
25-Jun	Geoprobe work and TG-1 preparation continue.	12
26-Jun	Geoprobe work and TG-1 preparation continue. Build tripod to use for running geophysical logs in existing wells.	12
27-Jun	Continue geoprobe work. Get permission to use BLM "gravel" and begin hauling it for access road improvement. Set up and run gamma log in last year's S-9 well.	12
28-Jun	Continue geoprobe, access road work, and preparation for well TG-1. Run gamma log on last year's S-1 well.	12
29-Jun	Continue geoprobe, access road work, and preparation for well TG-1. Disassemble and move last year's rig pallet from S-1 site to churchyard staging area. Dispose of last year's stored cuttings in S-1 dug sump and move tanks to staging area.	12
30-Jun	More geoprobe and access road work. Begin stockpiling road material at landing strip staging area for future use. Repair (weld) PHS entry gate.	12
1-Jul	More geoprobe work. Begin preparing site TG-1 (PS-12-1). Haul material in dump trailer for Louie Green to fill and repair trail leading to boat launch area in case we need to dispose of cuttings there. Run gamma log in well MI-1.	12
2-Jul	More geoprobe and moving of road material to runway staging area. Decide to set up rig pallet at PS-12-1 to allow for BOP installation w/o the need to move rig (raise rig on pallet to required height). Run 2-in water lines from boat-launch slough to site and fill tanks with water. Move mudpump and shaker trailer onto site.	12
3-Jul	After finding out that we can drill to 500 ft w/o AOGCC permits, drill and drive 10 ft of 10-in surface casing and finalize site to where we're ready to begin conductor casing drilling in morning. Finish geoprobe work and collect gamma log from well PS-5.	12
4-Jul	Drill 10-in hole to 100 ft disposing of liquid waste in sump behind garbage pile. Begin moving road material to build base on which backhoe and work to enlarge sump and dump solids.	12

5-Jul	Set and cement 6 5/8-in casing to 100 ft. Clean equipment and bring in new light-weight rotary rods for drilling below casing. Continue working on trash-pile cuttings disposal area.	12
6-Jul	Cut pumping sub from 6-in casing, drill cement out from inside casing, and drill 6-in hole to 290 ft. After tripping out drill steel at end of day, well begins flowing ~100 gpm at surface (clay boot around bit "swabbed" the well). Trip in rods to 120 ft and pump drill mud to stop flow. Trip to 220 ft, mix weighted mud and pump. Trip out pipe.	20
7-Jul	Trip to bottom and drill to 470 ft. Pull drill pipe from hole.	20
8-Jul	Trip to bottom and drill to 500 ft. Let rods stand w/o circulation for 2 hrs then run Kuster log inside pipe. Circulate and trip pipe from hole. Run gamma, caliper, induction, and resistivity logs in open hole.	20
9-Jul	Although we don't have AOGCC permit to drill below 500 ft, decide to hold off on cementing casing at this depth in the hopes that the permit-to-drill will be finalized today. Install knife-valve and 2-in kill lines on 6-in casing. Take geoprobe and pull rods from 2 sites that weren't yet pulled. Receive AOGCC permit at end of day.	20
10-Jul	Trip rods to bottom and drill to 730 ft. Pull rods from well.	20
11-Jul	Trip rods to bottom and drill to 1000 ft. Circulate and pull rods from well.	20
12-Jul	Trip and flush drill rods to bottom. Circulate and pull rod from hole. Run gamma, caliper, induction, and Kuster temperature logs in open hole. Prepare site and equipment to set and cement HW casing to 1000 ft. Run casing to 450 ft.	20
13-Jul	Finish running casing to 1000 ft and circulate. Mix and pump geolite cement thru casing to surface…..big mess but get it done. Clean equipment and site as much as possible.	22
14-Jul	Trip in drill pipe with 3 7/8-in bit and tag cement at 600 ft. Drill out cement to 990 ft leaving 10 ft in bottom. Flush well and fill with water. Trip pipe, install valve at surface, and clean equipment and site.	20
July 15-July 25	Crew returns to Denver for break. Jeff remains in Nome to take care of BOP-related and other issues (60 total hrs worked).	60
26-Jul	Crew flies Denver-Nome. Jeff and Don (arrived 7-25) move BOP to Pilgrim. Assist Josh and Charlie in running Kuster in 12-1 well….only get down to 400 ft.	10
27-Jul	Install BOP flange on 12-1 and trip steel to well bottom circulating and flushing fluid. Trip pipe and dig out well head for BOP installation	20
28-Jul	Install BOP and system. Trip steel to 200 ft and circulate per test requirements. Pressure system but it leaks. After Ron makes several calls, he opens/closes the bag in quick succession. Discover that we don't have the recording unit so test will have to wait until tomorrow.	20
29-Jul	Install pressure recorder and Ron Tate attempts to run test @ 3000 lbs pressure. The bag bursts and hyd fluid runs from the BOP head. Ron takes off and we remove the BOP and all plumbing from the well. Set up to run Kuster log in well. Begin clearing site and hauling rock material to runway.	20
BEGIN WORK ON PS-12-3, PERMIT NO.: 212-109		
30-Jul	Remove all equipment from site and install ball valve on well. Begin moving gravel to site 12-2	20
31-Jul	Set rig pallet on site and move rig onto pallet. Move rock onto access trail and lay tundra mats over the rock. Move equipment on site. Install 2-in water hose from slough to site and set up and fill water storage tanks.	20
1-Aug	Set and cement 10-in surface casing. Drilled 9 7/8-in hole to 125 ft.	20
2-Aug	Drill 9 7/8-in hole to 204 ft. Set and cement 6-in casing to 204 ft.	20
3-Aug	Pull 10-in casing and cement in large washout hole that was undercutting around the casing. Install 6-in knife valve and drill cement out of 6-in casing to bottom.	20
4-Aug	Drill 5 7/8-in hole to 464 ft. Trip pipe at day's end.	20
5-Aug	Drill to 754 ft. Trip pipe.	20
6-Aug	Intall new bit, trip pipe to bottom and drill to 1004 ft. Trip pipe from hole.	20
7-Aug	Trip to bottom and flush well. Set up for logging and log well to bottom. Run HW casing to 270 ft with cement sub and shoe installed.	20
8-Aug	Trip/wash HW casing to bottom. Mix cement and pump thru HW cement shoe. Shut in casing and begin moving BOP into place.	20
9-Aug	Install BOP flange and set BOP in place. Set up hyd actuator and run preliminary test. Run and record BOP test for AOGCC.	20
10-Aug	Trip 3 7/8-in bit to bottom and drill out aluminum float shoe. Drill to 1024 and conduct formation leak test per AOGCC. Drill to 1078….basement rock at about 1040? Trip bit from hole.	20
11-Aug	Tricone bit is very worn so install 3 7/8-in PDC bit and trip to bottom. Drill to 1223 ft and pull bit back into HW casing.	20
12-Aug	Trip to bottom and drill to 1249 ft…very slow drilling. Circulate well and trip out bit. Get rig set up for wireline coring and trip core rods to 980 ft.	20
13-Aug	Trip core rods to bottom, pump down inner-tube, and core from 1249 ft to 1294 ft thru biotite shist and other metasedimentary basement rock. Fill well with abandonment mud and pull core rods from well.	20
14-Aug	Set up for logging and collect geophysical and temperature logs from well. Run capped BQ rods to 1295 ft and fill with water. Begin moving equipment from site.	20

Alaska Center for Energy and Power
2012 Pilgrim Hot Springs Well Drilling Logs

BEGIN WORK ON PS-12-9, PERMIT NO.: 212-126		
15-Aug	Run tremie pipe in annular area to 160 ft and cement top of hole. Remove BOP and flanges. Begin building trail and running water line to site 12-3. Move rig pallet to site.	20
16-Aug	Use BSNC skid-steer to begin moving equipment onto 12-3 site. Very soft and muddy. Lay turf mats in worst spots.	20
17-Aug	Finish moving equipment and setting up site. Drill and set 5 ft of 10-in surface casing.	20
18-Aug	Drill 9 7/8-in hole to 144 ft. Trip out pipe and run geophysical logs.	20
19-Aug	Begin running 6-in casing but it stops at 30 ft. Pull casing and ream well to bottom. Trip out and run 6-in casing to 144 ft. Trip tremie to annular bottom and mix and pump cement.	20
20-Aug	Well flange to casing, install knife valve, and install diverter system. Trip 5 5/8-in tricone to bottom and drill to 263 ft. Trip pipe from well.	20
21-Aug	Install chisel-tooth tricone bit and drill to 423 ft. Very hard drilling in spots.Trip pipe from well.	20
22-Aug	Trip pipe to bottom and drill to 723 ft. Pull pipe.	20
23-Aug	Trip pipe to bottom w/o problem and drill to 983 ft. Still drilling numerous hard zones.	20
24-Aug	Trip pipe to bottom and monitor mud temp when ciculation starts (145 F max). Drill to 1133 thru varying hard and soft layers. Drills/looks like basement rock at 1083 ft. Trip pipe from well.	20
25-Aug	Trip pipe in hole but have to circulate every 40 ft from 700 ft to 1033 ft then ream to bottom. Drill to 1183…..very slow drilling through basement rock. Trip pipe from well.	20
26-Aug	Run steel to 860 ft and ream to bottom. Thin mud and trip rods from well. Begin geophysical logging but caliper tool becomes stuck at 1065 ft. Trip drill steel into hole to try and wash out logging tool but can't get it washed down to that depth. Pull pipe.	20
27-Aug	Run BQ rods with reaming shoe on bottom to 993 ft. Mix and circulate fresh mud from that point but discover rods are stuck when done circulating….still have perfect circ. Decide to leave rods at this depth rather than trying further to retrieve so that we can at least get temp logs to this depth. Further retrieval efforts will likely result in fractured rods and total loss of the well.	20
28-Aug	Cut logging cable. Circulate fluid thru rods. Mix and pump cement thru rods followed by rubber cement plug and 130 gallons fresh water. Begin moving equipment to town.	20
29-Aug	Well begins flowing 150-200 gpm hot water from annular area. Run tremie into annular and kill flow with heavy mud. Run tremie to 126 ft, mix and pump cement in annular.	20
DRILLING ACTIVITY SUSPENDED		
30-Aug	Begin moving equipment from site to runway with skid-steer. Weather conditions are horrible and everything is a total quagmire. Begin moving items to Nome at day's end.	20
31-Aug	Cleaning, packing, moving equipment from site to runway and from runway to Nome. With exception of what will be left in Nome for final P&A of wells next year (PU truck, white trailer, ATV, and ATV trailer) all items are moved to Northland to catch early Oct barge south.	20
1-Sep	Continue cleaning, packing and moving. Return skid-steer and ATVs to BSNC.	20
2-Sep	Continue cleaning, packing, and moving equipment to Nome.	20
3-Sep	Continue cleaning, packing, and moving equipment to Nome.	20
4-Sep	Make final Pilgrim-Nome run with equipment. Finish loading conex box for ACEP, make trash run, turn in rental vehicles, and leave truck, trailer, and ATV at BSNC Icy View yard .	20
5-Sep	Crews fly from Nome to Denver. END OF PROJECT.	
Sep 16 - Sep 21	Art and helper return to Nome to rehead logging cable, move equipment to Pilgrim, and collect gamma and equilibrated temperature logs from the 12-3 well.	

PS13-1 Drilling Logs

Date	Log
7-Sep-13	Auger conductor hole
8-Sep-13	Drive conductor to 20 feet below GL
9-Sep-13	Transport drill rod to drill pad. Install drag bit. Mix mud and begin circulating. Bit at 25' at midnight shift change
10-Sep-13	Continue drilling with 9 7/8" drag bit. Reach 140' at 06:40. Circulate hole for two hours. 09:45 finish tripping out. On site geologist elogs hole. 18-45':fine to med sand, grey and black. 45-76': Sand, black with some clay. 76 to 85': Course sand with some clay. 85-95': Fine sand with some clay. 95-110': fine and med sand. 110-120': sand, course with some gravel. Mud is hotter than before. 120-140': Sandy gravel, small. Tool Up 12 1/4" bit and collar. Enlarge hole to depth of 100' . As crew was adding joint, they began hearing a grinding noise like bearing is grinding. Tripped back up to shoe and discussed possible plan of action.
11-Sep-13	Night crew disassembled drill head housing, found cracked bearing and shipped back to ANC for repair. Drilling suspended until rig is repaired.
12-Sep-13	Drilling suspended due to breakdown
13-Sep-13	Drilling is still suspended. MW drilling has brought an older comparable size drill rig to the site to temporarily drill until the Schram rig is repaired early next week. Late afternoon, drilling resumed with T-4 rig. 12 1/4" hole rilled to 128'
14-Sep-13	Completed drilling the 12 1/4" hole from 128' to 140'. Circulated and tripped out of hole. Attached 17 1/2" bit with 22" reaming cones. Drilled 22" hole to 38'
15-Sep-13	Drill 22" hole to 140". Circulate hole one hour. Trip out of hole.
16-Sep-13	Trip down 22" hole opener to 140" and circulate. Run 18" casing. Rig up to pump cement.
17-Sep-13	Run 1" tremi pipe down hole and mix 3 batches of 26 sacks cement, 200 gal water, and 7 qts sack of gel and pump down hole. Cement is to top of 24" conductor.
18-Sep-13	Demobe replacement rig, move off the pad, position main Schram rig over hole, prepare for pressure test.
19-Sep-13	Replace drilling mud in hole with Water, Cut and weld top plate on top of 18" casing and attached pressure guage. Pressure checked hole to 250 psi for 30 min using duplex pump. Test began at 6:19 PM. Pressure held at 260 psi. Trip back into hole with 9 7/8" drag bit w/ collars. Completed tripping 60' into hole with stabilizer plate on the collar to center bit in 18" casing.
20-Sep-13	Continue tripping down with stabalizer ring, then circulate to displace water with mud. Trip out, cut off stabalizer ring, trip back down. Drill down to 216' . At 216' encounter quartz and pyrite. Trip out to change drag bit to tricone bit. 140'-185'-gravel with some clay, intermitant cobbles. 185'-190'-gravel increasing with clay. 190'-217'-clays, gray. 216'- quarts, pyrite.
21-Sep-13	Joint down, hard drilling at 333-335. Drilling goes smothly for rest of shift. Shift change at 437'. Mud temp is 103 deg f. drilling has slowed, drilling through mud with some gravel. At 537' bit began to ball up, pulled back and circulate hole for one hour.
22-Sep-13	Cuttings are silty clay with some gravel. At 587' divert more flow to desander to reduce mud weight. Continuie adding joints and circulating down to 687'. Add on and mix more mud. By end of shift, drilling was down to 787 ft. Had to run desanders the entire time to keep sand content of the mud down .
23-Sep-13	Drilling goes routinly for morning shift. Continue drilling 9 7/8" to 889'. Afternoon shift drilled to 909, then had to remix mud after vis got too high. After getting the mud back in check. At 930' passed from clay to gravel. At end of shift drillin progressd to 949'.

24-Sep-13	Continue jointing down and circulating to 1029 feet. Mud weight and viscosity is getting too high. Afternoon crew got vis and weight under control. 1033' drilling gets rough. TD at 1038'
25-Sep-13	Continue tripping out hole. Circulate after each joint. Setup block from rotary head to hang loggin tools. At 9AM when logging attempted, the Kuster took only able to descend to 960ft with sinker bar. Terresat equipment only able to descend to 350 feet. Afternoon crew trips back in the hole with a mill tooth tricone bit for wiper run. Crew continued moving a lot of clay out of the pit as they added on and circulated. The afternoon crew was able to get to 725 feet. Overall, it went down smooth, but pulled a lot more clay out of the hole.
26-Sep-13	Night shift progress slowed down. They reported at times it was like drilling a completely new hole. They got to 905' at crew changover at noon. Day crew added ConDet to the mud to try and help reduce the get the clay out and reduce the vis. Reached TD at 20:40 and circulated for one hour. Begin tripping out of hole, remove 260' of drill rod which came out smooth.
27-Sep-13	Continue tripping out drill rod, finish at 6A.M. Begin e logging hole. E logging complete at 14:00, hole TD 1036.5 ft. Run 1008' of 2" pipe into hole and fill with water as a conduit to run continued temp logs over the next couple days as temperatures equilibriate.
28-Sep-13	During morning check in, drillers discovered that a joint on the 2" pipe failed and 987' of pipe fell into the hole. Try and feel around for pipe with sandline, unable ot locate it.
29-Sep-13	Continue trying to locate 2". Evac some of the mud out of the top 18" casing to try and see the top of the pipe.
30-Sep-13	Grab onto the 2" pipe with a wall sweep, secure it to top of casing. Log downhole temperatures through the 2" pipe.
1-Oct-13	Drilling suspended for scheduled drill crew break.
2-Oct-13	Drilling suspended for scheduled drill crew break.
3-Oct-13	Drilling suspended for scheduled drill crew break.
4-Oct-13	Drilling suspended for scheduled drill crew break.
5-Oct-13	Crew arives back on site and wet trips out the 2" pipe. After pulling 28 sticks out of the hole, no pipe was left. 11 sticks had broken off and were still in hole. The bottom couplings of the string that was removed from the hole showed signs of damage from vertical force.
6-Oct-13	Cut lip wall sweep guide was constructed onto a Bowen overshot. The 2" pipe was first encountered 127' below the top of casing. Each time the drillers tried to rotate onto the fish, it dropped deeper into the hole. They were never able to attach onto it.
7-Oct-13	A wall sweep assembly attached to B rod is constructed is constructed, but they were never able to attach onto it. They tripped out of the hole, and then tripped in with a button bit assembly. They pushed the fish own to 425 feet.
8-Oct-13	They encountered the fish again at 700 feet. From 705-720 feet, drillers worked to drive the fish down in the hole. At 725 feet the rotational torque becamse high and the decision was made to attach a washover overshot tool.
9-Oct-13	Fabrication of overshot took place. It was deployed at 7PM and when it reached 219 feet the assembly hung up, presumably in a clay formation. The tool was pulled out and modified to include mud circulation. A cut lip guide was also added per the recomendation of an oil field drilling aquintance. The tool was lowered into the hole
10-Oct-13	The tool was tripped into the hole again. It was a slow process due the extra circulation required to clean mud out of hole. The fish was tagged at 730 feet just before midnight
11-Oct-13	Drillers were able to rotate the overshot on the fish, and it felt like it was slipping through the fingers. The washover was allowed to descend as far as it would go under the weight of the drill rod. It reached a depth of 840'. At this time the assembly was tripped out of the hole, and tripping was completed in the late afternoon. It contained no fish. Activities were suspended pending further discussion of future plans.
12-Oct-13	Drilling suspended pending a decision on future activities.

13-Oct-13	Drilling suspended pending a decision on future activities.
14-Oct-13	Drilling suspended pending a decision on future activities.
15-Oct-13	Drilling suspended pending a decision on future activities.
16-Oct-13	Drilling suspended pending a decision on future activities.
17-Oct-13	Drilling suspended pending a decision on future activities.
18-Oct-13	Drilling suspended pending a decision on future activities.
19-Oct-13	Ream hole to 17.5 inches down to 260 feet with a pass with 14 3/4" and a pass with 17.5" Circulate hole
20-Oct-13	Backfill bottom of hole with sand up to 260 feet. Pump down concrete plug.
21-Oct-13	Allow plug to set, and run 17.5 inch bit down hole for wiper run. Cement began mixing with mud. Get rid of the mud that was in the hole that is polluted with concrete.
22-Oct-13	Continue getting rid of mud that is polluted with cement, and allow hole to flow artisian to clean hole out. Mix new batch of mud and continue wiper run and allow to circulate. Begin welding casing and screen.
23-Oct-13	Weld bottom 55 feet of casing and screen assembly with 5 foot tailpipe section on bottom and 50 foot stainless screen above it. Continue welding 14" casing above surface to surface. Install packer at 55 feet and set assembly against plug. Grout with bentonite from packer to 21 feet, then with cement to surface.
24-Oct-13	Water jet mud out of hole from depth of 240 feet. Displace mud out of well and continue developing with water. Well is flowing about 50 GPM. Clean up and move rig off of pad.

Appendix K
2013 Electronic Drilling Logs and Aquifer Modeling

Terrasat Inc. was contracted by the University of Alaska to perform the mud logging and electronic well logging of well PS13-1 during the 2013 drilling operations. As part of their services, their report uses the information obtained from these logs to identify productive aquifers and calculate potential production of these aquifers. This production calculation uses the Theis equation which relies on several inputs explained in the memo below. Subtle changes to these inputs can yield significant changes to the calculated hydraulic conductivity.

The Terrasat report has very useful information, especially related to the comparisons of the elogs and mud logs that are used to identify productive aquifers. We feel it is important not to focus too heavily on the calculated productivities of the aquifers, as this could lead to overly optimistic expectations. Aquifers testing is necessary to get accurate transmissivity values.

Chris Pike, Project Manager

August 2014

TERRASAT, Inc.

Memo

To: Gwen Holdman and Chris Pike

Alaska Center for Energy and Power

From: Dan

Date: March 11, 2015

Re: Addendum to Pilgrim Hot Springs report, Clarification of Assumptions about Aquifer Yield Calculations

---

TERRASAT provided estimations of aquifer yields using an equation formulated by Theis in 1935. This equation, shown in the appendix of our report, calculates drawdown in a confined aquifer, based on pumping rate, transmissivity, and a well function. The well function is based on the distance from the well, aquifer storitivity, pumping time, pumping rate and transmissivity of the aquifer. We assumed the following values:

Distance from the well (**r**) is the radius of the casing. This value provides the maximum drawdown at the well, and thus the maximum aquifer yield from the well.

Storativity, or storage coefficient, typically ranges from 0.005 to 0.0005 for confined aquifers. Todd, and Mays, 2004, P. 58. We estimated storativity by multiplying aquifer thickness times 2.1×10^{-6} (unitless). This equation is provided by Kasenow, 2010, page 111. We choose this method so that our values are best estimates for each aquifer.

Time was assumed to be 365 days, continuous pumping. Continuous pumping assumes the aquifer does not fully recover during the pumping period. As a comparison, a domestic water well may pump for minutes to an hour and shut off. During the shut off period, the aquifer typically recovers or recharges fully. By assuming continuous pumping for an entire year, we are calculating a minimum yield for the well.

Transmissivity is defined as k (**hydraulic conductivity**) * **aquifer thickness**. Aquifer thickness was determined from the geophysical logs combined with the drilling logs. K, the hydraulic conductivity of the aquifer, is typically derived by conducting an aquifer flow test while measuring drawdown. Since aquifer test results are not available, we made the assumption that the aquifers behave either like fine-grained sand or medium-grained sand. We used average values from a text book for these two grain sizes and thus calculated a range of aquifer yields. The following table, from Batu, 1998, p . 35, is the source of our average hydraulic conductivities (refer to table 2-2 on next page).

We used these parameters with the Theis equation and iterated well yield until the drawdown matched the available drawdown in the well, considering a pump setting above the preferred screen zone.

The text book values show that hydraulic conductivity ranges over 3 to 4 orders of magnitude. That is why we recommend aquifer testing to get more accurate values of transmissivity and to verify if the aquifers behave as a Theis confined aquifer. Other potential aquifer types are confined with aquitard leakage or aquitard storage, or even various rock fracture configurations. Knowing how the aquifer behaves allows for a better estimate of yield.

Bibliography

Batu, Vedat, 1998, Aquifer Hydraulics, A comprehensive Guide to Hydrogeologic Data Analysis, John Wiley and Sons.

Kasenow, Michael, 2010, *Applied Ground-Water Hydrology and Well Hydraulics*, 3rd Ed.

Theis, Charles V. (1935). "The relation between the lowering of the piezometric surface and the rate and duration of discharge of a well using ground-water storage". *Transactions, American Geophysical Union* **16**: 519–524.

Todd, D. and Mays, L., 2004, Groundwater Hydrology, 3rd Ed. John Wiley and Sons.

TABLE 2-2 Hydraulic Conducitivity of Porous Materials

Group	Porous Material	Number of Analysis	Range of Hydraulic Conductivity, K (cm/s)	Arithmetic Mean Average Hydraulic Conductivity, K_{av} (cm/s)
Igneous rocks	Weathered granite	7	$(3.3–52) \times 10^{-4}$	1.65×10^{-3}
	Weathered gabbro	4	$(0.5–3.8) \times 10^{-4}$	1.98×10^{-4}
	Basalt	93	$(0.2–4250) \times 10^{-6}$	9.45×10^{-6}
Sedimentary materials	Sandstone (fine)	20	$(0.5–2270) \times 10^{-6}$	3.31×10^{-4}
	Siltstone	8	$(0.1–142) \times 10^{-8}$	1.9×10^{-7}
	Sand (fine)	159	$(0.2–189) \times 10^{-4}$	2.28×10^{-3}
	Sand (medium)	255	$(0.9–567) \times 10^{-4}$	1.65×10^{-2}
	Sand (coarse)	158	$(0.9–6610) \times 10^{-4}$	5.20×10^{-2}
	Gravel	40	$(0.3–31.2) \times 10^{-1}$	4.03×10^{-1}
	Silt	39	$(0.09–7090) \times 10^{-7}$	2.83×10^{-5}
	Clay	19	$(0.1–47) \times 10^{-8}$	9.00×10^{-8}
Metamorphic rocks	Schist	17	$(0.002–1130) \times 10^{-6}$	1.90×10^{-4}

Source: After Morris and Johnson (1967) and Mercer et al. (1982).

Source: Batu, V, 1998, p. 35.

TERRASAT, INC.
4203 Iowa Dr. Anchorage, AK 99517 (907) 344-9370 fax (907) 243-7870
Geological Consulting • Environmental Restoration • Regulatory Compliance

Pilgrim Hot Springs Geothermal Investigation Report

For
The Alaska Center for Energy and Power
Fairbanks, Alaska

Prepared For:
Gwen Holdmann, Director
Alaska Center for Energy and Power
University of Alaska
Physical Address: 814 Alumni Dr.
Mailing Address: PO Box 755910
Fairbanks, AK 99775-5910

Prepared By:
TERRASAT, Inc.
4203 Iowa Dr.
Anchorage, AK 99517

May 13, 2014

©Copyright TERRASAT, Inc. 2014

Table Of Contents

1. Introduction 1
2. Location and Setting 2
3. Site History 2
4. Methods 2
  4.1 Fluid Temperature and Resistivity 3
  4.2 Caliper 3
  4.3 Spontaneous Potential 4
  4.4 Single Point Resistance 4
  4.5 Normal Resistivity 5
  4.6 Natural Gamma 5
5 Findings 6
  5.1 PS-13-1 6
    5.1.1 PS-13-1 Introduction 6
    5.1.2 PS-13-1 Deep Aquifer 7
    5.1.3 PS-13-1 Middle Aquifer 8
    5.1.4 PS-13-1 Deeper Shallow Aquifer 8
    5.1.5 PS-13-1 Shallow Aquifer 9
    5.1.6 PS-13-1 Current Screened Interval 9
  5.2 PS4 10
6 Conclusions 11
  6.1 Screening Interval Conclusions 11
7. Disclaimer 13

Appendices

Appendix A – Field Well Log
Appendix B – Geophysical Well Logs
Appendix C- Field Notes
Appendix D – Theis Calculations

1. Introduction

TERRASAT, Inc. (TERRASAT) was retained by the Alaska Center for Energy and Power (ACEP) to field log borehole cuttings, conduct geophysical logging, interpret geophysical logs, and suggest screening intervals for optimum water production.

TERRASAT logged the well cuttings using the Unified Soil Classification System (U.S.C.S), which includes a description of: color, estimated percentage gravel, sand, silt, and clay, angularity of grains, grain size, a U.S.C.S designator, estimated water content, and other notable conditions. This method is applied for unconsolidated materials and can assist with geologic interpretation of aquifer characteristics. Cuttings were collected using a stainless steel sieve affixed to an extension pole and sampled from a discharge tube.

In addition to physically logging field cuttings, the well was geophysically logged using natural gamma, electrical resistivity, single point resistance, fluid resistivity, fluid temperature, and caliper probes. The natural gamma probe assists in determining the lithologic boundaries and determines the relative silt/clay content. The resistivity probe differentiates lithologic units, such as sand and gravel versus clay and shale. Single point resistance was employed to determine the depths of contacts for the underlying stratigraphy. Fluid resistivity and temperature were used to provide water quality information about the aquifers, aquifer properties, and if significant horizontal fluid movement occurs in the aquifer. Finally, the caliper probe was employed to determine the variability in size of the borehole and aid in the interpretation of the resistivity logs.

With the information gathered from the field and geophysical logging, screen settings determinations were made to provide the largest quantity and hottest water available from the well.

TERRASAT estimated the potential yields for each of four major aquifers. The aquifers were identified using the natural gamma log, the electrical resistivity and the single point resistance. Temperature, temperature differential and fluid conductivity logs were used to determine the zones within the aquifer where flow is expected to be the highest. The results were combined to identify the best screen settings, for maximum production.

Further, an additional well, termed PS4, was geophysically logged while onsite using the natural gamma, temperature, and resistivity probes.

The purpose of this investigation was to provide information regarding the highest temperature water producing zones and to recommend screen placement for optimum water production and geothermal heat.

2. Location and Setting

Pilgrim Hot springs is located approximately 60 miles northeast of Nome, Alaska on the Seward Peninsula at latitude 65.093°, longitude -164.9219°. Situated in the Pilgrim River Valley, the Pilgrim Hot springs have been a known geothermal resource since the late 1800s during the Nome gold rush.

3. Site History

Pilgrim Hot springs was initially used as a recreational site for gold miners during the late 1800s and was known at the time as "Kruzgamepa Hot Springs". It was purchased by Henry Bekus and hosted a dance hall, spa baths, a roadhouse, and a saloon. In 1908, the saloon burned down and the property was later transferred to the Catholic Church.

The Catholic Church built a mission and orphanage in 1917, run by Father Bellarmine Lafortune, after an influenza outbreak in Nome, AK. The orphanage was operational until 1941. From 1942 to 1943, during WWII, the United States Army housed troops at the Pilgrim Hot springs.

Pilgrim Hot springs was added to the National Register of Historic Places in 1977, and was considered, at the time, the most remote national park in the United States.

As early as 1917, the USGS had indicated that Pilgrim Hot springs might be an important geothermal target (Waring, 1917). In 1979, the University of Fairbanks Geophysical Institute conducted bedrock mapping, geophysical surveying, analysis and integration of field data, and preparation of a report setting forth the findings of the investigations.

The University of Alaska Fairbanks continued research at the Pilgrim Hot springs until 2013.

In 2010, Unaatuq, LLC became owner of the Pilgrim Hot Springs.

4. Methods

TERRASAT, Inc. employed borehole geophysical logging techniques to determine the optimum screen placement within well PS-13-1. Maximum heat and water production, as well as cleanliness of the producing sedimentary layers were the

determining factors in deciding screen placement. To identify these necessary features, TERRASAT used the following down-hole geophysical probes:

- Fluid Temperature
- Fluid Resistivity
- Caliper
- Single Point Resistance
- Spontaneous Potential
- Normal Resistivity (16 and 64 in)
- Natural Gamma

The probes were lowered down or raised up the well with a wench and pulley system, depending on the probe. The probe readings were gathered and recorded on a laptop using Mount Sopris Instruments' Logger software. The following is a brief description of what each probe measures, how it is used in the field, and what information can be inferred from the data it gathered.

4.1 Fluid Temperature and Resistivity

The fluid temperature/resistivity probe is used to measure the change in temperature and resistivity of the formation waters at varying depths in the well. The probe is lowered down the borehole at a rate of 8 ft/min, before other probes are deployed; at least 24 hour after drilling is complete, to allow borehole water to equilibrate with the formation waters. Information gathered from this probe allows the interpretation of water bearing zones, a relative estimate of water flow, and the influence of salinity from water bearing strata. Three geophysical logs are produced from this probe: a temperature log, a temperature differential log, and a fluid resistivity log. The temperature log compares water temperature *vs.* depth. The differential temperature log compares the temperature reading taken at any given point with the measurements taken before it. Both logs are used to detect water flow within the well. Areas within the well with a high water flow will be evidenced by a sharp change in temperature, warmer or cooler. An area of high water flow is indicative of an aquifer. In cases such as at Pilgrim Hot Springs, the fluid temperature probe can also be used to determine which aquifers contain the warmest water due to hydrothermal heat.

4.2 Caliper

The caliper probe is used to measure the well diameter in an uncased well, using 1-4 caliper arms that fold out upward on a pivot at the top of each arm. The probe is lowered closed down the well, engaged at the bottom of the well, and hauled up the well at a rate of 15 ft /min. As the probe ascends up the well, the caliper arms

open and close as the borehole widens and narrows and the borehole diameter is recorded. The caliper probe is only useful on uncased wells. If a well is to be cased, the caliper probe should be run before the well is cased. Borehole diameter is important in interpreting the logs created by many other geophysical probes, including spontaneous potential, single point resistivity, normal resistivity, and gamma probes.

4.3 Spontaneous Potential

The spontaneous potential probe can only be used in an uncased well. Casing will skew any measurements taken. The probe should be raised up the borehole at 15 ft/min. As it is raised, it measures the spontaneous potential or voltages that develop at the contacts between clay beds and sand beds or other dissimilar rock types during drilling. These spontaneous potentials or voltages are due to electrochemical, electrokinetic or streaming potentials, and redox effects. Electrochemical effects, the main cause of natural potentials in boreholes, result from the migration of ions from concentrated to more dilute solutions. When the fluid column in a borehole is fresher than the formation water, the spontaneous potential opposite sand beds is negative. When the fluid column in a borehole is more saline than the formation water, the spontaneous potential opposite sand beds is positive. If the fluid in the fluid column and the fluid in the formation are of the same salinity, a straight line spontaneous potential will be logged. Thus, the salinity of the fluid column in the borehole in comparison to the surrounding formation can be derived from the spontaneous potential log, as can the lithological boundaries. These contacts are located on the spontaneous potential logs at the point of curve inflection. Noisy intervals of spontaneous potential may be caused by streaming potential and indicative of depths where water is flowing into or out of a borehole. When possible a spontaneous potential probe should be used in conjunction with gamma probes and temperature probes. The gamma and temperature probes will assist with identification of sand layers areas where water flows into the borehole respectively.

4.4 Single Point Resistance

The single point resistance probe can only be used in an uncased well. Casing will skew any measurements taken. The probe should be raised up the borehole at 15 ft/min. As it is raised it measures the resistance, in ohms, between two electrodes, typically one with in the borehole and one on the surface, but sometimes between two within the borehole. Because the probe does not take into account the length or cross sectional area of the electrical currents flow path when the measurement is made, no intrinsic characteristics of the lithological layers, or fluid within the pore spaces or fractures can be determined. However, of the area surrounding the probe from which the resistance measurements are taken, the radius of influence, the measurements are predominately influence by the material closest to the lower electrode. Therefore, an electrode closer in diameter to that of the borehole is more desirable, because it will be less affected

by the empty space in the borehole and more by the surrounding lithological units. For this reason the single point resistance probe should be used in conjunction with a caliper probe for a more accurate interpretation of the log created. The changes in resistance with depth are used to infer the boundaries of the various lithological units within the borehole.

4.5 Normal Resistivity

The normal resistivity probe can only be used in an uncased well. Casing will skew any measurements taken. The probe should be raised up the borehole at 15ft/min. As it is raised, it measures the resistivity of the material including fluid and lithological units in the borehole. Depending on the spacing of the electrodes on the probe, the resistivity measurements include the material farther into the formation. The radius of the volume of investigation is approximately twice the distance between the current inducing electrode, and the voltage measuring potential electrode. The spacing between the electrodes is typically 4, 8, 16, 32, or 64 inches, depending on the zone of interest in the formation. During mud drilling, the fluid circulated within the borehole causes mud to invade the formation. This invaded mud, and possibly some of the drilling mud is then caked to the walls of the borehole. The caked mud is then picked up by and included in the measurements from the normal resistivity probe. For this reason, electrode spacings of 16 and 64 inches should be used; the 16 inch spaced electrodes to investigate the mud invaded zone near the borehole walls, and the 64 inch spaced electrodes to investigate both the invaded zone and the natural formation beyond. As with the single point resistance probe, as a borehole narrows or widens, more or less, respectively, of the surrounding lithological units, compared to the empty space within the borehole, will be influential in the recorded readings. For this reason the normal resistivity probe should also be used in conjunction with a caliper probe for a more accurate interpretation of the log created. The changes in resistivity with depth are used to infer the boundaries of the various lithological units within the borehole. However, the accuracy of the normal resistivity probe is limited by the thickness of the lithological units measured. Lithological units thicker than the electrode spacing used can indicate a lower resistivity and thinner beds than reality. Likewise, units that are half has thick or less than the electrode spacing can indicate higher resistivity and thicker beds than reality. For this reason, a normal resistivity probe should be used in conjunction with a single point resistance probe when possible.

4.6 Natural Gamma

The Gamma probe can be used on a cased or uncased well. The probe should be raised up the borehole at 15 ft/min. As it is raised, it measures the total gamma radiation. The levels of gamma radiation within sediments can be correlated to grain coarseness and can be used to relatively delineate lithology. The radius of investigation is related to the energy of the radiation measured, the density of the

material through which the radiation must pass, and the design of the probe. Sodium iodide crystals within the probe are used to measure the radiation. Probes with larger crystals can measure lower radioactivity levels. A probe with a sufficiently sized crystal should be selected for the lithologies expected in the area of study. The density of the material through which the radiation must pass affects the length of the travel path and can reduce the gamma readings. Therefore, borehole diameter and well casing will reduce the readings, however if the casing thickness or borehole diameter remains constant this reduction effect is constant and can be ignored. In wells where casing thickness and size or borehole diameter change with depth, this effect will also fluctuate accordingly, and adjustments will have to be made when interpreting the log. The correction factor for gamma readings within a cased well varies nearly linearly from 1.141 for 0.0625 in. thick casing to 1.891 for 0.375 in. thick casing. Position of the probe within the borehole can also affect the gamma log. When lowering or raising a probe in a borehole, there is a potential for probes to naturally decentralized or run along the borehole wall, due to common vertical deviation in most boreholes. When a gamma probe is centralized within the borehole, a reduction in gamma readings will be introduced. While there is no way to eliminate this error, knowledge of it will account for possible differences in rerun gamma logs. The readings upon repeated runs will depend on how the probe happens to descend the well, whether centralized or decentralized at any given depth.

Gamma radiation levels vary naturally within sediments. The most significant, naturally occurring gamma-emitting radioisotopes are potassium-40 and the daughter products of uranium- thorium- decay series. Potassium is abundant in some feldspars that weather to clays. Uranium and thorium can also exist in clay due to adsorption and ion exchange. Lithological layers composed of fine-grained detrital sediments that contain abundant clay tend to be more radioactive than coarser-grained sediments. Layers of clay tend to be more radioactive than layers of silt, which will be more radioactive than layers of sand. This inverse relationship in radioactivity versus coarseness continues as grain size coarsens. There are exceptions to this, and knowledge of the local geology is needed to recognize these exceptions. Layers of coal, limestone, dolomite, and silicic igneous rocks may contain more radioactive isotopes. Natural gamma probes cannot distinguish between natural and anthropogenic radioactive materials.

5 Findings

5.1 PS-13-1

5.1.1 PS-13-1 Introduction

TERRASAT identified four main aquifers. We refer to them as: deep, middle, deeper shallow, and shallow. For the purpose of this section, estimated yields are made for the aquifers in the event they are screened in the future. These aquifers are not screened at the time of this report. Further, a water production estimate

is made for the current screened zone (screened in Fall 2013), from 188 ft to 238 ft below top of casing.

Water production potential in these aquifers is estimated using the Theis equation (Appendix D). The Theis equation assumes the following:

- The aquifer has infinite areal extent
- The aquifer is homogeneous, isotropic, and of uniform thickness
- The pumping well is fully or partially penetrating
- The flow to the pumping well is horizontal when the pumping well is fully penetrating
- The aquifer is nonleaky and confined
- The flow is unsteady
- Water is released instantaneously from storage with a decline of hydraulic head
- The diameter of the pumping well is very small so that storage in the well can be neglected

TERRASAT also assumes the following general assumptions for each aquifer:

1. The well is 14 inches in diameter
2. The average hydraulic conductivity is assumed to be associated with fine-grained sandy soils to medium-grained sand (aquifer matrix)
3. Pumping will be continuous for 360 days, for purposes of this calculation

5.1.2 PS-13-1 Deep Aquifer

The deep aquifer extends from 874 ft to 990 ft from top of casing. Temperatures range from 69° C to 73.8° C on 9-27-13, but increase with time. This area includes fractured schist below coarse sands interbedded with clay/silt. The estimated yield, based on the Theis model and the individual aquifer assumptions, provide a general hydrogeologic water production estimate. Final designs should be based on an actual aquifer test as this model does not meet all the assumptions in the Theis (1935) equation.

TERRASAT assumes the following for well design and aquifer properties:

- The aquifer thickness is 116 feet based on field and geophysical logs
- The screened interval is a total of 100 feet, with blanks over the silt/clay layers to prevent entrainment
- The aquifer is artesian with a potentiometric surface 5 feet above the top of casing (TOC), based on field observations
- The available drawdown is from 5 feet above the top of casing to 5 feet above the top of the aquifer, 869 feet below top of casing.

Based on these assumptions, TERRASAT estimates this aquifer will produce between 3049 to 10,450 gal/min for 360 days of continuous pumping.

5.1.3 PS-13-1 Middle Aquifer

The middle aquifer extends from 411 ft to 480 ft from top of casing. Temperatures range from 58.3° C to 59.7° C on 9-27-13, but increase with time. This area includes coarse sand with silt and some minor amounts of fine gravel. The estimated yield, based on the Theis model and the individual aquifer assumptions provide a general hydrogeologic water production estimate. Final designs should be based on an actual aquifer test. The hydraulic conductivity should be measured during the aquifer test.

TERRASAT assumes the following for well design and aquifer properties:

- The aquifer thickness is 69 feet based on field and geophysical logs
- The screened interval is a total of 69 feet
- The aquifer is artesian with a potentiometric surface 5 feet above the top of casing (TOC), based on field observations
- The available drawdown is from 5 feet above the top of casing to 5 feet above the top of the aquifer, 406 feet below top of casing.

Based on these assumptions, TERRASAT estimates this aquifer will produce between 983 to 3370 gal/min for 360 days of continuous pumping.

5.1.4 PS-13-1 Deeper Shallow Aquifer

A second, deeper, shallow aquifer is located from 213 ft to 352 from top of casing. Temperatures range from 58.7° C to 63.3° C on 9-27-13, but increase with time. This aquifer consists of fine gravels interbedded with coarse sand and silty sand. The estimated yield, based on the Theis model and the individual aquifer assumptions provide a general hydrogeologic water production estimate. Final designs should be based on an actual aquifer test. The average hydraulic conductivity should be measured during the aquifer test.

TERRASAT assumes the following for well design and aquifer properties:

- The aquifer thickness is 139 feet based on field and geophysical logs
- The screened interval is a total of 139 feet
- The aquifer is confined based on the geophysical log and field observations
- The available drawdown is from 30 feet below top of casing to 5 feet above the top of the aquifer, 208 feet below top of casing.

Based on these assumptions, TERRASAT estimates this aquifer will produce between 1015 to 3478 gal/min for 360 days of continuous pumping.

5.1.5 PS-13-1 Shallow Aquifer

The shallow aquifer extends from 55 ft to 175 ft from top of casing. Temperatures range from 47° C to 63.6° C on 9-27-13, but increase with time. This aquifer consists of interbedded gravels and sands from 55 ft to 130 ft from top of casing and silty sands grading into gravels from 130 to 175 ft from top of casing. The estimated yield, based on the Theis model and the individual aquifer assumptions provide a general hydrogeologic water production estimate. Final designs should be based on an actual aquifer test. The average hydraulic conductivity should be measured during the aquifer test.

TERRASAT assumes the following for well design and aquifer properties:

- The aquifer thickness is 120 feet based on field and geophysical logs
- The screened interval is a total of 120 feet
- The aquifer is unconfined with static water at 30 ft below top of casing
- The available drawdown is from 30 ft below top of casing to 5 feet above the top of the aquifer, 50 feet below top of casing.

Based on these assumptions, TERRASAT estimates this aquifer will produce between 210 to 721 gal/min for 360 days of continuous pumping. The yield of this aquifer could be increased if the uppermost portion is not screened, allowing additional drawdown.

5.1.6 PS-13-1 Current Screened Interval

The current screened interval is from 188 ft to 238 ft from top of casing. Temperatures range from 62.2° C to 63.4° C on 9-27-13, but increase with time. This aquifer grades from predominantly silty sand from 180 ft to 217 ft to fine gravel interbedded with coarse sand from 217 ft to 238 ft from top of casing. This aquifer extends down to 352 ft below top of casing. The estimated yields, based on the Theis model and the individual aquifer assumptions provide a general hydrogeologic water production estimate. Final designs should be based on an actual aquifer test. The average hydraulic conductivity should be measured during the aquifer test.

TERRASAT assumes the following for well design and aquifer properties:

- The aquifer thickness is 164 feet based on field and geophysical logs
- The screened interval is a total of 50 feet
- The aquifer is unconfined with static water at 30 ft below top of casing

- The available drawdown is from 30 ft below top of casing to 5 feet above the top of the screen, 183 feet below top of casing.

Based on these assumptions, TERRASAT estimates this aquifer will produce between 1053 to 3610 gal/min for 360 days of continuous pumping.

5.2 PS4

PS4 was drilled prior to the September 2013 investigation. Well PS4 is blocked at 471 feet below the flange on top of the casing stick up. This well was geophysically logged to 471 feet below the flange on top of the casing stick up. The flange was used as the reference point for the below ground measurements. This well flows artesian; however the geophysical results did not indicate a substantial confining layer. It is possible the source of the artesian water is below 471 feet and a well obstruction is encountered at 471 feet that will not allow the geophysical probe to be lowered further down, but does allow artesian water to flow upwards. PS4 consists of many sandy gravel and silty sand/gravel layers to 471 feet. The warmest water is found in the fine sand/gravel aquifer from approximately 386 ft to 460 ft, at 48° C. However, flowing water is observed from 335 ft to 460 ft based on the temperature probe.

Water production potential in this aquifer is estimated using the Theis equation (Appendix D) and its assumptions.

- The aquifer has infinite areal extent
- The aquifer is homogeneous, isotropic, and of uniform thickness
- The pumping well is fully or partially penetrating
- The flow to the pumping well is horizontal when the pumping well is fully penetrating
- The aquifer is unconfined
- The flow is unsteady
- Water is released instantaneously from storage with a decline of hydraulic head
- The diameter of the pumping well is very small so that storage in the well can be neglected

TERRASAT assumes the following for well design and aquifer properties:

- The well is 9 7/8 inches in diameter
- The aquifer material has the hydraulic conductivity of fine sand
- The aquifer thickness is 125 feet
- Pumping will be continuous for 360 days
- The aquifer is artesian with a potentiometric surface 5 feet above the (TOC), based on field observations

- The available drawdown is from 5 feet above the top of casing to 5 feet above the top of the aquifer, 330 feet below top of casing

Based on these assumptions, TERRASAT estimates this aquifer will produce 1420 gal/min for 360 days of continuous pumping.

6 Conclusions

PS-13-1 was drilled to 1036 feet below the (TOC) and encounters numerous aquifers and aquitards. Four aquifers were identified as water producing zones of interest, for screening, and show flowing water based on the temperature differential logs. They are described as deep, middle, deeper shallow, and shallow.

6.1 Screening Interval Conclusions

The following discussion about screening intervals and water production potential is an estimate that should be verified by aquifer testing. These screening intervals were selected from an interpretation of multiple geophysical log traces and field observations. The Theis (1935) equation was applied to estimate aquifer yield in an addition to selecting screen locations.

The deep aquifer, from 874 ft to 990 ft from top of casing, is the warmest aquifer and is comprised of fractured schist below coarse sands interbedded with clay/silt. Temperatures range from 69° C to 73.8° C on 9-27-13, but increase with time. Based on the Theis equation for confined aquifers and 100 ft of screen, this aquifer may produce between 3049 to 10,450 gal/min for 360 days of continuous pumping. Screens could be set in this interval, minus the two silty areas (approximately 16 feet total), with a higher slot size from 915 ft to 951 ft from top of casing, as it appears to be the most productive portion of the aquifer and the coarsest grained.

The middle aquifer, from 411 ft to 480 ft from top of casing, is comprised of coarse sand with silt and some minor amounts of gravel. Temperatures range from 58.3° C to 59.7° C on 9-27-13, but increase with time. Based on the Theis equation for confined aquifers and 69 ft of screen this aquifer may produce between 983 to 3370 gal/min for 360 days of continuous pumping. Screens could be set in this interval because water production appears abundant and geophysical logs suggest coarse-grained soil with flowing water.

The deeper shallow aquifer, from 213 ft to 352 ft from top of casing, is comprised of fine gravels interbedded with coarse sand and silty sand. Temperatures range from 58.7° C to 63.3° C on 9-27-13, but increase with time. Based on the Theis equation for confined aquifers and 139 ft of screen this aquifer may produce between 1015 to 3478 gal/min for 360 days of continuous pumping. Screens

could be set in this interval because water production appears abundant and geophysical logs show soil media associated with aquifer material.

The shallow aquifer extends, from 55 ft to 175 ft from top of casing, is comprised of interbedded gravels and sands from 55 ft to 130 ft from top of casing and silty sands grading into gravels from 130 ft to 175 ft from top of casing. Temperatures range from 47° C to 63.6° C on 9-27-13, but increase with time. Based on the Theis equation for unconfined aquifers and 120 ft of screen, this aquifer may produce between 210 to 721 gal/min for 360 days of continuous pumping. Screens could be set in this interval because water production appears abundant and geophysical logs show soil media associated with aquifer material.

Finally, the current screened interval, from 188 ft to 238 ft from top of casing, is comprised predominately silty sand from 188 to 217 ft from top of casing grading to fine gravel interbedded coarse sand from 217 ft to 238 ft from top of casing. Temperatures range from 62.2° C to 63.4° C on 9-27-13, but increase with time. This aquifer extends to 352 ft below the top of casing. Based on the Theis equation for unconfined aquifers and 50 ft of screen, this aquifer may produce between 1053 to 3610 gal/min for 360 days of continuous pumping.

In the future of this project, it may be desirable to screen this well at an interval capable of producing warmer water for geothermal energy. It is TERRASAT's opinion the deep aquifer, from 874 ft to 990 ft from top of casing, may produce the desired pump rate of 2000 gallons per minute and contains the warmest water of all the identified aquifers.

In the event a different screening interval is deemed necessary in the future, it is advisable to select only one aquifer. Screening numerous aquifers, to provide additional water, may cause dewatering in the upper screen zones and subsequent screen encrustation. Further, there will no longer be available drawdown at the upper screens, which in turn will cause loss of water production.

7. Disclaimer

The data presented in this report should be considered representative of the time of our site observations. Changes in the conditions of the site and aquifers can occur with the passage of time. The findings we have presented within this report are based on limited test data; they should not be construed as a definite conclusion about aquifer characteristics at the site. In the event that future studies encounter subsurface conditions that appear different from those we encountered, we should be advised so we can review those conditions and reconsider our interpretations.

Prepared By:	Approved By:
Jeremy Stariwat Project Geologist	Dan Young Principal Hydrogeologist

Field Well Log

Terrasat Geotechnical Boring Log

Location Sketch Map

Test Pit / Excavation # PS-13-1 **Page 1 of 11**

Project # / Name: Piligrim Hotsprings **Location: Nome, Ak**

Client: Alaska Center for Energy and Power
Date Excavated: 9/10/13

Excavation / Sampling Method: Mud Rotary / Discharge Tube

Logged By: Jeremy Stariwat

			-			
			5-			
			-			
			10-			
			-			
			15-			
			-			
			20-			
			-			
			25-	SP @ 25'		Black/white fine to medium clean sand, ~100%, subangular. Mostly fine
			-			grained. At 30 ft sand becomes coarse, same composition as previous.
			30-			
			-			
			35-			
			-			
			40-			
			-	SC @ 42'		Black/white sand, fine to coarse, ~75%, subangular. Light gray clay, ~25%
			45-			Small clay lense from 45 to 46 ft. Increasing clay after 46 ft to ~60%.
			-			
			50-			
			-			At 52 ft increase coarse, subangular sand, ~60%.
			55-			
			-			
			60-	CL @ 60'		Light brown clay, ~75% with black/white sand, ~25%, subangular, fine
			-			to coarse.
			65-			
			-			
			70-			
			-			
			75-			
			-			
			80-			
			-			
			85-			
			-			
			90-			
			-			
			95-	SP @ 96'		Black/white sand, fine to coarse, subangular, ~75%. Gray clay, ~25%.
			-			Sand is coarse after 100 ft. Some fine gravel mix, ~10% of sand portion.

Terrasat Geotechnical Boring Log

Location Sketch Map

Test Pit / Excavation # PS-13-1 **Page** 2 of 11

Project # / Name: Pilgrim Hotsprings

Location: Nome, AK

Client: Alaska Center for Energy and Power
Date Excavated: 9/10/13 to 140 ft and 9/20/13 from 140 ft

Excavation / Sampling Method: Mud Rotary / Discharge Tube

Logged By: Jeremy Stariwat

			-			
			105-			
			-			
			110-			
			-			
			115-			Possible geothermal water encounterd at 115 to 120 ft based on mud heat.
			-			
			120-			
			-			
			125-	GP/SP @ 125'		Fine gravel, subangular, 50%, white/black, and coarse sand, subangular
			-			50%, white/black.
			130-			
			-			
			135-			
			-			
			140-			No data from 140 ft to 160 ft. Drilled while geologist was offsite.
			-			
			145-			
			-			
			150-			
			-			
			155-			
			-			
			160-	CL @ 160'		Gravelly clay, ~70% gray clay and ~30% subrounded black/white fine gravel.
			-			Increasing coarse sand at ~170 ft.
			165-			
			-			
			170-			
			-			
			175-			
			-			
			180-	CL/GP @ 180'		Increasing angular gravel at ~185 ft, ~35 to 40 %.
			-			
			185-			
			-			
			190-			Increasing clay at 190 to 195 ft, 10% coarse sand/fine gravel. Some pyrite.
			-			
			195-			
			-			

Terrasat Geotechnical Boring Log

Location Sketch Map

Test Pit / Excavation # PS-13-1 **Page** 3 of 11

Project # / Name: Pilgrim Hotsprings

Location: Nome, AK

Client: Alaska Center for Energy and Power
Date Excavated: 9/20/13

Excavation / Sampling Method: Mud Rotary / Discharge Tube

Logged By: Jeremy Stariwat

Blow Counts	Test Results	Sample ID	Depth (ft. BGL)	U.S.C.S	Graphic Log	Lithologic Description
			-	CL		Continued. Same as previous description.
			205-			
			-			
			210-			
			-			
			215-			
			-			At ~217 ft drilling becomes very slow. Return is 90% gray clay with 10%
			220-			quartz and pyrite
			-			
			225-			
			-			
			230-			
			-			
			235-			
			-			
			240-			
			-			
			245-			
			-			Note: 217 - 300 logged and sampled by Chris Westburg of MW-Drilling
			250-			during day shift.
			-			
			255-			
			-			
			260-			
			-			
			265-			
			-			
			270-			
			-			
			275-			
			-			
			280-			
			-			
			285-			
			-			
			290-			
			-			
			295-			
			-			

Terrasat Geotechnical Boring Log

Location Sketch Map

Test Pit / Excavation # PS-13-1 **Page** 4 of 11

Project # / Name: Pilgrim Hotsprings **Location:** Nome, AK

Client: Alaska Center for Energy and Power
Date Excavated: 9/21/13

Excavation / Sampling Method: Mud Rotary / Discharge Tube

Logged By: Jeremy Stariwat

Blow Counts	Test Results	Sample ID	Depth (ft. BGL)	U.S.C.S	Graphic Log	Lithologic Description
			-	GW @ 300'		Black angular gravel, up to 1 inch in diameter, ~50%. ~30% coarse black
			305-			sand, angular. And ~20% fines (likely silt). Drilling difficult at 300 ft, likely
			-			due to cobbly/gravelly material. Gravel clasts appear to be friable sand
			310-	GW/CL @ 310'		stone. Gravel shows quartz clasts at 308 ft. Increasing brown clay at 310 ft.
			-			~30%, and less gravel, ~40%.
			315-			
			-			
			320-			Gravel becomes fine at ~322 ft.
			-			
			325-	SW/CL @ 325'		Black/white sands, ~60%, subrounded to subangular, coarse. Lithologies
			-	SP @ 327'		include: quartz, black schists, and pyrite. Light brown clay, low plasticity,
			330-			~40%. Moderate drilling speed.
			-			Black/white, poorly graded sand. Same lithology and sizes as previous,
			335-			~90% and ~10% clay. Cobbles from 330 to 336 ft.
			-			
			340-			
			-			
			345-	SW @ 345'		Increased clay to ~30%
			-			
			350-			Little to no quartz. Mostly schist. Fast drilling from 337 to 362 ft.
			-			
			355-			
			-			
			360-			
			-	SP @ 362'		Clean, coarse sands, same description as previous, ~95% and 5% fines.
			365-			Increased quartz content.
			-			
			370-			
			-			
			375-			
			-			
			380-			
			-	SP/GP @ 382'		Coarse sand and fine gravel. ~50%/50%. Same material as above.
			385-			
			-			
			390-			
			-			
			395-			
			-			

Terrasat Geotechnical Boring Log

Location Sketch Map

Test Pit / Excavation # PS-13-1 **Page** 5 of 11

Project # / Name: Pilgrim Hotsprings

Location: Nome, AK

Client: Alaska Center for Energy and Power
Date Excavated: 9/21/13

Excavation / Sampling Method: Mud Rotary / Discharge Tube

Logged By: Jeremy Stariwat

Blow Counts	Test Results	Sample ID	Depth (ft. BGL)	U.S.C.S	Graphic Log	Lithologic Description
			-			
			405-			
			-			
			410-			
			-			Note: from 417 ft to 537 ft, cuttings logged by Chris Westburg of MW-
			415-			Drilling during the day shift.
			-			
			420-			According to driller's log at 437 ft - "Mostly silty clay, some gravel, drilling
			-			fast (2.6 ft/min)"
			425-			
			-			
			430-			
			-	CL @ 437'		
			435-			
			-			
			440-			
			-			
			445-			
			-			
			450-			
			-			
			455-			
			-			
			460-			
			-			
			465-			
			-			
			470-			
			-			
			475-			
			-			
			480-			
			-			
			485-			
			-			
			490-			
			-			
			495-			
			-			

Terrasat Geotechnical Boring Log

Location Sketch Map

Test Pit / Excavation # PS-13-1 **Page** 6 of 11

Project # / Name: Pilgrim Hotsprings

Location: Nome, AK

Client: Alaska Center for Energy and Power
Date Excavated: 9/22/13

Excavation / Sampling Method: Mud Rotary / Discharge Tube

Logged By: Jeremy Stariwat

Blow Counts	Test Results	Sample ID	Depth (ft. BGL)	U.S.C.S	Graphic Log	Lithologic Description
			-			
			505-			
			-			
			510-			
			-			
			515-			
			-			
			520-			
			-			
			525-			
			-			
			530-			
			-			
			535-			
			-	CH @ 537'		Light gray high plasticity clay, ~95%. The remaining 5% is fine sand mixed
			540-			with a small amount of fine gravel. Fast drilling.
			-			
			545-			
			-			
			550-			
			-			
			555-			
			-			
			560-			
			-			At 562 ft gravels become apparent in mud. Subrounded to subangular, up
			565-			to 1 inch, ~5 to 10%. Gravel stops at ~570 ft.
			-			
			570-			
			-			
			575-			
			-			
			580-			
			-			
			585-			
			-			
			590-			Increased coarse sand / fine gravel. Subrounded to subangular, white/black
			-			~10 to 20%.
			595-			
			-			

Terrasat Geotechnical Boring Log

Location Sketch Map

Test Pit / Excavation # PS-13-1 **Page** 7 of 11

Project # / Name: Pilgrim Hotsprings **Location:** Nome, AK

Client: Alaska Center for Energy and Power
Date Excavated: 9/22/13

Excavation / Sampling Method: Mud Rotary / Discharge Tube

Logged By: Jeremy Stariwat

Blow Counts	Test Results	Sample ID	Depth (ft. BGL)	U.S.C.S	Graphic Log	Lithologic Description
			-			Gravel/sand decreases at 602 ft to ~1-2%. Small fine gravel layer at
			605-			605 ft.
			-			
			610			
			-			
			615-			
			-			
			620-			
			-			
			625-			
			-			
			630-			
			-			
			635-			
			-			Increased coarse sand / fine gravel at 628 ft, ~10 to 20%.
			640-			
			-			Increased coarse sand / fine gravel at 644 ft, ~30 to 40%, angular.
			645-	CH/SP @ 644'		
			-			
			650-			
			-			
			655-			
			-			
			660-			
			-			
			665-			
			-			
			670-			
			-			
			675-	CH @ 675'		At 6775 ft there is little to no coarse sand or fine gravel.
			-			
			680-			
			-			
			685-			
			-			
			690-			
			-			
			695-			
			-			

Terrasat Geotechnical Boring Log

Location Sketch Map

Test Pit / Excavation # PS-13-1 **Page** 8 **of** 11

Project # / Name: Pilgrim Hotsprings

Location: Nome, AK

Client: Alaska Center for Energy and Power
Date Excavated: 9/23/13

Excavation / Sampling Method: Mud Rotary / Discharge Tube

Logged By: Jeremy Stariwat

Blow Counts	Test Results	Sample ID	Depth (ft. BGL)	U.S.C.S	Graphic Log	Lithologic Description
			-			
			705-			
			-			
			710-			
			-			
			715-			
			-			
			720-			
			-			
			725-			
			-			
			730-			Note: From 687 to 787 ft Chris Westburg of MW-Drilling has logged and
			-			sampled during the day shift.
			735-			
			-			
			740-			
			-			
			745-			
			-			
			750-			
			-			
			755-			
			-			
			760-			
			-			
			765-			
			-			
			770-			
			-			
			775-			
			-			
			780-			
			-			
			785-			
			-			
			790-	CH @ 787'		Light gray high plasticity clay, ~100%. Temp @ 790' = 113 F
			-			
			795-			
			-			

Terrasat Geotechnical Boring Log

Location Sketch Map

Test Pit / Excavation # PS-13-1 **Page 9 of 11**

Project # / Name: Pilgrim Hotsprings

Location: Nome, AK

Client: Alaska Center for Energy and Power
Date Excavated: 9/23/13

Excavation / Sampling Method: Mud Rotary / Discharge Tube

Logged By:Jeremy Stariwat

Blow Counts	Test Results	Sample ID	ø	U.S.C.S	Graphic Log	Lithologic Description
			-	CH		Continued from previous page.
			805-			
			-			
			810-			Temp = 100.6 F
			-			
			815-			At ~815 ft clay becomes light brown.
			-			
			820-			Temp = 98.9 F
			-			
			825-			
			-			
			830-			Temp = 107 F
			-			
			835-			
			-			
			840-			Temp = 102.1 F
			-			
			845-			
			-			
			850-			Temp = 104.1 F
			-			
			855-			At ~855 ft, ~2 to 5 % fine gravel / coarse sand is encountered in the sample
			-			Angular, black/white.
			860-			Temp = 105.6 F
			-			
			865-			
			-			
			870-			Temp = 104.4 F
			-			
			875-			
			-			
			880-			Temp = 103.1 F
			-			
			885-			
			-			
			890-			
			-			
			895-			
			-			

Terrasat Geotechnical Boring Log

Location Sketch Map

Test Pit / Excavation # PS-13-1 **Page** 10 of 11

Project # / Name: Pilgrim Hotsprings

Location: Nome, AK

Client: Alaska Center for Energy and Power
Date Excavated: 9/24/13

Excavation / Sampling Method: Mud Rotary / Discharge Tube

Logged By: Jeremy Stariwat

Blow Counts	Test Results	Sample ID	Depth (ft. BGL)	U.S.C.S	Graphic Log	Lithologic Description
			-			
			905-			
			-			
			910-			Note: From 886 to 948 ft Chirs Westburg of MW-Drilling logged and
			-			sampled during the day shift.
			915-			
			-			
			920-			
			-			
			925-			
			-			
			930-			
			-			
			935-			
			-			
			940-			
			-			
			945-			
			-			
			950-	SW/CH @ 950'		Sand with clay. Sand is ~60%, clay is ~40%. Sand is subrounded to
			-			subangular, quartz and schist, black/white. Clay is gray.
			955-			
			-			
			960-			Temp = 116.8 F
			-			
			965-	SW @ 965'		Increased coarse sand from ~965 ft, ~75%.
			-			
			970-	SW/CH @ 970'		At ~970 ft, clay increases to ~40%. Temp = 117.5 F
			-			
			975-			
			-			
			980-	CH @ 980'		At ~980 ft clay increases to ~60 to 70%
			-			
			985-			
			-	SW/CH @ 987'		Sand increases at 987 ft, ~50%.
			990-			Temp = 111.5 F
			-			
			995-			
			-			Temp @ 1000 ft = 99.8 F

Terrasat Geotechnical Boring Log

Location Sketch Map

Test Pit / Excavation # PS-13-1 **Page** 11 of 11

Project # / Name: Pilgrim Hotsprings

Location: Nome, AK

Client: Alaska Center for Energy and Power
Date Excavated: 9/24/13

Excavation / Sampling Method: Mud Rotary / Discharge Tube

Logged By: Jeremy Stariwat

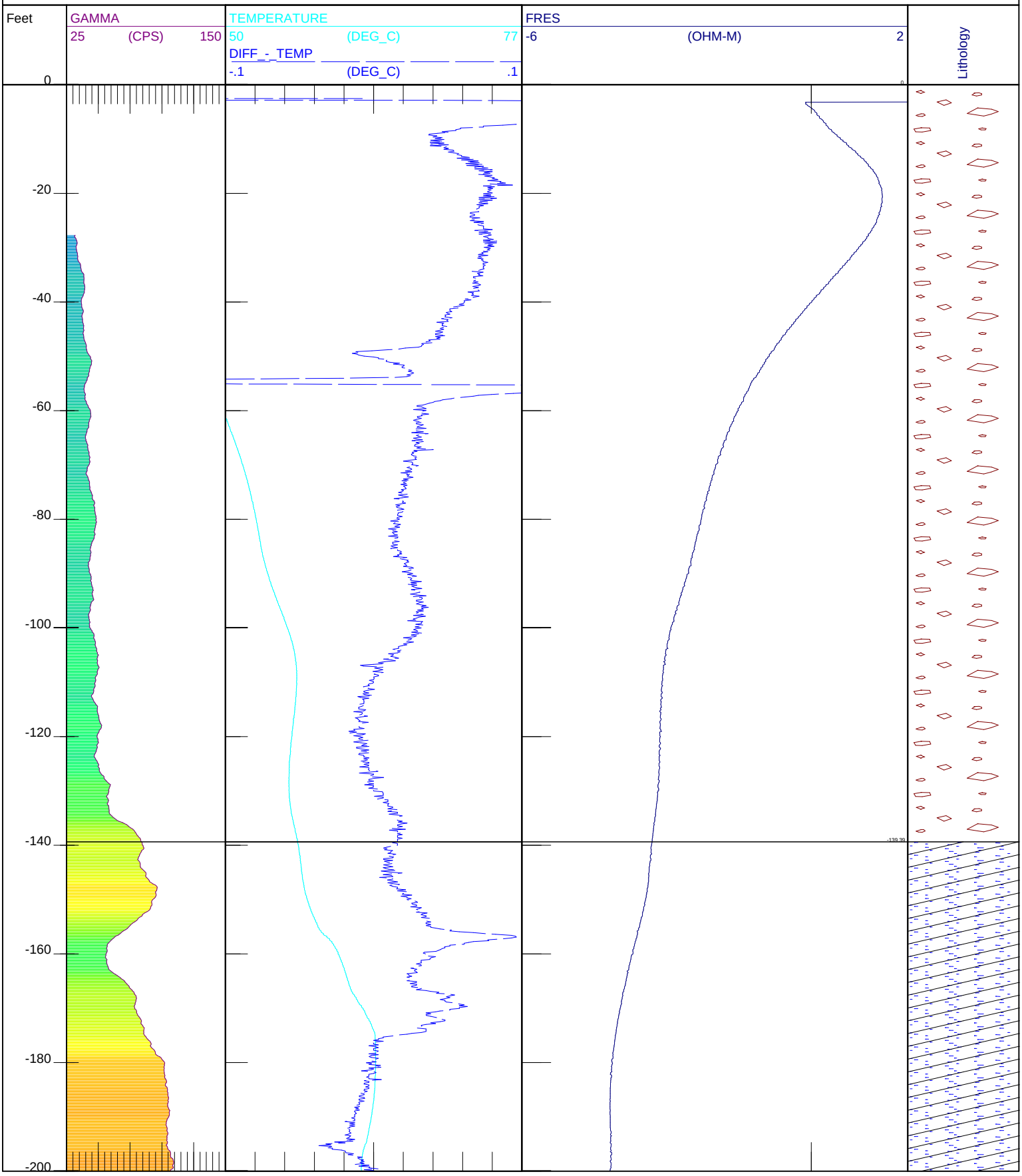
Blow Counts	Test Results	Sample ID	Depth (ft. BGL)	U.S.C.S	Graphic Log	Lithologic Description
			-			
			1005-			
			-			
			1010-	SW @ 1010'		Sand increases at ~1010 ft to ~65 to 70%, black/white, quartz and schist,
			-			rounded to subangular, medium to coarse grained. Temp = 106.1 F
			1015-			At 1014 ft cobbles are encountered based on drill rod response. However,
			-			cutting show clay and sand. The clay is likely residual.
			1020-			Temp = 107.1 F
			-			
			1025-			
			-			
			1030-			
			-			
			1035-			
			-			Total Depth = 1037 ft
			1040-			
			-			
			1045-			
			-			
			1050-			
			-			
			1055-			
			-			
			1060-			
			-			
			1065-			
			-			
			1070-			
			-			
			1075-			
			-			
			1080-			
			-			
			1085-			
			-			
			1090-			
			-			
			1095-			
			-			

Geophysical Well Logs

Well Name: PS-13-1 Gamma - Temperature - Fluid Log
Location: Pilgrim Hotsprings - Alaska
Reference: Top of casing

To of casing is 3.2 above current ground surface.
Logged by Jeremy Stariwat on 9/27/13.

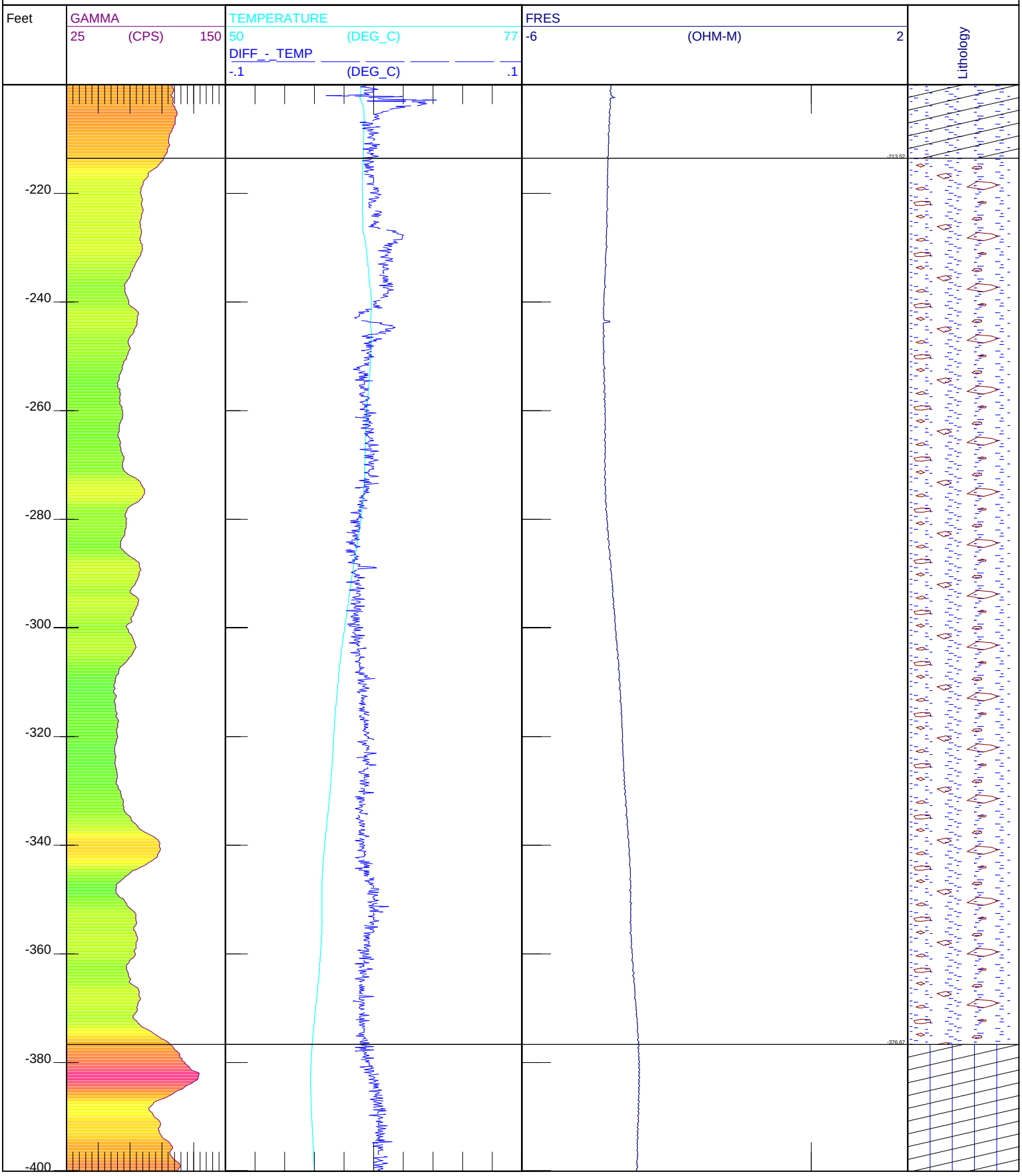
Note: Fluid conductivity is based on fluid resistivity readings. Fluid resisitivty was calibrated to attain measurements from 2 to 80 ohm-m. Due to the low fluid resistivity in the well water, likely less than 1 ohm-m, both fluid resistivity and conductivity measurements do not show true values. However, the measurements are useful for determining water flow when comparisons are made relative.



Well Name: PS-13-1 Gamma - Temperature - Fluid Log
Location: Pilgrim Hotsprings - Alaska
Reference: Top of casing

To of casing is 3.2 above current ground surface.
Logged by Jeremy Stariwat on 9/27/13.

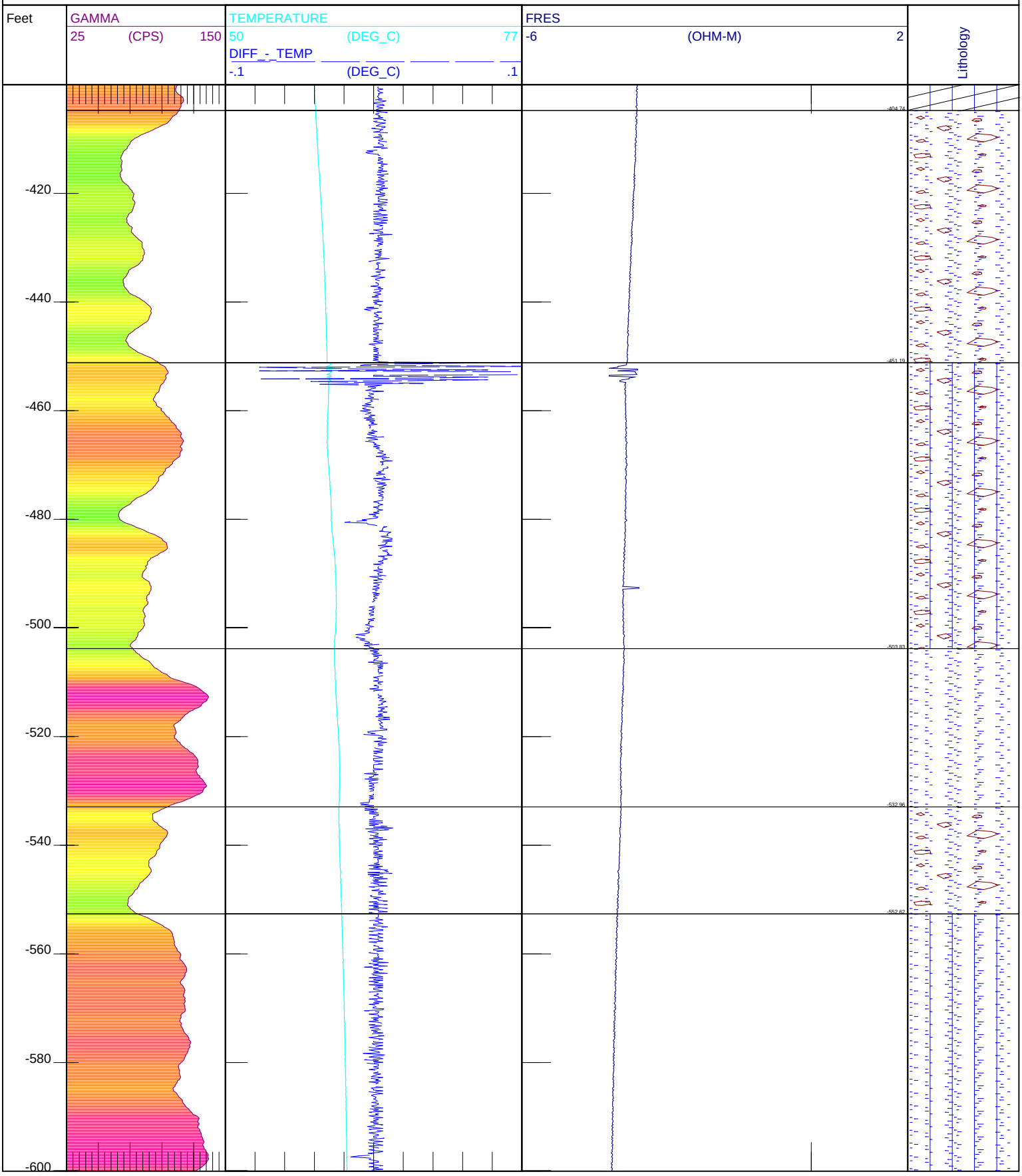
Note: Fluid conductivity is based on fluid resistivity readings. Fluid resisitivty was calibrated to attain measurements from 2 to 80 ohm-m. Due to the low fluid resistivity in the well water, likely less than 1 ohm-m, both fluid resistivity and conductivity measurements do not show true values. However, the measurements are useful for determining water flow when comparisons are made relative.



Well Name: PS-13-1 Gamma - Temperature - Fluid Log
Location: Pilgrim Hotsprings - Alaska
Reference: Top of casing

To of casing is 3.2 above current ground surface.
Logged by Jeremy Stariwat on 9/27/13.

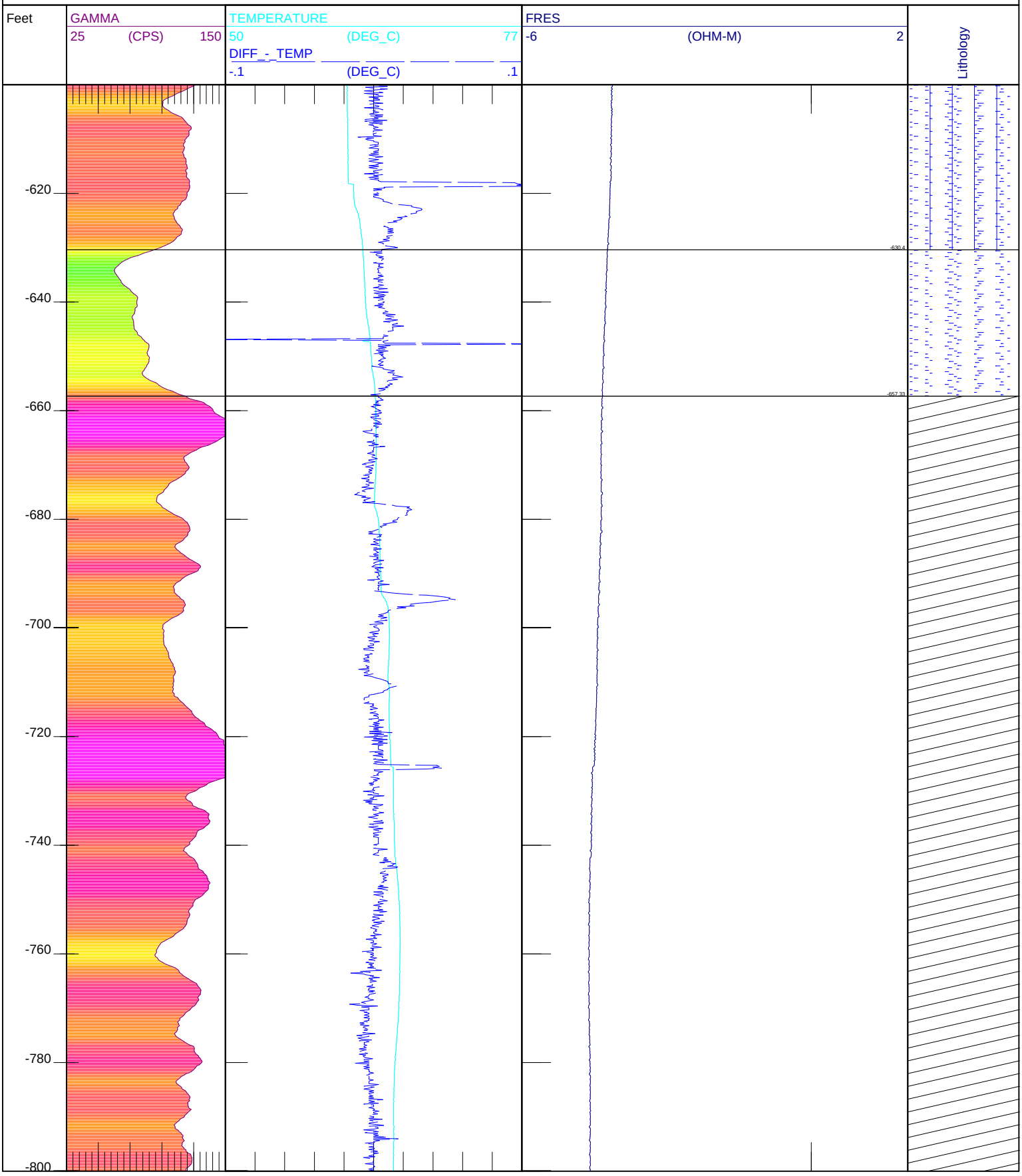
Note: Fluid conductivity is based on fluid resistivity readings. Fluid resisitivty was calibrated to attain measurements from 2 to 80 ohm-m. Due to the low fluid resistivity in the well water, likely less than 1 ohm-m, both fluid resistivity and conductivity measurements do not show true values. However, the measurements are useful for determining water flow when comparisons are made relative.



Well Name: PS-13-1 Gamma - Temperature - Fluid Log
Location: Pilgrim Hotsprings - Alaska
Reference: Top of casing

To of casing is 3.2 above current ground surface.
Logged by Jeremy Stariwat on 9/27/13.

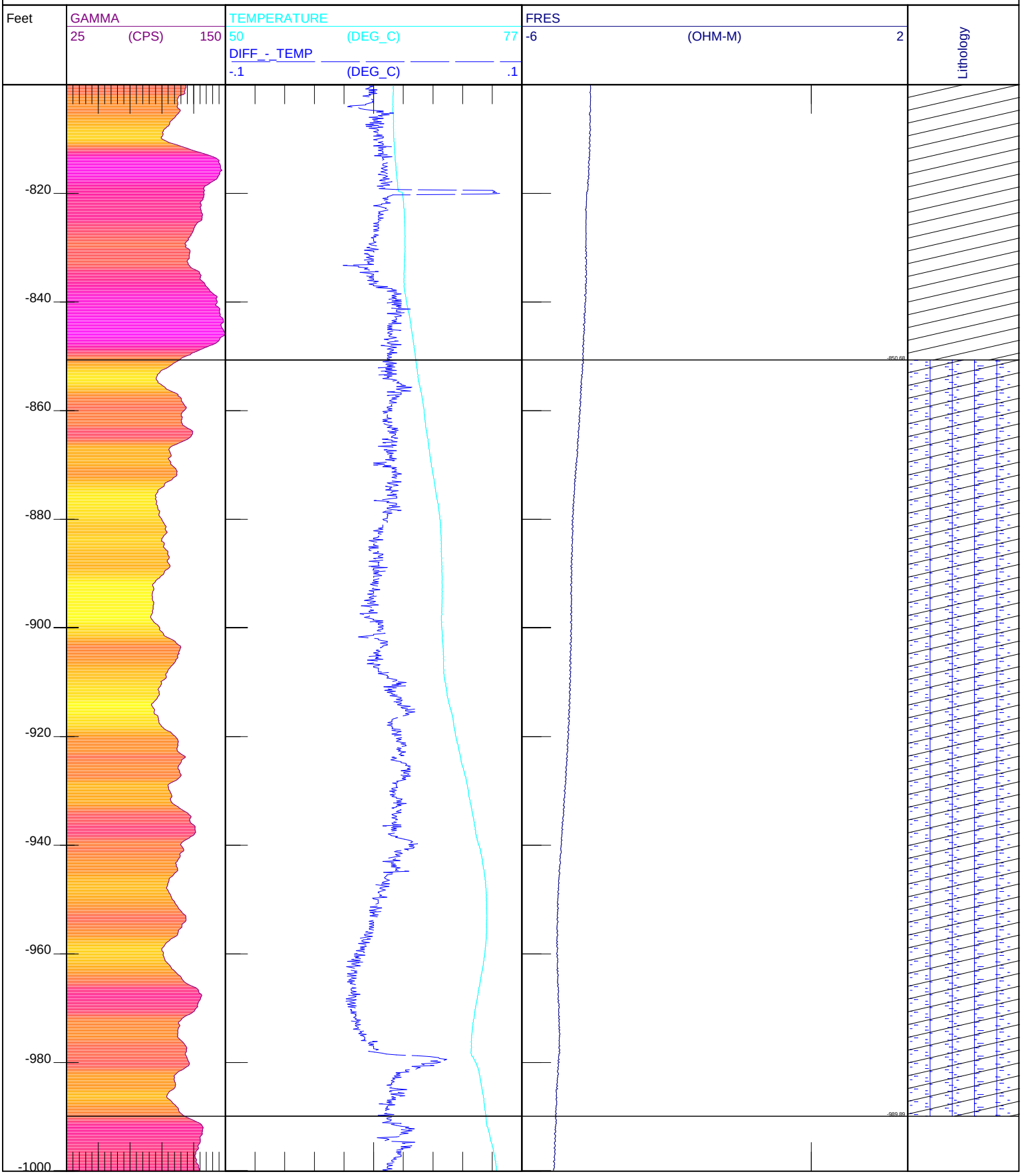
Note: Fluid conductivity is based on fluid resistivity readings. Fluid resisitivty was calibrated to attain measurements from 2 to 80 ohm-m. Due to the low fluid resistivity in the well water, likely less than 1 ohm-m, both fluid resistivity and conductivity measurements do not show true values. However, the measurements are useful for determining water flow when comparisons are made relative.



Well Name: PS-13-1 Gamma - Temperature - Fluid Log
Location: Pilgrim Hotsprings - Alaska
Reference: Top of casing

To of casing is 3.2 above current ground surface.
Logged by Jeremy Stariwat on 9/27/13.

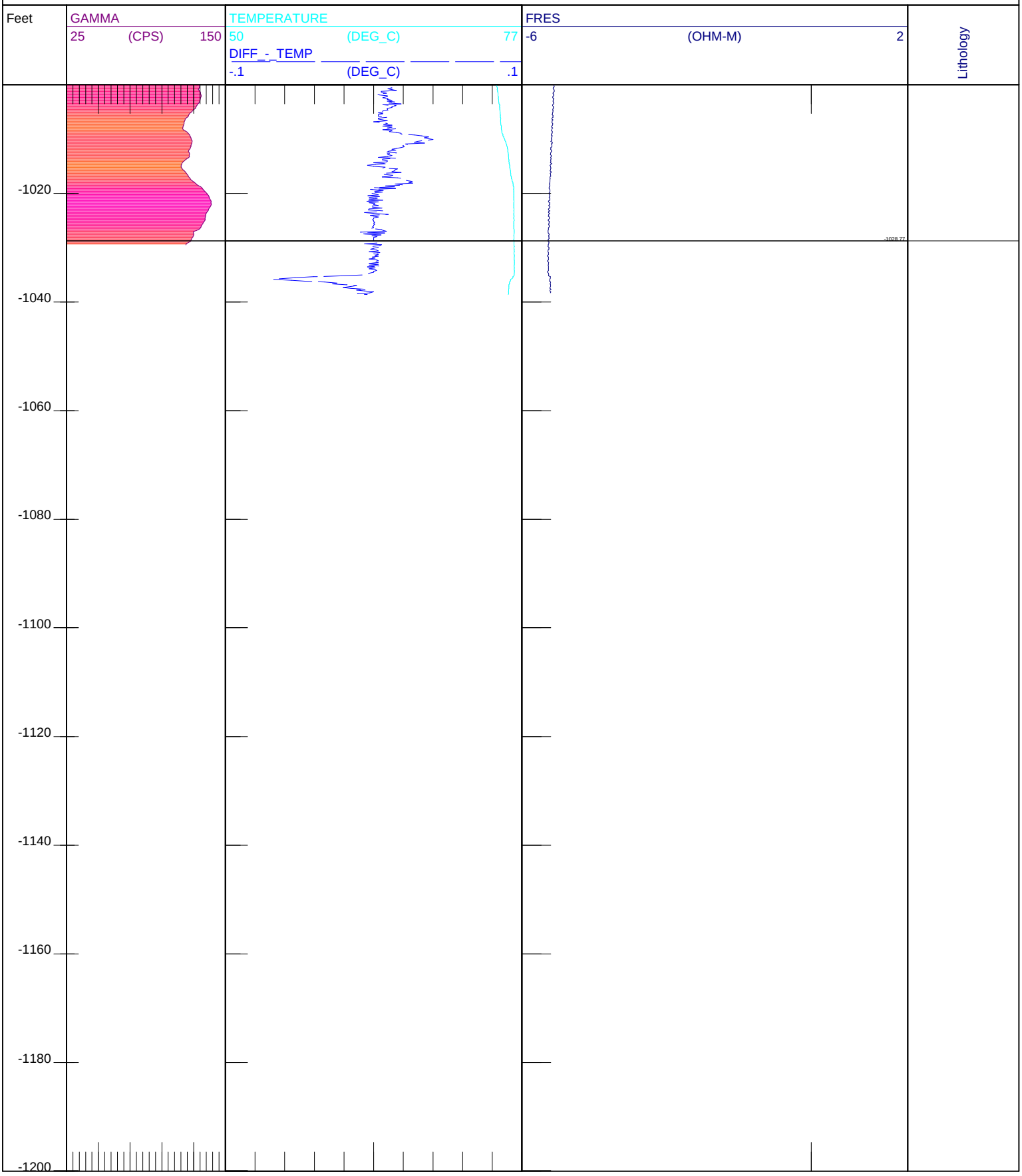
Note: Fluid conductivity is based on fluid resistivity readings. Fluid resisitivty was calibrated to attain measurements from 2 to 80 ohm-m. Due to the low fluid resistivity in the well water, likely less than 1 ohm-m, both fluid resistivity and conductivity measurements do not show true values. However, the measurements are useful for determining water flow when comparisons are made relative.



Well Name: PS-13-1 Gamma - Temperature - Fluid Log
Location: Pilgrim Hotsprings - Alaska
Reference: Top of casing

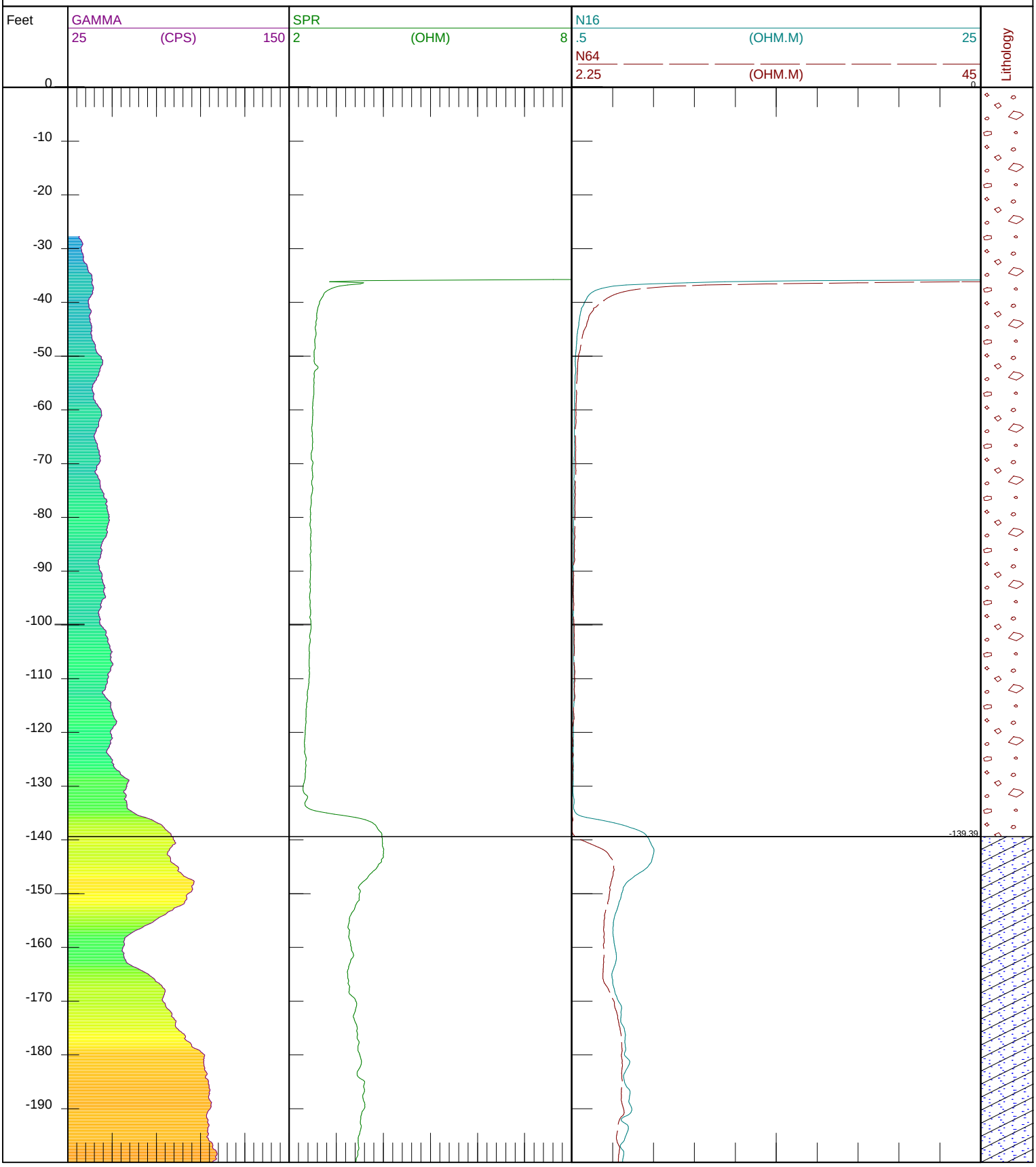
To of casing is 3.2 above current ground surface.
Logged by Jeremy Stariwat on 9/27/13.

Note: Fluid conductivity is based on fluid resistivity readings. Fluid resisitivty was calibrated to attain measurements from 2 to 80 ohm-m. Due to the low fluid resistivity in the well water, likely less than 1 ohm-m, both fluid resistivity and conductivity measurements do not show true values. However, the measurements are useful for determining water flow when comparisons are made relative.



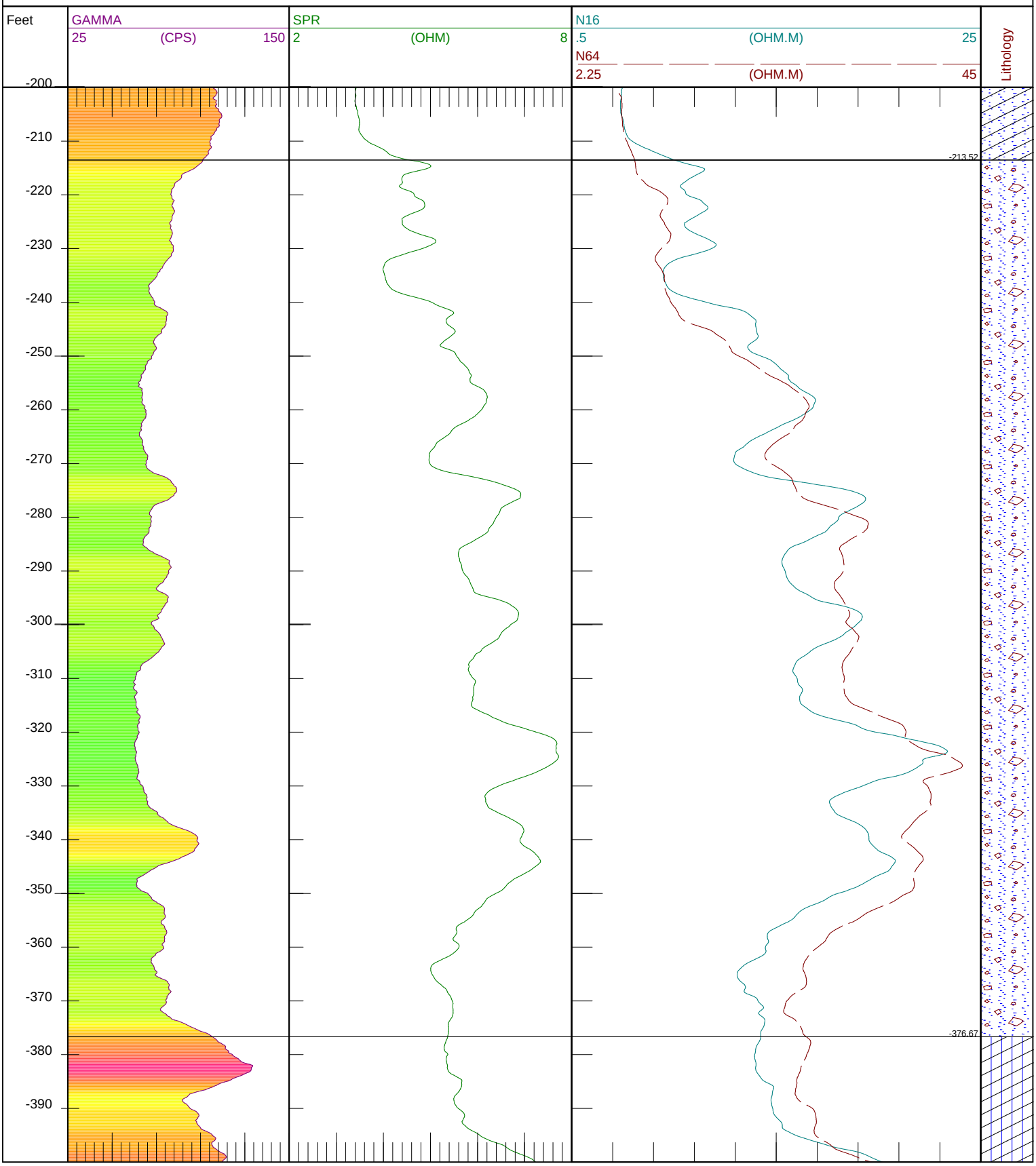
Well Name: PS-13-1 E-log
Location: Pilgrim Hotsprings - Alaska
Reference: Top of casing

To of casing is 3.2 above current ground surface.
Logged by Jeremy Stariwat on 9/27/13.



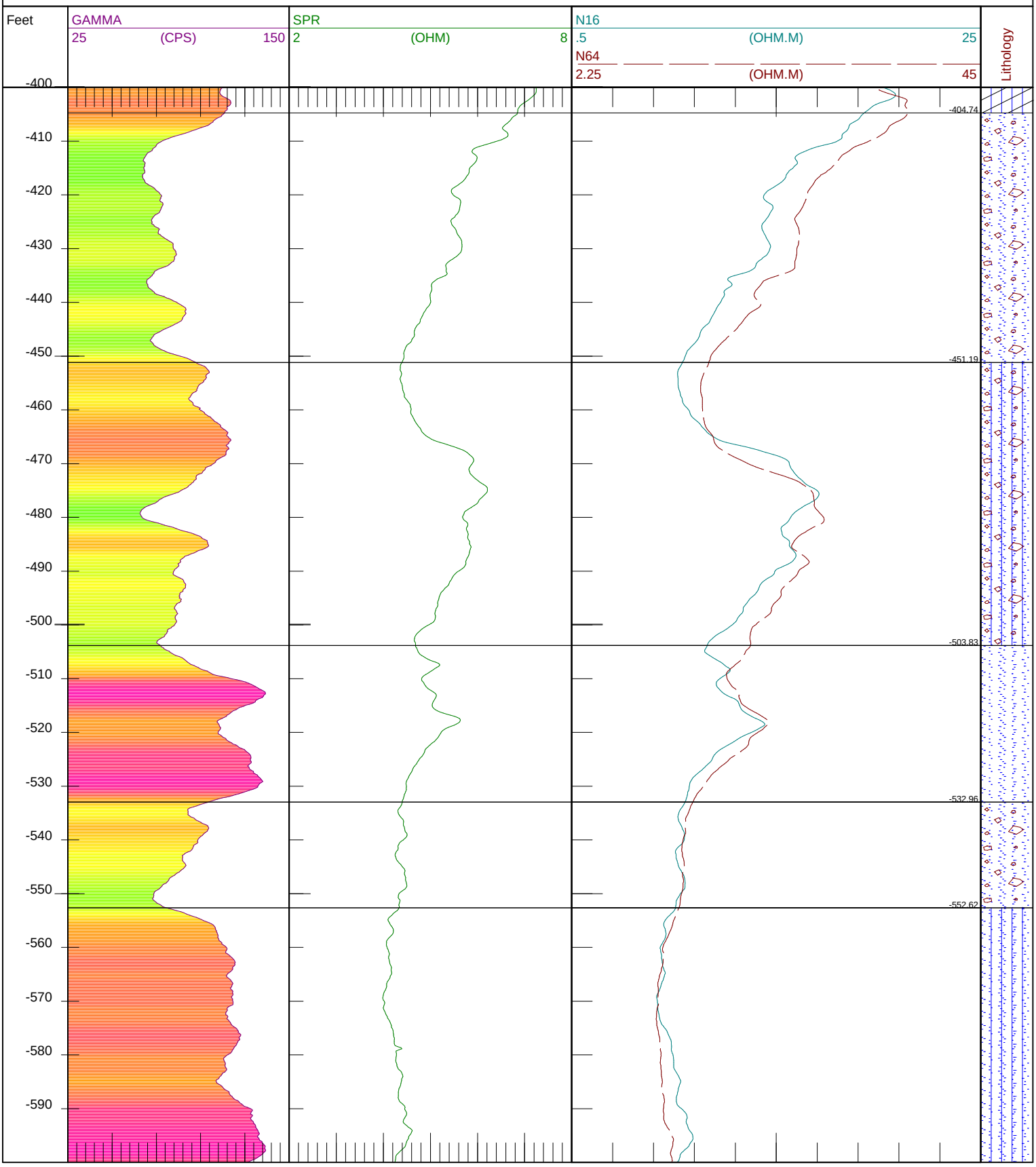
Well Name: PS-13-1 E-log
Location: Pilgrim Hotsprings - Alaska
Reference: Top of casing

To of casing is 3.2 above current ground surface.
Logged by Jeremy Stariwat on 9/27/13.



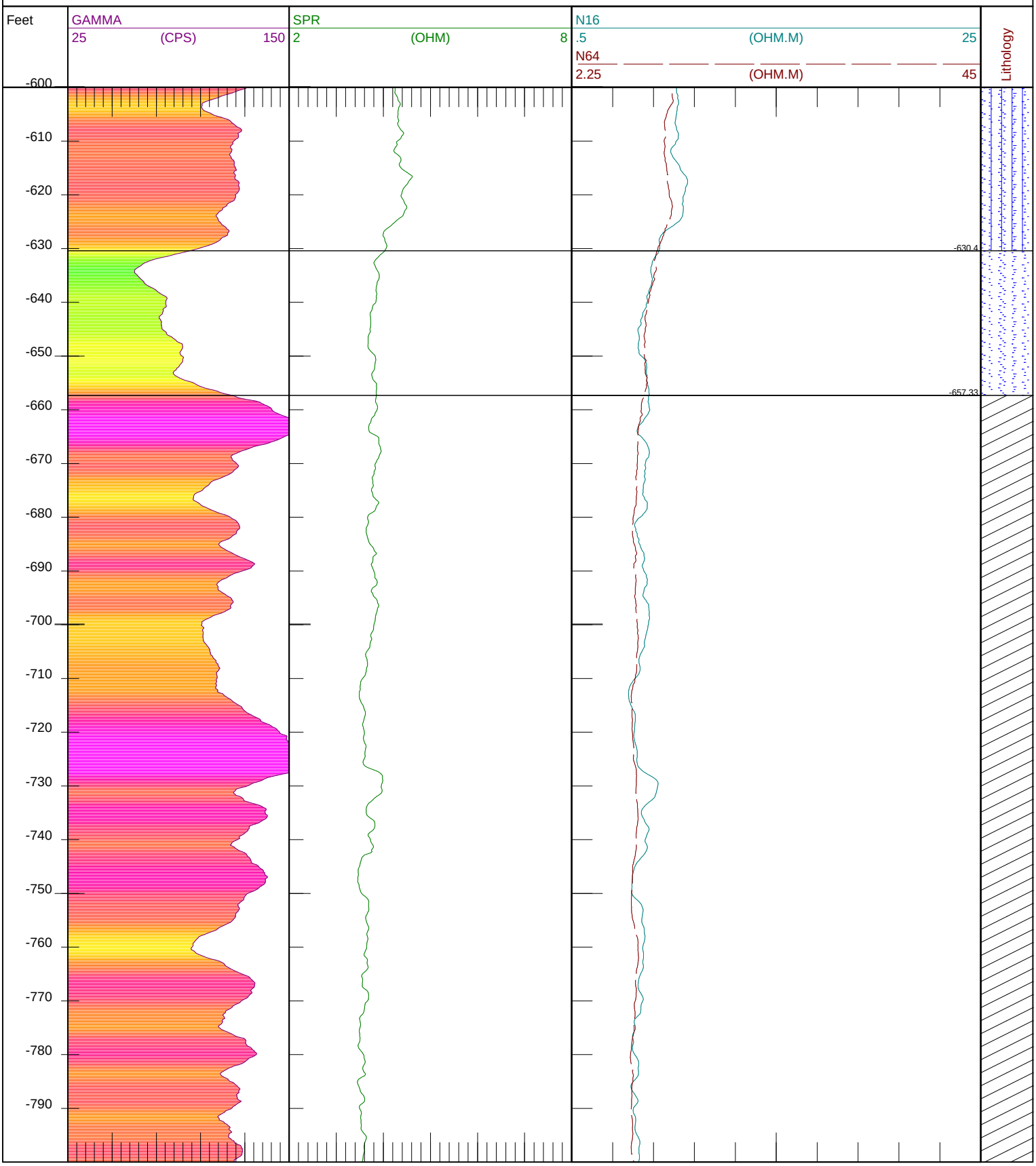
Well Name: PS-13-1 E-log
Location: Pilgrim Hotsprings - Alaska
Reference: Top of casing

To of casing is 3.2 above current ground surface.
Logged by Jeremy Stariwat on 9/27/13.



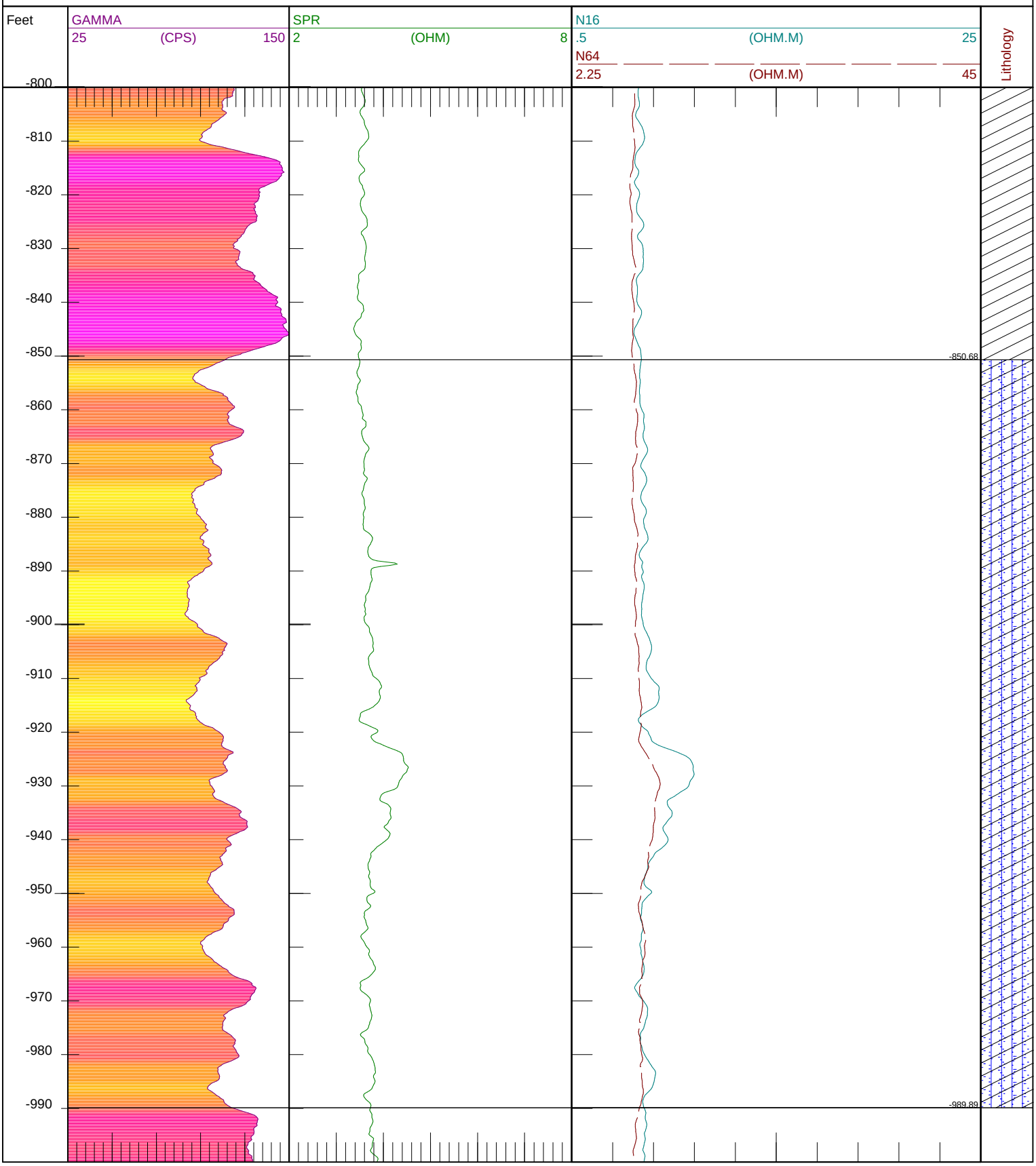
Well Name: PS-13-1 E-log
Location: Pilgrim Hotsprings - Alaska
Reference: Top of casing

To of casing is 3.2 above current ground surface.
Logged by Jeremy Stariwat on 9/27/13.



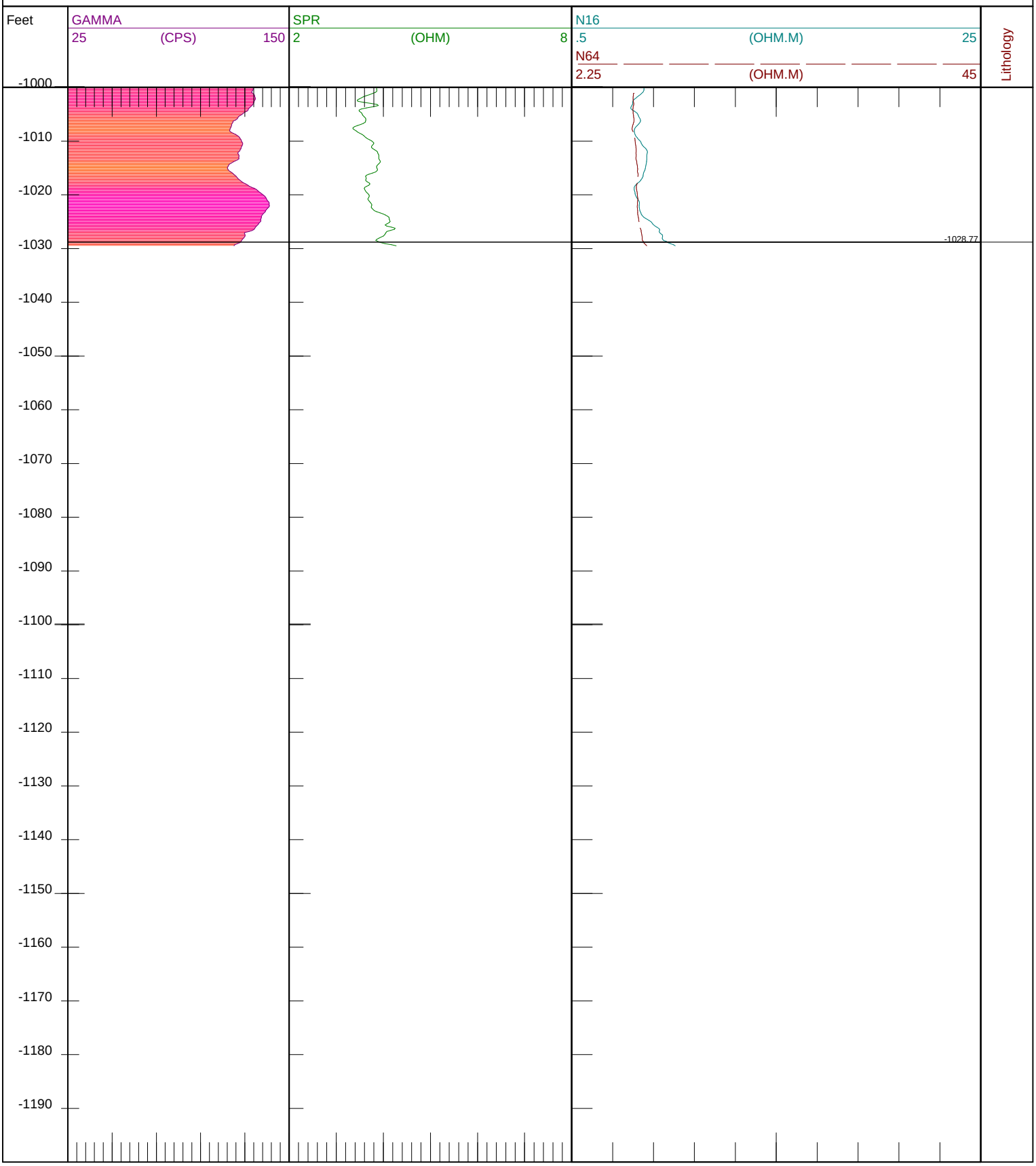
Well Name: PS-13-1 E-log
Location: Pilgrim Hotsprings - Alaska
Reference: Top of casing

To of casing is 3.2 above current ground surface.
Logged by Jeremy Stariwat on 9/27/13.



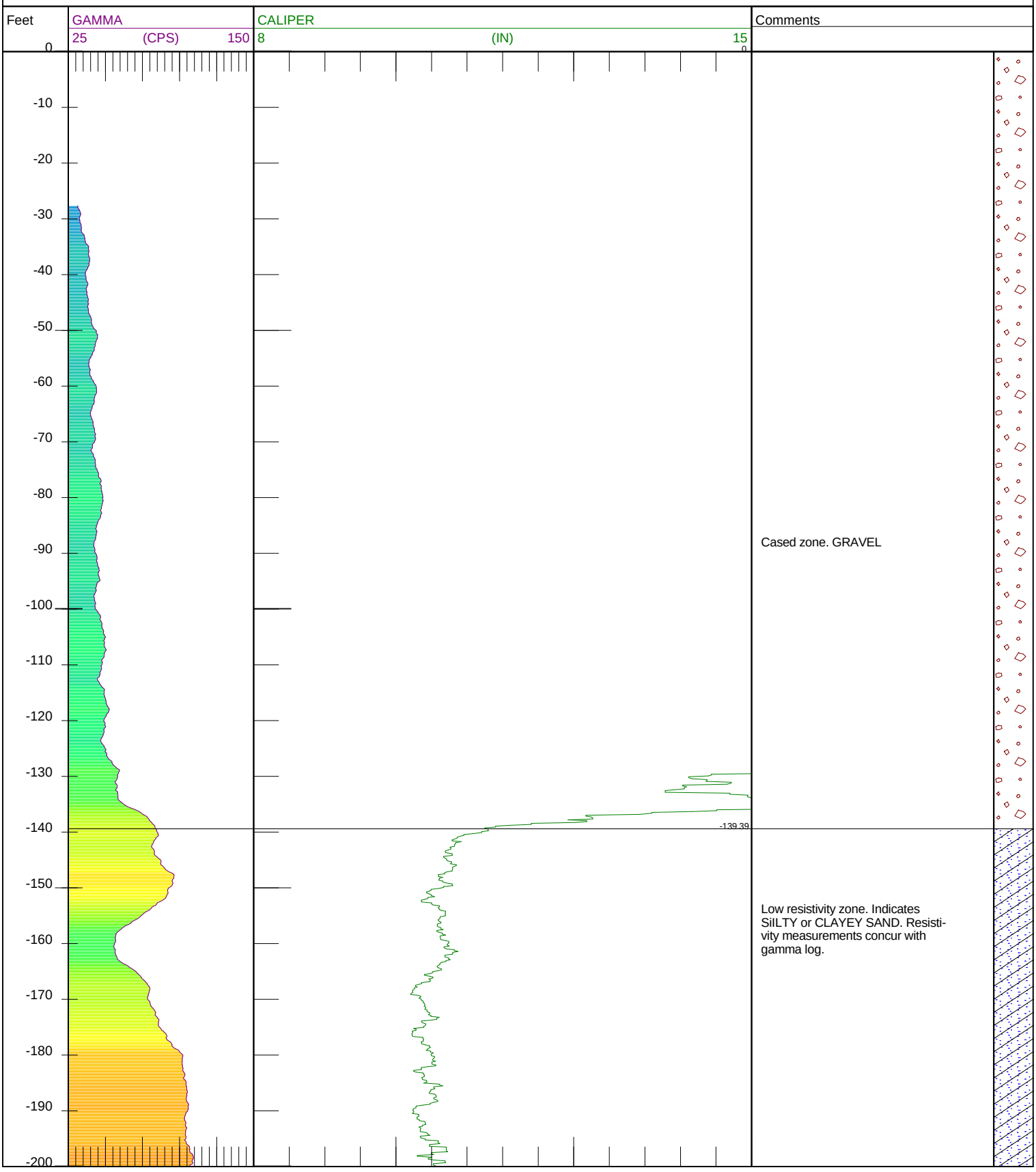
Well Name: PS-13-1 E-log
Location: Pilgrim Hotsprings - Alaska
Reference: Top of casing

To of casing is 3.2 above current ground surface.
Logged by Jeremy Stariwat on 9/27/13.



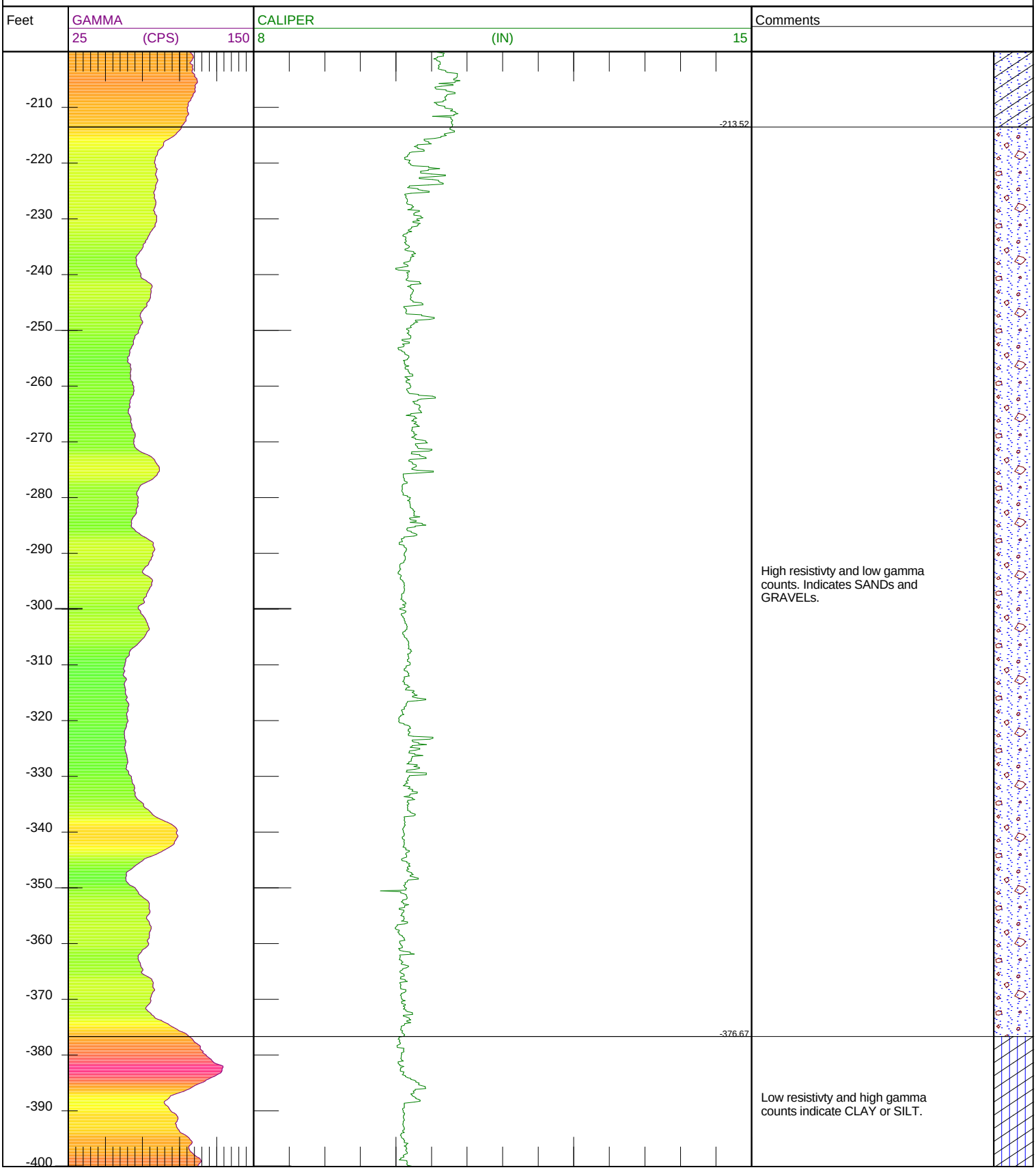
Well Name: PS-13-1 Caliper Log
Location: Pilgrim Hotsprings - Alaska
Reference: Top of casing

To of casing is 3.2 above current ground surface.
Logged by Jeremy Stariwat on 9/27/13.



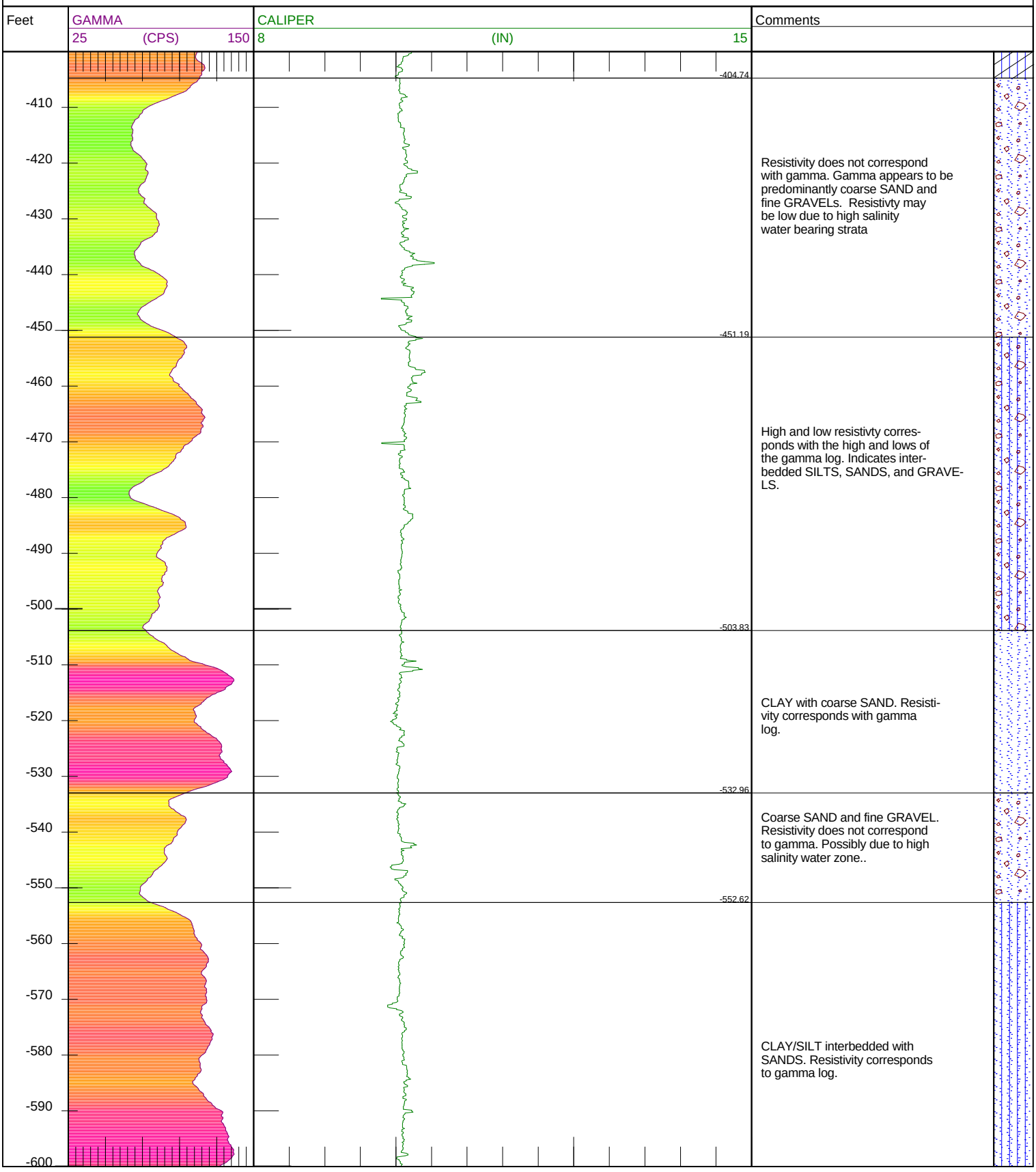
Well Name: PS-13-1 Caliper Log
Location: Pilgrim Hotsprings - Alaska
Reference: Top of casing

To of casing is 3.2 above current ground surface.
Logged by Jeremy Stariwat on 9/27/13.



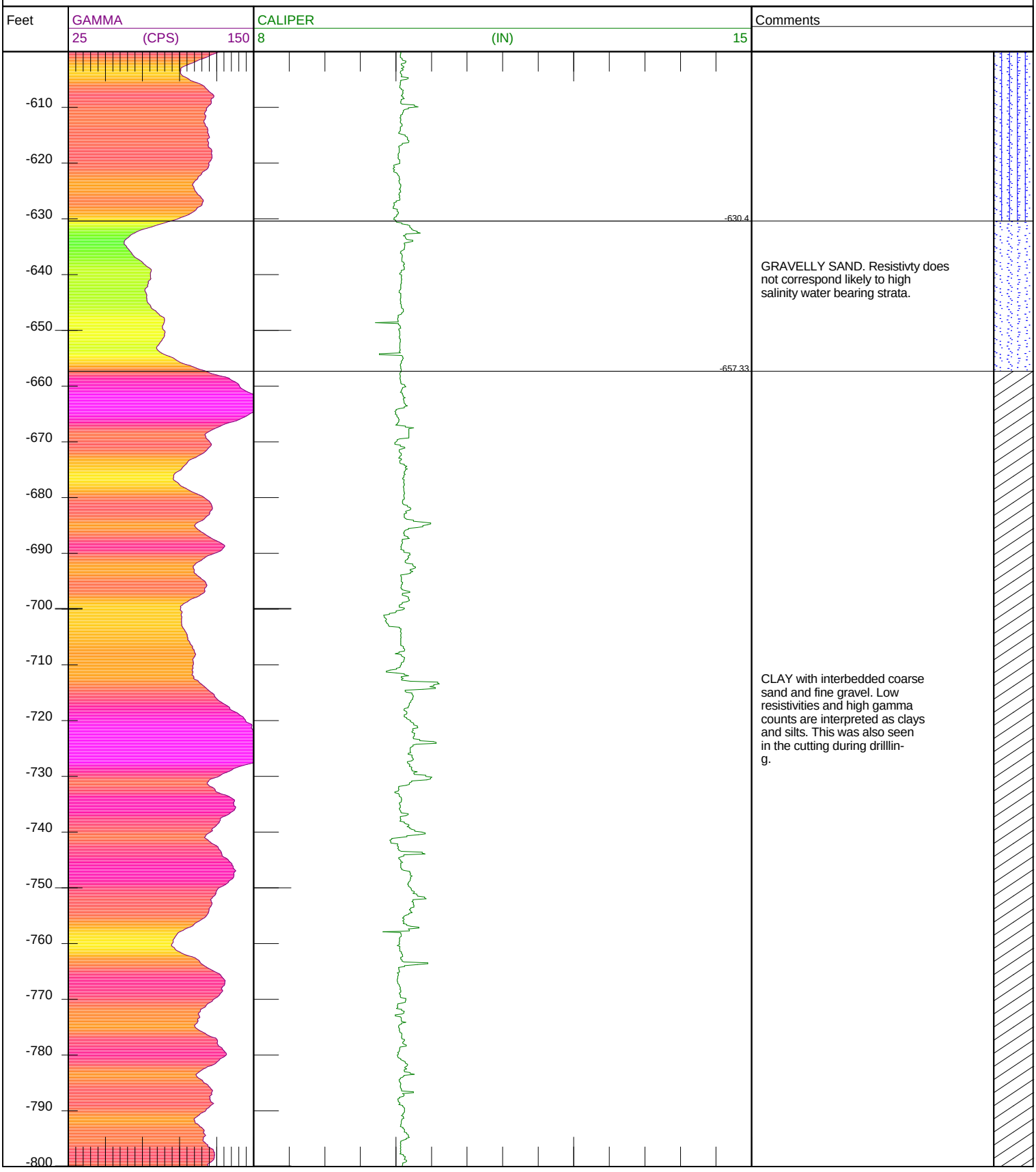
Well Name: PS-13-1 Caliper Log
Location: Pilgrim Hotsprings - Alaska
Reference: Top of casing

To of casing is 3.2 above current ground surface.
Logged by Jeremy Stariwat on 9/27/13.



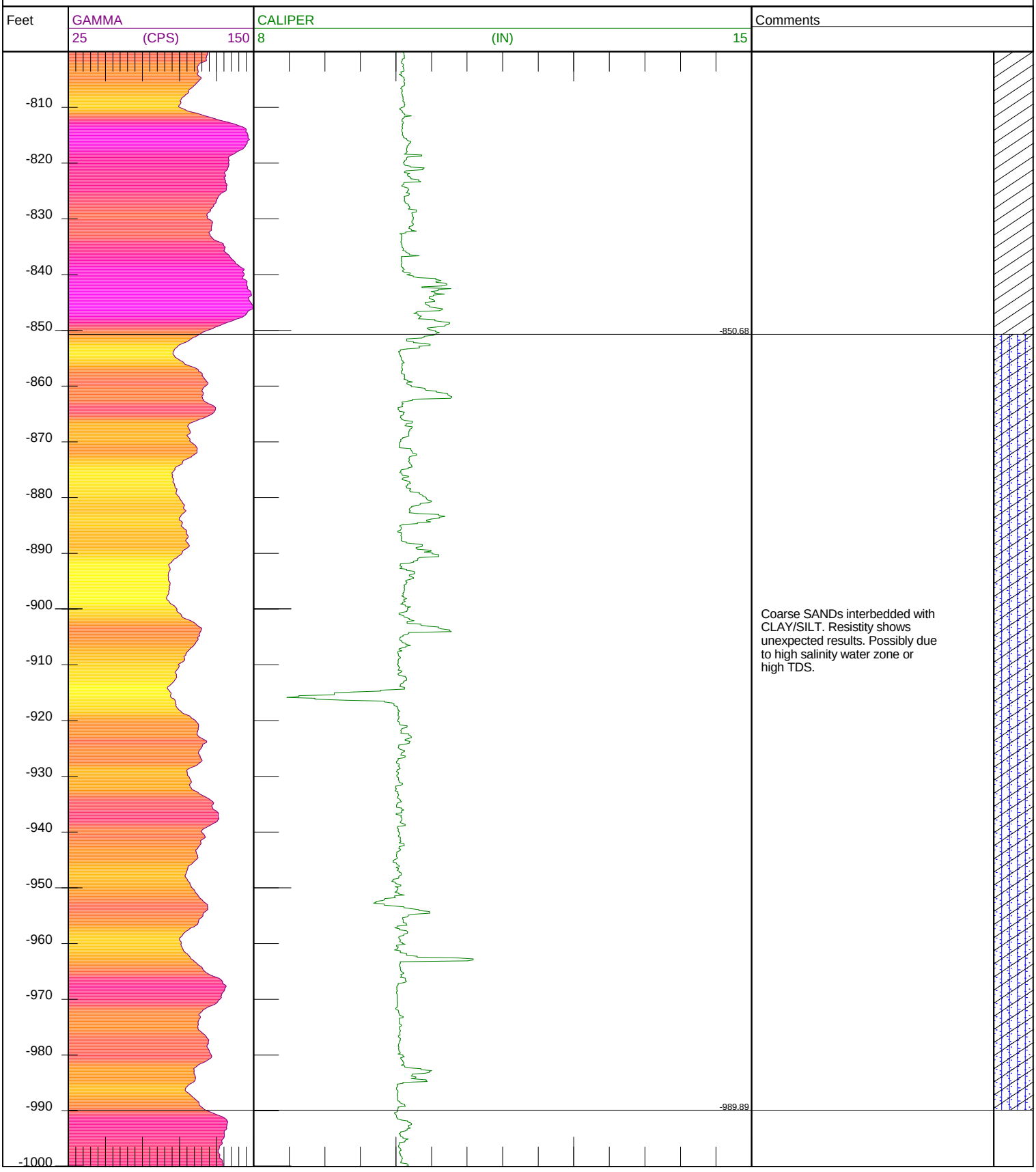
Well Name: PS-13-1 Caliper Log
Location: Pilgrim Hotsprings - Alaska
Reference: Top of casing

To of casing is 3.2 above current ground surface.
Logged by Jeremy Stariwat on 9/27/13.



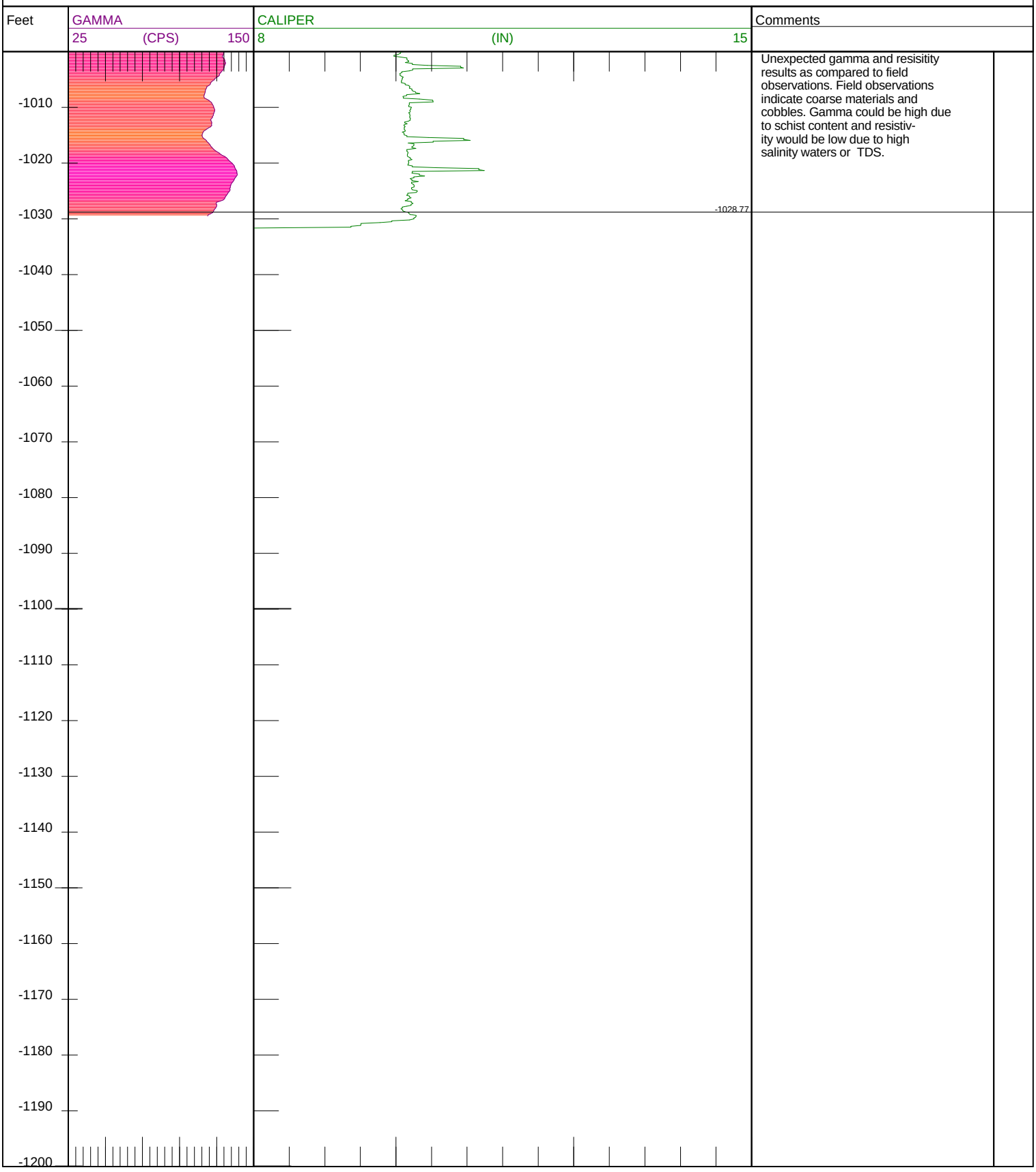
Well Name: PS-13-1 Caliper Log
Location: Pilgrim Hotsprings - Alaska
Reference: Top of casing

To of casing is 3.2 above current ground surface.
Logged by Jeremy Stariwat on 9/27/13.



Well Name: PS-13-1 Caliper Log
Location: Pilgrim Hotsprings - Alaska
Reference: Top of casing

To of casing is 3.2 above current ground surface.
Logged by Jeremy Stariwat on 9/27/13.



Field Notes

CONTENTS

PAGE	REFERENCE	DATE

9/7/13

1530: Arrive at airport in Anchorage. Check in baggage
1920: Arrive in Nome. Chris Pike arrives to pick me up. Drive to Pilgrim
2100: Arrive at site. End Day.

Total Hours: 8hrs

Scale: 1 square =

8/8/13

Project: Pilgrim Hotsprings Project.

Weather: Mostly clear, ~40°F

Field members: Jeremy Stanwat (note taker), Chris Pike, Dick (Geologist), Wayne Westburg (MW), Chris Westburg, Bryan, Kale, Dan.

0800: The geophysical equipment will arrive in Nome at 1300. Chris Pike and I tour site.

0900: Arrive at kitchen tent. Stand by while waiting for geophysical equipment.

1045: Depart to Nome to pick up geophysical equipment.

1430: Arrive back at site with geophysical equipment. Break for Lunch.

1515: Arrive at PS-4 and prepare to set up logging equipment.

1755: Arrive back at kitchen for dinner. Logging has not occured due to computer problems. Will retry after dinner.

1830: Arrive back at PS4 Temp/Fres (cond probe is functioning.

1848: PS4 opened. Tool "zeroed" at TOC. Logging at 8ft/min.

1945: We are currently at 360ft downhole. So far 3 files have been made due to probe hanging ups in the well.

2004: We have hit an area we cannot pass at 476.66, ~~but~~ below TOC. Prepare to log up at faster rate.

Logging rate up = 50ft/min.

2018: After numerous attempts we could not get logger to readi coming up at a fast

rate.
2100: Arrive back at camp.
End day.

Total hours: 13 hours
Billable: 6 hours
stand by: 7 hours.

9/9/13
Project: Pilgrim Hotsprings
Weather: Overcast, ~38°F
Feild members: Jeremy Stavinoha (Snowlake), Dick

0800: Call Mount Sopris regarding equipment concerns
0856: Arrive at PS4. Prepare to e-log.
0937: Bridle length = 75ft. Depth to TD = 145.28 meters
1032: E-log set at 32.22ft from TOC. due to cable length and bridal.
1046: Total depth = 478.41ft. Prepare to log. Logging rate = 18ft/min
1116: Cable / probe return to 33.76 ft.
1200: Arrive back at camp

Total hours: 4

Scale: 1 square =

Scale: 1 square =

9/10/13

Project: Pilgrim hot springs

Weather: Clear, dark, ~40°F

Feild members: Jeremy Stavinoha (note taker), Wade Westburg, Bryan Quinn, Dan.

2400: Arrive at site. Prepare to begin drilling. at PS-13-1

Top of casing is 3.2 ft above ground surface. We are currently at ~25 ft. from TOC. Measurements and observations will be from TOC.

0122: Generator to the mud tent has stopped. Wade and Bryan depart to get a fueling system.

0155: Drillers arrive back at site.

0216: Drilling continues. after fueling all equipment.

0251: Light plant has stopped working. We are still drilling, but with smaller lights.

0420: Samples are very small at PS-13-1 @60' due to low return. Shaker does not contain the same material as the discharge hose.

0615: Wayne westburg arrives onsite.

0640: We have reach 140ft below TOC. We will circulate mud in preparation of geophysical logging.

0644: Wayne Westburg departs site.

0800: Wayne westburg arrives onsite.

0845: Since last entry we have brought the geophysical equipment to site. I have told Dick there may be problems with the data because the hole has not

been stagnant for 24hrs.
0458: Since last entry Chris Pike is on site. We are preparing to e-log. Wade Westburg is assiting us with a pulley for the winch cable that will be centered over the hole.
1640: Begin temperature log. Dick is now on site.
1057: TD currently is 137.15ft at PS-13-1.
1121: TD for E-log is 137.15 ft.
1156: Depart site to camp
1430: Since last entry I have spoken to Chris Pike regarding budgetary issues and I have booked a plane ticket back to Anchorage for tonight.
1700: Gather gear and depart to Nome.
2130: Arrive back in Anchorage

Total = 19 hours
Billable = 16.5 hours
- 4.5 hrs @ $75/hr
- 12 hrs @ $150/hr
Standby = 2.5 hrs
- None billable.

9/17/13
Project: Pilgrim Hotsprings.
Weather: Clear, ~38°F

1530: Arrive at airport.
2000: Arrive in Nome.
2215: Arrive at camp.
End Day
Total = 6.75 hrs @ 87.5

9/18/13
Project: Pilgrim Hotsprings
Weather: ~32°F, Mostly clear, dark (0730).
Feild members: Jeremy Starinet (rock talker), Wade, Wayne, Chris Westburg, Bryan Quinn, Kale, Dan, Chris Pike, Doug.

0800: After speaking with MW and Chris Pike I will assist as a hand during the morning unit noon to 2 p.m. Then sleep until night shift when they will begin drilling.
1300: I have filled all camp equipment and site equipment with fuel and reviewed e-logs for other wells. I have sent Chris Pike an email with the preliminary PS-13-1 e-log.

Scale: 1 square = _____

End Day
Total: 5hrs @ $75

9/19/13
Project: Pilgrim Hotsprings
Weather, Mostly cloudy, ~35°F, dark
Feild members: Jeremy Stawart (note taker), Wade Westburg, Bryan Quinn, Dan

2400: Arrive onsite (PS-13-1)
2430: Wade and Bryan are currently moving the rig onsite.
2444: Wade has arrived with the rig.
0455: Drillers are currently tripping in to the hole to begin pressure test.
0552: Drillers are currently displacing mud from the boring.
0813: Bentonite chips have been poured down the hole (5-50lb bags).
0925: Drillers are currently testing that the pressure

system is functioning correctly before the test.
0951: The pressure gauge is malfunctioning. Bryan is welding on another to the well casing. Since last entry Wayne Westberg and Chris Pike have arrived onsite. I have shown Chris Pike where my sampling equipment is so day crew can sample in my absence.
1043: ~~900~~ 900 - 50lb bags of bentonite have been added to the borehole because the pressure would not stabilize when attempting a pressure test. Drillers assume the bottom of the hole blew out
1140: Drillers are preparing the pressure test for the day crew to perform.
1200: Depart site.
End Day

Total hours = 12
- Standby rate of $75

9/20/13
Project: Pilgrim Hotsprings
Weather: Mostly cloudy, ~34°F, Dark
Field members: Jeremy Stariwat (note taker), Wade, Bryan, Dan

2400: Arrive on site. Speak with day crew.
2488: Day crew has 160ft of rod tripped in hole. Drilling did not occur during the day shift.
0258: Since last entry drillers have tripped into the hole, drained the water, filled the rig with fuel, and began mixing mud. They will need to trip out to remove a centering piece and trip back in before we can begin drilling.
0506: Drillers have tripped in to 140ft from TOC. Currently circulating mud in preparation for drilling. 160ft
0552: Drilling begins at ~~140ft~~ from TOC
0916: Drillers are tripping out due to no advance past ~217ft.
1200: Depart site. Total footage = 160 - 217 ft.
END Day

Total = 12 hrs @150

9/21/13
Project: Pilgrim Hotsprings
Weather: Overcast, ~34°F, dark
Feild members: Jeremy Starwalt (note taker), Wade, Bryan, Dan

2400: Arrive onsite. We are currently at 302 ft. Drillers are logged and sampled in my absence.
1200: We have drilled and sampled (every 10 ft) from 302' to 412'. Total of 110'.
Depart site.
End Day

Total = 12hrs @ $50

9/22/13
Project: Pilgrim Hotsprings
Weather: Overcast, ~34°F, dark
Feild member: Jeremy Starwalt (note taker), Wade, Bryan, Dan

2400: Arrive at site. Hole is currently at 537' from TOC.
Media = Clay. According to Chris Westberg they encountered clay shortly after 417'.
1200: End drilling at 687'.
Total footage = 150 ft.
Depart site.
End Dan

Total = 12hrs @ $50

9/23/13
Project: Pilgrim Hotsprings
Weather: ~~the~~ Partly cloudy, ~34°F, dark
Feild naembers: Jeremy Starrwest (note taker), Wade, Bryan, Dan

2400: Arrive at site. Currently at 787'. Drillers logged and sampled in my absence.
1200: We have drilled and sampled from 787'-886'.
Total = 99'.
Depart site.
End days

TOTAL: 12hrs @150

9/24/13
Project: Pilgrim Hotsprings
Weather: Partly cloudy, ~34°F, dark
Field members: Jeremy Starrwest (note taker), Wade, Bryan, Dan
2400: Arrive at site. Currently at 948'. Drillers logged and sampled in my absence.
1200: We have drilled to ~1029 ft.
Total = 81 ft.
Depart site
End Day.

Total = 12hrs @150

9/25/13
Project: Pilgrim Hotsprings
Weather: Snowing, ~30°F
Feild members: Jeremy Sterwat (note taker), Chris Pike, Dick Benoit.

0900: Begin loading geophysical equipment to bring to site.
0936: Set up pulley off drill rig guill for logging equipment.
0957: Chris and Dick are setting up Kuster tool for first temperature pass.
0900: Begin Kuster logging.
1030: Finish Kuster logging. Prepare temp, fluid cond probe.
1102: Temp tool is ready. TD, based on Kuster tool, is ~964.6 ft. from TOC.

1104: Begin temp log. Tool zeroed at 1.99 ft. Speed = 8 ft/min going down.
1159: Temp probe will not pass 333 ft.
1257: Since last entry we have decided to have day crew clean up the hole. I depart to site to look at data collected.
1325: Show Dick the temperature profile in AutoCAD
Stand by.

Total = 8 hrs
Billable = 5 hrs @ 150
Standby = 3 hrs @ 75

9/26/13
Project: Pilgrim Hotsprings
Weather: Partly cloudy, ~35°F
Feild members: Jeremy Steinwert (note taker).
1030: Begin fueling camp.
1230: Finish fueling camp. I am on Standby until the rod has been tripped from the hole.

Total = 8hrs
Standby = 8hrs @ $75.

9/27/13
Project: Pilgrim Hotspring 3
Weather: Cloudy, ~28°F. Dark.
Feild members: Jeremy Steinwert
0540: Prepare to head to drill site. Bryan has informed me I can log in one hour.
0720: Begin temperature log at PS-13-1.
File calle "PS-13-1 Temp log 2". Logging at 8ft/min from TOC.
0744: Hang up at ~195ft.
0817: Hang up at ~430ft.
0840: Hang up at ~452 @ 18ft.

0845: Hang up at ~725ft.
0907: Hang up at ~819ft
0936: We have reached TD at ~~1036.~~ ~~1037.10ft~~ 1036.68ft
Pull up. Last temp = ~76.862
1009: Temp tool is out of hole. Prepare to

Deploy e-log.
1029: E-log set up.
File name = "PS-13-1 E-log"
1051: TD for e-log = 1035.89 ft.
1053: Begin e-log at
15.5 - 16 ft/min.
1209: Finish E-log,
Prepare to put caliper
to bottom of the hole.
1214: Deploy caliper.
1236: TD for Caliper = 1034.82 ft.
1300: Prepare to bring
up caliper. File name
= "PS-13-1 caliper log"
1403: Caliper has reached
the top of the borehole.
Prepare to demob equipment.
1600: Equipment has been
cleaned. Prepare to depart
to the airport.
2230: Since last entry
I have arrived in
Anchorage.
Total = 16.75

Billable = 10.25 @ 105
Travel = 6.5 @ 75

Theis Calculations

NONEQUILIBRIUM THEIS EQUATION
(after Driscol, 1995, Groundwater and Wells, pg. 218)

Deep Aquifer- Medium Sand

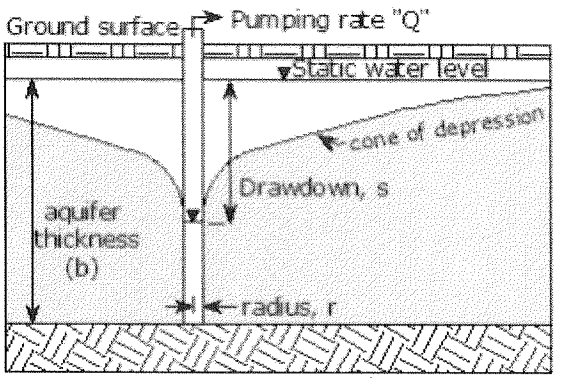
$r := 7 \cdot in$ distance from production well (ft)

$r_c := 7 \cdot in$ radius of casing

$Q := 10450 \cdot \frac{gal}{min}$ GPM

$S := 0.00021$ Specific capacity*

$b := 100 \cdot ft$ Aquifer thickness



$T := 34000. \cdot \frac{gal}{day \cdot ft}$ Transmissivity, GPD/ft

$t := 360 \cdot day$ days

$$test_{validity} := if\left(t > 250 \cdot \frac{r_c^{\,2}}{T}, \text{"valid"}, \text{"not"}\right) \qquad test_{validity} = \text{"valid"}$$

$$u := \frac{r^2 \cdot S}{4 \cdot T \cdot t} = 1.092 \cdot 10^{-11}$$ U is a well factor

$$s_{drawdown} := \frac{Q}{4 \cdot \pi \cdot T} \cdot \int_u^{\infty} \frac{e^{-u}}{u} du$$ Theis equation

$s_{drawdown} = 868.6\ ft$ feet of drawdown

$available_{drawdown} := 869 \cdot ft$

Specific capacity is calculated as $s_{calc} := 2.1 \cdot 10^{-6} \cdot \frac{b}{ft} = 2.1 \cdot 10^{-4}$ (Kasenow, 2005)

NONEQUILIBRIUM THEIS EQUATION
(after Driscol, 1995, Groundwater and Wells, pg. 218)

Deep Aquifer- Fine Sand

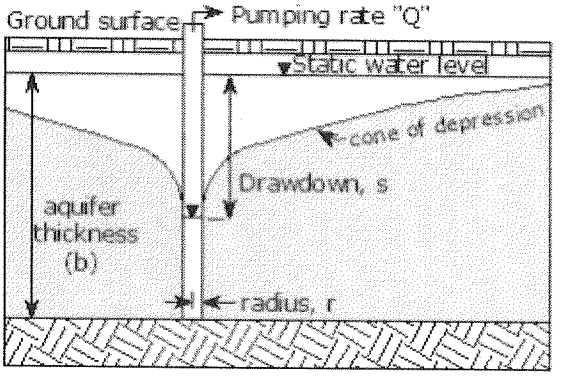
$r := 7 \cdot in$ distance from production well (ft)

$r_c := 7 \cdot in$ radius of casing

$Q := 3049 \cdot \frac{gal}{min}$ GPM

$S := 0.00021$ Specific capacity*

$b := 100 \cdot ft$ Aquifer thickness



$T := 9400. \cdot \frac{gal}{day \cdot ft}$ Transmissivity, GPD/ft

$t := 360 \cdot day$ days

$test_{validity} := \text{if}\left(t > 250 \cdot \frac{r_c^2}{T}, \text{"valid"}, \text{"not"}\right)$ $test_{validity} = \text{"valid"}$

$u := \frac{r^2 \cdot S}{4 \cdot T \cdot t} = 3.949 \cdot 10^{-11}$ U is a well factor

$s_{drawdown} := \frac{Q}{4 \cdot \pi \cdot T} \cdot \int_u^{\infty} \frac{e^{-u}}{u} du$ Theis equation

$s_{drawdown} = 868.9\ ft$ feet of drawdown

$available_{drawdown} := 869 \cdot ft$

Specific capacity is calculated as $s_{calc} := 2.1 \cdot 10^{-6} \cdot \frac{b}{ft} = 2.1 \cdot 10^{-4}$ (Kasenow, 2005)

NONEQUILIBRIUM THEIS EQUATION
(after Driscol, 1995, Groundwater and Wells, pg. 218)

Middle Aquifer- Medium Sand

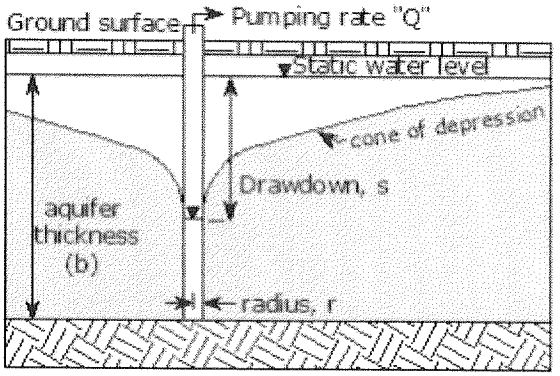
$r := 7 \cdot in$ distance from production well (ft)

$r_c := 7 \cdot in$ radius of casing

$Q := 3370 \cdot \frac{gal}{min}$ GPM

$S := 0.000145$ Specific capacity*

$b := 69 \cdot ft$ Aquifer thickness



$T := 23460. \cdot \frac{gal}{day \cdot ft}$ Transmissivity, GPD/ft

$t := 360 \cdot day$ days

$$test_{validity} := \text{if}\left(t > 250 \cdot \frac{r_c^2}{T}, \text{"valid"}, \text{"not"}\right) \qquad test_{validity} = \text{"valid"}$$

$$u := \frac{r^2 \cdot S}{4 \cdot T \cdot t} = 1.093 \cdot 10^{-11}$$ U is a well factor

$$s_{drawdown} := \frac{Q}{4 \cdot \pi \cdot T} \cdot \int_u^{\infty} \frac{e^{-u}}{u} \, du$$ Theis equation

$s_{drawdown} = 406\ ft$ feet of drawdown

$available_{drawdown} := 406 \cdot ft$

Specific capacity is calculated as $s_{calc} := 2.1 \cdot 10^{-6} \cdot \frac{b}{ft} = 1.449 \cdot 10^{-4}$ (Kasenow, 2005)

NONEQUILIBRIUM THEIS EQUATION
(after Driscol, 1995, Groundwater and Wells, pg. 218)

Middle Aquifer- Fine Sand

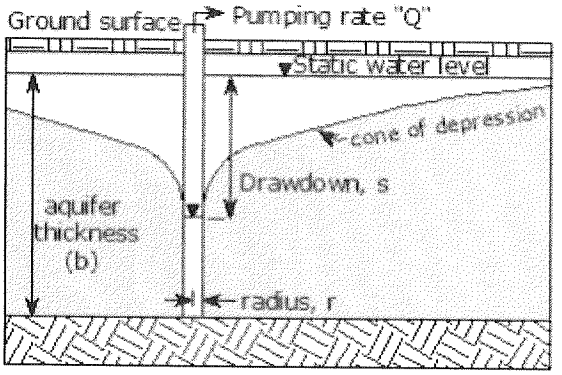
$r := 7 \cdot in$ distance from production well (ft)

$r_c := 7 \cdot in$ radius of casing

$Q := 983 \cdot \frac{gal}{min}$ GPM

$S := 0.000145$ Specific capacity*

$b := 69 \cdot ft$ Aquifer thickness



$T := 6486. \cdot \frac{gal}{day \cdot ft}$ Transmissivity, GPD/ft

$t := 360 \cdot day$ days

$$test_{validity} := \text{if}\left(t > 250 \cdot \frac{r_c^2}{T}, \text{"valid"}, \text{"not"}\right) \qquad test_{validity} = \text{"valid"}$$

$$u := \frac{r^2 \cdot S}{4 \cdot T \cdot t} = 3.952 \cdot 10^{-11}$$ U is a well factor

$$s_{drawdown} := \frac{Q}{4 \cdot \pi \cdot T} \cdot \int_u^{\infty} \frac{e^{-u}}{u} du$$ Theis equation

$s_{drawdown} = 406\ ft$ feet of drawdown

$available_{drawdown} := 406 \cdot ft$

Specific capacity is calculated as $s_{calc} := 2.1 \cdot 10^{-6} \cdot \frac{b}{ft} = 1.449 \cdot 10^{-4}$ (Kasenow, 2005)

NONEQUILIBRIUM THEIS EQUATION
(after Driscol, 1995, Groundwater and Wells, pg. 218)

Deeper Shallow Aquifer - Medium Sand

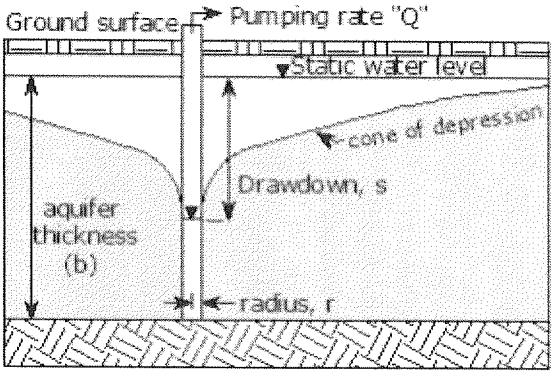
$r := 7 \cdot in$ distance from production well (ft)

$r_c := 7 \cdot in$ radius of casing

$Q := 3478 \cdot \frac{gal}{min}$ GPM

$S := 0.000292$ Specific capacity*

$b := 139 \cdot ft$ Aquifer thickness



$T := 47260. \cdot \frac{gal}{day \cdot ft}$ Transmissivity, GPD/ft

$t := 360 \cdot day$ days

$test_{validity} := if\left(t > 250 \cdot \frac{r_c^{\,2}}{T}, \text{"valid"}, \text{"not"}\right)$ $test_{validity} = \text{"valid"}$

$u := \frac{r^2 \cdot S}{4 \cdot T \cdot t} = 1.092 \cdot 10^{-11}$ U is a well factor

$s_{drawdown} := \frac{Q}{4 \cdot \pi \cdot T} \cdot \int_u^{\infty} \frac{e^{-u}}{u} du$ Theis equation

$s_{drawdown} = 208\ ft$ feet of drawdown

$available_{drawdown} := 208 \cdot ft$

Specific capacity is calculated as $s_{calc} := 2.1 \cdot 10^{-6} \cdot \frac{b}{ft} = 2.919 \cdot 10^{-4}$ (Kasenow, 2005)

NONEQUILIBRIUM THEIS EQUATION
(after Driscol, 1995, Groundwater and Wells, pg. 218)

Deeper Shallow Aquifer - Fine Sand

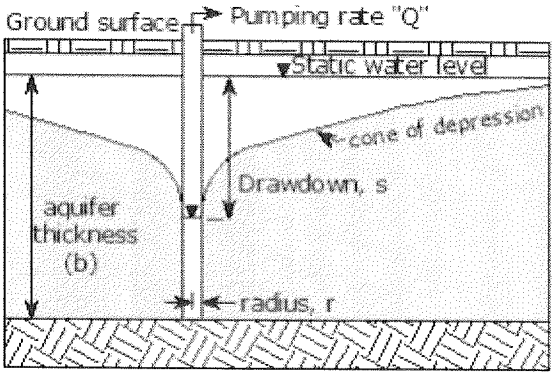
$r := 7 \cdot in$ distance from production well (ft)

$r_c := 7 \cdot in$ radius of casing

$Q := 1015 \cdot \frac{gal}{min}$ GPM

$S := 0.000292$ Specific capacity*

$b := 139 \cdot ft$ Aquifer thickness



$T := 13070. \cdot \frac{gal}{day \cdot ft}$ Transmissivity, GPD/ft

$t := 360 \cdot day$ days

$test_{validity} := \text{if}\left(t > 250 \cdot \frac{r_c^2}{T}, \text{"valid"}, \text{"not"}\right)$ $test_{validity} = \text{"valid"}$

$u := \frac{r^2 \cdot S}{4 \cdot T \cdot t} = 3.949 \cdot 10^{-11}$ U is a well factor

$s_{drawdown} := \frac{Q}{4 \cdot \pi \cdot T} \cdot \int_u^\infty \frac{e^{-u}}{u} du$ Theis equation

$s_{drawdown} = 208\ ft$ feet of drawdown

$available_{drawdown} := 208 \cdot ft$

Specific capacity is calculated as $s_{calc} := 2.1 \cdot 10^{-6} \cdot \frac{b}{ft} = 2.919 \cdot 10^{-4}$ (Kasenow, 2005)

NONEQUILIBRIUM THEIS EQUATION
(after Driscol, 1995, Groundwater and Wells, pg. 218)

Shallow Aquifer - Medium Sand

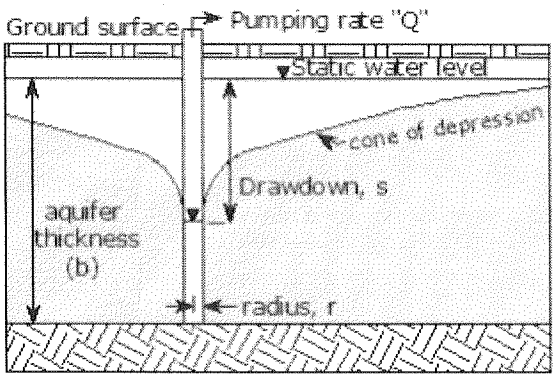
$r := 7 \cdot in$ distance from production well (ft)

$r_c := 7 \cdot in$ radius of casing

$Q := 721 \cdot \frac{gal}{min}$ GPM

$S := 0.000252$ Specific capacity*

$b := 120 \cdot ft$ Aquifer thickness



$T := 40800. \cdot \frac{gal}{day \cdot ft}$ Transmissivity, GPD/ft

$t := 360 \cdot day$ days

$test_{validity} := \text{if}\left(t > 250 \cdot \frac{r_c^2}{T}, \text{"valid"}, \text{"not"}\right)$ $test_{validity} = \text{"valid"}$

$u := \frac{r^2 \cdot S}{4 \cdot T \cdot t} = 1.092 \cdot 10^{-11}$ U is a well factor

$s_{drawdown} := \frac{Q}{4 \cdot \pi \cdot T} \cdot \int_u^{\infty} \frac{e^{-u}}{u} du$ Theis equation

$s_{drawdown} = 49.9\ ft$ feet of drawdown

$available_{drawdown} := 50 \cdot ft$

Specific capacity is calculated as $s_{calc} := 2.1 \cdot 10^{-6} \cdot \frac{b}{ft} = 2.52 \cdot 10^{-4}$ (Kasenow, 2005)

NONEQUILIBRIUM THEIS EQUATION
(after Driscol, 1995, Groundwater and Wells, pg. 218)

Shallow Aquifer - Fine Sand

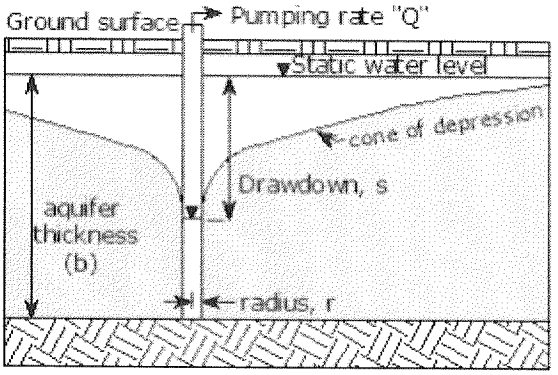
$r := 7 \cdot in$ distance from production well (ft)

$r_c := 7 \cdot in$ radius of casing

$Q := 210 \cdot \frac{gal}{min}$ GPM

$S := 0.000252$ Specific capacity*

$b := 120 \cdot ft$ Aquifer thickness



$T := 11280. \cdot \frac{gal}{day \cdot ft}$ Transmissivity, GPD/ft

$t := 360 \cdot day$ days

$test_{validity} := \text{if}\left(t > 250 \cdot \frac{r_c^2}{T}, \text{"valid"}, \text{"not"}\right)$ $test_{validity} = \text{"valid"}$

$u := \frac{r^2 \cdot S}{4 \cdot T \cdot t} = 3.949 \cdot 10^{-11}$ U is a well factor

$s_{drawdown} := \frac{Q}{4 \cdot \pi \cdot T} \cdot \int_u^{\infty} \frac{e^{-u}}{u} du$ Theis equation

$s_{drawdown} = 49.9\ ft$ feet of drawdown

$available_{drawdown} := 50 \cdot ft$

Specific capacity is calculated as $s_{calc} := 2.1 \cdot 10^{-6} \cdot \frac{b}{ft} = 2.52 \cdot 10^{-4}$ (Kasenow, 2005)

NONEQUILIBRIUM THEIS EQUATION
(after Driscol, 1995, Groundwater and Wells, pg. 218)

Currently Screened Zone - Medium Sand

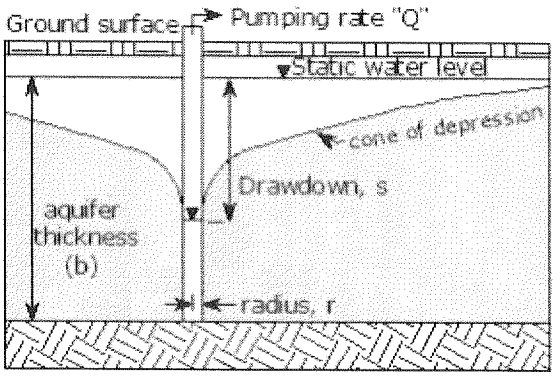
$r := 7 \cdot in$ distance from production well (ft)

$r_c := 7 \cdot in$ radius of casing

$Q := 3610 \cdot \frac{gal}{min}$ GPM

$S := 0.000344$ Specific capacity*

$b := 164 \cdot ft$ Aquifer thickness



$T := 55760. \cdot \frac{gal}{day \cdot ft}$ Transmissivity, GPD/ft

$t := 360 \cdot day$ days

$test_{validity} := \text{if}\left(t > 250 \cdot \frac{r_c^2}{T}, \text{"valid"}, \text{"not"}\right)$ $test_{validity} = \text{"valid"}$

$u := \frac{r^2 \cdot S}{4 \cdot T \cdot t} = 1.091 \cdot 10^{-11}$ U is a well factor

$s_{drawdown} := \frac{Q}{4 \cdot \pi \cdot T} \cdot \int_u^{\infty} \frac{e^{-u}}{u} du$ Theis equation

$s_{drawdown} = 183\ ft$ feet of drawdown

$available_{drawdown} := 183 \cdot ft$

Specific capacity is calculated as $s_{calc} := 2.1 \cdot 10^{-6} \cdot \frac{b}{ft} = 3.444 \cdot 10^{-4}$ (Kasenow, 2005)

NONEQUILIBRIUM THEIS EQUATION
(after Driscol, 1995, Groundwater and Wells, pg. 218)

Currently Screened Zone - Fine Sand

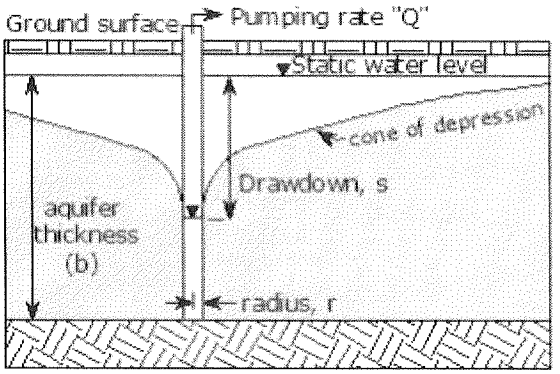
$r := 7 \cdot in$ distance from production well (ft)

$r_c := 7 \cdot in$ radius of casing

$Q := 1053 \cdot \frac{gal}{min}$ GPM

$S := 0.000344$ Specific capacity*

$b := 164 \cdot ft$ Aquifer thickness



$T := 15420. \cdot \frac{gal}{day \cdot ft}$ Transmissivity, GPD/ft

$t := 360 \cdot day$ days

$test_{validity} := if\left(t > 250 \cdot \frac{r_c^2}{T}, \text{"valid"}, \text{"not"}\right)$ $test_{validity} = \text{"valid"}$

$u := \frac{r^2 \cdot S}{4 \cdot T \cdot t} = 3.943 \cdot 10^{-11}$ U is a well factor

$s_{drawdown} := \frac{Q}{4 \cdot \pi \cdot T} \cdot \int_u^{\infty} \frac{e^{-u}}{u} du$ Theis equation

$s_{drawdown} = 182.9\ ft$ feet of drawdown

$available_{drawdown} := 183 \cdot ft$

Specific capacity is calculated as $s_{calc} := 2.1 \cdot 10^{-6} \cdot \frac{b}{ft} = 3.444 \cdot 10^{-4}$ (Kasenow, 2005)

MODIFIED NONEQUILIBRIUM EQUATION
Theis (after Driscol, pg 218)

PS4

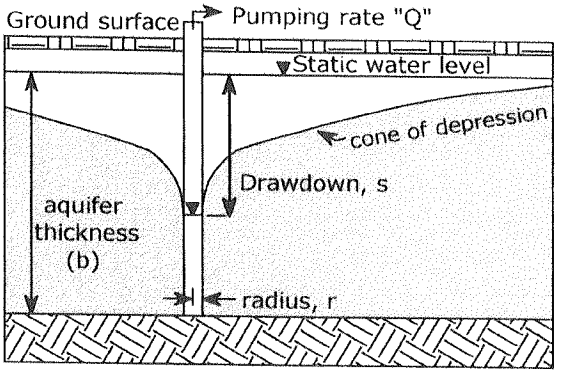
$r := \frac{4.9375}{12}\,ft$ distance from production well (ft)

$r_c := \frac{4.9375}{12}\,ft$ radius of casing

$Q := 1420 \cdot \frac{gal}{min}$ GPM

$S := 0.000263$ Specific yield*

$b := 125\,ft$ Aquifer thickness



$T := 11750 \cdot \frac{gal}{day \cdot ft}$ Transmissivity, GPD/ft

$t := 360 \cdot day$ days

$test_{validity} := if\left(t > 250 \cdot \frac{r_c^{\,2}}{T}, \text{"VALID"}, \text{"NOT"}\right)$ $test_{validity} = \text{"VALID"}$

$u := \frac{r^2 \cdot S}{4T \cdot t}$ $u = 1.969 \times 10^{-11}$ U is a well factor

$s_{drawdown} := \frac{Q}{4\pi \cdot T} \cdot \int_u^{\infty} \frac{e^{-u}}{u}\,du$ Theis equation

$s_{drawdown} = 333.4\,ft$ feet of drawdown

TERRASAT, Inc.

Memo

To: Gwen Holdman and Chris Pike

Alaska Center for Energy and Power

From: Dan

Date: February 12, 2015

Re: Addendum to Pilgrim Hot Springs report, Clarification of Assumptions about Aquifer Yield Calculations

---

TERRASAT provided estimations of aquifer yields using an equation formulated by Theis in 1935. This equation, shown in the appendix of our report, calculates drawdown in a confined aquifer, based on pumping rate, transmissivity, and a well function. The well function is based on the distance from the well, aquifer storitivity, pumping time, pumping rate and transmissivity of the aquifer. We assumed the following values:

Distance from the well (**r**) is the radius of the casing. This value provides the maximum drawdown at the well, and thus the maximum aquifer yield from the well.

Storativity, or storage coefficient, typically ranges from 0.005 to 0.0005 for confined aquifers. Todd, and Mays, 2004, P. 58. We estimated storativity by multiplying aquifer thickness times 2.1 x 10^{-6} (unitless). This equation is provided by Kasenow, 2010, page 111. We choose this method so that our values are best estimates for each aquifer.

Time was assumed to be 365 days, continuous pumping. Continuous pumping assumes the aquifer does not fully recover during the pumping period. As a comparison, a domestic water well may pump for minutes to an hour and shut off. During the shut off period, the aquifer typically recovers or recharges fully. By assuming continuous pumping for an entire year, we are calculating a minimum yield for the well.

Transmissivity is defined as k (**hydraulic conductivity**) * **aquifer thickness**. Aquifer thickness was determined from the geophysical logs combined with the drilling logs. K, the hydraulic conductivity of the aquifer, is typically derived by conducting an aquifer flow test while measuring drawdown. Since aquifer test results are not available, we made the assumption that the aquifers behave either like fine-grained sand or medium-grained sand. We used average values from a text book for these two grain sizes and thus calculated a range of aquifer yields. The following table, from Batu, 1998, p . 35, is the source of our average hydraulic conductivities (refer to table 2-2 on next page).

We used these parameters with the Theis equation and iterated well yield until the drawdown matched the available drawdown in the well, considering a pump setting above the preferred screen zone.

The text book values show that hydraulic conductivity ranges over 3 to 4 orders of magnitude. That is why we recommend aquifer testing to get more accurate values of transmissivity and to verify if the aquifers behave as a Theis confined aquifer. Other potential aquifer types are confined with aquitard leakage or aquitard storage, or even various rock fracture configurations. Knowing how the aquifer behaves allows for a better estimate of yield.

Bibliography

Batu, Vedat, 1998, Aquifer Hydraulics, A comprehensive Guide to Hydrogeologic Data Analysis, John Wiley and Sons.

Kasenow, Michael, 2010, *Applied Ground-Water Hydrology and Well Hydraulics*, 3rd Ed.

Theis, Charles V. (1935). "The relation between the lowering of the piezometric surface and the rate and duration of discharge of a well using ground-water storage". *Transactions, American Geophysical Union* **16**: 519–524.

Todd, D. and Mays, L., 2004, Groundwater Hydrology, 3rd Ed. John Wiley and Sons.

TABLE 2-2 Hydraulic Conducitivity of Porous Materials

Group	Porous Material	Number of Analysis	Range of Hydraulic Conductivity, K (cm/s)	Arithmetic Mean Average Hydraulic Conductivity, K_{av} (cm/s)
Igneous rocks	Weathered granite	7	$(3.3–52) \times 10^{-4}$	1.65×10^{-3}
	Weathered gabbro	4	$(0.5–3.8) \times 10^{-4}$	1.98×10^{-4}
	Basalt	93	$(0.2–4250) \times 10^{-6}$	9.45×10^{-6}
Sedimentary materials	Sandstone (fine)	20	$(0.5–2270) \times 10^{-6}$	3.31×10^{-4}
	Siltstone	8	$(0.1–142) \times 10^{-8}$	1.9×10^{-7}
	Sand (fine)	159	$(0.2–189) \times 10^{-4}$	2.28×10^{-3}
	Sand (medium)	255	$(0.9–567) \times 10^{-4}$	1.65×10^{-2}
	Sand (coarse)	158	$(0.9–6610) \times 10^{-4}$	5.20×10^{-2}
	Gravel	40	$(0.3–31.2) \times 10^{-1}$	4.03×10^{-1}
	Silt	39	$(0.09–7090) \times 10^{-7}$	2.83×10^{-5}
	Clay	19	$(0.1–47) \times 10^{-8}$	9.00×10^{-8}
Metamorphic rocks	Schist	17	$(0.002–1130) \times 10^{-6}$	1.90×10^{-4}

Source: After Morris and Johnson (1967) and Mercer et al. (1982).

Source: Batu, V, 1998, p. 35.

Appendix L
Fugro Magnetotelluric Report

PILGRIM SPRINGS - ALASKA

MAGNETOTELLURIC (MT) SURVEY

Final Report

For

University of Alaska

By

Fugro Electro Magnetics Italy Srl

With

Fugro Gravity and Magnetics Services, Huston

November 2012

This report has been authorised for release by:

Stephen Hallinan, General Manager, Fugro Electro Magnetics Italy

Disclaimer
Fugro assumes no responsibility for any direct or indirect consequences of using the information or opinions provided here.

Table of Contents

SUMMARY 1
1 INTRODUCTION 2
Coordinates 2
2 MAGNETOTELLURIC SURVEY 4
2.1 Equipment and Procedures 4
2.1.1 Equipment 4
2.1.2 Data acquisition 4
2.1.3 Overnight Data Recording Schedule 5
2.2 Data Processing 6
2.2.1 Robust Data Processing 6
2.2.2 Natural Signal Level 6
2.3 MT Sounding and Data Quality 8
2.4 Site Information Sheet 11
3 QUALITATIVE DATA ANALYSIS 12
3.1 Apparent Resistivity and Phase Parameter Maps 12
3.2 Magnetic Transfer Functions (Tipper) 17
4 1D MT MODELING 21
4.1 Tensor invariant 21
4.2 Impedance components at orientation N45ºW. 26
5 3D MT INVERSION 31
5.1 Mesh Dimensions 31
5.2 Inversion Settings and Data Fit 34
5.3 Blind 3D Inversion 35
5.4 Constrained 3D Inversion 49
6 INTEGRATION WITH WELL INFORMATION 56
7 BIBLIOGRAPHY 62
Appendix A SURVEY DETAILS A-1
A.1 Personnel A-1
A.2 Time Line A-1
A.3 Logistics A-1
A.4 Weather Conditions A-2
A.5 HSE Statistics A-2
Appendix B MT TIME SERIES FORMAT B-1
Appendix C 3-D MT INVERSION C-1

C.1 Output Data C-2
C.1.1 WinGLink OUT Format (ASCII). C-2
C.1.2 UBC Format (ASCII)..... C-3
C.1.3 4-Column ASCII format C-3
C.1.4 ECLIPSE format..... C-3
Appendix D DELIVERABLES D-1

List of Figures

Figure 1. MT site locations at Pilgrim Springs, on topographic map. 2

Figure 2. MT site locations at Pilgrim Springs, on topographic map. 3

Figure 3. Geomagnetic planetary Ap indices within the Pilgrim Springs survey period (red brackets). 7

Figure 4. MT site locations. Data plots from the marked sites are shown in Figure 5. 8

Figure 5. Example soundings illustrating data quality with data orientation geographic N. 9

Figure 6. Magnetic transfer function examples of selected 6 sites shown before. 10

Figure 7. *Apparent* resistivity in XY (left) and YX (right) polarization at 1000Hz (top) and 30Hz (bottom). Data rotation: N0ºE. 13

Figure 8. *Apparent* resistivity in XY (left) and YX (right) polarization at 1Hz (top) and 0.03Hz (bottom). 14

Figure 9. Impedance phase in XY (left) and YX (right) polarization at 1000Hz (top) and 30Hz (bottom). Data rotation: N0ºE. 15

Figure 10. Impedance phase in XY (left) and YX (right) polarization at 1Hz (top) and 0.03Hz (bottom). 16

Figure 11. Polar diagrams (Zxy component as a function of rotation angle) and induction vector strike (bar) at 0.01Hz. 17

Figure 12. Induction vectors (real parts) at 1000Hz and 30Hz. Arrows are plotted in the convention to point *away* from conductors. 18

Figure 13. Induction vectors (real parts) at 1Hz and 0.03Hz. Marked sites are displayed in the 1D modeling section (Figure 15 and Figure 16). 19

Figure 14. Real induction vectors at 3Hz overlaid on apparent resistivity at 10Hz (top) and temperature from wells at 40m depth – see section 6 for the well temperature data set. 20

Figure 15. Example soundings with 1D models. Green: layered model, purple: smooth Occam model, blue: Bostick curve (analytical conversion of impedances). The geometric average of the XY and YX impedance elements is modelled. 22

Figure 16. Example soundings with 1D models, as in Figure 15. 23

Figure 17. Resistivity at 25m and 100m depth from 1D smooth, Occam-type MT inversion (tensor *invariant*). 24

Figure 18. Resistivity at 300m and 500m depth from 1D smooth, Occam-type MT inversion (tensor *invariant*). 25

Figure 19. Cumulative *conductance* from 1D inversions (invariant) to 100m and 300m depth. 26

Figure 20. 1D modeling at site P072 in data orientation N45ºW, separately for components XY and YX, resulting in very significantly different resistivity distribution at depth >100m. 27

Figure 21. 1D inversion in different data rotation system (N45°W), separately for XY (top) and YX (bottom) component data. The resistivity map at 300m depth shows significant differences. 28

Figure 22. Resistivity at profiles 2 and C from smooth 1D MT inversion (Occam, XY component). 29

Figure 23. Resistivity at profile D from smooth 1D MT inversion (Occam, XY component). 30

Figure 24. Top view of 3D MT inversion mesh, core area (top) and full mesh area (bottom). 32

Figure 25. Side view of 3D MT inversion mesh, core area (top), and full section. 33
Figure 26. Profile locations for 3D resistivity structure visualization. 35
Figure 27. 3D MT inversion (#18) data fit for 4 example MT soundings. Faint: observed MT data, bold colors: predicted resistivity / phase and tipper from inversion #18. 36
Figure 28. Data fit as in Figure 27 for 2 more example soundings. 37
Figure 29. Resistivity map at 25m and 50m depth from blind 3D MT inversion (#18). 38
Figure 30. Resistivity map at 100m and 150m depth from blind 3D MT inversion (#18). 39
Figure 31. Resistivity map at 200m and 300m depth from blind 3D MT inversion (#18). 40
Figure 32. Resistivity map at 400m and 500m depth from blind 3D MT inversion (#18). 41
Figure 33. Resistivity map at 750m and 1000m depth from blind 3D MT inversion (#18). 42
Figure 34. Resistivity at profiles 0 and 1 from blind 3D MT inversion (#18). 43
Figure 35. Resistivity at profiles 2 and 3 from blind 3D MT inversion (#18). 44
Figure 36. Resistivity at profiles 4 and A from blind 3D MT inversion (#18). 45
Figure 37. Resistivity at profile B from blind 3D MT inversion (#18) 46
Figure 38. Resistivity at profiles C and D from blind 3D MT inversion (#18). 47
Figure 39. Resistivity at profile E from blind 3D MT inversion (#18) 48
Figure 40. Airborne differential resistivity at 20m depth. 49
Figure 41. Airborne differential resistivity at depths of 15m (left) and 60m (right). Note the gaps underneath conductive areas. 50
Figure 42. A priori information from Resolve airborne survey in starting model for MT inversion, shown with slices in X, Y, and Z direction from above (upper panel), and below (lower panel) 51
Figure 43. Resistivity map at 25m and 200m depth from constrained 3D MT inversion (#20). 53
Figure 44. Resistivity at profiles 1 from blind (top) and constrained (bottom) 3D MT inversion. 54
Figure 45. Resistivity at profile B from blind (top) and constrained (bottom) 3D MT inversion. 55
Figure 46. Temperature distribution of the 3 deeper PS-12-[1-3] drill holes. 56
Figure 47. Resistivity from blind 3D inversion (contours) on drill hole temperature data (color, in degrees Celsius), for 20m an 50m depth. 57
Figure 48. Resistivity from blind 3D inversion (contours) on drill hole temperature data (color, in degrees Celsius), for 100m and 200m depth 58
Figure 49. 3D MT inversion model (blind, #18), with resistivity-converted *conductivity* well logs at wells PS-12-[1-3]. View from west (top) and south (bottom). With respect to the deep well PS-12-2, the MT inversion images the low resistivity zone slightly too shallow when viewed from west, but at the same depth as the low resistivity further north 60
Figure 50. As previous figure, but from *resistivity* logs (16N), with significantly higher resistivity estimates. Note the bad data section (red) in the deep part of well PS-12-2. 61

List of Tables

Table 1. Projected map coordinates. 2

Table 2. MT Instrument and layout. 4
Table 3. MT acquisition parameters. 4
Table 4. MT Overnight recording schedule, one complete run cycles per 24 hours. 5
Table 5. 3D inversion mesh details 31
Table 6. 3D MT inversion settings. 34
Table 7. Field Personnel. A-1
Table 8. Project Time Line. A-1

SUMMARY

Under contract from University of Alaska, Fugro Gravity and Magnetics Services (Huston) with Fugro Electro Magnetics Italy Srl carried out a full tensor, broadband magnetotelluric survey of 59 soundings.

Two MT field teams deployed up to 3 MT systems each (ADU-07e Metronix receivers and sensors) for overnight recording, thus producing up to 6 MT soundings per day. Fieldwork was completed between August 13th and August 28th.

MT data processing to impedances functions was performed at the field office and delivered via e-mail throughout the project. With sufficient natural signal amplitudes during the survey period, absence of EM noise sources, the overall MT data quality was very good. During the survey 5 MT stations acquired were repeated for both improving data quality or technical failure. In a total of 10 days MT production, no LTI were recorded.

Inversion for 3D resistivity structure was performed using the recently developed Fugro RLM-3D MT code. Full tensor complex impedances were inverted in the frequency range from 0.032 Hz to 5.62 kHz, using 4 frequencies per decade, on a 384 core cluster.

Both unconstrained (blind) and constrained inversions were carried out. For the constrained inversion, the starting and a priori model in 3D inversions included shallow structure from resistivity-depth maps obtained from the Resolve airborne EM survey, conducted by Fugro Airborne Surveys Corp., Mississauga, Canada.

1 INTRODUCTION

The survey was carried out on lands centered on the Seward Peninsula about 70 km North of Nome, Alaska.

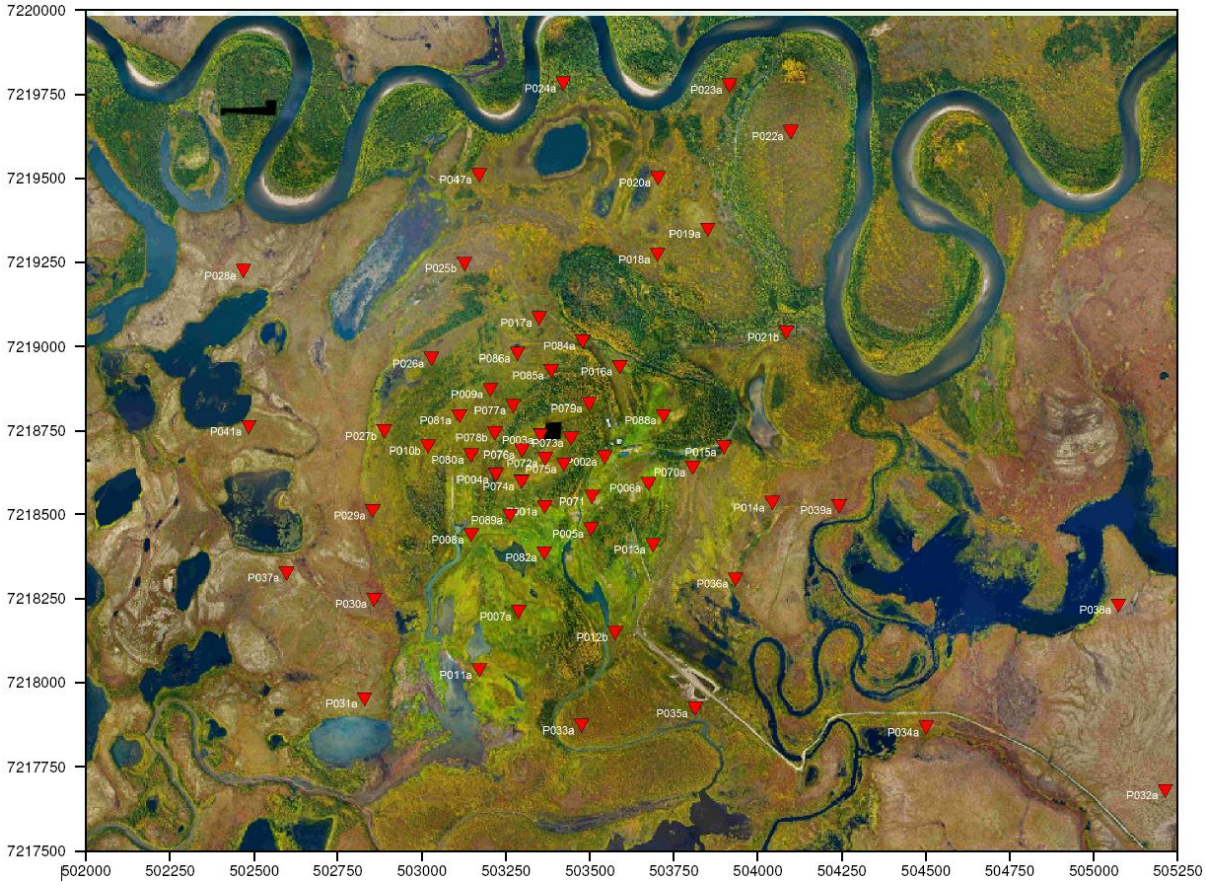


Figure 1. MT site locations at Pilgrim Springs, on topographic map.

Coordinates

Projected map coordinates are shown in kilometers on the UTM system, zone 03N.

Datum	WGS 1984
Spheroid	WGS 1984
Elevation	MT station elevations projected from NED DEM

Table 1. Projected map coordinates.

Coordinates in geographic latitudes and longitudes are in WGS84.

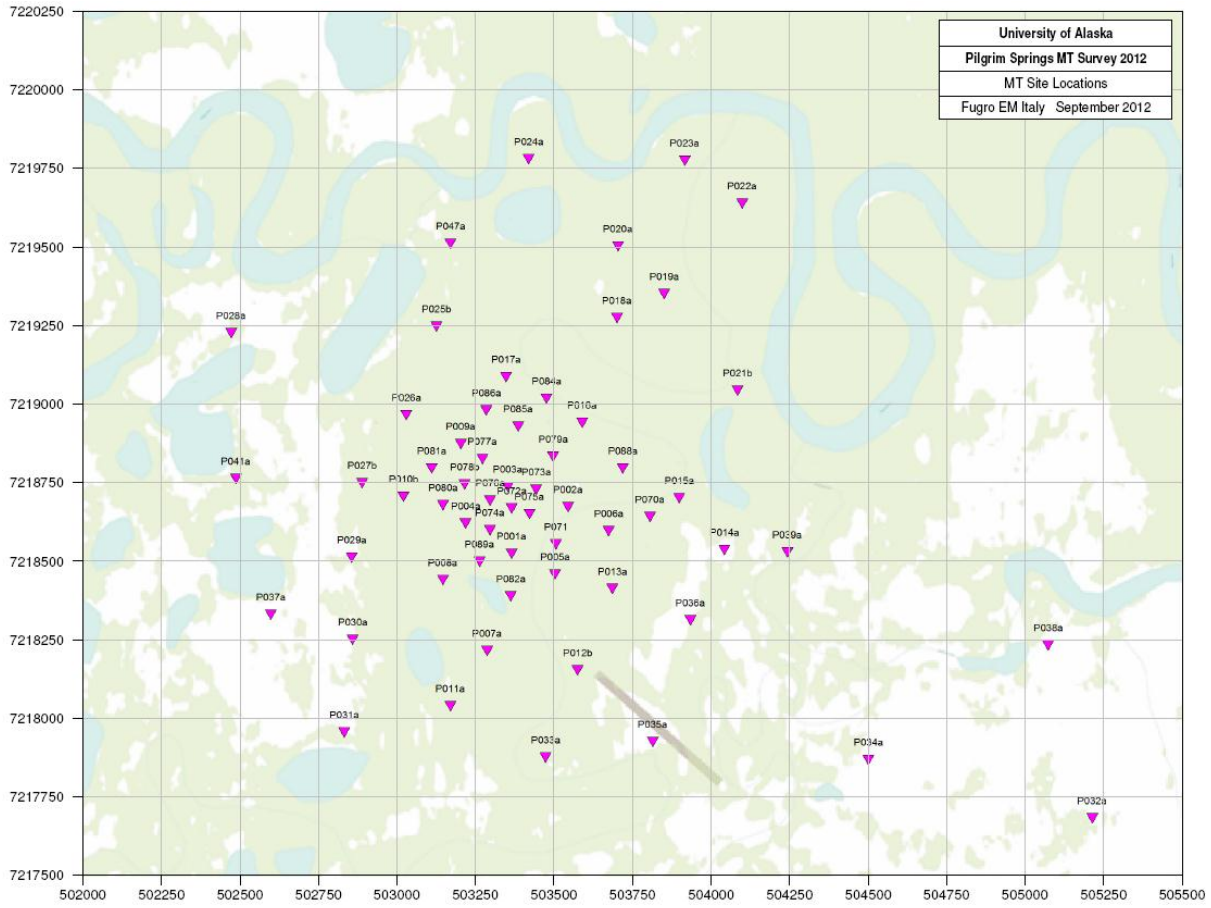


Figure 2. MT site locations at Pilgrim Springs, on topographic map.

2 MAGNETOTELLURIC SURVEY

2.1 Equipment and Procedures

2.1.1 *Equipment*

Receiver	Metronix ADU-07e (Germany) (http://178.63.62.205/mtxgeo/index.php/logger/adu-07e) 10 channel boards (5 HF, 5LF), 24 bit A/D.
Field components	5 components at each setup location (except site P023, which had electrics only): Ex, Ey, Hx, Hy, Hz
Electric field sensors	Wolf Chemical Ltd (Hungary). Non-polarizing PbPbCl
Magnetic field sensors	Metronix MSF-06e (Germany; Hx/Hy components) (http://178.63.62.205/mtxgeo/index.php/sensors/mfs-06e) Metronix MSF-07e (Germany; Hz component) (http://178.63.62.205/mtxgeo/index.php/sensors/mfs-07e)
Layout	Cross layout (4 dipoles): typically 50 m electric line length, i.e. 100 m dipoles azimuth: nominally 0º geomagnetic north ≈ 12.4º E

Table 2. MT Instrument and layout.

2.1.2 *Data acquisition*

MT method	5-component (full tensor) broadband MT with far remote reference
# of field teams	2
# instruments / team	3
# layouts per instrument / day	1 (overnight recording)
maximum production / day	6 sites
recorded frequency range	0.001 Hz – 10,000 Hz
station spacing	50 – 700 m, typically 100m in the central area
total # MT soundings	59

Table 3. MT acquisition parameters.

In addition to the field sites, one remote station was installed, approximately 5 km in SW direction from the survey area. Data from this site was used in the processing of the field sites applying the remote reference processing technique (e.g. Gamble, 1979).

2.1.3 *Overnight Data Recording Schedule*

The overnight recording schedule (Table 1) was configured to be repetitive with 24 hours periodicity, with absolute start time at 16.00 GMT every day, and recording started immediately after site installation with the run scheduled at that time. Times are *relative* with respect to 16:00 universal time or 8:00 local Pilgrim Springs time.

The repeated suite allows for high frequency recording during different time of the night, taking advantage of the naturally intermittent high frequency signal, originating from distant lighting activity. The total recording time at any station exceeded 14 hours, and the processed data covers the broadband frequency range from 10,000 Hz to 0.001 Hz.

Frequency [Hz]	Boards	Start [hh:mm:ss]	Stop [hh:mm:ss]	Duration [ss]	Gain Ex | Ey | Hx | Hy | Hz				
64 (2,048)	LF	[00:00:00]	09:59:00	[35,940]	1	1	1	1	1
2,048	LF	08:00:00	08:15:00	900	1	1	1	1	1
2,048	LF	09:00:00	09:15:00	900	1	1	1	1	1
65,536	HF	10:01:00	10:01:30	30	8	8	8	8	1
65,536	HF	10:03:00	10:03:30	30	64	64	64	64	1
8,192	HF	10:05:00	10:09:00	240	1	1	1	1	1
65,536	HF	10:11:00	10:11:30	30	8	8	8	8	1
64 (2,048)	LF	10:14:00	16:59:00	24,300	1	1	1	1	1
2,048	LF	11:00:00	11:15:00	900	1	1	1	1	1
2,048	LF	13:00:00	13:15:00	900	1	1	1	1	1
65,536	HF	17:01:00	17:01:30	30	8	8	8	8	1
65,536	HF	17:03:00	17:03:30	30	64	64	64	64	1
8,192	HF	17:05:00	17:09:00	240	8	8	8	8	1
65,536	HF	17:11:00	17:11:30	30	64	64	64	64	1
64 (2,048)	LF	17:14:00	23:58:00	24,240	1	1	1	1	1
2,048	LF	18:00:00	18:15:00	900	1	1	1	1	1
2,048	LF	20:00:00	20:15:00	900	1	1	1	1	1

Table 4. MT Overnight recording schedule, one complete run cycles per 24 hours.

2.2 Data Processing

2.2.1 *Robust Data Processing*

MT field data (raw time series) were processed using a robust, remote reference processing code with signal separation capability. Based on the methodology described in Larsen (1996), the Fugro robust processing software uses a sophisticated, for the most part iterative approach, including:

- Pre-whitening of spectra using first differences in time domain
- Removal of very large outliers of the raw (and low passed) time series in time domain
- Removal of large periodic variations, allowing for linear changes in frequency and amplitude over time
- Segment pre-selection and weighting based on coherence between local and remote channels
- Estimation of smooth continuous transfer function estimates using a quadratic or cubic spline fit
- Prediction of electric (or vertical magnetic) time series and calculation of residual data to identify outliers

When the update of the transfer function estimates approaches unity, the iterative procedure terminates.

Processed sub-bands from different recordings and sampling rates are then combined to a single result file containing tensor impedance and magnetic tipper transfer functions from nominally 0.001 Hz to 10 kHz.

These combined processing results are delivered in EDI format (SEG standard; Wight, 1988), one file per site.

2.2.2 *Natural Signal Level*

Natural MT signal relates to solar and lightning activity and the Earth's response to it. The spectrum exploited in broadband MT surveys typically lies within the frequency range from 10^{-3} Hz, and lower, to 10 kHz. At low frequencies, the signal largely stems from ionospheric currents excited from ionospheric and magnetospheric fluctuations due to interaction with solar radiations. Above 1 Hz, most signals originate from distant electric lightning sferics. Signal strengths at these higher frequencies depend on distance to lightening centers and on time: season, weather, and time of day. Signal propagation and attenuation depend on the geometry of the Earth-ionosphere waveguide and are therefore also time-dependent: a 20 km higher ionospheric base due to atmospheric expansion during daytime results in increased signal attenuation.

Natural signal lows occur at around 0.1-1 Hz; the high frequency end of ionospheric variations and the low frequency end of sferics, and at 1-2 kHz within the HF frequency band; due to a change of the dominant propagation mode (Volland, 1982).

Magnetic activity on the lower frequency band is quantified by a several established indices, e.g. K(p), a(p), A(p). The 3-hour K index quantifies the level of horizontal magnetic fluctuation from normal, quiet levels for single geomagnetic observatories, and the planetary Kp index represents the weighted average of the K indices from 13 global observatories (Bartels, 1939). The a(p) index is directly inferred from the K(p) index using a conversion table, and A(p) represents the daily average from the 8 3-hour a(p) values.

The Ap index for the survey period, displayed in Figure 3, shows MT signal was intermediate to high.

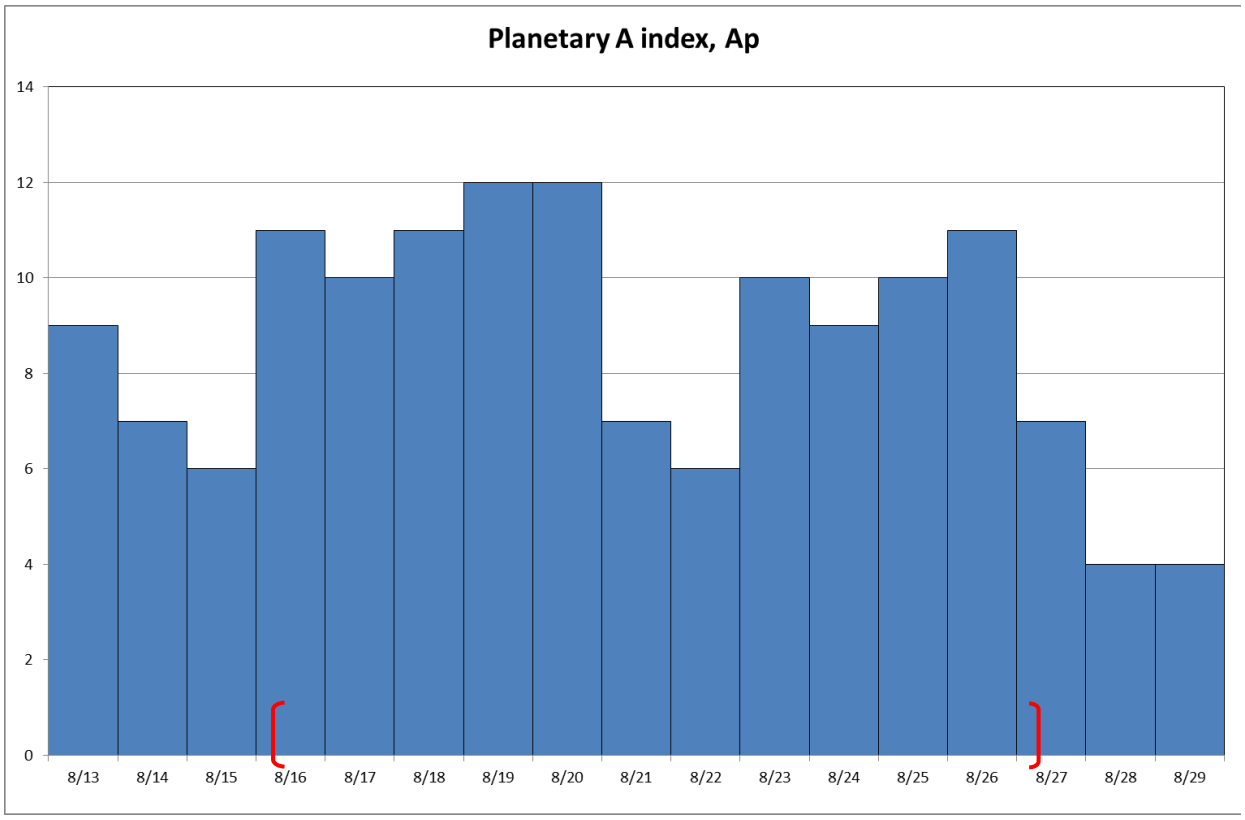


Figure 3. Geomagnetic planetary Ap indices within the Pilgrim Springs survey period (red brackets).

2.3 MT Sounding and Data Quality

Example soundings marked with dashed circles in Figure 4 are presented in Figure 5 and Figure 6. Masked data are shown in gray in the soundings shown below.

The complete set of soundings is plotted for both the edited data set and an unedited version, in PDF (in Appendix). For the edited version of the data a smoothed line from D+ analysis is shown as well (Beamish and Travassos, 1992).

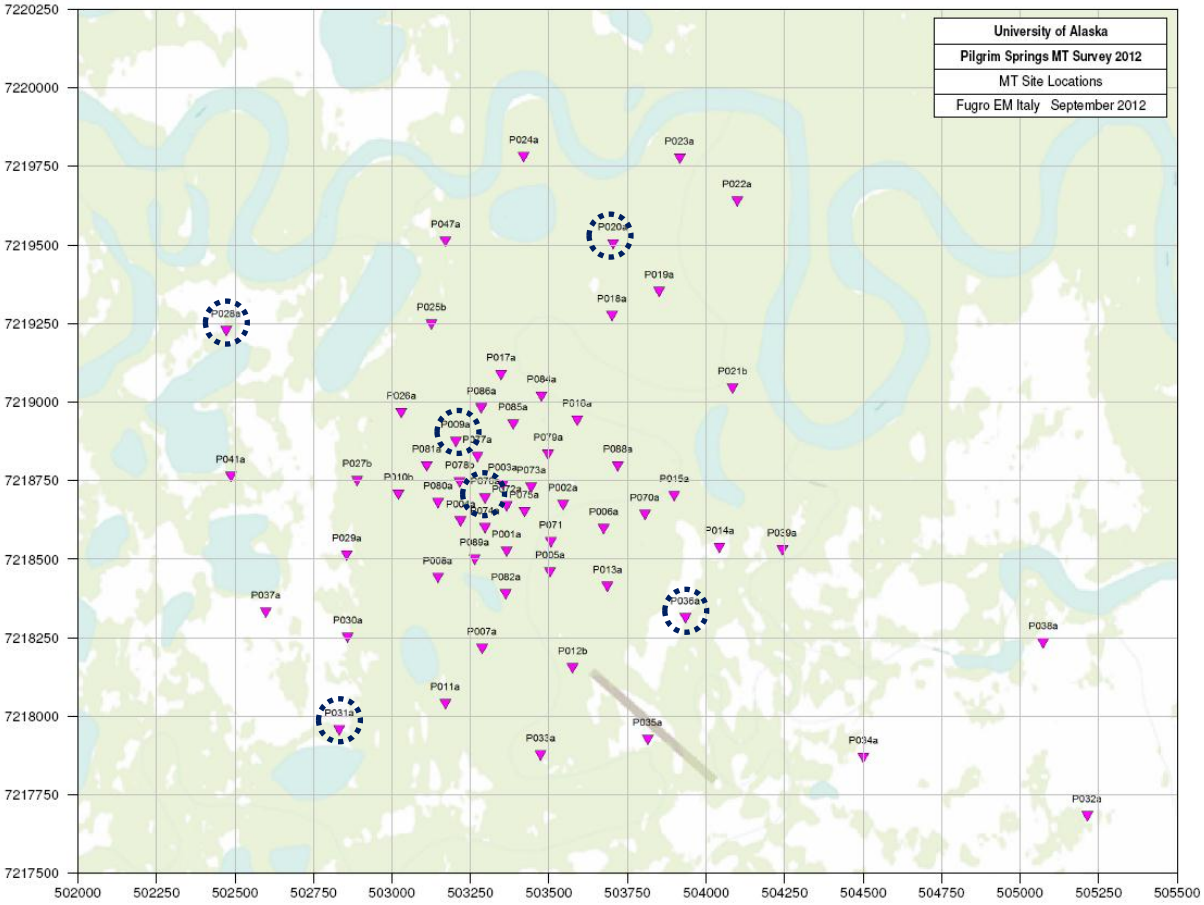


Figure 4. MT site locations. Data plots from the marked sites are shown in Figure 5.

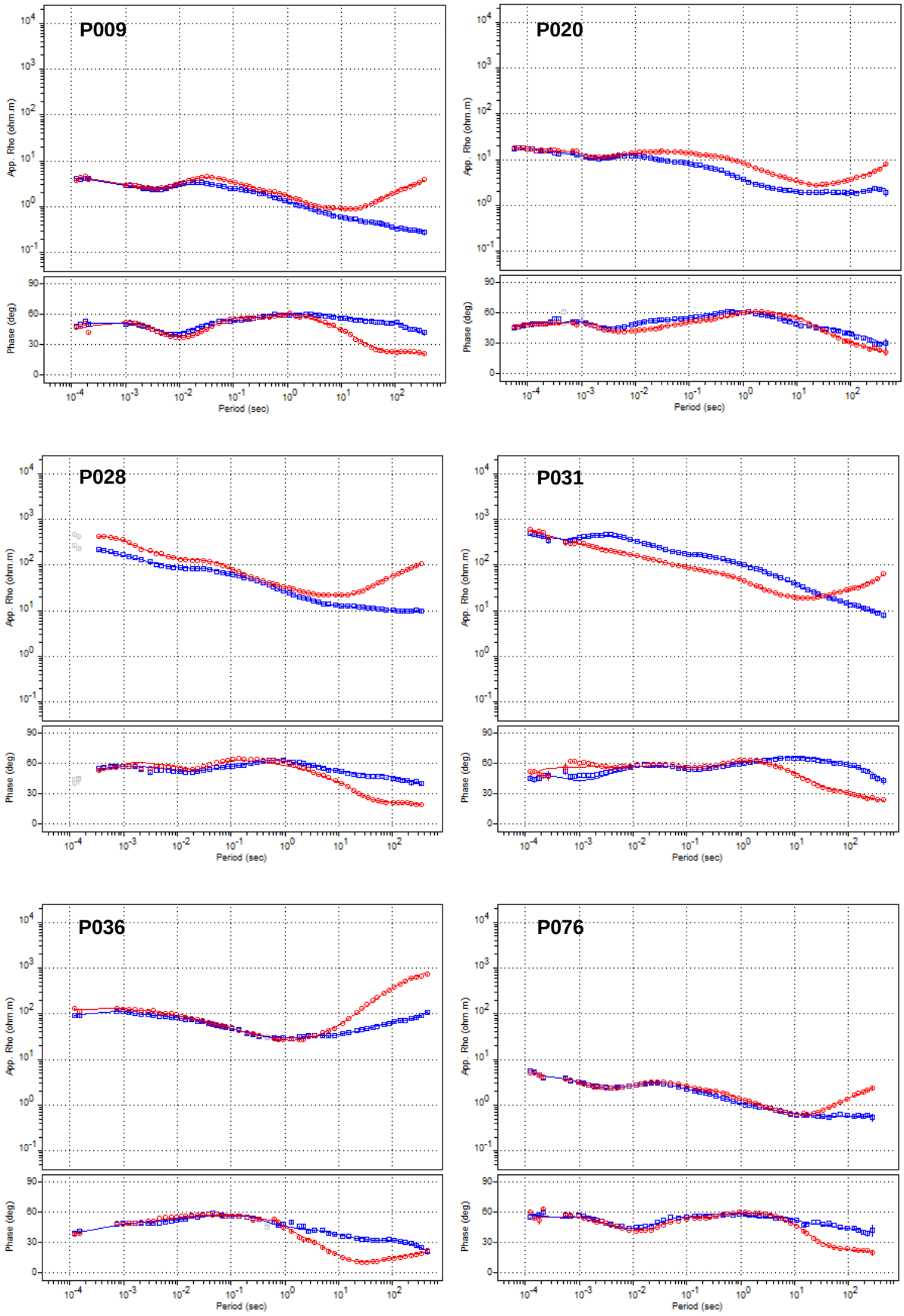


Figure 5. Example soundings illustrating data quality with data orientation geographic N.

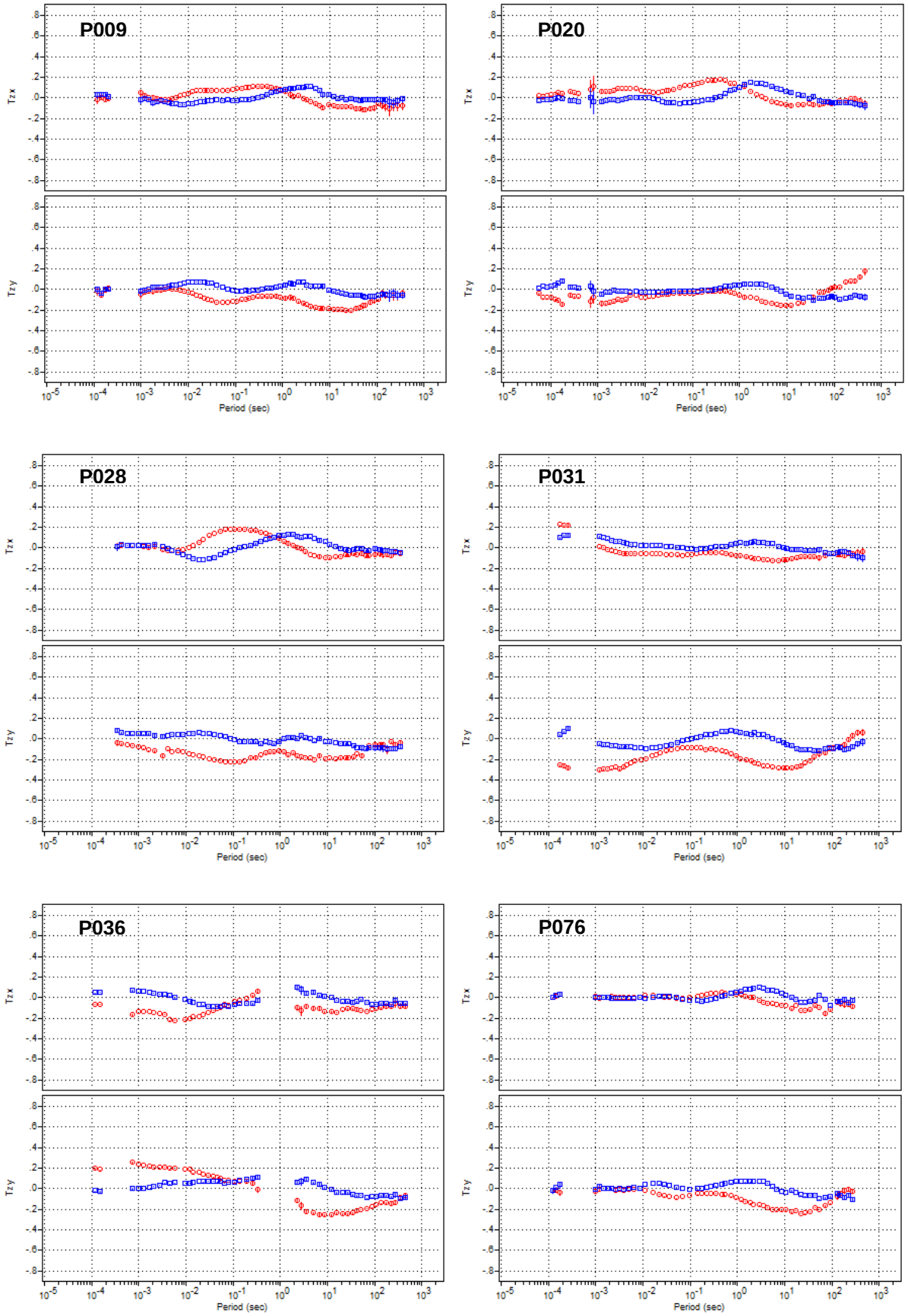


Figure 6. Magnetic transfer function examples of selected 6 sites shown before.

2.4 Site Information Sheet

This document provided as XLS document contains all relevant MT site-specific information:

- Site ID
- MT team
- Receiver instrument serial number
- Setup azimuth (clockwise from geomagnetic North)
- Electric field length (m)
- Magnetic sensor types and serial numbers
- Measured (GPS from time series) coordinates in DMS and UTM.
- Installation and Pickup Dates.

3 QUALITATIVE DATA ANALYSIS

Data are presented here in the coordinate system used also in 3D MT inversion, N0ºE, i.e. oriented within the geographic coordinate system. In this coordinate system, the impedance tensor's XY component corresponds *at first order* to currents flowing within this direction (NS), and the YX component accordingly to current perpendicular to this direction (EW).

Example soundings have been illustrated in the previous section. All soundings from the 2012 survey are plotted with the same vertical scale for apparent resistivity and phase in a separate PDF, see Appendix D.

3.1 Apparent Resistivity and Phase Parameter Maps

Parameter maps for XY and YX apparent resistivity are presented in Figure 7 and Figure 8 for 4 frequencies. Figure 9 and Figure 10 show gridded impedance phases for the same frequencies.

The color set chosen for the impedance phases has red tones for phases greater zero, and therefore those that indicate resistivity decrease with depth *at the respective frequency,* whereas blue shows a resistivity increase with depth. White marks phases around neutral 45 degrees. This simplification is of course only strictly valid for 1D resistivity structures.

As regularly observed, structure seen from impedances is mostly 1D (i.e. a function of depth) for the highest frequency range (here 1000Hz): both impedance components show similar structure, in both apparent resistivity (effectively the amplitude of the impedance) and phase.

From 30Hz to lower frequencies, differences between XY and YX emerge, i.e. data become higher dimensional, and at lowest frequencies (0.03Hz) the two components show very distinct structure.

The high frequency outline the zone of low resistivity already discovered in the airborne survey conducted by Fugro ("Resolve"), rhomb-shape and extending weakened towards NE. At decreasing frequency the low *apparent* resistivity anomaly somewhat shrinks in lateral dimension. To longer periods, a more regional NW-SE gradient in resistivity is indicated by impedances phases (at 1Hz), showing higher phases to the NW. Apparent resistivity at 0.03Hz indicates a similar contrast, mostly in the XY component.

Parameter maps at 1Hz and 0.03Hz underline the strong higher dimensionality of the data at the low frequency end. Polar diagrams indeed show a very strong polarization at long periods. These diagrams are obtained by plotting the absolute value of the XY off-diagonal impedance tensor component as a function of the rotation angle, rotating the tensor by 360 degrees, and dividing by the maximum value for normalization).

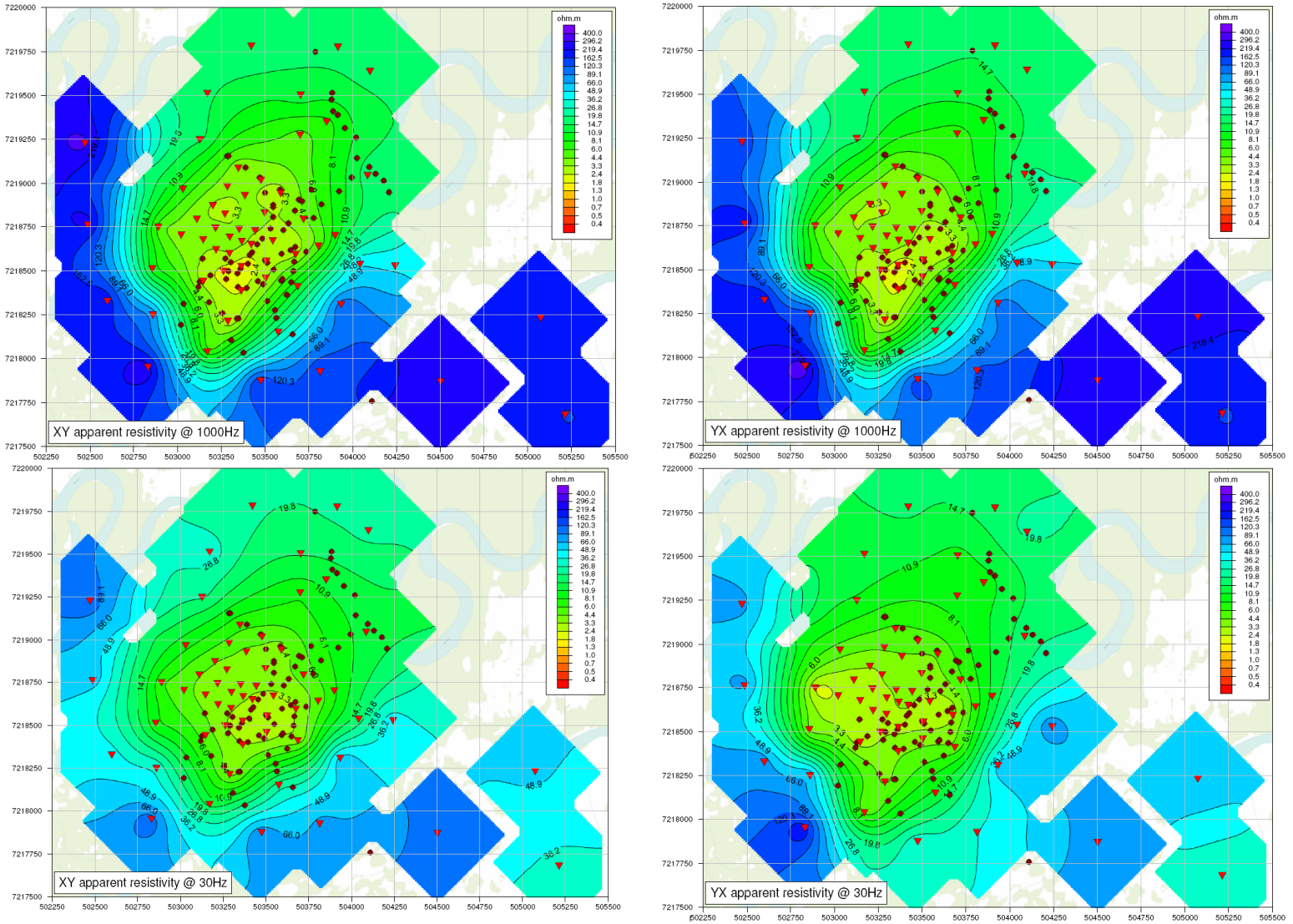


Figure 7. *Apparent* resistivity in XY (left) and YX (right) polarization at 1000Hz (top) and 30Hz (bottom). Data rotation: N0ºE.

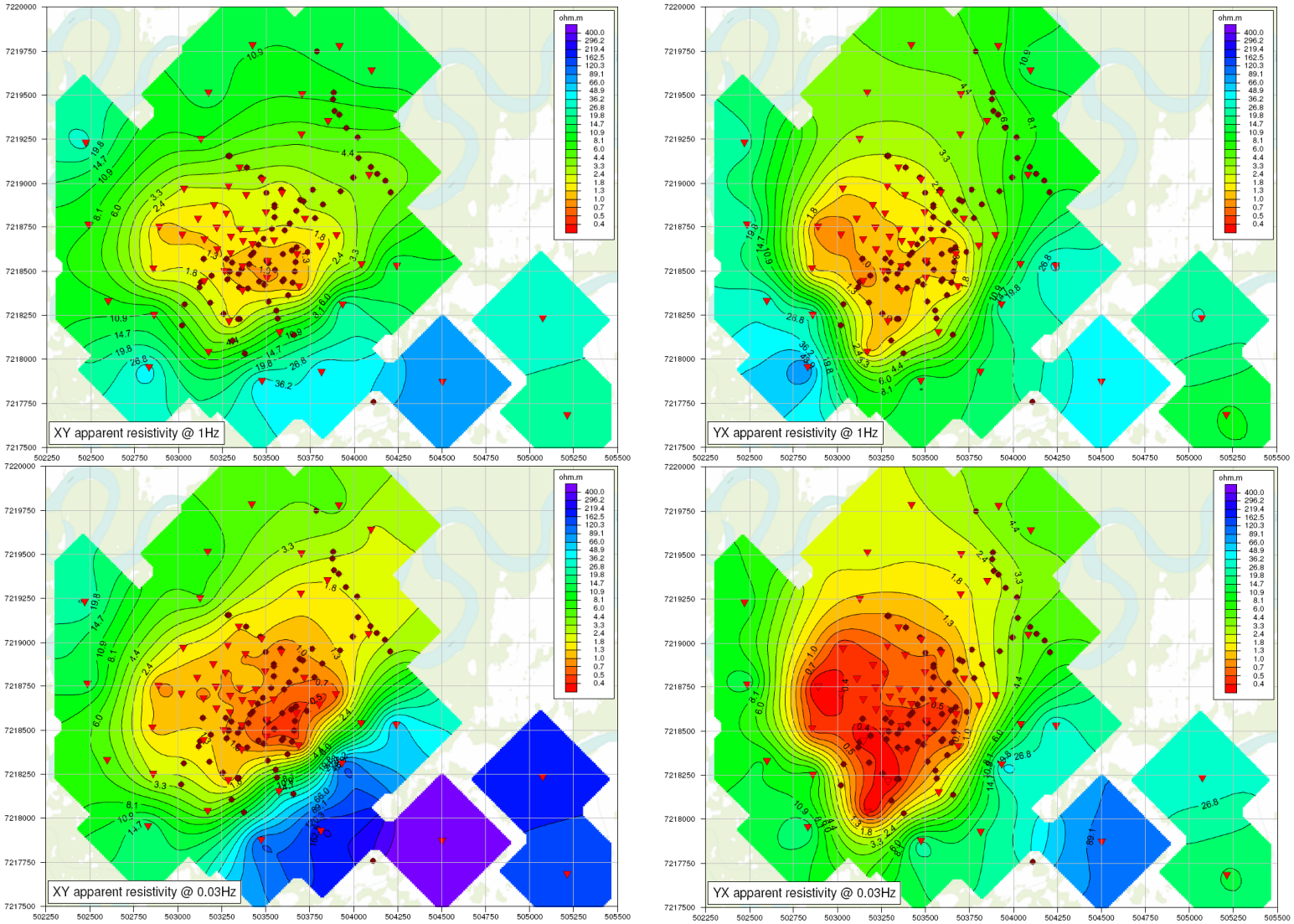


Figure 8. *Apparent* resistivity in XY (left) and YX (right) polarization at 1Hz (top) and 0.03Hz (bottom).

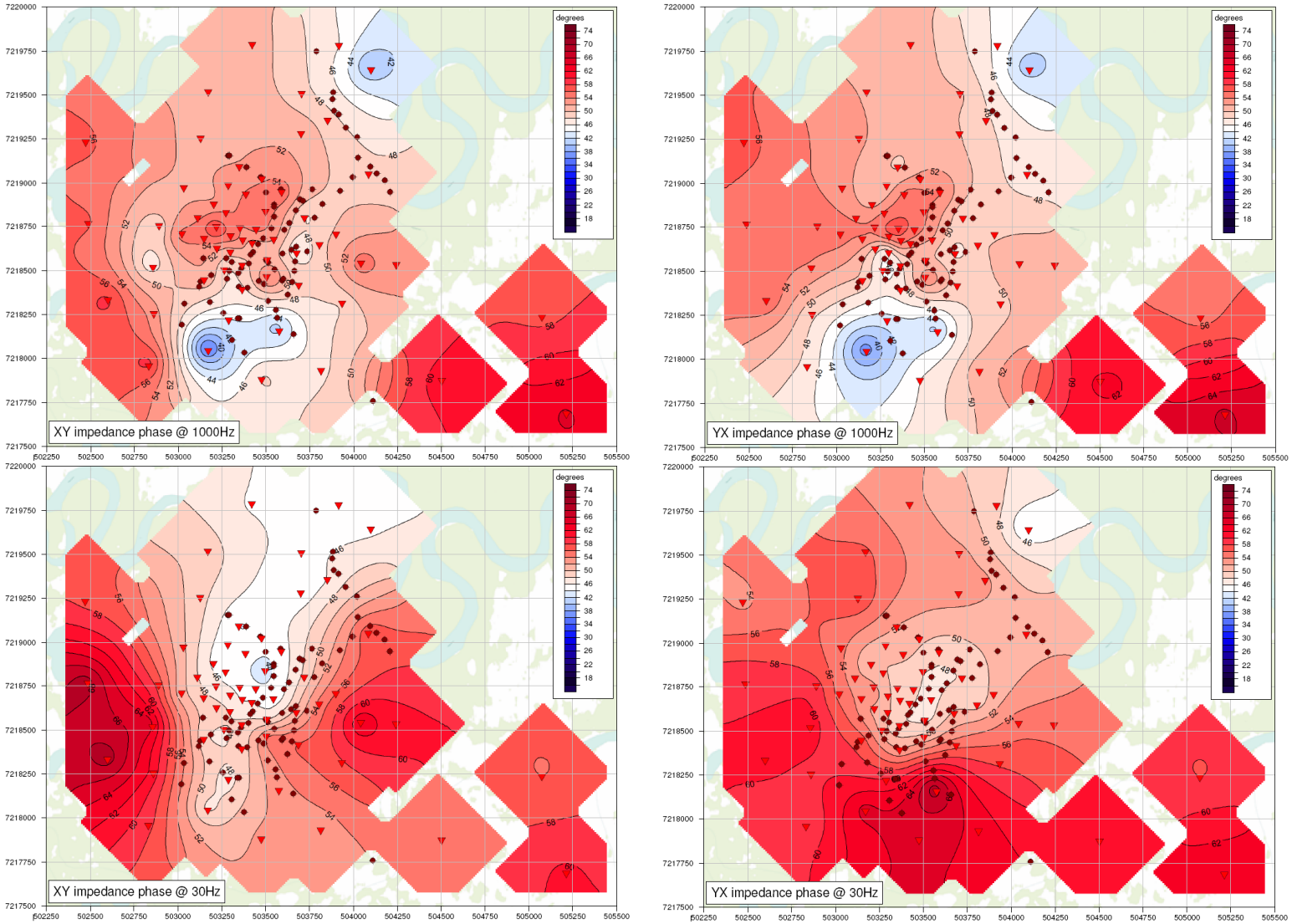


Figure 9. Impedance phase in XY (left) and YX (right) polarization at 1000Hz (top) and 30Hz (bottom). Data rotation: N0ºE.

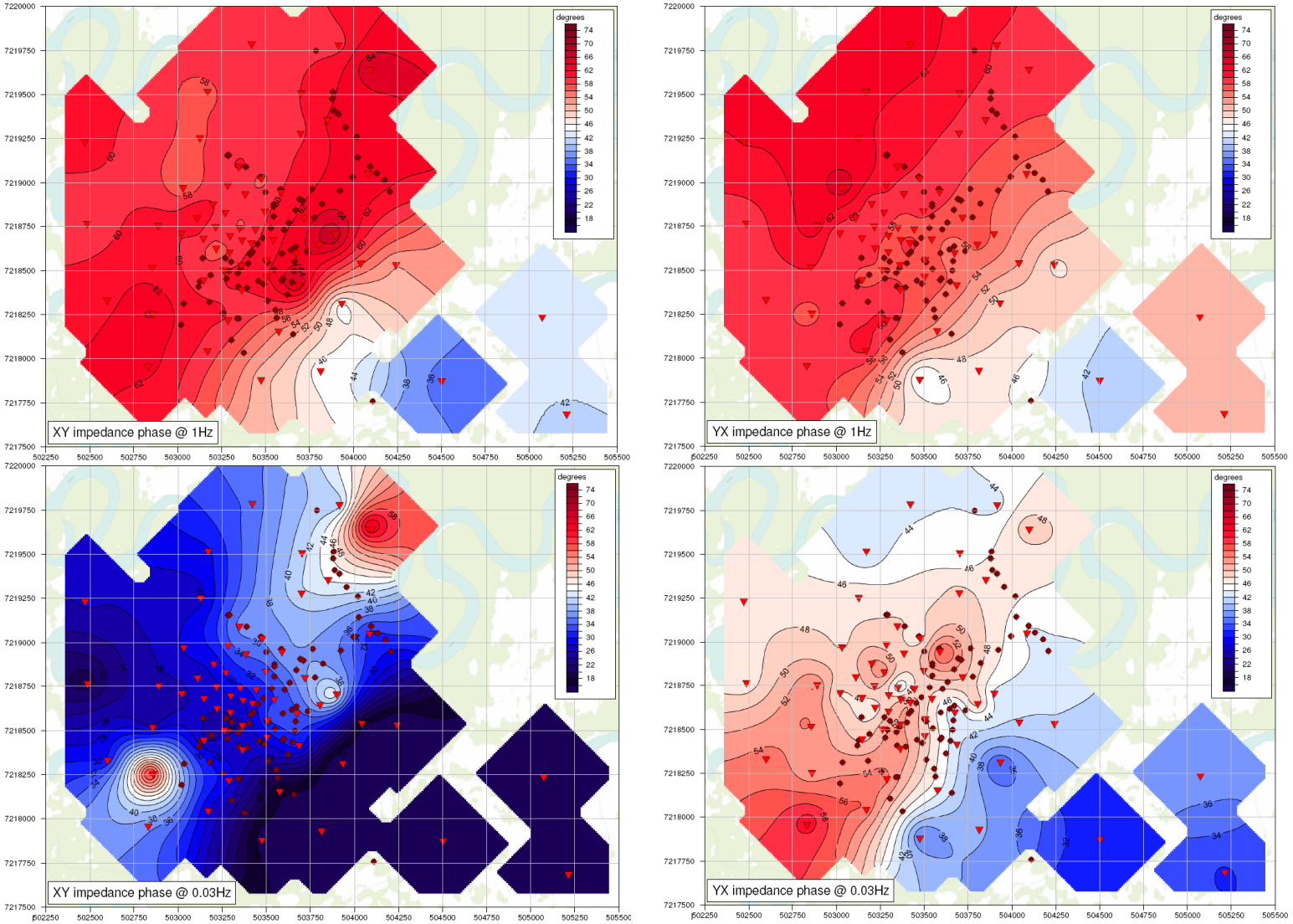


Figure 10. Impedance phase in XY (left) and YX (right) polarization at 1Hz (top) and 0.03Hz (bottom).

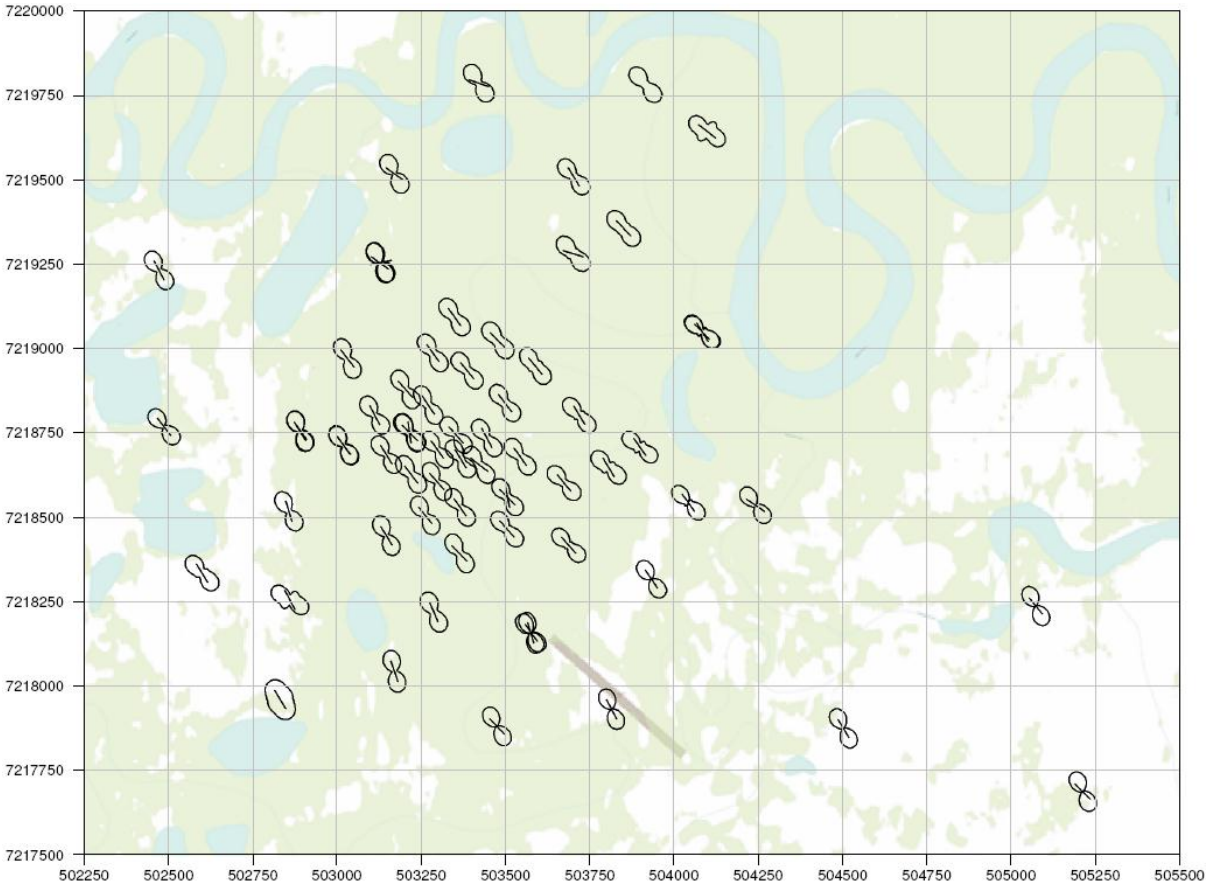


Figure 11. Polar diagrams (Zxy component as a function of rotation angle) and induction vector strike (bar) at 0.01Hz.

3.2 Magnetic Transfer Functions (Tipper)

Magnetic transfer functions – between the vertical and horizontal magnetic field components – are represented as induction vectors, or arrows, in Figure 12, for the frequencies 1000Hz and 30Hz, and Figure 13 for 1Hz and 0.03Hz. Induction arrows are a means to visualize lateral resistivity contrasts. Note that arrows are plotted in the Parkinson convention here, pointing *towards* zones of low resistivity (Wiese 1962, Parkinson, 1962).

At highest frequencies, they are sensitive to shallow resistivity contrasts in close vicinity and nicely outline the low resistivity zone observed in this frequency range, with longer arrows in the resistivity contrast zones.

At 30Hz arrows become laterally more homogeneous and radially point to the central zone of the high conductivity area. Note that with decreasing frequency, induction arrows are influenced by both deeper and laterally farther structure, and here therefore by both the extended shallow low resistivity zone found, and a deeper low resistivity anomaly.

At 1Hz the trend of the arrows is preferably in NW-SE direction, in good agreement with the phase gradient observed at that frequency in the previous sub-section.

At even longer periods induction arrows become very homogeneous laterally and are clearly influenced by structure outside the survey area, thus not resolvable from data in this laterally very small survey.

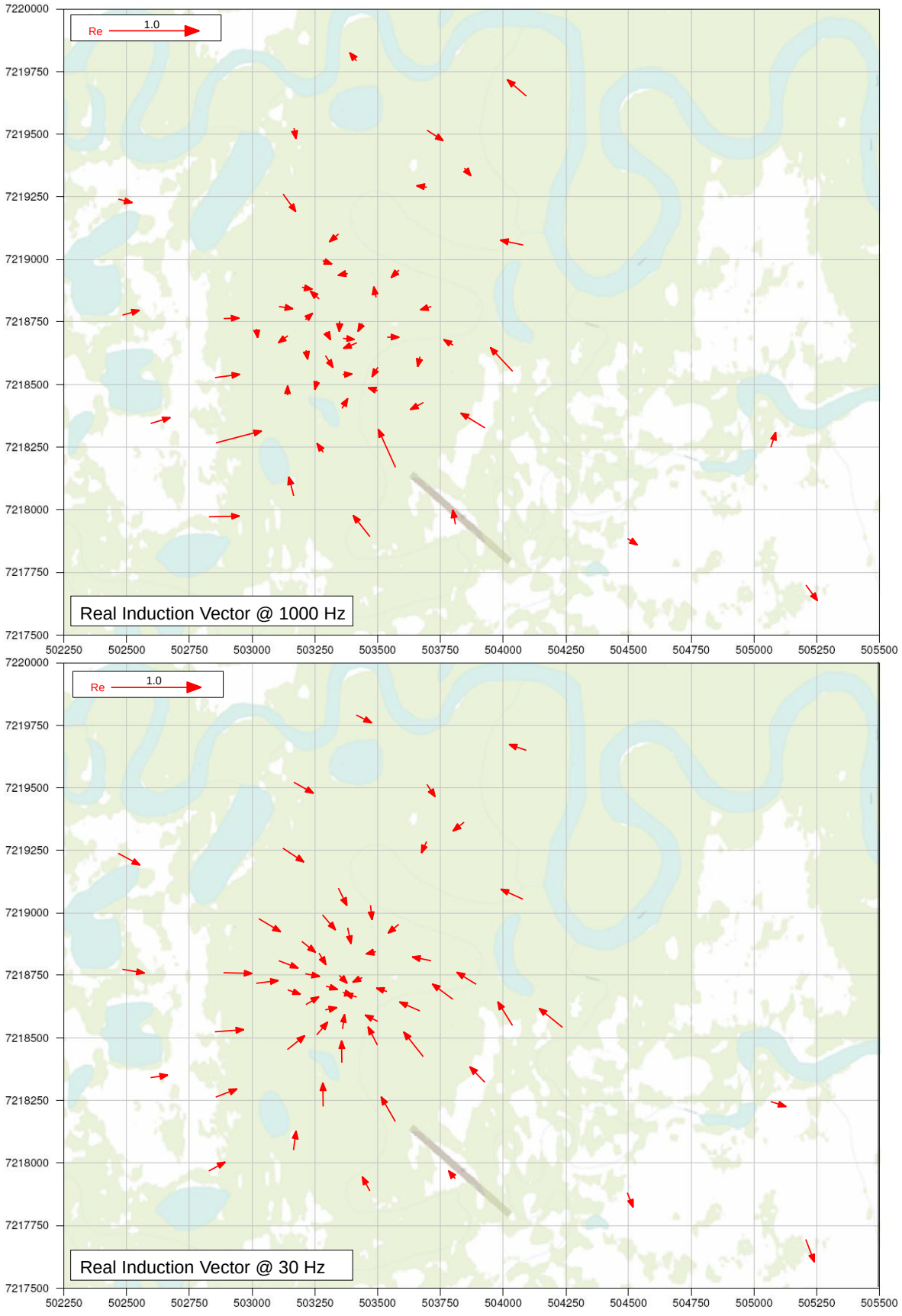


Figure 12. Induction vectors (real parts) at 1000Hz and 30Hz. Arrows are plotted in the convention to point *away* from conductors.

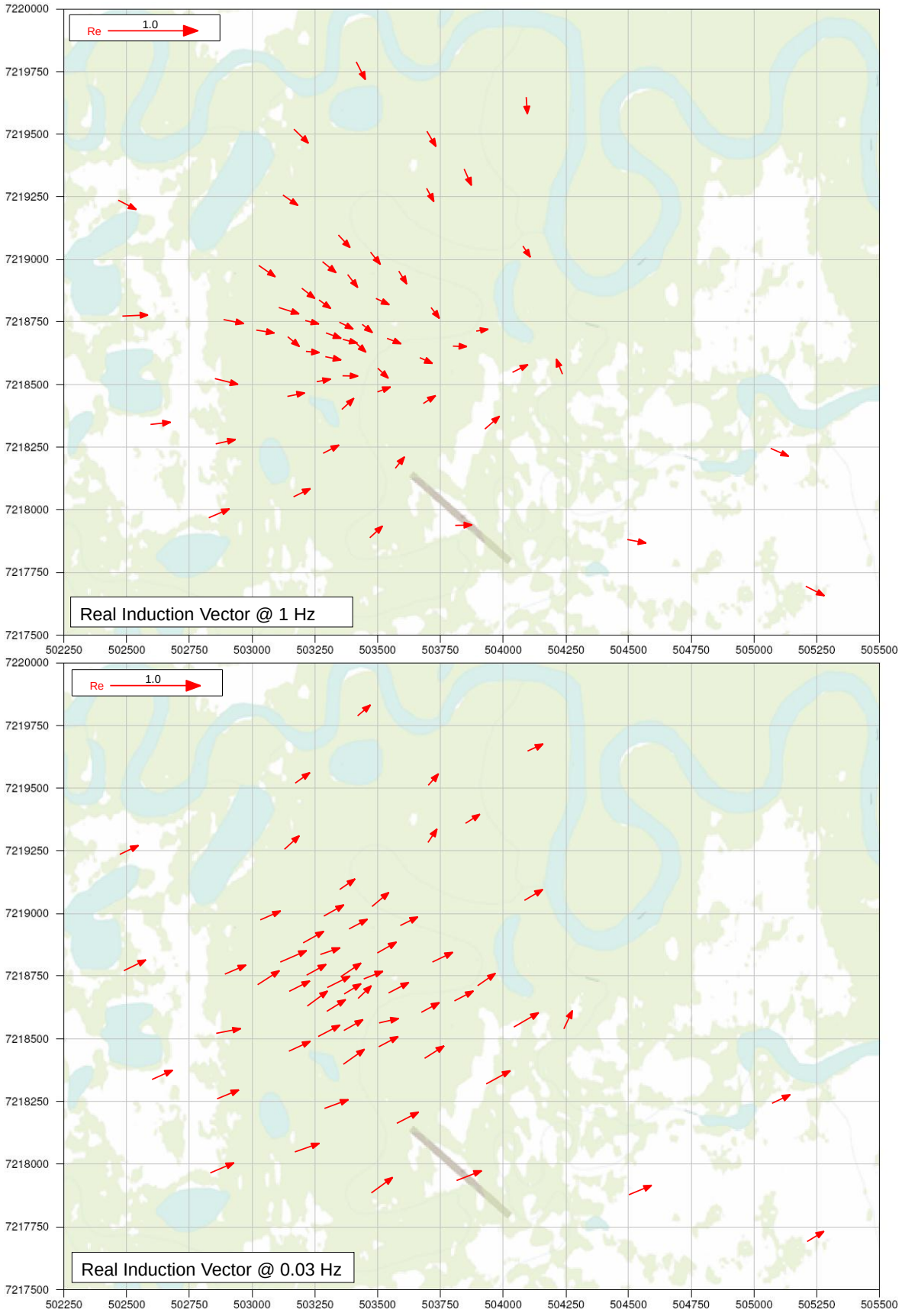


Figure 13. Induction vectors (real parts) at 1Hz and 0.03Hz. Marked sites are displayed in the 1D modeling section (Figure 15 and Figure 16).

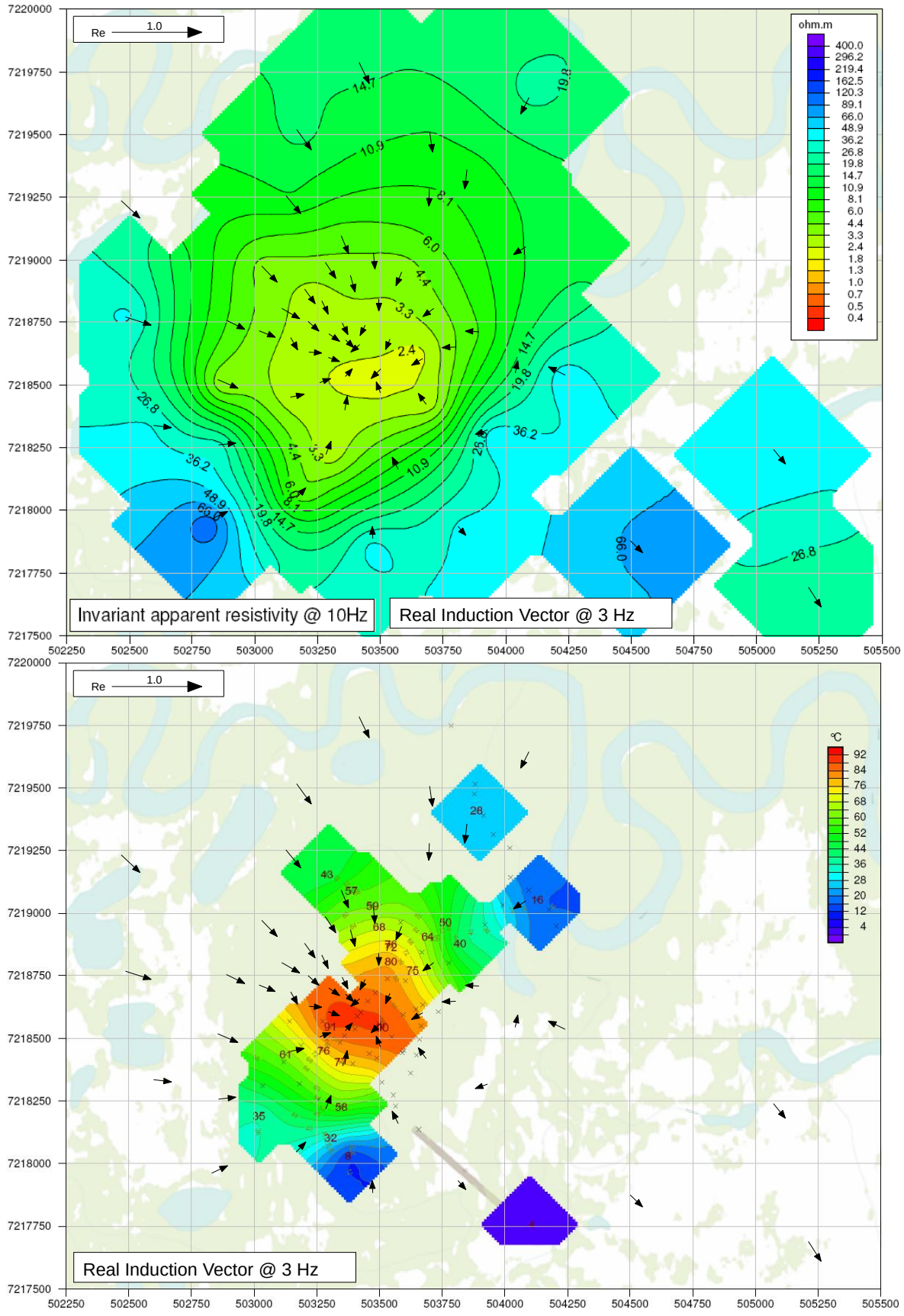


Figure 14. Real induction vectors at 3Hz overlaid on apparent resistivity at 10Hz (top) and temperature from wells at 40m depth – see section 6 for the well temperature data set.

4 1D MT MODELING

4.1 Tensor invariant

As for the data displays, data editing / masking used here is as for the 3D inversions presented for the first part of this section: input data are rotated to N0ºE, and the geometric average of XY and YX tensor elements was used (= referred to as *Invariant*).

All soundings were inverted for 1D structure, i.e. allowing for variations with depth only. The purpose of this effort is not to provide a full and comprehensive modeling of subsurface structure, but a different, more quantitative means to characterize the data set, in addition to the parameter maps shown before. Naturally, the higher dimensional the sounding (simply speaking the difference in XY and YX tensor elements), the less accurate, or misleading 1D modeling results will be. Another aspect are systematic shifts from galvanic distortions, which can be better accounted for in 3D inversion than in a 1D approach.

1D inversion involved both smooth multi-layer Occam-type inversions (purple in the figure, both for the model part and its response), and layered inversions with typically ~6 layers. Example inversions for 6 soundings are displayed in Figure 15 and Figure 16 (for locations of these, see Figure 5). For good comparison between the resulting layered resistivity, all scaling is identical in these graphs.

Resistivity maps obtained from the smooth 1D Occam-type inversions are shown in Figure 17 and Figure 18 for depths 25, 100, 300, and 500m bsl. A cumulative conductance (integral of conductivity – the inverse of resistivity – over depth) map is given in Figure 19 for the depth range from 0m to 100m.

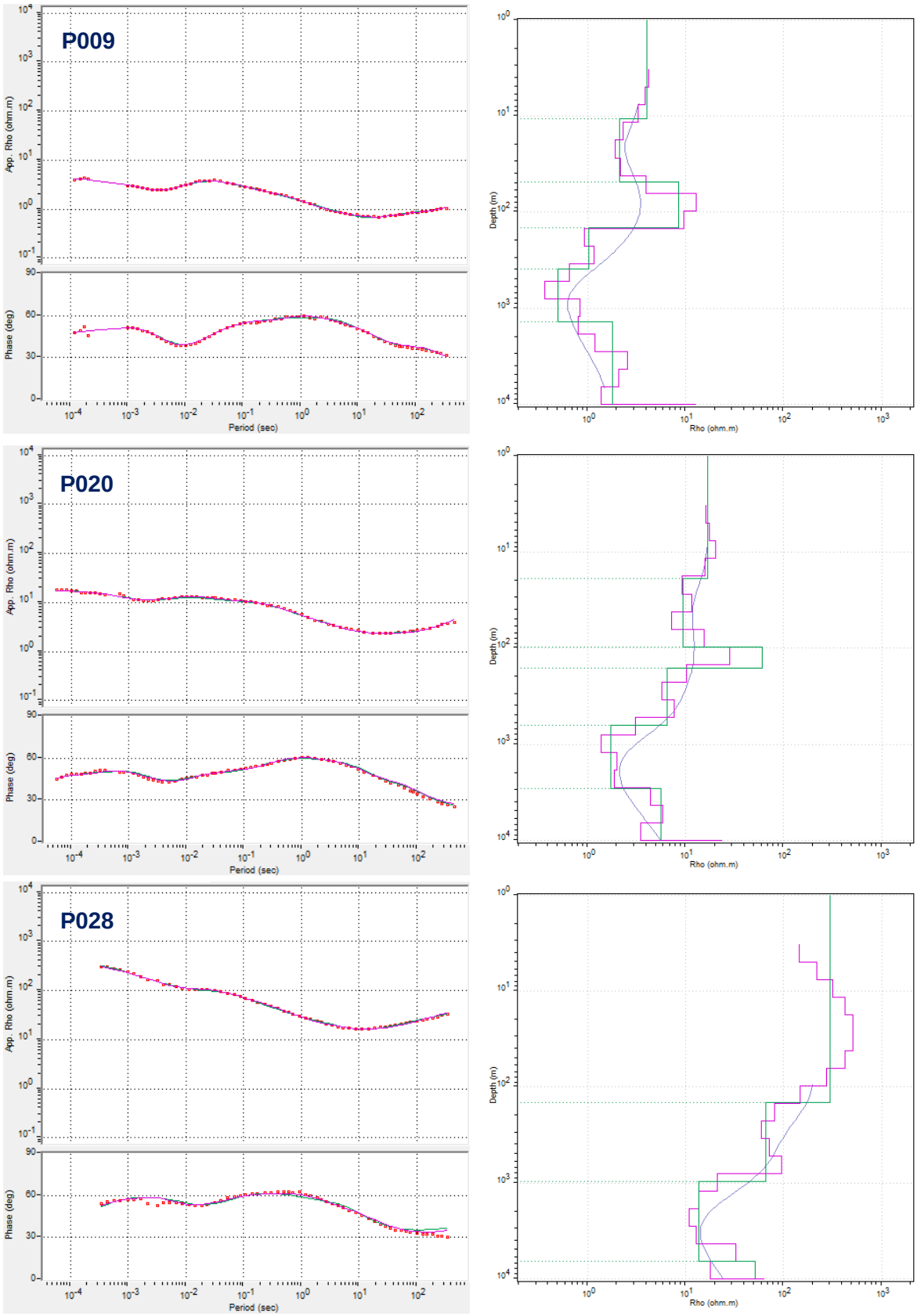


Figure 15. Example soundings with 1D models. Green: layered model, purple: smooth Occam model, blue: Bostick curve (analytical conversion of impedances). The geometric average of the XY and YX impedance elements is modelled.

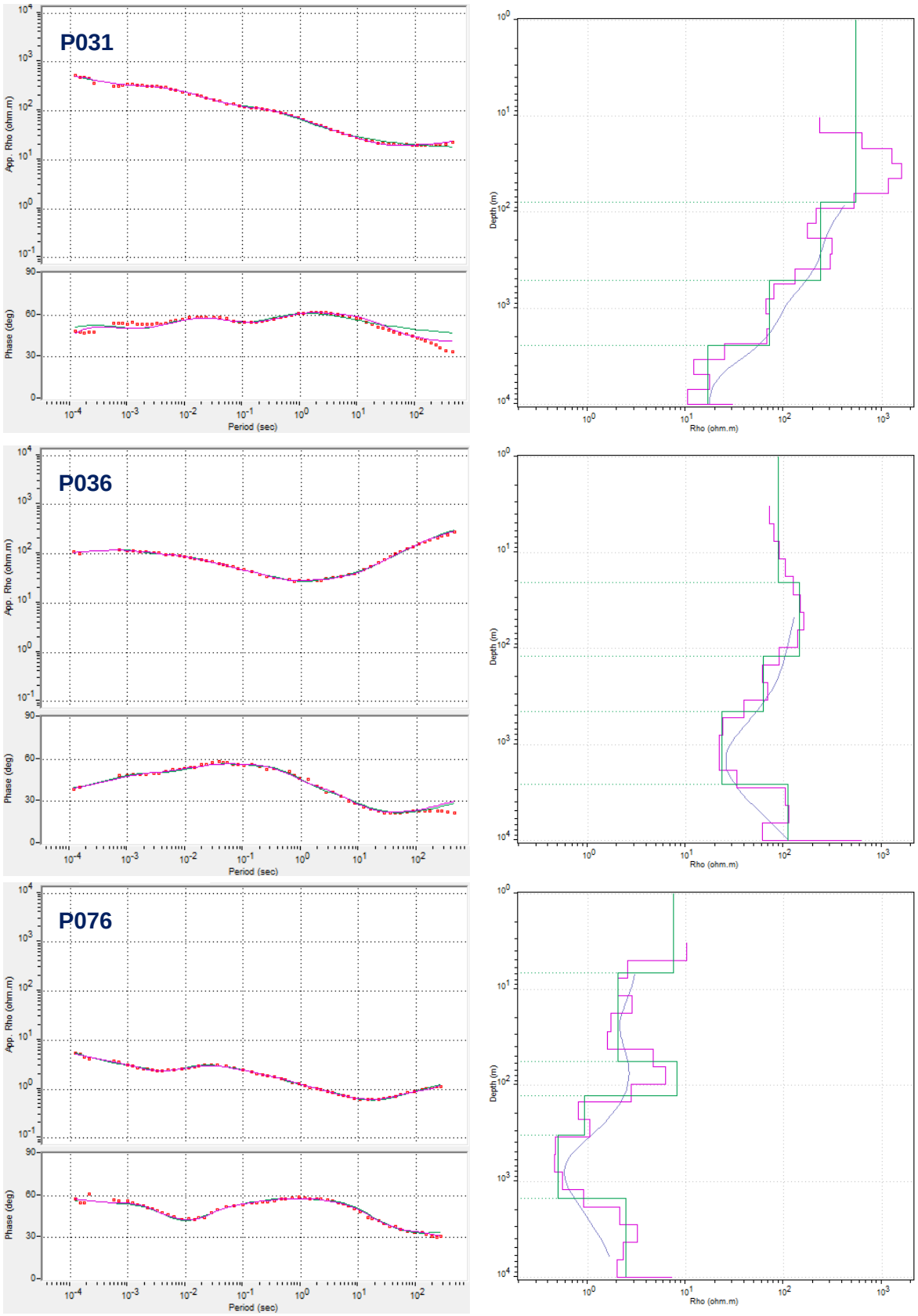


Figure 16. Example soundings with 1D models, as in Figure 15.

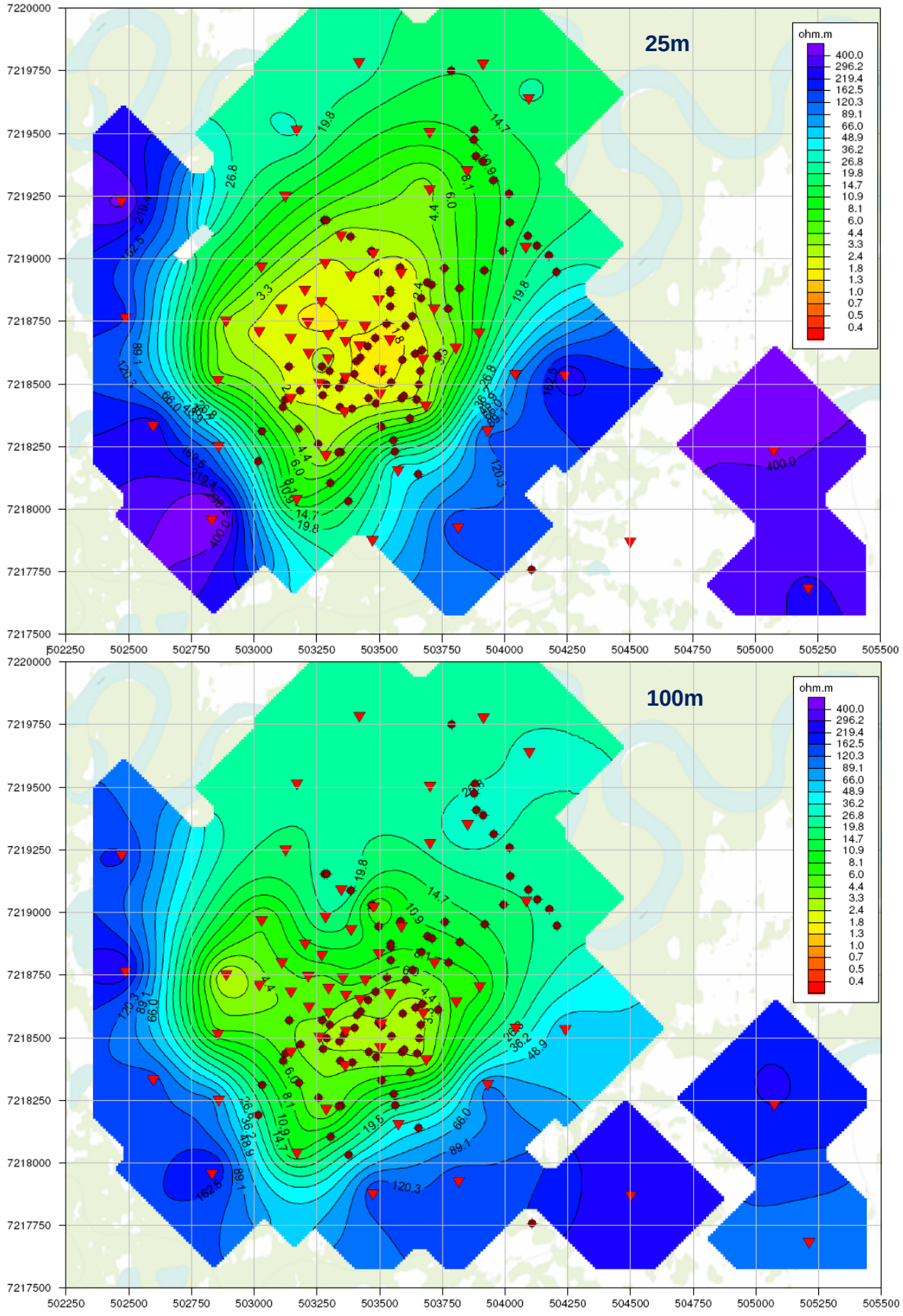


Figure 17. Resistivity at 25m and 100m depth from 1D smooth, Occam-type MT inversion (tensor *invariant*).

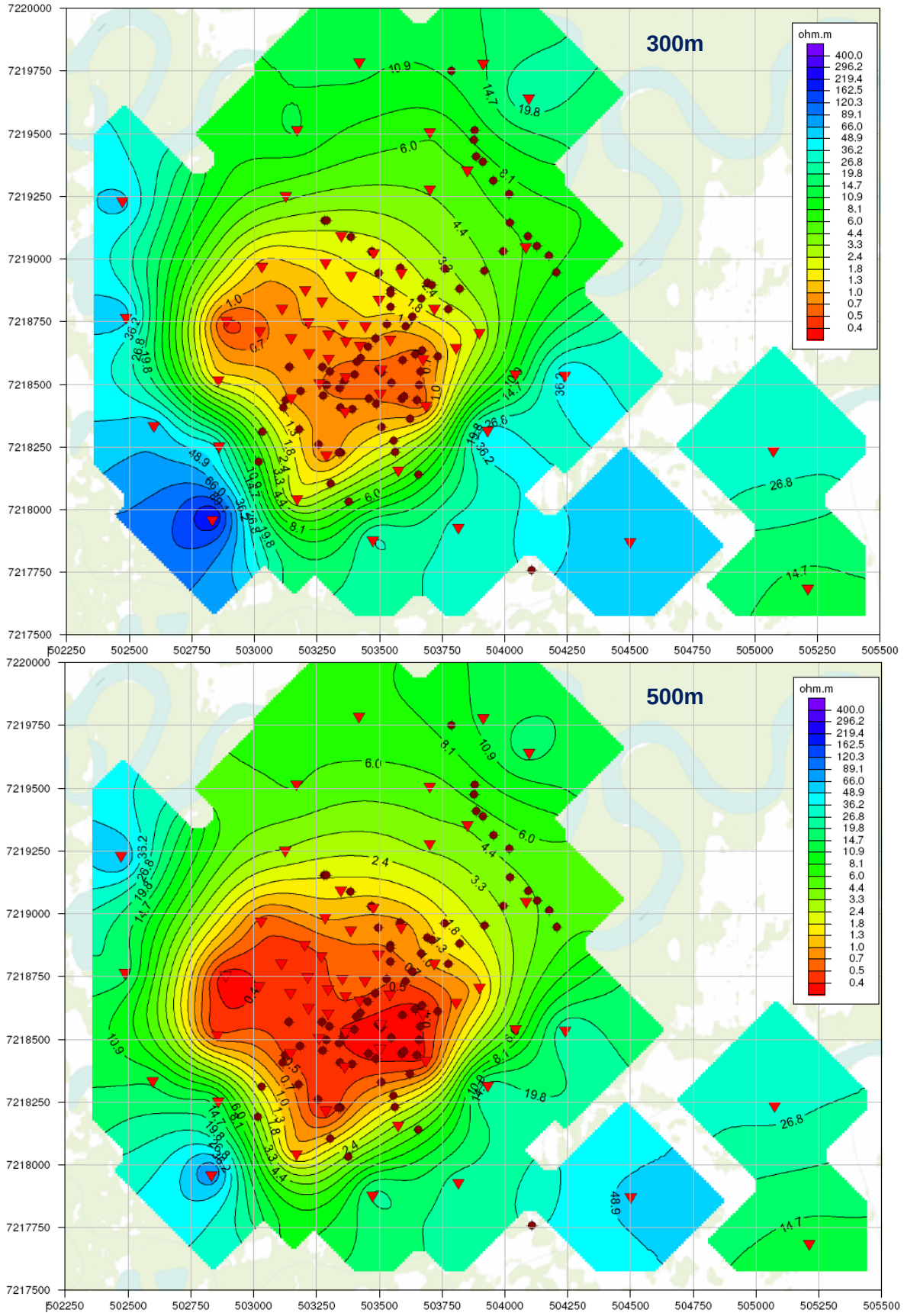


Figure 18. Resistivity at 300m and 500m depth from 1D smooth, Occam-type MT inversion (tensor *invariant*).

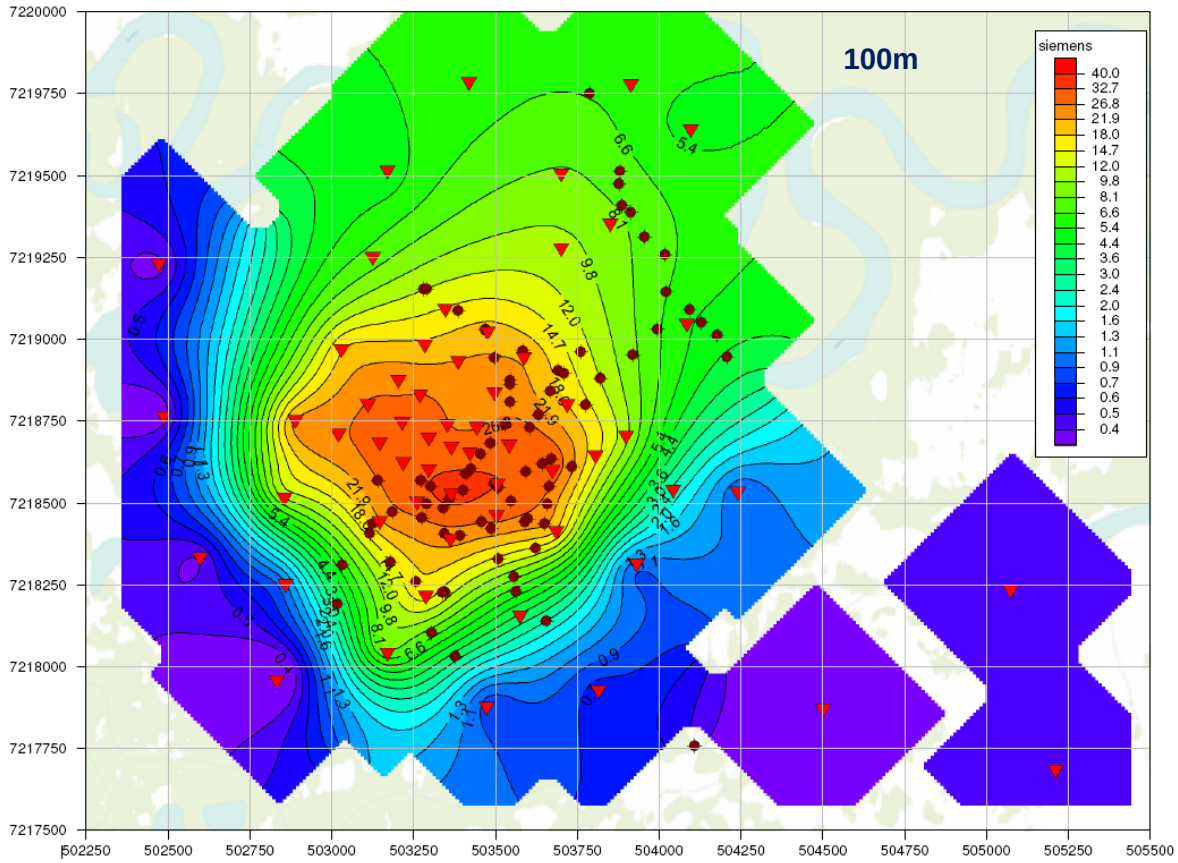


Figure 19. Cumulative *conductance* from 1D inversions (invariant) to 100m and 300m depth.

4.2 Impedance components at orientation N45ºW.

The long period strike direction indicated from impedance data was observed to be roughly around N45ºW (±90º), seen in polar diagrams (Figure 11). Rotated to this angle, the apparent resistivity and phase curve split is very strong (see Figure 20).

1D inversions are therefore very different between the two components, and in any attempts of 1D modeling it is critical what data is chosen. Resistivity maps from the previous section were based on the invariant – this is likely to underestimate resistivity at greater depth (> ~200m). For the selected stitched (interpolated) 1D inversion section displays, the XY component N45ºW data rotation is therefore chosen (Figure 22 and Figure 23).

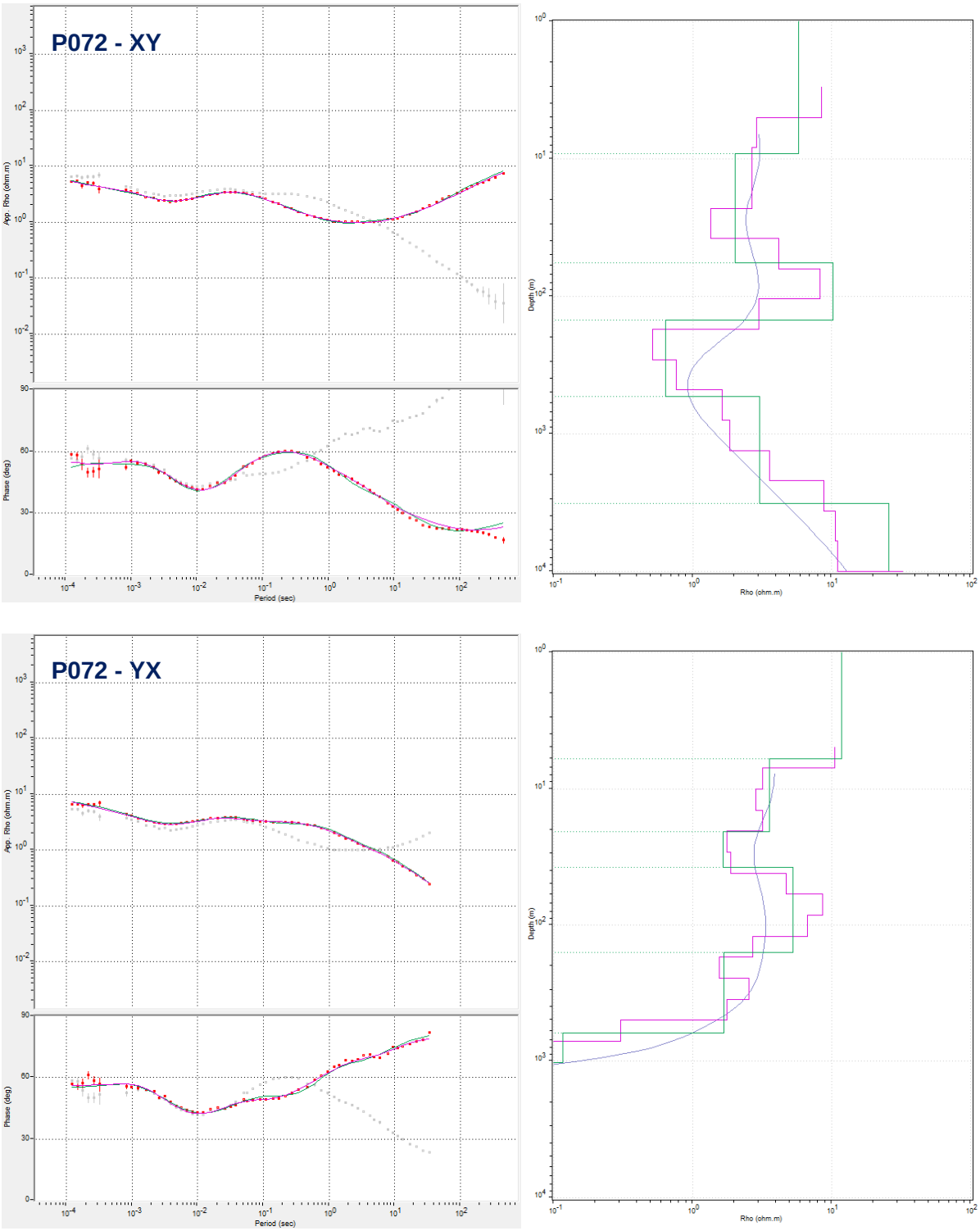


Figure 20. 1D modeling at site P072 in data orientation N45ºW, separately for components XY and YX, resulting in very significantly different resistivity distribution at depth >100m.

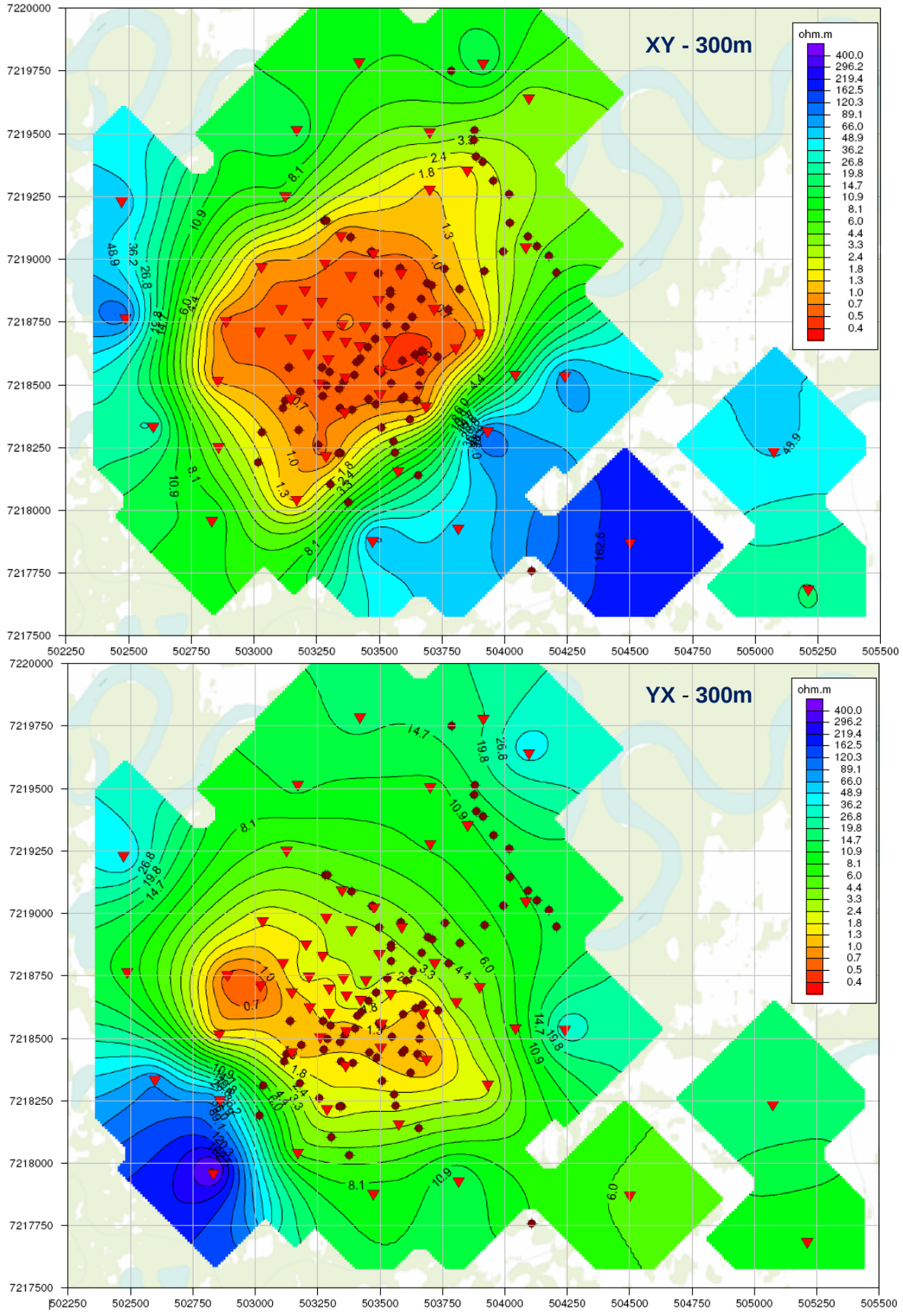


Figure 21. 1D inversion in different data rotation system (N45°W), separately for XY (top) and YX (bottom) component data. The resistivity map at 300m depth shows significant differences.

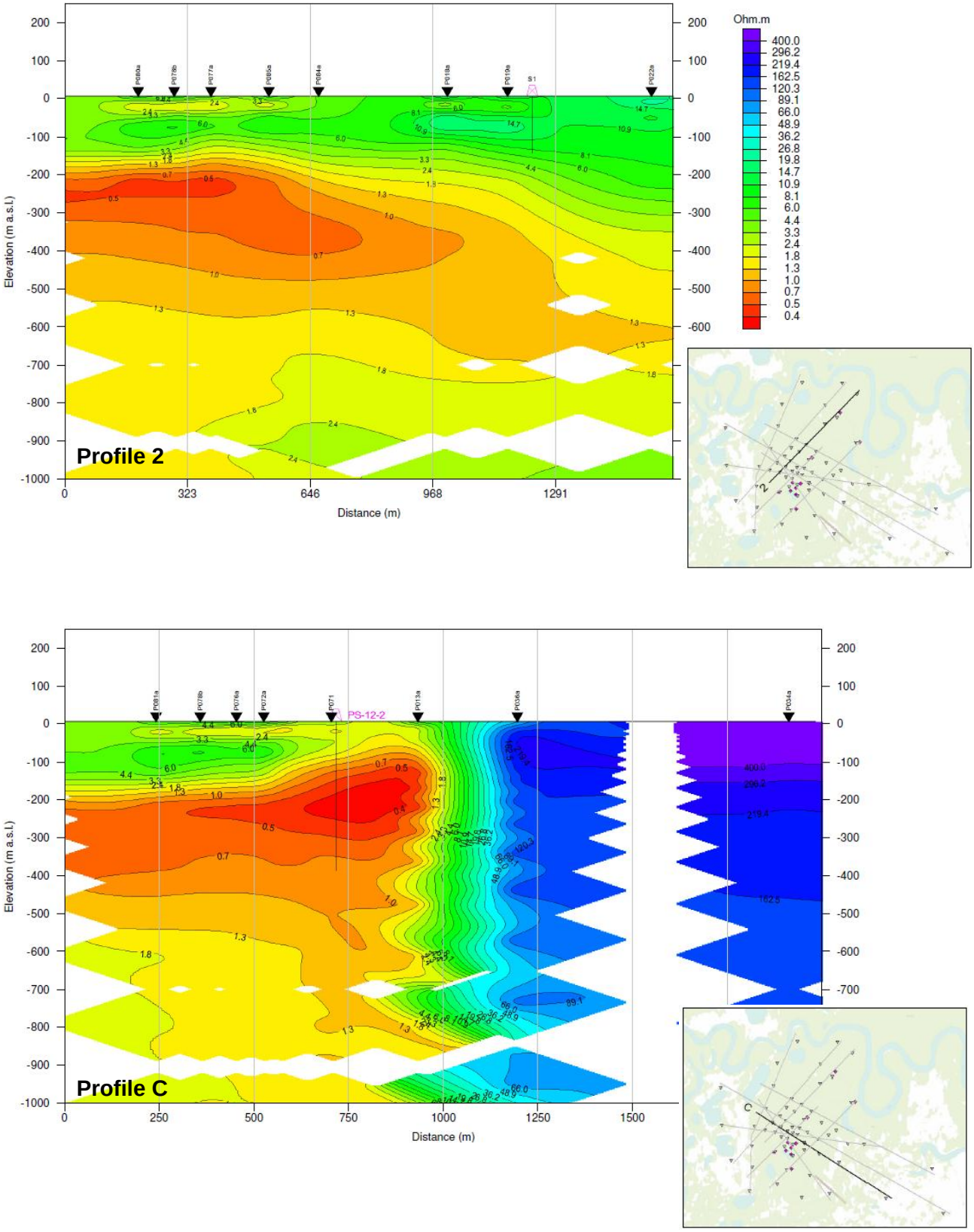


Figure 22. Resistivity at profiles 2 and C from smooth 1D MT inversion (Occam, XY component).

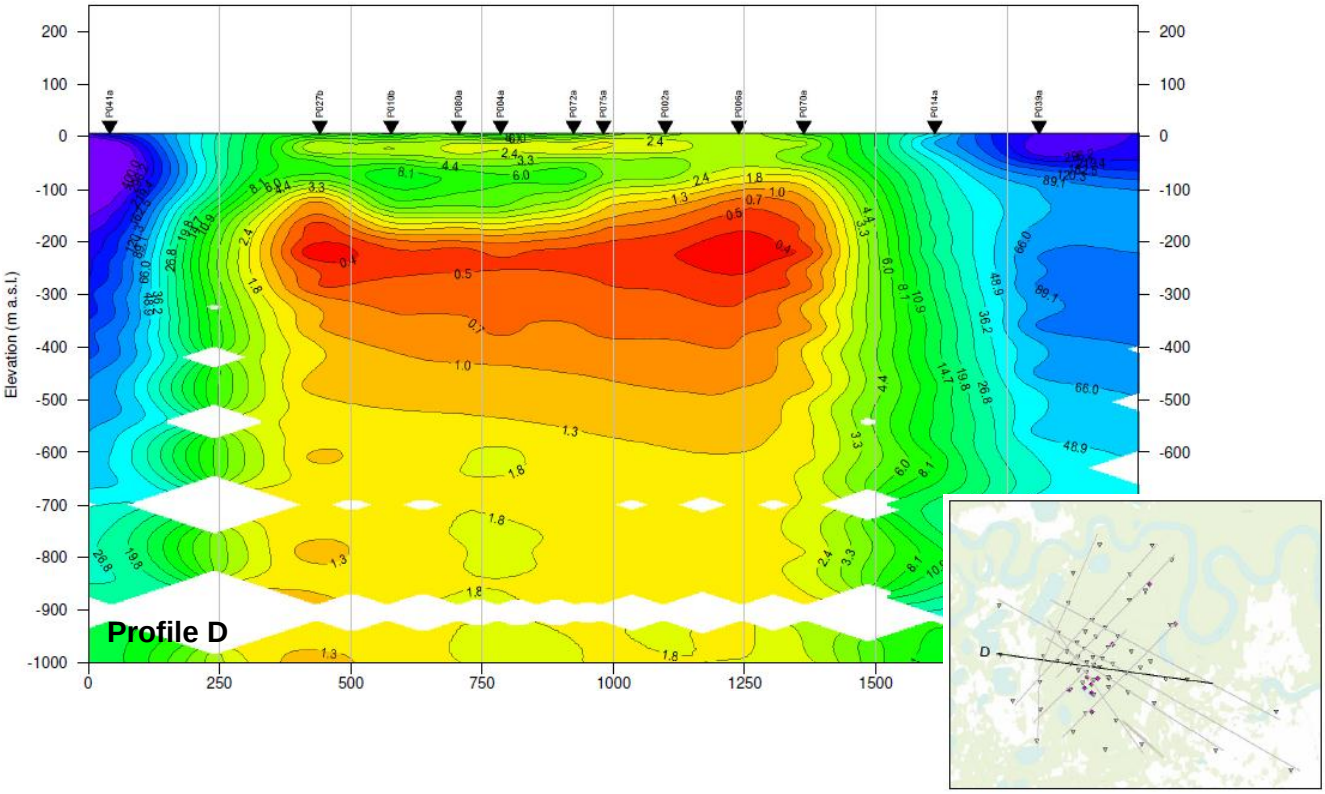


Figure 23. Resistivity at profile D from smooth 1D MT inversion (Occam, XY component).

5 3D MT INVERSION

Details on the Fugro 3D MT inversion code are given in Appendix C. All input data is rotated to the coordinate system of the 3D mesh (geographic North) and has undergone careful editing (= masking of data points).

5.1 Mesh Dimensions

The mesh technically includes topography (from NED DEM) – but is essentially flat - and air is given a conductivity value of 0 S/m. The 3D code inverts for conductivities, not resistivities.

Table 5. 3D inversion mesh details

orientation	N0ºE
# cells in X/Y/Z direction	80 x 70 x 87
# cells, total	487,200
# padding cells in X/Y direction	12
model size in X/Y/Z direction	80km x 80.7km x 60km
cell area, model core	40m x 40m – 100m x 100m
cell thickness, top layers	3m

The central zone is discretized laterally with 40m x 40m for the most central zone with very small MT site spacing – a zone of 26 x 20 cells or 1,040m x 800m extension. Beyond, cells size increase by 10% per cell up to 100m for the outer, sparser part of data coverage.

Layer thickness is 3m for the top 3 cells, increasing below by 20% until 10m at -45m depth. Underneath the vertical thickness increase per cell is reduced to 10% until reaching 100m at 1,100m depth, from where thickness is kept constant down to 3,100m. Finally layer thickness increases by 10% until 6,500m depth and then 20% until the bottom of the mesh.

In order to satisfy boundary conditions, the 3D mesh contains considerable padding to all sides and towards great depth: thickness of 12 lateral padding cells augments 50% per cell to a maximum of 13,0km.

Inversions with different mesh geometry were also run, with similar results.

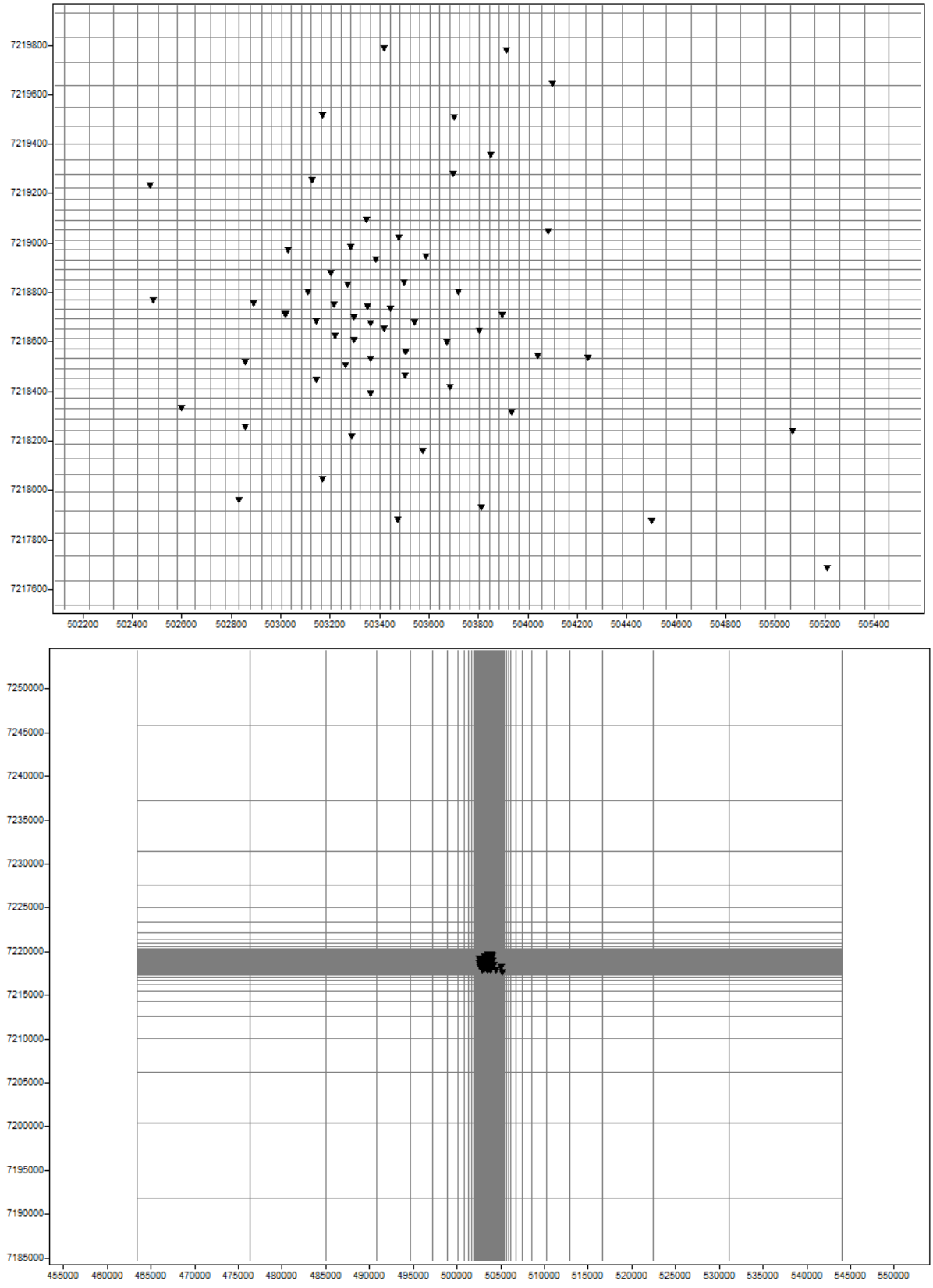


Figure 24. Top view of 3D MT inversion mesh, core area (top) and full mesh area (bottom).

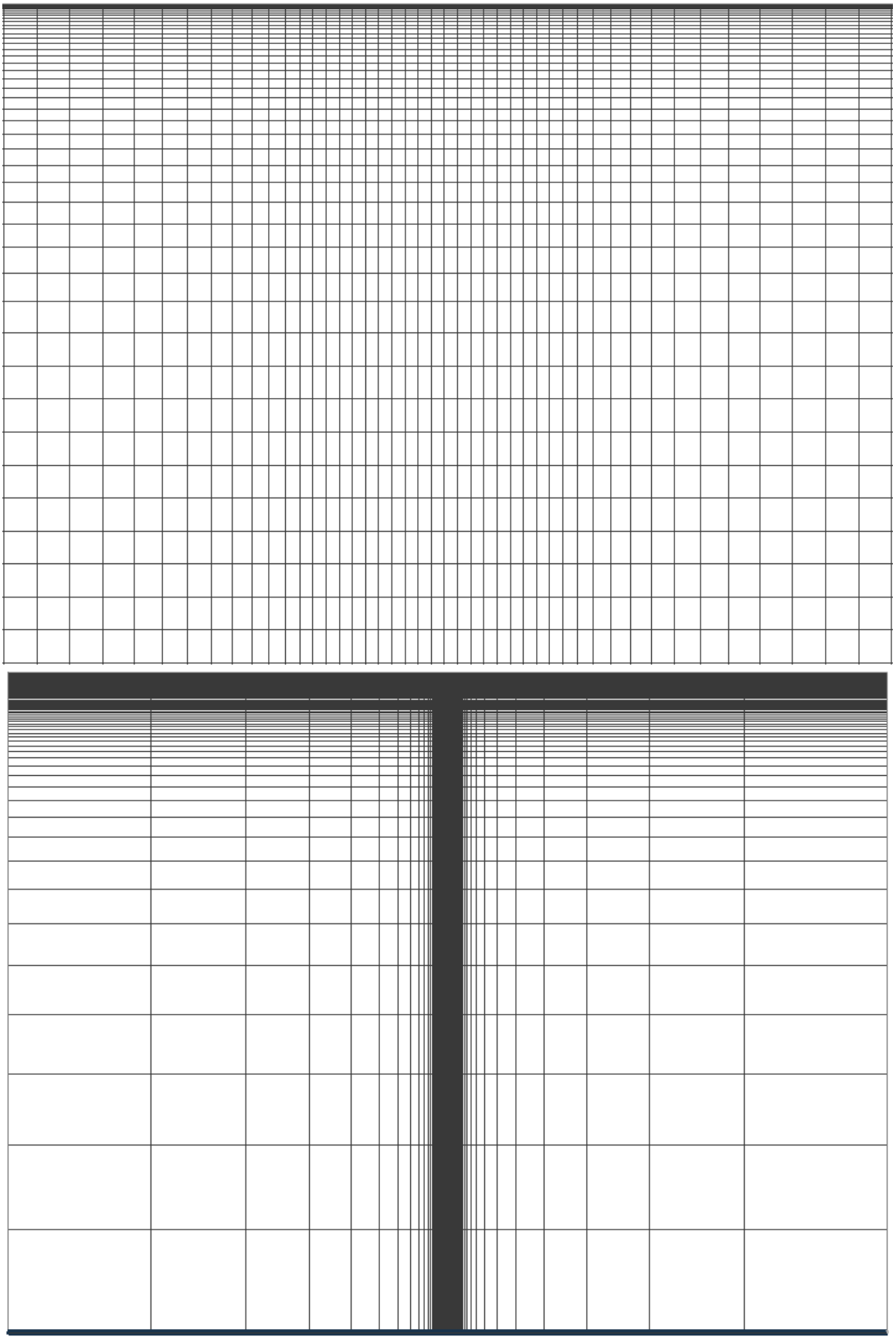


Figure 25. Side view of 3D MT inversion mesh, core area (top), and full section.

5.2 Inversion Settings and Data Fit

Both blind and constrained inversions were performed.

The blind inversion #17 started from a homogeneous model of 10 Ωm resistivity, running for 100 iterations. The result presented here (18) is a restart of this inversion (17) for another 50 iterations, lowering smoothness constraints tau and z0 by a factor of 2.

Constrained inversions were also run, incorporating imaged resistivities from the Resolve airborne survey conducted by Fugro Airborne Surveys Corp., Mississauga, Ontario, see section 5.4. These inversions were otherwise run with the same settings.

The main parameters for the inversion on input data and regularization constraints are listed below:

Table 6. 3D MT inversion settings.

Inversion #	17/18 (blind) & 19/20 (constrained)
Number of MT sites:	59
Quantity inverted	full tensor complex impedances *and* tipper
Error floors	2.5% (XY, YX), 25% (XX, YY)
Absolute error floor for Tipper	0.02
# of frequencies	22
Max frequency	5,623 Hz
Min frequency	0.03162 Hz (1 Hz for magnetic tipper data)
# frequencies per decade	4
Fields interpolated to precise site location within cell	no
Max resistivity	5,000 Ωm
Min resistivity	0.35 Ωm
Tradeoff parameter (tau) between data fit and model roughness	0.2 (17/19), 0.1 (restarts: 18/20)
Regularization for smoothest model or smoothest variation from a-priori model	*model* for blind, *variations* for constrained inversions.
Directional model regularization (alpha)	2/2/1 in X/Y/Z direction for the last run
Other regularization parameters	z0: 100 (17/19), 50 (restarts: 18/20)
Iterations	100 (17/19), 50 (restarts:18/20)
Data misfit, rms	1.421 (blind: 18), 1.417 (constrained: 20)

Overall final data fit is very good, and with 1.421 for the blind and 1.417 for the constrained inversion nearly identical (a value of 1.0 would correspond to the target data misfit, for the error floors chosen).

5.3 Blind 3D Inversion

This inversion started from a homogeneous half space of 10 Ωm resistivity.

Data fit is illustrated in Figure 27 and Figure 28 for the 6 example soundings shown in varying context previously.

Resistivity maps at 10 different depth levels are displayed in the following figures (Figure 29 to Figure 33) on topographic base map (outside the grid area).

Cross-sections through the 3D resistivity volume along profiles defined in Figure 26 below are shown in Figure 34 to Figure 39.

Note that for very deep imaging of lateral structure, the lateral dimension of the survey is not sufficient and structures models below 500m shall may not be interpreted literally.

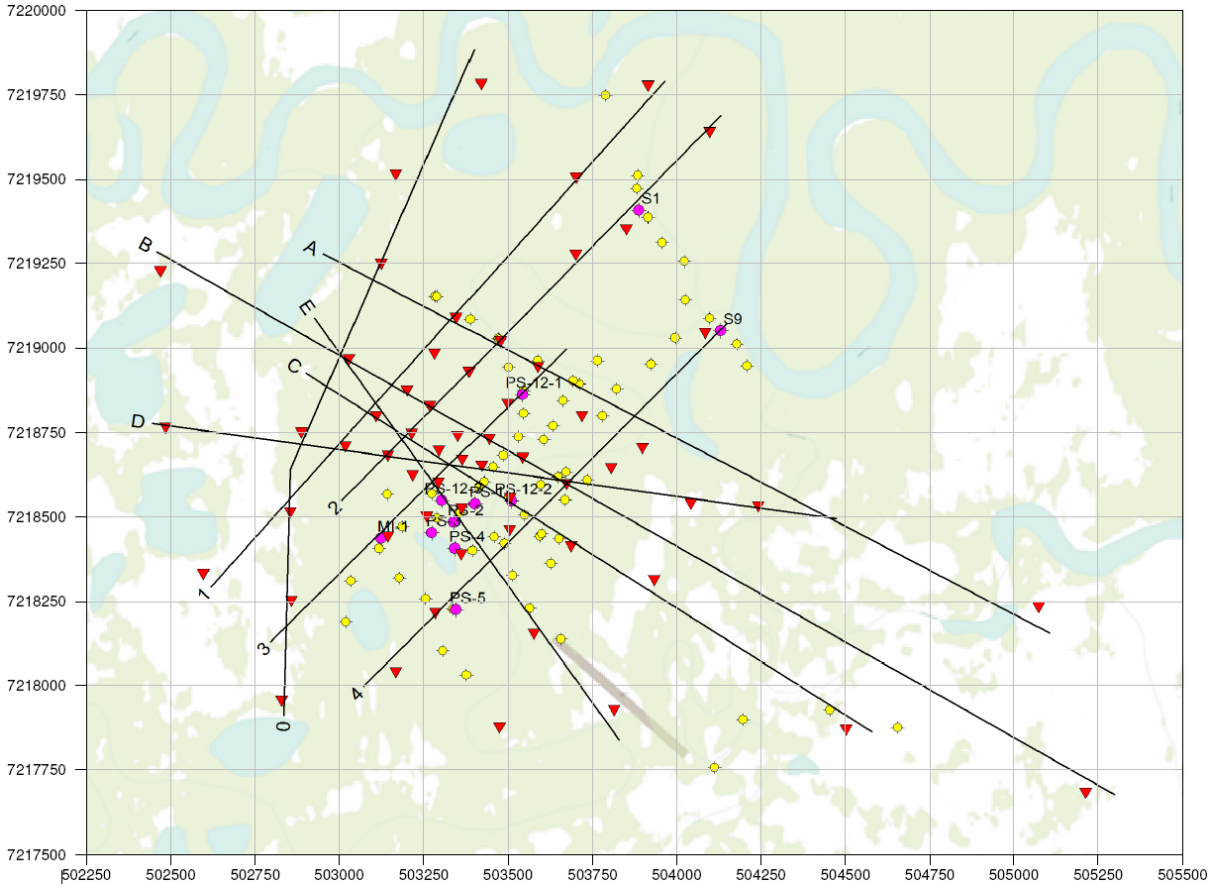


Figure 26. Profile locations for 3D resistivity structure visualization.

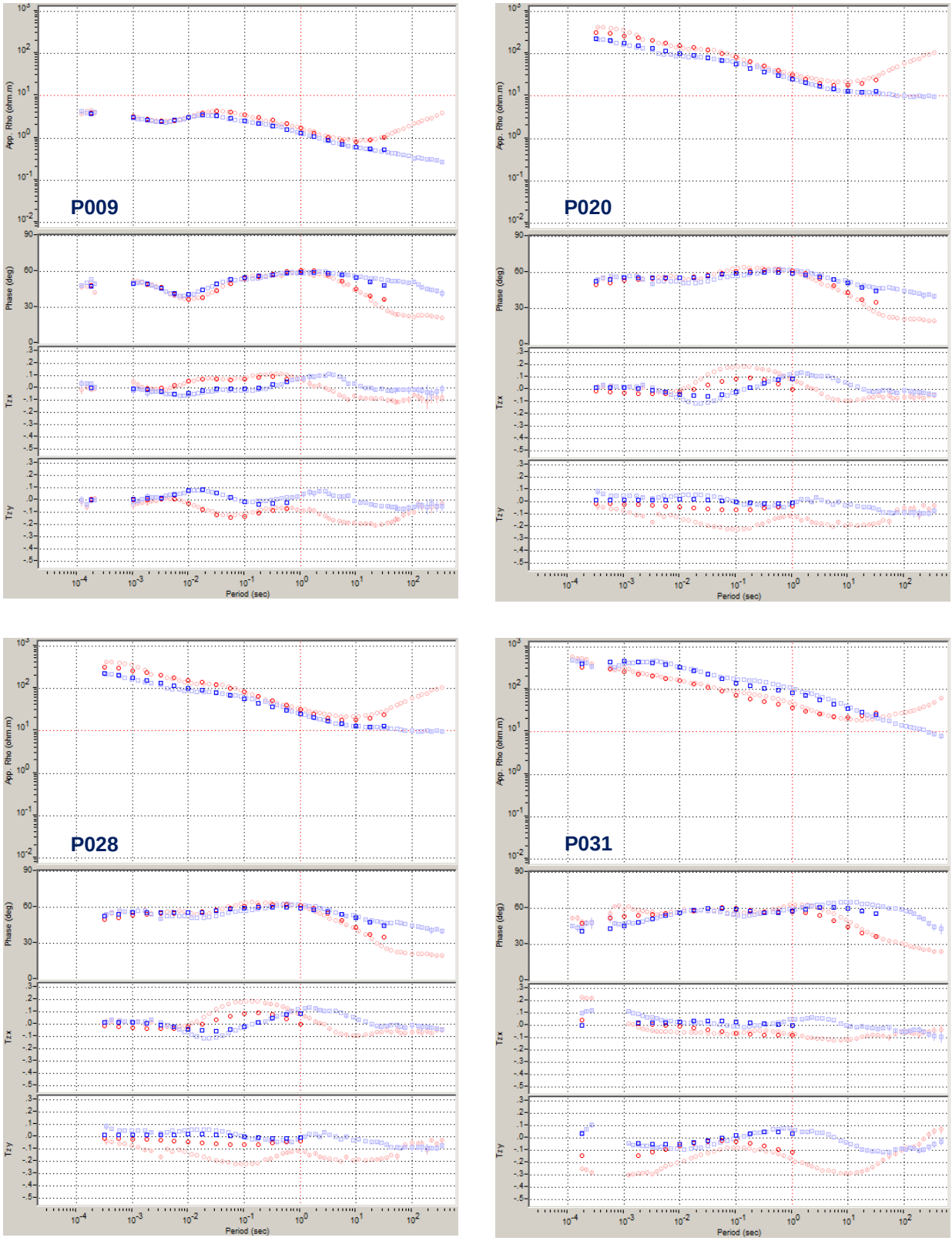


Figure 27. 3D MT inversion (#18) data fit for 4 example MT soundings. Faint: observed MT data, bold colors: predicted resistivity / phase and tipper from inversion #18.

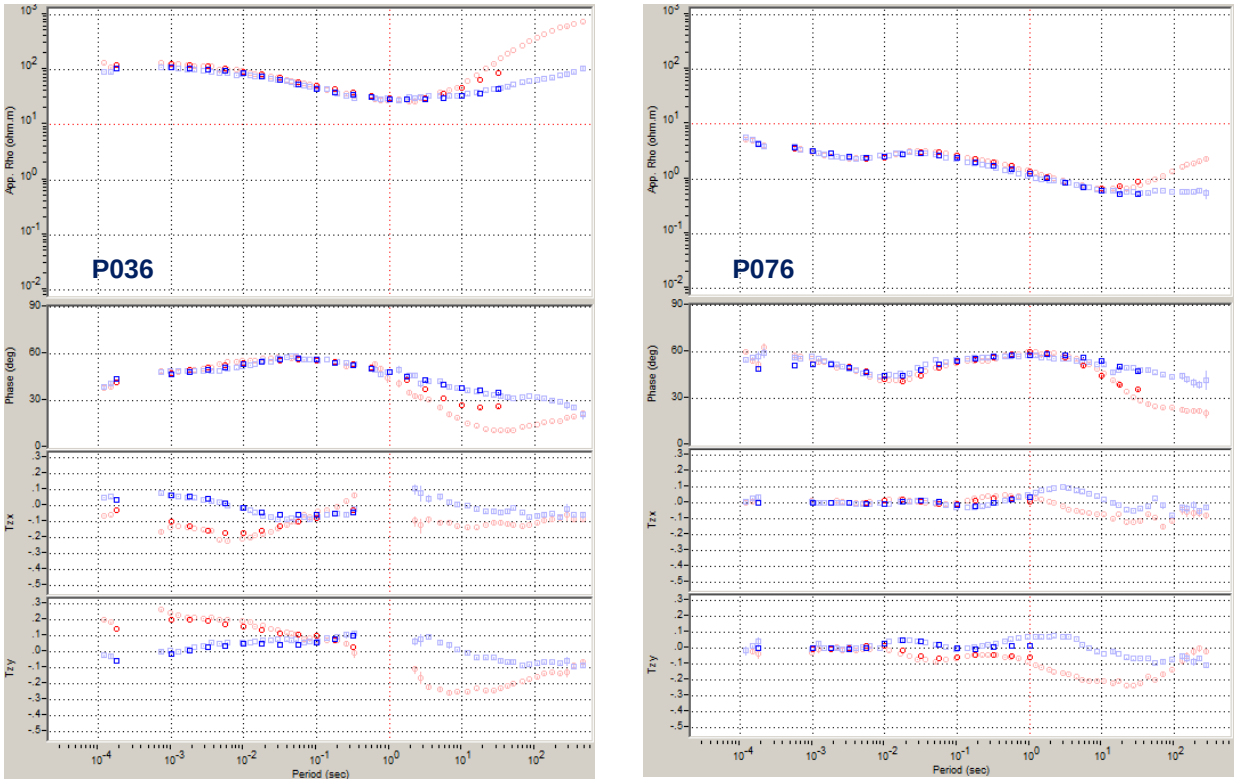


Figure 28. Data fit as in Figure 27 for 2 more example soundings.

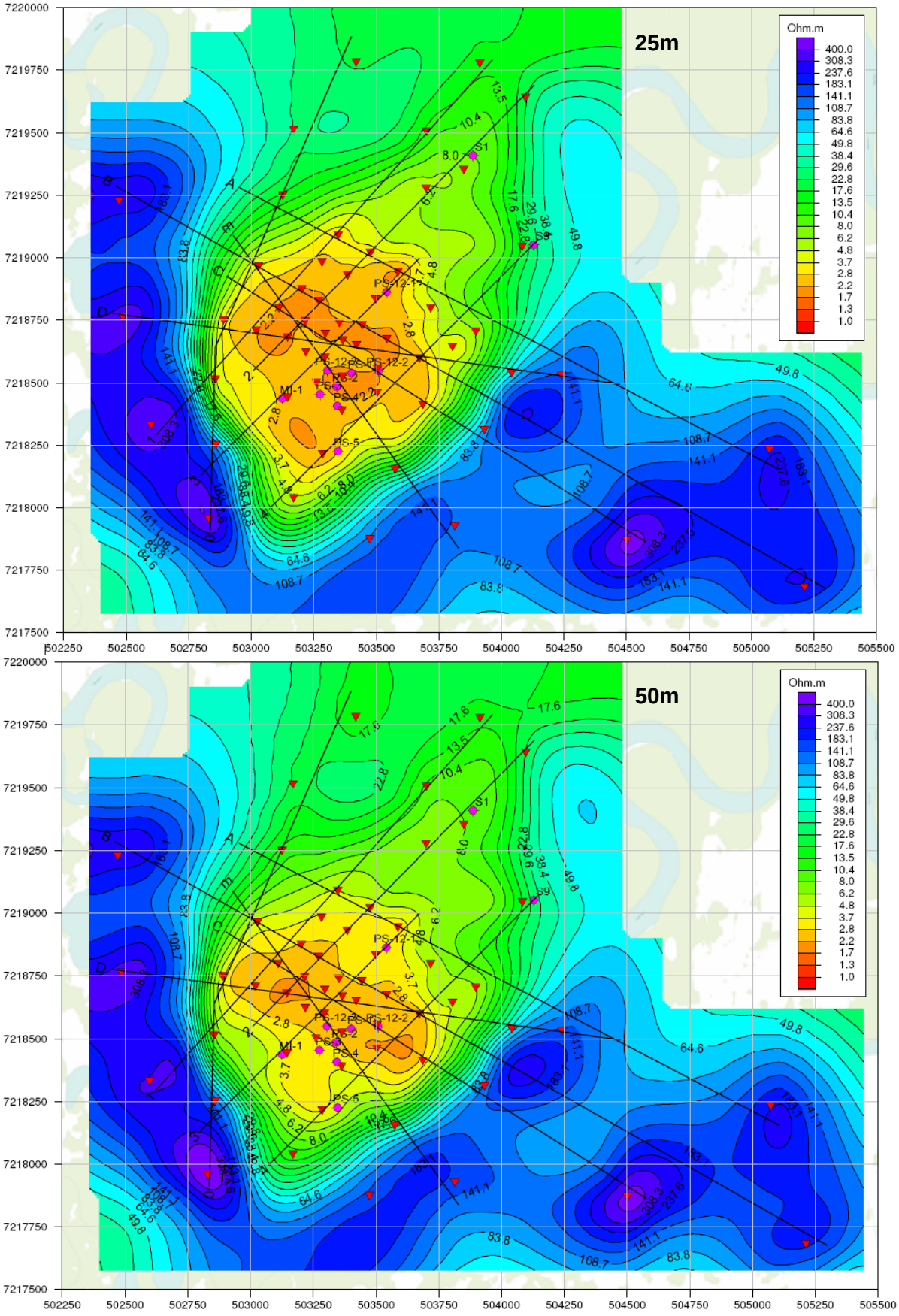


Figure 29. Resistivity map at 25m and 50m depth from blind 3D MT inversion (#18).

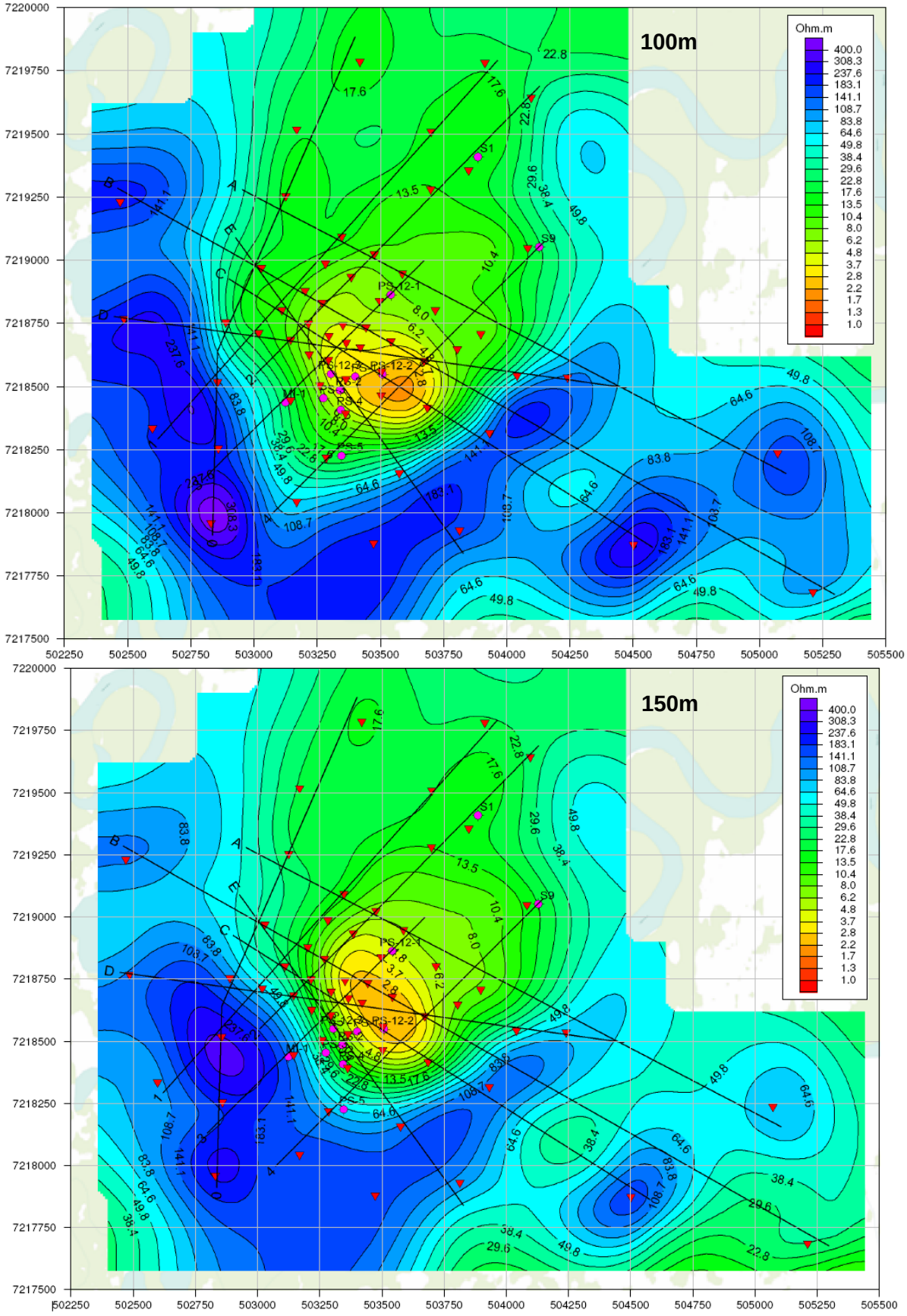


Figure 30. Resistivity map at 100m and 150m depth from blind 3D MT inversion (#18).

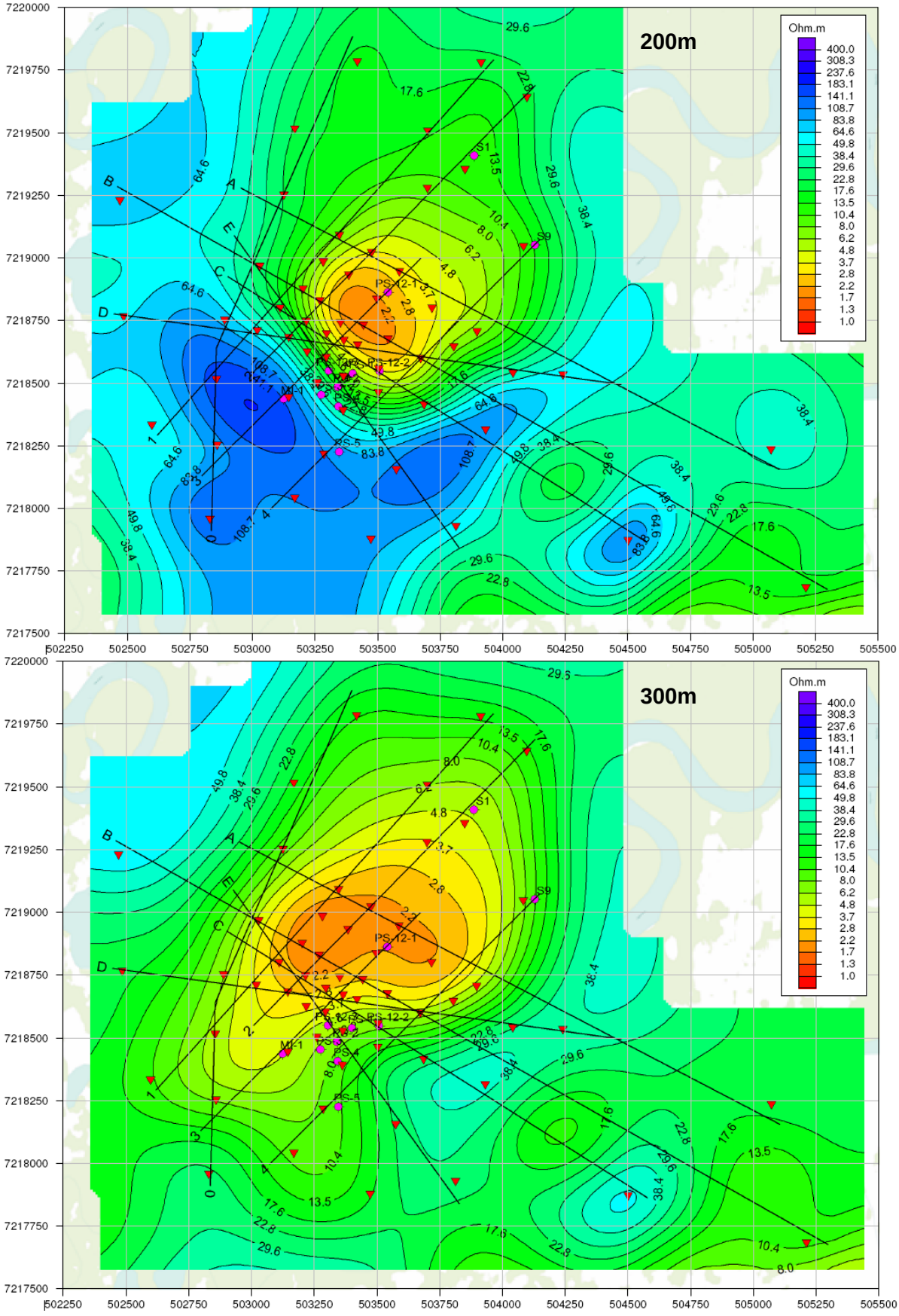


Figure 31. Resistivity map at 200m and 300m depth from blind 3D MT inversion (#18).

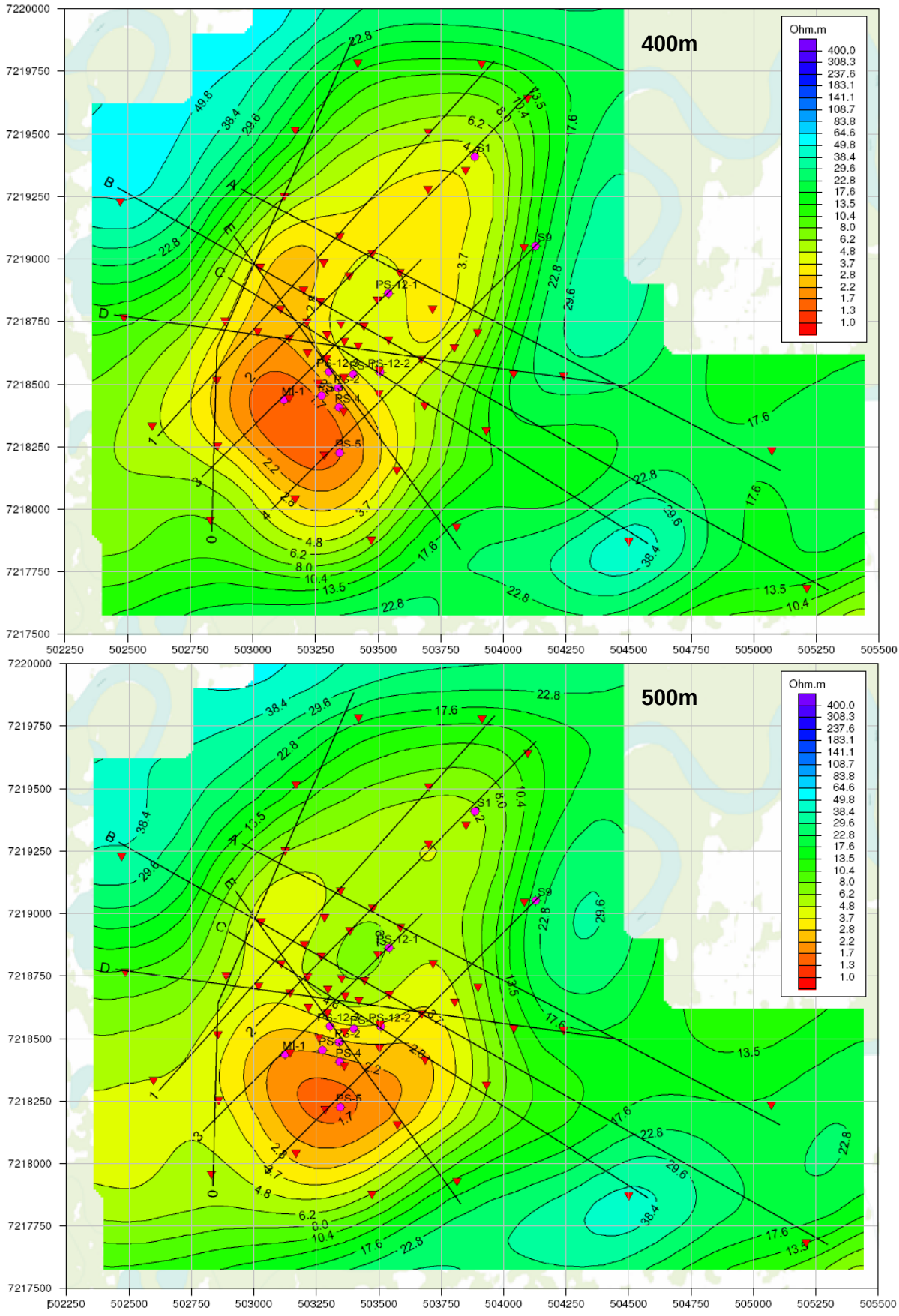


Figure 32. Resistivity map at 400m and 500m depth from blind 3D MT inversion (#18).

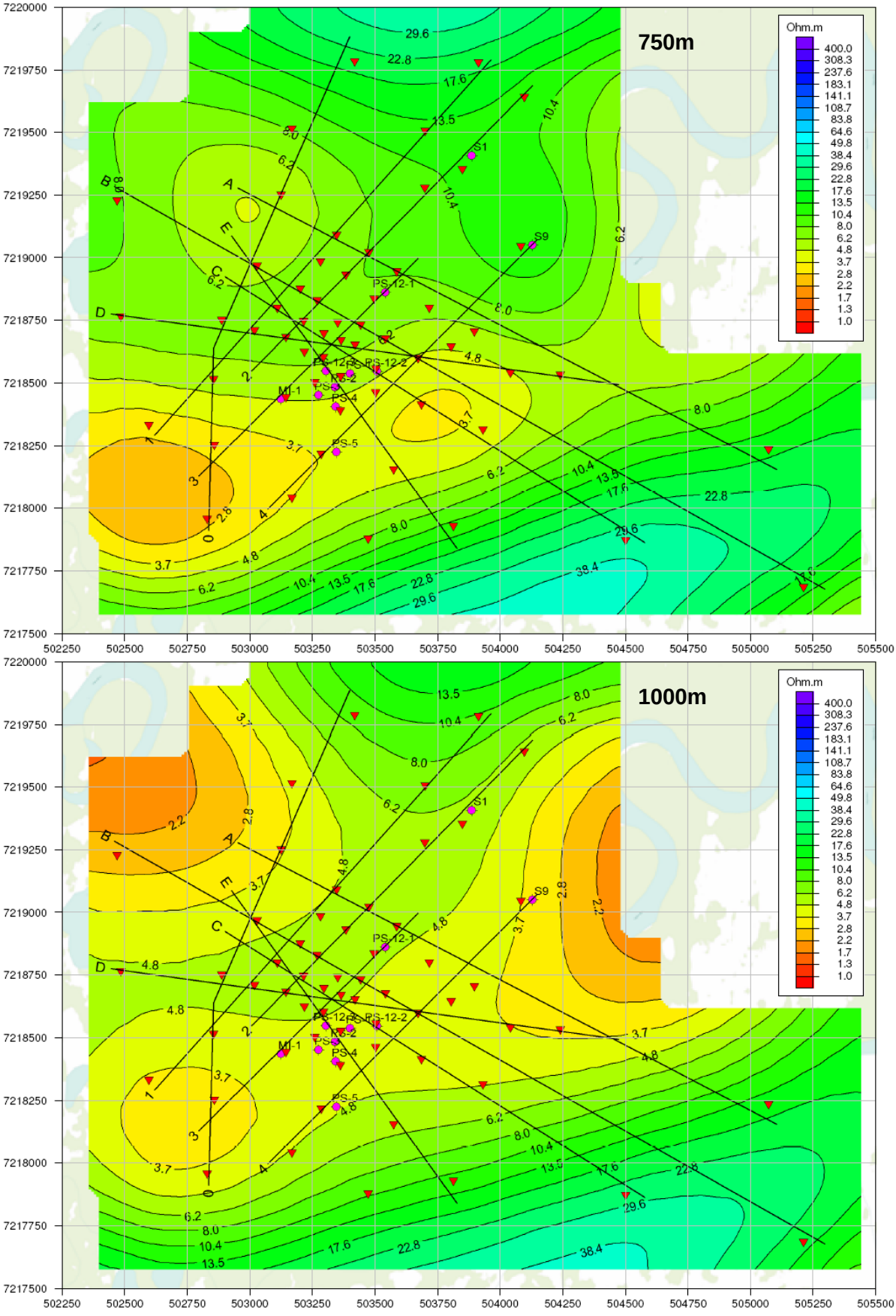


Figure 33. Resistivity map at 750m and 1000m depth from blind 3D MT inversion (#18).

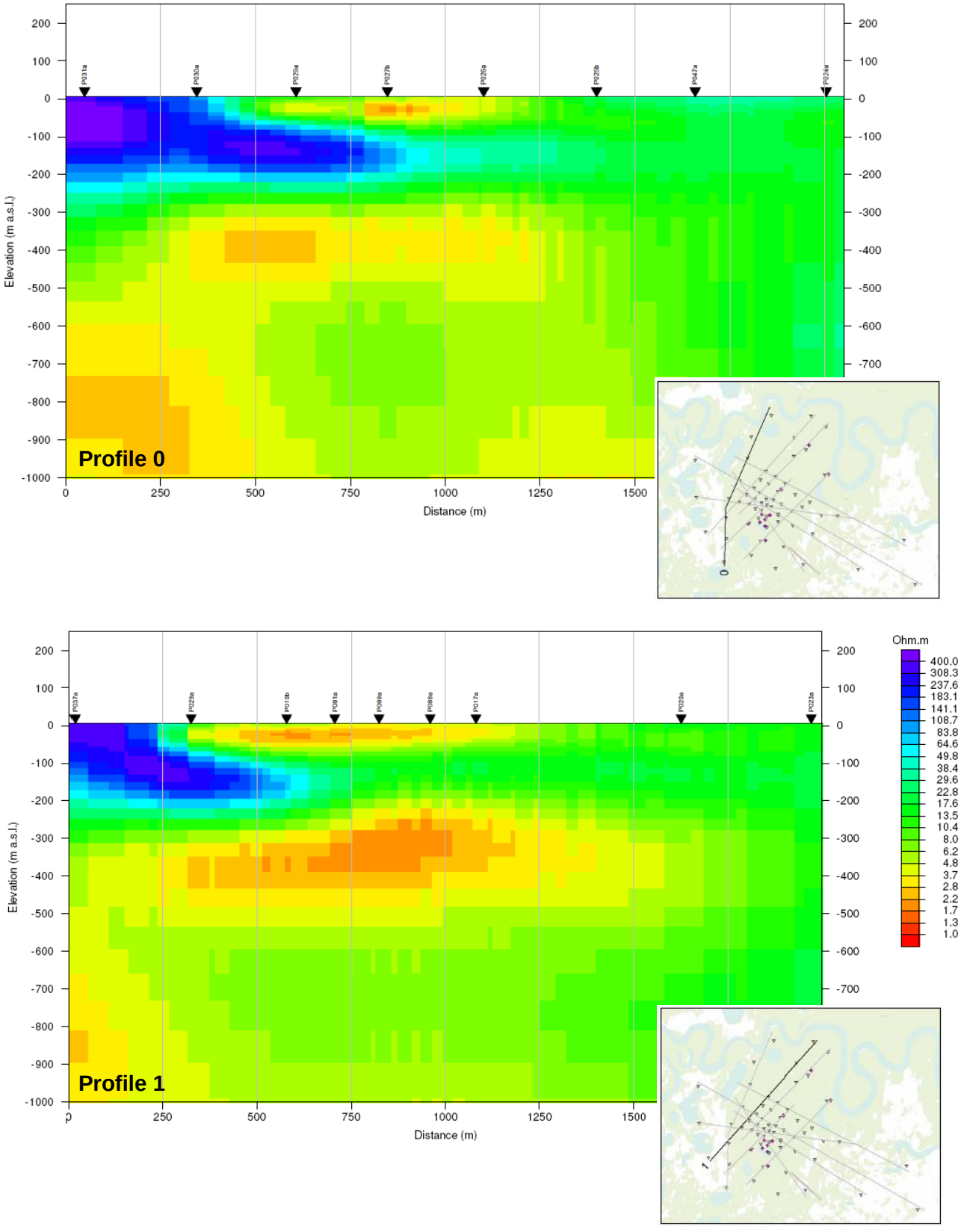


Figure 34. Resistivity at profiles 0 and 1 from blind 3D MT inversion (#18).

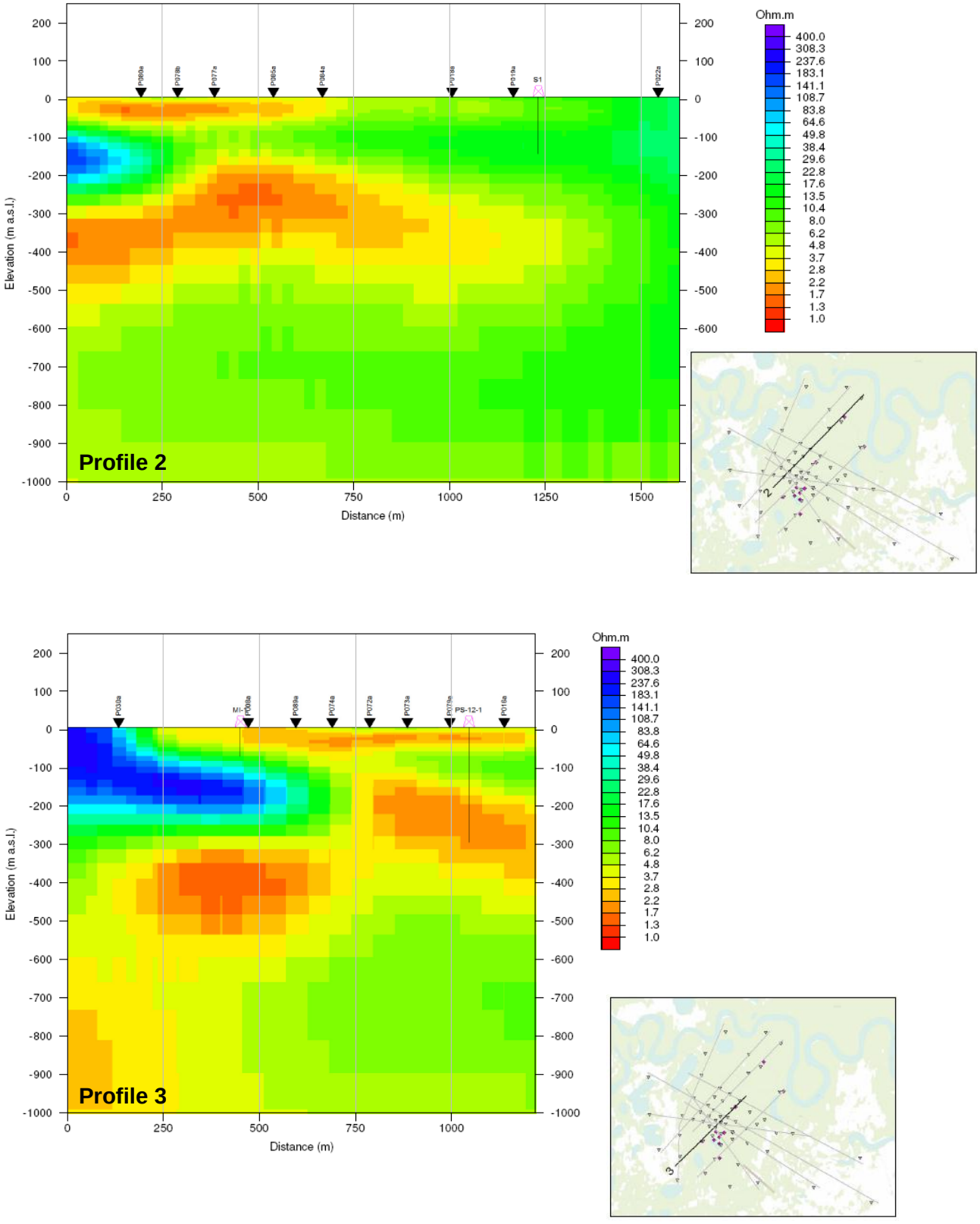


Figure 35. Resistivity at profiles 2 and 3 from blind 3D MT inversion (#18).

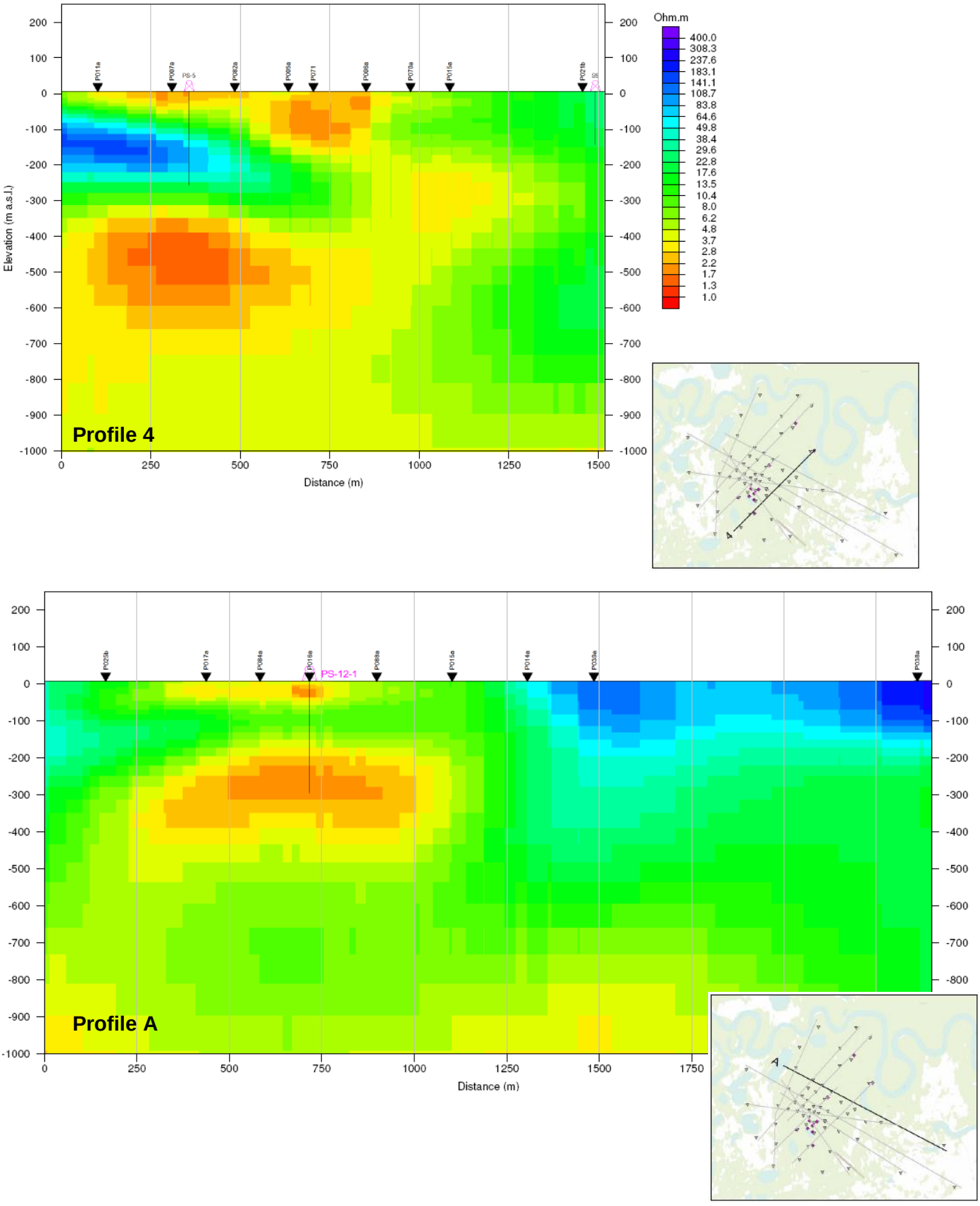
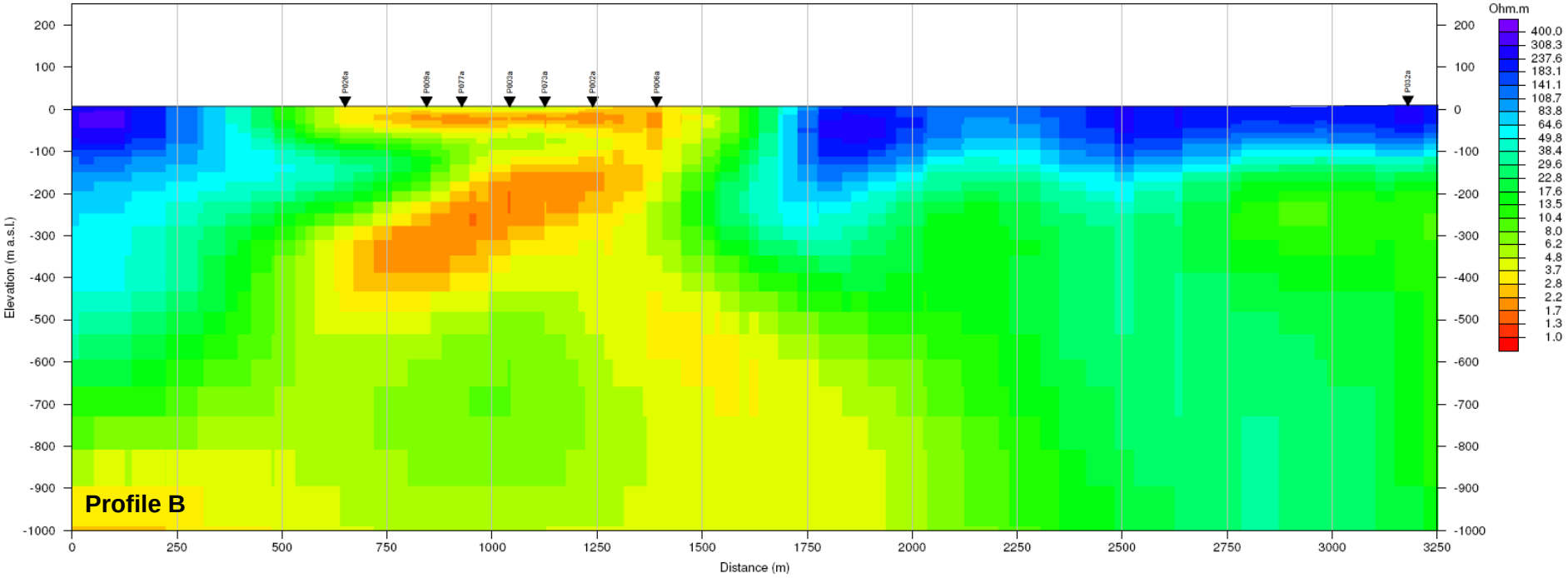


Figure 36. Resistivity at profiles 4 and A from blind 3D MT inversion (#18).



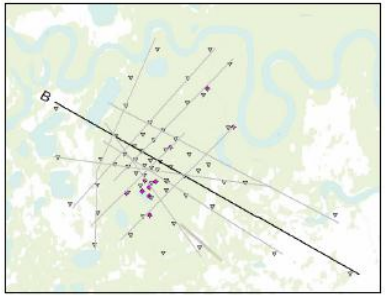


Figure 37. Resistivity at profile B from blind 3D MT inversion (#18).

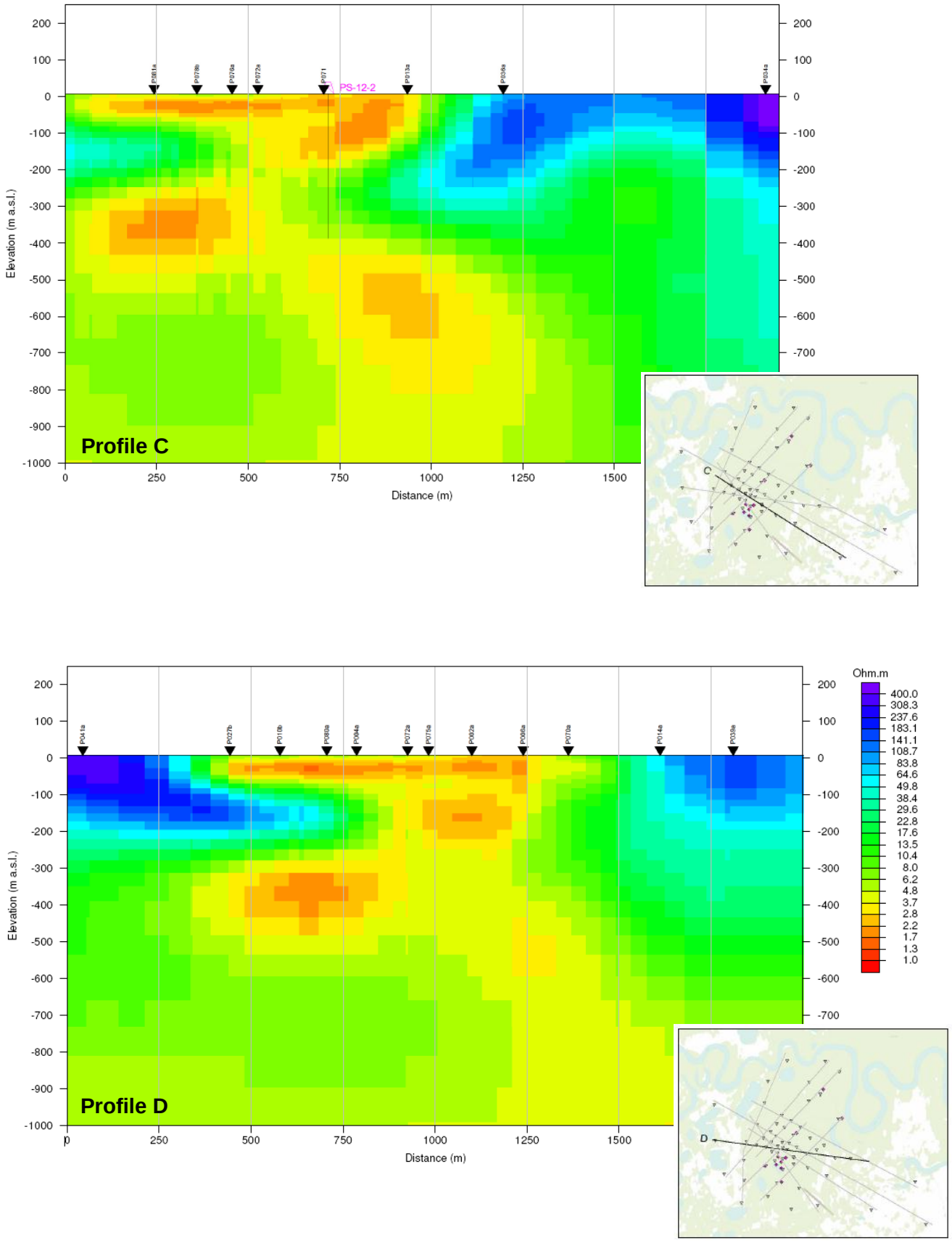


Figure 38. Resistivity at profiles C and D from blind 3D MT inversion (#18).

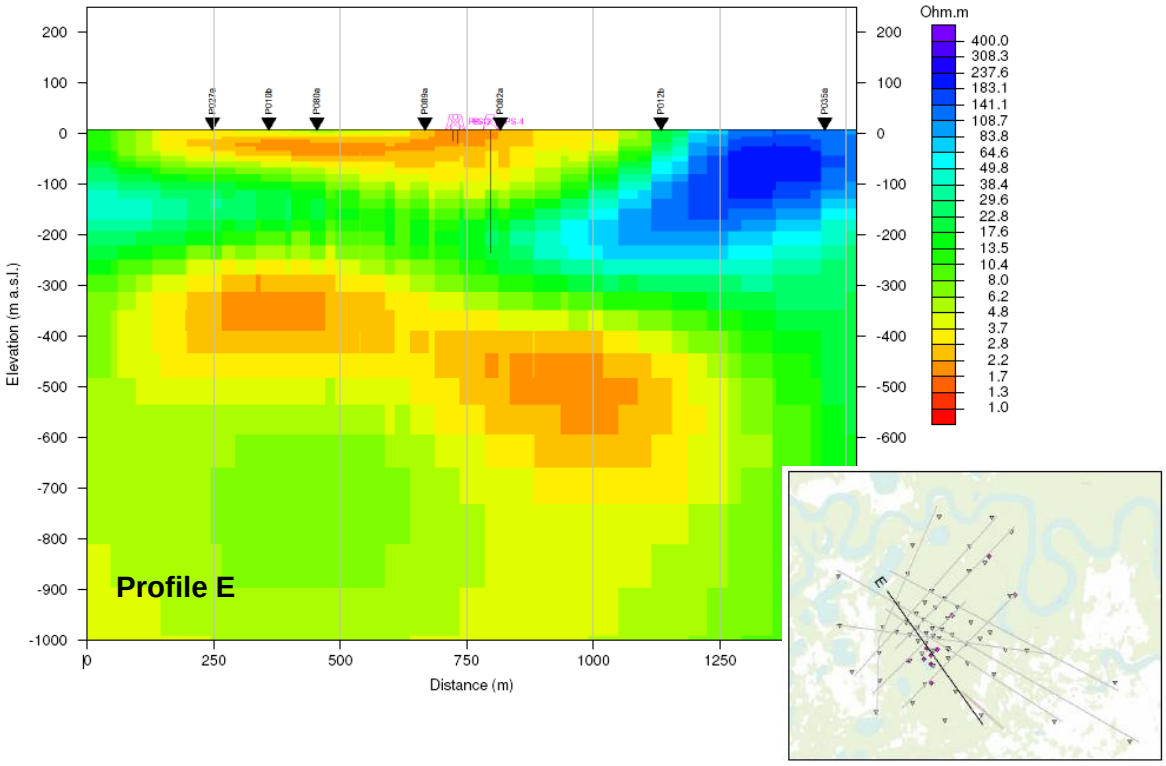


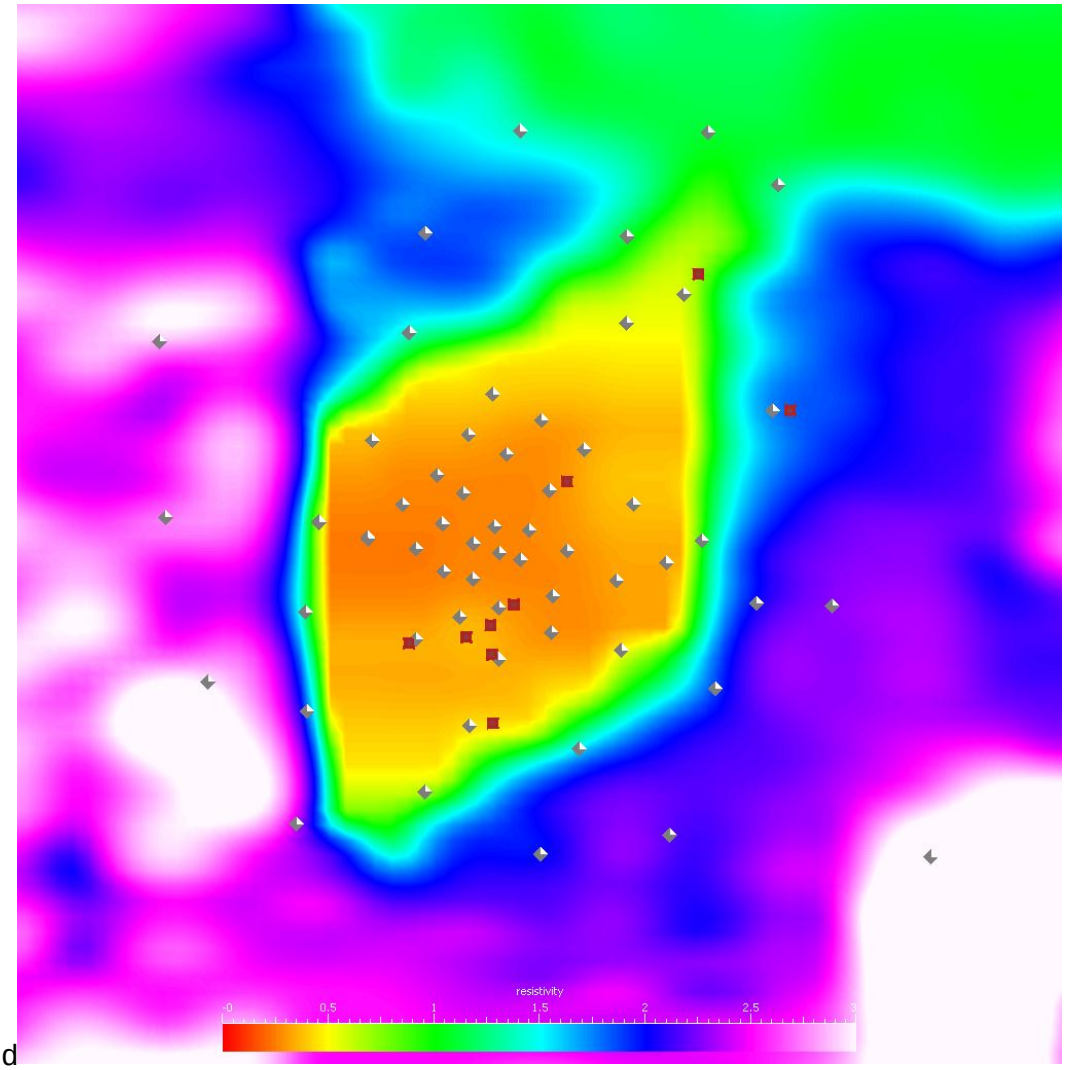
Figure 39. Resistivity at profile E from blind 3D MT inversion (#18).

5.4 Constrained 3D Inversion

Here the resistivity grid from differential resistivity imaging from the Resolve airborne EM data provided by Fugro was used to construct a 3D starting and a priori model for the 3D MT inversion.

Resistivity grids at the depth sections provided (5 / 10 / 15 / 20 / 40 / 60 / 80 / 100m) were loaded into a GOCAD data base and the resistivity information painted onto the 3D MT resistivity grid used for the inversion. The depth range covered was then interpolated to obtain a continuous resistivity distribution within the top ~0-100 meters. Note that in areas of high conductivity the depth extent imaged by the airborne data is reduced and the input grids for this procedure therefore had no information in the central area below ~40m depth (Figure 41).

Outside the area covered the starting model was given a homogeneous 10 Ωm as for the blind inversion. The two zones (defined by airborne resistivity and homogeneous) are separated by a tear surface used in the 3D inversion: the smoothing function of the 3D regularization does not act across the surface, i.e. a sharp boundary between the section with a priori information and underneath is permitted. Regularization was performed such that deviations from the a priori model were penalized.



d

Figure 40. Airborne differential resistivity at 20m depth.

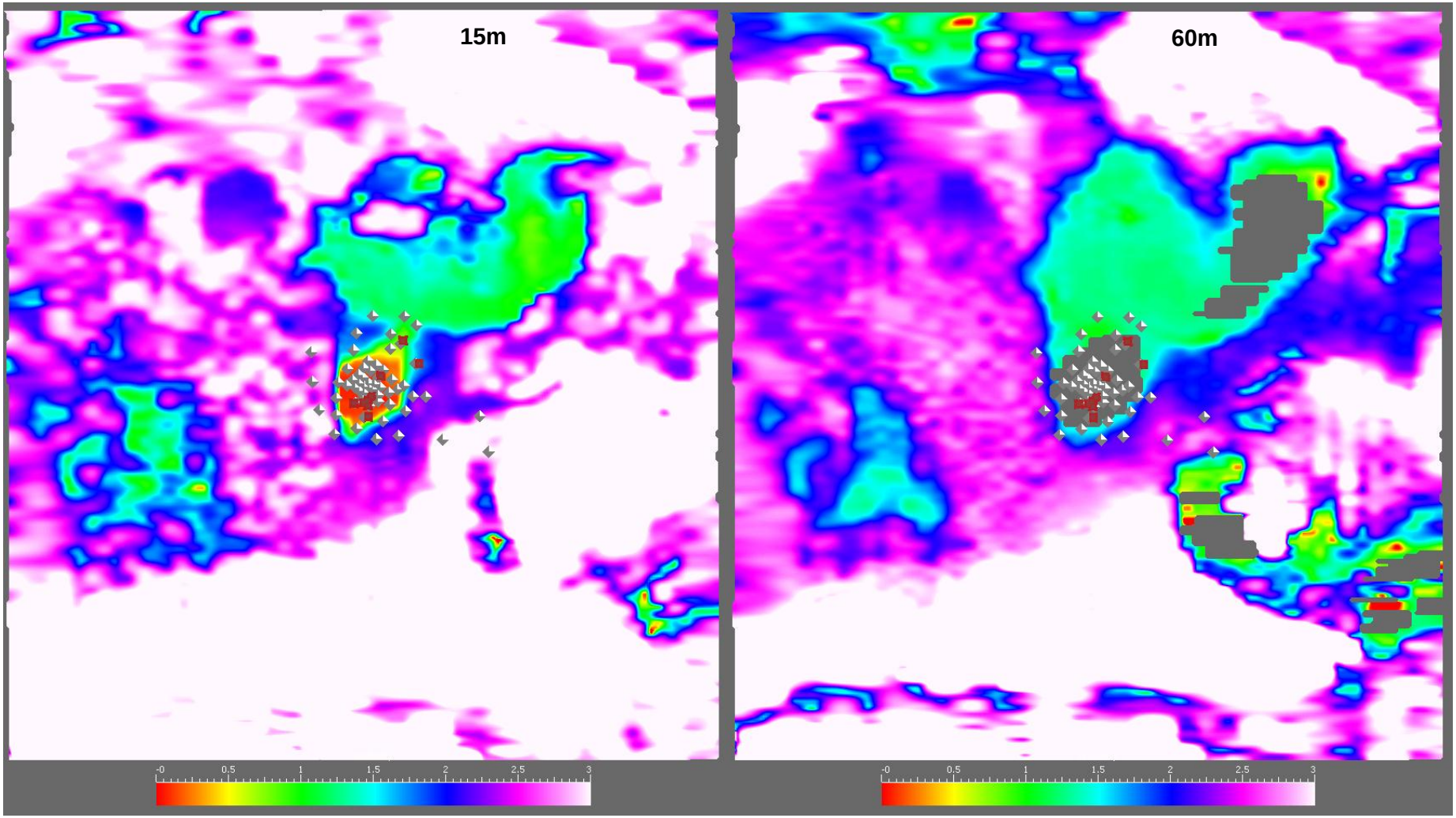


Figure 41. Airborne differential resistivity at depths of 15m (left) and 60m (right). Note the gaps underneath conductive areas.

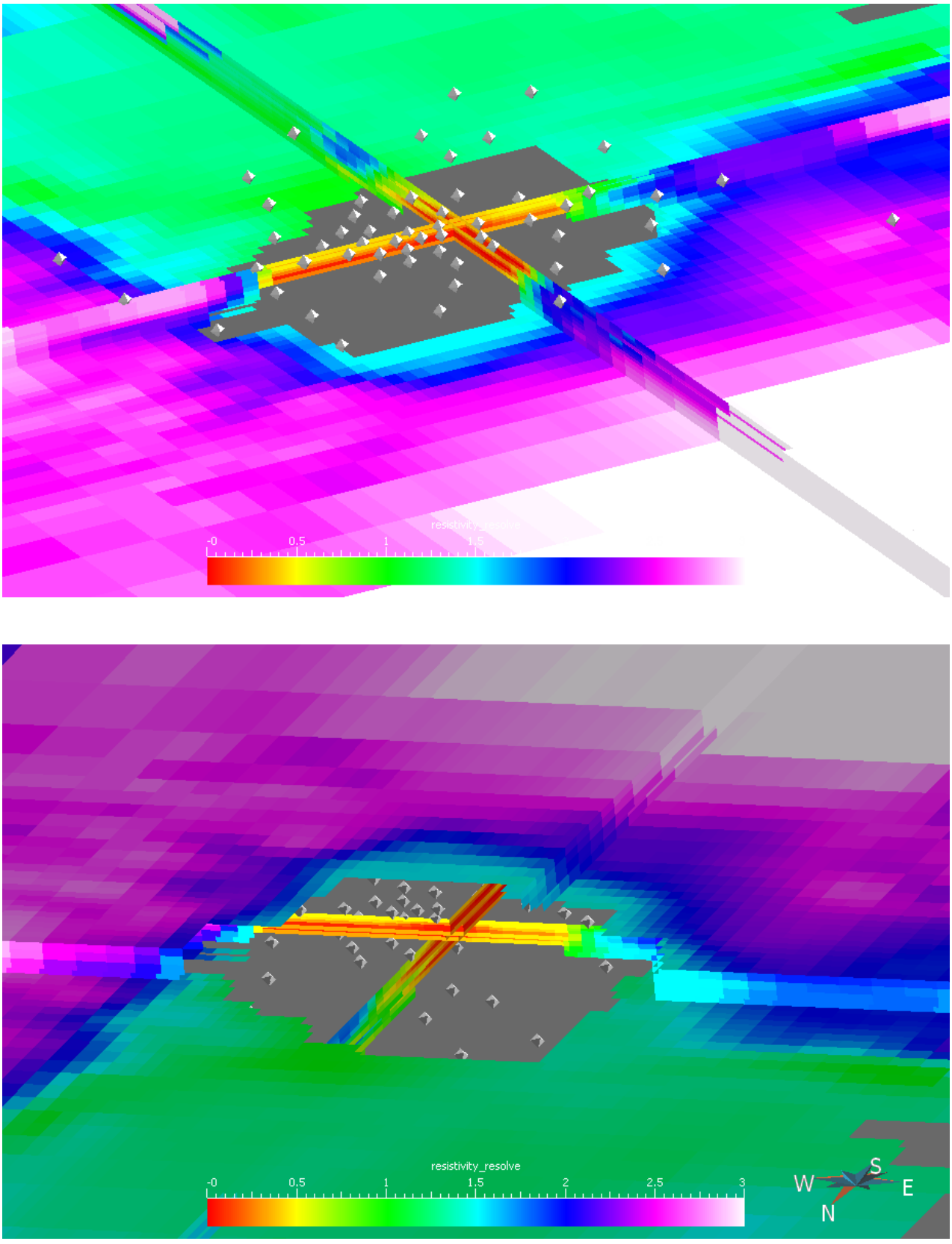


Figure 42. A priori information from Resolve airborne survey in starting model for MT inversion, shown with slices in X, Y, and Z direction from above (upper panel), and below (lower panel).

Flightlines of the airborne survey were oriented NS and about 200m apart in WE direction. While the airborne survey does have overall better lateral resolution, the central zone is also very well covered with MT sites, and the resistivity image at 25m depth from blind 3D MT inversion is indeed in excellent agreement with the airborne inferred one.

Resistivity depth maps from the 3D inversion using the Resolve information are shown at 25m and 200m bsl in Figure 29 below. Resistivity at 25m is close to the original airborne information. Deeper resistivity imaging however is very little influenced by the a priori inclusion of shallow structure.

Cross-section along profile 1 and B illustrate better the effect of the a priori aproach, and also show rather little differences to the blind inversion one (Figure 45).

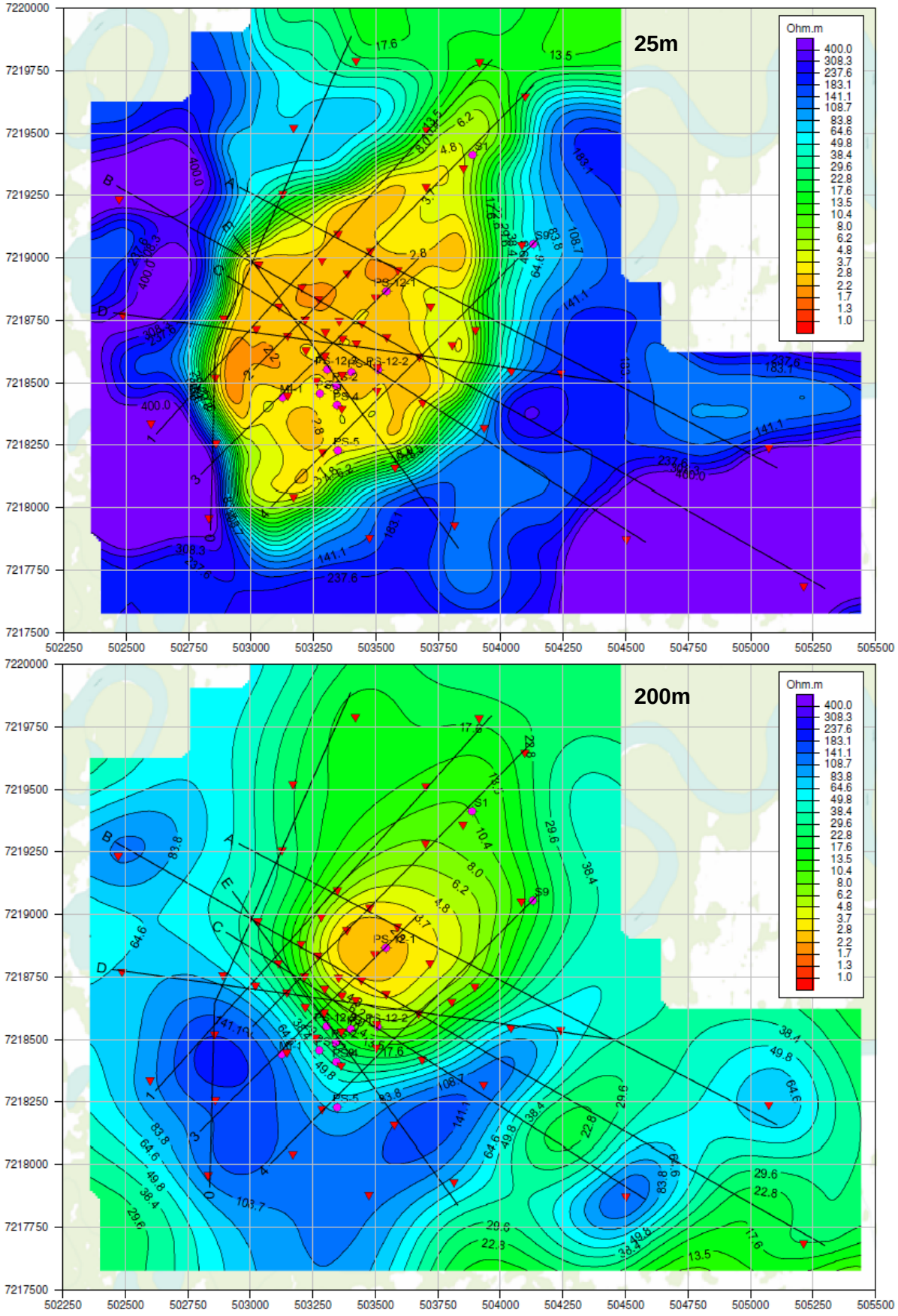


Figure 43. Resistivity map at 25m and 200m depth from constrained 3D MT inversion (#20).

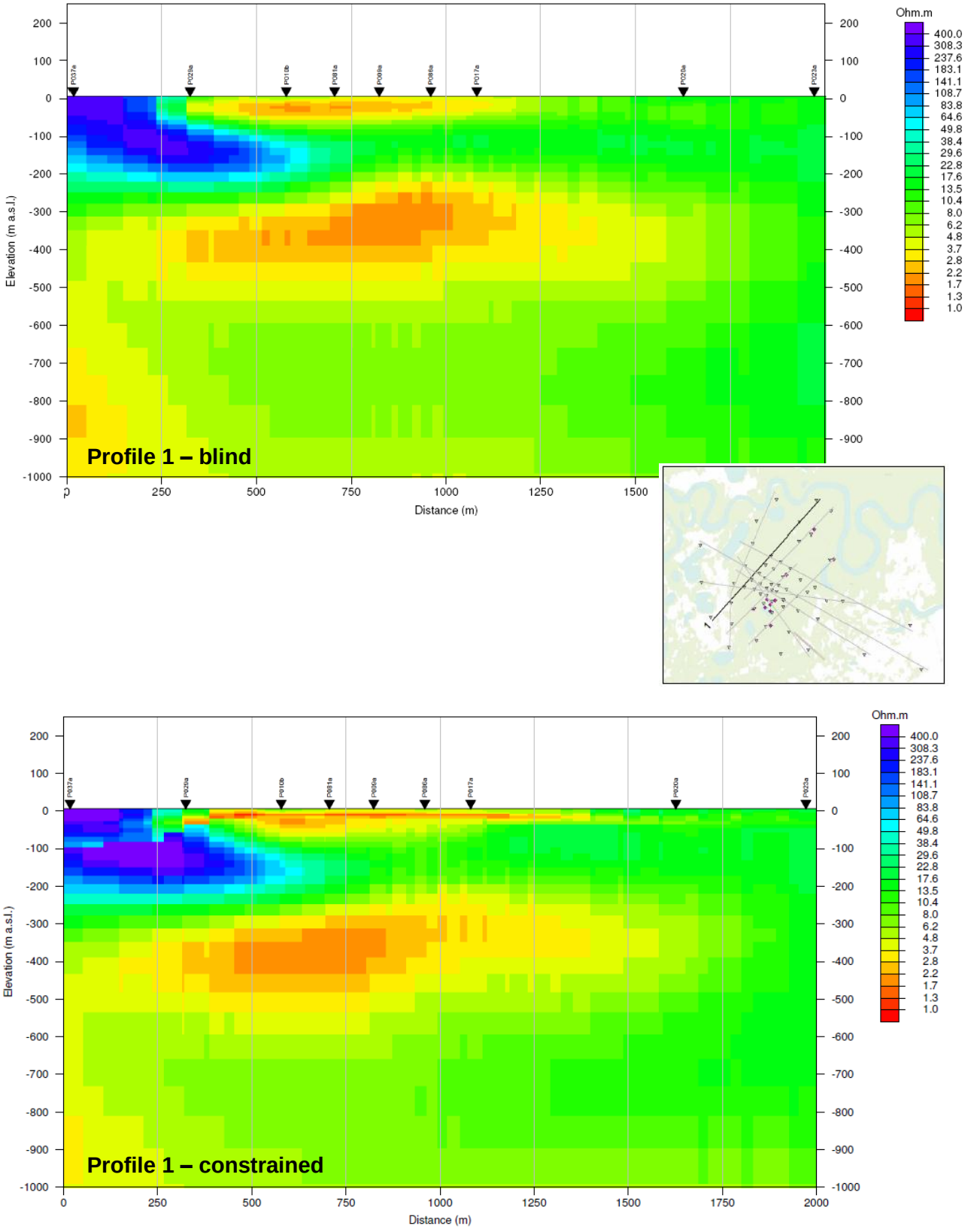


Figure 44. Resistivity at profiles 1 from blind (top) and constrained (bottom) 3D MT inversion.

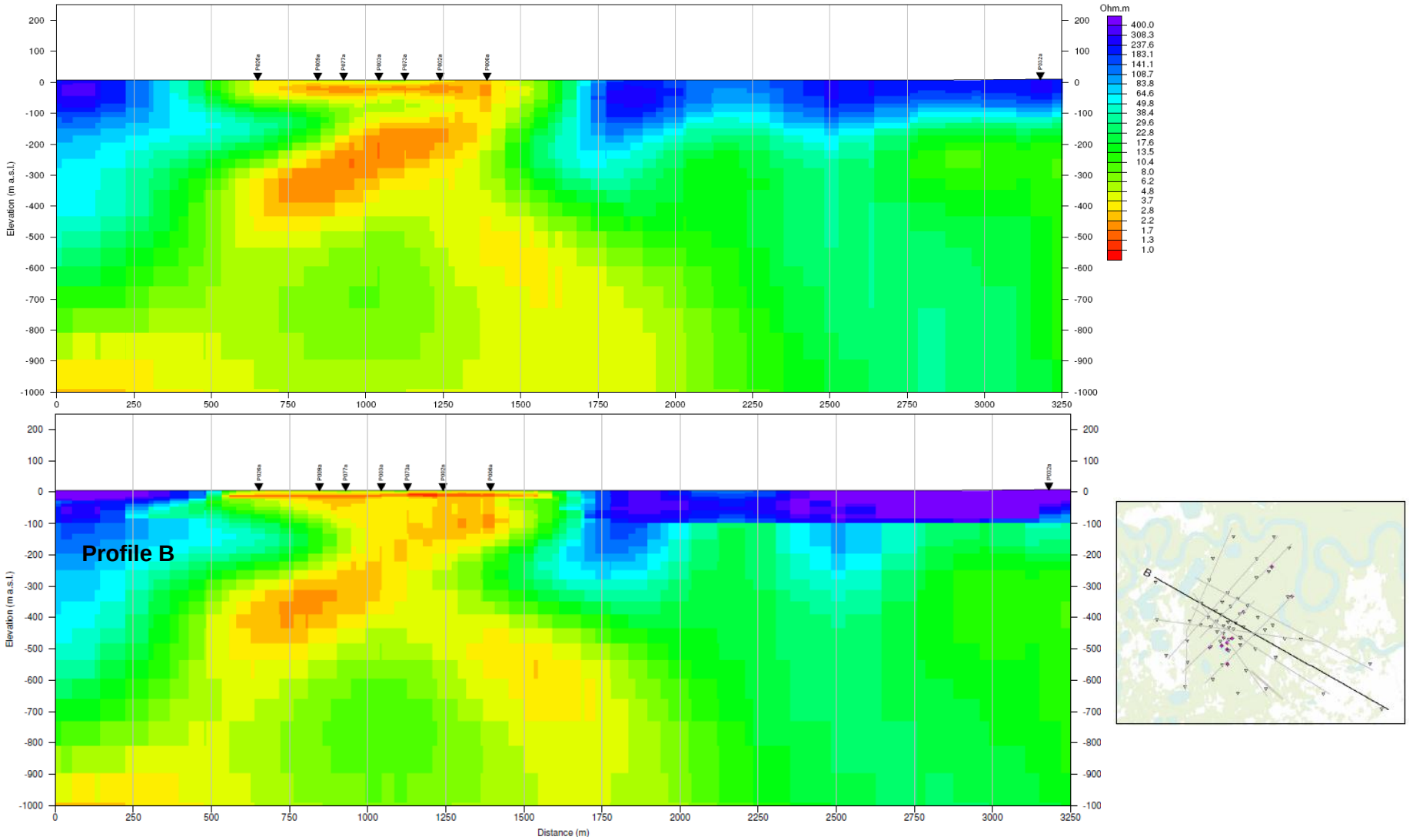


Figure 45. Resistivity at profile B from blind (top) and constrained (bottom) 3D MT inversion.

6 INTEGRATION WITH WELL INFORMATION

Temperature data from borehole measurements were provided by the Client for a number (11) of drillholes with varying depths (~25-400m), and 70 shallow (25m) Geoprobe geothermal gradient wells.

Temperature-depth maps were generated from these, shown below, overlaid by contours from blind 3D MT inversion modeling.

A good match is found at shallowest depth, considering also the different lateral data distribution of the samples from the two measurements. The strong temperature decrease with a local minimum at around 100m depth is not reflected in a strong resistivty high from the 3D modeling, keeping however in mind that a thin horizontal resistor is harder to image via MT than are conductive layers. At 200m anomalies from both measurements move consistently to the north.

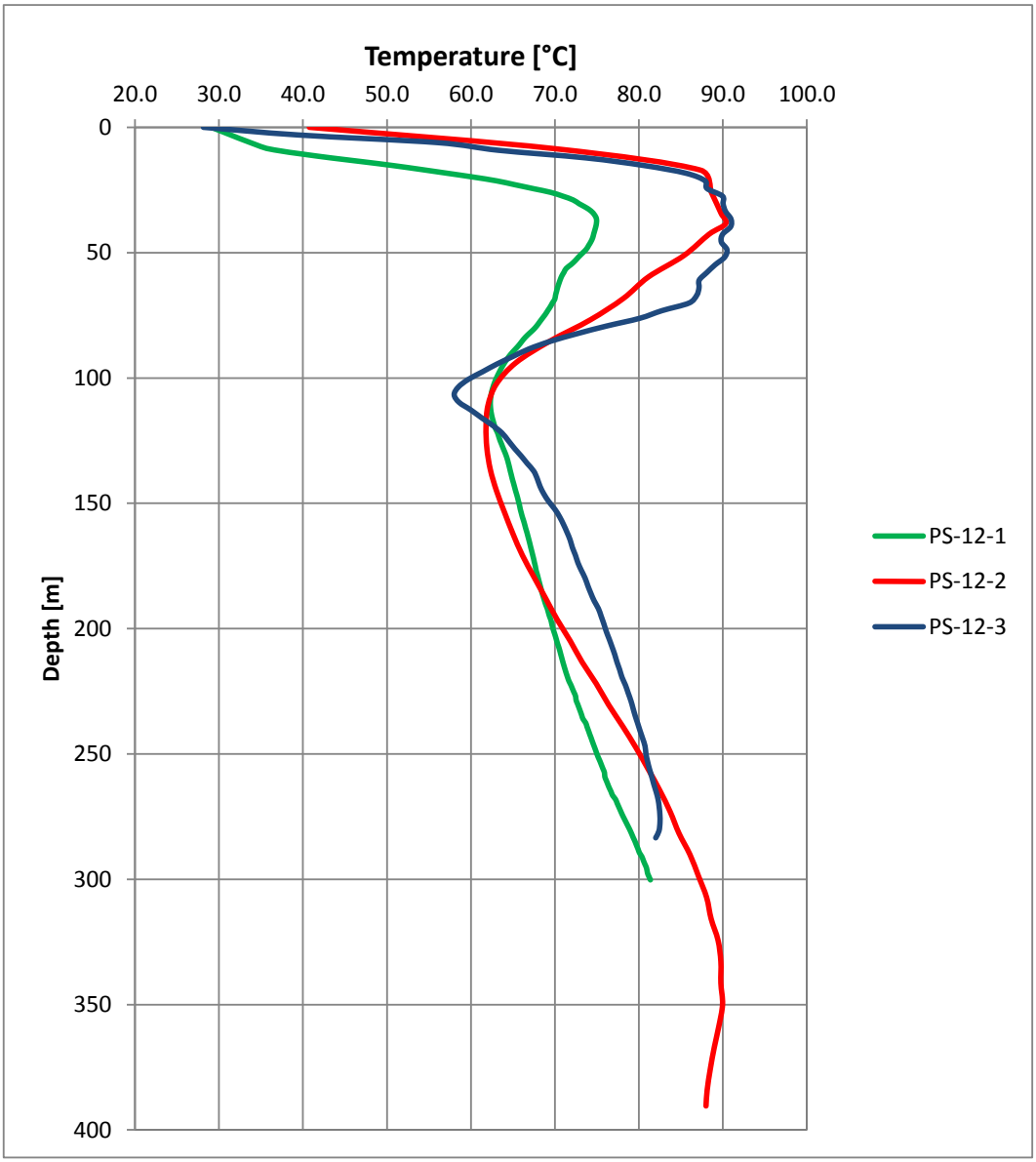


Figure 46. Temperature distribution of the 3 deeper PS-12-[1-3] drill holes.

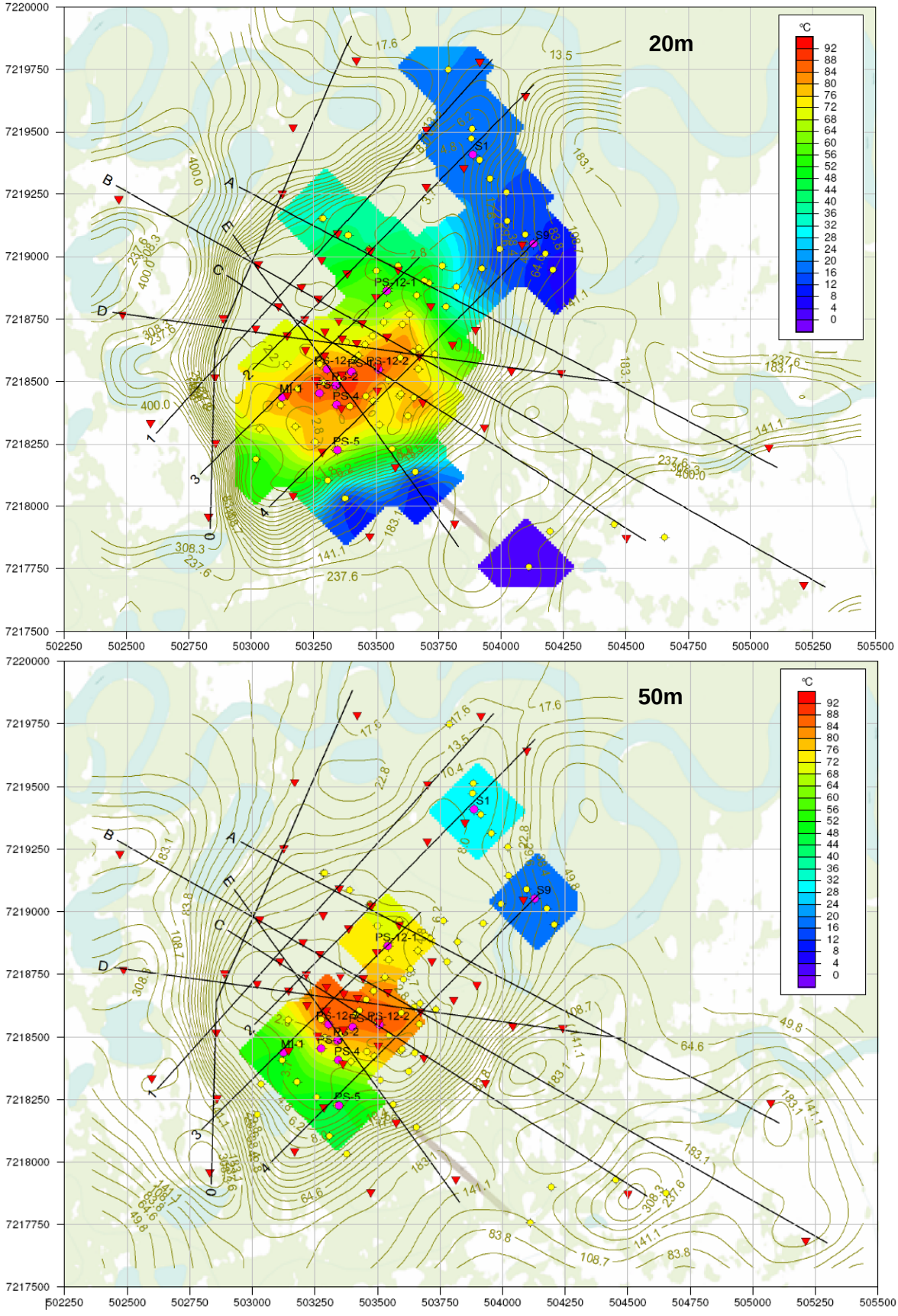


Figure 47. Resistivity from blind 3D inversion (contours) on drill hole temperature data (color, in degrees Celsius), for 20m an 50m depth.

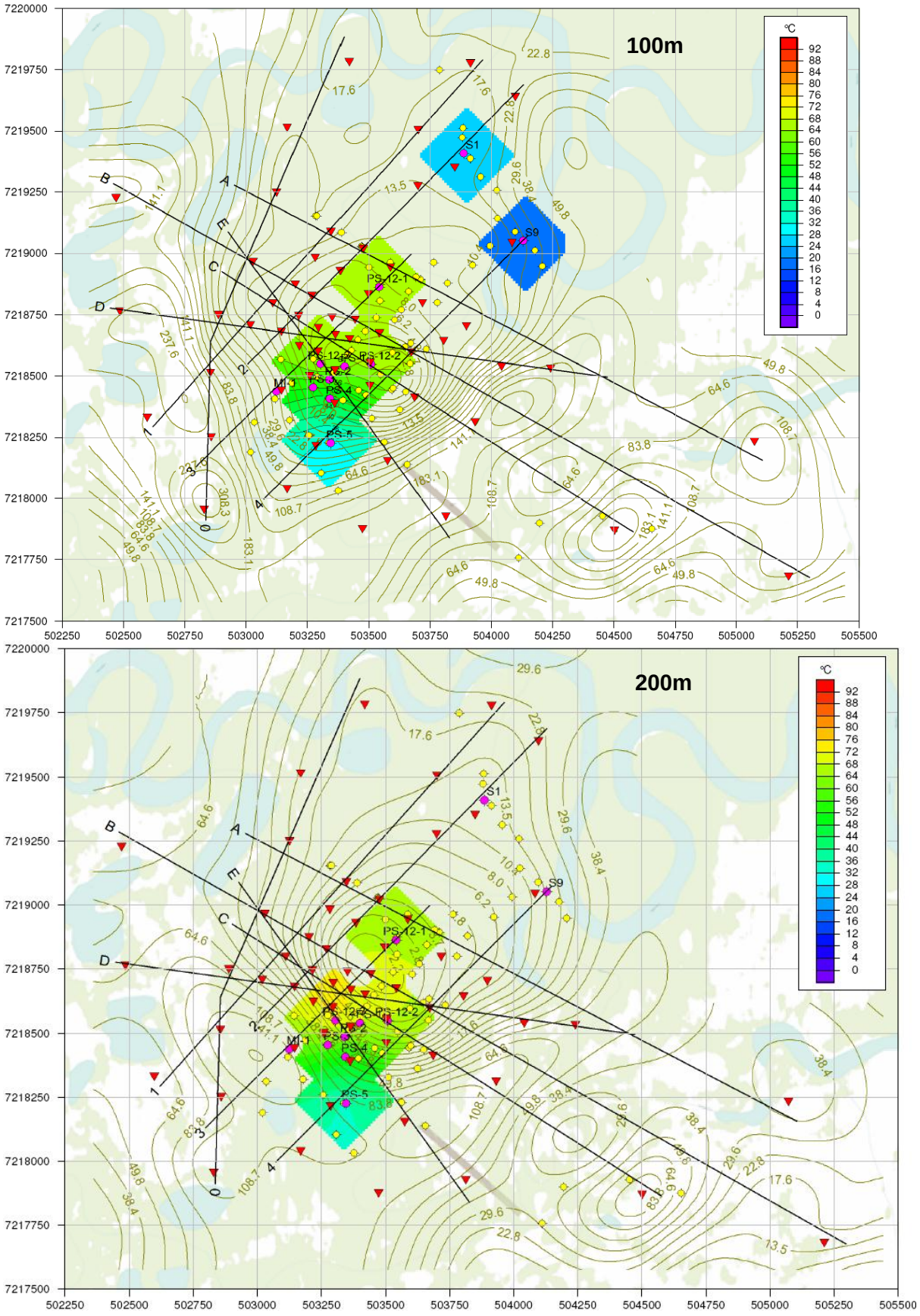


Figure 48. Resistivity from blind 3D inversion (contours) on drill hole temperature data (color, in degrees Celsius), for 100m and 200m depth.

Well logging files in LAS format were provided for wells MI-1, S-1, S-9, PS-12-1, PS-12-2, PS-12-3. Of these, all have gamma logs, but only PS-12-[1-3] contain resistivity or conductivity logs. Electrical resistivity is provided in 3 different log types, and partly (PS-12-2) separately for different ranges of measured depth:

Induction, uncalibrated [CPS = 'counts per second']	PS-12-2 (3-61m) PS-12-2 (61-278m) PS-12-2 (244-393m) PS-12-3 (3-43m)
Induction, calibrated [mmho = 1000 * $(\Omega m)^{-1}$]	PS-12-1 (30-152m) PS-12-2 (3-61m) PS-12-2 (244-393m) PS-12-3 (3-43m)
Resistivity [16N/64N – Ωm]	PS-12-1 (30-152m) PS-12-2 (61-268m) PS-12-2 (275-392m) PS-12-3 (3-43m)

Induction logs come partly also in temperature-corrected versions (AP-COND). From the log of PS-12-3, where the induction log was provided in both, CPS and mmho units, the following linear relationship was inferred between the two from linear regression, to obtain a means to infer physical units from the CPS measurements:

$$(CPS - 44416) / (72.75 * 1000) = \Omega m$$

Logs where loaded into GOCAD, merged, and units converted to Ωm.

Logging was likely performed using devices from Century Geophysical. Induction tools from Century would have an operating range of 1-500 Ωm. Several depth sections contain also negative conductivity values, necessarily masked before the conversion to Ωm. Some bad data sections still remain (see figures).

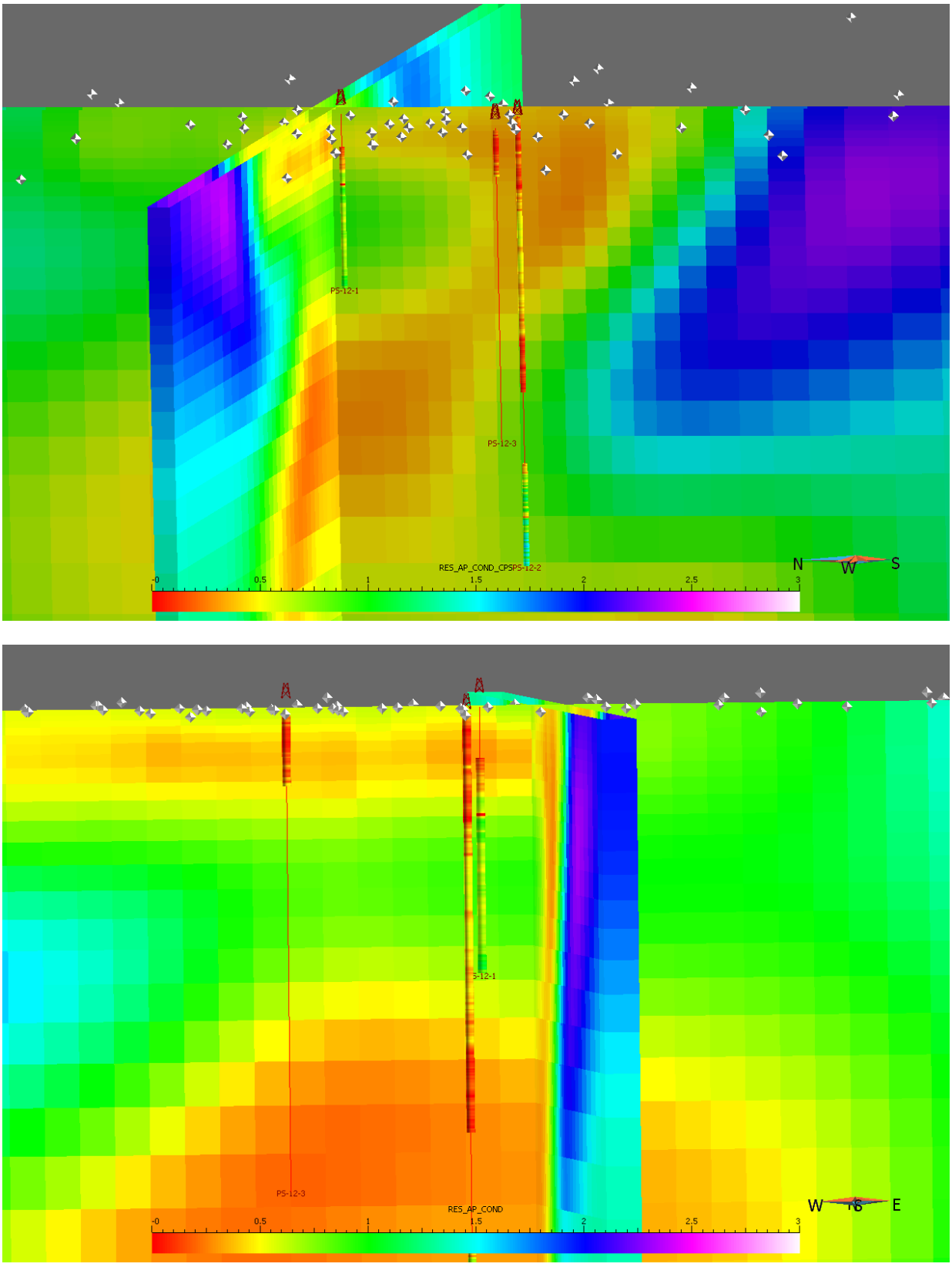


Figure 49. 3D MT inversion model (blind, #18), with resistivity-converted *conductivity* well logs at wells PS-12-[1-3]. View from west (top) and south (bottom). With respect to the deep well PS-12-2, the MT inversion images the low resistivity zone slightly too shallow when viewed from west, but at the same depth as the low resistivity further north.

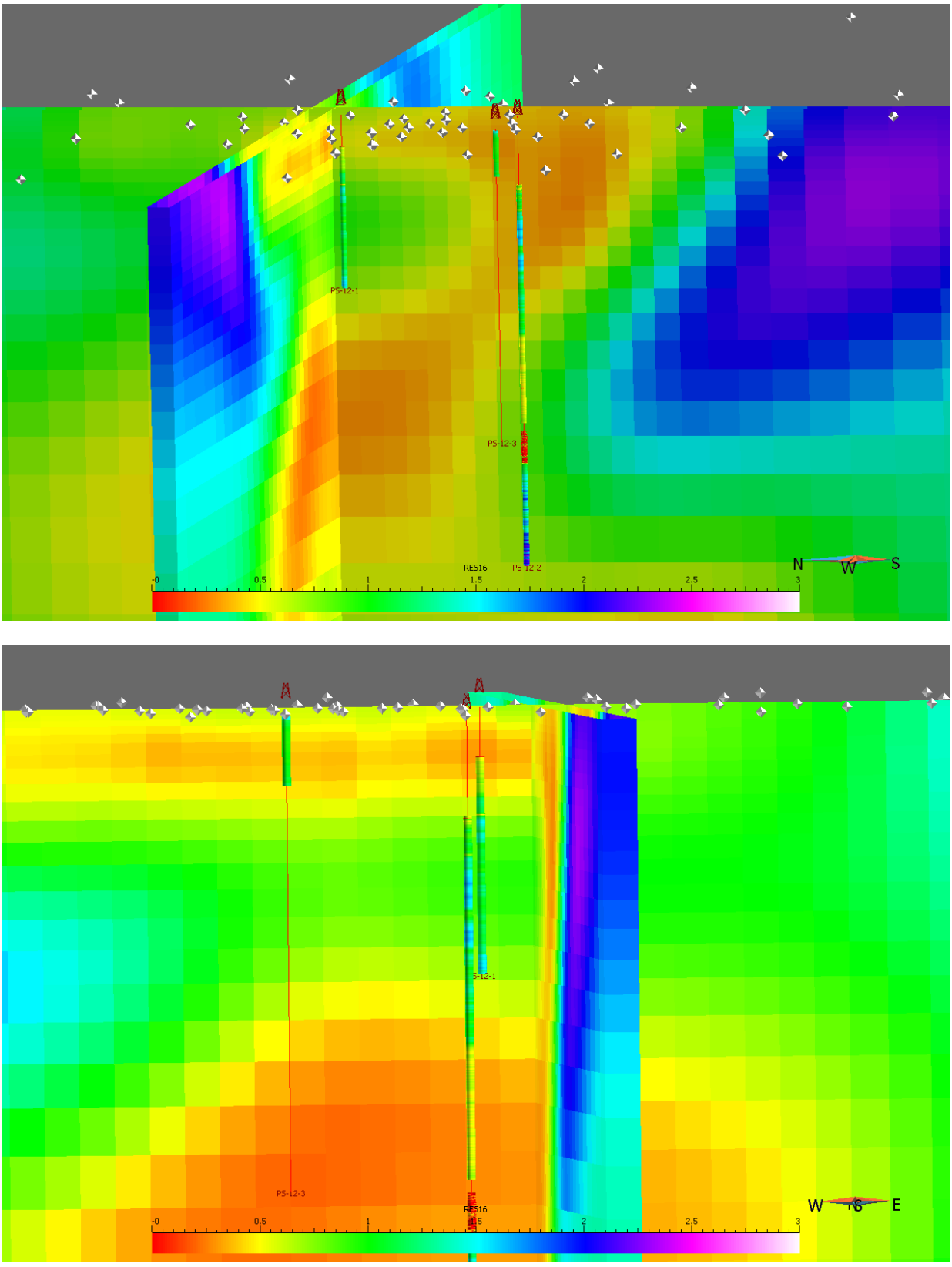


Figure 50. As previous figure, but from *resistivity* logs (16N), with significantly higher resistivity estimates. Note the bad data section (red) in the deep part of well PS-12-2.

7 BIBLIOGRAPHY

BARTELS J., HECK N. H. AND JOHNSTON H. F., 1939. The three-hour-range index measuring geomagnetic activity, Terr. Magn. Atmos. Elec., 44, pp. 411-454.

BEAMISH D. AND TRAVASSOS J., 1992. The use of D+ in Magnetotelluric interpretation: J. Appl. Geophys. 29, pp. 1-19.

CLEMENS, M. AND WEILAND, T., 2001, Discrete electromagnetism with the finite integration technique, *Progress in Electromagnetics Research*, 32, pp. 65-87.

CONSTABLE, S.C., PARKER, R.L., AND CONSTABLE, C.G., 1987, Occam's inversion: a practical algorithm for generating smooth models from electromagnetic sounding data: *Geophysics,* vol. 52, pp. 289-300.

FARR T. G. ET AL., 2007. The Shuttle Radar Topography Mission, Rev. Geophys., 45, RG2004, doi:10.1029/2005RG000183. [http://www2.jpl.nasa.gov/srtm/]

GAMBLE T. D. ET AL., 1979. Error analysis for remote reference magnetotellurics, Geophysics, 44, 5, pp. 959-968.

LARSEN J. C. ET AL., 1996. Robust smooth magnetotelluric transfer functions, Geophys. J. Int., 124, pp. 801-819.

KELLER AND FRISCHKNECHT, 1966, Electrical Methods in Geophysical Prospecting, Pergamon Press.

PARKINSON, W. D., 1962, The Influence of continents and oceans on geomagnetic variations, Geophys. *J. R. astr. Soc*., 6, pp. 441-449.

VOLLAND K., 1982. Low frequency radio noise *in* Volland, H., Ed., CRC Handbook of Atmospherics, vol. 1: CRC Press, Inc. pp. 179-250.

VOZOFF, K., 1991, The Magnetotelluric Method, *in* Electromagnetic Methods in Applied Geophysics, pub. SEG*.,* vol. 2B, pp. 641-711,

WIESE, H., 1962. Geomagnetische Tiefentellurik, II, Die Streichrichtung der Untergrundstrukturen des elektrischen Widerstandes, erschlossen aus geomagnetischen Variationen, *Geofis. Pura Appl.,* 52, pp. 83-103.

WEILAND, T., 1977, A discretization method for the solution of Maxwell's equations for six-component fields, *Electronics and Communications AEU*, 31, pp. 116-120.

WIGHT, D.E., 1988, SEG MT/EMAP Data Interchange Standard, Revision 1.0: SEG, Tulsa, OK, 91pp.

APPENDIX A SURVEY DETAILS

A.1 Personnel

Mark Kitchen of Fugro EM Italy was the Party Manager of the survey and the responsible for MT data acquisition and processing. Acquisition of MT signal was carried out by two MT teams, with T. Firestone and C. Rohe as Observers.

Mark Kitchen	Fugro EM Italy	Party Manager
Trey Firestone	Fugro EM Italy	MT-1 Observer
Chris Rohe	Fugro EM Italy	MT-2 Observer
Zach	Alaska Center for Energy and Power	MT-1 Operator
Lisa	Alaska Center for Energy and Power	MT-1 Operator
Charlie	Alaska Center for Energy and Power	MT-2 Operator
Jason	Alaska Center for Energy and Power	MT-2 Operator
Frank	Alaska Center for Energy and Power	MT-2 Operator

Table 7. Field Personnel.

A.2 Time Line

August 13 - 14	Logistics setup and mobilization to Nome
August 15	Gear preparation
August 16 – 26	MT Production
August 27 - 28	Pickup all gear, packing, processing last data set and leaving

Table 8. Project Time Line.

A.3 Logistics

The project base, accommodation, storage for all technical equipment, and the field office for data processing was set up at the Pilgrim Springs survey site.

ACEP provided food and accommodations, and motor vehicles for crew where practical (4WD and/or approved ATVs).

Communication between field teams and field office was maintained via satellite or mobile phones.

Internet communication and power were provided by ACEP at the field camp facilities.

Each MT team was composed by one MT observer with 2 additional field ACEP assistants.

A.4 Weather Conditions

Conditions were windy and raining days during most of the acquisition phase.

A.5 HSE Statistics

All personnel were HSE induced and trained by ACEP and Fugro.

Fugro induction consisted of the following topics:

- Driving and basic rules for passengers
- Journey management and reporting
- Reporting accidents and use of GPS. Emergency contact list
- Garbage & Waste policy
- Hiking in wet and swampy areas
- "AAA" - atitude, attention, action
- Take 5, 5 seconds 5 thought – Prevention
- Working with hand tools, special care of pickaxe

Daily morning meetings guaranteed continuous safety awareness.

No major accidents or LTI incidents occurred during the survey.

APPENDIX B MT TIME SERIES FORMAT

The raw time series on the external HD are organized with one folder per MT site, with corresponding name. Subfolders therein contain the time series data from each recording run, and are named after the start time of the measurement (meas_yyyy-mm-dd_hh-mm-ss).

Each recording in addition to the time series generates an XML file containing information on the instrument configuration for the recording plus sensor calibrations. The time series filenames (extension .ats) reflect the most critical information about the data file:

adu_Vvv_Ccc_Rrrr_Ttt_Bb_fffffH.ats, with:

adu	ADU serial number
vv	XML version (01)
cc	channel number (00/01/…/09)
rr	run-number (00/01/…)
tt	channel type (EX/EY/HX/HY/HZ)
b	board type (L: LF/ H: HF)

The time series data files, with one file per channel, are in a mixed binary format containing a header of 1024 bytes, followed by a row of four-byte integers with the actual data. The header contains all information required for data processing except for sensor calibration data, which are provided through separate ASCII files (.srv).

Metronix Time Series: ATS Format

B off-set	ADR	Byte	Type	Name	Info
1	000H	2	INT16	Header Length	Length of Header in Byte
3	002H	2	INT16	Header Version	Version Number of Header (*100)[4]
5	004H	4	UINT32	Samples	Number of Samples
9	008H	4	SINGLE	Sample Freq.	Sample Frequency
13	00CH	4	INT32		Start Time of Measurement (in seconds since 1.1.70)
17	010H	8	DOUBLE	LSBV	LSB Unit in MV[2]
25	018H	4	INT32		GPS Offset
29	01CH	4	SINGLE		Origin sample Rate
33	020H	2	INT16		Serial number of ADU07
35	022H	2	INT16		Serial number of ADB07 (ADC Board)
37	024H	1	INT8		Channel number (0…7)

B off-set	ADR	Byte	Type	Name	Info
38	025h	1	INT8		Chopper
39	026h	2	CHAR		Channel Type (Ex,Ey,Hx,Hy,Hz)
41	028H	6	CHAR		Sensor Type (MFS-06, MFS-07…)
47	02EH	2	INT16		Serial number of sensor
49	030H	4	SINGLE		x1 coordinates of 1. Dipole(m)
53	034H	4	SINGLE		y1
57	038H	4	SINGLE		z1
61	03CH	4	SINGLE		x2 coordinates of 1. Dipole (m)
65	040H	4	SINGLE		y2
69	044H	4	SINGLE		z2
73	048H	4	SINGLE		e-field dipole length (m)
77	04CH	4	SINGLE		Angle (0°=north) (degrees °)
81	050H	4	SINGLE		Probe resistivity (ohm)
85	054H	4	SINGLE		DC offset voltage[3] (MV)
89	058H	4	SINGLE		Internal gain amplification (1 or 30)[4]
93	05CH	4	SINGLE		Post Gain
97	060H	4	INT32		Latitude (msec)
101	064H	4	INT32		Longitude (msec)
105	068H	4	INT32		Elevation (cm)
109	06CH	1	CHAR		Lat/Long: ‘U’ user def, ‘G’ internal GPS clock
110	06DH	1	CHAR		Type of additional coordinates: ’U’ UTM, ‘G’ Gauss-Kruger
111	06EH	2	INT16		Reference median
113	070H	8	DOUBLE		X coordinate
121	078H	8	DOUBLE		Y coordinate
129	080H	1	CHAR		GPS/CLK status: ‘G’ GPS lock ‘C’ CLK sync ‘N’ CLK no sync
130	081H	1	INT8		Approximate accuracy of GPS/CLK: 9 means accuracy of 10^9
131	082H	2	INT16		UTC Offset
133	084H	12	CHAR		System Type
145	090H	12	CHAR		Survey header file name
157	09CH	4	CHAR		Type of measurement: MT or CSAMT
161	0A0H	12	CHAR		Log file of system self test
173	0ACH	2	CHAR		Result of self test ‘OK’ or ‘NO’
175	0AEH	2	BYTE		Reserved
177	0B0H	2	INT16		Number of calibration frequencies in file
179	0B2H	2	INT16		Length of frequency entry (32 byte)

B off-set	ADR	Byte	Type	Name	Info
181	0B4H	2	INT16		Version of calibration format (*100)
183	0B6H	2	INT16		Start address of calibration information in header (400H)
185	0B8H	8	INT8		1 to 8 LF Filters
193	0C0H	12	CHAR		File name of ADU07 cal file
205	0CCH	4	INT32		Date/time of calibration
209	0D0H	12	CHAR		File name of sensor calibration
221	0DCH	4	INT32		Date/time of calibration
225	0E0H	4	SINGLE		Power-line freq. 1
229	0E4H	4	SINGLE		Power-line freq.2
233	0E8H	8	INT8		1 to 8 HF Filters
241	0F0H	4	SINGLE		CSAMT transmitter frequency
245	0F4H	2	INT16		CSAMT time series block
247	0F6H	2	INT16		CSAMT stacks/block
249	0F8H	4	INT32		CSAMT block length
253	0FCH	4	CHAR		ADB Board Type
257	100H	16	CHAR		Client
273	110H	16	CHAR		Contractor
289	120H	16	CHAR		Area
305	130H	16	CHAR		Survey ID
321	140H	16	CHAR		Operator
337	150h	112	CHAR		Reserved
449	1C0H	64	CHAR		XML Header
513	200H	512	CHAR		Comments
	Header Length +n*20H	4 byte/ Sample	INT32		Time series data

Fields in gray are currently not used.

APPENDIX C 3-D MT INVERSION

The 3D models shown in this report were derived from a new 3D MT inversion code recently developed by Randall Mackie in late 2011 for Fugro EM Italy. The usual approach to MT inversion, and indeed the approach used in this new algorithm is that of Tikhonov regularization (Tikhonov and Arsenin, 1977). This algorithm seeks to find regularized inversion models that fit the data to within the prescribed errors. Typically, the regularization is of the form of minimum-structure models. We use the nonlinear conjugate gradients algorithm to minimize the nonlinear objective function, as described in Rodi and Mackie (2001). In this new algorithm, we invert for the complex impedance tensor values and the complex vertical magnetic transfer function (if present).

Doing a 3D MT inversion requires the solution of hundreds of 3D MT forward solutions. The new algorithm for forward modeling is based on the Finite Integration Technique (FIT) as described by Weiland (1977) and Clemens and Weiland (2001). The FIT is a discrete, but exact, reformulation of the Maxwell equations in their integral form that provides a generalized scheme for solving electromagnetic problems in discrete space and admits arbitrary geometries and coordinate systems. We currently apply FIT on orthogonal Cartesian grids, which is equivalent to the standard staggered grid finite difference solutions. In this algorithm, we define electric fields along block edges and magnetic fields are naturally defined as normals across block faces. Eliminating the magnetic fields results in a second-order system of equations in the electric fields. Because zero conductivity air layers lead to a singular system, we stabilize the solution by explicit inclusion of the gradient of the divergence of J in the earth and E in the non-conducting air. This system of equations is solved iteratively by the stabilized biconjugate gradient algorithm with incomplete LU decomposition of the diagonal sub-blocks as a preconditioner. Once the E and H fields have been determined for two linearly-independent source polarizations, the impedance tensor and vertical magnetic transfer function can be computed.

C.1 Output Data

The files associated with the 3-D inversions are:

- model files, which containing the mesh dimensions and the final resistivity values (see below).
- inversion LOG files, containing inversion statistics.
- RMS files, listing the misfit between observed and predicted values for each station.
- predicted data, in EDI format, with computed responses at each site.Model Formats

C.1.1 WinGLink OUT Format (ASCII).

- Coordinate axis: x = East, y = South, z = down (for orientation α=0)
- Origin / anchor: laterally - cell center of north-westernmost cell (index: 1, 1); vertically – top of model. Given in [km] at bottom of file (x0/ y0/ z0).
- Orientation: counterclockwise in degrees (α)

nx	ny	nz		
dx_1	dx_2	dx_3	...	dx_nx
dy_1	dy_2	dy_3	...	dy_ny
dz_1	dz_2	dz_3	...	dz_nz
1				
ρ_1,1,1	ρ_2,1,1	ρ_3,1,1	...	ρ_nx,1,1
...				
ρ_1,ny,1	ρ_2,ny,1	ρ_3,ny,1	...	ρ_nx,ny,1
...				
nz				
ρ_1,1,nz	ρ_2,1,nz	ρ_3,1,nz	...	ρ_nx,1,nz
...				
ρ_1,ny,nz	ρ_2,ny,nz	ρ_3,ny,nz	...	ρ_nx,ny,nz
WINGLINK				
Name				
1	1			
x0	y0			
α				
z0				

C.1.2 UBC Format (ASCII)

with mesh (MESH) and model (MOD) files, see also: http://www.eos.ubc.ca/ubcgif/iag/sftwrdocs/grav3d/elements.htm).

- Coordinate axis: x = East, y = North, z = down
- Origin / anchor: laterally – SW corner of south-westernmost cell (index: 1, 1); vertically – top of model. Given in [m] in second line of MESH file (x0/ y0/ z0).
- Orientation (NOT part of the standard UBC format): counterclockwise in degrees (α)

MESH file:

nx	ny	nz		
x0	y0	z0		
dx_1	dx_2	dx_3	...	dx_nx
dy_1	dy_2	dy_3	...	dy_ny
dz_1	dz_2	dz_3	...	dz_nz
α				

MOD file:

ρ_1,1,1
...
ρ_1,1,nz
...
ρ_nx,1,1
...
ρ_nx,1,nz
...
ρ_nx,ny,1
...
ρ_nx,ny,nz

C.1.3 4-Column ASCII format

Contains the cell center locations with respective resistivity values: X-Y-Z-resistivity.

Note that except for the original format (OUT), the lateral and vertical padding zones of the model have been removed for convenience.

C.1.4 ECLIPSE format

ASCII version of the format, readable e.g. by GOCAD and Petrel.

APPENDIX D DELIVERABLES

Raw time series for all MT sites, with sensor calibration files (on HD)

Maps of MT site locations

MT production sheet (XLS format) with site-specific information (instrumentation, layout, coordinates, etc.)

Processed MT Data (EDI format)

Data plots – 2 sets: masked/edited as for 3D inversion, and unmasked.

WinGLink data base, containing:

- Processed MT data
- 1D Inversion models
- Input data with editing as for 3D inversions (#18 & #20 - Observed)
- Forward response of 3D Inversion model (#18 & #20 - Predicted)
- Blind 3D Inversion model (#18)
- Constrained 3D Inversion model (#20)

3D Inversion output (inversions #18 & #20 - see Appendix C for format details)

Resistivity maps and cross sections (1D inversions, 3D inversions #18 & #20)

Appendix M
A Conceptual Model of the Pilgrim Hot Springs Geothermal System, Seward Peninsula, Alaska:
Joshua Miller Masters Thesis

A CONCEPTUAL MODEL OF THE PILGRIM HOT SPRINGS GEOTHERMAL SYSTEM, SEWARD PENINSULA, ALASKA

A

THESIS

Presented to the Faculty

of the University of Alaska Fairbanks

in Partial Fulfillment of the Requirements

for the Degree of

MASTER OF SCIENCE

By

Joshua K. Miller, B.S. Geology

Fairbanks, Alaska

December 2013

Abstract

This work has developed a conceptual geological model for the Pilgrim Hot Springs geothermal system supporting the exploration, assessment and potential development of this resource for direct use and electric power production. The development of this model involved the analysis of a variety of subsurface and geophysical data and the construction of a 3D lithostratigraphic block model. Interpretation of the data and block model aimed to establish the most likely scenario for subsurface geothermal fluid flow. As part of this work well cuttings were analyzed for permeability and correlated with geophysical logs from well to well to constrain the stratigraphic architecture of the unconsolidated sediments. Hydrothermal alteration of the sediments and bedrock core was also studied through reflectance spectroscopy and methylene blue titration in order to investigate past fluid migration pathways. The structure of the basin was interpreted through geophysical surveys including aeromagnetic resistivity, isostatic gravity, and magnetotelluric resistivity. Based on temperature, well logs, geophysical surveys, and lithologic data, the system is subdivided into a shallow outflow aquifer and a deeper reservoir beneath a clay cap connected by a conduit with 91°C hydrothermal fluid upflow. Stratigraphic correlations indicate several clay layers throughout the section with a dominant clay cap at 200-275 m depth. Extensive pyritization and the clay mineral assemblage suggest an argillic-style alteration facies indicative of past temperatures at or slightly elevated above current conditions of hydrothermal activity at Pilgrim Hot Springs. The conceptual model supports production from this resource in those subsurface zones where there is sufficient permeability and connectivity with the upflow zone.

Table of Contents

Page

Signature Page i

Title Page iii

Abstract v

Table of Contents vii

List of Figures xi

List of Tables xv

List of Appendices xvii

Acknowledgements xix

Chapter 1: Introduction 1

1.1 Overview 1

1.1.1 General Introduction 1

1.1.2 Research Objectives 2

1.1.3 Thesis Structure 3

1.2 Background 4

1.2.1 Geothermal Systems and Geothermal Energy 4

1.2.2 Alaska Geothermal Systems 5

1.2.3 History of Exploration at Pilgrim Hot Springs 6

Chapter 2: Study Area 9

2.1 Pilgrim Hot Springs Location 9

2.2 Regional and Local Geology and Physiography 11

2.2.1 Overview of the Regional Geology of Seward Peninsula 11

2.2.2 Seismicity of the Seward Peninsula 13

2.2.3. Surficial and Bedrock Geology of the Pilgrim River Valley....16

Chapter 3: Data and Data Products....19

3.1 Field Data....19

3.1.1 Rock Sample Collection....19

3.2 Geophysical Data....21

3.2.1 USGS Aeromagnetic and Electromagnetic (EM) Survey....23

3.2.2 Magnetotelluric (MT) Resistivity Survey....26

3.2.3 Ground-based Gravity Survey....32

3.3 Geoprobe Data....35

3.4 Drilling Data....37

3.4.1. Sediment Characterization....37

3.4.2 Geophysical Well Logs....42

3.4.3 Static Temperature Logs....44

3.5 Sample Analytical Techniques....47

3.5.1 Reflectance Spectroscopy....47

3.5.2 Methylene Blue Titration....57

3.5.3 X-ray Diffraction Analysis....59

3.5.4 Thin-section Characterization....62

3.6 Discussion of Analytical Results....64

Chapter 4: Lithostratigraphic and Temperature Model Development....70

4.1 RockWorks15 Model Parameters....70

4.2 Model Assumptions and Limitations....72

4.3 Data Integration....73

4.3.1 Lithostratigraphic Model....73

4.3.2 Temperature Model....78

Chapter 5: Development of the Conceptual Model 85

5.1 Introduction....85

5.2 Discussion of the Conceptual Model 87

5.3 Conceptual Model in a Regional Context....106

Chapter 6: Conclusions and Recommendations 113

6.1 Conclusions....113

6.2 Recommendations....114

References....117

Appendices....125

List of Figures

Page

Figure 2.1: Pilgrim Hot Springs location map with wells 10

Figure 2.2: Seismicity map of central and western Alaska.....15

Figure 2.3: Surficial and bedrock geology map of the Pilgrim River Valley.....18

Figure 3.1: Place map of rock sample locations 20

Figure 3.2: Logarithmic scale of resistivity values for geologic materials.....22

Figure 3.3: Flight path for aeromagnetic and electromagnetic survey 24

Figure 3.4: Different resistivity map at 20 m depth.....25

Figure 3.5: Locations of magnetotelluric resistivity recording stations 28

Figure 3.6: Magnetotelluric resistivity profile line D 29

Figure 3.7: Magnetotelluric resistivity profile line C 30

Figure 3.8: Magnetotelluric resistivity profile line 2 31

Figure 3.9: Isostatic gravity survey station location map 33

Figure 3.10: Isostatic gravity anomaly map of the Pilgrim River Valley.....34

Figure 3.11: Well and Geoprobe hole location map 36

Page

Figure 3.12: Logarithmic chart of particle diameter by sediment type.....41

Figure 3.13: Lithologic and gamma ray logs for selected wells.....43

Figure 3.14: Temperature curves for all Pilgrim Hot Springs wells.....45

Figure 3.15: Lithology, gamma ray, and temperature curves for selected wells.....46

Figure 3.16: AlOH and FeOH absorption features.....48

Figure 3.17: Hyperspectral image cube of PS-12-2.....51

Figure 3.18: The Spectral Geologist spectral analysis mineral results.....52

Figure 3.19: White Mica Alteration Index scatter plot for PS-12-2.....55

Figure 3.20: White Mica Alteration Index scatter plot for selected wells.....56

Figure 3.21: Methylene blue solution halos.....58

Figure 3.22: XRD results of PS-12-2 clay samples.....61

Figure 3.23: Thin-section photomicrographs of bedrock core samples.....63

Figure 3.24: AlOH absorption depths and methylene blue results combined plot.....66

Figure 3.25: Lithology, temperature, spectral, and methylene blue analysis plot.....67

Figure 4.1: RockWorks15 conceptual model dimensions.....71

Page

Figure 4.2: Southwest-northeast cross-section of interpolated lithologic logs 75

Figure 4.3: RockWorks15 3D model of the interpolated lithologic logs.....76

Figure 4.4: RockWorks15 3D model of major clay intervals and indurated zone 77

Figure 4.5: Southeastern view of the RockWorks15 temperature model 80

Figure 4.6: Vertical and horizontal slices of the RockWorks15 temperature model.....81

Figure 4.7: Three depth maps of the RockWorks15 temperature model result 82

Figure 4.8: Two cross-sections of the RockWorks15 temperature model.....83

Figure 5.1: Stratigraphic cross-section of the geologic model with isotherms.....88

Figure 5.2: AlOH absorption and methylene blue results plotted on MT profile.....90

Figure 5.3: MT and RockWorks15 temperature model plan maps at 50 m depth.....92

Figure 5.4: MT and RockWorks15 temperature model plan maps at 100 m depth.....93

Figure 5.5: MT and RockWorks15 temperature model plan maps at 200 m depth.....94

Figure 5.6: MT and RockWorks15 temperature model plan maps at 300 m depth.....97

Figure 5.7: Simple conceptual model cross-section utilizing the W-E Profile D of the MT survey.....102

Figure 5.8: 3D MT Profile 3 overlaid with lithostratigraphy.....103

Figure 5.9: USGS airborne electromagnetic resistivity survey of the Pilgrim River Valley surrounding the hot springs area 105

Figure 5.10: Interpreted basin cross-section of the Pilgrim River Valley 108

Figure 5.11: Location map of inferred transfer fault 111

Figure C.1: X-ray diffraction results of glycolated clay samples for well PS-12-1 130

Figure C.2: X-ray diffraction results of glycolated clay samples for well PS-12-2 131

Figure C.3: X-ray diffraction results of glycolated clay samples for well PS-12-3 132

List of Tables

Page

Table 3.1: Average porosity values for sediment size and sorting 39

Table 3.2: Grain diameter and intrinsic permeability by sediment type.....40

Table A.1: Mineral abundance for PS-12-1 125

Table A.2: Mineral abundance for PS-12-2.....125

Table A.3: Mineral abundance for PS-12-2 core.....126

Table A.4: Mineral abundance for PS-12-3.....126

Table B.1: Estimated smectite content per sediment sample for PS-12-1 127

Table B.2: Estimated smectite content per sediment sample for PS-12-2.....128

Table B.3: Estimated smectite content per sediment sample for PS-12-3.....129

List of Appendices

Page

Appendix A: Spectral assessment of mineral abundances.....125

Appendix B: Methylene blue (MeB) titration results 127

Appendix C: X-ray diffraction results of glycolated clay samples.....131

Acknowledgements

I am privileged to have experienced such a wonderful collection of people and organizations in my time at the University of Alaska Fairbanks. I would first like to thank my committee members Dr. Anupma Prakash, Dr. Christian Haselwimmer, Dr. Ronald Daanen, and Dr. Michael Whalen for their constant support and direction through the process of completing this thesis research. I would like to thank Gwen Holdmann and the rest of the Alaska Center for Energy and Power organization for the opportunities I have been able to enjoy ranging from fieldwork at Pilgrim Hot Springs, support during my research, and travel to Iceland and other places. I want to acknowledge Lesli Walls and Markus Mager for going well beyond their respective roles in the project to offer any help I needed as well. The funding agencies that allowed for me to participate in this project also deserve my gratitude: Department of Energy Geothermal Technologies Program (CID: DE-EE0002846) and the Alaska Energy Authority Renewable Energy Fund Round III. I want to thank all those involved in the project who have offered vast amounts of constructive advice including Bill Cumming, Dick Benoit, Art Clark, and Ralph Wilcox. I appreciate all of the help I received from other students who were involved in this project: Charles Parr and Zachary Woodbury. I'm also appreciative of the lab support given by Dr. Tom Trainor, Dr. Franta Majs, Susana Salazar Jaramillo, and the Advanced Instrumentation Lab at UAF. Finally, I want to acknowledge my appreciation for the support of my family, friends, and colleagues at the UAF Department of Geology and Geophysics, UAF Geophysical Institute, as well as other organizations including the Institute of the North and the Alaska Division of Geological and Geophysical Surveys.

Chapter 1: Introduction

1.1 Overview

1.1.1 General Introduction

Alaska is known for its richness in many resources such as oil, gas, and valuable ore deposits. One marginalized resource under renewed state-wide scrutiny is geothermal energy. Ultimately, the goal for exploration of geothermal resources is electric power production or direct use for the nearby communities. The geothermal system being evaluated for this research is Pilgrim Hot Springs located on the Seward Peninsula. The University of Alaska Fairbanks Geophysical Institute, Alaska Center for Energy and Power, Alaska Division of Geologic and Geophysical Surveys, and private contractors have mapped, drilled, and sampled the site over a period of 30 years.

Contributions of this research will provide a concise geologic assessment of the Pilgrim Hot Springs geothermal system helping to determine the viability of this resource. A conceptual model, the end result of this work, is needed to evaluate the potential for geothermal resource development by guiding future exploration of the system. Stratigraphy of the sediments and proximal structures will be shown through well log correlations. Subsurface conduits for geothermal fluid migration will be ascertained through temperature distributions, magnetotelluric (MT) and other geophysical survey maps, and stratigraphic correlations. Characterization of hydrothermal alteration in the collected samples and bedrock core will be fulfilled through multiple analytical methods. The final model will be the combination of a wide range of collected data and derived

data products which will also serve to complement and inform the numerical model for reservoir simulation and stimulation model scenarios.

1.1.2 Research Objectives

The hypothesis for this research is that Pilgrim Hot Springs can be an economically viable geothermal resource for both direct-use applications and electric power production. The desired outcome of the conceptual model is locating the deeper reservoir of hot fluids feeding the upflow from the bedrock through the synthesis of high-resolution MT survey maps, interpreted stratigraphy and structure, and temperature distributions. The conceptual model will also serve to direct the orientation and placement of proposed thermal conduits at depth. To test this hypothesis, several objectives have been proposed below:

- Describe sediment samples of five exploratory wells and estimate porosity and permeability.
- Correlate gamma ray and induction well logs to understand stratigraphic architecture.
- Assess the temperature distribution across the wells to model the mass transfer, thermal buoyancy, and transmissivity of upwelling hydrothermal fluids that interact with hydrologic barriers.
- Evaluate MT resistivity and other geophysical survey data to constrain the spatial extent of the geothermal system.

- Investigate the degree of hydrothermal alteration in clays to infer past hydrothermal activity at the site.
- Incorporate these data sets into a conceptual model of the geologic framework of the geothermal system.

1.1.3 Thesis Structure

The structure of this thesis research describes the construction, results, and interpretations of the conceptual model of the geologic framework of the Pilgrim Hot Springs geothermal system. The first chapter introduces the project and provides background information on geothermal systems and conceptual model development. Chapter two describes the geologic and physiographic setting of Pilgrim Hot Springs. The third chapter lists the data sets used in this research, along with methods used to derive data products as model inputs. The fourth chapter is the conceptualized geologic model that covers the development, inherent assumptions, limitations, and interpretations of the model. A discussion of marrying the data sets, sediment analysis results, and the conceptual model is provided in the fifth chapter. The final chapter emphasizes the principal findings of this research by reiterating the significance of the model results and also suggests future applications for this project.

1.2 Background

1.2.1 Geothermal Systems and Geothermal Energy

Glassley (2010) explains that geothermal energy and systems exist as interactions of heat escaping from the planet's interior to the outer crust. The heat, derived from early planetary formation and radioactive decay, can produce such features as hot springs, fumeroles, geysers, or sometimes no surface expression at all as in the case of blind geothermal systems. Total heat loss can be quantified for the entire Earth's surface and areas of elevated or anomalous heat flow may form a geothermal system. Different geologic settings contribute to the existence of geothermal systems. Regional extension of a continental plate thins the lithosphere resulting in a higher heat flow near the earth's surface. Intrusion of magmatic or plutonic bodies along fractures or fault systems conducive for the migration of heated fluids may also induce thermal springs. The energy of a geothermal system is transferred through conduction and convection processes. Conduction of heat occurs in low permeability settings such as a pluton or fine-grained sedimentary basin whereas convection cells are restricted to higher permeability pathways allowing for thermal buoyancy of geothermal fluids and significant thermal expansion which initiates hydrothermal systems (Glassley, 2010; Kolker et al., 2008). Several geologic settings conducive for low-high enthalpy geothermal systems exist within Alaska.

1.2.2 Alaska Geothermal Systems

Alaska contains abundant geothermal resources located in the Aleutian volcanic arc, south central Alaska, the southeastern Panhandle, and interior Alaska south of the Brooks Range. The Aleutian Islands have the greatest potential in Alaska for geothermal development as a result of Pacific plate subduction beneath North America (Swenson et al., 2012). The heat that fuels the hydrothermal activity is derived from magmatic bodies at depth generated through the melting of a subducting plate. Twelve hot springs have temperatures greater than 74°C, whereas only five springs of similar temperatures are located within mainland Alaska (Swenson et al., 2012). Several of these springs along the Aleutians produce surface discharge temperatures as high as 152°C and geothermometry estimates of reservoir temperatures up to 300°C (Swenson et al., 2012). Hot springs outside of the volcanic arc are typically low-moderate temperature systems with predicted reservoir temperatures of less than 150°C (Swenson et al., 2012). Kolker et al. (2008) concluded that within interior Alaska, with over 30 known hot springs, the principal sources of heat are proximal shallow high heat producing plutons, which was based on helium isotope studies. The regional tectonics resemble a backarc fault-block rotation in the eastern and central interior as suggested by Page et al. (1995) that provides the necessary fracturing for hydrothermal convection cells. However, the western interior/Seward Peninsula exhibits a different structural style related to the strongly transtensional tectonic regime (Biswas et al., 1986; Cross and Freymueller, 2008; Mackey et al., 1997; Ruppert, 2008). Geothermal systems associated with crustal extension are typified by deep convection cycles, circulating groundwater into and out of

the heat source along major normal fault systems that feed shallow reservoirs (Blackwell and Kelley, 1994; Kolker et al. 2008). Although the heat source remains elusive, a similar process is proposed for the Pilgrim Hot Springs geothermal system (Chittambakkam et al., 2013; Miller et al., 2013).

1.2.3 History of Exploration at Pilgrim Hot Springs

Pilgrim Hot Springs is located 96 km north of Nome, Alaska, and ~120 km south of the Arctic Circle in central Seward Peninsula. This region, principally the city of Nome, is in dire need of a low-cost, reliable alternative source of energy as opposed to costly imported diesel fuel. Also included in the energy demand are local mining operations. This geothermal anomaly has been known by the native community for centuries and locals have used the site since the early 20th century as a Catholic mission. Over the past 30 years, several exploration programs have been aimed at evaluating the site for its potential as an energy source.

There is a long history of exploration and assessment of the geothermal system at Pilgrim Hot Springs. Initially, the University of Alaska Fairbanks Geophysical Institute in cooperation with the Alaska Division of Geological and Geophysical Surveys provided a report to the U.S. Department of Energy on the geothermal energy potential of Pilgrim Hot Springs (Turner and Forbes, 1980). This work was completed in 1979 and involved mapping the regional surface and bedrock geology, geochemistry of the springs, possible radiogenic heat from nearby plutons, and geophysical surveys of the area. The map produced from the study indicated normal faulting along the Kigluaik Mountains to the

south as well as faults present across the basin evidenced by terraces and scarps in the adjacent hills. A radiogenic heat source was discounted after analyzing the mineralogy of the local intrusives and finding no elevated ratio of Th/U. Well testing of two 50 m wells, drilled during the 1979 exploration work, allowed estimates of permafrost depths to 100 m and established a local temperature gradient of up to 91 °C. Geochemical studies found the fluid composition to be alkali-chloride rich with dissolved carbon dioxide and hydrogen sulfide. Oxygen isotope and deuterium analysis suggested deep-seated water-rock reactions. The high-salinity and dissolved gases suggested a volcanic origin and a source temperature of ~130 °C. Geophysical surveys, resistivity and gravity, indicated a 1.5 km^2 reservoir and a downthrown block of basement to the southwest edge of the thawed ground bounded by intersecting faults at depth immediately below the springs. The recommendations from this study are complemented by exploration well data of the second phase of evaluation and are described below.

Early resource exploration, by the University of Alaska Fairbanks and Woodward Clyde Consultants, sought to determine the viability of Pilgrim Hot Springs as an energy resource (Woodward-Clyde, 1983). Initial temperature gradient wells were drilled in 1979, then resumed in 1982 with four wells of depths ranging from ~60-300 m. Drilling targets for the 1982 program were based on the earlier 1979 field work to demonstrate the extent of the resource. Wells were designed to provide detailed information on temperature variations and act as geothermal supply wells. The temperature gradients from the wells drilled from 1979-1983, coupled with soil-helium surveys, extrapolated the deeper reservoir to be 150°C at 1500 m depth. The total baseload energy that can be

derived from the hot springs was estimated at 1.5 MW based on a flow of 240 gpm at 90°C (Woodward-Clyde, 1983).

Recent exploration of Pilgrim Hot Springs is the product of collaboration between the Alaska Center for Energy and Power and the Geophysical Institute (University of Alaska Fairbanks). The project is testing the application of remote sensing using Forward Looking Infrared Radiometer (FLIR) to reduce the cost of preliminary geothermal exploration by quantifying geothermal surface heat losses. Five exploration slimhole wells were drilled (in addition to the existing six wells mentioned above) with two wells at ~150 m, two wells at ~300 m depth, and one at ~400 m. Over sixty shallow Geoprobe temperature gradient holes were drilled and both airborne and ground resistivity surveys at the site were also conducted. These data sets provide input to construct an improved conceptual model of the PHS geothermal system.

Chapter 2: Study Area

2.1 Pilgrim Hot Springs Location

Pilgrim Hot Springs is located on the Seward Peninsula in western Alaska, less than 200 km south of the Arctic Circle (Figure 2.1). The springs are within an alluvial basin in tundra underlain by discontinuous permafrost that is bounded by the glacially-eroded Kigluaik Mountains to the south and two prominent hills to the north, Marys Mountain and the Hen and Chicken Mountains. The basin is dissected by the east to west meandering Pilgrim River that borders the thawed ground of the springs, which occupies an ~1.5 km^2 area. The thawed ground is associated with anomalous vegetation that includes cottonwood trees, alders, grass, and various flowers. The site lies only a few meters above sea level and elevation changes are small.

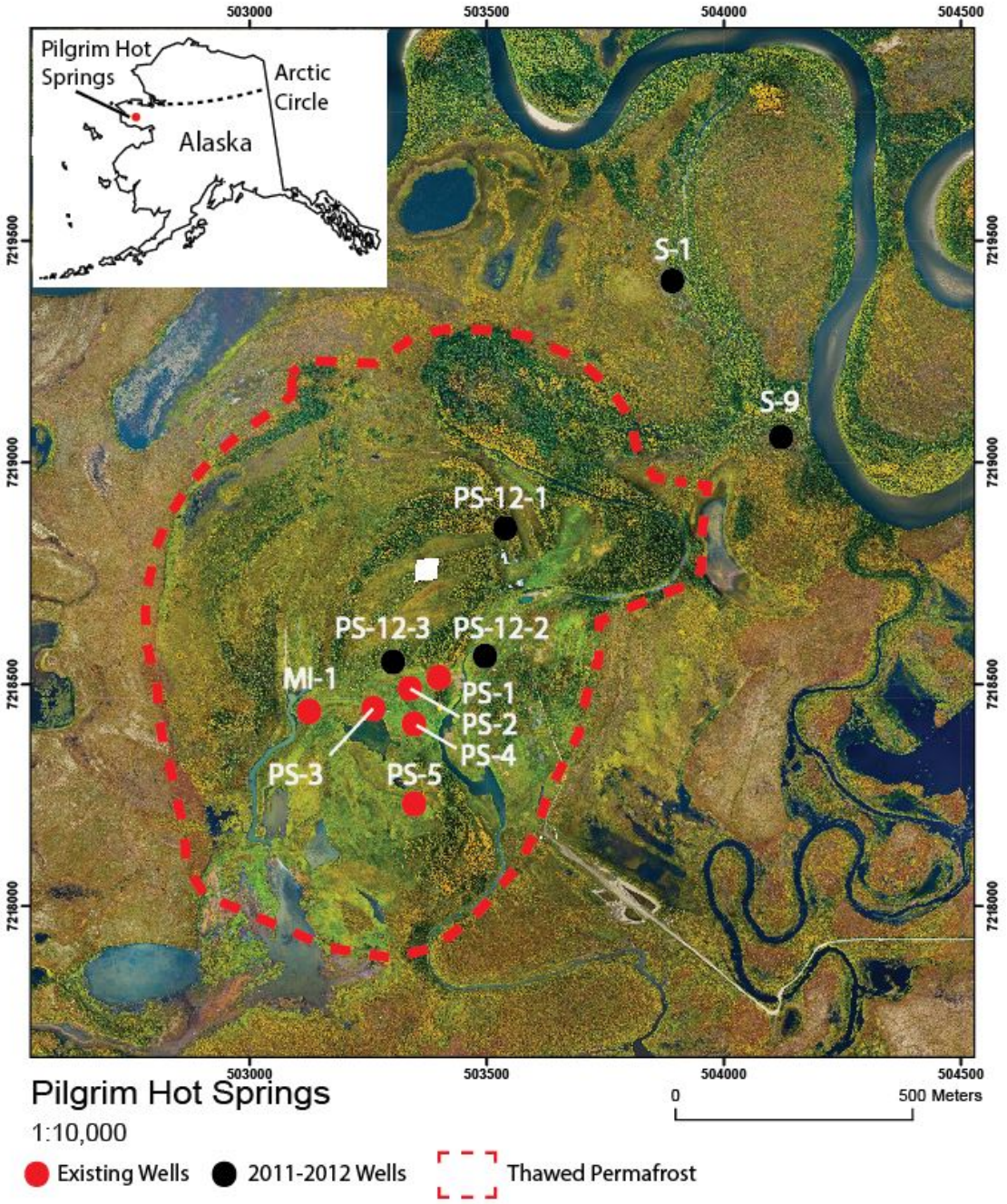


Figure 2.1: Pilgrim Hot Springs location map with wells. Map shows the distribution of wells, the boundary of discontinuous permafrost, and the extent of the thawed ground anomaly (Miller et al., 2013). Optical imagery modified from Haselwimmer et al. (2011).

2.2 Regional and Local Geology and Physiography

2.2.1 Overview of the Regional Geology of the Seward Peninsula

As summarized by Till and Dumoulin (1994), the Seward Peninsula is composed of two major geologic terranes: the older Seward terrane and the younger York terrane. Located in the central and eastern peninsula, the Seward terrane comprises Precambrian-early Paleozoic blueschist-, greenschist-, and amphibolite-facies schist and marble, and localized granitic intrusions. The York terrane is located in the western peninsula and along the Bering Straits and is comprised of Ordovician-late Cretaceous limestone, dolostone, phyllite, and local granite. The extent and contact of the terranes is marred by complex faulting, including the north-trending, east-vergent Koyuk-Kugruk fault zone in eastern Seward Peninsula, with possible thrusting between the terranes. Specifically, within the Seward terrane is the Nome Group, which contains a regionally extensive metamorphic stratigraphy of pelitic schist, interlayered marble and quartz-graphitic schist, a mafic schist, and impure chloritic schist. These units were exposed to high pressure-temperature blueschist metamorphism (~34-42 km burial) in the pre-Late Jurassic coeval with a similar event in the western Brooks Range. Greenschist metamorphism progressively overprints blueschist rocks to the south and also records a major deformational event that resulted in the north-south lineated isoclinal foliations of the Nome Group. This deformational event is related to Cretaceous magmatism, sharing a comagmatic history with plutonism throughout central Alaska and extending far into

eastern Siberia, represented by local Cretaceous granite and gneiss intrusives referred to as the Kigluaik Group.

The Kigluaik Mountains to the south of Pilgrim Hot Springs formed as a result of regional extension as an ascending intermediate mantle-derived magmatic diapir intruded and overprinted locally hot blueschist-facies rocks of the Nome Complex as indicated by a peripheral lack of quench textures (Amato et al., 1994; Amato et al., 2002; Amato et al., 2003; Amato et al., 2009; Amato and Miller, 2004). A granitic cap overlies the intermediate core of the pluton and is emplaced within metasedimentary rocks that grade from amphibolite to granulite facies toward the outer flanks of the mountain (Amato et al., 1994; Amato et al., 2003; Till et al., 2011). Ages obtained from U-Pb dating of zircons within the Kigluaik pluton reveal crystallization around 91 Ma (Amato et al., 1994; Amato et al., 2003; Till et al., 2011). The contact between the two groups is faulted (Till and Dumoulin, 1994). Alkalic and tholeiitc basalts from the Cenozoic basalt maar field in central and northern Seward Peninsula indicate recent volcanic activity (Beget et al., 1996; Turner and Swanson, 1981). The maar craters are the result of a particularly explosive combination of basalt eruption into overlying permafrost (Beget et al., 1996). The craters are dated to Pleistocene age and as young as 17500 years B.P. based on radiocarbon dating and tephrachronology (Beget et al., 1996).

The Kigluaik Mountains and surrounding exposures of bedrock have been subject to several intervals of Quaternary glaciation (Brigham-Grette, 2001; Calkin et al., 1998). A major advance of glaciation, the Nome River event, occurred between 580,000 and

280,000 yr ago and covered an area that stretched past Nome (Calkin et al., 1998). Several smaller advances have been noted for the Mid-Late Wisconsin glaciations and Holocene (Barclay et al., 2009; Calkin et al., 1998).

2.2.2 Seismicity of the Seward Peninsula

Seismicity and Holocene fault displacement across the Seward Peninsula is dominantly manifested by east-striking normal faulting with northwest-southeast extension, principally on the Kigluaik and Bendeleben faults (Biswas et al., 1986, Biswas and Tytgat, 1988; Cross and Freymueller, 2008; Finzel et al., 2011; Mackey et al., 1997; Page et al., 1991; Ruppert, 2008; Turner and Swanson, 1981). Seismicity across western Alaska appears diffuse and lacking any linear trends suggesting widespread movement across many active faults (Page et al., 1991). Semi-clustered activity of <2.0 M earthquakes around the Kilguaik fault occurs both north and south of the fault with uncertainty if the epicenters occur directly on the fault (Page et al., 1991). This region displays southeast-directed motion with a southwestern rotation into the Bering Sea (Cross and Freymueller, 2008; Finzel et al., 2011). The movement is attributed to the proposed Bering plate model (Cross and Freymueller, 2008). The Bering plate is defined as a clockwise-rotating, large rigid plate evidenced by GPS measurements and seismicity studies (Cross and Freymueller, 2008). The Bering plate appears to be rotating south-southwest relative to the North American plate along the eastern margin of the Bering Sea (Cross and Freymueller, 2008). The Bering plate is inferred to have a diffuse northern boundary cross-cutting the Seward Peninsula and is hinged on the Kigluaik and

Bendeleben faults (Cross and Freymueller, 2008; Fujita et al., 2002). This rotation could mark the boundary of the interpreted Bering plate. This could explain the continued extension in Seward Peninsula that extends as far inboard as the western Brooks Range (Finzel et al., 2011). Dumitru et al. (1995) proposed western Alaskan extension as accommodation for western movement of crustal fragments from interior and southern Alaska, although that is questioned by Finzel et al. (2011). A large mantle flow field or interacting microplates west of the Bering Sea may also impact ongoing western Alaska extension (Finzel et al., 2011). Regardless, continued southwestern rotation-induced tensional earthquakes coupled with Holocene offset of up to 10 m along faults in the region and the recent basaltic volcanism lends evidence to the proposed incipient rift model of Turner and Swanson (1981). Sampled alkali and tholeitic basalts from central and western Seward Peninsula reflect variable assimilation of ascending magma with country rock due to relatively rapid vertical movement common in back-arc environments (Turner and Swanson, 1981). Regional tectonic extension is evidenced by normal displacement along major faults in the Seward Peninsula. Combined with elevated heat flow throughout central Seward Peninsula, Turner and Swanson (1981) proposed a rift-related model for the sedimentary basins on the Seward Peninsula. The model is set in a back-arc extensional environment related to the Aleutian volcanic arc. This could explain the anomalous geothermal activity seen at Pilgrim Hot Springs.

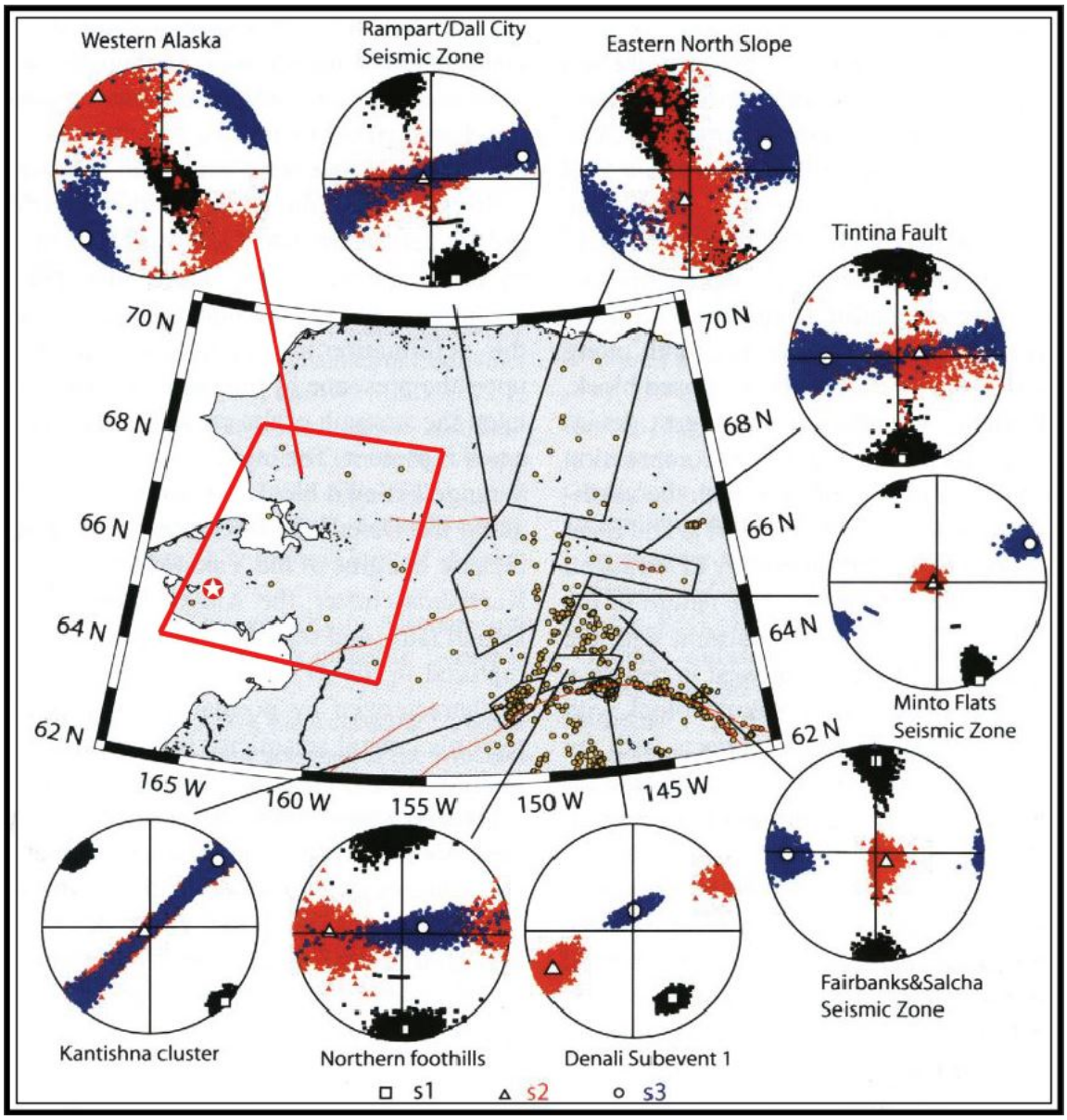


Figure 2.2: Seismicity map of central and western Alaska. Sigma 1, 2, and 3 are shown by color and symbols for the averaged sigma orientation (Ruppert, 2008). The location of Pilgrim Hot Springs is marked by the star.

2.2.3 Surficial and Bedrock Geology of the Pilgrim River Valley

Pilgrim Hot Springs is located in the middle of a graben valley with alluvial-fill derived from the glacially-eroded Kigluaik Mountains immediately to the south (Till et al., 2011; Turner et al., 1979). The surface expression of bedrock is only apparent in the nearby mountains (Figure 2.3). The composition of the basement block underlying the springs is described as Late Proterozoic-Early Paleozoic amphibolite to granulite facies metamorphic rock (Till et al., 2011; Turner et al., 1979). Only a few kilometers to the north lie Marys Mountain and the Hen and Chicken Mountains that are mainly composed of Late Proterozoic metasedimentary and metagranitic units intruded by undifferentiated Cretaceous granite present in both (Till et al., 2011). The older units are the same Late Proterozoic units exposed in the Kigluaik Mountains (Amato and Miller, 1994). The Kigluaik range-front fault at the northern base of the Kigluaik Mountains has an en echelon-style step over along the fault line and was previously mapped as a normal fault in a strongly extensional setting (Ruppert, 2008; Turner and Forbes, 1980). Abrupt truncation at the upper reaches of glacial moraines and outwash gravels approximately along the Kigluaik fault indicates recent movement (Turner and Forbes, 1980). A wide alluvial apron extends a couple of kilometers from the mountains where the Pilgrim River has reworked the valley floor leaving behind a visual trace of past channels and floodplains (Figure 2.3). Throughout the valley, the tundra is underlain by discontinuous permafrost with surface permafrost-related features such as thermokarst lakes, frost-heaves, and pingos (Turner et al., 1979). Pilgrim Hot Springs is located in the middle of the valley containing a variety of vegetation including cottonwood trees, wild flowers,

grassy fields, and farmed rhubarb, atypical for a predominantly tundra region. This vegetation aids in delineating the edges of the geothermal anomaly at the site by providing a clear and distinct boundary from forest to tundra. Thawed or absent near-surface permafrost and early snow-melt patterns also distinguish the areas of elevated heat flow and shallow subsurface hydrothermal upflow that feed the hot springs (Daanen et al., 2012; Haselwimmer et al., 2011). The thawed ground feature of the hot springs is only one aspect of the underlying geothermal system. A wide range of data is presented in the next chapter that provides a greater understanding of the nature of the Pilgrim Hot Springs geothermal system.

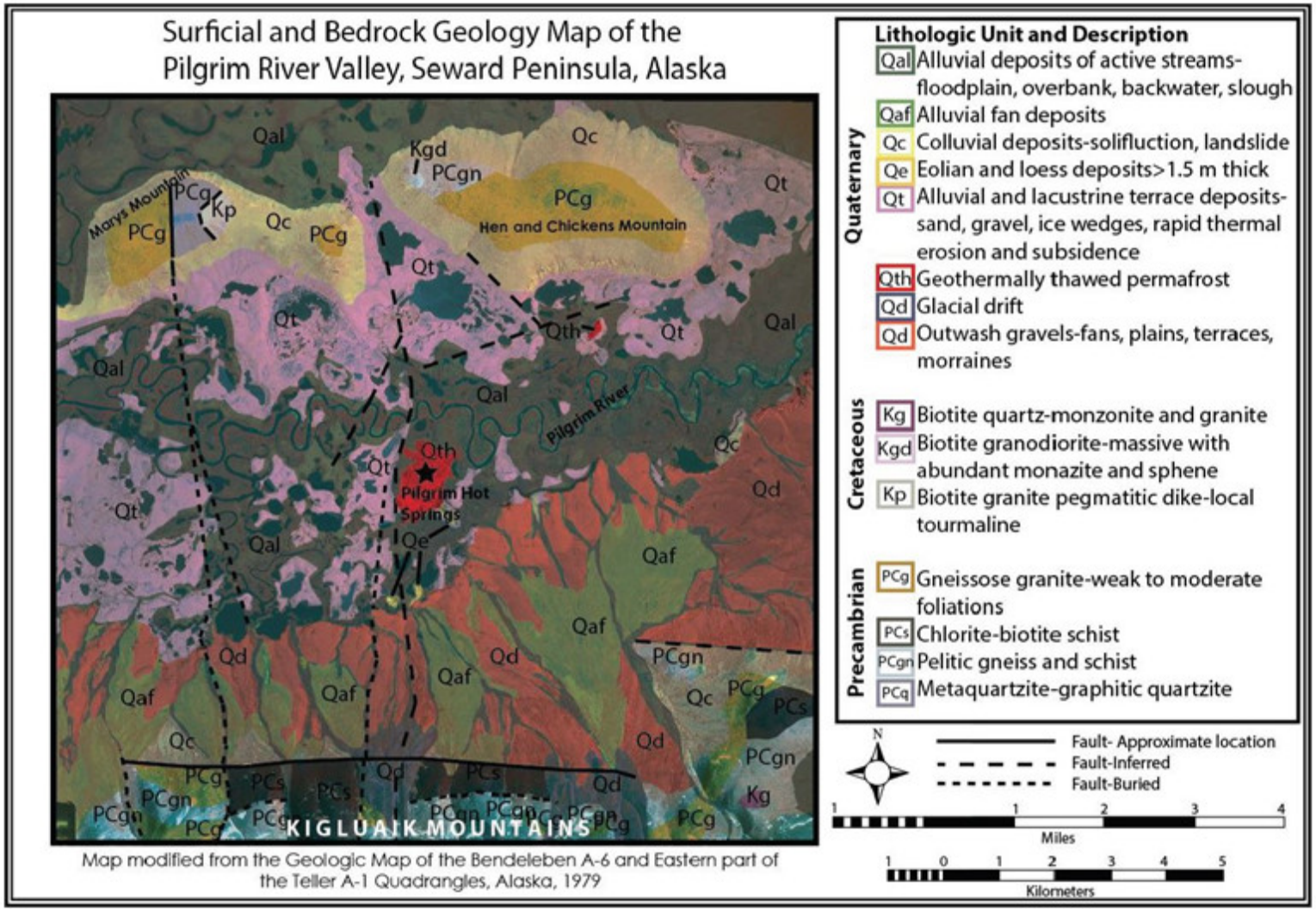


Figure 2.3: Surficial and bedrock geology map of the Pilgrim River Valley. Modified from Turner et al. (1979).

Chapter 3: Data and Data Products

A range of different data sets were collected and measured at Pilgrim Hot Springs from June to September 2012. The gathered data consist of rock samples, geophysical surveys, well cuttings descriptions, and geophysical and temperature logs. These are used to frame the model by determining the stratigraphic architecture, permeability, and hydrothermal fluid upflow and outflow pathways. Subsequent analysis of sediments was conducted through multiple analytical procedures: reflectance spectroscopy, methylene blue titration, x-ray diffraction, and thin-section characterization of rock samples and drill core. An array of analytical techniques is used to assess the degree of past hydrothermal alteration in the sediments and bedrock.

3.1 Field Data

3.1.1 Rock Sample Collection

Several rock samples were collected to study the range of lithologies exposed in the proximity of Pilgrim Hot Springs (Figure 3.1). The Kigluaik Mountain samples consist of mica schist to phyllite with locally abundant garnets and gneissose granites. Hen and Chicken has similar gneissose granite exposures. A pegmatitic dike outcrop northeast of the hot springs contains quartz, k-spar, fine-grained micas, and abundant, well-developed black tourmaline. A calcareous schist/impure marble adjacent to the pegmatitic dike was also sampled as it is seldom exposed in the immediate basin area.

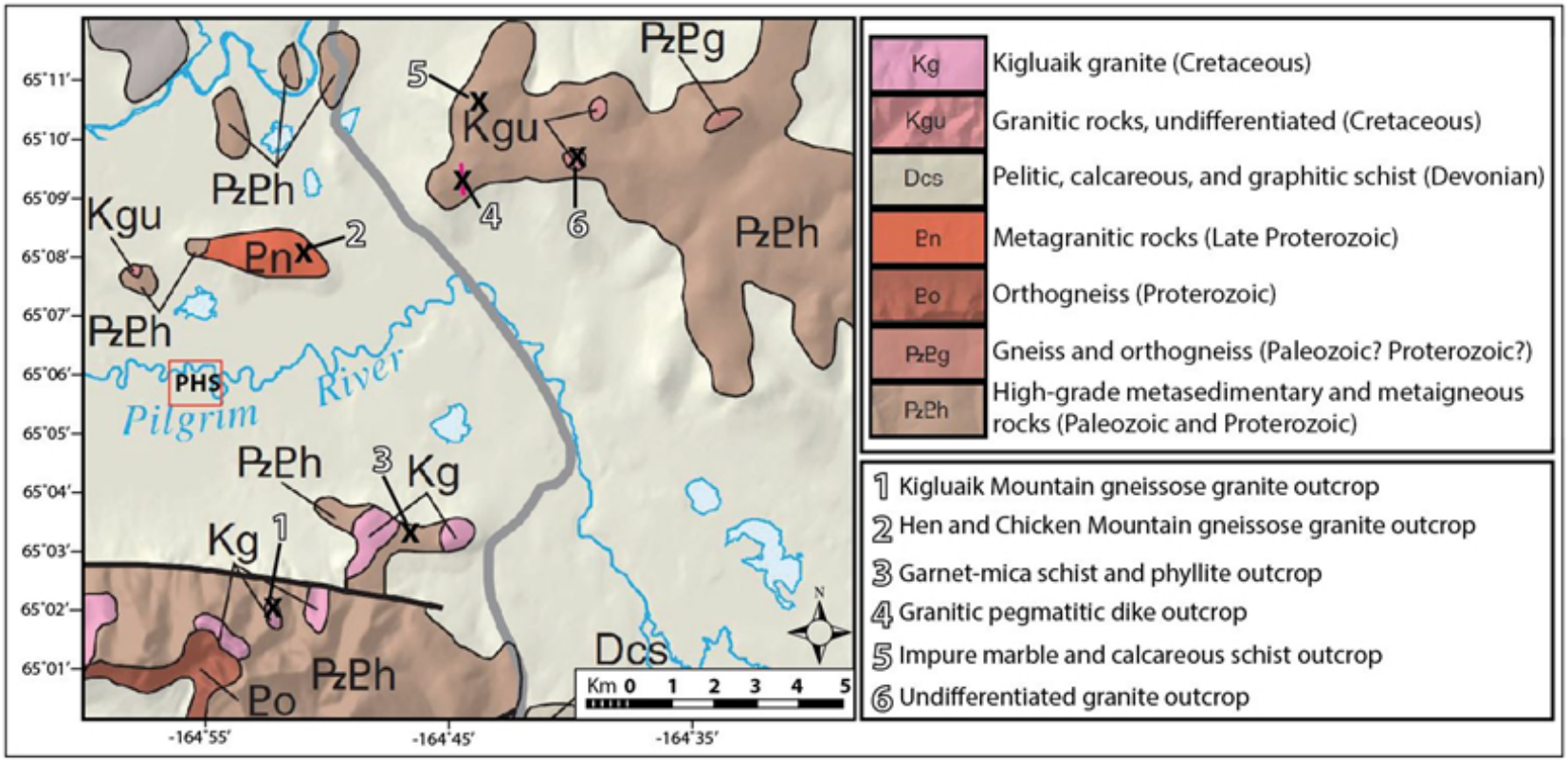


Figure 3.1: Place map of the rock sample collection sites. Outcrops are labeled by numbers and located on the geologic map to the left. Modified from Till et al. (2011).

3.2 Geophysical Data

The geophysical resistivity studies provide detailed information on the different types of sediment, fluid compositions, and conductive structures at depth in the basin. The contrast of resistivity and conductivity is associated with certain geologic materials (Figure 3.2) (Palacky, 1988). Unconsolidated glacial sediments, the most common sediment type in the basin, show a low resistivity value of ~10 ohm-m for clays and trending higher for gravels and sand. Saline fluids yield a very low resistivity (high conductivity) at <1 ohm-m and fresher fluids have a higher resistivity at >1-100 ohm-m. This is an important distinction where the resistivity surveys show areas of low resistivity associated with outflow of geothermal fluids with more dissolved constituents. At Pilgrim, the low resistivity of the hot springs are in marked contrast to a highly resistive boundary of permafrost at 1,000-100,000 ohm-m which conveniently isolates the extent of the geothermal system near the surface.

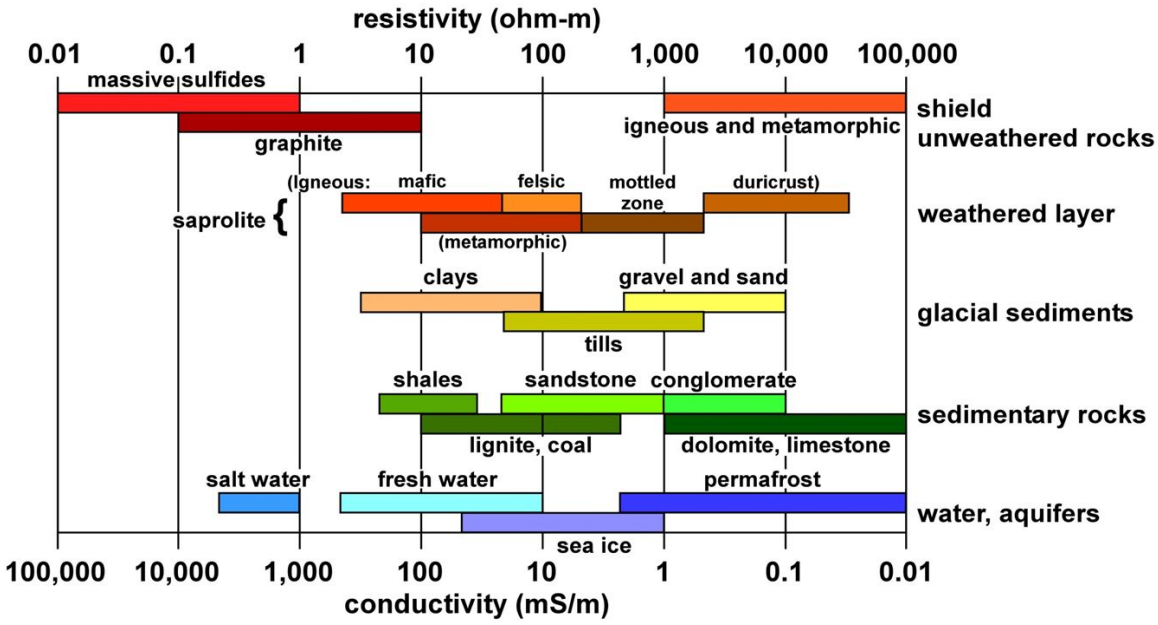


Figure 3.2: Logarithmic scale of resistivity values for geologic materials. Resistivity (ohm-m) and conductivity (mS/m) values are plotted for a range of sediments, rock types, and fluid compositions (Palacky, 1988).

3.2.1 USGS Aeromagnetic and Electromagnetic (EM) Survey

An aeromagnetic and electromagnetic survey was conducted over Pilgrim Hot Springs by FUGRO with funding support from the USGS and the Alaska Center for Energy and Power in the spring of 2011 (McPhee and Glen, 2012). The survey was conducted with a FUGRO-Resolve system flown by helicopter with a frequency range between 400 Hz and 140 kHz. A Cesium vapor magnetometer was used with a sample rate of 10 Hz and sensitivity of 0.01 nT. This survey includes diurnal corrections, differential GPS positions, 0.2-0.4 km spacing, and was acquired by helicopter at 60 m altitude. The helicopter towed a large induction coil that generated a magnetic field and measured the changes in resistivity from the ground below. Processing of the data was completed by the USGS and described in more detail in the Pilgrim Hot Springs Phase 1 Report (University of Alaska, 2012).

A differential resistivity map at 20 m depth produced by the USGS electromagnetic resistivity survey is provided below in Figure 3.4. The survey area spans the Pilgrim River valley between the Kigluaik Mountains and the hills to the north. Pilgrim Hot Springs is located in the center of the map that shows a low resistivity anomaly emanating from the site and extending north-northeast. Highly resistive zones correlate to more commonly resistive materials such as the exposed igneous and metamorphic bedrock as well as the discontinuous permafrost. The more conductive/low resistive zones outside of the hot springs site could be the result of conductive clay

formation through diagenetic processes independent of the geothermal system or conductive structures at depth connected to geothermal fluid outflow.

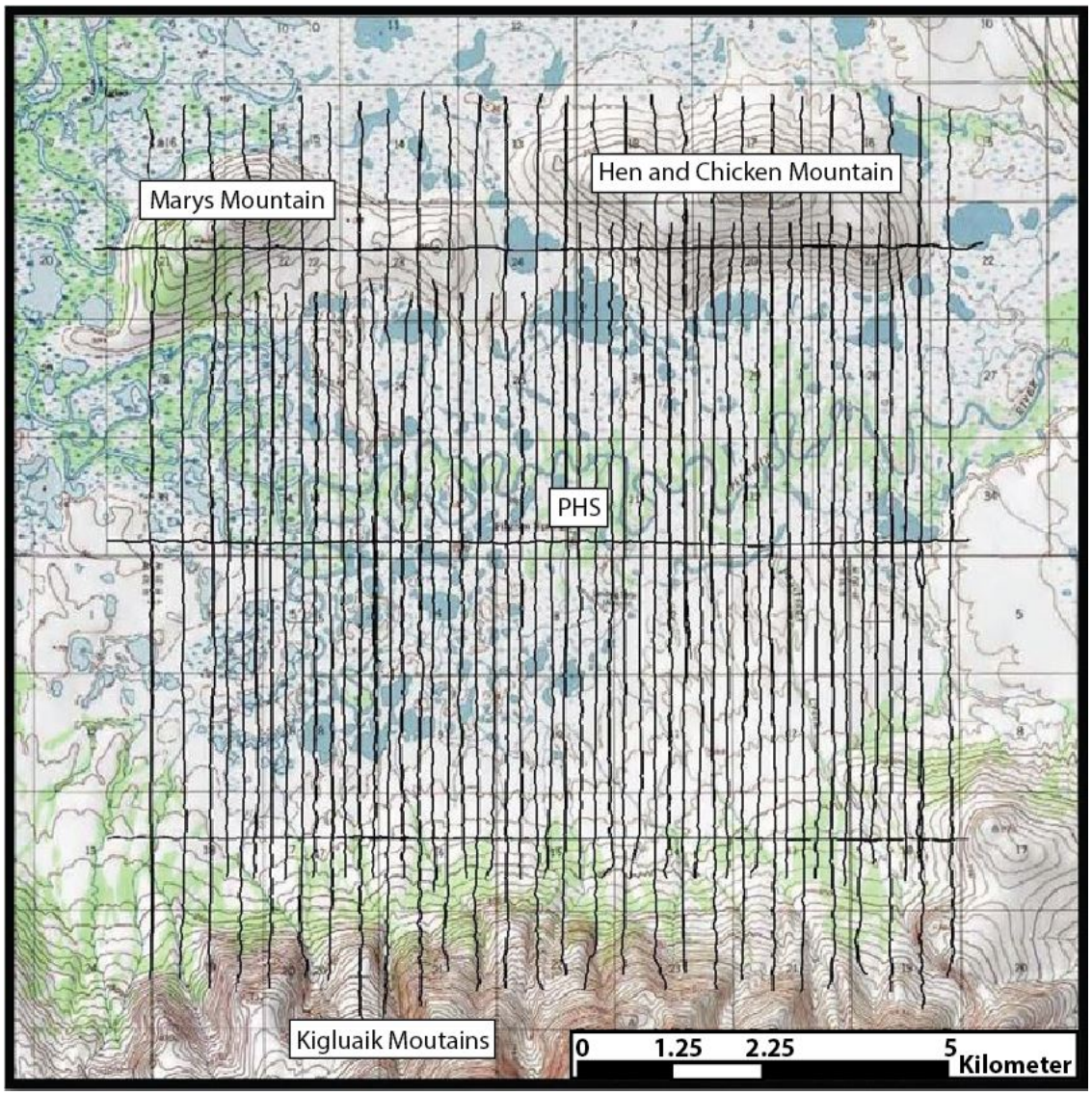


Figure 3.3: Flight path for aeromagnetic and electromagnetic survey (McPhee and Glen, 2012).

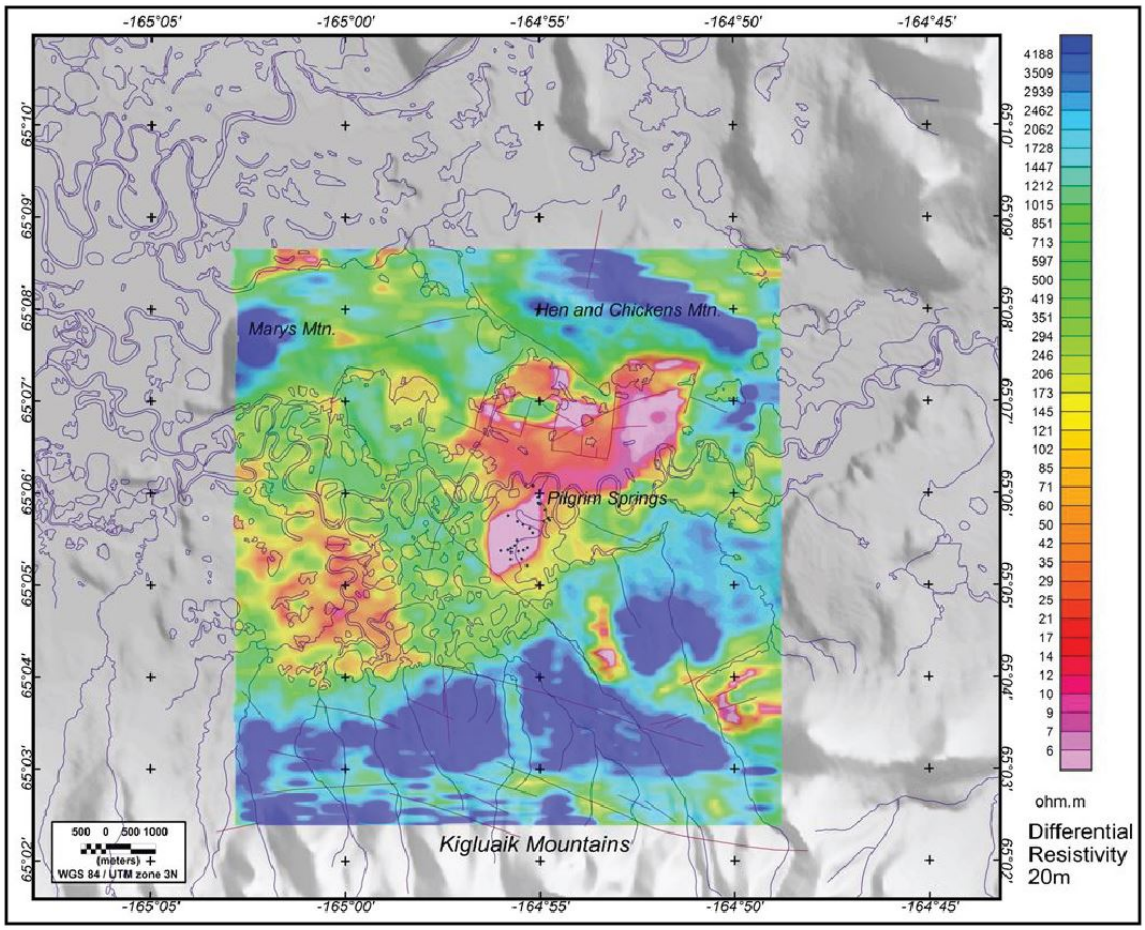


Figure 3.4: Differential resistivity map at 20 m depth. Produced by the USGS airborne electromagnetic resistivity survey (McPhee and Glen, 2012).

3.2.2 Magnetotelluric (MT) Resistivity Survey

The locations of the MT stations at Pilgrim Hot Springs were determined by maximum spacing for best resolution and constrained by accessibility. In total, 59 stations recorded at 0.001-10000 Hz range overnight with an average distance of 100 m apart with a remote station 5 km SE from the site (Figure 3.5). Data processing and recording equipment was provided by FUGRO Electric Magnetics Italy Srl. MT evaluation of the site provides insight into the changes in resistivity (decreasing resistivity is casually referred to as increasing conductivity in this discussion) to elucidate the geologic caps and plumbing of the reservoir. MT is a deeply focused electromagnetic method that measures the wide -range of surface recordings of natural fluctuations in the earth's magnetic and electric fields. This is recorded for both period and location beneath 24-hour recording stations emitting an induced current at different orders of magnitude (FUGRO, 2012). The relationship between the electric and magnetic field variations produces an impedance tensor that normalizes the observed electric resistivity in order to determine the distribution of resistivity at depth (Heise et al., 2007).

MT resistivity survey data highlights the spatial extent of the geothermal system. The dynamics of high conductivity, or inversely low resistivity, in outflowing and upflowing geothermal fluids, proximity to the heat source, and stratigraphic architecture of the hydrothermally altered swelling clays can be inferred from MT data (Cumming, 2009). Three 1D smoothed inversion profiles down to 1000 m that show resistivity variations with depth are present (Figures 3.6-3.8). A lack of station coverage over a

section of the profile results in poor or no resolution at depth as apparent in the profile lines as bank spaces. Figure 3.5 is a location map of the station coverage with the profile lines plotted. MT Profile D (Figure 3.6) shows a large, very low resistivity pattern (<1 ohm-m) from 150 m to 400 m that extends into the top of the basement at 320 m and is sharply bounded by increasingly resistive zones on the west (left) and east (right). A very thin, flat-lying conductive zone near the subsurface is also apparent in the profile. Areas of high resistivity values are interpreted as permafrost (0-100 m) and cold regional groundwater influx. The same low resistivity body is seen in Profile C (Figure 3.7) in the vicinity of PS-12-2 where it intersects the sharp highly resistive boundary to the southeast. Profile 2 (Figure 3.8) shows the low resistivity body dissipating to the northeast where it becomes less distinct. Well S-1, a relatively cold well, appears to have been drilled into the more resistive zone.

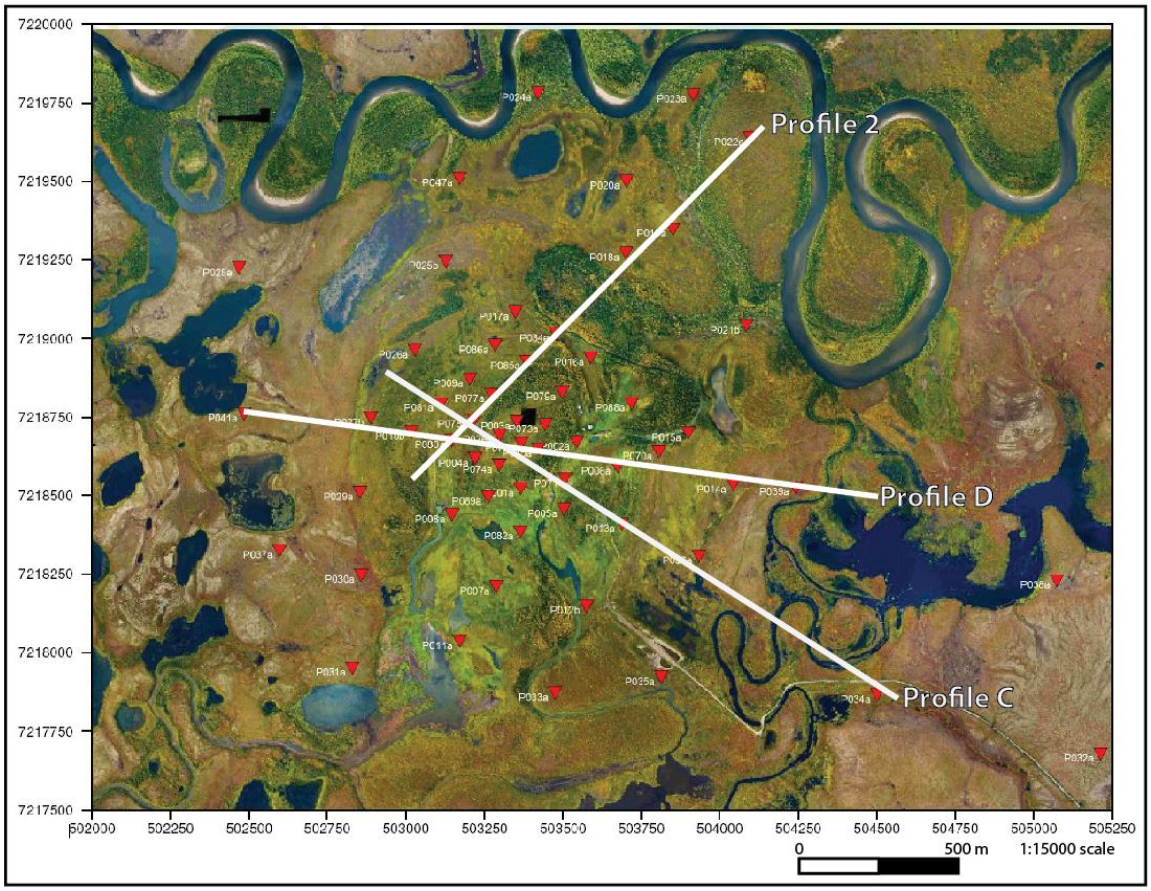


Figure 3.5: Locations of magnetotelluric resistivity recording stations (FUGRO, 2012).

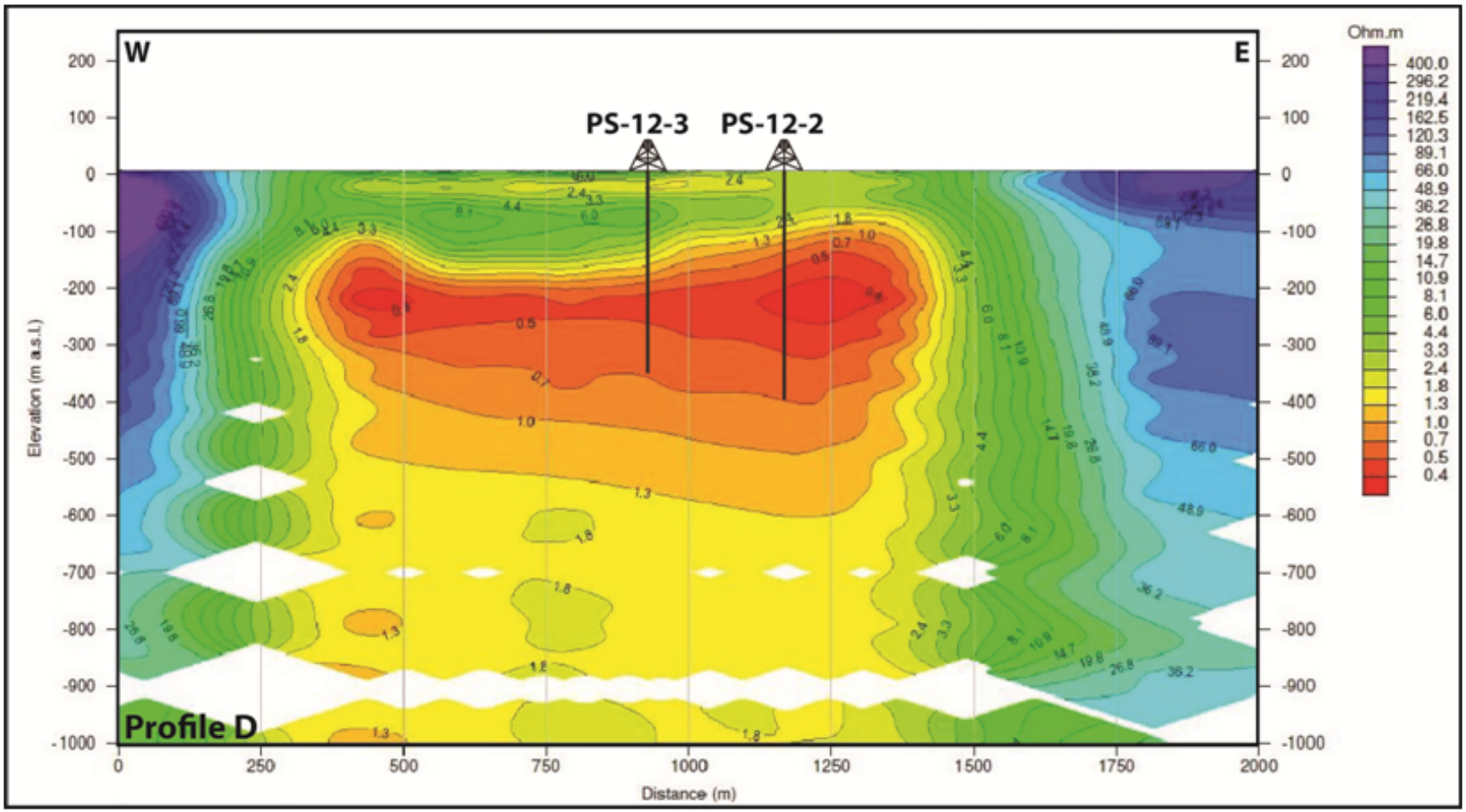


Figure 3.6: Magnetotelluric resistivity profile line D. Cross-section line is from the smoothed 1D MT inversion (FUGRO, 2012). The line is oriented west to east.

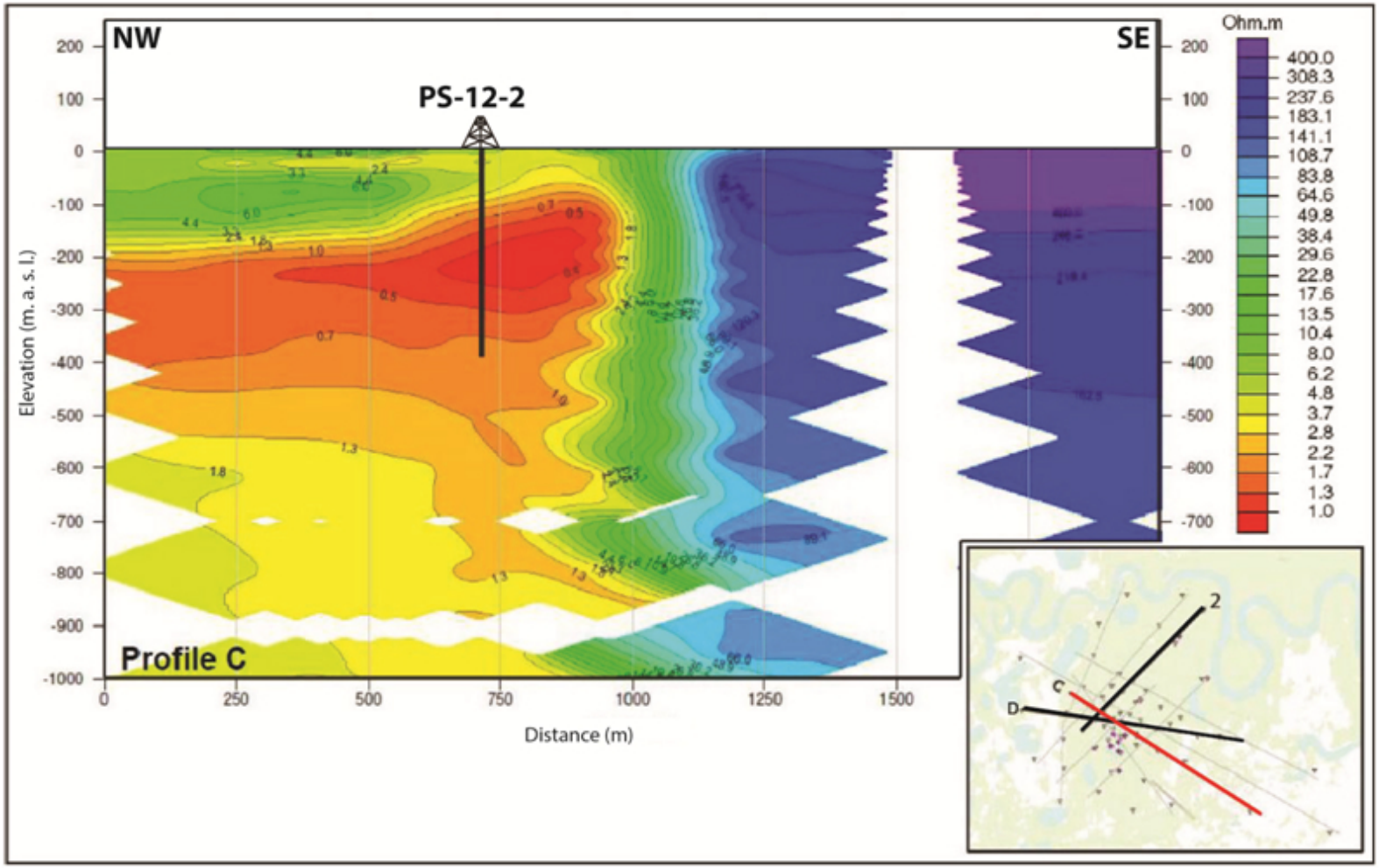


Figure 3.7: Magnetotelluric resistivity profile line C. Cross-section line is from the smoothed 1D MT inversion (FUGRO, 2012). The line is oriented northwest to southeast.

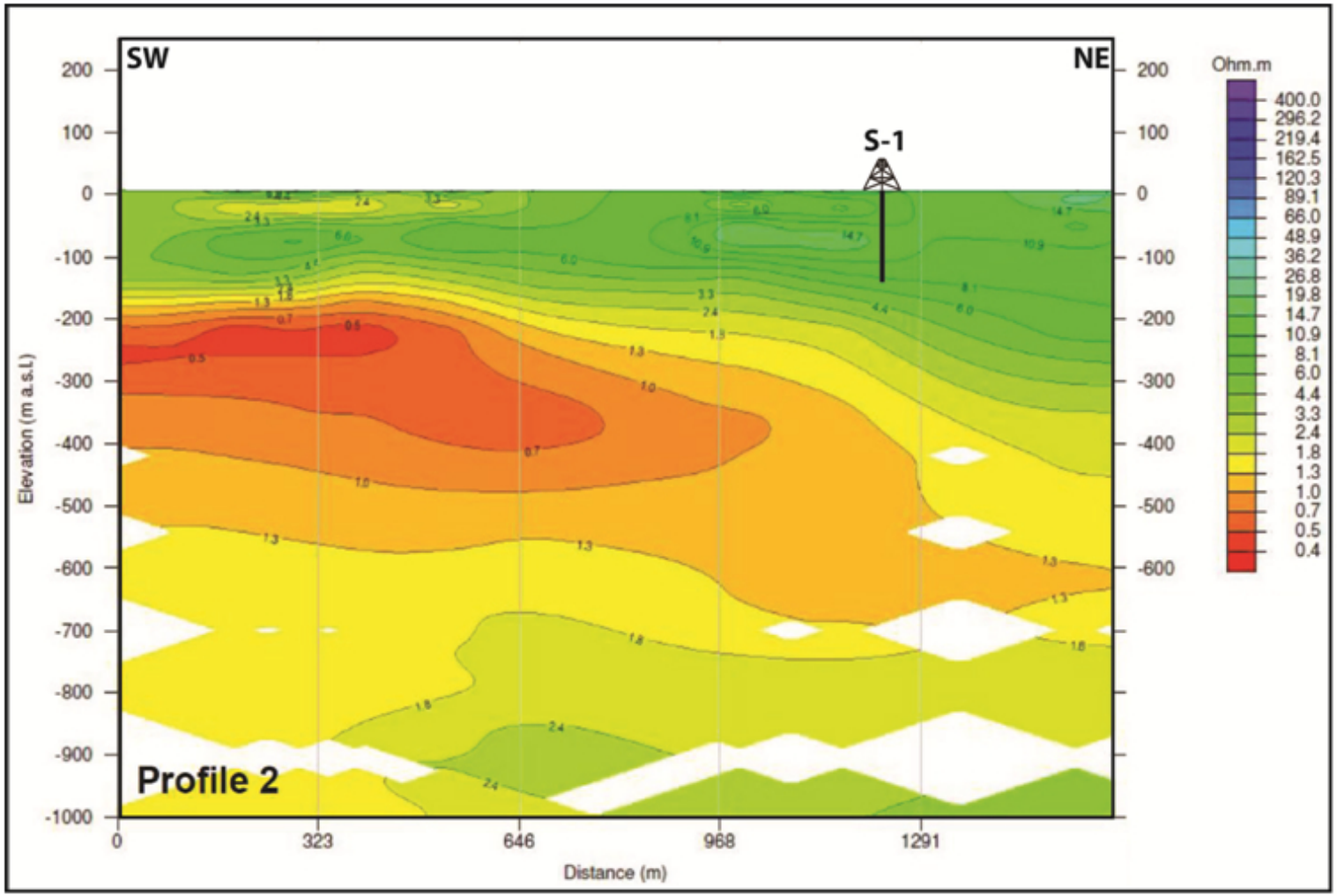


Figure 3.8: Magnetotelluric resistivity profile line 2. Cross-section line is from the smoothed 1D MT inversion (FUGRO, 2012). The line is oriented southwest to northeast.

3.2.3 Ground-based Gravity Survey

A ground-based isostatic gravity survey was conducted by the USGS Menlo Park team headed by Jonathan Glen in spring of 2010. Two teams ran several profile lines across the Pilgrim River valley. Each gravity meter station base was placed at a known elevation along the profile line. The field gravity readings were normalized to several base station gravity meters located at the site, the nearby camp, in the Nome Post Office and airport, as well as in Anchorage at the University of Alaska Anchorage and airport. By normalizing to gravity stations at known elevation points, topography can be extracted from the gravity meter readings and produce a map of changing elevation and basin depth.

Figure 3.9 shows the gravity survey lines and station locations with initial gravity readings. In general, the figure shows the shallow bedrock surface depth under much of the alluvial fan and glacial outwash deposits along the base of the Kigluaik Mountains and to the east and north of the hot springs. The blue color indicates the deeper basin appears to terminate beneath the hot springs and deepen to the southwest (Figure 3.10).

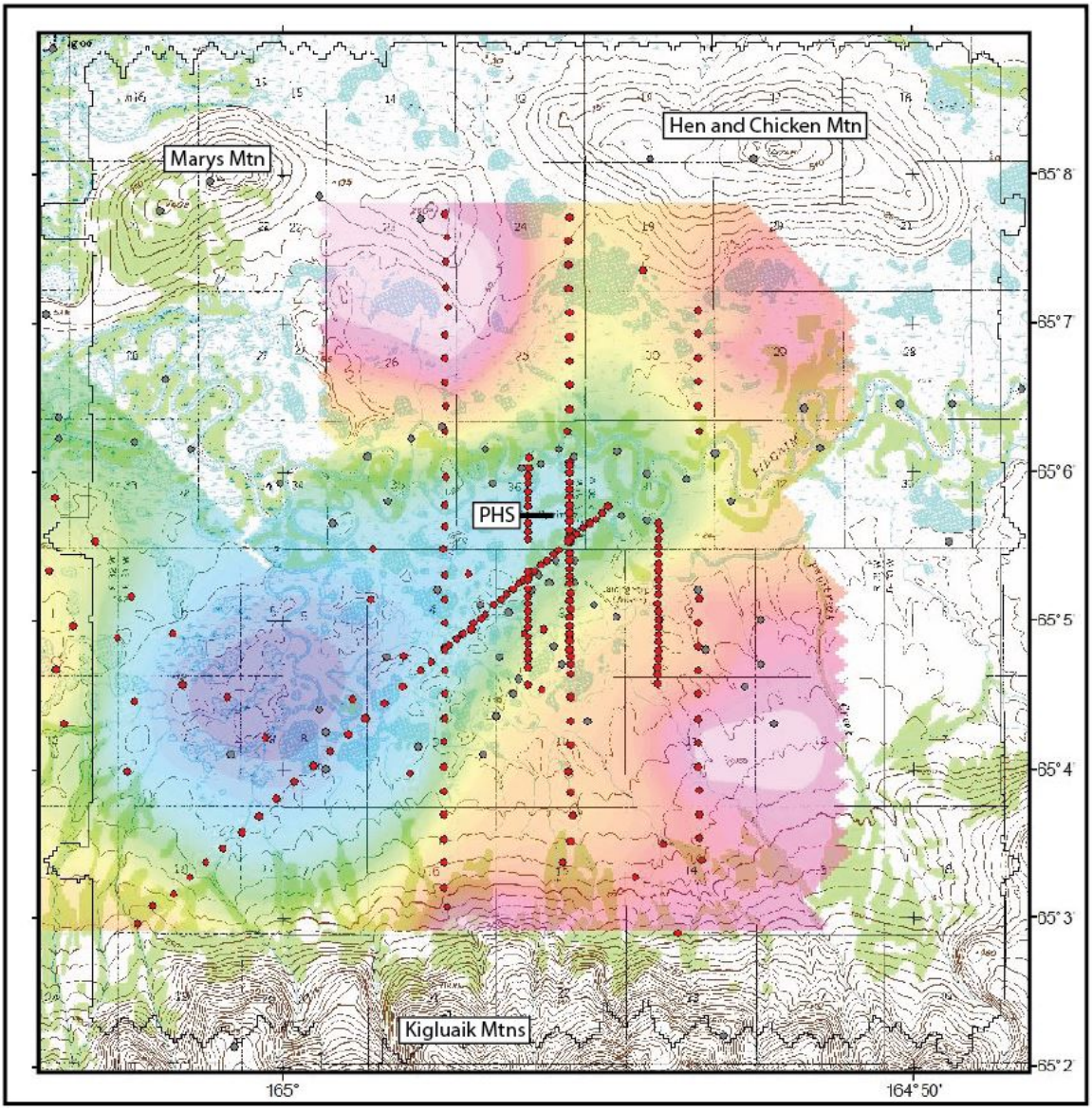


Figure 3.9: Isostatic gravity survey station location map. Map provided by Jonathan Glen. Warmer colors (orange and red) indicate above sea level, green equates to sea level, and cooler colors (blue and violet) are below sea level. In this case, light blue (immediately below Pilgrim) correlates to a basin depth to basement at 320 m (corroborated with drilling contact). The deeper basin indicated by the dark blue and violet colors, is estimated to be twice as deep as below Pilgrim to ~700 m depth (Jonathan Glen, personal communication).

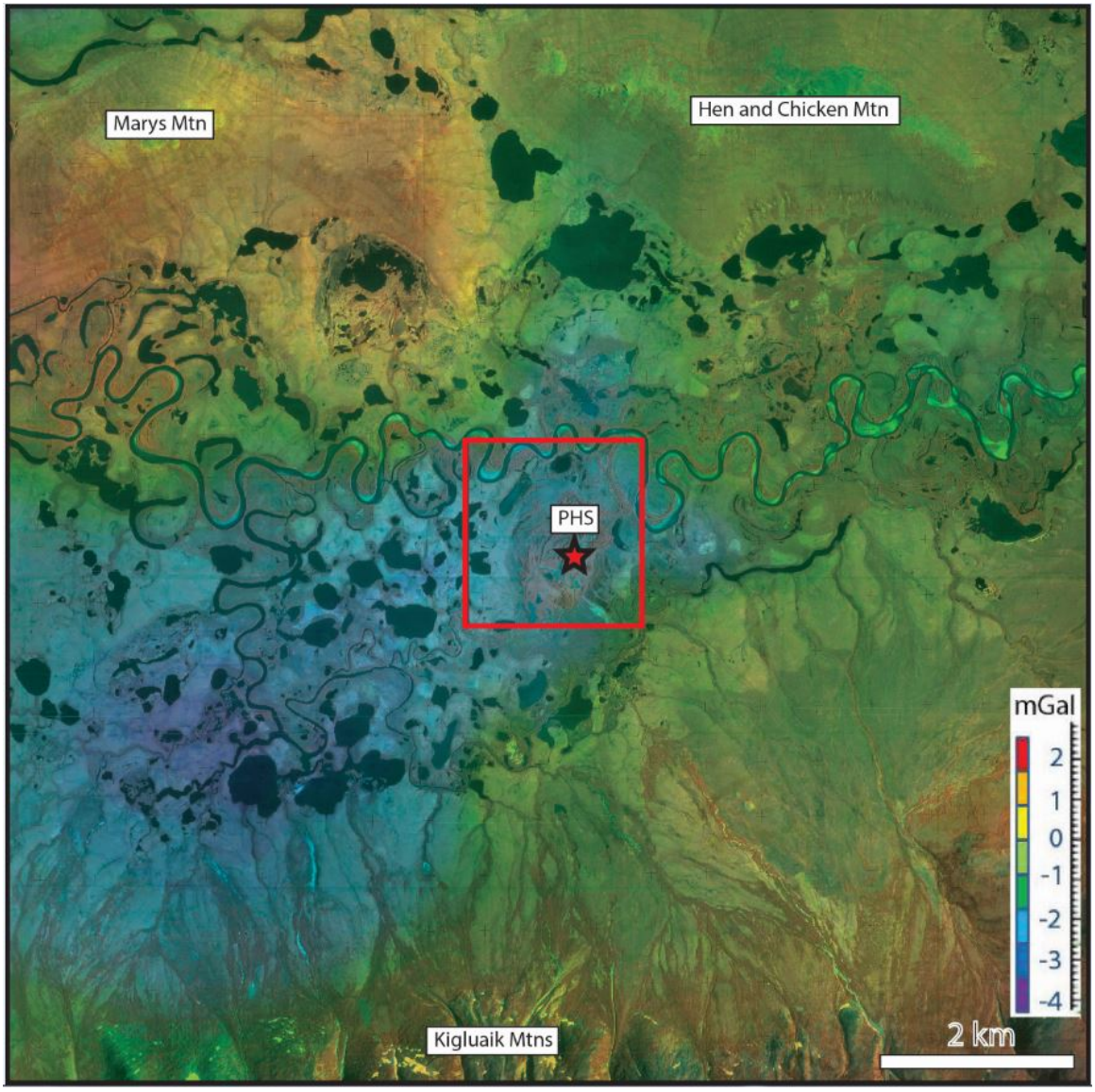


Figure 3.10: Isostatic gravity anomaly map of the Pilgrim River Valley. Overlaid by an Alaska High-Altitude Photography (AHAP) image of the Pilgrim River valley. Isostatic gravity anomaly map provided by Jonathan Glen, USGS Menlo Park. The red box around Pilgrim Hot Springs marks the edge of the conceptual model boundaries that encompasses the extent of the observed thermal anomaly at the surface.

3.3 Geoprobe Data

The Geoprobe, operated by the USGS Central Region Research Drilling Team and the Alaska Center for Energy and Power, is a small drilling track vehicle that uses the direct push method of hammering pipe to shallow depths via a small hydraulic system. This unit was used to conduct a shallow temperature survey with 64 holes of 10-60 m depths that covered the hot springs site as well as several holes in the surrounding tundra, some intercepting permafrost (Figure 3.11). The Geoprobe holes outside of the thermal expression provide a background temperature gradient that is not enhanced by the heat flux of the geothermal system. This wealth of data provides extensive coverage of temperature variations at the surface and in the shallow reservoir that complements the data obtained from the deeper drilling.



Figure 3.11: Well and Geoprobe hole location map. All Geoprobe holes drilled on site (red dots) with several of the deeper wells plotted (black dots). Image credits, Christian Haselwimmer.

3.4 Drilling Data

3.4.1 Sediment Characterization

Sediments obtained through sieve tables from reverse circulating mud while drilling were described and characterized to quantify the porosity and permeability of the sampled depth intervals. The descriptions of the sediments include grain size, shape, sorting, and mineralogy. These are critical input parameters for defining the lithostratigraphy of each drilling interval, making the construction of lithologic well logs and stratigraphic correlations possible. Also derived from this data is the calculation of the porosity and permeability of the sediments.

The permeability of a porous medium, k, is its natural ability to transmit fluids through interconnected pores. The unit of measurement for permeability, defined as m^2, is Darcy ($D=9.86923*10^{-23}$ m^2) (Bundschuh and Suarez Arriaga, 2010; Fitts, 2005). Permeability can be divided into four distinct types: permeability related to the intergranular spaces of the porous medium, micropermeability associated with interconnected microfractures, permeability related to nets of fractures, and macropermeability of open faults (Bundschuh and Suarez Arriaga, 2010; Fitts, 2005). The volume of intergranular space in the sediments is the focus of this assessment. Permeability also accounts for the fluid dynamic viscosity and pressure gradient of the aquifer (Bundschuh and Suarez Arriaga, 2010). However, without these fluid parameters, the intrinsic permeability can be estimated from sediment measurements.

To properly quantify intrinsic permeability, the sediment grain diameter, distribution, and porosity are calculated. Grain diameters of the clay to gravel-sized sediments are measured by grain size card. The distribution of the grain diameters for every given sample interval (~3 m of drilling depth) are also recorded through visual determination. For every sampled interval, a percent is given for clays through gravel adding to 100%. This allows for an average grain diameter to be estimated for that interval by multiplying the percent of each grain diameter by the representative diameter and summing the results for an average diameter for the interval. Porosity values are obtained from the table of average porosity values for unconsolidated sediments (Table 3.1). Beard and Weyl (1973) obtained porosities of the range of poorly to well-sorted sediments. The average porosity of each sorting parameter is multiplied by the average grain diameter for intrinsic permeability (Shepherd, 1989).

Bear (1972) showed distributions of various sediment types by plotting particle diameter versus percent clay finer by weight (Figure 3.12). Percent finer by weight plots the distribution of coarse to fine grains in a given mix of sediments by percent. Gravelly sand to common clay minerals (montmorillonite and kaolinite) also appear in the examined sediments of Pilgrim Hot Springs (Table 3.2). The particle diameters of the range of sediment types for the Pilgrim samples match closely to the diameters reported by Bear (1972) (Figure 3.12).

Table 3.1: Average porosity values for sediment size and sorting. Average porosity values are for very well to very poorly sorted, coarse to fine sands. The shaded section represents the values used in the intrinsic permeability calculations for the Pilgrim Hot Springs drill cuttings. Modified from Beard and Weyl (1973).

Size	**Coarse**		**Medium**		**Fine**		**Very Fine**		**AVG Porosity**	**Std. Dev. (%)**
Sorting	Upper	Lower	Upper	Lower	Upper	Lower	Upper	Lower		
V. Well	40.8	41.5	40.2	40.2	39.8	40.8	41.2	41.8	40.8	0.6
Well	38	38.4	38.1	38.8	39.1	39.7	40.2	39.8	39	0.8
Moderate	32.4	33.3	34.2	34.9	33.9	34.3	35.6	33.1	34	1
Poor	27.1	29.8	31.5	31.3	30.4	31	30.5	34.2	30.7	1.8
V. Poor	28.6	25.2	25.8	23.4	28.5	29	30.1	32.6	27.9	2.8
AVG Porosity	35	35.2	35.3	35	35.5	36.4	36.7	37.4		
Std. Dev. (%)	6	6.3	5.5	6.2	4.9	5.3	5	4.2		

Table 3.2: Grain diameter and intrinsic permeability by sediment type. Representative grain diameters (d) in mm and intrinsic permeability (mm^2) for sampled intervals in wells PS-12-1, PS-12-2, and PS-12-3. The samples are organized with gravel as the highest permeability to clay with the lowest. Listed representative diameters are the commonly accepted diameters of these sediment types.

Sediment Type	Diameter (mm)	Intrinsic Permeability (mm^2)
Gravel	2	2E+00
Very Coarse Sand	1.2	6E-01
Coarse Sand	0.6	1E-01
Medium Sand	0.3	4E-02
Fine Sand	0.08	3E-03
Silt	0.03	4E-04
Clay	0.002	2E-06
Indurated Sand	0.1	4E-03

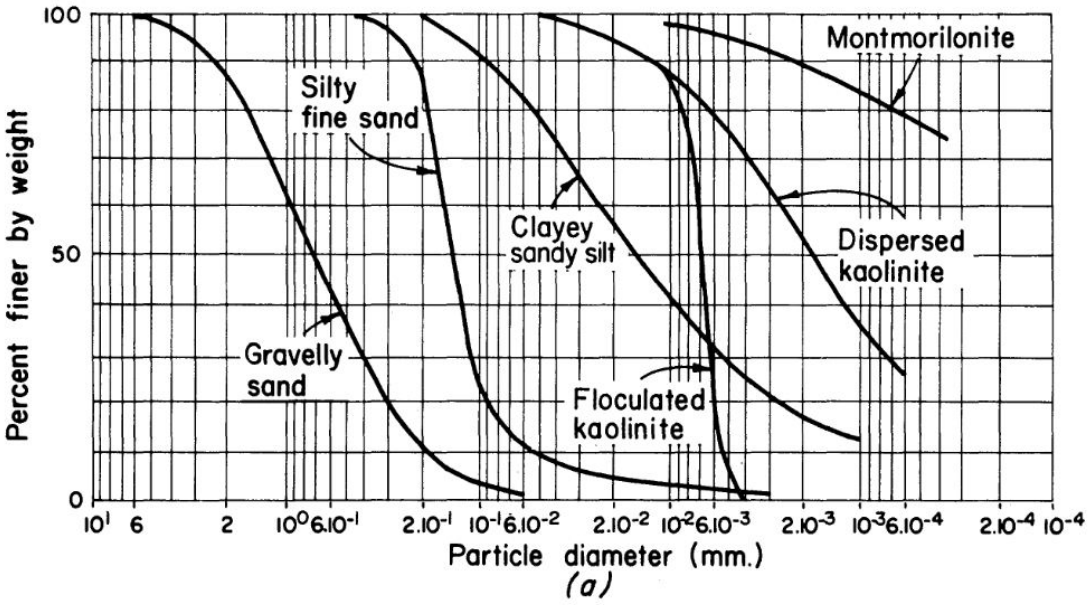


Figure 3.12: Logarithmic chart of particle diameter by sediment type. Figure from Bear (1972).

3.4.2 Geophysical Well Logs

The USGS Central Region Research Drilling Team ran geophysical logs for the Pilgrim Hot Springs wells consisting of gamma ray, conductivity, and resistivity. The equipment used to run the tools consisted of a computer-controlled winch system that lowered the tools downhole at a constant speed with real time depth readings. Gamma ray is the most valuable log as it allows for real time lithology prediction at the well site and can be run in cased holes, thus avoiding downhole logging issues with swelling clays. Conductivity and resistivity logs were only run for PS-12-1 and PS-12-2 due to the demanding drilling schedule and drilling issues in PS-12-3. Gamma ray logs are provided next to the lithologic logs for direct comparison (Figure 3.13).

Lithology and gamma ray logs for several wells are correlated by depth with equidistant spacing (Figure 3.13). The construction of the lithologic logs is guided by correlations of similar gamma ray peaks. Sticking issues with logging PS-5, PS-12-3, and PS-12-1 prevented more complete well log profiles to total depth. Gamma ray counts are highest and most definitive in clay at 175-300 API. Low counts from 0-100 API are observed for the gravels and mixed sands. Indurated zones are typically within 100-200 API. The thick clay interval at 180-260 m depth occurs in PS-12-1, PS-12-2, and PS-12-3.

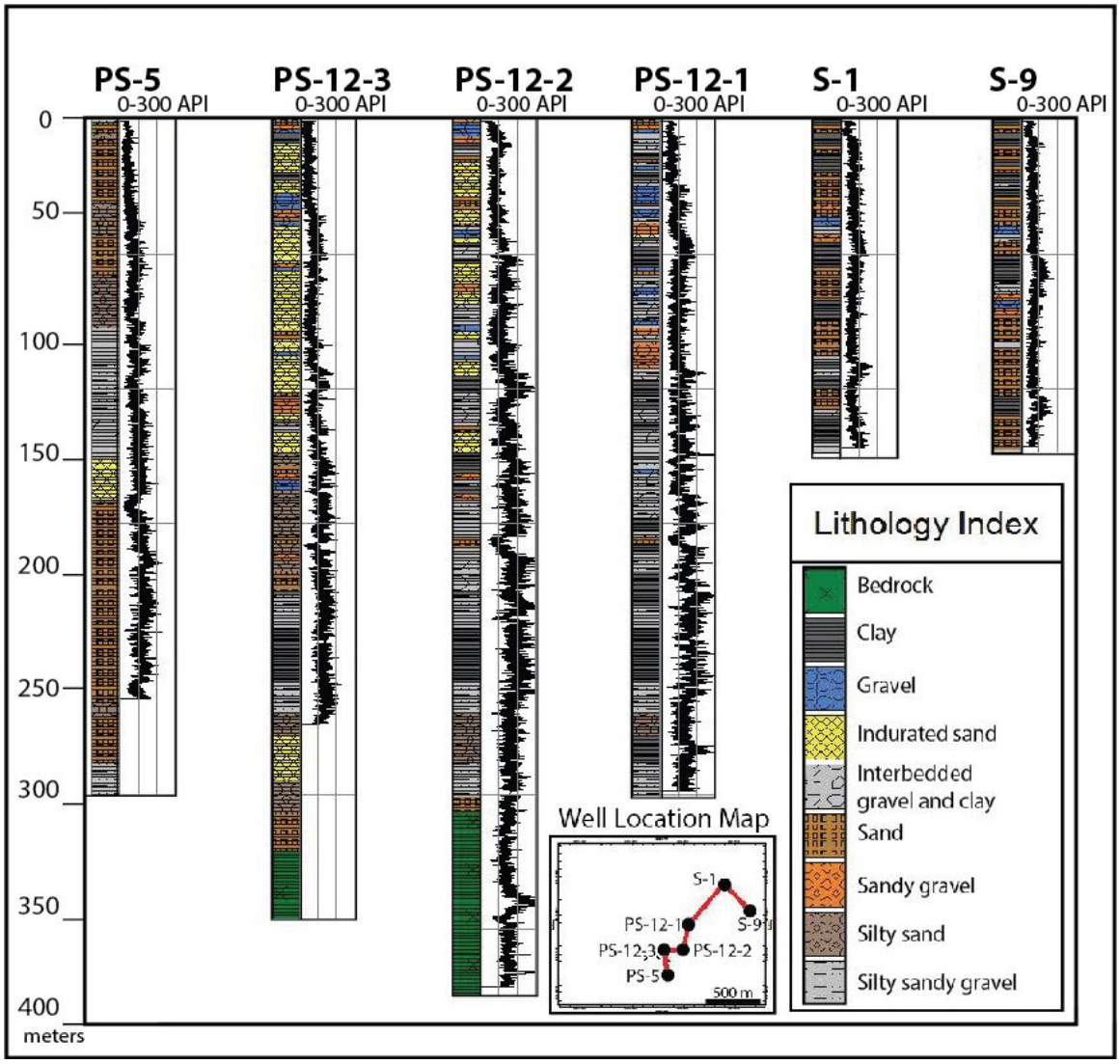


Figure 3.13: Lithologic and gamma ray logs for selected wells.

3.4.3 Static Temperature Logs

Well temperatures were recorded using a Kuster Strain temperature probe. A continuous logging technique of recording temperatures every 3 m per minute allowed the probe to measure the equilibrated ambient temperature in the well at detailed intervals. This approach was typically run at least a week after drilling ceased and the well was cased to allow for equilibration. Temperature curves for several wells on site show a spike in temperature up to 91 °C at 25-50 m and subsequent reversal at 30-100 m (Figure 3.14). All wells show an increasing temperature gradient below the reversal. The shallow temperatures are highest in wells PS-12-2 and PS-12-3 which also have the highest bottom hole temperatures of 91 °C and 80 °C, respectively. The influx of groundwater is estimated to have a flow rate of ~200 gpm flowing through the system from the south to the north, eventually feeding into the Pilgrim River (Lofgren, 1983). It should be noted that the curve for PS-4 is not reliable below 140 m and the multiple fluctuations in PS-5's curve are equipment-related. These measurements were recorded during earlier exploration in the 1980's (Woodward-Clyde, 1983). The shallow peak in temperature is the result of the outflow of geothermal fluids and the increasing temperature gradient is due to the heating of the deeper geothermal reservoir. Wells S-1 and S-9 seem to have only residual outflow fluids and a higher degree of mixing with meteoric groundwater water. These wells also have low temperatures compared to the other wells at the corresponding depth of peak outflow temperatures. The reversal from 30-100 m is attributed to a large degree of mixing with this colder meteoric water where permeability is sufficiently high (Daanen et al., 2012; Woodward-Clyde, 1983).

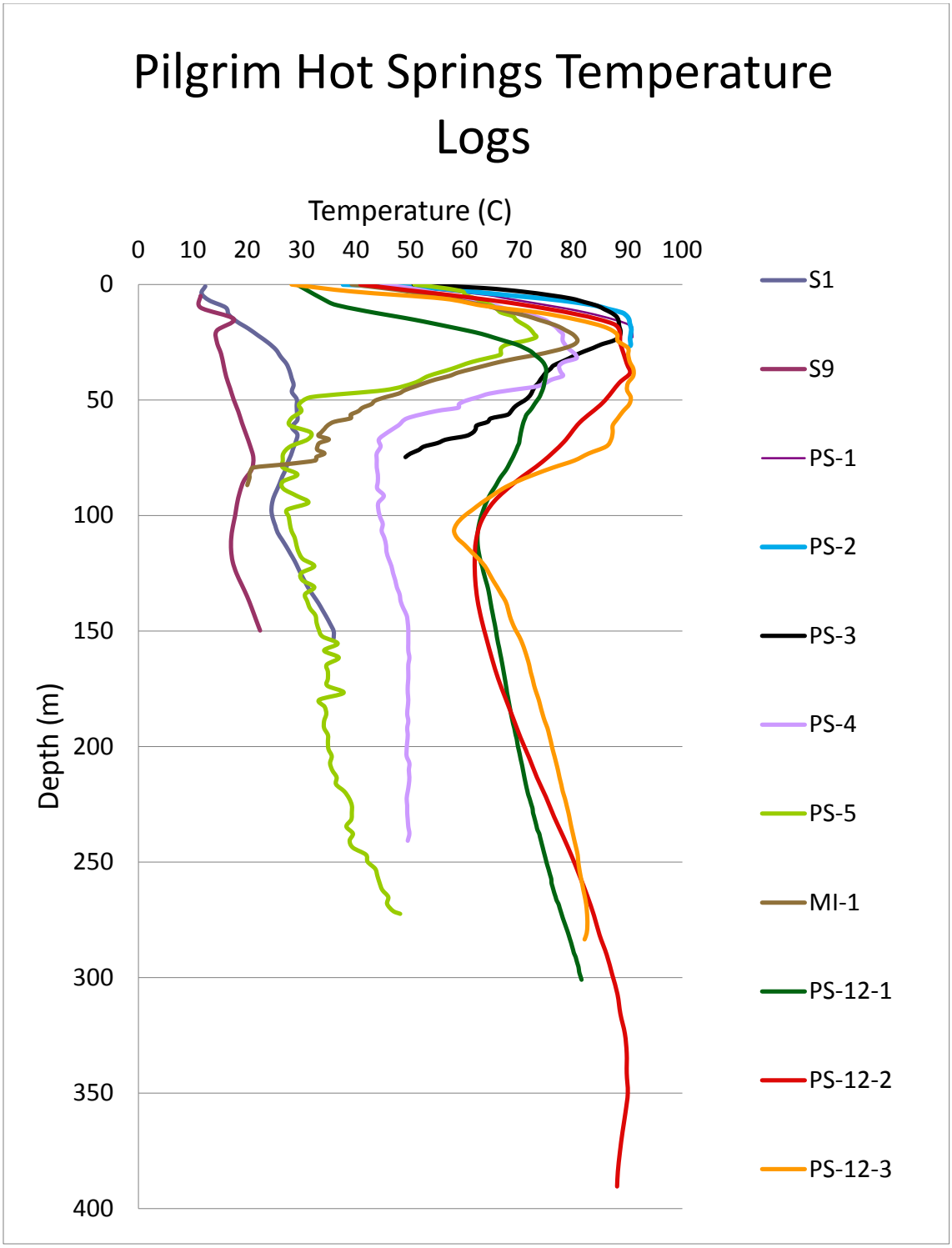


Figure 3.14: Temperature curves for all Pilgrim Hot Springs wells. Measured in Celsius from 0-400 m depths.

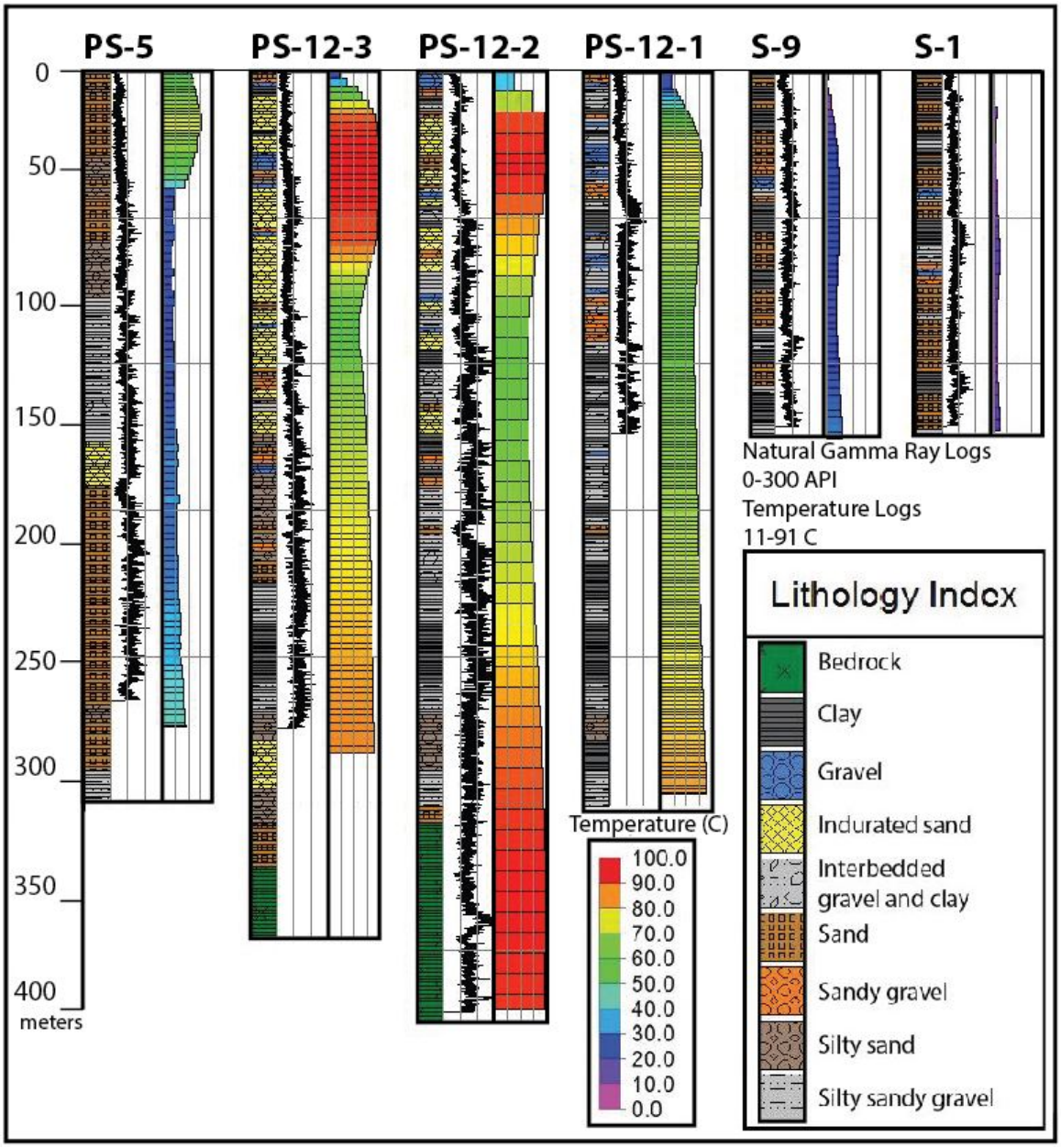


Figure 3.15: Lithology, gamma ray, and temperature curves for selected wells.

3.5 Sample Analytical Techniques

3.5.1 Reflectance Spectroscopy

Visible near infrared to shortwave infrared (VNIR-SWIR) reflectance spectra were acquired over the 400-2500 nm wavelength region with an Analytical Spectral Devices (ASD) FieldSpec Pro and a high-intensity contact probe using a white Spectralon panel as reference. Each sample was measured by holding the probe perpendicular to a preferentially flat or smooth surface to minimize measurement errors associated with stray light. Reflectance spectra were recorded every seven centimeters to detect detailed variations in the mineral spectral absorption features with depth. In the VNIR-SWIR wavelength region, hydroxyl, hydrate, and carbonate anions as well as transition elements (dominantly iron) produce distinctive absorption features (Hunt, 1977). These spectral features can be used to investigate mineral assemblages or variations in specific mineral chemistry that may be related to changing alteration conditions. For example, the depths and wavelength positions of absorption features, such as those related to AlOH and FeOH compounds, can be utilized as proxies for the extent and magnitude of hydrothermal alteration (Calvin et al., 2010; Haest et al., 2012; Harraden et al., 2013; van Ruitenbeek et al., 2005) (Figure 3.17). Geochemical signatures of hot fluids are recorded in subsequent alteration minerals where the fluids emanate from a deeper source. Reflectance spectroscopy is cost-effective and can accommodate large numbers of samples in a relatively short amount of time compared to XRD or XRF (Calvin et al., 2010).

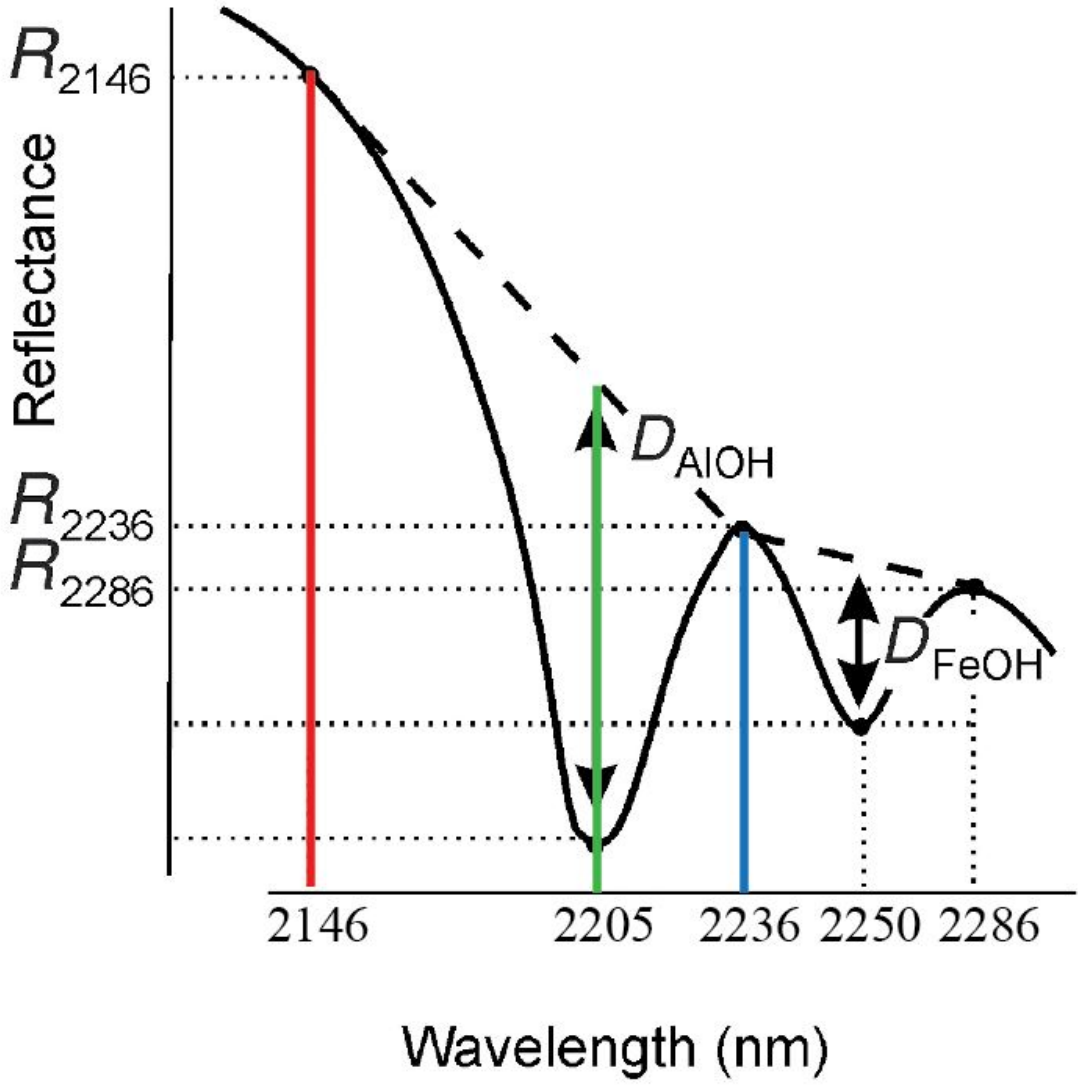


Figure 3.16: AlOH and FeOH absorption features. Red, green, and blue bands define the AlOH absorption feature. Modified from van Ruitenbeek et al. (2005).

Pre-processing of the acquired spectra involved calibrating the data to absolute reflectance using a reflectance spectrum of the Spectralon white reference panel and the use of a 'jump correction' to remove wavelength dependent offsets associated with the boundaries between the different sensor arrays of the ASD system. This pre-processing is

performed using the Spectral Analysis and Management System (SAMS) software package (SAMS, 2005). The pre-processed spectra are compiled into a spectral library file that was imported into the ENVI (Environment for Visualizing Images) software package. To better visualize the vertical changes in spectral reflectance properties an IDL (Interactive Data Language) script (provided by C Haselwimmer) was used to build a hyperspectral image cube that stacks spectral data against sample depth to provide a convenient method for visualizing the results (Figure 3.18). Using ENVI, false color composites of three spectral bands focused on specific mineral absorption features were produced to qualitatively investigate the range of mineral assemblages and variation in alteration intensity with depth. A continuum-removal procedure (Clark and Roush, 1984) was applied to the hyperspectral cube to better enhance the depth of specific absorption features as well as remove slope effects that impact the absorption depths and wavelength positions. Qualitative interpretation of major spectral classes manifested in the data was undertaken with reference to the USGS Digital Spectral Library (Clark et al., 2007) in order to identify the dominant mineral assemblages. Using scripts implemented in IDL, the continuum-removed depth and wavelength position of major mineral absorption features in the VNIR-SWIR was determined from the spectral data. These scripts were based on procedures adapted from Haest et al. (2012) that involved fitting polynomial curves of various orders of magnitude to the continuum-removed spectra for different absorption features. The spectra are stacked and continuum removed to highlight the profile subtleties for clarity of comparison (Figure 3.18). Red (2145 nm), green (2205 nm) and blue (2235 nm) define the ALOH absorption feature to distinguish Al-rich

mineral phases by color association as a function of absorption depth (Figure 3.18). The resultant spectral parameters were used to determine specific mineral assemblages following the procedures outlined by Haest et al. (2012) as well as providing variables that were cross-compared with the results of methylene blue and XRD analyses. Analysis of the sample spectra was also undertaken using The Spectral Geologist (TSG) software package to provide an independent check concerning the interpreted mineral assemblages (Figure 3.19).

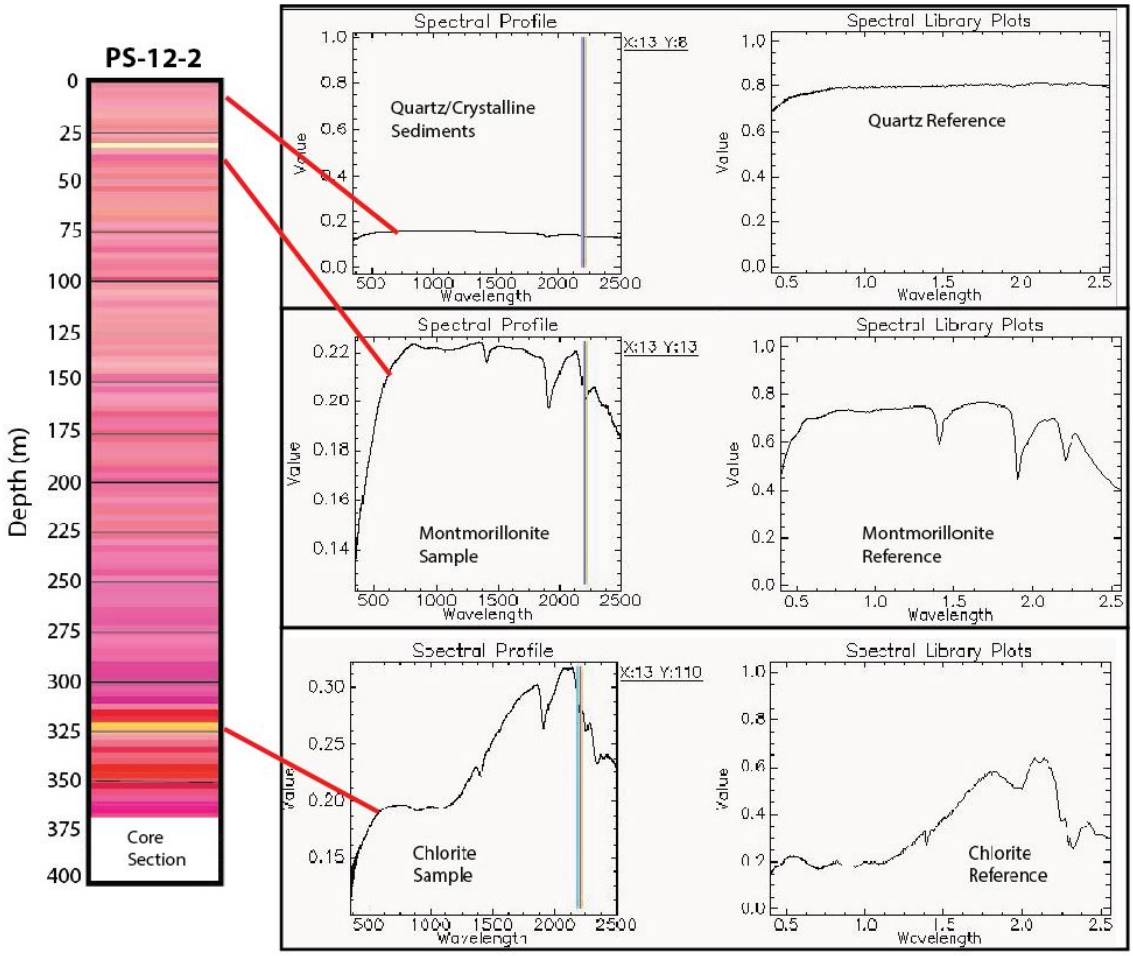


Figure 3.17: Hyperspectral image cube of PS-12-2. Stacked spectra corresponds to sample depth for a total of 375 m depth. Reference mineral spectra (USGS Spectral Library) have been selected: montmorillonite (magenta), chlorite (yellow), muscovite (red), illite and kaolinite (blue), and highly crystalline sediments with quartz as an example (white to very light pink-magenta).

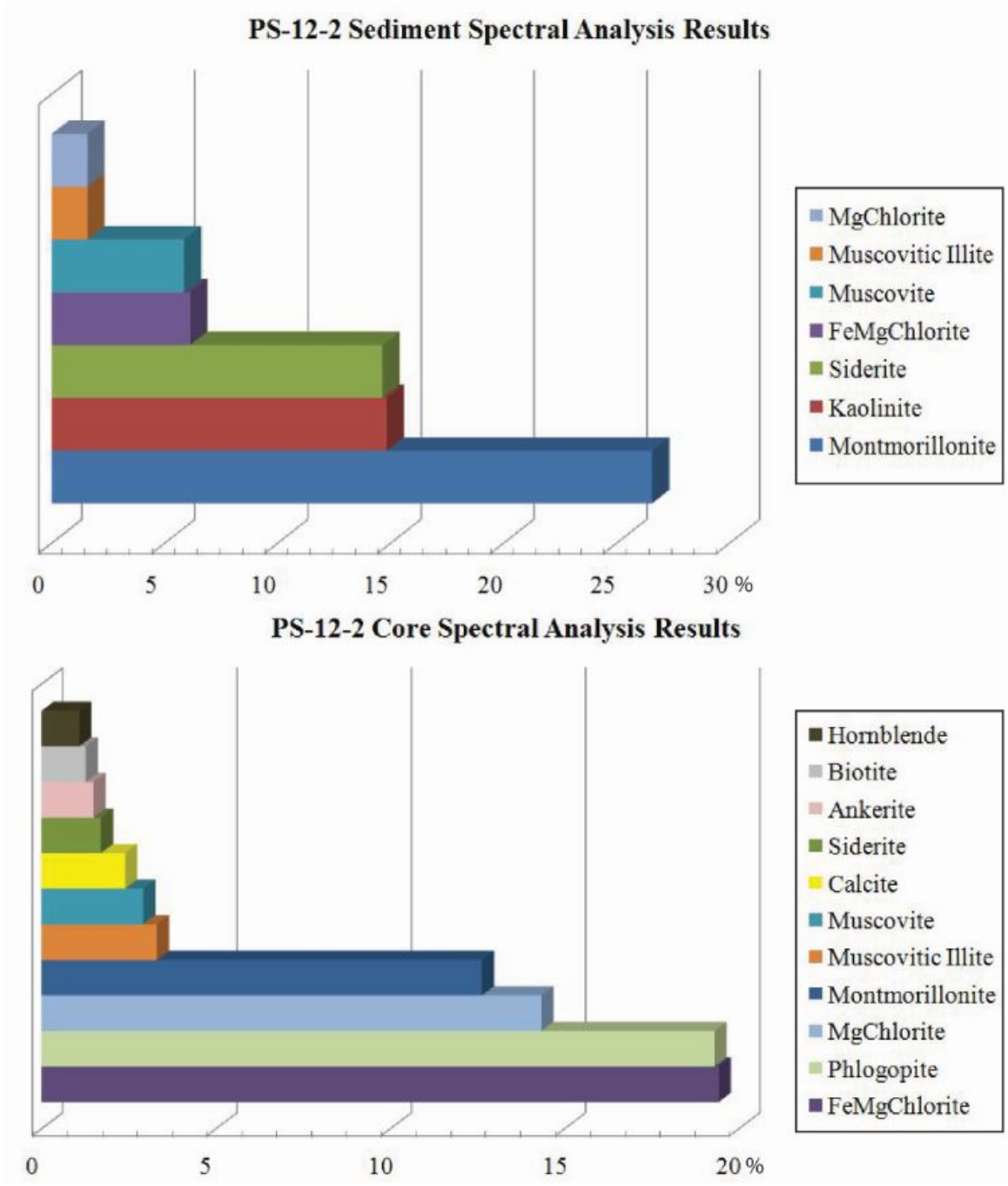


Figure 3.18: The Spectral Geologist spectral analysis mineral results. Results are listed from most abundant to least abundant for both PS-12-2 sediments and core.

Analysis of the reflectance spectra indicates alteration mineral assemblages within the well sediments and core samples comprised of various clays and micas. The dominant mineral assemblages include montmorillonite and chlorite (Figure 3.18). The absorption features of OH at 1400 nm, H_2O at 1900 nm, and specifically the AlOH absorption feature at 2205 nm with shoulder peaks at 2160 nm and 2240 nm are strong indicators of montmorillonite. Chlorite was identified by low reflectance in the visible spectrum, the multiple absorptions in the H_2O band, and a small AlOH absorption on the shoulder of the much more pronounced FeOH band at 2250 nm and MgOH band from 2330-2450 nm. However, muscovite and kaolinite, detected in XRD, were not as easily separated by visual determination in spectral analysis due to the mixed-layer nature of the clay samples and ambiguities in the spectral absorption features. The USGS reference spectra for mixed montmorillonite-kaolinite offered the closest resemblance to sample spectral profiles, but this particular mineral assemblage is almost indistinguishable from pure montmorillonite reference spectra.

To further characterize the extent of alteration within the samples, the White Mica Alteration Index (WMAI) was calculated. This index is the ratio of the AlOH absorption depth of white mica to the depth of the FeOH absorption feature in chlorite (van Ruitenbeek et al., 2005); the ratio increases with white mica relative to the abundance of chlorite (Figure 3.20). WMAI values that plot higher than 0.75 are interpreted to be mostly white mica while chlorite dominates the lower half at 0.5 and below (van Ruitenbeek et al., 2005). The relative Al content of the white micas determines the wavelength position of the AlOH absorption feature and changes with temperature,

hydrothermal fluid chemical substitution, and the mineral composition of the host rock type (van Ruitenbeek et al., 2005). Figure 3.20 is a WMAI scatter plot of wavelength values within 2190-2215 nm that is the characteristic range of the AlOH absorption band. The WMAI for the PS-12-2 sediments tend to exhibit a relatively low Al content possibly as a result of increased temperature (100+ °C) or evolving hydrothermal fluid chemistry (van Ruitenbeek et al., 2005). Figure 3.21 shows a similar distribution of WMAI values for the sediments of PS-12-1 and PS-12-3. The deeper sediments and shallow basement surface rock cuttings of PS-12-2 and PS-12-3 plot in or near the chlorite dominant range. The PS-12-2 core displays a wide spectrum of variable white mica-chlorite values. The Spectral Geologist program, designed for automated mineral detection using spectral data, produced results that indicate the abundance of (Fe,Mg) chlorite relative to a lesser amount of white micas such as muscovite and paragonite (Figure 3.19).

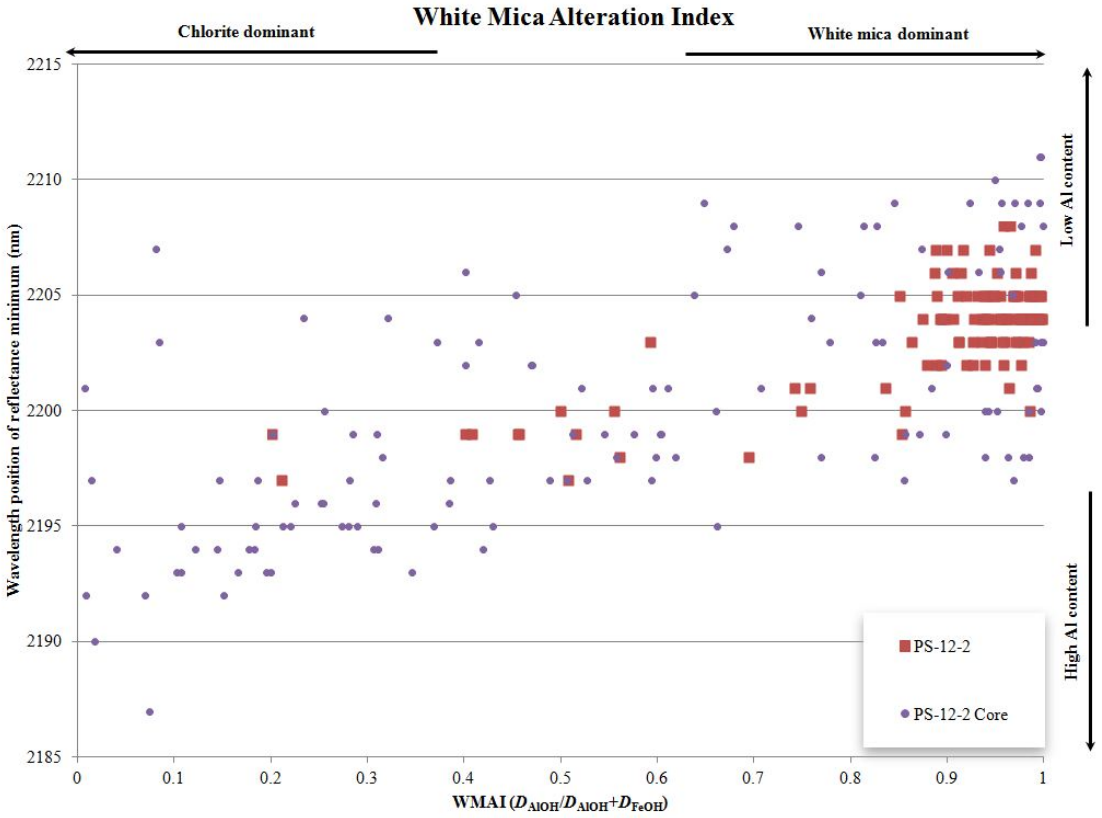


Figure 3.19: White Mica Alteration Index scatter plot for PS-12-2. AlOH and FeOH absorption feature depth and wavelength position changes are plotted.

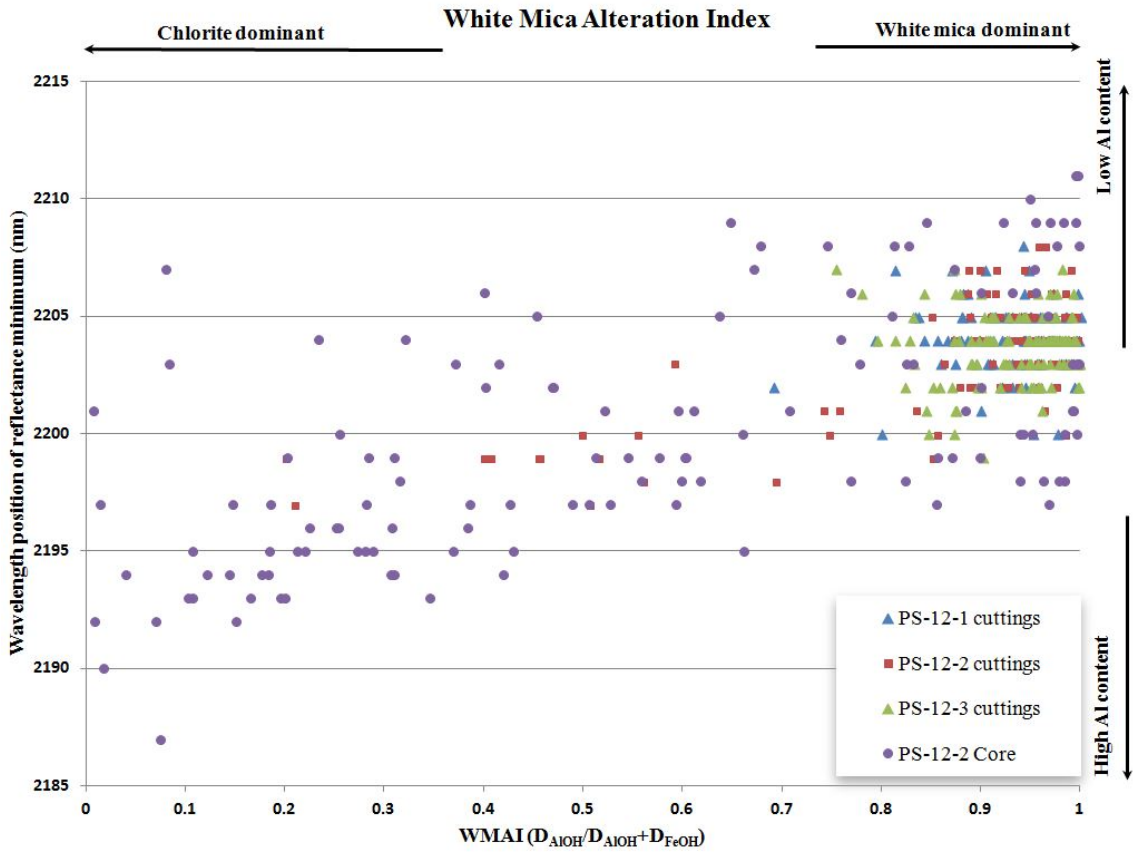


Figure 3.20: White Mica Alteration Index scatter plot for selected wells. PS-12-1, PS-12-2 (and core section), and PS-12-3 AlOH and FeOH absorption feature depth and wavelength position changes are plotted.

3.5.2 Methylene Blue Titration

Methylene blue (MeB) analysis is a common approach to determining the composition of clays intercepted in geothermal exploration (Gunderson et al., 2000). This analysis requires titration of methylene blue into solution containing a powdered sample of clay. In solution, methylene blue is a cationic dye with the molecular structure $C_{16}H_{18}N_3S^+$ that readily adsorbs onto smectite clays due to their very high cation exchange capacity and hydrogen bonding with the alumino-silicate lattice structure (Santamarina et al., 2002; Yukselen and Abidin, 2008). It is an important application as smectite clays form in temperatures in excess of 50 °C and conversion to illite composition begins at 80 °C and becomes increasingly dominant above 100 °C (Gunderson et al., 2000). The results of MeB analysis of clay-rich samples can be combined with zones of low resistivity to delineate areas of possible high-temperature alteration in association with the migration of geothermal fluids (Gunderson et al., 2000). For this analysis, 78 clay samples were analyzed with methylene blue titration.

The procedure used for the methylene blue analysis is provided in Harvey (1993). The main purpose of this method is to fully saturate the clay particles with a methylene blue solution. Drop counts of the methylene blue-clay solution are recorded until a blue halo forms on the paper (Figure 3.22). This halo forms as a result of full adsorption of methylene blue onto the clay structure where the excess methylene blue is suspended in the solution. For each one ml of methylene blue solution required for saturation, 1% swelling clay is estimated. The composition of the clay and a calibrated quantification

of $\%_{smectite}$ is typically ascertained by x-ray diffraction. A range of smectite content was detected in the clay samples in the MeB analysis.

For well PS-12-1, the MeB analysis showed an increase in smectite percentage with depth. The top of the well had an average of 2-3% smectite, which increased to 8.5% near the bottom of the well. In PS-12-2, high values of MeB saturation indicate smectite content up to 10% occurring at 200-300 m depth. PS-12-3 displayed a similar trend and average to PS-12-2. However, it only had a high of 7.5% smectite. The table of MeB values for these wells is located in Appendix B.1-B.3.

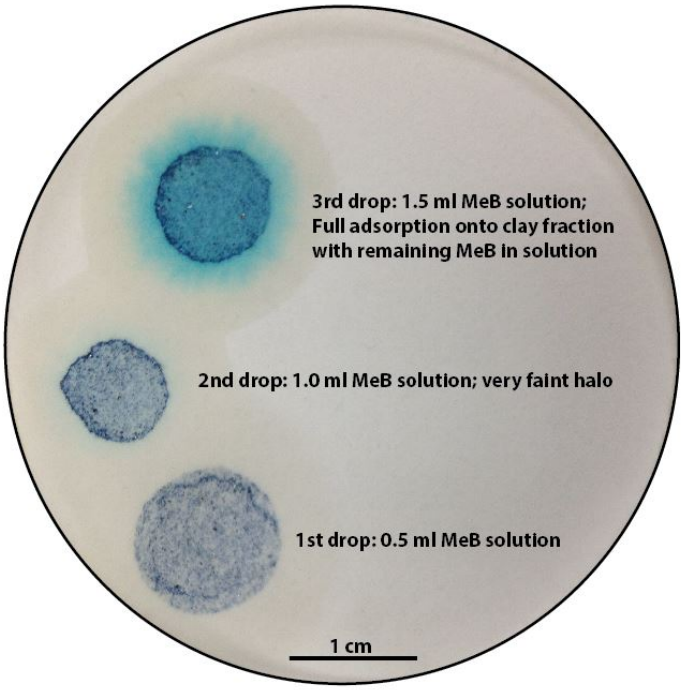


Figure 3.21: Methylene blue solution "halos". Halos indicate excess MeB (Methylene blue) remaining in solution after full adsorption onto free clay fraction in the prepared mixture.

3.5.3 X-ray Diffraction Analysis

Samples were analyzed using the PANalytical X'PERT PRO Materials Research Diffractometer (MRD) x-ray diffraction (XRD) in the Advanced Instrumentation Lab at the University of Alaska Fairbanks. Using a CuKα source, the analytical range was from 2-59 °2θ with a 0.01 step size and 15 seconds per step. Four clay samples obtained from drill cuttings from PS-12-2 were prepared for oriented clay x-ray diffraction analysis. The clays were decanted, separated from >2μm particles, and saturated with a 2M solution of $MgCl_2$ as expanding with an index cation yields predictable results that allow for differentiation of the clay mineralogy (Bain et al., 1987). The clays were then oriented in a vacuum filter apparatus and placed on glass slides. Separate XRD runs were completed after air-drying and ethylene glycolation. Expandable clays like smectites, principally montmorillonite, shift in measured Å peaks of 10 Å air-dried at 7 °2θ to 14 Å at 5 °2θ with ethylene glycol (Mosser-Ruck et al., 2005). The results of XRD analysis are compared to the results of the other methods to test the agreement of mineral determinations.

The common minerals detected in the XRD results include abundant montmorillonite, common illite/chlorite, kaolinite, and minor biotite (Figure 3.23). Peak matches within the 2-59 °2θ range and respective d-spacings for known minerals show a strong match with montmorillonite clay. Peak position and count intensity matches with other minerals may be slightly variable as the samples were oriented with the C-axis of the clays preferentially aligned. Thus, correlations to peaks of other mineral structures at

a specific °2θ are limited to the 001 line. Peaks on other lines and orientations may not show up. When considering a mineral identification, this orientation served as a mechanism for filtering out other mineral structures by looking at database results of measured °2θ angles and d-spacing values at the 001 line.

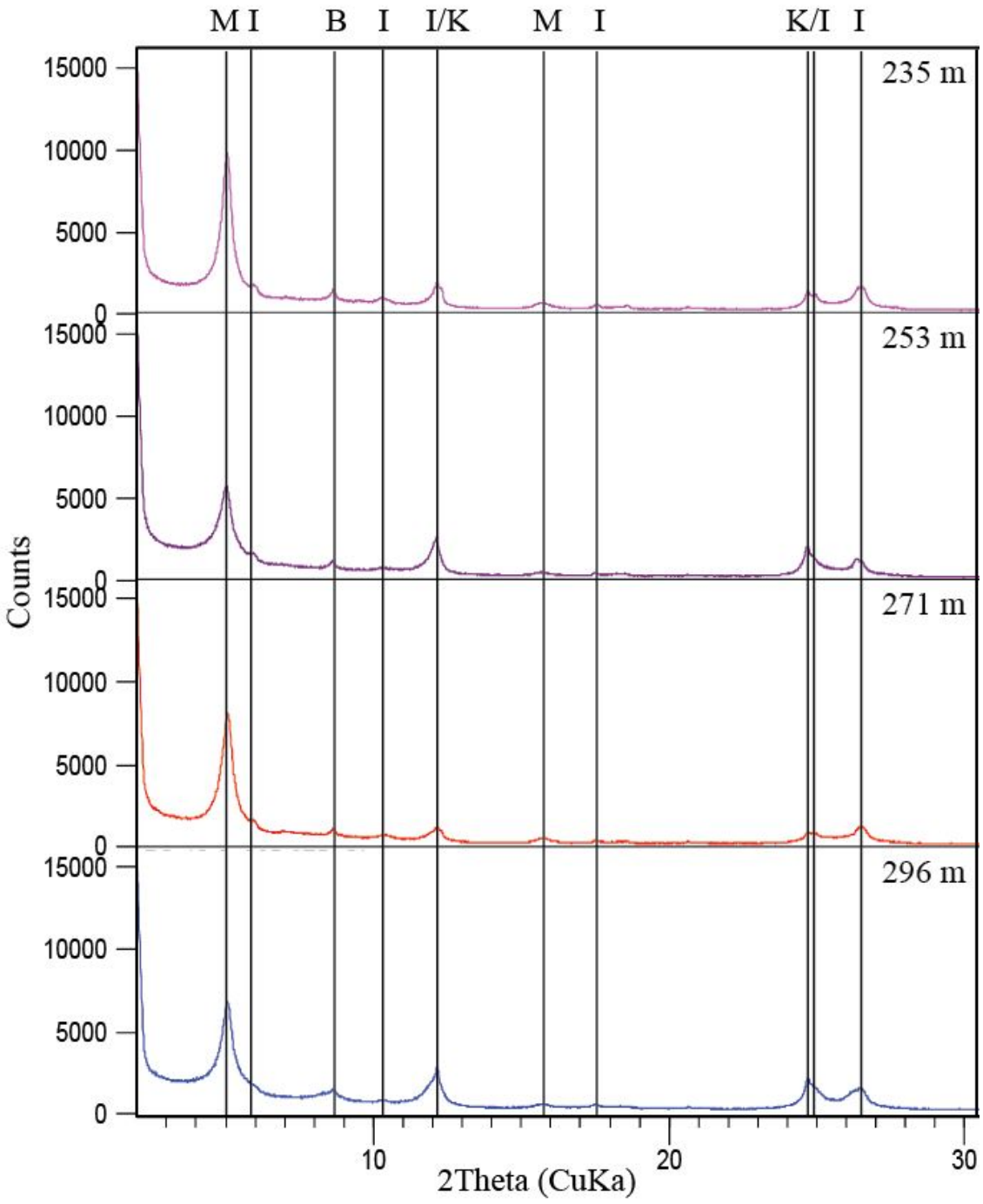


Figure 3.22: XRD results of PS-12-2 clay samples. XRD detected (M) Montmorillonite, (I) Illite, (K) Kaolinite, (B) Biotite from depths of 235-296 m in well PS-12-2. Results are dominated by montmorillonite with variable abundances of illite and kaolinite composition and minor biotite.

3.5.4 Thin-section Characterization

The thin-sections were created from selected samples that represent the three distinct lithologies present in the PS-12-2 core. The bedrock is composed of mica schist with a granitic pegmatite dike and a diabase dike. A thin-section was also created from a field sample of a previously identified granitic pegmatite dike for comparison (Turner et al., 1979). Photomicrographs of the biotite schist bedrock, pegmatitic dike, diabase dike, and the contact of the pegmatitic dike and biotite schist are illustrated (Figure 3.24). The pegmatitic dike contains plagioclase and quartz minerals of sizes ranging from 0.5-2 cm. Minor biotites are seen in the pegmatite at the contact with the biotite schist. The diabase dike has <3 mm sized hornblende crystals and several thin (<1 mm) quartz-filled veins with a groundmass of very fine plagioclase crystals. Fine-grained pyrite (only discernible in reflected light) is very common as a replacement mineral along both dike-schist contacts.

Mineral alteration seen in thin-sections of the core is limited to micas at or near dike contacts, pyritization in quartz veins and mineral contacts, and hornblende replacement in the deeper diabase dike sections. Minor alteration is present in some biotites producing a mottled sweeping extinction. Mineral degradation and the early stages of hornblende replacement by quartz are visible. The inspection for clay content in thin-section and precise alteration accessory mineralogy is best pursued in scanning electron microscopy and microprobe analysis, both of which are expensive endeavors and were not undertaken in this research.

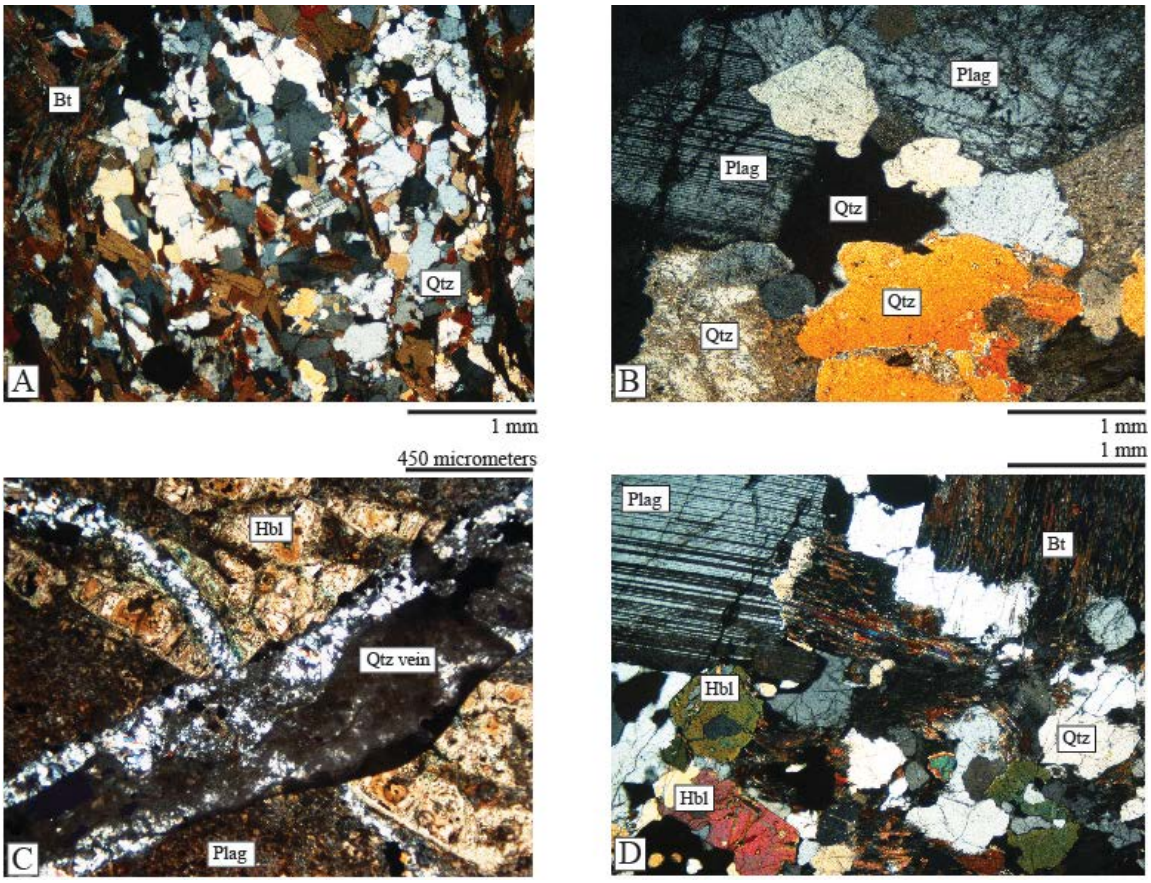


Figure 3.23: Thin-section photomicrographs of bedrock core samples. All images are under crossed polars. [A] Representative sample of the biotite (Bt) schist. Minor alteration is present in some biotites. [B] Pegmatitic dike with large plagioclase (Plag) and quartz (Qtz). [C] Diabase dike with a 3 mm hornblende (Hbl) crystal cut by two quartz veins with a groundmass of plagioclase. Mineral degradation and the early stages of hornblende replacement by quartz are visible. [D] Contact of the pegmatitc dike and biotite schist. Hornblende, quartz, plagioclase, and biotite are common.

3.6 Discussion of Analytical Results

The sediments and mica schist bedrock are experiencing hydrothermal alteration as evidenced by a mineral assemblage of montmorillonite, illite, and kaolinite, as well as a host of accessory minerals. The mixed montmorillonite, illite, and kaolinite clays suggest low-temperature alteration between 80-120 °C in both the sediments and bedrock.

The AlOH absorption depth and methylene blue estimated smectite content is plotted for wells PS-12-1, PS-12-2, and PS-12-3 with the aim of correlating montmorillonite-rich horizons as proxies for hydrothermal alteration (Figure 3.25). Discovering these zones of hydrothermal alteration can highlight the pathways, both past and present, of hydrothermal fluid flow in the geothermal system. The AlOH absorption depths for each well show a general increasing trend to the bedrock surface, yet smaller scale variations do not typically correlate directly well-to-well. One notable exception is the two data points in PS-12-1 at ~30 m depth that exhibit significant absorption up to 0.07-0.09%. These two points are indicators of montmorillonite on their respective spectral profiles. When compared to the other wells, AlOH absorption increases appear to occur at the same depth. However, this is limited to only a few data points and the absorption features of PS-12-2 and PS-12-3 are too subtle for a well-supported correlation. The methylene blue data for each well show a trend similar to the increasing trends of the AlOH absorption features to the bedrock surface. Each well exhibits low values (<3% smectite) until 130 m depth where the wells display an increase in smectite

content to the bedrock. Also, similar to the AlOH trends, small scale correlations between wells are not achievable. Increasing the sample data may help to resolve this issue.

Examination of the methylene blue and AlOH absorption data reveals broad similarities yet there is a lack of correlations at a higher frequency (Figure 3.25). Both methods produce trends with depth that signify increases in montmorillonite in all three wells. PS-12-2, for example, shows the trends with depth against lithology, temperature, and mineralogy as detected through The Spectral Geologist and XRD (Figure 3.26). Methylene blue and AlOH absorption both increase and decrease in identified clay-rich intervals. It is important to note that AlOH absorption is not uniquely a montmorillonite or smectite indicator and could be indicating the presence of other minerals as well. Also, the methylene blue analysis is only a measure of its affinity to the smectite clays in suspension. Montmorillonite is a specific smectite clay and other smectite clays in the sample solution could affect the outcome of estimated montmorillonite content. The discrepancy in the two trends may also be the result of heterogeneity of the clays and sediments. Increases in illite or kaolinite relative to montmorillonite could produce the variation observed in both trends. This is supported by Figure 3.26 where plotted XRD results show multiple clay minerals are detected throughout the selected well cutting samples. Temperature also does not appear to greatly influence the higher frequency changes of the two methods (Figure 3.26). This suggests the heterogeneity of the clay-rich intervals may be influenced by other environmental conditions.

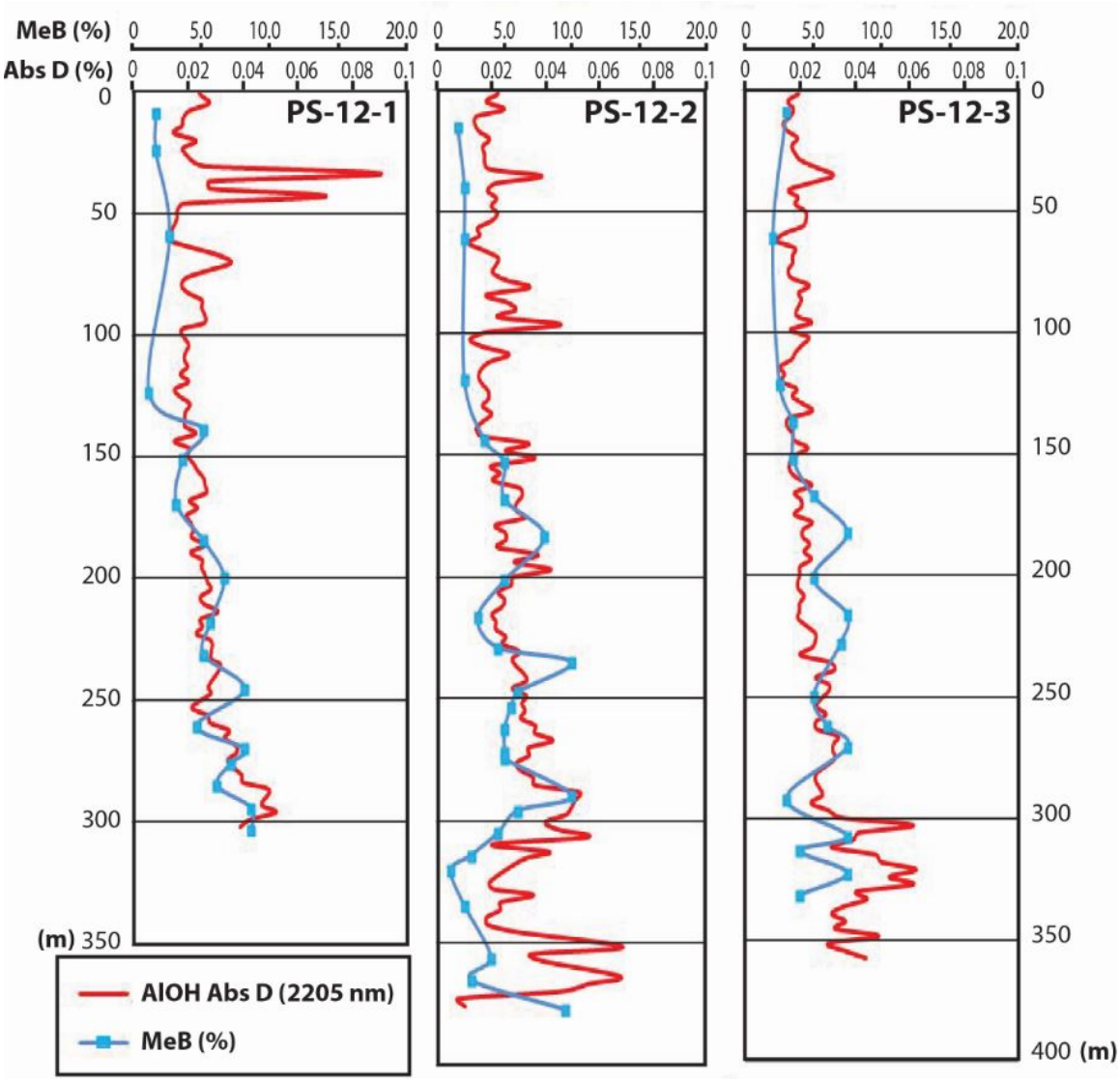


Figure 3.24: AlOH absorption depths and methylene blue results combined plot. AlOH absorption feature depth (AlOH D) at the 2200 nm wavelength (or approximately located at the maximum depth of absorption for this specific feature) and methylene blue estimated smectite content in percent (MeB %) plotted against depth for wells PS-12-1, PS-12-2, and PS-12-3. Absorption depth is measured in total percent absorbed light (not reflected).

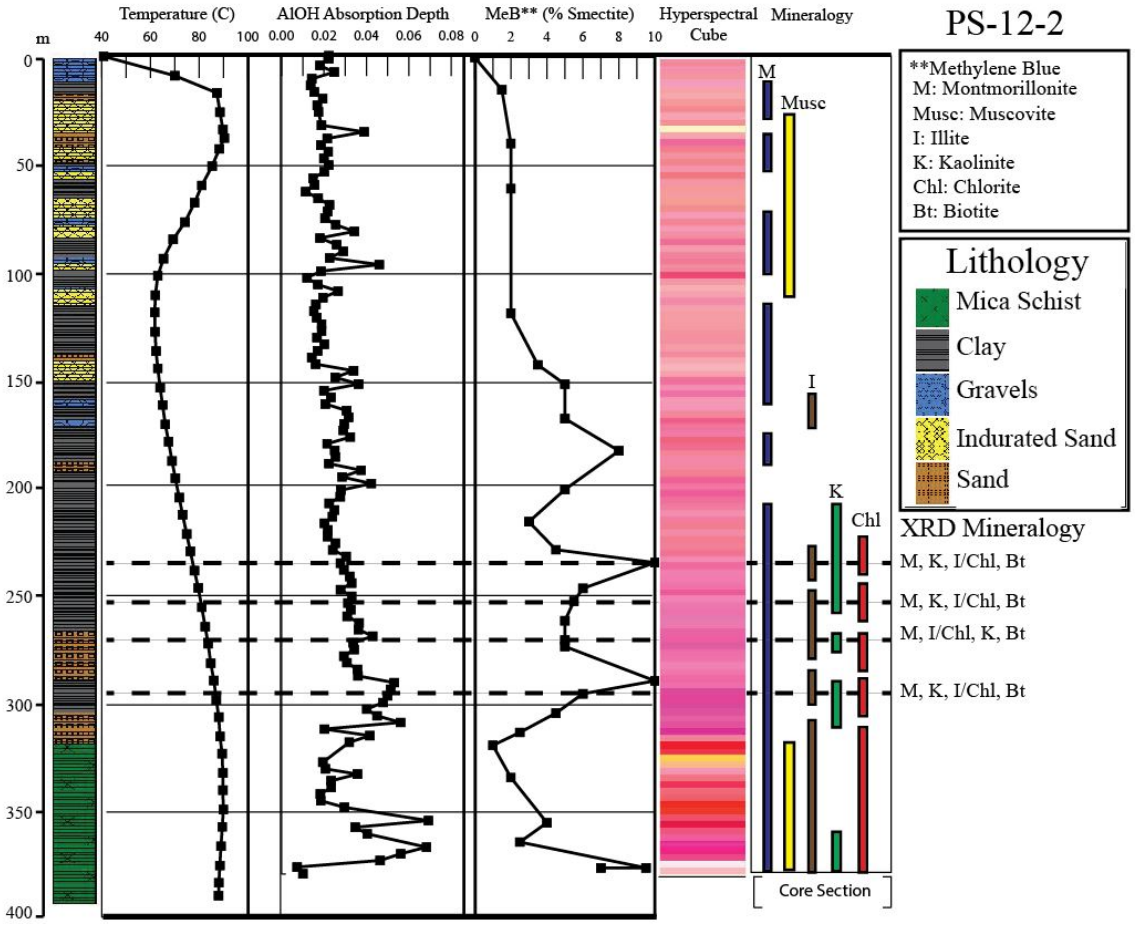


Figure 3.25: Lithology, temperature, spectral, and methylene blue analysis plot. A correlation of results for PS-12-2. All data sets are compared to detect changes in mineralogy that relate to the degree of past hydrothermal alteration.

The degree of alteration present in the Pilgrim Hot Springs wells resembles an argillic alteration facies with the assemblage of white micas and clays, dominantly kaolinite, montmorillonite, and illite (Mas et al., 2006). The formation of these clays is strongly dependent on fluid temperature and also on fluid chemistry (Browne, 1978). The presence of kaolinite indicates an environment with temperature and pH conditions necessary to strip the alkalis from muscovites as well as iron, calcium, and magnesium

from montmorillonite through the process of hydrolysis (Guilbert and Park, 1986). The montmorillonite in the PS-12-2 core provides further evidence for argillic-style alteration as it is a common alteration product in many ore vein deposits and hydrothermal systems (Guilbert and Park, 1986; Browne, 1978). Similarly, illite and chlorite typically require a temperature range of 100-200+ °C for formation and are commonly used as a geothermometer (Gunderson et al., 2000; Harvey and Browne, 2000; Lagat, 2007). The temperatures required for the mixed-layer smectite-illite clays detected in the well samples are most likely the result of the hydrothermal alteration within the system and would require greater burial depth for conversion to illite through diagenetic processes alone (Jennings and Thompson, 1986). Chlorite, although common in geothermal systems, is most likely derived from the low-grade metamorphics of the nearby mountains and dike intrusions in the basement that may have had more impact on mineralizing the shallow basement than hydrothermal processes. The low-grade metamorphism and dike intrusions of the bedrock may likely be responsible for the abundant presence of chlorite and mineral replacement in the dikes, as the temperatures required for their crystallization are well above any other hydrothermal alteration features observed in the sediments. Regardless, extensive pyritization and the clay mineral assemblage suggest an argillic-style alteration facies that is present in both the core and sediments.

The alteration assemblage points to past temperatures at or slightly elevated above current conditions of hydrothermal activity at Pilgrim Hot Springs. The presence of abundant pyrite and the clay mineral assemblage of montmorillonite, illite, and kaolinite

is a common feature of both low- and high-temperature geothermal systems around the world (Browne, 1978). The various geothermal systems of Yellowstone in Wyoming, The Geysers in California, many systems in New Zealand, the Philippines, and Iceland all contain the presence of these particular minerals (Browne, 1978). The lack of high temperature (>150 °C) alteration in the sediments may indicate that the heat source remained nearly constant through time.

Chapter 4: Lithostratigraphic and Temperature Model Development

4.1 RockWorks15 Model Parameters

RockWorks15, a geologic modeling program from Rockware, was used to create the visual model to generate cross-sections and maps for data comparison. All Pilgrim Hot Springs well data were imported into the program for mapping, contouring, visual analysis, and 3D modeling. The model encompasses an area of 4 km^2 that includes the observed anomalous thawed ground of the hot springs and surrounding boundary of permafrost (Figure 4.1). The node density of the model is 20 m laterally in the X-axis and Y-axis and ~2 m (5 ft) along the Z-axis. Lithologic observations made from describing drill cuttings were directly imported into the program as discrete intervals within each digital well log.

Well data points, both lithologic and temperature, are interpolated via an anisotropic modeling algorithm. The anisotropic algorithm constrains the interpolation of values to the nearest data points in the surrounding model nodes much like connecting a series of dots. This method is most applicable to continuous downhole data sets similar to the lithologic and temperature logs. The inverse method, isotropic modeling, assigns node values in between wells with an equal distribution in all directions. This interpolation of data does not reflect the real-world spatial variability of the sediments or hydrologic controls on the temperatures. The anisotropic algorithm more realistically constrains the data in interpolation as well as extrapolation to the model boundaries.

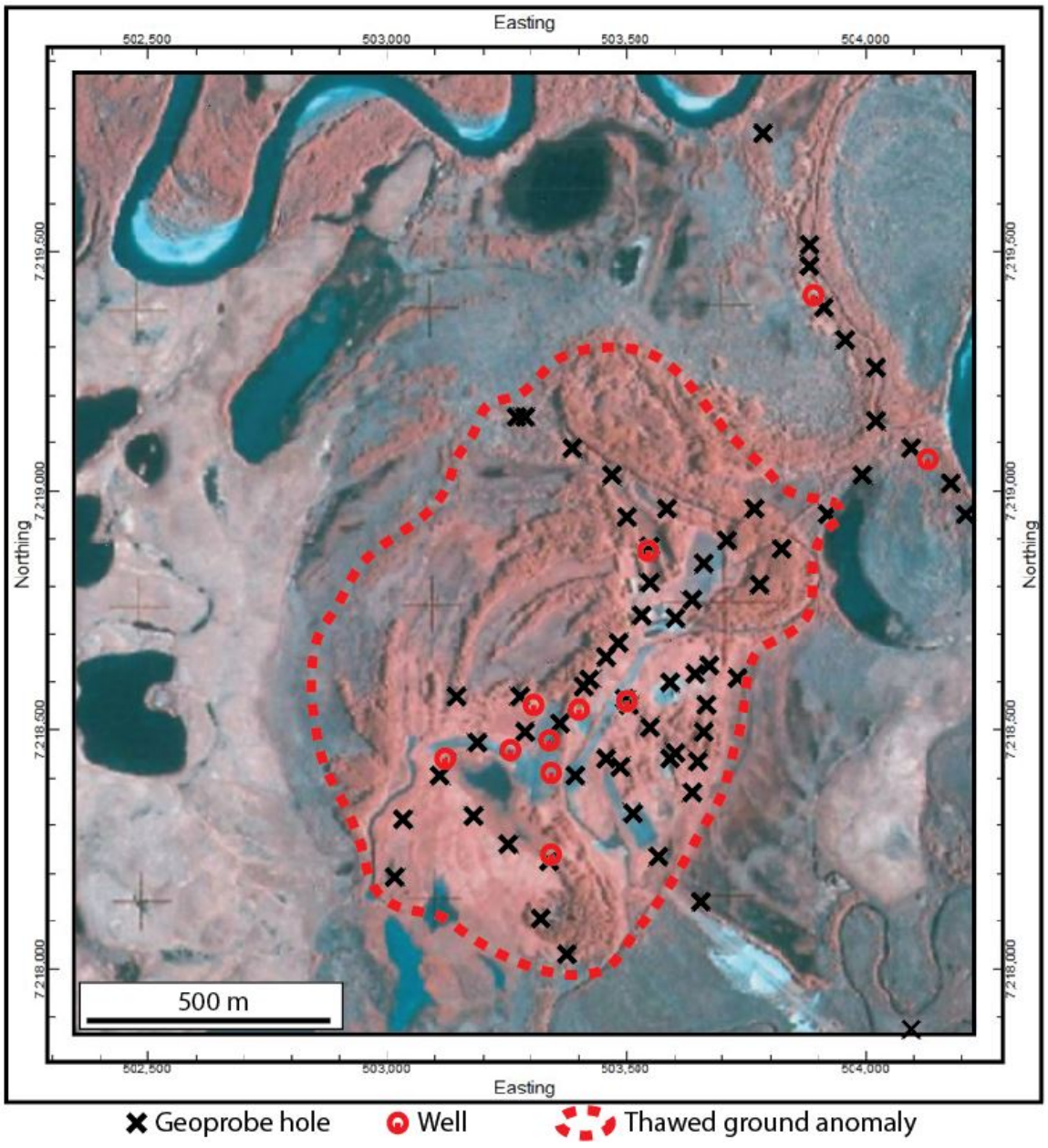


Figure 4.1: RockWorks15 conceptual model dimensions. Boundaries of the RockWorks15 model includes all Geoprobe and well locations. The model dimensions are 4 km^2. The map is a USGS Alaska High-Altitude Photography near-infrared image.

4.2 Model Assumptions and Limitations

Assumptions and Limitations

Several assumptions were integrated into the construction of this model:

- The porosity and permeability values obtained from published sources are accurate and can be applied to sediment analysis of well cuttings for this model.
- The geophysical well logs, most notably gamma ray, can be reliably correlated across the site to provide the best understanding of the subsurface stratigraphy.
- Well temperature data reflects a fully equilibrated ambient temperature.

The conceptual model is also restricted by limited understanding of the structural geology controlling fluid flow under Pilgrim Hot Springs. The placement and orientation of any faults at depth or offset in sediment layers between wells is difficult to ascertain due to relatively small area of exploration. The lack of any seismic reflection data makes interpreting the bedrock surface difficult as well. Another limitation to the model is the confidence in the sampling and sediment description reports of previous exploration drilling at the site. Without clarity on the conditions and procedure of sediment classification during the earlier drilling, previous lithologic logs utilized in the conceptual model have the potential to be overgeneralized or miss thinner, yet important sediment intervals.

4.3 Data Integration

4.3.1 Lithostratigraphic Model

Unconsolidated to poorly consolidated Quaternary alluvial, fluvial, glaciolacustrine, and brackish lagoon sediments ranging from clay to gravel were intercepted in the wells to depths of 320 m where the mica schist basement was encountered below. Characterization of the drill cuttings from each well were used to produce lithologic logs that provide the framework for development of a conceptual geological model of the geothermal system. The sediments were characterized based on mineralogy, grain shape, sorting, and distribution of grain size from clay, silt, very fine-coarse sand, and gravels. The sediment characterization also provides porosity and permeability values that are important as input parameters for the numerical reservoir model.

In Figure 4.2, a SW-NE cross-section is used to demonstrate the lithostratigraphic stacking of the underlying sediments. Both N-S and E-W cross-sections are seen in the 3D model image (Figure 4.3). Coarse sand is the most common sediment type derived from the edge of the proximal alluvial apron. Several laterally extensive clay layers are evident and are most abundant in PS-12-1. The thickest and most extensive clay-rich layer seems to be located between depths of 200-275 m, about 50 m above the buried basement surface, and is intercepted in wells PS-12-1, PS-12-2, and PS-12-3. Another clay layer above the basement at ~300 m is present in all of the deep wells except

PS-12-3. The extensive clay layers may have formed during periods of increased subsidence relative to sedimentation or during high sea level as a marine-influence brackish lagoon. Understanding more about these clay layers beyond their geometry and alteration is outside of the scope of this work. Beneath this clay is a zone of silty sand that extends down to the basement-sediment contact. There are other laterally extensive clay layers and they are typically grey and silty-sandy (Figure 4.2). The lenses of gravel, most likely fluvial channel lag, have the highest primary porosity of the sediments and allow for the best communication of groundwater into the system as well as hydrothermal fluid migration. The gravels are typically thin and interbedded with clay or form distinct layers in the indurated zones.

Indurated sediments occur in the subsurface to the basement with varying degrees of cementation. The indurated sediments have a clean silica cement and tend to be moderate to well-sorted silty sand. The cement was analyzed through XRD and was found to be principally silica with trace amounts of muscovite and calcite (Woodward-Clyde, 1983). Penetration of these zones occurred in every well with the exception of S-1 and S-9. Induration seems to be greatest around PS-4 and forms a "chimney" with various lateral splays up section (Figure 4.4).

The composition of the bedrock is a mica schist that was determined from the lowermost ~20 m of core from the well PS-12-2. Bedrock was also intercepted in PS-12-3 with possible difference in depth. Due to the obliqueness of the cross-section, the actual change in depth to bedrock between the two holes is less dramatic than Figure 4.2

indicates. The maximum difference is ~10 m where the depth to bedrock in PS-12-3 might be lower. The exact bedrock contact while drilling PS-12-3 was ambiguous and was only indicated by an increase in mica flakes in the well cuttings. If this is a small offset and not the effect of changing surface topography, this could be evidence of a fault at depth. However, the orientation and dip of the probable fault remains elusive.

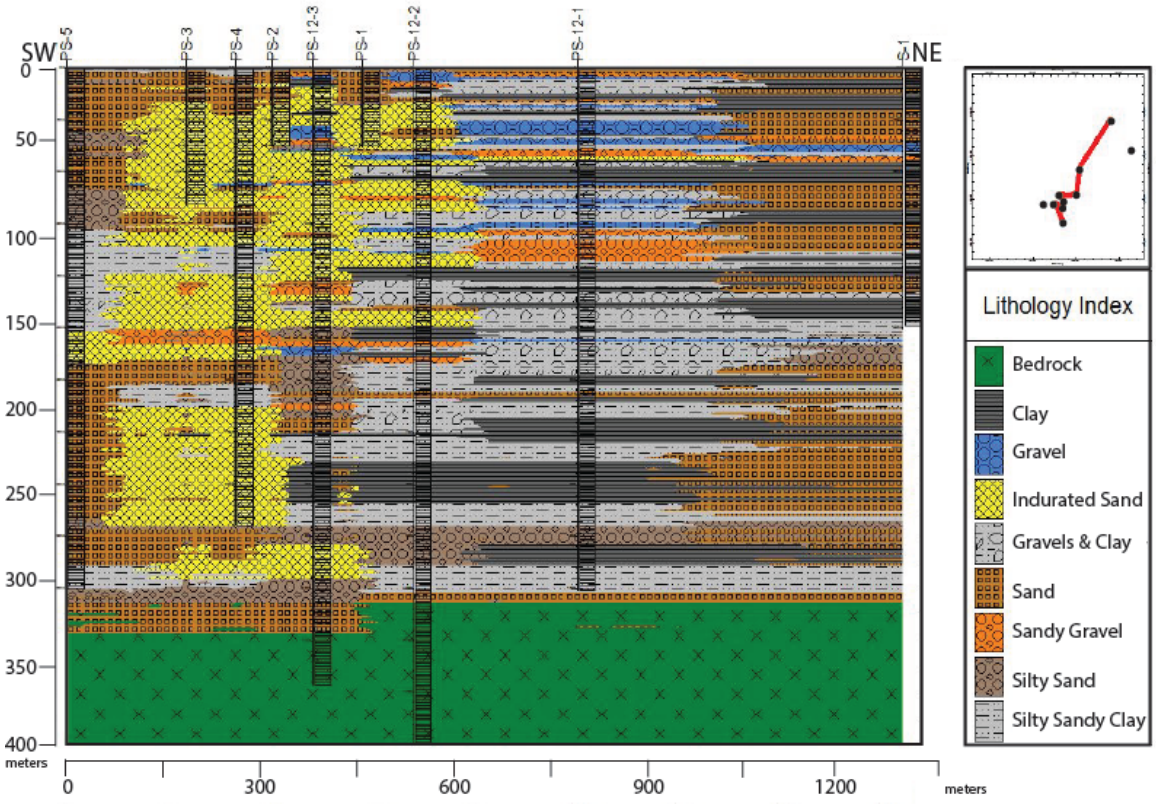


Figure 4.2: Southwest-northeast cross-section of interpolated lithologic logs. Created in RockWorks15.

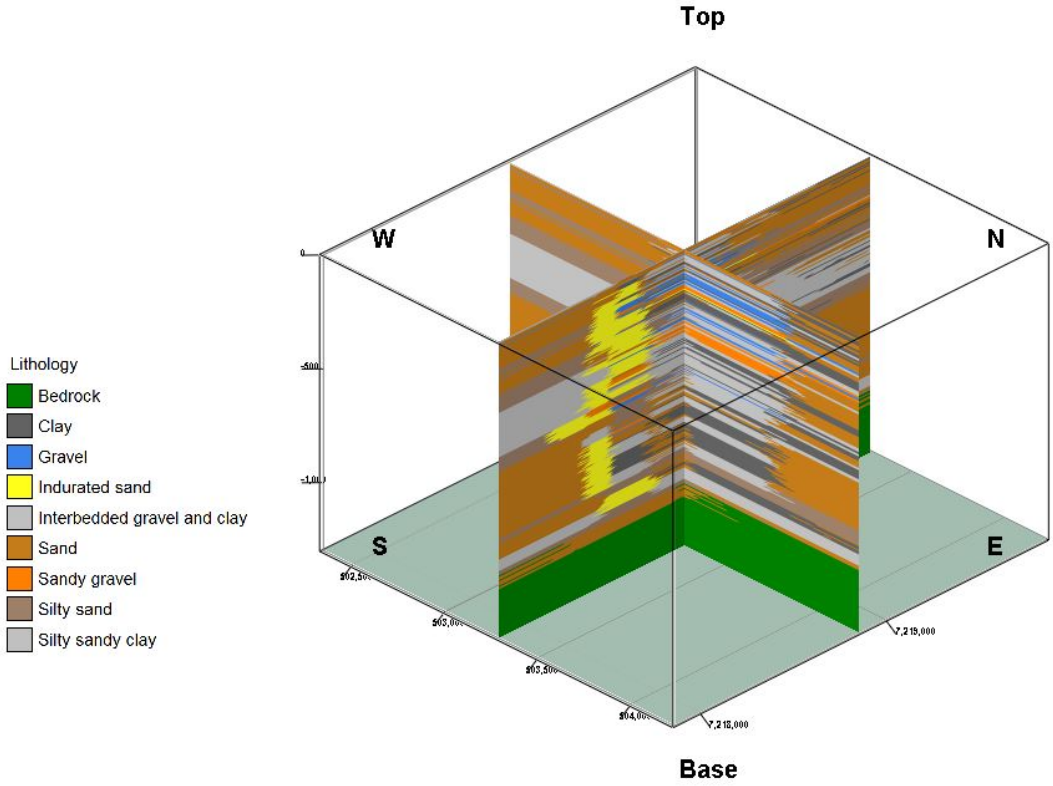


Figure 4.3: RockWorks15 3D model of the interpolated lithologic logs. Reservoir stratigraphy is interpolated between wells and extrapolated out of the model area.

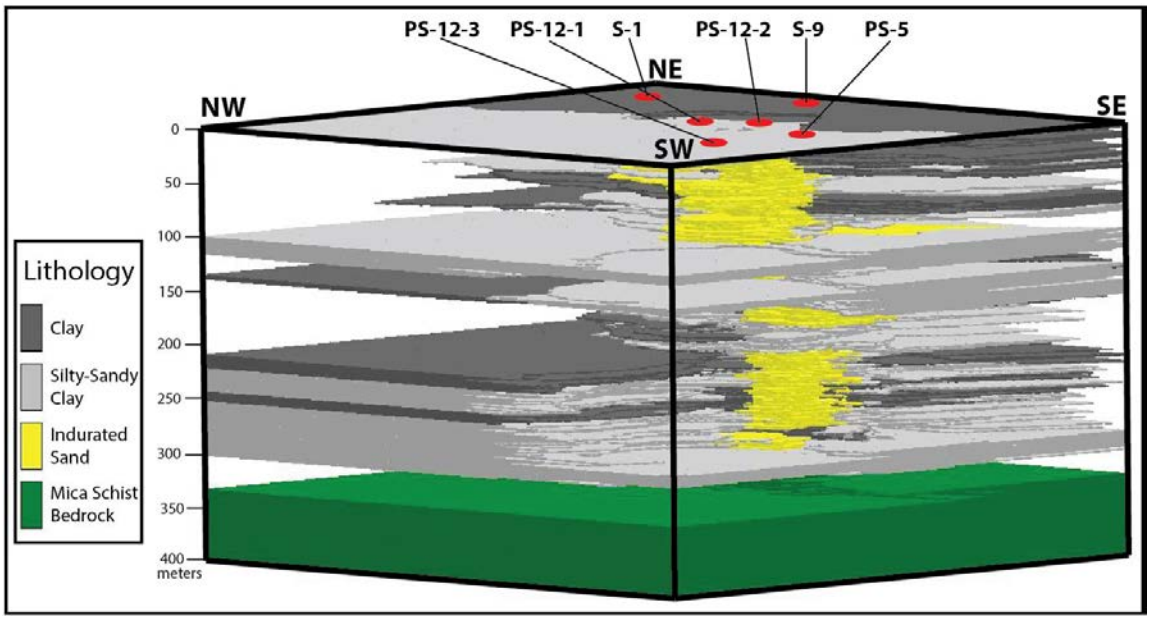


Figure 4.4: RockWorks15 3D model of major clay intervals and indurated zone. Modeled low permeability hydraulic barriers of clay intervals and the indurated zone with a "chimney-style" morphology extending from basement to surface. The six deepest wells are plotted on top.

4.3.2 Temperature Model

Temperature logs from the 11 wells and 64 Geoprobe holes were incorporated into the RockWorks15 isotropic model to produce the distribution (Figure 4.5). This temperature model has the same dimension of 4 km^2 as the lithostratigraphic model. The conditions of the model include the highest temperature 91 °C measured at depth to the lowest temperature of 1 °C measured in the permafrost. The permafrost temperatures were measured in Geoprobe holes to establish background temperatures. This range highlights the anomalously high heat of the hot springs in the center of the model. The western, southeastern, and eastern boundaries are marked by permafrost to depths of 100 m. The model extrapolated the cold background temperatures with a slightly increasing temperature gradient down to the bottom of the model. The increasing gradient of background temperatures surrounding the hot springs in the model is influenced by interaction with the hotter fluids at depth. The 40-50 °C isotherms extend from the center of the model to the southwest. Similarly, 40-50 °C isotherms are close to or below the basement surface on the edges of the model. The river cuts off the northwest corner of the model where no Geoprobe or well data is available.

To achieve an overall temperature distribution that reflects current observations from the field and other independent observations (Chittambakkam et al., 2013; Daanen et al., 2012; Haselwimmer et al., 2011), control wells were inserted into the model by using Geoprobe temperature data. The control wells were synthetically replicated from actual Geoprobe holes that intersected permafrost. The wells were placed at the model

boundaries to simulate realistic conditions and constrain the temperature model iteration. Three control wells (two on the western boundary and one in the southeast corner) were placed down to 30 m depth where the pink, ~1 °C isotherms are seen in the model to make the permafrost more robust (Figure 4.5). With a more constrained temperature model, the isotherms better reflect the nature of the geothermal reservoir.

The vertical and horizontal temperature distributions show the center of the geothermal system where the north-south and east-west cross-sections intersect (Figure 4.6). The geothermal system forms a large plume from the basement to the shallow subsurface. The width of the plume gradually decreases upwards where three depth slices and two cross-sections show the narrow neck of the 90+ °C temperatures of the plume between wells PS-12-1, PS-12-2, and PS-12-3 (Figure 4.7-4.8). The characteristics of the temperature model combined with the framework of the geologic model produce a cohesive conceptual model of Pilgrim Hot Springs discussed in the next chapter.

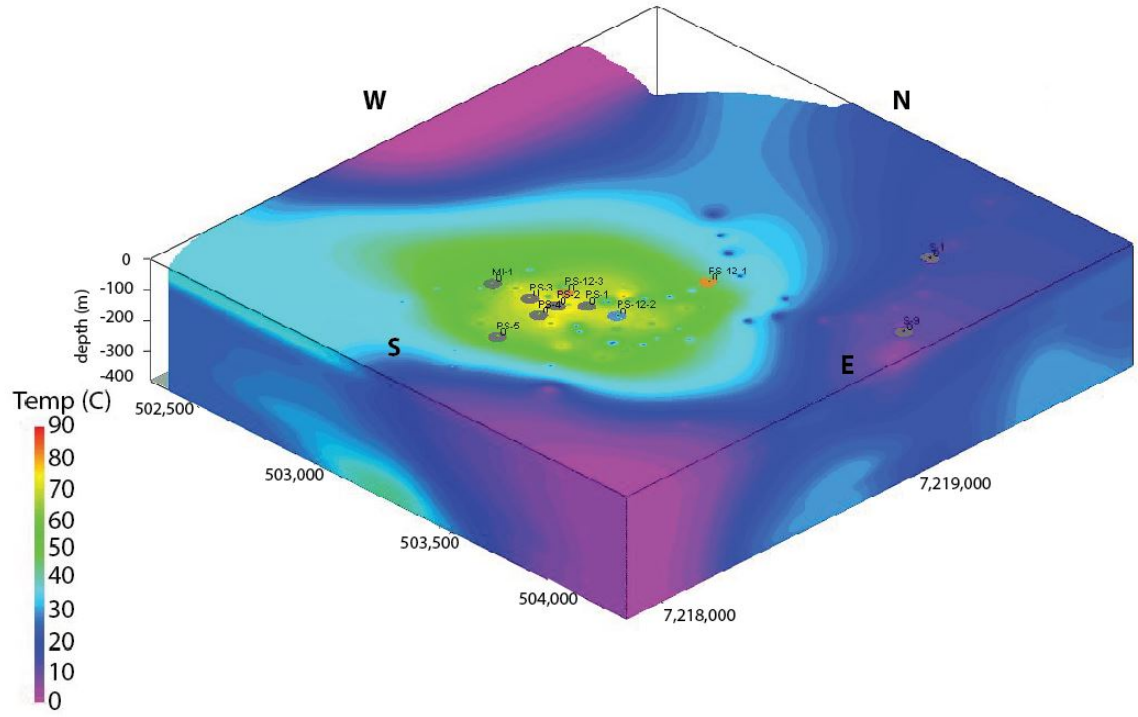


Figure 4.5: Southeastern view of the RockWorks15 temperature model. The total depth is 400 m and 4 km^2 wide. All eleven wells from the site are plotted.

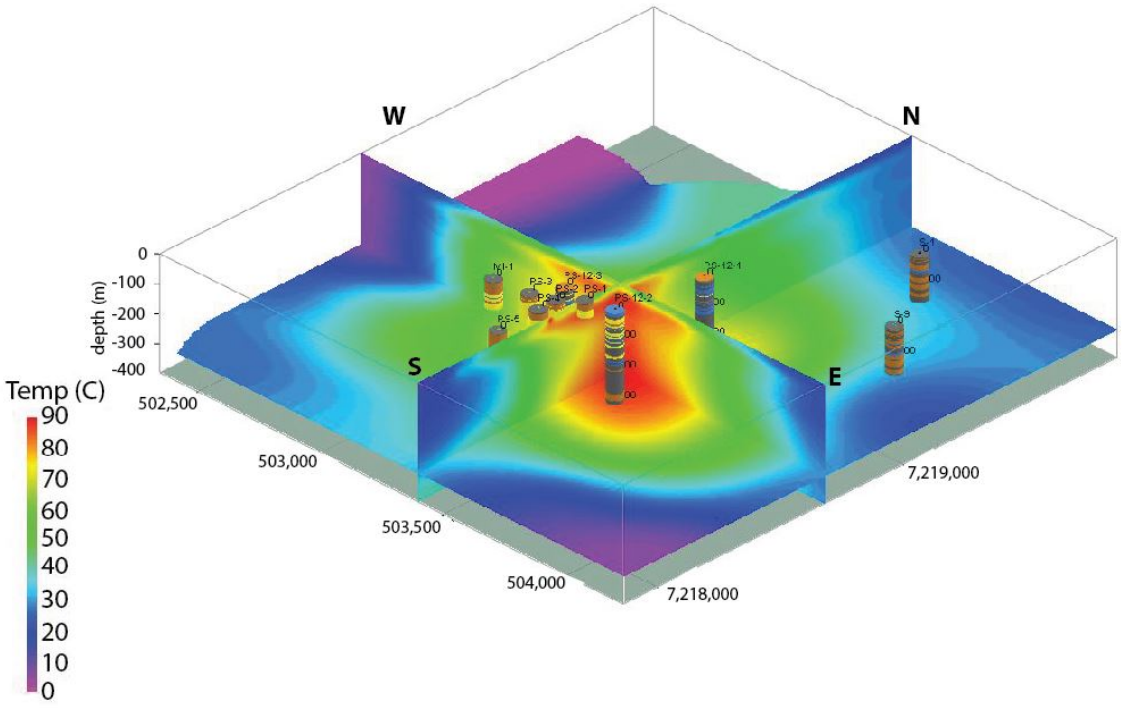


Figure 4.6: Vertical and horizontal slices of the RockWorks15 temperature model. A southeastern view of the RockWorks15 temperature model with north-south and east-west cross-sections and a 300 m depth horizontal temperature distribution slice slightly above the basement surface. All eleven wells are plotted as reference points.

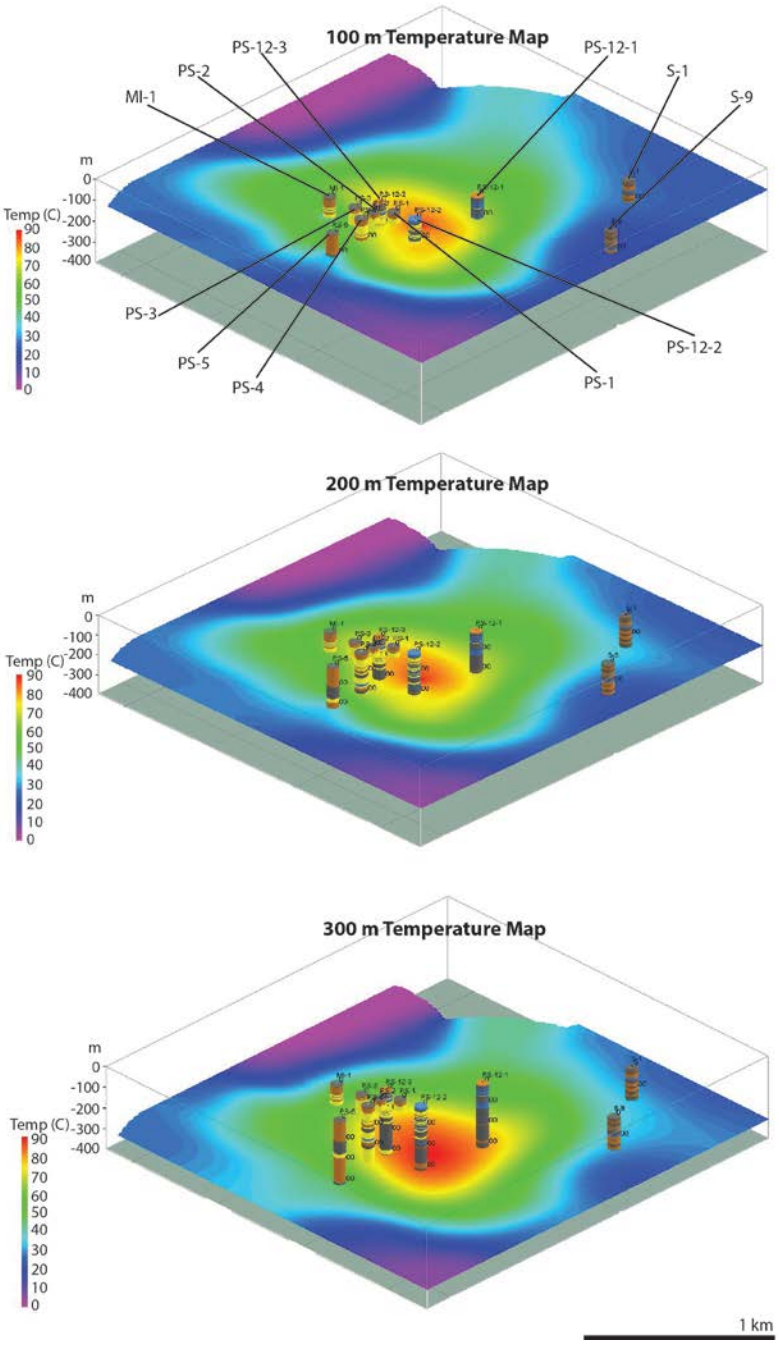


Figure 4.7: Three depth maps of the RockWorks15 temperature model result. A southeastern view of three depth slices at 100, 200, and 300 m from the RockWorks15 temperature model indicate the extent of the higher temperature distribution which narrows from the basement surface to the shallow subsurface. All eleven wells are plotted as reference points.

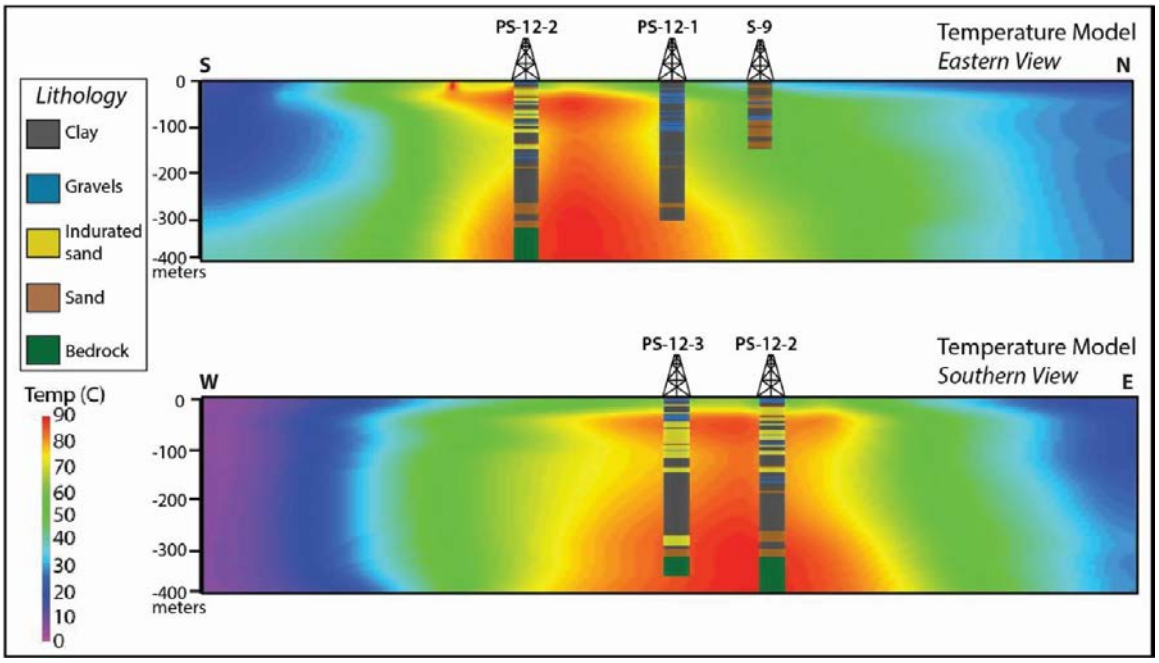


Figure 4.8: Two cross- sections of the RockWorks15 temperature model. The top is an eastern view (N-S) and the bottom is a southern view (W-E). Reference wells show lithostratigraphic units. The profiles are 2 km wide.

Chapter 5: Development of the Conceptual Model

5.1 Introduction

The goal of building a conceptual model of a particular resource is to best assess the gathered data as a cohesive picture of where different observed anomalies may correlate (Cumming, 2009). This provides possible targets for exploration. Essentially, this conceptual model integrates the cross-section of interpreted stratigraphy and structure, interpolated temperature isotherms, and mapped geophysical and geochemical surveys. These are overlaid to highlight the framework of the geothermal system. Understanding the geothermal system through a conceptual model allows for the prediction of subsurface conduits for the migration of hydrothermal fluids.

In order to achieve this understanding, several data sets are assessed and used to develop the conceptual model. Initially, lithostratigraphic relationships are surmised from lithologic and geophysical well logs. These relationships include comparing well log response to lithology and correlating from well to well. The correlations guide the construction of the 3D lithostratigraphic model as constraints to anisotropic interpolation and extrapolation to the model boundaries. The same process is conducted for temperature data with temperature logs being directly imported into the model software to create points for anisotropic interpolation. Temperature and lithostratigraphic integration demonstrates the geologic controls of isotherm placement through generating model profiles. The MT data can be directly applied to the lithostratigraphic and

temperature relationships as indicated by changes in low-to-high resistivity. These data sets comprise the conceptual model.

The interpretations of the geothermal system through this conceptual model are not without limitations. The spatial extent of the data gathered at the site was greatly limited by access on stable ground and existing trails. This includes the MT stations placed around the site that had to avoid flooded fields and permafrost, suitable ground for drill pad placement for the drilling locations of the deep wells, and general road/trail access for vehicle and heavy equipment. The largest constraint of the conceptual model is the lack of deep well lithostratigraphic and temperature data outside of the NE-SW lineated density of wells on site. The density of the well data, both Geoprobe and deep well, is greatest in the middle of the model which inherently produces biases on the consideration of various scenarios on the transport of hydrothermal fluids in the subsurface. However, no compelling evidence has been discovered as of yet that would justify drilling deeper wells outside of this trend on the hot springs site.

The conceptual model is complemented by the numerical model which evaluates the temperature and fluid flow conditions at Pilgrim Hot Springs for the purposes of testing the total energy flux estimation and deeper reservoir location. The sediment descriptions and lithostratigraphic architecture presented in this conceptual geologic model have been incorporated into the numerical model to provide permeability calculations for a more effective fluid flow model.

5.2 Discussion of the Conceptual Model

In general, the Pilgrim geothermal system can be subdivided into a shallow outflow aquifer and a deeper reservoir beneath a clay cap connected by a very narrow conduit with 91 °C upflow (Figure 5.1). Temperature logs increase to 91 °C at 25-50 m with a reversal at 30-100 m. The isotherm distribution is visually interpreted from temperature logs (Figure 5.1). The peak in temperature is the result of the outflow of geothermal fluids and the increasing temperature gradient is due to the heating of the deeper geothermal reservoir. The outflow direction is mostly concentrated to southwest and northeast. All wells show an increasing temperature gradient below the reversal with differing rates. The temperature gradients suggest the upflow is located between PS-12-1, PS-12-2, and PS-12-3. Stratigraphic correlations based upon well log data indicate several clay layers throughout the section with a dominant clay horizon at 200-300 m depth. Induration in the sediments is mostly concentrated between wells PS-4 and PS-12-3 and occurs from basement to the shallow subsurface with a chimney-like shape.

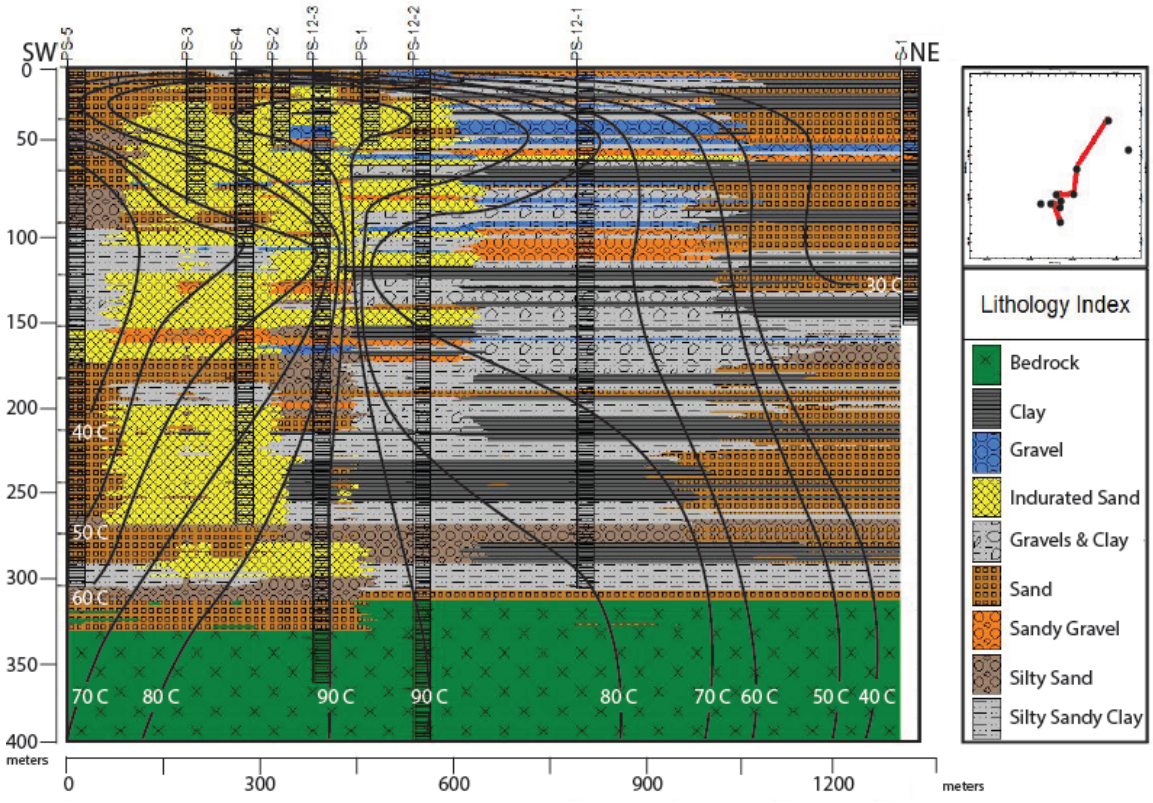


Figure 5.1: Stratigraphic cross-section of the geologic model with isotherms. Temperature isotherms are derived from the temperature model and indicate a shallow outflow aquifer above 100 m, a narrow upflow from 100 m to 300 m, and a deeper reservoir connecting to the system in the vicinity of PS-12-2 and PS-12-3.

Regarding the lithostratigraphic and temperature data, the conceptual model contains a data set greatly restricted in the size of inspection area. This is the result of the density of well data occurring in a small area, many as close as 100 m, and along a SW-NE trend. This trend makes confident extrapolation into other areas of the model that lack well data difficult. Inferring the extent of the modeled lithostratigraphic units and isotherms without well data is achieved through the geophysical surveys, notably the MT survey. The combination of MT ground-based resistivity and temperature data may delineate the upflow of hydrothermal fluids from depth. The temperature data of both the deep wells and shallow Geoprobe holes guide the modeled isotherms. However, the MT does not directly image the high-temperature fluids, but rather the associated hydrothermal alteration products in the sediments and bedrock (Cumming, 2009). The spectral investigation of AlOH absorption and estimated smectite content through methylene blue analysis reveal a close relationship of low MT resistivity and hydrothermal alteration (Figure 5.2). This can be used to elucidate the areas of past and present alteration through the interaction with hydrothermal fluids. By these proxies, the location of the upflowing fluids can be inferred.

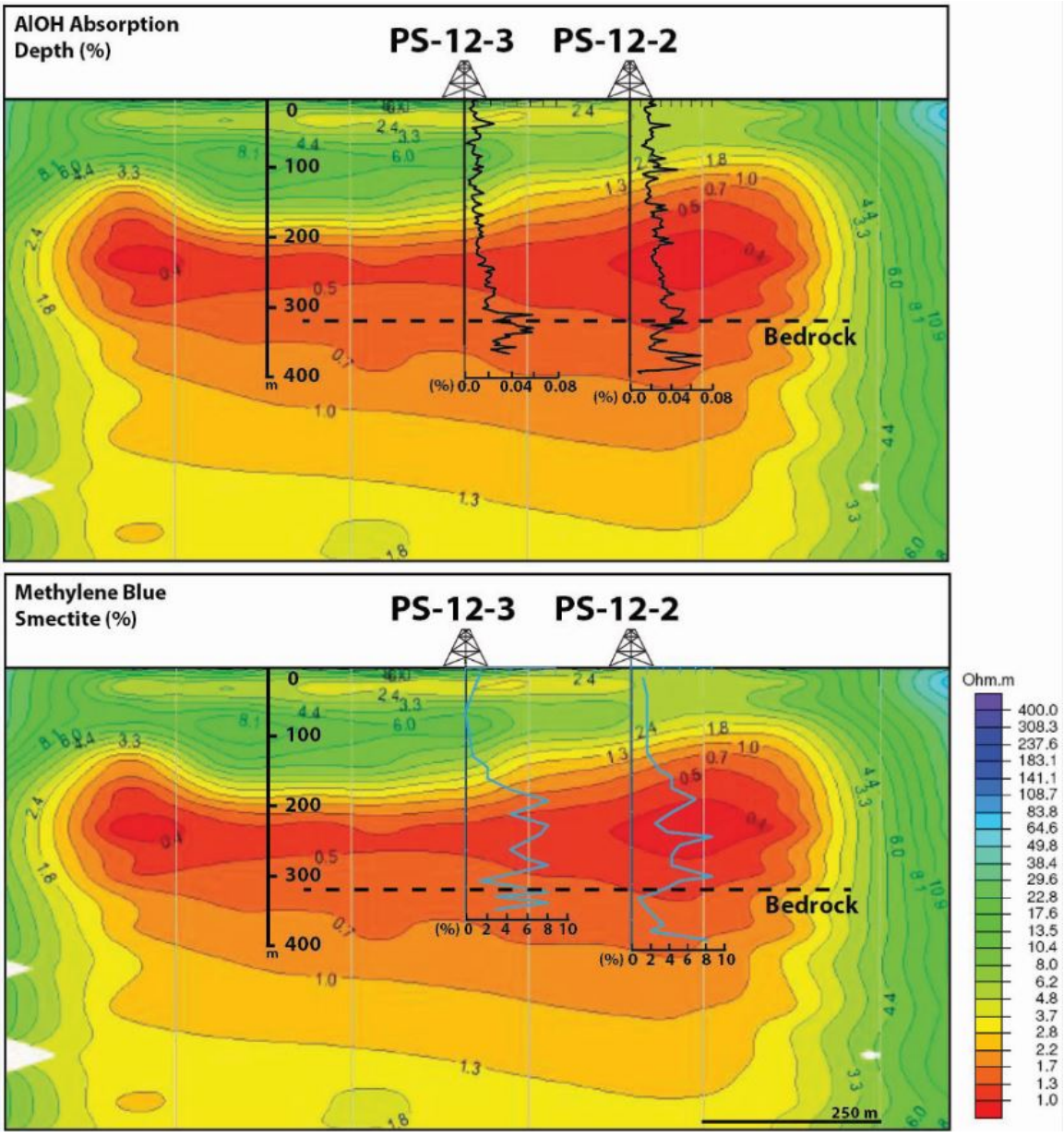


Figure 5.2: AlOH absorption and methylene blue results plotted on MT profile. An example MT resistivity profile is used for comparison to AlOH absorption (top) and methylene blue analysis (bottom). Both methods correspond with an increase in AlOH absorption and estimated smectite content as proxies for hydrothermal alteration in the low resistivity zone. MT data provided by FUGRO (2012).

MT and temperature distribution plan maps are used to highlight the various elements of the geothermal system and demonstrate the extent of associated alteration. The base of the shallow thermal aquifer is located at 50 m depth and shows an area of low resistivity (<3 ohm-m) constrained by >70+ °C isotherms between wells PS-12-1, PS-12-2, and PS-12-3 (Figure 5.3). The conductor is most likely discontinuous altered clay (smectite) layers, common low-temperature (<100 °C) hydrothermal alteration products, as no clay intervals appear laterally continuous through all the wells at this depth. The western and southern resistive zones bordering the hot springs are due to permafrost. With present day temperatures and interpreted alteration in the MT map showing a similar spatial extent, the outflow is apparently discharging hot fluids at this location and depth without much lateral movement or migration from this area through time. Both the 100 m and 200 m MT and temperature maps show similar-sized conductive and high temperature zones, respectively (Figures 5.4-5.5). At 100 m, the hottest temperatures are modeled to occur slightly to the northwest of PS-12-2 while the MT map shows a conductive zone of proportional size to the southeast of the same well. This discrepancy may result from the temperature model prediction of where the high temperatures occur. At this depth, the model is relying on 11 wells as control points for isotherm placement and all wells are displaying a temperature reversal at this depth. The higher temperatures could just as likely be placed at the approximate location of the conductive zone in the MT map. Both maps suggest the conduit feeding the outflow is narrow (<100 m) and difficult to predict as well as resolve through modeling.

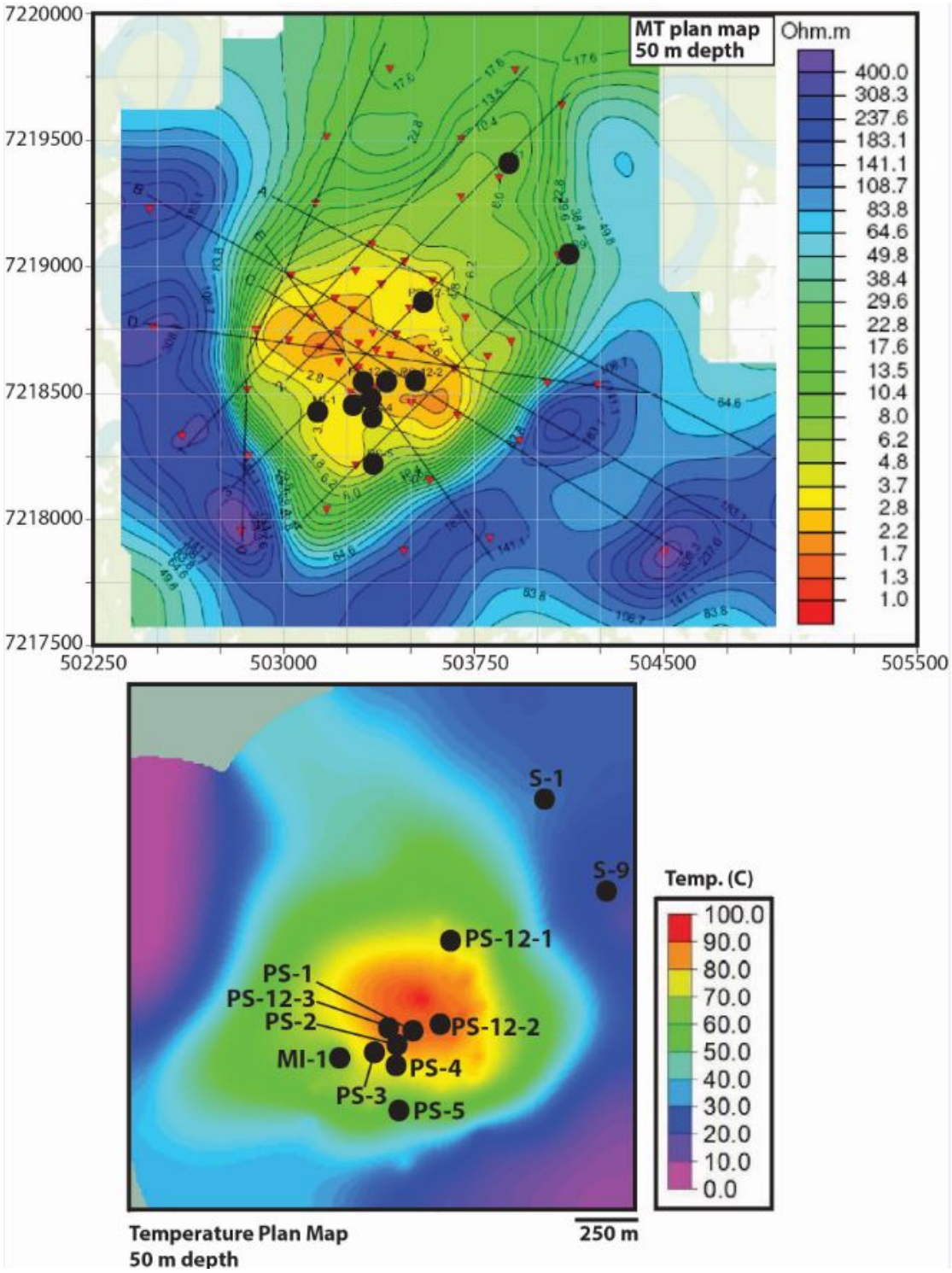


Figure 5.3: MT and RockWorks15 temperature model plan maps at 50 m depth. The red triangles indicate MT station location.

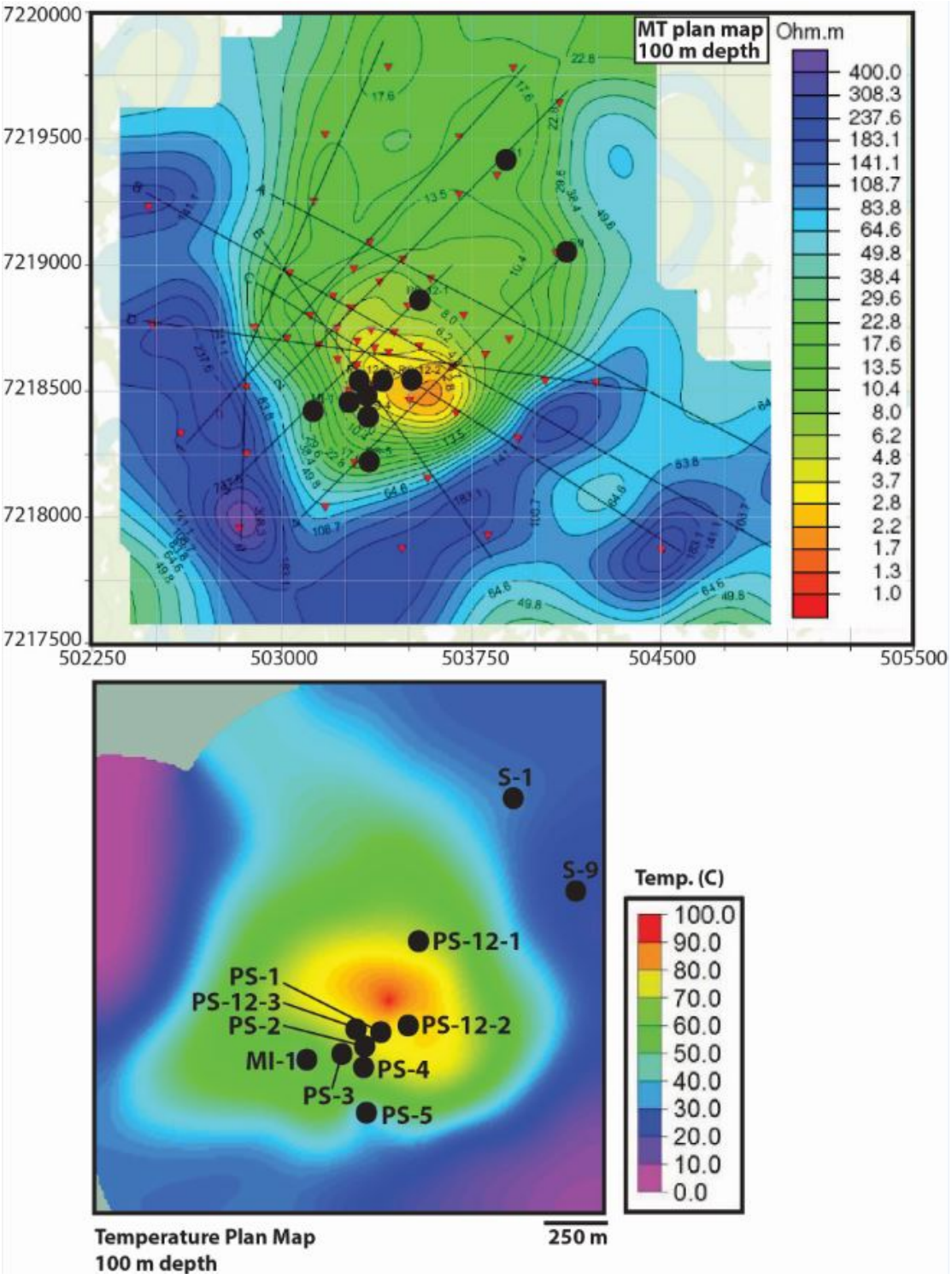


Figure 5.4: MT and RockWorks15 temperature model plan maps at 100 m depth. The red triangles indicate MT station location.

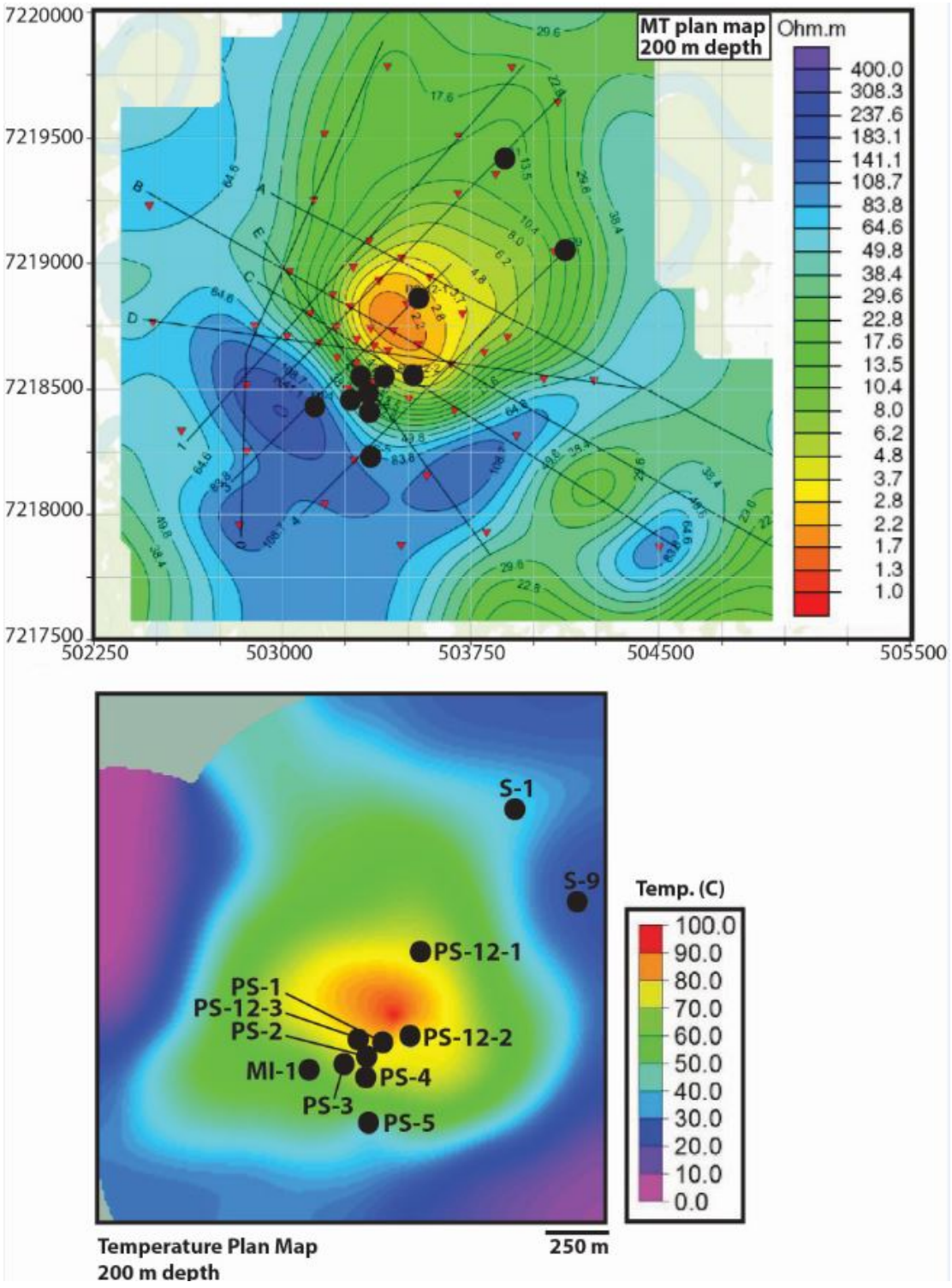


Figure 5.5: MT and RockWorks15 temperature model plan maps at 200 m depth. The red triangles indicate MT station location.

The 200 m depth maps both indicate a broader zone of conductivity and zone of higher temperatures as all the wells show an increasing temperature gradient. The numerous intervals of interbedded clays, sands, and gravels at this depth may be effectively transmitting hydrothermal fluid across the wells, protecting against the colder meteoric water. The 300 m depth maps show a significant difference in interpreted alteration due to high conductivity and the predicted zone of high temperatures. Until this depth, both data sets demonstrate a reliable correlation of alteration and high temperature fluids. However, the MT suggests a zone of increased conductivity in a large area that centers near PS-12-1 and bends back away from wells PS-12-2 and PS-12-3. This is surprising as the temperature map of the same depth indicates a large area of high temperatures centered between these wells with PS-12-2 being the hotter well at 91 °C and PS-12-1 at 80 °C. Both wells display similar values of estimated smectite content and AlOH absorption at this depth, indicating that both have experienced similar degrees of alteration. Also, the mineral assemblage of mixed smectite-illite and kaolinite clays have very similar abundances at this depth in both wells (Appendix B.1-B.3) and form in the active hydrothermal flow regime of fluid circulation (Mas et al., 2006). This means both wells have been subject to nearly the same extent of hydrothermal alteration in the past. However, the MT shows a more conductive signature at PS-12-1 and higher temperatures are centered on PS-12-2. This is interpreted to mean that the conductive signature, associated with smectite clay development, possibly shows a large clay layer extending from PS-12-1 to the north, west, east, and tapers around PS-12-2 and PS-12-3 where the clay abruptly pinches out and hot fluids may migrate up and around its edge. The pinch

out is supported by the southwestern wells PS-4 and PS-5 where this interval contains sands and indurated sediments, thus the loss of the conductive signature.

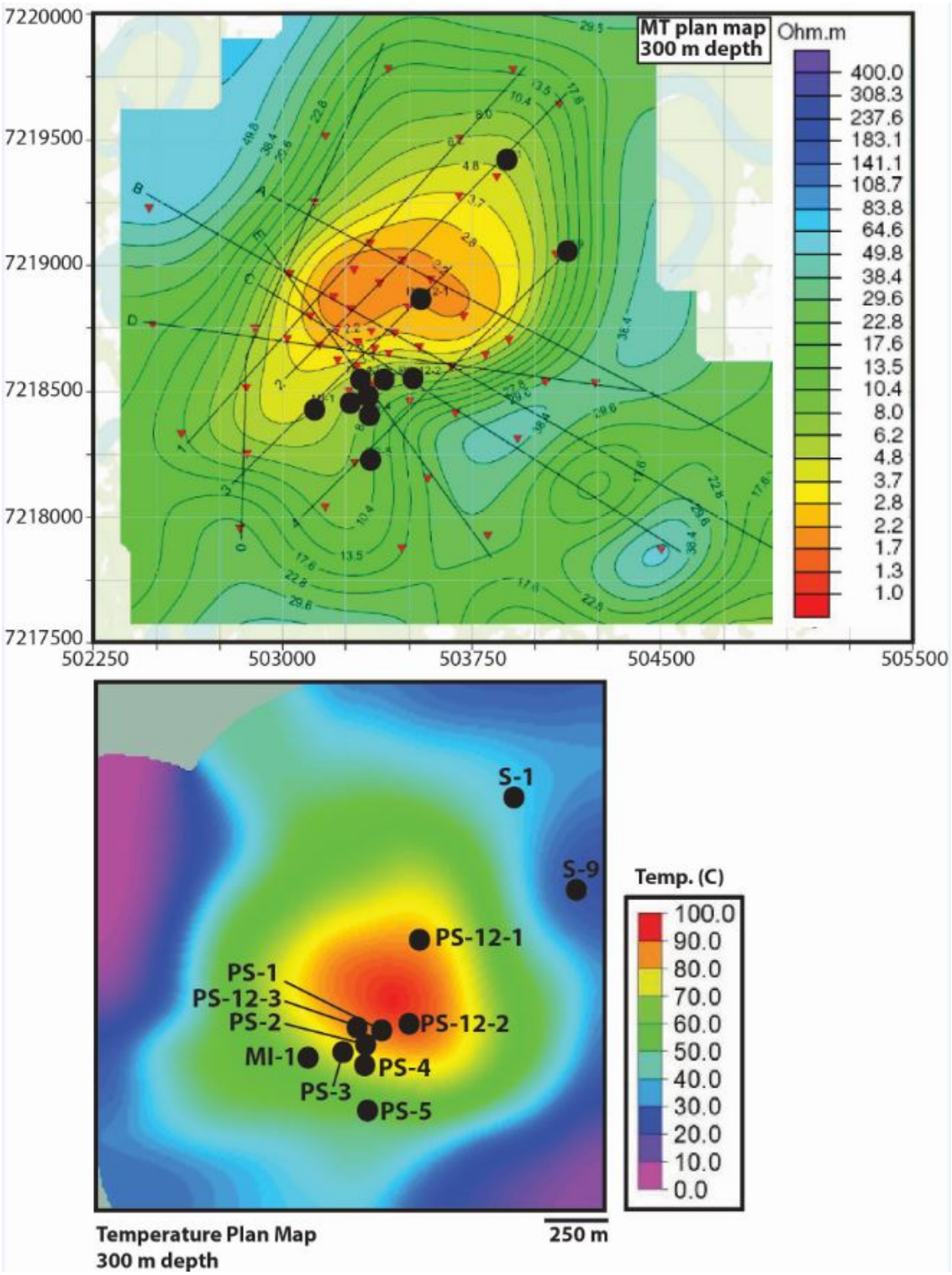


Figure 5.6: MT and RockWorks15 temperature model plan maps at 300 m depth.

The hot fluids are seemingly upwelling from a location closest to PS-12-2 due to the highest bottomhole temperature of 91 °C at the basement-sediment contact. The outflow temperatures in PS-12-2, PS-1, PS-2, PS-3, and PS-12-3 all exhibit 90-91 °C temperatures, meaning rapid and/or insulated transport to the shallow subsurface through a conduit of significant permeability. This interpreted location of the upflow is also supported by the extent of the indurated sediments. The cement of the indurated sand is dominantly composed of silica, as verified by x-ray diffraction analysis (Woodward-Clyde, 1983). All wells (with the exception of S-1 and S-9) show induration down to depths of 150 m (PS-12-1 with a very thin 3 m indurated interval at 60 m), PS-4 with induration to 250 m, and PS-12-3 being indurated to 275 m. PS-12-2 is not indurated at this interval above bedrock, maybe due to size of the sediments. From 300-320 m, PS-12-2 has coarse sand that is more porous than the silty-fine sand where induration occurs. Smaller pore spaces in the finer sediments tend to become cemented through precipitation from super-saturated fluids first whereas larger pore spaces in the coarse sand are often preserved and non-cemented (Cox et al., 2002). With high temperatures centered around PS-12-2 and dense induration occurring close to the bedrock surface in PS-12-3, the upflow is predicted to occur between the two wells from the bedrock fracture and/or fault conduit. This location plots underneath wells PS-1 and PS-2. Although both are shallow wells of only 50 m depth, these wells are very well indurated and PS-2 in particular, "vigorously degassed" at 15 m depth during drilling (Kline, 1980). The composition of the gas was guessed to be CO_2. Liss and Motyka (1994) sampled H_2 in Pilgrim wells and discovered the highest concentrations in PS-1. These gas

concentrations may imply close proximity to rapidly upwelling hot fluids where tightly-sealed indurated sediments retain the exsolved gases directly from the fluids. Regardless, considering an estimated diameter of <100 m for the upflow conduit, the best placement of this conduit appears to between PS-12-2 and PS-12-3.

A simple conceptual model of MT profiles and isotherms is shown in Figures 5.7-5.8. MT Profile D shows a large, very low resistivity pattern (<1 ohm-m) from 150 m to 400 m that extends into the top of the basement and is sharply bounded by increasingly resistive zones on the west (left) and east (right) (Figure 5.7). Areas of high resistivity values are interpreted as permafrost (0-100 m) and cold regional groundwater influx. The <0.5 ohm-m zone matches very closely to the modeled stratigraphy of the thick clays from 200-275 m in wells PS-12-2 and PS-12-3 (Figure 5.8). The clay interval is a mixed layer clay and resembles a low permeability, low resistivity clay cap to a geothermal reservoir underneath (Cumming, 2009). A shallow, flat, low resistivity layer of 2.4 ohm-m at 50 m depth aligns with the indurated zone in MI-1 and PS-12-1 (Figure 5.8). A deep conductor at ~800 m depth appears in Figure 5.8 as marked by the blue box. This is an artifact of the 3D MT modeling algorithm that projects the conductor into infinite size beyond the spatial boundaries of the survey data range. Above the blue box is a strongly conductive zone beneath MI-1 and stretches to PS-5 in other MT cross-sections. This zone could be the result of smectite clay development in the bedrock through hydrothermal fluid flow contact or localized heterogeneity in the mica schist bedrock. Turner et al. (1979) mapped local graphitic schist in the bedrock exposures in the Kigluaik Mountains. If graphite is present in the bedrock beneath Pilgrim, it would

result in a very conductive signature and would transmit fluids very efficiently due to its mineral structure (Cumming, 2012). Both interpretations are inherently difficult to prove or disprove with the lack of bedrock drilling on the western edge of the hot springs site. However, PS-5 has a bottomhole temperature of <50 °C just 50 m above the bedrock surface. This makes extensive smectite development in the shallow bedrock seem unlikely. In the event that it is smectite from past alteration, the clay is likely plugging fractures or faults and mitigating vertical flow to a point of entry into the sediments closer to the center of the hot springs area. This is incorporated into the cross-sections as lateral splays of decompressing heated fluids exiting the bedrock fractures shown as kinks in the isotherms at the bedrock surface.

Groundwater flows from the resistive western and eastern boundaries into the system where it eventually mixes with the outflow. A blue resistive zone under MI-1 shows how the cold water enters the system from the south and west from under the permafrost (Figure 5.8). Realistically, the flow is generally directed into the cross-section and continues to the north towards the Pilgrim River. The thermally-buoyant outflow emanates out from the top of the 91 °C plume with a stronger flow to the west and southwest above the influx. Isotherm placement is based on the distribution of temperatures from the wells. The tightly-spaced isotherms of 90-60 °C indicate low permeability correlating to clay layers and indurated sediments (Cumming, 2009) (Figure 5.7). Similarly, the close 30-80 °C isotherms converge at the top of the clay cap of the geothermal reservoir. A deeper heat source of 100+ °C has been placed under the

PS-12-2, although the exact depth and location is hypothetical and only corresponds with the dip of the low resistive zone into the bedrock.

The conceptual model proposes a shallow outflow aquifer in the indurated sediments with a thin clay cap at 50 m depth. The upflow has been placed between PS-12-2 and PS-12-3, although it is very narrow (<100 m) and the exact location is uncertain. A small convection cycle may feed into the influx of cold water where cooler outflowing fluid mixes with the meteoric water. The upflow of the 91 °C geothermal fluids is a vertical conduit from basement to outflow and is constrained by the low permeability indurated sediments. The upflow also correlates well with the indurated zone possibly due to the porosity and permeability of the cemented sand that acts as a reservoir for geothermal fluids and can vertically transmit fluid with less heat loss than unconsolidated sediments. When contemplating future drilling targets, drilling between PS-12-2 and PS-12-3, close to PS-1, is the most promising location. Both the MT and temperature maps suggest lower temperatures any direction more than 500 m outside of the area from MI-1 to PS-12-1. This is evidenced by colder Geoprobe hole data and an increase in resistivity.

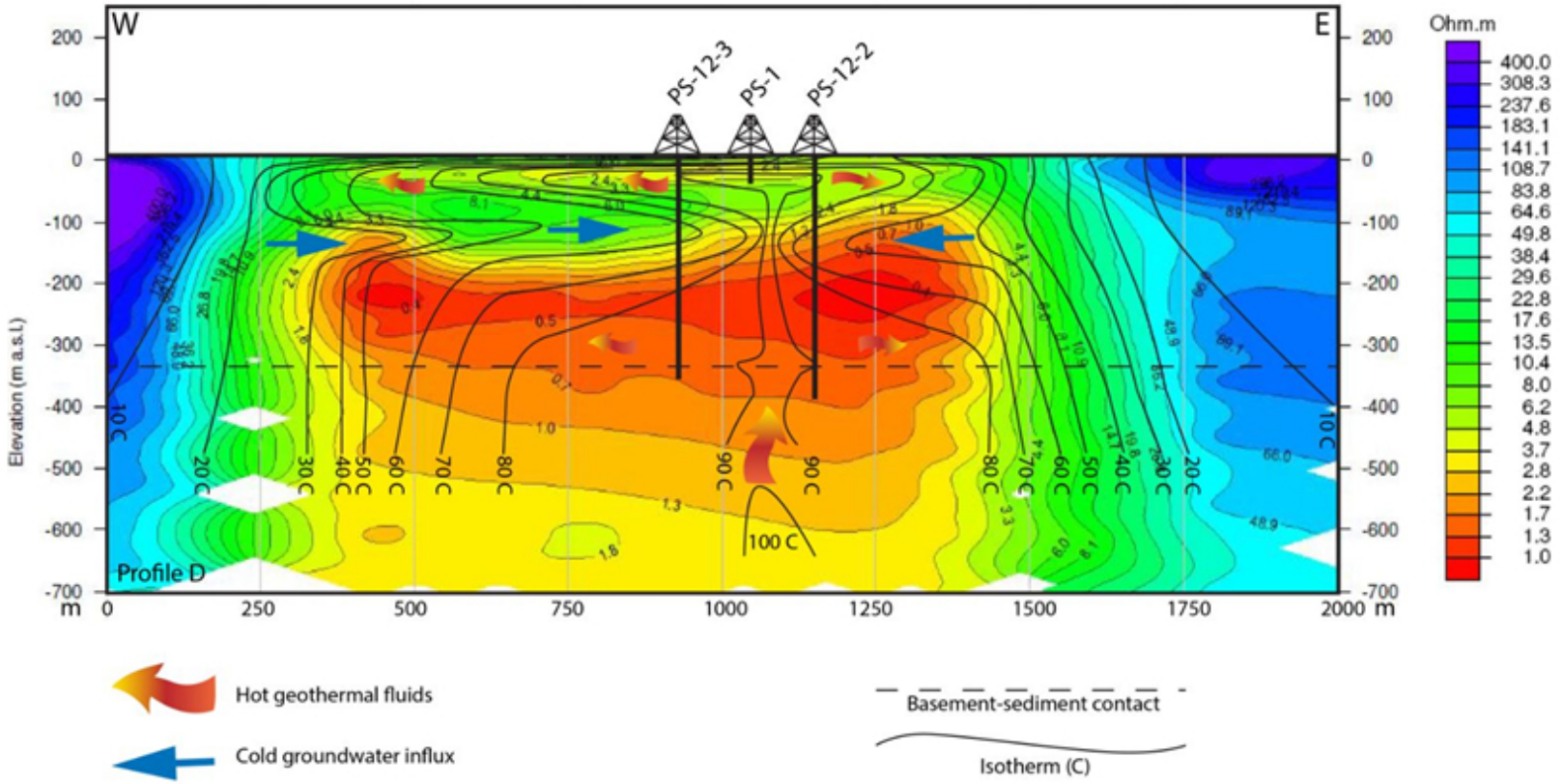


Figure 5.7: Simple conceptual model cross-section utilizing the W-E Profile D of the MT survey. Isotherms are plotted from 10-100 °C with hot fluid and cold fluid arrows to indicate direction of flow. Bedrock-sediment contact has been dashed to indicate approximate extent.

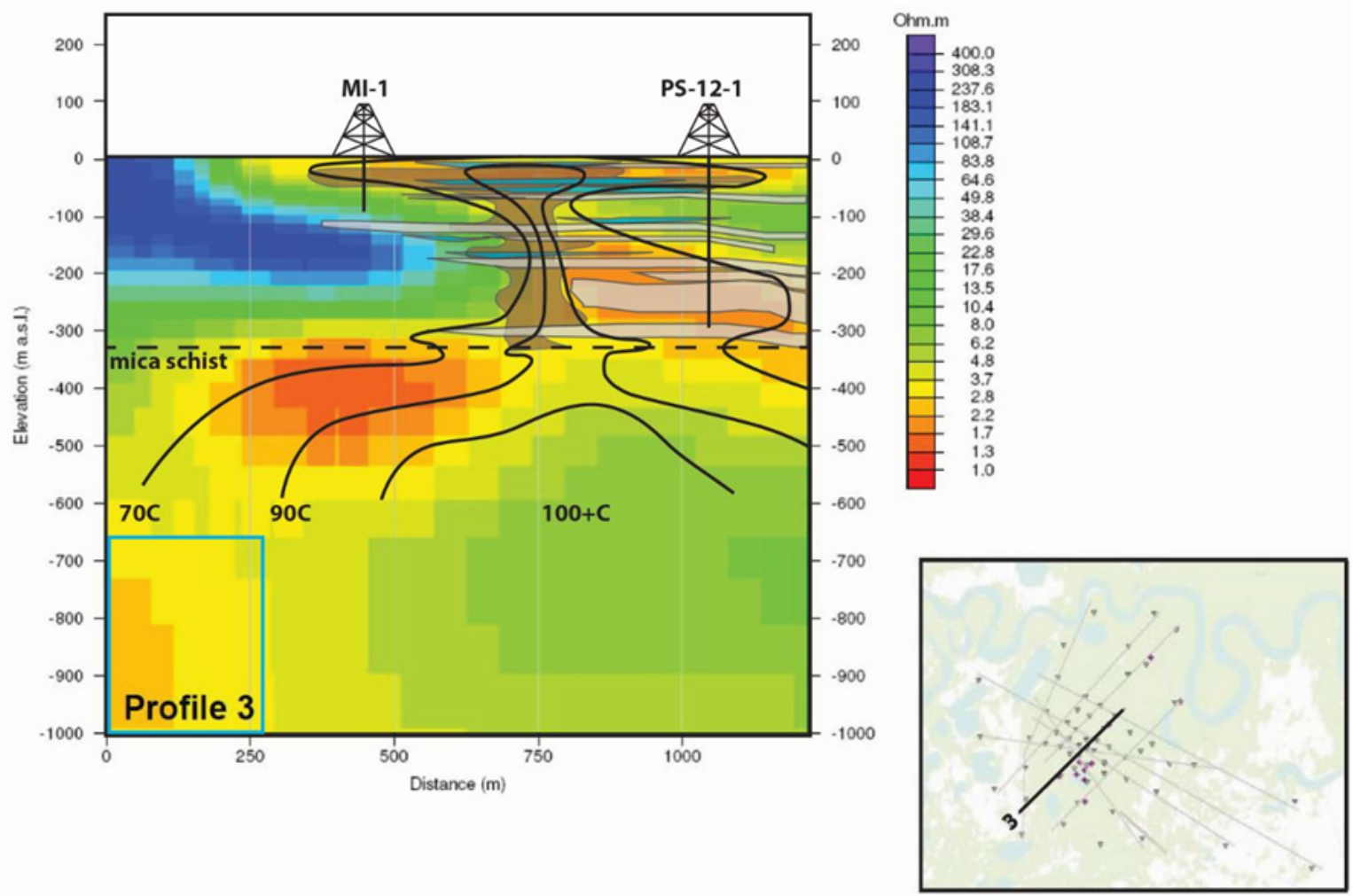


Figure 5.8: 3D MT Profile 3 overlaid with lithostratigraphy. Clay is gray, gravels are blue, and the induration is shaded in brown. SW is left and NE is right. MT data provided by FUGRO (2012).

As indicated in the broader, yet more shallowly focused electromagnetic survey, the conductive signature of the geothermal system at Pilgrim shows a narrow extent west-east and a larger extent north-south marked by the red boxes (Figure 5.9). The extent of the geothermal system is inferred from the occurrence of permafrost at the system's boundaries. With resolution only to 100 m depth, the shallow conductive response from outflowing hydrothermal fluids discharging into the groundwater and river extends as much as 4 km to the north at the base of Hen and Chicken Mountain. The conductive signal could be the result of the increased salinity of the northern directed regional groundwater flow mixing with the geothermal fluids which would make the system appear much larger in the north-south cross-section. Geoprobe shallow temperature surveying and an MT survey could be used to evaluate the conductive response, specifically to the northeast where Turner and Forbes (1980) identified a small thermal expression at the base of Hen and Chicken Mountain.

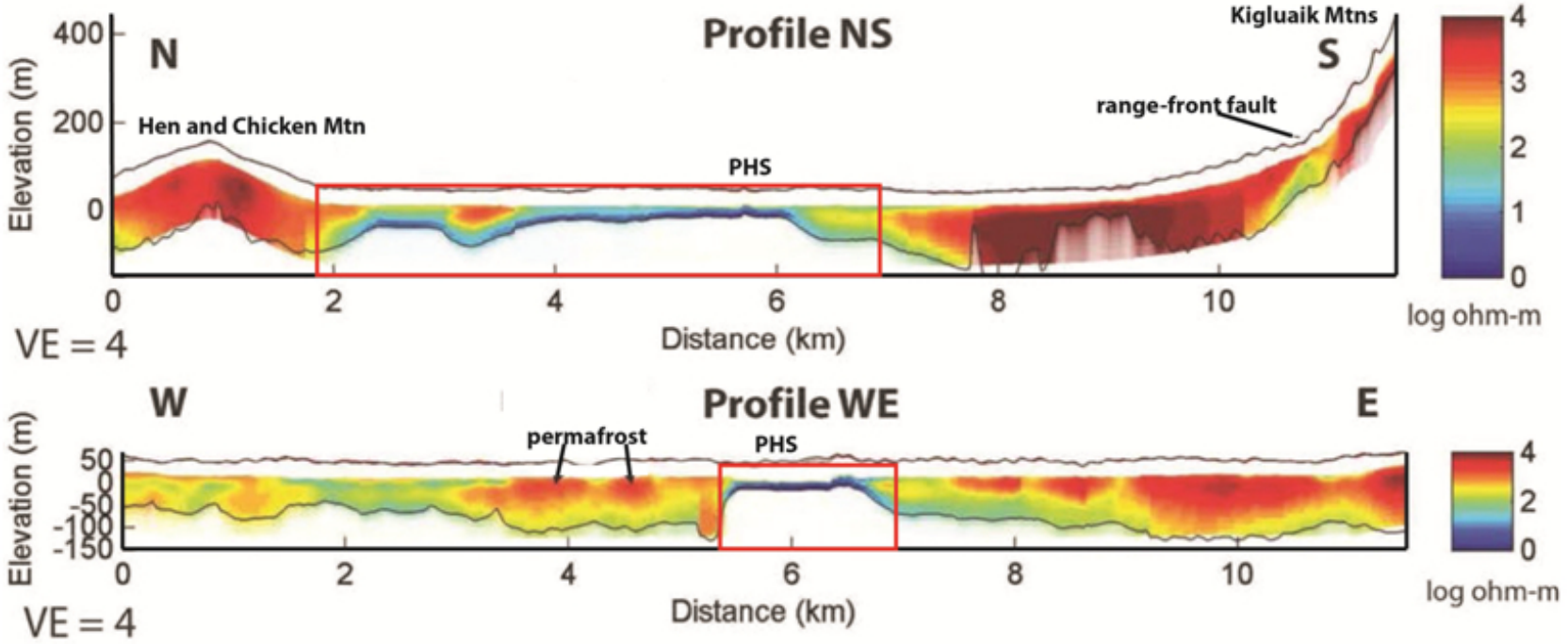


Figure 5.9: USGS airborne electromagnetic resistivity survey of the Pilgrim River Valley surrounding the hot springs area (McPhee and Glen, 2012).

5.3 Conceptual Model in a Regional Context

When considering the structural style and sedimentary architecture of the Pilgrim River valley alluvial basin with limited subsurface lithologic data, comparison to analogue basins can provide context for discerning the basin morphology. The Basin and Range geologic province in the Western U.S. contains many low-temperature geothermal systems that exhibit similar characteristics to Pilgrim. The structural controls on many Basin and Range systems are large normal faults commonly with step-overs, fault intersections, and terminations (Cashman et al., 2012). Heat for the geothermal systems is derived from deep circulation along the major fault systems (Blackwell and Kelley, 1994). Models for rift valley and asymmetric alluvial basin stratigraphy commonly include wide aprons of coarse-grained sand to gravel alluvium along the range faults and less extensive finer sediment fill in the center at the distal edges of the alluvial fans (Blackwell and Kelley, 1994; Bosworth and Morley, 1994; Okaya and Thompson, 1985). Lacustrine and floodplain clays, deposited during periods of subsidence in active extension, act as low permeability aquicludes that promote heat retention in the migrating hydrothermal fluids. The coarse-grained alluvial gravels form thick wedges along the deeper portions of the basin and thin distally (Blackwell and Kelley, 1994). These gravels allow mixing with groundwater or cross-range flow and typically exhibit depressed isotherms where heat loss is greatest (Blackwell and Kelley, 1994). Low permeability sediments are necessary for shallow geothermal systems to exist in alluvial basins because they facilitate heat conduction from upflowing fluids (Blackwell and Kelley, 1994).

The facies model examples mentioned above of asymmetric alluvial basin stratigraphy guided the understanding of the Pilgrim River Valley basin in the context of the geophysical survey results and field observations. Figure 5.10 shows the idealized cross-section of overlapped isostatic gravity, ground magnetic, and aeromagnetic resistivity data with fault orientations drawn to scale to illustrate the basin. The ground magnetic line shows an anomalously low value while the isostatic gravity dips in response to a relative increase in gravity. Low values in the ground electromagnetic survey possibly indicate hydrothermal fluid flow zones that reduce the magnetization of the bedrock (Schwering and Karlin, 2012). The Pilgrim Hot Springs conceptual model is placed in the context of this figure.

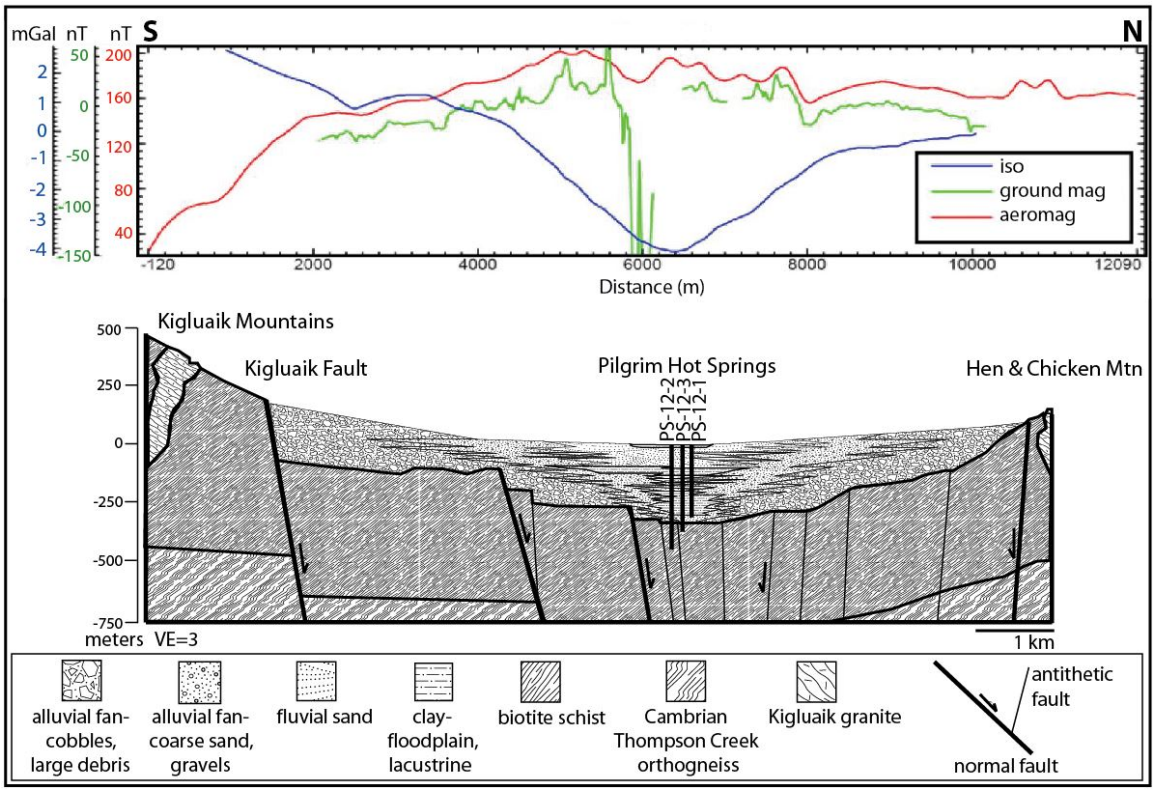


Figure 5.10: Interpreted basin cross-section of the Pilgrim River Valley. Interpreted from isostatic gravity (iso), ground magnetic (ground mag), aeromagnetic (aeromag), and drilling data as well as measured strikes and dips of fault planes that intersect the surface. The cross-section is south to north (left to right). Survey data provided by Jonathan Glen.

In a larger context, Pilgrim Hot Springs may be located in an area of significantly deep and numerous fractures and faults in the underlying graben. Miller et al. (1975) concluded from a regional aeromagnetic survey conducted in 1972 that the springs may be fed from an east-west trending conductive fault extending from the Bendeleben fault into the vicinity of Pilgrim Hot Springs. This was also previously proposed by Sainsbury et al. (1969). The bedrock and surficial geologic map, however, has a major ~N-S directed fault projected across the basin that transects the western edge of the thawed ground at Pilgrim (Turner et al., 1979). The fault is placed here due to a ~1 m terrace that runs roughly in the same direction. The terrace is most likely the result of frost-heaving in the active layer of the permafrost where frozen soils expand, causing an uplift in the immediate subsurface, as it forms an arc around the thawed ground anomaly. Both the Bendeleben and Kigluaik Mountains are bounded on the south and north respectively by range-front normal faults with opposite directions of dip (Figure 5.11). The convergence of these two faults can be explained by a transfer fault to accommodate the change in dip (McDannell, 2011). A series of offsets occur in the lithologic contacts south of the location of the proposed transfer fault (Figure 5.11). These offsets display movement consistent with the motion of the transfer fault orientation (Figure 5.11). The en echelelon-style step-overs of the Kigluaik range-front fault may be the result of movement along the transfer fault. The significance of this inferred fault may suggest locally deep faulting and intense fracturing of the bedrock which may be hydraulically conducive to deeply circulating hydrothermal fluids. However, any number of smaller fault splays from this transfer fault could be feeding directly into the hot springs and this

fault by itself is not a likely target for deep drilling. The fault could also be a remnant of older tectonism that resolved the difference in stress direction of the surrounding faults and is no longer active or conductive. Regardless, it is likely the mica schist bedrock below Pilgrim Hot Springs is significantly fractured and may explain the location of the hot springs and its connection to a deeper heat source.

The highly speculative heat source has been investigated by numerous researchers and at present, no single heat source has been identified (Liss and Motyka, 1994; Miller et al., 1975; Turner and Forbes, 1980; Woodward-Clyde, 1983). Liss and Motyka (1994) posit the source has a mantle component. This is based on gas chemistry of helium 3/4 isotope values of 0.9 that are well below volcanic origin, but elevated for a crustal source (Liss and Motyka, 1994). They favor a deep circulation origin of the heated fluids. Miller et al. (1975) mention that although Seward Peninsula has experienced geologically recent volcanic activity, no hot springs or any thermal expressions have been discovered in or around the basaltic or intermediate volcanic rocks. Evoking a magmatic source for Pilgrim related to the young volcanism must explain why no fumeroles or any other related-geothermal systems presently exist in those areas. Miller et al. (1975) conclude that the saline and nonsaline fluids sampled in Seward Peninsula geothermal systems resemble deeply circulating meteoric fluids based on preliminary chemical and isotopic data. These fluids may still be interacting with different heat sources such as radiogenic plutons at depth. However, evidence suggests these fluids have a strong component of deep-circulation through large fault systems and fracture networks as well.

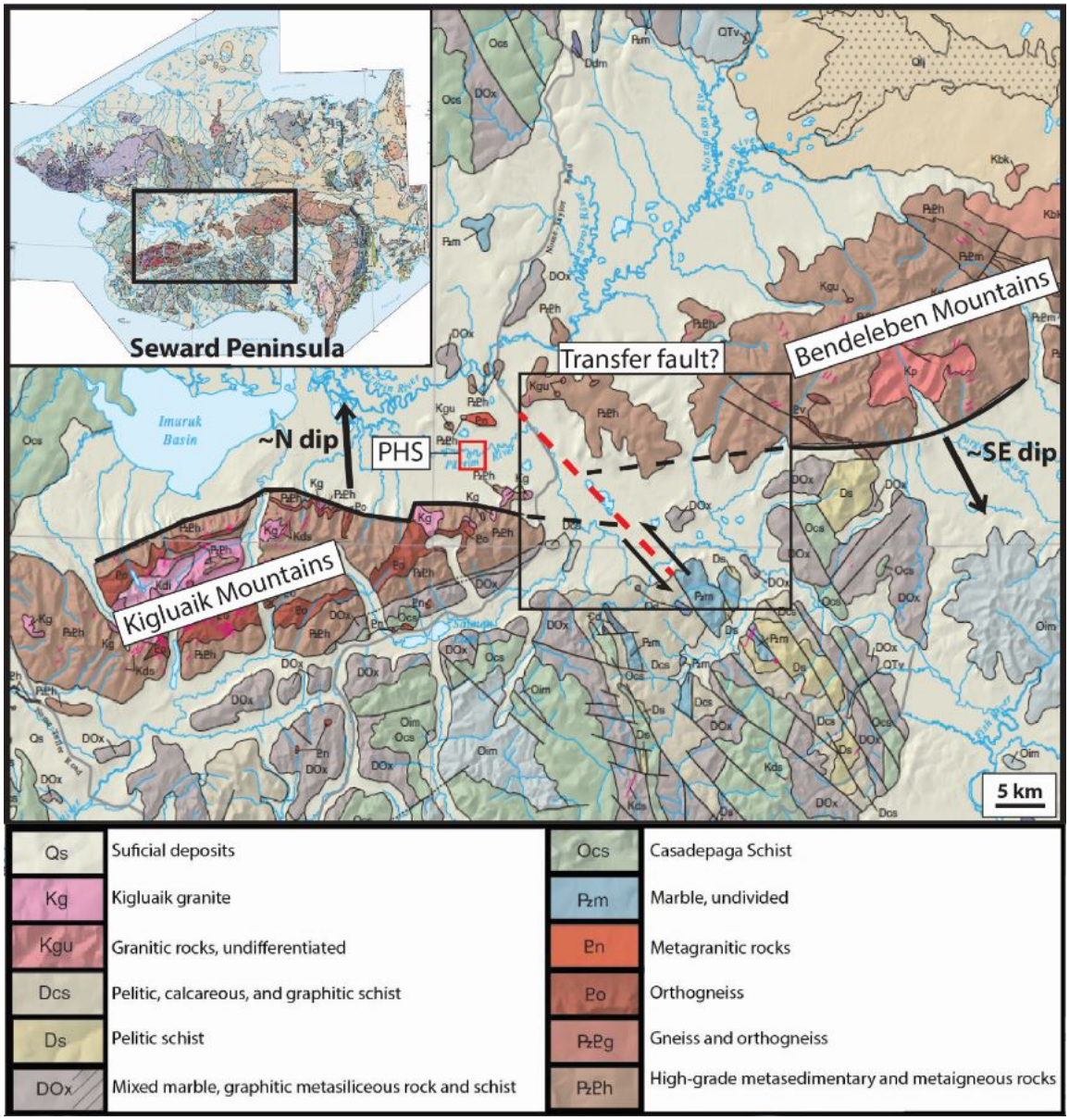


Figure 5.11: Location map of the inferred transfer fault. Map modified from Till et al. (2011).

Chapter 6: Conclusions and Recommendations

6.1 Conclusions

A conceptual model is presented to demonstrate the lithostratigraphic architecture as a control on the fluid migration pathways of the Pilgrim Hot Springs geothermal system. Results of the conceptual model show the geothermal system is comprised of Quaternary sediments down to 320 m depth that overlie a mica-schist basement. Based on temperature, geophysical well logs, MT survey, and lithologic data, the system can be subdivided into a shallow outflow aquifer and a deeper bedrock reservoir beneath a clay cap connected by a very narrow, <100 m wide, conduit with 91 °C upflow. The temperature gradients suggest the upflow is located between PS-12-2 and PS-12-3. Lithostratigraphic correlations based upon well log data indicate several clay layers throughout the section with significant clay horizons at 100 and 200-300 m depth. These clay layers act as major hydraulic barriers to vertical fluid migration and mitigate horizontal flow of geothermal fluids and regional groundwater. Magnetotelluric resistivity data matches closely to the modeled stratigraphy where thick clays from 200-300 m in wells PS-12-1, PS-12-2, and PS-12-3 correlate to the <0.5 ohm-m zone in the MT cross-sections. Reflectance spectroscopy and methylene blue titration detect highly conductive smectite clays in this zone as well as illite and kaolinite. Induration in the sediments is mostly concentrated between wells PS-4 and PS-12-3 and occurs from the shallow subsurface to the basement surface. The indurated sediments may also facilitate hydrothermal fluid flow by insulating higher permeability coarse sand and gravels.

Potential production from this resource is limited to where sufficient permeability exists in connection to the upflow. The silty sands beneath the clay layer at ~300 m close to PS-12-2 could have a high enough temperature and flow to be a feasible target for a large diameter production well. Additionally, extensive pyritization and a hydrothermal alteration clay mineral assemblage suggest an argillic-style alteration facies. This points to past temperatures at or slightly elevated above current conditions of hydrothermal activity at Pilgrim Hot Springs. The conceptual model supports production from this resource in those subsurface zones where there is sufficient permeability and connectivity with the upflow zone.

6.2 Recommendations

Further evaluation of the site is required to produce the upflow source from the bedrock fault or fracture network feeding the hot springs. A deep seismic survey would provide critically needed information for depth to bedrock changes across the basin as well as identify major structural features of the bedrock. If a large transfer fault is located nearby, seismic surveying would be needed to delineate zones of increased fracturing or faulting that may be directing upwelling hydrothermal fluids. Geoprobe shallow temperature surveying and a smaller, more targeted MT survey of the thermal expression at the base of Hen and Chicken Mountain would also be beneficial in understanding the deeper bedrock reservoir. If these two sites are connected by the same conduit, this may imply that Pilgrim Hot Springs is a surface expression of a much larger reservoir at depth.

The next step in assessing the Pilgrim Hot Springs geothermal resource is the integration of new drilling data to test the interpretations of the current conceptual model. The zone of high permeability coarse sands above the basement surface in connection to the upflow between PS-12-1, PS-12-2, and PS-12-3 is being targeted for drilling. A production well and temperature gradient slimhole wells will be drilled in the fall of 2013. This will serve to increase the accuracy of the predicted framework of the geothermal reservoir and the understanding of the upflow location and trajectory. Success of these efforts will determine the viability of Pilgrim Hot Springs as a resource with electric power production capability.

References

Amato, J. M., Wright, J. E., Gans, P. B., Miller, E. L., 1994. Magmatically induced metamorphism and deformation in the Kigluaik gneiss dome, Seward Peninsula, Alaska, Tectonics, 13, 2, 515-27.

Amato, J. M., Miller, E. L., 2004. Geologic map and summary of the evolution of the Kigluaik Mountains gneiss dome, Seward Peninsula, Alaska, Geological Society of America Special Papers, 380, 295-306.

Amato, J. M., Toro, J., Miller, E. L., Gehrels, G. E., Farmer, G. L., Gottlieb, E. S., Till, A. B., 2009. Late Proterozoic–Paleozoic evolution of the Arctic Alaska–Chukotka terrane based on U-Pb igneous and detrital zircon ages: Implications for Neoproterozoic paleogeographic reconstructions, Geological Society of America Bulletin, 121(9-10), 1219-1235.

Amato, J. M., Miller, E. L., Hannula, K. A., 2002. Orthogonal flow directions in extending continental crust: An example from the Kigluaik gneiss dome, Seward Peninsula, Alaska, Geological Society of America Special Papers, 360, 133-146.

Amato, J. M., Miller, E. L., Wright, J. E., McIntosh, W. C., 2003. Dike swarms on Seward Peninsula, Alaska, and their implications for the kinematics of Cretaceous extension in the Bering Strait region, Canadian Journal of Earth Sciences, 40, 6, 865-886.

Bain, D. C., Smith, B. F. L., Wilson, M.J., 1987. A handbook of determinative methods in clay mineralogy, Blackie, London, 1-248.

Barclay, D. J., Wiles, G. C., Calkin, P. E., 2009. Holocene glacier fluctuations in Alaska, Quaternary Science Reviews, 28, 21, 2034-2048.

Bear, J., 1972. Dynamics of fluids in porous media, American Elsevier, 765 p.

Beard, D. C., Weyl, P. K., 1973. Influence of texture on porosity and permeability of unconsolidated sand, AAPG Bulletin, 57, 2, 349-369.

Beget, J. E., Hopkins, D. M., Charron, S. D., 1996. The largest known maars on earth, Seward Peninsula, northwest Alaska, Arctic, 49, 1, 62-69.

Biswas, N.N., Pujol, J., Tytgat, G., Dean, K., 1986. Synthesis of seismicity studies for western Alaska, Tectnophysics, 131, 369-392.

Biswas, N. N., Tytgat, G., 1988. Intraplate seismicity in Alaska, Seismological Research Letters, 59, 4, 227-233.

Blackwell, D. D., Kelley, S., 1994. Implications of facies models on geothermal systems in the Basin and Range province, Geothermal Resources Council Transactions, 18, 3-5.

Bosworth, W., Morley, C.K., 1994. Structural and stratigraphic evolution of the Anza rift, Kenya, Tectonophysics, 236, 93-115.

Brigham-Grette, J., 2001. New perspectives on Beringian Quaternary paleogeography, stratigraphy, and glacial history, Quaternary Science Reviews, 20, (1–3), 15–24.

Browne, P.R.L., 1978. Hydrothermal alteration in active geothermal fields, Annual Review Earth Planetary Science, 6, 229-250.

Bundschuh, J., Suarez Arriaga, M.C., 2010. Introduction to the numerical modeling of groundwater and geothermal systems, fundamentals of mass, energy, and solute transport in poroelastic rocks, Multiphysics Modeling, vol. 2, Taylor & Francis Group, London, UK, 479 p.

Calkin, P. E., Kaufman, D. S., Przybyl, B. J., Whitford, W. B., Peck, B. J., 1998. Glacier regimes, periglacial landforms, and Holocene climate change in the Kigluaik Mountains, Seward Peninsula, Alaska, USA, Arctic and Alpine Research, 154-165.

Calvin, W., Lamb, A., Kratt, C., 2010. Rapid characterization of drill core and cutting mineralogy using infrared spectroscopy, Geothermal Resource Council Transactions, 34, 761-764.

Cashman, P. H., Faulds, J. E., Hinz, N. H., 2012. Regional variations in structural controls on geothermal systems in the Great Basin, Geothermal Resources Council Transactions, 36, 25-30.

Chittambakkam, A. Daanen, R. P., Haselwimmer, C., Prakash, A., Holdmann, G., 2013. Development of a reservoir stimulation model at Pilgrim Hot Springs, Alaska using Tough2, Proceedings, Thirty-eighth Workshop on Geothermal Reservoir Engineering, Stanford University, Stanford, California, SGP-TR-198.

Clark, R.N., Roush, T.L., 1984. Quantitative analysis techniques for remote sensing applications, Journal of Geophysical Research: Solid Earth, 89, 6329-6340.

Clark, R.N., Swayze, G.A., Wise, R., Livo, E., Hoefen, T., Kokaly, R., Sutley, S.J., 2007. USGS digital spectral library splib06a: U.S. Geological Survey, Digital Data Series 231.

Cox, M., Preda, M., Harbison, J., 2002. Importance of indurated sand layers to groundwater flow in Quaternary coastal settings, Moreton Bay, Balancing the Groundwater Budget, Proceedings of the 7th IAH National Groundwater Conference, Darwin.

Cross, R. S., Freymueller, J. T., 2008. Evidence for and implications of a Bering plate based on geodetic measurements from the Aleutians and western Alaska, Journal of Geophysical Research, 113.

Cumming, W., 2009. Geothermal resource conceptual models using surface exploration data, Proceedings, Thirty-Fourth Workshop on Geothermal Reservoir Engineering Stanford University, SGP-TR-18.

Cumming, W. 2012. Personal communication on MT inversion modeling and lithostratigraphic-temperature comparisons.

Daanen, R. P., Chittambakkam, A., Haselwimmer, C., Prakash, A., Mager, M., Holdmann, G., 2012. Use of COMSOL multiphysics to develop a shallow preliminary conceptual model for geothermal exploration at Pilgrim Hot Springs, Alaska, Geothermal Resource Council Transactions, 36, 631-635.

Dumitru, T.A., Miller, E.L., O'Sullivan, P.B., Amato, J.M., Hannula, K.A., Calvert, A.T., Gans, P.B., 1995. Cretaceous to recent extension in the Bering Strait region, Alaska, Tectonics, 14, 549-563.

Finzel, E. S., Flesch, L. M., Ridgway, K. D., 2011. Kinematics of a diffuse North America–Pacific–Bering plate boundary in Alaska and western Canada, Geology, 39, 9, 835-838.

Fitts, C. R., 2002. Groundwater science, Academic Press, An Imprint of Elsevier Science, London, England.

FUGRO, 2012, Pilgrim Springs-Alaska magnetotelluric (MT) survey final report for University of Alaska Fairbanks.

Fujita, K., Mackey, K. G., McCaleb, R. C., Gunbina, L.V., Kovalev, V. N., Imaev, V. S., Smirnov, V. N., 2002. Seismicity of Chukotka, northeastern Russia, in Miller, E.L., et al. eds., Tectonic evolution of the Bering Shelf-Chukchi Sea-Arctic margin and adjacent landmasses: Geological Society of America Special Paper 360, 259-272.

Glassley, W. E., 2010. Geothermal Energy: Renewable Energy and the Environment, Taylor & Francis US, 320 p.

Guilbert, J.M., Park, Jr., C.F., 1986. The geology of ore deposits, WH Freeman, 985 p.

Gunderson, R., Cumming, W., Astra, D., Harvey, C., 2000. Analysis of smectite clays in geothermal drill cuttings by the methylene blue method for well site geothermometry and resistivity sounding correlation, Proceedings, World Geothermal Congress, Kyushu-Tohoku, Japan, 1175-1181.

Haest, M., Cudahy, T., Laukamp, C., Gregory, S., 2012. Quantitative mineralogy from infrared spectroscopic data. I. Validation of mineral abundance and composition scripts at the Rocklea Channel iron deposit in Western Australia, Economic Geology, 107, 209-228.

Harraden, C.L., McNulty, B.A., Gregory, M.J., Lang, J.R., 2013. Shortwave infrared spectral analysis of hydrothermal alteration associated with the pebble porphyry copper-gold-molybdenum deposit, Iliamma, Alaska, Economic Geologist, 108, 483-494.

Harvey, C., 1993. Simplified methylene blue test for estimation of swelling clays, GNS Science, Annotated by W. Cumming, 2004 and 2010.

Harvey, C., Browne, P., 2000. Mixed-layer clays in geothermal systems and their effectiveness as mineral geothermometers, Proceedings World Geothermal Congress 2000, Kyushu-Tokoku, Japan, 1201-1205.

Haselwimmer, C., Prakash, A., Holdmann, G., 2011. Geothermal exploration in Pilgrim, Alaska using airborne thermal infrared remote sensing, Geothermal Resources Council Transactions, 35, 805-810.

Heise, W., Bibby, H. M., Caldwell, T. G., Bannister, S.C., Ogawa, Y., Takakura, S., Uchida, T., 2007. Melt distribution beneath a young continental rift: The Taupo Volcanic Zone, New Zealand, Geophysical Research Letters, 34, 6 p.

Hunt, G. R., 1977. Spectral signatures of particulate minerals in the visible and near infrared, Geophysics, 42, 3, 501-513.

Jennings, S., Thompson, G.R., 1986. Diagenesis of Plio-Pleistocene sediments of the Colorado River Delta, Southern California, Journal of Sedimentary Petrology, 56, 1, 89-98.

Kline, J.T., 1980. Test Drilling Report--Procedures and results of the two test holes drilled at Pilgrim Springs, Alaska in October and November 1979, Alaska Division of Geological and Geophysical Surveys report, 20 p.

Kolker, A.M., Kennedy, B.M., Newberry, R.J., 2008. Evidence for a crustal heat source for low-temperature geothermal systems in the Central Alaskan Hot Springs Belt, Geothermal Resources Council Transactions, 32, 225-230.

Lagat, J., 2007. Hydrothermal alteration mineralogy in geothermal fields with case examples from Olkaria Domes geothermal field, Kenya, United Nations University-Geothermal Training Programme Short Course II on Surface Exploration for Geothermal Resources.

Liss, S.A., Motyka, R.J., 1994. Pilgrim Springs KGRA, Seward Peninsula, Alaska: Assessment of fluid geochemistry, Geothermal Resources Council Transactions, 18, 213-219.

Lofgren, B.E., 1983. Results of drilling, testing, and resource confirmation-geothermal energy development at Pilgrim Hot Springs, Alaska: Unpublished report of Alaska, Woodward-Clyde Consultants to Alaska Division of Energy and Power Development.

Mackey, K. G., Fujita, K., Gunbina, L. V., Kovalev, V. N., Imaev, V. S., Koz'min, B. M., Imaeva, L. P., 1997. Seismicity of the Bering Strait region: Evidence for a Bering block, Geology, 25, 11, 979-982.

Mas, A., Guisseau, D., Mas, P., Beaufort, D., Genter, A., Sanjuan, B., Girard, J.P., 2006. Clay minerals related to hydrothermal activity of the Bouillante geothermal field (Guadeloupe), Journal of Volcanology and Geothermal Research, 158, 380-400.

McDannell, K. T., 2011. Exhumation in the Bendeleben Mountains (Seward Peninsula, Alaska) constrained by (U-Th)/He thermochronology, M.S. Geology thesis, West Virginia University, 46 p.

McPhee, D. K., Glen, J. M., 2012. Airborne geophysical surveys illuminate the geologic and hydrothermal framework of the Pilgrim Spring geothermal area, Alaska, American Geophysical Union Fall Meeting, Sand Francisco, California.

Miller, T. P., Barnes, I., Patton Jr., W.W., 1975. Geologic setting and chemical characteristics of hot springs in west-central Alaska, Journal Research U.S. Geological Survey, 3, 2, 149-162.

Miller, J. K., Prakash, A., Daanen, R. P., Haselwimmer, C., Whalen, M., 2013. Geologic model of the geothermal anomaly at Pilgrim Hot Springs, Seward peninsula, Alaska, 38th Workshop on Geothermal Reservoir Engineering, Stanford University, SGP-TR-198.

Mosser-Ruck, R., Devineau, K., Charpentier, D., Cathelineau, M., 2005. Effects of ethylene glycol saturation protocols on XRD patterns: A critical review and discussion, Clays and Clay Minerals, 53, 6, 631-638.

Okaya, D. A., Thompson, G. A., 1985. Geometry of Cenozoic extensional faulting: Dixie Valley, Nevada, Tectonics, 4, 107-125.

Page, R.A., Biswas, N.N., Lahr, J.C., Pulpan, H., 1991. Seismicity of continental Alaska, in Slemmons, D.B., Engdahl, E.R., Zoback, M.D., Blackwell, D.D., eds., Neotectonics of North America: Boulder, Colorado, Geological Society of America, Decade Map Volume 1.

Page, R. A., Plafker, G., Pulpan, H., 1995. Block rotation in east-central Alaska: A framework for evaluating earthquake potential, Geology, 23, 629-632.

Palacky, G.J., 1988. Resistivity characteristics of geologic targets, Electromagnetic methods in applied geophysics, 3, 53-129.

Ruppert, N. A., 2008. Stress map for Alaska from earthquake focal mechanisms, in Active Tectonics and Seismic Potential of Alaska, Geophys. Monogr. Ser., 179, edited by J. T. Freymueller et al., 351–367.

Sainsbury, C. L., Hudson, T., Kachadoorian, R., Richards, T. R., Todd, W. E., 1969. Reconnaissance geologic maps and sample data, Teller A-1, A-2, A-3, B-1, B-2, B-3, C-1, and Bendeleben A-6, B-6, C-6, D-5, D-6 quadrangles, Seward Peninsula, Alaska: U.S. Geological Survey open-file report, 49 p.

SAMS, 2005. Spectral Analysis and Management System, <sams.projects.atlas.ca.gov>, 25 October 2013.

Santamarina, J.C., Klein, K.A., Wang, Y.H., Prencke, E., 2002. Specific surface: determination and relevance, Canadian Geotechnical Journal, 39, 233-241.

Schwering, P. C., Karlin, R. E., 2012. Structural interpretation and modeling of the Dixie Meadows geothermal prospect using gravity and magnetic data, Geothermal Resources Council Transactions, 36, 53-58.

Shepherd, R. G., 1989. Correlations of Permeability and Grain Size, Ground Water, 27, 5, 633-8.

Swenson, R.F., Wartes, M.A., LePain, D.L., Clough, J.G., 2012. Fossil fuel and geothermal energy sources for local use in Alaska: Summary of available information, Special Report 66, State of Alaska DNR, Division of Geological & Geophysical Surveys.

Till, A. B., Dumoulin, J.A., 1994. Geology of Seward Peninsula and Saint Lawrence Island, The Geology of Alaska, The Geology of North America, 141-152.

Till, A. B., Dumoulin, J. A., Werdon, M. B. Bleick, H. A., 2011. Bedrock geologic map of the Seward Peninsula, Alaska, and accompanying conodont data, US Department of the Interior, U. S. Geological Survey.

Turner, D. L., Forbes, R. B., 1980. A geological and geophysical study of the geothermal energy potential of Pilgrim Springs, Alaska, Geophysical Institute, University of Alaska, UAF R-271, 165 p.

Turner, D. L., Swanson, S. E., 1981. Continental rifting; A new tectonic model for the central Seward Peninsula, Geophysical Institute, University of Alaska, UAG R-284, 7-36.

Turner, D.L., Swanson, S., Forbes, R. B., Maynard, D., 1979. Geologic map of the Bendeleben A-6 and eastern part of the Teller A-1 quadrangles, Alaska.

University of Alaska Fairbanks, 2012. Validation of innovative exploration techniques, Pilgrim Hot Springs, Phase 1 Final Report for the DOE Grant DE-EE0002846, September 2012, 103 p.

van Ruitenbeek, F. J.A., Cudahy, T., Hale, M., van der Meer, F. D., 2005. Tracing fluid pathways in fossil hydrothermal systems with near-infrared spectroscopy, Geology, 33, 7, 597-600.

Woodward-Clyde, 1983. Results of drilling, testing, and resource confirmation: Geothermal energy development at Pilgrim Springs, Alaska, Woodward-Clyde Report, 102 p.

Yukselen, Y., Abidin, K., 2008. Suitability of the methylene blue test for surface area, cation exchange capacity, and swell potential determination of clayey soils, Engineering Geology, 102, 38-45.

Appendix A

Spectral assessment of mineral abundances.

Table A.1: Mineral abundance for PS-12-1.

PS-12-1	
Mineral	**%**
Montmorillonite	34.18
Siderite	15.89
Kaolinite	14.22
Muscovite	6.39
Palygorskite	4.33
Magnesite	3.22
Aspectral	3.16
Muscovitic Illite	1.65
Ankerite	1.36

Table A.2: Mineral abundance for PS-12-2.

PS-12-2	
Mineral	**%**
Montmorillonite	26.57
Kaolinite	14.83
Siderite	14.64
FeMgChlorite	6.13
Muscovite	5.86
Aspectral	3.25
Palygorskite	2.51
Ankerite	2.08
Magnesite	1.75
Muscovitic Illite	1.58
MgChlorite	1.58

Table A.3: Mineral abundance for PS-12-2 core.

PS-12-2 Core	
Mineral	**%**
FeMgChlorite	19.43
Phlogopite	19.31
MgChlorite	14.34
Montmorillonite	12.64
Palygorskite	6.94
Muscovitic Illite	3.31
Muscovite	2.92
Calcite	2.4
Siderite	1.71
Ankerite	1.49
Biotite	1.27
Hornblende	1.09

Table A.4: Mineral abundance for PS-12-3.

PS-12-3	
Mineral	**%**
Montmorillonite	25.65
Siderite	18.48
Kaolinite	13.8
Aspectral	4.24
Muscovite	2.3
Muscovitic Illite	1.37
Ankerite	1.07

Appendix B

Methylene blue (MeB) titration results.

Table B.1: Estimated smectite content per sediment sample for PS-12-1.

PS-12-1				
MeB concentration: 3.742 g/L				
Duplicate sample (D)				
Sample (ft)	**Depth (m)**	**Weight (g)**	**MeB (mls)**	**%Smectite**
25-35	9	1.002	1.5	1.5%
75-85	24	1.000	1.5	1.5%
190-200	59	1.001	2.5	2.5%
400-410	123	1.003	1.0	1.0%
450-460	139	1.003	5.0	5.0%
490-500	151	1.003	3.5	3.5%
550-560	169	1.003	3.0	3.0%
550-560D*	169	1.000	3.0	3.0%
600-610	184	1.002	5.0	5.0%
650-660	200	1.000	6.5	6.5%
710-720	218	1.000	5.5	5.5%
753-763	231	1.002	5.0	5.0%
800-810	245	1.003	8.0	8.0%
850-860	261	1.000	4.5	4.5%
880-890	270	1.001	8.0	8.0%
900-910	276	1.002	7.0	7.0%
930-940	285	1.001	6.0	6.0%
960-970	294	1.000	8.5	8.5%
990-1000	303	1.000	8.5	8.5%
*D=Duplicate analysis for QC				

Table B.2: Estimated smectite content per sediment sample for PS-12-2.

PS-12-2				
MeB concentration: 3.742 g/L				
Duplicate sample (D)				
Sample (ft)	**Depth (m)**	**Weight (g)**	**MeB (mls)**	**%Smectite**
45-55	15	1.002	1.5	1.5%
125-135	40	1.003	2.0	2.0%
195-205	61	1.002	2.0	2.0%
385-395	119	1.004	2.0	2.0%
465-475	143	1.004	3.5	3.5%
495-505	152	1.003	5.0	5.0%
545-555	168	1.002	5.0	5.0%
595-605	183	1.002	8.0	8.0%
655-665	201	1.000	5.0	5.0%
705-715	216	1.001	3.0	3.0%
705-715D*	216	1.002	3.0	3.0%
745-755	229	1.002	4.5	4.5%
765-775	235	1.003	10.0	10.0%
805-815	247	1.002	6.0	6.0%
825-835	253	1.003	5.5	5.5%
855-865	262	1.002	5.0	5.0%
885-895	271	1.002	5.0	5.0%
895-905	274	1.003	5.0	5.0%
945-955	290	1.004	10.0	10.0%
965-975	296	1.002	6.0	6.0%
995-1005	305	1.002	4.5	4.5%
1025-1035	314	1.001	2.5	2.5%
1045-1055	320	1.003	1.0	1.0%
1093-1103	335	1.003	2.0	2.0%
1163-1173	356	1.000	4.0	4.0%
1193-1203	365	1.003	2.5	2.5%
1233-1243	377	1.003	9.5	9.5%
1233-1243D*	377	1.002	8.0	8.0%
*D=Duplicate analysis for QC				

Table B.3: Estimated smectite content per sediment sample for PS-12-3.

PS-12-3				
MeB concentration: 3.742 g/L				
Duplicate sample (D)				
Sample (ft)	**Depth (m)**	**Weight (g)**	**MeB (mls)**	**%Smectite**
24-34	9	1.002	3.0	3.0%
193-203	60	1.003	2.0	2.0%
393-403	121	1.002	2.5	2.5%
443-453	137	1.003	3.5	3.5%
493-503	152	1.002	3.5	3.5%
543-553	167	1.003	5.0	5.0%
593-603	182	1.004	7.5	7.5%
653-663	201	1.002	5.0	5.0%
703-713	216	1.003	7.5	7.5%
743-753	228	1.002	7.0	7.0%
813-823	249	1.001	5.0	5.0%
853-863	262	1.003	6.0	6.0%
883-893	271	1.001	7.5	7.5%
953-963	292	1.003	3.0	3.0%
953-963D*	292	1.001	3.0	3.0%
1003-1013	307	1.004	7.5	7.5%
1023-1033	313	1.003	4.0	4.0%
1083-1093	332	1.001	7.5	7.5%
1153-1163	322	1.000	4.0	4.0%
*D=Duplicate analysis for QC				

Appendix C

X-ray diffraction results of glycolated clay samples.

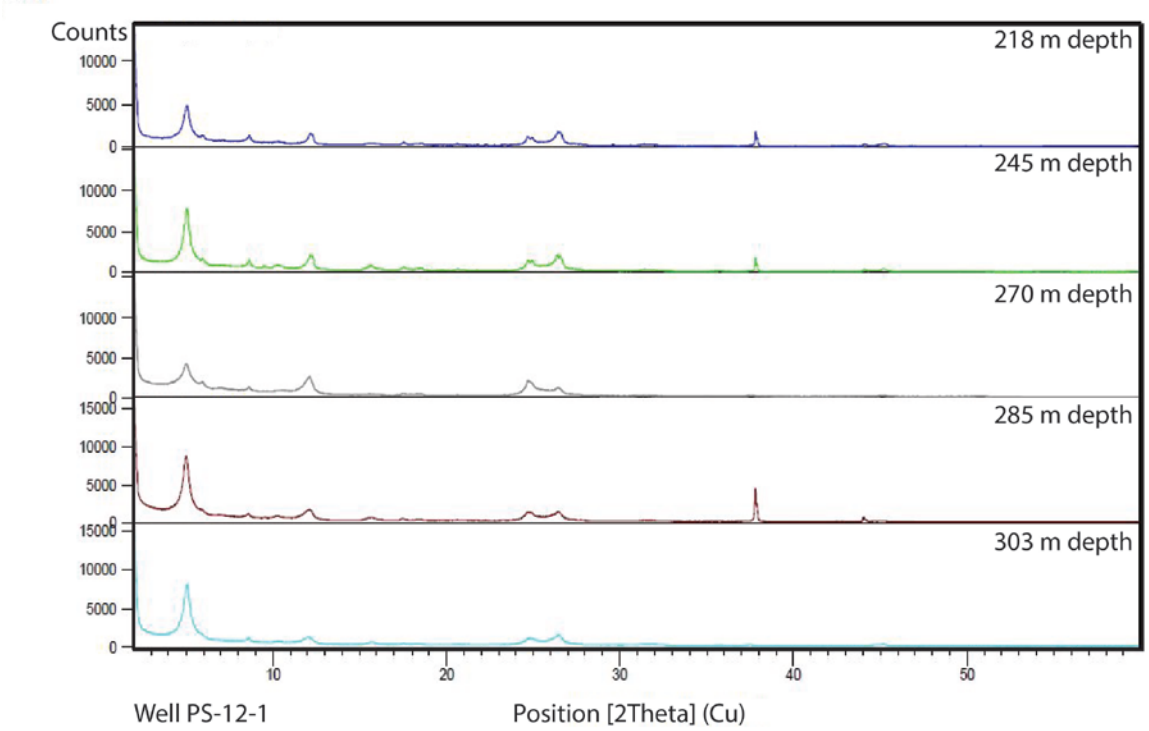


Figure C.1: X-ray diffraction results of glycolated clay samples for well PS-12-1.

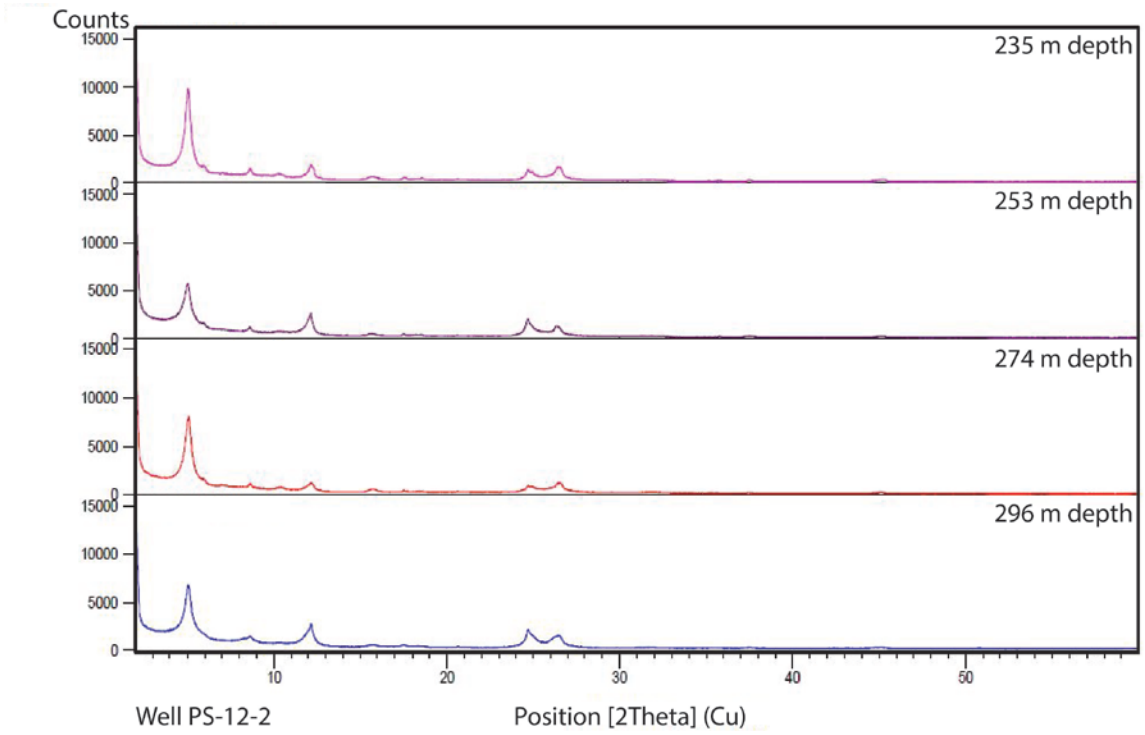


Figure C.2: X-ray diffraction results of glycolated clay samples for well PS-12-2.

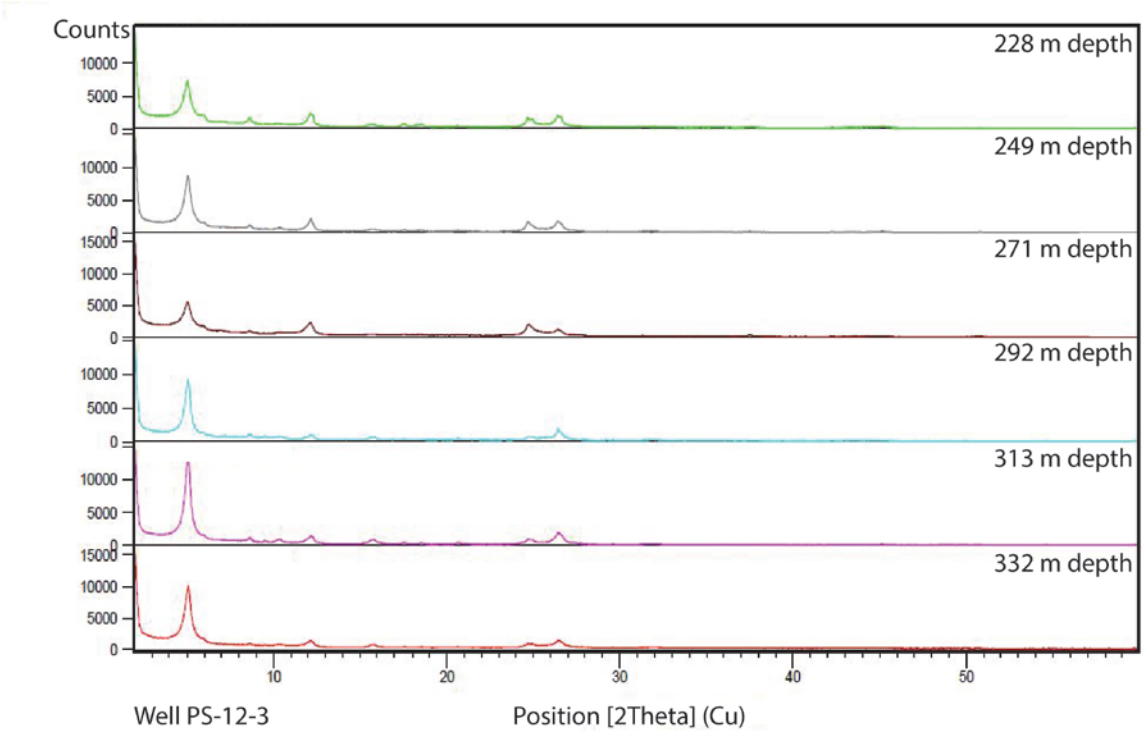


Figure C.3: X-ray diffraction results of glycolated clay samples for well PS-12-3.

Appendix N
Reservoir Simulation Modeling: Arvind Chittambakkam Thesis

DEVELOPMENT OF A RESERVOIR STIMULATION MODEL AT PILGRIM HOT SPRINGS, ALASKA USING TOUGH2

A

THESIS

Presented to the Faculty

of the University of Alaska Fairbanks

in Partial Fulfillment of the Requirements

for the Degree of

MASTER OF SCIENCE

By

Arvind A. Chittambakkam, B.Tech, M.E.

Fairbanks, Alaska

August 2013

Abstract

This study has developed numerical simulations of the Pilgrim Hot Springs geothermal system, Alaska using the TOUGH2 software package for the purposes of assessing the resource potential for both direct use applications and electrical generation. This work has included the development of two simulation models, describing fluid and heat flow in the geothermal system, that were built using geological and geophysical constraints with model simulation parameters optimized via a history matching of subsurface temperature profiles. The reservoir simulation models were used to predict the heat loss from the system for both conductive and convective heat fluxes. These reservoir simulation models served as the basis for the development of reservoir stimulation models encompassing three production scenarios with various configurations of production and injection wells. These reservoir stimulation models were used to estimate the thermal energy from the production wells. The major significance of these stimulation models is that they help to determine the feasibility of development of the reservoir for production. The reservoir simulation models estimate about 26-28 $MW_{Thermal}$ energy and the stimulation models estimate about 46-50 $MW_{Thermal}$ energy for the Pilgrim Hot Springs geothermal system. These estimated values indicate a favorable resource when compared to other low temperature systems such as, Chena Hot Springs, Alaska; Wabuska, Nevada; Amedee, California; and Wineagle, California.

Table of Contents

Page

Signature Page i

Title Page iii

Abstract v

Table of Contents vii

List of Figures xi

List of Tables xvii

List of Appendices xix

Acknowledgements xxi

Chapter 1 Introduction 1

1.1 Overview 1

1.1.1 General Introduction 1

1.1.2 Research Objectives 2

1.1.3 Thesis Structure 3

1.2 Background 4

1.2.1 Geothermal Systems 4

1.2.2 Geothermal Energy and Production 6

1.2.3 Geothermal Development 7

Chapter 2 Study Area and Data 11

2.1 Study Area (Pilgrim Hot Springs) 11

2.1.1 General Setting 11

2.1.2 Geological Overview 14

2.1.3 Previous Work 17

2.2 Data 23

2.2.1 Remote Sensing Data 23

2.2.2 Airborne Electromagnetic (EM) Survey 24

2.2.3 Magnetotelluric Survey 27

2.2.4 Temperature Logs 30

2.2.5 Geophysical Logs 30

Chapter 3 Reservoir Modeling Methodology 31

3.1 TOUGH2: Modeling Background 31

3.2 Reservoir Modeling Setup 39

3.3 Reservoir Domain 40

3.4 Gridding 48

3.5 Initial Conditions and Boundary Conditions 49

3.5.1 Top Layer 49

3.5.2 Base Layer 50

3.5.3 Permafrost 51

3.5.4 Cold Water Influx 52

3.5.5 Heat Source Location and Plumbing 53

3.5.5.1 Reservoir Simulation Model #1 53

3.5.5.2 Reservoir Simulation Model #2 60

3.5.5.3 Reservoir Stimulation Model 66

3.5.6 Lithology 69

Chapter 4 Results 75

4.1 Simulated Temperature Sections 75

4.1.1 Reservoir Simulation Model #1 75

4.1.2 Reservoir Simulation Model #2 80

4.2 Heat Flux Estimation 85

4.2.1 Reservoir Simulation Model #1 85

4.2.2 Reservoir Simulation Model #2 87

4.3 Well Temperature Plots 87

4.3.1 Reservoir Simulation Model #1 87

4.3.2 Reservoir Simulation Model #2 95

4.4 Reservoir Stimulation Models 100

4.4.1 Reservoir Stimulation Model #1 100

4.4.2 Reservoir Stimulation Model #2 103

4.4.3 Reservoir Stimulation Model #3 105

Chapter 5 Discussion 111

5.1 Reservoir Simulation Models 111

5.1.1 Heat Flux Estimation and History Matching 111

5.1.2 Well Temperature Plots 118

5.1.3 Reservoir Models and Remote Sensing Derived Heat Fluxes 121

5.2 Reservoir Stimulation Models 123

5.2.1 Comparison to Analogs of Pilgrim Hot Springs 130

5.3 Limitations 131

5.3.1 Reservoir Simulation Models 131

5.3.2 Reservoir Stimulation Models 132

5.3.3 Model Temporal and Spatial Resolutions 133

Chapter 6 Conclusions and Recommendations 137

6.1 Conclusions 137

6.2 Recommendations 138

References 141

Appendices 145

List of Figures

Page

Figure 1.1: Example of a geothermal system with heat source. 5

Figure 1.2: Distribution of geothermal energy production plants around the world. 8

Figure 2.1: Pilgrim Hot Springs area located in the Seward Peninsula, Alaska. 12

Figure 2.2: Pilgrim Hot Springs area 13

Figure 2.3: Surficial and bedrock geology map of the Pilgrim River Valley. 15

Figure 2.4: Location of all the drill holes across Pilgrim Hot Springs. 18

Figure 2.5: Various types of surface land features interpreted from the high resolution optical image. 24

Figure 2.6: Basic working principle behind the airborne EM survey. 25

Figure 2.7: Relationship between the lithologies and resistivity values. 26

Figure 2.8: Typical resistivity values of common material types. 29

Figure 3.1: Schematic diagram of a fault-bounded valley floor. 32

Figure 3.2: A flowchart indicating the various steps incorporated in the reservoir modeling setup. 39

Figure 3.3: Airborne EM survey at Pilgrim Hot Springs showing the differential resistivity slices at 5 m and 100 m. 41

Figure 3.4: Six different classes from the classification result. 42

Figure 3.5: Map view of a triangular shaped reservoir domain representing the Pilgrim Hot Springs. 44

Figure 3.6: Static temperature logs from all wells located across Pilgrim Hot Springs. 45

Figure 3.7: Layers in the model setup. 47

Page

Figure 3.8: Top layer of the reservoir model 50

Figure 3.9: Base layer of the reservoir model. 51

Figure 3.10: Walls of the domain represented by the blue-colored grid cells. 52

Figure 3.11: Resistivity across profile D through a smoothed 1D MT inversion. 55

Figure 3.12: Resistivity across profile C through a smoothed 1D MT inversion. 56

Figure 3.13: Resistivity across profile 2 through a smoothed 1D MT inversion. 57

Figure 3.14: Location of the heat source cell. 59

Figure 3.15: Resistivity across profile 4 from a blind 3D MT inversion. 61

Figure 3.16: Resistivity across profile 3 from a blind 3D MT inversion. 62

Figure 3.17: Resistivity across profile C from a blind 3D MT inversion. 63

Figure 3.18: Location of the heat source cell represented by pink color cell at a depth of 1000 m. 64

Figure 3.19: Orientation of the plumbing system at the depth of 500-750 m for reservoir model #2. 64

Figure 3.20: Orientation of the plumbing system at a depth of 300 m for reservoir model #2. 65

Figure 3.21: Location of the two production wells in the first reservoir stimulation model. 67

Figure 3.22: Location of the single production well in the second reservoir stimulation model. 67

Figure 3.23: Location of the injection well and production well in the third reservoir stimulation model. 68

Figure 3.24: Lithology, gamma ray, and temperature logs for several wells correlated by depth with equi-distant spacing. 70

Page

Figure 3.25: Lithology slice at 300 m. 72

Figure 3.26: Lithology slice at 295 m 73

Figure 3.27: Lithology slice at 270 m 73

Figure 4.1: Simulated temperature section in the west-east direction for reservoir model #1. 76

Figure 4.2: Simulated temperature section in the south-north direction for reservoir model #1. 77

Figure 4.3: Comparison of the simulated temperature profiles for grid cells at 295 m and 300 m for reservoir simulation model #1. 79

Figure 4.4: Simulated pressure profile for a grid cell that represents the conduit at a depth of 300 m for reservoir model #1. 79

Figure 4.5: Simulated temperature section in the west-east direction for reservoir simulation model #2. 81

Figure 4.6: Simulated temperature section in the south-north direction for reservoir model #2. 82

Figure 4.7: The flow of up-welling fluids through the plumbing of the second reservoir simulation model. 83

Figure 4.8: Comparison of the simulated temperature profiles for grid cells at 290 m and 300 m for reservoir simulation model #1. 84

Figure 4.9: Simulated pressure profile for a grid cell that represents the conduit at a depth of 300 m for reservoir simulation model #2. 85

Figure 4.10: Comparison of the simulated well temperature to the actual well temperature for well PS 1 for reservoir simulation model #1. 88

Figure 4.11: Comparison of the simulated well temperature to the actual well temperature for well PS 2 for reservoir simulation model #1. 89

Page

Figure 4.12: Comparison of the simulated well temperature to the actual well temperature for well PS 12-2 for reservoir simulation model #1. 90

Figure 4.13: Comparison of the simulated well temperature to the actual well temperature for well PS 12-3 for reservoir simulation model #1. 90

Figure 4.14: Comparison of the simulated well temperature to the actual well temperature for well S1 for reservoir simulation model #1. 91

Figure 4.15: Comparison of the simulated well temperature to the actual well temperature for well S9 for reservoir simulation model #1. 92

Figure 4.16: Comparison of the simulated well temperature to the actual well temperature for well MI 1 for reservoir simulation model # 1. 93

Figure 4.17: Comparison of the simulated well temperature to the actual well temperature for well PS 5 for reservoir simulation model #1. 94

Figure 4.18: Comparison of simulated temperatures to the measured static temperatures for PS 12-2 for reservoir simulation model #2. 96

Figure 4.19: Comparison of simulated temperatures to the measured static temperatures for PS 12-3 for reservoir simulation model #2. 97

Figure 4.20: Comparison of simulated temperatures to the measured static temperatures for PS 5 for reservoir simulation model #2. 98

Figure 4.21: Comparison of simulated temperatures to the measured static temperatures for PS 4 for reservoir simulation model #2. 99

Figure 4.22: Estimated thermal energy from production well # 1 is around 48 MW for reservoir stimulation model # 1. 101

Figure 4.23: Simulated temperature section in the west-east direction for reservoir stimulation model #1. 102

Figure 4.24: Simulated temperature section in the south-north direction for reservoir stimulation model #1. 102

Figure 4.25: Estimated thermal energy from production well # 1 is around 46 MW for reservoir stimulation model # 2. 103

Page

Figure 4.26: Simulated temperature section in the west-east direction for reservoir stimulation model #2. 104

Figure 4.27: Simulated temperature section in the south-north direction for reservoir stimulation model #2. 104

Figure 4.28: Estimated thermal energy from production well # 1 is around 50 MW. 106

Figure 4.29: Simulated temperature section in the west-east direction for reservoir stimulation model #3. 107

Figure 4.30: Simulated temperature section in the south-north direction for reservoir stimulation model #3. 107

Figure 4.31: Comparison of temperature of fluids entering the completed interval for the production well in the three reservoir stimulation models. 108

Figure 4.32: Comparison of the effects of the reservoir stimulation scenarios on reservoir pressure. 110

Figure 5.1: Conceptual model of a low temperature geothermal system 111

Figure 5.2: A schematic heat and water balance for the modeled part of geothermal system 122

List of Tables

Page

Table 3.1: Variation of the grid sizes along the X axis of the domain 48

Table 3.2: Variation in the grid sizes along the Y axis of the domain..... 48

Table 3.3: Well properties related to the operation of the production wells and injection wells incorporated in three stimulation models 69

Table 3.4: Lithology types and their respective properties which have been incorporated in the reservoir simulation model 71

List of Appendices

Page

Figure A.1: Comparison of the simulated well temperature to the actual well temperature for well PS 3 for the first reservoir model. 145

Figure A.2: Comparison of the simulated well temperature to the actual well temperature for well PS 4 for the first reservoir model. 146

Figure A.3: Comparison of the simulated well temperature to the actual well temperature for well PS 12-1 for the first reservoir model. 146

Figure B.1: Comparison of the simulated well temperature to the actual well temperature for well PS 2 for the second reservoir model..... 147

Figure B.2: Comparison of the simulated well temperature to the actual well temperature for well PS 3 for the second reservoir model..... 148

Figure B.3: Comparison of the simulated well temperature to the actual well temperature for well MI 1 for the second reservoir model. 148

Figure B.4: Comparison of the simulated well temperature to the actual well temperature for well PS 12-1 for the second reservoir model. 149

Figure B.5: Comparison of the simulated well temperature to the actual well temperature for well PS 1 for the second reservoir model..... 149

Figure B.6: Comparison of the simulated well temperature to the actual well temperature for well S1 for the second reservoir model. 150

Figure B.7: Comparison of the simulated well temperature to the actual well temperature for well S9 for the second reservoir model. 150

Acknowledgements

I would like to commence by thanking the Almighty (Lord Krishna, Lord Venkateshwara, Lord Varahi and Lord Ganesha) for guiding me through the paths of life. I am really appreciative of my exceptional committee members: Dr. Anupma Prakash, Dr. Ronald Daanen and Dr. Christian Haselwimmer. They have gone above and beyond to ensure my successful completion of this research work. They have been role models for me both professionally and personally. My advisor, Dr. Anupma Prakash deserves special thanks for being patient and for constantly encouraging, believing and supporting me to achieve greater heights through the highs and lows of graduate life. I would like to thank Gwen Holdmann for having given me this opportunity to work on this project. I also appreciate Dr. Cathy Hanks, Dr. Joanna Mongrain and Dr. Rudiger Gens for their encouragement and support during my time in Alaska. I'd like to thank Carol Holz and Sue Wolfe from the International Office for making my stay at UAF a pleasant and wonderful experience. I would like to thank the funding agencies, Department of Energy and Geothermal Technologies Program (CID: DE-EE0002846) and the Alaska Energy Authority Renewable Energy Fund Round III. I appreciate the other members of the Alaska Center for Energy and Power Team and Markus Mager. I also appreciate my friends, colleagues at UAF and my family back in India. I would like to thank Dr. Paul McCarthy for his excellent review of my thesis. I'd finally like to thank Antje Thiele for helping me format my thesis. I also appreciate Juan Antonio Goula and Hope Bickmeier from the Graduate School.

Chapter 1: Introduction

1.1 Overview

1.1.1 General Introduction

The technology, reliability, economics, and environmental acceptability of direct use of geothermal energy have been demonstrated throughout the world. Alaska more than any other single region in North America, probably has the greatest number of potential geothermal energy sites (Miller, 1994). The remoteness of many of the geothermal areas, the sparse population base, the difficulty in delivering energy to distant markets, and high front-end development costs are factors that affect the utilization of the resource (Miller, 1994). The development of the Pilgrim Hot Springs, for direct or indirect application will help to support the communities near Nome, Alaska and may be the answer to the energy insecurities and power generation in this remote region of Alaska.

Thermal springs in Alaska, outside of the Aleutian volcanic arc, are characterized by relatively low surface temperatures as indicated by geothermometry (usually less than 150 ℃). They appear to be associated with fractured margins of granitic plutons and have low porosity (Miller, 1994). Pilgrim Hot Springs on the Seward Peninsula is one such low temperature resource and may have sufficient porosity and volume to be a viable geothermal resource for development (Miller, 1994). The most studied geothermal area north of the Alaska Range is Pilgrim Hot Springs, located in the west-central Seward Peninsula. The thermal springs are located in an oval-shaped area of thawed ground surrounded by permafrost.

The preliminary exploration between 1979 and 1982 consisted of drilling six holes to depths of 45-305 m (Woodward-Clyde Report, 1983). The current exploration work involves acquiring remote sensing images, geophysical data, drill holes temperature logs and lithologs, followed by the development of a conceptual geologic model, reservoir simulation models and reservoir stimulation models. The reservoir simulation and stimulation models will help to determine the viability of power production from Pilgrim Hot Springs, Seward Peninsula, Alaska. The hypothesis for this research is that Pilgrim Hot Springs has the potential to be a viable geothermal resource for direct use applications and possible power production. This thesis work presents the reservoir simulation models which best represent the geological and geophysical studies at Pilgrim Hot Springs. These models have been utilized to estimate the heat flux near the surface. The thesis also presents three reservoir stimulation models that incorporate production scenarios which help to determine the viability of power production from Pilgrim Hot Springs.

1.1.2 Research Objectives

The objectives of this study are to utilize the various geological and geophysical data: remote sensing, airborne electromagnetic (EM) survey, magnetotelluric (MT) survey, gravity anomaly, temperature logs, and lithology and a stratigraphic section from Pilgrim Hot Springs in order to:

- Develop reservoir simulation models.
- Estimate the heat flux near the surface based on the reservoir simulation models.

- Compare the simulated well temperatures to the actual well temperatures recorded from the field.
- Attain steady-state conditions for the reservoir simulation model.
- Compare the heat flux estimated by the reservoir simulation model to the heat flux estimated via remote sensing.
- Generate production scenarios which convert the reservoir simulation model into a reservoir stimulation model.

1.1.3 Thesis Structure

This thesis describes the development and results of the reservoir simulation models and stimulation models for the Pilgrim Hot Springs geothermal system in western Alaska. In the remaining part of Chapter 1 of this thesis an overview of the geothermal systems, energy production, and developments is presented. Chapter 2 describes the location, geologic setting and previous investigations of Pilgrim Hot Springs including existing datasets that have been applied within this research. Chapter 3 describes the methodology utilized to develop the reservoir simulation models using geological and geophysical data and a recently developed conceptual geologic model of the geothermal system. Two reservoir simulation models have been developed based on the interpretations and analysis of the relevant data. Finally, three production case scenarios are created using the reservoir simulation model which converts the simulation model into stimulation models. Chapter 4 describes the results and validation of the reservoir simulation models that include predictions of the near surface heat flux.

This chapter also outlines the conversion of the reservoir simulation model into stimulation models by incorporating different production well scenarios. Chapter 5 of the thesis includes the discussion of results and describes the major conclusions from the reservoir simulation and stimulation models, the significance of the results for reservoir development and potential future directions for this research.

1.2 Background

1.2.1 Geothermal Systems

Geothermal energy is the thermal energy generated and stored in the earth's core, mantle and crust. This thermal energy is manifested as rising temperatures in the crust with increasing depth, with an average rate of 25-30 ℃ km^{-1} (Fridleifsson and Freeston, 1994). The transfer of geothermal energy towards the Earth's surface occurs by a combination of conduction and convection with the former dominating in hot springs. Geothermal systems occur in regions of anomalously high crustal heat flow that may be related to the presence of igneous activity or be caused by deep circulation and heating of sub-surface fluids in regions of crustal extension. Crustal extension leads to brittle deformation of the upper crust and breakage into slivers that are oriented perpendicular to the direction of extension. Geothermal systems occur in a number of geological environments (Fridleifsson, 1986). Often igneous activity associated with various settings provides the heat source for geothermal fluids and the heat source may be intrusive or extrusive (Figure 1.1). Igneous rocks which are formed by crystallization of liquid or magma may be classified into intrusive or extrusive.

Volcanic or extrusive rocks form when magma cools and crystallizes on the surface of Earth. Intrusive or plutonic igneous rocks form when magma cools and crystallizes at a depth in the Earth. As described by Muffler (1976), the geothermal systems which are non-igneous are divided into four types. These include those that involve (i) deep circulation of meteoric water along faults and fractures, (ii) resources in high porosity rocks at hydrostatic pressure, (iii) resources in high porosity rocks in excess of hydrostatic pressures (geopressured), and (iv) resources in low porosity rock formations (hot, dry rock).

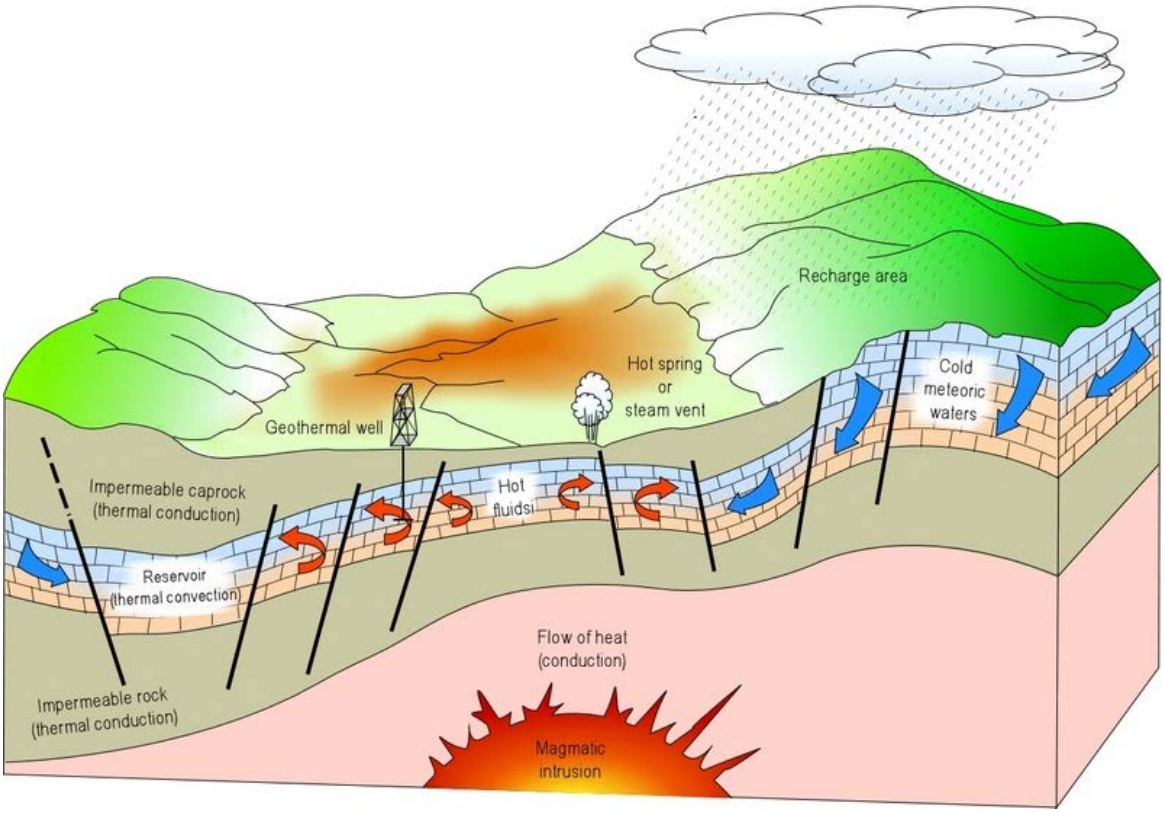


Figure 1.1: Example of a geothermal system with heat source due to igneous activity (Energy Information Administration, 2011).

1.2.2 Geothermal Energy and Production

The utilization of geothermal energy may be divided into two categories: electric production and direct use. Most existing geothermal electrical production occurs with hydrothermal systems where fluid temperatures are above 150 ℃. In electrical production from a geothermal source, the efficiency of extraction is governed by the efficiency of the steam-turbine generators and the theoretical limitations of the Carnot cycle (Bertani, 2011).

There are three main types of geothermal electrical production systems currently in use: dry steam, flash steam and binary steam. Dry steam power plants draw from underground resources of steam. The steam is piped directly from underground wells to the power plant where it is directed into a turbine/generator unit (Bertani, 2011). Flash steam power plants are the most common and use geothermal reservoirs of water with temperatures greater than 360 °F (182 °C). This very hot water flows up through wells in the ground under its own pressure (Bertani, 2011). As it flows upward, the pressure decreases and some of the hot water boils into steam. The steam is then separated from the water and used to power a turbine/generator. Any leftover water and condensed steam is injected back into the reservoir to sustain the resource.

Binary cycle power plants operate on water at lower temperatures of about 225–360 °F (107–182 °C). They use the heat from the hot water to boil a working fluid, usually an organic compound with a low boiling point (Bertani, 2011). The working fluid is vaporized in a heat exchanger and used to turn a turbine.

The water is then injected back into the ground to be re-heated. The water and the working fluid are kept separated during the whole process, so there are little or no air emissions. Pilgrim Hot Springs, on the Seward Peninsula, is a low temperature resource with geothermometry of 150 °C, but measured temperatures around 90 °C. The possibility of developing Pilgrim Hot Springs as a low temperature geothermal system lies in utilizing binary cycle power plants. Thus, with the advancements made in the technology, low temperature systems may be developed by utilizing the binary cycle power plants.

1.2.3 Geothermal Development

A total of twenty-four countries now generate electricity from geothermal resources (Figure 1.2) with the top five producers being the USA, Philippines, Indonesia, Mexico and Italy. In these and other countries geothermal is an important source of energy that accounts for an increasingly large proportion of installed capacity: for example, Iceland. Total installed capacity worldwide of geothermal energy is currently 10,898 $MW_{Thermal}$ (Bertani, 2011). Geothermal energy installed capacity is forecast to increase to around 19.8 $GW_{Thermal}$ by the year 2015 (Bertani, 2011).

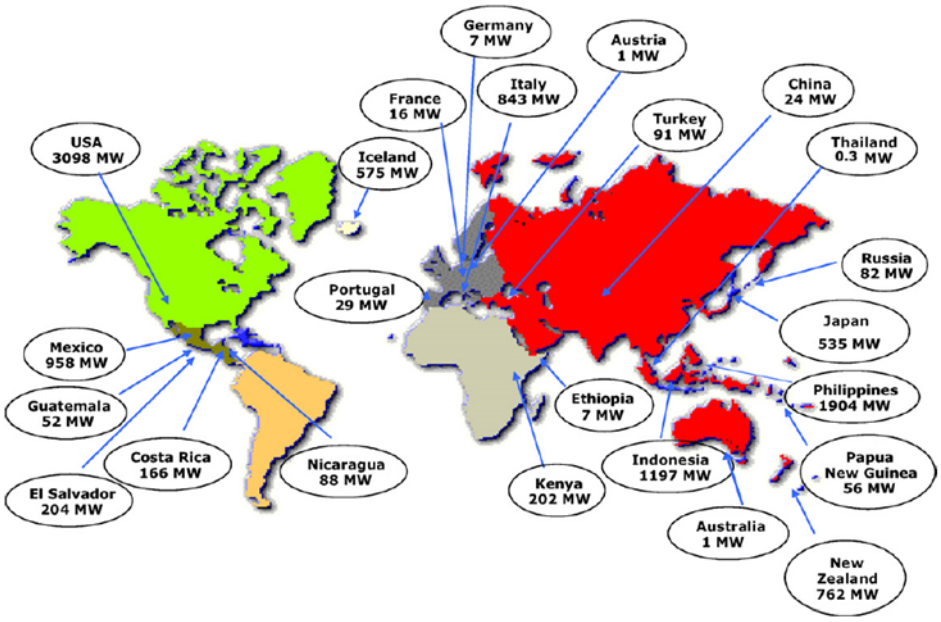


Figure 1.2: Distribution of geothermal energy production plants around the world, along with production capacities (Bertani, 2011).

The United States is the world's largest producer of geothermal energy with an installed capacity of 2979 $MW_{Electric}$. Developed geothermal systems are found in Alaska, California, Florida, Hawaii, Idaho, Nevada, New Mexico, Oregon, Utah and Wyoming (Lund et al., 2010). Most geothermal plants in the USA are concentrated in the Geysers in Northern California and the Imperial Valley in Southern California (Fridleifsson and Freeston, 1994).

The utilization of low enthalpy fluids has also been rapid in the USA (Fridleifsson and Freeston, 1994). In the State of Alaska there are abundant geothermal resources (Miller, 1994). The largest geothermal resource is the Aleutian volcanic arc, which extends some 2500 km from the Hayes volcano 130 km west of Anchorage. There are over 60 major volcanic centers of Quaternary age, ranging in volume from 5 to more than 400 km^3, that are part of this island-arc and continental margin system (Miller, 1994).

These volcanic centers are associated with many thermal areas consisting of fumaroles, mud pots, and more than 30 thermal springs. Unlike the thermal springs elsewhere in Alaska, they are associated with areas of active volcanism. This is well supported by the high surface temperature of the spring waters and reservoir temperatures. Thermal springs in Alaska, outside of the Aleutian volcanic arc, are characterized by relatively low surface temperatures, as indicated by geothermometry (usually less than 150 °C). They appear to be associated with fractured margins of granitic plutons and have low porosity. The first geothermal power plant in the State of Alaska was installed in 2006, at Chena Hot Springs. This resource produces 225 $kW_{Electric}$ from the coldest geothermal resource worldwide, with maximum temperature around 74 °C (Bertani, 2011). A second twin unit has been added and the third unit is under construction. The total installed capacity of 730 $kW_{Electric}$ provides off-grid power in a rather remote location (Bertani, 2011).

Chapter 2: Study Area and Data

2.1 Study Area (Pilgrim Hot Springs)

2.1.1 General Setting

Pilgrim Hot Springs is located on the Seward Peninsula, Alaska, approximately 97 km north of Nome and 130 km south of the Arctic Circle (Figure 2.1). The study area is centered at latitude 65° 06’ N, longitude 164° 55’ W. The geothermal area is marked by a 5 km^2 area of thawed ground populated by broadleaf trees such as poplar, that is in marked contrast to the surrounding sub-Arctic vegetation cover lying on discontinuous permafrost located at shallow depths below the surface. This permafrost impedes both the downward and lateral movement of water, so that in the broader study area most precipitation runs-off as surface water. Pilgrim Hot Springs is located immediately south of the east-west meandering Pilgrim River that lies in a relatively flat valley, which is bounded by Kigluaik Mountain in the south and Mary’s Mountain and Hen and Chicken Mountain in the north (Figure 2.2).

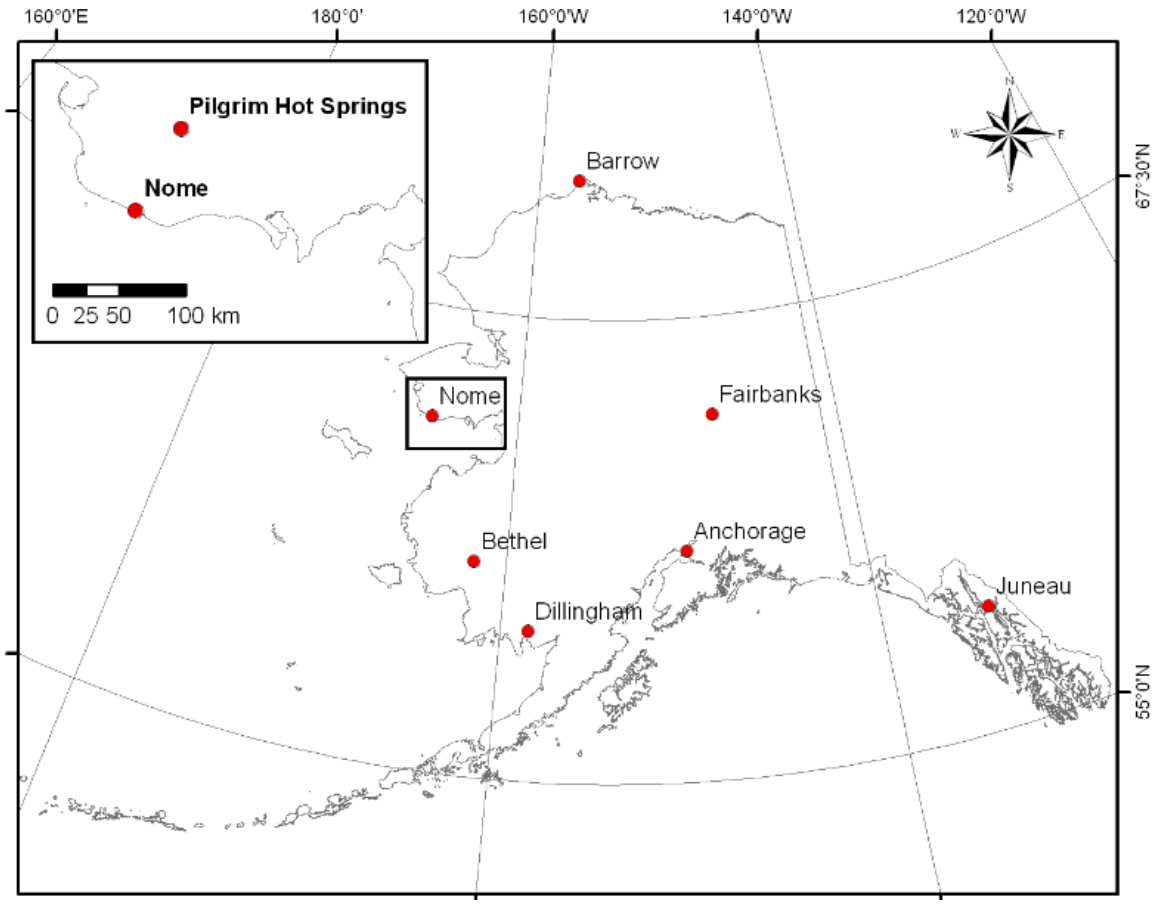


Figure 2.1: Pilgrim Hot Springs area located in the Seward Peninsula, Alaska (Dr. Rudiger Gens).

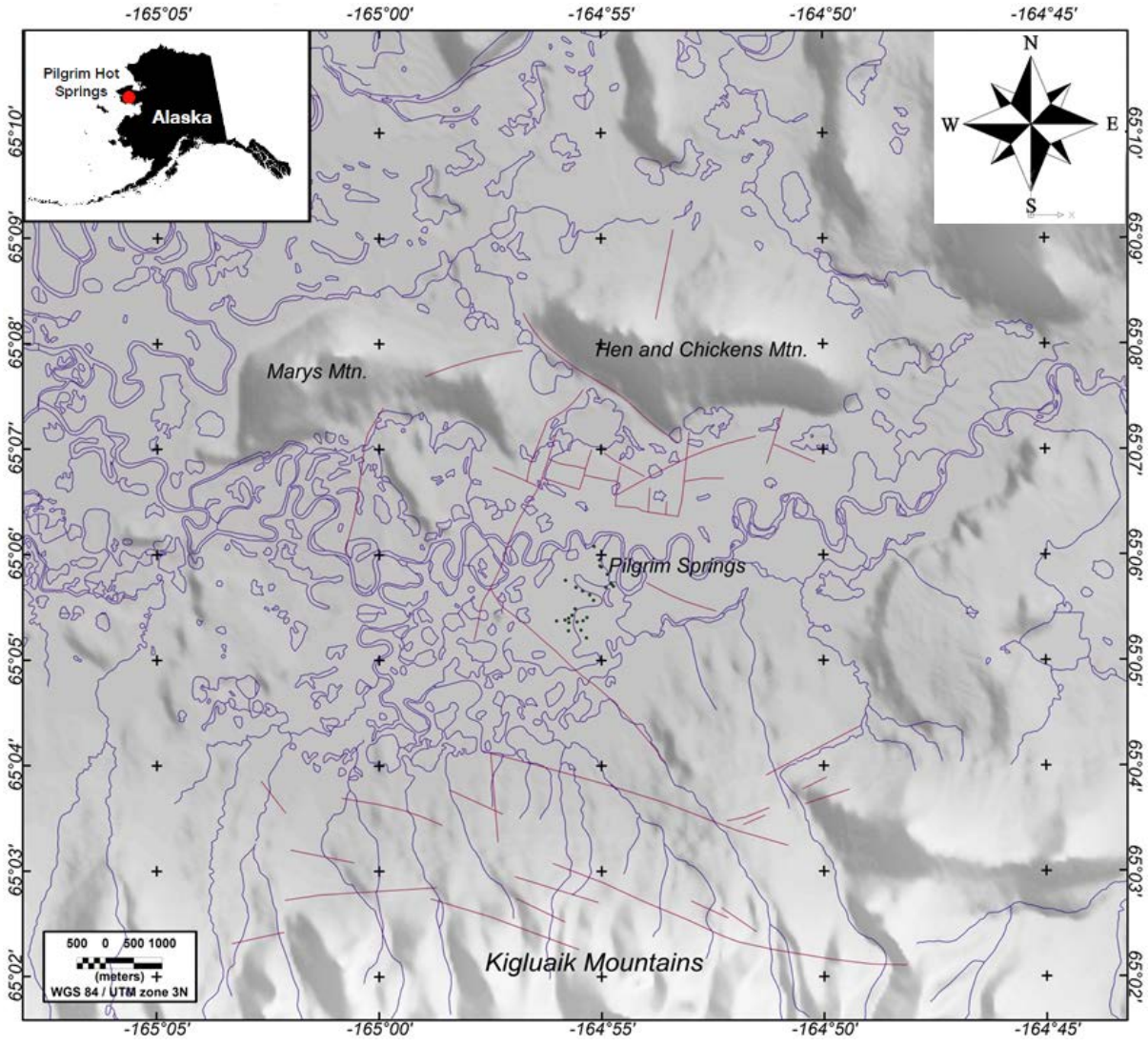


Figure 2.2: Pilgrim Hot Springs area bounded by Kigluaik Mountains to the south and Mary's and Hen and Chicken Mountains to the north (McPhee and Glen, 2012).

2.1.2 Geological Overview

A summary of the surficial and bedrock geology of the study area is shown in Figure 2.3 (Miller et al., 2013). The Pilgrim River Valley, considered to represent a valley graben system, is bounded on the south by the Kigluaik Mountains, which rise from the valley floor as a north-facing escarpment developed along a range-front fault (Turner and Forbes, 1980). This fault is seismically active and has experienced displacement during the Holocene. Mary's Mountain and Hen and Chicken Mountain are located on the low ridge about 5 km north of Pilgrim Hot Springs and are composed of granitic gneisses, intrusive granites and rare amphibolites (Turner and Forbes, 1980). Fault traces on both sides of the valley indicate that the valley is down-thrown. The valley fill includes both alluvial and glaciofluvial deposits, and possible lacustrine sands and silts of Quaternary age (Turner and Forbes, 1980).

Crystalline basement rocks contain an anomalously high uranium-thorium content that provides one potential source of geothermal heat through radiogenic decay, which is a heat generation mechanism suggested for other hot springs of the Central Alaskan Hot Springs Belt (Turner and Forbes, 1980). Tertiary sedimentary rocks overlie the crystalline basement rocks at Pilgrim Hot Springs. Recent volcanic activity includes basalt flows that are located to the east and west of Pilgrim Hot Springs, which may be related to tectonic extension in the area. This volcanism is believed to have begun about 30 million years ago and has continued up to the present (Turner and Swanson, 1981).

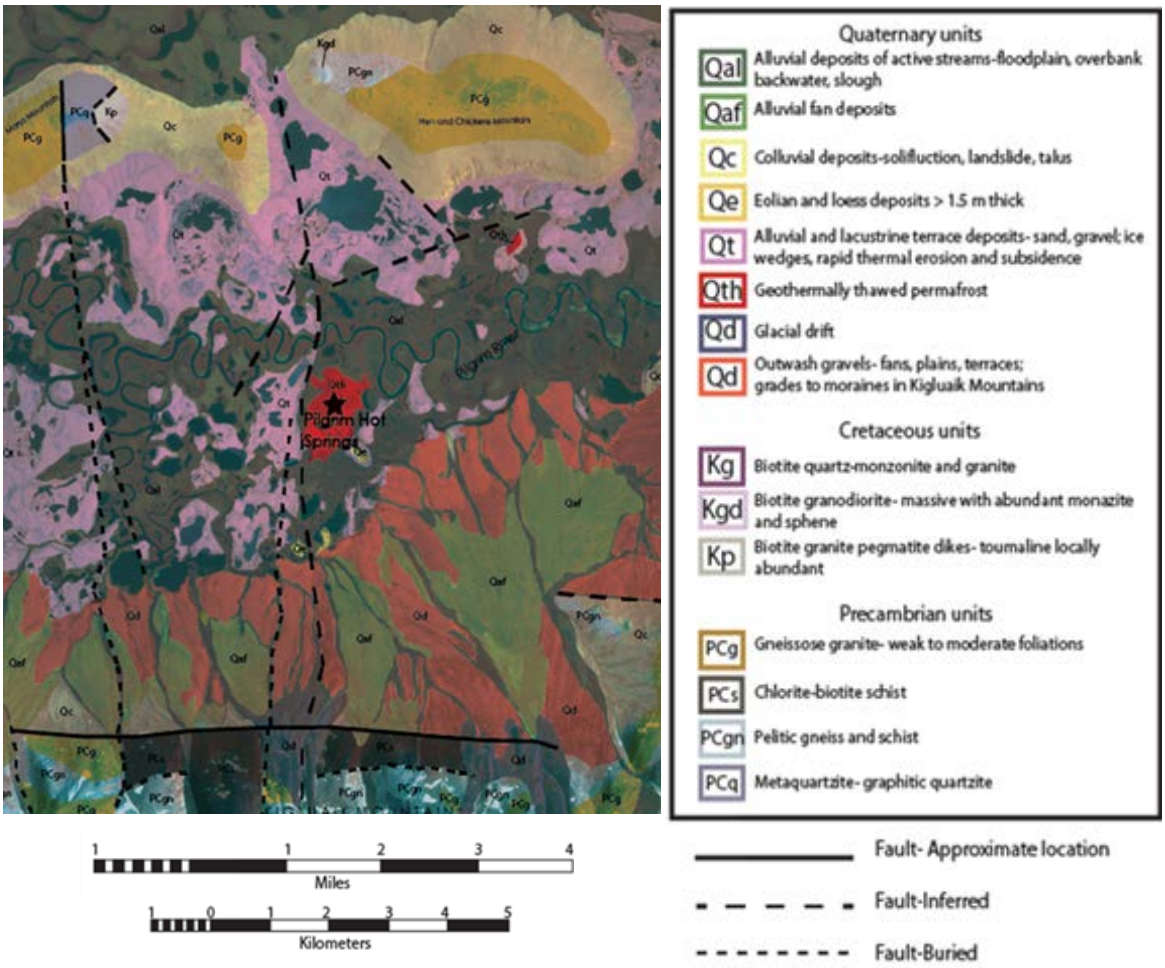


Figure 2.3: Surficial and bedrock geology map of the Pilgrim River Valley, Seward Peninsula, Alaska (Miller et al., 2013). Quaternary, Cretaceous, and Precambrian units are found in the immediate area. Many surface deposits are the result of Quaternary glaciation and permafrost-related features.

Although recent basalt flows and vents have not occurred in the immediate vicinity of Pilgrim Hot Springs, the possibility of subsurface emplacement of basaltic magma in the valley section has to be considered in the geothermal models. The major geologic units found around Pilgrim Hot Springs are Quaternary units, Cretaceous units and Precambrian units. The Kigluaik Mountains in the south mainly comprise Precambrian units, such as gneissose granite, chlorite-biotite schist, politic gneiss and schist and metaquartzite and graphitic quartzite. There are also traces of Quaternary units: outwash gravels, glacial till, alluvial and lacustrine terrace deposits, colluvial deposits and alluvial deposits.

Alluvial fan deposits from the Kigluaik Mountains lead into the Pilgrim Hot Springs valley. Pilgrim Hot Springs is well-contained within the geothermally thawed permafrost area. In the vicinity of Pilgrim Hot Springs, there are alluvial deposits of active streams-floodplain, overbank backwater, and slough. There are also alluvial and lacustrine terrace deposits: sand, gravel, ice wedges, rapid thermal erosion and subsidence. Mary’s Mountain and Hen and Chicken Mountains mainly consist of Precambrian units and Quaternary units.

2.1.3 Previous Work

The University of Alaska Geophysical Institute, in co-operation with the Alaska Division of Geological and Geophysical Surveys, undertook exploration and assessment of Pilgrim Hot Springs from 1978-1981 as a part of a U.S. Department of Energy (DOE) funded grant. This work included shallow temperature surveys, a soil-helium survey, exploration drilling, well testing and a variety of geophysical investigations.

The soil-helium investigation suggested that a reasonable correlation exists between the helium concentrations and shallow temperature contours. The following text summarizes the findings of Turner and Forbes (1980). In 1980, Turner and Forbes had prepared a report on Pilgrim Hot Springs for the U.S. Department of Energy. Geophysical studies including seismic refraction, geomagnetic profiling, electrical resistivity surveys, hydrologic studies, and He and Hg soil surveys, delineated a shallow geothermal reservoir which was confirmed by drilling. However, the bedrock and the conduit feeding the geothermal fluids to the shallow reservoir were not determined. Six out of the eleven wells across Pilgrim Hot Springs were drilled during the period 1979 to 1982 (Figure 2.4). The water chemistry suggested that waters produced from PS 1 and PS 2 in 1979 were identical, and more concentrated, versions of spring waters. The stable isotope composition of thermal waters was nearly the same as Pilgrim River which suggested that the river was the major source of recharge to the thermal aquifer. The wells PS 3 and PS 4 drilled in 1982 produced diluted versions of the more concentrated PS 1 well waters.

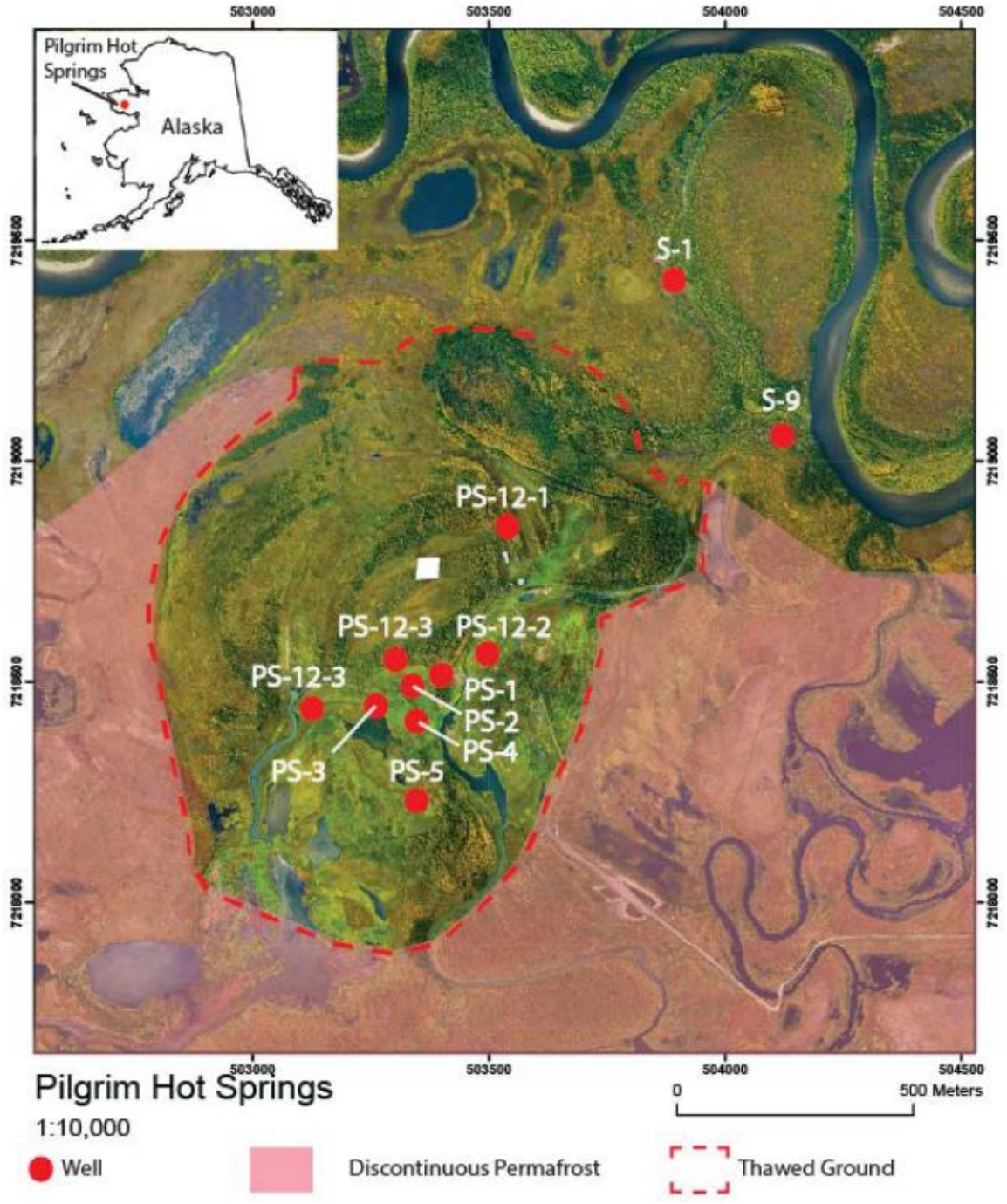


Figure 2.4: Location of all drill holes across Pilgrim Hot Springs are shown by the red colored dots where six of these wells were drilled from1979 to 1982 (Haselwimmer and Prakash, 2012).

Re-sampling of wells in 1993 suggested that waters from PS1 became more diluted while PS 3, PS 4, MI 1 had become more concentrated. While the temperatures at the wells declined very slightly between 1982 and 1993, springs waters had cooled substantially. This was probably the result of diversion of the ascending thermal waters from the bedrock by the flowing wells. Geothermometry suggested temperatures of a deep reservoir to be around 150 °C. The gas geothermometry suggested even higher reservoir temperatures. Isotopic chemistry suggested that the deep aquifers are likely charged by surface meteoric waters migrating along the faults. The $^{3}He/^{4}He$ ratio does suggest magmatic input to the system (Turner and Forbes, 1980).

The seismic refraction program at Pilgrim Hot Springs suggested three layers below the surficial zone. The fluvial sediments were found to be 30 m thick, glacio-fluvial gravels were found to be 38-40 m thick and a third layer was poorly defined. The gravity survey was conducted to define the regional crustal structure and estimate the depth to the crystalline basement. The gravity survey suggested that the Pilgrim valley is a sedimentary trough and elongated in a southwest-northeast direction. At the springs, the crystalline basement lies around a depth of 200 m while the deepest part of the trough could be around 400-500 m depth. The data suggested that the hot springs appeared to be located at the northeastern corner of this subsided basement block.

An electrical resistivity survey was conducted in order to delineate the hot water reservoir underlying the Pilgrim Hot Springs. The model suggested that permafrost, up to a depth of 100 m, existed towards the east and west of the springs as indicated by high resistivity values. The most important feature of this modeling work suggested that the permafrost did not extend to basement, and waters were free to migrate in aquifers beneath the permafrost. Finally, the power potential of the geothermal system was assessed using the temperature distribution of the area, both in plan view and at depth. Surface measurements, in the form of stream temperature and flow measurements, allowed an estimation of the power produced by the surface flow from the main hot springs area. The power carried by the main hot springs 81 °C water was calculated to be 1.4 MW. Borehole measurements allowed the power estimation from vertical flow of fluids at 10 MW (Turner and Forbes, 1980).

In 1983, Woodward-Clyde consultants prepared a report on Pilgrim Hot Springs. Four types of well test data were collected: pressure-interference effects among wells; geochemistry of well-discharge waters; temperature gradients; and hydraulic tests to evaluate reservoir-system parameters. The interference tests involved monitoring the pressure head at shut-in wells when a nearby discharge well was opened. However, the drawdown test indicated subtle changes in head due to differences in depths of well perforations. This suggested that a series of horizontal aquitards may effectively separate wells of different depths in the reservoir (Woodward-Clyde Report, 1983).

Geochemical studies concluded the fluid composition of hot springs water to be alkali-chloride-rich, with dissolved carbon dioxide and hydrogen sulfide. Oxygen and deuterium isotope analysis suggested deep-seated water-rock reactions. The high-salinity and dissolved gases suggested a volcanic origin and a source temperature of ~130 °C (Woodward-Clyde Report, 1983). Geophysical surveys, resistivity and gravity, indicated a 1.5 km^2 reservoir and a downthrown block of basement to the southwest edge of the thawed ground bounded by intersecting faults at depth immediately below the springs.

The temperature profiles from all the wells suggested that two types of heat transfer occur here: Horizontal movement of groundwater at shallow depths which might be the reason for the high temperatures above a depth of 60 m, and convective heat transfer which brings the heat upward from the underlying heat source (Woodward-Clyde Report, 1983). However, there was little evidence to indicate the direction of either the groundwater flow or the heat source. Flow tests were conducted to evaluate the hydraulic characteristics of saturated sediments. The two main parameters were transmissivity (T) and storage coefficient (S). Transmissivity is a measure of the ability of the formation to transmit groundwater; the storage coefficient is a measure of the ability of the rock to store and release groundwater. The transmissivities (T) for the wells were estimated by plotting draw-down pressures versus time on semi-logarithmic graphs and analyzing them using a straight-line technique (Jacob and Lohman, 1952). A conceptual model of the Pilgrim Hot Springs was developed and the discharge of energy was estimated from the modeled geothermal system (Woodward-Clyde Report, 1983).

The modeled geothermal system considered: discharge of energy to the atmosphere, discharge of energy from numerous springs, discharge of energy in groundwater away from the area and discharge of energy via conductive heat transfer to deeper zones. The accessible geothermal resource base for the modeled part of the geothermal system was estimated to be about 24 MW (Woodward-Clyde Report, 1983). Lorie M. Dilley prepared a preliminary feasibility report for Pilgrim Hot Springs in 2007 for the Alaska Energy Authority. According to this report (Dilley, 2007), assuming 5 MW of accessible energy, power production from the shallow and deep reservoirs is possible at high flow rates of 480 gpm for every 1 MW in the deeper source and 1200 gpm for the shallow aquifer using a reverse-refrigeration binary plant.

Recent exploration work of Pilgrim Hot Springs involved satellite-based and airborne-based anomaly mapping. Time series ASTER data indicated snow free areas and vegetation growth anomalies (Haselwimmer and Prakash, 2012). Thermal infrared data were collected over the study area during September 2010 and April 2011 using a Forward Looking Infrared (FLIR) camera mounted on an aircraft. The objectives of these FLIR surveys were to identify the thermal anomalies outside the main spring's site. The second airborne thermal survey successfully provided new observations of anomalous snow melt which was consistent with the conductive/convective surface heating around the main Pilgrim Hot Springs area (Haselwimmer and Prakash, 2012). The total heat flux near the surface of the geothermal anomaly estimated from remote sensing is 4.7-6.7 $MW_{Thermal}$ (Haselwimmer et al., 2013).

Current exploration work also involved a variety of other data collection efforts including: airborne electromagnetic survey, magnetotelluric survey, gravity survey, drilling geoprobe temperature gradient holes across the reservoir, drilling exploratory wells, lithology analysis and stratigraphy development, and development of a conceptual geologic model. This conceptual model aids in developing the reservoir simulation model for Pilgrim Hot Springs.

2.2 Data

There is a wealth of data available for the Pilgrim Hot Springs area. Here we only report and discuss the datasets which have been used and applied to this research work. The relevant datasets utilized to develop the reservoir simulation model at Pilgrim Hot Springs, Alaska are listed and briefly described below.

2.2.1 Remote Sensing Data

The high resolution optical image (Figure 2.4) is utilized to visually interpret the various types of surface features surrounding the Pilgrim Hot Springs area. These include polygon permafrost, hummocks, horse tail drain permafrost, sorted circles, thermokarst lakes, rivers, lakes, geothermal areas and vegetated areas (Figure 2.5).

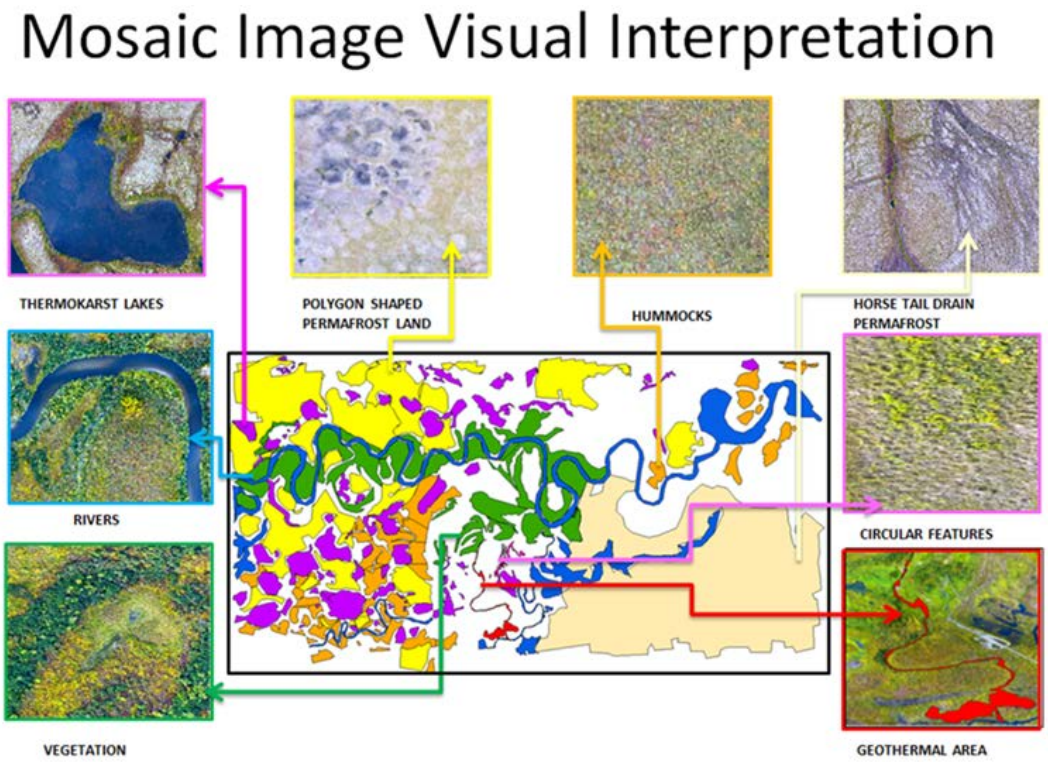


Figure 2.5: Various types of surface land features interpreted from the high resolution optical image (Arvind).

2.2.2 Airborne Electromagnetic (EM) Survey

Commercial airborne electromagnetic (EM) survey data was collected by FUGRO using the RESOLVE helicopter electromagnetic system. This airborne EM system provides measurements of the ground conductivity or resistivity with depths up to 100 m. The frequency domain consists of the primary field oscillating smoothly over time (sinusoidal), inducing a similarly varying electric current in the ground. The airborne EM system had a frequency range between 400 Hz to 140 KHz. The length of the survey covered a distance of 546 km with the height above the ground being 60 m.

The six nominal frequencies utilized in this survey were 400 Hz, 1800 Hz, 3300 Hz, 8200 Hz, 40000 Hz and 140000 Hz (McPhee and Glen, 2012). The working principle of the airborne EM survey (Figure 2.6) involves creating a magnetic field by inducing current in the coil. This magnetic field is utilized to induce eddy currents which are recorded by the receiver coils. The magnitude of eddies generated in the field is measured in terms of resistivity.

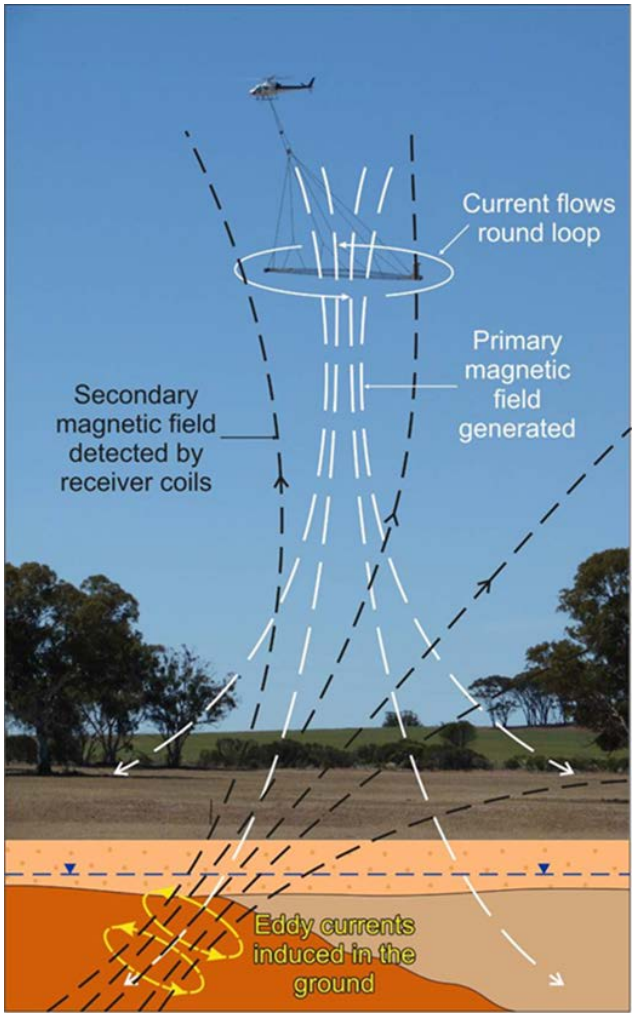


Figure 2.6: Basic working principle behind the airborne EM survey (Fitzpatrick et al., 2010).

A general relationship between common material types and resistivity (Figure 2.7) was published by Palacky (1988). As indicated in this figure, igneous and metamorphic rocks have very high resistivity values ranging from 1000-100000 ohm-m. Permafrost indicates high resistivity values ranging from 500-100000 ohm-m, glacial sediments have relatively lower resistivity values, and the lowest range of resistivity values are shown for salt water (0.1-1 ohm-m) and fresh water (1-100 ohm-m). The analysis and interpretation of the airborne EM survey data will be discussed in detail in Chapter 3. The airborne EM survey data have been utilized to distinguish frozen and unfrozen ground. The reservoir model's size, shape and extent have been developed based on the interpretation of the airborne EM survey.

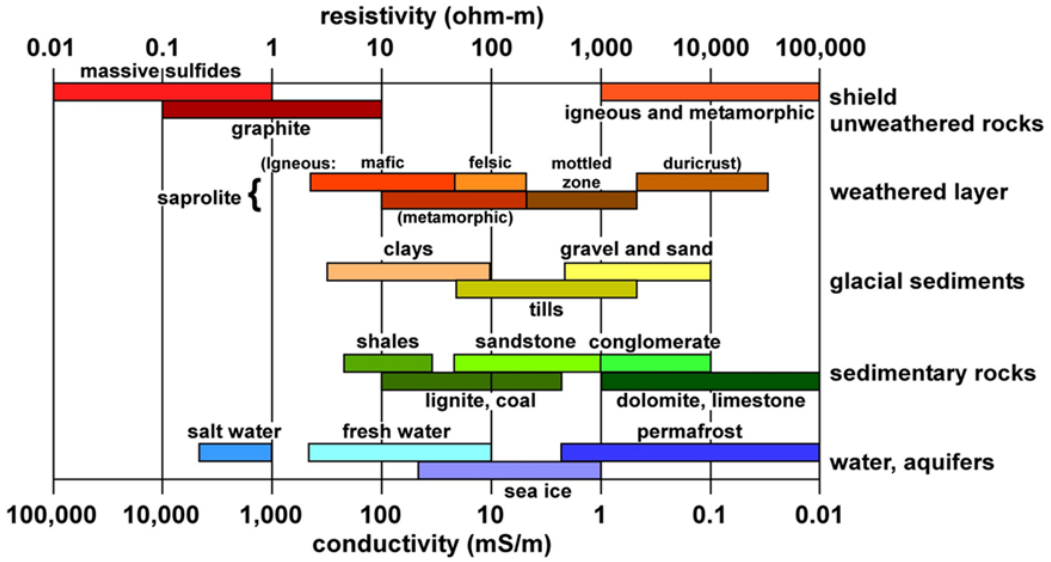


Figure 2.7: Relationship between the lithologies and resistivity values (Palacky, 1988).

2.2.3 Magnetotelluric Survey

A magnetotelluric (MT) survey was conducted at Pilgrim Hot Springs accounting for the best possible resolution considering accessibility constraints. In total, 59 stations recorded at 0.001-10000 Hz range overnight with an average distance of 100 m apart, with a remote station 5 km SE of the site. 1D MT inversion and 3D MT inversion data was collected by Fugro Electric Magnetics, Italy, Srl. A MT survey is a frequency domain technique which utilizes naturally occurring magnetic and electric signals as a source to obtain a resistivity map of the subsurface. Temperature, pressure, lithology and permeability control the electrical resistivity measured in the formation. Lower frequencies help to probe deeper into the Earth (Vozoff, 1991).

Natural fluctuations in the Earth's magnetic field are used as signal source (Hx, Hy). These fluctuations induce current in the ground which is measured at the surface (Ex and Ey). The measured MT time series are Fourier transformed into the frequency domain. The best solution which represents the relation between the magnetic field and the electric field is given by Equation 2.1 and Equation 2.2.

$$\begin{bmatrix} E_X \\ E_Y \end{bmatrix} = \begin{bmatrix} Z_{XX} & Z_{XY} \\ Z_{YX} & Z_{YY} \end{bmatrix} \begin{bmatrix} H_X \\ H_Y \end{bmatrix} \tag{2.1}$$

$$\vec{E} = Z\vec{H} \tag{2.2}$$

E and H are the electric and magnetic field vectors in the frequency domain (Hersir et al., 2013). Z represents the impedance tensor which contains all the information about the subsurface resistivity structure. From the impedance tensor, apparent resistivity and phases for each frequency are calculated. 1D and 3D inversion are performed on the impedance tensor.

The relationship between the material types and resistivity values (Figure 2.8) show that salt water and fresh water are strong to moderate conductors. However, permafrost, as well as igneous and metamorphic rocks, are very strong resistors. Glacial sediments, such as clays, behave as moderate conductors. A MT survey helps to better visualize the deeper structures of the reservoirs and to identify sharp contrasts in resistivity values which may relate to sudden changes in lithology due to faulting (Lugao et al., 2002). The low resistivity values in the reservoir may be due to the presence of thermal waters, high temperature, lithology, and high permeability indicating fractures or faults. High temperature saline fluids will form an electrically conducting medium which, combined with hydrothermal alteration of the surrounding rock, will lower the resistivity (Bertrand et al., 2011). Thus, A MT survey in our case will help to identify the possible flow path of the geothermal fluids or the plumbing of the system and location of the heat source.

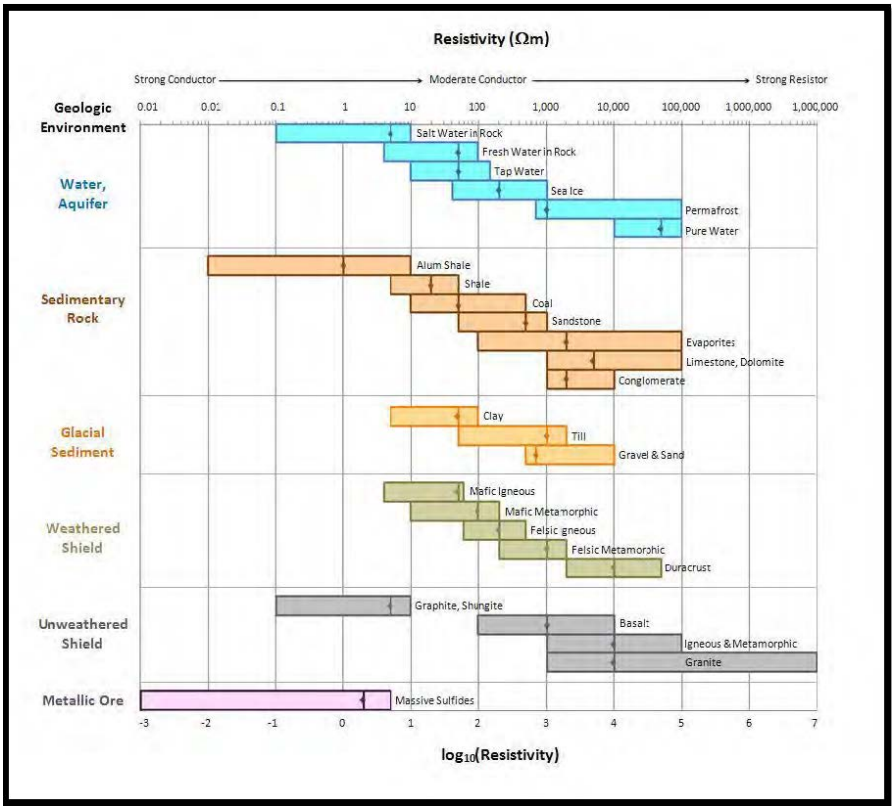


Figure 2.8: Typical resistivity values of common material types (Lugao et al., 2002).

The analysis and interpretation of the MT survey data and its use within the simulation model will be discussed in detail in Chapter 3. The MT survey data have been utilized to determine the possible location of the heat source and the plumbing system within the reservoir model. Two reservoir simulation models have been developed based on different plumbing systems and different locations of the heat sources.

2.2.4 Static Temperature Logs

Drilling logs and temperature profiles for the eleven wells drilled at Pilgrim Hot Springs are available for analysis and data interpretation. The eleven wells which exist in Pilgrim Hot Springs are: PS 1, PS 2, PS 3, PS 4, PS 5, MI 1, S1, S9, PS12-1, PS12-2 and PS12-3. There are temperature profiles available from the 50+ shallow geoprobe temperature gradient holes. The analysis and the interpretations of the temperature logs and geoprobe temperature gradient holes will be discussed in detail in Chapter 3. The geoprobe holes and temperature logs have been utilized to determine the intervals of cold water influx and outflow from the reservoir model. The temperature logs indirectly help to determine possible regions of upflow and outflow of hotter geothermal fluids when correlated with MT survey data.

2.2.5 Geophysical Logs

Characterization of the drill cuttings from the wells have been used to generate lithological logs that have formed a framework for the development of a conceptual geological model of the geothermal system. The sediment characterization from all the wells has resulted in estimation of porosity and permeability values which are important input parameters for the numerical reservoir model. The geologic model of the Pilgrim Hot Springs has been developed with the preceeding information using RockWorks 15 (Miller et al., 2013). Analyses and interpretations from the conceptual geologic model and their use within the simulation model will be discussed in detail in Chapter 3.

Chapter 3: Reservoir Modeling Methodology

3.1 TOUGH2 Modeling Background

A number of numerical models have been developed for geothermal systems that are based upon steady-state simulation of the flow regime associated with up-flow along permeable faults (Pruess, 1988). Characterization of reservoirs necessary for building these models is based upon determining key characteristics such as temperature profiles, heat flow, the geometry and the properties of subsurface stratigraphy and geological structures (Blackwell, 1983).

Most geothermal systems are associated with upflow paths having relatively high permeability. However, there are some geothermal systems where up-flow paths have relatively low permeability that may lead to cross-range flow (Blackwell, 1983). Under these circumstances temperature inversions can arise due to fluid flow within a thin horizontal or shallowly dipping fracture or aquifer (Bodvarsson, 1969, 1983). In developing numerical models of geothermal systems with significant cross-range flow, bulk permeability is an important parameter that needs to be considered. Previous simulation work has consisted of modeling domains which typically consist of a valley floor surrounded by mountain ranges (Figure 3.1). The valley floor has a thick sequence of clastic sediments (Blackwell and McKenna, 2004). A high-angle fault acts as the main conduit for the subsurface fluids. This common and simplified scenario is quite likely to be the case at Pilgrim Hot Springs.

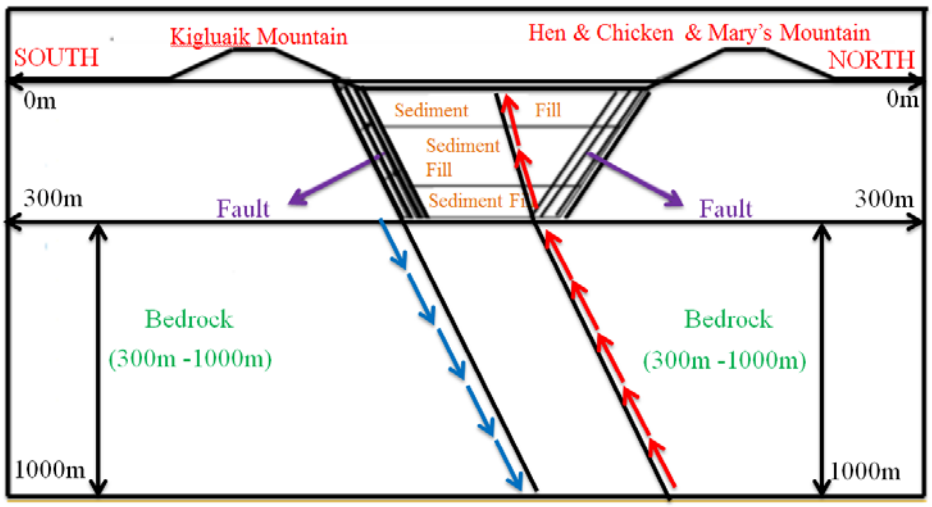


Figure 3.1: Schematic diagram of a fault-bounded valley floor surrounded by mountain ranges, which is a common setup for many geothermal systems (Blackwell and McKenna, 2004).

There exists an approximate proportionality between the rate of natural heat loss (conduction and advection) and electric power production (Williams, 2005). Various models have been developed to predict surface heat flows by variation in bulk rock permeability, and presence and absence of faults. The simulations have indicated that the basin and range geothermal systems are highly time dependent and the geologic history can dramatically modify the maximum reservoir temperature and time-frame of occurrence (Blackwell and McKenna, 2003). Most relationships between the structure, heat input, and permeability distribution for extensional geothermal systems have been determined on the basis of steady-state modeling.

For these models, the maximum temperatures and heat flow via the fault or conduit are proportional to the basal heat flow – that is, heat released from the base layer of the model. Topography may provide an additional kick to the fluid circulation as fluids flow from higher elevations towards lower elevations due to a difference in the pressure heads. In general, flow from the mountain ranges to the fault dominates the fluid circulation. The fault may also create a cross-range flow in the valley. The higher bulk permeability creates additional deep circulation cells in the valley (Blackwell and McKenna, 2004). For this work, the modeling approach being used considers utilizing the steady-state modeling technique. The key to setting up a steady-state model is to understand the movement of the hot water from the bedrock up to the surface without mixing with the cross-flowing cold water lower in the reservoir. We assume that there has to be an up-flow path with relatively higher permeability when compared to the surrounding geology. Thus, the high angle fault acts as a conduit to allow the up-flow of hotter fluids from the bedrock. The geothermal fluid is propelled to the surface through density induced pressure differences. The differences in the density between the up-welling, hotter fluids and surrounding cooler fluids allow fluid movement within a domain which may be viewed as a convection chamber.

This work consists of building a reservoir domain which represents a valley composed of a thick sequence of clastic sediments overlying the bedrock, surrounded by mountains on the north and south side that possibly control the cross-flow of cooler fluids. Temperatures and heat flow within the domain are proportional to the basal heat flow.

The software utilized to build the model is Petrasim. Petrasim belongs to the TOUGH family of codes. The numerical code used to solve the coupled, non-linear equations of heat and fluid flow is TOUGH2 (Pruess, 1988). The equation of state (EOS) used in this work is (EOS3) air, water and heat flow. We assume water under one phase condition. The physical properties of water are determined for 0-150 °C and 0-100 MPa, by means of lookup/interpolation tables (Pruess, 1988).

Single Phase Flow: The TOUGH family of codes (PetraSim) simulates flow in porous media with a basic assumption that the flow is described by Darcy's Law.

Darcy's Law: Darcy's Law is expressed to represent the fluid flow where the discharge Q is proportional to the difference in the height of water, h (hydraulic head), and inversely proportional to the flow length L as given by Equation 3.1:

$$Q = -KA\left(\frac{h_A - h_B}{L}\right) \tag{3.1}$$

Where, Q = discharge ($m^3\ sec^{-1}$); K = hydraulic conductivity ($m\ sec^{-1}$); A = cross sectional area of flow (m^2); h_A = hydraulic head at point A (m); h_B = hydraulic head at point B (m) and L = flow length (m).

Specific Discharge: The specific discharge which is also known as Darcian velocity or Darcy flux is given by Equation 3.2:

$$q = -K\frac{dh}{dl} \tag{3.2}$$

Where, q = specific discharge ($m\ sec^{-1}$); K = hydraulic conductivity ($m\ sec^{-1}$) and dh/dl = hydraulic gradient (dimensionless).

The reservoir modeling work at Pilgrim Hot Springs involves fluid flow under a single phase condition. Thus, the equations of heat balance and mass balance also consider a single phase condition.

Heat Transfer due to Thermal Conduction: The basic relation for conductive heat transport is given by the Fourier's law (Equation 3.3) which states that the heat flux, or the flow of heat per unit area and per unit time, at a point in a medium is directly proportional to the temperature gradient at the point. Fourier's law is given by Equation 3.3:

$$q = \frac{k\Delta T}{L} \tag{3.3}$$

Where, k = thermal conductivity [W m^{-1} K^{-1}]; ΔT = temperature [°C]; L= distance between the hot point and cold point [m] and Q = heat flux [W m^{-2}].

Heat Transfer due to Thermal Conduction in 3D: The thermal conduction can also be represented by Fourier's law in 3-D which is given by the Equations 3.4, 3.5 and 3.6:

$$\nabla k = \left(\frac{d}{dx}\vec{x} + \frac{d}{dy}\vec{y} + \frac{d}{dz}\vec{z}\right).\left(k_x\vec{x} + k_y\vec{y} + k_z\vec{z}\right) \tag{3.4}$$

$$\nabla T = \left(\frac{d}{dx}\vec{x} + \frac{d}{dy}\vec{y} + \frac{d}{dz}\vec{z}\right).\left(T_x\vec{x} + T_y\vec{y} + T_z\vec{z}\right) \tag{3.5}$$

$$\nabla k \nabla T = \frac{d}{dx}(k_x T_x) + \frac{d}{dy}\left(k_y T_y\right) + \frac{d}{dz}(k_z T_z) \tag{3.6}$$

Where, ∇k = divergence of permeability (variation of permeability with space in x, y, z direction) and ∇T = divergence of temperature (variation of temperature with space in x, y, z direction).

Heat Transfer due to Convection: Convection is the displacement of volume of a substance in liquid or gaseous phase. Natural or free convection is caused by buoyancy forces due to density differences as a result of temperature variations in the fluid. Heat transfer by thermal convection is given by Equation 3.7:

$$q = hA\,(T_s - T_\infty) \tag{3.7}$$

Where, q = heat transferred per unit time [W]; A = heat transfer area of surface [m^2]; h = convective heat transfer coefficient (volumetric heat capacity multiplied with Darcian flux) [W m^{-2} K^{-1}]; $(T_s - T_\infty)$ = temperature difference between surface and bulk fluid [K]; Ts = temperature of the system [K] and

T_∞ = reference temperature [K].

Mass Balance Equation: The change in the fluid mass within a fixed volume is given by the sum of the net fluid inflow across the surfaces of the volume and the net gain of fluid from the sinks and sources of the volume. The mass balance is given by Equation 3.8:

$$\frac{d}{dt}\int_0^{Vn} M^{\kappa} dV_n = \int_0^{\tau_n} F^{\kappa}.\, n d\tau_n + \int_0^{V_n} q^{\kappa} dV_n \tag{3.8}$$

Where,Vn = volume of arbitrary subdomain [m^3]; τ_n= closed surface [m^2]; n = normal vector on surface element $d\tau n$, pointing inward into Vn; M^{κ} = specific mass of component κ [kg m^{-3}] ; F^{κ} = specific mass flux of component κ [kg m^{-2} s^{-1}] and

q^{κ} = specific mass sink/source [kg m^{-3}].

Heat Balance Equation:

The change in heat within a fixed volume is given by the sum of net heat flow across the surfaces of the volume and the net gain or loss of heat from the sinks and sources of the volume. The heat balance is given by the Equation 3.9:

$$\frac{d}{dt}\int_0^{V_n} M^h dV_n = \int_0^{\Gamma_n} F^h . n d\Gamma_n + \int_0^{V_n} q^h dV_n \quad (3.9)$$

Where M^h is the specific bulk heat capacity which is given by Equation 3.10:

$$M^h = (1-\varphi)\rho_R c_R T + \varphi \sum_\beta S_\beta \rho_\beta \mu_\beta \quad (3.10)$$

Where,

M^h= energy in Joules per unit volume or bulk heat capacity [J m^{-3}]; Ø = porosity;

ρ_R = density of fluid [kg m^{-3}]; c_R= specific heat capacity [J kg^{-1} K^{-1}]; T = temperature [K]; μ_β = specific internal energy [J kg^{-1}]; $\varphi S_\beta \rho_\beta$= specific mass of phase β; F^h = specific heat flux [W m^{-2}] and q^h = specific volumetric heat source [W m^{-3}].

Heat Source Cell: The heat associated with the heat source cell (Equation 3.11) is a function of cell volume, density of rock, specific heat and temperature gradient:

$$Q = V\rho C_p \frac{\Delta T}{\Delta t} \quad (3.11)$$

Where, Q = heat (W); V = cell volume (m^3); ρ = density of rock (kg m^{-3}); Cp = specific heat capacity of rock (J kg^{-1} °C $^{-1}$); ΔT = change in temperature (°C); and Δt = change in time (seconds). The Equation 3.11 is utilized in Petrasim software to estimate the heat associated with, and released from, the heat source cell or grid which exists within the reservoir modeling domain.

Mass Flow Rate in Source Cells: The mass flow rate (Equation 3.12) is a function of density of fluid, porosity, volume of cell, compressibility of rock and pressure gradient:

$$m = \rho_{water} \emptyset V C \frac{\Delta P}{\Delta t} \quad (3.12)$$

Where, m = mass flow rate (kg sec^{-1}); ρ_{water} = density of water (kg m^{-3}); $\emptyset$ = porosity of cell; V = volume of cell (m^3); C = pore compressibility ($pascal^{-1}$); ΔP = change in pressure (pascal); and Δt = change in time (seconds).The Equation 3.12 is utilized in Petrasim accounts for the mass flow rate associated with source cells or grids. This equation helps to apply the required pressure conditions to the source cells which involve creation of mass within a fixed volume domain.

3.2 Reservoir Modeling Setup

There are several steps involved in the development of the reservoir simulation model. These include:

- Step 1- Selecting the dimensions and shape of the reservoir model: The reservoir shape and dimensions of the reservoir model are referred to as reservoir domain. This step also involves dividing the domain into a pre-selected number of layers.
- Step 2 – Gridding: The process of selecting the grid density across the reservoir domain for all the layers existing in the domain.
- Step 3 - Applying the initial and boundary conditions: Initial and boundary conditions are applied to the top layer and base layer of the model.

This step also involves locating and incorporating all necessary features such as permafrost, cold water influx and heat source based on the interpretation of the geological and geophysical data.

- Step 4 – Assigning lithology: In this step each layer in the model is assigned a representative lithology and corresponding thermal properties.
- Step 5 – Incorporating fractures and plumbing: Orientation of fracture systems and a possible plumbing route is incorporated in the model domain.

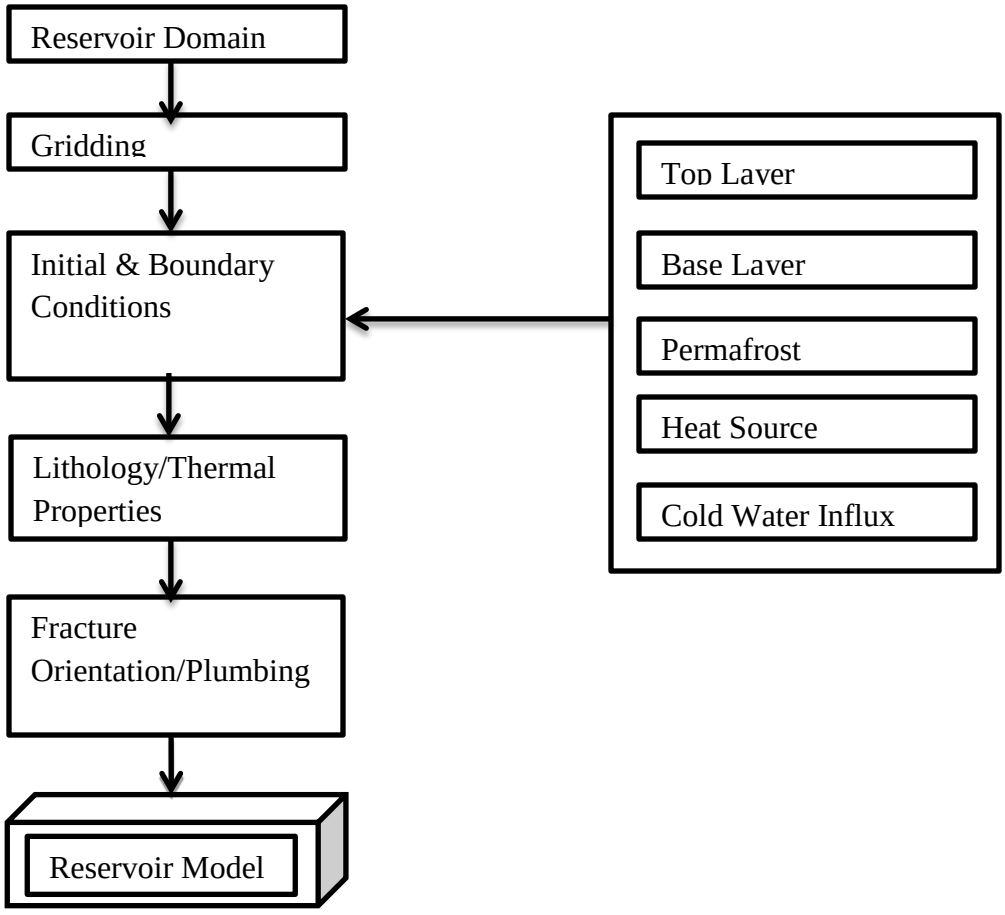


Figure 3.2: A flowchart indicating the various steps incorporated in the reservoir modeling setup.

3.3 Reservoir Domain

The extent of unfrozen area which has been identified using the airborne EM survey and optical remote sensing images defines the extent of the reservoir domain in this study. The frozen areas on the ground correspond to very high resistivity values and the unfrozen areas correspond to very low resistivity values in the airborne EM data. The unfrozen areas are assumed to be the areal extent for the containment of geothermal fluids which allows the area to remain unfrozen. A high resolution optical image was used for visual interpretation of surface features in the vicinity of Pilgrim Hot Springs. These included polygon permafrost, hummocks, horse tail drain permafrost, sorted circles, thermokarst lakes, rivers, lakes, geothermal areas and vegetated areas (see Figures 2.6 and 2.7 in Chapter 2).

The airborne EM data showed resistivity values ranging from -2400-42000 ohm-meters at various depths. The differential resistivity depth slices at 5 m and 100 m (Figure 3.3) helped to distinguish the relatively high resistivity areas from low resistivity areas. The airborne EM data layers were stacked and a six class unsupervised classification was carried out on this data-stack. This classification result (Figure 3.4) was compared with the surface features identified by visual interpretation of the high resolution optical image.

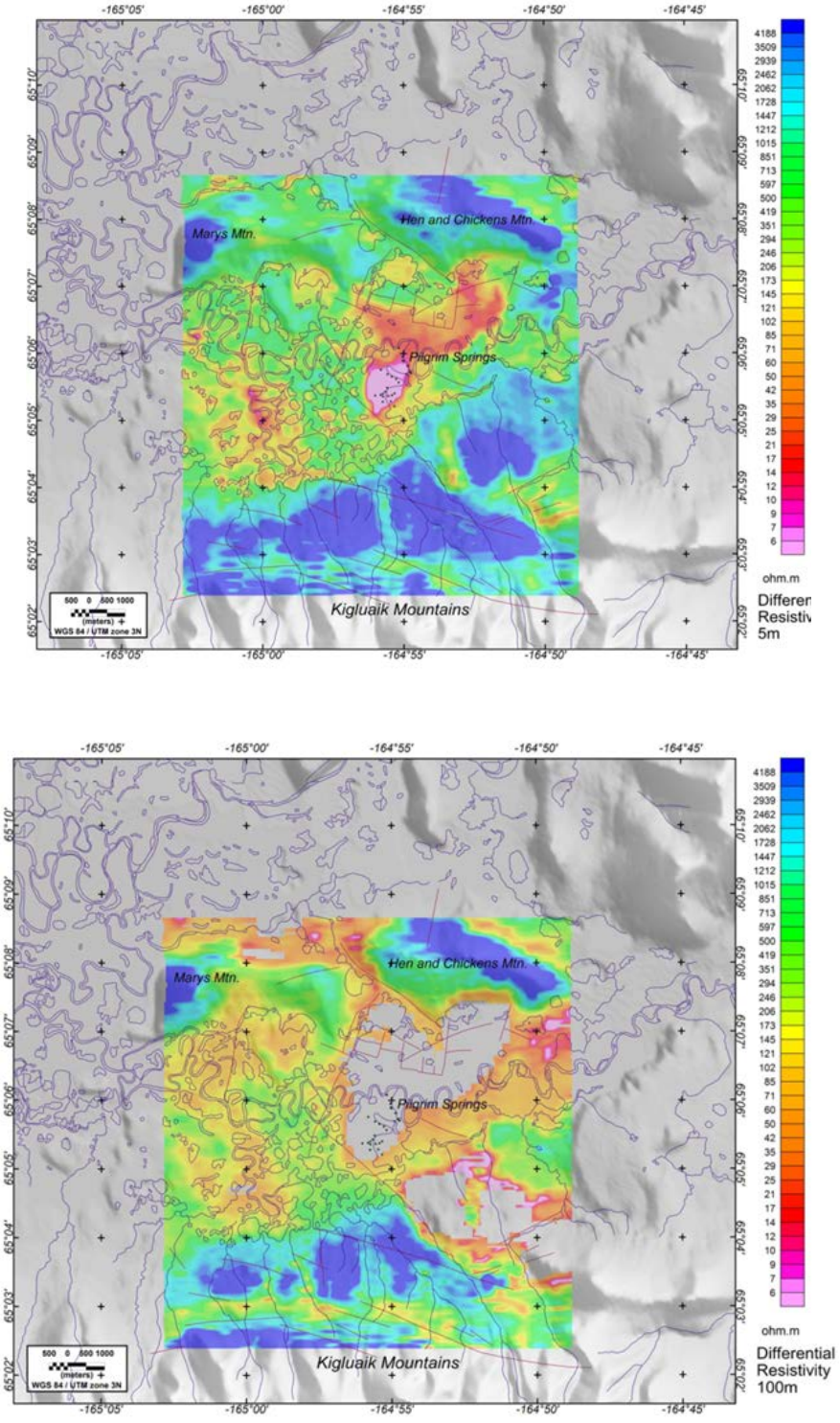


Figure 3.3: Airborne EM survey at Pilgrim Hot Springs showing the differential resistivity slices at 5 m and 100 m (McPhee and Glen, 2012).

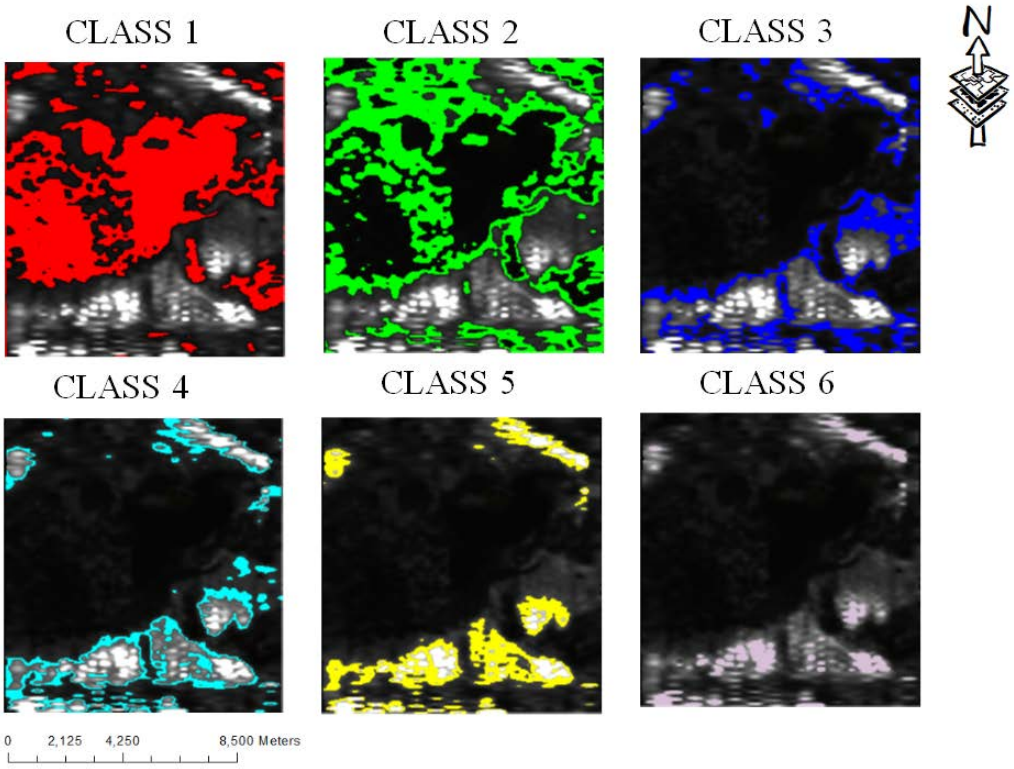


Figure 3.4: Six different classes from the classification result relate to various types of surface features in the high resolution optical image.

Broadly, Class 1 represents the lowest resistivity value range which may indicate the presence of geothermal fluids, unfrozen areas and thermokarst lakes. The other five classes have higher ranges of resistivity values which may be representative of a higher percentage of frozen ground. Class 2 broadly corresponds to surface features such as polygon permafrost, hummocks, and some thermokarst lakes. Class 3 relates closely to the horse tail drain permafrost land features. Class 4 represents a very high percentage of frozen ground and very high resistivity values.

Class 5 represents an even higher percentage of frozen ground and resistivity values, in comparison to Class 4. Class 6 represents the highest percentage of frozen ground and highest range of resistivity values. All six classes extracted from the unsupervised classification broadly correspond to distinctly different surface features interpreted from visual analysis of the high resolution optical image.

The reservoir domain utilized for the modeling work consists of an initial box set-up with dimensions of 2000 m x 2000 m x 1000 m. This square-shaped domain initially consisted of 100,000 cells. The boundaries of this domain have been edited and reshaped into a triangular domain (Figure 3.5) based on the interpretations of the extent of unfrozen areas from the airborne EM survey and the extent of availability of geologic information in the Pilgrim Hot Springs area. The triangular domain consists of 68,481 cells. The reservoir domain has been classified into a shallow zone (0-30 m), deeper sediment zone (30-300 m) and bedrock (300-1000 m). These regions are based on the interpretations and inferences made from the static temperature logs (Figure 3.6).

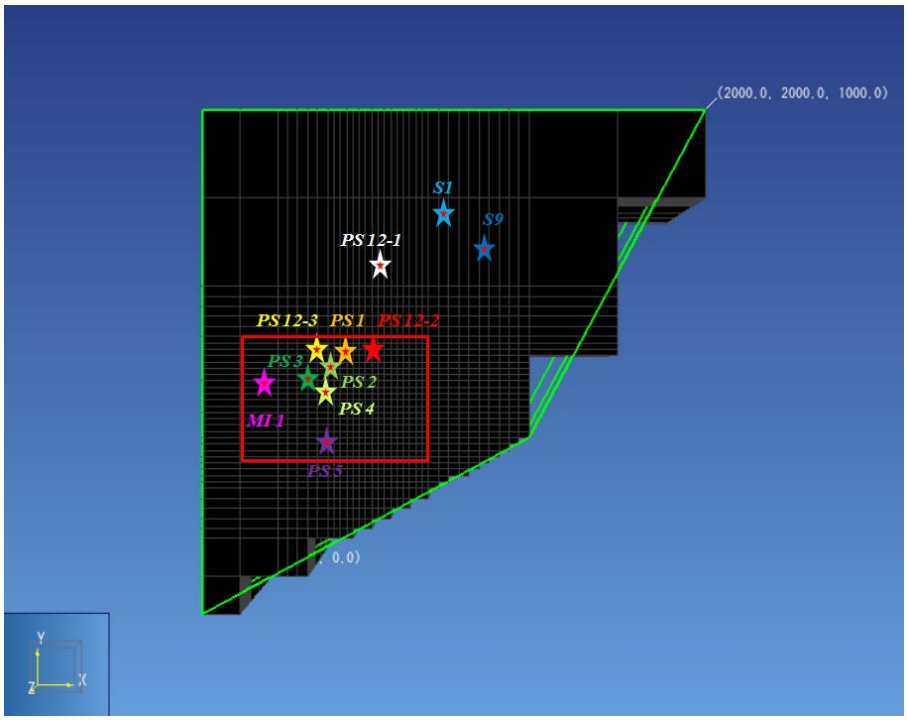


Figure 3.5: Map view of a triangular shaped reservoir domain representing the Pilgrim Hot Springs.

The static temperature logs from all wells across Pilgrim Hot Springs, Alaska, (Figure 3.6) indicate a spike in temperatures up to 91 °C around 25-50 m and subsequent reversals occur around 30-100 m.

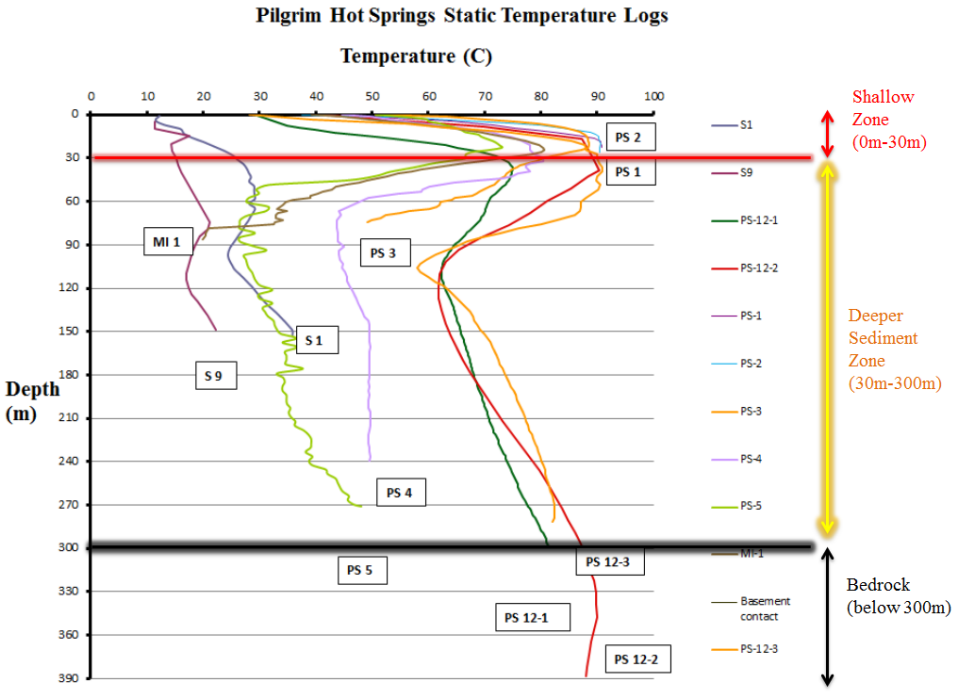


Figure 3.6: Static temperature logs from all wells located across Pilgrim Hot Springs.

The working assumption is that the cold water is fed by snow melt in the Kigluaik Mountains in the south of the domain and is forced to flow across the reservoir causing a temperature reversal between 30-100 m. Finally, the cold water flows into the Pilgrim River to the north. The peak in the temperatures in the shallow aquifer is the result of the outflow of the geothermal fluids.

There is a possibility of mixing of the cross-flowing cold water with the up-welling hotter fluids from basement rock. This mixing cools the system as a whole. It is also important to know that some of the warmer water enters the Pilgrim River. The shallow zone has been selected from 0-30 m which is marked by outflow. Upflows occur in a deeper sediment zone which is fed from the faulted basement rock via the deeper aquifer. Characterization of drill cuttings from each well has been used to produce lithologic logs which provide the framework for the development of a conceptual geologic model of the Pilgrim Hot Springs (Miller et al., 2013). The lithologic logs from deep wells in the reservoir suggest that the basement contact occurs around a depth of 300 m (Miller et al., 2013). This contact represents the boundary which separates upper sedimentary rocks from the deeper bedrock. Thus, the basement rock and the deep faulted aquifer are represented in the model at depths between 300-1000 m.

The reservoir domain has been divided into three categories: shallow zone, deeper sediment zone, and basement rock, where the shallow zone acts as region of outflow of geothermal fluids and the up-flow of hotter fluids originates from the bedrock and flows through the deeper sediment zone feeding the shallow zone, as inferred from the static temperature logs. In order to accommodate the maximum information from the conceptual geologic model, the vertical resolution of all the layers in the reservoir model has been set up so that the lithologic logs have the same vertical resolution.

The shallow zone consists of 6 layers, with each layer having 5 m vertical resolution. The deeper sediment zone consists of 54 layers, each with 5 m resolution, and the bedrock region consists of 3 layers, each with 333.33 m vertical resolution (Figure 3.7).

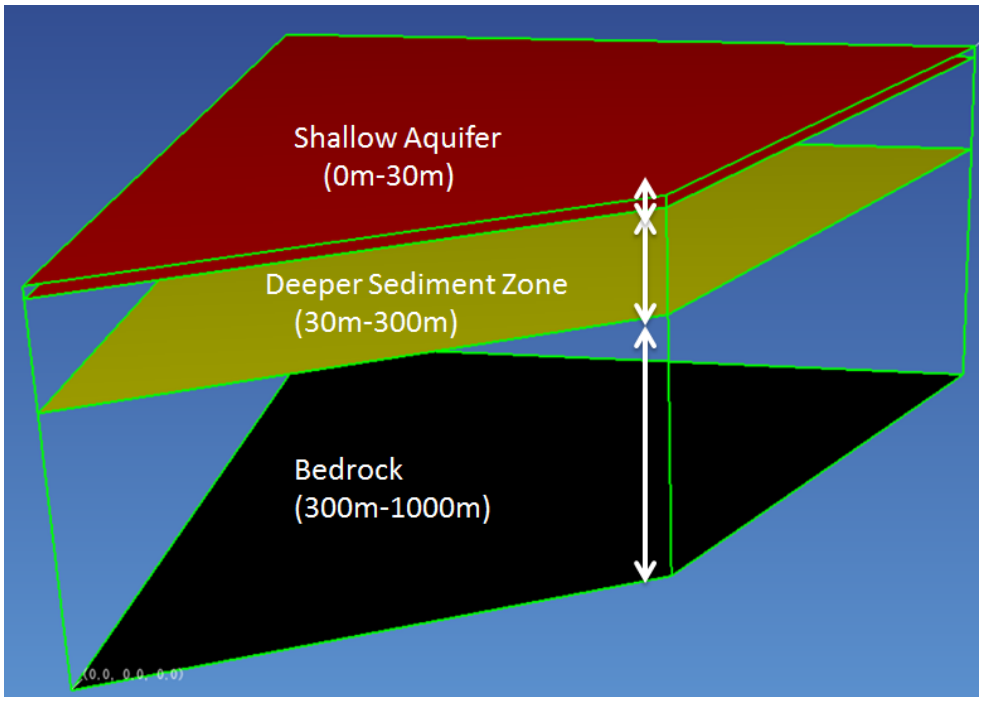


Figure 3.7: Layers in the model setup. The red region shows the shallow aquifer, yellow layer represents the base of deeper sediment zone and black layer represents the base of bedrock. The shallow aquifer layers have 5 m vertical resolution and 6 layers. The deeper sediment zone layers have 5 m vertical resolution and 54 layers. The bedrock region has 3 layers with 333.3 m vertical resolution.

3.4 Gridding

The gridding density of the triangular-shaped reservoir domain was varied according to the density of the wells at Pilgrim Hot Springs, with higher gridding density where the wells are closely spaced. As a result, the model grid is non-uniform throughout the domain (Table 3.1 and Table 3.2).

Table 3.1: Variation of the grid sizes along the X axis of the domain.

Gridding Axis [X]	Number of Grids	Grid Size [m]	Total Distance[m]	Cumulative Distance [m]
X	2	150	300	300
X	5	40	200	500
X	16	25	400	900
X	10	40	400	1300
X	2	350	700	2000

Table 3.2: Variation of the grid sizes along the Y axis of the domain.

Gridding Axis [Y]	Number of Grids	Grid Size [m]	Total Distance [m]	Cumulative Distance [m]
Y	2	150	300	300
Y	5	40	200	500
Y	24	25	600	1100
Y	5	40	200	1300
Y	2	350	700	2000

For both the X and Y axes, the modeling domain extends over a distance of 2000 m with a maximum grid density of 25 m in the region where wells are most closely spaced. There are currently 11 wells, which range from shallow to deep, that have been drilled across the Pilgrim Hot Springs area (Figure 3.5).

The wells PS 12-3, PS 12-2 and PS 12-1 were drilled during the summer of 2012. The wells S1 and S9 were drilled during the summer of 2011. The remaining six wells, namely PS 1, PS 2, PS 3, PS 4, PS 5 and MI 1, were drilled during the exploratory phase in the 1970's. Geoprobe data were collected during the summer of 2012 from over 60 holes across Pilgrim Hot Springs. These data have not been utilized directly for developing this reservoir model domain.

The deepest well in the reservoir is PS 12-2, with the bottom of the wellbore at a depth of 388 m. The bedrock contact occurs at approximately 300 m. The wells PS 12-1 and PS 12-3 are 300 m and 280 m deep, respectively. The wells PS 12-1, PS 12-2 and PS 12-3 originate at the surface and pass deep into the reservoir via the shallow aquifer, and deeper sediment zone until they reach the basement contact. Wells S1 and S9 are each 150 m deep. Wells PS 1 and PS 2 are each approximately 30 m deep. Wells PS 4 and PS 5 are 240 m and 270 m deep, respectively. Wells PS 3 and MI 1 are 75 m and 85 m deep, respectively.

3.5 Initial Conditions and Boundary Conditions

3.5.1 Top Layer

The top layer of the reservoir model is assumed to be the ground or the surface (Figure 3.8). We assume that the surface layer is subject to atmospheric pressure and mean annual air temperature. The mean annual air temperature is set at -6 °C (Liljedahl et al., 2009). The atmospheric pressure is assumed to be an average of 96516 Pascal. These conditions are applied as fixed boundary conditions to the top layer.

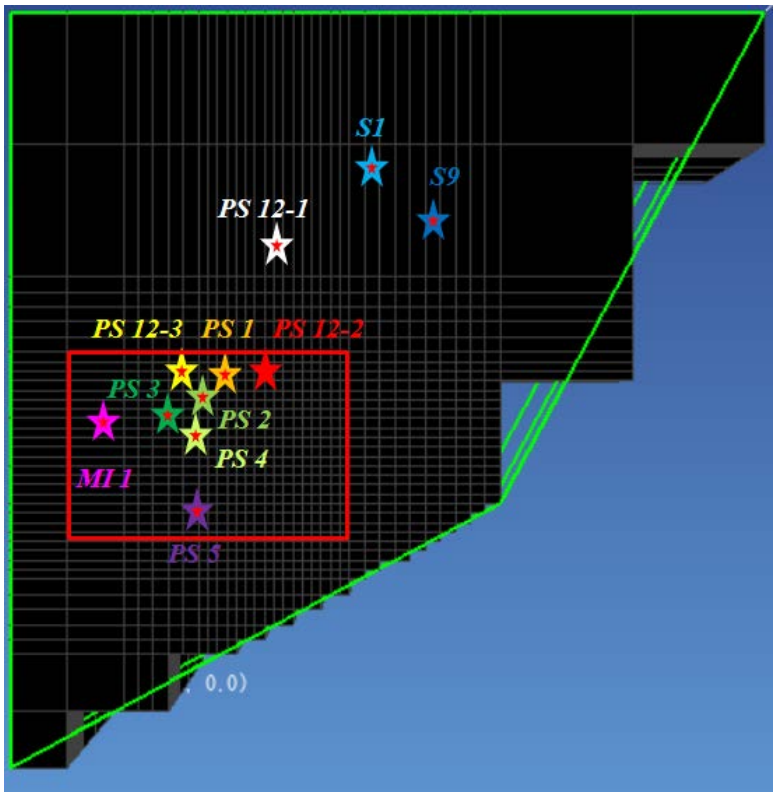


Figure 3.8: Top layer of the reservoir model which is subject to atmospheric pressure and mean annual air temperature.

3.5.2 Base Layer

The base layer of the domain is at a depth of 1000 m (Figure 3.9). The basement rock or bedrock is the deepest layer in the reservoir model. Bedrock grid cells are represented by green color and have set initial conditions of 90 °C and pressure of 9.95×10^{06} Pascal. The pressures for the grid cells in this layer represent the hydrostatic pressures for 1000 m depth. The temperature and pressure for all the grid cells in this layer are applied as fixed boundary conditions.

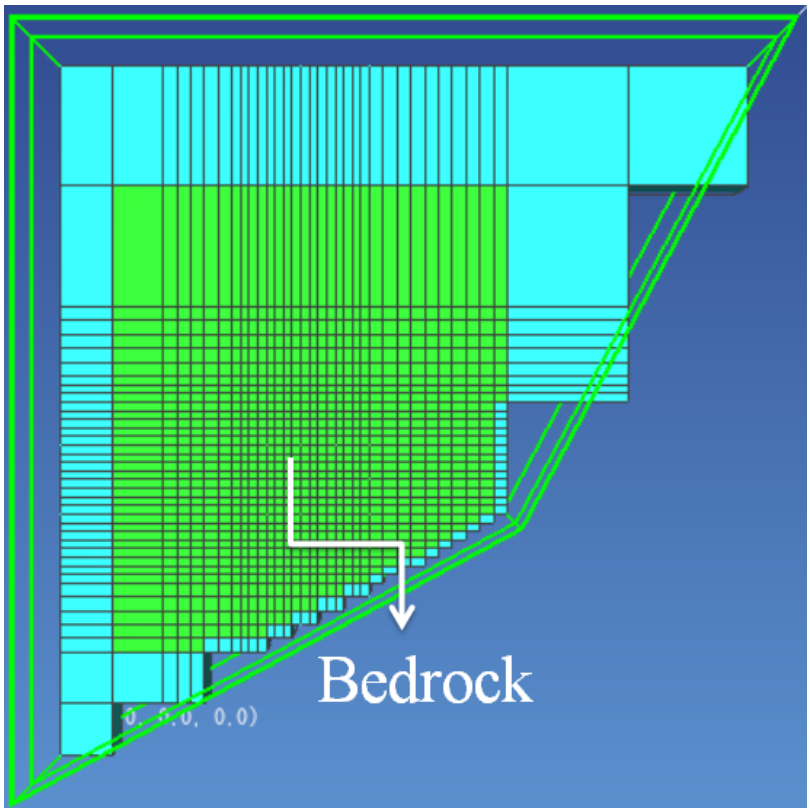


Figure 3.9: Base layer of the reservoir model which represents the bedrock at 1000 m.

3.5.3 Permafrost

Permafrost, or perennially frozen ground, is defined as 'ground (soil or rock and included ice and organic material) that remains at or below 0 °C for at least two years, for natural climatic reasons' (Van Everdingen, 1998). Based on our previous discussion about the interpretation of the airborne EM survey at Pilgrim Hot Springs and inferences from the survey, we consider that any area surrounding the reservoir model domain is frozen ground and that permafrost exists from 0-100 m (Figure 3.10) along the boundaries of the reservoir. We assume that artesian ground water exists below the permafrost along the boundaries of the reservoir model domain from 100-300 m depth.

Permafrost is represented by the blue-colored grid cells along the boundaries of the reservoir modeling domain between 0-100 m. Grid cells representing permafrost are set at -6 °C, having respective hydrostatic pressures and fixed boundary conditions.

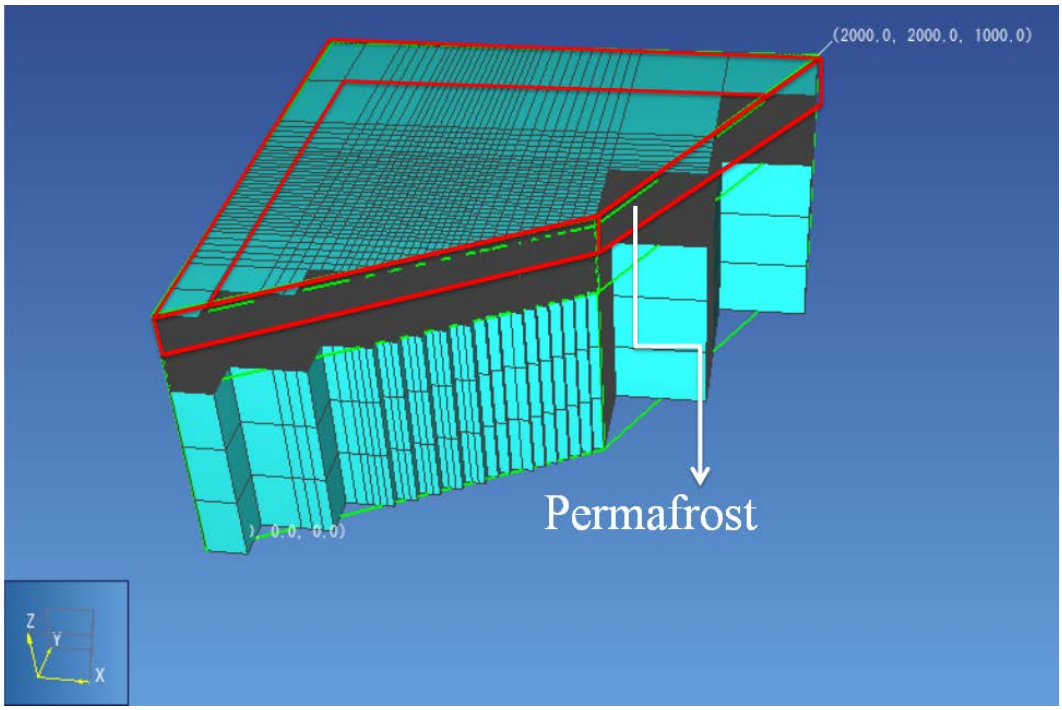


Figure 3.10: Walls of the domain represented by the blue-colored grid cells between 0-100 m represent the permafrost.

3.5.4 Cold Water Influx

The intervals of cold water influx into the reservoir modeling domain and outflow of cold water is determined by the interpretation of the static temperature logs of all wells located across Pilgrim Hot Springs. The differential pressure heads between the north and the south account for the forced flow of cold water from the south towards the north.

The piezometric heads for the old wells drilled during the 1970's exploration phase have been recorded and estimated (Woodward-Clyde Report, 1983). Based on these data, we determine the pressure head along the south and north of the domain by extrapolation of the pressure gradient across the reservoir domain in a horizontal direction. The source cells in the south are provided with an additional pressure head of 18 m. The sink cells in the north are provided with a lowered pressure head of 3 m, relative to the surface elevation.

The mass flow rate across any source cell or sink cell may be estimated using Equation 3.12 in Chapter 3, and is a function of the fluid density, volume of the cell, porosity, compressibility of formation, and pressure gradient. The pressure gradient in this equation accounts for the additional pressure head or lowered pressure head for every source cell or sink cell. We assume that the temperature of the cold water is 4 °C. The enthalpy of the cold water at 4 °C is 16900 Jkg^{-1}. The temperature and enthalpy of the cold water are set as fixed condition in the source cells.

3.5.5 Heat Source Location and Plumbing

3.5.5.1 Reservoir Simulation Model #1

The MT survey data have been utilized to determine the possible location of the heat source and the plumbing system within the reservoir model. Two reservoir simulation models have been developed based on different plumbing systems and different locations of the heat sources. MT data helped to identify the possible flow path of the geothermal fluids or the plumbing of the system and location of the heat source.

MT data with 1D inversions accounted for variations with depth only while 3D inversions accounted for modeling with length, width and depth covering a large volume. Thus, 3D inversions of the data are better and more accurate than 1D inversion.

However, for this analysis we have used the relevant MT data to identify and locate the plumbing and heat source irrespective of the MT data inversion type. The resistivity across profile D from a smooth 1D MT inversion (Figure 3.11) shows that the basement contact exists around a depth of 300 m. A high conductive zone, represented by the red and yellow colors present at 300 m in the vicinity of wells PS 1 and PS 12-2, extends in an east-west direction. The highly conductive area seems to migrate vertically near the vicinity of wells PS 1 and PS 12-2. A relatively conductive area exists in the shallow parts of the profile between 0-50 m which also spreads in an east-west direction.

The highly conductive layer at 300 m depth and the shallow conductive layer both correspond to zones enriched in smectite clays (Miller et al., 2013). One hypothesis is that the thick clay package at a depth of 200-300 m acts as a cap for the deeper, primary geothermal reservoir and the shallow clay layer acts as a cap for the secondary geothermal reservoir (Miller et al., 2013).

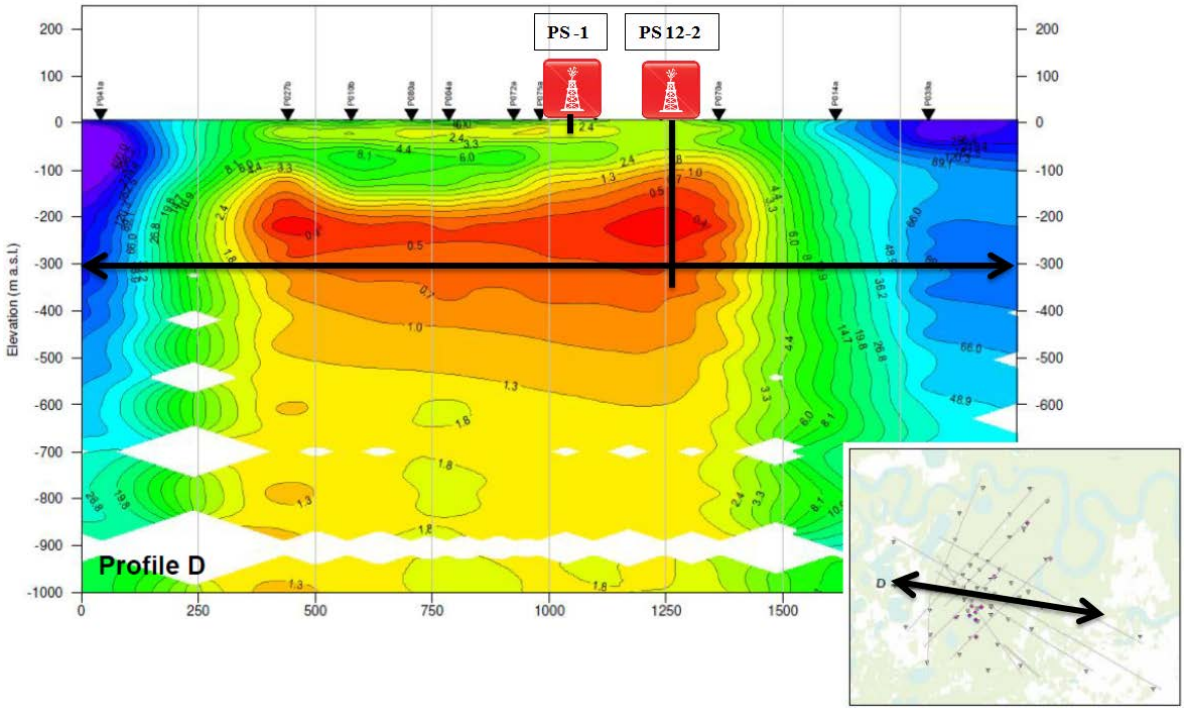


Figure 3.11: Resistivity across profile D through a smoothed 1D MT inversion at Pilgrim Hot Springs (Fugro, 2012). Inset map indicates the orientation of this profile at the site. The black lines represent the area of up-welling and outflow of geothermal fluids.

Another section showing resistivity across profile C from a smoothed 1D MT inversion in the NW-SE direction is analyzed and interpreted to identify the possible location of the heat source and plumbing of the system (Figure 3.12). This section shows that a highly conductive zone exists at 300 m (basement depth) in the vicinity of well PS 12-2. It is also clearly evident that the vertical migration of this highly conductive area occurs in the vicinity of well PS 12-2. There also seems to be a north-westerly extending conductive area.

Conductivity of both of these zones can be attributed to the presence of clay layers which also act as caps for the primary deeper reservoir and secondary reservoir, respectively.

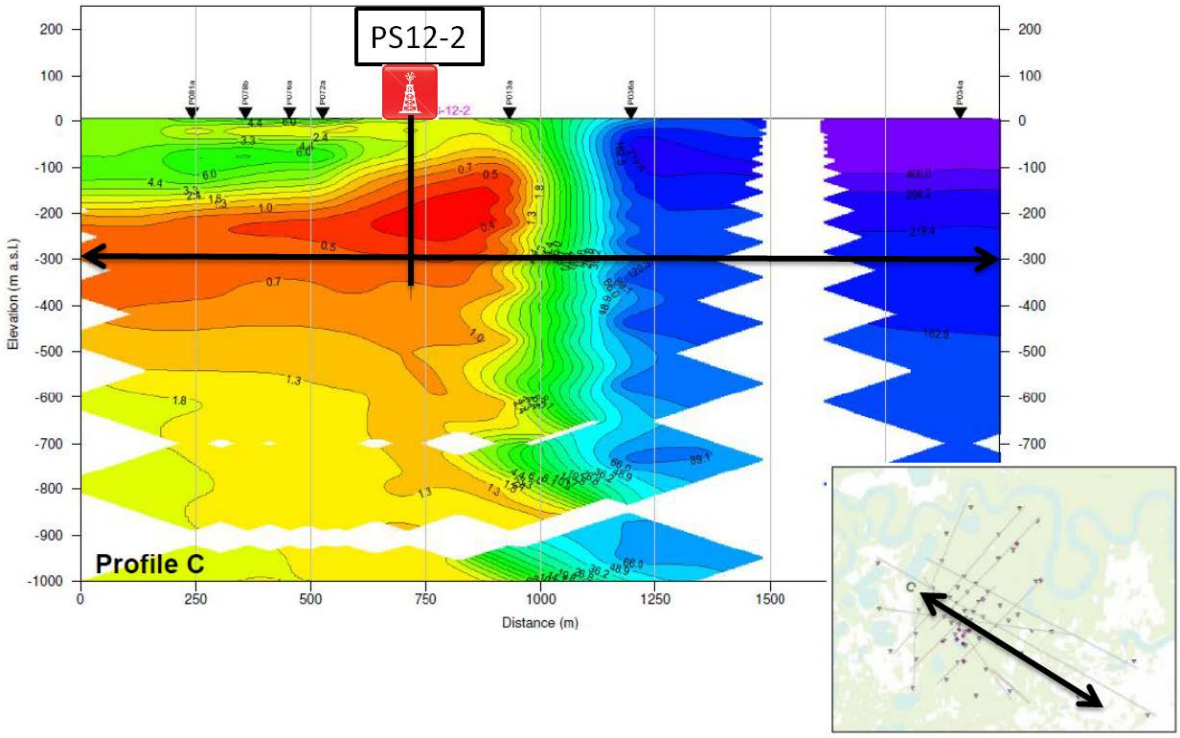


Figure 3.12: Resistivity across profile C through a smoothed 1D MT inversion at Pilgrim Hot Springs (Fugro, 2012). Inset map indicates the orientation of this profile at the site. The black lines represent the area of up-welling and outflow of geothermal fluids.

Resistivity across profile 2 through a smoothed 1D MT inversion (Figure 3.13) indicates a highly conductive zone between 200-300 m depth in the south-west portion of the section. There is also a shallow conductive area between 0-50 m depth. This shallow conductive region seems to extend towards the north-east direction and south-west direction.

These suggest that the heat source and the up-welling of the hotter fluids from the bottom of the basement rock until the basement contact may occur in the vicinity of the wells PS 12-2 and PS 1. Further up-welling of hotter fluids from the deeper sediment zone to the shallow zone may occur between wells PS 12-2 and PS 1. The highly conductive region near a depth of 300 m may indicate the lateral orientation of the conduit.

The shallow conductive region between 0-50 m may indicate the outflow of the hotter geothermal fluids.

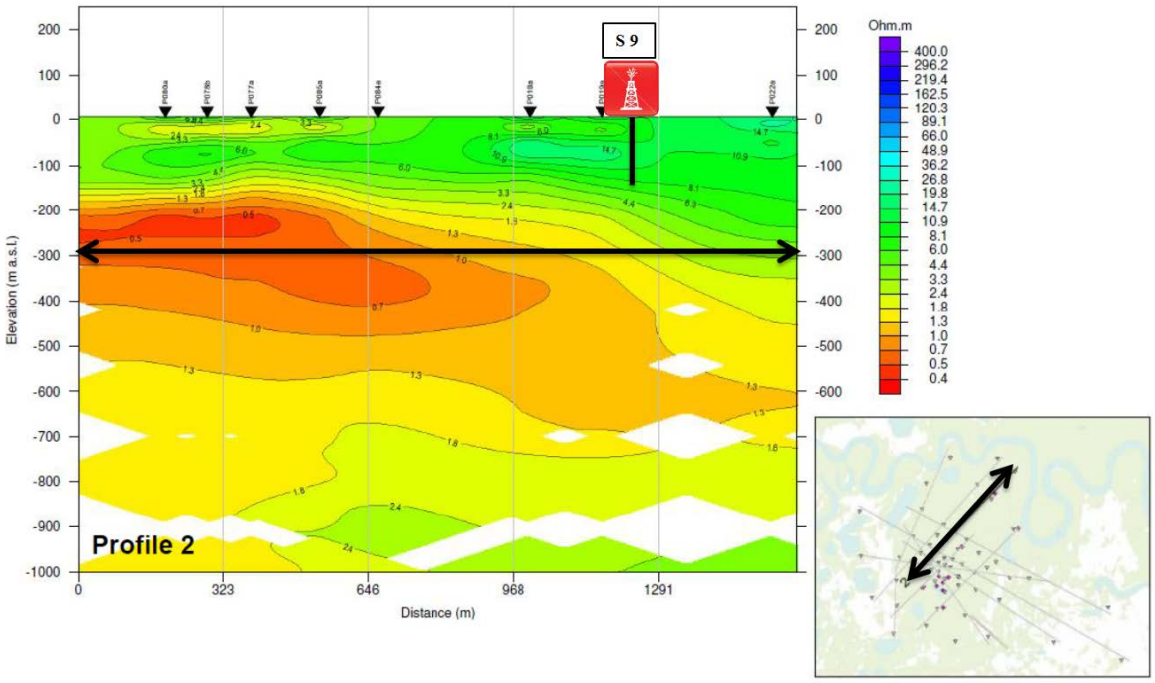


Figure 3.13: Resistivity across profile 2 through a smoothed 1D MT inversion at Pilgrim Hot Springs (Fugro, 2012). Inset map indicates the orientation of this profile at the site. The black lines represent the area of up-welling and outflow of geothermal fluids.

The plumbing of the system is set to originate from the bedrock at a depth of 1000 m. The conduit is initially oriented vertically until the basement contact is reached in the vicinity of well PS 12-2, and then it is oriented horizontally as it moves toward the vicinity of well PS 1 at a depth of 300 m. The hotter fluids are forced to flow from the basement rock to the shallow aquifer via the deeper aquifer.

These preliminary interpretations of the MT survey are incorporated in the first reservoir simulation model. The heat source cell at a depth of 1000 m is located in the base layer of the reservoir model in the vicinity of PS 12-2 (Figure 3.14). The heat source cell is set at 95 °C and given an enthalpy of 400,000 Jkg^{-1}, for 95 °C water. The enthalpy accounts for the amount of energy carried by the water. The heat source is set at a volume factor of 1×10^{20} to account for an infinite influx of magmatic fluids in the model. The large volume factor allows the heat source cell to maintain constant temperature and pressure over the duration of the simulation. The heat source in the model is also provided with additional pressure head to account for buoyancy effects in the faulted bedrock.

The additional pressure head, set to the heat source cell, is determined by trial and error where the simulated well temperature profiles are compared to the actual field-estimated well temperature profiles. The actual pressure head of the heat source is the value which yields a match of the simulated well temperature profiles and the actual well temperature profiles.

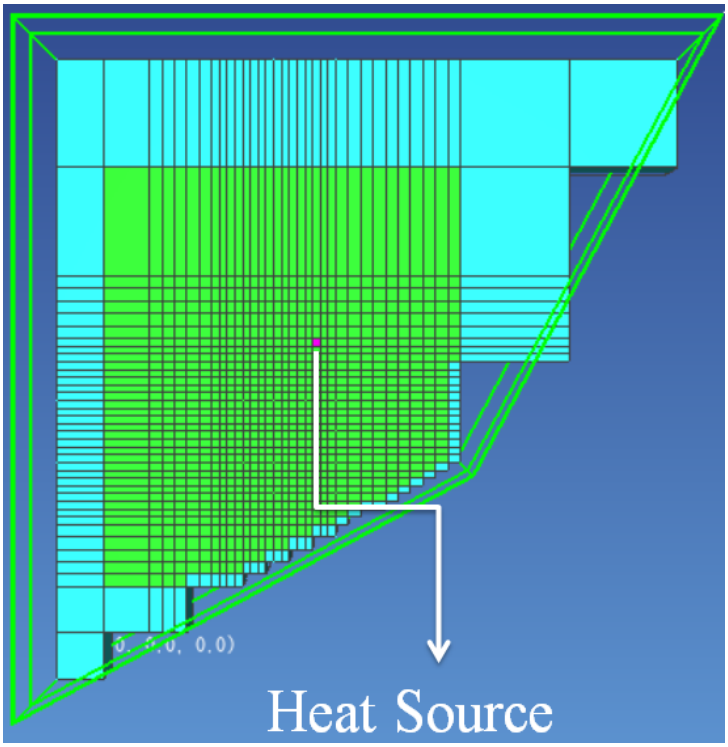


Figure 3.14: Location of the heat source cell represented by pink color cell at a depth of 1000 m for the first reservoir simulation model.

The heat associated with the heat source cell, calculated using the Equation 3.11, is 6.87×10^{18} J sec^{-1}. The values of the parameters used to calculate this heat are: ρ_{rock} = 2740 kgm^3, V = 1×10^{20} m^3, C_p = 790 $Jkg^{-1}°C^{-1}$, ΔT = 100 °C,

Δt = 3.15E09 seconds.

3.5.5.2 Reservoir Simulation Model #2

Based on the interpretations and the analysis of the MT data, we determined a possible alternative location of the heat source and alternative plumbing of the geothermal system, and developed a second reservoir simulation model to represent this alternate scenario. The resistivity across profile 4 from the blind 3D MT inversion (Figure 3.15) shows a highly conductive area represented by the red color to the south-west of well PS 5 at a depth of 500-600 m. The shallow area from 0-50 m also shows a very high conductive area in the south-west and north-east direction. The highly resistive region represented by the blue color at a depth of 100-300 m indicates the possible influx of cold water from the south-west. The highly conductive area may be due to the flow of hotter fluids subject to a highly permeable pathway. These regions may be subject to possible hydrothermal alteration which may be due to flow of geothermal fluids. The high temperature saline fluids will form an electrically conducting medium which, combined with hydrothermal alteration of surrounding rock, will lower the resistivity (Bertrand et al., 2011).

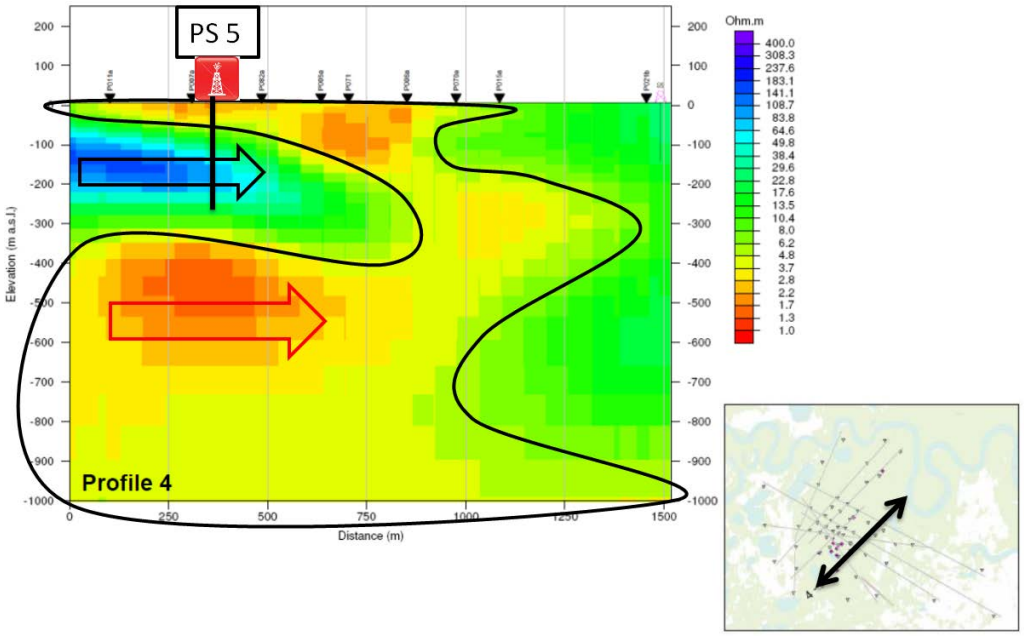


Figure 3.15: Resistivity across profile 4 from a blind 3D MT inversion at Pilgrim Hot Springs (Fugro, 2012).

The resistivity across profile 3 from the blind 3D MT inversion (Figure 3.16) which is parallel and north of profile 3 shows a highly conductive area represented by red color is at a depth of 400-500 m to the south-west of well MI 1. The highly conductive area also exists in the shallower parts of the reservoir between 0-50 m and spreads toward the south-west and north-east from well MI 1 toward well PS 12-1. This high resistivity area might be indicative of cold water influx from the south-west. There is also a highly conductive area near the basement contact at a depth of 300 m which occurs from the south-west to north-east of well PS 12-1.

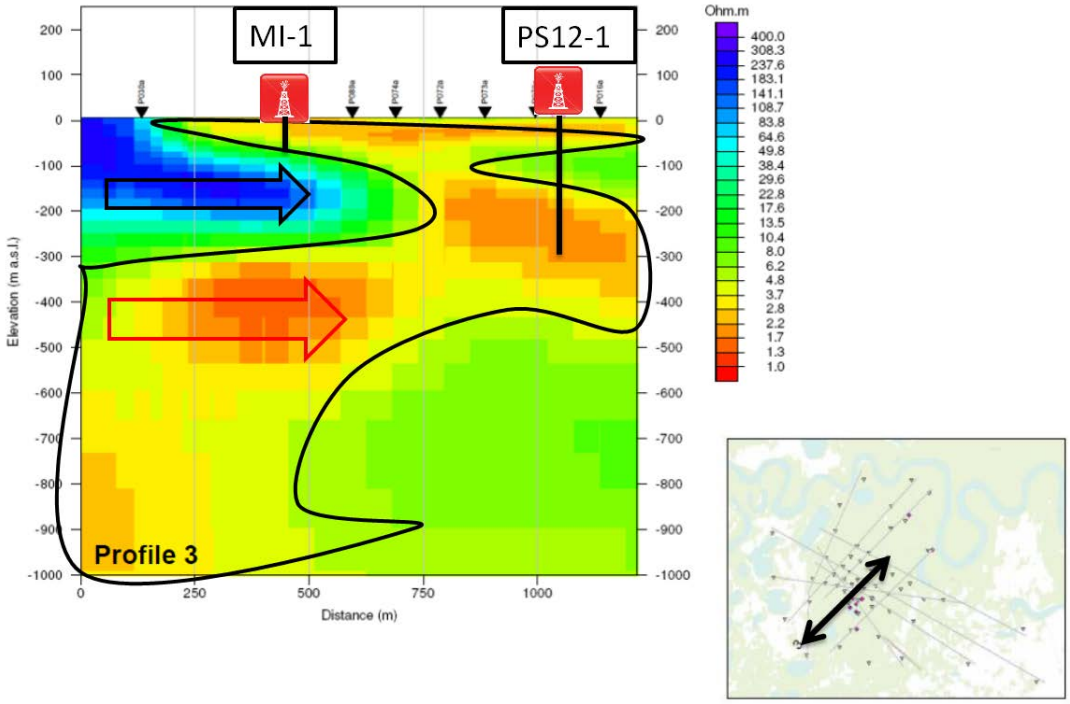


Figure 3.16: Resistivity across profile 3 from a blind 3D MT inversion at Pilgrim Hot Springs (Fugro, 2012).

The resistivity across profile C from the blind 3D MT inversion (Figure 3.17) shows a highly conductive area represented by red color at a depth of 300 m and migration in a vertical direction near the vicinity of well PS 12-2 between 0-300 m. The highly conductive area spreads into the shallower part of the reservoir between 0-50 m toward the north-west direction of well PS 12-2. The vertical migration of the highly conductive area near well PS 12-2 suggests a possible area of up-welling of hotter fluids from the bedrock. The high resistivity areas represented by the blue and green colors exist between 100-300 m toward the north-west and south-east of well PS 12-2. This may also suggest a possible cold water influx from the south-east direction.

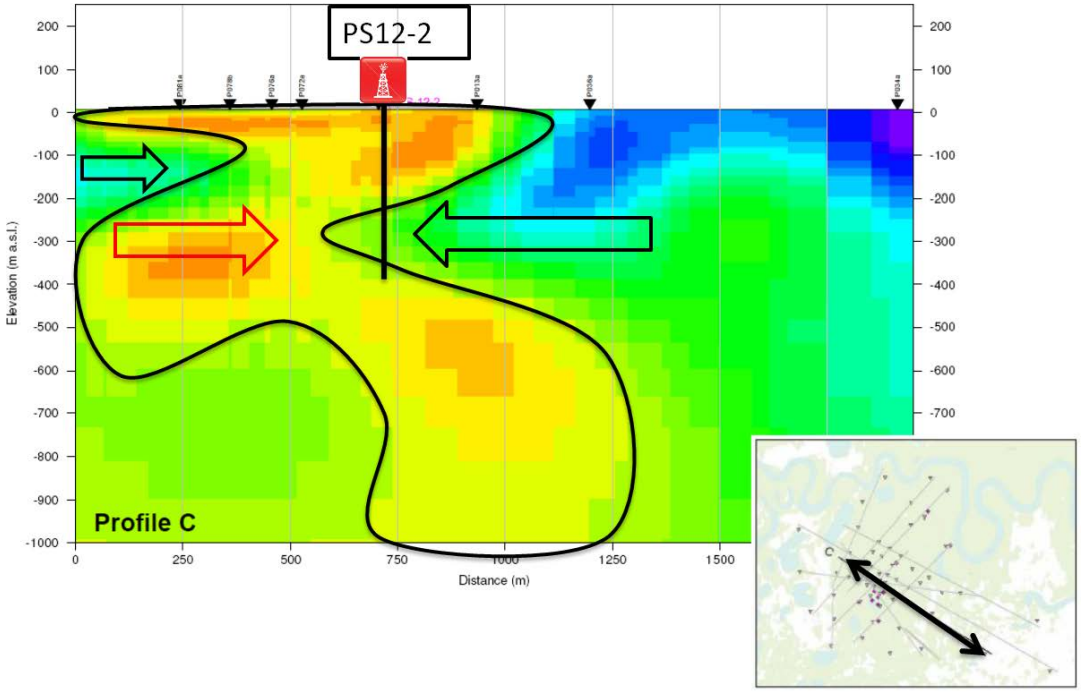


Figure 3.17: Resistivity across profile C from a blind 3D MT inversion at Pilgrim Hot Springs (Fugro, 2012).

Based on the interpretation and analysis of the MT survey from the blind 3D MT inversion at Pilgrim Hot Springs, we can propose the following hypothesis. The cold water influx into the reservoir modeling domain occurs from both the south-west and south-east direction. The conduit originates at the base layer of 1000 m towards the south-west of well PS 5 (Figure 3.18) up to a depth of 500-600 m (Figure 3.19) and moves laterally towards the vicinity of well MI 1 between 400-500 m. Finally, it moves laterally toward the vicinity of well PS 12-2 at a depth of 300 m (Figure 3.20). The up-welling of hotter fluids from the heat source cell in the bedrock occurs via this conduit. These interpretations from the 3D MT inversions are incorporated in the second reservoir simulation model.

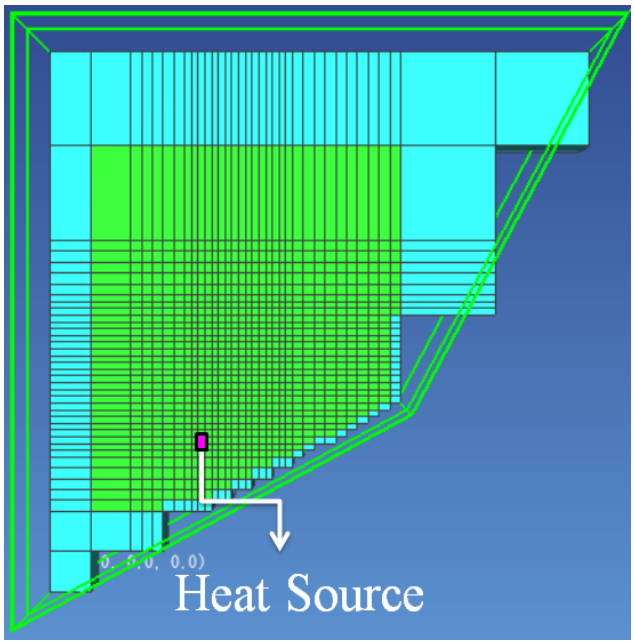


Figure 3.18: Location of the heat source cell represented by pink color cell at a depth of 1000 m to the south-west of well PS 5 for reservoir model #2.

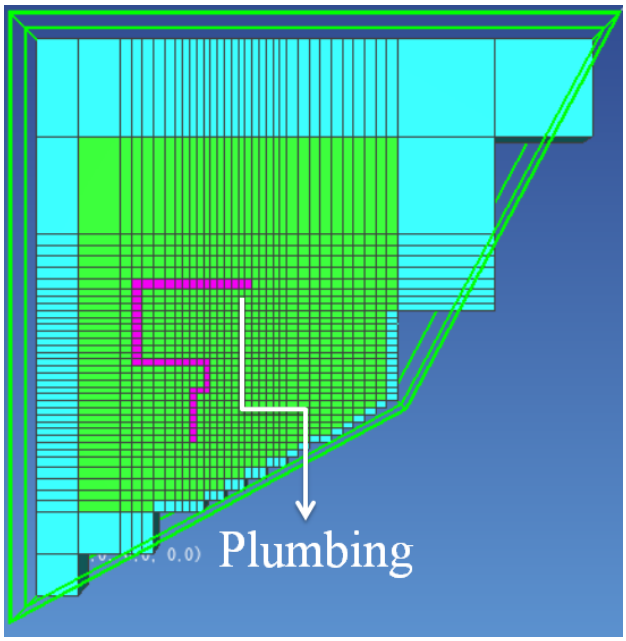


Figure 3.19: Orientation of the plumbing system at the depth of 500-750 m for reservoir model #2.

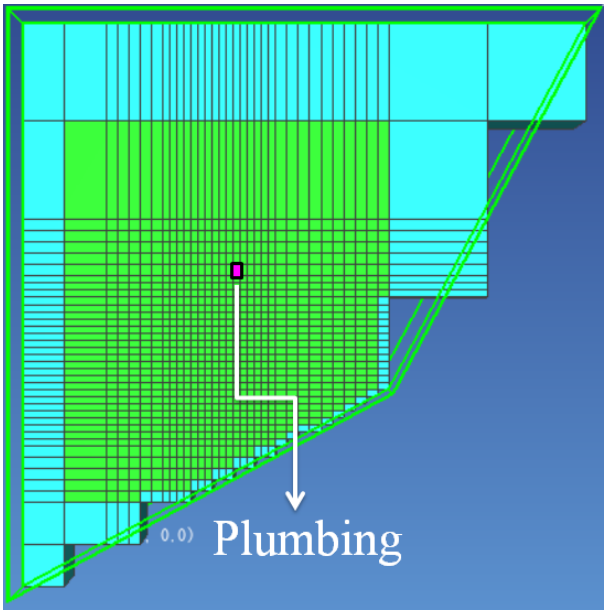


Figure 3.20: Orientation of the plumbing system at a depth of 300 m for reservoir model #2.

Thus, we assign the heat source cell at a depth of 1000 m (Figure 3.18) in the vicinity of well PS 5 which is set at 120 °C and provided with an enthalpy of 400,000 Jkg^{-1}, for 120 °C water. The heat from the heat source cell is calculated using the Equation 3.11 to be 2.7 x 10^{19} $Jsec^{-1}$. The values of the parameters used to calculate heat associated with heat source cell are: ρ_{rock} = 2740 kgm^3, V = 1x10^{20} m^3, C_p = 790 Jkg^{-1} $°C^{-1}$, ΔT = 125 °C, Δt = 3.15E09 seconds.

3.5.5.3 Reservoir Stimulation Model

Three production case scenarios are created using the reservoir simulation model which converts the simulation model into three stimulation models that represent the case of (i) two production wells, (ii) one production well and (iii) a production and injection well. The production wells operate based on the prescribed bottom hole flowing pressure and productivity index. The productivity index of a well may be defined as the ratio of the flow rate to the draw-down pressure (Equation 3.10).

$$PI = Q_{sc}/(P_{reservoir} - P_{bottom\ wellbore}) \quad (3.10)$$

Where, Q_{sc} = Volumetric Flow rate (m^3day^{-1}); $P_{reservoir}$ = Reservoir pressure (Pascals); and $P_{bottom\ wellbore}$ = Bottomhole flowing pressure (Pascals).

For a steady state radial flow, the productivity index (Pruess, 1988) is given by Equation 3.11.

$$PI = \frac{2\pi(k\Delta z)}{\ln(r_e/r_w)+s-1/2} \quad (3.11)$$

Where, k = permeability of medium (m^2); Δz = saturation thickness or completion thickness (m); r_e = radius of the producing grid cell (m); s = skin factor or fracturing effect (dimensionless); and r_w = radius of wellbore (m). When the radius of the producing grid cell does not have a cylindrical shape, the productivity index can be calculated using the effective radius (re) using Equation 3.12.

$$r_e = \sqrt[2]{A/\pi} \quad (3.12)$$

Where, re = radius of the producing grid cell (m) and A = area of producing grid cell (m^2).

The first stimulation model (Figure 3.21) indicates the location of the two production wells.

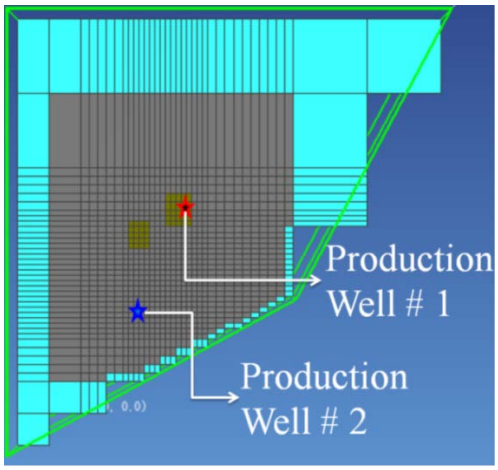


Figure 3.21: Location of the two production wells in the first reservoir stimulation model.

The second stimulation model involves a production scenario involving one production well (Figure 3.22).

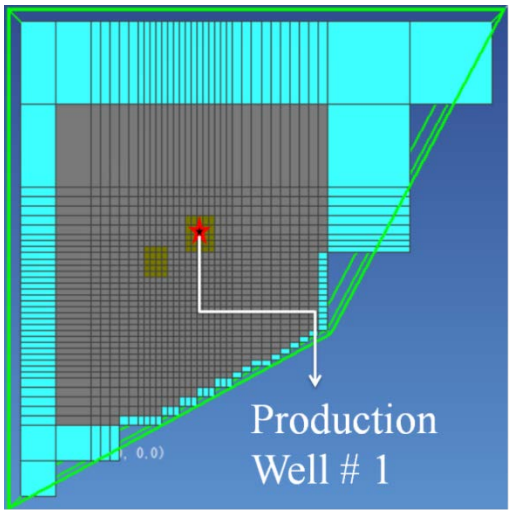


Figure 3.22: Location of the single production well in the second reservoir stimulation model.

The third, and final, stimulation model involves having both a production and injection well (Figure 3.23).

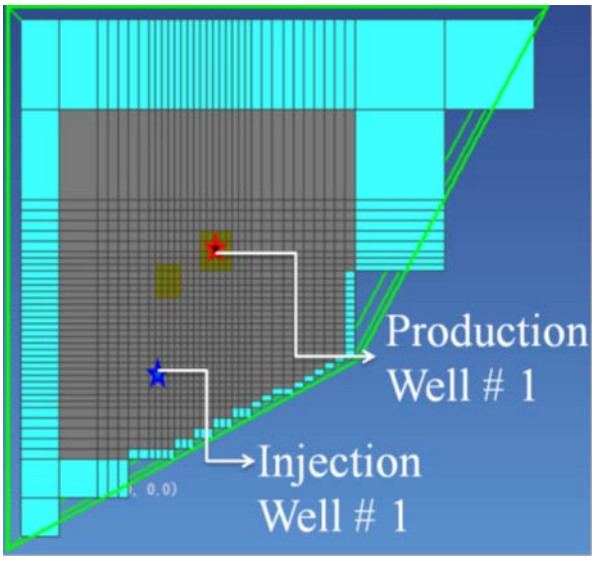


Figure 3.23: Location of the injection well and production well in the third reservoir stimulation model.

The various properties related to the operation of the production wells and injection wells incorporated in the three stimulation models are indicated in Table 3.3. These properties have been incorporated for the wells for the respective stimulation scenarios.

Table 3.3: Well properties related to the operation of the production wells and injection wells incorporated in the three stimulation models.

	Stimulation Model 1	**Stimulation Model 1**	**Stimulation Model 2**	**Stimulation Model 3**	**Stimulation Model 3**
	Production well 1	**Production well 2**	**Production well 1**	**Production well 1**	**Injection well**
Completion depth (m)	270-295	200-300	270-295	270-295	200-300
Flow rate (gpm)	2000	2000	2000	2000	2000
Productivity Index (m^3)	$5x10^{-5}$	$4x10^{-5}$	$5x10^{-5}$	$5x10^{-5}$	Not Applicable
Permeability (m^2)	$2.58x10^{-7}$	$2.58x10^{-7}$	$2.58x10^{-7}$	$2.58x10^{-7}$	$2.58x10^{-7}$
Radius of grid cell (re) (m)	33	33	33	33	33
Radius of wellbore (rw) (m)	0.33	0.33	0.33	0.33	0.33
Completion top pressure (Pa)	$2.76x10^{6}$	$2.76x10^{6}$	$2.76x10^{6}$	$2.76x10^{6}$	$2.76x10^{6}$

3.5.6 Lithology

A characterization of drill cuttings from each well were used to produce lithological logs that provide the framework for development of a conceptual geological model of the geothermal system (Miller et al., 2013). Porosity and permeability values were determined from the sediment characterization, which act as input parameters for the numerical reservoir model. The lithology, gamma ray, and temperature logs for several wells were correlated by depth with equi-distant spacing for development of the conceptual geologic model (Figure 3.24).

Stratigraphic correlations based upon the well log data indicate several clay layers throughout the section with a dominant clay package at 200-275 m. The induration of sands is mainly concentrated between wells PS 4 and PS 12-3. The indurated sands occur from the shallow aquifer to near the basement surface. The MT data also supports the modeled stratigraphy where thick clays occur from 200-275 m in wells PS 12-3, PS 12-2, and PS 12-1 correlate to the low resistivity zone in the MT cross-section and occurs at 200 m depth. The conceptual geologic model also suggests shallow outflow aquifer with a thin clay cap at a depth of 50 m.

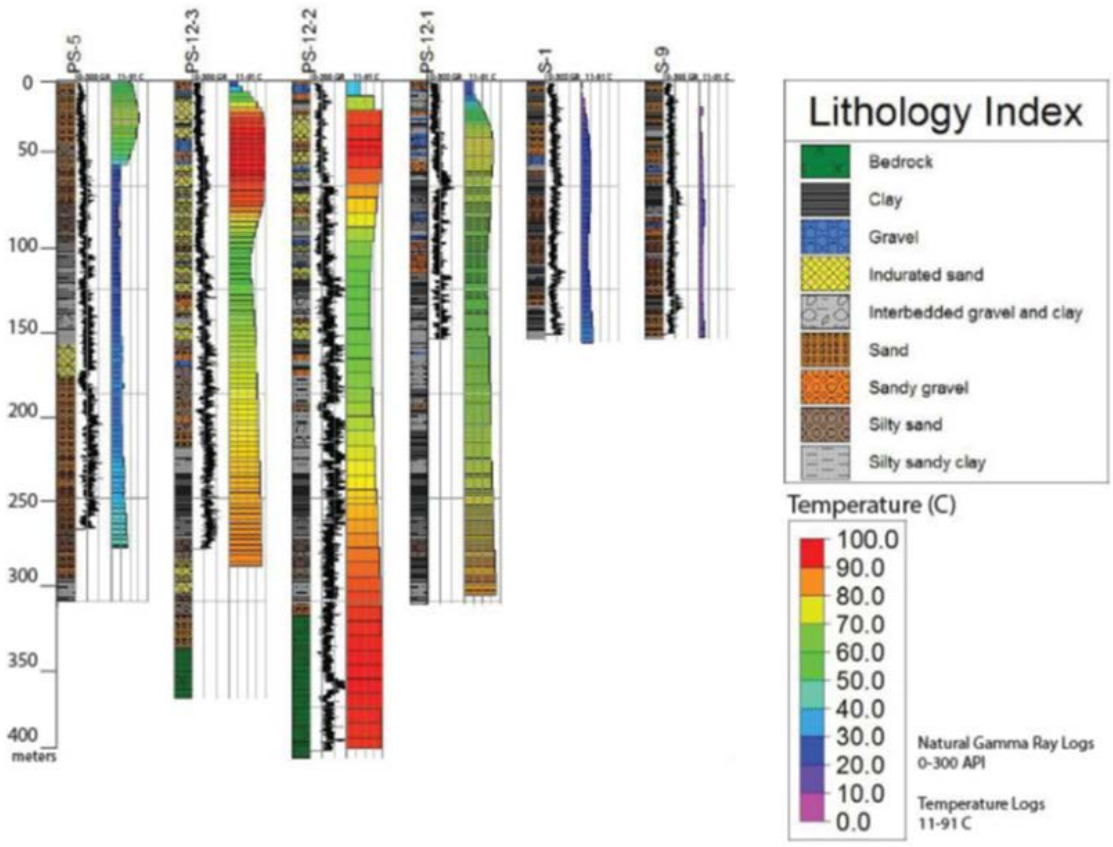


Figure 3.24: Lithology, gamma ray, and temperature logs for several wells correlated by depth with equi-distant spacing (Miller et al., 2013).

The conceptual model also suggests that the upflow correlates with the indurated sand zones which might be due to the porosity and higher intrinsic permeability of the cemented sands. The transfer of geothermal fluids in the indurated sand zones also accounts for less heat loss than unconsolidated sands. Potential production from the reservoir may be influenced by regions of very high permeability and high hydraulic conductivity which support the up-flow of hotter fluids. Silty sands beneath the thick clay package at around 270-300 m may have sufficient permeability to make it feasible for a large diameter production well. In order to accommodate the maximum information from the conceptual geologic model, the vertical resolution of all the layers in the reservoir model have been set up in a manner so that they have the same vertical resolution as the lithologic logs. The lithology types and their respective properties, with color codes which have been incorporated in the reservoir simulation model, are shown in Table 3.4.

Table 3.4: Lithology types and their respective properties which have been incorporated in the reservoir simulation model.

Lithology	Density (Kgm^{-3})	Porosity (%)	Permeability (m^2)	Thermal Conductivity ($Wm^{-1}K^{-1}$)	Specific Heat ($JKg^{-1}K^{-1}$)
CLAY	2680	35	3.33E-08	2.68	860
INDURATED SAND	2640	1	5.8E-08	2.5	840
SANDY SILTY CLAY	2680	34	1.39E-07	1.73	860

Table 3.4: Continued

INTERBEDDED GRAVEL AND CLAY	2700	35	2.48E-07	1.8	920
SAND	2640	32	2.58E-07	1.7	775
SILTY SAND	2640	34	2.64E-07	1.93-2.06	775
SANDY GRAVEL	2640	31	4.19E-07	2.82-3.07	920
GRAVEL	2700	32	5.58E-07	1.8	920
BEDROCK/SCHIST	2740	2	1E-13	4	790

The hotter up-welling fluids are forced from the base layer of the bedrock at 300 m (Figure 3.25) toward the basement contact through a conduit or fault. The silty-sands beneath the thick clay package, commencing at around 270 m (Figure 3.26) and terminating at a depth of 300 m (Figure 3.27), may have sufficient permeability to conduct the up-welling hotter fluids fed from the bedrock basement.

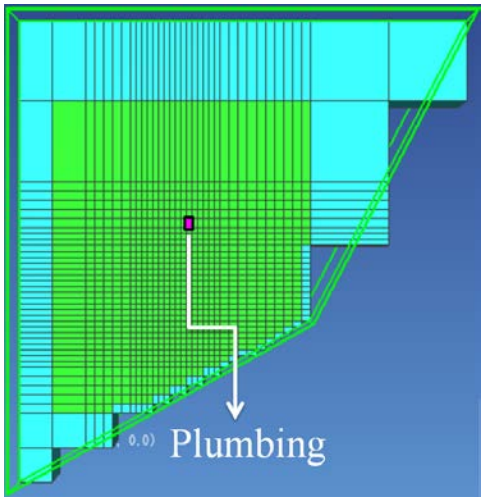


Figure 3.25: Lithology slice at 300 m indicating the bedrock (green color) and the conduit (pink color).

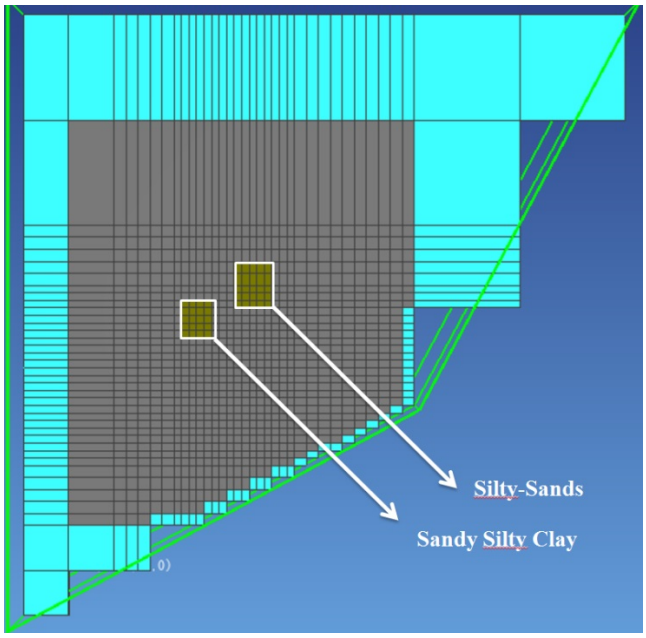


Figure 3.26: Lithology slice at 295 m indicating the silty-sands (dirty green color) and the sandy silty-clay (light grey color).

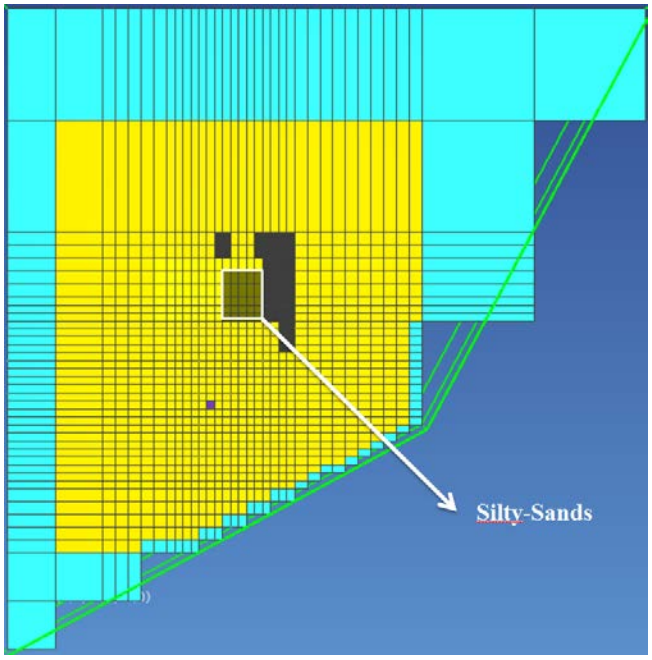


Figure 3.27: Lithology slice at 270 m indicating the presence of silty-sands (dirty green color) beneath the thick clay package

Chapter 4: Results

4.1 Simulated Temperature Sections

4.1.1 Reservoir Simulation Model #1

The first reservoir simulation model has been developed based on the methodology discussed in Chapter 3. The results obtained have been attained using the following conditions:

- A heat source cell is located at 1000 m in the vicinity of well PS 12-2 and PS 1, set as a fixed boundary condition with a temperature of 95 °C and an additional pressure head of 10 m.
- The conduit is oriented vertically from the base layer until the basement contact is reached, and is oriented horizontally to allow lateral movement towards well PS 1 at a depth of 300 m.
- All 63 layers within the model have respective hydrostatic pressures as initial conditions. The top layer and the base layer have been set as fixed boundary conditions.
- The boundaries of the reservoir domain represent permafrost from 0-100 m depth, and cold water influx from the south from 100-300 m with the sink cells in the top layer representing the river and the spring.

The simulated temperature section (Figure 4.1) in the west-east direction and south-north direction (Figure 4.2) show up-welling and outflow of geothermal fluids into the shallow aquifer.

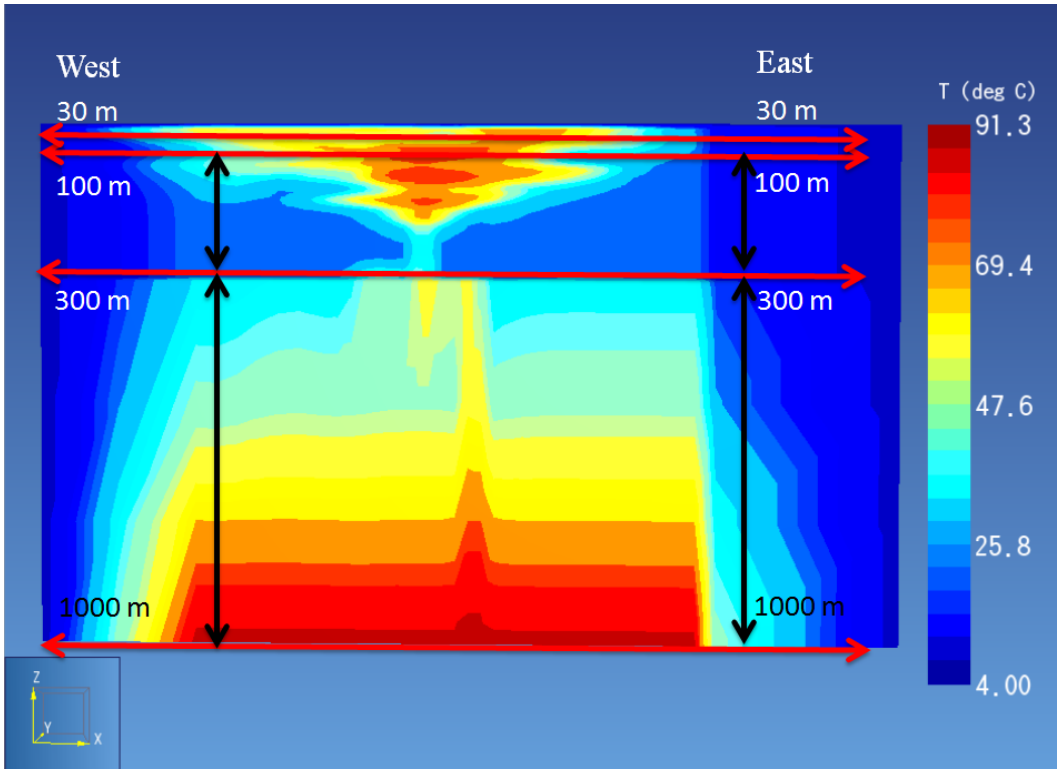


Figure 4.1: Simulated temperature section in the west-east direction for reservoir model #1. The successive red, orange, yellow, green and cyan peaks in the central part of the figure indicate the passage of up-welling geothermal fluids.

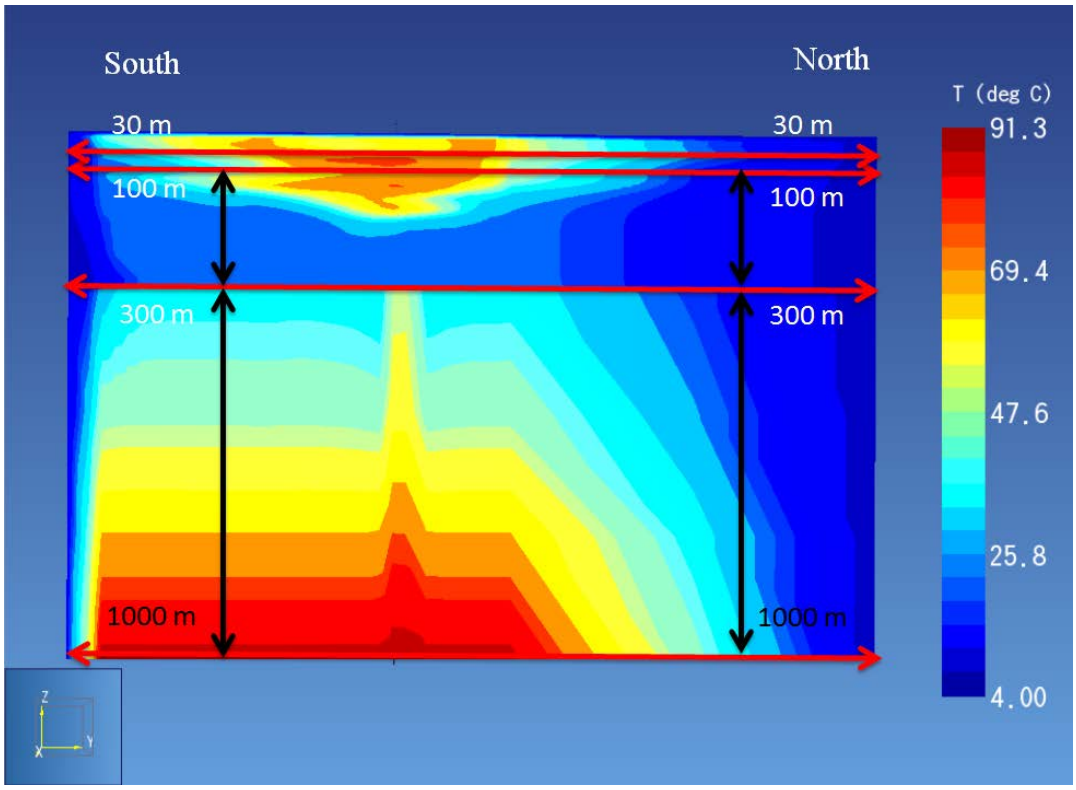


Figure 4.2: Simulated temperature section in the south-north direction for reservoir model#1. The complete path of up-welling of geothermal fluids is not as visible in this direction as the section does not pass through the core of the up-welling region. However, lateral migration of the fluids in the shallow aquifer (the basin-like structure) is clearly visible at the top.

A fault or fractures in the bedrock feeds the geothermal fluids from the base layer until the basement contact is reached. The additional pressure head of 10 m allows the fluids to be forced into the upper sedimentary layers. The silty-sands between 270-300 m may have sufficient permeability to conduct the warmer up-welling fluids that then pass around the thick clay package at 200-270 m by flowing via the indurated sands. These indurated sands might offer high porosity and higher vertical permeability due to possible fractures or pipes in the consolidated sands.

The indurated sands support the up-welling of the hotter fluids and feed them into the shallow aquifer. The outflow of geothermal fluids occurs in the shallow aquifer and is controlled by the highly permeable layers of sands and gravels. The dark blue color at the boundaries of the reservoir domain represents the permafrost from 0-100 m and cold water influx occurs below that depth. We can observe the cold water represented by various shades of blue below the plume. These observations are common for both the simulated vertical temperature sections. However, the connection in the up-welling of hotter fluids from the basement rock towards the shallow aquifer is not observed in Figure 4.2 as this temperature section does not pass precisely through the up-welling region.

The colors within the plume for both the simulated temperature sections, that represent the temperatures in the plume, show only minor variations possibly due to the current resolution of the grids. Higher grid resolutions are expected to capture more details on the spatial variability of temperatures. A grid cell at a depth of 300 m shows a temperature of 94 °C and at a depth of 295 m it shows a temperature of 91 °C (Figure 4.3). It is also known that the temperature of the heat source cell for this model is 95 °C. The cooling of the up-welling fluid between 295-300 m is only about 3 °C, and between 270-300 m is about 9 °C. The high pressure of 5.59×10^6 Pascal for the grid cell at 300 m (Figure 4.4) and buoyancy effects forces the hotter geothermal fluids to flow into the upper sedimentary layers which experience some degree of cooling enroute due to the cross-flowing cold waters.

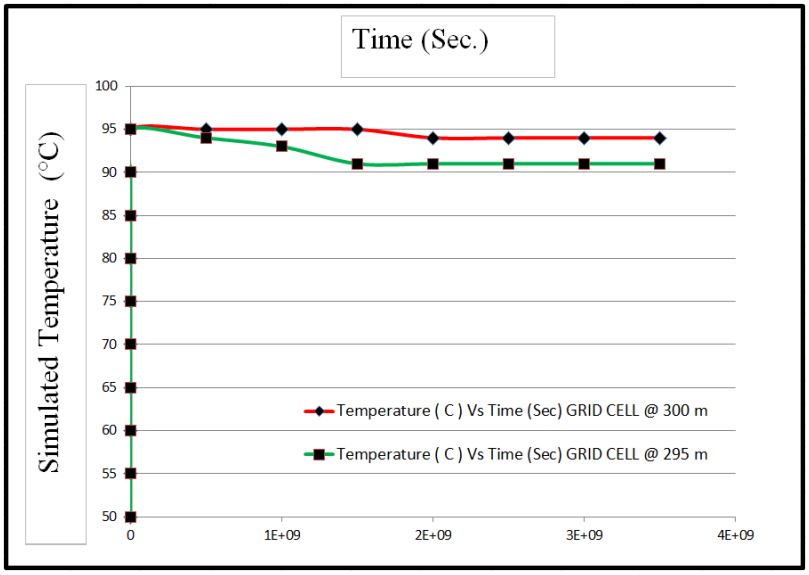


Figure 4.3: Comparison of the simulated temperature profiles for grid cells at 295 m and 300 m for reservoir simulation model #1. The figure shows that at the end of the model run, grid cell temperatures of 94 °C at 300 m and 91 °C at 295 m are obtained.

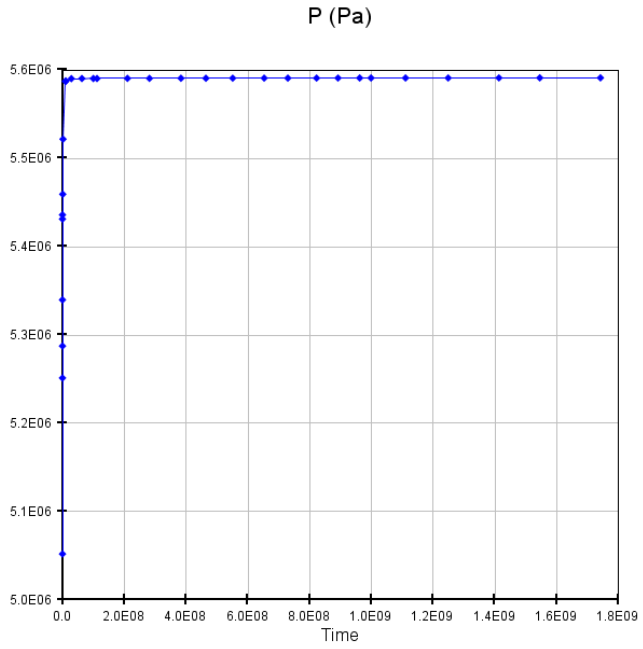


Figure 4.4: Simulated pressure profile for a grid cell that represents the conduit at a depth of 300 m for reservoir model #1. At the end of the model run, this pressure is 5.59 x 10^6 Pascals.

The temperature differential of 9 °C reflects the amount of cooling which occurs in the silty-sands located between 270-300 m below the thick clay package. The temperature profiles (Figure 4.3) show that there are minor changes in temperatures over the simulation time period. These temperature profiles also suggest that the reservoir model is very close to attaining a steady state condition where temperatures and pressures across the reservoir remain constant with time. Allowing this reservoir model to run for a longer time period will certainly allow it to attain a steady state condition.

4.1.2 Reservoir Simulation Model #2

The second reservoir simulation model has been established and run using the following conditions:

- A heat source cell is located at 1000 m in the vicinity of well PS 5. It is set as a fixed boundary condition with a temperature of 120 °C and an additional pressure head of 12 m.
- The conduit originates from the base layer near the vicinity of well PS 5 and orients laterally toward the vicinity of well PS 12-2 at the basement contact at a depth of 300 m. The details of the plumbing have been discussed in Chapter 3.
- Other conditions are the same as in reservoir simulation model #1.

The second reservoir simulation model has been developed based on increasing the temperature gradient for the well PS 5 at a depth of 240 m. Further investigations have been made to analyze and interpret the MT survey and static temperature logs for all the wells. Thus, based on the interpretations of the geological and geophysical data, we have developed the second reservoir simulation model with a different plumbing and heat source location as discussed in Chapter 3.

The simulated temperature section in the west-east direction (Figure 4.5) and in the south-north direction (Figure 4.6) for the second reservoir simulation model show the directions of up-welling and outflow of geothermal fluids into the shallow aquifer.

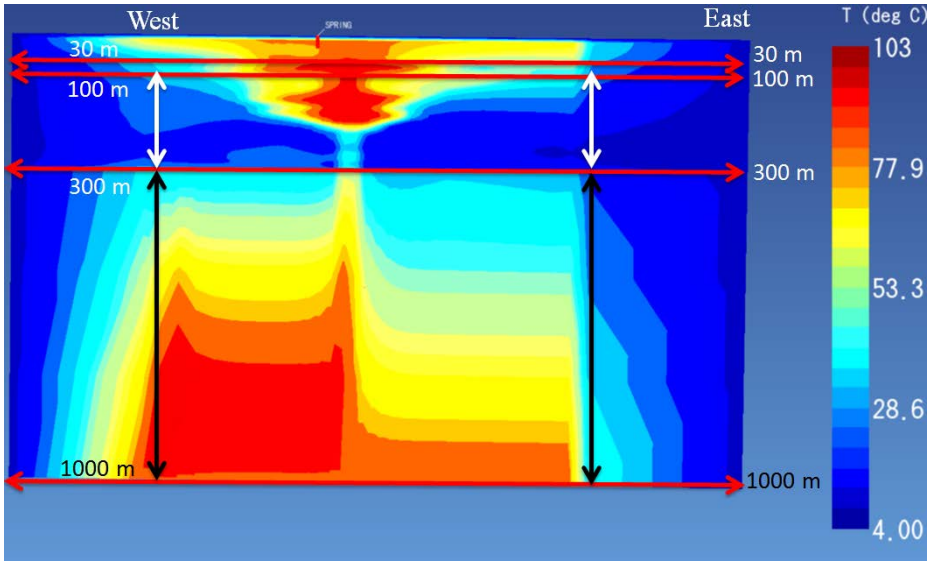


Figure 4.5: Simulated temperature section in the west-east direction for reservoir simulation model #2. The successive red, orange, green, yellow and cyan peaks in the central part of the figure indicate the passage of up-welling geothermal fluids.

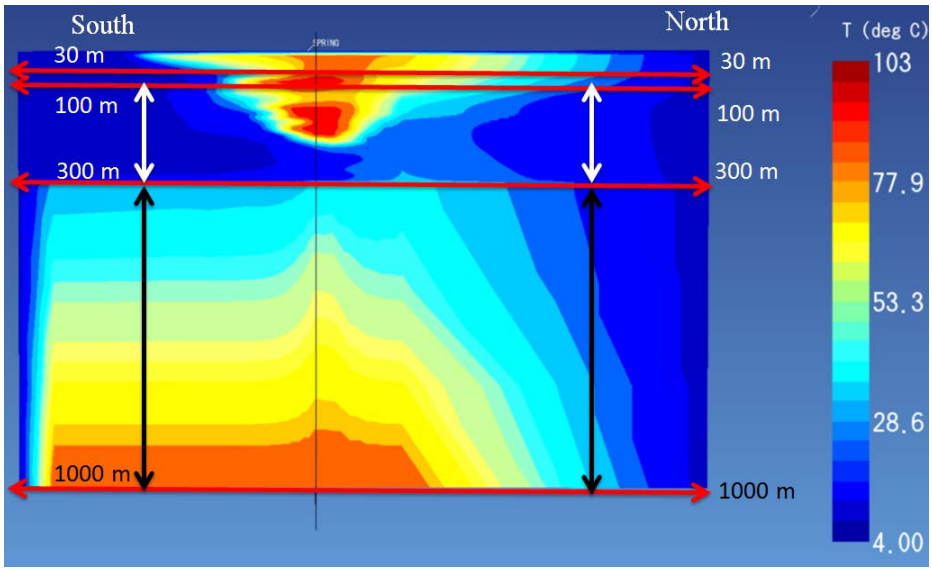


Figure 4.6: Simulated temperature section in the south-north direction for reservoir model #2. The complete path of up-welling of geothermal fluids is not as visible in this direction as the section does not pass through the core of the up-welling region. However, the lateral migration of the fluids in the shallow aquifer (the basin-like structure) is clearly visible at the top.

An important difference between this model and the previous reservoir simulation model is that the heat source is located near the vicinity of well PS 5. The plumbing is setup such that despite the hotter fluid being fed into the model near the vicinity of well PS 5, the up-welling of the hotter fluids from bedrock into the upper sedimentary layers still occur near the vicinity of the wells PS 1, PS 12-2 and PS 12-1 (Figure 4.7).

In fact, the up-welling occurs in the sedimentary layers to the north-west of well PS 12-2. The heat source cell has been set at 120 °C. The heat source cell has also been set with an additional pressure head of 12 m to force the fluids via a longer flow path.

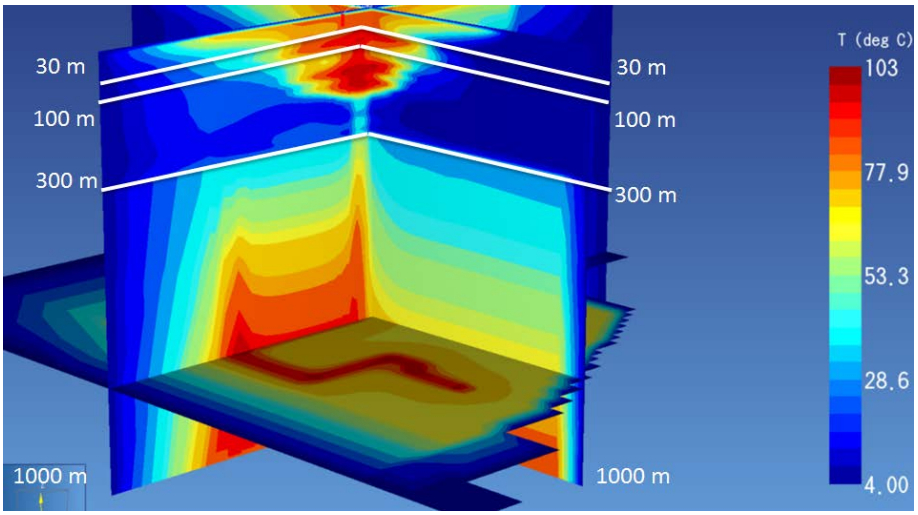


Figure 4.7: The flow of up-welling fluids through the plumbing of the second reservoir simulation model which originates in the south near well PS 5 and moves laterally towards the well PS 12-2.

Similar to the previous simulation model, the simulated vertical temperature sections are highly influenced by the grid resolutions which affect the plume, deeper sediment zone and the shallow aquifer. However, extracting temperature profiles from the grid cells that represent the well locations gives a better sense of variations in temperatures. During influx of cold water into the domain towards the north, there may be mixing with hot up-welling fluids. The grid cell at a depth of 300 m shows a temperature of 118 °C, and at a depth of 290 m (Figure 4.8), a temperature of 90 °C, indicating a cooling of 28 °C as geothermal fluids rise between these depths.

It is also known that the temperature of the heat source cell for this model is 120 °C. The pressure of the grid cell at 300 m (Figure 4.9) is 5.63 x 10^6 Pascal, which is the pressure of the fluid which exits the conduit at the basement contact level. The pressure of fluids expelled from the conduit at 300 m is greater in this model when compared with the first reservoir simulation. The up-welling of the geothermal fluids in this scenario is also dominated by the greater buoyancy effects of the 120 °C fluid and the additional pressure head of 12 m. The combination of these two factors contributes to the enhanced up-welling of the geothermal fluids and stronger cooling.

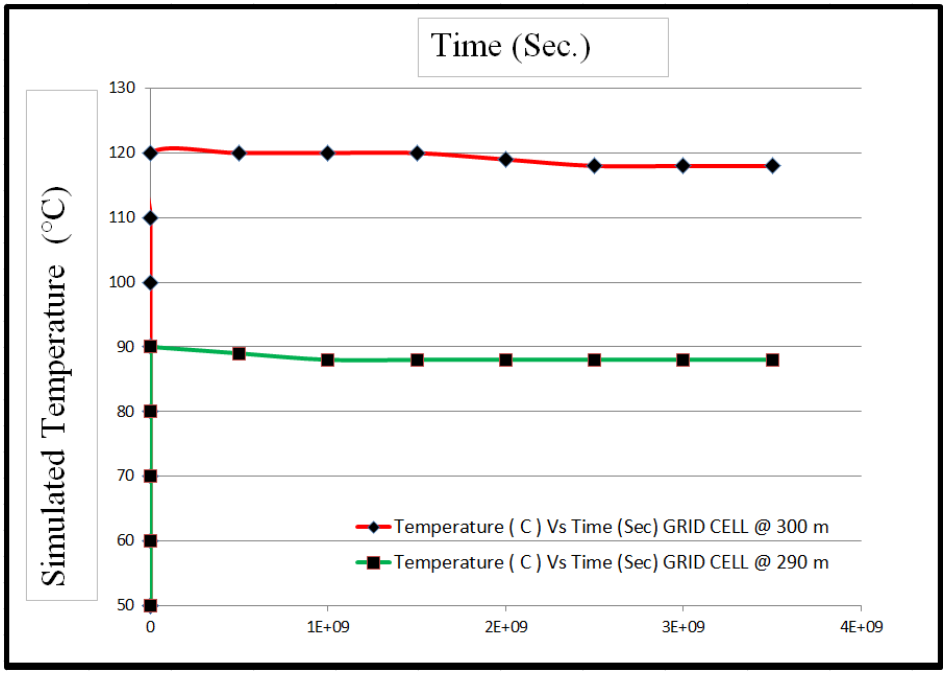


Figure 4.8: Comparison of the simulated temperature profiles for grid cells at 290 m and 300 m for reservoir simulation model #1. The figure shows that at the end of the model run, grid cell temperatures of 118 °C at 300 m and 90 °C at 290 m were obtained.

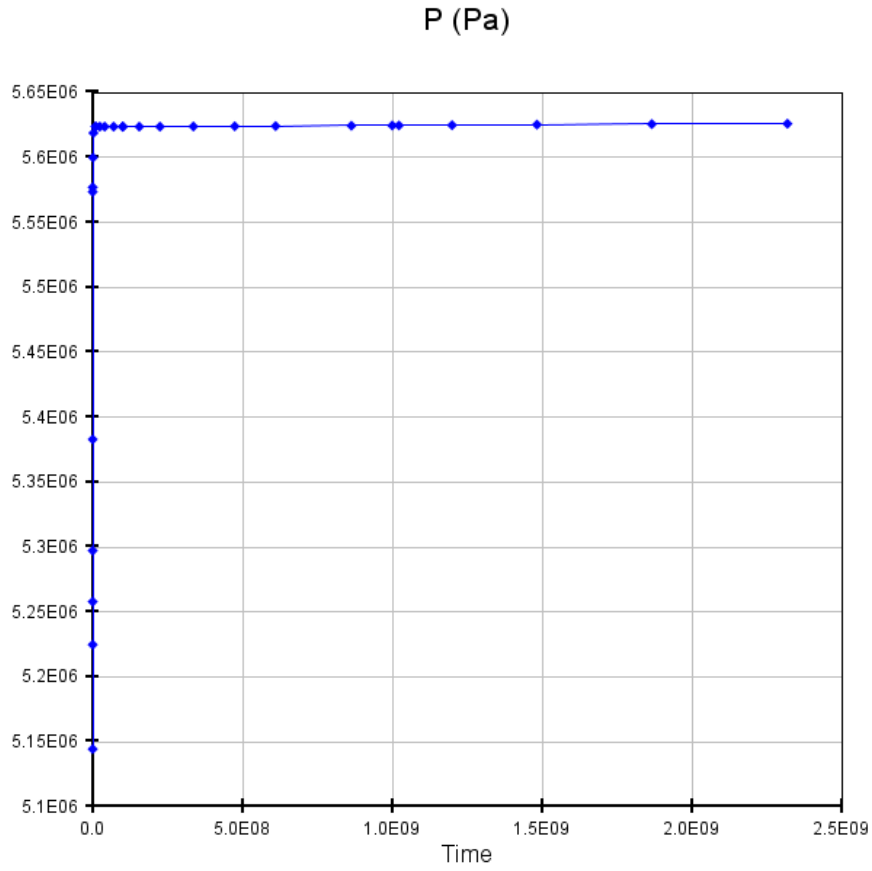


Figure 4.9: Simulated pressure profile for a grid cell that represents the conduit at a depth of 300 m for reservoir simulation model #2. At the start of the model run, this pressure is set at 5.63 x 10^6 Pascals.

4.2 Heat Flux Estimation

4.2.1 Reservoir Simulation Model #1

The reservoir simulation model was used to estimate the total heat energy near the surface by calculating a cumulative heat flux (z-direction) for every cell in the top layer within the domain. The layer closest to the surface was utilized to estimate the total heat flux in W/m^2 near the surface.

The thermal energy for every cell in the layer nearest to the surface was estimated using Equation 4.1:

$$\text{Thermal Energy per cell} = \text{Area of cell} * \text{Heat Flux for cell} \quad (4.1)$$

The total thermal energy near the surface is estimated using Equation 4.2:

$$\text{Total Thermal Energy near the surface} = \sum \text{Area of cell} * \text{Heat Flux for cell} \quad (4.2)$$

The total thermal energy estimation from the layer closest to the surface does not incorporate the cells which represent the permafrost at the reservoir boundaries. The estimated thermal energy is 26 MW which is much higher than the value of 6.7 MW estimated from remote sensing of surface geothermal features (Haselwimmer et al., 2013). The reason for this substantial difference is that the model considers the discharge of groundwater near and away from the area, the discharge of energy near the surface towards the atmosphere, discharge of energy from springs, and discharge of energy via the Pilgrim River. Thus, the area and volume covered by the reservoir model covers a larger domain and deeper system while the remote sensing technique estimates the heat associated with hot springs and some areas of geothermally-heated ground.

4.2.2 Reservoir Simulation Model #2

Simulation model # 2 uses the same set of assumptions and equations for evaluating the total surface thermal energy as Model #1. The thermal energy estimated from the model # 2 is 28 MW with a 120 °C heat source when both the models have the same boundary and initial conditions. The major differences between the models are the conditions applied to the heat source cell. The heat source cell for the first model has an additional pressure head of 10 m, but for the second model the additional pressure head is 12 m. This additional pressure head forces the fluids to feed into the upper sedimentary layers so the simulated temperature profiles match the static temperature logs for all wells across the domain. Small variations in estimated values may be due to the varying buoyancy effects on the up-welling fluids and the varying pressure and temperature of fluids expelled from the conduit at the basement contact.

4.3 Well Temperature Plots

4.3.1 Reservoir Simulation Model #1

The accuracy of any reservoir simulation model depends on the success of history matching. The history matching process involved ensuring simulated well temperatures closely matched the static temperatures from all the wells at Pilgrim Hot Springs. This successful matching was attained by varying the pressure conditions at the heat source cell for every individual run. This process is also known as reservoir model calibration. As a result of history matching, the simulated temperature profiles and measured static temperature profiles for the wells were in very close agreement.

This model indicated that the heat source and up-welling of hotter fluids may be in the vicinity of wells PS 12-2, PS 12-3 and PS 1. A comparison of simulated temperatures to the measured static temperatures for PS 1 (Figure 4.10) and PS 2 (Figure 4.11) shows that the outflow of the hotter water occurs in the shallow aquifer at 30 m.

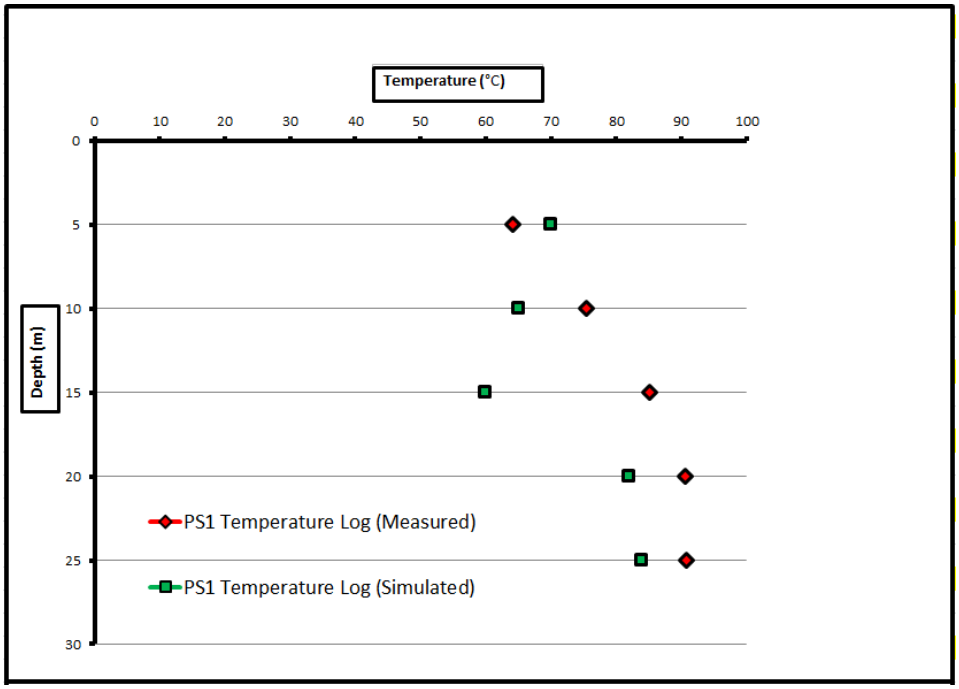


Figure 4.10: Comparison of the simulated well temperature to the actual well temperature for well PS 1 for reservoir simulation model #1. The presence of 80 °C water at 30 m indicates the outflow of fluids in the shallow aquifer.

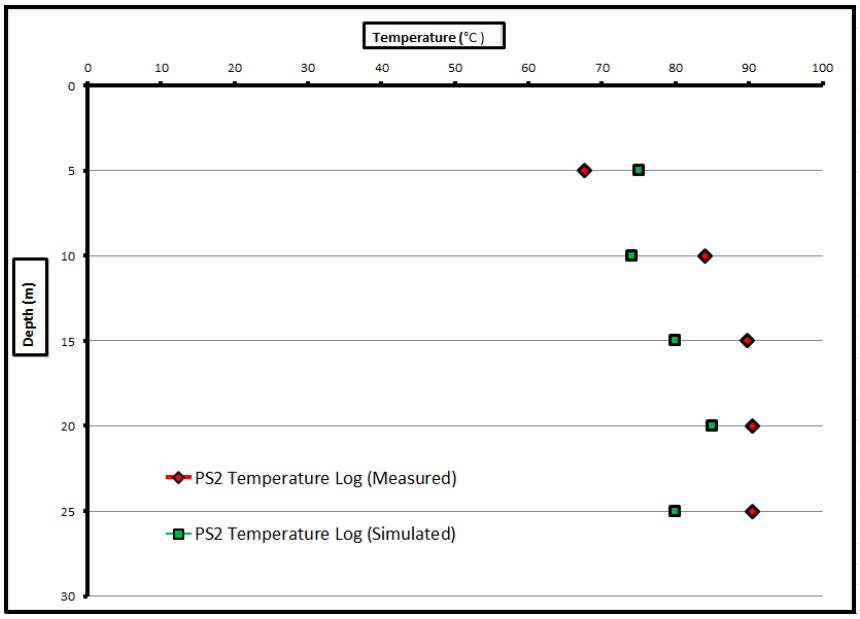


Figure 4.11: Comparison of the simulated well temperature to the actual well temperature for well PS 2 for reservoir simulation model #1. The presence of 80 °C water at 30 m indicates the outflow of fluids in the shallow aquifer.

A comparison of simulated temperatures to the measured static temperatures for PS 12-2 (Figure 4.12) and PS 12-3 (Figure 4.13) indicates the highest temperature of 80 °C near the basement contact at a depth of 300 m and at the base of the shallow aquifer at 30 m. The 80 °C fluids at both these depths suggest that the up-welling of hotter fluids occurs at 300 m, while the outflow of hotter fluids occurs at 30 m.

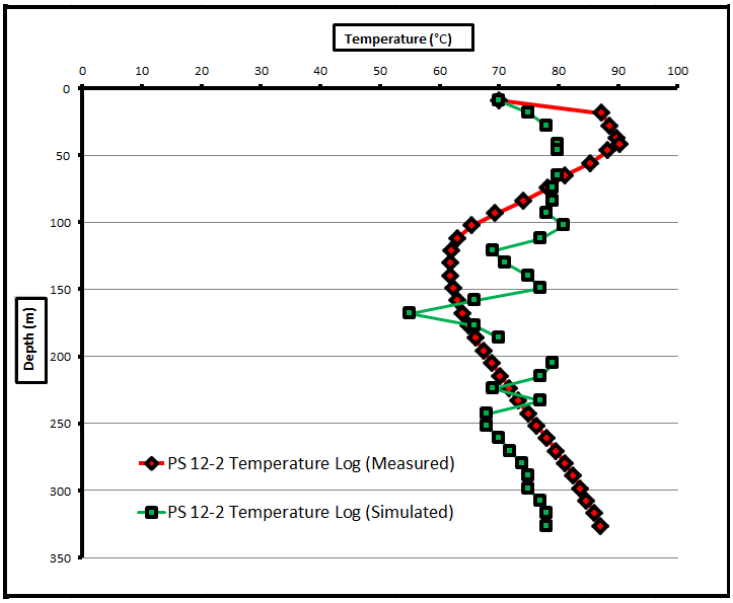


Figure 4.12: Comparison of the simulated well temperature to the actual well temperature for well PS 12-2 for reservoir simulation model #1. The 80 °C fluid at 30 m indicates outflow, while up-welling occurs at 250 m.

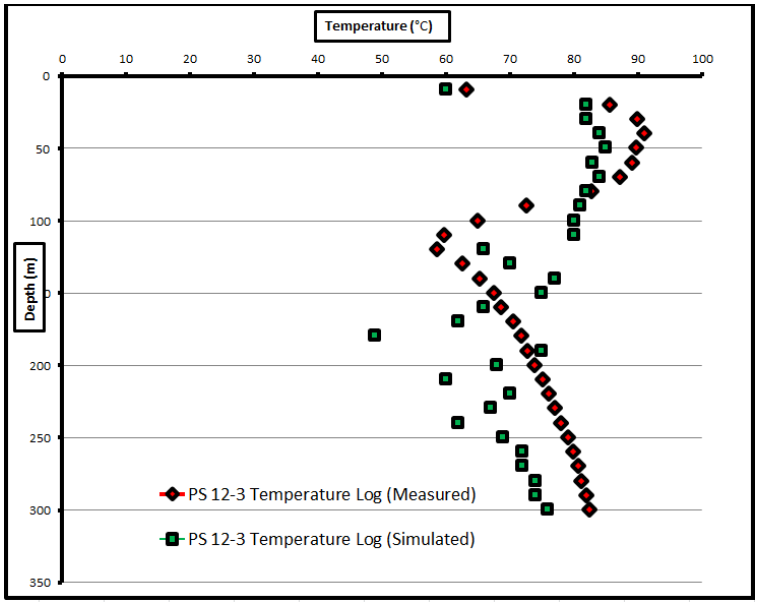


Figure 4.13: Comparison of the simulated well temperature to the actual well temperature for well PS 12-3 for reservoir simulation model #1. The 80 °C fluid at 30 m indicates outflow, while up-welling occurs at 300 m.

These observations for wells PS 12-2, PS 12-3 and PS 1 suggest that an up-welling of hotter fluids from the 95 °C heat source is feasible, but the model is slightly colder than the observed values. It assumed that cold groundwater influx from the Kigluaik Mountains was fed into a domain flowing towards the north. The interaction of the hot and cold liquids results in mixing. The mixed waters are eventually fed into the Pilgrim River. Wells S1 and S9 are located in the northern part of the domain. A comparison of simulated temperatures to the measured static temperatures for S1 (Figure 4.14) and S9 (Figure 4.15) shows that both the simulated and measured temperatures are relatively lower than the temperatures observed in the other wells in the domain, with a very low temperature gradient that suggests mixing of fluids.

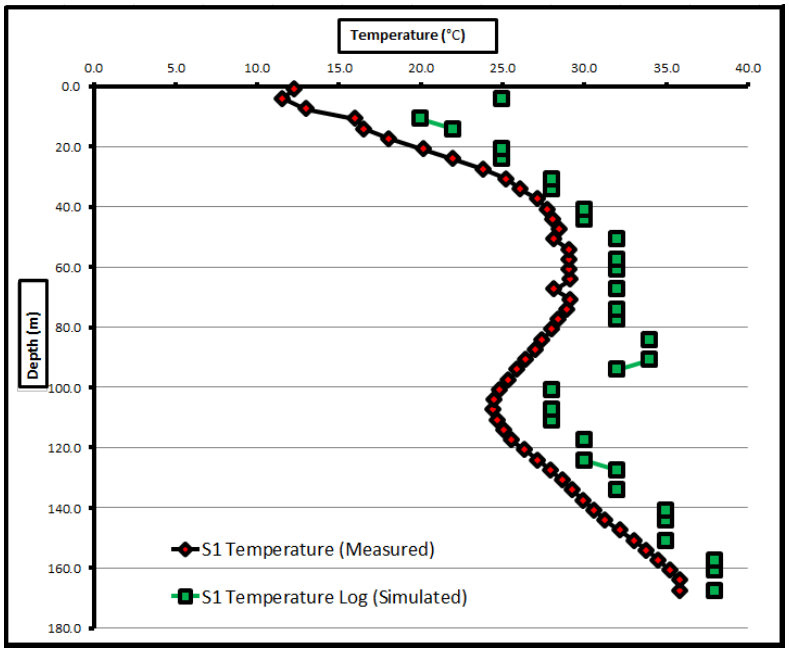


Figure 4.14: Comparison of the simulated well temperature to the actual well temperature for well S1 for reservoir simulation model #1 that indicates very low temperatures and low gradient, which suggests mixed fluids in the area.

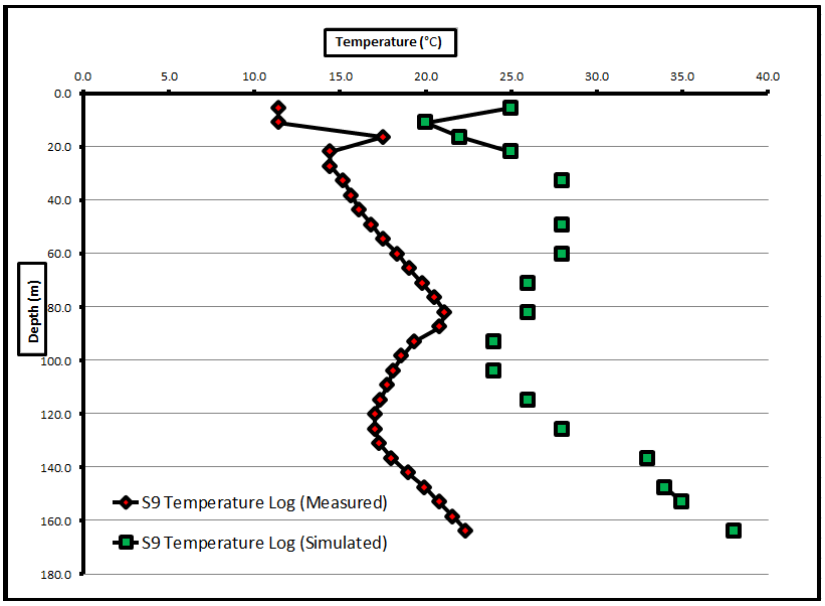


Figure 4.15: Comparison of the simulated well temperature to the actual well temperature for well S9 for reservoir simulation model #1 that indicates very low temperatures and low gradient, which suggests mixed fluids in the area.

Wells PS 5 and MI 1 are located in the southern part of the reservoir domain. Wells PS 5 and MI 1 are closest to the cold water influx that can be observed from the reversals of temperature profiles near the surface. The comparison of simulated temperatures to the measured static temperatures for MI 1 (Figure 4.16) shows that the temperature at a depth of 100 m is the lowest temperature for this well.

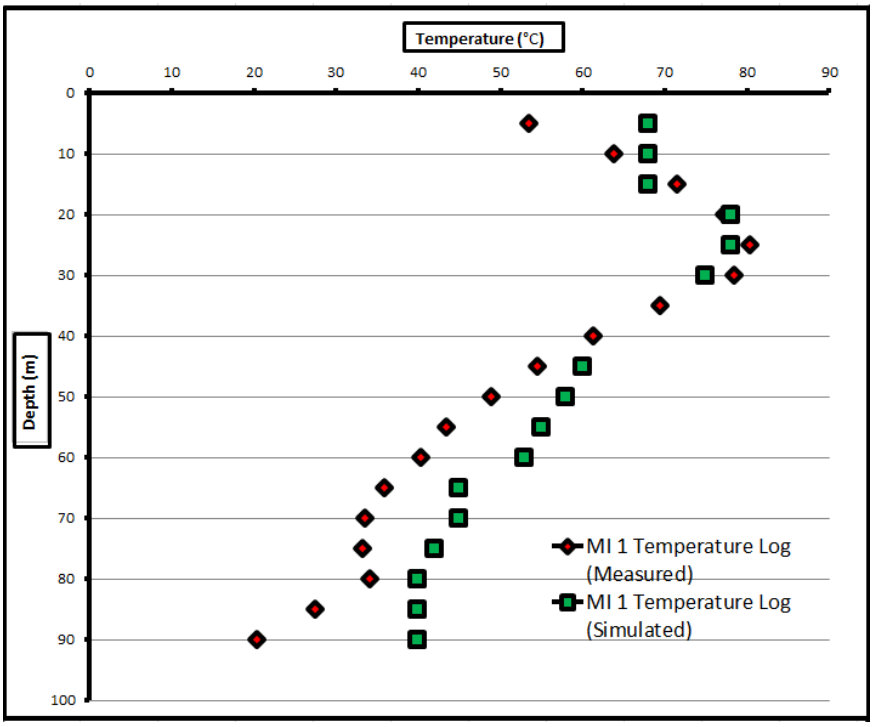


Figure 4.16: Comparison of the simulated well temperature to the actual well temperature for well MI 1 for reservoir simulation model # 1 shows the lowest temperature of 40 °C at 90 m, suggesting the influence of cold water influx at 100 m.

A comparison of simulated temperatures to the measured static temperatures for PS 5 (Figure 4.17) shows that there is a notable temperature gradient between 220-260 m in the static temperature logs measured from the field.

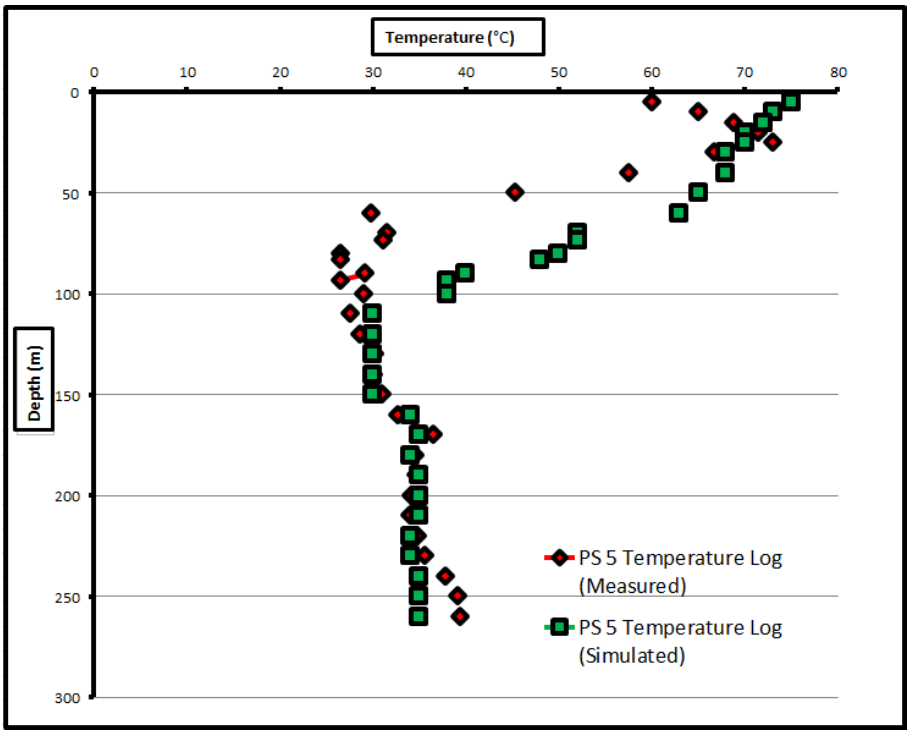


Figure 4.17: Comparison of the simulated well temperature to the actual well temperature for well PS 5 for reservoir simulation model #1 showing a notable temperature gradient at 240 m only for the measured temperature log.

One possible explanation for an increasing temperature gradient irrespective of cold water influx is the presence of a plumbing system or heat source in the vicinity of this well. However, we do not observe this increasing temperature gradient in the simulated results due to the absence of any plumbing or heat source near the vicinity of this well. As per discussions in Chapter 3, another reservoir simulation model has been developed based on alternative plumbing and location of heat source in the vicinity of well PS 5 that corroborates with the increasing temperature gradient at a depth of 240 m even when influenced by the cold water influx.

The results of the comparison of the simulated well temperatures to the actual measured temperatures for wells PS 3, PS 4 and PS 12-1 are included in Appendix A to document the history matching for the other wells at Pilgrim Hot Springs for this model.

4.3.2 Reservoir Simulation Model #2

The heat source cell in the second reservoir simulation model has been set at 120 °C based on the isotherms derived from the MT survey and static temperature logs for all wells across Pilgrim Hot Springs. The temperature profiles for the wells PS 5 and PS 12-2 support the feasibility of the idea that the heat source and plumbing could be in the vicinity of well PS 5, with up-welling of hotter fluids to the north-west of well PS 12-2. In this reservoir model, both the heat source and cold water influx into the domain occurs from the southern end of the domain. However, the plumbing has been reoriented in order for the up-welling of hotter fluids to occur in the vicinity of wells PS 12-2 and PS 1. A comparison of simulated temperatures to the measured static temperatures for PS 12-2 (Figure 4.18) and PS 12-3 (Figure 4.19) shows the vicinity of the well to the up-welling of hotter fluids and their outflow regions.

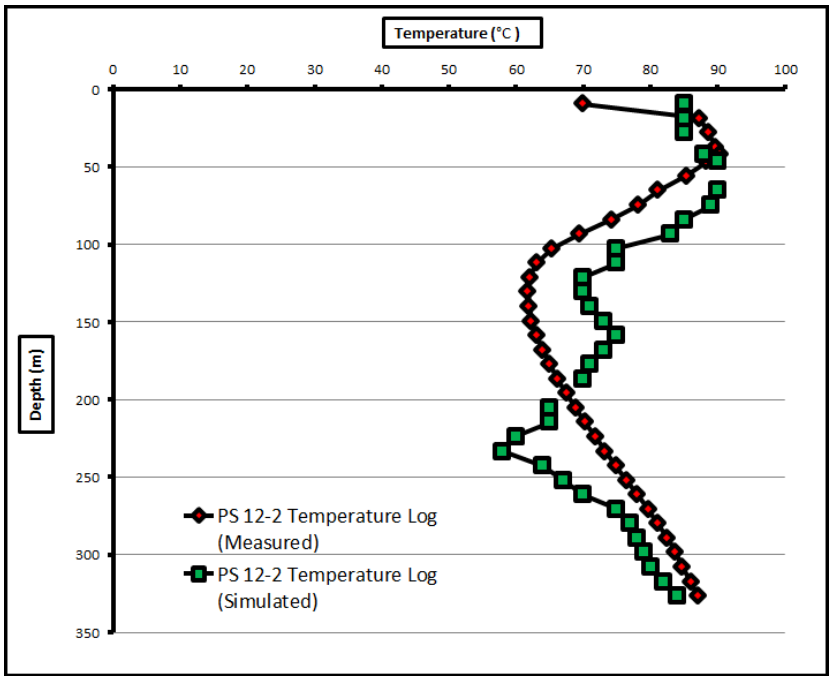


Figure 4.18: Comparison of simulated temperatures to the measured static temperatures for PS 12-2 for reservoir simulation model #2. The 85 °C fluid at 30 m suggests outflow of geothermal fluid, while at 320 m it suggests up-welling.

We observe that there is better matching of the simulated temperature profiles to the static temperature logs for the second reservoir simulation model for all the wells across the domain.

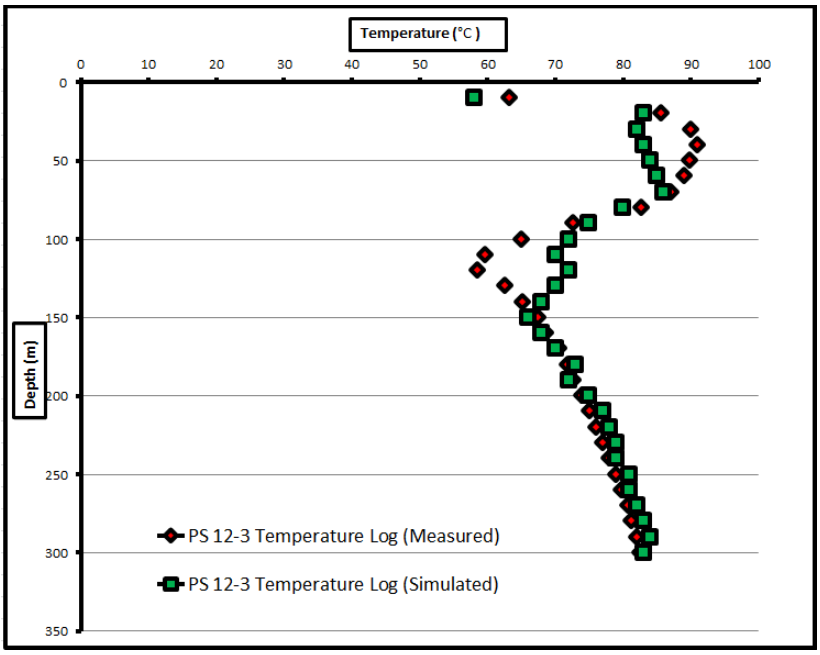


Figure 4.19: Comparison of simulated temperatures to the measured static temperatures for PS 12-3 for reservoir simulation model #2. The 85 °C fluid at 60 m suggests outflow of geothermal fluid, while at 300 m it suggests up-welling.

For well PS 5 (Figure 4.20), the maximum temperature of 75 °C occurs at the base of the shallow aquifer at 30 m. It is very interesting to note that there is a very sharp temperature gradient between 220-260 m in the static measured temperature log, and we observe a sharp temperature gradient between 250-280 m for the simulated temperature profile which was not evident in reservoir simulation model #1. The increasing temperature gradient, irrespective of cold water influx into the domain, could be due to the possible existence of a plumbing system or heat source in the vicinity of this well.

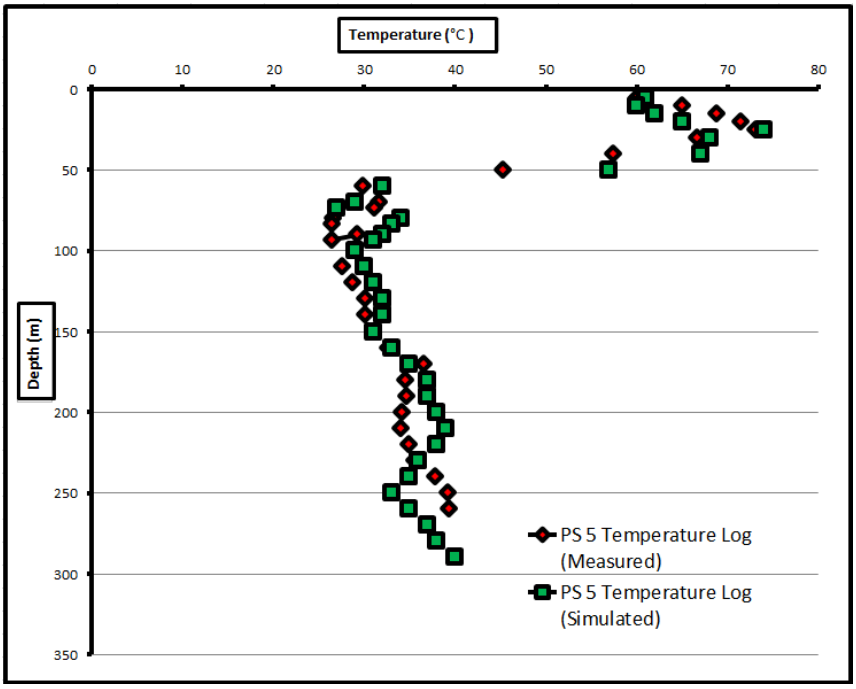


Figure 4.20: Comparison of simulated temperatures to the measured static temperatures for PS 5 for reservoir simulation model #2 where both profiles indicate increasing temperature gradient at 240 m possibly due to vicinity to the plumbing or heat source.

These observations for wells PS 12-2, PS 12-3 and PS 5 suggest that it is feasible for a heat source at 120 °C to exist in the vicinity of PS 5, and also an up-welling of hotter fluids to the north-west of PS 12-2. The history matching for well PS 5 compares much better to the measured values than does the previous model. This shows the right balance between the up-welling hotter fluids and cross-flowing cold water. This matching has been obtained after running many trials with varied additional pressure heads at the heat source cell.

A comparison of simulated to measured static temperatures for PS 4 (Figure 4.21) shows a maximum temperature of 80 °C at the base of the shallow aquifer. Also notable is that the simulated temperature profile differs from the measured temperature profile between 200-250 m. The isothermal signature in the measured temperature profile is due to instrument error. However, the simulated temperatures between 50-150 m indicate a positive temperature gradient which suggests that this well may also be in the vicinity of the up-welling of hotter fluids, with a maximum temperature of 80 °C.

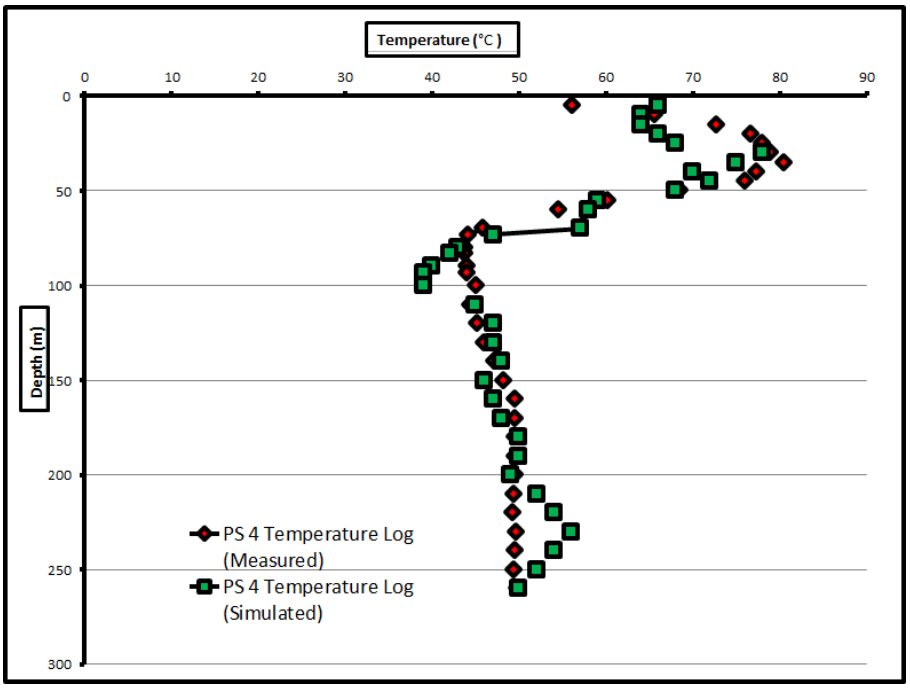


Figure 4.21: Comparison of simulated temperatures to the measured static temperatures for PS 4 for reservoir simulation model #2. The mismatch between the profiles is due to the incorrectly measured isothermal signature due to instrument error.

All results of comparisons of the simulated to the actual measured temperatures for wells S1, S9, PS 1, PS 2, PS 3, MI 1 and PS 12-1 are included in Appendix B.

The limitations to this second reservoir simulation model are similar to the first reservoir model. However, the second model shows a better match in the trends between measured and simulated temperature profiles. Both of the reservoir simulation models utilize the same boundary conditions and initial conditions. However, the first reservoir simulation model utilizes an additional pressure head of 10 m with a 95 °C heat source, whereas the second reservoir simulation model utilizes an additional pressure head of 12 m with a 120 °C heat source. For both models, the additional pressure head at the heat source cell was varied until a better match of the simulated temperature profiles to the static temperature profiles was obtained. Thus, it seems that the better fit in the second case is likely dependent on conditions applied to the heat source cell.

4.4 Reservoir Stimulation Models

4.4.1 Reservoir Stimulation Model #1

Reservoir simulation model # 2 with a 120 °C heat source located at a depth of 1000 m, including all the boundary and initial conditions, has been utilized to execute all three reservoir stimulation models (Figure 3.24). Based upon this, the first reservoir stimulation model uses two production wells (Figure 3.27). The heat transfer rate associated with any production well is a product of specific heat, mass flow rate and change in temperature, given by Equation 4.3:

$$Q = m\, C_p \Delta T \qquad (4.3)$$

Where, Q = heat transfer rate (W); m = mass flow rate (kg sec^{-1}); C_p = specific heat capacity (J Kg^{-1} $°C^{-1}$); and ΔT = difference between reference temperature and final temperature (°C).This stimulation model estimates 48 MW of thermal energy (Figure 4.22). Using Equation 4.3, the temperature of the production fluid was calculated to be 85 °C. We assumed the values for the following parameters: m = 135 kg sec^{-1}, C_p= 4200 J Kg^{-1} $°C^{-1}$, Q = 48 MW. The reference temperature for this calculation is assumed to be 0 °C. Due to computational demands this model has only been run for a 10 year period. As such, the simulation has not yet reached steady-state conditions due to minor changes in the slope of the thermal energy curve. Running this model for longer time periods would help to attain steady state conditions.

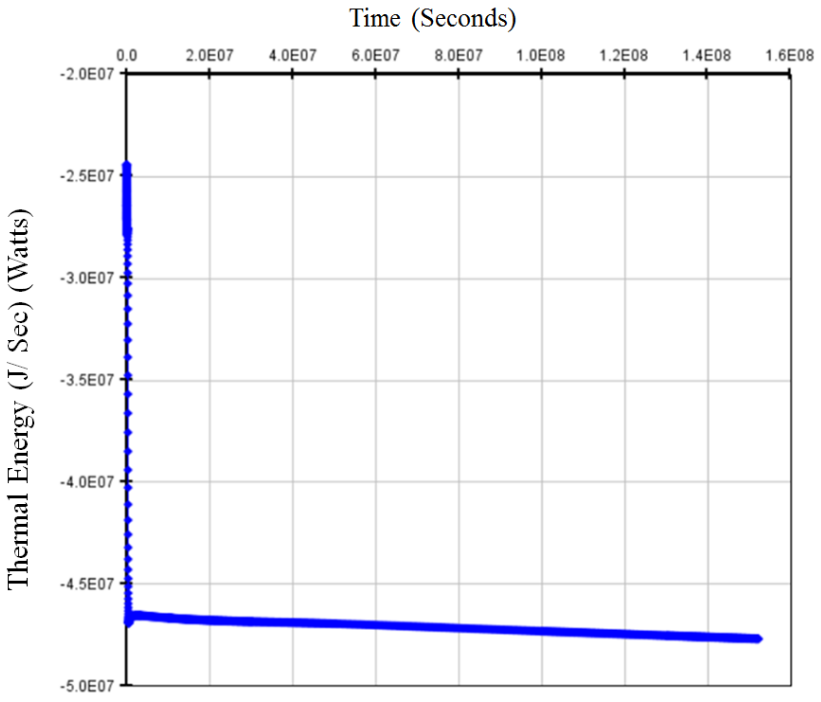


Figure 4.22: Estimated thermal energy from production well # 1 is around 48 MW for reservoir stimulation model # 1 with calculated temperature of production fluid of 85 °C.

The simulated temperature section in the west-east direction (Figure 4.23) and south-north direction (Figure 4.24) shows that the shallow zone has become warmer than the initial conditions at the start of the simulations.

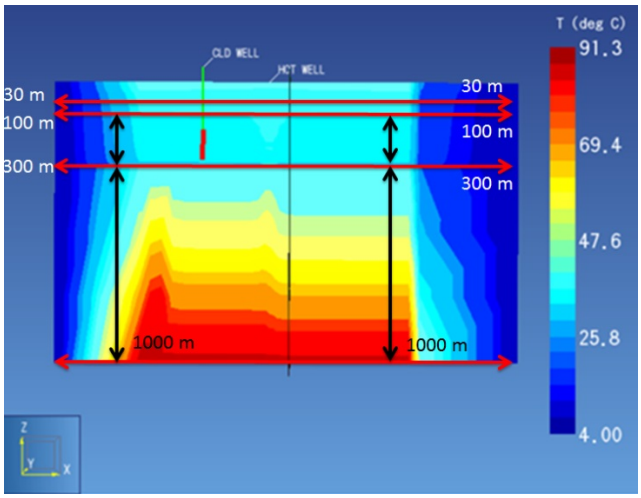


Figure 4.23: Simulated temperature section in the west-east direction for reservoir stimulation model #1 indicates a warmer shallow zone and deeper sediment zone.

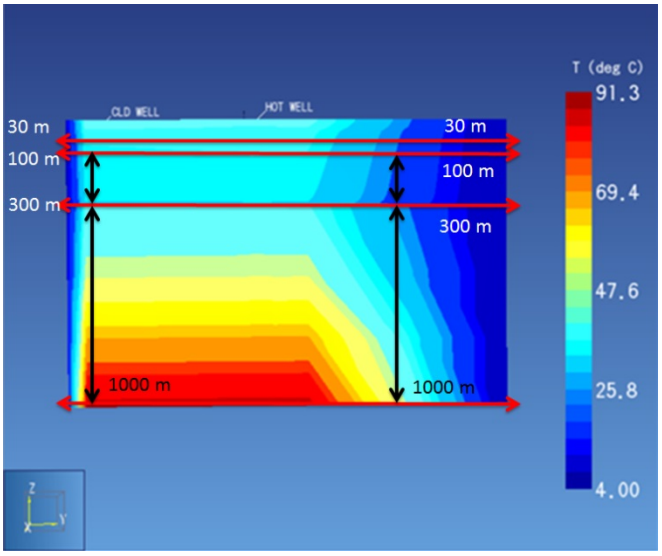


Figure 4.24: Simulated temperature section in the south-north direction for reservoir stimulation model #1 indicates a warmer, shallow aquifer and deeper sediment zone.

4.4.2 Reservoir Stimulation Model #2

The second reservoir stimulation model involved a scenario with one production well (Figure 3.28). This reservoir stimulation model estimates 46 MW of thermal energy (Figure 4.25) which is lower than stimulation model #1. Using Equation 4.3, the temperature of the production fluid was calculated to be 82 °C. We assume the values for the following parameters: m = 135 kg sec^{-1}, C_p= 4200 J $Kg^{-1}°C^{-1}$, q = 46 MW. The reference temperature for this calculation was assumed to be 0 °C. In this model, changes in the slope of the thermal energy curve occurred that indicate it has not yet reached steady state conditions over the relatively short 10 year model run. As with reservoir stimulation model #1, running the simulation for longer time periods would help to attain steady state conditions.

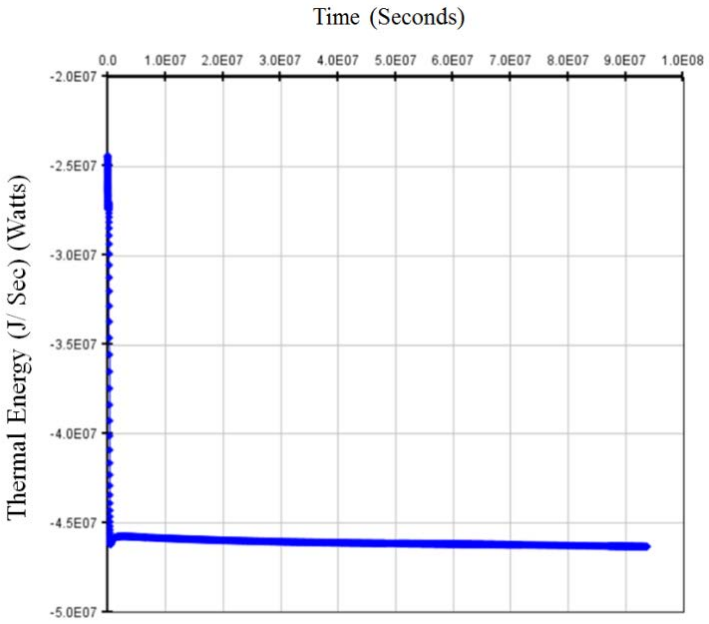


Figure 4.25: Estimated thermal energy from production well # 1 is around 46 MW for reservoir stimulation model # 2 with calculated temperature of production fluid of 82 °C.

The simulated temperature section in the west-east direction (Figure 4.26) and south-north direction (Figure 4.27) shows that the shallow zone and deeper sediment zone remain cool, and become cooler with time.

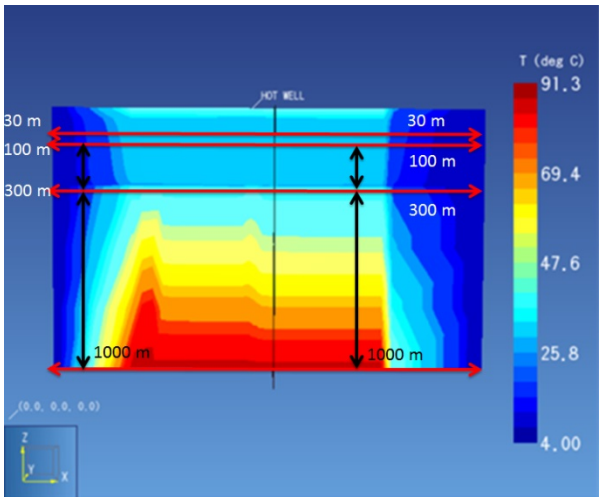


Figure 4.26: Simulated temperature section in the west-east direction for reservoir stimulation model #2 indicates a cooler shallow zone and deeper sediment zone.

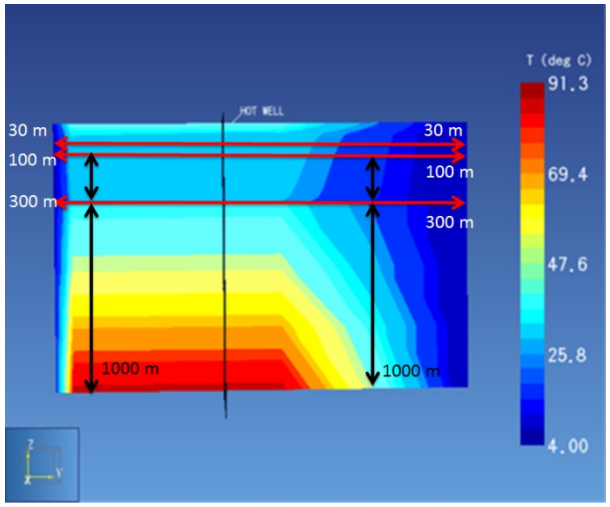


Figure 4.27: Simulated temperature section in the south-north direction for reservoir stimulation model #2 indicates a cooler shallow zone and deeper sediment zone.

The temperatures of the shallow aquifer and deeper sediment zone have not been modified as much as in reservoir stimulation model #1. The temperatures of the shallow aquifer and deeper sediment zone for this stimulation model are cooler than for reservoir stimulation model #1. Calculated thermal energy from the production well is lower when compared to reservoir stimulation model # 1.

4.4.3 Reservoir Stimulation Model #3

The third reservoir stimulation model involved an injection and production scenario (Figure 3.29). The injection well inputs 80 °C water into the domain which has an enthalpy of 335,000 Jkg^{-1} with a rate of injection of 2000 gpm. This reservoir stimulation model estimates 50 MW of thermal energy (Figure 4.28), which is higher than the other two reservoir stimulation models. Using Equation 4.3, the temperature of the production fluid was calculated to be 88 °C. We assumed the values for the following parameters: m = 135 kg sec^{-1}, C_p= 4200 J $Kg^{-1}°C^{-1}$, Q = 50 MW. The reference temperature for this calculation was assumed to be 0 °C. Due to minor changes in the slope of the thermal energy curve, it is observed that this model is not in a steady state condition over the short 10 year length of the model run.

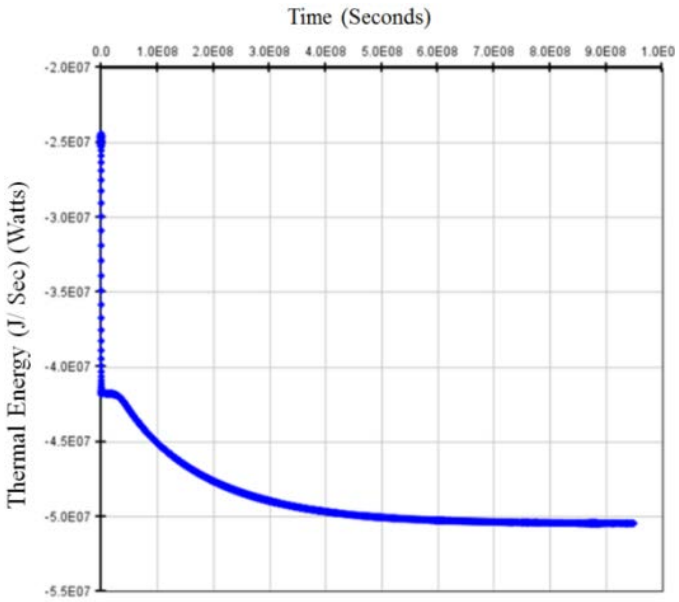


Figure 4.28: Estimated thermal energy from production well # 1 is around 50 MW for reservoir stimulation model # 3 with estimated temperature of production fluid of 88 °C.

The simulated temperature section in the west-east direction (Figure 4.29) and south-north direction (Figure 4.30) shows that both the shallow zone and the deeper sediment zone have warmed significantly when compared to the other two reservoir stimulation models.

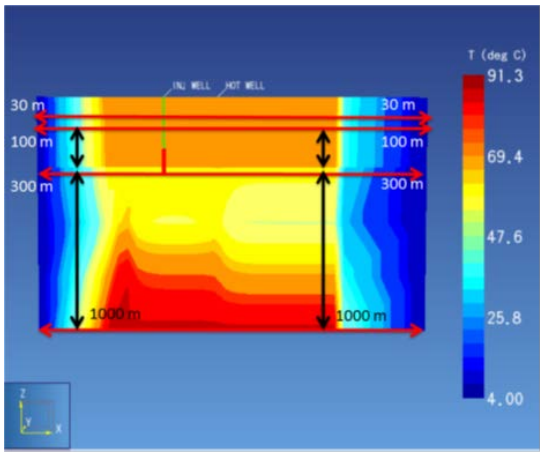


Figure 4.29: Simulated temperature section in the west-east direction for reservoir stimulation model #3 indicates significant warming of the shallow aquifer and deeper sediment zone.

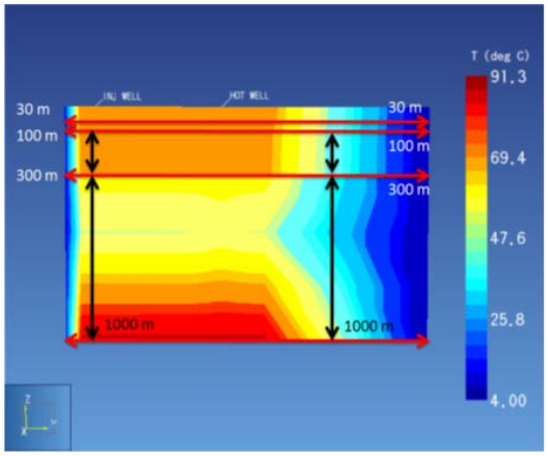


Figure 4.30: Simulated temperature section in the south-north direction for reservoir stimulation model #3 indicates significant warming of the shallow aquifer and deeper sediment zone.

The reason for this observation is that the injection well inputs 80 °C water back into the deeper sediment zone between 200-300 m. This re-injected water interacts with the cooler water in the southern part of the domain. The shallow zone and the deeper sediment zone become warmer. This allows the production well to maintain warmer temperatures.

The temperature of fluids entering the completion interval for production well #1 (Figure 4.31) indicates that relatively hotter fluids are produced when compared to the other two reservoir stimulation models.

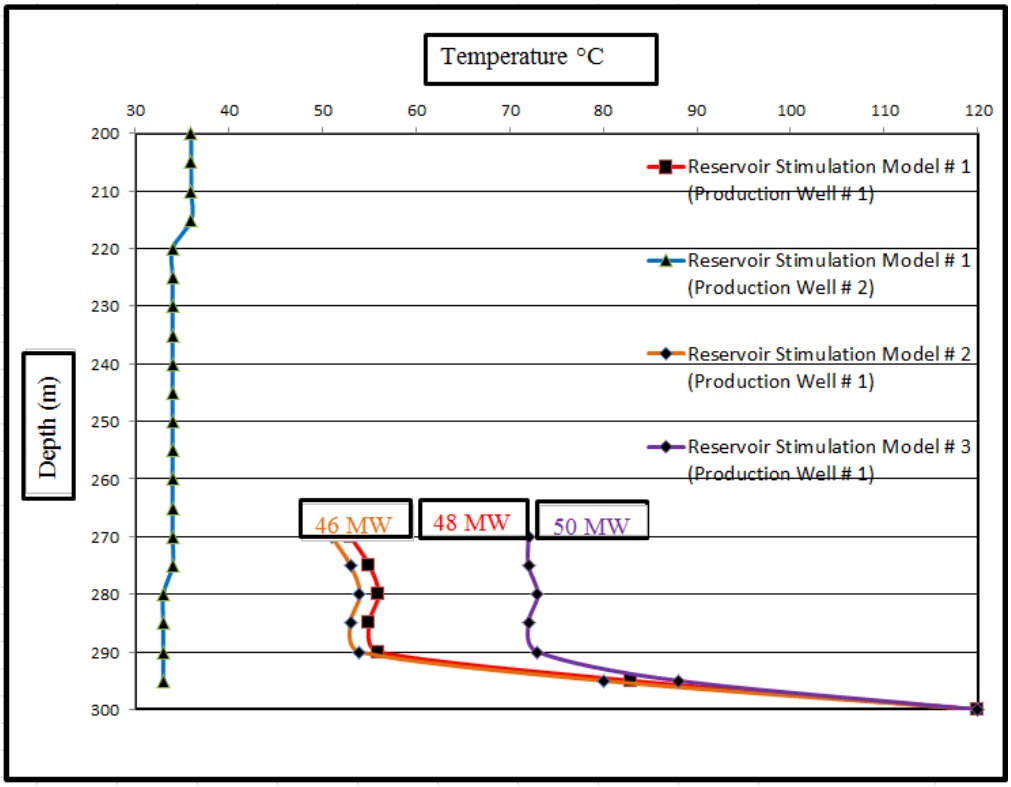


Figure 4.31: Comparison of temperature of fluids entering the completed interval for the production well in the three reservoir stimulation models which suggests the maximum temperature of produced fluid occurs in reservoir stimulation model #3.

Thus, the combination of production and injection is feasible with flow rates of 2000 gpm. This cyclic process of production and re-injection of 80 °C water back into the domain indirectly helps to sustain the reservoir pressure and simultaneously helps to improve the efficiency of the production well.

The efficiency of the production well derives from attaining greater volumes of hot fluids compared to the total volume of fluids produced. This combination of re-injection and production helps to complete the cyclic process which helps to sustain the system and improve the efficiency and life of the reservoir. Thus, this production scenario suggests that with one production well and one injection well, production well #1 produces about 50 MW of thermal energy. The effects of the reservoir stimulation scenarios on springs (Figure 4.32) show that excessive production from the reservoir results in a lower or negative differential pressure head in the springs. When the reservoir system is well-balanced as a cyclic process, the differential pressure head in the springs is positive and the difference is almost negligible.

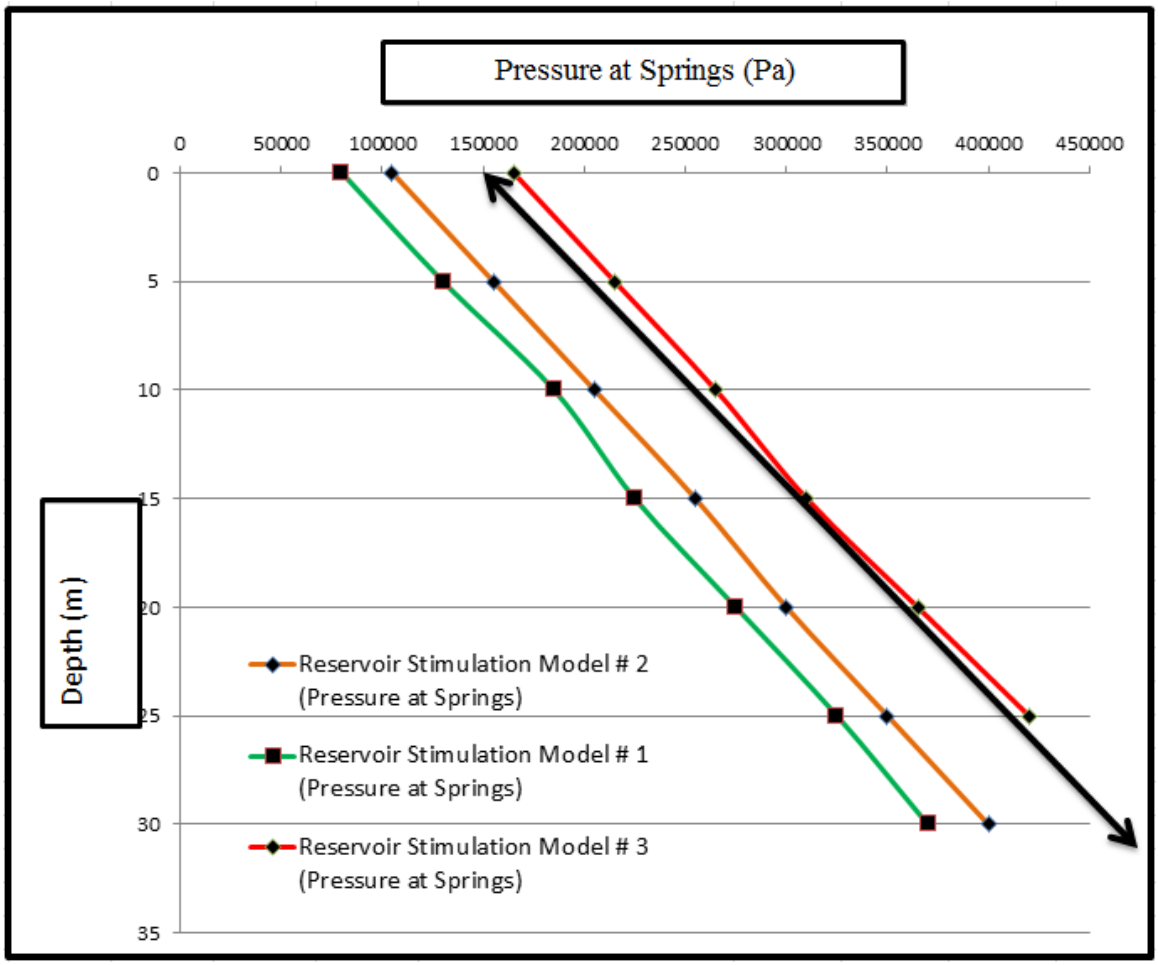


Figure 4.32: Comparison of the effects of the reservoir stimulation scenarios on reservoir pressure suggests decline in pressure at the springs due to excessive production from the first and second stimulation models. However, the third stimulation model is able to sustain the reservoir pressure due to the cyclic process of injection and production.

Chapter 5: Discussion

5.1 Reservoir Simulation Models

5.1.1 Heat Flux Estimation and History Matching

Pilgrim Hot Springs belongs to the classification of low-temperature fluid systems, which by definition have reservoir temperatures below 150 °C at 1 km depth (Axelsson et al., 2010). A general conceptual model of a low temperature geothermal system in Iceland (Figure 5.1) suggests that there may be two feed points: one for the deep inflow of geothermal water, and another for the shallow inflow of cold ground water (Steinberg et al., 1981). We believe that this is also the case for the Pilgrim Hot Springs geothermal system.

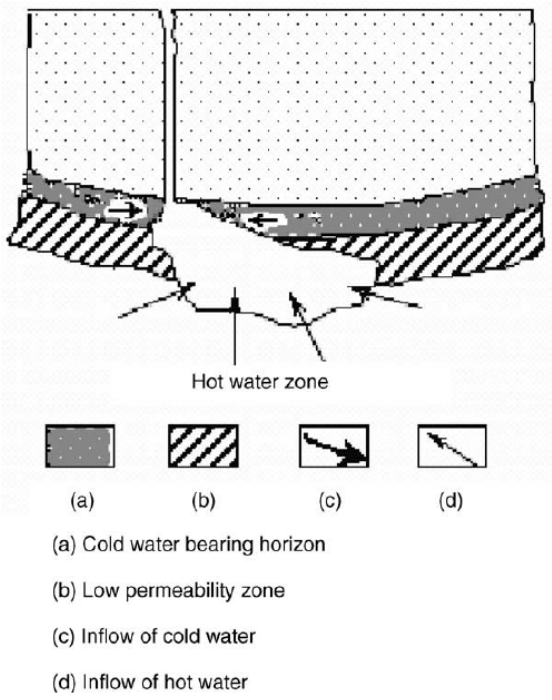


Figure 5.1: Conceptual model of a low temperature geothermal system in Iceland (Steinberg et al., 1981).

For modeling purposes, the conceptual model of Steinberg et al., (1981) has been considered to develop the reservoir simulation models. The adapted model developed in this research considers the heat source and inflow of hot water to result from the base layer in the model, such that the fluids are forced to flow vertically due to higher temperature and pressure conditions at the heat source cell. The hotter geothermal fluids are forced to flow via a fault or conduit until the basement contact is reached at a depth of 300 m. Thus, the up-welling, hotter geothermal fluids are expelled from the bedrock into the upper sedimentary layers. However, the up-welling of the hotter fluids needs to be sustained against the cross-flowing cold water in order to feed geothermal fluids into the shallow aquifer via the deeper sediment zone.

Lithologic logs and stratigraphic sections across Pilgrim Hot Springs suggest that there is a good correlation between the flow path of the hotter fluids and indurated sands (Miller et al., 2013). Literatures on other geothermal systems have also indicated the significance of indurated sands as pathways for fluid migration. Ward et al., (1979) reported that various forms of cemented sands are present across a wide range of geographic settings in Australia where they are referred to as ‘hardpan,’ ‘sandrock,’ ‘beachrock,’ and ‘coffeerock.’ The indurated sands are formed by hardening of zones within sandy deposits related to dissolution, leaching and precipitation of organic and inorganic complexes.

Scanning electron microscope (SEM) images of these indurated sands reveal that the cements tend to be present as grain coatings and they infill smaller interstitial pores, with the large pores usually open (Ward et al., 1979). Greater relative hardness and platy clay structures are present when sands have a high proportion of kaolinite. Indurated sands are a product of cementation during periods of super-saturation under fluctuating groundwater flow conditions (Fairbridge, 1967; Thompson et al., 1996; Strachotta, 2004). It is believed that, based on the properties of indurated sands, these sands account for very high vertical intrinsic permeability due to large open pores and fractures while they are coated by cement in the horizontal direction. This allows hotter fluids to flow in a vertical direction when encountered in indurated sands and it shields them from any cross-flowing cold waters (Brooke et al., 2008). Thus, for modeling purposes, we have considered the vertical permeability of indurated sands to be greater than the horizontal permeability by a factor of ten.

The next step in modeling involved setting boundary conditions and characteristics of the heat source cell. Both the reservoir simulation models have similar boundary conditions and initial conditions, with the exception of the conditions applied to the heat source cell. The reservoir simulation models have their respective top layer as a fixed boundary condition with no-flow, with the exception of cells representing the river and springs. The heat source cell location was fixed using interpreted isotherms from MT data. As the MT data indicated two possible heat sources at different temperatures and depths, the two models were run with the heat source cells at these two locations using the corresponding temperature values of 95 °C and 120 °C, respectively.

The other variable parameter in both models involved applying differing pressure heads to the heat source cell. The simulation runs with the closest possible matching of the simulated temperatures to the actual static temperatures (history matching) revealed that, though the degree of successful matching varied, additional pressure heads of 10 m and 12 m were optimal for the first and second simulation models, respectively.

Lower additional pressure heads resulted in cooler and smaller plumes while higher additional pressure heads resulted in warmer and bigger plumes. This may be viewed as a candle-in-the-wind scenario where there should be a correct balance between the cross-flowing wind and the plume formed by the candle for it to remain lit successfully while the winds blow across it. This analogy may also be applied to the reservoir simulation models. History matching involves the process of obtaining the right balance between the cross-flowing cold water and the up-welling hotter fluids which will result in a stable plume with cold water flowing across without killing the plume. These additional pressure heads were estimated by running many simulation models and comparing the simulated temperatures to the actual temperatures.

In some trial runs, the pressure head was too small to sustain a stable plume without being affected by the cold water influx from the south. When the pressure of the cross-flowing cold water was greater than the pressure of the up-welling fluids, we observed disappearance of the plume over the duration of the simulation. The plume seemed to extend toward the north while the southern end of the plume is affected by cold water influx followed by complete extinguishing of the plume.

However, when the pressure of the up-welling fluid was greater than the pressure of the cold water influx, the plume was sufficiently large and hot to overcome the dampening effects of the cold water influx from the south. Published literature lacks a body of work that discusses the development of reservoir models encompassing scenarios where cross-flowing cold waters and up-welling hot geothermal fluids reach a stable steady state condition. In the model developed in this work, steady-state conditions were achieved by varying the additional pressure heads provided to the heat source cells.

The rate of cooling of up-welling fluids due to cold water influx is greater in the second reservoir model, compared to the first model. By setting the source cell to a higher temperature of 120 °C in the second model, the difference in temperatures between the up-welling fluids and the external cooler fluids is greater, leading to increased convection of hotter fluids towards the shallow zone. This meant that more thermal energy was lost as a result of this process, compared to the first simulation model. This enhanced convection within the system allowed better matching of the simulated temperatures to static temperature logs.

The heat flux estimated by the first reservoir model was 26 MW, while it was 28 MW from the second model that included all the sink cells for the river. A difference of 2 MW was observed between the simulation runs from both models. However, they have similar temperature profiles. This suggests that the heat flux near the surface may be influenced by some other factors as well.

The heat source cell in the second model provides 2.7×10^{19} $Jsec^{-1}$ of energy when compared to the 6.8×10^{18} $Jsec^{-1}$ of energy for first model. The additional heat allowed enhanced convection within the system, as observed from the higher differences in temperatures between up-welling fluids and the external cooler fluids in the second model. Results from the first and second models suggested a pressure of 5.59×10^{6} Pascal and 5.63×10^{6} Pascal, respectively, for fluids exiting the conduit at the basement contact. The pressure and temperature of fluids expelled in the second model was greater than in the first model. However, in order to obtain similar temperatures for wells for both models, the up-welling fluid in the second model underwent more rapid cooling compared to the first model. The 120 °C fluid rose faster and more efficiently compared to the 95 °C fluid due to the effects of buoyancy. Thus, the combined effect of buoyancy for higher temperature fluid, and higher pressures of fluids expelled in the conduit near the basement contact in the second model, may explain the relatively higher heat flux near the surface.

It is also important to consider the driving mechanism in the model for the up-welling of geothermal fluids from the bedrock to the surface. Traditional conceptual models for thermal springs consist of an underground chamber, a channel connecting the chamber to the ground surface, and a heat source at the lower part of the chamber. The intermittent boiling within the chamber is considered to be the main driver for the periodic ejection or eruption (Lu et al., 2005). There are also a few examples of deep wells that erupt like springs, with pulses where the discharge is at a temperature significantly less than 100 °C (Lu et al., 2005).

These concepts can be related to observations from both the reservoir simulation models that explain better the driving mechanism of eruption and up-welling of 120 °C water in the second model, with a pressure of 5.63×10^6 Pascal at the end of the conduit, compared to the first model, with a pressure of 5.59×10^6 Pascal. The additional pressure allows greater flow rates of fluids and greater momentum that enables high temperature fluids to easily rise to the surface due to higher pressures and greater buoyancy.

The heat source cells for both models have been defined as a fixed boundary condition where the source of hotter fluids is unlimited and remains constant over the period of simulation. This condition ensures that the influx of hotter fluids into the domain from the heat source cell remains constant with respect to thermodynamic properties. This does not represent the real world scenario as the influx of the hotter fluids will vary with time, affecting reservoir conditions. A realistic heat source will have declining influx of hotter fluids along with declining pressures and temperatures.

Assuming a more realistic variable heat source cell then, it is likely that the values of heat flux near the surface from both the reservoir simulation models will be smaller. Incorporating a more realistic heat source cell will also result in lower values of thermal energy extracted from the production wells in the stimulation scenarios. The second model is not affected by this additional temperature and pressure of the heat source cell as the rate of cooling of up-welling fluids is greater due to greater temperature differences between the up-welling fluids and external cold fluids.

This additional pressure provides for additional momentum for fluids to rise toward the surface, and the temperature of fluids provides the buoyancy. As higher temperature fluids rise toward the surface, they lose more heat via convection causing a greater heat flux near the surface for the second reservoir model. In this study history matching has helped to predict the conditions required at the heat source cell and the conduit terminating at bedrock. This modeling work has been unique in the way that the reservoir model has been calibrated to attain the conditions of fluid expulsion from the heat source.

5.1.2 Well Temperature Plots

Based on the earlier discussion, the successful history matching was highly dependent on the initial and fixed conditions applied to the heat source cell. The history matching process indirectly allowed an estimation of the pressure and temperature of the geothermal fluid influx into the system and at the point of up-welling from the bedrock. However, matching of the simulated temperature profiles and static temperature profiles was also notably affected by the lithology. Lithology slices applied within the model influenced the exact matching of temperature profiles. For example, in Figure 4.10 at a depth of 15 m, the simulated temperature is cooler than the actual static temperature due to lithology. This is due to the fact that there is cold water influx at this depth as a relatively impermeable layer of permafrost occurs between 0-100 m. Similarly, the simulated temperatures are cooler than actual static temperature logs for well PS 12-3 between 10-60 m.

This is possibly due to the presence of low permeability silty sandy-clays that prevent the up-welling hot fluids from flowing easily into this horizon, keeping the temperatures cooler (Figure 4.19). It seems that the matching of the temperature profiles is also similarly affected by the lithology in the vicinity of the wells. The history matching for the first reservoir model was obtained by applying an additional pressure head of 10 m for the heat source cell located in the vicinity of wells PS 1, PS 12-2 and PS 12-3. For example, Figures 4.10 through 4.13 indicate up-welling of fluids near these wells and outflow into the shallow zone may be supported by the temperature logs where peak temperatures are observed around 30 m and 300 m. Peak temperatures around 300 m indicate up-welling of hotter fluids near the basement. Peak temperatures around 30 m indicate outflow of hotter fluids. For example, Figures 4.16 and 4.17 show that wells PS 5 and MI 1 are the most affected by cold water influx, shown by the lowest minimum temperatures.

The static temperature profile for PS 5 (Figure 4.17) indicated an increasing temperature gradient around 240 m while it was not evident in the simulated temperature profile. The observation of this increasing temperature gradient for this well along with interpretations of MT data led to the development of the second simulation model. For example, Figures 4.14 and 4.15 show that wells S1 and S9 were fed with mixed fluids, due to lower temperatures, compared to other wells in the domain.

The second reservoir model has been developed based on the observed increasing temperature gradient around 240 m for well PS 5 (Figure 4.20) which was also obtained in the simulated result for this well for the second reservoir model.

Simulated results for well PS 5 in the second model indicated an increasing temperature gradient between 240-300 m. This temperature profile for well PS 5 matches very closely with the static temperature log for this well. A possible explanation for this result is the existence of a plumbing and heat source to the south-west of well PS 5 which maintained the increasing temperature gradient at that depth in spite of the cold water influx from the south. History matching for the second simulation model seems to be better than the first model due to the correct balance between up-welling hotter fluids and cross-flowing cold water. Striking the right balance is highly dependent on the conditions applied to the heat source cell. Allowing more simulation runs with additional variable pressure heads for the heat source cell for the first simulation model would have potentially helped to improve the degree of success of history matching. However, the second model serves as an excellent example of the degree of successful history matching and estimating the pressure and temperature of the heat source cell (Figures 4.18 through 4.21).

5.1.3 Reservoir Models and Remote Sensing Derived Heat Fluxes

The estimated thermal energy of 26 MW and 28 MW from the two simulation models are greater than the value estimated from remote sensing (Haselwimmer et al., 2013). The remote sensing method gave a value of 4.7-6.7 MW for the heated waters and 2 MW for the snow-melt areas. The reason for this substantial difference is that, in calculating the heat flux, the reservoir simulation model considers the discharge of groundwater near and away from the area, the discharge of energy near the surface towards the atmosphere, the discharge of energy from springs, and the discharge of energy via the Pilgrim River, which was covered by the surface layer analyzed. The reservoir model covers a larger domain and emulates a deeper system while the remote sensing technique estimates heat flux from a very shallow region and a limited area.

In an earlier study, a conceptual model of Pilgrim Hot Springs was developed and the discharge of energy was estimated at 24 MW from the modeled geothermal system (Woodward-Clyde Report, 1983). The modeled geothermal system considered: discharge of energy to the atmosphere, discharge of energy from numerous springs, discharge of energy in groundwater away from the area and discharge of energy via conductive heat transfer to deeper zones (Figure 5.2). Of the total 24 MW of energy produced, energy lost from the springs and thawed ground is estimated at 2 MW and 6 MW respectively. The amount of energy lost due to the ground water outflow is 15 MW.

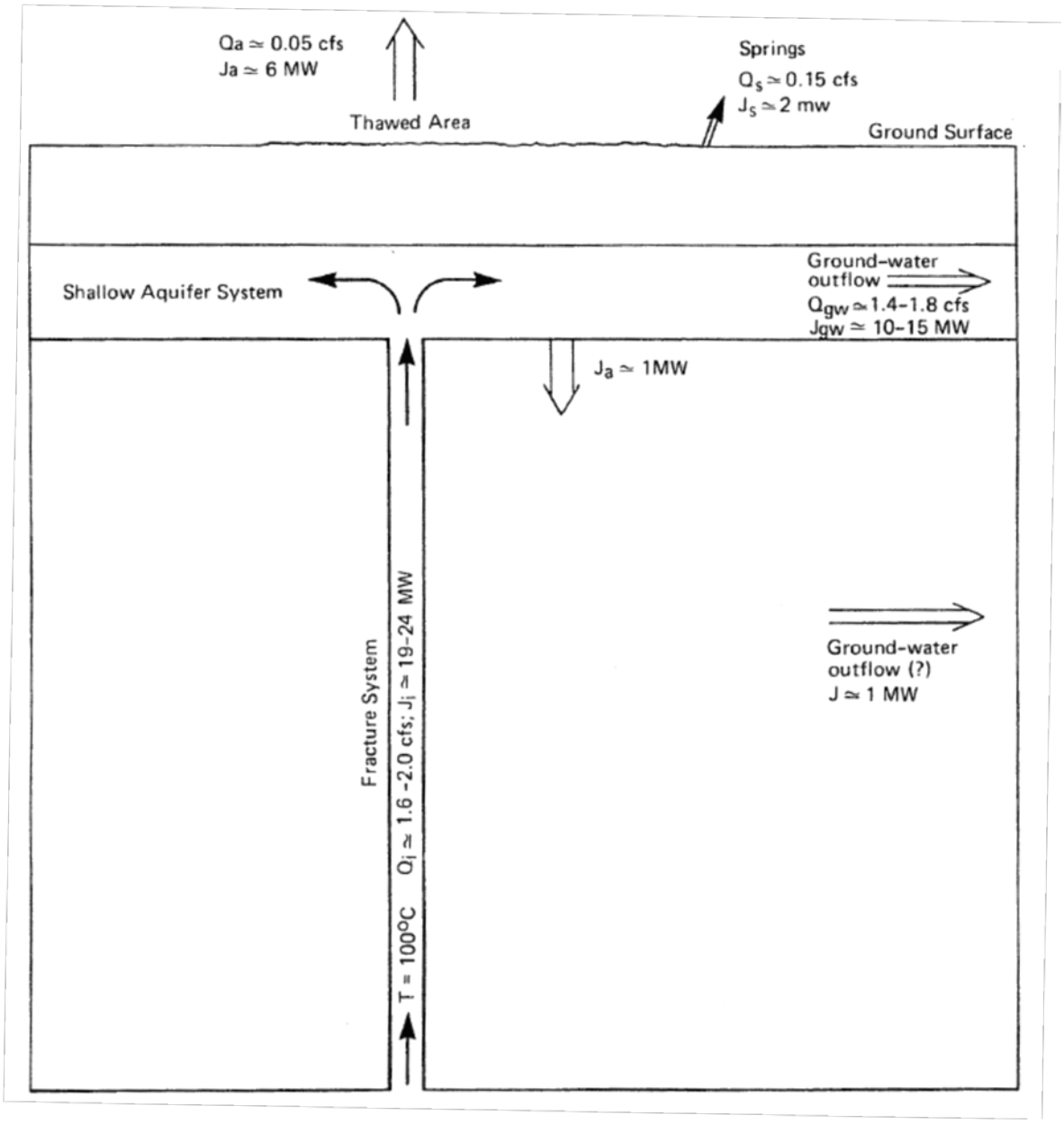


Figure 5.2: A schematic heat and water balance for the modeled part of geothermal system (Woodward-Clyde Report, 1983).

This estimate matches closely the thermal flux estimated from the present modeling efforts, possibly due to the fact that both studies similarly accounted for heat loss from thawed ground, springs, groundwater movement and from river outflow. The close match of the two estimates provides added confidence in the results of the current modeling effort. The 4.7-6.7 MW estimate from Haselwimmer et al. (2013) are higher than the 2 MW thermal energy estimated for the hot springs in the Woodward-Clyde Report (1983). This is because the former estimates heat loss from all sources of thermal waters, including hot springs, thermal pools, and hot water in seeps and streams, whereas the latter represents heat flux associated with a sub-set of the hot springs.

5.2 Reservoir Stimulation Models

The three reservoir stimulation models developed here utilize the second reservoir simulation model with the 120 °C heat source and the same boundary conditions and initial conditions. However, the top layers for the stimulation models have been set up as open to flow conditions where the top layer accepts fluids. This open flow boundary condition allows fluid to flow to the surface and also ensures that the pressure changes in the springs, which relate to the individual production scenarios, are captured. The effect of production on the reservoir has been studied by observing the pressure at the springs for the three production scenarios. Although the second reservoir simulation model was utilized to generate the three production scenarios, the end results of the simulation models have not been considered as initial conditions for the stimulation models.

The initial plume in these stimulation scenarios would have provided a better estimate of temperature changes in the production well. The stable conditions were attained after running the simulation models for a period of 150 years. The production well in all the three stimulation scenarios has been located in the region of up-welling of hotter fluids near well PS 12-2. In the stimulation models, all production wells have been completed between 270 -295 m. This means that the wells do not communicate with or contact the bedrock and the fracture network within the bedrock.

The first stimulation model incorporates two production wells, where one well is located in the region of up-welling of hotter fluids in the vicinity of wells PS 1, PS 12-2 and PS 12-3. The other well is located in the southern part of the domain in the vicinity of well PS 5. The well in the vicinity of PS 5 aims to remove cold water from the domain while the main production well produces hotter fluids. Results of this model indicate 48 MW of thermal energy and production of 85 °C water. The effects of production using two wells are reflected by the spring pressure which has a lowered head of 3 m which suggests that the springs will stop flowing. The thermal energy lost between 295-300 m is calculated using Equation 4.3 assuming the values for the following parameters: m = 135 kg sec^{-1}, C_p= 4200 J $Kg^{-1}°C^{-1}$, ΔT = 120 °C – 85 °C = 35 °C. The thermal energy lost is around 20 MW. This estimated value of energy lost might have been recoverable if the well had been completed to a depth of 300 m such that it communicated with the fractured bedrock.

The heat source cell also has a major impact on the results as it was defined as unlimited in size, which allows a constant supply of heat and up-welling fluids throughout the simulation time. This does not represent the real case scenario. However, it is important to remember that the probability of a production well hitting a major fault is debatable in this scenario. The thermal energy produced by this well might have been greater than the estimated value of 48 MW if either the well had been completed to the depth below the basement contact, or if the stimulation models were started with the end results of the simulation model as an initial condition. However, due to the uncertainty in the location of faulting within the system and limitations in the software to incorporate the results of previous simulation runs, these could not be used as new initial conditions, limiting the presentation of other possible production scenarios.

The second stimulation model involves production with only one well located in the vicinity of wells PS 1, PS 12-2 and PS 12-3. Results of this model indicate 46 MW of thermal energy and production of 82 °C water. The effect of production using one well is reflected by the springs pressure which has a lowered head of 1 m. The thermal energy lost between 295-300 m is calculated using Equation 4.3 assuming the values for the following parameters: m = 135 kg sec^{-1}, C_p= 4200 J $Kg^{-1}°C^{-1}$, ΔT = 120 °C – 82 °C = 38 °C. Thermal energy lost is around 22 MW. However, since both models have their completion depths between 270-295 m, a difference of 2 MW thermal energy for a temperature difference of 3 °C was observed.

One reason for the cooler shallow aquifer and lower thermal energy is the absence of production well #2, which had a flow rate of 2000 gpm. Without the flow rate of 2000 gpm, cold water was able to reach production well # 1. The main objective of this second production well was to produce cold fluids from the reservoir. Production well #1 is fed with hotter fluids from the bedrock via a conduit with a heat source at 120 °C. There is a significant degree of mixing of the cross-flowing cold water and the up-welling hotter fluids in the vicinity of the completion interval of production well #1. The higher degree of mixing may be due to the absence of production well # 2, which removed the vast majority of the cooler water entering the domain.

The third reservoir stimulation model was developed to incorporate an injector-producer scenario. This incorporates the cyclic process of injection and production into the domain. This scenario incorporated the re-injection of 80 °C water back into the domain after production. The assumption of re-injecting 80 °C water back into the system is supported by the idea that 95 °C water can be harvested. However, this assumption was sustainable in this model, therefore, this model over-estimates the amount of heat produced.

Low temperature geothermal systems can utilize binary cycle power plants to generate electricity (Bertani, 2011). In these systems the low temperature geothermal fluids are used to warm up a working fluid which has a low boiling point, which can then drive a turbine. The water that has heated the working fluid, which has been cooled, is then injected back into the ground to be re-heated by the geothermal system.

The water and the working fluid are kept separated during the whole process, so there are little or no air emissions. Chena Hot Springs uses the binary cycle power plants to generate power and allows re-injection of fluids back into the reservoir at the same rate of production providing higher efficiency (Erkan et al., 2008). This may also be applicable at Pilgrim Hot Springs. The flow rate of 2000 gpm has been selected for all wells in the three scenarios assuming that binary cycle power plants will allow this scenario to re-inject fluids back into the system with the same flow rate due to their greater efficiency (Fridleifsson and Freeston, 1994). Generally, only 30 % of the produced fluids are available for re-injection with geothermal power plants where the fluids are used to directly drive the turbines (Stefansson, 1997). This highlights the benefits of binary cycle electricity generation.

The higher the temperature of fluids produced, the better the chance of re-injecting higher temperature fluids. Recovery of the injected fluids during production depends on a good connection between the production wells and injection wells.

Thermal breakthrough usually refers to the speed of communication between the re-injected fluids and the reservoir fluids. Thermal breakthroughs are usually considered an adverse reaction since usually the re-injected fluids are relatively cooler than the reservoir fluids. However, when the re-injected fluids are warmer than the reservoir fluids at certain depth intervals, then the thermal breakthrough becomes a positive thermal breakthrough (Stefansson, 1997).

In the producer-injector model stimulation scenario, the process of re-injecting 80 °C fluids back into the southern part of the domain allows a positive thermal breakthrough where the re-injected fluids are warmer than the reservoir fluids at the area of injector. The reason for the existence of the cooler area near the injector is the cold water influx into the domain from the Kigluaik Mountains in the south. Thus, in this stimulation model, the objective of the injector well is to counteract the effects of cold water recharge and warm the deeper sediment zone. The results of this model indicate 50 MW of thermal energy and the production of 88 °C water. This scenario seems to indicate the highest thermal energy extracted and the highest temperature of fluid produced. However, it is important to remember that this scenario is only feasible when the re-injected fluid temperature is around 80 °C.

A more realistic scenario will consist of reinjection of fluid with a temperature lowered by 15 °C, which should be around 70 °C. At this temperature the liquids are still considerably warmer than the liquids in the cold water aquifer at depths of 100 m in the domain. The effect of production on the reservoir pressure has been analyzed by comparing the pressure at the springs for the three stimulation models.

The third stimulation model was able to sustain the spring pressure at the end of simulation. One reason for sustaining the spring pressure was the cyclic process of injection and production at a rate of 2000 gpm. The two other stimulation models indicated decreases in the pressure at the springs at similar production rate. The third stimulation model indicates the differential spring pressures to be 0.5 m positive head, which is interpreted as a modeling artifact.

The additional pressure head comes from stimulating the upflow in the geothermal liquid allowing more liquids to enter the domain and be forced into the ground in the injector well. Pressures at 270 m and 295 m to inject fluids into the domain are 3×10^6 Pascals and 2.7×10^6 Pascals, respectively. This means that the pressure differential in springs is almost negligible and this is inferred as maintaining the reservoir pressure. When fluids with temperatures lower than 80 °C are allowed to be re-injected in the third stimulation model, the thermal energy estimates are expected to be higher than 46 MW and below 50 MW and the temperature of produced fluid is greater than 82 °C and lower than 88 °C. The main advantages of this scenario are that the produced fluids are better utilized to sustain the reservoir pressure and reduce the cost of disposing of the produced fluids.

5.2.1 Comparisons to Analogs of Pilgrim Hot Springs

There are many analogs to Pilgrim Hot Springs, Alaska that are classified as low-temperature spring-dominated geothermal systems. These analogs may be considered as low-temperature geothermal systems which have shallow thermal aquifers and have been developed using binary cycle systems. A comparison to analogs is useful to assess the relationship between surface heat flux and production capacity.

The Wabuska geothermal system in Nevada consists of 103 °C waters at 130 m (Garside et al., 2002). The energy extracted from this geothermal system is estimated to be around 2 $MW_{Electric}$. Similarly, at Amedee geothermal system in California, 103 °C waters are found at 240 m (Juncal and Bohm, 1987). The energy from this system is estimated to be 1.6 $MW_{Electric}$. The energy from the Wineagle geothermal system in California is estimated to be 7 $MW_{Thermal}$ (Juncal and Bohm, 1987). The first low temperature geothermal system developed in Alaska is at Chena Hot Springs (Erkan et al., 2008). The estimated energy produced is around 0.5 $MW_{Electric}$ and consists of 80 °C water. These geothermal systems provide a range of values of 5 $MW_{Thermal}$ to 20 $MW_{Thermal}$.

The energy estimated from the two simulation models indicates 26 $MW_{Thermal}$ to 28 $MW_{Thermal}$ which, when compared to the analogs, suggests that current estimates are optimistic due to relatively higher values. However, the values are of the same order and magnitude and are close to the analogs. Our energy estimate for Pilgrim Hot Springs is 2.5 $MW_{Electric}$ which suggests that it is 5 times greater than the Chena Hot Springs low temperature geothermal system.

5.3 Limitations

5.3.1 Reservoir Simulation Models

The modeling carried out in this work is inherently limited by the availability of subsurface geological and geophysical data concerning the Pilgrim Hot Springs geothermal system. Although varied, the current data is hampered by the relatively limited exploration of this area. The availability of further information pertaining to the subsurface geological and hydrological conditions will undoubtedly improve the ability to robustly model the hydrothermal system through better parameterization of model parameters and boundary conditions. Given the lack of data concerning Pilgrim Hot Springs, a number of assumptions had to be made in building the simulation models during this work.

For example, the pressure from the wells at Pilgrim Hot Springs had to be extrapolated to estimate the pressure gradient, and subsequently, the pressures for cold water influx from the south toward the north of the domain. The exact location of the heat source and respective plumbing within the system or in the bedrock had to be determined from the available data that has limited coverage. The fracture properties and other thermal properties for modeling were considered by taking values from published literature and the geologic model developed by Miller et al (2013). Also, incorporation of the lithology and stratigraphy into the model required extrapolation into areas where data was unavailable.

Another major limitation of the simulation models was the characteristics of the heat source cell that were set as an unlimited source of heat and hot water influx. This does not represent a real world scenario although it helped to maintain the required pressure and temperature conditions in the model. This unrealistic heat source likely resulted in higher estimates of thermal energy and heat flux near the surface. However, incorporating a realistic heat source in these models would have resulted in lower estimates of heat flux and thermal energy. Similarly, the stimulation scenarios would have resulted in lower values of thermal energy from production wells with a more realistic heat source cell.

5.3.2 Reservoir Stimulation Models

The stimulation scenarios have incorporated production from wells at a constant flow rate of 2000 gpm throughout the simulation time period based on the idea that the usage of binary cycle power plants provides higher efficiency by allowing maximum re-injection of fluids back into the system. The assumption of re-injecting the 80 °C fluid back into the reservoir after production is valid only if the temperatures of the produced fluids are greater than 95 °C. However, re-injection of fluids lower than 80 °C back into the system will generate thermal energy in the range of 46 MW to 50 MW. Re-injecting higher temperature fluids will allow the generation of higher values of thermal energy.

Another assumption is that the production well is located in the region of up-welling of geothermal fluids from the bedrock such that the well communicates with the up-welling fluid at the completion depth of 270-295 m.

This region of up-welling has been selected based on the interpretations of the MT survey and isotherms. These results are going to be different from the scenarios with production wells which communicate with the bedrock and the fracture. The well communicating with the bedrock and fractures will produce higher values of thermal energy.

Finally, another limitation has been to run these stimulation models with the end results of the simulation model as initial conditions. This estimates higher values of thermal energy due to an already existing stable plume within the domain. This plume will, however, dissipate over time resulting in a temperature distribution as observed in the stimulation models, where the plume is not allowed to form due to continuous production from the reservoir.

5.3.3 Model Temporal and Spatial Resolutions

The reservoir simulation models have been built and simulations have been run for a 150 year time period. The simulated vertical temperature sections from both the reservoir simulation models indicate that there is not much variation in the color within the plume which represents spatially distributed temperatures. For example, Figures 4.1 and 4.2 indicate minor variations in the temperatures within the plume for the simulated temperature sections. Figures 4.5 through 4.7 indicate minor variations in the temperatures within the plume for simulated temperature sections due to current resolution of grids.

Similarly, there is not much variation in the temperatures within the deeper sediment zone which represents cooler fluids. The resolution of the grids and density of the grids varies along the X-axis direction and the Y-axis direction. However, the model has layers in the shallow aquifer and deeper sediment zone with 5m vertical resolution.

Variation of the density of the grids and resolution of grids along both the X-axis and Y-axis results in varying inter-nodal distances between grid cells. Inter-nodal distance may be defined as the distance between the nodes of the two grid cells when the nodes are at the center of the grid cells. The grid size, shape, and density affect the results of the reservoir simulation. The modeling approach utilized in this case consists of finite-difference models. These models replace the continuous model with a set of discrete points arranged in a grid pattern. Every grid is associated with a node point, where the equation is solved to obtain the unknown values. Also every node block is associated with known values such as storativity and transmissivity.

In this case, the models deal with the block-centered grids where the node points fall at the center of the grid. The finite-difference equation is solved by iterative methods. Simulations are run through iterative methods until values at each node have been recomputed until the difference between the initial estimate and recomputed value is determined and is less than the pre-set value. This is known as the convergence criterion. When the inter-nodal distances between the grid cells become larger, the unknown values determined cover larger areas, and a greater averaging is involved in estimation of values. Thus, the results tend to be more deviated and less accurate.

Conversely, when the inter-nodal distances between the grid cells are smaller or the grids are finer, the solution for unknown values is improved, providing a more accurate solution. However, finer grids significantly increase the simulation time and complexity for solving for the unknown values.

The coarseness of the grids also limits the representation of the real stratigraphy. A 5 m grid is still very coarse considering that water flows rapidly in much smaller gravel layers and at rates much greater than 2000 gpm. These minor variations are due to the current resolution of the grids. Higher grid resolutions are expected to capture more details on the spatial variability of temperatures. Extracting information from every grid cell from node points allows us to better visualize the temperature changes within the plume. Smaller inter-nodal distances between grid cells allow capturing of more details with spatial variations.

The stimulation models were run only for a period of 10 years due to attaining the maximum number of time steps allowed by the software. However, the simulation models were able to run the models for a period of 150 years. The main reason for this difference between the maximum simulation time depended on the convergence criteria to attain the required solutions at every node point. The stimulation models required more time-steps to solve for the unknown values at the node points within the grids. This resulted in utilizing the maximum number of time-steps allowed by the software much earlier in the stimulation models compared to the simulation models. The solution was more complex for the stimulation model due to the additional conditions applied within the model due to the production wells and injection well.

Chapter 6: Conclusions and Recommendations

6.1 Conclusions

The first reservoir simulation model estimates the heat flux near the surface to be about 26 $MW_{Thermal}$. The second reservoir simulation model estimates a similar, but slightly higher value of about 28 $MW_{Thermal}$. The history matching of the static temperature logs with the simulated temperature logs for both the models provides confidence on the value of heat flux estimated near the surface. Both these scenarios represented by the reservoir simulation models are feasible based on the current interpretations from the geological and geophysical data. Assuming the efficiency of converting thermal energy into electrical energy to be about 10 %, the electrical energy production potential projected from the current heat flux estimates from simulation models, is about 2.6 $MW_{Electric}$ or 2.8 $MW_{Electric}$.

Based on current estimates of the thermal energy from the stimulation scenarios, the estimated electrical energy production capacity at PHS is about 4.8 $MW_{Electric}$ or 5.0 $MW_{Electric}$. Based on the modeling work using the two simulation models and three stimulation scenarios, the geothermal system at Pilgrim Hot Springs seems like a promising resource which can be developed for future direct use applications and power production for providing an alternative source of energy for Nome and its community. These models help to understand the hydrology of the area and the working mechanism of the geothermal system at Pilgrim Hot Springs, Alaska. These models may also be utilized in the near future to execute various stimulation scenarios.

6.2 Recommendations

A preliminary step in order to develop the Pilgrim Hot Springs geothermal resource is to drill a production well in the vicinity of wells PS 12-2, PS 1 and PS 12-3 which the model determines as the region of up-welling hot fluids. In fact, the region north-west of PS 12-2 seems promising such that a well drilled there would likely communicate with fractures or conduits in the bedrock. The production capacities of this well should be tested with varying flow rates. Draw-down tests during production at a constant flow rate, and build-up tests after shutting the well, will help to estimate the key reservoir parameters such as well-bore storativity, permeability of completed zone, efficiency of well, ideal flow rate, and recovery factor. Tracer tests should be conducted to monitor fluid communication between the various wells spread across Pilgrim Hot Springs. These tests will also help in the estimation of the required reservoir parameters. Based on the information obtained from the tracer tests, the location of the injector well should be decided such that maximum efficiency is affected for re-injecting the waters into the deeper sediment zone. This will counteract the effect of the cold water recharge zone from the south end of the domain.

Complete analysis should be done to consider the various re-injection parameters such as: disposal cost of waste fluid, cost of drilling a re-injection well, reservoir temperature for thermal breakthrough, reservoir pressure to determine production decline, temperature of re-injected fluid, location of re-injector, subsidence, chemistry changes of fluid and recovery of injected fluid.

A better analysis to estimate a range of values of thermal energy can be carried out by running Monte Carlo simulations which will help to predict different ranges of thermal energy estimates based on variations in the reservoir properties. This analysis might make it feasible to relate the logistics and economics of development to thermal energy estimate.

References

Axelsson, G., Gunnlaugsson, E., Jonasson, T., Olafsson, M., 2010. Low-temperature geothermal utilization in Iceland – Decades of experience, Geothermics, 39, 329-338.

Bertani, R., 2011. Geothermal power generation in the world from 2005-2010 update report, Geothermics, 41, 1-29.

Bertrand, E. A., Caldwell, T.G., Bennie, S.L., 2011. Magnetotelluric imaging of the upper crustal convection plumes beneath the Taupo volcanic zone, New Zealand, Geophysical Research Letters, 39, American Geophysical Union.

Blackwell, D. D., 1983. Heat flow in northern Basin and Range province, Geothermal Resource Council, 24, 223-228.

Blackwell, D. D., McKenna, J.R., 2003. Numerical modeling of transient Basin and Range extensional geothermal systems, Geothermics, 33, 457-476.

Blackwell, D. D., McKenna J.R., 2004. Numerical modeling of Basin and Range geothermal systems, Geothermics, 33, 713-741.

Bodvarsson, G., 1969. On the temperature of water flowing through fractures, Journal of Geophysics, 74, 1987-1992.

Bodvarsson, G., 1983. Temperature flow statistics and thermo-mechanics of low-temperature geothermal systems in Iceland, Journal of Volcanology and Geothermal Research, 19, 255-280.

Brooke, B., Preda, M., Lee, R., Cox, M., Olley, J., Pietsch, T., Price, D., 2008. Development, composition and age of indurated sand layers in the late Quaternary coastal deposits of northern Moreton Bay, Queensland, Australian Journal of Earth Sciences, 55, 141-157.

Dilley, L.M., 2007. Preliminary feasibility report, Alaska Energy Authority.

Energy Information Administration, 2011. Website available at http://tuffbiz.wordpress.com/2012/12/31/geothermal-energy-philippines-part1/geothermal-energy-diagram/ Last Accessed on July 7th 2013.

Erkan, K.,Holdmann, G., Benoit, W., Blackwell, D., 2008.Understanding the Chena Hot Springs, Alaska, geothermal system using temperature and pressure data from exploration borehole, Geothermics, 37, 565-585.

Fairbridge, R. W., 1967. Phases of diagenesis and authigenesis, Development in Sedimentology, Elsevier, 8, 19-90.

Fitzpatrick, A., Munday, T., Cahill, K., Berens, V., 2010. Redefining the ground water resource of the Eyre Peninsula, South Australia using AEM data, Symposium on the Application of Geophysics to Engineering and Environmental Problems, 287-293.

Fridleifsson, B. I., 1986. Geothermal resources: present status and future potential in the world energy supply, 13th Congress of the World Energy Conference, Cannes.

Fridleifsson, B. I., Freeston D.H.,1994. Geothermal energy research and development, Geothermics, 23, 175-214.

Fugro, 2012. Magnetotelluric Survey Report, Report to UAF, 2012.

Garside, L.J., Shevenell, L.A., Snow, J.H., Hess, R.H., 2002. Status of Nevada Geothermal Resource Development – Spring 2002, Geothermal Resource Councils Transactions, 26, 527-532.

Haselwimmer, C., Prakash, A., 2012. Investigating geothermally-heated ground at Pilgrim Hot Springs, Alaska using remote sensing observations of the anomalous snow-melt and in-situ shallow temperature measurements, American Geophysical Union Fall Meeting, San Francisco, California.

Haselwimmer, C., Prakash, A., Holdmann, G., 2013. Quantifying the heat flux and outflow rate of hot springs using airborne thermal imagery: Case study from Pilgrim Hot Springs, Alaska, Remote Sensing of Environment, 136, 37-46.

Hersir, G. P., Arnason , K., Vilhjalmsson, A.M., 2013. 3D Inversion of magnetotelluric (MT) resistivity data from Krysuvik high temperature geothermal area in SW Iceland, 38th workshop, Geothermal Reservoir Engineering, Stanford University.

Jacob, C. E., Lohman, S. W., 1952. Non steady flow to a well of constant drawdown in an extensive aquifer, American Geophysical Union Transactions, 33, 559-569.

Juncal, R.W., Bohm, B., 1987. A conceptual model of the Wendel-Amedee geothermal system, Lassen County, CA, Geothermal Resources Council, 11, 601-606.

Liljedahl, A. K., Schulla, J., Hinzman, L. D., 2009. The first application and validation of the hydrologic model WaSiM-ETH at a watershed underlain by permafrost, American Geophysical Union Fall Meeting, San Francisco, California.

Lu, X., Watson, A., Gorin, A.V., Deans, J., 2005. Measurements in a low temperature CO_2 – driven geysering well, viewed in relation to natural geysers, Geothermics, 34, 389-410.

Lugao, P. P., LaTerra, E.F., Kreigshauser, B., Fontes, S.L., 2002. Magnetotelluric studies of the Caldas Novas geothermal reservoir, Brazil, Journal of Applied Geophysics, 49, 33-46.

Lund, J. W., Gawell, K., Boyd, T. L., Jennejohn, D., 2010. The United States of America country update the 2010, Proceedings of the 2010 World Geothermal Congress, Bali, Indonesia, 18.

McPhee, K. D., Glen, M. J., 2012. Airborne geophysical surveys illuminate the geologic and hydrothermal framework of the Pilgrim Springs geothermal area, Alaska, American Geophysical Union Fall Meeting, San Francisco, California.

Miller, J. K., Prakash, A., Daanen, R. P., Haselwimmer, C., Whalen, M., 2013. Geologic model of the geothermal anomaly at Pilgrim Hot Springs, Seward peninsula, Alaska, 38th Workshop on Geothermal Reservoir Engineering, Stanford University, Stanford, California.

Miller, P. T., 1994. Geothermal resources of Alaska, Geological Society of America, The Geology of North America, G-1.

Muffler, L. J. P., 1976. Tectonic and hydrologic control of the nature and distribution of the geothermal resources, 2nd UN Geothermal Symposium Proceedings, Lawrence Berkeley Lab, University of California, 499-507.

Palacky, G. J., 1988. Resistivity characteristics of geologic targets in Nabighian, Electromagnetic Methods in Applied Geophysics Theory, Society of Exploration Geophysics Investigation in Geophysics, 3, 53-129.

Pruess, K., 1988. TOUGH User's Guide, Lawrence Berkeley Laboratory, Berkeley, CA, 78.

Stefansson, V., 1997. Geothermal Reinjection experience, Geothermics, 26, 1, 99-139.

Steinberg, G. S., Merzhanov, A. G., Steinberg, A. S., 1981. Geyser Process: its theory, modeling, and field experiment, Modern Geology, 8, 67-70.

Strachotta, C., 2004. Water management concepts for the proposed pacific harbor golf course, Proceedings of the Coastal Zone Asia Pacific Conference, Brisbane, 210-218.

Thompson, C. H., Bridges, E.M., Jenkins, D.A.,1996. Pans in humus podzols in coastal southern Queensland, Australian Journal of Soil Research, 34, 161-182.

Turner, D. L., Forbes, R.B., 1980. A geological and geophysical study of the geothermal energy potential of Pilgrim Hot Springs, Alaska: Alaska Geophysical Institute, Report UAF-R-271.

Turner, D. L., Swanson, S., 1981. Continental rifting- A new tectonic model for the central Seward Peninsula, in geothermal reconnaissance survey of the central Seward Peninsula, Alaska, University of Alaska Fairbanks, Geophysical Institute Report UAG R-284.

Van Everdingen, R.O., 1998. Multi-language glossary of permafrost and related ground ice terms, International Permafrost Association, Circumpolar Active-Layer Permafrost System (CAPS), Boulder, CO, NSIDC, University of Colorado Boulder, 48, CD-ROM. Available from National Show and Ice Data Center.

Vozoff, K., 1991. The magnetotelluric method in Nabighian, Electromagnetic Methods in Applied Geophysics, Society of Exploration Geophysicists, Tulsa, OK, 641-707.

Ward, W. T., Little, I.P., Thompson, C.H., 1979. Stratigraphy of two sandrocks at Rainbow Beach, Queensland, Australia, and note on humate composition, Palaeogeography, 26, 305-316.

Williams, F. C., 2005. Evaluating heat flow as a tool for assessing geothermal resources, 13th workshop, Geothermal Reservoir Engineering, Stanford University.

Woodward-Clyde Report, 1983. Results of drilling, testing and resource confirmation: Geothermal energy development at Pilgrim Springs, Alaska, 1-102.

Appendix A

Additional results of the history matching from reservoir simulation model # 1 are summarized below.

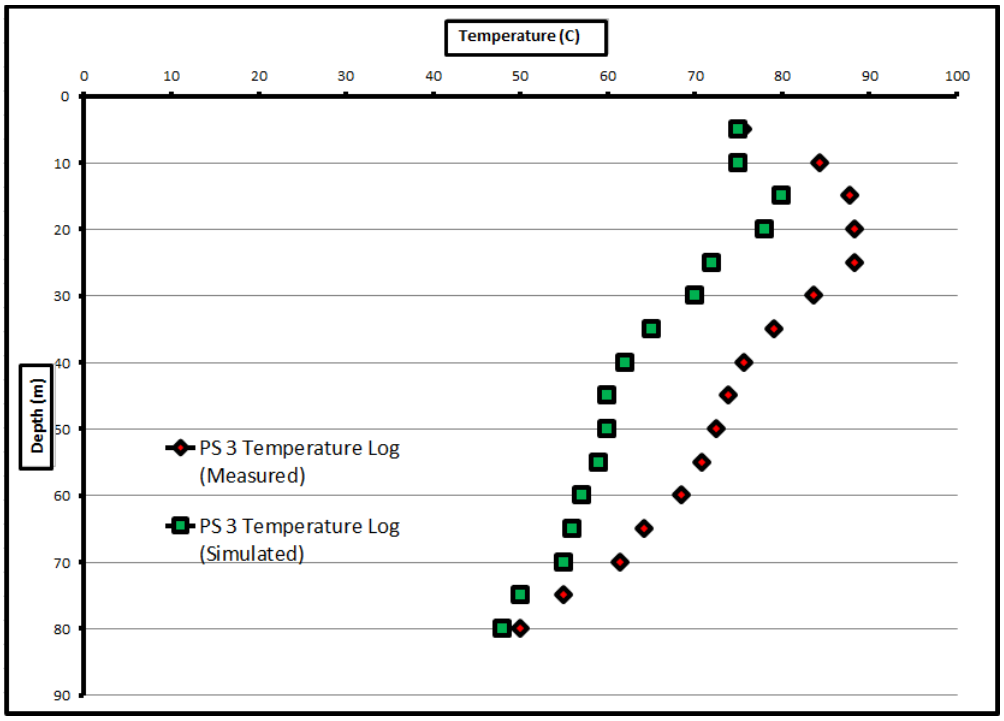


Figure A.1: Comparison of the simulated well temperature to the actual well temperature for well PS 3 for the first reservoir model.

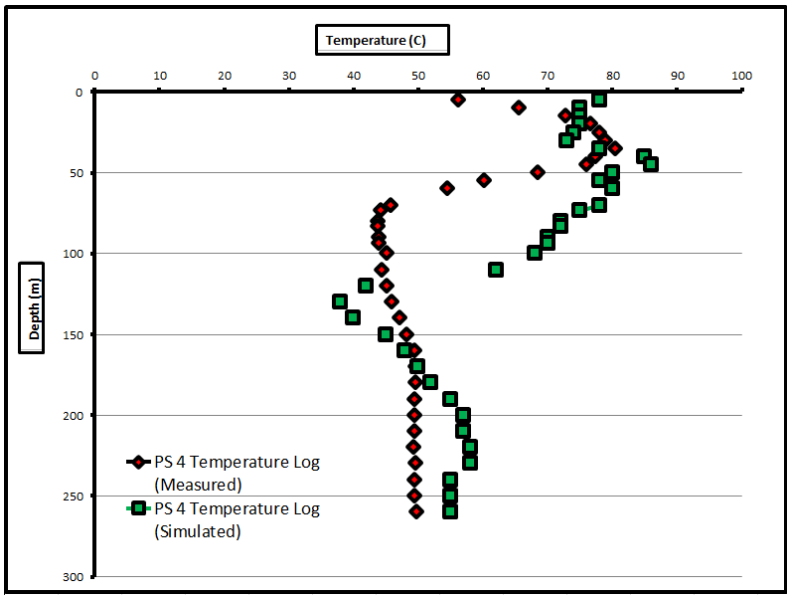


Figure A.2: Comparison of the simulated well temperature to the actual well temperature for well PS 4 for the first reservoir model.

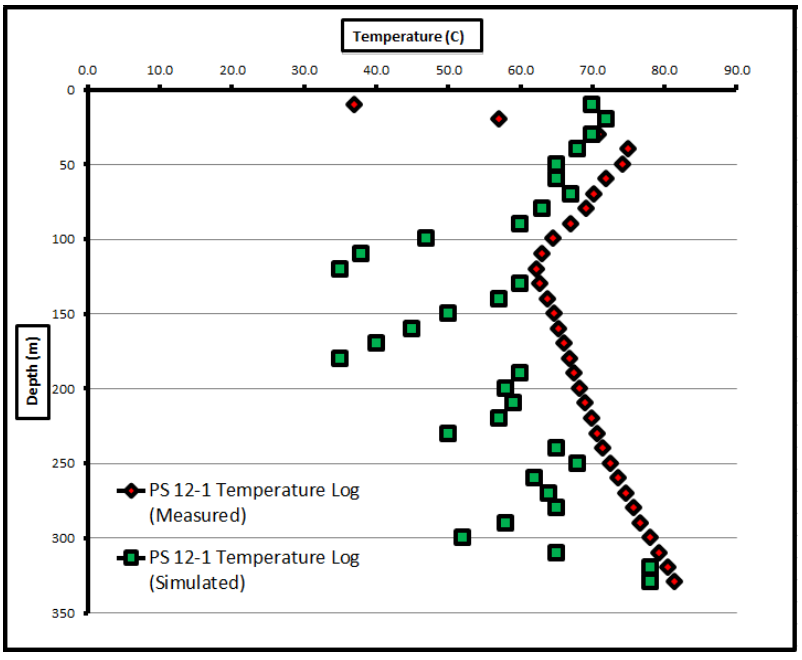


Figure A.3: Comparison of the simulated well temperature to the actual well temperature for well PS 12-1 for the first reservoir model.

Appendix B

Additional results of the history matching from reservoir simulation model # 1 are included here.

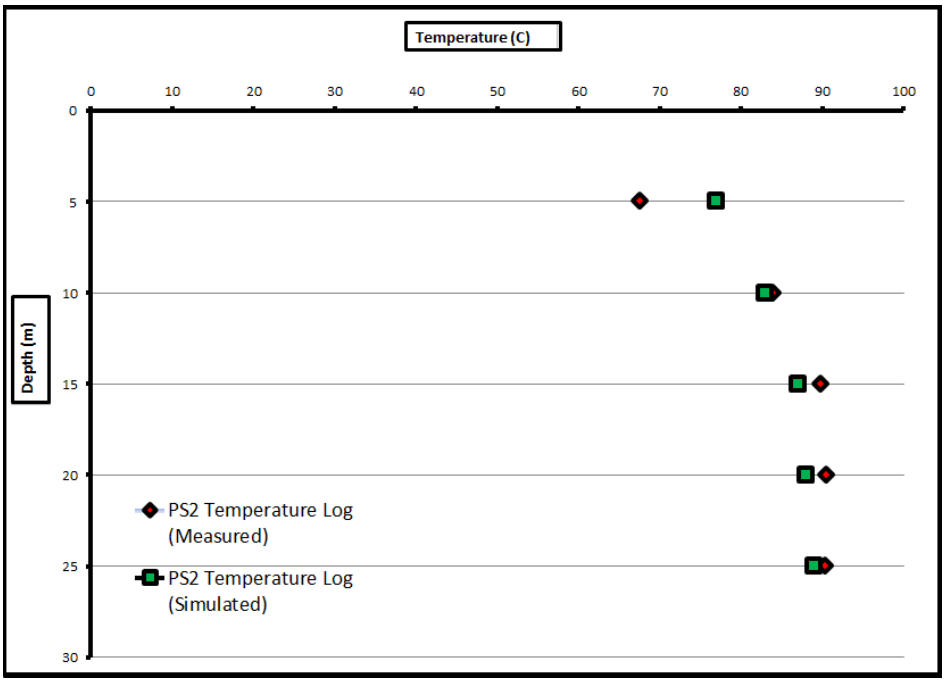


Figure B.1: Comparison of the simulated well temperature to the actual well temperature for well PS 2 for the second reservoir model.

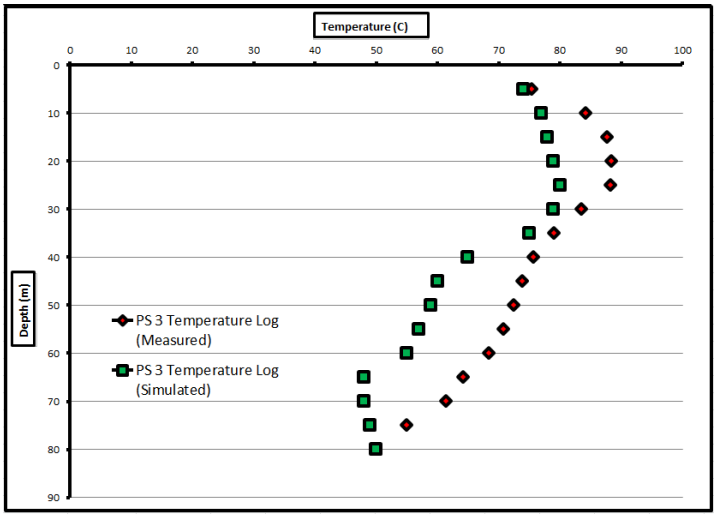


Figure B.2: Comparison of the simulated well temperature to the actual well temperature for well PS 3 for the second reservoir model.

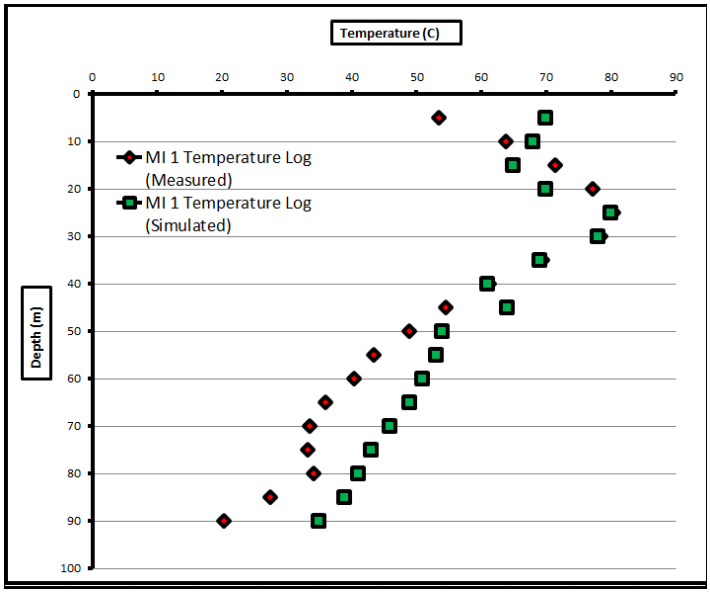


Figure B.3: Comparison of the simulated well temperature to the actual well temperature for well MI 1 for the second reservoir model.

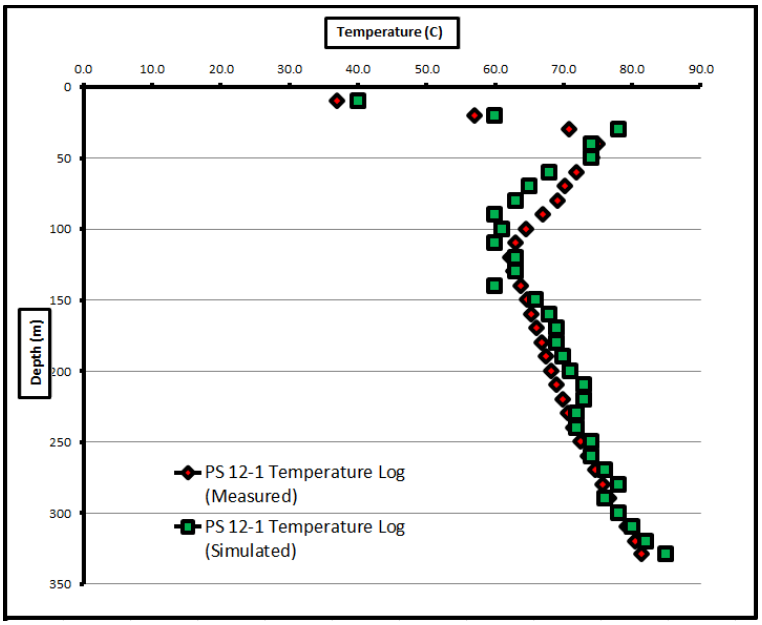


Figure B.4: Comparison of the simulated well temperature to the actual well temperature for well PS 12-1 for the second reservoir model.

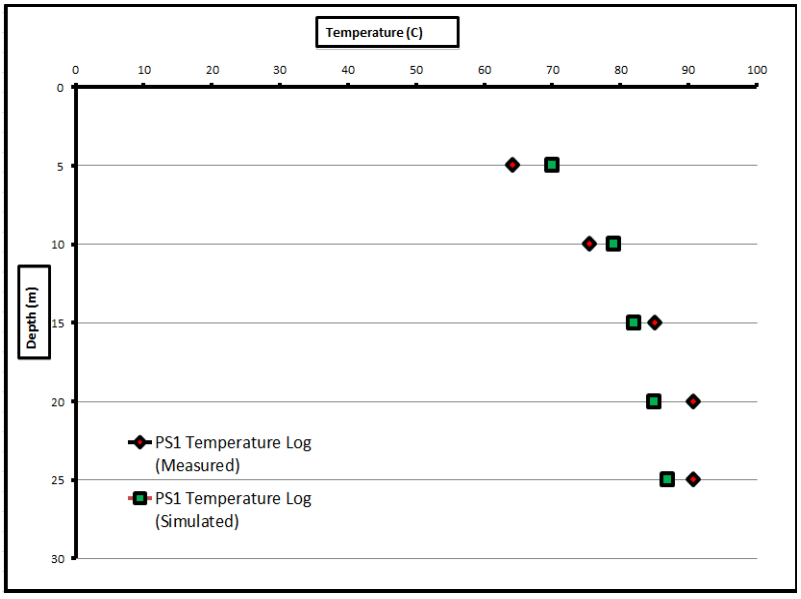


Figure B.5: Comparison of the simulated well temperature to the actual well temperature for well PS 1 for the second reservoir model.

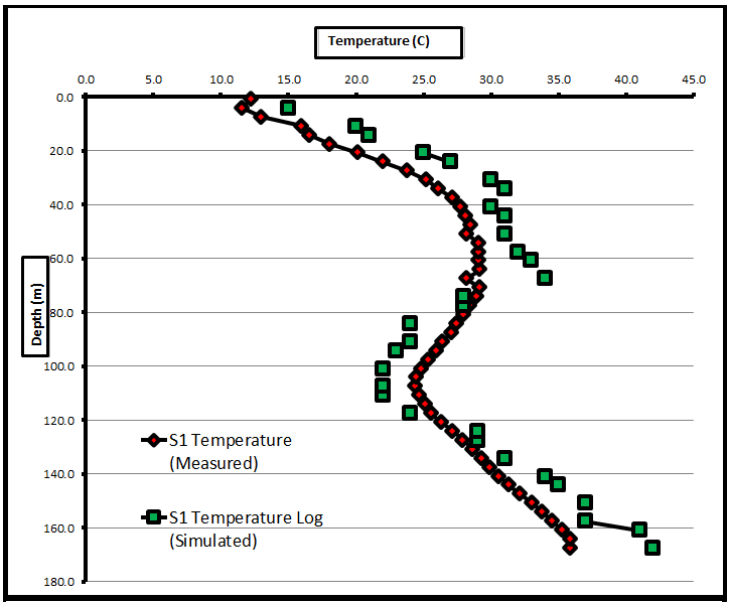


Figure B.6: Comparison of the simulated well temperature to the actual well temperature for well S1 for the second reservoir model.

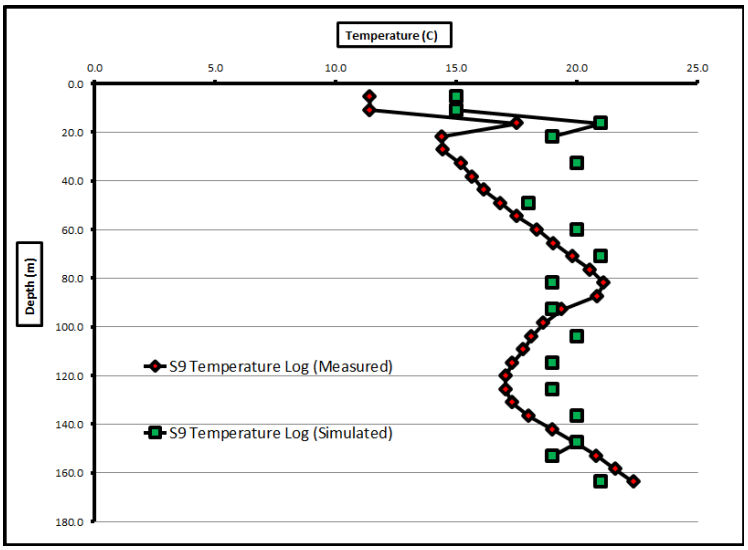


Figure B.7: Comparison of the simulated well temperature to the actual well temperature for well S9 for the second reservoir model.

Appendix O
Tectono-thermal History of Pilgrim Hot Springs, Alaska

Tectono-thermal history of Pilgrim Hot Springs, Alaska

Jeff Benowitz[1], Christian Haselwimmer[1], Jim Metcalf[2], Paul B. O'Sullivan[3], Rebecca Flowers[2], Gwen Holdmann[4] Joshua Miller[1]

1 jbenowitz@alaska.edu Geophysical Institute University of Alaska Fairbanks, Alaska, USA
2 University of Colorado Boulder, Colorado, USA
3 Apatite to Zircon, Idaho, USA
4 Alaska Center for Energy and Power University of Alaska Fairbanks, Alaska, USA

Energy security and energy access in remote communities is a priority for the state of Alaska. Consistent with an emphasis on local renewable resource development to support community-based energy needs, geothermal resources are under renewed consideration as a potential energy source. One of the fundamentals of evaluating a geothermal resource is understanding both the tectonic regime and spatio-temporal evolution of the thermal anomaly. This project served as a pilot study to a) use thermochronology modeling to constrain the tectonic regime responsible for the Pilgrim Hot Springs thermal anomaly of the Seward Peninsula and b) integrate geological time scale thermal modeling with remote sensing imagery, cation geothermometry, and modern temperature drill logs to investigate the thermal anomaly's evolution.

Pilgrim Hot Springs was selected as the subject of this analysis because it is undergoing serious evaluation for development of a 2 MW geothermal power plant to serve the nearby population of Nome. This site is located ~5 km north of the Kigluiak Range Front Fault, a normal fault with geomorphological evidence of Quaternary slip. Rock and sediment samples were collected from regional surface gneiss and granitic bedrock outcrops, mica-schist, felsic and mafic dikes, and indurated muscovite-rich sediment cores that were obtained from coring of the modern expression of the thermal anomaly (i.e. the hot springs site). These samples were analyzed using multiple thermochronology methods with a range of closure temperatures from ~400 ˚C to ~ 70 ˚C.

Preliminary $^{40}Ar/^{39}Ar$ analysis of chlorite on a felsic dike sampled during coring of the modern expression of the thermal anomaly produced an age (~82 Ma) similar to a known regional magmatic event (~85 Ma). Apatite fission track ages from both bedrock and detrital samples (indurated sediments) from the Pilgrim Hot Springs thermal anomaly region were all approximately ~65 Ma. HeFTy thermal modeling of these samples indicate that the samples cooled very quickly to below ~20 ˚C. This ~65 Ma timing coincides with the timing of the final docking of the Wrangellia Terrane and the initiation of major strike-slip fault movement on the Denali Fault System. Further work is planned to better understand the tectonic significance of this ~65 Ma rock cooling event of the Seward Peninsula. Additionally, HeFTy thermal models of apatite fission track data from bedrock and sediment core samples collected in the immediate vicinity of the present day thermal springs demonstrate evidence of subsequent reheating in the last 0.1 Ma.

(U-Th)/He single grain apatite ages from both bedrock and detrital samples (indurated sediments) from the Pilgrim Hot Springs thermal anomaly region ranged from ~62 Ma to ~0.5 Ma. The youngest (U-Th)/He single grain age was produced from a sediment core sample apatite collected at the modern expression of the thermal anomaly. The He dates are therefore recording a younger thermal history than the corresponding fission track dates, but fission track length shortening to a lesser degree also reflects this young thermal event. The data are qualitatively consistent with more recent thermal events with temperatures sufficient to primarily affect the He data. Thermal modeling of multiple data sets from the same sample will allow for exploration of possible thermal

histories consistent with the data and provide insight into the behavior of these systems during short duration reheating events. Overall the combination of a full range of thermochronometers allowed for a more complete reconstruction of the Pilgrim Hot Springs region tectono-thermal history.

The maximum well log temperature measured at Pilgrim Hot springs to date (summer 2013) was 91 ˚C. Na-K-Ca geothermometry predict subsurface temperatures of 145 ˚C[1]. Combined HeFTy thermal modeling indicated the Pilgrim thermal anomaly is young (< 10,000 years) and the hot springs region cored has likely reached a temperature of ~150 ˚C in the recent past (<1,000 years). This is consistent with the range of temperatures estimated using a variety of common geothermometers.

We infer based on the overall thermochronology data set that the thermal anomaly at Pilgrim Hot Springs is related to the youthful extensional setting of the Kigluiak Range Front Fault and is not thermally equilibrated. It is quite likely that the hottest thermal fluids have not been accessed to date. We suggest that stressing the resource by artificially increasing the total discharge from the system through pumping could draw up hotter fluids which could improve the efficiency of a hypothetical power plant.

References

1. Liss, S. A., & Motyka, R. J. Pilgrim Springs KGRA, Seward Peninsula, Alaska: Assessment of fluid geochemistry. Transactions-Geothermal Resources Council 213-213 (`1994).

Appendix P
Wind-Diesel-Geothermal Micrigrid Development: Jeremy VanderMeer Thesis



Wind-Geothermal-Diesel Hybrid Micro-Grid Development: A Technical Assessment for Nome, AK

by

Jeremy B. VanderMeer

Master Thesis

in the Postgraduate Programme
RENEWABLE ENERGY

Energy and Semiconductor Research Laboratory
Department of Physics
Faculty of Mathematics & Science
Carl von Ossietzky University
Oldenburg / F.R. Germany

Day of Examination: 28th March 2014

1. Examiner: Prof. Dr. C. Agert
2. Examiner: Dipl. Phys. M. Golba M.A.

LICENSE

Terms and Conditions for Copying, Distributing, and Modifying

Items other than copying, distributing, and modifying the Content with which this license was distributed (such as using, etc.) are outside the scope of this license.

1. You may copy and distribute exact replicas of the OpenContent (OC) as you receive it, in any medium, provided that you conspicuously and appropriately publish on each copy an appropriate copyright notice and disclaimer of warranty; keep intact all the notices that refer to this License and to the absence of any warranty; and give any other recipients of the OC a copy of this License along with the OC. You may at your option charge a fee for the media and/or handling involved in creating a unique copy of the OC for use offline, you may at your option offer instructional support for the OC in exchange for a fee, or you may at your option offer warranty in exchange for a fee. You may not charge a fee for the OC itself. You may not charge a fee for the sole service of providing access to and/or use of the OC via a network (e.g. the Internet), whether it be via the world wide web, FTP, or any other method.

2. You may modify your copy or copies of the OpenContent or any portion of it, thus forming works based on the Content, and distribute such modifications or work under the terms of Section 1 above, provided that you also meet all of these conditions:

a) You must cause the modified content to carry prominent notices stating that you changed it, the exact nature and content of the changes, and the date of any change.

b) You must cause any work that you distribute or publish, that in whole or in part contains or is derived from the OC or any part thereof, to be licensed as a whole at no charge to all third parties under the terms of this License, unless otherwise permitted under applicable Fair Use law.

These requirements apply to the modified work as a whole. If identifiable sections of that work are not derived from the OC, and can be reasonably considered independent and separate works in themselves, then this License, and its terms, do not apply to those sections when you distribute them as separate works. But when you distribute the same sections as part of a whole which is a work based on the OC, the distribution of the whole must be on the terms of this License, whose permissions for other licensees extend to the entire whole, and thus to each and every part regardless of who wrote it. Exceptions are made to this requirement to release modified works free of charge under this license only in compliance with Fair Use law where applicable.

3. You are not required to accept this License, since you have not signed it. However, nothing else grants you permission to copy, distribute or modify the OC. These actions are prohibited by law if you do not accept this License. Therefore, by distributing or translating the OC, or by deriving works herefrom, you indicate your acceptance of this License to do so, and all its terms and conditions for copying, distributing or translating the OC.

NO WARRANTY

4. BECAUSE THE OPENCONTENT (OC) IS LICENSED FREE OF CHARGE, THERE IS NO WARRANTY FOR THE OC, TO THE EXTENT PERMITTED BY APPLICABLE LAW. EXCEPT WHEN OTHERWISE STATED IN WRITING THE COPYRIGHT HOLDERS AND/OR OTHER PARTIES PROVIDE THE OC ”AS IS” WITHOUT WARRANTY OF ANY KIND, EITHER EXPRESSED OR IMPLIED, INCLUDING, BUT NOT LIMITED TO, THE IMPLIED WARRANTIES OF MERCHANTABILITY AND FITNESS FOR A PARTICULAR PURPOSE. THE ENTIRE RISK OF USE OF THE OC IS WITH YOU. SHOULD THE OC PROVE FAULTY, INACCURATE, OR OTHERWISE UNACCEPTABLE YOU ASSUME THE COST OF ALL NECESSARY REPAIR OR CORRECTION.

5. IN NO EVENT UNLESS REQUIRED BY APPLICABLE LAW OR AGREED TO IN WRITING WILL ANY COPYRIGHT HOLDER, OR ANY OTHER PARTY WHO MAY MIRROR AND/OR REDISTRIBUTE THE OC AS PERMITTED ABOVE, BE LIABLE TO YOU FOR DAMAGES, INCLUDING ANY GENERAL, SPECIAL, INCIDENTAL OR CONSEQUENTIAL DAMAGES ARISING OUT OF THE USE OR INABILITY TO USE THE OC, EVEN IF SUCH HOLDER OR OTHER PARTY HAS BEEN ADVISED OF THE POSSIBILITY OF SUCH DAMAGES.

Abstract

The City of Nome, Alaska, is powered by a remote wind-diesel micro-grid. The average electrical load is 4 MW, the base load is 2.5 MW and the wind power capacity is 2.7 MW. Recent geological exploration has determined there to be 2 MW of electrical potential from a nearby geothermal resource. Incorporating 2 MW of geothermal power into the grid would not be trivial, as this would push the power generation from renewable sources well above the base electrical load. The proposed geothermal power source would not be able to load follow or supply spinning reserve capacity (SRC) to the grid, requiring the diesel generators or possible energy storage systems (ESS) to supply the total required SRC. When the diesel generators are required to supply the SRC, this limits the amount of renewable energy that can be incorporated into the grid.

This study presents the results of time dependent energy balance simulations performed in the MATLAB software environment from MathWorks Inc.. A range of geothermal capacities, different additions to the current diesel fleet, different ESS and different diesel and ESS schedules were simulated. The results show a sharp increase in diverted geothermal energy after geothermal capacities ranging from 2.5–3 MW. Below this geothermal capacity, the diversion of wind energy increased quadratically, while the displaced diesel generator output increased linearly, at around ten times the rate of the diverted wind energy.

Adding diesel generators to the fleet to create a more even step size between the capacities of the diesel generating options was found to reduce the diesel generator output. Using a diesel schedule which attempts to minimize the diesel consumption instead of minimizing the diesel generator output was found to significantly reduce diesel consumption as long as there was a difference in the efficiencies of the available diesel generators.

Adding ESS to the grid was able to displace a significant amount of diesel generator output by supplying SRC to the grid. The ESS was most effective when its ability to supply SRC was taken into account in the selection process for possible diesel generating options during the diesel schedule. The generic ESS used in the simulation were shown to be a good representation of lead acid ESS, and likely other ESS technologies, with some scaling. However, for accurate results, it is recommended to model the specific ESS technology in the simulation.

Version of 22nd July 2014

I would like to thank the Alaska Center for Energy and Power (ACEP), based at the University of Alaska, Fairbanks, for allowing me to work on this project in conjunction with my thesis. I would also like to thank the funding and working partners who have made this research possible: the Alaska Experimental Program to Stimulate Competitive Research (EPSCoR), the U.S. Department of Energy (DOE), the Alaska Energy Authority (AEA), Unaatuq LLC, The City of Nome/NJUS, the Bering Straits Native Corporation, the White Mountain Native Corporation, the Sitnasuak Native Corporation, the Nome Chamber of Commerce, the Norton Sound Economic Development Corporation and the Artic Region Supercomputing Center.

Many people were instrumental in accomplishing this project, predominantly Dr. Marc Mueller-Stoffels, the lead researcher in this project who provided the topic of research and invaluable guidance and support. I would like to thank Prof. Dr. Carsten Agert and Dipl. Phys. Michael Golba M.A. who took time out of their busy schedules to supervise my work. Finally, I would like to thank the rest of the ACEP team for being great to work with and for inviting me to come back.

"Time is a non-renewable resource. Some people in our program try hard to find out about this basic fact…." – Prof. Dr. Konrad Blum

Declaration

I state and declare that this thesis was prepared by me and that no means or sources have been used, except those, which I cited and listed in the References section.The thesis is in compliance with the rules of good practice in scientific research of Carl von Ossietzky Universität Oldenburg[1].

Fairbanks, 17^{th} of March 2014 _____

[1] http://www.gremien.uni-oldenburg.de/download/good_scientific_practice_neu_10.05.2011pdf.pdf

Contents

1 INTRODUCTION **1**

1.1 Introduction to Nome and Pilgrim Hot Springs, Alaska 1

1.2 Problem Formulation 2

1.3 Research Scope 2

1.4 Existing Research on Wind Integration 3

1.4.1 Grid restrictions on wind power 3

1.4.2 Unit commitment 3

1.4.2.1 Conventional grid 3

1.4.2.2 Islanded wind-diesel micro-grids 4

1.4.3 Wind power forecasting 6

1.4.4 Sizing of diesel generators 6

1.4.5 Energy storage 6

1.4.5.1 Energy storage in Alaska 7

1.4.5.2 Energy storage research 7

1.4.6 Controllable loads 8

2 METHODS **9**

2.1 Load 10

2.2 Wind Power 10

2.2.1 Resource 10

2.2.1.1 Deriving an output for Farm A 13

2.2.1.2 Deriving an output for Farm B 15

2.2.1.3 Sensitivity analysis 17

2.2.1.4 Summary 19

2.2.2 Control 20

2.3 Geothermal 23

2.3.1 Resource 23

2.3.2 Control 24
2.4 Grid 24
2.5 Diesel generators 25
2.5.1 Resource 25
2.5.2 Control 26
2.5.3 Schedule 27
2.5.3.1 Initiating the diesel schedule 27
2.5.3.2 Schedule 1 28
2.5.3.3 Schedule 2 28
2.6 Energy Storage System 29
2.6.1 Resource 29
2.6.2 Schedule 30
2.6.2.1 ESS schedule 31
2.6.2.2 ESS-Diesel Schedule 1 32
2.6.2.3 ESS-Diesel Schedule 2 32
2.6.2.4 ESS-diesel schedule 3 33
2.7 Simulation flow 33

3 RESULTS 35

3.1 Diesel Schedule 1, No Energy Storage System 35
3.1.1 Diverted renewable energy and displaced diesel output 35
3.1.2 Diesel operation 39
3.1.3 2 MW geothermal scenario 43
3.1.4 Summary 43
3.2 Diesel Schedule 2, No Energy Storage System 46
3.3 Generic Energy Storage 52
3.3.1 Results for ESS-diesel schedule ESD1 53
3.3.1.1 Displaced diesel generator output 53
3.3.1.2 Diesel operation 57
3.3.1.3 Energy storage system operation 60
3.3.1.4 Summary 61
3.3.2 Results for ESS-diesel schedule EDS2 62
3.3.2.1 Displaced diesel generator output 62
3.3.2.2 Diesel operation 63
3.3.2.3 Energy storage system operation 64

3.3.2.4 Summary 65
3.3.3 Results for ESS-diesel schedule EDS3 68
3.3.4 Overview for 2 MW of geothermal capacity 69
3.4 Lead Acid Energy Storage, ESS-Diesel Schedule 1 71

4 SUMMARY **73**

A ESS discharge sequences **77**

B ESS charge sequences **79**

C Entegrity Wind Turbine Specs **81**

D EWT Wind Turbine Specs **82**

E Surrette 2-YS-31PS Specs **84**

F Simulation Results for EDS1 **86**

G Simulation Results for EDS2 **90**

H Simulation Results for EDS3 **94**
H.1 Displaced Diesel Generator Output 94
H.2 Diesel Operation 99
H.3 Energy Storage System Operation 101

I Lead acid ESS simulation results **103**
REFERENCES 77

List of Figures

2.1 Control Structure 10
2.2 Simulation Structure 10
2.3 Load CDF 11
2.4 Wind farm layout 13
2.5 Power demand for one week on Farm A's feeder. 14
2.6 Binning actual Farm A output vs initial Farm A estimate. 15
2.7 Farm A scaling factor 16
2.8 Comparison between actual and calculated Farm B time series 17
2.9 Binning theoretical Farm B output vs initial Farm A estimate. 18
2.10 Comparison between theoretical and calculated Farm A time series. . . . 19
2.11 Scaling factor for Farm B. 20
2.12 Compare time series of calculated and theoretical Farm B output. 21
2.13 Wind diversion sensitivity analysis 21
2.14 Diesel switching sensitivity analysis 22
2.15 Two years of geothermal output for a 2MW installation beginning in May. 24
2.16 Per unit diesel efficiency curve 26
2.17 Scenarios where ESS must provide SRC and discharge 32

3.1 Diverted wind and geothermal energy 36
3.2 Operating ranges of **Case 1** 37
3.3 Operating ranges of **Case 4** 38
3.4 Comparison of diverted wind and displaced diesel 39
3.5 Displaced diesel and diverted RE equal geothermal energy 40
3.6 Average diesel loading 41
3.7 Diesel switching 42
3.8 Diesel run times 44
3.9 Average capacity of online diesel generating options 45
3.10 Average diesel efficiency compare 47

3.11 Average diesel loading compare 48
3.12 Wind diversion compare 48
3.13 Diesel consumption compare 49
3.14 Diesel switching compare 49
3.15 Average diesel capacity compare 50
3.16 Diesel run time compare 51
3.17 ESS comparison 52
3.18 Displaced diesel output for 2 MW goethermal 54
3.19 Displaced diesel output for optimal ESS 55
3.20 Yearly increas in displaced diesel over ESS capacity 55
3.21 Diesel switching with no ESS 56
3.22 ESS scenarios that do and do not result in a reduction of diesel switching . 58
3.23 Decrease in diesel switching per year 58
3.24 Increase in average diesel loading 59
3.25 ESS cycles per year 60
3.26 ESS discharge per year 61
3.27 Displaced diesel output with optimal ESS using EDS2 62
3.28 Displaced diesel output per optimal ESS using EDS2 63
3.29 Decrease in diesel switching for optimal ESS using EDS2 64
3.30 Increase in diesel loading for optimal ESS using EDS2 65
3.31 ESS yearly discharge with EDS2 66
3.32 ESS cycles with EDS2 67
3.33 ESS SRC coverage with EDS2 67

A.1 Diesel output time series 77
A.2 ESS discharge time series 78
A.3 Diesel MOL time series 78

B.1 RE Diversion time series 79
B.2 ESS charging time series 80

C.1 Entegrity wind turbine specifications 81

D.1 EWT wind turbine specifications, page 1. 82
D.2 EWT wind turbine specifications, page 2. 83

E.1 Surrette 2-YS-31 specifications, page 1. 84

E.2 Surrette 2-YS-31 specifications, page 2. 85

F.1 Displaced diesel output for 0 MW goethermal 86
F.2 Displaced diesel output for 1 MW goethermal 87
F.3 Displaced diesel output for 1.5 MW goethermal 87
F.4 Displaced diesel output for 2 MW goethermal 88
F.5 Displaced diesel output for 2.5 MW goethermal 88
F.6 Displaced diesel output for 3 MW goethermal 89
F.7 Displaced diesel output for 3.5 MW goethermal 89

G.1 Displaced diesel output for 0 MW goethermal 90
G.2 Displaced diesel output for 1 MW goethermal 91
G.3 Displaced diesel output for 1.5 MW goethermal 91
G.4 Displaced diesel output for 2 MW goethermal 92
G.5 Displaced diesel output for 2.5 MW goethermal 92
G.6 Displaced diesel output for 3 MW goethermal 93
G.7 Displaced diesel output for 3.5 MW goethermal 93

H.1 Displaced diesel output for 0 MW goethermal 94
H.2 Displaced diesel output for 1 MW goethermal 95
H.3 Displaced diesel output for 1.5 MW goethermal 95
H.4 Displaced diesel output for 2 MW goethermal 96
H.5 Displaced diesel output for 2.5 MW goethermal 96
H.6 Displaced diesel output for 3 MW goethermal 97
H.7 Displaced diesel output for 3.5 MW goethermal 97
H.8 Displaced diesel output for optimal ESS 98
H.9 Displaced diesel output per ESS power 98
H.10 Reduction in diesel switching using EDS3 99
H.11 Increase in the average diesel loading using EDS3 100
H.12 ESS cycles with EDS3 101
H.13 ESS SRC coverage with EDS3 102

I.1 Displaced diesel generator output, lead acid ESS 103
I.2 Yearly lead acid ESS discharge for 104
I.3 Decrease in diesel switching for lead acid ESS 104
I.4 Yearly lead ESS cycles 105
I.5 Increase in diesel loading for lead acid ESS 105

List of Tables

2.1 Data sets used to calculate an estimate for wind farm outputs. 12
2.2 Diesel generator operating attributes and parameters. 25
2.3 Diesel scenarios. 26
2.4 Effective capacities of 2YS31P 30

3.1 Simulation results for 2 MW of geothermal 45
3.2 ESS comparison 53
3.3 Comparison of different ESS-diesel schedules 70
3.4 Comparison between generic and lead acid ESS for 2 MW geothermal . . 72

Glossary

C/20: The rate of discharge that will discharge the ESS in 20 h. C/5 refers to the rate of discharge that will discharge the ESS in 5 h.

Case 1: The diesel scenarios with the current diesel fleet: 1.9 MW, 3.7 MW and two 5.2 MW diesel generators. See Table 2.3.

Case 2: The diesel scenarios with 0.4 MW, 1.9 MW, 3.7 MW and two 5.2 MW diesel generators. See Table 2.3.

Case 3: The diesel scenarios with 1 MW, 1.9 MW, 3.7 MW and two 5.2 MW diesel generators. See Table 2.3.

Case 4: The diesel scenarios with 0.4 MW, 1 MW, 1.9 MW, 3.7 MW and two 5.2 MW diesel generators. See Table 2.3.

Data1: A two year set of data from the grid at Nome.

Data2: A six month set of data from the grid at Nome including outputs for the wind farms.

Data3: A nine month set of data from a metereological tower near the wind farms at Nome.

Diesel generating option: One possible combination of diesel generators.

Diesel schedule: The process by which diesel generators are turned on and off in a diesel grid. It is a special case of the unit commitment problem.

Diesel switching: Changes in the online combination of diesel generators.

DOD: Depth of Discharge, given as a percentage of the ESS capacity.

EDS1: ESS-diesel schedule 1. It adds ESS charging as an event to initiate the diesel schedule **Schedule 1**.

EDS2: ESS-diesel schedule 2. It incorporates ability of the ESS to supply SRC into the criteria to select possible diesel generating options before performing the diesel schedule to **EDS1**.

EDS3: ESS-diesel schedule 3. It adds ESS discharging to **EDS2** as an event which will initiate the diesel schedule.

Energy Diversion: Excess energy is diverted either by curtailing the ouput of the generating source or by diverting it into a diversion load, such as a hot water tank.

ESS: Energy storage system

ESS cycles: One ESS cycle refers to the ESS going from charging to discharging.

ESS schedule: The schedule which determines when the ESS charges and discharges.

Farm A: A wind farm at Nome with eighteen 50 kW turbines.

Farm B: A wind farm at Nome with two 900 kW turbines.

High penetration: A significant percentage of the power generation within the grid comes from renewable sources.

Islanded micro-grid: A micro-grid that is not connected to a main grid. This could refer to a remote micro-grid, or a section of a main grid that has been temporarily disconnected.

Load following: When a generating source follows the load. A generating source that is able to load follow can change its power output quick enough to match the demand of the load.

MOL: Minimum optimal loading. It is the lowest loading of a diesel generator, or a combination of diesel generators, at which they can optimally run, measured in percentage. The MOL of a combination of diesel generators is the highest MOL of the individual generators.

MOT: Minimum on time. It is the minimum amount of time a diesel generator must be run after being brought online before it can be brought offline.

MWe: MW of electrical output.

PGS: Pilgrim geothermal system, located 37 miles north of Nome.

RE: Renewable energy.

Remote micro-grid: A micro-grid that is permanently not connected to a main grid.

Schedule 1: The diesel schedule which maximizes the import of wind energy and minimizes the diesel generator output.

Schedule 2: The diesel schedule which minimizes fuel consumption.

SOC: State of charge, given as a percentage of the ESS capacity.

SRC: Spinning reserve capacity. It refers to the amount of unused online generating capacity there is at a given moment, measured in MW. It is needed to buffer against increases in the load or a drop in the wind power production.

Unit commitment: The process by which generating units are scheduled to turn on or off. In conventional grids, this is usually done as part of an economic optimization.

Chapter 1

INTRODUCTION

1.1 Introduction to Nome and Pilgrim Hot Springs, Alaska

Nome, population 3760, is the largest settlement on the Seward Peninsula in Alaska. There is no road access to Nome, and it is not connected to the main electrical grid. Like most remote micro-grids in Alaska, Nome's grid relies mainly on diesel generation to produce electricity. Transporting diesel is expensive and the cost of diesel has been rising and is volatile (AEA,2013). Before the subsidy, residents pay $0.37/kWh. Security of supply is also an issue. Recently, the HSS Healy ice breaker and a tanker were required to deliver a shipment of fuel after they missed a fall shipment.

The Pilgrim geothermal system (PGS) is located 37 miles north of Nome, Alaska. Drilling first began in 1979 to test the geothermal resource. Following the success of a low temperature (76° C) geothermal project at Chena Hot Springs, Alaska, in 2007, a renewed interest was taken in the PGS. A feasibility assessment was performed, funded by the U.S. Department of Energy and National Energy Technology Laboratory, which concluded that geothermal energy could be economical for that region. In 2008, the Alaska Center for Energy and Power (ACEP) submitted a proposal to the U.S. Department of Energy to resume exploration of the resource. Since the acceptance of the proposal, five more wells have been drilled at depths up to 1294 ft (394 m), 54 Geoprobe temperature probes installed and satellite imagery, forward looking infrared radiometry (FLIR) and high-resolution airborne magnetic and EM surveys assessed to map the geothermal resource (Haselwimmer, Prakash, & Holdmann, 2013). The models resulting from these studies have shown there to be a shallow basin of hot water being fed at 90° C from 1050 ft (320 m) below the surface by a narrow conduit. The final recommendation of the study was to drill into the upflow zone to increase the potential flow rate. Based on conservative estimates, a 2 MWe[1] binary electric power plant could be possible. An agreement was made in 2013 between the landowner, Unaatuq LLC, and Potelco Inc. to develop this resource and to export to Nome should there be a minimum of 2 MWe possible.

[1] MWe refers to electrical output

1.2 Problem Formulation

The potential 2 MWe geothermal resource at Pilgrim hot springs represents an opportunity for the City of Nome to reduce their dependence on diesel for electricity generation. Nome has a mean load of 4 MW and a base load of 2.5 MW. The wind energy capacity was recently upgraded from 0.9 MW to 2.7 MW. Adding geothermal power to the system is not trivial, as this would push the combined capacity of wind and geothermal power production well above the base load.

Diesel generators are the prime movers of the grid, thus they are responsible for maintaining grid power quality by compensating for the variations in the loads and renewable energy sources. In order to accomplish this, and to avoid damaging the diesel generators, they must be operated within certain bounds. One of these bounds is that the diesel generators must maintain the spinning reserve capacity (SRC) in the grid. SRC is refers to the amount of online unused generating capacity. For example, a 5 MW generator running at 4 MW is supplying 1 MW of SRC. This is to handle sudden drops in the wind power or an increase in the load. Due to this, with the current grid setup, the diesel generators cannot be shut off and a combination of diesel generators with sufficient capacity must remain online to supply the SRC, regardless of how much renewable energy is being generated.

Another parameter, the minimum optimal loading (MOL), dictates that there is a minimum loading at which a diesel generator should be run. Thus, not only must there always be diesel generators running online, but they must also be supplying a certain minimum amount of the load. This limits how much renewable energy can be accepted into the grid and surplus generation needs to be diverted. [2]

Geothermal energy would have a steady output with a slight seasonal variation. It would not have load following capabilities. This means that it would not be able to quickly reduce or increase its power output in response to changes in the load demand or wind power generation. Thus, if geothermal energy were added to the grid, it would not be able to contribute to the SRC of the grid, which would still need to be met by the diesel generators.

An economic assessment must be performed by Nome to determine the feasibility of utilizing geothermal energy. The following questions are central:

- How much diesel generator output would be displaced?
- How much more wind energy would be diverted?
- How would the operation of the diesel generators be affected?

1.3 Research Scope

This study seeks to answers to the questions listed in Section 1.2 through the use of time dependent energy balance simulations. Results are given not only for added geothermal

[2] Diversion of energy refers to either curtailing the production of energy (for example reducing the output of wind turbines) or diverting the excess energy to a diversion load (for example a water boiler. Electric boilers are used in Nome and generating heat is of significant economic value, but is not addressed in this study.

energy, but also for changes to the diesel fleet, the addition of energy storage systems (ESS) and changes to the control schedules of the diesel generators and ESS.

The goal of this study is not to perform an economic assessment, but to produce the data that is necessary for one. This study also seeks to gain a more general understanding of how changing the energy mix affects the operation of an islanded micro-grid. In line with this goal, the results of the simulations are analyzed to determine their underlying causes. This study seeks to be useful not only for the specific situation at Nome, AK, but also to the general field of integrating high pentration renewable energy in micro-grids.

1.4 Existing Research on Wind Integration

One of the main factors affecting the value of adding geothermal energy to the grid is how to maintain power quality while minimizing the diversion of wind energy. Already, the suboptimal use of its wind power is one of the main challenges facing Nome. An increase in diverted wind energy would negatively affect how much diesel generator output is displaced. This section gives some examples of current innovations and research being done to integrate high penetration wind energy into grids, with a special focus on diesel micro-grids.

1.4.1 Grid restrictions on wind power

Grid restrictions are becoming increasingly strict on the required ability to control the output power of a wind turbine in order to connect to the main grid. Examples include the ability to ride through a fault, to limit power output to specified amount and to be able to supply reactive power to the grid (IEC, 2005). In this way, a wind turbine can behave more like a conventional power station, allowing a higher penetration of wind energy at a lower risk to the grid.

1.4.2 Unit commitment

Unit commitment (UC) refers to the problem of scheduling which generating units will run when within a power system to meet operating constraints and minimise generating costs (Padhy, 2004) (Fossati, 2012). The formulation of the unit commitment problem has a significant impact on how much wind energy is integrated into the grid. How the unit commitment problem is solved can be very different between a conventional grid and an islanded micro-grid. The following sections summarize the current situation in these two fields.

1.4.2.1 Conventional grid

In a conventional grid, the unit commitment problem is usually quite complex, as there are many factors affecting costs which must be considered as well as power purchase agreements and government regulations which must be followed when finding the lowest cost generating solution. Reducing fuel costs by as little as 0.5% can result in millions of

dollars of savings per year for large utilities (Padhy, 2004). Included in the UC problem are the start-up and shutdown times and costs, minimum run times, minimum off times, ramp rates, fixed operating costs and incremental energy costs (Padhy, 2004).

The challenge is to find a method that will allow the UC problem to be solved in an adequately short amount of time. A typical time frame for the UC problem is every hour (Wright, 2013). There is a large body of literature on different algorithms which are used to solve this problem. Padhy (2004) has created a summary of some of the algorithms currently being implemented or developed and some of the main ones are listed here:

- **Exhaustive enumeration** goes through all possible combinations of generating units to find the optimal one. This is very slow but gives an accurate solution.
- **Priority Listing** pre-arranges combinations according to typical lowest operating cost. Combinations are chosen until the load is met.
- **Dynamic programming** is the earliest optimization-based method applied to UC and is used extensively throughout the world. It is a method of breaking down the problem into sub problems and then combining the solutions.
- **Branch and bound** separates the decision variables into subsets and performs an iterative process to sort the subsets.
- **Lagrangian relaxation** incorporates the operating constraints into the cost function using Lagrangian multipliers to reduce the complexity of the problem. Lagrangian relaxation is used regularly by some utilities and there are many modifications to it in the literature. The performance improves with the number of generating units.
- **Simulated Annealing** decomposes the problem into binary (unit status) and continuous (power output) variables, which are solved separately.
- **Fuzzy systems** use fuzzy logic, which uses gradients instead of binary values, to handle uncertain decision making variables.
- **Artificial Neural networks** simulate a biological neural network and can take advantage of parallel processors and incorporates learning algorithms.
- **Genetic algorithms** simulate 'survival of the fittest', where potential solutions go through successive selection processes.
- **Evolutionary Programming** simulates an evolutionary process, where combinations of solutions evolve through random changes, competition and selection.
- **Hybrid Models** combine different solution techniques, often into different steps of the problem.

1.4.2.2 Islanded wind-diesel micro-grids

Islanded wind-diesel micro-grids are much smaller than conventional grids, and typically have fewer generating units and simpler control schemes. This paper focusses specifically on remote islanded micro grids (or remote micro-grids) which are never connected to a main grid.

In many remote diesel micro-grids in Alaska and around the world, the diesel generators are switched on and off by an operator or a control system to keep them within their operating bounds without solving a UC problem. An experienced operator knows how to switch the diesel generators in response to the load. This is generally referred to as diesel scheduling instead of unit commitment. Recently there have been studies showing that significant savings could be possible by incorporating the UC problem into remote diesel micro-grids, especially when incorporating RE (Brouhard Jr., 2008). First, diesel scheduling at Nome is presented followed by several examples of UC in remote micro-grids from literature.

Nome currently operates with two Wärtzillä 5.2 MW diesel generators, which usually alternate to supply power. A 3.7 MW Caterpillar generator is used during the morning summer hours when the demand is low, and a 1.9 MW Caterpillar generator is used to supply peak loads during winter afternoons. There is also a 0.4 MW diesel generator which is used as a black start unit in case of a black out. The diesel generators are connected to a SCADA system and automated (Devine, 2011).

With the addition of wind energy to the grid, the 5.2 MW diesel generators are often oversized and operated below an optimal loading. In addition, their MOL is set to 50%, which means they must (if possible) supply at least 2.6 MW of the load. This means with a base load of 2.5 MW, and a wind energy capacity of 2.7 MW, wind generation often needs to be diverted. Due to this, the wind energy generation has been contributing less than its full potential. Adding geothermal energy will increase the amount of wind generation that needs to be diverted.

The **Peng-Hu Island power system, Taiwan** was simulated by Chen (2008) in order to develope a UC problem and an algorithm with which to solve it which would maximise the profits from increasing wind penetration. He compares a full dynamic programming (FDP) algorithm, hybrid dynamic programming algorithm without approximate economic dispatch strategy (HDP) and a hybrid dynamic programming algorithm with an approximate economic dispatch strategy(HDP*). Economic dispatch refers to economic optimization of real time power output levels of the generating units. The Peng-Hu power system was simulated with minimum and maximum loads of 20 MW and 64 MW respectively, 12 diesel units totalling 128 MW and up to 8 wind turbines totalling 4.8 MW capacity. The HDP* strategy was shown to find the optimal solution in significantly less time.

Katiraei & Abbey (2007) modelled the island grid of **Ramea Island, Canada,** with 390 kW of wind power and a peak load of 1.2 MW in order to determine the benefit of adding smaller diesel generators to the grid. In the simulation they used a very simple UC problem, where the generator combination with the lowest MOL that met the operating bounds was chosen. This allows the diesel generators to operate at a higher load factor and maximise wind import to the grid. No special algorithm was needed to solve the UC problem, since it was simple and there are few generating units. Thus, all possible combinations could be compared (exhaustive enumeration) and the best chosen quickly with little computing power.

Logenthiran & Srinivasan (2009) simulated a **generic islanded microgrid** while comparing the performance of Lagrangian reduction (LR), genetic (GA), and Lagrangian-genetic (LRGA) hybrid algorithms to schedule thermal, renewable and energy storage units. The algorithms were modelled with a grid with a 1.4 MW PV system, 0.6 MW wind power capacity, a 1 MW and 2.5 MWh battery bank and 10 thermal units totalling 2.3 MW. The average load was 1.8 MW. This paper focussed on the cost savings between the different

algorithms. It was found that with thermal units only, LRGA had significant cost savings, while with the introduction of the renewable and energy storage units, the difference became negligible.

The results from Logenthiran & Srinivasan are interesting when considering Nome's case, since the sizes of the grids are comparable. The simulation compared the cost savings between different algorithms used to solve the unit commitment problem. Nome does not currently perform a unit commitment problem when scheduling its diesels. Thus, the results of this simulation indicate not only the possible savings between different algorithms to solve the unit commitment problem, but also of solving a unit commitment problem in the first place. A key difference between this simulation and Nome is that in the simulation, there are 10 thermal units for an average load of 1.8 MW, while Nome has 4 thermal units for an average load of 4 MW. Thus Nome would benefit less from using an economic dispatch since there are less possible generation options to choose from.

1.4.3 Wind power forecasting

The ability to predict wind power output allows the scheduling of other generating units to compensate for the changes in wind power and reduces the requirement for spinning reserve capacity in the system (SRC). Different companies are now offering detailed wind power forecasts for wind parks based on empirical and mathematical models (Costa et al., 2008). For example, Vestas, a wind turbine manufacturer, offers short term (0–24 hr), day ahead and extended (up to 98 hr) wind power forecasts to its customers. Overspeed GmbH , a wind speed consulting company based in Oldenburg, Germany, offers wind power forecasting to its customers using its proprietary Anemos system (Kariniotakis et al., 2003). Nome currently does not have wind power forecasting ability.

1.4.4 Sizing of diesel generators

The sizing of diesel generators significantly affects the amount of wind energy that can be integrated into a remote diesel micro-grid. Communities in Alaska often have loads that experience large diurnal and seasonal fluctuations. In order to deal with the fluctuations and to accommodate future growth, diesel generators are installed that are much larger than required for the average load (Brouhard Jr., 2008). This reduces the amount of wind energy that can be integrated into the grid due to the MOL and SRC requirements of the diesel generators and reduces the efficiency of the diesel generators. Katiraei & Abbey (2007) simulated the high penetration remote mirco-grid on Ramea island, Canada, and showed that a significant increase in wind energy import into the grid could be achieved by adding a smaller diesel generator to the fleet.

1.4.5 Energy storage

Energy storage can help increase the import of wind energy into a grid by storing it when there is an excess and supplying it when there is a need. How energy storage will affect the grid, and the type of energy storage that should be used, depends on how the energy storage is scheduled.

The charge and discharge cycles can be over a long time scale, 'leveling out the peaks' in the wind energy so to speak, where storage with a large capacity is needed. Examples of this include pumped hydro, electric vehicles or hydrogen storage (Conte, Prosini, & Passerini, 2004).

Energy storage can also help supply power for quick ramp rates in either the load, a variable generation source like wind energy or a grid fault. In this case, the energy storage needs to be capable of large ramp rates and a high power output. An example of this type of energy storage would the flywheel (Cimuca, Saudemont, Robyns, & Radulescu, 2006).

A third use of energy storage is to replace some, or all, of the required SRC in the grid. In a wind-diesel micro-grid, the diesel generators typically supply the required SRC. However, depending on the power, ramp rate and capacity of the energy storage, it can replace a certain amount of the SRC (Kirby et al., 2010).

1.4.5.1 Energy storage in Alaska

This section provides three examples of energy storage implementations in Alaska. It is not meant to be a comprehensive overview.

A 32 kWh nickel-cadmium SAFT system was installed in Wales, Alaska, for short-term storage. The average load at Wales is around 50 kW and there is 130 kW of wind power capacity with a class 7 wind resource. The goal was to implement a high penetration of wind energy that would allow the diesel generators to turn off and allow the wind to provide 50–100% of the load. Some problems were encountered, as the control system was not capable of handling 'diesel-off' mode (Drouilhet, 2001).

A 1.4 MWh, 1 MW lead-acid battery was installed at Metlakatla, Alaksa, in 1997. The average load is 4–5 MW, 25–30% of which is due to a sawmill. The electricity is supplied by a 4 MW hydro-electric generator and two diesel generators totalling 8 MW. The battery handled the large power demand swings of the sawmill, which the hydro-electric generator was unable to do on its own (Parker & Garche, 2004).

Golden Valley Electric Association (GVEA) in Fairbanks, Alaska, has installed a 40 MW NiCd battery system rated for a 15 min discharge. Fairbanks is connected by a single transmission line to the grid in southern Alaska, and so is not a remote grid, but still provides a significant example of an energy storage solution in Alaska. The peak power capacity is about 20% of the peak power capacity of GVEA. Its chief role is to supply reactive power to the grid and if a generating unit goes offline it can support the grid until a backup unit comes on (Roberts & Mcdowall, 2005).

1.4.5.2 Energy storage research

Abbey & Joós (2009) propose a stochastic method to sizing an energy storage system for an islanded wind-diesel system. Significantly increased savings resulted if the system allowed the turning off of diesel generators, while negligible savings resulted without the ability to turn diesel generators off. However, the paper did not present the thermal unit commitment or energy storage scheduling strategies used in the model.

Weis & Ilinca (2008) simulated the use of energy storage to allow for a higher penetration of wind energy into small remote wind-diesel grids in Canada. These grids are in a similar

situation to those in Alaska, with small grid sizes and high fuel costs. Assuming an electricity cost of 0.30 $Cdn/kWh and installed costs in 2008, wind energy is feasible at an average wind speed of 6.0 m/s. Energy storage systems become viable at wind speeds greater than 7 m/s, if the installed cost is 1000 $Cdn/kWh and can achieve over 75% overall efficiency.

1.4.6 Controllable loads

Controllable loads can be used to consume energy when there is an excess of wind energy. This reduces the amount of wind energy that would otherwise be diverted. Examples of controllable loads include thermal storage, certain industrial loads and large home appliances.

An example of an implementation of controllable loads is St Paul Island located in the Bering Sea off the coast of Alaska. They installed a 225 kW wind turbine and two 150 kW diesel generators to supply an industrial complex and airport with an average load of 65 kW . The wind energy allows the diesel generators to be shut off for significant amounts of time, resulting in significant diesel savings. This is possible due to the excellent wind resource (Class 7) at the site. A 27,000 l hot water tank was installed to take advantage of excess wind energy and thermal energy from the diesel generators. 70% of energy needs (electricity and heating) were met through wind power. In 2009, a study was performed to assess the value of using excess wind energy to power alternative forms of transportation (Keith & Witmer, 2009).

Lu et al. (2011) simulated centralized and decentralized control schemes for a remote wind-diesel micro-grid with controllable loads and energy storage. The simulation showed that demand response and energy storage could significantly reduce stress on the diesel generators and frequency deviations as a result of wind power variability.

Chapter 2

METHODS

For Nome to determine the feasibility of utilizing geothermal energy in their grid, the following questions must be answered (Section 1.2):

- How much diesel generator output would be displaced?
- How much more wind energy would be diverted?
- How would the operation of the diesel generators be affected?

A time-dependent energy balance simulation was developed to simulate the current Nome grid with the addition of geothermal energy. The simulation was performed using the MATLAB software environment from MathWorks Inc.. In addition to geothermal energy, the following modifications were also simulated:

- Addition of strategically sized diesel generators
- Diesel schedules
- Energy storage systems (ESS)

The simulated grid control structure is shown in Figure 2.1. A central controller utilizes feedback information on the operation of the generation and storage units to perform their scheduling while maintaining grid requirements. The central controller determines which diesel units will run online (2.5.3), the charge and discharge rate of the ESS (2.6.2), and the maximum import of wind (2.2.2) and geothermal power (2.3.2). The local controllers at each of the generation and storage units receive this information and adjust their operation accordingly.

Figure 2.2 shows the layout of the simulation. Ten minute interval time series for the full capacity wind and geothermal power outputs were generated prior to the simulation using the models for the wind and geothermal plants. A time series of the demand of Nome's grid was used as the load input to the model (2.1). The energy balance model performed the central controller function and simulated the output of each of the generating and storage units, performing an energy balance to match them to the load . Measured outputs of the simulation included diverted wind and geothermal power, displaced diesel generator output, diesel consumption and statistics on the operation of the diesel generators and ESS. The following sections first describe the different components of the grid simulation and then the flow of the simulation (2.7).

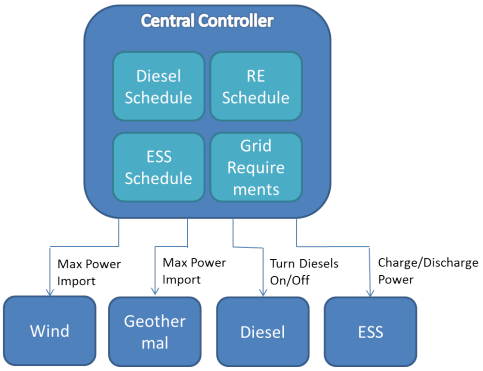


Figure 2.1: The control structure of the grid which was used in the simulation.

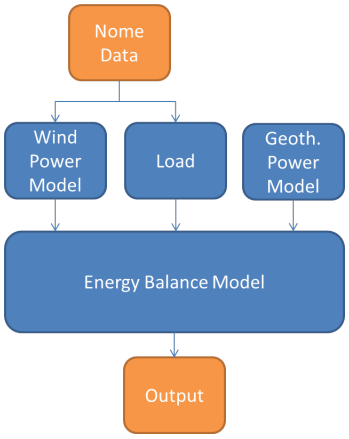


Figure 2.2: The simulation setup.

2.1 Load

Two years of grid demand data were available from Nome's grid. Ten-minute averages were taken of the demand data and used as the load in the simulation. The load had a seasonal variation, with a higher consumption in winter and a lower consumption in summer. The overall average was 4 MW, which rose to around 4.5 MW in January, and dropped to around 3.5 MW in July. The base load was 2.5 MW and the peak load 6 MW. Figure 2.3 shows the cumulative distributions of the load for January, July and the whole year.

2.2 Wind Power

2.2.1 Resource

The City of Nome has two wind farms, listed here as Farm A and Farm B. Farm A was installed in 2008 and is compromised of 18 Entegrity eW15 50 kW turbines, which have induction generators and stall speed control (see Appendix C for turbine specs). Farm B was installed in July, 2013, and has is compromised of two EWT 900 kW turbines, which have synchronous generators and pitch speed control (see Appendix D for turbine specs). Table 2.1 shows the different data sets available from the wind farms.

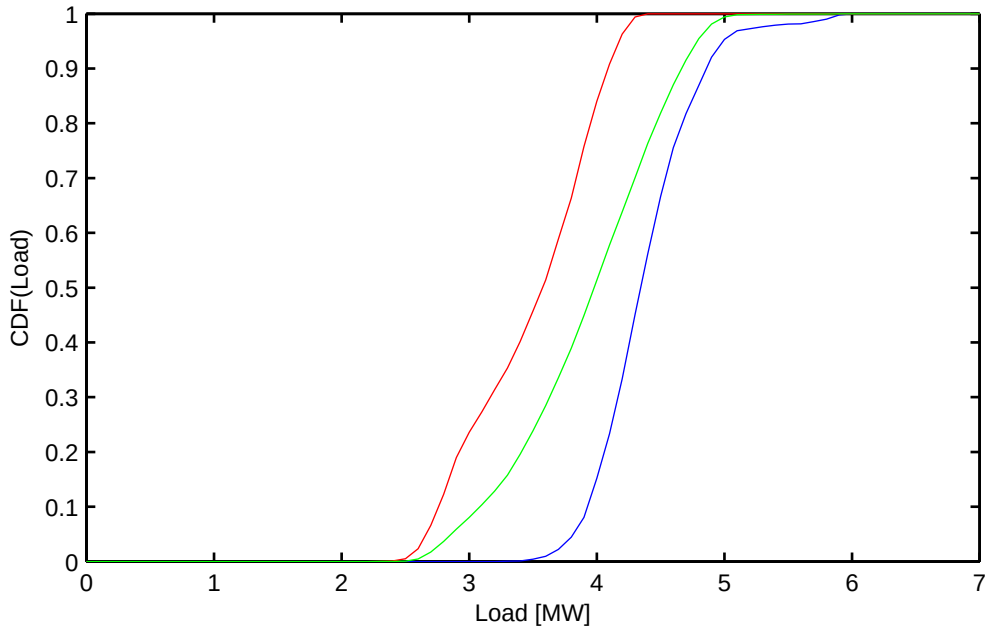


Figure 2.3: Cumulative distribution functions of the load for the entire year (green), July (red) and January (blue).

The two years of grid data (**Data1**) used in the simulation were from May, 2011, to April, 2013, and thus only had production data for Farm A. Wind power output measurements were only made at the feeder level (Figure 2.5). Thus, wind energy outputs for Farm A and B had to be estimated for those two years. This section describes how those estimations were made using the available data sets listed in Table 2.1.

The data set **Data2** consists of six months of grid data including measurements made at the wind farms. Both Farm A and Farm B were in operation at this time; however Farm B was just being commissioned and had severely curtailed outputs.

The data set **Data3** consists of nine months of wind speed measurements from a met tower, six of which overlap **Data1**. Figure 2.4 shows the layout of the Banner Creek wind farm (Farm A), where the eighteen 50 kW Entegrity turbines are located, indicated by the red markers. Two meteorological towers were installed on either end of the ridge, indicated with yellow markers and titled the North and South met towers. The wind speed levels at the South Met Tower corresponded to the output levels of the wind turbines, but their time sequenses did not correspond. The reason for this is not known, but could be caused by innaccurate date/time records or faults with the annenometer. For this reason, the South Met Tower could not be used to find an estimate for the outputs of Farm A and B.

The wind speeds at the North Met Tower corresponded sequentially with the power outputs from the wind farm, but the wind speeds were much lower, since the met tower was on the far side of the ridge from the ocean. **Data3**, from Table 2.1 consists of the wind speeds measured at the North Met Tower and the lower wind speeds were taken into account when using them to derive an estimate for the output of Farm A and B.

Table 2.1: Data sets used to calculate an estimate for wind farm outputs.

Data set	**Duration**	**Farm A**	**Farm B**	**Feeder Level data**	**Wind farm level data**	**Wind speed data**	**Description**
Data1	01/05/2011 to 27/04/2013	Yes	No	Yes	No	No	Grid data used in the simulation. Measurements only made at the feeder level, combining loads and wind production.
Data2	01/04/2013 to 13/10/2013	Yes	Yes	Yes	Yes	No	Grid data including measured outputs for each farm. Farm B came online in July. Much of the available data is from the commissioning phase, when the turbines were often curtailed.
Data3	13/03/2011 to 10/12/2011	Yes	Yes	No	No	Yes	Wind speed measurements from a met tower. The met tower was on the far side of the ridge from the ocean, thus measured lower wind speeds than actually seen at the wind farm.

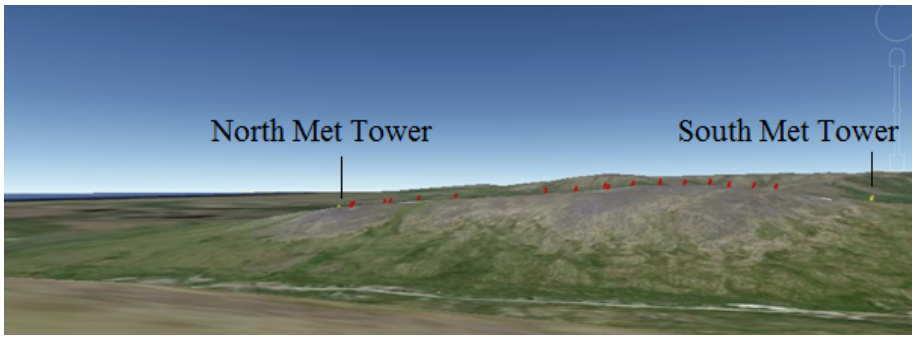


Figure 2.4: The layout of Banner Creek wind farm, where the red markers indicate wind turbines, and the yellow markers on either end indicate met towers. The ocean is on the left. Image source: googleearth.

2.2.1.1 Deriving an output for Farm A

This section describes the process of deriving an output for Farm A for **Data1**. First a relationship was calculated between the power measurements at Farm A's feeder with the measured outputs of Farm A in **Data2**. This relationship was then applied to Farm A's feeder in **Data1** to get an estimate of the output of Farm A.

In **Data1** and **Data2**, the main load on Farm A's feeder was a moth-balled mine, which was found to have a relatively constant load. For an initial estimate ($P_{A,init}$) of the wind power production of Farm A, a constant load ($P_{A,feederload}(t)$) was estimated for each week and subtracted from the total feeder demand ($P_{A,feeder}(t)$), as in the following equation,

$$P_{A,init}(t) = P_{A,feeder}(t) - P_{A,feederload}(\bar{t}) \tag{2.1}$$

Where time t is measured in 10 minute intervals and time $\bar{t}$ is measured in weekly intervals. The constant weekly load, $P_{A,feederload}(\bar{t})$, was calculated from the power draw of Farm A's feeder. Figure 2.5 shows an example of one week. There appears to be a relatively constant load (measured as positive) on the feeder when there is no wind power (measured as negative). To get an approximation for the constant load, a cumulative distribution function (CDF) was calculated for each week. The load was estimated to be the maximum for 99% of the demand on the feeder. For the week in Figure 2.5, the constant load was calculated to be 78 kW.

Using Equation 2.1, $P_{A,init}(t)$ was calculated for **Data2** and then compared with the actual output measured at Farm A ($P_{A,act}(t)$) in **Data2**. A relationship was then calculated between $P_{A,act}$ and $P_{A,init}$.

First, $P_{A,act}$ was binned according to $P_{A,init}$ to obtain $P_{A,act}(P_{A,init})$ and then the average taken for each bin. Figure 2.6 shows the result, where the red crosses represent the average of $P_{A,act}$ at each bin of $P_{A,init}$. The blue is the initial estimate, $P_{A,init}$. $P_{A,act}$ tends to range from equalling to around 200 kW below $P_{A,init}$.

Twenty iterations of a moving average with a 5.5 kW window size were performed on the averaged $P_{A,act}(P_{A,init})$ to obtain $P_{A,act,ave}(P_{A,init})$, shown by the blue line in Figure 2.6. A disadvantage of taking an average is that the resulting output will have a reduce range. A greater range means higher wind power outputs, which are less likely to be able to be fully

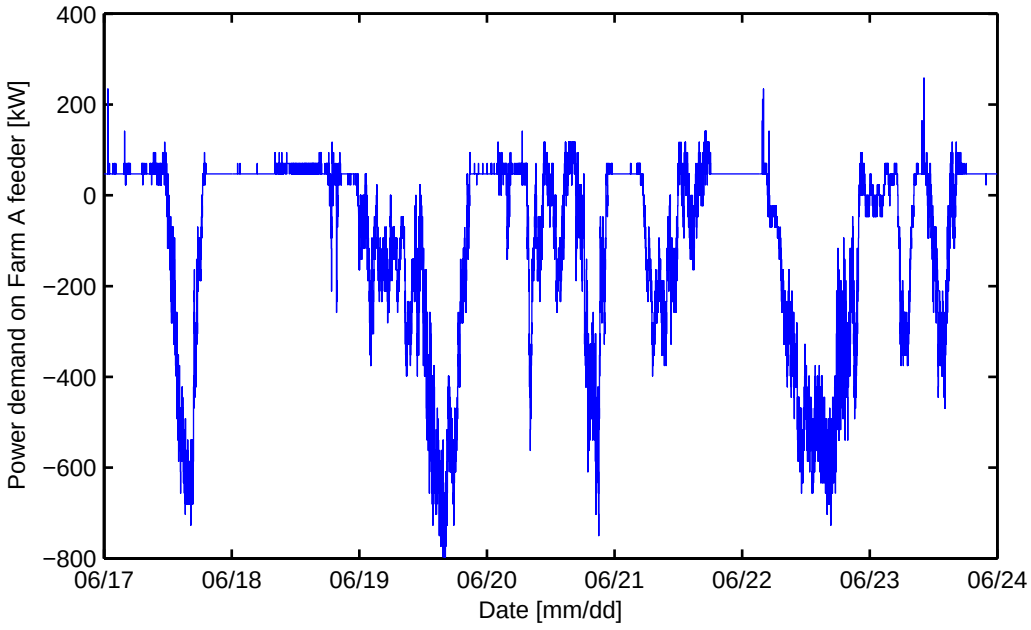


Figure 2.5: Power demand for one week on Farm A's feeder.

imported into the grid, and leads to greater diversion of wind energy. A disadvantage of not taking an average is that the outputs are much noisier. A noisy output signal means the wind power outputs change quickly, which make it difficult for the grid to change the diesel schedule accordingly to accommodate the changing wind power outputs.

Thus, not enough averaging would result in too much diversion of wind energy in the output, while too much averaging would result in not enough diversion of wind energy in the output of the simulation. There is only around a 60 kW difference between the range of $P_{A,act,ave}\ (P_{A,init})$ and $P_{A,act}(P_{A,init})$, thus it can be considered to be a good approximation. A comparison between the final calculated wind power output and the measured wind power output $(P_{A,act})$ is shown in Figure 2.8. The range is only slightly reduced and there is a strong correlation between the two series, indicating an appropriate level of averaging.

The next step was to determine a relationship between $P_{A,init}$ (Figure 2.6, black line) and $P_{A,act,ave}(P_{A,init})$ (Figure 2.6, blue line) to improve upon the initial estimate of Farm A's output. A scaling factor (S_A) was calculated for the different values of $P_{A,init}$ with the Equation 2.1. Figure 2.7 shows S_A plotted for different values of $P_{A,init}$.

$$S_A(P_{A,init}) = \frac{P_{A,act,ave}(P_{A,init})}{P_{A,init}} \tag{2.2}$$

A wind power output for Farm A $(P_A(t))$ was calculated for **Data2** by scaling $P_{A,init}(t)$ by $S_A\ (P_{A,init})$, as shown by Equation 2.3.

$$P_A(t) = P_{A,init}(t) \cdot C_A(P_{A,init}) \tag{2.3}$$

The resulting $P_A(t)$ had an average of 171 kW compared to the 168 kW average of the actual measured Farm A output, $P_{A,act}(t)$. This results in a capacity factor of 19%, which matches the capacity factor of the actual Farm A. The correlation between $P_A(t)$ and $P_{A,act}(t)$ is 93%, as calculated with Equation 2.4.

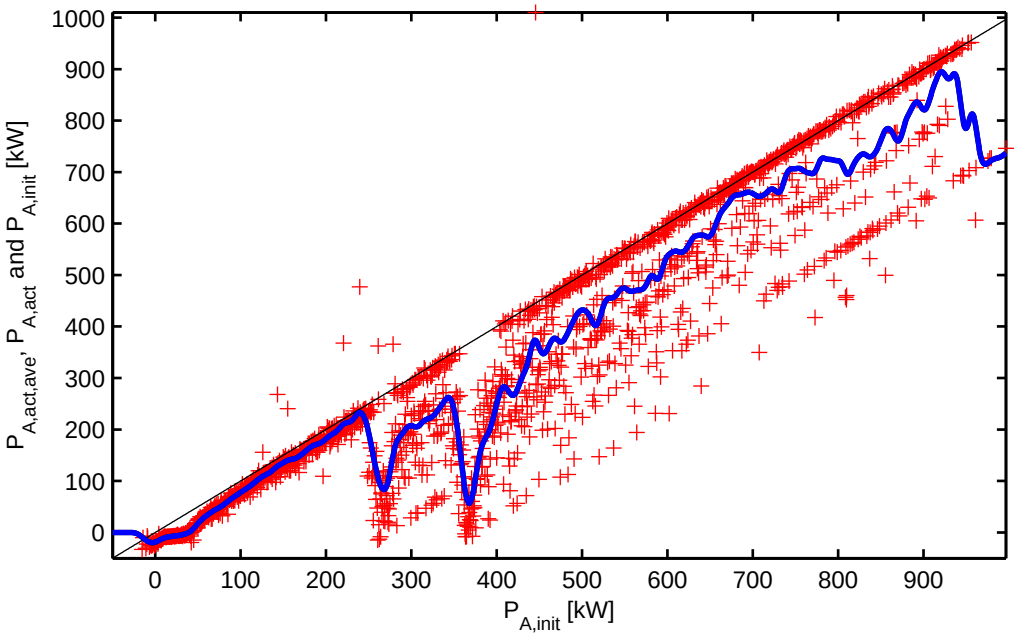


Figure 2.6: The average at each bin for the actual wind power outputs of Farm A (red '+'), binned against the initial estimate for Farm A output (black). The blue line results from 20 iterations of a moving average with a 5.5kW window size on the red data points.

$$r_{xy} = \frac{(\sum_{i=1}^{n}(x_i - \bar{x})(y_i - \bar{y}))}{((n-1)s_x s_y)} \tag{2.4}$$

Where $(x_i - \bar{x})$ and $(y_i - \bar{y})$ represent the differences between each sample of X and Y with the mean of X and Y, n is the number of samples being compared in X and Y and s_x and s_y are the standard deviations of X and Y.

Figure 2.8 shows a section of $P_A(t)$ (blue) and $P_{A,act}(t)$ (green). The synthesized signal is a good estimate of the actual Farm A output. $P_A(t)$ was calculated for **Data1** and used in the simulation as Farm A's output.

2.2.1.2 Deriving an output for Farm B

This section describes the process of deriving an output for Farm B for **Data1**. First a relationship was calculated between the power measurements at Farm A's feeder in **Data1** with calculated outputs for Farm B using corresponding wind speed measurements from **Data3**. This relationship was then applied to Farm A's feeder in **Data1** to obtain an estimate for the output of Farm B.

In **Data2**, Farm B was still being integrated into the grid and not operating at full capacity, thus it could not be used in the calculations. To estimate the actual output of Farm B over the course of two years, the wind speeds in **Data3** were used with the power curves for the turbines to determine the theoretical wind turbine outputs. The met tower from **Data3** was located on the far side of the ridge from the ocean on which the wind farms were located (see Figure 2.4). Thus the measured wind speeds were lower than wind speeds that have been measured at the wind farm. To compensate, no loss factor was used when calculating the turbines' theoretical output with their power curves.

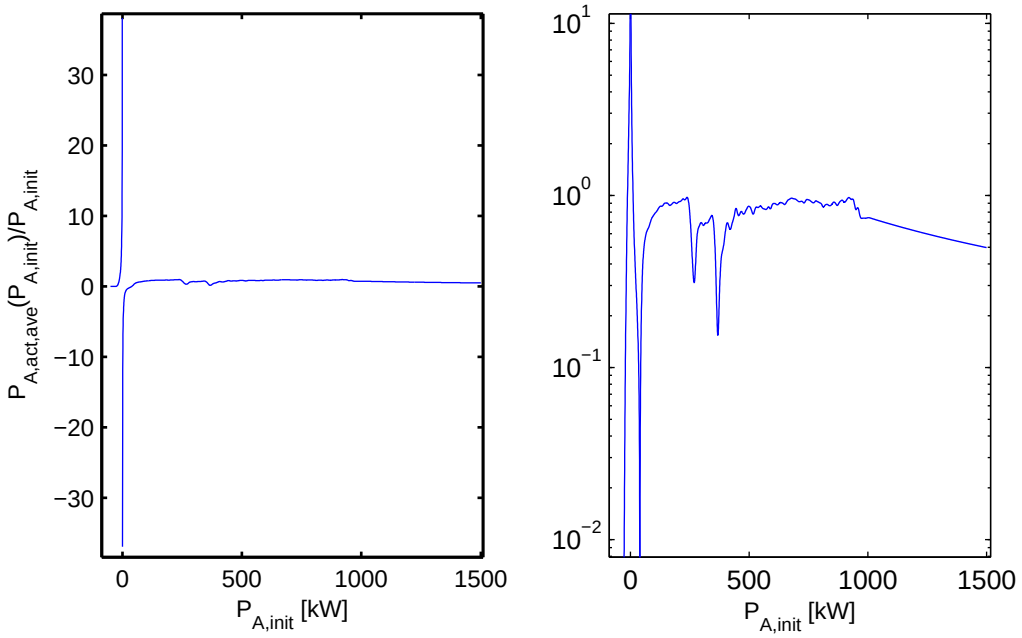


Figure 2.7: The scaling factor for the different values of the initial estimate of Farm A's output is shown on the left and its absolute is plotted on a log scale on the right.

The Alaska Energy Authority performed a simulation during the assessment phase of the installation of Farm B, in which a capacity factor of 31.5% was predicted (Devine, 2011). Meanwhile, the actual measured outputs from Farm B in **Data2** result in a capacity factor of 9%. The capacity factor calculated from the wind speeds in **Data3**, without using a loss factor, was 22%. Thus, it is higher than what is currently being measured, and lower than what was predicted. The wind output for Farm B used in this simulation is considered to be a conservative estimate for Farm B's potential output.

Using the wind speeds in **Data3** and the power curves for the turbines in Farm B, a theoretical output for Farm B was calculated ($P_{B,th}(t)$). $P_{B,th}(t)$ was binned according to values of $P_{A,init}(t)$ to obtain $P_{B,th}(P_{A,init})$. The average of each bin of $P_{B,th}(P_{A,init})$ is shown in Figure 2.9 by the red crosses. The black line is the initial estimate for Farm A, $P_{A,init}$. There is a larger spread in the binned data points than there was for Farm A (Figure 2.6). This can be expected, since they represent a comparison between the calculated outputs for Farm B and A instead of a comparison between the calculated and actual outputs of Farm A. The blue line shows $P_{B,th,ave}(P_{A,init})$, which represents averaged bin values of $P_{B,th}(P_{A,init})$ after 10 iterations of a moving average was applied with a window size of 5.5 kW.

As discussed in the previous section, averaging too much results in a diminished range which would reduce the amount of wind diversion in the solution. Not averaging enough results in a noisy output which would increase the amount of wind diversion in the solution. Thus, the right balance must be found. Figure 2.10 shows a section of the final calculated output for Farm B if no moving average was performed on the averaged bin values of $P_{B,th}(P_{A,init})$ (blue) and if 10 iterations of a moving average with a window of 5.5 kW were performed on the averaged bin values of $P_{B,th}(P_{A,init})$ (green). The high level of noise resulting from not averaging compared to the reduced range from averaging can be seen. The wind series resulting from the moving average was used in the simulation, and a sensitivity analysis is presented in Section 2.2.1.3 which indicates how this may

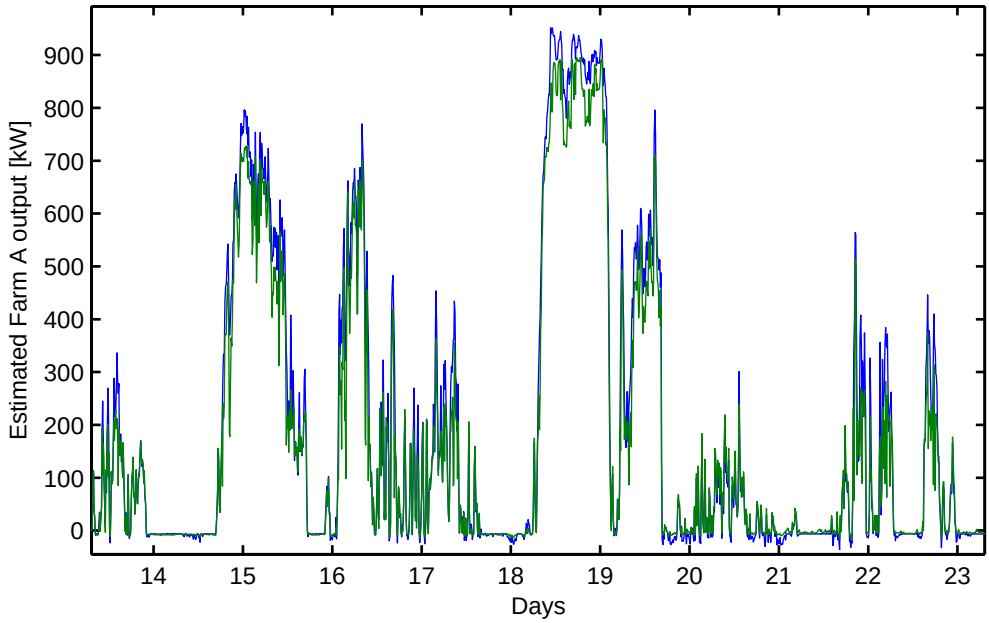


Figure 2.8: Comparing the calculated Farm A output (green) with the measured Farm A output (blue).

affect the results of the simulation.

The next step was to determine a relationship between $P_{B,th}$ and $P_{A,init}$, which will allow the calculation of Farm B's output from Farm A's feeder. A scaling factor (S_B) was calculated for the different values of the initial estimate of Farm A's output ($P_{A,init}$) with the Equation 2.5. Figure 2.11 shows S_B plotted for different values of $P_{A,init}$.

$$S_B(P_{A,init}) = P_{B,th,ave}(P_{A,init})/P_{A,init} \tag{2.5}$$

The output for Farm B, $P_B(t)$, was calculated by applying $S_B(P_{,init})$ to $P_{A,init}(t)$, using the following equation:

$$P_B(t) = P_{A,init}(t) \cdot S_B(P_{A,init}) \tag{2.6}$$

The resulting P_B had an average of 194 kW compared to the 192 kW average of the theoretical Farm B output. The correlation between the two was 71%. Figure 2.12 shows a section of $P_B(t)$ (blue) and $P_{B,th}(t)$ (green). While the two time series have a similar average and capacity factor, $P_B(t)$ does not reach as high or low values as $P_{B,th}(t)$ does. This is a result of averaging, and a sensitivity analysis is presented in Section 2.2.1.3 which indicates how this may affect the results of the simulation.

2.2.1.3 Sensitivity analysis

In order to determine how sensitive the results of the simulation are to the moving average which was performed when synthesizing the outputs for Farm A and B, a sensitivity analysis was performed, comparing this report's simulation results (**Result A**) to the results of a simulation where no moving average was performed when synthesizing the wind farm

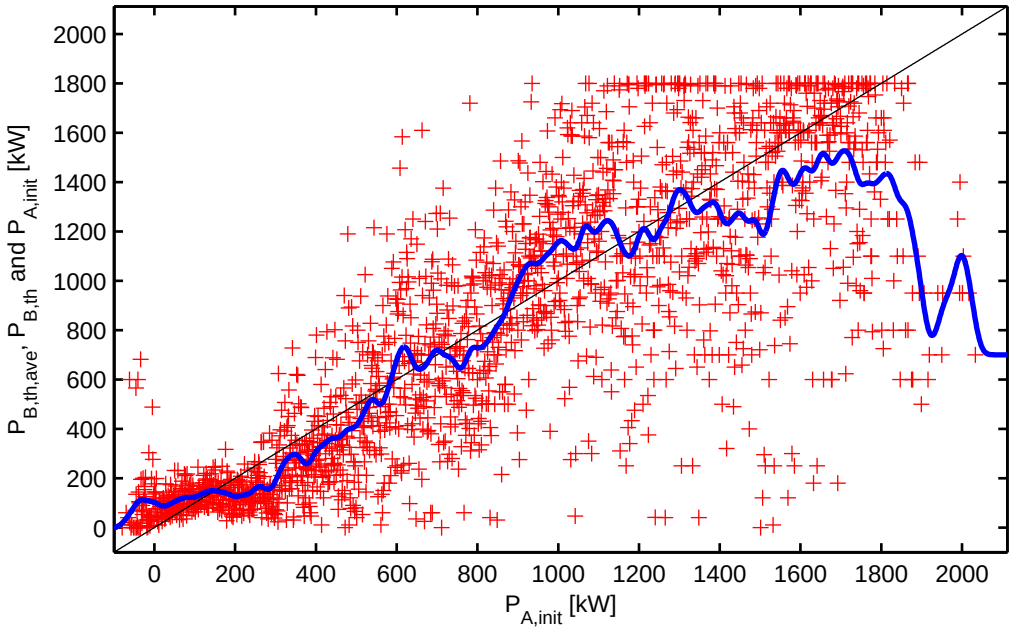


Figure 2.9: The average at each bin of the theoretical wind power outputs for Farm B (red '+') binned against the initial estimate for Farm A output (black). The blue line results from applying 10 iterations of a moving average with a 5.5kW window size to the red data points.

outputs (**Result B**). **Result B** represents the 'worst case scenario' for wind farm outputs, with an unrealistic amount of noise.

Figure 2.13 shows the diversion of wind energy per year for **Result A** (+), and **Result B** (o). The different colors represent the diesel scenarios which are outlined in Section 2.5. There is a reduced difference between the two results for increasing levels of average geothermal output. At 2 MW of geothermal capacity there is an average of 70 MWh/a difference in wind diversion, which represents a difference of 5–10% between scenarios.

Result A displaces 10–20 MWh/a more diesel generator output per year than **Result B**. This represents a difference of around 0.07% between the results.

The average loading of the diesel generators remains unchanged. The number of times the online combination of diesel generators changes per year is shown in Figure 2.14. **Result B** has a higher number of changes per year. The most affected diesel scenario was **Case 4** (purple - see Table 2.3). For **Case 4**, at 2 MW of geothermal capacity, **Result B** had 236 more diesel changes per year than **Result A**, a 21% difference. Diesel scenario **Case 1** is least affected, and at 2 MW of geothermal capacity, **Result B** has 7 more diesel changes per year, a 1% difference.

Thus, the main differences between the results of the simulations using the 'worst case scenario' wind power time series and the one which was used in this study were diesel switching and diverted wind energy. At 2 MW of geothermal capacity 5–10% more wind energy was diverted per year, and there was up to 21% more diesel switching. The difference in displaced diesel was minimal, and the differences between the two scenarios decreased with increasing geothermal capacity.

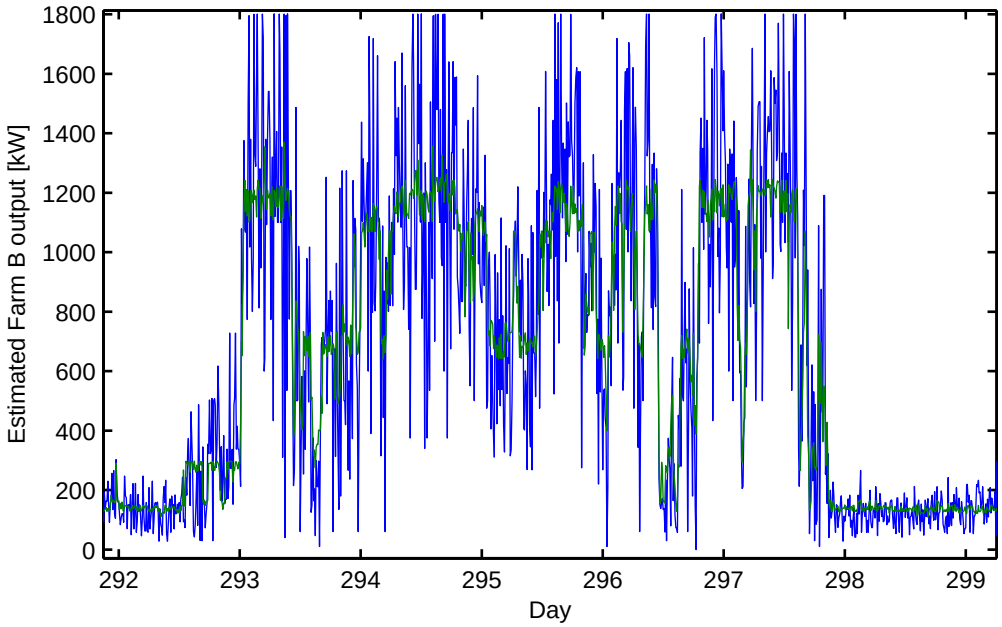


Figure 2.10: Comparison of a section of Farm B's output calculated using the binned theoretical outputs of Farm B with a moving average (green) and without a moving average (blue). Averaging results in a reduced range, while not averaging results in 'noisy' data.

2.2.1.4 Summary

Wind production data was only available for Farm A in **Data1**, with measurements made at the feeder level. An initial approximation ($P_{A,init}$) was obtained for Farm A's output by subtracting a constant load, recalculated for each week of the time-series, from the feeder measurements in **Data1**. An improvement to $P_{A,init}$ was obtained by calculating a scaling factor (S_A) between it and the actual Farm A outputs measured in **Data2**.

A scaling factor (S_B) was also calculated between $P_{A,init}$ and a theoretical output for Farm B using the wind speed measurements in **Data3**. $P_{A,init}$ was calculated for **Data1** and S_A and S_B applied to obtain an approximation for Farm A and Farm B's outputs in **Data1**.

During the process of synthesizing wind outputs, a moving average was applied to the binned values of the measured and theoretical outputs for Farm A and B. This had the effect of reducing the 'noise' (the rate at which the wind farm outputs switched between significant differences in output levels) and reducing the range (how much the wind farm outputs varied from the mean output). Both had the effect of reducing the diversion of wind energy in the simulation and the number of changes in online diesel generators year.

Not using a moving average would result in too much diversion of wind energy and changes in diesel generators and too much averaging would result in not enough for a realistic representation of the grid. Thus, a sensitivity analysis was performed to determine how much the result could be affected by the level of averaging performed. It was found that the displaced diesel and average loading of diesel generators were not greatly affected. There was a 5–10% less wind diversion and up to 21% less changes in online diesel generators per year between averaging and not averaging. These are comparisons to the 'worst case scenario' in terms of the quality of the wind farm output.

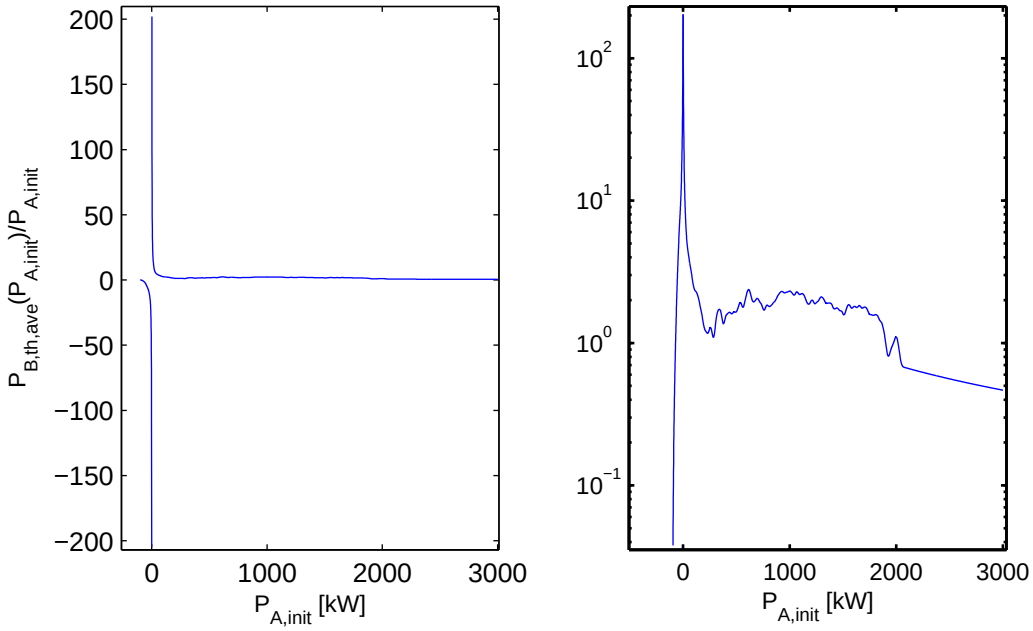


Figure 2.11: The scaling factor used to convert the different values of the initial estimate of Farm A's output into Farm B's output is shown on the left. On the right is its absolute on a log scale.

2.2.2 Control

The main controller determined the maximum amount of wind energy that could be accepted into the grid. If this was less than what the turbines were currently generating, then their output needed to be diverted.

The output of Farm A could be diverted by either turning off turbines, or diverting the excess energy to an electric boiler. Farm A consists of eighteen 50 kW turbines and turning a turbine offline can reduce the wind farm output by up to that much. While running, their outputs cannot be controlled.

Farm B consists of two 900 kW turbines, which can be turned off or have their output clamped to levels below their full capacity generation.

Considered together, the output for both wind farms was modelled to be fully controllable up to full capacity generation in the simulation.

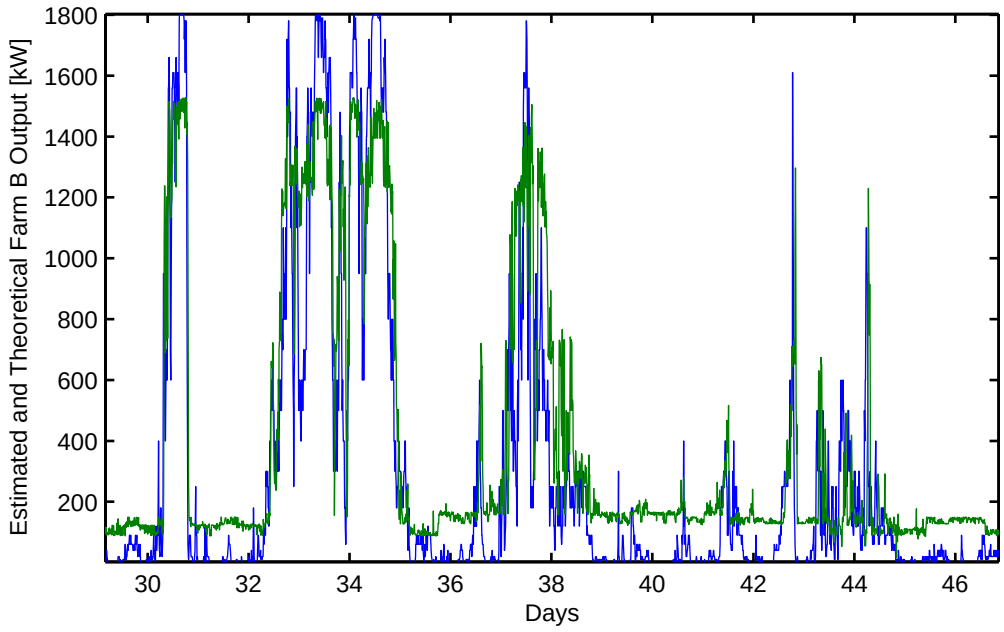


Figure 2.12: A comparison of Farm B's output calculated from Farm A's feeder (green) with Farm B's output calculated from the wind speeds of the North Met Tower (blue).

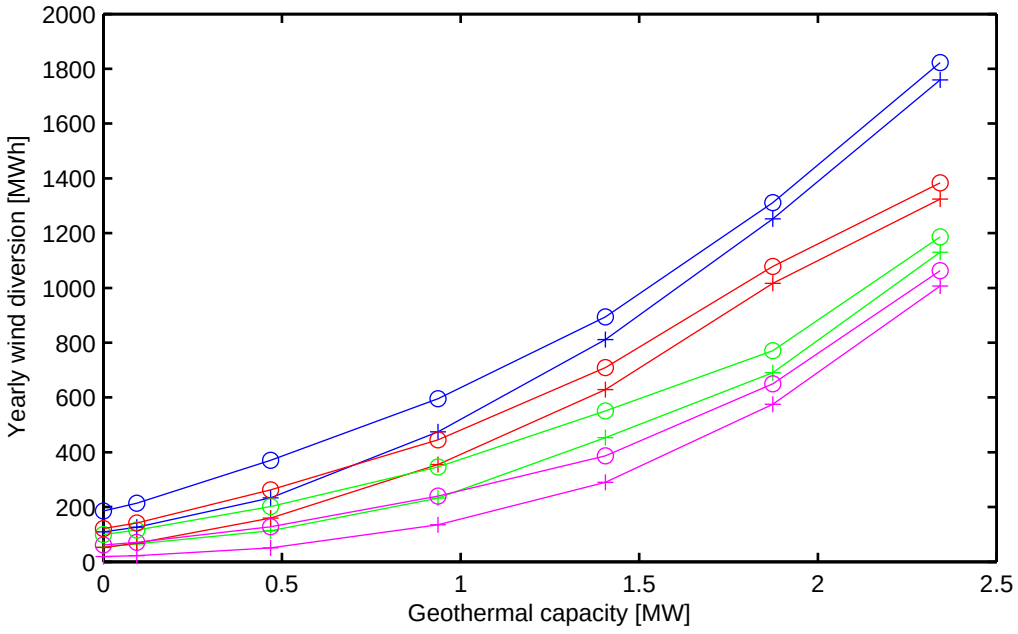


Figure 2.13: Comparing the yearly diversion of wind energy when a moving average was applied to the binned measured outputs of Farm A and theoretical outputs of Farm B (+) with the yearly diversion of wind energy when no moving average was applied (o). The different colors represent the different diesel scenarios used in the simulation, listed in Table 2.3.

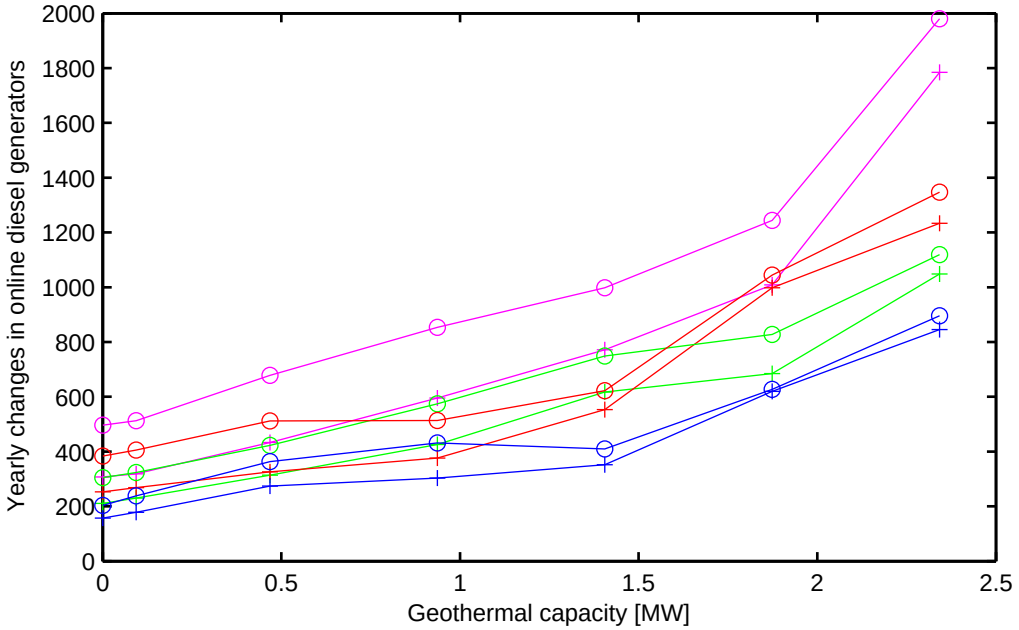


Figure 2.14: Comparing the changes in online diesel generators per year when a moving average was applied to the binned measured outputs of Farm A and theoretical outputs of Farm B (+) with the changes in online diesel generators when no moving average was applied (o). The different colors represent the different diesel scenarios used in the simulation, listed in Table 2.3.

2.3 Geothermal

2.3.1 Resource

There are, in general, three types of geothermal power plants: direct steam, flash steam and binary plants (Rafferty, 2000). A direct steam plant can be used when the geothermal resource directly produces steam, which can be fed directly into a turbine. A flash steam plant is used when the geothermal resource produces either high temperature water, or a combination of water and steam. The hot water is put into a flash tank where a portion turns into steam and can be used to run the turbine. A binary plant is used with low temperature geothermal resources. The geothermal resource is used to heat a secondary loop, causing the fluid in the secondary loop to vaporize and run the turbine.

With the 90°C temperatures predicted in the model for the Pilgrim geothermal system, a binary plant would most likely be used. The maximum theoretical efficiency (η_{th}) in converting the energy from the steam to electricity is determined by the Carnot efficiency (Rafferty, 2000):

$$\eta_{th} = \frac{(T_H - T_L)}{T_H} \tag{2.7}$$

where T_H is the temperature of the steam and T_L the temperature of the condenser, given in Kelvin. The actual efficiency is usually much lower and overall efficiency also takes into account losses in the boiler and in the electrical generator. Equation 2 gives the electrical power output of a geothermal plant.

$$P_e = c_{water} \cdot \dot{m}_{water} \cdot \Delta T \cdot \eta_{overal} \tag{2.8}$$

The electrical output (P_e) from a geothermal resource is determined by the temperature differential (ΔT), water flow rate ($\dot{m}_{water}$) and the overall system efficiency in converting thermal power into electrical power ($\eta_{overall}$), which is also a function of the temperature differential.

A lower temperature differential requires a higher flow rate to generate the same amount of power, which requires larger plant equipment (Holdmann, 2006) and increases the cost of electricity. However, due to the high cost of electricity in Nome, a geothermal power plant is still projected to be economical.

Since the geothermal resource remains relatively constant, during winter a higher temperature differential is possible. Due to this, a higher power output can be expected than in the summer. This corresponds to the load, which also increases in the winter (Holdmann, 2006). This was modelled in the simulation, with the lowest output in July, at 75% of the maximum capacity, shown by Figure 2.15.

Geothermal power plants are usually operated to supply the base load and have a hard time load following. There is some research being conducted to improve their ability to load follow (Brown, 1993), but no feasible solution is apparent for this application. In the simulation, the geothermal plant was assumed not to be able to load follow.[1]

[1]Load following refers to the ability of a power source to modulate its output in response to the demand.

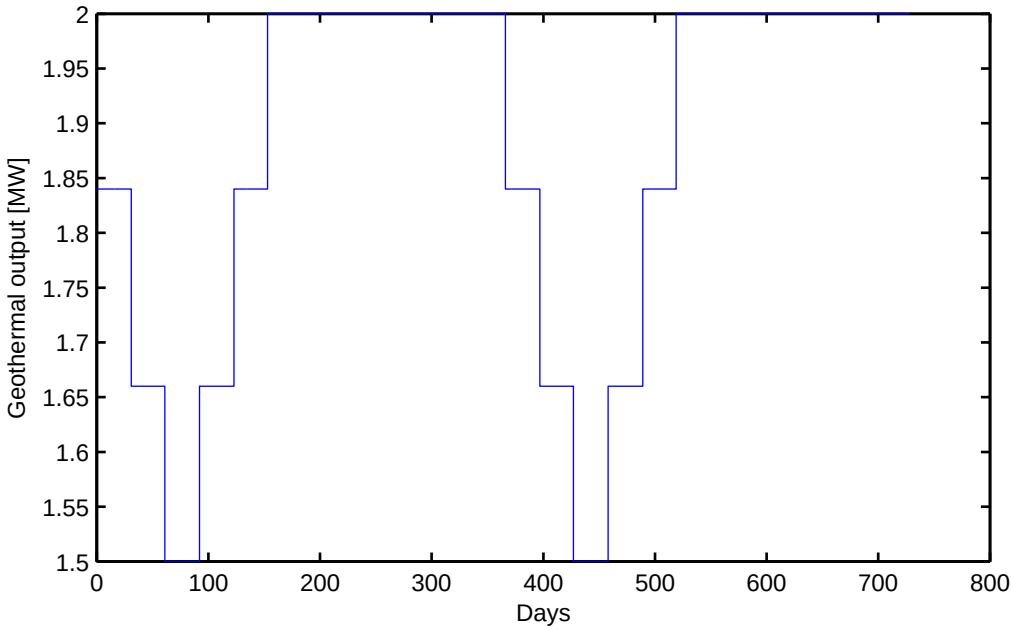


Figure 2.15: Two years of geothermal output for a 2MW installation beginning in May.

From the geological exploration performed by ACEP (Haselwimmer et al., 2013), a potential capacity of 2 MWe was considered likely, but a range of geothermal capacities from 0–5.5 MWe were simulated in order to understand the underlying principles of how geothermal power would affect this type of hybrid system, and how to plan for a range of possible outputs.

The Pilgrim Geothermal Resource (PGS) is located 37 miles from Nome. Thus, it is too far to use the thermal energy from the plant in town. However, the heat resource would be used locally in the power plant and could be used for other local development.

2.3.2 Control

The central controller determined how much geothermal energy could be imported into the grid. Ideally, the grid could accept the entire geothermal output. If there was excess renewable generation, wind power was diverted first, since it had a controllable output, unlike the assumed geothermal source. Diverting geothermal was considered to be a sub-optimal scenario for this simulation, as a means of handling the excess energy generation would have to be found. This paper focusses on the scenarios in which little geothermal generation must be diverted.

2.4 Grid

A spinning reserve capacity (*SRC*) must be maintained in the grid to maintain the power quality. The simulation copies the current grid operation by covering a fixed amount (0.25 MW) of the load (SRC_{load}), and the entire wind import into the grid (SRC_{wind}) with the SRC. The total SRC in the grid is the combination of the two, as given in the following in equation:

$$SRC = SRC_{load} + SRC_{wind} \tag{2.9}$$

This SRC is able to handle a complete loss in wind power as well as a sudden 0.25 MW increase in load at the same time. This is a conservative amount of SRC, as there is a low probability of these two events coinciding. Other grid control systems in literature do not cover the full wind import, but have a dynamic relationship between wind import and SRC_{wind}. Chen (2008) simulated the Peng-Hu remote power grid in Taiwan with a linearly decreasing relationship between the SRC and wind import. The percentage of wind import covered by the SRC_{wind} reduced with increasing levels of wind import into the grid. Significant savings are possible by decreasing the level of required SRC_{wind}, and this is a recommendation for future simulations.

2.5 Diesel generators

2.5.1 Resource

The Nome grid currently has two 5.2 MW Wärtzillä diesel generators, and one 3.6, 1.9 and 0.4 MW Caterpillar diesel generator each. A hypothetical 1 MW diesel generator was also added to some simulations, which was chosen to allow for an even step size in between generator capacities. The Table 2.2 shows the generator operating attributes and parameters that reflect Nome's current grid operation and performance.

Table 2.2: Diesel generator operating attributes and parameters.

Diesel generator	**Capacity [MW]**	**Max. Efficiency [%]**	**MOL [%]**	**Warm-up/cool-down time [min]**	**Warm-up/cool-down cons. [gal/hr]**	**Min run time [min]**
G1	0.4	34	30	10	7.8	90
G2	1	34	30	20	19.6	90
G3	1.9	34	30	20	36.6	90
G4	3.7	34	40	20	70.5	180
G5 and G6	5.2	42	60	30	80.9	180

The MOL is largely a function of the size of the diesel generator, with the larger diesel generators having a higher MOL. When a combination of diesel generators are running together, the MOL of the group is equal the highest MOL of the individual generators.

Each diesel generator was assumed to have an identically shaped efficiency curve (Figure 2.16), which was scaled according to the maximum efficiency listed in Table 2.2. The two 5.2 MW diesel generators were newer and larger than the others which led to them having a higher efficiency.

Each diesel generator had to run a certain amount of time before it could be brought online on and after being brought offline. This is referred to as the warm-up and cool-off periods.

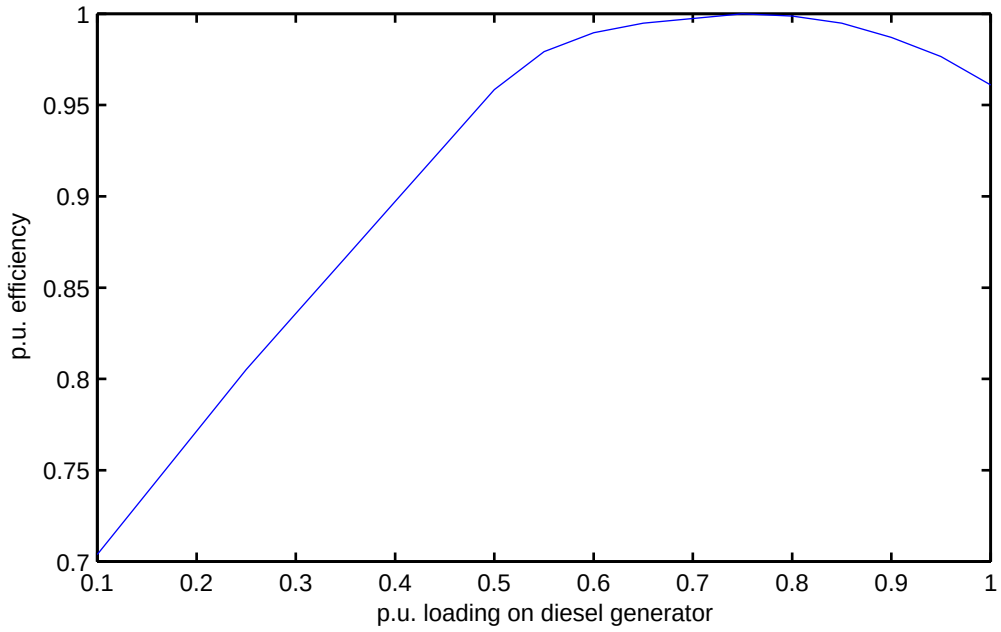


Figure 2.16: Per unit efficiency (scaled by the maximum efficiency for the given diesel generator) for the per unit loading (scaled by the capacity of the diesel generator).

Larger diesel generators had longer warm-up and cool-off periods. During the warm-up and cool-off periods, the diesels ran at no load, but still consumed diesel. This is what is referred to by the warm-up/cool-down consumption in Table 2.2.

Finally, after being switched online, each diesel generator had to run for a certain amount of time before switching offline again. This is what is referred to by the minimum run time. The larger diesel generators had to run for a longer amount of time.

Table 2.3 lists the four different diesel scenarios which were simulated, using the diesel generators from Table 2.2. **Case 1** represents the base case, with the current fleet of diesel generators. **Case 2** includes the 0.4 MW diesel generator which is currently only used for black starts, **Case 3** includes the hypothetical 1 MW diesel generator and **Case 4** includes both the 0.4 MW and 1 MW diesel generators.

Table 2.3: Diesel scenarios. **Case 1** is the base (current) case. See Table 2.2 for a description of the diesel generators.

Diesel scenario	Available diesel generators	Color on plots
Case 1	G3, G4, G5, G6	Blue
Case 2	G1, G3, G4, G5, G6	Red
Case 3	G2, G3, G4, G5, G6	Green
Case 4	G1, G2, G3, G4, G5, G6	Purple

2.5.2 Control

The diesel schedule turns the diesel generators on and off but does not determine the generation share of each diesel generator. This is performed by the local isochronous

controllers on each diesel generator which share the load equally between the diesel generators based on their capacities and makes up the difference between the load and the import of RE.

2.5.3 Schedule

Diesel scheduling refers to the decision making process by which diesel generators are turned on and off. It is a special case of unit commitment, and as discussed in the Section 1.4.2, many different algorithms are being used to solve the unit commitment problem. In a conventional grid, unit commitment is often solved as part of an economic optimization, where the lowest cost combination of generating units is chosen. Section 2.5.3.1 lists the events which will initiate the diesel schedule and the criteria for choosing potential diesel generating options. Sections 2.5.3.2 and 2.5.3.3 present the two diesel schedules which were used in the simulations.

2.5.3.1 Initiating the diesel schedule

One of the following events would initiate the diesel schedule:

- The SRC in the system was less than what was required
- The diesel generators were operating below their MOL
- Renewable energy was being diverted

As discussed in Section 2.6.2, additional initiating events were added with the use of energy storage systems (ESS) in the grid.

After an initiating event and before the diesel schedule could be performed, the potential diesel generating options were determined by whether or not they met the following criteria:

1 The load ($P_{Load}(i)$) was not less than the MOL ($P_{MOL,n}$) of the generating option n:

$$P_{Load}(i) >= P_{MOL,n} \tag{2.10}$$

2 The capacity of generating option n ($P_{Cap,n}$) could supply the difference between the load ($P_{Load}(i)$) and the RE import ($P_{import}(i)$) as well as the SRC ($P_{SRC}(i)$):

$$P_{Cap,n} >= P_{Load}(i) + P_{SRC}(i) - P_{import}(i) \tag{2.11}$$

3 Switching to the new combination would not switch off diesel generators that had not yet run for their minimum operating time (MOT)

The diesel schedule was then performed on all diesel generating options which meet the criteria. As discussed in Section 2.6.2, there were some scenarios where the criteria were changed based on the use of energy storage systems (ESS).

2.5.3.2 Schedule 1: Maximize renewable energy import into grid

The goal of the main diesel schedule used in this simulation was to maximize the amount of renewable energy that could be imported into the grid. This was accomplished by choosing the diesel generator combination with the lowest minimum optimal loading (MOL) which which met the criteria listed in Section 2.5.3.1. This allowed the maximum amount of RE to be imported into the grid (Katiraei & Abbey, 2007). It also maximized the loading of the diesel generators.

If there was no cost associated with switching diesel generators, and if the diesel generators had identical characteristics (running costs and efficiency curves) then this schedule would also minimize the amount of diesel consumed and find the lowest cost solution. In reality, this is not the case. As seen in the Section 2.5.1, the larger diesels have higher start-up, shut-down and running costs, but also can operate at a higher efficiency. Thus, while this diesel scheduling scheme maximizes the amount of wind energy imported into the grid, it does not minimize the overall cost. It does however give a good approximation. The advantage of using this scheduling scheme is that it is a very simple problem to solve, thus it does not need much computational power and the simulation can be performed quickly. It also does not require operating costs and efficiency curves for the generators, which were not available.

2.5.3.3 Schedule 2: Minimize consumption of diesel

A second diesel schedule was also simulated, with the goal of minimizing the amount of consumed diesel. This was accomplished by predicting the overall diesel efficiency that each possible combination of diesel generators would run at, i.e. the total load divided by the power equivalent of the diesel required to supply that load. Equation 2.12 was applied to each combination of diesel generators that met the criteria listed in Section 2.5.3.1.

$$\eta_{overall,i} = \frac{P_{load}}{\frac{P_{load} - P_{import,i}(P_{geo}+\bar{P}_{wind})}{\eta_{state,i}} + \vec{P}_{sw,i} \cdot \frac{\vec{t}_{sw,i}}{120}} \tag{2.12}$$

$\eta_{overall,i}$ is the overall diesel efficiency at meeting the current load for the i^{th} combintation. P_{load} is the current electrical load. P_{geo} is the current geothermal output. $\bar{P}_{wind}$ is the average wind farm output for the last hour. $P_{import,i}(P_{geo} + \bar{P}_{wind})$ is the amount of P_{geo} and $\bar{P}_{wind}$ that could be imported into the grid with the i^{th} combination of diesel generators. $\eta_{state,i}$ is the combined efficiency of the i^{th} combination of diesel generators while supplying a load of $P_{load} - P_{geo} - \bar{P}_{wind}$ (the combined efficiency is compromised of the individual efficiencies weighted according to the capacities of the diesel generators, in the same way that the diesel generators would share the load). $\vec{P}_{sw,i}$ is the vector of the power equivalent of the gal/hour diesel consumed by each diesel generator during cool-off or warm-up that would need to be switched on or off in order to bring in the i^{th} combination of diesel generators online. $\vec{t}_{sw}$ is the vector of the time in minutes that each generator would run while starting up or cooling off.

$\vec{t}_{sw}$ is divided by 120 min because the assumption is that each diesel generator will be online for 2 hours. The power consumption of each generator during warm-up or cool-off is averaged out over the entire 2 hour period each diesel generator is assumed to run for. This is a weak part of the equation, as an assumption is made about the amount of time

the diesel generators will be online for. Two hours is a very low estimate, which is erring on assigning a higher (diesel) cost to switching.

When applying the diesel schedule, the overall diesel efficiency is calculated for each possible combination of diesel generators that meet the diesel and grid operating requirements. The combination with the highest overall efficiency is chosen. This tries to predict the combination of diesel generators which will consume the least amount of diesel. This schedule tries to minimize diesel consumption, not overall cost. While diesel is the main cost, there are additional costs to consider, such as running, maintenance, start-up and shut-down costs. However, it does get closer to minimizing overall costs than **Schedule 1**.

2.6 Energy Storage System

2.6.1 Resource

In order to determine the optimal type of energy storage, a generic energy storage system (ESS) was simulated with different combinations of power and capacity to find the optimal combination. The ratio of power to capacity was used to find an appropriate type of energy storage. The generic energy storage had an overall assumed efficiency of 81% and the capacity was not affected by the rate of discharge.

In addition to generic energy storage, a lead acid battery storage unit was simulated. The 2YS31P Surrette battery was used in the simulation (spec sheet in Appendix E). It was a 2 V cell and had a total of 2.4 kAh capacity at a 20 hour discharge rate (C/20). The energy efficiency of a lead acid battery can be defined as the product of its voltage efficiency and its coulomb efficiency (Masters, 2004), shown in Equation 2.13.

$$\eta_{energy} = \eta_{voltage} \cdot \eta_{coulomb} = \left(\frac{V_D}{V_C}\right)\left(\frac{I_D \Delta T_D}{I_C \Delta T_C}\right) \tag{2.13}$$

Where η_{energy} is the energy efficiency, $\eta_{voltage}$ is the voltage efficiency,$\eta_{coulomb}$ is the Coulomb efficiency, V_D is the voltage at which the battery discharges, V_C is the voltage at which the battery charges, $I_D \Delta T_D$ is the discharged Amp hours and $I_C \Delta T_C$ is the charged Amp hours.

The voltage efficiency relates the effect charging and discharging the battery at different voltages has on the overall energy efficiency. The higher the discharge current, the lower the discharge voltage will be, decreasing the voltage efficiency. This is modelled by having different effective battery capacities for different discharge currents. Table 2.4 shows the effective capacity of the 2YS31P battery normalized to its C/20 capacity for different discharge currents. These can also be considered as the voltage efficiencies for the different discharge currents. This was modelled in the simulation with Equation 2.14.

$$SOC(i+1) = SOC(i) - P_{dis}(i)\Delta t / \eta_{voltage} \tag{2.14}$$

Where $SOC(i+1)$ is the state of charge of the next time step, $SOC(i)$ is the current state of charge, $P_{dis}(i)$ is the power being drawn from the battery at the current time step, Δt

Table 2.4: The effective capacity of the 2YS31P battery, normalized to the capacity at C/20, for different discharge currents. This is derived from the spec sheet in Appendix E.

Discharge rate [hr]	20	15	12	10	8	6	5	4	3	2	1
Normalized capacity ($\eta_{voltage}$)	1	0.94	0.90	0.85	0.8	0.74	0.7	0.65	0.6	0.51	0.36

is the length of the time step in hours and $\eta_{voltage}$ is the voltage efficiency taken from Table 2.4 for the current discharge power.

The maximum discharge current was set to be C/3 and the maximum depth of discharge (DOD) was set to 80%.

The Coulomb efficiency results from the electrolysis of the water during charging and the gassing that results during which some of the charging electrons escape with the gasses. At a low state of charge (SOC) the Coulomb efficiency is close to 100%, but can drop to below 90% during the final stages of charging. A typical Coulomb efficiency is 90% (Masters, 2004).

One way to reduce the gassing and keep the battery temperature within acceptable limits is to decrease the maximum charging current with increasing state of charge. A rule of thumb for valve regulated lead acid batteries is that the battery can accept a current resulting in a 1 hour charge time for the given SOC (C&DTechnologies, 2012). For example, a completely discharged 100 Ah battery could be charged at 100 A, at 50% SOC it could be charged with 50 A and at 90% SOC it could be charged with 10 A. The maximum charging current was determined this way in the simulation and an efficiency of 90% was used (see Appendix B for examples of charging sequences). Equation2.15 shows the relation between the SOC and the charging power.

$$SOC(i+1) = SOC(i) + P_{ch}(i)\Delta t/\eta_{coulomb} \tag{2.15}$$

Where P_ch (i) is the current charging current and $\eta_{coulomb}$ is the Coulomb efficiency which is assumed to be 90%.

2.6.2 Schedule

This section describes how the ESS was scheduled in the simulations. The role of the ESS was to allow smaller diesel generating options to remain online by delaying the switching to larger capacity options. A diesel generating option with a lower MOL allows a greater import of wind energy into the grid. The diesel **Schedule 1** (Section 2.5.3.2) was used when simulating ESS in the system.

The same ESS schedule was used for each simulation, as described in Section 2.6.2.1. However, three different variations on the interaction between the ESS schedule and the diesel schedule were simulated, as described in Sections 2.6.2.2–2.6.2.4. They differ in the following two areas:

- What to do when the ESS begins to discharge

- The criteria for choosing the next diesel generating option

2.6.2.1 ESS schedule

Allowing a smaller diesel generating option to stay online was achieved by allowing the ESS to supply part of the spinning reserve capacity (SRC). In other words, if the capacity of the online diesel generating option was too small to cover the SRC and if the state of charge and power capabilities of the ESS were sufficient, instead of switching to a larger capacity generating option, the ESS would cover the remaining SRC. To cover a portion of the SRC, the ESS must have the necessary power capabilities and enough charge to sustain that discharge power for a least one 10 minute time step.

Figure 2.17 shows figuratively when the ESS must provide SRC into the grid, and when the ESS must also discharge. In the scenario on the left, the ESS does not need to discharge as long as the diesel generating capacity and the wind power can supply the difference between the load and the geothermal power. It must supply the required SRC for the wind import and load which is not covered by the diesel generator. The following equation shows the relation between the SRC supplied by the ESS ($SRC_{wind,ESS} + SRC_{load,ESS}$), diesel generating capacity (CAP_{diesel}), load (P_{load}), geothermal power (P_{geo}) and SRC required for the load (SRC_{load}):

$$SRC_{wind,ESS} + SRC_{load,ESS} = P_{load} + SRC_{load} - P_{geo} - CAP_{diesel} \tag{2.16}$$

If the ESS is unable to supply the required SRC, then a larger capacity diesel generating option must be brought online. This will raise the MOL. If the difference between the load, geothermal power and the MOL is less than the current wind production, then the excess wind power will have to be diverted.

In the scenarion on the right, the sum of the wind power generation (P_{wind}) and the diesel output (P_{diesel}) no longer add up to the difference between the load (P_{load}) and geothermal power (P_{geo}). In this case the diesel generating option is operating at full capacity, and the ESS must discharge to supply the difference ($P_{discharge}$), as shown in the following equation:

$$P_{discharge} = P_{load} - P_{geo} - P_{diesel} - P_{wind} \tag{2.17}$$

If a larger diesel generating option was brought online at this point, then no wind energy would be diverted, since the difference between the load, geothermal power and the MOL will not be less than the current wind production. In the long run, it reduce the diversion of wind energy when the wind generation increases again, by reducing the need to bring a smaller capacity generating capacity online in the future. Advantages of allowing the ESS to discharge instead of bringing a new diesel generating option online are to reduce diesel switching as well as displacing diesel generator output. The disadvantage of discharging is that the SOC of the ESS will decrease, lowering the amount of SRC it is able to supply to the grid until it is recharged.

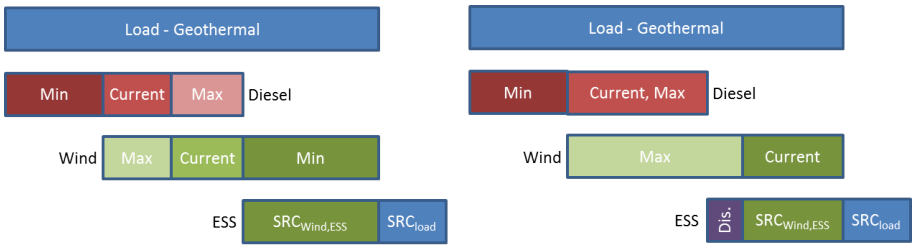


Figure 2.17: The scenario on the left shows a situation where the ESS is supplying SRC without discharging. The scenario on the right shows a situation where the ESS needs to discharge.

2.6.2.2 ESS-Diesel Schedule 1

ESS-Diesel Schedule 1 (**EDS1**) was the initial schedule used when integrating ESS into the simulations. The only change made to the base diesel schedule was to include the charging of the ESS with excess RE as an event which would trigger the diesel shedule. This was because using the RE to supply the load was a more optimal use than using it to charge the ESS. Thus, the set of events which would initiate the diesel schedule were as follows:

- The SRC in the system was less than what was required
- The diesel generators were operating below their MOL
- Renewable energy was being diverted
- Renewable energy was being used to charge the ESS

The ESS was allowed to discharge as long as it was required by the online diesel generating option. When the SOC of the ESS became too low, it would not be able to supply the required SRC, which would trigger the diesel schedule. The criteria for choosing potential diesel generating options remained the same as described in Section 2.5.3.1.

2.6.2.3 ESS-Diesel Schedule 2

ESS-Diesel Schedule 2 (**EDS2**) was the same as **EDS1**, except that it added a modification to the criteria for choosing potential diesel generating options as described in Section 2.5.3.1. Instead of requiring the diesel generating option to be able to supply all of the SRC, the ESS, based on its available power and capacity, was able offset the amount of SRC that the diesel generating option was required to be able to cover. The new criteria for choosing potential diesel generating options were as follows:

1 The load ($P_{Load}(i)$) was not less than the MOL ($P_{MOL,n}$) of the generating option n:

$$P_{Load}(i) >= P_{MOL,n} \tag{2.18}$$

2 The capacity of generating option n ($P_{Cap,n}$) could supply the difference between the load ($P_{Load}(i)$) and the RE import ($P_{import}(i)$) as well as the difference between the SRC ($P_{SRC}(i)$) and the maximum possible ESS contribution towards the SRC ($P_{max,ESS}$):

$$P_{Cap,n} >= P_{Load}(i) + P_{SRC}(i) - P_{import}(i) - P_{max,ESS} \tag{2.19}$$

3 Switching to the new combination would not switch off diesel generators that have not yet run for their minimum operating time (MOT)

2.6.2.4 ESS-diesel schedule 3

ESS-diesel schedule 3 (**EDS3**) was the same as **EDS2**, except that it added ESS discharging as a even which would intiate the diesel schedule. The resulting events which would trigger the diesel schedule were as follows:

- The SRC in the system was less than what was required
- The diesel generators were operating below their MOL
- Renewable energy was being diverted
- Renewable energy was being used to charge the ESS
- The ESS was discharging

EDS1 and **EDS2** allow the ESS to discharge as long as the diesel generating option has insufficient capacity to meet the load, while staying below the maximum discharge power and maximum DOD.

The goal of the ESS was to allow a smaller capacity diesel generating option to remain online in order to allow a higher import of RE into the grid. As described in Section 2.6.2, discharging the ESS to supply the difference not supplied by the online diesel generating option did not directly increase the import of wind energy, and had the potential to lower the import of wind energy into the grid by discharging the ESS and reducing the amount of SRC it could supply until it was recharged. Advantages of allowing the ESS to discharge included displacing diesel generator output and potentially reducing diesel swithching. Both **EDS3** and **EDS2** were simulated to determine which schedule performed better in different scenarios.

2.7 Simulation flow

This section describes the chronological sequence of the energy balance performed at each 10 minute interval of the simulation (see Figures 2.1 and 2.2).

RE import: The first step was to determine how much renewable energy could be imported into the grid, which depended on the current load demand and combination of diesel generators online. The maximum import of power (P_{limit}) into the grid was the difference between the current load (P_{load}) and the MOL of the current online combination of diesel generators (P_{MOL}), shown in Equation 2.20.

$$P_{limit}(i) = max(P_{load}(i) - P_{MOL}(i), 0) \tag{2.20}$$

ESS charging: Surplus energy generation from the renewables charged the ESS, up to the maximum allowed charging current. The battery was not allowed to charge above its rated capacity.

RE diversion: If there was wind (P_{wind}) or geothermal (P_{geo}) power that was not imported to the grid (P_{import}), or used to charge the ESS (P_{ch}), it had to be diverted (P_{div}), as shown in Equation 2.21

$$P_{div}(i) = max(P_{wind}(i) + P_{geo}(i) - P_{import}(i) - P_{ch}(i), 0) \tag{2.21}$$

ESS covering SRC: If the online diesel generating capacity could not supply the difference between the load and the import of RE as well as the SRC, the ESS would supply up to the entire SRC, depending on its capabilities.

ESS discharging: If the diesel generators could not supply the difference between the load and the imported RE, then the ESS discharged up to its full capability to make up the difference.

ESS SOC: The state of charge of the energy storage for the next time step was calculated with Equations 2.15 and 2.14. For generic ESS, $\eta_{coulomb}$ and $\eta_{voltage}$ were set to 90%.

Diesel generator output: The diesel generators supplied the difference between the load (P_{load}), RE import (P_{import}) and ESS discharge (P_{dis}), as shown in Equation 2.22.

$$P_{diesel}(i) = P_{load}(i) - P_{import}(i) - P_{dis}(i) \tag{2.22}$$

Diesel scheduling: The diesel schedule was intitiated by one of the events listed in Sections 2.5.3.1, 2.6.2.2, 2.6.2.3 and 2.6.2.4, depending on the use of ESS in the grid. The potential diesel generating options were determined by the criteria listed in those same sections. Finally, one of the diesel schedules listed in Sections 2.5.3.2 and 2.5.3.3 were performed on the potential diesel generating options to find the most optimal.

Chapter 3

RESULTS

This section presents the results of the simulations. Sections 3.1 and 3.2 compare diesel schedules **Schedule 1** and **Schedule 2** with no ESS. Then, results of simulations using a generic ESS with ESS-diesel schedules **EDS1**, **EDS2** and **EDS3** in Sections 2.6.2.2, 2.6.2.3 and 2.6.2.4. Finally, results for simulations using a lead acid ESS with ESS-diesel schedule **EDS1** was presented in Section 3.4.

3.1 Diesel Schedule 1, No Energy Storage System

This section presents the results of the simulation for different diesel (Table 2.3) and geothermal scenarios in which diesel schedule **Schedule 1** (Section 2.5.3.2 and no ESS were used. The first section discusses how much diesel generator output was displaced and how much renewable energy was diverted under geothermal integration scenarios from 0 MW to 5.5 MW. Section 3.1.2 discusses how the diesel generator operation was affected. An overview of the results for the different scenarios with 2 MW geothermal capacity is presented in Section 3.1.3, and a summary is presented in Section 3.1.4.

3.1.1 Diverted renewable energy and displaced diesel output

This section presents the results of the simulation for diverted renewable energy and displaced diesel generator output for the simulated scenarios. Diverted renewable energy can be split into diverted wind and diverted geothermal energy. Since the geothermal power source is assumed not to load follow, wind energy is diverted first. Geothermal power is only diverted when the maximum RE import into the grid is less than the geothermal power output. Figure 3.1 shows the diverted wind energy per year (+) and the diverted geothermal energy per year (o) for different levels of geothermal power output, where the colors represent the different diesel scenarios as described in Table 2.3.

A key result is that there is a critical level of geothermal capacity at which there is a significant increase in the diversion of geothermal energy, around 2.5 MW for diesel **Cases 1** and **2** and around 3 MW for **Cases 3** and **4**. Figures 3.2 and 3.3 show that at 2.5 MW and 3 MW of geothermal capacity, the load on the diesel generators begins to fall below the MOL of the smallest available diesel generating option, which explains the increase in diverted geothermal energy.

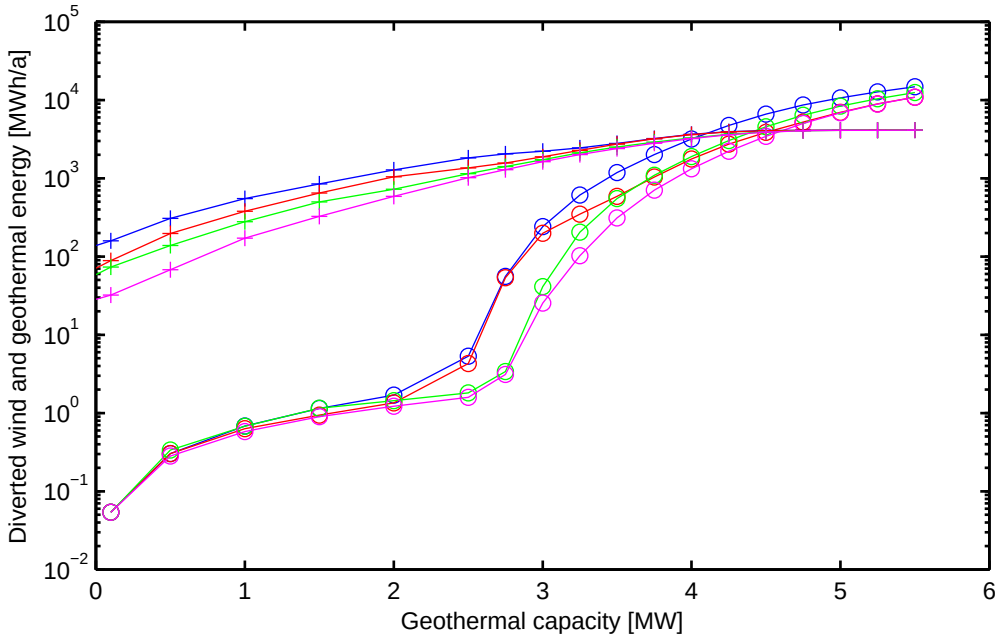


Figure 3.1: Diverted wind energy (+) and geothermal energy (o). Different diesel scenarios are represented by the different colors and outlined in Table 2.3. The y axis is a log scale.

Figure 3.2 shows the operating bounds for the diesel generating options for **Case 1**. The upper limit (brown bar) is the difference between the combined capacity of the generating option and the SRC required to cover the load (0.25 MW). This is the upper limit because the diesel generators are required to maintain at least enough surplus capacity to supply the SRC to cover the load.

The lower limit (blue bar) is the MOL of the generating option. The blue line represents the load and the red line represents the difference between the load and the output of a 2.5 MW geothermal plant over a two year time span. With 2.5 MW of geothermal in the grid, this is the amount that must be covered by the diesel generators, by actively supplying what is not supplied by wind power and maintaining enough SRC to cover what is supplied by wind power.

With 2.5 MW of geothermal, the load that must be covered by the diesel generators begins to go below the MOL of the smallest diesel generating option. At this point, geothermal energy must begin to be diverted to allow the diesel generators to operate within their bounds. Figure 3.3 shows the same for diesel **Case 4** with 3 MW of geothermal capacity. Diesel **Case 4** has two additional diesel generators compared to **Case 1** and many more generating options.

Thus, the more diverse diesel fleets allowed for a higher integration of geothermal into the grid without diverting a significant amount. Diesel **Cases 2** and **3** have the same number of generating options, but the 0.4 MW unit of **Case 2** is too small to act as a stand alone generating option except for extremely small loads, thus **Case 3** effectively has the lowest possible MOL with the 1 MW generator.

With the high levels of geothermal diversion above 2.5 and 3 MW capacity, a solution beyond what is presented in this section would have to found to deal with the diverted energy. This could involve a controllable load that could accept the excess energy, or an

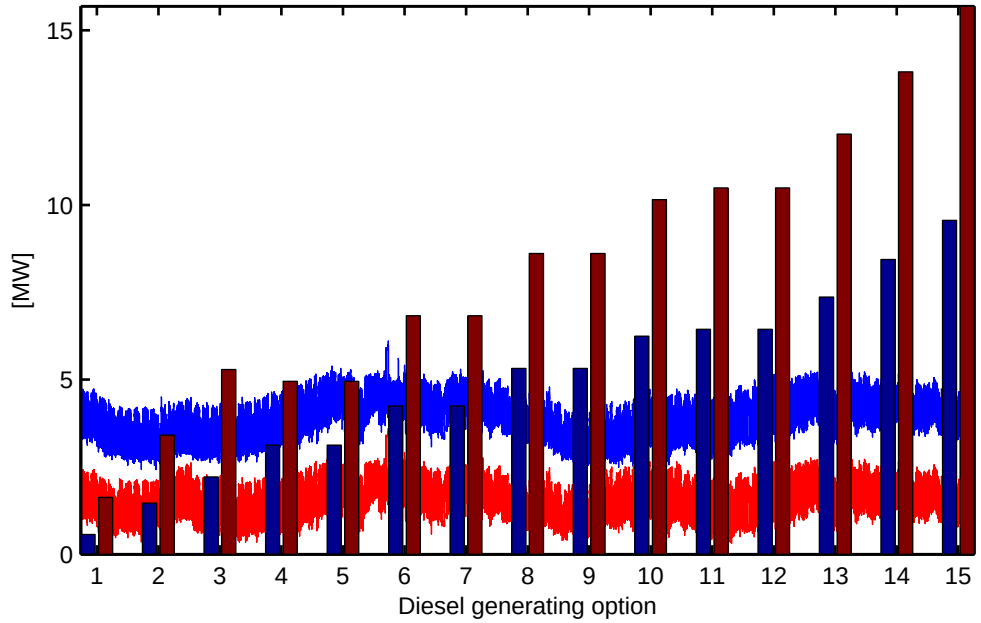


Figure 3.2: The bar graph shows the upper and lower operating limit for each of the diesel generating options for diesel **Case 1**. The brown bars represent the difference between the capacity of the generating option and the SRC required for the load (0.25 MW). The blue bars represent the MOL of the diesel generating option. The blue line represents the load, and the red line represents the difference between the load and the output of the geothermal plant with a 2.5 MW capacity.

engineered solution that would allow the geothermal power source to load follow. As a result, geothermal outputs of 0 to 2.5 MW are the focus of this section.

Another result is that adding diesel generators can significantly decrease the amount of wind energy diversion for a given level of geothermal power. For example, at 2 MW of geothermal capacity, there is a total diversion of 1254 MWh for **Case 1**, 1018 MWh for **Case 2**, 692 Wh for **Case 3** and 576 MWh for **Case 4**. Thus, **Case 3** and **Case 4** have about half the total diversion of renewable energy compared to **Case1**.

Figure 3.4 shows the diverted wind energy and the displaced diesel output for geothermal capacities up to 2.5 MW. At these levels of geothermal capacities, due to low levels of geothermal diversion, wind diversion can be assumed to represent the entire diversion. The diversion of wind energy increases with a predominantly quadratic slope for increasing geothermal output. The displaced diesel increases with a predominantly linear slope for increasing geothermal output. The displaced diesel output is one order of magnitude greater than the diversion of wind energy.

The energy balance in Equation 3.1 is used to determine the relationship between the diesel generator output (E_{DEG}), wind energy (E_{WTG}), load (E_{load}), diverted wind energy (E_{div}) and average geothermal power production ($\tilde{P}_{GTG}$) per year (8760 h):

$$E_{DEG} + E_{WTG} + 8760 \cdot \tilde{P}_{GTG} = E_{load} + E_{div} \tag{3.1}$$

Changing the value of $\tilde{P}_{GTG}$ changes the energy balance. The change in the energy balance is shown by Equation 3.2. E_{load} and E_{WTG} are not affected by a change in $\tilde{P}_{GTG}$ and thus cancel out:

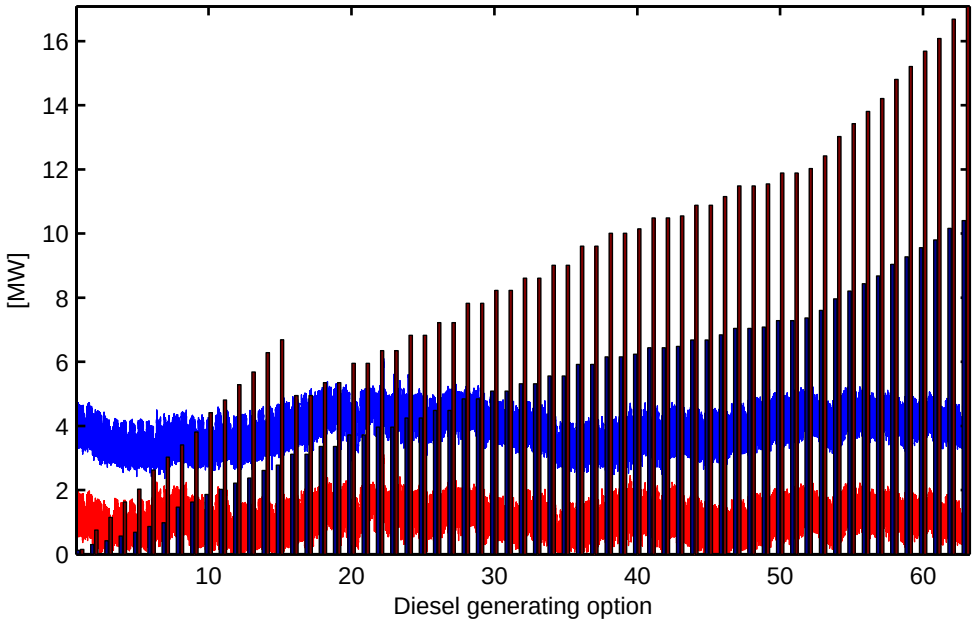


Figure 3.3: The bar graph shows the upper and lower limit for each of the diesel generating options for diesel **Case 4**. The brown bars represent the difference between the capacity of the generating option and the SRC required for the load (0.25 MW). The blue bars represent the MOL of the diesel generating option. The blue line represents the load, and the red line represents the difference between the load and the output of the geothermal plant with a 3 MW capacity.

$$\Delta E_{DEG} + 8760 \cdot \tilde{P}_{GTG} = \Delta E_{div} \tag{3.2}$$

If the base case scenario had no geothermal production, then $\tilde{P}_{GTG_0} = 0\,MW$ and $\Delta\tilde{P}_{GTG} = \tilde{P}_{GTG}$. Displaced diesel generator output resulting from adding geothermal production equals a negative change in diesel generator output; $E_{disp} = -\Delta E_{DEG}$. Equation 3.3 results from substituting these definitions into Equation 3.2:

$$E_{disp} + \Delta E_{div} = 8760 \cdot \tilde{P}_{GTG} \tag{3.3}$$

Based on Equation 3.3, the total displaced diesel generator energy and the increase in wind energy diversion should add up to a linear line with a slope of 8760 h as a function of the average geothermal power. This relationship holds true for each diesel case listed in Table 2.3 and is shown in the Figure 3.5, where E_{disp} (o) and $E_{disp} + \Delta E_{div}$ (+) are plotted against $\tilde{P}_{GTG}$ for the different diesel cases. $E_{disp} + \Delta E_{div}$ have a slope of 8760 h as expected, while the slopes of E_{disp} are the differences between 8760 h and the increased diversion of renewable energy.

For geothermal capacities up to 2.5 MW, the diversion of renewable energy is almost entirely wind energy and has a quadratic slope, as shown in Figure 3.4. Thus, for 0 to 2.5 MW of geothermal capacity, the difference between the generated geothermal energy ($8760 \cdot \tilde{P}_{GTG}$) and displaced diesel output (E_{disp}) increases quadratically and represents a diminishing return for increasing geothermal output.

At geothermal capacities above 2.5 MW, geothermal as well as wind energy are diverted in significant amounts. Thus the difference between the generated geothermal energy

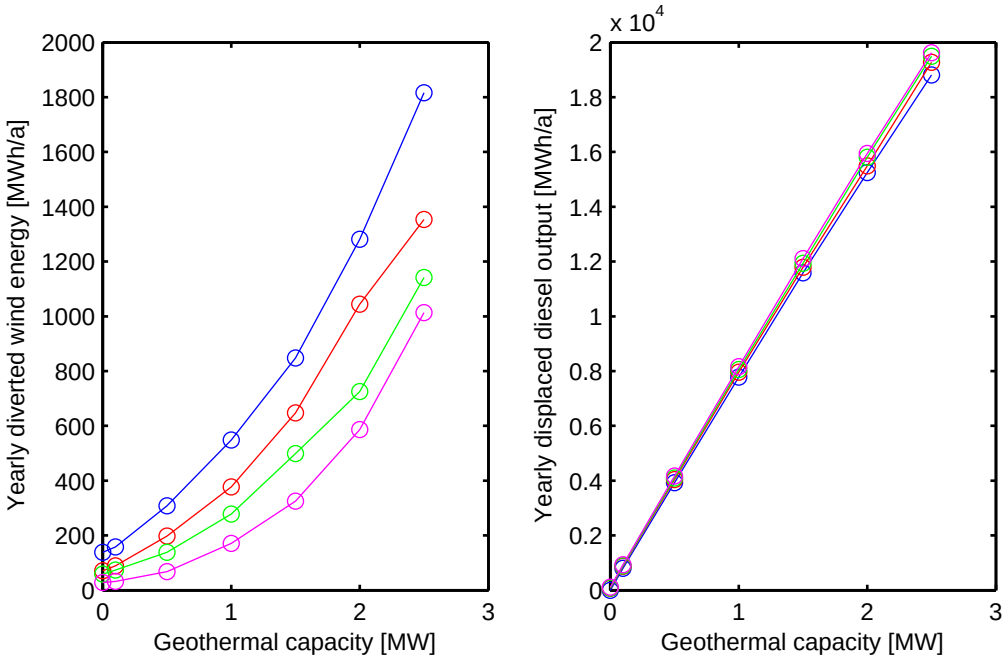


Figure 3.4: Displaced diesel generator output and diverted wind energy per year. The different colors represent difference diesel scenarios, outlined in Table 2.3. The scale of the y axis for displaced diesel generator output is one order of magnitude greater than the diverted wind energy.

and displaced diesel output increases at a quicker rate, with the displaced diesel output eventually leveling off at a maximum value.

3.1.2 Diesel operation

In the current grid setup, the diesel generators are the prime movers. They are responsible for supplying the difference between the load and the import of renewable energy, maintaining the frequency and voltage within acceptable limits and supplying the spinning reserve capacity (SRC). The diesel generators must be operated within specified bounds (Table 2.2). Adding a new energy source into the grid changes how the diesel generators will operate. It is important that the operation of the diesel generators stays within the operating bounds. Also, within the operating bounds, there are optimal and suboptimal regions of operation with regard to single unit efficiency and stress.

Figure 3.6 shows the average loading[1] of diesel generators for different levels of geothermal capacity. The different color lines represent the different diesel scenarios outlined in Table 2.3. Diesel generators must be operated over a certain minimum optimal loading (MOL) (see Table 2.2), and tend to operate most optimally (with respect to efficiency and reduced stress) between 50 and 90% (see Figure 2.16).

The average loading of diesel generators decreases with increasing geothermal capacity. Each scenario has the same amount of wind energy production. However, with a higher geothermal capacity, smaller capacity diesel generating options are being run (Figure 3.9). This effectively raises the wind penetration with respect to the diesel generators

[1] Loading refers to the output of the diesel generator divided by its capacity.

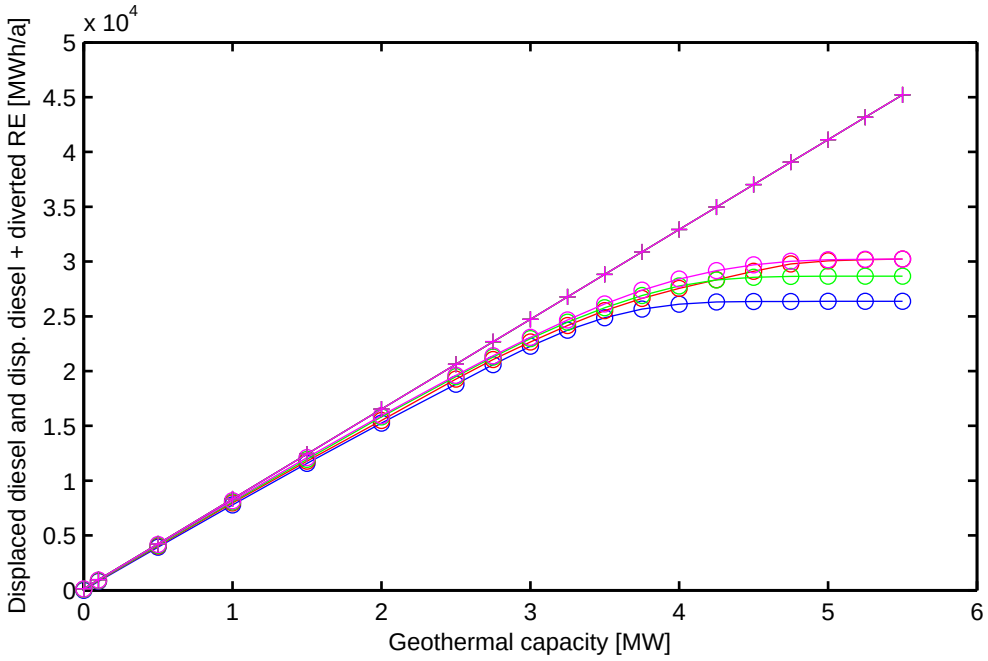


Figure 3.5: Displaced diesel generator output (o) and the sum of the displaced diesel generator output and diverted renewable energy (+). The different colors represent the different diesel scenarios, outlined in Table 2.3. The sum of the displaced diesel generator output and diverted renewable energy (+) for each diesel scenario is identical with a slope of 8760 h.

and causes them to run at a lower loading in order to accept more wind energy into the grid.

Up to 2.5 MW of geothermal capacity (at which significant diversion of geothermal energy begins), the average loading stays above 48%, which is within the optimal range of a diesel generator. This is the average loading, so there will be times when the diesels are operating in a suboptimal region. At high levels of geothermal capacity, the average loading of the diesel generators levels out at 30%. This is the MOL of the smallest diesel generator, which is the only diesel generator running at that point.

A more diverse diesel fleet with more generating options results in a higher average loading. Table 2.3 summarizes the different diesel cases. **Case 2** and **Case 3** both have the same number of generating options, but **Case 3** has a more even step size in between the capacities of generating options. **Case 3** tends to result in a higher loading, which indicates an advantage of having a more even step size between diesel generator capacities to match a wide range of power demands.

There are levels of geothermal capacity at which **Case 2** results in a higher loading than **Case 3**; 1.5 MW for example. This is a level at which one generating option within **Case 1** matches the load well and the added 0.4 MW diesel generator of **Case 2** is used as a peaking unit.

The discontinuities in the slopes for the different diesel cases represent the transition from one predominant diesel generating option to another. The slope maxima (where the slope of the curve is less negative) represent points at which there is one predominant generating option which matches the load well. The slope minima represent transitions between predominant generating options. Diesel cases with a smaller overlap between

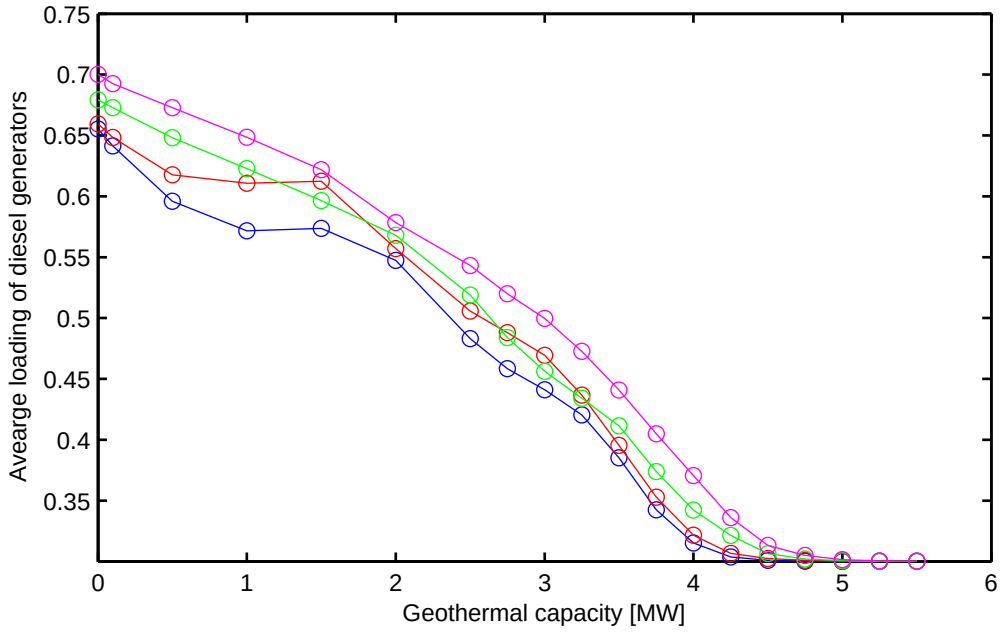


Figure 3.6: Average loading of diesel generators for different levels of geothermal output. The different colors represent different diesel scenarios (see Table 2.3).

the capacities of diesel generating options (**Cases 1** and **2**) have a longer transition period between predominant generating options and a more discontinuous slope. Thus, while for a wide range of power demands, an even step size between diesel generators results in an optimal loading of diesel generators, for a limited range of power demands (for example the power demand on the diesel generators for one level of geothermal capacity) this is not always the case, and the sizing of the diesel generators can be optimized for that specific scenario.

Figure 3.7 shows the number of changes in the online combination of diesel generators per year (diesel switching). According to Table 2.2, after being brought online, a diesel generator must run for a minimum on time (MOT) before being brought offline. However, ideally the diesel generators are being switched at a much lower frequency than indicated by the MOT. Switching diesel generators results in additional fuel consumption during diesel generator warm-up and cool-off and causes stress which increases maintenance costs.

Below 2.5 MW of geothermal capacity, diesel switching increases with increasing geothermal capacity. The increase in switching is due to the fact that the lower capacity diesel generating options have smaller operating ranges (see Figures 3.2 and 3.3), requiring an increase in switching to keep the diesel generators within their operating bounds.

Switching reaches a maximum just before the point where a significant amount of geothermal energy begins to be diverted. This corresponds to the point at which the load on the diesel generators begins to fall below the MOL of the generating options (see Figures 3.2 and 3.3). As the load decreases, there are less diesel generating options within range of the load resulting in less switching. The switching eventually goes to zero for very high levels of geothermal capacity, in which only the smallest diesel generating option is running. This corresponds to Figure 3.6, where at high levels of geothermal capacity only the smallest diesel generating option is running at its MOL.

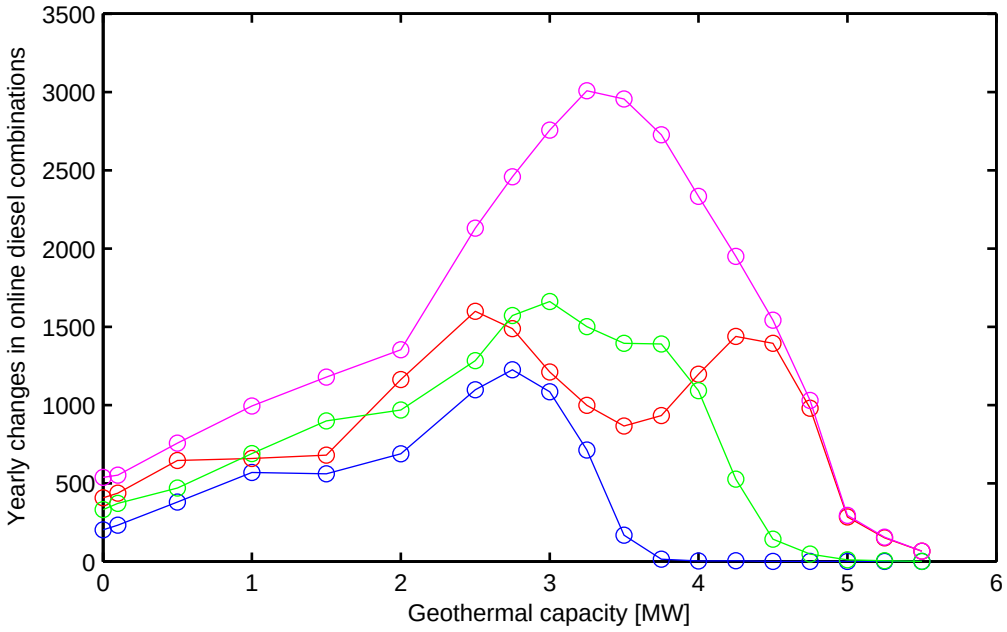


Figure 3.7: The number of changes in the online combination of diesel generators per year. The different colors represent different diesel scenarios (see Table 2.3).

The diesel cases with the more diverse diesel fleets tend to have more diesel switching. This is partly a result of the diesel schedule, where the cost of switching is not taken into account. When there are more diesel generating options available, more switching will occur to match the best one to the load. Switching should not go above 4–6 times a day, or 1460–2190 times per year. Note that switching refers to changes in the online combination of diesel generators, not of individual generators. Individual switching counts will be less.

If Nome was to implement a solution where a high level of switching is indicated, a change to the diesel schedule would be needed to take into account the cost of switching. Reducing the switching will also reduce some of the benefits of a more diverse diesel fleet including the higher loading of diesels, reduced diversion of RE and increased displaced diesel output.

There are discontinuities in the slope of diesel switching for different geothermal capacities. For diesel **Case 1** (blue) and **2** (red), there are slope minima at 1.5 MW of geothermal capacity. These correspond to slope maxima for the average loading of diesel generators (see Figure 3.6). Again, these points correspond to predominant diesel generating options which match the demand well. Since for diesel **Case 1** and **2**, the operating ranges of the different generating options have less overlap than for **Case 3** and **4**, they are less likely to switch to a different generating option, resulting in less switching. Thus, the slope maxima and minima of diesel switching tend to line up with the slope minima and maxima of the average diesel generator loading, respectively.

Figure 3.8 shows the run time of each diesel generator per year for different levels of geothermal capacity and different diesel cases (see Table 2.3). The color of the lines representing the diesel generators (Table 2.2), which from smallest to largest capacity are: G1 (blue), G2 (red), G3 (green), G4 (purple), G5 (black) and G6 (light blue).

With increasing geothermal capacity, there is a transition from larger diesel generators to smaller diesel generators. Figure 3.9 shows the decrease in the average capacity of

online diesel generators with added geothermal capacity, corresponding to the decrease in the load supplied by the diesel generators. The more diverse diesel fleets tend to have a smaller online capacity. This corresponds with the higher loading shown in Figure 3.6.

With diesel schedule **Schedule 1** generators G5 and G6 (both 5.2 MW units) are never used. This is because the MOL of G5 and G6 is 60%, compared to 40% and 30% for the other diesel generators, and the goal of **Schedule 1** was to minimize the MOL of the online diesel generating option to maximize the import of RE. G5 and G6 are represented as generating options 4 and 5 in Figure 3.2 and 16 and 17 in Figure 3.3. The relatively high MOL compared to other generating options is apparent from these figures. Thus for diesel **Case 1** (top left plot), only two diesel generators are used.

Geothermal capacities at which there are predominant diesel generating options can be seen. At 0 MW geothermal capacity, G3 and G4 run together most of the year. At 1.5 MW of geothermal capacity, there is a near minima in the run time of G3 while G4 still runs most of the year. This corresponds to where G4 runs by itself for most of the year. At around 3.5 MW of geothermal capacity, only G3 runs. These points represent where the operating range of a diesel generating option matches the demand well and runs most of the year. These points correspond to maxima of the slope for the average loading curve in Figure 3.6 and minima of the slope for the diesel switching curve in Figure 3.7 for diesel **Case 1**. Between these points, there are transitions between predominant generating options. The same can be observed for the other diesel cases, where more diesel generators result in more and less noticeable transitions.

3.1.3 2 MW geothermal scenario

Table 3.1 outlines the results of the simulations for 2 MW of geothermal capacity and different diesel scenarios. With the current diesel fleet, a reduction of 15,300 MWh of diesel generator output is possible. By upgrading to diesel **Case 3** or **4**, an additional 500 to 600 MWh of diesel generator output can be displaced. As well as increasing the displaced diesel generator output and reducing the diversion of RE, the diesel generators will operate at a slightly higher loading, though not enough to notice much of a difference in the operation of the diesel generators. There will also be more diesel switching, which comes with additional fuel and maintenance costs. For **Case 1**, the online diesel generating option changes around 2 times a day. For **Case 4** it changes 3 to 4 times a day.

3.1.4 Summary

In this section, the results of the simulations for diesel **Schedule 1** and no ESS were presented. It was found that at a certain geothermal capacity, around 2.5 MW, there was a drastic increase in the diversion of geothermal energy. This was a result of the load on the diesel generators (the difference between the load and geothermal power) falling below the MOL of diesel generating options. Having a more diverse diesel fleet increased the geothermal capacity at which this occurred by adding diesel generating options with a lower MOL.

For levels of geothermal up to 2.5 MW, increasing geothermal capacity:

- Displaced diesel generator output in a linear fashion

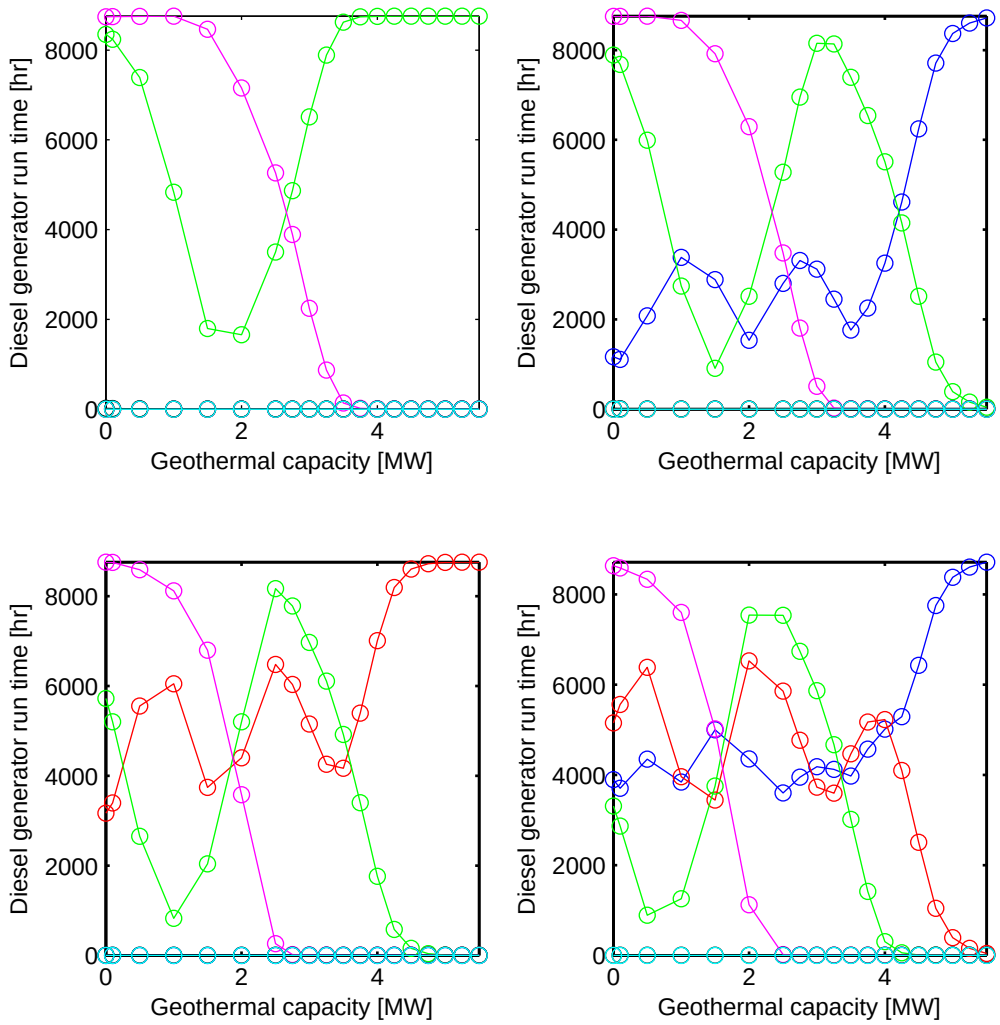


Figure 3.8: The run time of diesel generators. The lines represent the diesel generators (see Table 2): G1 (blue), G2 (red), G3 (green), G4 (magenta), G5 (black) and G6 (cyan). The different plots represent different diesel cases (see Table 3): Top left: Diesel Case 1, Top right: Diesel Case 2. Bottom left: Diesel Case 3. Bottom right: Diesel Case 4.

- Increased the diversion of RE in a quadratic fashion
- Increased the switching of diesel generators
- Reduced the loading on diesel generators

Adding diesel generators for a more varied fleet:

- Reduced the diversion of RE
- Displaced diesel generator output
- Increased the loading on the diesel generators
- Increased the switching of the diesel generators

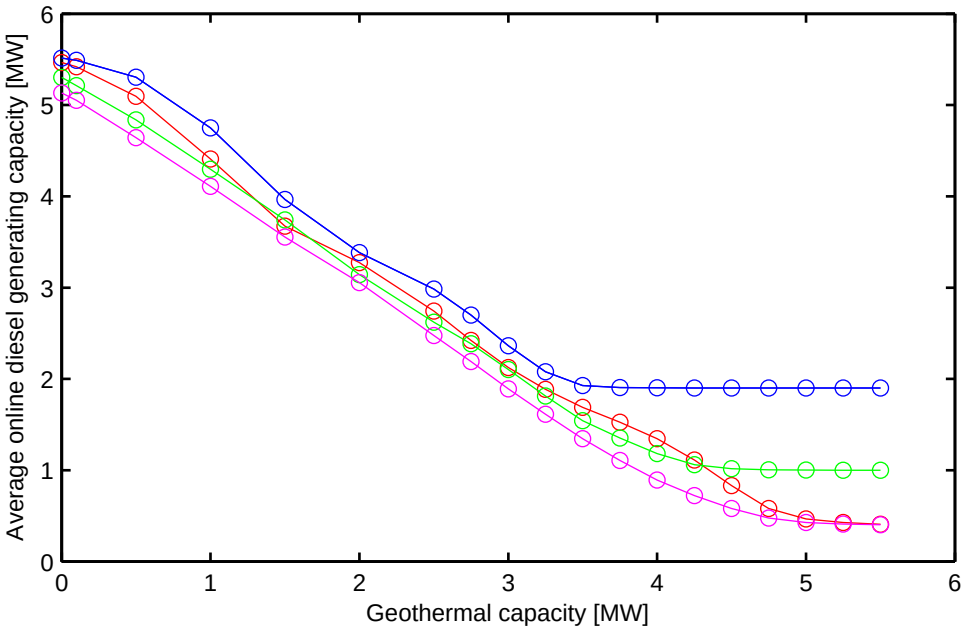


Figure 3.9: Average capacity of online diesel generating options. The different colors represent different diesel scenarios (see Table 2.3).

Table 3.1: Simulation results for 2MW of geothermal capacity and different diesel scenarios.

Diesel Scenario	**Displaced diesel output [MWh]**	**Diverted Wind [MWh]**	**Diverted geothermal [MWh]**	**Average diesel loading [%]**	**Yearly Diesel switching**
Case 1	15,300	1,252	1.42	54.7	689
Case 2	15,500	1,017	1.36	55.7	1162
Case 3	15,800	691	1.29	56.8	968
Case 4	15,900	575	1.21	57.9	1353

The increase in diesel switching and decrease in diesel loading were found to be a result the reduced operating ranges of the smaller capacity diesel generating options which were run with higher levels of geothermal capacity. The switching began to decrease after the load on the diesel generators began to fall below the MOL of the diesel generating options, due to there being less generating options within range of the load. This is also the point at which significant amounts of geothermal began to be diverted.

Maxima of the slopes for average diesel generator loading and minima of the slopes for diesel switching correspond to points at which there was one predominant diesel generating option which matched the load well. This resulted in less switching to other generating options. Maxima were especially apparent in diesel cases with fewer generating options which had less overlap between their operating ranges.

3.2 Diesel Schedule 2, No Energy Storage System

The goal of **Schedule 1** was to maximize the amount of renewable energy imported into the grid. This also resulted in minimizing the electrical output of the diesel generators (according to Equation 3.3). However, it did not necessarily minimize the amount of diesel consumed. This is because **Schedule 1** did not take into account the efficiency at which the diesel generators were running or the diesel consumed while switching.

Schedule 2 tried to minimize the diesel consumption. Minimizing diesel consumption does not minimize overall cost, as there are costs other than diesel consumption to consider. However, it does result in a lower cost solution than maximizing RE import. While the goal of this schedule was to minimize diesel consumption, it can only give an approximation to the solution with the lowest diesel consumption. This is because certain assumptions need to be made about the future operation of the grid.

The p.u. diesel efficiency curve used in the schedule is shown in Figure 2.16. This is a generic efficiency curve and is not the result of measurements of the actual diesel generator performance or from their manufacturer specifications. The diesel efficiency curves were scaled by a maximum efficiency, listed in Table 2.2, which reflects the observed performance of the generators in the grid. Table 2.2 also gives the diesel consumption of the generators while warming up or cooling off, which is used to calculate the cost of diesel switching. This information is used to predict which diesel generating option will result in the highest overall diesel efficiency using Equation 2.12.

Figure 3.10 shows the average operating efficiency of the diesel generators for **Schedule 2** (o) compared to **Schedule 1** (+). There is a significant increase in diesel efficiency for **Schedule 2** compared to **Schedule 1** for geothermal capacities up to 2 MW. This is a result of increasing the usage of diesel generators G5 and G6 (see Figure 3.15) which have the highest efficiency with a maximum of 42% compared to 34% for the other generators (see Table 2.2). G5 and G6 also have the highest capacity at 5.2 MW and the highest MOL. Because of the high MOL of G5 and G6, they were never used in **Schedule 1**. The actual average capacity of the online diesel generating option either did not change or went down a little compared to **Schedule 1**, as shown in Figure 3.16, while the average loading stayed the same or went up, as shown in Figure 3.11.

Since diesel generating options with a higher MOL are being run, one would expect an increase in diverted wind energy compared to **Schedule 1**. This is shown in Figure 3.12, where there is a significant increase in diverted wind energy below 2 MW of geothermal capacity for **Schedule 2**. Since diverted RE and displaced diesel generator output are inversely related, this means the diesel generators are supplying more of the load in **Schedule 2** than in **Schedule 1**. However, the gains made in diesel efficiency are enough that the diesel consumption actually decreases in **Schedule 2**, as shown in Figure 3.13.

Figure 3.14 shows the diesel switching for **Schedule 1** and **Schedule 2**. Below 2 MW of geothermal capacity there is an increase in diesel switching for **Schedule 2** compared to **Schedule 1**, but not to a suboptimal amount. At the very high levels of switching for diesel **Case 4**, **Schedule 2** reduces switching compared to **Schedule 1**, but not to an acceptable level of switching below 2200 times per year and preferably under 1500 times per year. Thus, to implement these scenarios, an additional cost would need to be assigned to switching in the diesel schedule, besides just the fuel cost.

The results of the simulations for **Schedule 2** are very dependent on the efficiency curves

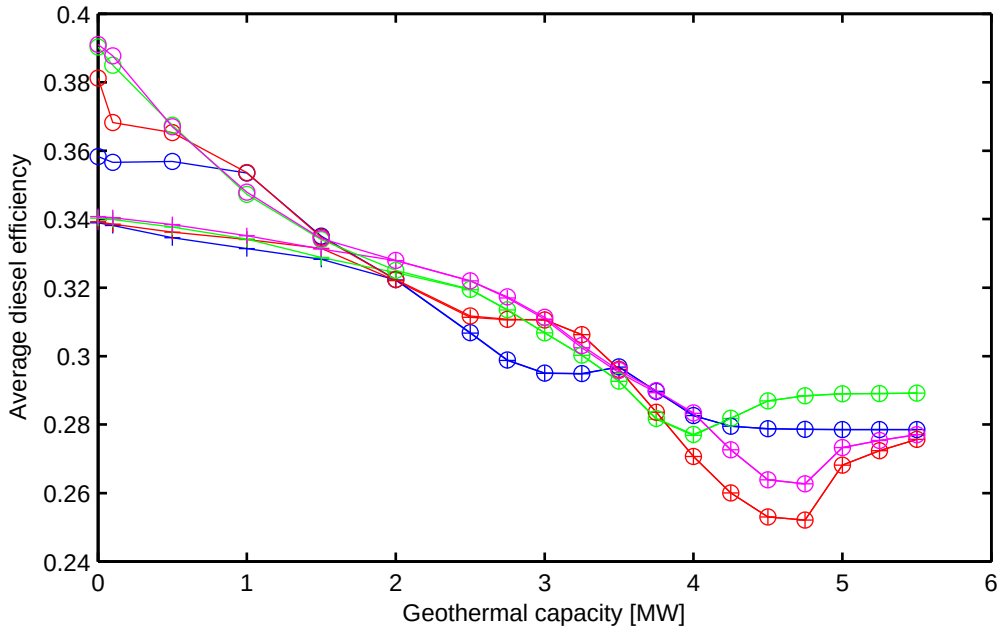


Figure 3.10: Average efficiency of Diesel Generators for diesel schedules Schedule 1 (+) and Schedule 2 (o). The different colors represent different diesel scenarios (see Table 2.3).

and diesel operating parameters (such as MOL) used. However, they give an indication of the fuel savings possible by using a more detailed diesel schedule. The greater the differences between the efficiencies, MOLs and warm-up and cool-down fuel consumptions of the diesel generators are, the greater the diesel savings resulting from **Schedule 2** compared to **Schedule 1** will be.

After 2 MW of geothermal capacity, **Schedule 1** and **Schedule 2** produce essentially the same results. Thus, when considering the 2 MW geothermal scenario, there is no added advantage to **Schedule 2**. However, without the addition of geothermal energy, significant fuel savings are possible by using **Schedule 2** compared to **Schedule 1**. With no changes to the diesel fleet, 117,000 gal of diesel savings are projected. If the 0.4 MW black start unit is added to the main fleet, 255,000 gal of diesel savings are projected.

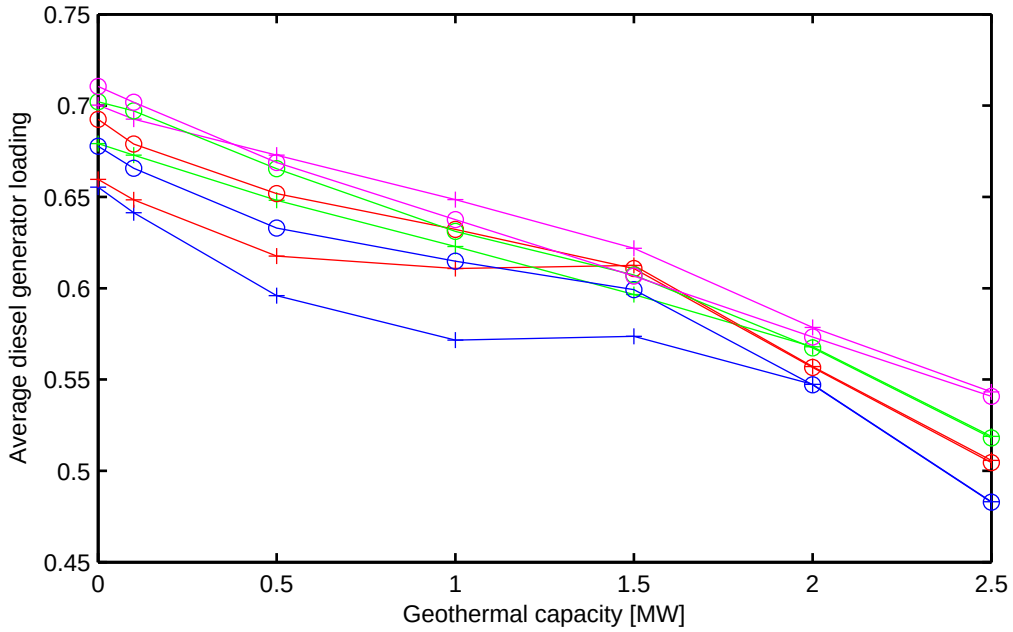


Figure 3.11: Average loading of diesel generators for diesel schedules Schedule 1 (+) and Schedule 2 (o). The different colors represent different diesel scenarios (see Table 2.3).

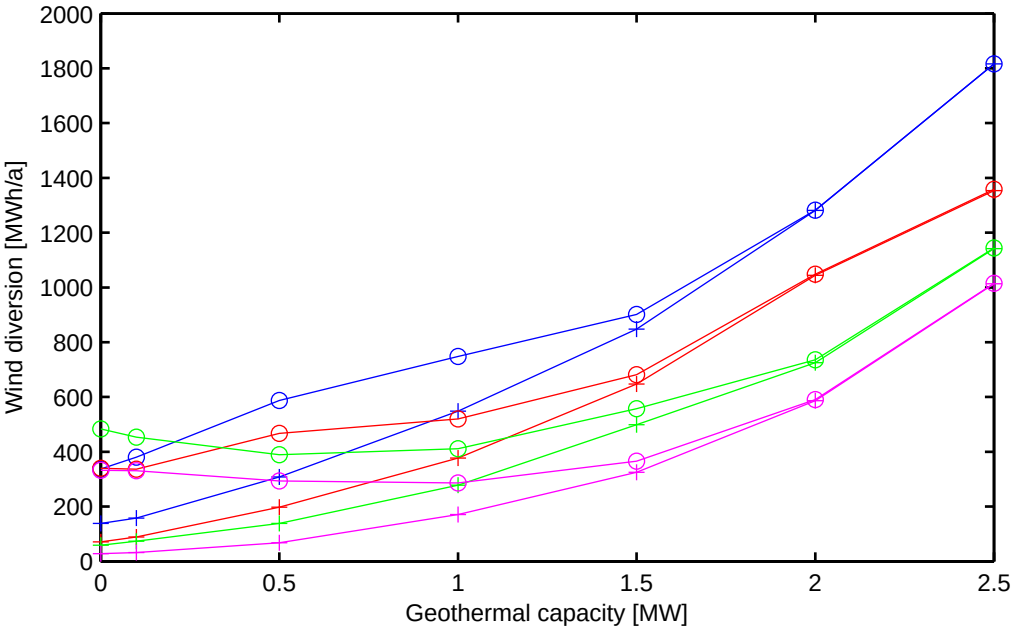


Figure 3.12: Yearly diverted wind energy for Schedule 1 (+) and Schedule 2 (o). The different colors represent different diesel scenarios (see Table 2.3).

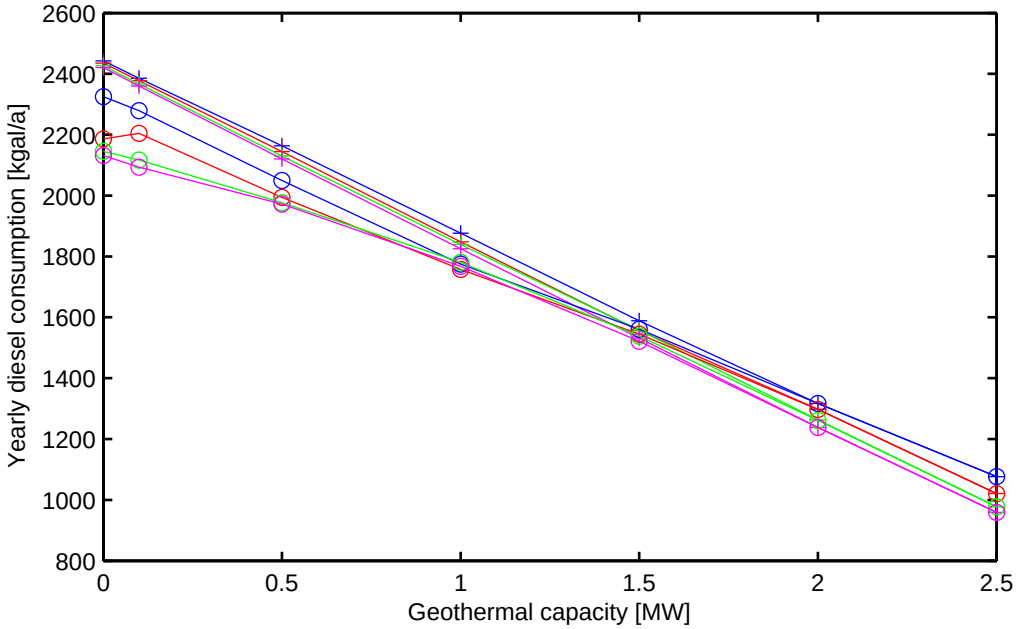


Figure 3.13: Yearly diesel consumption for Schedule 1 (+) and Schedule 2 (o). The different colors represent different diesel scenarios (see Table 2.3).

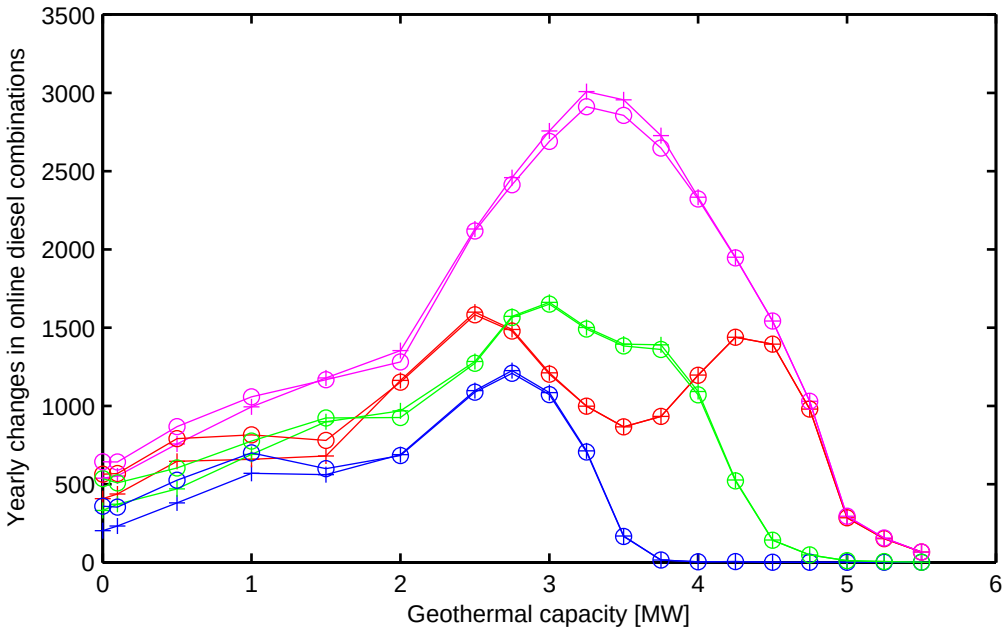


Figure 3.14: The yearly number of changes in the online combination of diesel generators for Schedule 1 (+) and Schedule 2 (o). The different colors represent different diesel scenarios (see Table 2.3).

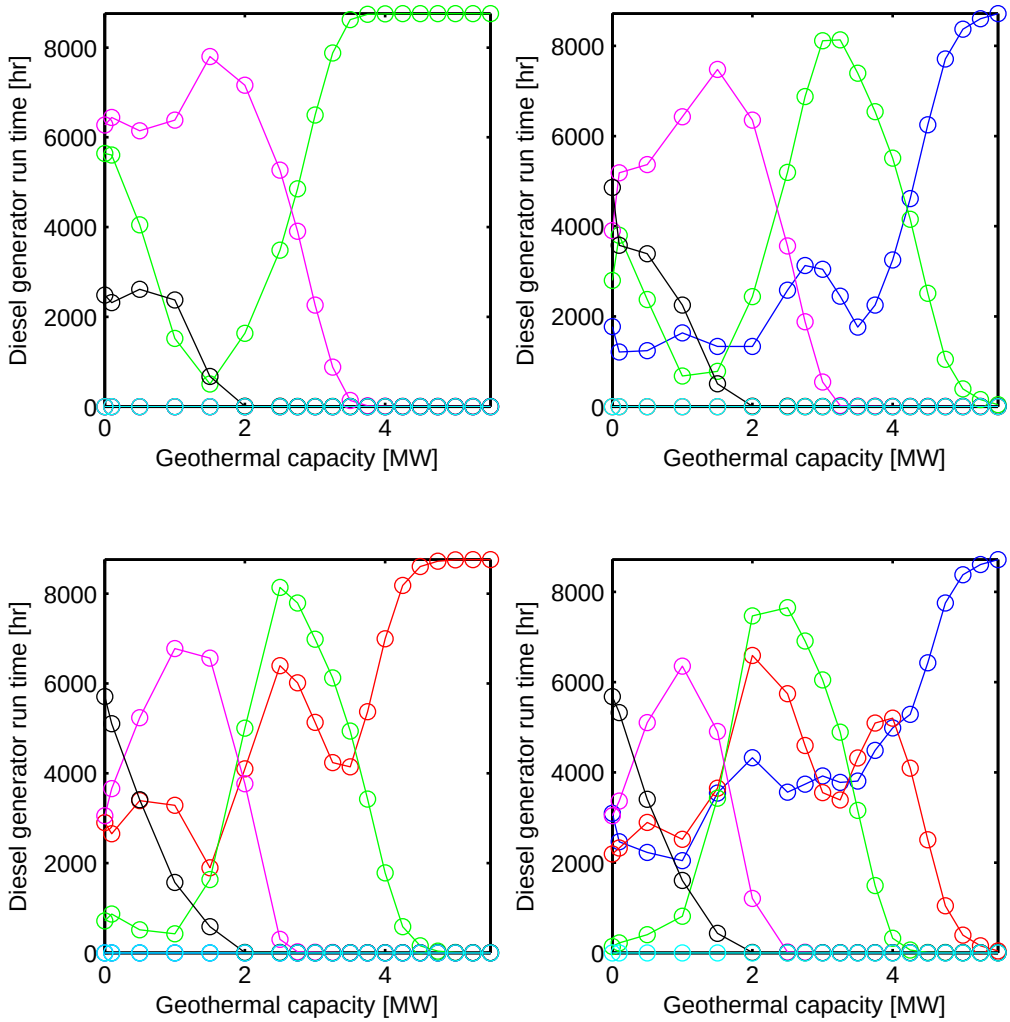


Figure 3.15: Average capacity of the online diesel generating option for diesel schedules Schedule 1 (+) and Schedule 2 (o). The different colors represent different diesel scenarios (see Table 2.3).

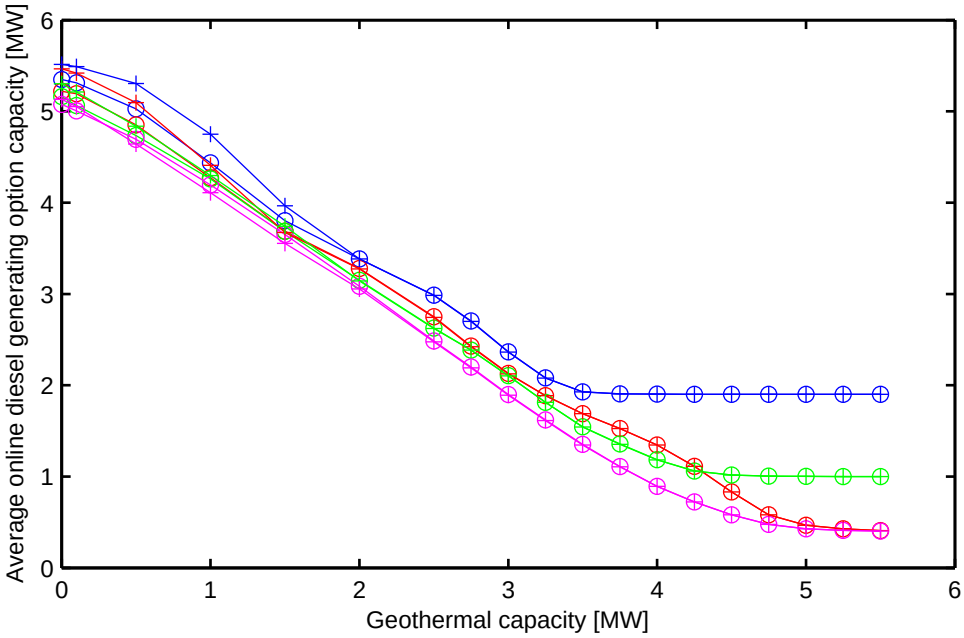


Figure 3.16: The run time of diesel generators. The lines represent the diesel generators (see Table 2.2): G1 (blue), G2 (red), G3 (green), G4 (magenta), G5 (black) and G6 (cyan). The different plots represent different diesel cases (see Table 2.3): Top left: Diesel Case 1, Top right: Diesel Case 2. Bottom left: Diesel Case 3. Bottom right: Diesel Case 4.

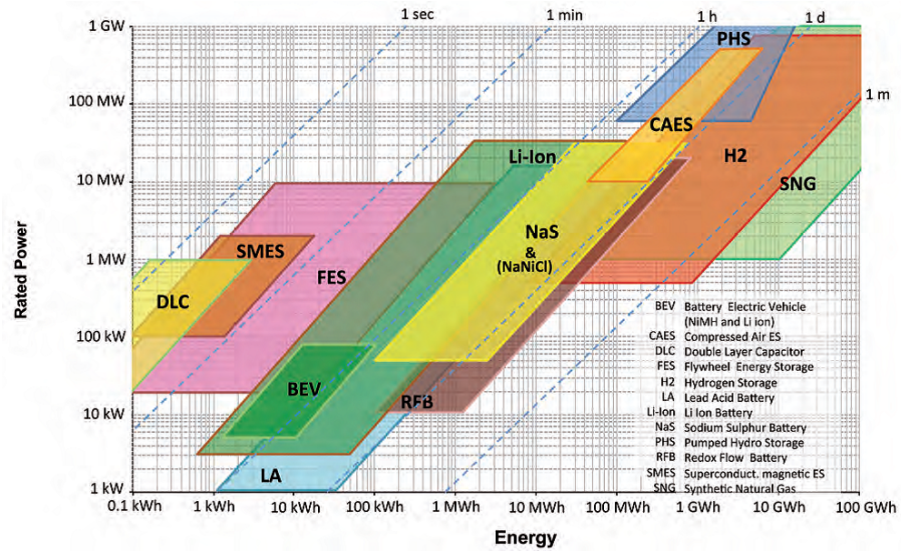


Figure 3.17: Comparison of rated power and energy of different ESS technologies (IEC, 2011).

3.3 Generic Energy Storage

The goal of using an energy storage system (ESS) in the grid, as outlined in Section 2.6, was to allow smaller capacity diesel generating options to run online, which would allow a greater import of RE into the grid and increase the displacement of diesel generator output. This was achieved by allowing the ESS to supply some of the SRC to the grid.

To get an indication for what type of ESS would be best suited for Nome's grid, a generic ESS (Section 2.6.1) was simulated. The power and capacity of the ESS were treated as independent variables when generating scenarios. The increase in displaced diesel generator output was plotted against ESS capacity and power for different levels of geothermal capacity and diesel scenarios. The resulting plots can be seen in Appendices F, G and H for the ESS-Diesel scenarios **EDS1**, **EDS2** and **EDS3** (Sections 2.6.2.2 to 2.6.2.4). These plots show by how much the displaced diesel generator output increases for added ESS capacity or power. Each contour represents a 20 MWh increase. From these figures, an ideal relationship between ESS capacity and power can be deduced.

Overlaid on the plots are the average slopes relating power to capacity for different ESS technologies taken from Figure 3.17 (IEC, 2011). Technologies were chosen which had possible installation sizes ranging up to 10 MWh. The different ESS technologies that were plotted are listed in Table 3.2 along with their average capacity to power ratio and line color in the plots. An example plot is shown in Figure 3.18 for ESS-diesel schedule **EDS1** and 2 MW of geothermal capacity.

An optimal ratio of capactiy to power was determined for each ESS-diesel schedule, and the results for that ESS presented in the following sections. Results include displaced diesel generator output, diesel generator operation and ESS operation. Finally, a summary is given for the different ESS and schedules for 2 MW of geothermal capacity and compared with the corresponding results for no ESS.

Table 3.2: Overview of different ESS from Figure 3.17 that are in the 0–10MWh range.

Name	Average Capacity/Power [hours]	Typical Minimum Installation Size [MWh]	Projected Maximum Installation Size [MWh]	Line Color
Battery EV (NiMH and Li-ion)	0.5	1e-3	0.1	Black
DLC (double layer capacitor)	6 e-4	1e-4	1e-3	Blue
FES (flywheel energy storage)	1.7e-2	1e-4	1	Green
LA (lead acid battery)	3	1e-3	10	White
Li-ion (lithium ion battery)	1	1e-3	100	Purple
NaS (Sodium Sulpher battery)	6	0.1	1000	Yellow
RFB (redox flow battery)	20	0.1	1000	Red
SMES (super conductor magnetic energy storage)	4.2e-3	1e-4	1e-2	Light Blue

3.3.1 Results for ESS-diesel schedule ESD1

This section presents the results of the simulations where a generic ESS was simulated using the ESS-diesel schedule **EDS1** from Section 2.6.2.2.

3.3.1.1 Displaced diesel generator output

Figures F.1 to F.7 in Appendix F show the increase in displaced diesel generator output for different combinations of ESS capacity and power. They indicate an ideal ESS capacity to power ratio of around 5 h, which from Figure 3.17 is in the range of lead acid, Sodium Sulphite, redox flow and Li-ion ESS types. Thus, a capacity to power ratio of 5 h was chosen for further analysis. Figure 3.19 shows the displaced diesel generator output for different levels of ESS and geothermal capacity, using a capacity to power ratio of 5 h for the ESS.

One key obervation from Figure 3.19 is that the increase in displaced diesel generator output corresponds to the level of diesel switching in the corresponding scenarios with no ESS from Section 3.1. The diesel switching for no ESS is presented again in Figure 3.21.

In the no ESS scenarios, increasing levels of diesel switching resulted from the smaller capacity diesel generating options being run online with increasing geothermal capacity. The maxima in the slope of diesel switching with respect to geothermal capacity were caused by transitions between predominant diesel generating options, as described in Section 3.1.2.

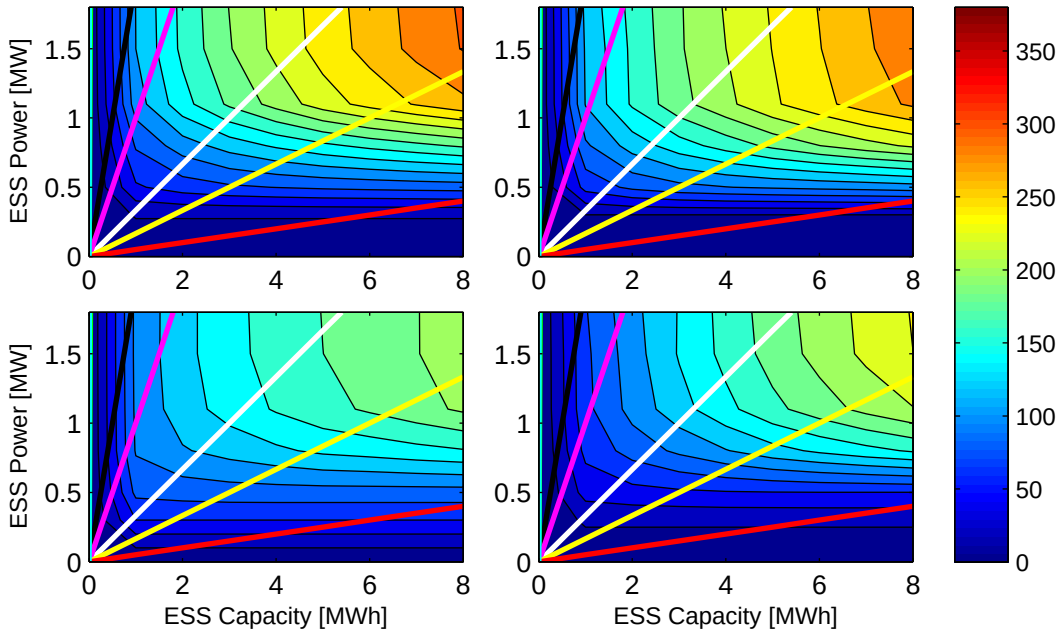


Figure 3.18: Displaced diesel generator output for different levels of ESS power and capacity and 2 MW of geothermal capacity. The different plots represent different diesel cases (see Table 2.3): Top left: Diesel Case 1, Top right: Diesel Case 2. Bottom left: Diesel Case 3. Bottom right: Diesel Case 4.

Both smaller capacity diesel generating options and having the load in between the operating ranges of two diesel generating options reduce the amount of power the ESS must supply to keep a smaller diesel generating option online. This results in a smaller capacity ESS being able to displace a larger amount of diesel output. Thus, the level of increased displaced diesel generator output due to ESS corresponds to the initial level of switching in each scenario.

Another significant result is the amount of displaced diesel generator output per ESS capacity in the system, shown in Figure 3.20. A typical increase in displaced diesel generator output per added ESS capacity is 30–60 MWh/MWh. The goal of this study is not to perform an economical analysis, however, it is unlikely that ESS would be economical with this kind of return.

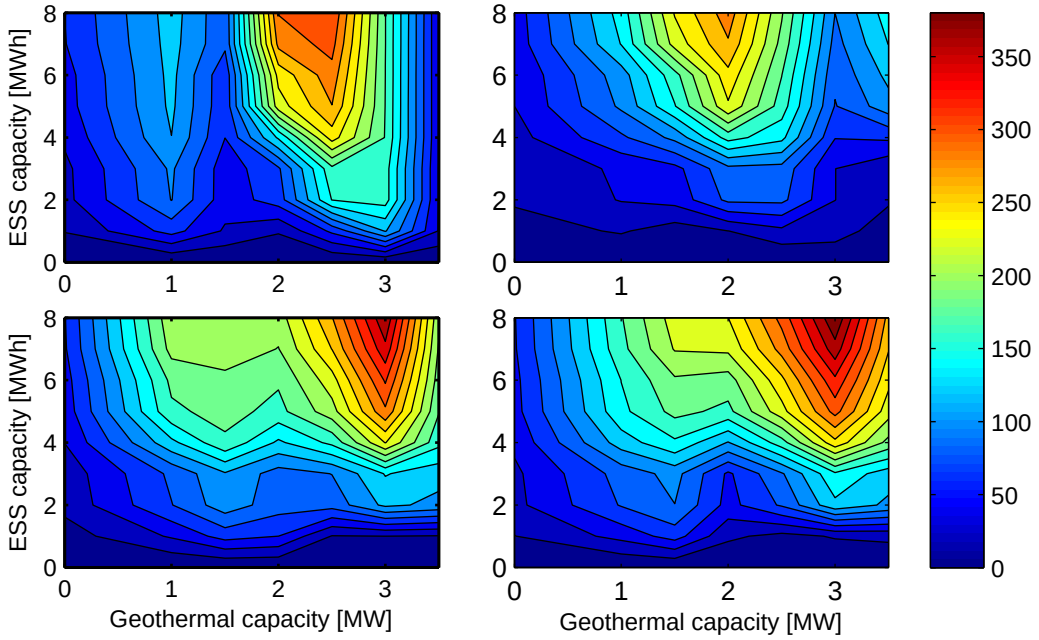


Figure 3.19: Displaced diesel generator output for different levels of ESS power and capacity and 3.5 MW geothermal capacity. The different plots represent different diesel cases (see Table 2.3): Top left: Diesel Case 1, Top right: Diesel Case 2. Bottom left: Diesel Case 3. Bottom right: Diesel Case 4.

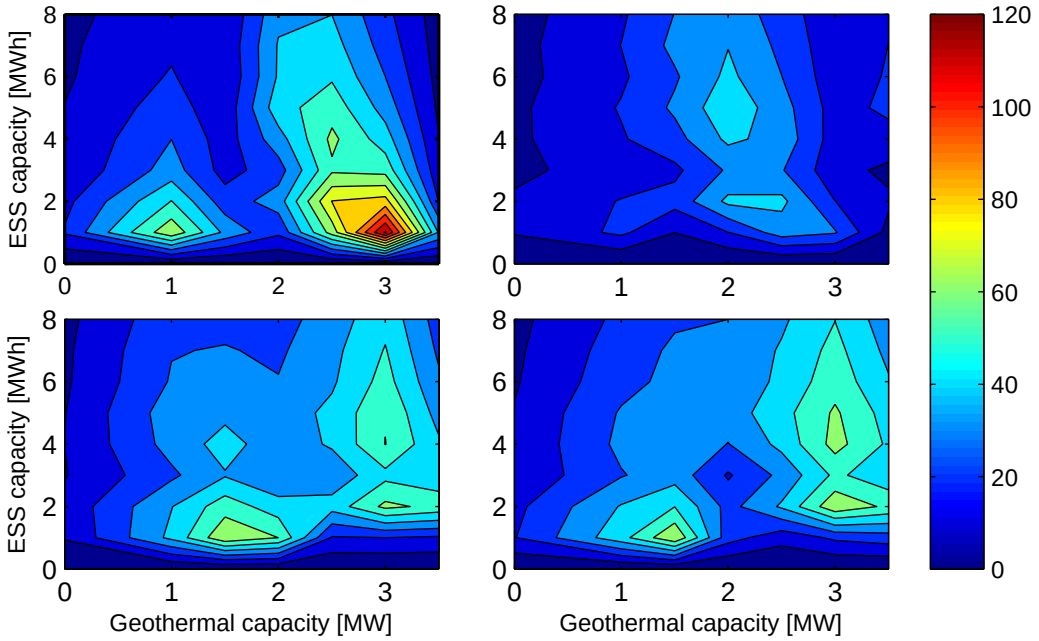


Figure 3.20: Yearly increas in displaced diesel over ESS capacity [MWh/MWh] for different diesel scenarios. Top left: Case 1, Top right: Case 2, Bottom left: Case 3 and Bottom right: Case 4. Each contour represents an increment of 10.

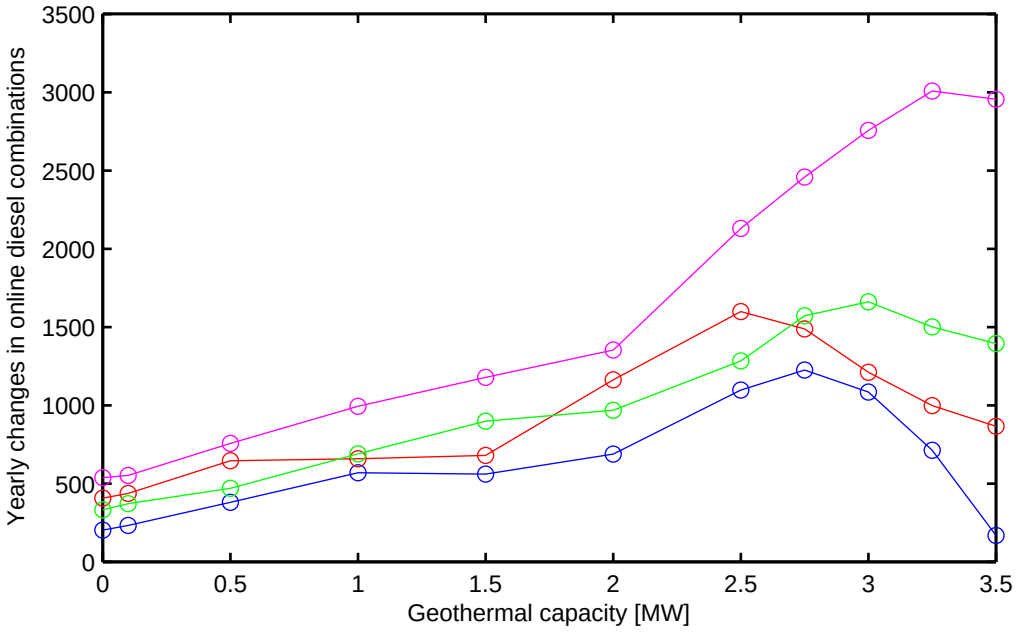


Figure 3.21: The number of changes in the online combination of diesel generators per year with no ESS. The different colors represent different diesel scenarios (see Table 2.3: Diesel scenarios. Case 1 is the base (current) case. The capacity of G1 is 0.4MW, G2 is 1.0MW, G3 is 1.9MW, G4 is 3.7MW, G5 is 5.2 MW and G6 is 5.2MW).

3.3.1.2 Diesel operation

Figure 3.23 shows the reduction in diesel switching for different levels of ESS. The greatest reduction in diesel switching occured at the scenarios where there was inititally a high amount of diesel switching before the addition of ESS (see Figure 3.21). For example, 2 MWh of ESS reduced the extremely high levels of diesel switching for diesel **Case 4** at 2 MWh of geothermal capacity down to 1841 timer per year, or around 5 times a day. This is still high, but in the range of what would be considered acceptable.

Displaced diesel generator output also was highest at levels of geothermal capacity where there was high levels of switching before adding ESS (Figure 3.19). While the reduction in diesel switching and increase in displaced diesel generator output behaved similarly along the geothermal axis, they behaved very differently along the ESS axis (see Figures 3.23 and 3.19). The displaced diesel generator output increased relatively constantly for increases in ESS capacity, but the decrease in diesel switching leveled off after 2 MWh of ESS capacity.

A reduction in diesel switching is the result of instances where the ESS was able to delay the diesel switching for longer than one switching cycle. Figure 3.22 shows two examples where the ESS delays the switching of the online diesel generating option to a larger capacity. The blue and green lines represent the output and MOL of the diesel generators with no ESS, and the red and the purple lines represent the output and MOL of the diesel generators with a 5 MWh 1.5 MW ESS. The change in the MOL of the online diesel generating option indicates a change in the generating option, where a higher MOL indicates a higher capacity generating option. The plot on the left shows a reduction of 2 in diesel switching, while the plot on the right shows no reduction diesel switching.

Thus, after 2 MWh of ESS, additional ESS mainly delays switching instead of reducing it. The main objective is to displace diesel genetor output, not necessarily to reduce diesel switching, and the displaced diesel generator output continues to increase after the diesel switching reduction has plateaued (Figure 3.19). However, Figure 3.20 shows the maximum ratio of increased diplaced diesel generator output per ESS capacity tends to be greatest around 2 MWh of ESS capacity for the different geothermal scenarios, indicating some relation between displaced diesel generator output and the reduction of diesel switching.

Figure 3.24 shows the increase in loading for added ESS. Switching and loading were found to have an inverse relationship in Section 3.1.2, and the same relationship can be observed in their increase and decrease with added ESS. The increase in loading ranges from around 2–9% and gives an indication of the success of the ESS in allowing smaller capacity diesel generating options to run online.

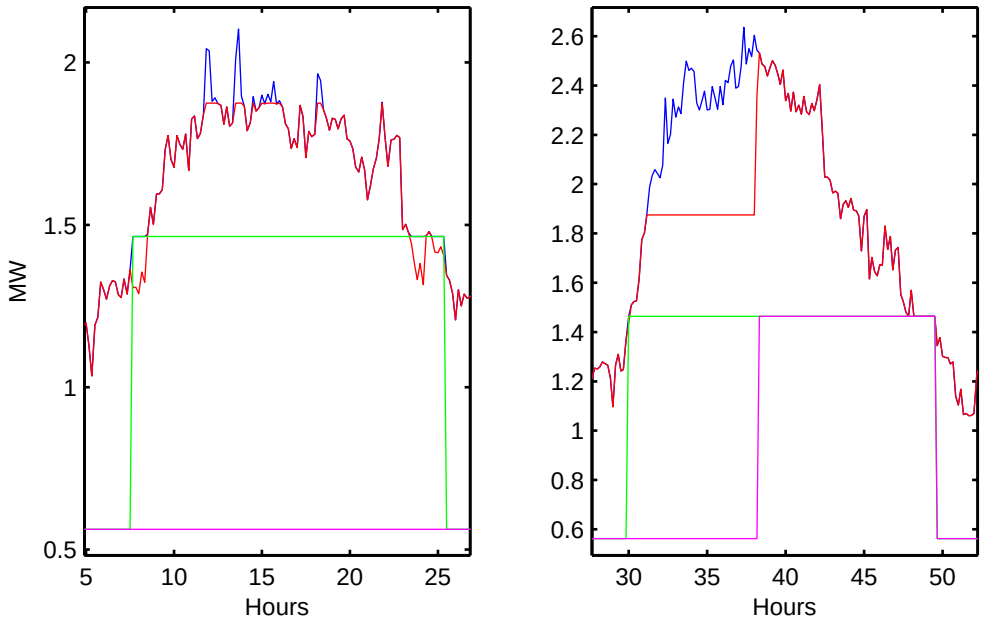


Figure 3.22: The blue and green lines represent the output and MOL of the diesel generators with no ESS, and the red and the purple lines represent the output and MOL of the diesel generators with a 5 MWh 1.5 MW ESS. The figure on the left shows the a reduction of two changes in diesel swithing while the figure on the right shows no reduction in diesl switching for added ESS.

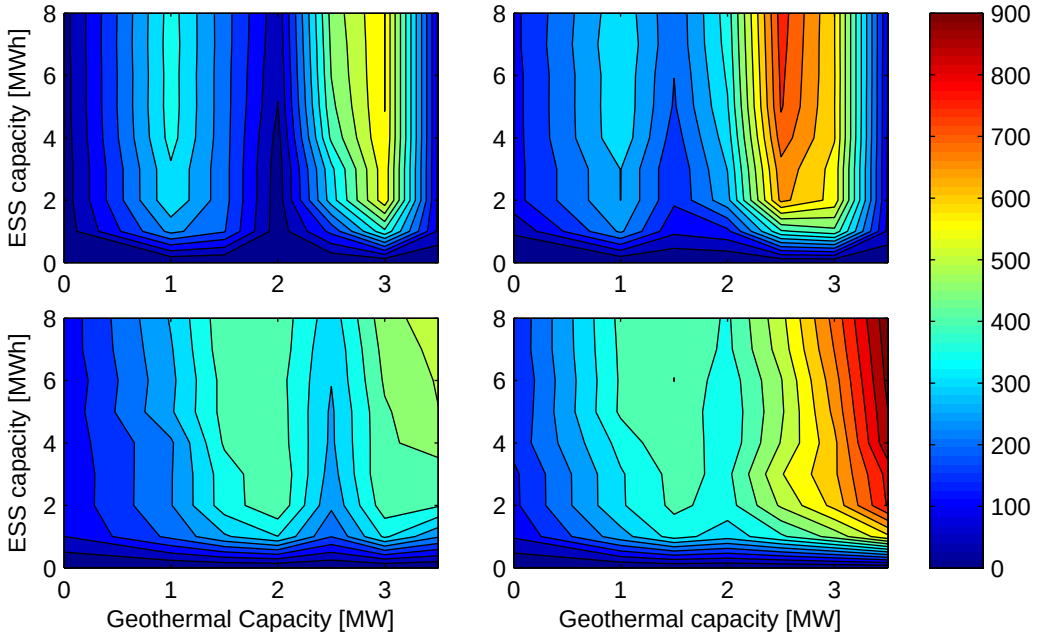


Figure 3.23: Decrease in diesel switching per year for different diesel scenarios. Top left: Case 1, Top right: Case 2, Bottom left: Case 3 and Bottom right: Case 4.

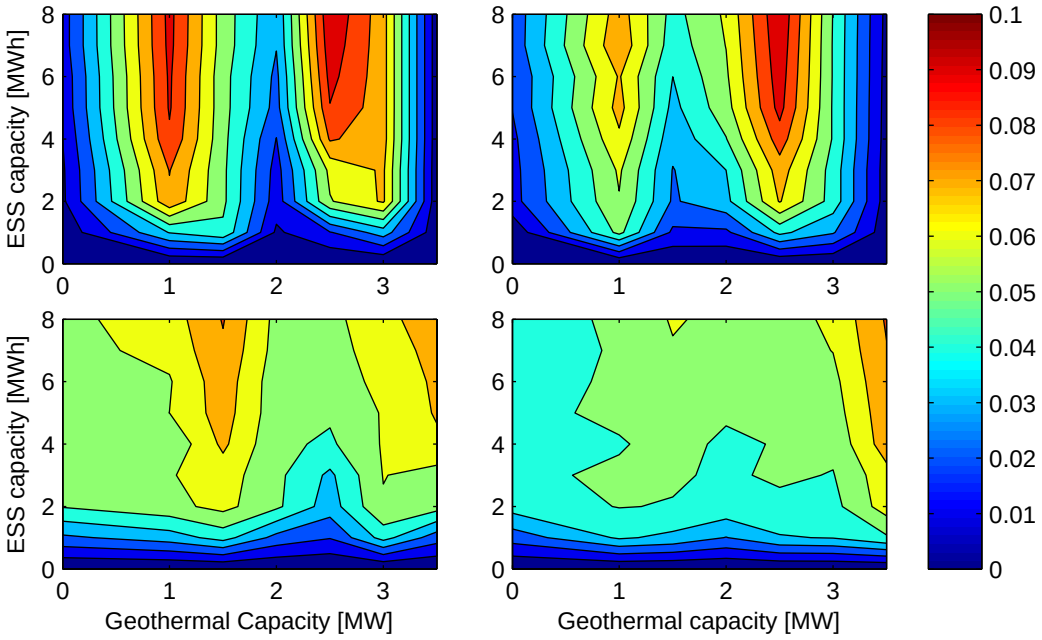


Figure 3.24: Increase in average diesel generator loading per year for different diesel scenarios. Top left: Case 1, Top right: Case 2, Bottom left: Case 3 and Bottom right: Case 4.

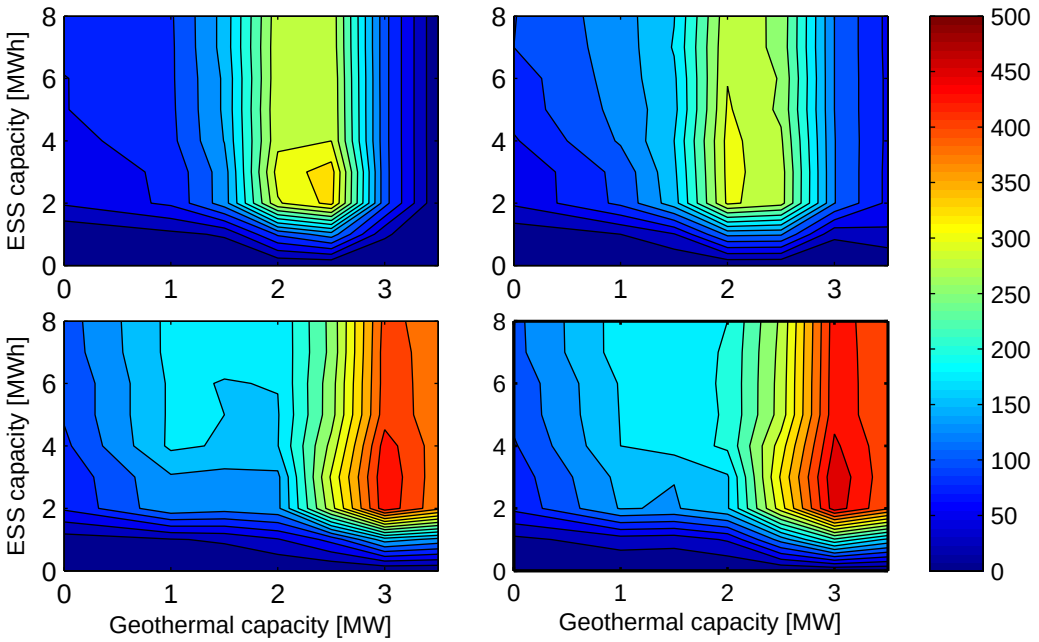


Figure 3.25: ESS cycles per year for different diesel scenarios. Top left: Case 1, Top right: Case 2, Bottom left: Case 3 and Bottom right: Case 4.

3.3.1.3 Energy storage system operation

There are two ways the ESS can allow a smaller diesel generating option to remain online in order to allow a greater import of wind energy into the grid: supplying SRC and actively discharging. As described in Section 2.6.2, supplying SRC allows a higher level of wind import. Actively discharging allows a smaller diesel generating option to remain online, but does not directly affect the import of wind energy into the grid, although it does displace diesel generator output. Increasing the import of wind energy by supplying SRC is a much more efficient use of ESS than directly discharging to displace diesel generator output.

Figure 3.26 shows the total ESS discharge per year. The total ESS discharge corresponds well with the displaced diesel output along the geothermal and ESS axes. The ESS discharge ranges from 50%–100% of the displaced diesel generator output in the corresponding scenarios. This indicates that nearly all the displaced diesel generator output is a result of the ESS discharging, and not a result of it providing ESS. This is one indication that the ESS-diesel schedule (**EDS1**) used here is not utilizing the ESS optimally. The ratio of yearly ESS discharge over its capacity typically ranges from 15–50 MWh/MWh in these scenarios. In other words, the ESS will discharge around 15–50 times its capacity per year, which is not a heavy use of the ESS. See Appendix A for examples of discharge sequences for different capacities of ESS.

Figure 3.25 shows the number of ESS cycles per year. A cycle represents the battery going from charging to discharging.The number of ESS cycles levels off after 2 MWh of ESS capacity, similar to the reduction in diesel switching.

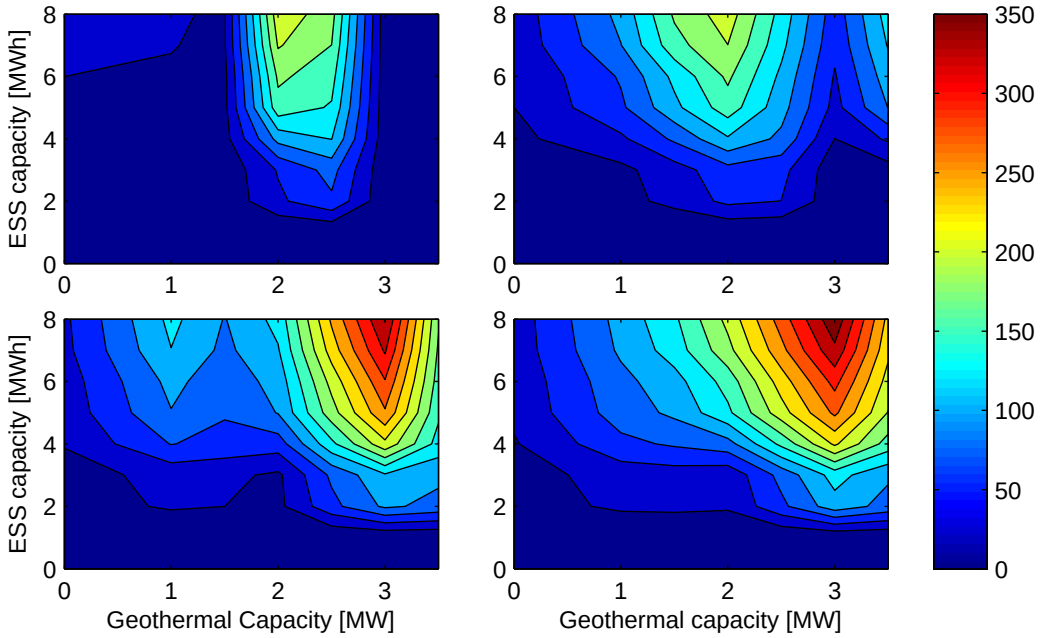


Figure 3.26: ESS discharge per year for different diesel scenarios. Top left: Case 1, Top right: Case 2, Bottom left: Case 3 and Bottom right: Case 4.

3.3.1.4 Summary

In this section, a generic ESS was included in the simulation using the ESS-diesel schedule **ESD1** (Section 2.6.2.2). A power to capacity ratio of 5 h was chosen to maximize the displaced diesel generator output using Figures F.1–F.7 in Appendix F. From Figure 3.17, this is in the range of lead acid, Sodium Sulphite, redox flow and Li-ion ESS types.

The decrease in diesel switching, increase in diesel loading, ESS cycles, displaced diesel generator ouput and ESS disharge per year had an irregular slope with increasing geothermal capacity which tended to align with the level of the diesel switching in the corresponding no ESS scenarios. This is intuitive, since high levels of switching were shown to be a result of running smaller capacity diesel generating options and of the average load being in between the operating ranges of two different diesel generating options. These also increase the ability of the ESS to delay switching to a higher capacity diesel generating option.

The decrease in diesel switching and increase in diesel loading and ESS cycles leveled off for ESS capacities greater than around 2 MWh. The displaced diesel generator output and ESS discharge both increased up till the maximum ESS simulated, 3.5 MWh. This corresponded with the maximum increase in displaced diesel generator output per ESS capacity typically being around 2 MWh.

A ratio of yearly displaced diesel generator output to ESS capacity ranged around 30–60 MWh/MWh for most simulations. This is not a high return for an ESS. The ratio of yearly displaced diesel generator output to ESS discharge generally ranged from 1–2 MWh/MWh. This indicates that most of the displaced diesel generator output is a result of the ESS discharging and not from supplying SRC. This is a suboptimal usage of the ESS and ESS-diesel schedules **EDS2** and **EDS3** were developed to try to improve the usage of the ESS. The following sections present their results.

3.3.2 Results for ESS-diesel schedule EDS2

This section presents the results of the simulations where a generic ESS was simulated using the ESS-diesel schedule **EDS2** from Section 2.6.2.3. The difference between **EDS2** and **EDS1** was that **EDS2** included the ESS into the criteria for selecting possible diesel generating options before running the diesel schedule. The ESS reduced the capacity requirements on the diesel generating options, allowing smaller diesel generating options to run online.

3.3.2.1 Displaced diesel generator output

Figures G.1 to G.7 in Appendix G show the increase in displaced diesel generator output for different combinations of ESS capacity and power. They indicate an ideal ESS capacity to power ratio of around 15 min, in the range of flywheel, Li-ion and BEV ESS types. The results in this section are shown for an ESS with a ratio of capacity to power of 12 min to be able to compare it to **EDS3**. This value reflects the amount of time needed to bring another diesel generating option online, which was 10 min in this simulation. Depending on the application, this value could change. This is a significant difference from the results of **EDS1**, which had an ideal ratio of 5 h.

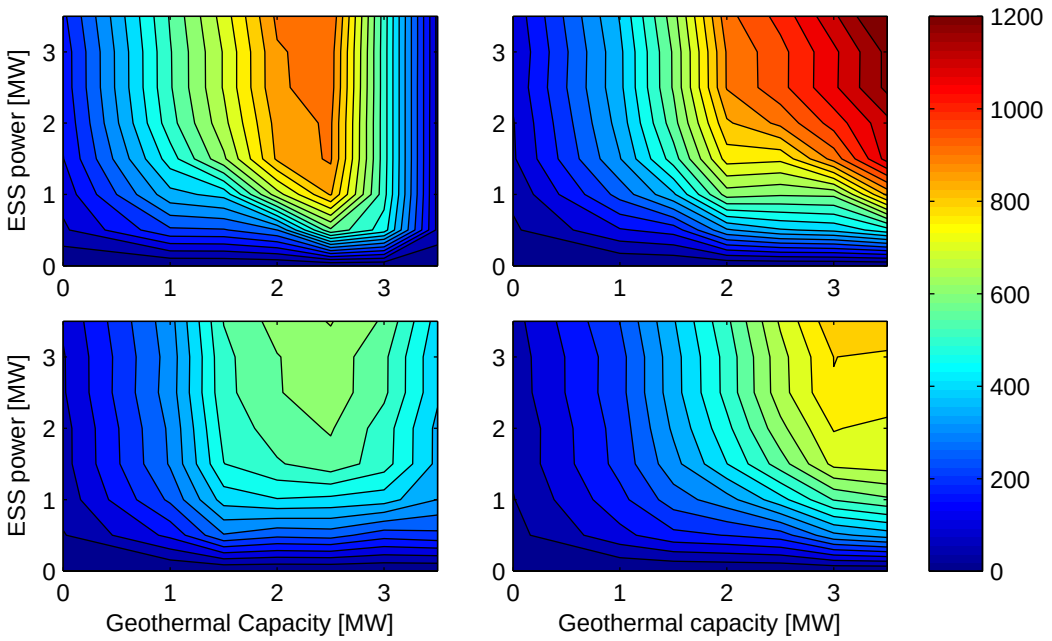


Figure 3.27: Displaced diesel generator output [MWh] for ESS with a capactiy to power ratio of 0.2 h and different levels of geothermal capacity. The different plots represent different diesel cases (see Table 2.3): Top left: Diesel Case 1, Top right: Diesel Case 2. Bottom left: Diesel Case 3. Bottom right: Diesel Case 4.

Figure 3.27 shows the displaced diesel generator output for different levels of ESS power and geothermal capacity, using a capacity to power ratio of 15 min for the ESS. Note that the ESS axis shows power and not capacity as in Section 3.3.1. The increase in displaced diesel seems to correspond less to the intial level of diesel switching in the corresponding no ESS scenarios than it did for **EDS1**. The diesel scenarios with the least diverse diesel

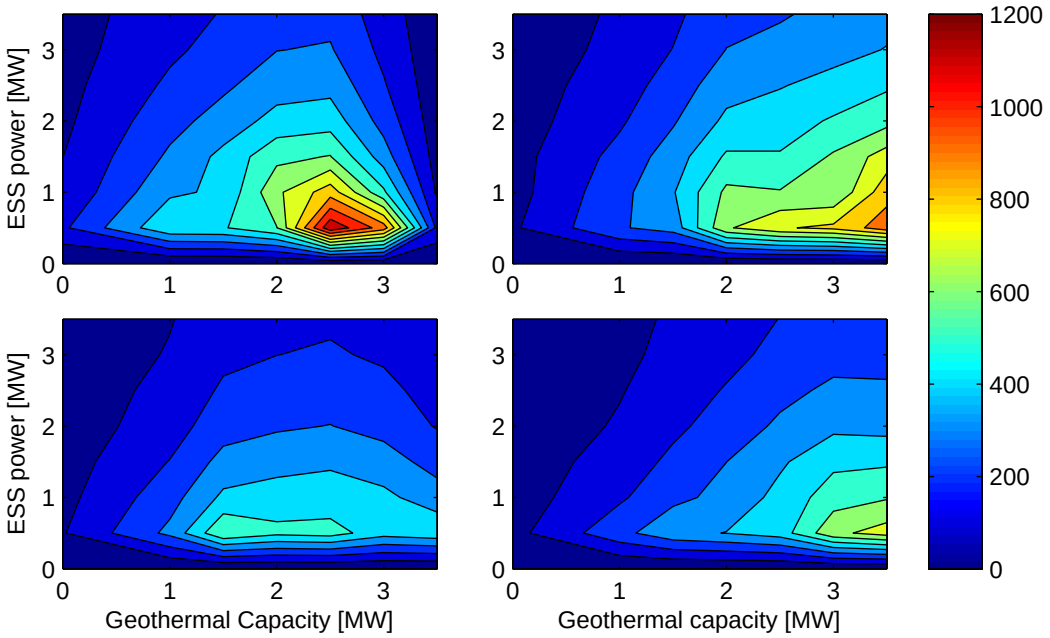


Figure 3.28: The ratio of displaced diesel generator output [MWh] over ESS power [MW] with a capactiy to power ratio of 0.2 h and different levels of geothermal capacity. The different plots represent different diesel cases (see Table 2.3): Top left: Diesel Case 1, Top right: Diesel Case 2. Bottom left: Diesel Case 3. Bottom right: Diesel Case 4.

fleets (**Cases 1** and **2**, see Table 2.3) had a higer increase in displaced diesel generator output. Also, the the diesel scenarios with the smallest (0.4 MW) diesel generator (**Cases 2** and **4**) had a higher increase in displaced diesel generator output than the diesel scenarios that did not.

Figure 3.28 shows the ratio of displaced diesel generator output over ESS power (MWh/MW). The ratio typically varied between 400–700 MWh/MW in the scenarios. This is a better result than was measrured with **EDS1**, which had a typical displaced diesel generator output over ESS capacity ratio of around 30–60 MWh/MWh. It depends on relative cost of the ESS types how much more economical **EDS2** is compared to **EDS1**. However, even if the 5 h ESS from **EDS1** was used for **EDS2**, with a ratio of 500 MWh of displaced diesel generator output per MW of ESS, this would result in a ratio of 100 MWh of displaced diesel generator output per MWh of ESS capacity, assuming the extra capacity does increase the displaced diesel output. Thus, regardless of the ESS type, **EDS1** performs better, and it would be a trade off between the optimal ESS type and the relative costs of the ESS types.

3.3.2.2 Diesel operation

Figures 3.29 and 3.30 show the reduction in diesel switching and the increase in the average loading of the diesel generator per year. Similar to Figures 3.23 and 3.24 for **ESD1**, the higest reduction in diesel switching and increase in average loading occured at the geothermal scenarios where there was initially a relatively high amount of diesel switching before the addition of ESS.

Along the ESS axis, the reduction in diesel switching and increase in average diesel load-

ing leveled off after around 0.5 MW of ESS power. This was also the ESS power which had the highest ratio of displaced diesel generator output over ESS power for most geothermal scenarios (Figure 3.28). Figures 3.23 and 3.24 had the same characteristics at 2 MWh with **EDS1**.

The ESS sizes simulated with **ESD2** reduced the high levels of switching to a greater degree than the ESS sizes simulated with **ESD1**. At geothermal capacities where there was initially relatively low levels of diesel switching, **ESD2** actually increased the level of switching. All diesel switching was kept within reasonable limits. Simlarly, the ESS sizes simulated in **ESD2** resulted in a 1–2% higher loading than the ESS sizes simulated in **ESD1**.

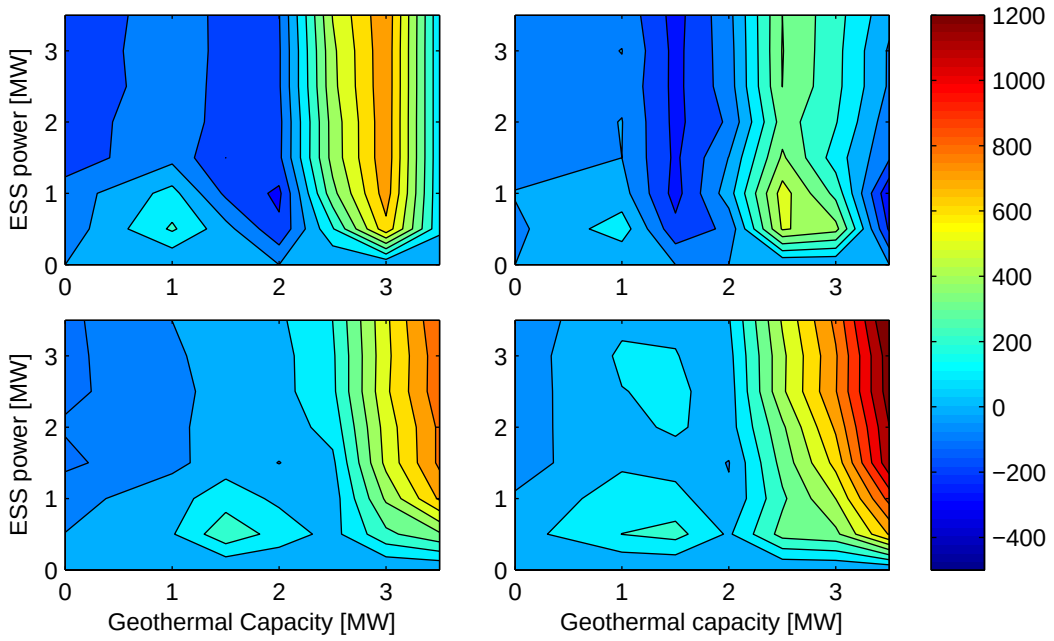


Figure 3.29: Reduction in diesel switching per year with an ESS with a capactiy to power ratio of 0.2 h and different levels of geothermal capacity. The different plots represent different diesel cases (see Table 2.3): Top left: Diesel Case 1, Top right: Diesel Case 2. Bottom left: Diesel Case 3. Bottom right: Diesel Case 4.

3.3.2.3 Energy storage system operation

Figures 3.31 and 3.32 show the yearly cumulative ESS discharge (in MWh) and cycles of the ESS. The typical discharge ranges between 50–200 MWh per year. This is 1–15% of the displaced diesel generator output, significantly less than the 50–100% when using **ESD1**. Thus, only 1–15% of the displaced diesel generator output is a direct result of the ESS discharging, indicating a much more optimal use of the ESS.

The ratio of ESS discharge over ESS capacity is typically in the range of 50–350 MWh/MWh, which is much higher than the typical range of 15–50MWh/MWh for **ESD1**. Thus, the ESS will discharge 50–350 times its capacity during the year. This is a much higher usage of the battery. The number of ESS cycles per year is typically in the range of 200–1000, which is around twice the number of ESS cycles with **ESD1**. A higher usage will in-

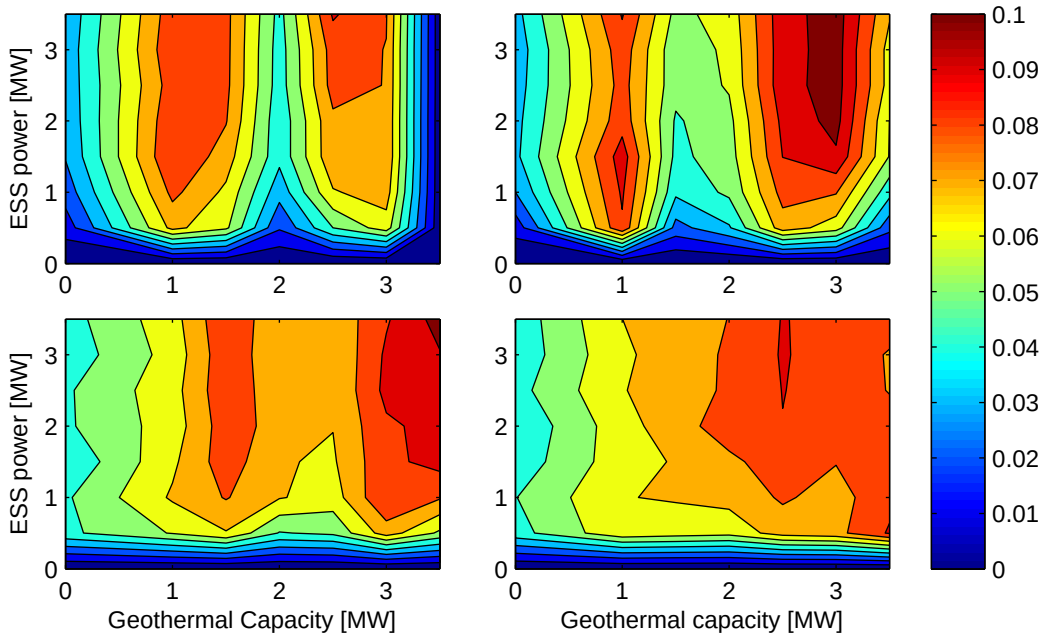


Figure 3.30: Increase in average diesel generator loading with an ESS with a capactiy to power ratio of 0.2 h and different levels of geothermal capacity. The different plots represent different diesel cases (see Table 2.3): Top left: Diesel Case 1, Top right: Diesel Case 2. Bottom left: Diesel Case 3. Bottom right: Diesel Case 4.

crease the wear and shorten the lifetime of the ESS. The extent depends on the specific ESS technology.

Figure 3.33 shows the yearly amount of SRC provided by the ESS, with a typical range of 400–2000 MWh. This is significantly more than the discharge of the ESS. While the discharge of the ESS results in a one to one saving in displaced diesel generator output, covering SRC has a 15–90% return in displaced diesel generator output. Since supplying SRC displaces diesel generator output by increasing the import of wind energy, it is most effective in scenarios where there is a high amount of wind energy diversion.

3.3.2.4 Summary

In order to improve the usage of the ESS when using the ESS-diesel schedule **ESD1** (Section 3.3.1), ESS-diesel schedules **ESD2** and **ESD3** were developed (Sections 2.6.2.3 and 2.6.2.4). The results for **ESD2** were presented in this section.

EDS2 resulted in an optimal ESS with a much lower capacity to power ratio than **EDS1**. It also resulted in a much higher level of displaced diesel generator output for the sizes of ESS simulated with each schedule. This was a result of a more optimal use of the ESS, with 80–90% of the increase in displaced diesel generator output resulting from the increase in wind energy import due to the SRC supplied by the ESS. Although supplying SRC does not result in the one to one displacement of diesel generator output that discharging does, it does not require the ESS to discharge, greatly reducing its capacity requirements.

The ESS sizes simulated with **EDS2** also resulted in a higher average diesel generator loading and a reduction in diesel switching than the ESS sizes simulated with **EDS1**.

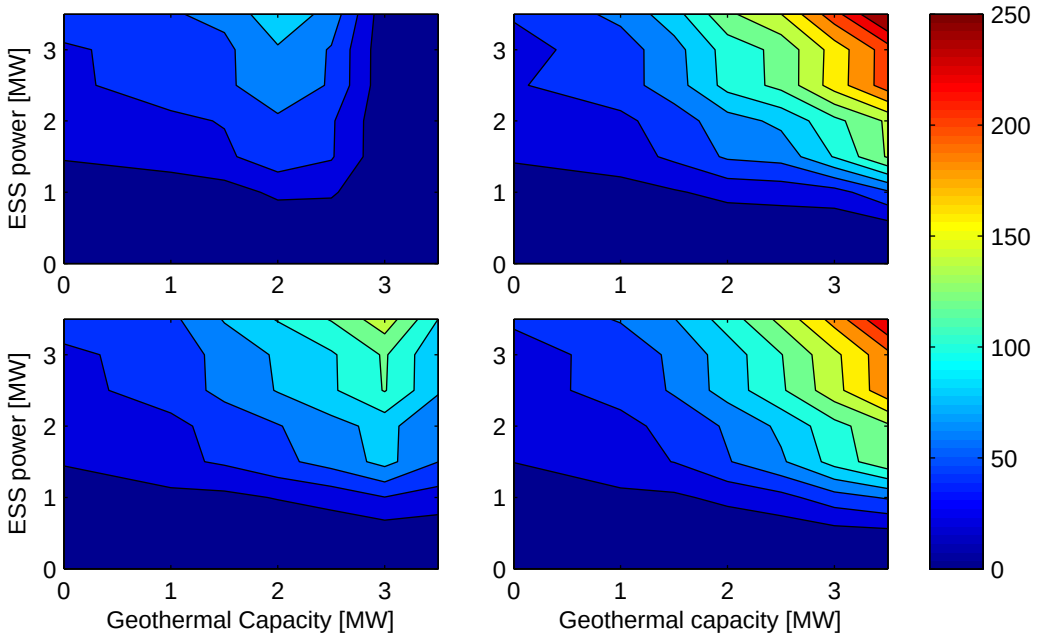


Figure 3.31: ESS yearly discharge [MWh] for an ESS with a capactiy to power ratio of 0.2 h and different levels of geothermal capacity. The different plots represent different diesel cases (see Table 2.3): Top left: Diesel Case 1, Top right: Diesel Case 2. Bottom left: Diesel Case 3. Bottom right: Diesel Case 4.

This allows for a more optimal operation of the diesel generators. However, **EDS2** also resulted in a much heavier usage of the ESS than **EDS1**. How the usage will affect the life of the ESS depends on the ESS technology.

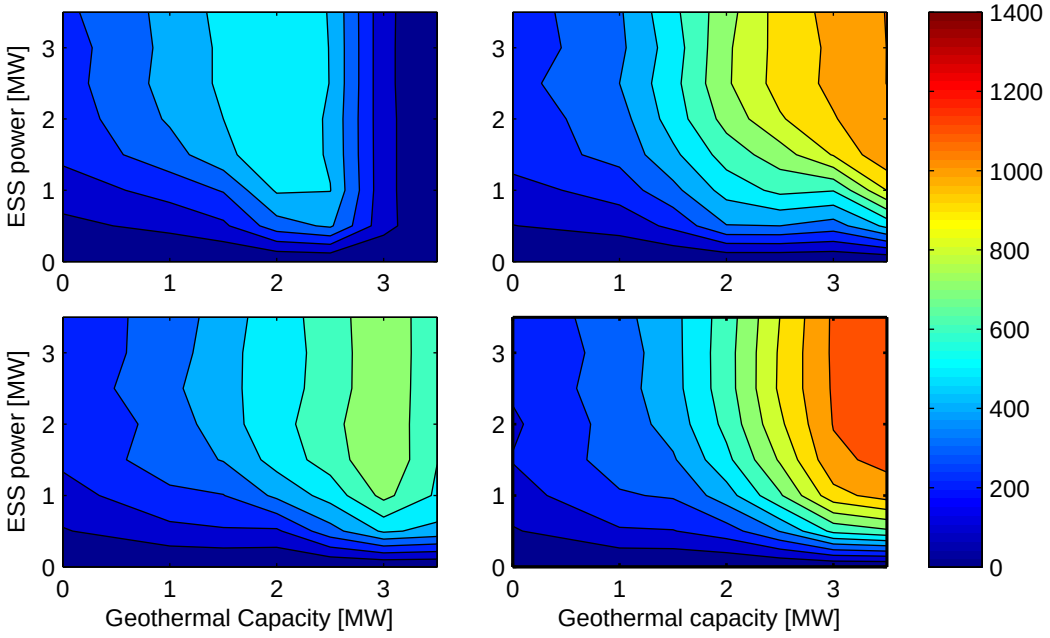


Figure 3.32: ESS cycles per year for an ESS with a capactiy to power ratio of 0.2 h and different levels of geothermal capacity. The different plots represent different diesel cases (see Table 2.3): Top left: Diesel Case 1, Top right: Diesel Case 2. Bottom left: Diesel Case 3. Bottom right: Diesel Case 4.

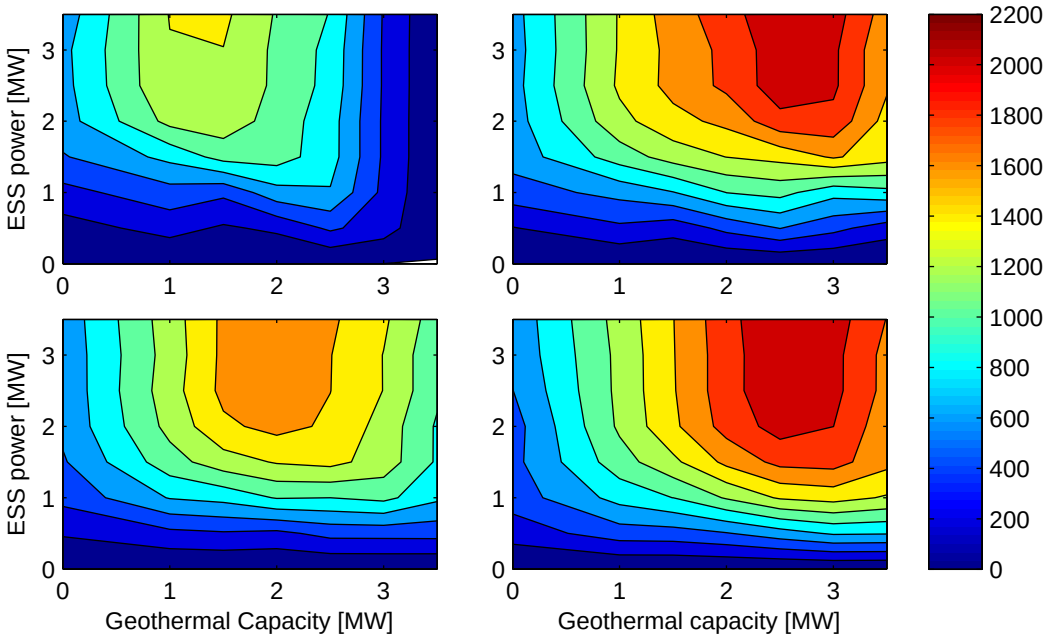


Figure 3.33: SRC supplied be the ESS per year [MWh] for an ESS with a capactiy to power ratio of 0.2 h and different levels of geothermal capacity for **EDS2**. The different plots represent different diesel cases (see Table 2.3): Top left: Diesel Case 1, Top right: Diesel Case 2. Bottom left: Diesel Case 3. Bottom right: Diesel Case 4.

3.3.3 Results for ESS-diesel schedule EDS3

This section presents the results of the simultions where a generic ESS was used with the ESS-diesel schedule **EDS3**. The difference between **EDS3** and **EDS2** (Section 3.3.2) is that **EDS3** adds ESS discharging as an event that will initiate the diesel schedule. The ESS discharges when the online diesel generating option is not able to supply the difference between the load and the import of RE. When the diesel schedule is run, a larger capacity diesel gernating option will be chosen to run online. This will not, however, directly cause the diversion of wind power since the MOL of the new generating option will not be higher than the difference between the current load and RE import (Section 2.6.2.4).

It could potentially lower the import of RE by discharging the ESS, reducing the amount of SRC that it can supply. It could also potentially increase the import of RE into the grid and reduce diesel switching by keeping a smaller capacity diesel generating option online which would reduce future wind diversion.

Figures H.1 to H.7 show the increase in displaced diesel generator output for different levels of ESS power and capacity. The optimal ratio of capacity to power was found to be around 12 min, slightly less than it was for **EDS2** which was 15 min. Identical ESS sizes were plotted for the results of **EDS2** and **EDS3** to enable easier comparison.

The simulation results for **EDS3** can be seen in Appendix H. There was actually very little overall difference in the SRC supplied by the ESS between **EDS3** and **EDS2**, which varied by up to +/- 60% from each other. In the scenarios where there was a high level of increase in displaced diesel generator output **EDS2** tended to result in the ESS supplying a higher level of SRC than **EDS3**. In the scenarios where there was a low level of increase in displaced diesel generator output, **EDS3** tended to result in the ESS supplying a higher amount of SRC than **EDS2**.

The greatest difference between **EDS2** and **EDS3** was the level of ESS discharge, which was up to 20 times higher in **EDS2**. Since there was no overall difference in the amount of SRC provided by the ESS, this led to an up to 35% greater increase in displaced diesel generator output in **EDS2** compared to **EDS3**.

The very low capacity to power ratio of the ESS allowed it charge quickly, minimizing the amount of time it could only supply a low amount of SRC due to a low SOC. This minimized the impact of allowing the ESS to nearly fully discharge on its ability to supply SRC in **EDS2** and is most likely the main reason why there was no overall difference in the amount of SRC suplied by the ESS between **EDS2** and **EDS3**.

If a greater capacity to power ratio was used, the results of **EDS3** and **EDS2** would be different. **EDS3** would not benefit much from the increased capacity. However, **EDS2** would be able to discharge more, which would displace more diesel generator output. At some point, this would likely begin to impede its ability to supply SRC to the grid. Thus, when using ESS with a higher capacity to power ratio, a hybrid between **EDS2** and **EDS3** would work best, allowing a limited amount of ESS discharge before initiating the diesel schedule.

EDS3 resulted in an up to 500% lower reduction in diesl switching compared to **EDS2**. The average loading on the diesel generators varied by around +/- 50% between **EDS2** and **EDS3**. Thus, the operation of the diesel generators was in general better with **EDS2** compared to **EDS3**, especially in areas where there was initially a high level of diesel switching.

EDS3 resulted in up to 20 times less ESS discharge and up to 50% more ESS cycles per year per year than **EDS2**. How this affects the usage of the ESS depends on the technology. However, having 20 times less ESS discharge is a significant reduction, despite the increase in cycles. Thus, it is likely that **EDS3** results in a lighter usage of the ESS, resulting in a longer life expectancy.

In conclusion, **EDS3** was expected to be able to deliver a higher amount of SRC to the grid than **EDS2**. This was not the case. As a result, since **EDS2** was also able to discharge as well as supply SRC, it displaced more diesel generator output than **EDS3**. In general it also resulted in a more optimal operation of the diesel generators, and a heavier usage of the ESS compared to **EDS3**.

3.3.4 Comparison of ESS-diesel schedules for 2 MW of geothermal capacity

Figures 3.20, 3.28 and H.9 show the ratio of displaced diesel generator output over the capacity or power of the ESS in the system. These figures are usefull when determining the return on investment for ESS. Table 3.4 summarizes the results for the 2 MW geothermal capacity schenarios with **EDS1**, **EDS2** and **EDS3** ESS-diesel schedules and no ESS.

At 2 MW of geothermal capacity, the highest return in displaced diesel generating output for **EDS1** was at 5 MWh of ESS capacity for each of the diesel cases except for **Case 3**, which had the highest return at 1 MWh. Thus, 5 MWh of ESS capacity was used for Table 3.4.

At 2 MWh of geothermal capacity, the highest return in displaced diesel generating output for **EDS2** and **EDS3** was at 0.5 MW of ESS power. This is also the lowest ESS power simulated. Instead, an ESS with 1 MW of power was used for Table 3.4.

This table provides a summary of result which can be used for an economic analysis of integrating geothermal energy into the grid at Nome. For example, installing a 1 MW 0.2 MWh ESS with ESS-diesel schedule **EDS2** to diesel **Case 1** will result in similar displaced diesel generator output as adding a 1 MW and 0.4 MW diesel generator to the fleet to get diesel **Case 4**. As well as displaced diesel generator output, the changes to the diesel and ESS operation must also be taken into account. Also, these are results for a generic ESS with an 81% overall efficiency. The return for a specific ESS technology should be scaled by its expected performance as well as modelled in the simulation to understand how it interacts with the system. A lead acid ESS was modelled and its results are presented in Section 3.4.

Table 3.3: Results for different diesel and ESS scenarios with 2 MW of geothermal capacity using ESS-diesel schedules **EDS1**, **EDS2** and **EDS3**, decribed in Sections 2.6.2.1 and for no ESS. **EDS2** and **EDS3** were simulated with a 0.2 MWh, 1 MW battery and **EDS1** was simulated with a 5 MWh, 1.1 MW battery.

Diesel Scenario	**ESS Scenario**	**Displaced diesel output [MWh]**	**Diverted Wind [MWh]**	**Diverted geothermal [MWh]**	**Average diesel loading [%]**	**Yearly Diesel switching**	**ESS Cycles per year**	**Yearly ESS discharge [MWh]**	**Yearly ESS SRC provided [MWh]**
Case 1	EDS1	15,490	1,025	3.4	57.3	582	296	165	377
	EDS2	15,940	603	3.8	58.1	853	513	24	725
	EDS3	15,900	636	4.1	57.6	946	633	6.3	671
	No ESS	15,260	1,252	1.4	54.7	689			
Case 2	EDS1	15,720	800	3.3	60.6	758	303	164	655
	EDS2	16,100	441	3.0	60.3	1,048	539	25.7	1002
	EDS3	16,090	449	3.2	60.0	1,224	700	8.2	1016
	No ESS	15,480	1,017	1.4	55.7	1,162			
Case 3	EDS1	15,930	597	3.2	61.9	471	173	101	437
	EDS2	16,210	342	3.0	63.6	816	421	21.2	1014
	EDS3	16,190	351	3.0	63.0	881	494	6.7	982
	No ESS	15,760	691	1.3	56.8	968			
Case 4	EDS1	16,090	436	3.0	62.5	875	203	144	542
	EDS2	16,250	304	3.0	64.6	1,227	454	25.1	1,220
	EDS3	16,240	313	3.0	64.8	1,302	452	9.3	1,250
	No ESS	15,920	575	1.2	57.9	1,353			

3.4 Lead Acid Energy Storage, ESS-Diesel Schedule 1

This section compares the simulation results for a lead acid ESS with a generic ESS. The lead acid ESS was simulated with the ESS-diesel schedule **EDS1**, which was shown in Section 3.3 to result in a suboptimal usage of the ESS. Thus, these results do not reflect the total savings possible by using a lead acid ESS. They do however give an indication on how much the performance of a lead acid ESS would differ from the simulation of a generic ESS. This could give an indication of how a lead acid ESS would work with other ESS-diesel schedules as well.

The main differneces between the lead acid ESS and generic ESS models are as follows:

- The lead acid ESS had a maximum discharge rate of C/3[2], while the generic ESS had a maximum discharge rate of C/5
- The lead acid ESS had a maximum DOD of 80%, while the generic ESS could fully discharge
- The maximum charging current for the lead acid ESS decreased with increasing SOC, while the maximum charging current for the generic ESS did not.
- The discharge efficiency of the ESS depended on the rate of discharge, while the generic ESS used a fixed discharge efficiency of 90%.

The higher discharge current and lower maximum DOD of the lead acid ESS effectively changed its capacity to power ratio to 2.4 h, compared to the 5 h ratio simulated with the generic ESS.

The impact of the lead acid ESS on the system followed the same general trends as the generic ESS, as they were both scheduled in the same way. The full results of the lead acid ESS simulations can be seen in Appendix I. Following is a summary of the lead acid ESS results compared to the generic ESS results:

- **Average diesel generator loading increase:** Nearly identical for diesel **Case 1** and **Case 2**. Up to 10% higher for diesel **Case 3** and **Case 4**.
- **Diesel switching reduction:** 0–5% less
- **ESS cycles:** Up to 20% more
- **ESS discharge:** Up to 50% more below 3 MWh of ESS. Above 3 MWh of ESS, 0–5% less.
- **Displaced diesel output increase:** Up to 50% more below 3 MWh of ESS. Above 3 MWh of ESS, 0–5% less.

The lead acid ESS discharges more and displaces more diesel generator output at lower ESS capacities, which is likely due to the higher discharge power of the lead acid ESS. The lead acid discharges less and displaces less at higher capacities than the generic ESS.

[2] C/3 refers the current required to discharge the ESS in 3 h, C/5 to the current required to discharge in 5 h, etc

Table 3.4: Comparison between the simulation results for a 5 MWh lead acid ESS with 2 MW of geothermal capacity and a 5 MWh generic ESS with 2 MW of geothermal capacity.

Diesel Scenario	**ESS Scenario**	**Displaced diesel output [MWh]**	**Diverted Wind [MWh]**	**Diverted geothermal [MWh]**	**Average diesel loading [%]**	**Yearly Diesel switching**
Case 1	L.A. ESS	15,300	1,190	3.1	56	606
	Gen. ESS	15,490	1,025	3.4	57.3	582
Case 2	L.A. ESS	15,600	957	2.8	59	788
	Gen. ESS	15,720	800	3.3	60.6	758
Case 3	L.A. ESS	15,900	681	2.8	62	468
	Gen. ESS	15,930	597	3.2	61.9	471
Case 4	L.A. ESS	16,090	556	2.6	62	870
	Gen. ESS	16,090	436	3.0	62.5	875

This is likely due to the fact that the lead acid ESS had a higher discharge power and a lower effective capacity.

Table 3.4 compares the simualation results for a lead acid ESS with a generic ESS. A 5 MWh ESS was used in both scenarios. Differences in the relative capacity and power of the lead acid ESS compared to the generic ESS result in differences in the simulation results. However the results show the same tendencies along the ESS and geothermal capacity axes. This indicates that the generic ESS model gives a good indication of how a lead acid ESS, and likely other ESS types, would operate in the system after some scaling was applied.

Chapter 4

SUMMARY

Nome, AK, is currently powered by a remote wind-diesel micro-grid. Due to the high cost of fuel, electricity is expensive. Recent geological exploration has determined that a nearby geothermal resource has the potential to economically produce 2 MW of electricity. The proposed geothermal plant would not be able to load follow or supply SRC to the grid. In order to determine the feasibility of incorporating geothermal energy into their grid, the following questions are central:

- How much diesel generator output would be displaced?
- How much more wind energy would be diverted?
- How would the operation of the diesel generators be affected?

This study provides answers to these questions through the use of time dependent energy balance simualations. The goal of this study was to provide the data required to do an economical assesment on integrating geothermal energy into the grid at Nome as well as to gain a more general understanding on how changing the energy mix affects the operation of an islanded micro-diesel grid.

It was found that there was one level of geothermal capacity at which the diversion of geothermal energy drastically increased. This level was different for the different diesel cases and corresponded to the MOL of the smallest diesel generating option.

Below this level of geothermal, the diversion of wind energy increased with a quadratic slope while the displaced diesel generator output increased with a linear slope which was an order of magnitude greater than the diverted wind energy.

For levels up to 2.5 MW, increasing the geothermal capacity:

- Displaced diesel generator output in a linear fashion
- Increased the diversion of RE in a quadratic fashion
- Increased the switching of diesel generators
- Reduced the loading on diesel generators

Adding diesel generators for a more varied fleet:

- Reduced the diversion of RE
- Displaced diesel generator output
- Increased the loading on the diesel generators
- Increased the switching of the diesel generators

Two different diesel schedules were simulated: **Schedule 1** and **Schedule 2**. The goal of **Schedule 1** was to maximize the import of wind energy into the grid while the goal of **Schedule 2** was to minimize the fuel consumption. **Schedule 2** resulted in significant fuel savings below 2 MW, above which there was no difference between **Schedule 1** and **Schedule 2** since the more efficient 5.2 MW diesel generators became too large to use.

While modeling a generic ESS in the simulations, several different ESS-diesel schedules were used. While determining potential diesel generating options for the diesel schedule, it was found that lowering the requirement on the diesel generating options to be able to supply SRC by taking into account the ability of the ESS to supply SRC significantly increased the displaced diesel generator output and reduced the capacity to power ratio of the optimal ESS. The optimal ESS for this schedule was found to be in the range of a Li-ion, flywheel or electric vehicle ESS. Adding the discharge of the ESS as an event which would initiate the diesel schedule was found to reduce the displaced diesel generator output but also reduce the usage of the ESS, increasing its life.

Finally, a lead acid ESS was modeled in the simulations. Its results were consistant with those of the generic ESS with some scaling to take into account differences in effective capacity, discharge power and efficiency. This indicates that the generic ESS can give a good indication of the operation of a lead acid ESS, and possibly other ESS types, with some scaling. However, for more accurate results, it is best to model the specific ESS technology in the simulation.

References

Abbey, C., & Joós, G. (2009). A Stochastic Optimization Approach to Rating of Energy Storage Systems in Wind-Diesel Isolated Grids, 24(1), 418-426.

AEA. (2013). Alaska Energy Data Gateway - Nome.pdf. Retrieved March 06, 2014, from https://akenergygateway.alaska.edu/community-data-summary/1407125/#detail-fuel

Brouhard Jr., L. G. (2008). Economic Dispatch and Control for Efficiency Improvements on Diesel Electric Power Systems in Alaska Rural Villages. University of Alaska.

Brown, D. (1993). Experimental Verificaiton of the Load-Following Potential of a Hot Dry Rock Geothermal Resevoir.

C&DTechnologies. (2012). Charging Valve Regulated Lead Acid Batteries.

Chen, C.-L. (2008). Optimal Wind-Thermal Generating Unit Commitment. IEEE Transactions on Energy Conversion, 23(1), 273-280. doi:10.1109/TEC.2007.914188

Cimuca, G. O., Saudemont, C., Robyns, B., & Radulescu, M. M. (2006). Control and Performance Evaluation of a Flywheel Energy-Storage System Associated to a Variable-Speed Wind Generator, 53(4), 1074-1085.

Conte, M., Prosini, P. ., & Passerini, S. (2004). Overview of energy/hydrogen storage: state-of-the-art of the technologies and prospects for nanomaterials. Materials Science and Engineering: B, 108(1-2), 2-8. doi:10.1016/j.mseb.2003.10.107

Costa, a, Crespo, a, Navarro, J., Lizcano, G., Madsen, H., & Feitosa, E. (2008). A review on the young history of the wind power short-term prediction. Renewable and Sustainable Energy Reviews, 12(6), 1725-1744. doi:10.1016/j.rser.2007.01.015

Devine, M. (2011). Analysis of Wind-Diesel Power System in Nome , Alaska. Drouilhet, S. (2001). Preparing an Existing Diesel Power Plant for a Wind Hybrid Retrofit: Lessons Learned in the Wales , Alaska , Wind-Diesel Hybrid Power Project, (August).

Fossati, J. P. (2012). UNIT COMMITMENT AND ECONOMIC DISPATCH IN Despacho económico y de unidades en Micro Redes, 10, 83-96.

Haselwimmer, C., Prakash, A., & Holdmann, G. (2013). Geothermal Exploration at Pilgrim Hot Springs , Alaska Using Airborne Thermal Infrared Remote Sensing, 1-12.

Holdmann, G. (2006). The Chena Hot Springs 400kW Geothermal Power Plant: Experience Gained During the First Year of Operation (pp. 1-9).

IEC. (2005). International Standard IEC 61400-1, Third Edition.

IEC. (2011). Electrical Energy Storage White paper. Geneva.

Kariniotakis, G., Mayer, D., Moussafir, J., Kintxo, J., Usaola, J., Sanchez, I., ... Cruz, I. (2003). ANEMOS: Development of a Next Generation Wind Power Forecasting System for the Large-Scale Integration of Onshore & Offshore Wind Farms., 1-4.

Katiraei, F., & Abbey, C. (2007). Diesel Plant Sizing and Performance Analysis of a Remote Wind-Diesel Microgrid, 1-8.

Keith, K., & Witmer, D. (2009). ALTERNATIVE TRANSPORTATION OPTIONS ON ST . PAUL ISLAND Phase One Final Report Prepared for Tanadgusix Corporation by?:, (September 2009).

Kirby, B., Milligan, M., Denholm, P., Ela, E., Kirby, B., & Milligan, M. (2010). The Role of energy storage with renewable electricity generation The Role of Energy Storage with Renewable Electricity Generation.

Logenthiran, T., & Srinivasan, D. (2009). Short term generation scheduling of a Microgrid. TENCON 2009 - 2009 IEEE Region 10 Conference, 1-6. doi:10.1109/TENCON.2009.5396184

Lu, S., Elizondo, M. a., Samaan, N., Kalsi, K., Mayhorn, E., Diao, R., ... Zhang, Y. (2011). Control strategies for distributed energy resources to maximize the use of wind power in rural microgrids. 2011 IEEE Power and Energy Society General Meeting, 1-8. doi:10.1109/PES.2011.6039787

Padhy, N. P. (2004). Unit Commitment-A Bibliographical Survey. IEEE Transactions on Power Systems, 19(2), 1196-1205. doi:10.1109/TPWRS.2003.821611

Parker, C. ., & Garche, J. (2004). Valve-Regulated Lead-Acid Batteries. Elsevier.

Rafferty, K. (2000). GEOTHERMAL POWER GENERATION, 1-12.

Roberts, B., & Mcdowall, J. (2005). Commercial Successes in Power Storage, (april), 24-30.

Weis, T. M., & Ilinca, A. (2008). The utility of energy storage to improve the economics of wind-diesel power plants in Canada. Renewable Energy, 33(7), 1544-1557. doi:10.1016/j.renene.2007.07.018

Wright, B. (2013). A Review of Unit Commitment, 1-14.

Appendix A

ESS discharge sequences

The following three figures show a sequence where the load went above the capacity of the current diesel fleet. In each case the ESS discharge to allow the smaller capacity diesel generating option to stay online. Figure A.3 shows the MOL of the online generating combination.

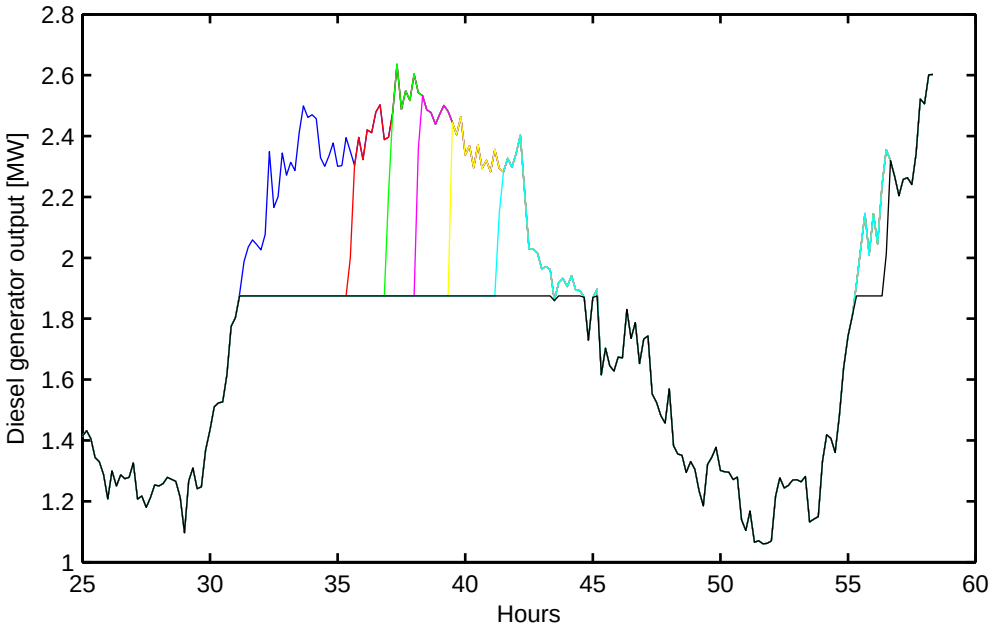


Figure A.1: Diesel outputs for differnt ESS scenario: 2 MW ESS (blue), 3 MW ESS (red), 4 MW ESS (green), 5 MW ESS (purple), 6 MW ESS (yellow), 7 MW ESS (light blue), 8 MW ESS (black).

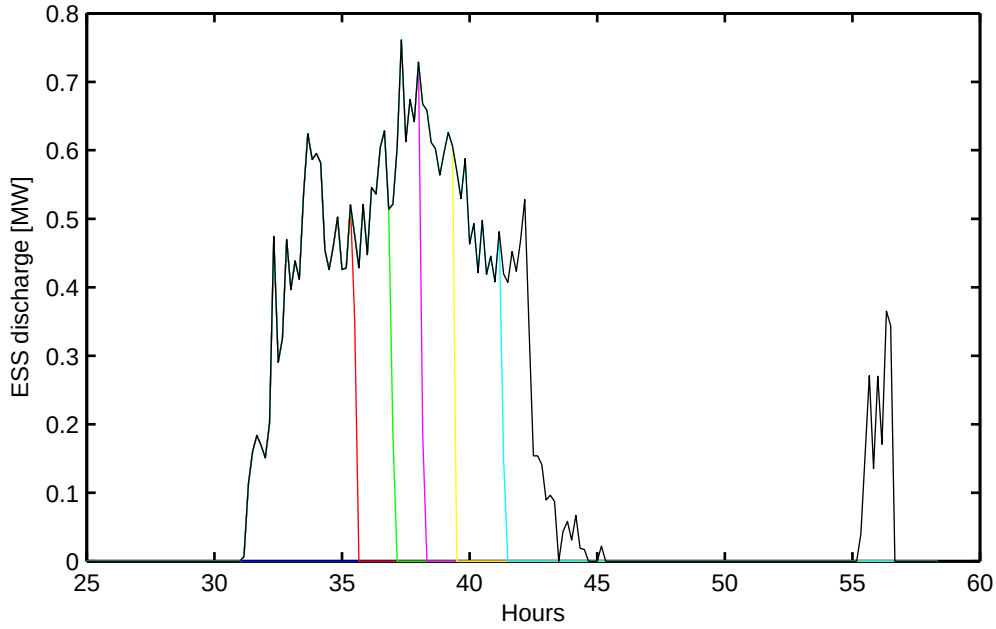


Figure A.2: ESS discharge for differnt ESS scenario: 2 MW ESS (blue), 3 MW ESS (red), 4 MW ESS (green), 5 MW ESS (purple), 6 MW ESS (yellow), 7 MW ESS (light blue), 8 MW ESS (black).

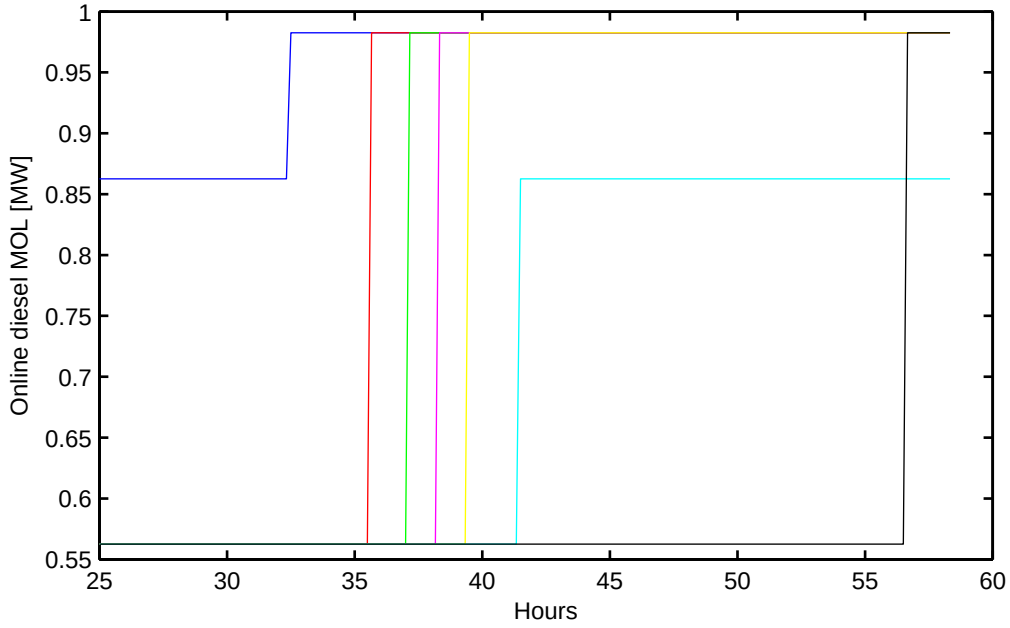


Figure A.3: Diesel MOL for differnt ESS scenario: 2 MW ESS (blue), 3 MW ESS (red), 4 MW ESS (green), 5 MW ESS (purple), 6 MW ESS (yellow), 7 MW ESS (light blue), 8 MW ESS (black).

Appendix B

ESS charge sequences

The following figures show the interaction of Lead Acid ESS charging and the diversion of RE. Notice the decreasing charging power as the SOC of the ESS reaches full capacity.

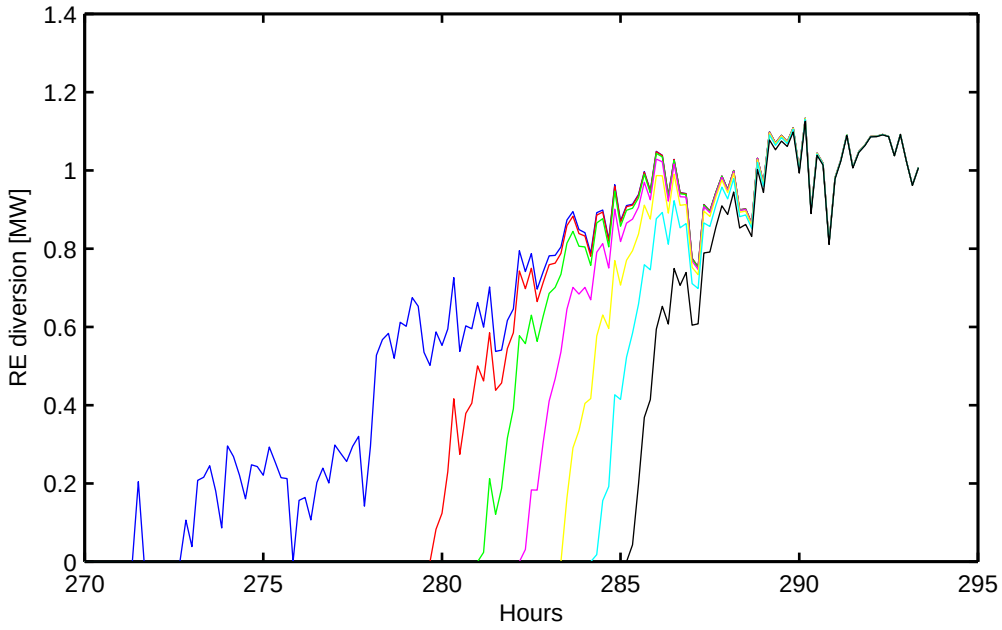


Figure B.1: Diversion of RE [MWh] for different ESS scenarios: 2 MW ESS (blue), 3 MW ESS (red), 4 MW ESS (green), 5 MW ESS (purple), 6 MW ESS (yellow), 7 MW ESS (light blue), 8 MW ESS (black).

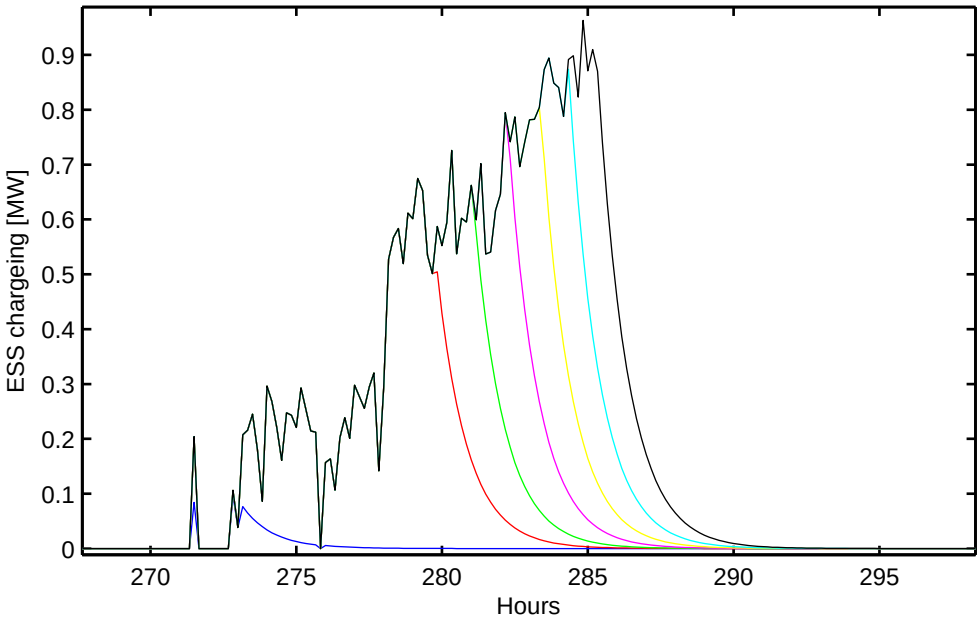


Figure B.2: ESS charging for differnt ESS scenario: 2 MW ESS (blue), 3 MW ESS (red), 4 MW ESS (green), 5 MW ESS (magenta), 6 MW ESS (yellow), 7 MW ESS (cyan), 8 MW ESS (black).

Appendix C

Entegrity Wind Turbine Specs

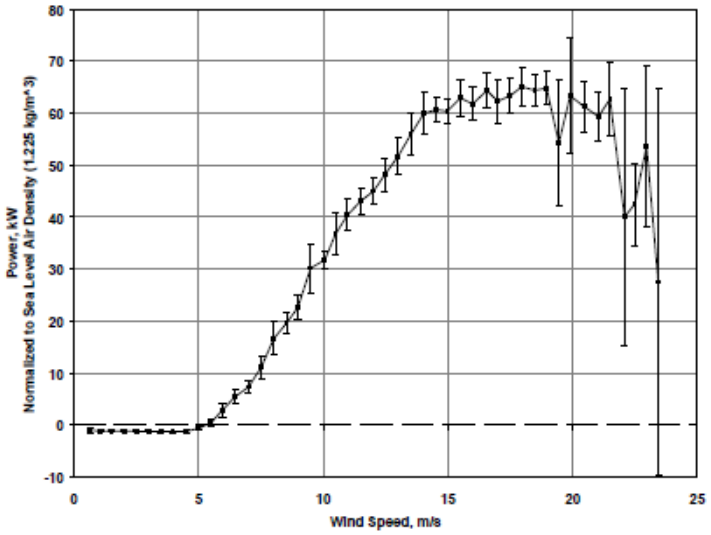


Figure 8. Power curve at sea-level air density, 1.225 kg/m^3.

Table 8. Annual Energy Production at Sea-Level Air Density, 1.225 kg/m^3

Estimated Annual Energy Production				
	Reference air density: 1.225 kg/m^3			
	Cut-out wind speed: 22.3 m/s			
Hub-Height Annual Average Wind Speed (Rayleigh)	**AEP-Measured** (from measured power and zero from last bin to cut-out)	**Standard Uncertainty in AEP-Measured**		**AEP-Extrapolated** (from measured power and constant power from last bin to cut-out)
m/s	MWh	MWh	%	MWh
4	11	5	44%	11
5	42	8	19%	42
6	83	10	13%	83
7	128	13	10%	128
8	172	14	8%	172
9	211	15	7%	211
10	243	15	6%	243
11	268	15	6%	268

Figure C.1: Entegrity wind turbine specifications

Appendix D

EWT Wind Turbine Specs

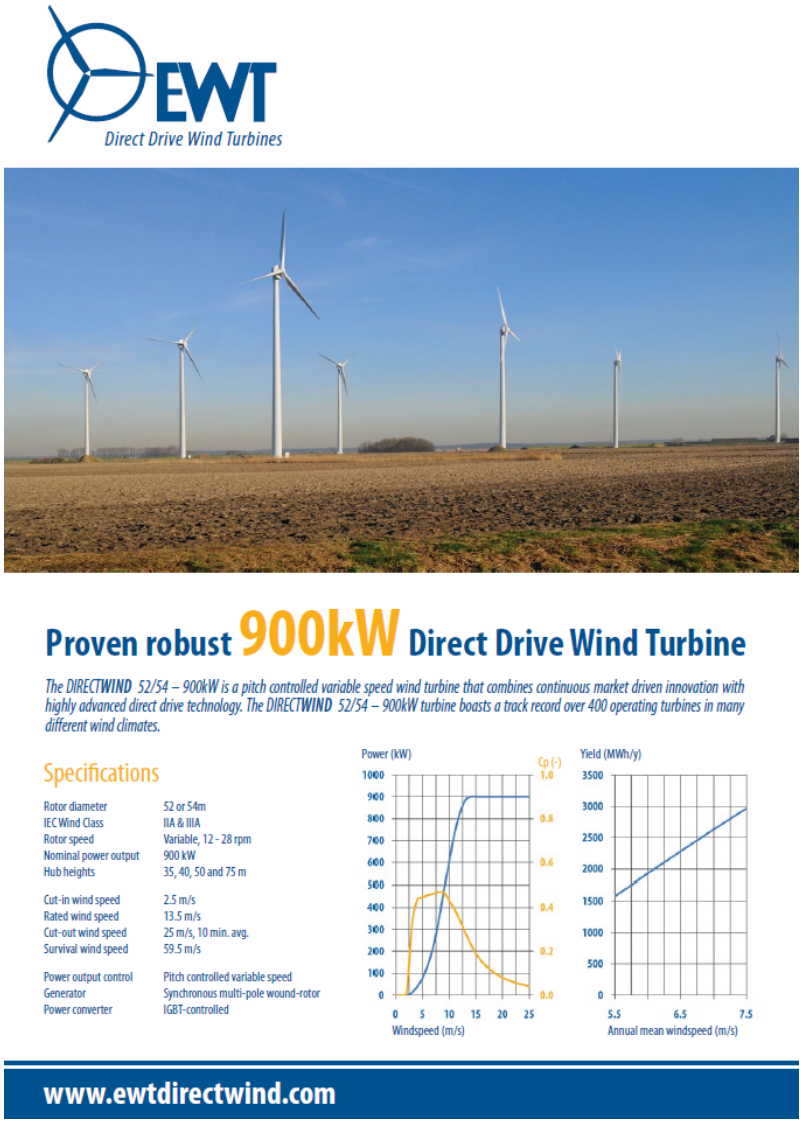


Figure D.1: EWT wind turbine specifications, page 1.

EWT
Direct Drive Wind Turbines

Direct Drive Wind Technology

In EWT turbines the rotor directly drives the synchronous generator, without the use of a gearbox. This is important because various studies have concluded that the dominant cause of downtime is malfunctioning of gearboxes. The generated energy is fed into the grid via a modern back-to-back full-power converter which controls the output, so grid requirements can be met. This makes the *DIRECT**WIND*** turbine suitable to operate in weak grids.

Advantages of EWT's Direct Drive Technology:

- Superior availability levels
- No need to replace gearboxes
- High yields / return on investment
- Low maintenance costs
- Reduced noise levels
- Low cost of ownership



Power quality & Site conditions

The *DIRECT**WIND*** turbine feeds generator power into the grid by means of a modern 'back-to-back' type full-converter system. This converter contains a number of programmable functions like a capability to control the reactive power output. Built-in grid-fault-ride-through technology is available on demand.

All the advanced grid-connection features combined make the *DIRECT**WIND*** the perfect choice for solitary applications, weak grids and demanding locations with constrains in site access.

The combination of advanced control features and proven wind technology makes the DIRECTWIND also a first-class choice with regard to energy yield. Fewer components, high reliability, reduced maintenance and excellent energy yield ensure an optimal return on investment. We are looking forward to showing you what our *DIRECT**WIND*** systems can offer.



DSP - *DIRECT**WIND*** Service Program

EWT stands for high-quality direct drive turbines characterized by reliability and cost efficiency. To ensure optimal performance and trouble-free operation of our DIRECTWIND turbines, we have a extensive service and maintenance program in place. The DIRECTWIND Service Program offers:

- Preventive maintenance
- Availability guarantee
- Extended product warranty
- Corrective maintenance
- Power curve guarantee
- Business Interruption compensation

The company

EWT is a designer and manufacturer of direct drive wind turbines active in Europe, North America and Asia. EWT was established in 2004 and is based in the Netherlands. The company has an extensive product line, an engineering department covering all relevant disciplines and a dedicated service and maintenance organisation.

EWT B.V.
Lindeboomseweg 51
3825 AL Amersfoort
The Netherlands
T +31 (0)33 454 05 20
F +31 (0)33 456 30 92
sales@ewtdirectwind.com
www.ewtdirecwind.com

Disclaimer: The information included herein is provided to you for general information purposes only. Although every effort has been made to ensure the accuracy of such information, EWT makes no representation or warranty of any kind, express or implied, as to the correctness, accuracy, reliability or completeness of the information.

Copyright EWT 2013 ©

Figure D.2: EWT wind turbine specifications, page 2.

Appendix E

Surrette 2-YS-31PS Specs

Surrette

DEEP CYCLE - SOLAR

SERIES: 5000
MODEL: 2 YS 31PS

BATTERY TYPE: **2 VOLTS**

DESIGN CRITERIA: **10 YEAR WARRANTY** **15 YEAR LIFE** **3300 CYCLES**

DIMENSIONS:

LENGTH	394	MM	15 1/2	INCHES	WEIGHT DRY	91	KG	200 LBS.
WIDTH	229	MM	9	INCHES	WEIGHT WET	129	KG	285 LBS.
HEIGHT	803	MM	31 5/8	INCHES				

CONTAINER CONSTRUCTION:

CONTAINER (INNER):	POLYPROPYLENE	**HANDLES:**	MOLDED
CONTAINER (OUTER):	HIGH DENSITY POLYETHYLENE	**CELLS:**	1
COVER (INNER):	POLYPROPYLENE - HEAT SEALED TO INNER CONTAINER	**PLATES / CELL:**	33
COVER (OUTER):	HIGH DENSITY POLYETHYLENE SNAP FIT TO OUTER CONTAINER		
TERMINALS:	FLAG WITH STAINLESS STEEL NUTS AND BOLTS		

PLATES:

POSITIVE PLATE DIMENSION:

HEIGHT	600	MM	23.625	INCHES
WIDTH	143	MM	5.625	INCHES
THICKNESS	6.99	MM	0.275	INCHES

NEGATIVE PLATE DIMENSION:

HEIGHT	600	MM	23.625	INCHES
WIDTH	143	MM	5.625	INCHES
THICKNESS	4.57	MM	0.180	INCHES

SEPARATOR:

THICKNESS	3	MM	0.105	INCHES

INSULATION:

GLASS MAT	1	MM	0.020	INCHES

POSITIVE PLATE DOUBLE WRAPPED WITH SLYVER ENVELOPED WITH HEAVY DUTY SEPARATOR

ELECTROLYTE RESERVE: (ABOVE PLATES)
95 MM 3.75 INCHES

CAPACITY: **20 HR RATE** **2430**

CRANK AMPS:

COLD (CCA)	0ºF / -17.8º	5740
MARINE (MCA)	32ºF / 0ºC	7175

RESERVE CAPACITY:
RC @ 25A 7772 MINUTES

	HOUR RATE	SPECIFIC GRAVITY	CAP / AH	CURRENT / AMPS
CAPACITY @	**20 HOUR RATE**	**1.280 SP. GR.**	**2430**	**121.5**
CAPACITY @	15 HOUR RATE	1.280 SP. GR.	2284	152.3
CAPACITY @	12 HOUR RATE	1.280 SP. GR.	2163	180.2
CAPACITY @	10 HOUR RATE	1.280 SP. GR.	2066	206.6
CAPACITY @	8 HOUR RATE	1.280 SP. GR.	1944	243.0
CAPACITY @	6 HOUR RATE	1.280 SP. GR.	1798	299.7
CAPACITY @	5 HOUR RATE	1.280 SP. GR.	1701	340
CAPACITY @	4 HOUR RATE	1.280 SP. GR.	1580	395
CAPACITY @	3 HOUR RATE	1.280 SP. GR.	1434	478
CAPACITY @	2 HOUR RATE	1.280 SP. GR.	1239	620
CAPACITY @	1 HOUR RATE	1.280 SP. GR.	875	875

Rev.1 Oct. -09 RDSPECS 09

Figure E.1: Surrette 2-YS-31 specifications, page 1.

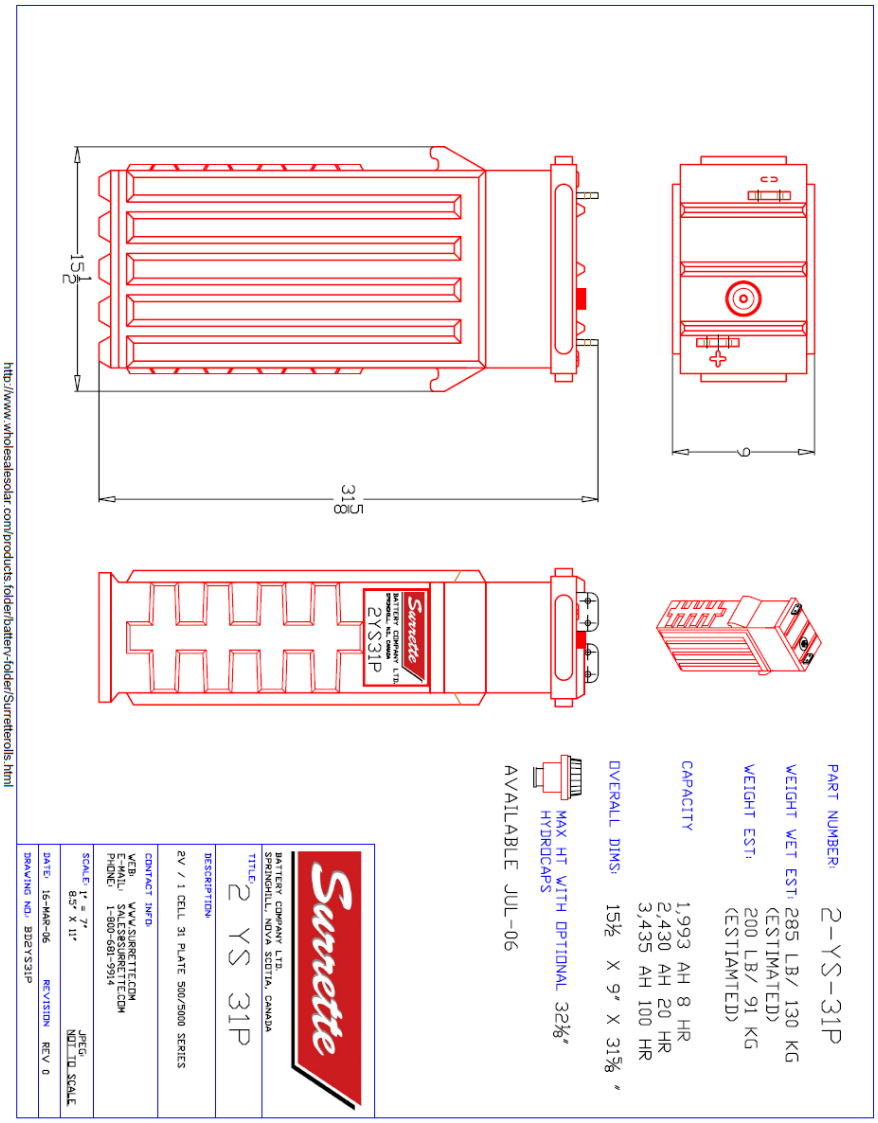


Figure E.2: Surrette 2-YS-31 specifications, page 2.

Appendix F

Simulation Results for EDS1

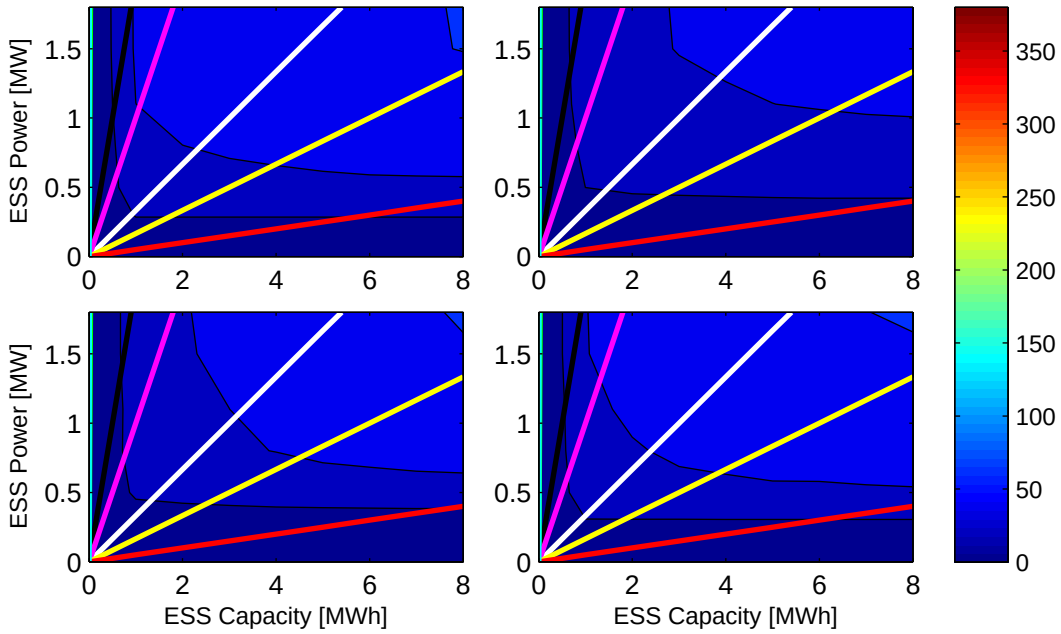


Figure F.1: Displaced diesel generator output for different levels of ESS power and capacity and 0MW of geothermal capacity. The different plots represent different diesel cases (see Table 2.3): Top left: Diesel Case 1, Top right: Diesel Case 2. Bottom left: Diesel Case 3. Bottom right: Diesel Case 4.

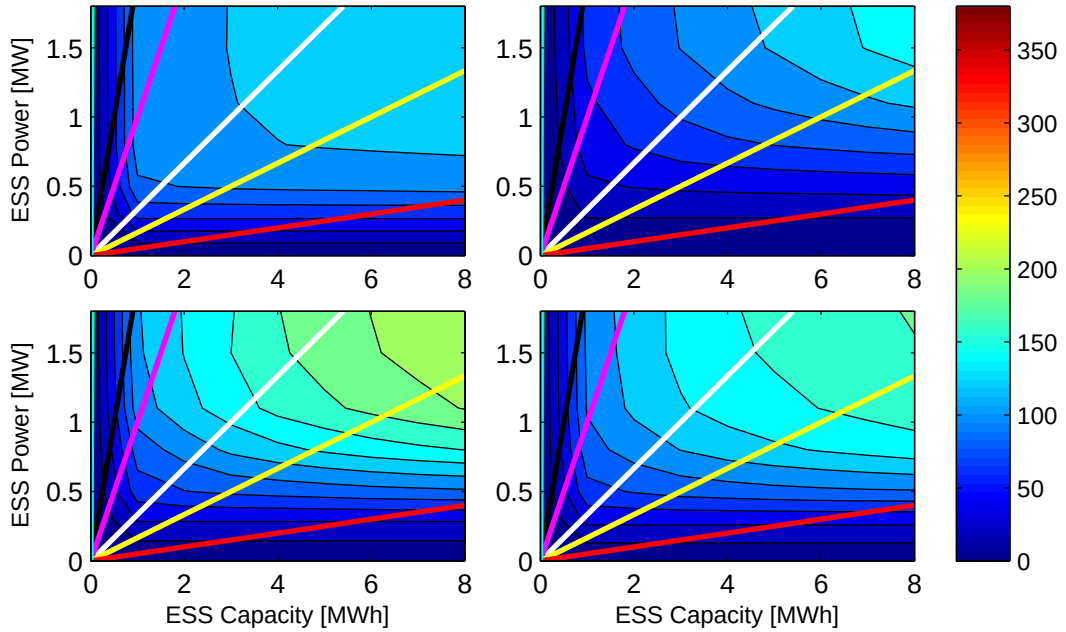


Figure F.2: Displaced diesel generator output for different levels of ESS power and capacity and 1MW of geothermal capacity. The different plots represent different diesel cases (see Table 2.3): Top left: Diesel Case 1, Top right: Diesel Case 2. Bottom left: Diesel Case 3. Bottom right: Diesel Case 4.

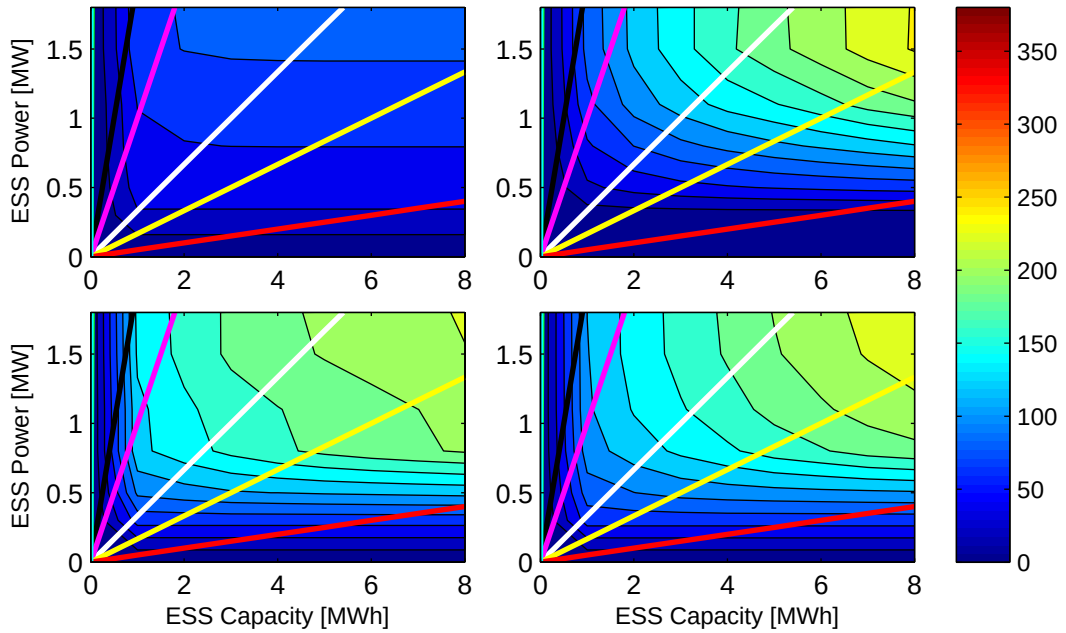


Figure F.3: Displaced diesel generator output for different levels of ESS power and capacity and 1.5 MW of geothermal capacity. The different plots represent different diesel cases (see Table 2.3): Top left: Diesel Case 1, Top right: Diesel Case 2. Bottom left: Diesel Case 3. Bottom right: Diesel Case 4.

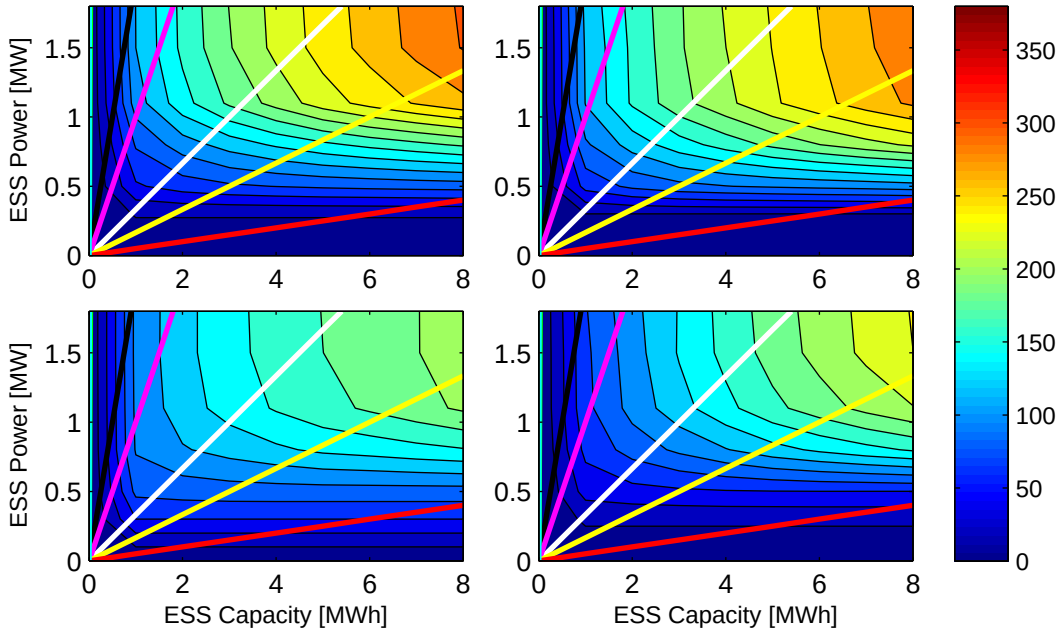


Figure F.4: Displaced diesel generator output for different levels of ESS power and capacity and 2 MW of geothermal capacity. The different plots represent different diesel cases (see Table 2.3): Top left: Diesel Case 1, Top right: Diesel Case 2. Bottom left: Diesel Case 3. Bottom right: Diesel Case 4.

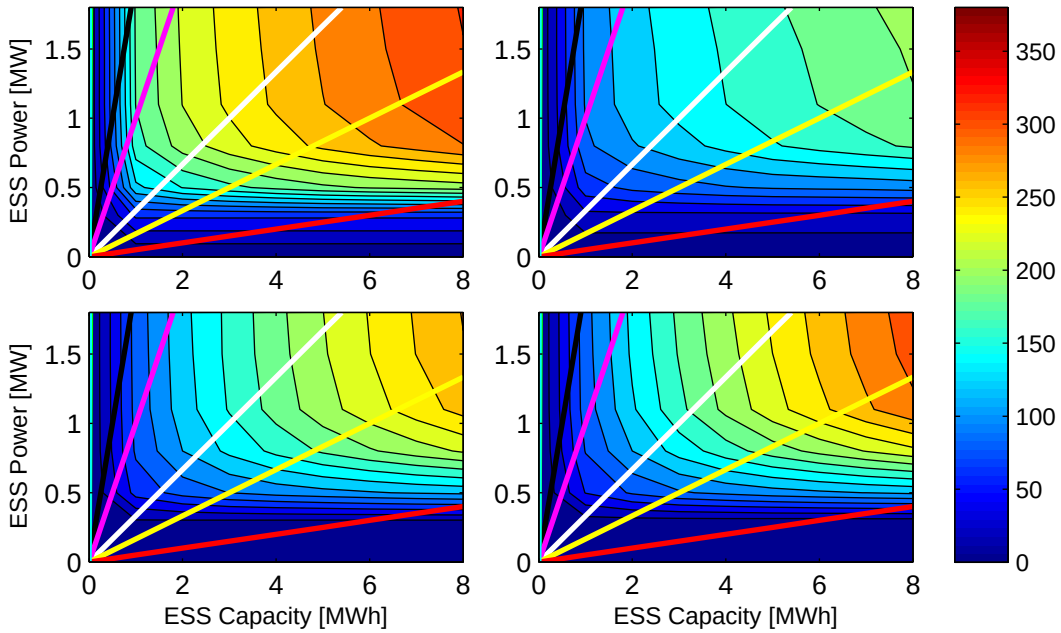


Figure F.5: Displaced diesel generator output for different levels of ESS power and capacity and 2.5 MW of geothermal capacity. The different plots represent different diesel cases (see Table 2.3): Top left: Diesel Case 1, Top right: Diesel Case 2. Bottom left: Diesel Case 3. Bottom right: Diesel Case 4.

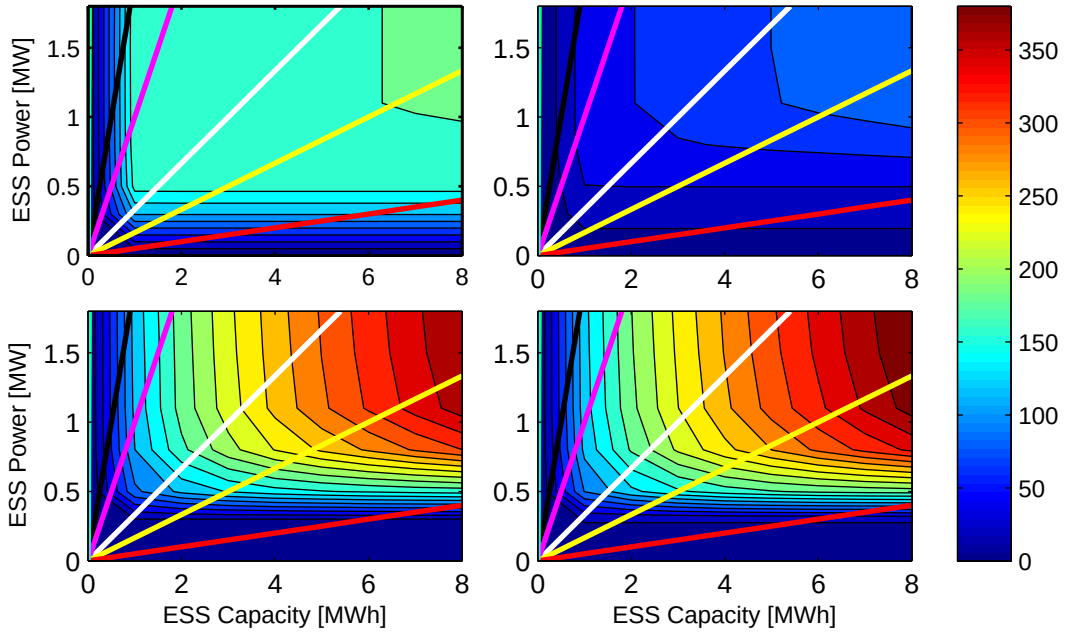


Figure F.6: Displaced diesel generator output for different levels of ESS power and capacity and 3 MW of geothermal capacity. The different plots represent different diesel cases (see Table 2.3): Top left: Diesel Case 1, Top right: Diesel Case 2. Bottom left: Diesel Case 3. Bottom right: Diesel Case 4.

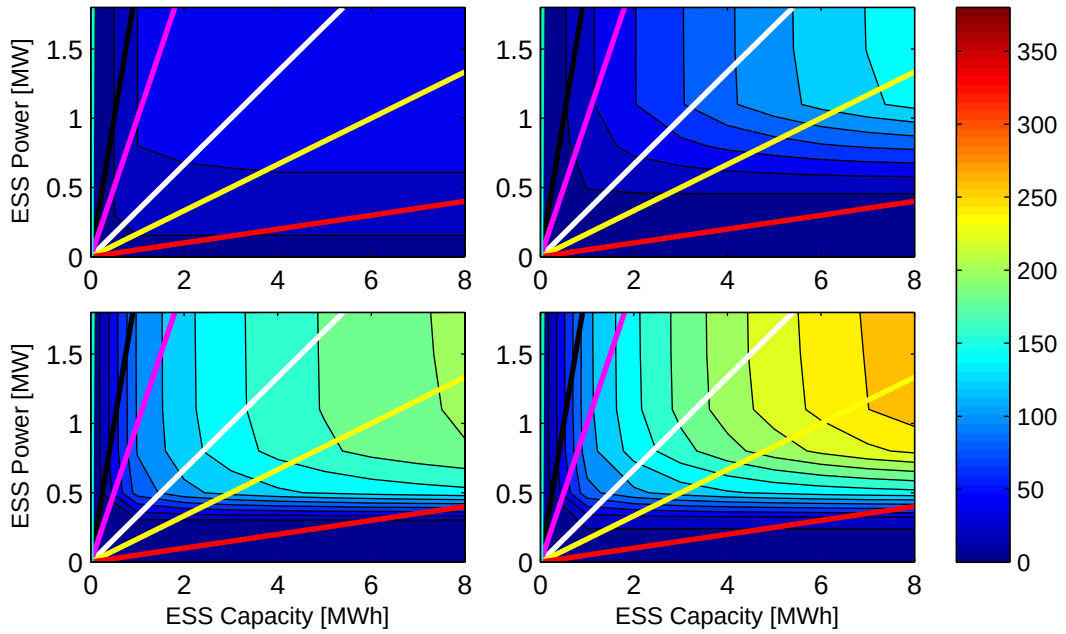


Figure F.7: Displaced diesel generator output for different levels of ESS power and capacity and 3.5 MW of geothermal capacity. The different plots represent different diesel cases (see Table 2.3): Top left: Diesel Case 1, Top right: Diesel Case 2. Bottom left: Diesel Case 3. Bottom right: Diesel Case 4.

Appendix G

Simulation Results for EDS2

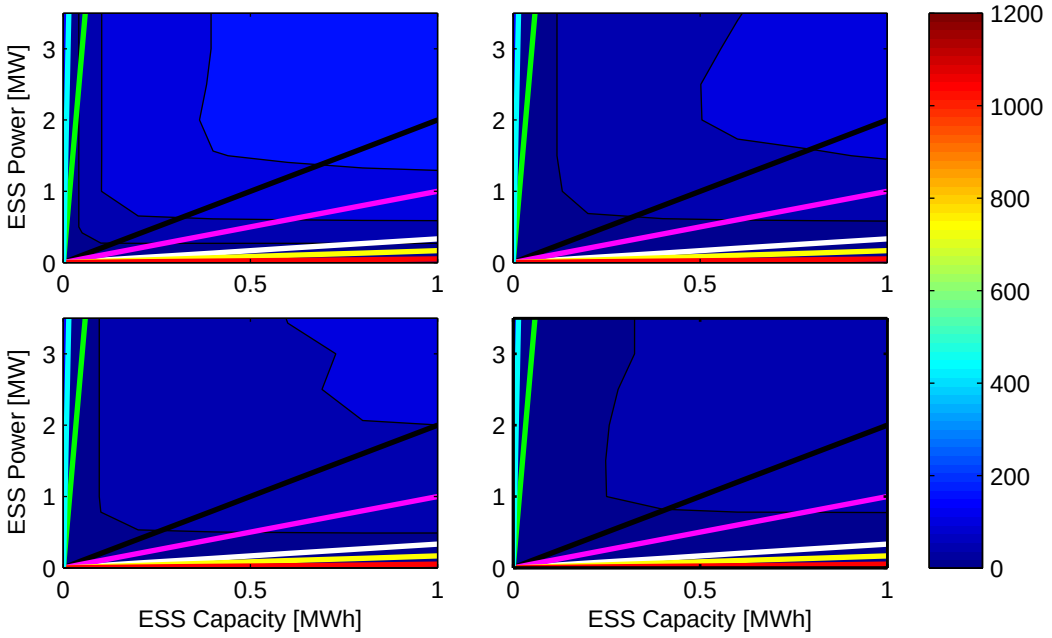


Figure G.1: Displaced diesel generator output [MWh] for different levels of ESS power and capacity and 0 MW of geothermal capacity. The different plots represent different diesel cases (see Table 2.3): Top left: Diesel Case 1, Top right: Diesel Case 2. Bottom left: Diesel Case 3. Bottom right: Diesel Case 4.

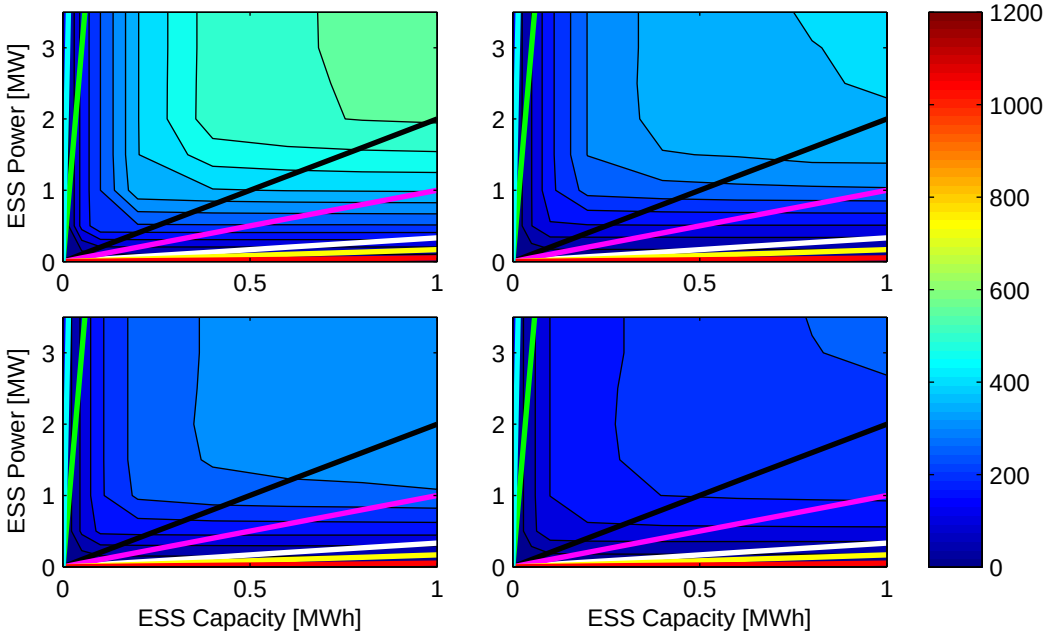


Figure G.2: Displaced diesel generator output [MWh] for different levels of ESS power and capacity and 1 MW of geothermal capacity. The different plots represent different diesel cases (see Table 2.3): Top left: Diesel Case 1, Top right: Diesel Case 2. Bottom left: Diesel Case 3. Bottom right: Diesel Case 4.

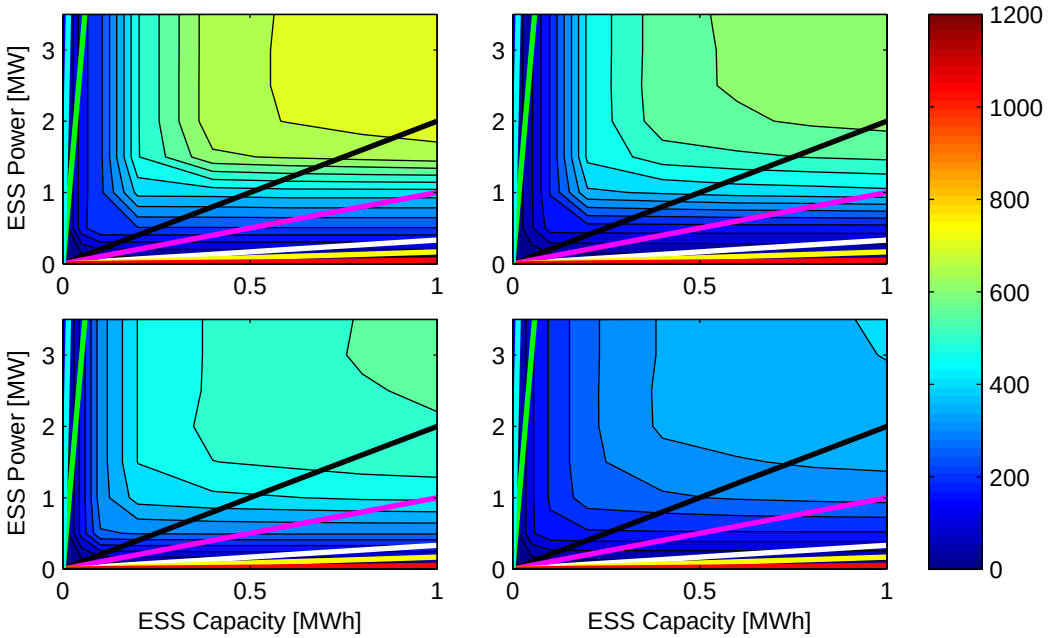


Figure G.3: Displaced diesel generator output [MWh] for different levels of ESS power and capacity and 1.5 MW of geothermal capacity. The different plots represent different diesel cases (see Table 2.3): Top left: Diesel Case 1, Top right: Diesel Case 2. Bottom left: Diesel Case 3. Bottom right: Diesel Case 4.

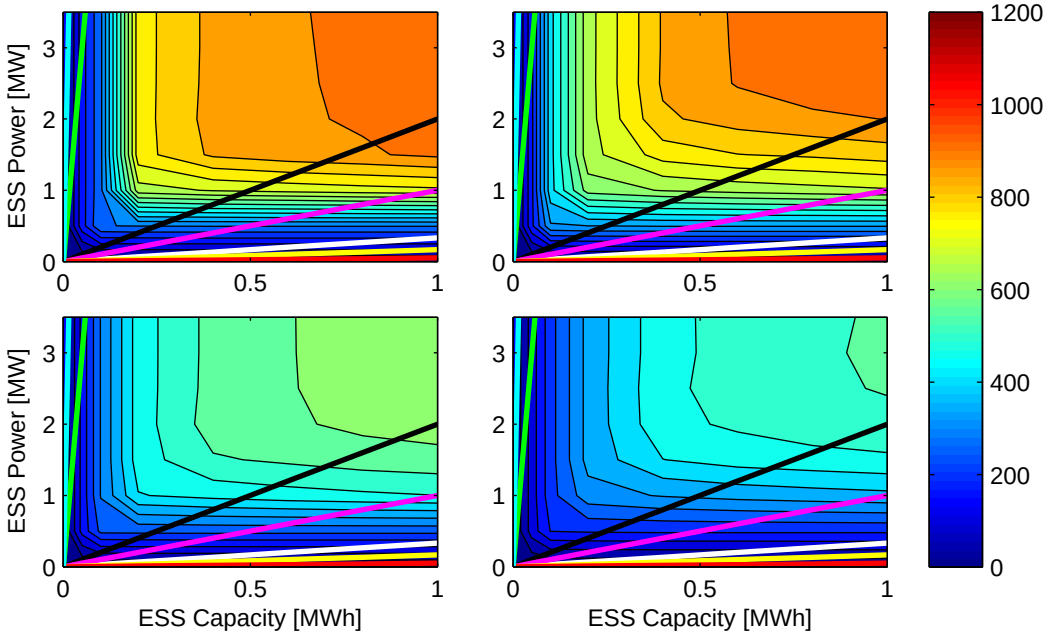


Figure G.4: Displaced diesel generator output [MWh] for different levels of ESS power and capacity and 2 MW of geothermal capacity. The different plots represent different diesel cases (see Table 2.3): Top left: Diesel Case 1, Top right: Diesel Case 2. Bottom left: Diesel Case 3. Bottom right: Diesel Case 4.

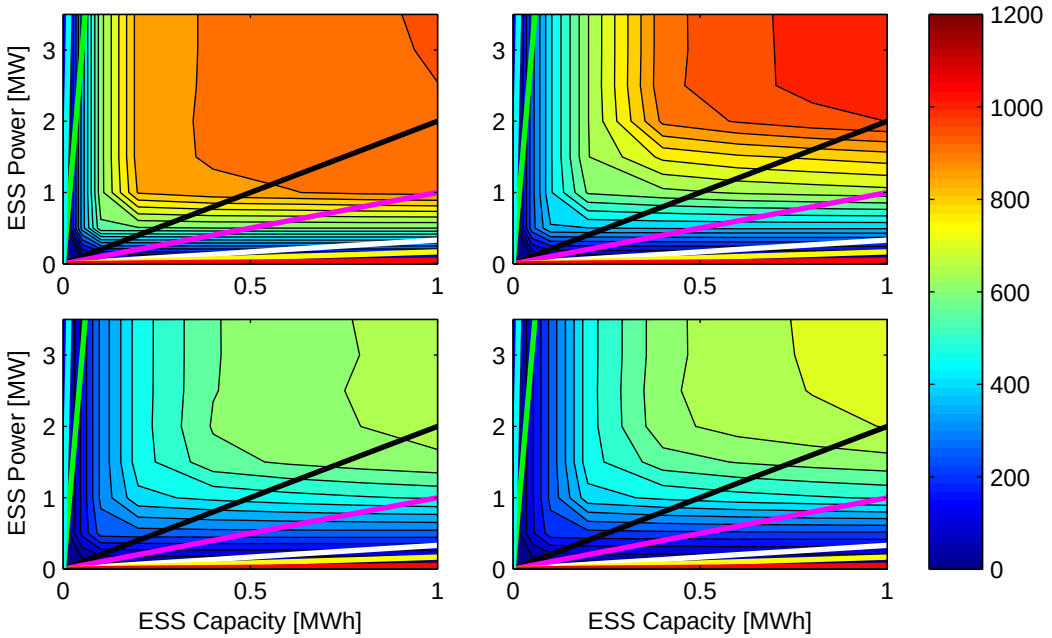


Figure G.5: Displaced diesel generator output [MWh] for different levels of ESS power and capacity and 2.5 MW of geothermal capacity. The different plots represent different diesel cases (see Table 2.3): Top left: Diesel Case 1, Top right: Diesel Case 2. Bottom left: Diesel Case 3. Bottom right: Diesel Case 4.

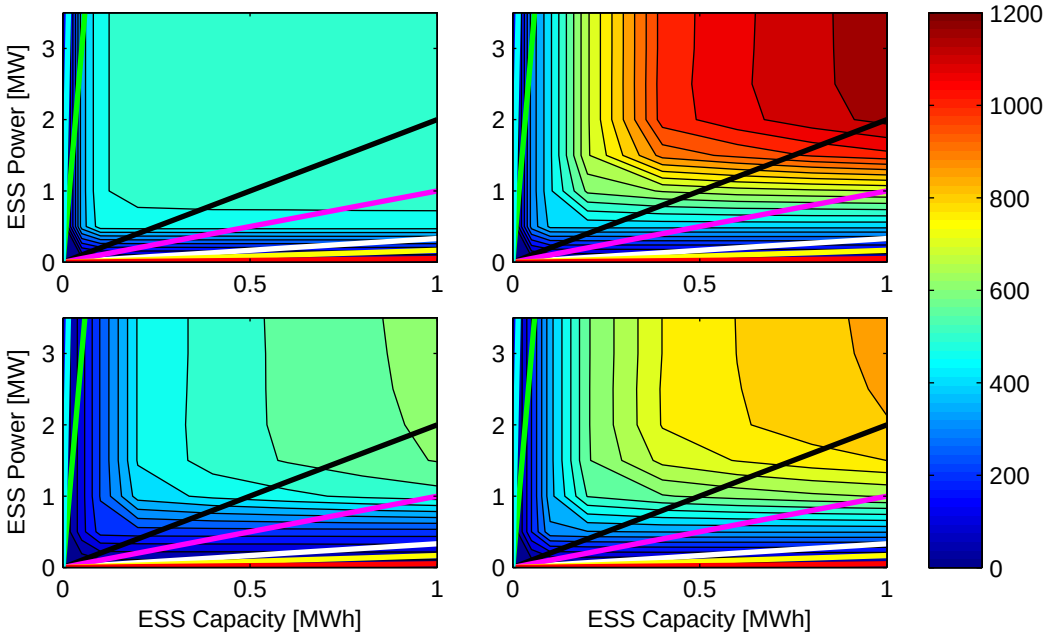


Figure G.6: Displaced diesel generator output [MWh] for different levels of ESS power and capacity and 3 MW of geothermal capacity. The different plots represent different diesel cases (see Table 2.3): Top left: Diesel Case 1, Top right: Diesel Case 2. Bottom left: Diesel Case 3. Bottom right: Diesel Case 4.

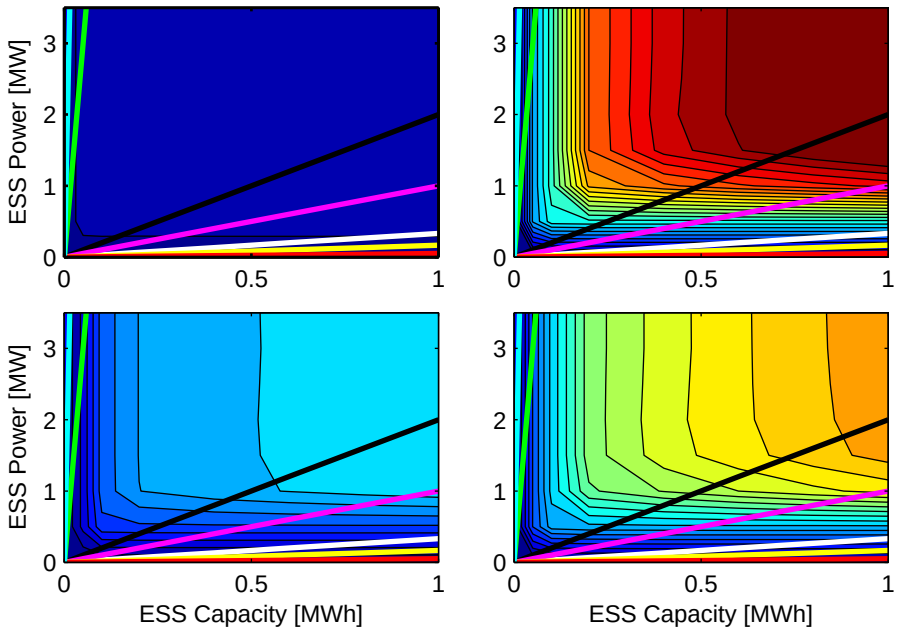


Figure G.7: Displaced diesel generator output [MWh] for different levels of ESS power and capacity and 3.5 MW of geothermal capacity. The different plots represent different diesel cases (see Table 2.3): Top left: Diesel Case 1, Top right: Diesel Case 2. Bottom left: Diesel Case 3. Bottom right: Diesel Case 4.

Appendix H

Simulation Results for EDS3

H.1 Displaced Diesel Generator Output

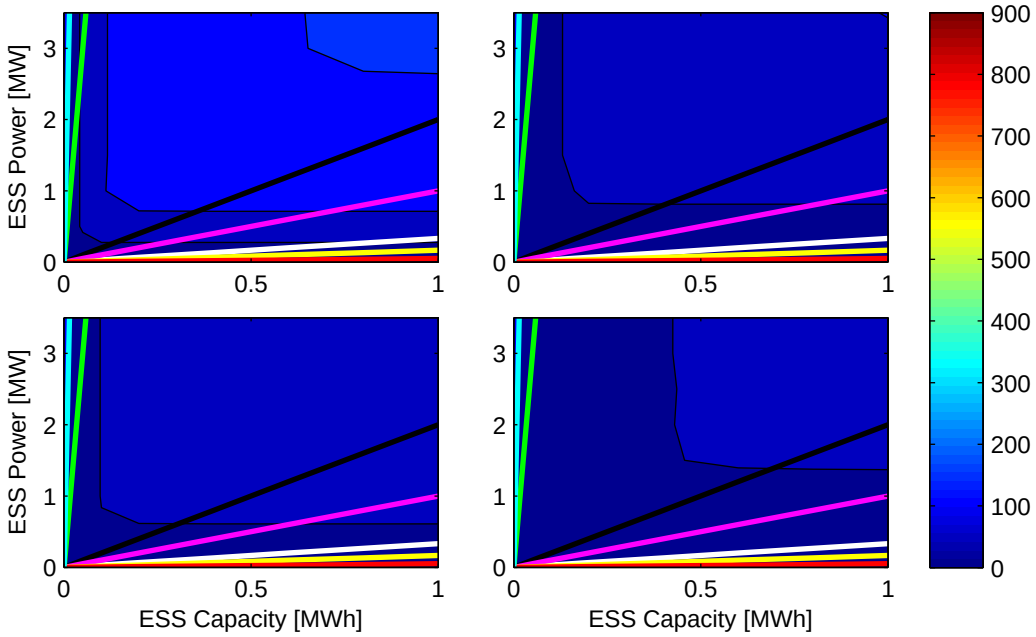


Figure H.1: Displaced diesel generator output [MWh] for different levels of ESS power and capacity and 0 MW of geothermal capacity. The different plots represent different diesel cases (see Table 2.3): Top left: Diesel Case 1, Top right: Diesel Case 2. Bottom left: Diesel Case 3. Bottom right: Diesel Case 4.

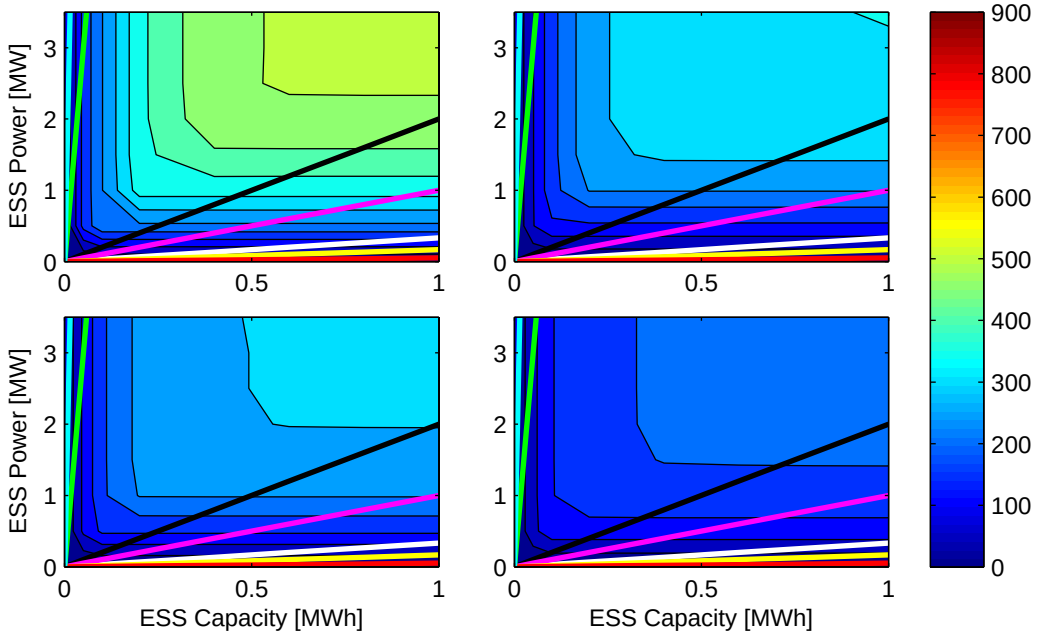


Figure H.2: Displaced diesel generator output [MWh] for different levels of ESS power and capacity and 1 MW of geothermal capacity. The different plots represent different diesel cases (see Table 2.3): Top left: Diesel Case 1, Top right: Diesel Case 2. Bottom left: Diesel Case 3. Bottom right: Diesel Case 4.

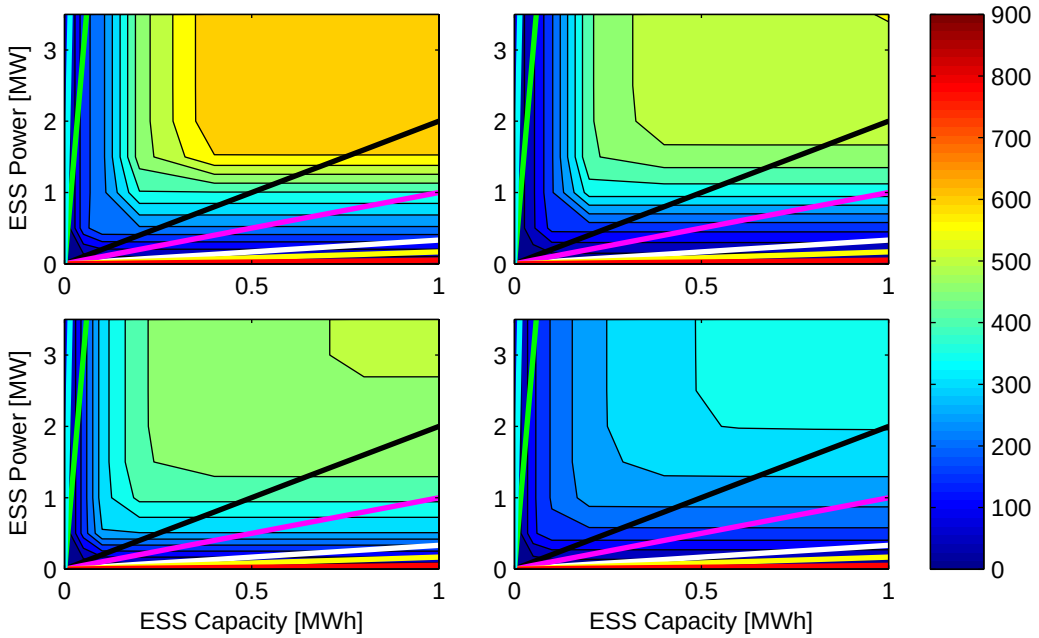


Figure H.3: Displaced diesel generator output [MWh] for different levels of ESS power and capacity and 1.5 MW of geothermal capacity. The different plots represent different diesel cases (see Table 2.3): Top left: Diesel Case 1, Top right: Diesel Case 2. Bottom left: Diesel Case 3. Bottom right: Diesel Case 4.

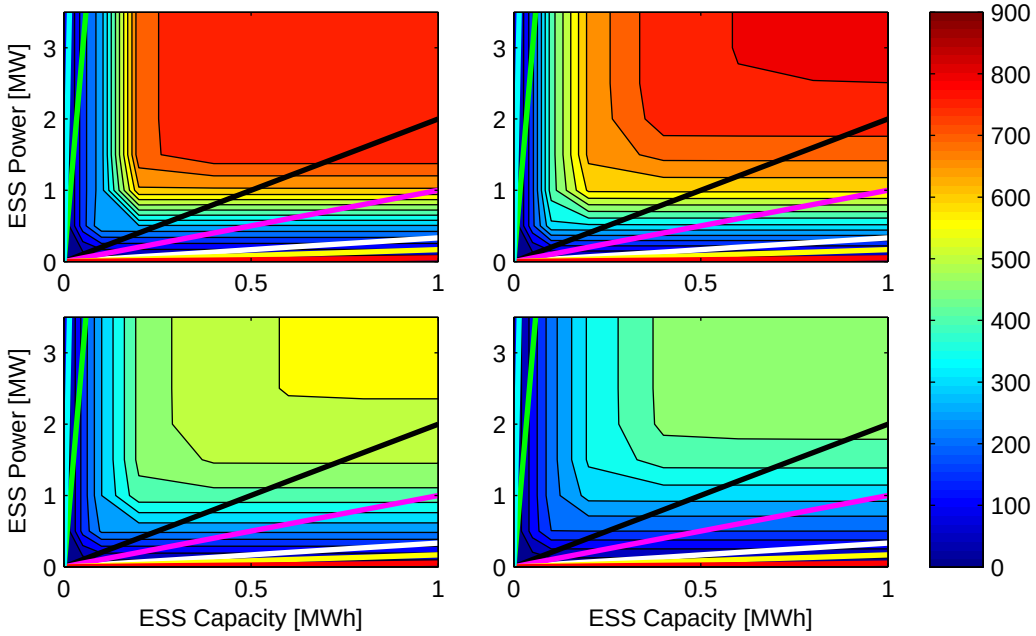


Figure H.4: Displaced diesel generator output [MWh] for different levels of ESS power and capacity and 2 MW of geothermal capacity. The different plots represent different diesel cases (see Table 2.3): Top left: Diesel Case 1, Top right: Diesel Case 2. Bottom left: Diesel Case 3. Bottom right: Diesel Case 4.

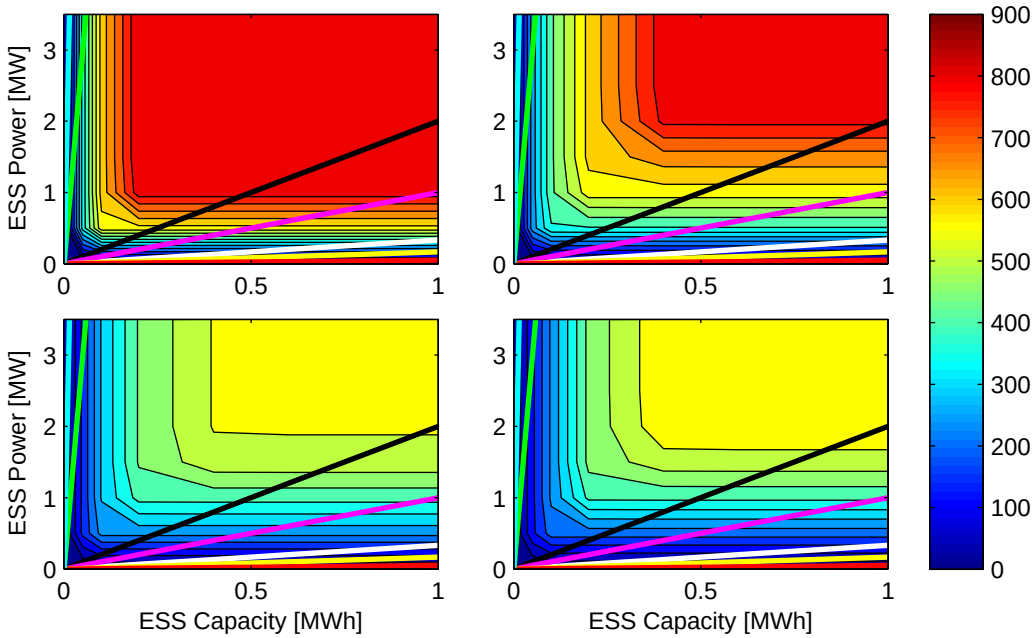


Figure H.5: Displaced diesel generator output [MWh] for different levels of ESS power and capacity and 2.5 MW of geothermal capacity. The different plots represent different diesel cases (see Table 2.3): Top left: Diesel Case 1, Top right: Diesel Case 2. Bottom left: Diesel Case 3. Bottom right: Diesel Case 4.

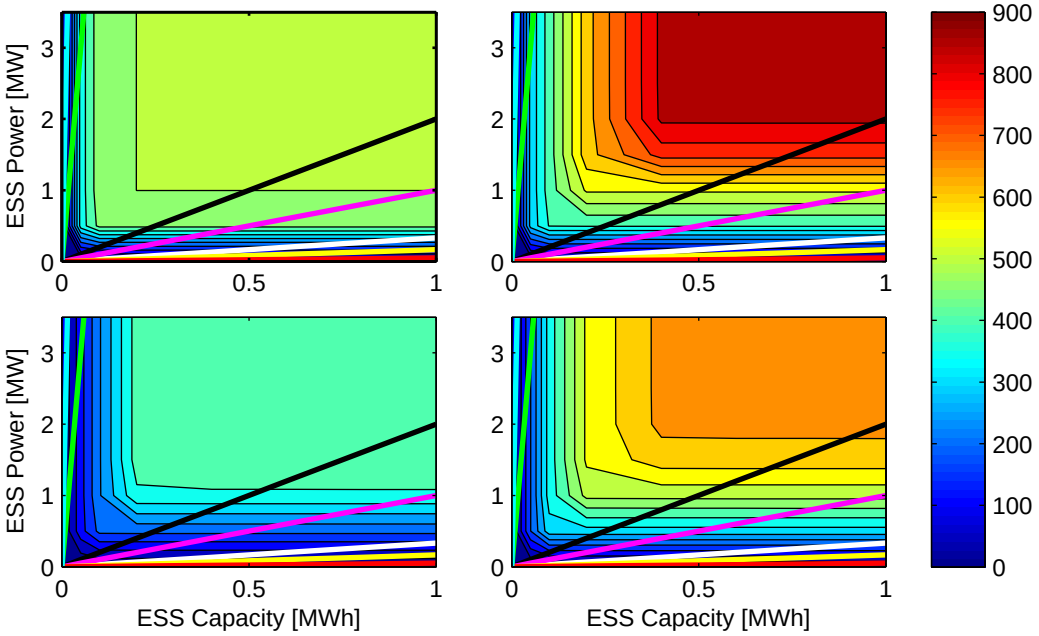


Figure H.6: Displaced diesel generator output [MWh] for different levels of ESS power and capacity and 3 MW of geothermal capacity. The different plots represent different diesel cases (see Table 2.3): Top left: Diesel Case 1, Top right: Diesel Case 2. Bottom left: Diesel Case 3. Bottom right: Diesel Case 4.

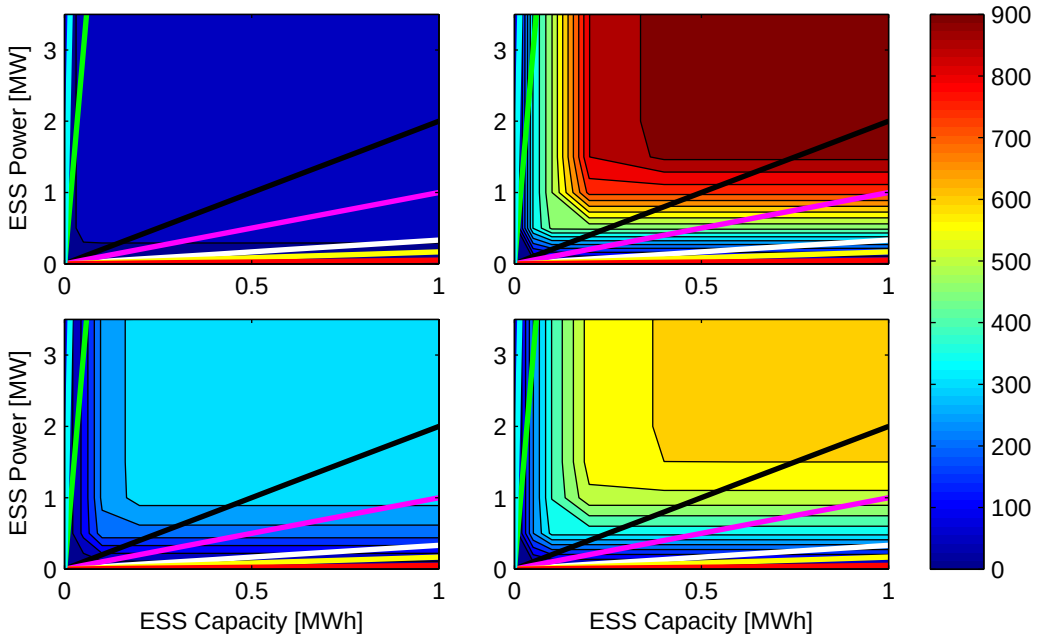


Figure H.7: Displaced diesel generator output [MWh] for different levels of ESS power and capacity and 3.5 MW of geothermal capacity. The different plots represent different diesel cases (see Table 2.3): Top left: Diesel Case 1, Top right: Diesel Case 2. Bottom left: Diesel Case 3. Bottom right: Diesel Case 4.

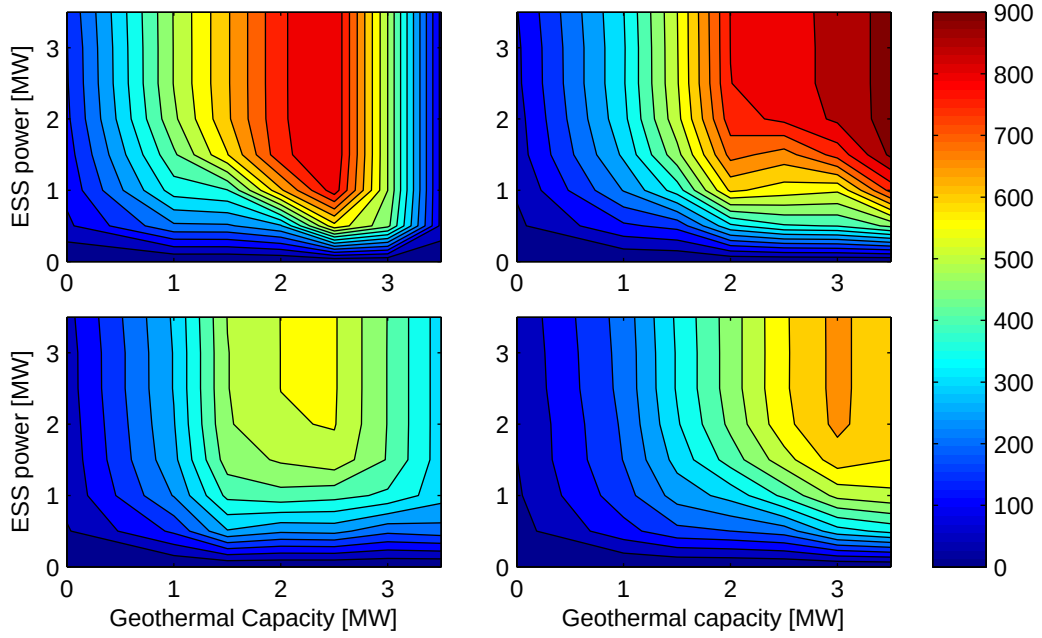


Figure H.8: Displaced diesel generator output [MWh] for ESS with a capactiy to power ratio of 0.2 h and different levels of geothermal capacity. The different plots represent different diesel cases (see Table 2.3): Top left: Diesel Case 1, Top right: Diesel Case 2. Bottom left: Diesel Case 3. Bottom right: Diesel Case 4.

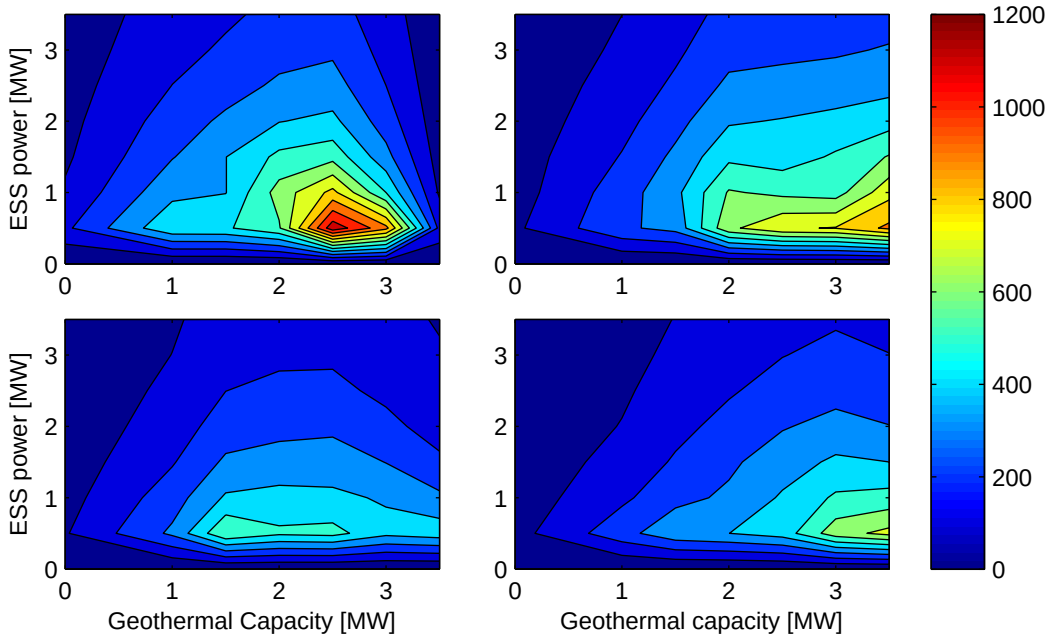


Figure H.9: The ratio of displaced diesel generator output [MWh] over ESS power [MW] for ESS with a capactiy to power ratio of 0.2 h and different levels of geothermal capacity. The different plots represent different diesel cases (see Table 2.3): Top left: Diesel Case 1, Top right: Diesel Case 2. Bottom left: Diesel Case 3. Bottom right: Diesel Case 4.

H.2 Diesel Operation

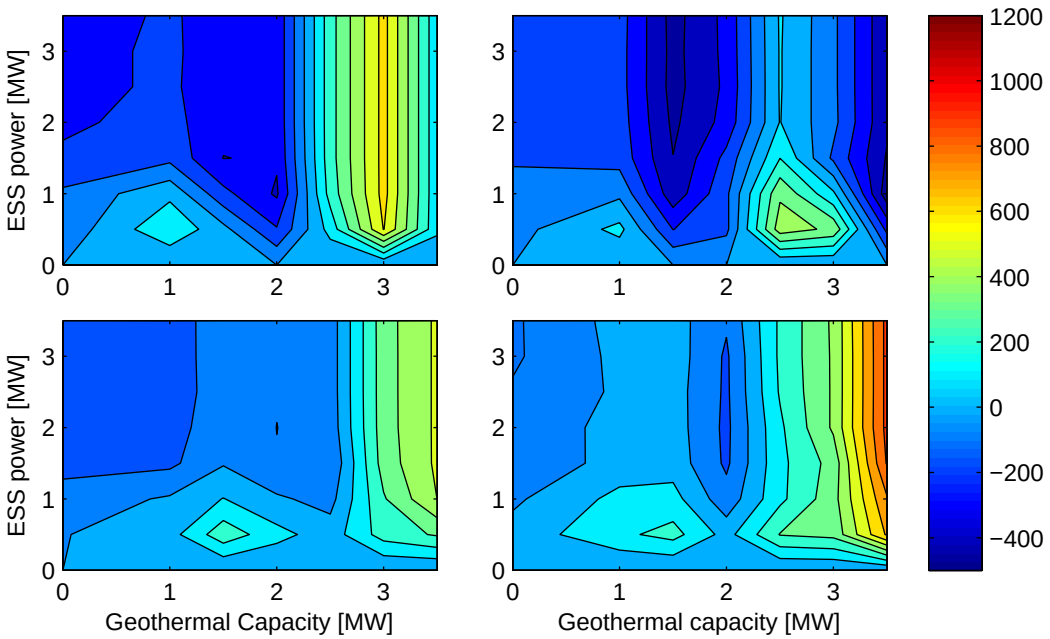


Figure H.10: Reduction in diesel switching with an ESS with a capactiy to power ratio of 0.2 h and different levels of geothermal capacity. The different plots represent different diesel cases (see Table 2.3): Top left: Diesel Case 1, Top right: Diesel Case 2. Bottom left: Diesel Case 3. Bottom right: Diesel Case 4.

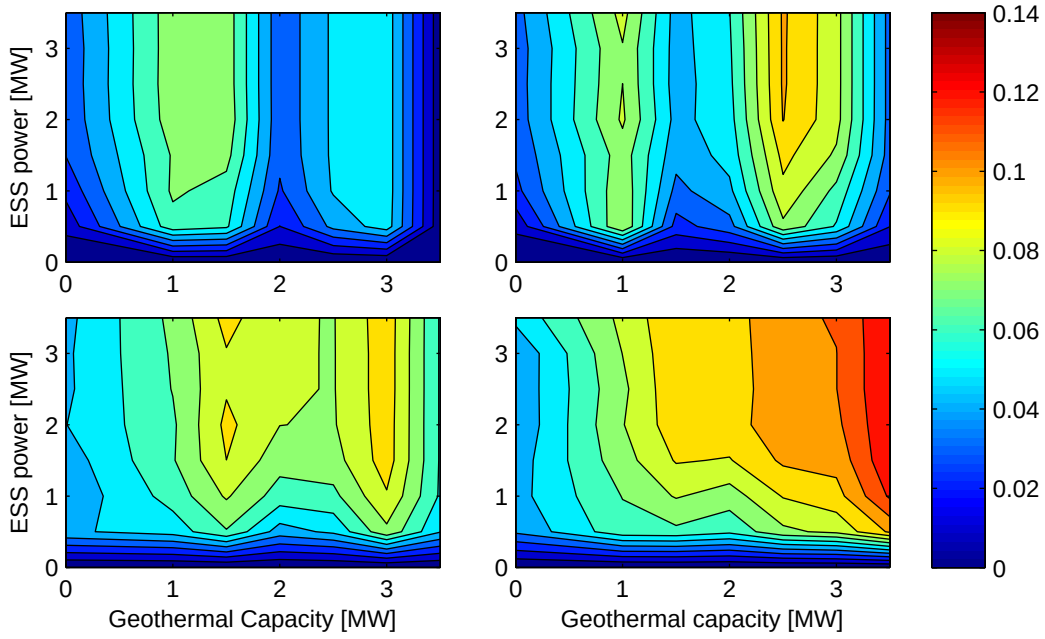


Figure H.11: Increase in the average loading of diesel generators with a capactiy to power ratio of 0.2 h and different levels of geothermal capacity. The different plots represent different diesel cases (see Table 2.3): Top left: Diesel Case 1, Top right: Diesel Case 2. Bottom left: Diesel Case 3. Bottom right: Diesel Case 4.

H.3 Energy Storage System Operation

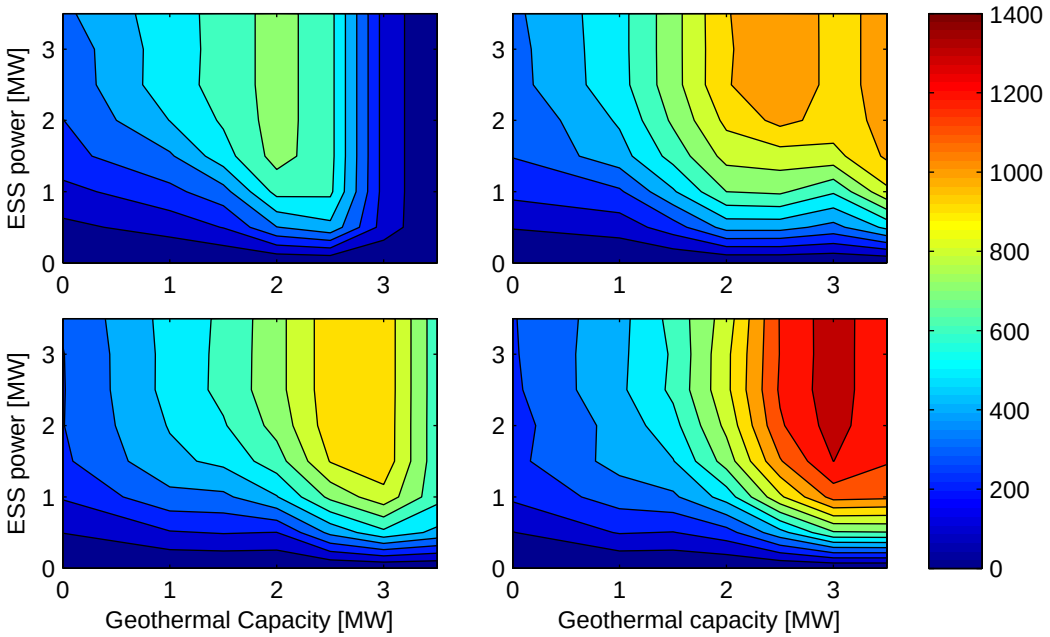


Figure H.12: ESS cycles per year for an ESS with a capactiy to power ratio of 0.2 h and different levels of geothermal capacity. The different plots represent different diesel cases (see Table 2.3): Top left: Diesel Case 1, Top right: Diesel Case 2. Bottom left: Diesel Case 3. Bottom right: Diesel Case 4.

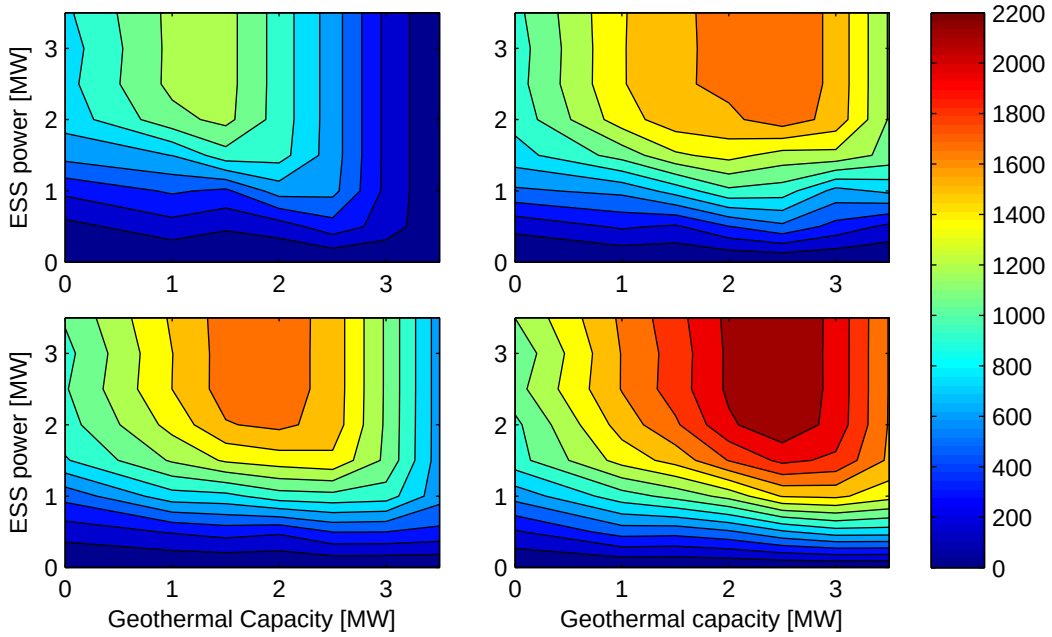


Figure H.13: SRC supplied be the ESS per year [MWh] for an ESS with a capactiy to power ratio of 0.2 h and different levels of geothermal capacity. The different plots represent different diesel cases (see Table 2.3): Top left: Diesel Case 1, Top right: Diesel Case 2. Bottom left: Diesel Case 3. Bottom right: Diesel Case 4.

Appendix I

Lead acid ESS simulation results

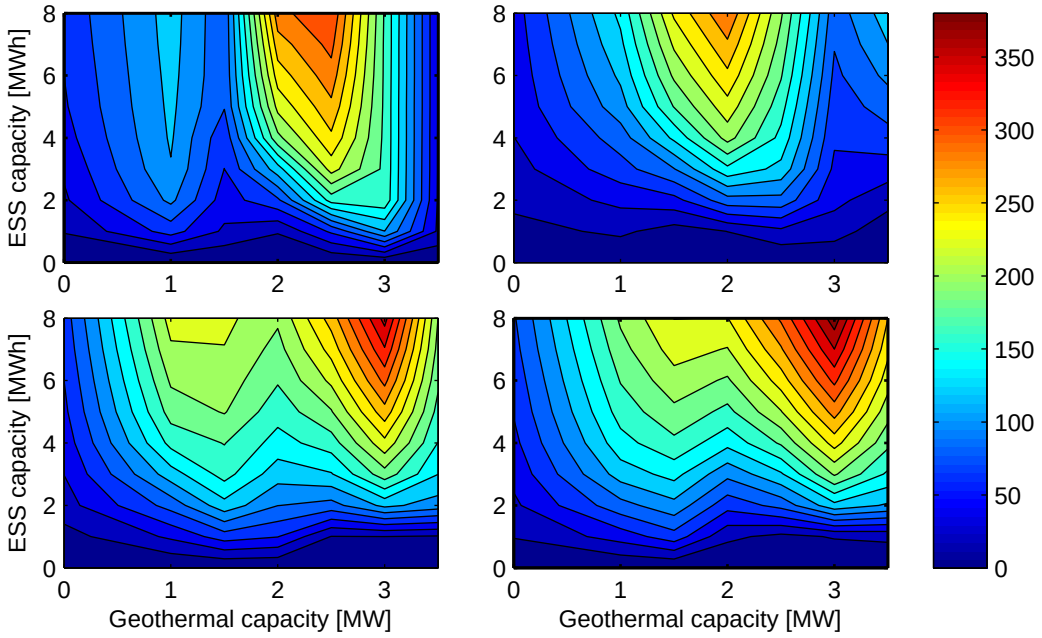


Figure I.1: Displaced diesel generator output [MWh] for different levels of lead acid ESS and geothermal capacity. The different plots represent different diesel cases (see Table 2.3): Top left: Diesel Case 1, Top right: Diesel Case 2. Bottom left: Diesel Case 3. Bottom right: Diesel Case 4.

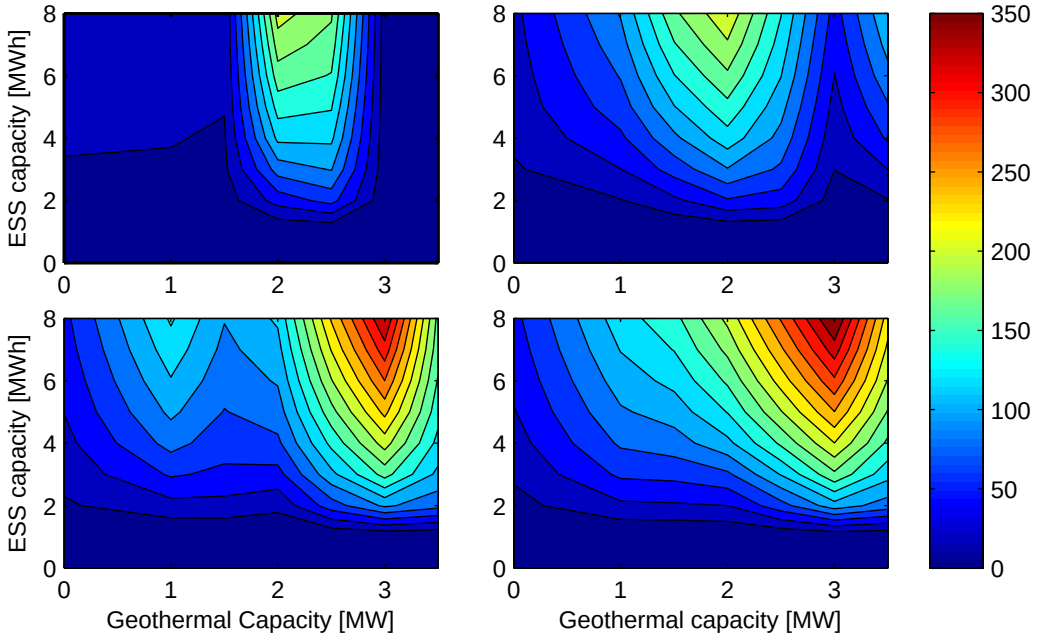


Figure I.2: Yearly ESS discharge [MWh] for different levels of lead acid ESS and geothermal capacity. The different plots represent different diesel cases (see Table 2.3): Top left: Diesel Case 1, Top right: Diesel Case 2. Bottom left: Diesel Case 3. Bottom right: Diesel Case 4.

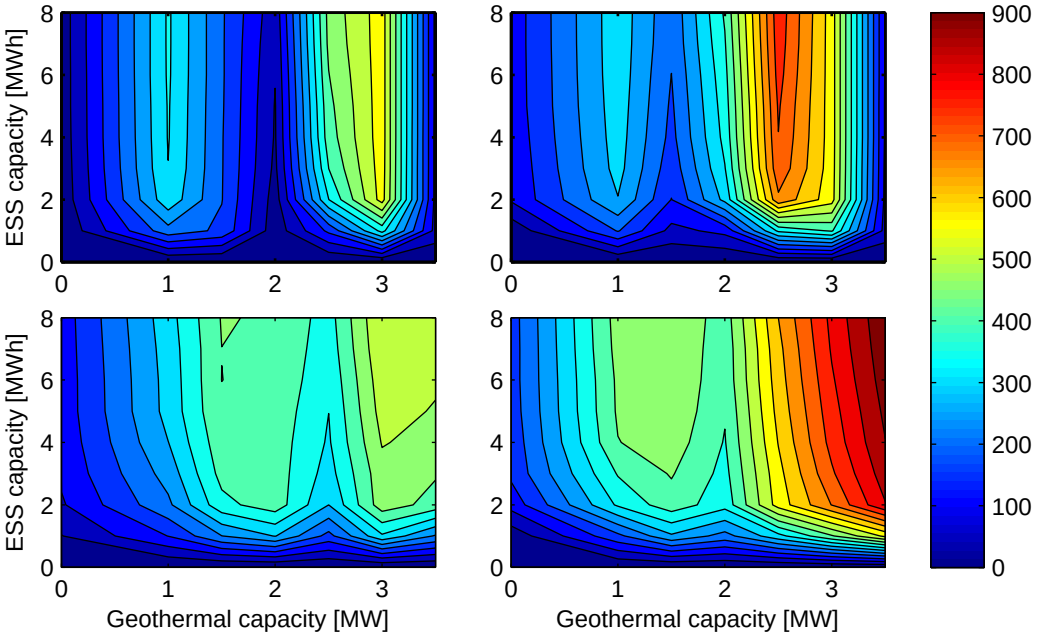


Figure I.3: Decrease in diesel switching for different levels of lead acid ESS and geothermal capacity. The different plots represent different diesel cases (see Table 2.3): Top left: Diesel Case 1, Top right: Diesel Case 2. Bottom left: Diesel Case 3. Bottom right: Diesel Case 4.

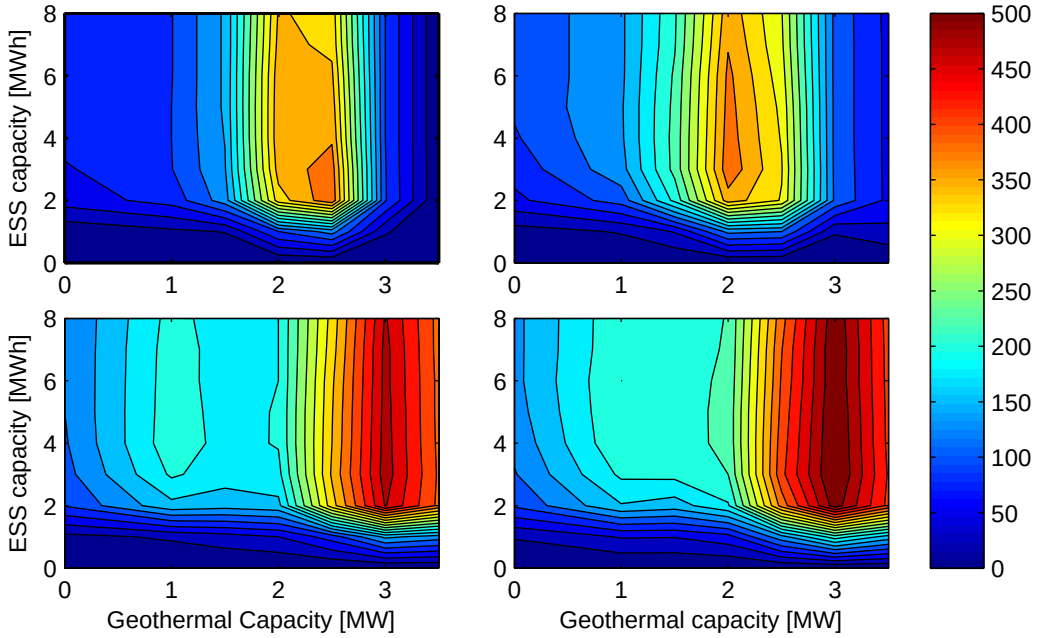


Figure I.4: Yearly ESS cycles for different levels of lead acid ESS and geothermal capacity. The different plots represent different diesel cases (see Table 2.3): Top left: Diesel Case 1, Top right: Diesel Case 2. Bottom left: Diesel Case 3. Bottom right: Diesel Case 4.

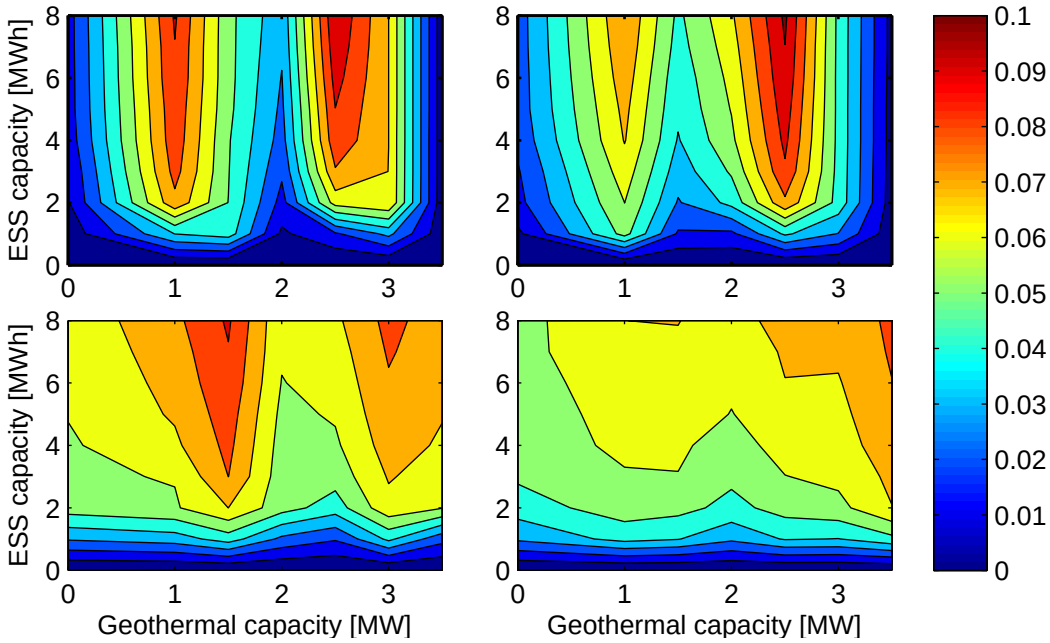


Figure I.5: Increase in average loading for different levels of lead acid ESS and geothermal capacity. The different plots represent different diesel cases (see Table 2.3): Top left: Diesel Case 1, Top right: Diesel Case 2. Bottom left: Diesel Case 3. Bottom right: Diesel Case 4.

Appendix Q
Fuel Oil Volatility – Complications for Evaluating A Proposed Power Purchase Agreement for Renewable Energy in Nome, AK

Fuel Oil Volatility – Complications for Evaluating A Proposed Power Purchase Agreement for Renewable Energy in Nome, AK

Antony G Scott (agscott@alaska.edu)
Alaska Center for Energy and Power, University of Alaska Fairbanks
Fairbanks, AK, USA

Abstract

Private development of a geothermal project to bring electric power to Nome, AK, will require a power purchase agreement between the developer and local utility. Small loads and difficult logistics increase fuel costs for the existing diesel based system, suggesting potential economic benefit from geothermal power. But tools for evaluating future diesel prices in remote, rural markets are sparse – in large part because only 1-3 deliveries determine diesel prices for the year. This paper leverages standard tools to help clarify consequences for Nome citizens of replacing a portion of their stochasticly diesel-based power with stable-priced geothermal energy. It finds that accounting for the unusual nature of episodic fuel deliveries significantly adds to normal annual fuel-oil volatility.

Keywords: Renewable energy; power purchase contracts; economic evaluation; diesel prices; risk; microgrids.

Introduction

While government or donor resources are often stretched, private capital resources for investment in renewable energy systems are vast and their deployment increasing. But many factors inhibit commercial diffusion of renewable technologies to remote rural communities. High counterparty risk, and inadequate commercial prizes given transaction costs can be disincentives to would-be suppliers of wholesale renewable electricity. In remote roadless regions that currently rely on diesel fuel, another factor may be important for would-be power purchasers: the complexity of evaluating the comparative economics associated with a proposed renewable energy "deal".

Electricity costs in remote Alaskan communities are driven by poor economies of scale and difficult logistics. Community grids are islanded and serve small loads. Lack of roads significantly increases costs of diesel fuel delivery, upon which baseload electricity generally depends. Barged fuel delivery may occur only a few times during the summer ice-free season, increasing price volatility. In Nome, AK, the fuel portion of electricity costs last year exceeded $0.22/kWh, with total costs of $0.55/kWh. Such conditions would appear to enable renewable energy to cost effectively displace diesel fuel.

The Pilgrim Hot Springs geothermal resource lies 60 miles from Nome. Down-hold resource assessment began in 1979; sporadic but substantial efforts since that have reduced geological uncertainty (Holdmann et al, 2013). Commercial development would require new-build construction of single-purpose transmission to from the site to Nome, making up roughly three-fourths of the project's $40 million in capital costs. While the costs create scale potentially sufficient to render the investment attractive to an investor, it also shifts project economics from slam-dunk to close thing.

The Nome Joint Utility System (NJUS) and a private investor have been engaged for the last year in negotiating a long-term take-or-pay power purchase agreement. The contract might enable development of Pilgrim Hot Springs. The range for discussions appears to be $.22-$.25/kWh, subject to annual escalation (Doogan, 2013).

For the private developer, aside from residual geologic uncertainty, a contract substantially shields it from business risks outside its control. As well, the developer enjoys risk mitigation associated with having a portfolio of other current and future renewable energy investments.

For Nome the value proposition is more uncertain and more material. The stochastic path of future diesel prices determines whether purchased power "pays off", yet sporadic fuel deliveries add to uncertainty inherent in long-term diesel fuel price forecasts. As well, the size of the geothermal resource is large relative to Nome's annual average (4 MW) and baseload (2.5 MW) demand (Vander Meer and Mueller-Stoffels, 2014). Accordingly, so too might be the "hedging" benefit of replacing volatile diesel with flat-priced geothermal power. In short, a contractual commitment could have potentially broad, rather than marginal, welfare impacts. The relatively high proportion of cash income allocated to energy expenditures compounds the stakes.

Research Objectives

This paper seeks to leverage standard tools to help clarify economic consequences for Nome citizens of entering into a power purchase agreement for geothermal power. Specifically, we:

1) Present a simple method to correlate Nome diesel prices to benchmark crude oil prices that would facilitate assessing future Nome equilibrium prices given availability of public third party crude oil price projections;
2) Describe and simulate the unusual form of price uncertainty engendered by irregular and episodic fuel purchases;
3) Assess representative household welfare impacts of displacing modeled volatile diesel fuel with stable-priced geothermal power.

Methods

Nome's excess generating capacity and slow load growth suggests that contract price should be compared to the existing system's short-run marginal costs. Although roughly 2.7 MW of installed wind capacity complicates assessment, it turns out that geothermal penetration reduces diesel fuel consumption essentially linearly

(Vander Meer and Mueller-Stoffels, 2014). Accordingly, the existing system's marginal costs are reasonably captured by the cost of diesel.[1]

Thinness of market complicates assessment of future diesel prices. The NJUS receives 1-3 barge deliveries of diesel fuel during the ice-free season. This inventory sets diesel costs for the year. Negotiated during the winter, delivered prices typically reflect a 3-day average published indexed product price at the time of refinery lift, plus some negotiated margin to cover expected distributer costs and profit (Bristol Bay Native Association, 2013). At most three distributers compete to supply Nome's need. (Wilson et al, 2008)

The remainder of this section describes methods used to model future Nome diesel price paths given the data.

Price Levels

We use OLS to regress Alaska North Slope West Coast (ANS WC) crude oil spot prices on Nome product prices:

$$Pdiesel_t = \alpha + \beta(Poil)_{\hat{t}} \quad (1)$$

Here $Pdiesel_t$ is the product price per gallon at delivery date t, as recorded by invoices on file with the Regulatory Commission of Alaska; there are 16 observations between 2003 and 2013. $Poil_{\hat{t}}$ is the 3-day moving average ANS WC price per barrel on dates 25 or 35 days prior to t, reflecting respectively average time of transport between refinery lift and delivery to Nome for early and late-summer deliveries (A. Morris, personal communication, 12/17/2013). $Poil_{\hat{t}}$ are calculated from data available from the Alaska Department of Revenue's Tax Division web site (http://tax.alaska.gov/programs/oil/index.aspx).

Crude and product prices are adjusted to 2013 dollars using CPI-U. US DOE projections of annual oil prices are then run through the OLS parameter estimates to obtain equilibrium Nome product price projections. Effective prices paid by consumers reflect 2% uplift for the cost of financing bulk fuel purchases with commercial paper.

Price Volatility

Annual volatility of electricity prices is modeled as a function of diesel fuel volatility. Diesel price volatility is simulated as a linear function of crude prices, conditional on the OLS parameter estimates linking diesel and crude oil prices. Two price volatility components are modeled.

First, we address year-to-year volatility by assuming a mean-reverting Brownian motion process for crude oil prices. ANS WC crude prices are modeled as:

$$d\ln(P_{t+1}) = \eta(\mu - \ln(P_t) - \frac{\sigma^2}{2\eta})dt + \sigma dW_t \quad (2)$$

where P_t and P_{t+1} are prices for time t and time $t+1$, η is the mean-reversion rate, σ is a measure of volatility, μ is the logarithm of mean price to which the process converges, and W_t is a Brownian motion. Following Dixit-Pindyck (1994), we obtain parameter estimates for (2) by using simple regression to estimate its discrete form:

$$\ln(P_{t+1}) - \ln(P_t) = (1 - e^{-\eta\Delta t})\mu - (e^{-\eta\Delta t} - 1)\ln(P_t) + \varepsilon_t \quad (3)$$

That is, we estimate

$$\ln(P_{t+1}) - \ln(P_t) = \alpha + \beta\ln(P_t) + \varepsilon_t \quad (4)$$

to recover

$$\mu = -\frac{\alpha}{\beta} \quad (5)$$

$$\eta = -\ln(1+\beta) \quad (6)$$

$$\sigma = \sigma_\varepsilon \sqrt{\frac{2\ln(1+\beta)}{(1+\beta)^2 - 1}} \quad (7)$$

Parameter estimates are based on annual ANS WC price data for 2003 through 2013. This coincides with the public availability of NJUS invoice data, and broadly captures a period when real oil price levels and movement have substantially departed from prior dynamics.

Second, we address the product price volatility caused by Nome's small number of erratic deliveries within a year. That is, limited sampling from the daily price process – 1-3 realizations per year, taken during the summer – creates additional annual price volatility that is worn by consumers for the entire year. We non-parametrically model this variability as follows.

The 3-day moving average ANS WC crude price path generates an "implied" Nome diesel price path. For each day in a given summer season – May 15 through September 20 (the chronological end-points for product lifts associated with invoiced deliveries) – we calculate the percentage price difference from that year's implied mean diesel price. Aggregating these percentage differences across all years generates a dimensionless distribution of daily differences from annual mean prices.

Household Welfare Effects

Given knowledge of future equilibrium crude oil prices, and of power purchase terms, Nome households' expected present value of displacing diesel with geothermal power could readily be calculated. Lacking knowledge of either, we focus on the degree to which stochastic diesel prices create variability in household electricity expenditures.[2] Risk-averse consumers should value reduced variability that geothermal power could bring. We rely on the foregoing characterization of diesel price volatility to develop measures of associated power cost volatility.

Diesel price movements are translated to household expenditures given data on NJUS fuel consumption and assuming perfectly inelastic electricity demand. (While extreme, estimates of rural Alaska demand lend support towards the assumption of perfect inelasticity. (Villalobos Melendez, 2012) This may be due to extant conservation efforts encouraged by high costs and comparatively low income.) Household expenditures on the diesel portion of NJUS electricity costs are the residential sector share of

[1] While reduced diesel run-time could also reduce generator overhaul and maintenance, interviews with utility management

[2] Experience with making and applying them erodes confidence in the accuracy of any long-term oil price projection. Price volatility however seems an inescapable fact of life (even if its magnitude may not be stationary).

total sales. Data for Nome sector power sales, as well as its annual total diesel fuel consumption, were taken from annual Power Cost Equalization program reports (e.g. Alaska Energy Authority, 2013).

Household diesel expenditure changes are modeled using Monte Carlo simulations of 10,000 trials. Price paths generated by (2) are augmented by multiplicative shocks drawn from the seasonal and refinery lift non-parametric distribution. Central tendencies of household expenditure risk is measured by the coefficients of variation of the present value of expenditures over the course of Nome's contractual obligation (e.g., 20 years), and of expenditures within a single (year 3) year. The first measure incorporates information on the full expenditure time path; the second better indicates the magnitude of the shocks that a household must manage in any given year.

Results

The model, (1), linking Nome diesel prices to crude oil prices yields statistically significant parameter estimates but leaves unexplained much of the diesel price variation.

Table 1: Diesel Price Model

Parameter	Coeff	T statistic
Intercept	1.30	2.33
Poil	.0206	3.39
		R square = .47

The parameter estimates enable translation of US Energy Information Administration's (EIA) projections of crude oil prices into Nome's equilibrium diesel prices and, given generator efficiency, costs per kWh. (Figure 1) EIA brackets their "reference" projection with high and low price scenarios. (EIA, 2013)

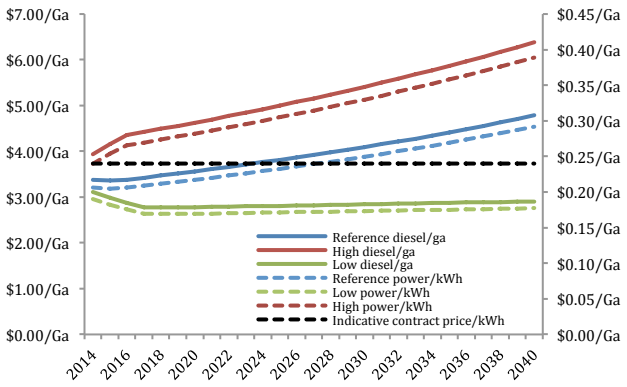


Figure 1: Implied real equilibrium Nome diesel prices and kWh costs given EIA oil price projections, with indicative power purchase price/kWh as reference.

The non-linear estimate of (5) suggests a long-run equilibrium oil price of $99.62/Bbl, which translates (via estimates in Table 1) to an equilibrium diesel price of $3.36/gallon. This is somewhat below EIA's reference case, but appears to lie within a credible range (Figure 1). Together with the estimated mean-reversion (.447) and volatility (19.51%) estimates the model generates sample price paths that broadly capture price dynamics that reasonably resemble the recent past.

The distribution of percentage "shocks" associated with seasonal variation and episodic refinery lift dates is both fat-tailed and skewed. (Figure 2)

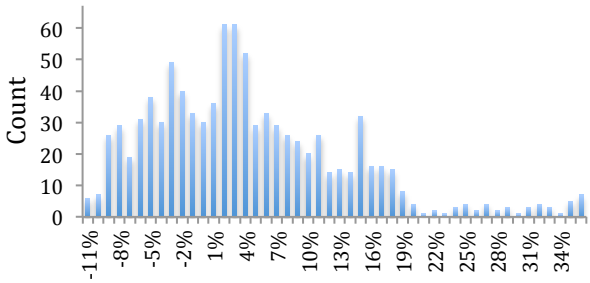


Figure 2: Truncated histogram (2%, 98%); Summer 3-day moving average ANS WC percentage price differences from yearly means, 2003-2013.

Incorporating such shocks into the annual stochastic price paths generated by (2) increases apparent volatility of modeled diesel prices. (Figure 3)

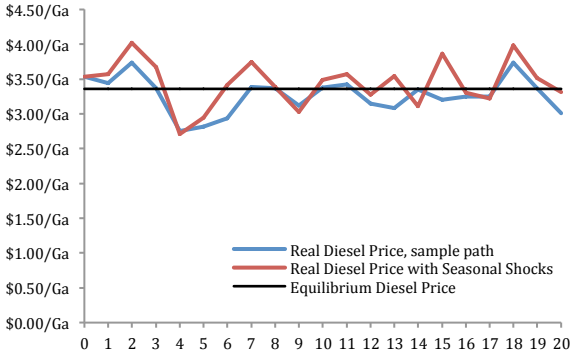


Figure 3: Sample Monte Carlo paths showing annual mean-reversion Brownian motion, and effect of seasonal and lift-date shocks, on modeled diesel prices.

The seasonal, episodic lift-date shocks affect household expenditure uncertainty. If 2 MWe of geothermal power were connected into the Nome grid, the average household would have to pay for roughly half of the approximately 367 gallons of diesel now annually consumed. At a 4% discount rate the expected present worth of displaced fuel rises from $10,730 to $11,013 if seasonal-lift shocks are considered; the coefficient of variation (CV) of expenditure present worth rises from 4.56% to 4.84% – a 6% relative increase.[3]

The CV of household expenditures in a given year is significantly greater than for the present worth of 20 years of expenditures. This is owing to the non-linear telescoping effect of discounting on future-year expenditure differences. The price process (2) generates a CV of 11.77% – more than double the full-path figure. Adding seasonal and lift date variability further increases

[3] The CV was essentially unchanged when calculated at discount rates of 2% and 6%.

the CV to 13.47% – an increase of 14%. The standard deviation of yearly household expenditures in this latter case exceeds $86, and the difference between P98 and median expenditure levels exceeds $217. (Figure 4)

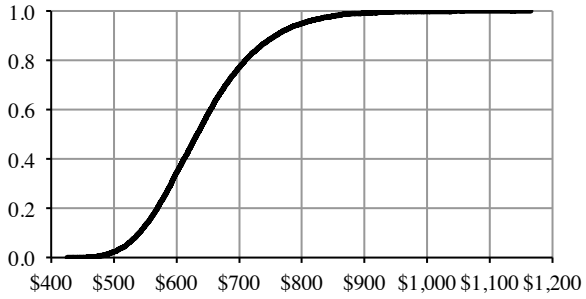


Figure 4: Cumulative probability function of single-year representative household expenditures for diesel fuel that would be displaced by 2 MWe of geothermal power

The cost of diesel volatility is linear in the quantity of fuel displaced. It is therefore worth noting that the reported measure of household responsibility for displaced diesel fuel – 184 gallons – is a lower bound, conditional on 2 MWe of geothermal power. If local residents are ultimately responsible for the cost of electricity used in community or local government facilities, then average household cost responsibility might be as much as 310 gallons.

Discussion

A linch-pin of this work's precision rests in the correlation of limited Nome diesel-price data with ANS WC crude oil prices. Unfortunately, the regression explains a substantially smaller portion of diesel price variation than when more and better data are available. The simple specification in (1) typically explains about 95% – almost twice what we find here – of the variation in product prices when correlating several years of daily NY Harbor #2 and marker crude prices (Wilson et al, 2008). This might be due to errors in variables. Fuel invoices to not indicate the precise period between a given delivery and its date of lift, which if known would allow selecting the contractually-correct daily crude prices. Alternatively, a relatively large portion of Nome's diesel prices may reflect negotiated outcomes in imperfectly competitive markets, rather than the distributer's cost.

Even so, the value in this work lies less in prediction than in providing a framework to inform decision makers as to a logically-consistent set of possible stylized outcomes. Since 2003 NJUS managers have experienced only 16 diesel price transactions. The resultant ambiguity makes evaluation of alternatives difficult.

If commodity prices evolved smoothly, Figure 1 might capture the relevant information for Nome decision makers. But one of the more compelling aspects of the potential addition of geothermal power lies in the opportunity to reduce volatility in Nome electricity prices. Characterizing that volatility directly is difficult, but diesel price volatility (Figure 3) has bearing on purchase power contract value. Indeed, reducing diesel expenditure volatility (Figure 4) may be particularly relevant in smaller communities where households have fewer economic opportunities to absorb price shocks. To our knowledge this is the first attempt to quantify diesel price risk in remote places that receive only a few, highly episodic deliveries per year.

More work remains. An obvious extension would be to graft the risk framework developed here to EIA or other structural model projections of oil prices. This would result, in essence, in a model with a "mean"-reversion term that drifts towards the equilibrium projection path.

Even more, research is needed on measuring the value that remote rural residents place on the volatility of diesel price expenditures to which they are exposed. Comparing measures of central tendencies of volatility, especially against median or average incomes, generates results that are underwhelming. A standard deviation in expenditures of $86 seems small, even against the P20 Nome household income of $35,000. But it is one thing to describe the distribution of potential diesel price outcomes in a given year (Figure 4); it is another to understand how residents value that uncertainty.

Acknowledgements

This work was supported in part by the U.S. Department of Energy, Office of Science, Basic Energy Sciences, under Award # *DE-SC0004903.*

References

Alaska Energy Authority. (2013). Statistical Report of the Power Cost Equalization Program, Fiscal Year 2012. Anchorage, AK: Alaska Energy Authority.

Bristol Bay Native Association (2013). Bristol Bay Bulk Fuel: Purchasing Potential and Interest in a Cooperative Buying Program. Fairbanks, AK: Information Insights.

Dixit, A. & R. Pindyck (1994). *Investment Under Uncertainty*. Princeton, NJ: Princeton University Press.

Doogan, Sean. 2013. Geothermal could be key to figuring out Nome's costly power problem. *Alaska Dispatch*. September 23, 2013. Retrieved from http://www.alaskadispatch.com/article/20130923/geothermal-could-be-key-figuring-out-nomes-costly-power-problem

Holdmann, G., D. Benoit, R. Daanan, A. Prakash & C. Haselwimmer (2013). Summary: Pilgrim Geothermal System Conceptual Model. Fairbanks, AK: The University of Alaska Fairbanks.

Vander Meer, J.B. & M. Mueller-Stoffels (2014). Wind-Geothermal-Diesel Hybrid Microgrid Development: A Technical Assessment for Nome, AK. *In review*

Villalobos Melendez, A. (2012). Aligning Electricity Energy Policies in Alaska: Analysis of the Power Cost Equalization and Renewable Energy Fund Programs (Master's thesis). Fairbanks, Alaska: University of Alaska Fairbanks.

Wilson, M., B. Saylor, N. Szymoniak, S. Colt & G. Fay (2008). Components of Delivered Fuel Prices in Alaska. Prepared for the Alaska Energy Authority, Anchorage: University of Alaska Anchorage Institute of Social and Economic Research.

Appendix R
Report Excerpt, High Voltage Direct Current Transmission at Pilgrim Hot Springs



B.4.2 Pilgrim Hot Springs – Nome

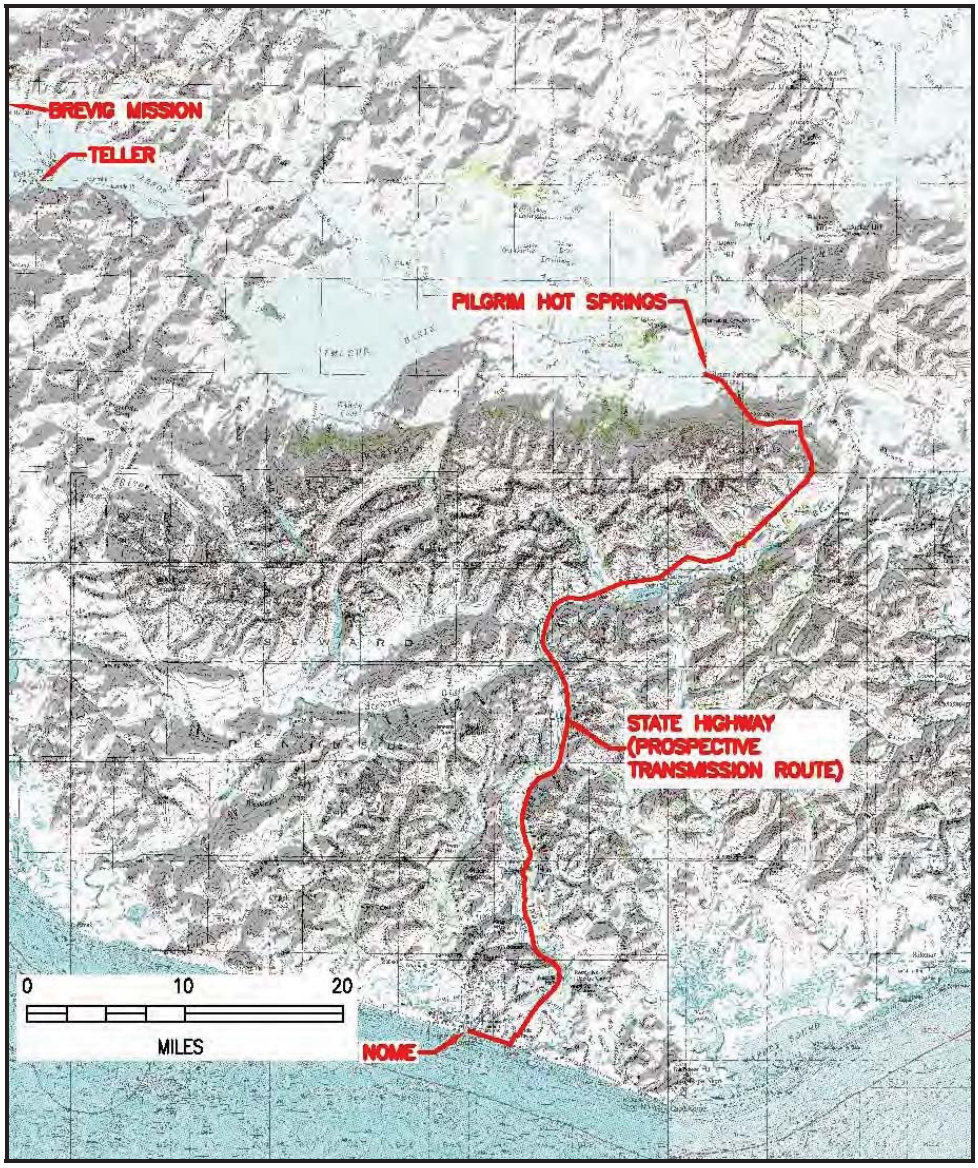
Pilgrim Hot Springs is a geothermal resource located approximately 60 miles north of Nome. It has been proposed as a power source to reduce Nome's reliance on diesel fuel for electrical generation. ACEP is currently studying the Pilgrim Hot Springs geothermal resource to better characterize the resource's potential for power generation and other applications. For purposes of sizing the transmission line from Pilgrim Hot Springs, an electrical generating capacity and transmission capacity of 5 MW is assumed, based on conversations with ACEP's manager for the Pilgrim Hot Springs assessment project.[28] The proposed transmission route is shown on Figure B-4.

A bipolar HVDC circuit using overhead lines was selected for the HVDC intertie. The bipolar configuration was selected because it provides increased reliability compared to a monopolar line at a reasonable additional cost.

Conceptual power line costs for overhead AC and HVDC interties were estimated to evaluate the benefits of connecting Pilgrim Hot Springs to Nome using an HVDC intertie. The cost estimates indicate that an HVDC transmission line would cost 29% less than an AC transmission line.

[28] Personal communication with Marcus Mager, 2012.

Figure B-4 Prospective Transmission Route from Pilgrim Hot Springs to Nome



B.4.2.1 Conceptual Design Basis

A routing study was not performed as part of this case study. The intertie route is assumed to follow the approximately 70-mile road corridor from Nome to Pilgrim Hot Springs. This is assumed to be the least-cost route for the power lines, as the road can be used to support the construction and long-term maintenance of the line. A routing study may identify other routes that are more favorable due to geotechnical, land status, environmental, or other factors.

For this analysis, the transmission route distance is assumed to be 60 miles.



B.4.2.1.1 Load

Nome's average annual electricity usage is approximately 3,500 kW, and monthly peak demand is between 4 and 10 MW. The assumed size of the Pilgrim Hot Springs geothermal power plant is assumed to be 5 MW. The intertie is therefore assumed to have a capacity of 5 MW and operate at between 2 and 5 MW, depending on instantaneous demand in Nome.

B.4.2.1.2 Conceptual AC Intertie Design

The conceptual design for the AC intertie is a three-wire 69-kV AC overhead line set on 45-foot wood poles with a ruling span of 400 feet. All poles are assumed to be fastened to steel pile foundations for moment support and to resist frost jacking forces.

The AC transmission system would consist of the following major components:

- A 5-MW geothermal power plant at Pilgrim Hot Springs generating at 4,160 V.
- A substation and switch yard to increase voltage from 4,160 V to 69 kV.
- An approximately 60-mile-long overhead intertie from Pilgrim Hot Springs to Nome.
- A substation and switchyard in Nome to isolate Nome from the transmission line and step down the voltage from 69 kV to 12.47 kV for distribution in Nome.

B.4.2.1.3 Conceptual HVDC Intertie Design

The conceptual design for the HVDC intertie is a bipolar circuit operating at +50 and –50 kV DC. The two circuits would be supported on a guyed glass-fiber-reinforced polymer (GFRP) pole fitted with a cross arm and suspension insulators. A ruling span of 1,000 feet is assumed. The design is similar to that shown on Figure C-9.

The HVDC transmission system would consist of the following major components:

- A 5-MW geothermal power plant at Pilgrim Hot Springs generating at 480 V. It may be preferable to instead generate at 4,160 V and have a step-down transformer to the 480 V interface voltage to the power converters.
- A bipolar HVDC converter station consisting of two banks of five 500-kW power converters. Each bank would form a 2.5-MW pole on the bipolar transmission system.
- An approximately 60-mile-long bipolar HVDC transmission line from Pilgrim Hot Springs to Nome.
- A second bipolar HVDC converter station in Nome.
- An AC transformer to step up the AC output from the converters from 480 V up to 7.2/12.47 kV for distribution in Nome.



B.4.2.2 Economic Analysis

Table B-5 presents the economic analysis for the Pilgrim Hot Springs – Nome intertie alternatives. The estimated installed cost for the HVDC intertie alternative is $25.7 million, as compared to the cost of $36.3 million for a conventional AC intertie.

No information is available for the installed cost of a geothermal power plant at Pilgrim Hot Springs or the cost of the energy it would generate, so a benefit-cost ratio of the intertie alternatives was not evaluated.

Table B-5 Estimated Installed Cost for a 5-MW Pilgrim Hot Springs – Nome Intertie

Cost Item	Estimated Installed Cost for Bipolar HVDC Intertie	Estimated Installed Cost for AC Intertie	Estimated HVDC Savings	Percent Cost Savings
Preconstruction Activities *(right-of way acquisition, design, survey, permitting)*	$3,400,000	$3,400,000	-	-
Administration/Management	$1,000,000	$1,300,000	-	-
Converter Station Construction	$4,600,000	$3,000,000	-	-
Overhead Intertie Construction	$10,800,000	$20,200,000	-	-
Contingency (30%) [1]	$5,900,000	$8,400,000	-	-
Total Estimated Cost	**$25,700,000**	**$36,300,000**	**$10,600,000**	**29%**

Note:

1. A 30% contingency was applied to the costs for this project because no information was available for the transmission route. This lack of data creates risks due to factors such as land availability, geotechnical conditions, structural (wind and ice) loadings, and environmental (bird, wildlife, and aesthetics) factors.

   Some of these risks are mitigated by the use of cost data for the robust conceptual designs (i.e., Alaska-specific construction) used for the HVDC system. The Alaska-specific conceptual design is assumed to be adequate for the expected geotechnical and structural conditions along the route. Environmental and land availability issues, which could require a longer route or departure from the road corridor, pose relatively greater risks than line design considerations. The net result of these factors results in the 30% contingency used for the case study economics.

Appendix S
Wind-Geothermal-Diesel Hybrid Microgrid Development: A Technical Assessment for Nome, AK

Wind-Geothermal-Diesel Hybrid Microgrid Development: A Technical Assessment for Nome, AK

Jeremy B Vander Meer (jbvandermeer@alaska.edu)
Department of Physics, University of Oldenburg
Oldenburg, Germany

Marc Mueller-Stoffels (mmuellerstoffels@alaska.edu)
Alaska Center for Energy and Power, University of Alaska Fairbanks
Fairbanks, AK, USA

Abstract

This paper investigates the effect of adding a geothermal electric power source to the remote wind-diesel microgrid of Nome, AK. The proposed geothermal source would displace most of the base load and not be able to load follow. A time step simulation was created to model the grid behavior for different levels of geothermal power and additions to the diesel generator fleet. With increased geothermal power input, the diverted[1] wind energy increased quadratically while the diesel generators' displaced output increased linearly, average load factor decreased and switching increased. Adding diesel generators of varying size to the fleet decreased the diverted wind energy, increased the displaced energy and average load factor of diesel generators, but also increased the diesel generator switching.

Keywords: Microgrid; geothermal power; wind power; diesel scheduling.

Introduction

The City of Nome, Alaska, population 3,759, has an average electrical load of about 4 MW and is powered by an islanded wind-diesel grid. Nome has recently increased its nameplate wind power capacity to 2.7 MW. Currently, the potential for electrical low temperature geothermal power (Organic Rankin Cycle) is being explored near Nome. Models suggest that there is potential for 2 MW_e power from this resource. This poses several key questions for Nome: How would adding the geothermal power affect the operation of the grid? What would the added value of the geothermal power be? What grid modifications could help with the integration of geothermal energy by improving grid performance?

Research Objectives

This paper seeks to answer the following questions:

1. How would adding geothermal power and diesel generators affect the operation of the diesel fleet?
2. How much would diesel generator output be reduced?
3. How much wind power would have to be diverted[1]?

Methods

A time step simulation was created to model the Nome grid using two years of grid data in 10 minute intervals. The following sections describe the load, how wind production data was generated from partial data, how the diesel fleet was scheduled and the specifics of the geothermal resource.

Load Characteristics

The measured grid consumption over two years was used in the simulation as the load. The load had a seasonal variation, with an overall average of 4 MW, which rose to around 4.5 MW in January, and dropped to around 3.5 MW in July. The base load was 2.5 MW and peak load was 6 MW.

Estimating Wind Power Available

The City of Nome has two wind farms. Farm A has 18 older 50 kW turbines and Farm B has two 900 kW turbines. There was only 6 months of production data for both wind parks. There was 2 years of grid data during which Farm A was in operation, but measurements were only made at the feeder level. The main load on Farm A's feeder was a mothballed mine and found to be relatively constant. Thus a calculated constant load was subtracted to obtain an approximation for Farm A's output. The approximation was then compared with the 6 months of actual measured wind park outputs to obtain a correlation between the two. In addition, measured wind speeds from nearby met towers and theoretical power curves were used to validate the model of wind power output. The resulting estimated power outputs for Farm A and B had the same average output as the actual outputs, with correlation coefficients of 93% and 71% respectively. The estimates were then applied to the 2 years of grid data to obtain an approximation for what the wind farm outputs would have been during those 2 years.

Diesel Fleet Scheduling

The current grid has 1.9, 3.7, and two 5.2 MW diesel generators. There is a 0.4 MW generator that could be brought online in the future. Different combinations of these generators, along with a hypothetical 1 MW diesel generator, were simulated.

The following operating bounds were placed on the diesel generators in the simulation:

1. Minimum operating time (MOT): Each diesel generator has a minimum amount of time it must run before it can be switched off.

[1] Diverted is to be understood as supplying managed loads, or curtailment of wind turbine output. Electric boilers are used in Nome and generating heat is of significant economic value, but is not addressed as part of this study.

2. Warm up/cool off: Each diesel generator must run a certain amount of time before coming online and after going offline.
3. Minimum optimal loading (MOL): Each diesel generator has a size dependent minimum power output below which it should not be operated.
4. Spinning reserve capacity (SRC): A set amount of online diesel generator capacity must remain available to handle a sudden increase in load.
5. Cover wind production: In addition to the required SRC, there must be online available diesel generator capacity equal to the wind production that is supplying unmanaged loads. This would allow the grid to handle a sudden drop in wind production.

These operating bounds were set to model the current grid operation and are fairly conservative. While more advanced control schemes involving a dynamic relationship between the SRC and covering wind production (Chen, 2008), demand response and energy storage (Lu et al., 2011) are possible, for this simulation it was important to obtain results that are directly applicable to the current grid setup.

When scheduling the diesel generators, the combination with the lowest combined MOL that met the above requirements was chosen. This allowed for a maximum import of wind power into the grid and for the diesel generators to operate with a higher load factor (Katiraei & Abbey, 2007). More complex scheduling algorithms are possible that minimize operating costs but require more operating and cost information about the grid and generating units than was available at Nome (Logenthiran & Srinivasan, 2009)(Cecati, Citro, Piccolo, & Siano, 2011).

Geothermal Resource Integration

Preliminary drilling and models suggest that there is a 2 MW_e potential geothermal resource near Nome (Miller, McIntyre & Holdmann, 2014). If developed, this power source is not expected to be able to load follow and will have a seasonal variation due to a reduced temperature differential during the summer months. The seasonal variation was modelled as being the nameplate capacity from October to April, 92% capacity in May and September, 83% capacity in June and August and 75% capacity in July. Geothermal power production cannot be curtailed quickly, unlike wind power, and the grid must accept whatever is produced. Although there is a potential of 2 MW_e, outputs ranging from 0 to 5.5 MW_e were simulated to understand underlying principles that may govern this type of hybrid system.

Results

The results of the simulation of adding geothermal power to Nome's grid are presented in this section. First, the effect on the operation of the diesel generators is discussed and then the displaced diesel generator energy and diverted wind energy.

Diesel Generator Operation

Four different groupings of diesel generators were simulated, as listed in Table 1.

Table 1: Groupings of diesel generators; Case 1 is the base (current) case.

Case #	Available Diesel Generator Capacities [MW]	Marker-style on plots
1	5.2, 5.2, 3.7, 1.9	circle
2	5.2, 5.2, 3.7, 1.9, 0.4	square
3	5.2, 5.2, 3.7, 1.9, 1	diamond
4	5.2, 5.2, 3.7, 1.9, 1, 0.4	cross

Figure 1 shows the average diesel generator load factor for the different levels of geothermal input to the grid. The different lines represent the different combinations of available diesel generators, as outlined in Table 1.

Four main observations can be made:

1. By adding smaller diesel generators to the fleet, the average diesel load factor at a given geothermal power increases, as the online capacity can be better matched to the load. In this case, adding a 1 MW generator generally results in a higher load factor than a 0.4 MW, since it allows a more even step size between generator combination capacities. In general, a higher load factor results in increased efficiency and optimal operation for diesel generators.
2. At very high geothermal power output, the diesel generator load factor bottoms out at the MOL of the smallest generator, which also means that all wind power is diverted.
3. There are distinct maxima in the slope of the line for Case 1 (blue) around 0, 1.5 and 3 MW geothermal output. These represent scenarios at which there is one predominant diesel generator combination online, since the average diesel generator output falls in the middle of its operating range. The local minimum in the curve between these peaks represent scenarios switching between predominant online generator combinations. With added diesel generators, the local minimum is removed, as there is less of a difference between the capacities of possible diesel generator combinations. Again, adding a 1 MW generator improves performance more than the 0.4 MW, since it allows for a more even step size between generator combination capacities.
4. Diesel generator switching increases with geothermal power output and with a larger diesel generator fleet (see Figure 2). The smaller diesel generators tend to switch more often than the larger ones. Increased switching consumes diesel and can increase the stress on the diesel generators. Changes to the generator scheduling can reduce the switching, but would also reduce the positive effects listed in the previous points.

In summary, adding smaller capacity diesel generators to the fleet increased the average diesel generator load factor and allowed a more constant change in the load factor for changes in geothermal power output. Also, adding diesel generators which allow for a more constant step size between generator combination capacities increased both these results. In general, the amount of diesel generator switching increased with an increase in the number of available diesel generators and geothermal power output.

While operating at a higher load factor generally results in a higher efficiency and optimal operation for diesel generators, switching consumes diesel and can increase the stress on the diesel generators.

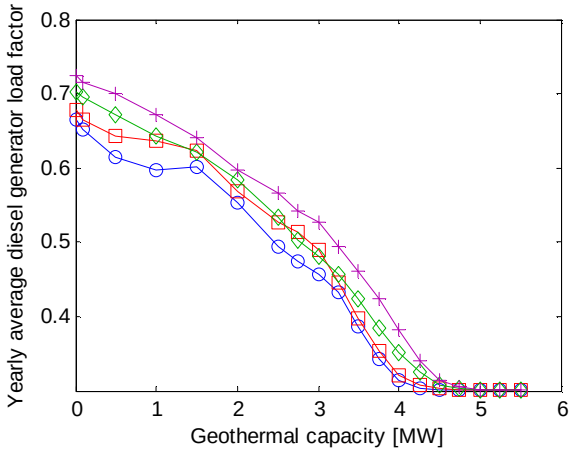


Figure 1: Average diesel generator load factor for different diesel generator scenarios (see Table 1).

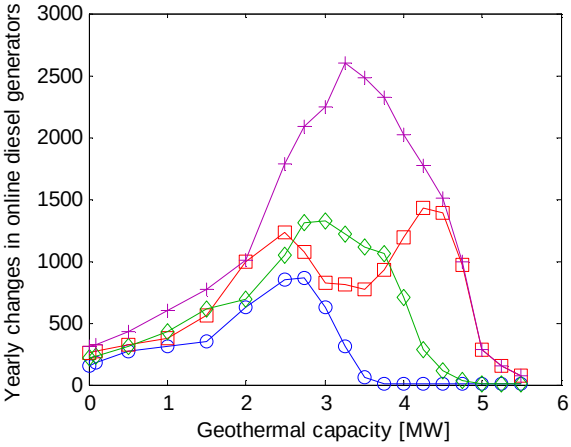


Figure 2: Number of changes of online diesel generator combinations per year for different diesel generator scenarios (see Table 1).

Wind Energy Diversion and Displaced Diesel Output

This section investigates the relationship between increased diverted wind energy and saved diesel generator output for increased geothermal power output. Discussion is limited to results of geothermal capacity less than the base load. Exceeding base load leads to diversion of significant amounts of geothermal energy.

An energy balance shows the relationship between diesel generator output (E_{DEG}), wind energy (E_{WTG}), diverted wind energy (E_{div}), the load (E_{load}) and average geothermal power production ($\tilde{P}_{GTG}$) per year (8760 h):

$$E_{DEG} + E_{WTG} + 8760\ h \cdot \tilde{P}_{GTG} = E_{load} + E_{div} \quad (1)$$

Changing the value of $\tilde{P}_{GTG}$ changes the energy balance. The change in the energy balance is shown by Equation 2. E_{load} and E_{WTG} are not affected by a change in $\tilde{P}_{GTG}$ and thus cancel out.

$$\Delta E_{DEG} + 8760\ h \cdot \Delta\tilde{P}_{GTG} = \Delta E_{div} \quad (2)$$

If the base case scenario had no geothermal production, then $\tilde{P}_{GTG_0} = 0$ MW and $\Delta\tilde{P}_{GTG} = \tilde{P}_{GTG}$. Displaced diesel generator output resulting from adding geothermal production equals a negative change in diesel generator output; $E_{disp} = -\Delta E_{DEG}$. Equation 3 results from substituting these definitions into Equation 2:

$$E_{disp} + \Delta E_{div} = 8760 * \tilde{P}_{GTG} \quad (3)$$

Based on Equation 3, the total displaced diesel generator energy and the increase in wind energy diversion should add up to a linear line with a slope of 8760 h as a function of average geothermal power for different fleet cases.

Several key simulation results follow:

1. Geothermal outputs above the maximum displaceable base load (base load – MOL of the smallest diesel generator) either need to be diverted at times or be able to load follow. Load following capabilities would significantly change the outcome of this study, with 100% diesel displacement being possible at times.
2. A second order polynomial fits the relationship between increasing wind energy diversion and increasing average geothermal output well (see Figure 3). Adding smaller diesel generators to the fleet lowers the slope of the curve, resulting in less diverted wind energy. Again, adding a 1 MW diesel generator (case 3) performs better than adding the 0.4 MW diesel generator (case 2).
3. The displaced diesel generator output has an equal and opposite quadratic component to the diverted wind, but is predominantly linear (see Figure 4). The quadratic and linear coefficients for wind diversion and displaced diesel generator output can be seen in Table 2. The quadratic coefficients cancel out and the linear coefficients add up to roughly 8760 h.
4. The displaced diesel generator output is predominantly linear, with approximate slopes shown in Figure 4. Thus, with the diesel generator fleet in case 1, the annually displaced diesel generator output will increase with a slope of 8060 h per MW of average geothermal power input to the grid.

In summary, the annual displaced diesel generator output and diverted wind energy, as functions of added geothermal power, add up to a linear line with a slope of 8760 h. Less wind energy is diverted with a larger number of diesel generators of varying size, which means more diesel generator energy is displaced. The diverted wind energy has a significant quadratic component, while the displaced diesel generator energy is predominantly linear.

Table 2: Diverted wind and displaced diesel vs average geothermal power output curve coefficients.

Case #	Diverted wind coefficients		Displaced diesel coefficients	
	X^2	X	X^2	X
1	2.2e2	1.9 e2	-2.2e2	8.6e3
2	1.5e2	2.2e2	-1.5e2	8.5e3
3	1.9e2	-5.1	-1.9e2	8.7e3
4	2.3e2	-1.2e2	-2.3e2	8.9e3

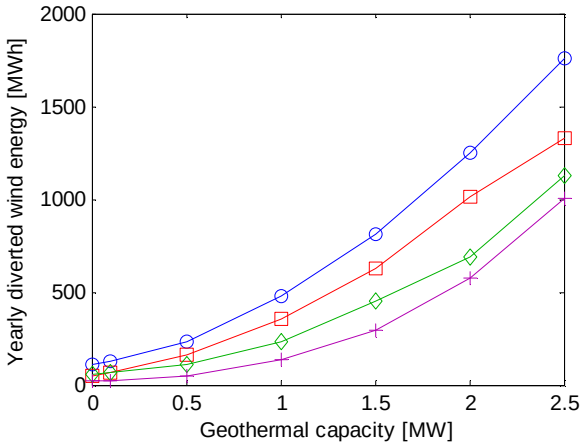


Figure 3: Annual wind electrical energy diversion for different diesel generator scenarios (see Table 1).

Discussion

The effects of adding geothermal power to the operation of the wind-diesel grid at Nome have been summarized for the current grid setup and for possible upgrades to the diesel generator fleet. These results can be used to help determine the value of adding geothermal power and diesel generators to the grid.

The slopes of the displaced diesel generator energy and diverted wind energy as functions of added geothermal power add up to a linear line with a slope of 8760 h. The diverted wind energy was found to have a quadratic increase. Due to a predominant linear term, the displaced diesel generator energy could be approximated as a linear increase.

The diesel generators' average load factor was found to decrease and switching to increase for added geothermal power to the grid. Adding to the diesel generator fleet to create smaller, more constant, differences between the combined capacities of diesel generator combinations resulted in less diverted wind energy, more displaced diesel generator energy, a higher diesel generator load factor and more diesel generator switching.

Thus, when determining the value of adding geothermal power to the grid, the decrease in diesel generator performance due to increased switching and decreased load factor needs to be considered. Similarly, when determining the value of adding diesel generators to the fleet, the advantages will have to be weighed against the increase in switching.

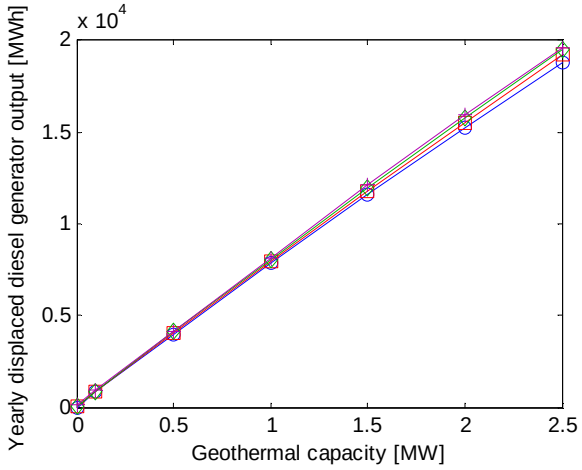


Figure 4: Displaced diesel generator output for different diesel generator scenarios (see Table 1). The slope of Case1 is 8060 h, Case2 is 8200 h, Case3 is 8320 h and Case4 is 8360 h.

Acknowledgements

MMS is supported by the U.S. Department of Energy, Office of Science, Basic Energy Sciences, under Award # *DE-SC0004903*. JBV is supported by the U.S. Department of Energy, Office of Energy Efficiency & Renewable Energy, Geothermal Technologies Office under Award # *DE-EE0002846*.

References

Cecati, C., Citro, C., Piccolo, a., & Siano, P. (2011). Smart Operation of Wind Turbines and Diesel Generators According to Economic Criteria. *IEEE Transactions on Industrial Electronics*, *58*(10), 4514–4525. doi:10.1109/TIE.2011.2106100

Chen, C.-L. (2008). Optimal Wind–Thermal Generating Unit Commitment. *IEEE Transactions on Energy Conversion*, *23*(1), 273–280. doi:10.1109/TEC.2007.914188

Katiraei, F. & Abbey, C. (2007). Diesel Plant Sizing and Performance Analysis of a Remote Wind-Diesel Microgrid, 1–8.

Logenthiran, T., & Srinivasan, D. (2009). Short term generation scheduling of a Microgrid. *TENCON 2009 - 2009 IEEE Region 10 Conference*, 1–6. doi:10.1109/TENCON.2009.5396184

Lu, S., Elizondo, M. a., Samaan, N., Kalsi, K., Mayhorn, E., Diao, R., … Zhang, Y. (2011). Control strategies for distributed energy resources to maximize the use of wind power in rural microgrids. *2011 IEEE Power and Energy Society General Meeting*, 1–8. doi:10.1109/PES.2011.6039787

Miller, L., Mcintyre, H., Holdmann, G. (2014). Small Scale Distributed Geothermal Applications for Islanded Microgrids. *To be submitted MES2014*